

# Handbook on the Physics and Chemistry of Rare Earths, volume 32

Elsevier, 2001

Edited by: Karl A. Gschneidner, Jr., LeRoy Eyring and Gerry H. Lander  
ISBN: 978-0-444-50762-4

## PREFACE

Karl A. GSCHNEIDNER, Jr., LeRoy EYRING, and  
Gerry H. LANDER

---

*These elements perplex us in our rearches [sic], baffle us in our speculations, and haunt us in our very dreams. They stretch like an unknown sea before us – mocking, mystifying, and murmuring strange revelations and possibilities.*

Sir William Crookes (February 16, 1887)

---

This volume of the Handbook covers a variety of topics with three chapters dealing with a range of lanthanide magnetic materials, and three individual chapters concerning equiatomic ternary ytterbium intermetallic compounds, rare-earth polysulfides, and lanthanide organic complexes. Two of the chapters (206 and 210) also include information on the actinides and the comparative lanthanide/actinide behaviors.

The lead chapter by N.H. Duc deals with giant magnetostrictions in lanthanide (Sm, Tb, and Dy)–transition metal (Fe and Co) thin films. Magnetostrictions (changes in the dimensions of a solid) arise in magnetically ordered substances when they are subjected to a change in the magnetic field. Magnetostrictions can also occur when the magnetic state of the solid is changed by a temperature or pressure variation. Magnetostrictive thin films are particularly promising for use as microactuator elements, such as cantilevers or membranes, since they combine a high energy output at high operating frequencies, and also offer the possibility of remote control operation. In his review Duc covers lanthanide–iron thin films, including Terfenol-related compositions  $[(\text{Tb}_{1-x}\text{Dy}_x)\text{Fe}_2]$ ; lanthanide–cobalt films; giant magnetostrictive spring magnet type multilayers (materials which combine giant magnetostrictions with soft-magnetic properties); and lanthanide–transition-metal sandwich films.

G.M. Kalvius, D.R. Noakes and O. Hartmann in a detailed and comprehensive review treat muon spin resonance ( $\mu\text{SR}$ ) spectroscopy of both lanthanide and actinide materials. As the authors point out,  $\mu\text{SR}$  spectroscopy is a useful technique which complements other, more commonly used experimental methods (such as, magnetic susceptibility, magnetization, NMR and neutron scattering) for studying lanthanide and actinide materials. They note that the muon: (1) is quite sensitive to small variations in spin structures and these measurements have shown that even in small “well established” systems, the magnetic structure is not fully understood; (2) is a highly local probe and thus is well suited for detecting and studying short-range-order magnetism; and

(3) samples the entire volume of the specimen and thus is useful in studying systems which simultaneously exhibit more than one cooperative state, e.g. the coexistence of superconductivity and magnetic order. Also,  $\mu$ SR spectroscopy has a high sensitivity to a small magnetic moment, which is important in studying Kondo lattices and heavy-fermion systems; and possesses a unique time window for spin-dynamical processes. In this chapter the authors cover the pure elements, various simple and complex intermetallic compounds, non-metallic compounds, superconductors (including the high- $T_c$  cuprates), disordered magnetism, and correlated electron systems.

R. Pöttgen, D. Johrendt and D. Kussmann cover the structure–property relationships of ternary equiatomic  $\text{Yb}TX$  intermetallic compounds, where  $T$  is a transition metal and  $X$  is a third or fourth main group element. These authors review the synthesis, crystal chemistry and bonding, various physical properties (magnetism, electrical resistivity, and heat capacity), and spectroscopic data ( $L_{\text{III}}$  spectra and Mössbauer) of the  $\text{Yb}TX$  compounds. These compounds are of interest because ytterbium can be divalent, trivalent, or mixed-valent, which can lead to heavy-fermion and Kondo-like behaviors. The bonding in the  $\text{Tb}TX$  compounds is governed by strong  $T$ – $X$  covalent interactions within the polyanions rather than ionic  $\text{Yb}$ – $T$  or  $\text{Yb}$ – $X$  bonds. Some of the more unusual  $\text{Yb}TX$  compounds are ferromagnetic  $\text{YbNiSn}$ , intermediate-valent  $\text{YbCuAl}$  and the heavy-fermion compound  $\text{YbPtBi}$  with an extremely large effective electronic mass.

K. Kobayashi and S. Hirosawa discuss rare-earth permanent magnets [ $\text{SmCo}_5$ ,  $\text{Sm}_2\text{Co}_{17}$ ,  $\text{Nd}_2\text{Fe}_{14}\text{B}$ ,  $\text{Sm}_2\text{Fe}_{17}\text{X}_3$  (where  $X = \text{N}$  or  $\text{C}$ ) and  $\text{Nd}(\text{Fe},\text{Ti})_{12}\text{N}$ ], reviewing the fundamentals involved and commenting on the state-of-the-art. Included in their discussions are sintered magnets, the HDDR (hydrogenation, disproportionation, desorption, recombination) process for preparing some of these materials, nanocomposite permanent magnets prepared by rapid solidification and mechanical alloying, and exchange-coupled (or spring) magnets. They also review the coercivity and corrosion of these materials, especially  $\text{Nd}_2\text{Fe}_{14}\text{B}$ , and discuss the relationship between the two properties.

I.G. Vasilyeva reviews polysulfides, i.e. compounds which have more sulfur atoms than the ideal ionic  $\text{R}_2\text{S}_3$  composition ( $>66.6$  at.% S). The polysulfides are grouped into three classes: the hypostoichiometric  $\text{RS}_{2-x}$  phases, the stoichiometric  $\text{RS}_{2.0}$  disulfides, and the hyperstoichiometric phases. The author gives a brief history of these materials, which have been known for about 90 years, and then discusses their occurrence, preparative methods, crystal growth, phase equilibria, structural properties, thermodynamic properties, chemical bond and electronic structures, and finally their physical properties (electrical, magnetic and optical). Although these polysulfides have not yet generated practical applications, their scientific interest remains large.

D.K.P. Ng, J. Jiang, K. Kasuga and K. Machida conclude this volume with an overview of rare-earth and actinide half-sandwich tetrapyrrole complexes. When tetrapyrrole molecules, such as porphyrins or phthalocyanines, are reacted with the rare earths and actinides, they are split in half, forming the half-sandwich complexes because the metal atoms are larger than the core size of the macrocyclic ligands. They also can form sandwich-type complexes in which the metal centers are sandwiched between the macrocycles. However, this chapter is devoted to the former class of compounds. Ng and co-workers discuss the synthesis, structure, and spectroscopic and electrochemical properties of half-sandwich complexes of porphyrins and phthalocyanines. The authors

note that these complexes are potentially useful as biological probes for biomolecules, imaging agents, and photosensitizers in photodynamic therapy.

With this volume of the Handbook Prof. LeRoy Eyring is retiring as a co-editor. The editorial duties of future issues of the Handbook will continue to be handled by the senior editor (Karl A. Gschneidner, Jr.) with the assistance of two new editors: Prof. Jean-Claude Bünzli, Swiss Federal Institute of Technology, Lausanne, and Prof Vitalij K. Pecharsky, Iowa State University.

## CONTENTS

Preface v

Contents vii

Contents of Volumes 1–31 ix

205. N.H. Duc  
*Giant magnetostriction in lanthanide–transition metal thin films* 1
206. G.M. Kalvius, D.R. Noakes and O. Hartmann  
*μSR studies of rare-earth and actinide magnetic materials* 55
207. Rainer Pöttgen, Dirk Johrendt and Dirk Kußmann  
*Structure–property relations of ternary equiatomic YbTX intermetallics* 453
208. Kurima Kobayashi and Satoshi Hirosawa  
*Permanent magnets* 515
209. I.G. Vasilyeva  
*Polysulfides* 567
210. Dennis K.P. Ng, Jianzhuang Jiang, Kuninobu Kasuga and Kenichi Machida  
*Half-sandwich tetrapyrrole complexes of rare earths and actinides* 611
- Author index* 655
- Subject index* 733

## CONTENTS OF VOLUMES 1–31

### VOLUME 1: Metals

1978, 1st repr. 1982, 2nd repr. 1991; ISBN 0-444-85020-1

1. Z.B. Goldschmidt, *Atomic properties (free atom)* 1
  2. B.J. Beaudry and K.A. Gschneidner Jr, *Preparation and basic properties of the rare earth metals* 173
  3. S.H. Liu, *Electronic structure of rare earth metals* 233
  4. D.C. Koskenmaki and K.A. Gschneidner Jr, *Cerium* 337
  5. L.J. Sundström, *Low temperature heat capacity of the rare earth metals* 379
  6. K.A. McEwen, *Magnetic and transport properties of the rare earths* 411
  7. S.K. Sinha, *Magnetic structures and inelastic neutron scattering: metals, alloys and compounds* 489
  8. T.E. Scott, *Elastic and mechanical properties* 591
  9. A. Jayaraman, *High pressure studies: metals, alloys and compounds* 707
  10. C. Probst and J. Wittig, *Superconductivity: metals, alloys and compounds* 749
  11. M.B. Maple, L.E. DeLong and B.C. Sales, *Kondo effect: alloys and compounds* 797
  12. M.P. Dariel, *Diffusion in rare earth metals* 847
- Subject index 877

### VOLUME 2: Alloys and intermetallics

1979, 1st repr. 1982, 2nd repr. 1991; ISBN 0-444-85021-X

13. A. Iandelli and A. Palenzona, *Crystal chemistry of intermetallic compounds* 1
  14. H.R. Kirchmayr and C.A. Poldy, *Magnetic properties of intermetallic compounds of rare earth metals* 55
  15. A.E. Clark, *Magnetostrictive RFe<sub>2</sub> intermetallic compounds* 231
  16. J.J. Rhyne, *Amorphous magnetic rare earth alloys* 259
  17. P. Fulde, *Crystal fields* 295
  18. R.G. Barnes, *NMR, EPR and Mössbauer effect: metals, alloys and compounds* 387
  19. P. Wachter, *Europium chalcogenides: EuO, EuS, EuSe and EuTe* 507
  20. A. Jayaraman, *Valence changes in compounds* 575
- Subject index 613

### VOLUME 3: Non-metallic compounds – I

1979, 1st repr. 1984; ISBN 0-444-85215-8

21. L.A. Haskin and T.P. Paster, *Geochemistry and mineralogy of the rare earths* 1
  22. J.E. Powell, *Separation chemistry* 81
  23. C.K. Jørgensen, *Theoretical chemistry of rare earths* 111
  24. W.T. Carnall, *The absorption and fluorescence spectra of rare earth ions in solution* 171
  25. L.C. Thompson, *Complexes* 209
  26. G.G. Libowitz and A.J. Macland, *Hydrides* 299
  27. L. Eyring, *The binary rare earth oxides* 337
  28. D.J.M. Bevan and E. Summerville, *Mixed rare earth oxides* 401
  29. C.P. Khattak and F.F.Y. Wang, *Perovskites and garnets* 525
  30. L.H. Brixner, J.R. Barkley and W. Jeitschko, *Rare earth molybdates (VI)* 609
- Subject index 655

**VOLUME 4: Non-metallic compounds – II**

1979, 1st repr. 1984; ISBN 0-444-85216-6

31. J. Flahaut, *Sulfides, selenides and tellurides* 1
32. J.M. Haschke, *Halides* 89
33. F. Hulliger, *Rare earth pnictides* 153
34. G. Blasse, *Chemistry and physics of R-activated phosphors* 237
35. M.J. Weber, *Rare earth lasers* 275
36. F.K. Fong, *Nonradiative processes of rare-earth ions in crystals* 317
- 37A. J.W. O'Laughlin, *Chemical spectrophotometric and polarographic methods* 341
- 37B. S.R. Taylor, *Trace element analysis of rare earth elements by spark source mass spectroscopy* 359
- 37C. R.J. Conzemius, *Analysis of rare earth matrices by spark source mass spectrometry* 377
- 37D. E.L. DeKalb and V.A. Fassel, *Optical atomic emission and absorption methods* 405
- 37E. A.P. D'Silva and V.A. Fassel, *X-ray excited optical luminescence of the rare earths* 441
- 37F. F.W.V. Boynton, *Neutron activation analysis* 457
- 37G. S. Schuhmann and J.A. Philpotts, *Mass-spectrometric stable-isotope dilution analysis for lanthanides in geochemical materials* 471
38. J. Reuben and G.A. Elgavish, *Shift reagents and NMR of paramagnetic lanthanide complexes* 483
39. J. Reuben, *Bioinorganic chemistry: lanthanides as probes in systems of biological interest* 515
40. T.J. Haley, *Toxicity* 553
- Subject index 587

**VOLUME 5**

1982, 1st repr. 1984; ISBN 0-444-86375-3

41. M. Gasgnier, *Rare earth alloys and compounds as thin films* 1
42. E. Gratz and M.J. Zuckermann, *Transport properties (electrical resistivity, thermoelectric power and thermal conductivity) of rare earth intermetallic compounds* 117
43. F.P. Netzer and E. Bertel, *Adsorption and catalysis on rare earth surfaces* 217
44. C. Boulesteix, *Defects and phase transformation near room temperature in rare earth sesquioxides* 321
45. O. Greis and J.M. Haschke, *Rare earth fluorides* 387
46. C.A. Morrison and R.P. Leavitt, *Spectroscopic properties of triply ionized lanthanides in transparent host crystals* 461
- Subject index 693

**VOLUME 6**

1984; ISBN 0-444-86592-6

47. K.H.J. Buschow, *Hydrogen absorption in intermetallic compounds* 1
48. E. Parthé and B. Chabot, *Crystal structures and crystal chemistry of ternary rare earth-transition metal borides, silicides and homologues* 113
49. P. Rogl, *Phase equilibria in ternary and higher order systems with rare earth elements and boron* 335
50. H.B. Kagan and J.L. Namy, *Preparation of divalent ytterbium and samarium derivatives and their use in organic chemistry* 525
- Subject index 567

**VOLUME 7**

1984; ISBN 0-444-86851-8

51. P. Rogl, *Phase equilibria in ternary and higher order systems with rare earth elements and silicon* 1
52. K.H.J. Buschow, *Amorphous alloys* 265
53. H. Schumann and W. Genthe, *Organometallic compounds of the rare earths* 446
- Subject index 573

**VOLUME 8**

1986; ISBN 0-444-86971-9

54. K.A. Gschneidner Jr and F.W. Calderwood, *Intra rare earth binary alloys: phase relationships, lattice parameters and systematics* 1
55. X. Gao, *Polarographic analysis of the rare earths* 163
56. M. Leskelä and L. Niinistö, *Inorganic complex compounds I* 203
57. J.R. Long, *Implications in organic synthesis* 335
- Errata 375
- Subject index 379

**VOLUME 9**

1987; ISBN 0-444-87045-8

58. R. Reisfeld and C.K. Jørgensen, *Excited state phenomena in vitreous materials* 1
59. L. Niinistö and M. Leskelä, *Inorganic complex compounds II* 91
60. J.-C.G. Bünzli, *Complexes with synthetic ionophores* 321
61. Zhiqian Shen and Jun Ouyang, *Rare earth coordination catalysis in stereospecific polymerization* 395
- Errata 429
- Subject index 431

**VOLUME 10: High energy spectroscopy**

1988; ISBN 0-444-87063-6

62. Y. Baer and W.-D. Schneider, *High-energy spectroscopy of lanthanide materials – An overview* 1
63. M. Campagna and F.U. Hillebrecht, *f-electron hybridization and dynamical screening of core holes in intermetallic compounds* 75
64. O. Gunnarsson and K. Schönhammer, *Many-body formulation of spectra of mixed valence systems* 103
65. A.J. Freeman, B.I. Min and M.R. Norman, *Local density supercell theory of photoemission and inverse photoemission spectra* 165
66. D.W. Lynch and J.H. Weaver, *Photoemission of Ce and its compounds* 231
67. S. Hüfner, *Photoemission in chalcogenides* 301
68. J.F. Herbst and J.W. Wilkins, *Calculation of 4f excitation energies in the metals and relevance to mixed valence systems* 321
69. B. Johansson and N. Mårtensson, *Thermodynamic aspects of 4f levels in metals and compounds* 361
70. F.U. Hillebrecht and M. Campagna, *Bremsstrahlung isochromat spectroscopy of alloys and mixed valent compounds* 425
71. J. Röbner, *X-ray absorption and emission spectra* 453
72. F.P. Netzer and J.A.D. Matthew, *Inelastic electron scattering measurements* 547
- Subject index 601

**VOLUME 11: Two-hundred-year impact of rare earths on science**

1988; ISBN 0-444-87080-6

- H.J. Svec, *Prologue* 1
73. F. Szabadvány, *The history of the discovery and separation of the rare earths* 33
74. B.R. Judd, *Atomic theory and optical spectroscopy* 81
75. C.K. Jørgensen, *Influence of rare earths on chemical understanding and classification* 197
76. J.J. Rhyne, *Highlights from the exotic phenomena of lanthanide magnetism* 293
77. B. Bleaney, *Magnetic resonance spectroscopy and hyperfine interactions* 323
78. K.A. Gschneidner Jr and A.H. Daane, *Physical metallurgy* 409
79. S.R. Taylor and S.M. McLennan, *The significance of the rare earths in geochemistry and cosmochemistry* 485
- Errata 579
- Subject index 581



**VOLUME 12**

1989; ISBN 0-444-87105-5

80. J.S. Abell, *Preparation and crystal growth of rare earth elements and intermetallic compounds* 1
81. Z. Fisk and J.P. Remeika, *Growth of single crystals from molten metal fluxes* 53
82. E. Burzo and H.R. Kirchmayr, *Physical properties of  $R_2Fe_{14}B$ -based alloys* 71
83. A. Szytuła and J. Leciejewicz, *Magnetic properties of ternary intermetallic compounds of the  $RT_2X_2$  type* 133
84. H. Maletta and W. Zinn, *Spin glasses* 213
85. J. van Zytveld, *Liquid metals and alloys* 357
86. M.S. Chandrasekharaiah and K.A. Gingerich, *Thermodynamic properties of gaseous species* 409
87. W.M. Yen, *Laser spectroscopy* 433
- Subject index 479

**VOLUME 13**

1990; ISBN 0-444-88547-1

88. E.I. Gladyshevsky, O.I. Bodak and V.K. Pecharsky, *Phase equilibria and crystal chemistry in ternary rare earth systems with metallic elements* 1
89. A.A. Eliseev and G.M. Kuzmichyeva, *Phase equilibrium and crystal chemistry in ternary rare earth systems with chalcogenide elements* 191
90. N. Kimizuka, E. Takayama-Muromachi and K. Siratori, *The systems  $R_2O_3$ – $M_2O_3$ – $M'O$*  283
91. R.S. Houk, *Elemental analysis by atomic emission and mass spectrometry with inductively coupled plasmas* 385
92. P.H. Brown, A.H. Rathjen, R.D. Graham and D.E. Tribe, *Rare earth elements in biological systems* 423
- Errata 453
- Subject index 455

**VOLUME 14**

1991; ISBN 0-444-88743-1

93. R. Osborn, S.W. Lovesey, A.D. Taylor and E. Balcar, *Intermultiplet transitions using neutron spectroscopy* 1
94. E. Dormann, *NMR in intermetallic compounds* 63
95. E. Zirngiebl and G. Güntherodt, *Light scattering in intermetallic compounds* 163
96. P. Thalmeier and B. Lüthi, *The electron–phonon interaction in intermetallic compounds* 225
97. N. Grewe and F. Steglich, *Heavy fermions* 343
- Subject index 475

**VOLUME 15**

1991; ISBN 0-444-88966-3

98. J.G. Sereni, *Low-temperature behaviour of cerium compounds* 1
99. G.-y. Adachi, N. Imanaka and Zhang Fuzhong, *Rare earth carbides* 61
100. A. Simon, HJ. Mattausch, G.J. Miller, W. Bauhofer and R.K. Kremer, *Metal-rich halides* 191
101. R.M. Almeida, *Fluoride glasses* 287
102. K.L. Nash and J.C. Sullivan, *Kinetics of complexation and redox reactions of the lanthanides in aqueous solutions* 347
103. E.N. Rizkalla and G.R. Choppin, *Hydration and hydrolysis of lanthanides* 393
104. L.M. Vallarino, *Macrocyclic complexes of the lanthanide(III) yttrium(III) and dioxouranium(VI) ions from metal-templated syntheses* 443
- Errata 513
- Subject index 515

**MASTER INDEX, Vols. 1–15**

1993; ISBN 0-444-89965-0

**VOLUME 16**

1993; ISBN 0-444-89782-8

105. M. Loewenhaupt and K.H. Fischer, *Valence-fluctuation and heavy-fermion 4f systems* 1  
 106. I.A. Smirnov and V.S. Oskotski, *Thermal conductivity of rare earth compounds* 107  
 107. M.A. Subramanian and A.W. Sleight, *Rare earths pyrochlores* 225  
 108. R. Miyawaki and I. Nakai, *Crystal structures of rare earth minerals* 249  
 109. D.R. Chopra, *Appearance potential spectroscopy of lanthanides and their intermetallics* 519  
 Author index 547  
 Subject index 579

**VOLUME 17: Lanthanides/Actinides: Physics – I**

1993; ISBN 0-444-81502-3

110. M.R. Norman and D.D. Koelling, *Electronic structure, Fermi surfaces, and superconductivity in f electron metals* 1  
 111. S.H. Liu, *Phenomenological approach to heavy-fermion systems* 87  
 112. B. Johansson and M.S.S. Brooks, *Theory of cohesion in rare earths and actinides* 149  
 113. U. Benedict and W.B. Holzapfel, *High-pressure studies – Structural aspects* 245  
 114. O. Vogt and K. Mattenberger, *Magnetic measurements on rare earth and actinide mononictides and monochalcogenides* 301  
 115. J.M. Fournier and E. Gratz, *Transport properties of rare earth and actinide intermetallics* 409  
 116. W. Potzel, G.M. Kalvius and J. Gal, *Mössbauer studies on electronic structure of intermetallic compounds* 539  
 117. G.H. Lander, *Neutron elastic scattering from actinides and anomalous lanthanides* 635  
 Author index 711  
 Subject index 753

**VOLUME 18: Lanthanides/Actinides: Chemistry**

1994; ISBN 0-444-81724-7

118. G.T. Seaborg, *Origin of the actinide concept* 1  
 119. K. Balasubramanian, *Relativistic effects and electronic structure of lanthanide and actinide molecules* 29  
 120. J.V. Beitz, *Similarities and differences in trivalent lanthanide- and actinide-ion solution absorption spectra and luminescence studies* 159  
 121. K.L. Nash, *Separation chemistry for lanthanides and trivalent actinides* 197  
 122. L.R. Morss, *Comparative thermochemical and oxidation–reduction properties of lanthanides and actinides* 239  
 123. J.W. Ward and J.M. Haschke, *Comparison of 4f and 5f element hydride properties* 293  
 124. H.A. Eick, *Lanthanide and actinide halides* 365  
 125. R.G. Haire and L. Eyring, *Comparisons of the binary oxides* 413  
 126. S.A. Kinkad, K.D. Abney and T.A. O'Donnell, *f-element speciation in strongly acidic media: lanthanide and mid-actinide metals, oxides, fluorides and oxide fluorides in superacids* 507  
 127. E.N. Rizkalla and G.R. Choppin, *Lanthanides and actinides hydration and hydrolysis* 529  
 128. G.R. Choppin and E.N. Rizkalla, *Solution chemistry of actinides and lanthanides* 559  
 129. J.R. Duffield, D.M. Taylor and D.R. Williams, *The biochemistry of the f-elements* 591  
 Author index 623  
 Subject index 659

**VOLUME 19: Lanthanides/Actinides: Physics – II**

1994; ISBN 0-444-82015-9

130. E. Holland-Moritz and G.H. Lander, *Neutron inelastic scattering from actinides and anomalous lanthanides* 1
131. G. Aeppli and C. Broholm, *Magnetic correlations in heavy-fermion systems: neutron scattering from single crystals* 123
132. P. Wachter, *Intermediate valence and heavy fermions* 177
133. J.D. Thompson and J.M. Lawrence, *High pressure studies – Physical properties of anomalous Ce, Yb and U compounds* 383
134. C. Colinet and A. Pasturel, *Thermodynamic properties of metallic systems* 479
- Author index 649
- Subject index 693

**VOLUME 20**

1995; ISBN 0-444-82014-0

135. Y. Ōnuki and A. Hasegawa, *Fermi surfaces of intermetallic compounds* 1
136. M. Gasgnier, *The intricate world of rare earth thin films: metals, alloys, intermetallics, chemical compounds, ...* 105
137. P. Vajda, *Hydrogen in rare-earth metals, including  $RH_{2+x}$  phases* 207
138. D. Gignoux and D. Schmitt, *Magnetic properties of intermetallic compounds* 293
- Author index 425
- Subject index 457

**VOLUME 21**

1995; ISBN 0-444-82178-3

139. R.G. Bautista, *Separation chemistry* 1
140. B.W. Hinton, *Corrosion prevention and control* 29
141. N.E. Ryan, *High-temperature corrosion protection* 93
142. T. Sakai, M. Matsuoka and C. Iwakura, *Rare earth intermetallics for metal–hydrogen batteries* 133
143. G.-y. Adachi and N. Imanaka, *Chemical sensors* 179
144. D. Garcia and M. Faucher, *Crystal field in non-metallic (rare earth) compounds* 263
145. J.-C.G. Bünzli and A. Milicic-Tang, *Solvation and anion interaction in organic solvents* 305
146. V. Bhagavathy, T. Prasada Rao and A.D. Damodaran, *Trace determination of lanthanides in high-purity rare-earth oxides* 367
- Author index 385
- Subject index 411

**VOLUME 22**

1996; ISBN 0-444-82288-7

147. C.P. Flynn and M.B. Salamon, *Synthesis and properties of single-crystal nanostructures* 1
148. Z.S. Shan and D.J. Sellmyer, *Nanoscale rare earth–transition metal multilayers: magnetic structure and properties* 81
149. W. Suski, *The  $ThMn_{12}$ -type compounds of rare earths and actinides: structure, magnetic and related properties* 143
150. L.K. Aminov, B.Z. Malkin and M.A. Teplov, *Magnetic properties of nonmetallic lanthanide compounds* 295
151. F. Auzel, *Coherent emission in rare-earth materials* 507
152. M. Dolg and H. Stoll, *Electronic structure calculations for molecules containing lanthanide atoms* 607
- Author index 731
- Subject index 777

**VOLUME 23**

1996; ISBN 0-444-82507-X

153. J.H. Forsberg, *NMR studies of paramagnetic lanthanide complexes and shift reagents* 1  
 154. N. Sabbatini, M. Guardigli and I. Manet, *Antenna effect in encapsulation complexes of lanthanide ions* 69  
 155. C. Görller-Walrand and K. Binnemans, *Rationalization of crystal-field parametrization* 121  
 156. Yu. Kuz'ma and S. Chykhrij, *Phosphides* 285  
 157. S. Boghosian and G.N. Papatheodorou, *Halide vapors and vapor complexes* 435  
 158. R.H. Byrne and E.R. Sholkovitz, *Marine chemistry and geochemistry of the lanthanides* 497  
 Author index 595  
 Subject index 631

**VOLUME 24**

1997; ISBN 0-444-82607-6

159. P.A. Dowben, D.N. McIlroy and Dongqi Li, *Surface magnetism of the lanthanides* 1  
 160. P.G. McCormick, *Mechanical alloying and mechanically induced chemical reactions* 47  
 161. A. Inoue, *Amorphous, quasicrystalline and nanocrystalline alloys in Al- and Mg-based systems* 83  
 162. B. Elschner and A. Loidl, *Electron-spin resonance on localized magnetic moments in metals* 221  
 163. N.H. Duc, *Intersublattice exchange coupling in the lanthanide–transition metal intermetallics* 339  
 164. R.V. Skolozdra, *Stannides of rare-earth and transition metals* 399  
 Author index 519  
 Subject index 559

**VOLUME 25**

1998; ISBN 0-444-82871-0

165. H. Nagai, *Rare earths in steels* 1  
 166. R. Marchand, *Ternary and higher order nitride materials* 51  
 167. C. Görller-Walrand and K. Binnemans, *Spectral intensities of f–f transitions* 101  
 168. G. Bombieri and G. Paolucci, *Organometallic  $\pi$  complexes of the f-elements* 265  
 Author Index 415  
 Subject Index 459

**VOLUME 26**

1999; ISBN 0-444-50815-1

169. D.F. McMorro, D. Gibbs and J. Bohr, *X-ray scattering studies of lanthanide magnetism* 1  
 170. A.M. Tishin, Yu.I. Spichkin and J. Bohr, *Static and dynamic stresses* 87  
 171. N.H. Duc and T. Goto, *Itinerant electron metamagnetism of Co sublattice in the lanthanide–cobalt intermetallics* 177  
 172. A.J. Arko, P.S. Riseborough, A.B. Andrews, J.J. Joyce, A.N. Tahvildar-Zadeh and M. Jarrell, *Photoelectron spectroscopy in heavy fermion systems: Emphasis on single crystals* 265  
 Author index 383  
 Subject index 405

**VOLUME 27**

1999; ISBN 0-444-50342-0

173. P.S. Salamakha, O.L. Sologub and O.I. Bodak, *Ternary rare-earth–germanium systems* 1  
 174. P.S. Salamakha, *Crystal structures and crystal chemistry of ternary rare-earth germanides* 225  
 175. B.Ya. Kotur and E. Gratz, *Scandium alloy systems and intermetallics* 339  
 Author index 535  
 Subject index 553

**VOLUME 28**

2000; ISBN 0-444-50346-3

176. J.-P. Connerade and R.C. Karnatak, *Electronic excitation in atomic species* 1  
 177. G. Meyer and M.S. Wickleder, *Simple and complex halides* 53  
 178. R.V. Kumar and H. Iwahara, *Solid electrolytes* 131  
 179. A. Halperin, *Activated thermoluminescence (TL) dosimeters and related radiation detectors* 187  
 180. K.L. Nash and M.P. Jensen, *Analytical separations of the lanthanides: basic chemistry and methods* 311  
 Author index 373  
 Subject index 401

**VOLUME 29: The role of rare earths in catalysis**

2000; ISBN 0-444-50472-9

- P. Maestro, *Foreword* 1  
 181. V. Paul-Boncour, L. Hilaire and A. Percheron-Guégan, *The metals and alloys in catalysis* 5  
 182. H. Imamura, *The metals and alloys (prepared utilizing liquid ammonia solutions) in catalysis II* 45  
 183. M.A. Ulla and E.A. Lombardo, *The mixed oxides* 75  
 184. J. Kašpar, M. Graziani and P. Fornasiero, *Ceria-containing three-way catalysts* 159  
 185. A. Corma and J.M. López Nieto, *The use of rare-earth-containing zeolite catalysts* 269  
 186. S. Kobayashi, *Triflates* 315  
 Author index 377  
 Subject index 409

**VOLUME 30: High-Temperature Superconductors – I**

2000; ISBN 0-444-50528-8

187. M.B. Maple, *High-temperature superconductivity in layered cuprates: overview* 1  
 188. B. Raveau, C. Michel and M. Hervieu, *Crystal chemistry of superconducting rare-earth cuprates* 31  
 189. Y. Shiohara and E.A. Goodilin, *Single-crystal growth for science and technology* 67  
 190. P. Karen and A. Kjekshus, *Phase diagrams and thermodynamic properties* 229  
 191. B. Elschner and A. Loidl, *Electron paramagnetic resonance in cuprate superconductors and in parent compounds* 375  
 192. A.A. Manuel, *Positron annihilation in high-temperature superconductors* 417  
 193. W.E. Pickett and I.I. Mazin,  *$R\text{Ba}_2\text{Cu}_3\text{O}_7$  compounds: electronic theory and physical properties* 453  
 194. U. Staub and L. Soderholm, *Electronic  $4f$  state splittings in cuprates* 491  
 Author index 547  
 Subject index 621

**VOLUME 31: High-Temperature Superconductors – II**

2001; ISBN 0-444-50719-1

195. E. Kaldis, *Oxygen nonstoichiometry and lattice effects in  $\text{YBa}_2\text{Cu}_3\text{O}_x$ . Phase transitions, structural distortions and phase separation* 1  
 196. H.W. Weber, *Flux pinning* 187  
 197. C.C. Almasan and M.B. Maple, *Magnetoresistance and Hall effect* 251  
 198. T.E. Mason, *Neutron scattering studies of spin fluctuations in high-temperature superconductors* 281  
 199. J.W. Lynn and S. Skanthakumar, *Neutron scattering studies of lanthanide magnetic ordering* 315  
 200. P.M. Allenspach and M.B. Maple, *Heat capacity* 351  
 201. M. Schabel and Z.-X. Shen, *Angle-resolved photoemission studies of untwinned yttrium barium copper oxide* 391

202. D.N. Basov and T. Timusk, *Infrared properties of high- $T_c$  superconductors: an experimental overview* 437
203. S.L. Cooper, *Electronic and magnetic Raman scattering studies of the high- $T_c$  cuprates* 509
204. H. Sugawara, T. Hasegawa and K. Kitazawa, *Characterization of cuprate superconductors using tunneling spectra and scanning tunneling microscopy* 563
- Author index 609
- Subject index 677

## Chapter 205

# GIANT MAGNETOSTRICTION IN LANTHANIDE-TRANSITION METAL THIN FILMS

NGUYEN HUU DUC

*Cryogenic Laboratory, Faculty of Physics, National University of Hanoi,  
334 Nguyen Trai, Thanh xuan, Hanoi, Vietnam*

---

### Contents

Abbreviations	1	5.1.2.2. $(\text{Tb}_{0.27}\text{Dy}_{0.73})(\text{Fe}_{1-x}\text{Co}_x)_2$ thin films	29
List of symbols	2	5.1.2.3. $(\text{Tb}_{1-x}\text{Dy}_x)(\text{Fe}_{0.45}\text{Co}_{0.55})_{2.1}$ thin films	33
1. Introduction	2	5.1.2.4. Sm-Co thin films	36
2. Magnetoelastic phenomena	3	5.2. Giant magnetostrictive spring-magnet- type multilayers	37
3. Magnetostrictive constants in thin films	7	5.3. Magnetostriction of R-T sandwich films	41
4. Magnetism in amorphous lanthanide- transition metal alloys	10	6. Potential applications of magnetostrictive microsystems	43
5. Giant magnetostrictive thin film materials	17	7. Summary and recent developments	46
5.1. Thin film systems	17	Acknowledgements	50
5.1.1. R-Fe thin films	17	References	50
5.1.1.1. Tb-Fe thin films	17		
5.1.1.2. (Tb,Dy)-Fe thin films	21		
5.1.1.3. Sm-Fe thin films	24		
5.1.2. R-Co thin films	25		
5.1.2.1. Tb-Co and (Tb,Dy)-Co thin films	25		

---

### Abbreviations

a	amorphous	p	polycrystalline
c	crystalline	R	lanthanide
CEF	crystalline electric-field	HR	heavy lanthanide
EDW	extended domain wall	LR	light lanthanide
EMD	easy magnetisation direction	T	transition metal
n	nanocrystalline		

---

## List of symbols

$A_{ij}$	spin-spin coupling parameter	$t$	film thickness
$B$	external magnetic field ( $\mu_0 H$ )	$T_C$	Curie temperature
$B_{\text{exch}}$	exchange field	$Z_{ij}$	number of nearest neighbours
$b$	elastic coefficient	$\alpha_j$	Stevens factor
$D$	magnetocrystalline coupling constant	$\alpha_i$ ( $i=x, y, z$ )	direction cosines of magnetisation
$E$	Young's modulus	$\beta_i$ ( $i=x, y, z$ )	direction cosines of measured magnetostriction
$g_R$	Landé factor	$\Gamma$	exchange integral
$J_R$	total angular momentum for 4f ions	$\theta$	sperimagnetic cone angle
$J$	quantum number of $J_R$	$\lambda$	magnetostriction
$K$	anisotropy constant	$\nu$	Poisson's ratio
$M_i$	sublattice magnetisation	$\sigma$	stress
$M_R, M_T$	magnetisations of R and T sublattices	$\chi$	magnetic susceptibility
$M_s$	spontaneous magnetisation		
$n_{ij}$	molecular-field coefficient		

## 1. Introduction

Magnetostriction is a well-known phenomenon of magnetoelastic coupling which exhibits a change in dimensions and a change in the elastic modulus of a magnetic substance induced by a change in its magnetic state. Generally, the dimensions of a magnetostrictive material change when the material is subjected to a change in magnetic field. This is the (linear) Joule magnetostriction associated with the distribution of the orientation of the magnetic moments. It results in a relative replacement of atoms due to the modification of the electrostatic configuration. Another type is the (volume) spontaneous magnetostriction associated with the change of the magnetic state by a temperature variation. Magnetostrictive materials as well as piezoelectric and shape memory ones are the transducer materials which directly convert electrical energy into mechanical energy. They are useful in the manufacture of sensors, actuators, controllers, force and displacement as well as other electro-acoustic devices. For these applications, transducer materials in the form of thin films are of special interest as they are capable of cost-effective mass-production compatible to microsystem process technologies. In addition, magnetostrictive thin films are particularly promising for the microactuator elements like cantilevers or membranes as they combine high energy output, high frequency and remote control operation. Due to this potential, interest in such giant magnetostrictive thin films has rapidly grown over the past few years. Owing to the specifications related with microsystem applications, the materials research has focused upon thin-film materials showing giant magnetostriction in combination with soft magnetic properties.

With regard to the Joule magnetostriction, the lanthanide metals and lanthanide-iron intermetallic compounds have constituted very interesting systems for research. In 1971, A.E. Clark at the Naval Ordnance Laboratory (NOL), now Naval Surface Warfare Center



discovered that bulk TbFe<sub>2</sub> (Terfenol) has the highest room-temperature magnetostriction, and his Terfenol-D (Tb<sub>x</sub>Dy<sub>1-x</sub>Fe<sub>2</sub>, where  $x \approx 0.3$ ) alloy is still the best known and exploits huge magnetostriction in combination with reduced magnetocrystalline anisotropy. (The name he gave to these alloys – Terfenol- indicate the constituents: ter for Tb, fe for iron, -D for dysprosium, and nol for the place where these alloys had been discovered) (Clark and Belson 1972). As a tradition, research on the giant magnetostrictive thin films have also been based on the lanthanide–iron alloys. However, progress has been obtained with the development of lanthanide–cobalt alloys, and a record of magnetostriction of  $1020 \times 10^{-6}$  has been achieved at the Laboratoire Louis Néel, Grenoble (France) on the amorphous Tb(Fe<sub>0.55</sub>Co<sub>0.45</sub>)<sub>2.1</sub> thin film (Duc et al. 1996). Composite materials are known to exhibit outstanding properties sometimes, which cannot be predicted from the constituent behaviour. Actually, a very high magnetostrictive susceptibility has recently been observed in TbCo/FeCo and TbFe/Fe multilayers.

Information on the magnetoelastic properties has been reviewed by Clark on “Magnetostrictive rare-earth RFe<sub>2</sub> compounds” (1980), by Morin and Schmitt on “Quadrupolar effects in rare earth intermetallics” (1990) and by du Trémolet de Lacheisserie (1993) on “Magnetostriction: theory and applications of magnetoelasticity” (1993). In case of thin films, which is the topic of this review, the research on magnetostriction also concentrates on the lanthanide–transition metal materials. However, additional attempts to further lower the macroscopic anisotropy are based on the use of amorphous, nanocrystalline or multilayered states of the R–Fe and R–(Fe,Co) alloys. For the best comprehension of readers, it is necessary to present in this chapter not only an introduction to magnetostriction, but also a brief summary of the magnetism and magnetocrystalline anisotropy of amorphous lanthanide–transition metal compounds. This chapter is organised as follows. Section 2 is devoted to magnetoelastic phenomena. Problems in the determination of the magnetostrictive coefficients of thin films are presented in sect. 3. In sect. 4, magnetism and magnetostriction in crystalline and amorphous lanthanide–transition metal compounds are summarised, and the possibilities to develop a giant magnetostriction in thin films are discussed. Section 5 presents an overview on the research of magnetostrictive lanthanide–transition metal thin films, sandwich and multilayer systems. Potential applications of magnetostrictive films in microsystems are briefly discussed in sect. 6. Finally, summary and concluding remarks are presented in sect. 7.

## 2. Magnetoelastic phenomena

The elasticity and magnetism in magnetic materials are explained by electrostatic interactions between the nucleus and the electrons. Thus, the magnetoelasticity is strongly related to these interactions. In order to describe the elastic effects, the following magnetic interactions are usually taken into account:

- The dipolar interactions are responsible for the energy of the demagnetisation field. The minimization of this energy leads to the form effect, which is always small ( $\leq 10^{-6}$ ).

- The exchange interactions are isotropic to first order. They describe a coupling between the magnetic moments and dominate the magnetic ordering in the materials. The variation of these interactions with the interatomic distance is the reason for a spontaneous deformation (i.e., the volume magnetostriction).
- The pseudo-dipolar exchange interactions, which are anisotropic and vary rapidly with the increasing interatomic distance, are one of origins of the Joule magnetostriction.
- The crystalline electric-field (CEF) interactions are the principle origin of the magnetocrystalline anisotropy. They cause a notable contribution to the (linear) Joule magnetostriction.

These interactions are generally considered for bulk magnetic materials, even for those which are ribbon-shaped and have a thickness of some micrometers, still very substantial as compared with the interatomic distances. For thin films and multilayers, the surface (and/or interface) magnetostriction is important. Up to now, however, it is not clear which mechanism is responsible for the surface magnetism. But, since the magnetostriction and magnetic anisotropy have, generally speaking, the same origin, the non-linear contributions to the bulk magnetoelastic coefficients due to surface strains and surface roughness effects are expected to be considerable. Principally, the problem of surface magnetostriction can be developed in the spirit of the Néel model of the surface anisotropy (Zuberek et al. 1994). Detailed theoretical calculations of the surface magnetostriction, however, have been performed only in frames of the dipolar model (Szumiata et al. 1993). This implies that surface magnetostriction is an intrinsic property, which does not necessarily arise due to large surface strains. The surface/interface contributions to magnetostriction will be discussed in sect. 5.2 for multilayers. Presently, however, mechanisms of the bulk magnetostriction will be discussed and only the CEF interaction origin of the Joule magnetostriction will be described.

The demagnetised state is determined by a local magnetic anisotropy. This anisotropy is based on the CEF interactions, which couple the orbitals of the electrons with the crystal lattice or atomic environment. As a consequence, the orbital moments and the spin moments (through the spin-orbit coupling  $\lambda LS$ ) tend to orient along a well-defined direction, referred to as the easy magnetisation direction (EMD). For an ordered crystalline structure, the anisotropy establishes the parallel alignment of the moments up to the macroscopic scale. It is responsible, through this mechanism, for the long-range magnetic order.

For the case where the spin-orbit coupling is relatively weak ( $\sim 0.015$  eV per atom), the spin moments with the stronger exchange interactions ( $\sim 0.1$  eV) can easily be rotated into the applied-field direction, but the orbitals are almost unaffected (fig. 1a). To the first order, the anisotropy energy represents the change in the spin-orbit coupling energy occurring when the spin moment rotates from the easy direction to the difficult one. In this case, the anisotropy and then the magnetostriction is small. This is usually observed in the 3d transition metals.

For the case where the CEF interactions are dominant, e.g., the case of the lanthanides and their alloys, the electron orbitals tend to follow the local symmetry of the

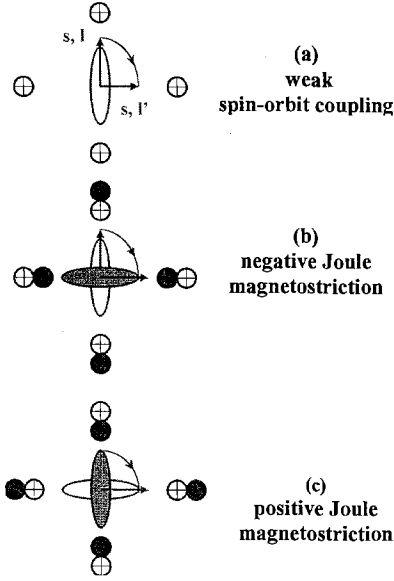


Fig. 1. Schematic representation of the phenomena of magnetostriction. The atoms, schematised as positive charges, are displaced from their initial symmetrical position (open circles) to their final strained positions (solid circles) due to the electrostatic interactions with the aspherical electron distribution.

environment. The spin-orbit coupling is strong and the rotation of the total moment  $J$  forces simultaneously the rotation of the orbitals. This results in not only a change in the magnetocrystalline anisotropy but also in a deformation of the crystal lattice. Different deformations of the lattice, i.e., different (positive or negative) magnetostriction are associated with different orientations of the 4f shell. As illustrated in fig. 1(b,c), the magnetostriction is negative when the distribution of the charge density is prolate, whereas the magnetostriction is positive when the charge density is oblate (see also sect. 4). This process occurs at low temperatures in the lanthanides and even at room temperature in the lanthanide-transition metal intermetallics.

For the Joule magnetostriction, the deformation reaches its limit value,  $\lambda_s$  at the magnetic saturation. When the magnetic state is isotropic in the absence of the field, one can measure a relative change of the length along the applied-field direction, which corresponds to the magnetostrictive coefficient  $(\Delta/l)_{\parallel} = \lambda_{\parallel} = \lambda_s$  and a relative change in the plane perpendicular to the field, which corresponds to  $(\Delta/l)_{\perp} = \lambda_{\perp} = \frac{1}{2}\lambda_s$ . As the materials always present an anisotropic demagnetised state, it is necessary to measure  $\Delta/l$  along two perpendicular directions to determine  $\lambda_s$ . In this case,  $\lambda_s = \frac{2}{3}(\lambda_{\parallel} - \lambda_{\perp})$  is independent of the demagnetised state of the magnetic materials.

The magnetostrictive properties imply the symmetry of the crystal lattice when a piece of material is present in the form of a single crystal. In that case, the length changes observed at the magnetic saturation depend on the measurement direction as well as on the initial and final direction of magnetisation of the single crystal. In cubic materials,

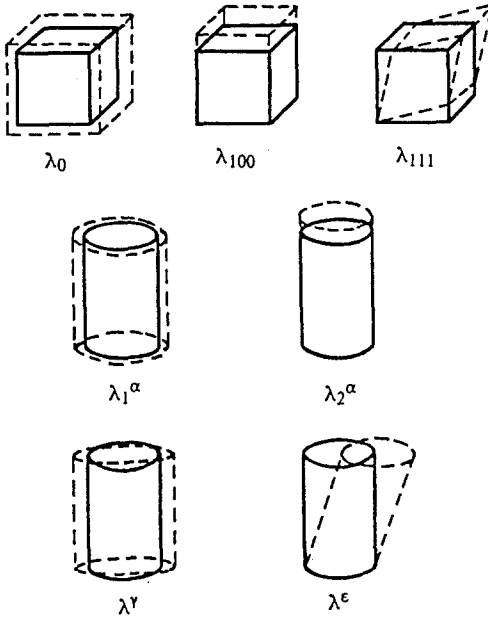


Fig. 2. Magnetostriction modes for cubic and uniaxial symmetries.

the magnetostriction is given by the phenomenological expression (Akulov 1928, Becker and Döring 1939)

$$\begin{aligned} \Delta/l = & \lambda_0 + 1.5\lambda_{100}(\alpha_x^2\beta_x^2 + \alpha_y^2\beta_y^2 + \alpha_z^2\beta_z^2 - \frac{1}{3}) \\ & + 3\lambda_{111}(\alpha_x\beta_x\alpha_y\beta_y + \alpha_y\beta_y\alpha_z\beta_z + \alpha_x\beta_x\alpha_z\beta_z). \end{aligned} \quad (1)$$

In this expression,  $\alpha_i$  ( $i=x, y, z$ ) represent the direction cosines of the magnetisation direction with respect to the  $i$ -axes of the crystal and  $\beta_i$  represent the direction cosines of the measurement direction with respect to the crystal axes. The quantity  $\lambda_0$  describes the isotropic (volume) magnetostriction which depends on neither the magnetisation direction nor the crystal direction. The magnetostriction constants  $\lambda_{100}$  ( $\lambda_{111}$ ) represent the change in length in the [100] ([111]) directions when the magnetisation direction is also along the [100] ([111]) directions. These two magnetostriction constants describe the anisotropic magnetostriction which transfers the lattice symmetry to tetragonal ( $\lambda_{100}$ ) or rhombohedral ( $\lambda_{111}$ ). The magnetostriction modes for the cubic symmetry is shown in fig. 2.

For uniaxial crystals, also included in fig. 2, the magnetostriction modes are given as:

- the  $\alpha$ -magnetostriction describes the changes in the interatomic distance within the basal plane ( $\lambda_1^\alpha$ ) and along the  $c$ -axis ( $\lambda_2^\alpha$ ). In more detailed descriptions, the  $\alpha$ -magnetostriction is divided into terms with zero-order  $\alpha$ -magnetostriction ( $\lambda_1^{\alpha,0}$  and  $\lambda_2^{\alpha,0}$ ) similar to  $\lambda_0$  in cubic crystals and with the second-order  $\alpha$ -magnetostriction ( $\lambda_1^{\alpha,2}$  and  $\lambda_2^{\alpha,2}$ ) when the magnetisation rotates in the crystal under the effect of a magnetic field during a spontaneous spin reorientation.

- the  $\gamma$ -magnetostriction ( $\lambda^\gamma$ ) represents an orthorhombic distortion in the basal plane when the magnetisation direction does not coincide with the  $c$ -axis. The second-order  $\gamma$ -magnetostriction relates to  $\lambda_{100}$  as  $\lambda^{\gamma,2} = \frac{3}{2}\lambda_{100}$ .
- the  $\epsilon$ -magnetostriction ( $\lambda^\epsilon$ ) describes a deviation of an angle between the basal plane and the  $c$ -axis from the  $90^\circ$  arrangement. The second-order  $\epsilon$ -magnetostriction relates to  $\lambda_{111}$  as  $\lambda^{\epsilon,2} = \frac{3}{2}\lambda_{111}$ .

### 3. Magnetostrictive constants in thin films

For bulk ferromagnetic materials, the magnetostriction is described by the function of the magnetic field  $\lambda(H) = \Delta l/l$ , which corresponds to a relative deformation in one direction. For thin films, the experimental determination of the magnetostriction is not an easy task. First, the two dimensional character of thin films implies that only one ‘ $\lambda_s$ ’ magnetostrictive coefficient cannot describe correctly the physics of such magnetic substances, since the symmetry may not be higher than uniaxial. This leads to the fact that one must use at least four Joule magnetostriction modes,  $\lambda_1^{\alpha,2}$ ,  $\lambda_2^{\alpha,2}$ ,  $\lambda^{\gamma,2}$  and  $\lambda_1^{\epsilon,2}$  which are relevant to the cylindrical symmetry (see sect. 2). Moreover, magnetic films have always been deposited on the planar surface of a non-magnetic substrate. In such a bimorph, the observed strains, when applying a magnetic field, are not strictly Joule magnetostriction, but it contains also contributions of the elastic properties of the substrate.

Various experimental methods have been developed for investigating the magnetoelastic properties of thin films. Indirect methods are based on the stress dependence of any magnetic properties, e.g., susceptibility or resonance frequency, while the most common direct method was introduced as early as 1976 by Klokhholm (1976, 1977) who observed the deflection of the end of a bimorph when subjected to a magnetic field.

Assuming that the magnetic film is thin in comparison to the substrate, the deflection  $D$  ( $\approx L \cdot \vartheta$ ) at the distance  $L$  from the clamping edge to the measurement location (fig. 3) is given by

$$D = \frac{2}{9} t_f \lambda_s \left( \frac{L}{t_s} \right)^2 \frac{E_f(1 - \nu_s)}{E_s(1 + \nu_f)}. \quad (2)$$

Here,  $t$  is the thickness,  $E$  is Young’s modulus,  $\nu$  is Poisson’s ratio,  $\lambda$  is the magnetostriction; f stands for film, and s for substrate. Numerical values of  $E_s$  and  $\nu_s$  are illustrated in table 1 for several magnetostrictive films and related substrates.

From eq. (2)  $\lambda_s$  can be calculated by

$$\lambda_s = \frac{2}{9} \frac{D}{t_f} \left( \frac{t_f}{L} \right)^2 \frac{E_s(1 + \nu_f)}{E_f(1 - \nu_s)}. \quad (3)$$

The above cantilever-bending technique requires a sensitive displacement detection [such as capacitance probe (Klokhholm 1976, 1977), optical interferometry (Sontag and

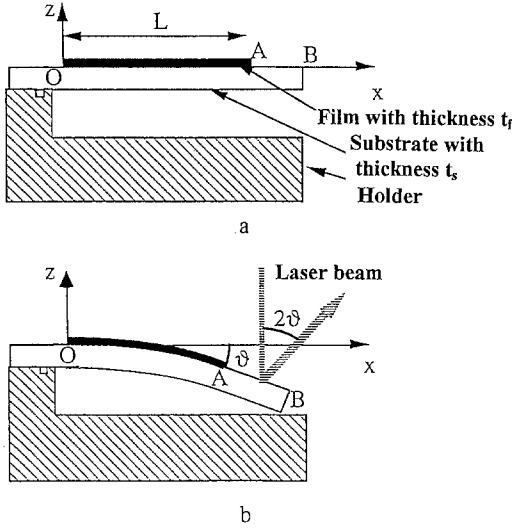


Fig. 3. (a) Fixation of a bimorph on its sample holder and (b) measurement principle of the deformation of any magnetostrictive bimorph using the deflection of a laser beam. After Betz et al. (1996a).

Table 1  
Young's modulus ( $E$ ) and Poisson's ratio ( $\nu$ ) for several magnetostrictive films and different substrates

Material	$E_s$ (GPa)	$\nu_s$	Reference
a-R-Fe	40	0.4	Wada et al. (1997c)
a-R-Fe	50	0.3	Quandt (1997)
n-R-Fe	80	0.3	Quandt (1997)
a-R-Co	80	0.31	Duc et al. (1996)
W	345	0.28	Wada et al. (1997c)
Ta	186	0.3	Wada et al. (1997c)
Other metals	$\approx 200$	0.31	Betz (1997)
Glass	72	0.21	Duc et al. (1996)
Si [100]	130.19	0.278	Betz (1997)
Si [110]	169.16	0.037	Betz (1997)

Tam 1986) or a tunneling tip (Wandass et al. 1988)] or angular detection (e.g., laser beam deflection, Sontag and Tam 1986, Trippel 1977, Tam and Schroeder 1988).

Schatz et al. (1993) have proposed a formula which can be applied for thin films, but again without any demonstration. The utilisation of the 'Klokholm' formula (i.e., eq. 3), however, is doubtful. Dirne and Denissen (1989) have modified this formula by suppressing the  $(1 + \nu_f)$  term and adding a multiplying  $\frac{2}{3}$  without any explanation. Kaneko et al. (1988) have argued that the term  $(1 - \nu_s)$  should occur only for the case of a uniform thermal stress and have dropped the ratio  $(1 + \nu_f)/(1 - \nu_s)$ . This modified formula gives again a correction for  $\lambda_s$  in the order of  $\frac{1}{2}$ . Nozières (see du Trémolet de Lacheisserie and

Peuzin 1994, 1996) found the magnetostriction coefficient for thick nickel films twice as large as observed in bulk nickel. The same problem of calibration has probably led van de Riet (1994) and Weber et al. (1994) to the recalculation of the Klokholm's formula. Their results are consistent with those reported independently by du Trémolet de Lacheisserie and Peuzin (1994) that the true formula to determine the magnetostriction of thin films is (also referred to as TL,P's formula)

$$\lambda_s = \frac{2}{9} \frac{D}{t_f} \left( \frac{t_f}{L} \right)^2 \frac{E_s(1 + \nu_f)}{E_f(1 + \nu_s)}. \quad (4)$$

Equations (3) and (4) differ respectively by  $(1 - \nu_s)$  and  $(1 + \nu_s)$ . For substrates of Corning glass,  $\nu_s = \frac{1}{4}$ , hence for Stokholm's formula  $(1 - \nu_s) = \frac{3}{4}$ , while for TL,P  $(1 + \nu_s) = \frac{5}{4}$ . Thus,  $\lambda_s$  calculated from eq. (3) would be larger than  $\lambda_s$ , from eq. (4), by a factor of  $\frac{5}{3}$ .

Finally, we note that it is in general difficult to determine correctly the elastic parameters  $E_f$  and  $\nu_f$  of thin films. This may introduce a large uncertainty in the  $\lambda_s$  value. On the other hand, the relevant parameters for technical applications, e.g., in microsystems, are the magnetoelastic coupling coefficient  $b^{\gamma,2}$  of the film and the elastic parameters of the substrate, but not the magnetostriction of the film. du Trémolet de Lacheisserie and Peuzin (1994) and Betz (1997) thus preferred to determine  $b^{\gamma,2}$  rather than  $\lambda_s$ . The magnetoelastic coupling coefficient  $b^{\gamma,2}$  is simply derived by taking the difference between the parallel and perpendicular deflections,  $D_{||}$  and  $D_{\perp}$ , and is given as

$$b^{\gamma,2} = \frac{E_s}{3(1 + \nu_s)} \frac{D_{||} - D_{\perp}}{L^2} \frac{t_s^2}{t_f}. \quad (5)$$

The two magnetoelastic coefficients measured along the two applied field directions are

$$b_i = \frac{E_s}{3(1 + \nu_s)} \frac{D_i}{L^2} \frac{t_s^2}{t_f}, \quad (6)$$

where  $i$  stands for  $||$  and  $\perp$  and  $b^{\gamma,2} = b_{||} - b_{\perp}$  in accordance with the definition for bulk materials  $\lambda^{\gamma,2} = \lambda_{||} - \lambda_{\perp}$ .

Nevertheless, in order to easily compare with the results traditionally reported in the literature, it is possible to determine the magnetostrictive coefficients from  $b_i$  and  $b^{\gamma,2}$  by applying the formulas

$$\lambda_i = -\frac{b_i(1 + \nu_f)}{E_f}, \quad \lambda^{\gamma,2} = \frac{3}{2}\lambda_s = -\frac{b^{\gamma,2}(1 + \nu_f)}{E_f}. \quad (7a,b)$$

In the following sections, for instance in sects. 5.1.2 and 5.1.3, both the magnetoelastic,  $b^{\gamma,2}$ , and magnetostrictive,  $\lambda^{\gamma,2}$ , data will be reported. As an illustration, we present

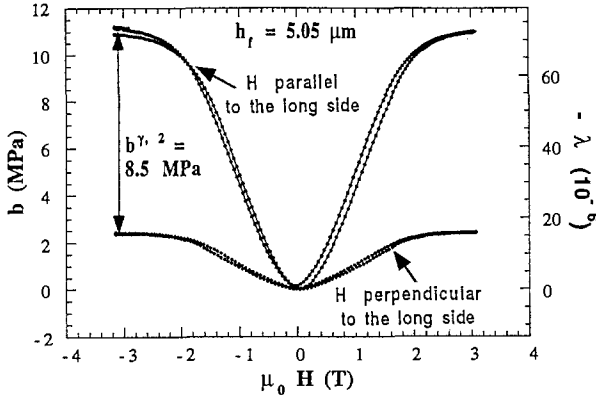


Fig. 4. Field dependence of the magnetoelastic and magnetostrictive coefficients for a vacuum-evaporated nickel thin film. After Betz (1997).

in fig. 4 a typical magnetostriction curve described with all the parameters  $\lambda_{\parallel}$ ,  $\lambda_{\perp}$ ,  $\lambda^{\gamma,2}$ ,  $b_{\parallel}$ ,  $b_{\perp}$  and  $b^{\gamma,2}$  for a vacuum-evaporated nickel film.

#### 4. Magnetism in amorphous lanthanide–transition metal alloys

The lanthanide–transition metal compounds have been considered to be formed by the association of the relatively narrow 3d band with a wider 5d band with higher energy. The electronegativity difference between the constituents gives rise to a transfer of 5d electrons towards the unfilled 3d band. Since the screening of the nuclear potentials by the electrons is modified, the two bands draw together, leading to 3d–5d hybridisation states at the top of the 3d band and at the bottom of the 5d one. This strong 3d–5d hybridisation does not only result in the formation of the lanthanide intermetallics, but also determines the physical properties of the existing compounds. In the compounds based on the lanthanides and transition metals, it is found, as a general rule that, due to the hybridisation between the 3d and 5d states, the 4f–3d spin–spin coupling is always antiferromagnetic (Campbell 1972, Duc 1997). Taking into account the coupling between the spin and orbital moments of the 4f electrons, one can explain the parallel and antiparallel alignments of the 3d(Fe,Co,Ni)- and 4f-moments in the light- ( $J = |L - S|$ ) and heavy- ( $J = L + S$ ) lanthanide compounds (fig. 5).

As already mentioned, the lanthanide elements can be separated into two groups: the light Ce, Pr, Nd, Pm, Sm, Eu, and the heavy Gd, Tb, Dy, Ho, Er, Tm, Yb. Within these two groups, one can divide them once more into two subgroups according to the sign of the Stevens factor  $\alpha_J$ . This division put on the angular distribution of the charge density of the 4f electrons, which is in the oblate ( $\alpha_J < 0$ ) or prolate ( $\alpha_J > 0$ ) form (fig. 6). As mentioned in sect. 2 (fig. 1), with the oblate distribution ( $\alpha_J < 0$ ), the magnetic moment is perpendicular to the plate (e.g., Nd and Tb). In this case, the magnetostriction is positive. When  $\alpha_J > 0$ , i.e., the electronic density distribution in the prolate form, the magnetic moment is aligned along the axis of a prolate spheroid, and the magnetostriction is negative.



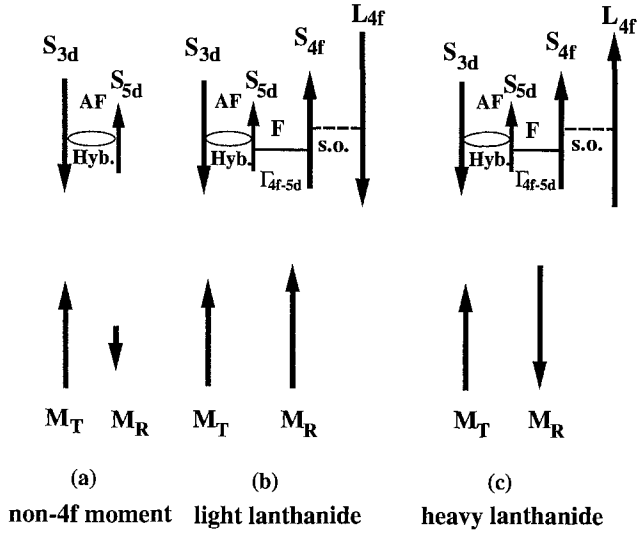




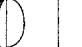








Fig. 5. Schematic description of the compositions of, and interactions between, magnetic moment in R-T compounds. F and AF denote ferromagnetic and antiferromagnetic spin coupling, respectively. The hybridisation (hyb.), 4f-5d local exchange, and spin-orbital interactions (s.o.) are shown. After Duc (1997).

Light-lanthanide elements					
$J =  L - S $					
$\alpha_J < 0$			$\alpha_J > 0$		
					Eu
Ce	Pr	Nd	Pm	Sm	Eu

Heavy-lanthanide elements					
$J = L + S$					
$\alpha_J < 0$			$\alpha_J > 0$		
					
Tb	Dy	Ho	Er	Tm	Yb



La		
La	Gd	Lu

Fig. 6. Angular distribution of the 4f charge density of lanthanide atoms for  $J_z = J$  (effective moment parallel to the z-axis). After Thole cited by Coehoorn (1990). In Ce, Pr, Nd, Tb, Dy, Ho the charge density is oblate ( $\alpha_J < 0$ ); in Pm, Sm, Er, Tm, Yb it is prolate ( $\alpha_J > 0$ ). In Gd and Lu ( $L=0$ ), the charge density has spherical symmetry.

The huge magnetostriction is expected to occur in compounds which combine a high lanthanide concentration with a high ordering temperature. This is the case in the Laves-phase  $RFe_2$  compounds. Magnetic and magnetostrictive properties of  $RFe_2$

are presented in table 2. These compounds exhibit a magnetostriction which is always larger along the [111] direction than along the [100] axis. The highest known room-temperature anisotropic magnetostriction has been found in  $\text{TbFe}_2$  (Clark and Belson 1972) as  $\lambda_{111} = 2.4 \times 10^{-3}$ .  $\text{SmFe}_2$  exhibits a  $\lambda_{111}$  value of similar magnitude, but negative. In  $\text{DyFe}_2$ , the magnetostriction is somewhat smaller than in the other two compounds. This difference has been related to the fact that the easy magnetisation direction in  $\text{TbFe}_2$  and  $\text{SmFe}_2$  is [111], whereas it is [100] in  $\text{DyFe}_2$ . For all these binary alloys, however, a relatively large magnetic field is needed to achieve the technical saturation, due to the rather large magnetocrystalline anisotropy energy. Clark has tried to minimise the fourth-order anisotropy constant  $K_4$  by alloying two different binary  $\text{RFe}_2$  compounds having anisotropy coefficients of different sign. This was possible without dramatically reducing the magnetostriction since in the Laves-phase  $\text{RFe}_2$  compounds, magnetostriction arises mainly from pseudo-dipolar interactions ( $l=2$ ), whereas magnetocrystalline anisotropy is governed by higher order interactions ( $l=4, 6$ ). He succeeded in finding the technically important  $\text{Tb}_{0.27}\text{Dy}_{0.73}\text{Fe}_2$  alloys (Terfenol-D) in which the magnetostriction at room temperature is still sufficient, but the anisotropy is extremely low, because the fourth-order contributions of Tb and Dy almost cancel each other. Lanthanide contribution to the anisotropic magnetostriction in  $\text{RFe}_2$  is well expected within the framework of the single-ion model, where giant magnetostriction as well as magnetocrystalline anisotropy originate from the electrostatic interactions between the anisotropic 4f electron shell of the R ion and the crystal field (Clark 1980).

In the crystalline  $\text{RCO}_2$  compounds, the Curie temperature ( $T_C$ ) has a value much lower than in  $\text{RFe}_2$ . Only in  $\text{GdCo}_2$   $T_C$  exceeds the room temperature (see table 3). For this reason, these compounds are not interesting for application. However, the huge  $\lambda_{100}$  and  $\lambda_{111}$  magnetostriction observed in these compounds should be a point of great attention. While  $\text{GdAl}_2$ ,  $\text{GdNi}_2$  and  $\text{GdFe}_2$  have a magnetostriction not larger than  $8 \times 10^{-5}$ ,  $\text{GdCo}_2$  exhibits at low temperatures a tetragonal distortion corresponding to  $\lambda_{100} = -1.2 \times 10^{-3}$  (Levitin and Markosyan 1990). Similar or even larger  $|\lambda_{100}|$  values have been found also for  $\text{TbCo}_2$ ,  $\text{DyCo}_2$ ,  $\text{HoCo}_2$  and  $\text{ErCo}_2$  (table 3). Additionally, neither the sign nor magnitude of  $\lambda_{100}$  follow the trend expected in the case of an R contribution. This high  $\lambda_{100}$  value was thought to have its origin from the Co atom. The  $\lambda_{111}$  value of  $\text{RCO}_2$ , however, is comparable with that of  $\text{RFe}_2$ , showing the important role of the R sublattice in the formation of this magnetostrictive mode. This seems to suggest that in the  $\text{RCO}_2$  compounds the main condition for the huge magnetostriction, i.e., the local environment, is still satisfied. For applications one would like to increase the ordering temperature of these alloys. Fortunately, this condition can be reached in the amorphous state. This will be presented below and as will be seen in sect. 5, the room-temperature magnetostriction of the amorphous  $\text{RCO}_2$  alloys is comparable to that observed in the amorphous  $\text{RFe}_2$ .

The amorphous alloys are characterised by a structural disorder where each atom constitutes a structural unit. In this state, the small mass density and the loss of the periodicity enhance the localisation of the 3d electrons in the lanthanide-transition metal alloys. In amorphous alloys, at a certain concentration, the 3d magnetic moment

Table 2

Magnetic and magnetostrictive properties of the RFe<sub>2</sub> compounds: Curie temperature ( $T_C$ ), saturation magnetic magnetization ( $M_s$ ), easy magnetization direction (EMD),  $\lambda_s$ ,  $\lambda_{100}$ ,  $\lambda_{111}$ ,  $\lambda^{N^2}$ ,  $\lambda^{E^2}$ , and magnetocrystalline anisotropy coefficient  $K_4$  at 4.2 K (the values in parentheses are data obtained at room temperature)

	CeFe <sub>2</sub>	SmFe <sub>2</sub>	GdFe <sub>2</sub>	TbFe <sub>2</sub>	DyFe <sub>2</sub>	HoFe <sub>2</sub>	ErFe <sub>2</sub>	TmFe <sub>2</sub>	Terfenol-D
$T_C$ (K)	230	660	790	697	624	586	577	560	640
$M_s$ ( $\mu_B$ /f.u.)	2.3	3.1	3.8	5.8	6.8	6.9	6.0	3.7	6.5
EMD	[100]	[110]	[100]	[111]	[100]	[100]	[111]	[111]	[110]*
$\lambda_s$ ( $10^{-6}$ )	0	(-1560)	(39)	(1753)	(433)	(80)	(-300)	(-125)	(1100)
$\lambda_{100}$ ( $10^{-6}$ )	60	30	50		-70	-750			
$\lambda_{111}$ ( $10^{-6}$ )	(-2100)		(2460)	(1260)	(200)	(-300)	(-210)		
	-4100					-1850	-3600		
$\lambda^{N^2}$ ( $10^{-6}$ )					(6)	(-90)	(-450)	(-315)	(2400)
$\lambda^{E^2}$ ( $10^{-6}$ )		(-3150)		(3690)	(1890)	(285)	(-2640)	-5280	
$K_4$ ( $10^{-6} \times J/m^3$ )				(-7.63)	(2.1)	(0.58)	(-0.33)	(-0.053)	
References	[1,2]	[3-5]	[1,6]	[3,6,7]	[3,8-10]	[3,8-11]	[8,9,12]	[3,13]	[9,15]

\* Data determined at 310 K.

#### References

- [1] Franse and Radwanski (1993)
- [2] Deryagin et al. (1985)
- [3] Clark (1980)
- [4] Andreev (1990)
- [5] Korolyov et al. (1990)
- [6] Babara et al. (1977)
- [7] Clark et al. (1978)
- [8] Deryagin et al. (1981)
- [9] Zavorokin (1987)
- [10] Kudrevayikh (1994)
- [11] Abbundi et al. (1979)
- [12] Andreev et al. (1985)
- [13] Abbundi and Clark (1978)
- [14] Deryagin et al. (1984)
- [15] Popov et al. (1980)
- [16] Andreev (1979)

Table 3

Magnetic and magnetostrictive properties of the RCo<sub>2</sub> compounds: Curie temperature ( $T_C$ ), saturation magnetic magnetization ( $M_S$ ), easy magnetisation direction (EMD),  $\lambda_{100}$  and  $\lambda_{111}$  at 4.2 K

	GdCo <sub>2</sub>	TbCo <sub>2</sub>	DyCo <sub>2</sub>	HoCo <sub>2</sub>	ErCo <sub>2</sub>	TmCo <sub>2</sub>
$T_C$ (K)	398	235	137	78	32.4	5
$M_S$ ( $\mu_B$ /f.u.)	5.0	6.3	7.0	7.5	6.9	3.8
EDM	[100]	[111]	[100]	[110]	[111]	[111]
$\lambda_{100}$ ( $10^{-6}$ )	-1200	-1200	-1900	-2200	-1000	750
$\lambda_{111}$ ( $10^{-6}$ )	100	4500	5000	500	-2550	-4100
Refs.	[1,2,3]	[2,3,4]	[2,3]	[2,3]	[2,3,5]	[4]

#### References

- |                                 |                              |
|---------------------------------|------------------------------|
| [1] Franse and Radwanski (1993) | [4] Morin and Schmitt (1990) |
| [2] Markosyan (1988)            | [5] Andreev et al. (1985)    |
| [3] Nakamura (1983)             |                              |

is higher but the 4f–3d exchange interactions are somewhat weaker in comparison with the crystalline alloys. These parameters, however, follow the same tendencies with varying concentrations (Duc and Givord 1996). These results confirm again the systematic variation of the 3d–5d hybridisation and their role in the magnetism of the lanthanide–transition metal compounds. The decrease of the transfer and of the associated hybridisation allow the conservation of the strongly ferromagnetic character over a large range of the concentrations, i.e., there exists a large value for the critical lanthanide concentration where the magnetism disappears in the amorphous alloys. These effects lead to the enhancement of the Curie temperature when going from the crystalline state to the amorphous state for the R–Co alloys: the ordering temperature of a-TbCo<sub>2</sub> is comparable with that of a-TbFe<sub>2</sub> ( $T_C > 400$  K) (see fig. 7) (Hansen et al. 1989, Hansen 1991). For the a-RFe compounds, however, the magnetic properties are not improved by the amorphisation, but just the opposite. Due to the amorphous structure, the Fe–Fe interatomic distance is distributed and the Fe–Fe exchange interactions can sometimes be positive or negative. This leads to the effects of the frustration and freezing of the magnetic moments in the Fe sublattice and to form the speromagnetism as observed for Y<sub>1-x</sub>Fe<sub>x</sub> (Coe 1978, Chappert et al. 1981).

Speromagnetism occurs in two-sublattice structures like lanthanide–transition metal alloys of composition R<sub>1-x</sub>T<sub>x</sub> where the 4f–3d exchange interactions are not modified (Duc and Givord 1996, Danh et al. 1998), but the large spin–orbit coupling of the non-S-state lanthanides gives rise to large local anisotropies (local easy magnetisation axis). For the two classes of alloys distinguished with light and heavy lanthanides, we can again divide the amorphous R–T alloys into four groups of sperimagnetic structures as illustrated in fig. 8:

- an asperomagnetic LR sublattice with a collinear T sublattice (like Sm–Co),
- an asperomagnetic HR sublattice with a collinear T sublattice (like Tb–Co),

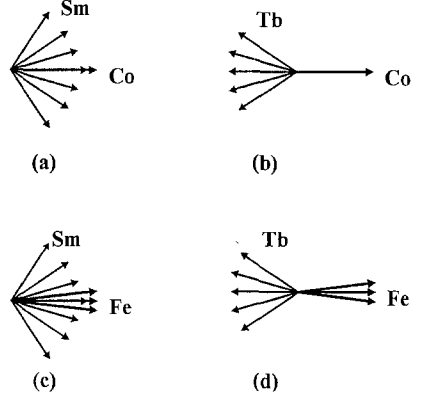
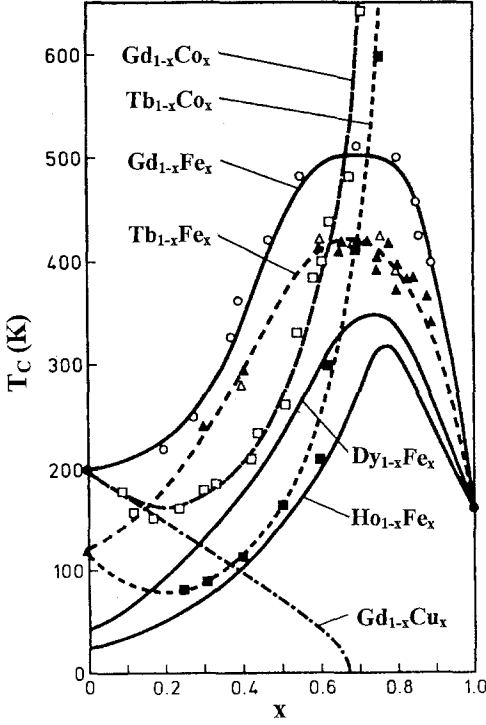


Fig. 8. Sperimagnetic structures in amorphous alloys: (a) Sm-Co; (b) Tb-Co; (c) Sm-Fe; (d) Tb-Fe.

Fig. 7. Compositional variation of the Curie temperature for amorphous  $R_xT_{1-x}$  alloys. After Hansen (1991) and references therein.

– an asperomagnetic LR sublattice with a non-collinear T sublattice (like Sm-Fe),  
 – an asperomagnetic HR sublattice with a non-collinear T sublattice (like Tb-Fe).  
 In these sperimagnetic structures, the subnetwork magnetisations are reduced. The influence of the exchange interactions and a random axial anisotropy on the average magnetic moment can be described using the Hamiltonian (Harris et al. 1973)

$$H = - \sum A_{ij} J_i J_j - \sum D_i (n_i J_i)^2 - g_R \mu_B \sum B J_i, \quad (8)$$

where  $i, j = R, T$ ,  $A_{ij}$  is the exchange-coupling parameter,  $D$  is the magnetocrystalline coupling constant,  $J$  is the total moment, and  $B$  is the external magnetic field. In this case, the energy at  $T = 0$  K can be expressed as

$$E_i = -(B + B_{\text{exch}}) J_R \cos \theta_i - D J_R^2 \cos^2(\phi_i - \theta_i), \quad (9)$$

where the exchange interactions were treated in the molecular field approximation.  $\theta_i$  and  $\phi_i$  represent the angles between the direction of the magnetic field and the magnetic moment with respect to the local easy axis, respectively. Neglecting R-R interactions, the exchange field  $B_{\text{exch}}$  is given as (Duc 1997)

$$B_{\text{exch}} = -Z_{RT} A_{RT} S_R / \mu_B,$$

with  $Z_{RT}$  the number of T-nearest neighbours of one R atom.

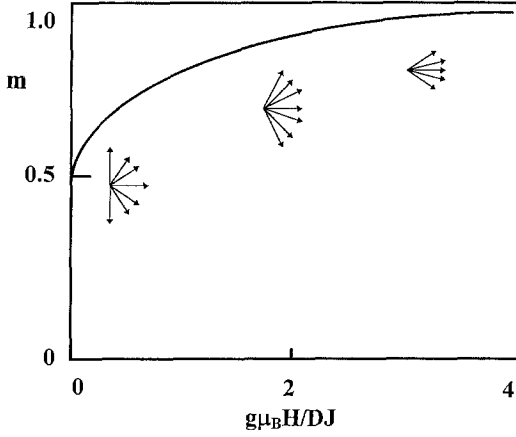


Fig. 9. Relative magnetisation curves for an array of magnetic ions with random easy axis anisotropy at  $T=0\text{K}$ .

The reduced magnetic moment of the lanthanide sublattice  $m = \langle J_z \rangle / J$  can then be calculated as

$$m = \int_0^{\pi/2} \cos \theta_i \sin \phi_i d\phi_i. \quad (10)$$

With increasing magnetic field, however, the fanning angle of the asperomagnetic structure is reduced and saturation can only be reached when the applied field significantly exceeds the local anisotropy field (see fig. 9). Practically, for most amorphous  $R_{1-x}T_x$  compounds, this limit cannot be reached even in fields up to 30 T. To solve this problem, the strengthening of the R–T exchange field may help. Indeed, as will be presented in sect. 5.2, this solution has successfully been applied to the a-(Tb,Dy)(Fe,Co) system, where the R–(Fe,Co) exchange energy was thought to exceed both that of R–Fe and that of R–Co (Duc et al. 1996, 2000a).

At  $T > 0\text{K}$ , besides the average of the spatial projection (identified with angle brackets), one must also take account of the thermal average of the magnetic moment (identified by an overline). Thus, the total average lanthanide magnetic moment is

$$\langle \overline{J_R} \rangle = J_R \int_0^\pi \sin \phi_i d\phi_i \frac{\int_{\theta_i \psi_i} \cos \theta_i \sin \theta_i \exp(-E_i/k_B T) d\theta_i d\psi_i}{\int_{\theta_i \psi_i} \sin \theta_i \exp(-E_i/k_B T) d\theta_i d\psi_i}. \quad (11)$$

The direction cosine for each lanthanide moment with respect to the field direction is expressed as

$$\alpha_z = \int_0^\pi \sin \phi_i d\phi_i \frac{\int_{\theta_i \psi_i} \cos^2 \theta_i \sin \theta_i \exp(-E_i/k_B T) d\theta_i d\psi_i}{\int_{\theta_i \psi_i} \sin \theta_i \exp(-E_i/k_B T) d\theta_i d\psi_i}. \quad (12)$$

Equations (11) and (12) will be used to discuss the sperimagnetic structure of the magnetostrictive Tb–Co alloys in sect. 5.2.

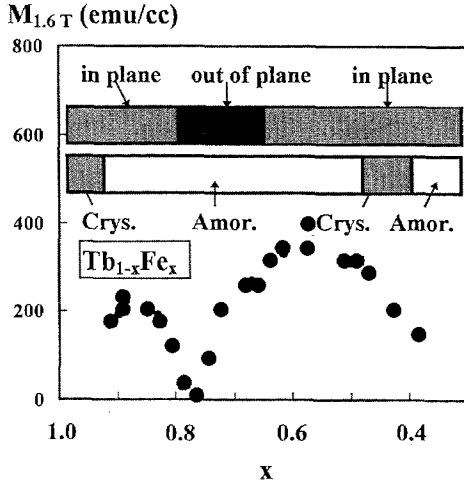


Fig. 10. Room-temperature magnetisation as a function of Tb concentration for  $Tb_{1-x}Fe_x$  films. The corresponding crystal and magnetic structures are shown. After Miyazaki et al. (1997).

## 5. Giant magnetostrictive thin film materials

### 5.1. Thin film systems

#### 5.1.1. R-Fe thin films

5.1.1.1. *Tb-Fe thin films.* Traditionally, the R-Fe based alloys are thought to be the best candidates giving giant magnetostriction in the bulk as well as in film materials. The common approach to amorphous R-Fe magnetostrictive thin films is to reduce the macroscopic anisotropy to achieve the magnetostriction saturation in low magnetic fields. The magnetic and magnetostrictive properties and magnetic anisotropy of the amorphous binary  $Tb_{1-x}Fe_x$  films as a function of the Tb concentration have been the subject of many investigations (Forester et al. 1978, Hansen et al. 1989, Hayashi et al. 1993, Quandt 1994a, Grundy et al. 1994, Huang et al. 1995, Hernando et al. 1996 and Miyazaki et al. 1997). Results of these investigations on the Tb-concentration dependence of the magnetization, the easy magnetisation direction (EMD) and the structural behaviours are shown in fig. 10. Low saturation magnetisation around  $x=0.77$  implies the compensation of the subnetwork Tb- and Fe-magnetisations. Around this compensation point ( $0.8 \leq x \leq 0.65$ ), the EMD is along the film normal. The existence of this perpendicular anisotropy suggests potentials for application as perpendicular magnetic and magneto-optic recording materials. The origin of this perpendicular anisotropy, however, is still not well understood. Local magnetic anisotropy in the R-T alloys results from the combination of the electrostatic interaction between 4f cloud with its electric environment, and the large spin-orbit coupling. The 4f-electronic cloud of Tb has the shape of an oblate ellipsoid with magnetic moment perpendicular to the equatorial plane. If the macroscopic EMD of the sample is along the film normal, the equatorial plane of the 4f cloud has to be preferentially in the film plane. Such a configuration should correspond to either an excess of environment negative charge along the polar direction or an excess of environment positive charge

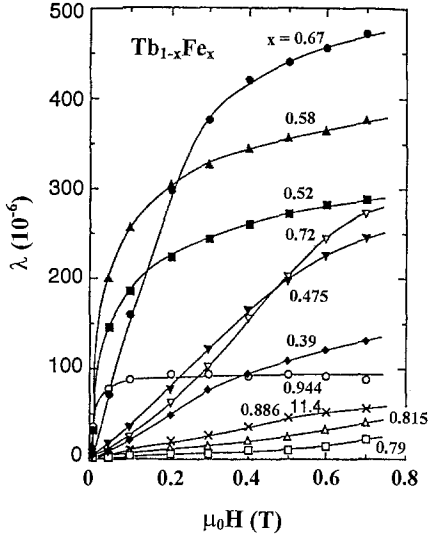


Fig. 11. Room-temperature magnetostriction for  $Tb_{1-x}Fe_x$  films. After Miyazaki et al. (1997).

along the equatorial directions. The EXAFS and magnetic anisotropy studies performed by Huang et al. (1995) and Hernando et al. (1996) have suggested that the origin of the perpendicular anisotropy in *a*-TbFe thin films should be the excess of the positive charge in the equatorial direction of the 4*f* cloud. They also show that Tb–Fe bonds mainly lie along the in-plane directions for films with  $x < 0.7$ , where anisotropy and magnetostriction are high and stable. This supports a “point-charge” model for the explanation of the structural origin of the anisotropy.

Magnetostriction curves measured in magnetic fields up to 0.7 T applied parallel to the film plane for several *a*- $Tb_{1-x}Fe_x$  thin films are presented in fig. 11. For all samples, except for  $x = 0.944$  which has the bcc-Fe structure, the field dependence of the magnetostriction shows a relatively large random anisotropy. The values of the magnetostriction in the as-deposited TbFe thin films collected from different sources are summarised in fig. 12a,b. Although there is some scatter they show a compositional variation of the magnetostriction, which is very similar to that observed for polycrystalline Tb–Fe compounds. A magnetostriction maximum occurs around  $0.55 \leq x \leq 0.67$ . In fact, at  $\mu_0 H = 0.7$  T, the largest magnetostriction of about  $480 \times 10^{-6}$  was found at  $x = 0.67$  which corresponds to an alloy of the  $TbFe_2$  composition (Miyazaki et al. 1997, see fig. 12b). This confirms again the role of the optimal combination of the lanthanide concentration and the magnetic ordering temperature (see fig. 7, sect. 4) on the giant magnetostriction. The magnetostriction maximum shifts to higher Tb content with decreasing the applied magnetic field and a magnetostriction maximum of  $220 \times 10^{-6}$  was obtained at  $x = 0.58$  in  $\mu_0 H = 0.1$  T.

The hard magnetostrictive property of the sample with  $x = 0.67$  is thought due to its perpendicular anisotropy. In order to obtain a soft magnetostrictive behaviour for this alloy, attempts to reduce the magnetic anisotropy have been undertaken. Altering



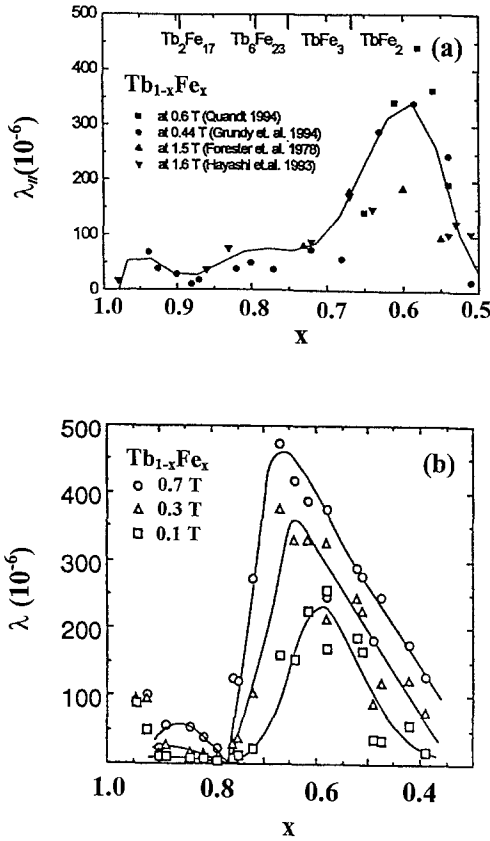


Fig. 12. Magnetostriction as a function of Tb concentration for  $Tb_{1-x}Fe_x$  films. After (a) Quandt (1997) and (b) Miyazaki et al. (1997).

the deposition conditions, e.g., by applying a r.f. bias voltage (Quandt 1994a), the tensile stress obtained can lead to an in-plane magnetic easy axis and to dramatically improved magnetostriction at low fields. Miyazaki et al. (1997), Wada et al. (1997a,b) have also succeeded to enhance the low field magnetostriction, however, by varying the substrate temperature and the heat treatments. Miyazaki et al. showed that the soft magnetostrictive property of the Tb-Fe films can be improved by the heat treatments just below the crystallisation temperature ( $T_x$ ) at about 600 K. With these treatments, however, a perpendicular magnetic anisotropy appears in the mixed state of amorphous and crystalline structures (see sect. 5.1.1.2, fig. 17). In this case, therefore, the origin of the recovery of the soft magnetostrictive behaviour is not due to the reduction of perpendicular anisotropy, but the main reason is related to phase segregations (Miyazaki et al. 1997). The role of heat treatment, here, is to separate the single amorphous phase in the as-deposited state into two Tb-rich and Tb-poor phases before the alloy is crystallised. As already mentioned above, the Tb-rich phase is magnetically (and magnetostrictively) rather soft. In this state, the weak magnetic character is mainly governed by this Tb-

rich phase. With further increase of the annealing temperature, the Tb-rich phase may decompose into a TbFe<sub>2</sub> Laves-phase and Tb oxides. Also, the Tb-poor phase may decompose into a TbFe<sub>2</sub> Laves-phase and pure iron and/or its oxides. Therefore, after crystallisation, the magnetic and magnetostrictive properties become very hard. From X-ray diffraction data, however, only the TbFe<sub>2</sub> Laves-phase and Tb oxides were observed to occur, see below in the following section.

The EMD of a magnetostrictive film is directly related to the film's stress. The change of the orientation of the film's EMD can be determined by considering the minimum of the magnetoelastic energy for an isotropic ferromagnet (du Trémolet de Lacheisserie 1993):

$$E_{me} = -\frac{3}{2} \sigma \cdot \lambda_s \cos^2 \alpha, \quad (13)$$

where  $\sigma$  is film stress and  $\alpha$  is the angle between the directions of the magnetisation and of the application of the stress.

For a material with a given saturation magnetostriction, the EMD depends on the sign of the film stress  $\sigma$ . Equation (13) implies an in-plane EMD for a positive product  $\sigma \cdot \lambda_s$ , while a negative product results in a perpendicular anisotropy. In the case of positive magnetostrictive Tb-based films, tensile stress is required for parallel anisotropy, and compressive stress results in a perpendicular anisotropy. The sign and the magnitude of the film's stress were controlled by the fabrication conditions (Quandt 1994a), by the thermal expansion coefficients of the substrate (Schatz et al. 1994) or by stress annealing (Duc et al. 1996). Films deposited on silicon and on titanium substrates show tensile stress of about 200 MPa whereas films on CuBe and on stainless steel exhibit compressive stress of the same order.

The different magnetostrictive behaviours were explained by considering the nature of the magnetisation processes (Schatz et al. 1994). A spin rotation induces a change in magnetisation as well as magnetostriction. This corresponds to the the motion of 90°-domain walls. A magnetisation caused only by the motion of 180°-domain walls, however, cannot lead to any magnetostriction. According to the rotation of the magnetic moments out of the easy axis, the magnetostriction as a function of magnetisation and magnetic field can be given as (Chikazumi 1964)

$$\frac{\lambda(H)}{\lambda_s} = \left( \frac{M(H)}{M_{\max}} \right)^2. \quad (14)$$

For amorphous alloys described by the random anisotropy model (Cochrane et al. 1978) as well as for polycrystalline materials, the EMD is isotropically distributed. In this case, spin orientation and domain walls are randomly distributed. The magnetisation process therefore consists of two steps: (i) the motion of 180°-domain walls leading to a magnetisation of  $M_s/2$  without any magnetostriction, and (ii) the rotation of spins into

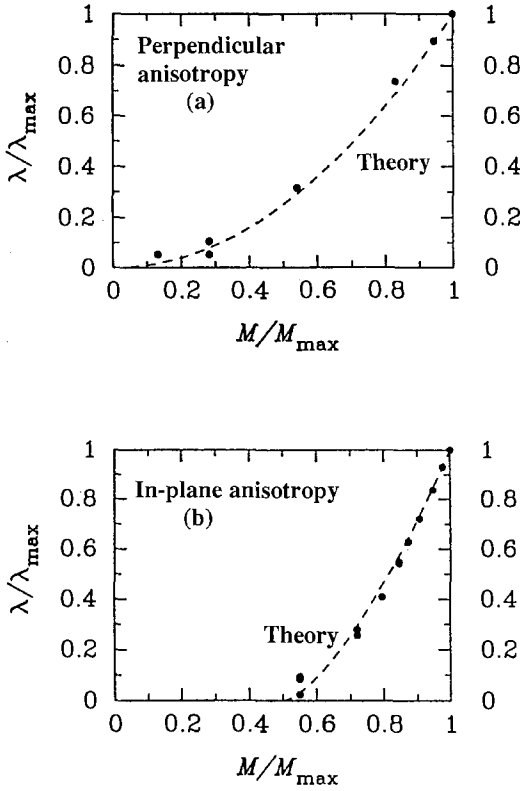


Fig. 13. Normalised magnetostriction as a function of normalised magnetisation for  $(\text{Tb}_{0.27}\text{Dy}_{0.73})_{0.42}\text{Fe}_{0.58}$  films with (a) perpendicular and (b) parallel anisotropies. Dashed curves indicate the theoretical behaviour described by eqs. (14) and (15), respectively. After Schatz et al. (1994).

the direction of the applied magnetic field. Instead of eq. (14), the relationship between magnetostriction and magnetisation now becomes (Schatz et al. 1994)

$$\frac{\lambda(H)}{\lambda_s} = \left( \frac{2M(H)}{M_{\max}} - 1 \right)^{3/2}. \quad (15)$$

Normalised magnetostriction as a function of normalised magnetisation for films with perpendicular and parallel anisotropies is plotted in figs. 13a,b. It was derived that the films with in-plane anisotropy show high magnetostriction at low fields due to the easy rotation of the spins in the isotropic plane even if the motion of  $180^\circ$ -domain walls does not contribute to magnetostriction. For the films with perpendicular anisotropy, the magnetisation is governed only by rotations into the plane. In contrast to the rotations in the isotropic easy plane, these rotations out of the EMD require larger external fields.

5.1.1.2. *(Tb,Dy)-Fe thin films.* By assuming that the same local environment in the amorphous state is similar to the crystalline one, a further approach to lower the remaining anisotropy is by eliminating the fourth-order anisotropy by substitution of Tb by Dy (Williams et al. 1994, Wada et al. 1996, 1997a-d, Miyazaki et al. 1997).

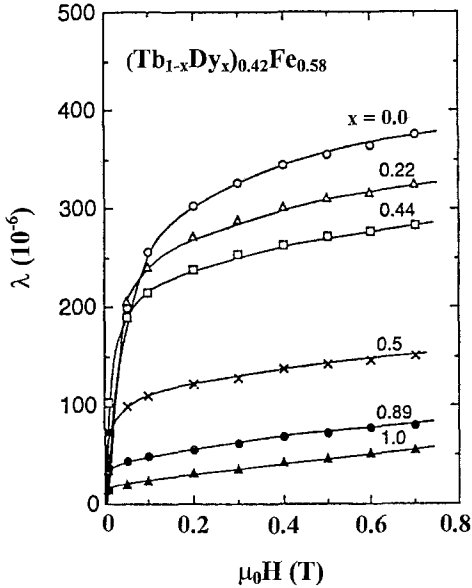


Fig. 14. Room-temperature magnetostriction for  $(\text{Tb}_{1-x}\text{Dy}_x)_{0.42}\text{Fe}_{0.58}$  films. After Miyazaki et al. (1997).

The well-known composition of the bulk Terfenol-D alloy is  $\text{Tb}_{0.3}\text{Dy}_{0.7}\text{Fe}_2$ . Recently, however, Miyazaki et al. have succeeded to confirm the compensation of the magnetic anisotropy in the  $a\text{-(Tb,Dy)}_{0.42}\text{Fe}_{0.58}$  thin films also occurs at the 3:7 Tb:Dy ratio. Room temperature magnetostriction curves for the  $a\text{-(Tb}_{1-x}\text{Dy}_x)_{0.42}\text{Fe}_{0.58}$  thin films are presented in fig. 14. Note that with increasing  $x$  the value of  $\lambda$  decreases and tends to saturate with smaller magnetic field. In addition, the magnetostriction data measured at  $\mu_0H=0.008$ , 0.05 and 0.7 T are plotted as a function of  $x$  in fig. 15a. At  $\mu_0H=0.05$  and 0.7 T,  $\lambda$  does not decrease monotonically with  $x$  but exhibits a broad peak around  $x=0.7$ . This concentration dependence of  $\lambda$  is rather similar to that of bulk polycrystalline  $(\text{Tb}_{1-x}\text{Dy}_x)\text{Fe}_2$  compounds (see fig. 15b). It indicates the near-zero magnetic anisotropy in a film of Terfenol-D composition. The atomic short-range order of sputtered amorphous films, thus, can be considered as quite similar to that of crystalline bulk samples and the same origin of the magnetic anisotropy as well as magnetostriction can be expected for both film and bulk alloys. We will return to this aspect in the discussion of  $a\text{-(Tb,Dy)(Fe,Co)}$  films in sect. 5.1.2.2.

Effects of the substrate temperature, of the annealing treatment on the microstructure, magnetic domains and then on the magnetic and magnetostrictive properties of the Terfenol-D films have been investigated by Wada et al. (1997c,d). Their results showed that a high magnetostrictive susceptibility ( $\partial\lambda/\partial H$ ) can only be observed in films formed at substrate temperature below 405 K. In these films, nanocrystalline structures with grains below 5 nm were evidenced. The measured hysteresis loops and the observations of the magnetic domains in applied magnetic fields seem to indicate a preferential perpendicular magnetisation by spin rotations with low anisotropy in these nanocrystalline

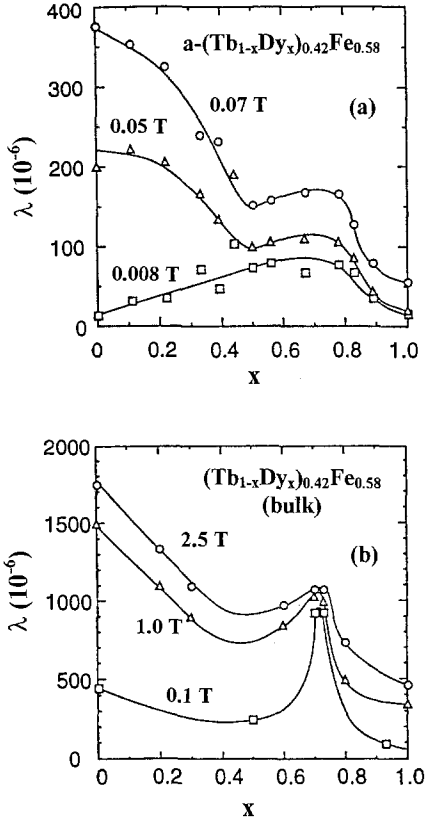


Fig. 15. Magnetostriction as a function of Dy content for (a)  $a-(Tb_{1-y}Dy_y)_{0.42}Fe_{0.58}$  films and (b) bulk  $(Tb_{1-y}Dy_y)_{0.42}Fe_{0.58}$  alloys. After Miyazaki et al. (1997) and references therein.

films (n-films). The films formed at temperatures between 410 K to 600 K were found to have grains with a size from 5 nm to 10 nm. It was recently reported by Ried et al. (1998) that samples annealed at 600°C for 10 minutes also have grains with a size around 10 nm and exhibit an in-plane magnetostriction of  $860 \times 10^{-6}$ . For these grown polycrystalline films (p-films), however, the results suggested that the magnetisation is governed by the motion of domain walls at low magnetic fields. The change in the normalised in-plane magnetostriction  $\lambda_{||}/\lambda_s$  as a function of the normalised magnetisation of these films is plotted in fig. 16. It can be seen that at low magnetic fields, the n-film shows a much higher magnetostrictive response to the magnetisation than the grown p-film. The parabolic dependence of the in-plane magnetostriction on in-plane magnetisation observed for the n-film is in good agreement with the as-mentioned arguments and with the experimental results for the motion of  $90^\circ$  domain walls, i.e., the rotation of spins with perpendicular anisotropy into the plane (see also eq. 14 and fig. 13a). For the p-film, almost no magnetostriction takes place up to  $M/M_{\max} = 0.2$ . This behaviour seems to be the case, and was described by Schatz et al. (1994) (see also eq. 15), for random distributions of spins.

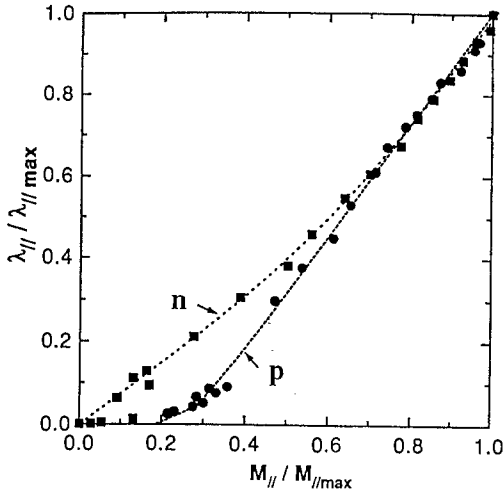


Fig. 16. Normalised magnetostriction as a function of normalised magnetisation for nanocrystalline (n) and polycrystalline (p)  $(\text{Tb}_{0.3}\text{Dy}_{0.7})\text{Fe}_2$  films. After Wada et al. (1997c).

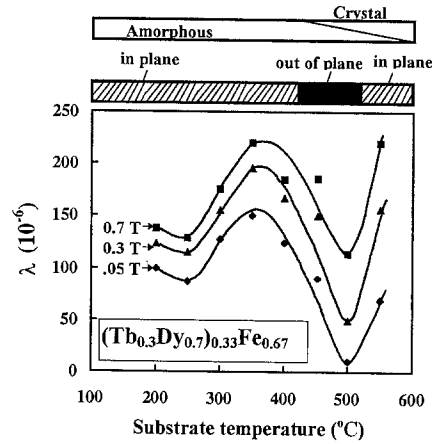


Fig. 17. Magnetostriction as a function of substrate temperature for  $(\text{Tb}_{0.3}\text{Dy}_{0.7})\text{Fe}_2$ . After Miyazaki et al. (1997).

The appearance of a perpendicular anisotropy in the mixed state of both amorphous and crystalline structure, where the magnetostriction becomes hard was reported by Miyazaki et al. (1997) for the  $(\text{Tb}_{0.3}\text{Dy}_{0.7})_{0.33}\text{Fe}_{0.67}$  films fabricated above 673 K (400°C) (see fig. 17). Study of the thermal stability and the reproducibility of those films was also carried out. For films prepared with substrate temperatures above 673 K (400°C), the magnetostriction changes remarkably after 3 months. This is due to aging effects, which lead to the formation of the Laves phase  $(\text{Tb,Dy})\text{Fe}_2$  compound.

**5.1.1.3. Sm-Fe thin films.** A negative magnetostriction was actually observed in amorphous Sm-Fe thin films (Hayashi et al. 1993, Honda et al. 1993, 1994). For these films, the room-temperature magnetostriction increases rapidly in low fields due to the in-plane anisotropy. The maximum absolute  $\lambda$ -values of about  $250\text{--}300 \times 10^{-6}$  at 0.1 T and  $300\text{--}400 \times 10^{-6}$  at 1.6 T were obtained on films with 30–40 at.% Sm. Honda et al. (1994) have used these magnetostrictive films for the fabrication of trimorph TbFe/polyimide/SmFe cantilevers (see fig. 43a, below). Applying a bias voltage, it was again possible to alter the stress state to tensile stress, which resulted in a perpendicular anisotropy due to the negative but increased saturation magnetostriction (Quandt 1997). In contrast to Tb-Fe films, crystallisation of Sm-Fe films does not result in a higher saturation magnetostriction, but only the hysteresis was found to be significantly increased. Boron added to the  $\text{SmFe}_2$  alloy improves the formability of the amorphous state, reduces the local magnetic anisotropy energy (Polk 1972) and, thus, can enhance the low-field magnetostriction. This was examined by Kim (1993)

on the dc-sputtered  $(\text{SmFe}_2)_{100-x}\text{B}_x$  system with a thickness of 0.3 mm. In these alloys, the saturation magnetisation decreases with increasing  $x$ , whereas the saturation magnetostriction significantly increases. The highest saturation magnetostriction of  $-670 \times 10^{-6}$  at 1.0 T with an effective magnetostriction of  $-490 \times 10^{-6}$  at 0.03 T can be obtained for the  $a\text{-(SmFe}_2)_{99.26}\text{B}_{0.74}$  alloy. A similar result was also reported for amorphous bulk  $(\text{Sm,Tb})\text{Fe}_2\text{-B}$  alloys (Fujimori et al. 1993, Shima et al. 1997).

### 5.1.2. R-Co thin films

5.1.2.1. *Tb-Co and (Tb,Dy)-Co thin films.* The magnetostriction of  $a\text{-Tb}_{1-x}\text{Co}_x$  ( $0.78 \geq x \geq 0.38$ ) thin films was studied intensively by Betz et al. (1999) (see also Givord et al. 1995, Betz 1997). These alloys are ferrimagnets. Their Curie temperatures are above room temperature for  $x \geq 0.62$ . For  $x \approx 0.67$ ,  $T_C$  reaches approximately 500 K which is already higher than that of the  $a\text{-TbFe}_2$ . Room-temperature magnetostriction is shown fig. 18 for several  $a\text{-Tb}_{1-x}\text{Co}_x$  films. The magnetostriction is always positive. The compositional variation of magnetostriction is shown in fig. 19. It is clearly seen that the magnetostriction increases rapidly with the increasing Co content when the films become magnetic at room temperature and reaches a maximum around  $x = 0.71$  ( $b_{\parallel} = 20$  MPa,

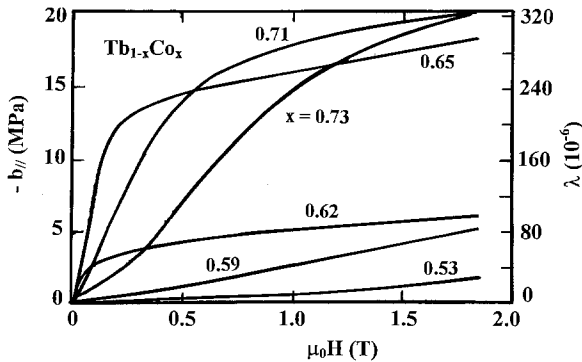


Fig. 18. Room-temperature magnetostriction for several  $a\text{-Tb}_{1-x}\text{Co}_x$  alloys. After Givord et al. (1995).

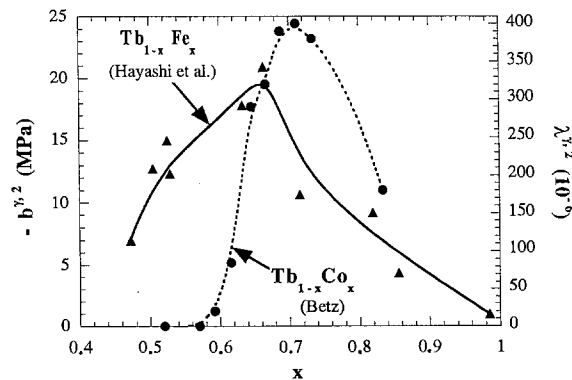


Fig. 19. Magnetostriction as a function of Tb concentration for thin films of  $a\text{-Tb}_{1-x}\text{Co}_x$  (after Betz 1997) and  $a\text{-Tb}_{1-x}\text{Fe}_x$  (after Hayashi et al. 1993).

$b^{\gamma,2} = 23.5$  MPa under  $\mu_0 H = 1.9$  T which corresponds to  $\lambda_{\parallel} = 320 \times 10^{-6}$ ,  $\lambda^{\gamma,2} = 400 \times 10^{-6}$  assuming  $E_f = 80$  GPa and  $\nu_f = 0.3$ ). For comparison, the magnetostriction results for a-TbFe measured at a field of 1.6 T by Hayashi et al. (1993) are also included in the same fig. 19. These early published results were corrected by multiplying a corrected-term  $(1 - \nu_s)/(1 + \nu_s)$  for the use of the former Klokholm's formula (Betz 1997, Betz et al. 1999). It is also meaningful to consider the magnetostrictive susceptibility  $\partial b/\partial H$  (and/or  $\partial \lambda/\partial H$ ), which is of significance for applications. For the films under consideration, at low applied magnetic field, however, the magnetostrictive susceptibility is maximum for  $x = 0.65$ . The fact that  $b^{\gamma,2}$  is larger for the a-Tb-Co system than for a-Tb-Fe is probably due, on the one hand, to the higher Tb-Co exchange energies for the Tb-Co films even though the Co moments are smaller than those of Fe. So the higher values of  $b^{\gamma,2}$  can be explained by the ferromagnetic Co-Co interactions which increase the magnetoelastic coupling. On the other hand, it may be caused by the ordering temperature, which is higher in the case of a-Tb-Co. Betz et al. (1999) thus have succeeded to show the similarity of the compositional variation of the magnetostriction in both a-TbFe and a-TbCo alloys and opened up a promising series of magnetostrictive alloys for potential applications.

A biaxial anisotropy, which is characterised by the linear part between the saturation and the hysteresis in the magnetisation loops was observed for as-deposited Tb-Co films. This is due to the competition of the in-plane and the perpendicular anisotropy. As the observed stresses are compressive and the magnetostriction of a-TbCo is positive, the anisotropy tends to create an EMD along the film normal. In this case, however, the biaxial anisotropy still appears because the stresses is not strong enough to dominate the demagnetisation field. Within the biaxial anisotropy model and combining the eqs. (7) and (13), Betz et al. (1999) have deduced the stresses in a-TbCo films. Logically, a decrease of  $\sigma$  as a function of the film thickness ( $t$ ) (a roughly  $1/t$  dependence, but with a high initial stress) was found (fig. 20). If the in-plane stresses were isotropic, then only a perpendicular component would be generated by this mechanism. We know, however, that the stress is rather inhomogenous – perhaps due to the substrate clamping during the deposition. This stress creates also an anisotropy between the different directions in the film plane (see also Takagi et al. 1979).

The comparison between  $b_{\parallel}(\lambda_{\parallel})$  and  $b_{\perp}(\lambda_{\perp})$  indicates clearly the anisotropy state of the sample. If the zero-field state is fully isotropic, then  $b_{\parallel} = -2b_{\perp}$ , and if it is isotropic in the plane, then  $b_{\parallel} = -b_{\perp}$ . For a well-defined in-plane uniaxial system, which is usually perpendicular to the sample length in the experimental set-ups (Duc et al. 1996, Betz 1997), magnetisation reversal under a field applied along the easy axis, occurs by the displacement of the  $180^\circ$ -domain walls. Neglecting the domain-wall contributions, no magnetostriction is associated with this process. Thus,  $b_{\perp}$  should be zero and  $b_{\parallel} = b^{\gamma,2}$ . Figures 21a,b show the magnetostriction for the rf-sputtered  $\text{Tb}_{0.27}\text{Dy}_{0.73}(\text{Co}_{0.83}\text{Fe}_{0.17})_2$  and  $\text{Tb}_{0.27}\text{Dy}_{0.73}\text{Fe}_2$  films. Here we see that for the as-deposited  $\text{Tb}_{0.27}\text{Dy}_{0.73}(\text{Co}_{0.83}\text{Fe}_{0.17})_2$ ,  $b_{\parallel} \approx -b_{\perp}$  indicating an in-plane isotropy, whereas the as-deposited  $\text{Tb}_{0.27}\text{Dy}_{0.73}\text{Fe}_2$  has already a certain initial anisotropy evidenced by  $b_{\perp} = -0.12b_{\parallel}$ . After field annealing at  $250^\circ\text{C}$ , opposite effects are observed:  $b_{\parallel}$  increases and  $b_{\perp}$  is significantly reduced ( $b_{\perp} = 0.25b_{\parallel}$ , see fig. 21a), i.e., a well-defined in-plane,



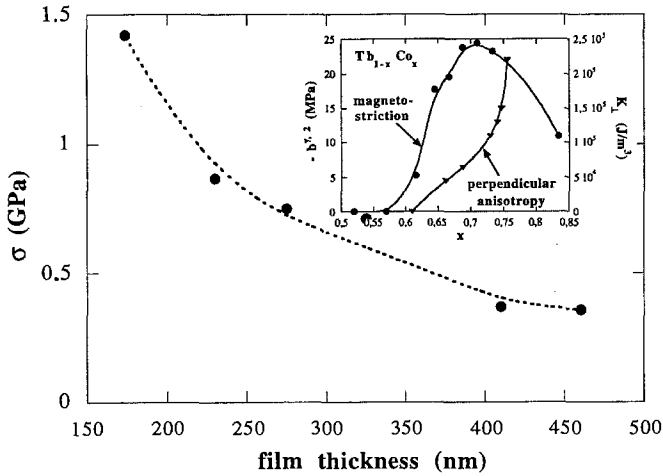


Fig. 20. Calculated stress  $\sigma$  as a function of film thickness for Tb-Co films. The variations of perpendicular anisotropy and magnetoelastic coefficient as functions of composition are shown in the inset. After Betz et al. (1999).

uniaxial anisotropy is created for  $\text{Tb}_{0.27}\text{Dy}_{0.73}(\text{Co}_{0.83}\text{Fe}_{0.17})_2$ , whereas the sample becomes in-plane isotropic for  $\text{Tb}_{0.27}\text{Dy}_{0.73}\text{Fe}_2$  ( $b_{\parallel} = -b_{\perp}$ , fig. 21b). This effect will be analysed in more detail in sect. 5.1.2.2. Annealing effects under magnetic field, thus, are interesting not only to relax the film stresses but also to create a uniaxial anisotropy in the Tb-Co films. In the case of R-Fe films, however, only the first effect plays a role. This effect increases  $b^{1/2}$  in R-Fe films, however, it is not so interesting for applications as R-Co, where the magnetostrictive properties are mainly improved in the preferential direction. Field-annealing effects in the (Tb,Dy)(Fe,Co) systems will be discussed in sect. 5.1.2.2.

The maximum magnetostriction found in the amorphous state for both Tb-Fe and Tb-Co alloys is much lower than in the crystalline state. There are three reasons to be considered for this difference. (i) The structure is not the same in the crystalline and the amorphous state. Nevertheless, it is often argued that the local environment in the amorphous state is reminiscent of that found in the crystalline one. As a starting point for the discussion, differences in the local environment can be neglected. The measured differences in magnetostriction between the crystalline and amorphous states might then be attributed to the facts that (ii) some compositions have a lower ordering temperature in the amorphous state which means that the magnetocrystalline anisotropy and so the magnetoelastic coupling coefficient is lower, and (iii) the sperimagnetic arrangement of the Tb-moment in the amorphous case gives rise to a distribution of the Tb-moments which lower the projected magnetisation and magnetostriction. In order to verify the latter argument, Betz (1997) has compared the mean Tb-magnetic moment in the a- $\text{Tb}_{1-x}\text{Co}_x$  and c- $\text{Tb}_{1-x}\text{Co}_x$  alloys and determined the variation of the low-temperature Tb-sperimagnetic cone angle  $\theta$  as shown in fig. 22. This result is comparable with that published in the literature (Cochrane et al. 1978, Danh et al. 1998).

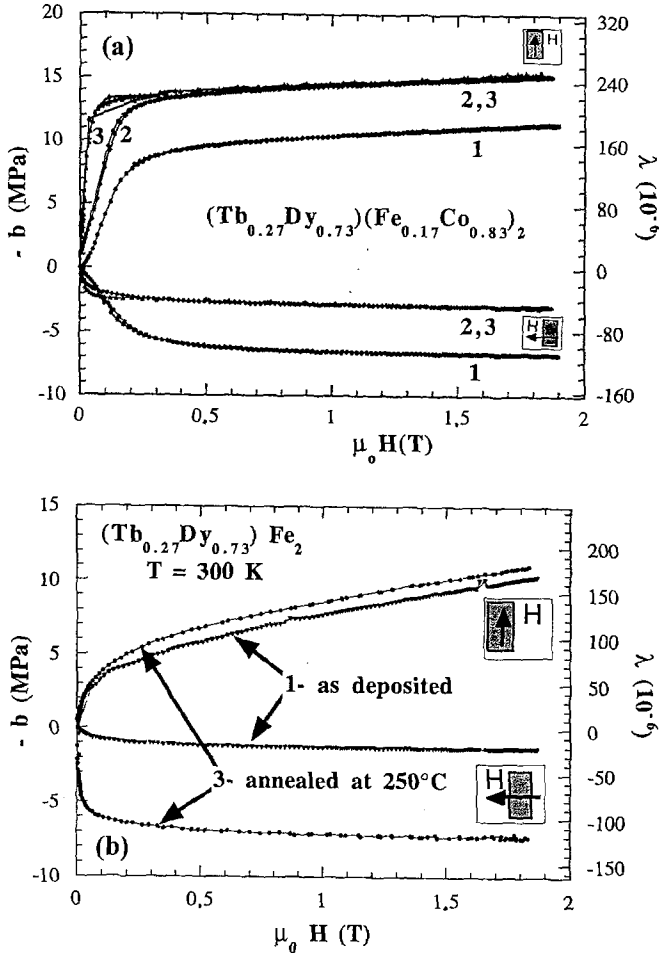


Fig. 21. Room-temperature magnetostriction for  $\text{Tb}_{0.27}\text{Dy}_{0.73}(\text{Co}_{0.83}\text{Fe}_{0.17})_2$  and  $\text{Tb}_{0.27}\text{Dy}_{0.73}\text{Fe}_2$  films: (1) as-deposited; (2) annealed at 150°C; (3) annealed at 250°C. The measured directions along and perpendicular to the sample length are indicated. After Duc et al. (2000a).

In general, the lanthanide saturation magnetisation can be calculated by applying eq. (11) and the magnetostriction of a sperimagnetic system can be evaluated by using the expression

$$\lambda^{\gamma,2} = \frac{3}{2} \lambda_{\text{int}}^{\gamma,2} (\langle \alpha_z^2 \rangle - 1), \quad (16)$$

where  $\lambda_{\text{int}}^{\gamma,2}$  is an intrinsic magnetoelastic coupling coefficient of the corresponding collinear ferrimagnet and  $\alpha_z$  is the direction cosine for each lanthanide moment with respect to the field direction, which was already introduced in sect. 4 (see eq. 12). In fact, Betz (1997) has succeeded to calculate the magnetisation  $M_S$  and magnetostriction  $\lambda^{\gamma,2}$

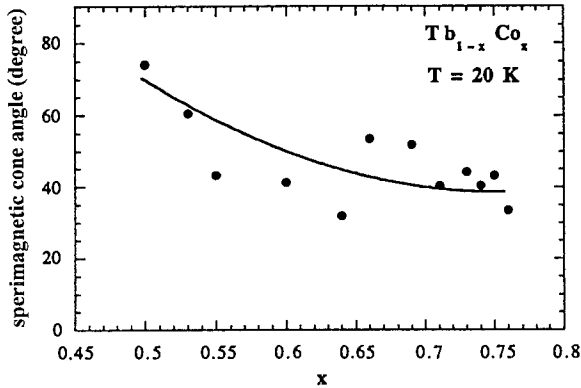


Fig. 22. Variation of the low-temperature Tb-sperimagnetic cone angle  $\theta$  as a function of composition for a-Tb-Co films. After Betz (1997).

at 300 K for a-Tb<sub>1-x</sub>Co<sub>x</sub> alloys. Although there is still a deviation between the calculated and experimental results, their approach is important to understand the influence of the sperimagnetic structure on the magnetostriction.

5.1.2.2. *(Tb<sub>0.27</sub>Dy<sub>0.73</sub>)(Fe<sub>1-x</sub>Co<sub>x</sub>)<sub>2</sub> thin films.* Up until now the optimisation of the magnetostriction in thin films was focussed on the lanthanide concentration and on the internal stresses. One of the crucial ways to obtain a larger magnetostriction at room temperature, however, as mentioned in the preceding section, is to enhance the lanthanide magnetisation by increasing the ordering temperature and by diminishing the sperimagnetic cone angle. For these attempts, Duc et al. (1996) have succeeded by substituting Co for Fe in the a-R-(Fe,Co) alloys. The simple arguments were that, in general, R-Fe exchange energies are larger than the equivalent R-Co interaction energies (Liu et al. 1994, Duc 1997). This arises from the fact that the Fe moment is significantly larger than the Co one, while the R-T intersublattice exchange constant is approximately the same for T=Fe and Co. Fortunately, the T-T interactions tend to be stronger in (Fe,Co)- than in either Fe- or Co-based alloys (Gavigan et al. 1988). This results in an increase of  $T_C$  for a given R:T ratio. The stronger R-FeCo exchange energies should then lead to a closing of the sperimagnetic cone angle and thus to an enhancement of the magnetostriction. Duc et al. (1996) have started a study on the (Tb<sub>0.27</sub>Dy<sub>0.73</sub>)(Fe<sub>1-x</sub>Co<sub>x</sub>)<sub>2</sub> system, in which the Tb:Dy ratio of 1:2.7 was fixed as the same as that of Terfenol-D. At low temperature, all these as-deposited compounds of the composition (Tb<sub>0.27</sub>Dy<sub>0.73</sub>)(Fe<sub>1-x</sub>Co<sub>x</sub>)<sub>2</sub> are magnetically rather hard. The coercive fields reach their highest value of 3.4 T for  $x=0$  then decrease rapidly with increasing Co concentration down to about 0.5 T for  $0.67 \leq x \leq 1.0$ . At 4.2 K, the high-field magnetic susceptibility ( $\chi_{hf}$ ) shows a minimum and the saturation magnetisation exhibits a maximum at  $x=0.47$  (see fig. 23). This compositional variation of  $M_S$  is in contrast to the behaviour observed for the corresponding crystalline alloys where  $M_S$  always shows a minimum in the middle of the composition range due to the enhancement of the 3d(Fe,Co) magnetic moment. In the amorphous case, however, an increase in  $M_{3d}$  will close the sperimagnetic cone. The maximum observed at  $x=0.47$  reflects that, at low temperatures,

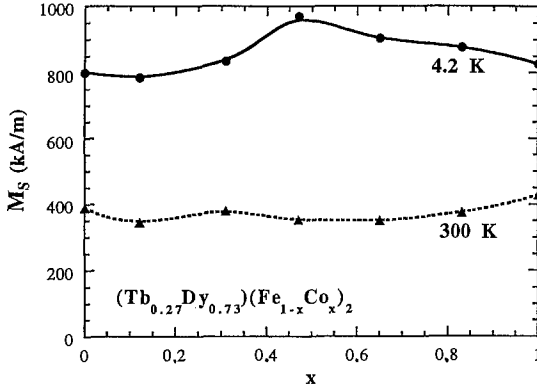


Fig. 23. Variation of spontaneous magnetisation as a function of  $x$  at 4.2 K and 300 K for  $\text{Tb}_{0.27}\text{Dy}_{0.73}(\text{Co}_x\text{Fe}_{1-x})_2$  thin films. After Duc et al. (2000a).

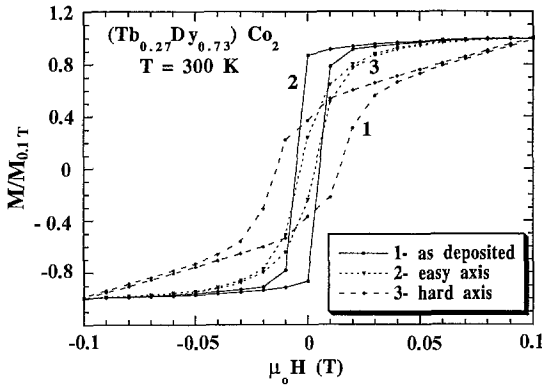


Fig. 24. Hysteresis loops for  $\text{Tb}_{0.27}\text{Dy}_{0.73}\text{Co}_2$  thin film: (1) as-deposited; (2,3) annealed at 250°C along (2) induced easy axis and (3) hard axis. After Duc et al. (2000a).

the enhancement of  $M_{3d}$  is smaller than the associated increase in  $\langle M_{\text{Tb}} \rangle$ . The observed minimum of  $\chi_{\text{hf}}$  also confirms the above arguments. At room temperature, the films become magnetically rather soft. The strongest coercive field (of 0.015 T only) is found at  $x=0.63$ . The room-temperature spontaneous magnetisation  $M_S$ , however, is independent of the Co-concentration (see fig. 23).

Samples were annealed at temperatures between 425 K and 525 K in an applied magnetic field of 2.2 T. The magnetic hysteresis loops before and after annealing are presented in fig. 24 for  $x=1$ . For the as-deposited samples, the magnetisation reversal process is progressive and isotropic with rather large coercive field. This property is often observed in sperimagnetic systems where domains of correlated moments are formed due to the competition between exchange interactions and random local anisotropy. These domains, termed Imry and Ma domains (Imry and Ma 1975, Boucher et al. 1979), are oriented more or less at random in zero field but can be reoriented relatively easily under applied field. After annealing, there are a number of clear differences in the magnetisation process. Firstly, the coercive field is strongly reduced, e.g., after annealing at 525 K,  $\mu_0 H_c$  is less than 0.002 T. Secondly, for  $x=1.0$ , there is now a well defined easy axis with an

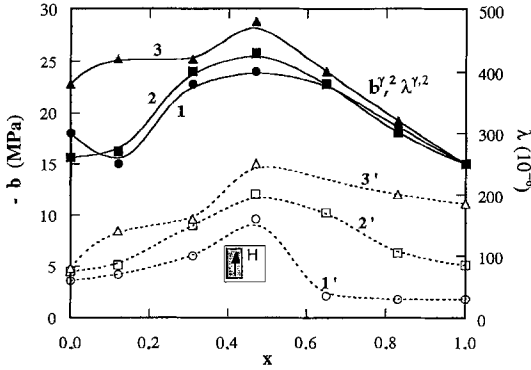


Fig. 25. Magnetostriction  $b^{\gamma,2}(\lambda^{\gamma,2})$  and  $b_{\parallel}(\lambda_{\parallel})$  (at 0.06 T) for  $\text{Tb}_{0.27}\text{Dy}_{0.73}(\text{Co}_x\text{Fe}_{1-x})_2$  thin films: (1, 1') as-deposited; (2, 2') annealed at 150°C; (3, 3') annealed at 250°C. The measured direction along the sample length is indicated. After Duc et al. (2000a).

increased low-field susceptibility. These properties are characteristic of systems which show uniaxial anisotropy. That such anisotropy is induced by annealing, suggests that a process of single ion directional ordering (Néel 1953) has occurred, in which there is a local reorientation of the Tb easy axis along the field direction. The composition dependence of the uniaxial anisotropy is, however, more complex and will be discussed further in connection with the magnetostriction data. Finally, the field annealing also causes a reduction in  $\chi_{\text{hf}}$ , indicating that the cone distribution of the Tb moments is somewhat closed.

Different field-annealing effects on the magnetostriction of the two amorphous Fe-rich and Co-rich  $(\text{Tb,Dy})(\text{Fe,Co})_2$  films were shown in fig. 21 (sect. 5.2.1.1). These differences are evident across the whole composition range as summarised in fig. 25. For the Co-rich alloys,  $b_{\parallel}$  increases significantly after annealing while  $b^{\gamma,2}$  remains virtually unchanged. For the Fe-rich alloys we see the opposite effect,  $b^{\gamma,2}$  increases significantly after annealing while  $b_{\parallel}$  remains virtually unchanged. The increase in  $b^{\gamma,2}$  may be associated to the decrease of the saturation field after annealing. In fact, the largest magnetostriction of  $\lambda^{\gamma,2} = 480 \times 10^{-6}$  and  $\lambda_{\parallel} = 250 \times 10^{-6}$  is found in the middle of the composition range (at  $x = 0.47$ ) and it can be obtained in rather low applied magnetic-field of 0.06 T. Note that, due to the replacing Fe by Co the ordering temperature in the c- $\text{Tb}(\text{Fe}_{1-x}\text{Co}_x)_2$  was increased but no enhancement of magnetostriction was observed (Dwight and Kimball 1974 and Belov et al. 1975). At present, the increase of magnetostriction is considered as originating from the close of the sperimagnetic cone angle due to the enhancement in  $M_{3d}$  in the substituted a-R $(\text{Fe,Co})_2$  alloys. The analysis is as follows. Introducing  $b_{\text{int}}^{\gamma,2} = 127 \text{ MPa}$ , the room temperature value of  $b^{\gamma,2}$  in isotropic polycrystalline  $(\text{Tb}_{0.27}\text{Dy}_{0.73})\text{Fe}_2$  (du Trémolet de Lacheisserie, private communication) into eq. (16) and assuming an uniform probability distribution of the easy axes within a cone, the sperimagnetic cone angle  $\theta$  can be deduced from the obtained magnetostriction data. In this case, it gives values of between  $48^\circ$  and  $53^\circ$  which are typical of those reported in the literature (Coe et al. 1981, Hansen 1991, Danh et al. 1998). This variation in  $\theta$  implies that there is a variation in the average  $(\text{Tb,Dy})$  moment as a function of  $x$ . Using  $M_{(\text{Tb,Dy})} = 7.27 \mu_{\text{B}}$ , the room-temperature value for  $(\text{Tb}_{0.27}\text{Dy}_{0.73})\text{Fe}_2$  (Clark 1980), one

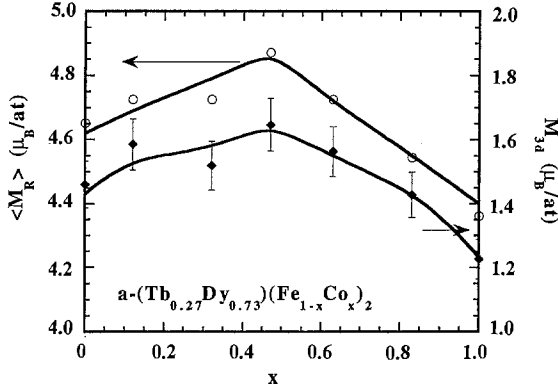


Fig. 26. Variation of  $\langle M_R \rangle$  and  $M_{3d}(\text{Fe,Co})$  calculated from magnetostriction data as a function of  $x$  for  $\text{Tb}_{0.27}\text{Dy}_{0.73}(\text{Co}_x\text{Fe}_{1-x})_2$  thin films. After Duc et al. (2000a).

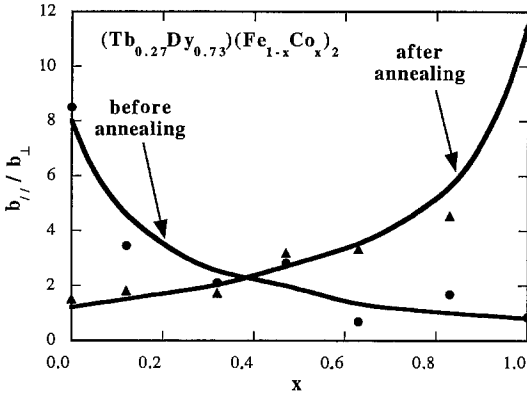


Fig. 27. Ratio  $b_{\parallel}/b_{\perp}$  as a function of  $x$  in  $\text{Tb}_{0.27}\text{Dy}_{0.73}(\text{Co}_x\text{Fe}_{1-x})_2$  thin films before and after annealing.

can deduce  $\langle M_{\text{TbDy}} \rangle = M_{(\text{TbDy})} \langle \alpha_Z \rangle$ , as a function of  $x$ , and this is plotted in fig. 26. From the measured magnetisation data, the value of  $M_{3d}$  as a function of  $x$  can also be evaluated (see also fig. 26). Clearly, a similar composition dependence of  $M_{3d}$  as observed in the crystalline R-(Fe,Co) alloys is found and a maximum is reached for  $x=0.47$  where there is sufficient Co to ensure good ferromagnetic T-T coupling as well as sufficient Fe giving the larger magnetic moment.

Figure 27 shows the variation of  $b_{\parallel}/b_{\perp}$  as a function of Co concentration. It clearly indicates a systematic variation of the anisotropy before and after annealing when going from the Co-poor alloy to the Co-rich one. The ratio of  $b_{\parallel}/b_{\perp}$  decreases indicating that the initial as-deposited uniaxial anisotropy is destroyed with increasing Co content in the films, whereas its increase indicates that the induced uniaxial anisotropy becomes better defined after annealing. These differing anisotropies seen in the as-deposited state are more difficult to account for precisely, but it has often been noted that Fe-based RT-compounds have an opposite anisotropy state compared to their Co-based counterpart (Thuy et al. 1988). The differences in the effects of annealing under a magnetic field, however, may be accounted for as follows. During the annealing process, it is the local

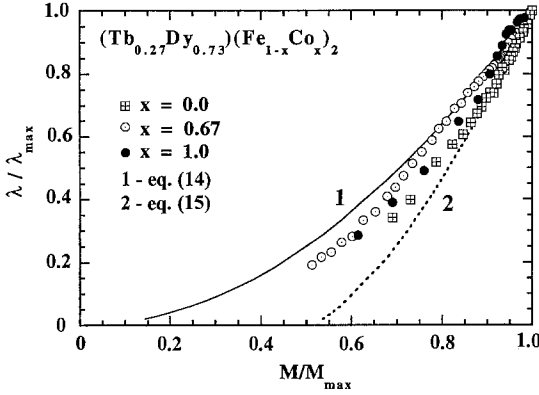


Fig. 28. Experimental normalised magnetostriction as a function of normalised magnetisation for  $\text{Tb}_{0.27}\text{Dy}_{0.73}(\text{Co}_x\text{Fe}_{1-x})_2$  films. Lines (1) and (2) are theoretical curves described by eqs. (14) and (15), respectively. After Duc et al. (2000a).

internal molecular field that is responsible for the reorientation of the R-moments. The external field merely saturates the material in a given direction. For Fe-rich alloys, the sperimagnetic nature of the Fe sublattice distribution is conveyed to the R sublattice and gives no net anisotropy. In Co-rich alloys, however, the strongly ferromagnetically coupled Co sublattice is well ordered and its molecular field acts to orient the R sublattice in one direction, giving rise to the observed uniaxial anisotropy. This variation in anisotropy was illustrated by associating the field dependence of the magnetostriction with different types of the magnetisation process as already mentioned in sect. 5.1.1.2 (i.e., eqs. 14 and 15). The results of this analysis are presented in fig. 28. The experimental data for the (Tb,Dy)Fe<sub>2</sub> film are well described by eq. (15) for the case where the motion of 180°-domain walls leads to a magnetisation of  $M_0 = M_{\text{max}}/2$  without any contribution to magnetostriction. With increasing Co concentration,  $\lambda/\lambda_{\text{max}}$  vs.  $M/M_{\text{max}}$  curves shift towards the line described by eq. (14). This further confirms that the Co substitution is advantageous to the creation of a well-defined easy axis in this system.

It is well known that the substitution of Dy for Tb gives rise to the increase of the magnetostriction at low magnetic fields through the reduction of the saturation field. However, it is also accompanied by a reduction of the saturation magnetostriction. The Co substitution in the R-(Fe,Co) alloys, coupled with the effects of field annealing, results in an enhancement of both the low-field and saturation magnetostriction. Thus, it shows a possibility to enhance the magnetostriction in this type of alloys by increasing the Tb concentration. Indeed, a record giant magnetostriction of  $\lambda^{y,2} = 1020 \times 10^{-6}$  at  $\mu_0 H = 1.8$  T with  $\lambda_{\parallel} = 585 \times 10^{-6}$  at  $\mu_0 H = 0.1$  T in a-Tb(Fe<sub>0.45</sub>Co<sub>0.55</sub>)<sub>2.1</sub>. This will be discussed below.

5.1.2.3. *(Tb<sub>1-x</sub>Dy<sub>x</sub>)(Fe<sub>0.45</sub>Co<sub>0.55</sub>)<sub>2.1</sub> thin films.* Figure 29 shows the field dependence of the magnetostriction for a-Tb(Fe<sub>0.45</sub>Co<sub>0.55</sub>)<sub>2.1</sub> (Duc et al. 1996). Here we see that a magnetostriction of  $\lambda^{y,2} (= \lambda_{\parallel} - \lambda_{\perp}) = 800 \times 10^{-6}$  at 1.8 T is already observed for the as-deposited film. In this state,  $b_{\perp} = \frac{1}{4}b_{\parallel}$ , indicating a certain initial anisotropy. After annealing,  $b_{\parallel}$  increases and  $b_{\perp}$  is significantly reduced (in absolute magnitude) in agreement with the fact that the easy axis becomes better defined. In addition, it is

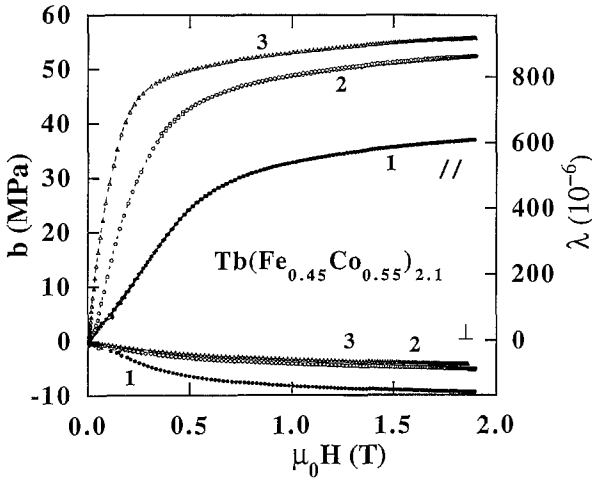


Fig. 29. Room-temperature magnetostriction for  $\text{Tb}(\text{Fe}_{0.45}\text{Co}_{0.55})_{2.1}$ : (1) as-deposited; (2) annealed at  $150^\circ\text{C}$ ; (3) annealed at  $250^\circ\text{C}$ . After Duc et al. (1996).

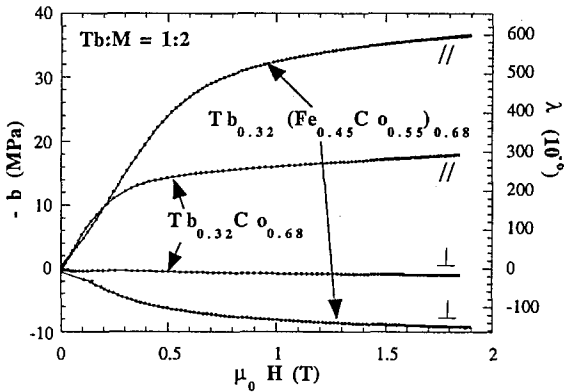


Fig. 30. Room-temperature magnetostriction for as-deposited  $\text{Tb}(\text{Fe}_{0.45}\text{Co}_{0.55})_{2.1}$  and  $\text{TbCo}_{2.1}$ . After Betz (1997).

important to note that  $b^{\gamma,2}$  actually increases after annealing at  $250^\circ\text{C}$  leading to the very large magnetoelastic coupling coefficient of 60 MPa (i.e.,  $\lambda^{\gamma,2} = 1020 \times 10^{-6}$ ) at saturation. This result is particularly interesting as the magnetostriction was almost completely developed at only 0.3 T. In comparison, the magnetostriction of  $\text{Tb}_{0.32}(\text{Fe}_{0.45}\text{Co}_{0.55})_{0.68}$  and  $\text{Tb}_{0.32}\text{Co}_{0.68}$  is presented in fig. 30. Clearly, the Fe substitution increases the magnetostriction by a factor of 2. The temperature dependence of the magnetostriction is shown in fig. 31 for the  $\text{Tb}_{0.36}(\text{Fe}_{0.5}\text{Co}_{0.5})_{0.64}$  film. The magnetostriction decreases linearly with increasing temperature up to the ordering temperature which is about 423 K.

Figure 32 presents low-field magnetostriction data for  $a\text{-(Tb}_{1-x}\text{Dy}_x)(\text{Fe}_{0.45}\text{Co}_{0.55})_2$  thin films with different Tb/Dy ratios after annealing at  $250^\circ\text{C}$ . It exhibits obviously a decrease in the magnetostriction and saturation field with increasing Dy content but with a maximum in the initial magnetostrictive susceptibility for  $x=0.73$  as observed in other Terfenol-D based alloys. As shown in fig. 33, the ratio  $b_{\parallel}/b_{\perp}$  has also a minimum for this



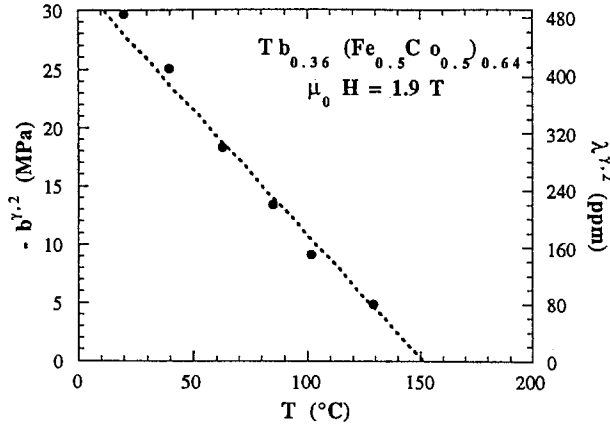


Fig. 31. Magnetostriction of  $\text{Tb}(\text{Fe}_{0.55}\text{Co}_{0.45})_{2.1}$  as a function of temperature. After Betz (1997).

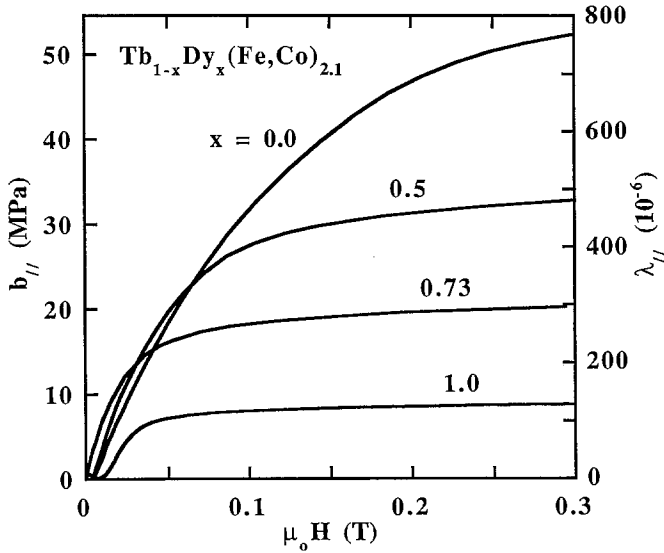


Fig. 32. Room-temperature parallel magnetostriction for  $(\text{Tb}_{1-x}\text{Dy}_x)(\text{Fe}_{0.55}\text{Co}_{0.45})_{2.1}$  measured along the hard axis and after annealing at  $250^\circ\text{C}$ . After Duc et al. (1996).

composition, implying that the anisotropy is then less well defined. In the same figure, the anisotropy constants  $K$  deduced from the magnetisation measurements are plotted. Here, we see a partial anisotropy compensation for  $x=0.73$  as found for crystalline  $(\text{Tb}_{0.27}\text{Dy}_{0.73})\text{Fe}_2$ . This indicates that even in amorphous samples, in which the uniaxial  $K_2$  terms are expected to dominate due to the local distortions from cubic symmetry, there is still a significant contribution from the  $K_4$  cubic anisotropy terms. It is interesting to contrast this with the numerical simulations for a- $\text{TbFe}_2$  which have shown that the fourth-

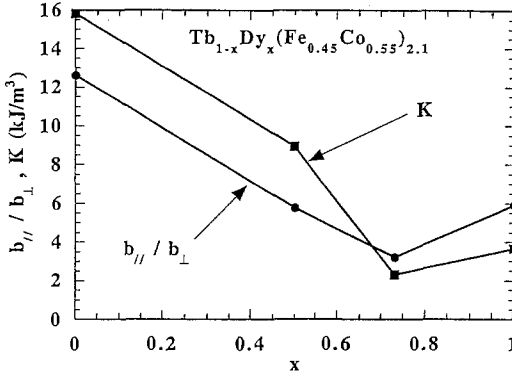


Fig. 33. Variation of the ratio  $b_{||}/b_{\perp}$  and anisotropy constant  $K$  as functions of  $x$  for  $(\text{Tb}_{1-x}\text{Dy}_x)(\text{Fe}_{0.45}\text{Co}_{0.55})_{2.1}$ . After Duc et al. (1996).

order anisotropy energy per atom was an order of magnitude smaller than the second-order anisotropy energy per atom albeit the fourth-order term was of the same order of magnitude as in the crystalline  $\text{TbFe}_2$  Laves-phase (Kaneyoshi 1984). The present result implies that  $K_4$  tends to be larger than expected and the local environment is reminiscent of that in the cubic Laves phase.

5.1.2.4. *Sm-Co thin films.* A comparison of the magnetostriction of Sm-Co and Tb-Co systems is shown in fig. 34 for  $\text{Sm}_{0.37}\text{Co}_{0.63}$  and  $\text{Tb}_{0.36}\text{Co}_{0.64}$ . The Sm-Co alloy shows a comparable behaviour as the Tb-Co one but with the opposite and a somewhat smaller magnetostriction in absolute value. In addition, the Sm-Co alloy is magnetically harder than Tb-Co: its magnetostriction saturates around 0.3 T and the coercive field is about 0.03 T. The high-field magnetostrictive susceptibility, however, is smaller in the case of Sm-Co. It is particularly interesting to compare the Stevens factors,  $a_J\langle O_2^0 \rangle$ , of these two alloys with the observed magnetostriction. The values of  $a_J\langle O_2^0 \rangle$  are  $+41.3 \times 10^{-2}$  and  $-66.6 \times 10^{-2}$  and the values of  $b^{J,2}$  at 300 K are  $+11.0$  and  $-18.3$  MPa for the corresponding Sm-Co and Tb-Co films, respectively. One finds that the ratio between the operators is comparable with that between the two magnetoelastic coefficients:

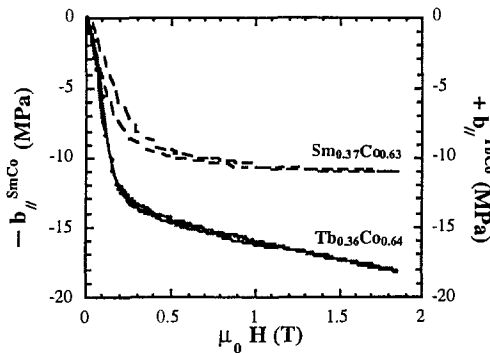


Fig. 34. Magnetostriction of  $\text{Sm}_{0.37}\text{Co}_{0.63}$  and  $\text{Tb}_{0.36}\text{Co}_{0.64}$ .

$\left| \alpha_J \langle O_2^0 \rangle^{\text{TbCo}} / \alpha_J \langle O_2^0 \rangle^{\text{SmCo}} \right| = 1.61$  and  $\left| b_{\parallel}^{\text{TbCo}} / b_{\parallel}^{\text{SmCo}} \right| = 1.67$ . A few amorphous Sm-Co alloys have also been studied by Quandt (1994b). A (negative) magnetostriction somewhat smaller (by 30–50%) than that of Tb-based alloys have been confirmed.

### 5.2. Giant magnetostrictive spring-magnet-type multilayers

Up to now, the giant magnetostrictive material research has been based on R-T homogeneous alloys. For these alloys, as already described in the sect. 5.1, attempts to reduce the driving fields required for giant magnetostriction are concentrated around techniques for reducing the macroscopic anisotropy, e.g., to control the Tb:Dy ratio in order to achieve compensation of fourth order anisotropy, to use amorphous or nanocrystalline materials to reduce anisotropy, etc. Furthermore, the saturation field  $H_s$  can be reduced by increasing the saturation magnetisation  $M_s$ , instead of decreasing anisotropy constant  $K$ , as  $H_s = K/2M_s$ . For a given R concentration, which is optimised on the point of view of giant magnetostriction, e.g., at the 1:2 R:T ratio, the possibility to increase the T-sublattice magnetisation by substitution, for instance, will increase slightly the total magnetisation in the R- alloys with R = light lanthanide. This, however, will reduce the total magnetisation in the alloys with a heavy lanthanide (due to the ferrimagnetic nature). An increase in the R concentration can increase  $M_s$ , however, this results in a lowering of the ordering temperature. Thus, it is difficult to see how  $M_s$  can be notably increased using homogeneous R-T alloys. This, however, can be achieved by combining two different magnetic materials using a similar approach those developed for the permanent “spring magnets”. For the spring magnets, one matches a material which has a high magnetisation with another which possesses a strong coercive field. These two materials are coupled magnetically. Here, multilayers are fabricated by combining also two different materials, one with a large room-temperature magnetostriction (like, e.g., a-Tb-(T,T') alloys, T,T' = Fe, Co) and the other magnetically soft and with a high magnetisation (like, for example, (T,T') alloys). The structure of this spring-magnet type multilayer is illustrated in fig. 35. The thickness of these layers must be enough for magnetic coupling but they must be thinner than the magnetic exchange length, for which domain walls cannot be formed at the interfaces, i.e., it should range between 1 nm to 20 nm (Givord et al. 1993, 1996, Wüchner et al. 1995, see also sect. 5.3). In this state, the 3d-3d exchange interactions ensure that parallel coupling of the (T,T')-magnetic moments persists throughout the entire thickness of multilayers. Without creating domain walls at the interfaces, the multilayer behaves as a unique material. Then, magnetisation processes

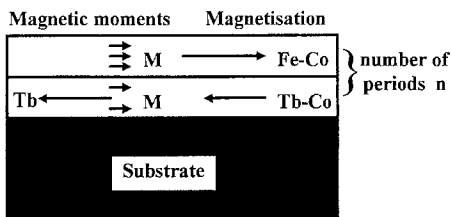


Fig. 35. Schematic of “spring magnet” type giant magnetostriction multilayers.

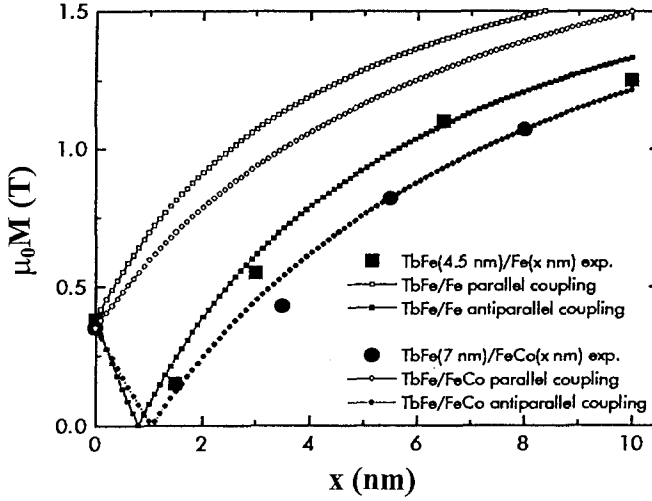


Fig. 36. Saturation magnetisation of TbFe/Fe and TbFe/FeCo multilayers as a function of the thickness of the transition-metal sublayer in comparison with a simple model for exchange-coupled layers considering either parallel or antiparallel coupling of the TbFe and the transition-metal layers. After Quandt and Ludwig (1997).

result from the average of the magnetic characteristics of each individual layer. Assuming that the 3d–3d exchange interactions are infinite and the interfacial magnetic anisotropy is neglected, it is possible to calculate the magnetisation, anisotropy and magnetostriction of the multilayers from the corresponding values of the simple alloys and the individual Tb–T ( $t_{\text{Tb}}$ ) and T ( $t_{\text{T}}$ ) layer-thicknesses as follows (Betz 1997)

$$\langle M \rangle = \frac{M_{\text{T}}t_{\text{T}} - M_{\text{Tb}}t_{\text{Tb}}}{t_{\text{T}} + t_{\text{Tb}}}, \quad (17)$$

$$\langle K \rangle = \frac{K_{\text{T}}t_{\text{T}} + K_{\text{Tb}}t_{\text{Tb}}}{t_{\text{T}} + t_{\text{Tb}}}, \quad (18)$$

$$\langle b^{\gamma,2} \rangle = \frac{(b^{\gamma,2})_{\text{T}}t_{\text{T}} + (b^{\gamma,2})_{\text{Tb}}t_{\text{Tb}}}{t_{\text{T}} + t_{\text{Tb}}}. \quad (19)$$

In the as-deposited composite Tb–T/T and Tb–(T,T')/(T,T') multilayers, Tb-based layers were formed in the amorphous state while T or (T,T') layers were found to be nanocrystalline with a mean grain size being equal to the layer thickness (Quandt and Ludwig 1997). In spite of the compressive stress, these multilayers exhibit an in-plane EMD. Magnetisation of the TbFe/Fe and TbFe/FeCo multilayer series as a function of the transition-metal sublayer-thickness is presented in fig. 36 (Quandt and Ludwig 1997, Quandt et al. 1997a,b). The experimental data can be compared with the theoretical one for spring-magnet-type multilayers by considering either the parallel and antiparallel coupling between the Tb–Fe and the T layers. As seen in fig. 36 the agreement between the experimental data and the theoretical calculations strongly support the antiparallel

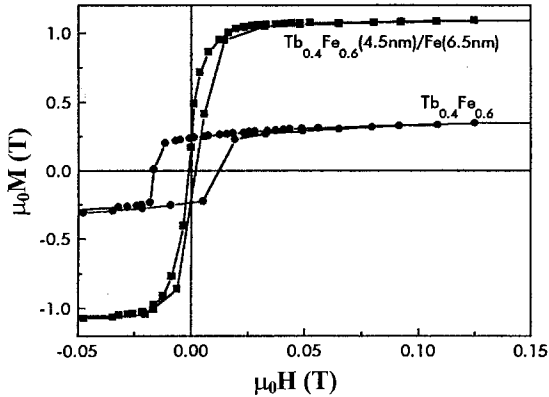


Fig. 37. In-plane magnetisation of TbFe single layer and TbFe/Fe multilayer. After Quandt and Ludwig (1997).

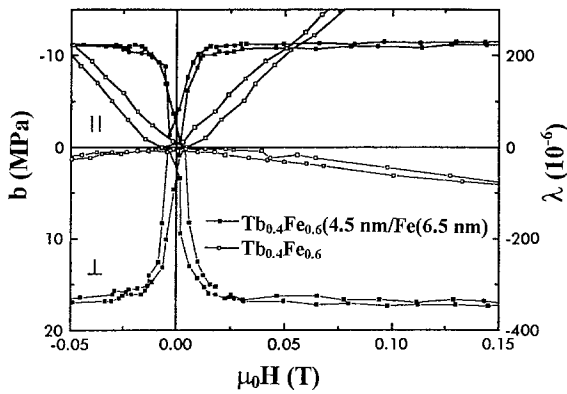


Fig. 38. Magnetostrictive hysteresis loops of a TbFe/Fe multilayer showing increased magnetostriction at low fields. After Quandt and Ludwig (1997).

coupling of the magnetisation of the layers due to the dominating Tb moments in the ferrimagnetic TbFe layers and to the parallel coupling of the (T,T')- and Fe-magnetic moments throughout the entire thickness of multilayers. The in-plane magnetisation loops of a  $\text{Tb}_{0.4}\text{Fe}_{0.6}(4.5 \text{ nm})/\text{Fe}(6.5 \text{ nm})$  multilayer which was annealed at  $280^\circ\text{C}$  is plotted in fig. 37 together with the corresponding loop of a giant-magnetostrictive TbFe single-layer film. It reveals the strong increase of magnetisation of the multilayer film combined with the reduced but (non-neglectable) hysteresis and saturation field. Figures 38 and 39 show the magnetostrictive hysteresis loops of the TbFe/Fe and TbFe/FeCo multilayers, respectively. For both multilayer systems, high saturation magnetoelastic coefficients  $\lambda^{\parallel,2}$  ( $=\lambda_{\parallel} - \lambda_{\perp}$ ) of 29 MPa (TbFe/Fe) and 42 MPa (TbFe/FeCo) were obtained at field as low as 20 mT. Unfortunately, these saturation magnetostriction values are still lower than those of the best TbFeCo single-layer films and also the uniaxial easy axis does not seem to be well established in these systems. The magnetostriction improved in TbFe/FeCo compared to TbFe/Fe multilayers is due to the magnetostrictive contribution of the FeCo layers, which exhibits a saturation magnetostriction exceeding  $100 \times 10^{-6}$  (Quandt and Ludwig 1997, Betz 1997). This may imply that the exchange field and the annealing effects are

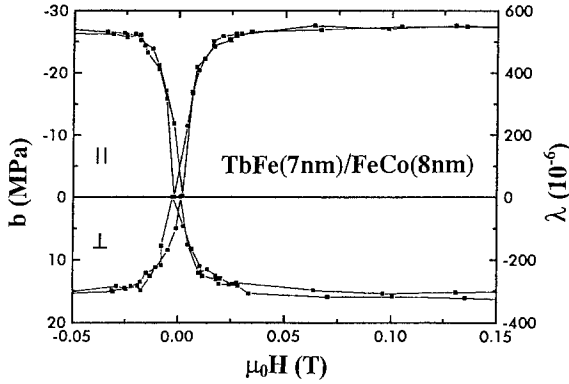


Fig. 39. Magnetostrictive hysteresis loops of a TbFe/FeCo multilayer. After Quandt and Ludwig (1997).

not effective in closing the Tb sperimagnetic cone angle in these multilayers as in the single layer films. The reason may be associated to the antiparallel orientation between the dominant magnetisation of the sample and the magnetisation of Tb, which creates a rather strong demagnetisation field in the Tb subsystem. This demagnetisation field opens the sperimagnetic cone, leading to the decrease of the magnetoelasticity. During field annealing, the Tb moments remain antiparallel with the applied field. The Tb moments are thus dispersed (instead of aligned). In order to avoid this antiparallel ordering, one can use a light lanthanide element, for example Sm. At present, however, the question is still open.

The magnetostriction of the multilayers is found to change as the thickness  $t$  of the magnetic layer is changed (Zuberek et al. 1987, 1988, Awano et al. 1988, Dirne and Denissen 1989, Nagi et al. 1988). The changes in the magnetoelastic properties have been attributed to magnetostrictive strains which are localised at the interface. These strains lead to the linear variation of the effective magnetostriction with the inverse layer thickness  $t^{-1}$ . Such magnetostrictive effects are called “surface magnetostriction” (Szymczak et al. 1988). In addition, it is often claimed that the changes in elastic and magnetoelastic properties of multilayers are due to the presence of interdiffusion layers which are formed at the interfaces. In many multilayers as well as in the magnetostrictive multilayers under consideration, the interface diffusion and considerable surface anisotropy and magnetostriction have been neglected. For Gd/Fe multilayers, however, a surfacial magnetostriction ( $\lambda_{\text{sur}}$ ) of  $10.2 \times 10^{-6}$  which is larger than the observed bulk magnetostriction ( $\lambda_{\text{bulk}} = 6.5 \times 10^{-6}$ ) has been found (Zuberek et al. 1995). In fact, investigations on the SmFeB/TbFeB multilayers have shown that the strain and stress are transferred effectively at the interface (Shima et al. 1997). In these SmFeB/TbFeB multilayers, magnetostriction was varied with ratio of each layer thickness and it was found that the magnetostriction is sensitively affected by Young’s modulus, Poisson ratio and the thickness of the constituent layers. From a better understanding of the nature of interfaces, we can expect better performance of these magnetostrictive materials.

### 5.3. Magnetostriction of R-T sandwich films

Sandwich films of the type RT/R'T/RT made by stacking coupled layers with a typical thickness of 100 nm have been intensively studied at Louis Néel Laboratory in Grenoble, France in the last decade (Dieny et al. 1990, 1991, Givord et al. 1993, 1996, Wüchner et al. 1995). Because properties such as magnetisation or anisotropy differ from one layer to the next, the reversal of the magnetisation in each layer occurs at the different value of the coercive field. When the reversal takes place in a given layer but not in the adjacent one, a domain wall will be formed at the interface between the layers, in order to minimise the exchange energy. Such a domain wall has the particular feature of extending over the whole film surface and it was referred to as an extended domain wall (EDW). In these systems the magnetostriction, which is fundamentally different to that observed in the above mentioned multilayers, is associated with the creation of this domain wall. Magnetostriction associated with domain wall formation has been known for a long time as due to the progressive rotation of magnetic moments making up the domain wall. Normally, this effect is small since the volume occupied by the domain wall is always quite small and it contributes to the magnetostriction measured along the easy axis. In the systems with EDWs, however, the domain wall can occupy an extremely large fraction of the total volume of the sample.

The effects of EDW formation were investigated on the sandwiches consisting of Nd-Co/Tb-Co/Nd-Co (system 1) and Tb-Co/Nd-Co/Tb-Co (system 2), in which the uniaxial easy axis was well created by field annealing at 150°C and the Tb magnetic moment is dominant in the Tb-Co layers at room temperature (Givord et al. 1996, Betz 1997). In order to better understand the magnetisation process, the coupling between one pair of layers was suppressed by a thin oxide layer at the interface. The configuration of magnetisation and of the magnetic moments in zero-magnetic field is illustrated in fig. 40a for the sandwich system 2.

Magnetostriction of the sandwich Tb-Co/Nd-Co/Tb-Co system is shown in fig. 41. While the high-field magnetostriction exhibits the similar behaviour as observed in the single Tb-Co layer films, the low-field magnetostriction measured along the easy axis shows a rather complex field dependence with magnetostriction anomalies and, in particular, extremely large magnetostrictive susceptibilities. (In the Nd-Co/Tb-Co/Nd-Co sandwich system, a magnetostrictive susceptibility ( $\partial b/\partial\mu_0H$ ) of 556 MPa/T was observed even at  $\mu_0H=2$  mT). The magnetisation loop at room temperature is shown in fig. 42. for the sandwich Tb-Co/Nd-Co/Tb-Co system. Starting from the high-field state, where the magnetisation of the system is well saturated in the applied field direction, we see that the Co moments between layers are antiparallely coupled and an EDW is formed at the coupled interface (fig. 40b). As the field decreases, a (positive) critical field (of 8.5 mT) is reached, where the EDW at the Nd-Co/Tb-Co coupled interface is suppressed by the reversal of the moment in the Nd-Co layer (fig. 40c). The reversal of the uncoupled TbCo layer occurs at -46 mT, and, finally, for the coupled TbCo at a higher field of -96 mT due to the re-creation of an EDW (figs. 40d,e). Taking into account these demagnetisation processes, the field dependence of the magnetostriction measured along

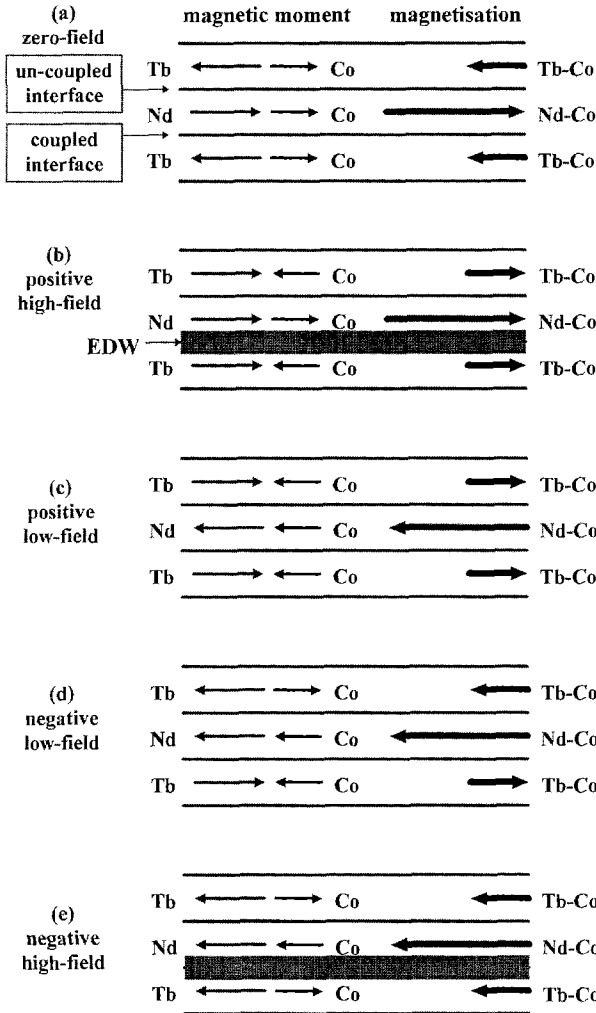


Fig. 40. Configuration of magnetisation and magnetic moment in a sandwich TbCo/NdCo/TbCo film in zero magnetic field and during demagnetisation processes (b–e).

the easy direction can be understood as follows. At saturation, the magnetostriction (which can be either positive or negative) is maximum. As the field is reduced from saturation, the magnetostriction decreases as the EDW becomes larger. At around 8.5 mT, the EDW is destroyed. This is associated with the Tb moments being better aligned along the field, and a large change in magnetostriction is observed. When the external field changes its direction, the cone of Tb moments being opposite to the applied magnetic field opens up, leading to the observed decrease of the magnetostriction. At the coercive field for reversal of the magnetisation in the uncoupled TbCo layer ( $-46$  mT), a discontinuity in the magnetostriction takes place since these Tb moments become more aligned along the applied field. Further variation of the field makes the coupled TbCo layer again



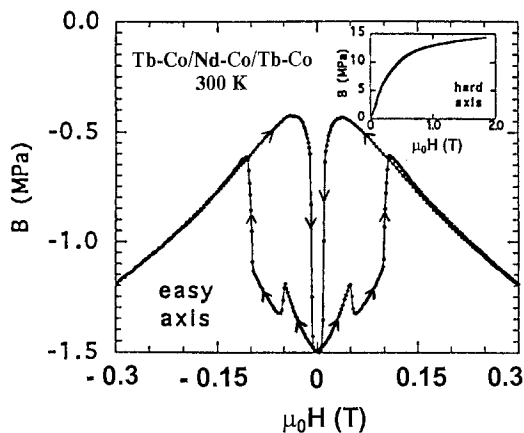


Fig. 41. Magnetostrictive hysteresis loops of a sandwich Tb-Co/Nd-Co/Tb-Co system at 300 K. After Givord et al. (1995).

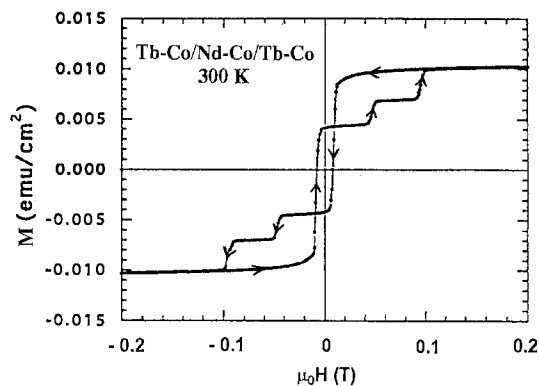


Fig. 42. Magnetic hysteresis loops of a sandwich Tb-Co/Nd-Co/Tb-Co system at 300 K. After Givord et al. (1995).

more disordered. Finally, at  $-95$  mT the EDW is re-created with an sudden increase of the disorder in the magnetic configuration giving rise to a large transition in the magnetostriction.

The sandwich system is a composite material, which gives evidence for the magnetostriction of the domain wall. These systems are not optimised in magnetostriction. Only their high magnetostrictive susceptibility is interesting.

## 6. Potential applications of magnetostrictive microsystems

Technical aspects and potential applications of magnetostrictive materials have been presented by du Trémolet de Lacheisserie (1993). Different kinds of magnetostrictive devices based on Terfenol-D were recently reviewed by Zhu et al. (1997) and Claeysen et al. (1997). Today, interest is mounting in physical micro-systems of reduced dimensions, typically between  $10$  and  $10^3$   $\mu\text{m}$ . Such systems may satisfy the need to perform functions which are not fulfilled by existing electronic circuits, i.e., sensing

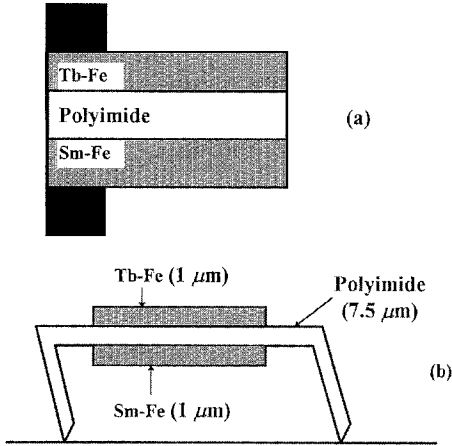


Fig. 43. (a) Side view of a cantilever actuator fabricated by combining TbFe and SmFe films. After Honda et al. (1994). (b) Two-leg linear magnetostrictive micromotor. After Honda et al. (1994).

functions (micro-sensors) and functions of interacting with the environment (micro-actuators). In cases where a simple motion is to be obtained, magnetostrictive amorphous R-T thin films which combine several specific properties are very promising. Their advantages with respect to their piezo-electric competitors are the larger deformations, higher forces and energy densities, lower sound velocity and Young's modulus, and low operating voltage. Therefore, they can reach, as well as possibly drive, the considered systems without a direct electric contact. The disadvantage is the coil which is difficult to make small because of the field requirements. These problems can be solved by developing films with giant magnetostriction at low fields. In addition, as magnetostrictive devices using thin films are very small, the price of material is not a problem. Thus, such microsystems could find large scale applications, for instance in electronics, optics, medicine, the automobile industry, geophysical explorations, and ocean environmental protection as well. At the moment, some devices are already used for specific applications. We present here some typical examples, such as the micro mechanical switch, micromotor and micropump, demonstrating the above-mentioned advantages of magnetostriction, owing especially to the fact that the moving parts are wireless.

The simplest motion which can be thought of is realised by a bimorph bending (as schematised in fig. 3) as a mechanical switch. In this case, although Sm-T films exhibit less pronounced magnetostriction compared to the Tb-T thin films, the combination of a negative- with a positive-magnetostriction film allows the fabrication of magnetostrictive bimorphs which enhance the total deflection, and reduce the initial curvature of cantilevers (fig. 43a, see Honda et al. 1994). A 3-mm long cantilever actuator is found to exhibit a large deflection of above  $100\ \mu\text{m}$  in a magnetic field as low as 0.03 T. With this cantilever, a deflection of more than  $500\ \mu\text{m}$  at resonant frequency in an alternating field of 0.03 T has been reached.

One of the main drawbacks of the magnetostrictive actuators is their thermal drift. For the bulk Terfenol-D actuators, it has been known that the thermal expansion ( $10^{-5}\ \text{K}^{-1}$ ) develops strains comparable to the magnetostrictive ones for  $\Delta T = 150\ \text{K}$ . For a simple

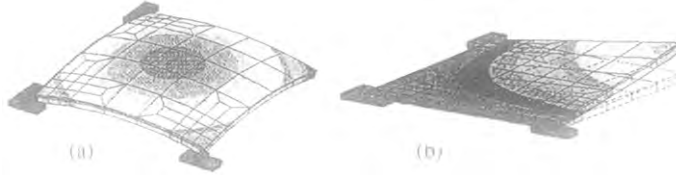


Fig. 44. Drift-free microactuator: (a) thermal deformation; (b) magnetostriction deformation. After Betz (1997).

rectangular bimorph cantilever as illustrated in fig. 43a, the strains due to thermal expansion and to the magnetoelastic coupling are comparable only for  $\Delta T = 75$  K (du Trémolet de Lacheisserie et al. 1998). The torsion-based, thermal-drift free microactuator was invented (Betz et al. 1996b, Betz 1997). It is basically a unimorph structure composed of one magnetostrictive film deposited on a passive substrate. The special feature is a square shape maintained by hinges at three corners (fig. 44a,b). The useful displacement due to magnetostriction is obtained at the fourth free corner, without thermal displacement. The different deformed shapes are due to the anisotropy of magnetostriction strains and the isotropy of thermal strains.

Various types of the so-called magnetostrictive “inchworm” type of motor have been proposed and built. A two-leg travelling machine using a magnetostrictive bimorph actuator with  $7.5 \mu\text{m}$ -thick polyimide was fabricated by Honda et al. (1994), see fig. 43b. In an alternating magnetic field, it can travel in one direction. The maximum speed of approximately  $5 \text{ mm/s}$  was obtained around the mechanical resonant frequency of  $200 \text{ Hz}$ . Similarly, a many-leg linear-motor was also fabricated using a micromachined Si(110) substrate and TbFe films, see fig. 45 (Halstrup et al. 1996, Claeysen et al. 1997). The  $13 \mu\text{m}$ -thick TbFe films were deposited on both sides of the substrate. Applying a magnetic excitation field of  $15 \text{ mT}$  at a frequency of approximately  $750 \text{ Hz}$  and a magnetic bias field of  $30 \text{ mT}$ , this motor can be operated at a speed of  $3 \text{ mm/s}$ .

The world’s first magnetostrictive thin film micropump prototype was made of four laser micro-machined Si(100) wafers in combination with a bimorphous TbDyFe( $15 \mu\text{m}$ )/Si(100)( $50 \mu\text{m}$ )/SmFe( $15 \mu\text{m}$ ) membrane and cantilever-type passive valves (fig. 46) (Quandt and Seemann 1996, Quandt 1997). The radial magnetic field circuit is directly placed on the membrane to permit a good penetration by the magnetic field. The micropump is operated using an oscillating rectangle pulse for the membrane actuation.

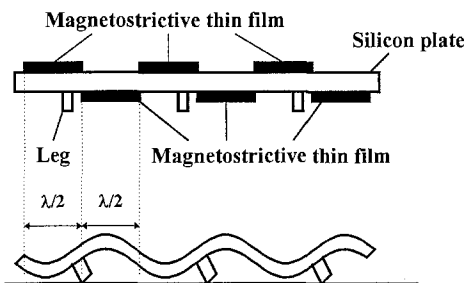


Fig. 45. Many-leg linear magnetostrictive micromotor. After Claeysen et al. (1997).

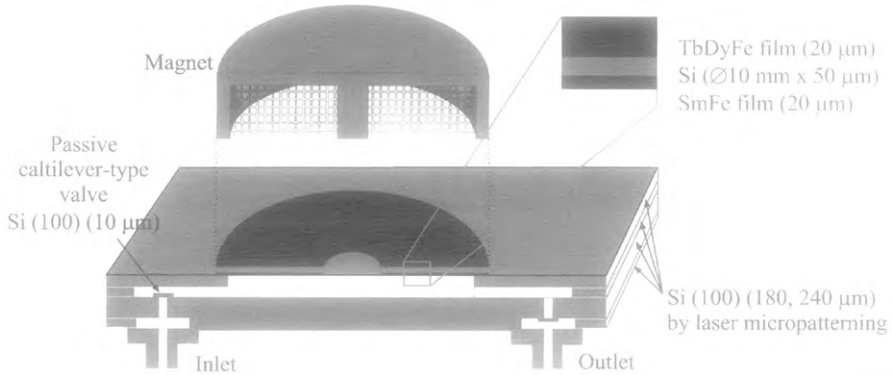


Fig. 46. Schematic cross-section of a magnetostrictive membrane-type micropump. After Quandt (1997).

At the frequency of 2 Hz a maximum yield of approximately 10 μl/min. of methanol or an outlet pressure of 1 mbar can be reached.

## 7. Summary and recent developments

Thin films having giant magnetostriction at low fields and an ordering temperature high enough for the applications as magnetostrictive microactuators have been the goal of magnetostriction researches. Various attempts have been focused mainly on amorphous Terfenol and Terfenol-D ( $\text{TbDyFe}_2$ ) alloys. However, the magnetostriction of these amorphous alloys has been found to be one order of magnitude lower than that of its crystalline counterpart. Magnetic investigations have shown that such amorphous R-Fe alloys could never offer promising magnetostrictive performances, due to the distribution of the signs of the Fe-Fe interactions and the Fe- and R-sperimagnetic characters. Another great disadvantage of the amorphous R-Fe thin films, from the point of view of application in microsystems is the comparatively low Curie temperature ( $T_C \leq 400$  K for amorphous Terfenol-D films). The polycrystalline Terfenol-D film processes a room temperature magnetostriction of  $\lambda_s \approx 1500 \times 10^{-6}$  and  $T_C = 650$  K. This film is, however, not suitable for micro-mechanical applications due to its comparatively high coercive fields. Material designs always require a combination between the advantages of the crystalline films (giant magnetostriction and high  $T_C$ ) and the good magnetic softness of the amorphous films (low coercivity). In this context, the nanocrystalline structure is expected to be able to realise this objective (Schatz et al. 1993, 1994, Williams et al. 1994, Miyazaki et al. 1997, Wada et al. 1997c,d, Ried et al. 1998, Winzek et al. 1999, Farber and Kronmüller 2000a,b). In these alloys, the dimensions of crystallites are sufficiently large enough to allow the exchange coupling to be effective but small enough to prevent the appearance of any macroscopic anisotropy energy. Thus one may consider the material as an isotropic ferromagnet, in which the magnetostriction is expected to be the same but the magnetocrystalline anisotropy has disappeared. By

combining the annealing temperature and time, the magnetostriction value can be doubled. Indeed, the best magnetic properties were obtained on the ‘cold grown’  $(\text{Tb}_{0.3}\text{Dy}_{0.7})_{1-x}\text{Fe}_x$  (with  $x \approx 0.3$ ) films annealed at  $T_A = 600^\circ\text{C}$  for 10 minutes with a grain size around 10 nm: a saturation magnetostriction  $\lambda = 860 \times 10^{-6}$  and  $\mu_0 H_c = 120$  mT (Ried et al. 1998). In addition, high-temperature annealing is not desirable because of the formation of iron-rich phases, like  $\text{RFe}_3$  and  $\text{R}_6\text{Fe}_{23}$ , with even less magnetostriction and higher magnetic coercivity.

According to the random anisotropy model (Herzer 1990, Hofmann et al. 1992), a further reduction of the crystal size will reduce the coercive field if the exchange length is larger than the average grain size. Hence, technologies which at the same time enhance grain nucleation and limit grain size must be applied to achieve a fine nanocrystalline structure. For this purpose Zr and Mo have been chosen as additives in order to enhance grain nucleation and to limit grain growth, respectively. Practically, the influence of the Zr and Mo additives on the crystallisation and the magnetic properties was studied by Winzek et al. (1999). Films with 3 at% Zr, crystallised at 973 K for 10 minutes, showed  $\lambda_{\parallel} = 430 \times 10^{-6}$  at  $\mu_0 H = 1.0$  T and  $\mu_0 H_c = 120$  mT, which was a large improvement compared to the starting alloys:  $\lambda_{\parallel} = 230 \times 10^{-6}$  and  $\mu_0 H_c = 300$  mT. These additives were also thought to enhance the growth of the  $\text{RFe}_2$  grains and to hinder the formation of  $\text{RFe}_3$  ones. It is assumed that the latter was responsible for the high coercivity values above 150 mT.

In general, it should be noted that a reduction of the average grain size of the cubic Laves phases below 10 nm and, therefore, the coercivity values below 100 mT could not be achieved in single layer films. Grain growth, however, enabled one to control nanometer-scaled multilayers with interlayers of Nb (Fischer et al. 1999, Winzek et al. 1999). These authors fabricated a multilayer system containing  $\text{TbDyFe} + \text{Zr}$  with a thickness of 5 nm separated by Nb-layers with an average thickness of 0.25 nm. The introduction of a partial Nb layer in this multilayer structure was thought to cause reduced dimensions and increase the amount of inner surfaces, while Zr is assumed to play a dominant role in forming nucleation centers for the nanograins. After 10 min. annealing at temperatures from 873 K to 973 K the magnetic phase transition temperature increased from  $T_C = 333$  K to 592 K accompanied by an increase of the magnetostriction from  $265 \times 10^{-6}$  to  $520 \times 10^{-6}$ , while the coercive fields increased from  $\mu_0 H_c = 5$  to 75 mT, which lies distinctively below 100 mT. Research is in progress to prevent not only the growth of crystallites but also aging effects.

In the amorphous state, however, it is preferable to replace the iron by cobalt because the amorphous alloys near to the composition  $a\text{-RCO}_2$  (named  $a\text{-TercoNéel}$ , where Néel identifies the laboratory where the magnetostriction of this composition was studied first; Duc 2001) have higher ordering temperatures and higher magnetostrictions than the equivalent iron-based alloys. In fact, the magnetostriction has been optimised in a series of thin films of the type  $a\text{-(Tb,Dy)(Fe,Co)}_n$ : the material  $\text{Tb}(\text{Fe}_{0.45}\text{Co}_{0.55})_{2.1}$  showed a high record magnetoelasticity of  $\gamma_b^{1,2} = 63.5$  Mpa and  $\lambda^{\gamma,2} = 1020 \times 10^{-6}$ , which is almost fully developed at low fields. The giant magnetostrictions obtained in this series of alloys has been explained in terms of an increase in the 3d–3d exchange

coupling within (Fe,Co) sublattice. Recently, Danh et al. (2000) and Duc et al. (2000b) have reported a value of the magnetoelastic susceptibility  $\chi_{\lambda\parallel} = 1.8 \times 10^{-2} \text{ T}^{-1}$  (or  $\chi_{b\parallel} = 1100 \text{ MPa}$ ) for a-Tb(Fe<sub>0.55</sub>Co<sub>0.45</sub>)<sub>1.5</sub>. (denoted a-TerfecoHan, where Han stands for Hanoi, the capital where studies on this composition have been carried out; Duc 2001). Values of magnetostriction and magnetostrictive susceptibility which are interesting from the applications viewpoint are summarised in table 4. It is clearly seen that this magnetostrictive susceptibility is comparable to that of the magnetostrictive multilayers.

Even better performances were obtained from magnetostrictive multilayers of the novel type of "Spring Magnets", where the saturation field of the magnetostrictive, amorphous Tb-FeCo is lowered by increasing the average magnetisation through exchange coupling with the soft-magnetic Fe-Co layers. In addition to this, increasing magnetisation by closing the cone angle in a sperimagnetic structure is also an efficient means of increasing low field magnetostrictive susceptibility, since this reduces the saturation field, and the magnetoelastic coupling is strongly correlated to the mean value of the magnetic moments correlation function. This process can be achieved by increasing the molecular field. Experimentally, the molecular field of R-T may be strengthening in the neighbourhood of the strongly magnetic FeCo layer. In this case, layers must be sufficiently thin, then, a noticeable volume of the R-T layer may be submitted to the large molecular field. In the last two years, important progress has been achieved in magnetostrictive multilayer research. Ludwig and Quandt (2000) reported the possibility of controlling the orientation of the magnetic easy axis by magnetic annealing and, thus, were able to enhance the magnetostriction in the desired direction. An induced uniaxial anisotropic multilayer TbFe/Fe can also be created by deposition under a magnetic polarisation field. High amplitude flexural and torsional oscillation modes were observed for these films (Le Gall et al. 2000). Duc et al. (2001a) reported a large magnetostrictive susceptibility and discussed the so-called working point for the magnetostrictive multilayers in microactuator devices.

In attempts to prepare the magnetostrictive multilayers consisting of nanocrystalline magnetostrictive layers with soft magnetic interlayers, Farber and Kronmüller (2000b) have studied TbDyFe/Finemet multilayers (Finemet is a nanocrystalline FeSiBNbCu soft magnetic alloy). The contribution of the individual layers to the magnetoelastic couplings was deduced from their magnetoelastic data, where an opposite contribution of the Finemet ( $b^{\gamma,2} = 15$ ) with respect to that of the TbDyFe ( $b^{\gamma,2} = -18$ ) was found. In the TbDyFe/Fe multilayers, however, the magnetoelastic coupling has the same sign:  $b^{\gamma,2} = -22$  and  $-6$  for TbDyFe and Fe layers, respectively (Farber and Kronmüller 2000b).

Attempts to reduce  $\mu_0 H_c$  also imply the possibility of shifting the working point to lower fields. For this purpose, Quandt and Ludwig (1999) have prepared the TbFe/FeCoBSi multilayers. It was shown that the FeCoBSi layers improved the magnetic softness of the multilayer. Recently, Duc et al. (2001b) have succeeded in preparing Tb(Fe<sub>0.55</sub>Co<sub>0.45</sub>)<sub>1.5</sub>/(Y<sub>0.2</sub>Fe<sub>0.8</sub>) (i.e., a-TerfecoHan/n-YFe, Duc 2001) multilayers with  $\mu_0 H_c = 0.5 \text{ mT}$ . Initially, this multilayer consists of the amorphous TbFeCo and not-well crystallised FeCo layers. In this state, a soft magnetic and magnetostrictive character with a coercivity  $\mu_0 H_c = 3 \text{ mT}$  and a parallel magnetostrictive susceptibility

Table 4  
Comparison of the magnetoelastic data for magnetostrictive bulk and thin-film materials

Materials	$b^{\gamma,2}$ (MPa)	$\lambda^{\gamma,2}$ ( $10^{-6}$ )	$\partial b_{\parallel}/\partial B$ (Mpa/T)	References
<i>Bulk crystalline</i>				
Terfenol-D Tb <sub>0.27</sub> Dy <sub>0.73</sub> Fe <sub>2</sub>	-101	2400	568	[1]
<i>Single layer films</i>				
a-TbFe <sub>2</sub>	-19.4	321	20	[2]
a-Tb <sub>0.27</sub> Dy <sub>0.73</sub> Fe <sub>2</sub>	-17.2	300	50	[3]
n-Tb <sub>0.27</sub> Dy <sub>0.73</sub> Fe <sub>2</sub>	-49.0	800		[4]
a-TbCo <sub>2</sub>	-24.5	400	155	[5]
a-Tb <sub>0.27</sub> Dy <sub>0.73</sub> Co <sub>2</sub>	-15.1	260	190	[3]
a-Tb(Fe <sub>0.45</sub> Co <sub>0.55</sub> ) <sub>2</sub>	-63.5	1040	300	[6,7]
a-Tb(Fe <sub>0.55</sub> Co <sub>0.45</sub> ) <sub>1.5</sub>	-65.9	1080	1100	[8]
a-Tb <sub>0.27</sub> Dy <sub>0.73</sub> (Fe <sub>0.45</sub> Co <sub>0.55</sub> ) <sub>2</sub>	-20.15	330	430	[6,7]
a-SmFe <sub>1.6</sub>	25.9	-380		[9]
a-(SmFe <sub>2</sub> ) <sub>99.26</sub> B <sub>0.74</sub>	45.6	-670		[10]
a-SmCo <sub>2</sub>	11.0	-161	40	[7]
a-Sm(Fe <sub>0.58</sub> Co <sub>0.42</sub> ) <sub>1.54</sub>	27.4	-320	76	[11]
<i>Multilayers</i>				
Tb <sub>0.4</sub> Fe <sub>0.6</sub> /Fe	-20	300		[12]
Tb <sub>0.27</sub> Dy <sub>0.73</sub> Fe <sub>2</sub> /Fe	-12		650	[13]
Tb <sub>0.27</sub> Dy <sub>0.73</sub> Fe <sub>2</sub> /Finemet			300	[13]
Tb(Fe <sub>0.55</sub> Co <sub>0.45</sub> ) <sub>1.5</sub> /Fe	-39		3040	[14]
Tb <sub>0.4</sub> Fe <sub>0.6</sub> /Fe <sub>0.5</sub> Co <sub>0.5</sub>	-28	410	1000	[12]
Tb <sub>0.37</sub> Fe <sub>0.63</sub> /Fe <sub>0.65</sub> Co <sub>0.35</sub>	-31.1	600	4000	[12]
Tb <sub>0.27</sub> Fe <sub>0.73</sub> /Fe <sub>0.75</sub> Co <sub>0.25</sub>	-27	348	4800	[12]
Tb <sub>0.18</sub> Fe <sub>0.82</sub> /Fe <sub>0.75</sub> Co <sub>0.25</sub>	-44.5	890		[12]
Tb(Fe <sub>0.55</sub> Co <sub>0.45</sub> ) <sub>1.5</sub> /Fe <sub>0.85</sub> Co <sub>0.15</sub>	-32	530	7850	[15]
<i>Sandwich system</i>				
Nd <sub>0.25</sub> Co <sub>0.75</sub> /Tb <sub>0.28</sub> Co <sub>0.72</sub> /Nd <sub>0.25</sub> Co <sub>0.75</sub>	-15.2	248	560	[8]
Tb <sub>0.28</sub> Co <sub>0.72</sub> /Nd <sub>0.25</sub> Co <sub>0.75</sub> /Tb <sub>0.28</sub> Co <sub>0.72</sub>	-16.5	270	117	[7,8,16]

*References*

- |                           |                                 |                                    |
|---------------------------|---------------------------------|------------------------------------|
| [1] Clark (1980)          | [7] Betz (1997)                 | [12] Quandt and Ludwig (1997)      |
| [2] Hayashi et al. (1993) | [8] Duc et al. (2000b)          | [13] Farber and Kronmüller (2000b) |
| [3] Duc et al. (2000a)    | [9] Honda et al. (1994)         | [14] Duc et al. (2001a)            |
| [4] Ried et al. (1998)    | [10] Kim (1993)                 | [15] Duc et al. (2001b)            |
| [5] Betz et al. (1999)    | [11] S. David, unpublished data | [16] Givord et al. (1996)          |
| [6] Duc et al. (1996)     |                                 |                                    |

$\chi_{\lambda\parallel, \max} = 3.8 \times 10^{-2} \text{ T}^{-1}$  had been achieved. This magnetostrictive softness was strongly improved by heat treatments:  $\mu_0 H_c = 0.5 \text{ mT}$  and  $\chi_{\lambda\parallel} = 13 \times 10^{-2} \text{ T}^{-1}$  in a field of 1.8 mT. These novel properties are associated with the development of YFe nanostructure layers.

Aside from technical considerations, we must stress that studies on magnetoelastic effects in thin films also present a fundamental interest. The magnetoelastic coupling is quite dependent on the symmetry of the material. At the surface of any alloy, the symmetry is broken since there are no neighbouring atoms. The surface contribution to the magnetoelastic coupling, thus, must be considered. This contribution is usually negligible in bulk materials, but it is no longer true for thin films where surface effects are essential. In particular, for magnetostrictive multilayers the nature of the interfaces is critical; their contributions to the magnetic and magnetostrictive properties needs to be considered. In this context, a general consideration of the magnetoelasticity in the heterogeneous magnetic materials (including nanoscale thin films, multilayers, superlattices, nanocrystalline magnetic alloys and magnetic granular films) may be useful. As noted above the contributions of interfaces to the magnetic and magnetostrictive properties have been experimentally verified in heterogeneous magnetic systems. However, the magnetoelastic interactions as well as magnetic properties of these materials are complex and need further experimental as well as theoretical studies. At the moment, only phenomenological models can describe their properties.

Finally, significant improvements in the field of giant magnetostrictions have allowed the design and test of some prototypes of microactuators and motors taking advantage of a wireless magnetic excitation.

### Acknowledgements

The support of the Vietnam National University, Hanoi under projet QG.99.08 is useful for the completion of this work. The collaborations with Dr. D. Givord, Dr. K. Mackay, Dr. J. Betz and Dr. E. du Trémolet de Lacheisserie at the Laboratoire Louis Néel, CNRS, Grenoble (France) are very useful, not only to become familiar with the field, but also to expand my research in this area. Special thanks are due to J. Betz for permission to include his work prior to this overview. I am particularly grateful to Prof. Dr. T.D. Hien, Prof. Dr. N.H. Luong, Dr. N.H. Chau and co-workers, who have started together with me to build equipment for measuring the thermal expansion and magnetostriction using the capacitance method, and to develop research on magnetovolume effects and magnetostriction of the lanthanide–transition metal intermetallics at the Cryogenic Laboratory in Hanoi since 1981. Dr. N.T. Hien and Prof. Dr. N.P. Thuy have greatly encouraged me to write this chapter.

### References

- |  |  |
|--|--|
| Abbundi, R., and A.E. Clark, 1978, <i>J. Appl. Phys.</i> <b>49</b> , 1969.           | Akulov, N.S., 1928, <i>Z. Phys.</i> <b>52</b> , 389.                         |
| Abbundi, R., A.E. Clark and N.C. Coon, 1979, <i>J. Appl. Phys.</i> <b>50</b> , 1671. | Andreev, A.V., 1979, Thesis (Ural State University, Sverdlovsk). In Russian. |
|  | Andreev, A.V., 1990, Dissertation of Doctor of Sci-                          |



- ences, Thesis (Ural State University, Sverdlovsk). In Russian.
- Andreev, A.V., A.V. Deryagin and S.M. Zadvorkin, 1985, *Phys. Met. Metallogr.* **59**, 57.
- Awano, H., O. Taniguchi, T. Katayama, F. Inoue, A. Itoh and K. Kawanishi, 1988, *J. Appl. Phys.* **64**, 6107.
- Babara, B., J.P. Girard, J. Laforet, R. Lemaire, E. Siaud and J. Schweizer, 1977, *Physica B* **88-86**, 155.
- Becker, R., and W.D. Döring, 1939, *Ferromagnetismus* (Springer, Berlin).
- Belov, K.P., O.P. Yelyutin, G.I. Katayev, D. Kim, S.A. Nikitin, G.V. Pshechenkova, L.I. Solntseva, G.N. Surovaya and V.P. Taratynov, 1975, *Phys. Met. Metallogr.* **39**, 50.
- Betz, J., 1997, Thesis (University of Grenoble).
- Betz, J., E. du Trémolet de Lacheisserie and L.T. Baczewski, 1996a, *Appl. Phys. Lett.* **68**(1), 132.
- Betz, J., K. Mackay, J.C. Peuzin, B. Halstrup and N. Lhermet, 1996b, in: *Proc. Actuator 96 Conf.*, Bremen, Germany (Axon Technology Consult) pp. 283-286.
- Betz, J., K. Mackay and D. Givord, 1999, *J. Magn. Magn. Mater.* **207**, 180.
- Boucher, B., A. Liénard, J.P. Rebouillat and J. Schweizer, 1979, *J. Phys. F* **9**, 1421.
- Campbell, I.A., 1972, *J. Phys. F* **2**, L47.
- Chappert, J., J.M.D. Coey, A. Liénard and J.P. Rebouillat, 1981, *J. Phys. F* **11**, 2727.
- Chikazumi, S., 1964, *Physics of Magnetism* (Wiley, New York).
- Claeyssen, F., N. Lhermet, R. Le Letty and P. Bouchilloux, 1997, *J. Alloys Compounds* **258**, 61.
- Clark, A.E., 1980, in: *Handbook of Ferromagnetic Materials*, Vol. 1, ed. E.P. Wohlfarth (North-Holland, Amsterdam) p. 539.
- Clark, A.E., and H. Belson, 1972, *AIP Conf. Proc.* **5**, 1498; *Phys. Rev. B* **5**, 3642; *IEEE Trans. Magn. MAG-8*, 477.
- Clark, A.E., R. Abbundi and W.G. Gillmor, 1978, *IEEE Trans. Magn. MAG-14*, 542.
- Cochrane, R.W., R. Harris and M.J. Zuckermann, 1978, *Phys. Rep.* **48**, 1.
- Coehoorn, R., 1990, in: *Proc. NATO-ASI, Supermagnets, Hard Magnetic Materials*, eds G.J. Long and F. Grandjean (Kluwer, Dordrecht).
- Coey, J.M.D., 1978, *J. Appl. Phys.* **49**, 1646.
- Coey, J.M.D., D. Givord, A. Liénard and J.P. Rebouillat, 1981, *J. Phys. F* **11**, 2707.
- Danh, T.M., N.H. Duc and N.P. Thuy, 1998, *J. Magn. Magn. Mater.* **185**, 105.
- Danh, T.M., N.H. Duc, H.N. Thanh and J. Teillet, 2000, *J. Appl. Phys.* **87**, 7208.
- Deryagin, A.V., N.V. Kudrevatykh, V.N. Moskaev, A.V. Andreev and S.M. Zavorkin, 1981, *Ukr. Phys. J.* **26**, 1734. In Russian.
- Deryagin, A.V., G.M. Kvshnin and A.M. Kapitonov, 1984, *Sov. Phys. Solid State* **26**, 1871.
- Deryagin, A.V., A.A. Kazakov, N.V. Kudrevatykh, V.N. Moskaev, V.N. Mushnikov and S.V. Terent'yev, 1985, *Phys. Met. Metallogr.* **60**, 81.
- Dieny, B., D. Givord, J.M. Ndjaka and J.M. Alameda, 1990, *J. Appl. Phys.* **67**, 5677.
- Dieny, B., D. Givord and J.M. Ndjaka, 1991, *J. Magn. Magn. Mater.* **93**, 503.
- Dirne, F.W.A., and C.J.M. Denissen, 1989, *J. Magn. Magn. Mater.* **78**, 122.
- du Trémolet de Lacheisserie, E., 1993, in: *Magnetostriction: Theory and Applications of Magnetoelasticity*, CRC press (Boca Raton, FL).
- du Trémolet de Lacheisserie, E., and J.C. Peuzin, 1994, *J. Magn. Magn. Mater.* **136**, 189.
- du Trémolet de Lacheisserie, E., and J.C. Peuzin, 1996, *J. Magn. Magn. Mater.* **152**, 231.
- du Trémolet de Lacheisserie, E., K. Mackay, J. Betz and J.C. Peuzin, 1998, *J. Alloys Compounds* **275**, 685.
- Duc, N.H., 1997, in: *Handbook on the Physics and Chemistry of Rare Earths*, Vol. 24, eds K.A. Gschneidner Jr and L. Eyring (Elsevier Science, Amsterdam), Vol. **24**, p. 339.
- Duc, N.H., 2001, in: *Proc. Joint European Magnetic Symp.*, Grenoble, *J. Magn. Magn. Mater.*, to be published.
- Duc, N.H., and D. Givord, 1996, *J. Magn. Magn. Mater.* **157/158**, 169.
- Duc, N.H., K. Mackay, J. Betz and D. Givord, 1996, *J. Appl. Phys.* **79**, 973.
- Duc, N.H., K. Mackay, J. Betz and D. Givord, 2000a, *J. Appl. Phys.* **87** 834.
- Duc, N.H., T.M. Danh, H.N. Thanh, J. Teillet and A. Liénard, 2000b, *J. Phys.: Condens. Matter* **12**, 8283.
- Duc, N.H., T.M. Danh, N.A. Tuan and J. Teillet, 2001a, *Appl. Phys. Lett.* **78**, 3648.
- Duc, N.H., F. Richomme, N.A. Tuan, D.T. Huong Giang, T. Verdier and J. Teillet, 2001b, *Proc. Joint European Magnetic Symp.*, Grenoble, *J. Magn. Magn. Mater.*, to be published.

- Dwight, A.E., and C.W. Kimball, 1974, *Acta Crystallogr. B* **30**, 2791.
- Farber, P., and H. Kronmüller, 2000a, *J. Magn. Magn. Mater.* **195**, 159.
- Farber, P., and H. Kronmüller, 2000b, *J. Appl. Phys.* **88**, 2781.
- Fischer, S.F., M. Kelsch and H. Kronmüller, 1999, *J. Magn. Magn. Mater.* **195**, 545.
- Forester, D.W., C. Vittoria, J. Schelleng and P. Lubitz, 1978, *J. Appl. Phys.* **49**, 1966.
- Franse, J.J.M., and R.J. Radwanski, 1993, in: *Ferromagnetic Materials*, Vol. 7, ed. K.H.J. Buschow (North-Holland, Amsterdam) p. 307.
- Fujimori, H., J.Y. Kim, S. Suzuki, H. Morita and N. Kataoka, 1993, *J. Magn. Magn. Mater.* **124**, 115.
- Gavigan, J.P., D. Givord, H.S. Li and J. Voiron, 1988, *Physica B* **149**, 345.
- Givord, D., A.D. Santos, Y. Souche, J. Voiron and S. Wüchner, 1993, *J. Magn. Magn. Mater.* **121**, 216.
- Givord, D., J. Betz, N.H. Duc, K. Mackay and E. du Trémolet de Lacheisserie, 1995, in: *Proc. 2nd Int. Workshop on Materials Science, Hanoi, 10/1995*, eds F.F. Becker, N.D. Chien, J.J.M. Franse and T.D. Hien, p. 287.
- Givord, D., J. Betz, K. Mackay, J.C. Toussaint, J. Voiron and S. Wüchner, 1996, *J. Magn. Magn. Mater.* **159**, 71.
- Grundy, P.J., D.G. Lord and P.I. Williams, 1994, *J. Appl. Phys.* **76**, 7003.
- Halstrup, B., J. Betz, K. Mackay, J.-C. Peuzin and N. Lhermet, 1996, in: *Micro Systems Technologies 96*, eds H. Reichl and A. Heuberger (VDE, Berlin) p. 457.
- Hansen, P., 1991, in: *Handbook of Magnetic Materials*, Vol. 6, ed. K.H.J. Buschow (Elsevier Science, Amsterdam) p. 289.
- Hansen, P., C. Clausen, G. Much, M. Rosenkranz and K. Witer, 1989, *J. Appl. Phys.* **66**, 756.
- Harris, R., M. Plischke and M.J. Zuckermann, 1973, *Phys. Rev. Lett.* **31**, 160.
- Hayashi, Y., T. Honda, K.I. Arai, K. Ishiyama and M. Yamaguchi, 1993, *IEEE Trans. Magn.* **MAG-29**, 3129.
- Hernando, A., C. Prados and C. Prieto, 1996, *J. Magn. Magn. Mater.* **157/158**, 501.
- Herzer, G., 1990, *IEEE Trans. Magn.* **MAG-26**, 1397.
- Hofmann, B., T. Reninger and H. Kronmüller, 1992, *Phys. Status Solidi a* **134**, 247.
- Honda, T., Y. Hayashi, K.I. Arai, K. Ishiyama and M. Yamaguchi, 1993, *IEEE Trans. Magn.* **MAG-29**, 3126.
- Honda, T., K.I. Arai and M. Yamaguchi, 1994, *J. Appl. Phys.* **76**, 6994.
- Huang, J., C. Prados, J.E. Evetts and A. Hernando, 1995, *Phys. Rev. B* **51**, 297.
- Imry, Y., and S. Ma, 1975, *Phys. Rev. Lett.* **35**, 1399.
- Kaneko, M., S. Hashimoto, M. Hayakawa and K. Aso, 1988, *J. Phys. Sci. Instrum.* **21**, 487.
- Kaneyoshi, T., 1984, *Amorphous Magnetism* (CRC, Boca Raton, FL).
- Kim, J.Y., 1993, *J. Appl. Phys.* **74**, 2701.
- Klokholm, E., 1976, *IEEE Trans. Magn.* **MAG-12**, 819.
- Klokholm, E., 1977, *IBM Tech. Disc. Bull.* **19**, 4030.
- Korolyov, A.V., V.N. Mushnikov, A.V. Andreev and V.A. Gaviko, 1990, *Phys. Met. Metallogr.* **69**, 88.
- Kudrevatykh, N.V., 1994, *Dissertation of Doctor of Sciences* (Ural State University, Sverdlovsk). In Russian.
- Le Gall, H., J. Ben Youssef, F. Socha, N. Tiercelin, V. Preobrazhensky and P. Pernod, 2000, *J. Appl. Phys.* **87**, 5783.
- Levitin, R.Z., and A.S. Markosyan, 1990, *J. Magn. Magn. Mater.* **84**, 247.
- Liu, J.P., F.R. de Boer, P.F. de Châtel, R. Coehoorn and K.H.J. Buschow, 1994, *J. Magn. Magn. Mater.* **134**, 159.
- Ludwig, A., and E. Quandt, 2000, *J. Appl. Phys.* **87**, 4691.
- Markosyan, A.S., 1988, *Dissertation of Doctor of Sciences* (Moscow State University, Moscow). In Russian.
- Miyazaki, T., T. Saito and Y. Fujino, 1997, *J. Magn. Magn. Mater.* **171**, 320.
- Morin, P., and D. Schmitt, 1990, in: *Handbook of Magnetic Materials*, Vol. 4, ed. K.H.J. Buschow (North-Holland, Amsterdam) p. 4.
- Nagi, Y., M. Senda and T. Toshima, 1988, *J. Appl. Phys.* **63**, 2356.
- Nakamura, Y., 1983, *J. Magn. Magn. Mater.* **31-34**, 829.
- Néel, L., 1953, *C.R. Acad. Sci.* **237**, 1468, 1954; *J. Phys. Radium* **15**, 225.
- Polk, D.E., 1972, *Acta Metall.* **20**, 485.
- Popov, Yu.F., R.Z. Levitin, A.V. Deryagin, M. Zelery and A.V. Andreev, 1980, *Sov. Phys. JETP* **51**, 1223.
- Quandt, E., 1994a, *J. Appl. Phys.* **75**, 5653.
- Quandt, E., 1994b, *J. Appl. Phys.* **76**, 7000.
- Quandt, E., 1997, *J. Alloys Compounds* **258**, 126.

- Quandt, E., and A. Ludwig, 1997, *Mater. Res. Soc. Symp. Proc.* **459**, 565.
- Quandt, E., and A. Ludwig, 1999, *J. Appl. Phys.* **85**, 6232.
- Quandt, E., and K. Seemann, 1996, in: *Micro Systems Technologies 96*, eds H. Reichl and A. Heuberger (VDE, Berlin) p. 451.
- Quandt, E., A. Ludwig, J. Mencik and E. Nold, 1997a, *J. Alloys Compounds* **258**, 133.
- Quandt, E., A. Ludwig, J. Betz, K. Mackay and D. Givord, 1997b, *J. Appl. Phys.* **81**, 5420.
- Ried, K., M. Schnell, F. Schatz, M. Hirscher, B. Ludescher, W. Sigle and H. Kronmüller, 1998, *Phys. Status Solidi a* **167**, 195.
- Schatz, F., M. Hirscher, G. Flik and H. Kronmüller, 1993, *Phys. Status Solidi a* **137**, 197.
- Schatz, F., M. Hirscher, M. Schnell, G. Flik and H. Kronmüller, 1994, *J. Appl. Phys.* **76**, 5380.
- Shima, T., H. Yokoyama and H. Fujimori, 1997, *J. Alloys Compounds* **258**, 149.
- Sontag, H., and A.C. Tam, 1986, *IEEE Trans. Ultrason. Ferroelectr. Freq. Cont.* **UFFC-33**, 500.
- Szumiata, T., H. Szymczak and R. Zuberek, 1993, *IEEE Trans. Magn.* **MAG-29**, 3132.
- Szymczak, H., R. Zuberek, R. Krishnan, M. Tessier, K.B. Youn and C. Sella, 1988, *ICMFS-12 Conf.*, Le Creusot, p. 3.
- Takagi, H., S. Tsunashima and S. Uchiyama, 1979, *J. Appl. Phys.* **50**, 1642.
- Tam, A.C., and H. Schroeder, 1988, *J. Appl. Phys.* **64**, 5422.
- Thuy, N.P., N.M. Hong, T.D. Hien and J.J.M. Franse, 1988, *J. Phys. Paris* **49**, C8.
- Trippel, G., 1977, *IBM Tech. Rep.* **TR28.094**.
- van de Riet, E., 1994, *J. Appl. Phys.* **76**, 584.
- Wada, M., H.H. Uchida, Y. Matsumura, H. Uchida and H. Kaneko, 1996, *Thin Solid Films* **281**, 503.
- Wada, M., H.H. Uchida and H. Uchida, 1997a, *J. Alloys Compounds* **258**, 143.
- Wada, M., H. Uchida and H. Kaneko, 1997b, *J. Alloys Compounds* **258**, 169.
- Wada, M., H.H. Uchida and H. Uchida, 1997c, *J. Alloys Compounds* **258**, 174.
- Wada, M., H. Uchida and H. Kaneko, 1997d, *J. Alloys Compounds* **258**, 42.
- Wandass, J.H., J.S. Murday and R.J. Colton, 1988, Preprint (Naval Research Laboratory, Washington).
- Weber, M., R. Koch and K.H. Rieder, 1994, *Phys. Rev. Lett.* **73**, 116.
- Williams, P.L., D.G. Lord and P.J. Grundy, 1994, *J. Appl. Phys.* **75**, 5257.
- Winzek, B., M. Hirscher and H. Kronmüller, 1999, *J. Alloys Compounds* **283**, 78.
- Wüchner, S., J. Voiron, J.C. Toussaint and J.J. Prejean, 1995, *J. Magn. Magn. Mater.* **148**, 264.
- Zavorkin, S.M., 1987, Thesis (Ural State University, Sverdlovsk). In Russian.
- Zhu, Houqing, Liu Jianguo, Wang Xiurong, Xing Yanhong and Zhang Hongping, 1997, *J. Alloys Compounds* **258**, 49.
- Zuberek, R., H. Szymczak, R. Krishnan, K.B. Youn and C. Sella, 1987, *IEEE Trans. Magn.* **MAG-23**, 3699.
- Zuberek, R., H. Szymczak, R. Krishnan and M. Tessier, 1988, *J. Phys. Paris* **49**, C8-1761.
- Zuberek, R., D. Zymierska and H. Szymczak, 1994, *Acta Phys. Pol. A* **85**, 439.
- Zuberek, R., K. Fronc, H. Szymczak, A. Nabialek, T. Stobiecki and J. Sokulski, 1995, *J. Magn. Magn. Mater.* **139**, 157.

## Chapter 206

# **μSR STUDIES OF RARE-EARTH AND ACTINIDE MAGNETIC MATERIALS\***

G.M. KALVIUS

*Physics Department, Technical University Munich, 85747 Garching, Germany*

D.R. NOAKES

*Department of Physics, Virginia State University, Petersburg, VA 23806, USA*

O. HARTMANN

*Department of Physics, University of Uppsala, 75121 Uppsala, Sweden*

---

### Contents

List of symbols	58	3.2.3. Longitudinal field measurements	102
List of acronyms	59	3.3. μSR spectroscopy of ordered magnets	105
1. Introduction	60	3.4. Double relaxation	110
2. The μSR technique	62	3.5. Data analysis	111
2.1. General aspects	62	3.6. Determination of the muon site	114
2.2. Properties of the muon	66	3.7. Modeling of the internal field	116
2.3. Muon generation and decay	67	3.8. Muon diffusion and magnetism (site averaging)	121
2.4. Muon implantation	69	4. Elemental metals	122
2.5. Muon beam characteristics	71	4.1. Anisotropic spin fluctuations	124
2.6. The recording of μSR spectra	76	4.2. Gadolinium	126
2.7. Special applications	81	4.2.1. Paramagnetic region and critical behavior	127
2.7.1. Extreme temperatures	81	4.2.2. Ferromagnetic region	129
2.7.2. High magnetic fields	82	4.2.3. High-pressure measurements	131
2.7.3. High pressure	83	4.3. Holmium, dysprosium and erbium	132
2.7.4. Small samples	85	4.3.1. Ambient pressure	132
2.7.5. Low-energy muons	86	4.3.1.1. Holmium	132
3. μSR magnetic response	88	4.3.1.2. Dysprosium	134
3.1. The local field at the muon site	88	4.3.1.3. Erbium	136
3.2. μSR spectroscopy of dia- and paramagnets	92	4.3.2. High-pressure measurements	138
3.2.1. Transverse field measurements (Knight shift)	93	5. Intermetallics	140
3.2.2. Zero field measurements	97	5.1. Singlet ground state systems	140

---

\* This work has been supported by the BMBF, Federal Republic of Germany under contract 03-KA4-TU1-9, by US DOD grants F-49620-97-0297 (AFOSR) and -0532 (BMDO), and by the Swedish National Research Council.

5.1.1. Crystalline electric field (CEF) effects	140	5.4. Binary compounds and alloys (other than Laves phases)	208
5.1.2. $\mu$ SR in singlet ground state systems	145	5.4.1. $\text{MX}_2$ compounds	208
5.1.2.1. Praseodymium metal	146	5.4.1.1. $\text{PrCu}_2$	208
5.1.2.2. $\text{PrNi}_5$	147	5.4.1.2. $\text{NdCu}_2$	208
5.1.2.3. $\text{PrIn}_3$	148	5.4.1.3. R dihydrides and dideuterides	208
5.1.2.4. $\text{PrCu}_2$	149	5.4.2. $\text{MX}_3$ compounds	209
5.1.2.5. $\text{PrP}_x$	149	5.4.2.1. $\text{EuAs}_3$	209
5.1.2.6. $\text{PrRu}_2\text{Si}_2$	150	5.4.2.2. $\text{UPd}_3$	209
5.1.2.7. $\text{HoBa}_2\text{Cu}_3\text{O}_7$	150	5.4.3. $\text{MX}_5$ compounds	210
5.1.3. Muon-induced effects	151	5.4.3.1. $\text{GdNi}_5$	210
5.2. Simple cubic compounds	152	5.4.3.2. $\text{TbNi}_5$	213
5.2.1. NaCl structure	154	5.4.3.3. $\text{DyNi}_5$	213
5.2.1.1. UAs	156	5.4.3.4. $\text{ErNi}_5$	213
5.2.1.2. UN	160	5.4.3.5. $\text{TmNi}_5$	214
5.2.1.3. UP	160	5.4.3.6. $\text{YbNi}_5$	215
5.2.1.4. USb	160	5.4.4. $\text{RGa}_6$ compounds	215
5.2.1.5. $\mu$ SR response in AFM simple cubic compounds	162	5.4.4.1. $\text{CeGa}_6$	215
5.2.1.6. CeAs	162	5.4.4.2. $\text{NdGa}_6$	216
5.2.1.7. CeSb	166	5.4.4.3. $\text{GdGa}_6$	216
5.2.1.8. DySb	167	5.4.4.4. $\text{TbGa}_6$	216
5.2.1.9. Uranium monochalcogenides	167	5.5. Ternary compounds	218
5.2.2. CsCl structure	170	5.5.1. MTX	218
5.2.2.1. $\text{LaAg}_{1-x}\text{In}_x$	171	5.5.1.1. CeCuSn	218
5.2.2.2. CeAg and $\text{CeAg}_{0.97}\text{In}_{0.03}$	171	5.5.1.2. UNiGa	219
5.2.2.3. DyAg	172	5.5.1.3. UNiAl	220
5.2.3. AuCu <sub>3</sub> structure	175	5.5.1.4. Other UTX compounds	221
5.3. Laves-phase compounds	178	5.5.2. $\text{MT}_2\text{X}_2$	222
5.3.1. $\text{MAl}_2$	179	5.5.2.1. Y and La intermetallics	222
5.3.1.1. $\text{RAl}_2$	179	5.5.2.2. $\text{CeRh}_2\text{Si}_2$	222
5.3.1.2. $\text{AnAl}_2$ (An = U, Np)	185	5.5.2.3. $\text{PrCo}_2\text{Si}_2$	224
5.3.2. $\text{MT}_2$ (T = Fe, Co, Ni)	189	5.5.2.4. $\text{PrRu}_2\text{Si}_2$	227
5.3.2.1. $\text{RT}_2$	189	5.5.2.5. $\text{NdRh}_2\text{Si}_2$	228
5.3.2.2. $\text{AnT}_2$	191	5.5.2.6. $\text{UT}_2\text{Si}_2$ with T = Co, Rh, Pt	228
5.3.3. $\text{MMn}_2$ and related compounds	193	5.5.2.7. $\text{U}(\text{Pd}_{1-x}\text{Fe}_x)_2\text{Ge}_2$	229
5.3.3.1. $\text{YMn}_2$	193	5.6. Other compounds	231
5.3.3.2. $\text{Y}(\text{Tb})\text{Mn}_2$	196	5.6.1. $\text{Gd}_{0.696}\text{Y}_{0.304}$	231
5.3.3.3. $\text{Y}(\text{Sc})\text{Mn}_2$	197	5.6.2. CeSi, CeGe	232
5.3.3.4. $\text{Y}(\text{Mn},\text{Al})_2$	199	5.6.3. $\text{R}_2\text{In}$	232
5.3.3.5. $\text{Y}(\text{Mn},\text{Fe})_2$	199	5.6.4. $\text{Y}_6(\text{Mn}_{1-x}\text{Fe}_x)_{23}$	233
5.3.3.6. $\text{Y}(\text{Al},\text{Fe})_2$	200	5.6.5. $\text{YMn}_{12}$	233
5.3.3.7. $\text{YMn}_2$ summary	201	5.6.6. $\text{CeAgSb}_2$	234
5.3.3.8. $\text{RMn}_2$ with R = Gd, Tb, Dy	201	5.6.7. $\text{RFe}_{9.5}\text{Mo}_{2.5}$	234
5.3.3.9. $\text{YCo}_2$	206	5.6.8. $\text{RFe}_6\text{Al}_6$	235
5.3.3.10. $\text{UMn}_2$	207	5.6.9. $\text{RFe}_4\text{Al}_8$	236
5.3.4. Other Laves phases	208	5.6.10. $\text{RTC}_2$	237
		5.7. Summary: $\mu$ SR studies in R and An intermetallics	237
		6. Non-metallic compounds	238

6.1. Binary oxides and halides	239	9.2.3. CeRhSb and $\text{La}_x\text{Ce}_{1-x}\text{RhSb}$	312
6.1.1. EuO	239	9.2.4. The Kondo insulator $\text{YbB}_{12}$	314
6.1.2. $\text{UO}_2$ and $\text{NpO}_2$	240	9.2.5. Other Kondo metals	316
6.1.3. Rare-earth halides	243	9.2.5.1. CePdSb	316
6.2. Orthoferrites and other perovskites	243	9.2.5.2. YbNiSn	318
6.3. Compounds showing giant magnetoresistance	245	9.2.5.3. $\text{Yb}(\text{Cu}_{1-x}\text{Ni}_x)_2\text{Si}_2$	318
6.4. Hard magnetic materials	248	9.2.5.4. $\text{UCu}_2\text{Sn}$	319
7. Superconductors	250	9.3. Heavy-fermion compounds	319
7.1. Non-cuprate f-electron superconductors	251	9.3.1. Ce intermetallics	319
7.2. Lanthanide magnetism in cuprates	255	9.3.1.1. CeRu <sub>2</sub>	319
7.2.1. The “214” phases	257	9.3.1.2. CeAl <sub>3</sub>	321
7.2.2. The “123” phases	259	9.3.1.3. CePb <sub>3</sub>	323
7.2.2.1. R = Gd	261	9.3.1.4. CeCu <sub>5</sub> , CeCu <sub>5-x</sub> Al <sub>x</sub> , CeCu <sub>5-x</sub> Ga <sub>x</sub>	323
7.2.2.2. R = Tb, Dy	262	9.3.1.5. CeB <sub>6</sub>	326
7.2.2.3. R = Ho	262	9.3.1.6. CeCu <sub>6</sub>	328
7.2.2.4. R = Er	263	9.3.1.7. CeRuSi <sub>2</sub>	329
7.2.2.5. R = Pr	264	9.3.1.8. CeCu <sub>2</sub> Si <sub>2</sub> and related compounds	331
7.2.2.6. R = Nd	264	9.3.1.9. CeCu <sub>2</sub> Ge <sub>2</sub>	334
7.2.2.7. Other studies	265	9.3.1.10. CeRu <sub>2</sub> Si <sub>2</sub> , Ce <sub>1-x</sub> La <sub>x</sub> Ru <sub>2</sub> Si <sub>2</sub> , Ce(Ru <sub>1-x</sub> Rh <sub>x</sub> ) <sub>2</sub> Si <sub>2</sub>	335
7.2.3. The “2212” phase	265	9.3.1.11. CeRu <sub>2</sub> Ge <sub>2</sub> , Ce(Ru <sub>1-x</sub> Fe <sub>x</sub> ) <sub>2</sub> Ge <sub>2</sub>	340
7.2.4. Ruthenate hybrids	266	9.3.1.12. CeT <sub>2</sub> Sn <sub>2</sub> (T = Cu, Pd, Pt)	342
8. Disordered magnetism	267	9.3.1.13. CePd <sub>2</sub> Al <sub>3</sub>	347
8.1. Dilute spin glasses	269	9.3.1.14. CeRh <sub>3</sub> B <sub>2</sub>	348
8.2. More-concentrated magnetic disorder	270	9.3.1.15. Ce <sub>3</sub> Au <sub>3</sub> Sb <sub>4</sub>	350
8.2.1. Varying-power exponential relaxation	271	9.3.1.16. Ce <sub>3</sub> Pd <sub>20</sub> Si <sub>6</sub> and Ce <sub>3</sub> Pd <sub>20</sub> Ge <sub>6</sub>	351
8.2.2. Kagomé dynamic relaxation	273	9.3.2. U intermetallics	352
8.2.3. Static relaxation for non-Gaussian and non-Lorentzian field distributions	273	9.3.2.1. UGe <sub>2</sub>	352
8.2.4. Inhomogeneous freezing	276	9.3.2.2. UPt <sub>3</sub> , U <sub>1-x</sub> Th <sub>x</sub> Pt <sub>3</sub> , U(Pd <sub>x</sub> Pt <sub>1-x</sub> ) <sub>3</sub>	352
8.3. Results on disordered f-magnetism	277	9.3.2.3. UCu <sub>5</sub>	361
8.3.1. Amorphous DyAg	277	9.3.2.4. UCd <sub>11</sub>	364
8.3.2. Highly frustrated rare-earth systems	279	9.3.2.5. UBe <sub>13</sub> , U <sub>1-x</sub> Th <sub>x</sub> Be <sub>13</sub> , U <sub>1-x</sub> Th <sub>x</sub> Be <sub>13-y</sub> By	364
8.3.3. Rare-earth quasicrystals	281	9.3.2.6. U <sub>2</sub> Zn <sub>17</sub>	367
8.3.4. Novel reduced-dimensionality systems	283	9.3.2.7. U <sub>14</sub> Au <sub>51</sub>	370
9. Correlated electron intermetallics	284	9.3.2.8. URu <sub>2</sub> Si <sub>2</sub> , URh <sub>2</sub> Si <sub>2</sub> and related compounds	370
9.1. Overview	284	9.3.2.9. URh <sub>2</sub> Ge <sub>2</sub>	375
9.2. Kondo metals, semimetals and insulators	293	9.3.2.10. UNi <sub>2</sub> Al <sub>3</sub> and UPd <sub>2</sub> Al <sub>3</sub>	376
9.2.1. CeTSn (T = 3d transition element)	293	9.3.2.11. UNi <sub>3</sub> B	381
9.2.1.1. CeNiSn	295	9.3.3. Other heavy-fermion compounds	382
9.2.1.2. CePtSn and CePdSn	301	9.3.3.1. PrInAg <sub>2</sub>	382
9.2.2. Pseudo-ternary compounds of type CeTSn	304	9.3.3.2. Sm <sub>3</sub> Se <sub>4</sub> (and Sm <sub>2</sub> Se <sub>3</sub> )	383
9.2.2.1. La <sub>x</sub> Ce <sub>1-x</sub> NiSn	304	9.3.3.3. Sm <sub>3</sub> Te <sub>4</sub>	385
9.2.2.2. U <sub>x</sub> Ce <sub>1-x</sub> NiSn	304		
9.2.2.3. CePt <sub>x</sub> Ni <sub>1-x</sub> Sn	305		
9.2.2.4. CeCu <sub>x</sub> Ni <sub>1-x</sub> Sn	306		

9.3.3.4. Yb <sub>4</sub> As <sub>3</sub>	385	9.4.2.5. CeCoGe <sub>3-x</sub> Si <sub>x</sub>	403
9.3.3.5. YbBiPt and Y <sub>0.5</sub> Yb <sub>0.5</sub> BiPt	386	9.4.2.6. Ce <sub>2</sub> Ni <sub>3</sub>	403
9.3.3.6. YbPdSb	388	9.4.2.7. CePt <sub>2</sub> Si <sub>2</sub>	406
9.3.3.7. YbAuCu <sub>4</sub>	390	9.4.2.8. U <sub>2</sub> Pt <sub>2</sub> In	407
9.3.3.8. Yb <sub>2</sub> Cu <sub>9</sub>	392	9.4.3. Summary: NFL compounds	407
9.3.4. Conclusions: heavy fermions	392	9.5. Intermediate valence	408
9.4. Non-Fermi-liquid behavior	393	9.5.1. CeSn <sub>3</sub> (and LaSn <sub>3</sub> ), CePd <sub>3</sub>	408
9.4.1. General considerations	393	9.5.2. Ce <sub>1-x</sub> Th <sub>x</sub>	409
9.4.2. Non-Fermi-liquid materials	394	9.5.3. EuPdAs (and NdPdAs)	410
9.4.2.1. CeCu <sub>6-x</sub> Au <sub>x</sub>	394	9.5.4. Sm <sub>0.9</sub> La <sub>0.1</sub> S	412
9.4.2.2. UCu <sub>5-x</sub> Pd <sub>x</sub>	398	10. Conclusions	412
9.4.2.3. Y <sub>1-x</sub> U <sub>x</sub> Pd <sub>3</sub>	400	Acknowledgements	414
9.4.2.4. Ce(Cu <sub>1-x</sub> Ni <sub>x</sub> ) <sub>2</sub> Ge <sub>2</sub>	402	References	414

### List of symbols<sup>1</sup>

$A(t)$	observed forward-backward asymmetry (of decay positron count rate)	$C(E)$	energy distribution function of emitted positrons
$a$	half width at half maximum of Lorentzian field distribution	$c$	speed of light
$a_0$	initial asymmetry (of decay positron emission)	$ce$	conduction electrons
$B$	magnetic field	$E$	energy (in general)
$B_{app}$	externally applied field in general	$E_f$	Fermi energy
$B_{con}$	contact field	$e$	elementary charge
$B_{dem}$	demagnetizing field	$G_x(t)$	transverse field (envelope) muon spin relaxation function
$B_{dip}$	dipolar field	$G_z(t)$	zero field or longitudinal field muon spin relaxation function
$B_{dip}^i$	dipolar field inside Lorentz sphere	$\mathcal{H}$	interaction Hamiltonian
$B_i$	cartesian component of local field	$\hbar$	Planck constant
$B_{int}$	field at the muon site from internal sources	$I$	nuclear spin
$B_L$	longitudinally applied field	$J$	total electronic angular momentum
$B_{lor}$	Lorentz field	$J$	exchange integral
$B_{rms}$	root mean square field of a (Gaussian) field distribution	$K$	(muon) Knight shift constant
$B_{sat}$	field required to achieve saturation magnetization	$k$	(neutron) wave vector
$B_T$	transverse applied field	$k$	Boltzmann constant
$B_\mu$	total magnetic field at muon site (local field)	$M_{dom}$	domain magnetization
$\langle B_\mu^2 \rangle$	second moment of local field distribution	$M_S$	sample magnetization
$C$	specific heat	$m$	mass
		$m_e$	electron mass
		$m_p$	proton mass
		$m_\mu$	muon mass
		$m_\pi$	pion mass
		$\mathcal{N}$	demagnetization factor

<sup>1</sup> Vectors are given in *boldface italic* type.

$N$	counts	$Z$	nuclear charge
$N_B$	backward counts	$\alpha$	ratio of backward/forward counter efficiency
$N_{bk}$	background counts	$\beta$	ratio of backward/forward initial asymmetry
$N_F$	forward counts	$\gamma$	Sommerfeld constant of electronic specific heat
$n$	neutron	$\gamma_p$	proton gyromagnetic ratio
$n^{\uparrow}, n^{\downarrow}$	up (down) spin density	$\gamma_{\mu}$	muon gyromagnetic ratio
$P$	pressure	$\Delta$	Gaussian width of field distribution
$P(B)$	probability of field magnitude $ B $ ; the magnetic field magnitude distribution	$\Lambda$	general muon spin relaxation rate
$P(T_K)$	distribution of Kondo temperatures	$\lambda$	muon spin relaxation rate (exponential decay)
$p$	proton	$\mu, (\mu^+, \mu^-)$	muon (positive, negative)
$p$	exponent in stretched exponential muon spin relaxation	$\vec{\mu}$	magnetic dipole moment
$p_{\mu}$	muon momentum	$\mu_B$	Bohr magneton
$p_{\nu}$	neutrino momentum	$\mu_e$	electron magnetic moment
$q$	wave vector	$\mu_N$	nuclear magneton
$S(q, \omega)$	(neutron) scattering function	$\mu_p$	proton magnetic moment
$S_{th}$	theoretical μSR signal function	$\nu, \nu_{\mu}, \nu_e$	neutrino, muon neutrino, electron neutrino
$S_{\mu}$	muon spin	$\nu_{\mu}$	muon spin precession frequency
$T$	absolute temperature	$\bar{\nu}$	antineutrino
$T_1$	spin–lattice relaxation time	$\pi, (\pi^+, \pi^-)$	pion (positive, negative)
$T_2$	spin–spin relaxation time	$\sigma$	muon spin relaxation rate (Gaussian decay)
$T_C$	Curie temperature	$\vec{\sigma}_{ce}$	spin of conduction electron
$T_c$	critical temperature (e.g., superconductors)	$\sigma_{VV}$	Van Vleck width (of field distribution)
$T_g$	glass transition temperature	$\tau_c$	correlation time in relaxation processes
$T_K$	(single ion) Kondo temperature	$\tau_s$	(magnetic) spin fluctuation time
$T^*$	Kondo lattice temperature	$\tau_{\mu}$	muon lifetime
$T_M$	magnetic transition temperature in general	$\tau_{\pi}$	pion lifetime
$T_N$	Néel temperature	$\chi$	magnetic susceptibility
$T_Q$	Quadrupolar ordering temperature	$\omega_{\mu}$	muon spin precession angular frequency
$T_{RKKY}$	Strength of RKKY interaction expressed as temperature		
$V$	volume		
$W(\theta)$	angular distribution of decay positrons		

### List of acronyms

AFM	antiferromagnetism or antiferromagnetic or antiferromagnet	BCS	Bardeen–Cooper–Schrieffer
An	actinide (or actinoid)	BOOM	Japanese pulsed muon facility at KEK
APW	augmented plane wave (approximation)	CEF	crystalline electric field
bcc	body-centered cubic (crystal structure)	CERN	European Center for Nuclear Research, Geneva (Switzerland)



dhcp	double hexagonal closed packed (crystal structure)	LAMPF	Los Alamos Meson Physics Factory (USA)
DOS	density of states	LCR	level crossing resonance
EFG	electric field gradient	LF	longitudinal field
EPR	electron paramagnetic resonance	LRC	long-range (magnetic) correlations
fcc	face centered cubic (crystal structure)	LRO	long-range (magnetic) order
FFLO	Fulde–Ferrel–Larkin–Ovchinnikov (state)	MFA	mean field approximation
FFT	Fast Fourier Transform	NFL	non Fermi liquid
FL	Fermi liquid	NMR	Nuclear Magnetic Resonance
FM	ferromagnetism or ferromagnetic or ferromagnet	PAC	perturbed angular correlations
GBG	Gaussian-broadened Gaussian (relaxation function)	PSI	Paul Scherrer Institute near Zürich (Switzerland)
GMR	giant magnetoresistance	RAL	Rutherford Appleton Laboratory, near Oxford (United Kingdom)
hcp	hexagonal closed packed (crystal structure)	R	rare earth (Sc, Y plus lanthanides)
HF	heavy fermion	RKKY	Ruderman–Kittel–Kasuya–Yosida
HWHM	half width at half maximum (of a distribution function)	SDW	spin density wave
ISDW	incommensurate spin density wave	SCR	self-consistent renormalization (theory of itinerant magnetism)
ISIS	neutron spallation source at RAL near Oxford (UK)	SRC	short-range (magnetic) correlations
IV	intermediate valence	SRO	short-range (magnetic) order
KEK	Japanese High Energy Laboratory at Tsukuba (Japan)	TF	transverse field
KT	Kubo–Toyabe (relaxation function)	TRIUMF	Tri-University Meson Facility, Vancouver (Canada)
		ZF	zero field

## 1. Introduction

Muon spin rotation/relaxation/resonance ( $\mu$ SR) spectroscopy has become an important tool for probing local static and dynamic magnetic properties. In over two decades a quite substantial body of  $\mu$ SR data has been collected from rare-earth and actinide materials, the latter, however, mostly restricted to samples containing uranium. To our knowledge no special review of  $\mu$ SR in f transition elements and their compounds exists. A comprehensive review on  *$\mu$ SR studies in magnetic materials* has been published by Schenck and Gygax (1995) and contains information on rare-earth and actinide magnets. The main emphasis is on samples showing long-range magnetic order, i.e., ferromagnets (FM) or antiferromagnets (AFM). More recently a very concise review by Dalmas de Réotier and Yaouanc (1997) under the title *Muon spin rotation and relaxation in magnetic materials* has appeared. Its emphasis is to show with pertinent examples the possibilities offered by  $\mu$ SR for gaining information on magnetic properties of various types. This is achieved on a high and comprehensive level. The paper only offers an overview on magnetic  $\mu$ SR studies after 1993 (i.e., of work not contained in the

review by Schenck and Gygax 1995) in the form of a table. Another review by Seeger and Schimmele (1992) entitled  *$\mu$ SR in magnetically ordered materials* concentrates on magnetic materials of the transition (3d) elements. In particular, the question of site occupation by the muon in those materials is discussed in detail there. Hartmann (1989) has briefly reviewed the basic aspects of *Positive muons as a probe in magnetism*. The latest addition to this theme is an article by Schenck (1999) entitled *Static magnetic properties of metallic systems explored by  $\mu$ SR-spectroscopy*. It is not a review, but discusses the theme on selected examples in good detail. Reviews on special aspects of compounds with f transition elements exist, such as  $\mu$ SR in heavy-fermion systems (Schenck 1993, Heffner 1994, Luke et al. 1994a, and especially Amato 1997) and high- $T_c$  superconductors (Nishida 1992, Uemura 1992, 1997, S.L. Lee 1999, Uemura and Cywinski 1999). We shall cover heavy-fermion and related compounds with respect to their often quite unusual magnetic behavior, but will not attempt a complete review of high- $T_c$  materials containing f transition elements. Usually the rare-earth constituent has little influence on the superconducting properties (with the notorious exception of Pr). We will address the acute question of how cuprates containing rare-earth elements move from magnetism into high- $T_c$  superconductivity. On this subject,  $\mu$ SR is able to give important insights.

The fundamental difference between 4f and 5f magnetism is the possibility of a substantial delocalization of the 5f wave function in the light actinides.  $\mu$ SR is not particularly well suited to give information on this aspect and, to our knowledge, the question how  $\mu$ SR reacts to highly delocalized magnetic moments has not been treated theoretically. In consequence, few investigations have been carried out with the declared goal to compare related actinide and rare-earth magnets and, in contrast to other contributions within this series of monographs, we cannot report results under the governing theme of evaluating differences between 4f and 5f magnets. However, we think a review on  $\mu$ SR magnetic studies of f element materials to be of use to the scientific community dealing with the properties of rare-earth and actinide materials. Several new aspects of magnetism have been discovered, especially in the realm of strongly correlated electron systems. Although we attempt a broad coverage of the subject we shall not list or comment on all data which have appeared in the literature. Often the early work which had been important in establishing the field has been superseded by more recent data. Since readers with expertise in other specializations in magnetism may not be familiar with this technique, we begin with a brief description of  $\mu$ SR, the experimental requirements and the physical meaning of the spectral parameters before we enter into a discussion of relevant data. We would be most happy if some of the readers would see advantage in performing  $\mu$ SR measurements in their fields of interest and join our growing community.

We had included in the original text of this review the literature (to the best of our knowledge) published up to the end of 1999 and some not-yet-published preprints that came to our attention. Delays in publication allowed us to update the article with publications having appeared in 2000. Their discussion is usually added at the end of the appropriate (sub)sections.

## 2. The $\mu$ SR technique

In this section we provide an overview of the technical aspects of  $\mu$ SR spectroscopy without going into details. The aim is to bring the reader to some understanding of what is involved in a  $\mu$ SR experiment and what is meant by the *termini technici* which he will encounter when studying original  $\mu$ SR literature.

### 2.1. General aspects

Basically,  $\mu$ SR is the measurement of the *temporal development of the spatial orientation of the spins of muons* which have been implanted in the material of interest with all spins initially fixed in one direction (complete muon spin polarization). The three names covered by the acronym  $\mu$ SR, namely muon spin rotation, relaxation or resonance, refer loosely to different means of observation.

When speaking of *Muon Spin Rotation* one emphasizes the measurement of *coherent* Larmor precession of the ensemble of muon spins in the magnetic field present at the site of the muons embedded in the sample. The spin rotation frequency is a direct measure of the magnitude of this field. To produce a precessional motion the field must have a component perpendicular to direction of the muon spin. Usually, this can be achieved by applying an external magnetic field in this direction, and Muon Spin Rotation is often synonymous with transverse field  $\mu$ SR.

*Muon Spin Relaxation* refers to the observation of *incoherent* motions of the muon spins which result in a loss of polarization with time. This will occur if the magnetic field sensed by the ensemble of implanted muons is broadly distributed. If the local field each muon sees in addition fluctuates randomly during a muon's life we observe what is called "dynamic depolarization", but also a stationary distributed field causes depolarization by phase incoherence ("static depolarization"). These two cases must be clearly distinguished. The situation corresponds to the two relaxation times  $T_1$  (spin-lattice) and  $T_2$  (spin-spin) in NMR. Muon Spin Relaxation measurements can be carried out without observing spin rotation and thus are possible in zero applied field or with a longitudinally applied field (i.e., a field applied parallel to the muon spin direction at the moment of implantation). Longitudinal field measurements are the most appropriate way to obtain a clear distinction between *static* and *dynamic* muon spin depolarization. Muon Spin Relaxation hence mostly refers to zero or longitudinal field  $\mu$ SR.

The term *Muon Spin Resonance* defines a NMR-type technique. In the presence of a static external field one induces muon spin flips by the application of resonant radio frequency (Kitaoka et al. 1982, Kreitzman 1990, Hampele et al. 1990, Nishiyama 1992, Scheuermann et al. 1997, Cottrell et al. 1997) or microwave field (Kreitzman et al. 1994). The resonance condition is detected *via* a loss of muon polarization. As in NMR, frequency shifts and linewidth are the sensitive parameters.

There are still other means to carry out  $\mu$ SR experiments. Most notably among them is the so-called (Avoided) Level Crossing Resonance (LCR or ALC, Kreitzman 1986, Kiefl 1986, Heming et al. 1986, Kiefl and Kreitzman 1992, Leon 1994). In this review we will

discuss only Muon Spin Rotation/Relaxation measurements since the other techniques have not yet been applied to the materials under consideration. LCR has its main impact on muon radical chemistry. Muon Spin Resonance experiments are most important for the study of semiconductors.

In principle,  $\mu$ SR can be performed either with positive or negative muons. The latter behave like heavy electrons and will be captured into Bohr orbits by the atoms in the sample material. They will quickly reach the 1s ground state, whose orbital radius, however, is comparable to nuclear radii. Negative muons thus sense predominantly the effects of the protonic charge distribution and the result is primarily of interest to nuclear physics. In addition, the  $\mu^-$  will be captured quickly by the nucleus, meaning that its life time is considerably shortened compared to the free muon lifetime ( $\sim 2.2 \mu\text{s}$ ), especially for atoms with large  $Z$ . Some aspects of  $\mu^-$ SR on oxygen are of interest to the study of high- $T_c$  superconductors (Nishida 1992) but in general, condensed matter physics or chemistry studies are carried out exclusively with positive muons. They act chemically like ions of a light isotope of hydrogen. As will be discussed in some detail further below, the  $\mu^+$  comes to rest at a site between the atoms (interstitial site in crystalline materials), since it is repelled by their nuclear charge. In consequence, it senses the magnetic field present near, but outside, the atoms. In the following, when speaking of  $\mu$ SR without further specification we always refer to *positive* muons.

The magnetic field at the site of the muon in a magnetic compound is, at least in part, created by the dipole moments on neighboring paramagnetic atoms or ions. As stated, we can gain information on the magnitude of the field from the muon spin rotation frequency and also (to a limited degree) on the spatial arrangement of the moments. From muon spin relaxation times we gain knowledge on the dynamics and the couplings of these atomic moments. Consequently, one of the important features of  $\mu$ SR is its capability to serve as a *microscopic probe of magnetism*.

Competing microscopic methods in magnetism are the hyperfine methods such as Mössbauer spectroscopy, Perturbed Angular Distribution, NMR or EPR. All these techniques measure the magnetic field *at the nucleus* of a probe atom, this being quite often the magnetic atom in a compound. EPR, like optical spectroscopy, actually measures the disturbance of electronic states by the electron–nuclear hyperfine coupling, and the hyperfine coupling constant is completely dominated by the magnetic field at the nucleus.  $\mu$ SR senses the *interstitial field*, a quite different quantity. Furthermore, the muon normally possesses no electron shell of its own in conductors and also in most magnetic non-metals. This is another basic difference from the hyperfine methods, where the field at the nucleus is either entirely created, or at least strongly influenced by, the electronic shell of the probe atom. In certain materials, notably in semiconductors, the muon may capture an electron forming *muonium*, which, however, is too sensitive to magnetic fields to be useful in the study of magnetic materials (see also sect. 2.4).

Relative to Mössbauer spectroscopy, which is probably the most important hyperfine technique for the study of magnetic materials, one has no limitation in temperature in  $\mu$ SR (no Lamb–Mössbauer factor). Also,  $\mu$ SR can be applied to liquids and gases, but

this is of course of little consequence in magnetism. A comparison between Mössbauer spectroscopy and  $\mu$ SR can be found in Asch et al. (1988a).

One of the advantages of  $\mu$ SR compared to NMR is the possibility of measuring relaxation rates of paramagnets in true zero field. The extremely high resolving power of microwave resonance techniques often causes the signal to be lost in disordered magnetic systems (strong inhomogeneous line broadening), while  $\mu$ SR, since it is mainly sensitive to interstitial dipolar fields rather than nuclear hyperfine (contact) fields, is still capable of detecting a spectrum. Finally, it should be pointed out, that for  $\mu$ SR no limitation exists as to the type of atoms contained in the sample material.

Clearly, the most important method for gaining information on intrinsic properties of magnets is neutron scattering, which is primarily a probe of long-range correlations.  $\mu$ SR, a local probe, cannot directly obtain a spin structure the way neutron diffraction can, but the dipolar contribution to the field at the muon site (see sect. 3.1) is strongly dependent on the spatial arrangement of the surrounding moments. Hence the  $\mu$ SR spectrum provides a consistency test on any spin structure derived by neutrons. Differences may well exist, however, because  $\mu$ SR is a much more local probe, which needs no large coherence length. Consequently,  $\mu$ SR is particularly sensitive to short-range order and other forms of disordered magnetism.

Magnetic scattering of photons can in principle provide similar information on magnetic structures as neutron diffraction. With neutrons, the cross sections for nuclear (lattice structure) and magnetic (spin structure) scattering are roughly of equal magnitude, but the magnetic photon scattering cross section is many orders of magnitude smaller than that for charge scattering. Only the development of powerful synchrotron X-ray sources has allowed this obstacle to be overcome and studies of magnetism *via* X-ray scattering have emerged in recent years (see, for example, Isaacs et al. 1989 and Hannon et al. 1989). A special case is X-ray *resonant* magnetic scattering (XRMS) where the photon energy is set exactly on an absorption edge energy. This enhances the magnetic scattering cross section by six orders of magnitude or more. The  $M_{IV}$  and  $M_V$  absorption edges of the actinides are particularly favorable, so this technique has been used largely for the study of actinide compounds to date. XRMS has the additional advantage that it is both element and site (through the slight variation of edge energy) sensitive. This method can be a competitor for  $\mu$ SR because it also allows the detection of weak magnetism (i.e., moments of the order  $10^{-2}\mu_B$  or less) as found, for example, in heavy-fermion compounds (Isaacs et al. 1990, 1995). In contrast to  $\mu$ SR, it is at present impossible to deduce the size (even the order of magnitude) of the moment from XRMS data. Nonetheless, the spin structure involving such small moments can be found. It also allows (especially in conjunction with a related method, X-ray magnetic dichroism), at least in principle, separation of *orbital* and *spin* contributions to the moment, which is a rather fundamental question of actinide magnetism.  $\mu$ SR can give no information in this respect.

There is also a considerable difference in the time window for the study of spin-dynamical processes when comparing  $\mu$ SR to other methods (see fig. 1). A brief discussion of the different time windows in the various nuclear techniques has been given by Dattagupta (1989). It is of special importance that  $\mu$ SR, as shown in fig. 1, bridges the

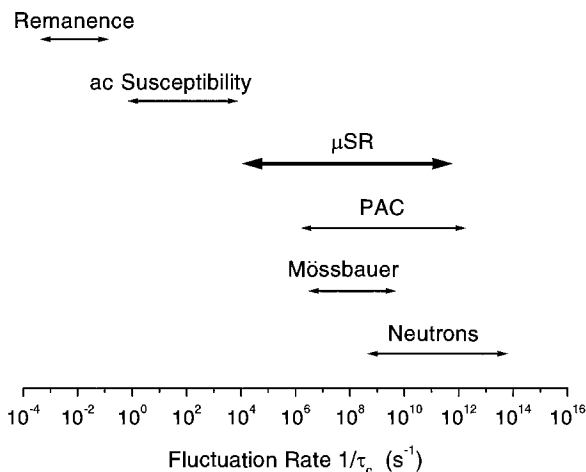


Fig. 1. Time scales of various techniques to study magnetism.  $1/\tau$  is the fluctuation rate of the field sensed by the nuclear probes or the rate of spin fluctuations.

gap between neutron scattering on the one side, and bulk magnetic measurements (i.e., ac susceptibility) on the other (Uemura 1989, Karlsson 1995). It is possible to relate the muon spin relaxation rate to the general scattering function  $S(\mathbf{q}, \omega)$  (Lovesey et al. 1990). μSR as a largely local method integrates over  $\mathbf{q}$  space. This is of course a serious loss of information. On the other hand, μSR measures at  $\omega \rightarrow 0$ , a region not accessible to neutron scattering.

Studies in magnetism are but one application of μSR. Other fields where μSR has given important information is the diffusion of light interstitials, especially with regard to quantum diffusion in metals, semiconductors and insulators (Kehr et al. 1982, Kondo 1986, Kadono 1990, Prokof'ev 1994, Storchak et al. 1996, Karlsson 1996). Other very active fields are applications to chemistry with emphasis on chemical kinetics especially in connection with radical formation (Brewer et al. 1975, Walker 1983, Fischer 1984, S.F.J. Cox and Symons 1986, Roduner 1990, 1999, Fleming and Senba 1992) and also the study of hydrogen states in semiconductors (Chow et al. 1995). μSR in life sciences is discussed by Nagamine (1999) in an article on *Exotic applications of muons*.

From the point of view of the physics involved, μSR is closely related to NMR (Slichter 1978). De Renzi (1999) offers in a recent review a detailed comparison between NMR and μSR using well selected examples. From the point view of apparatus and detection schemes, μSR is more akin to nuclear or particle physics experiments. Reviews covering the μSR technique are numerous (e.g.: Brewer et al. 1975, Karlsson 1982, 1995, Chappert 1984, Schenck 1985, S.F.J. Cox 1987, Schatz and Weidinger 1992, Davis and Cox 1996, S.L. Lee et al. 1999), but since the technique has advanced, the older ones have lost some of their relevance. Tri-annually, a special international conference on μSR is held. Its proceedings were published in the journal *Hyperfine Interactions* up to the 1996 conference in Nikko (Japan). Proceedings of the 1999 conference (Les Diablerets, Switzerland) have appeared in *Physica B* (Roduner et al. 2000). Although μSR emerged in the early 1970s, its application to magnetism became more widespread in the 1980s,

Table 1  
Some properties of the muon

Property	Symbol	Value	Units
Rest mass	$m_\mu$	206.77	$m_e$ (electron masses)
		0.1126	$m_p$ (proton masses)
		105.66	MeV/c <sup>2</sup>
Mean life	$\tau_\mu$	2.197	$\mu\text{s}$
Charge	$Q_\mu$	$\pm e$	(elementary charge)
Spin	$S_\mu$	$\hbar/2$	
<i>g</i> -factor	$g_\mu$	2.00233	
Magnetic moment	$\mu_\mu$	$4.84 \times 10^{-3}$	$\mu_B$ (Bohr magnetons)
		8.88	$\mu_N$ (nuclear magnetons)
		3.18	$\mu_p$ (proton moment)
Gyromagnetic ratio	$\gamma_\mu/2\pi$	135.54	MHz/T

particularly with respect to spin-dynamical studies. Disordered and frustrated magnets, spin glasses, critical phenomena, Kondo-lattice and heavy-fermion systems, the interplay of magnetism and superconductivity, especially in high- $T_c$  superconductors and related materials, are some of the subjects being actively studied with  $\mu\text{SR}$ .

## 2.2. Properties of the muon

The muon, when discovered in cosmic ray studies by Neddermeyer and Anderson (1938), was thought to be the Yukawa meson which transmits the strong forces between nucleons, but about 10 years later it became apparent that it is not the particle postulated by Yukawa (which is in fact the pion or  $\pi$  meson). Within the standard model, the muon is a fundamental particle. As such it is a point-like object without internal structure. With its neutrino it forms the second generation of the family of leptons, the first family being the electron and the third the tauon, always together with their neutrinos. Fundamental particles come in particle–antiparticle pairs. By convention, the  $\mu^+$  is the antiparticle and strictly speaking, we are concerned with “antimuon spin rotation/relaxation”. A short review of the history of the muon has recently been given by T.D. Lee (1994). Due to its past, the muon is still on occasion referred to as the  $\mu$  meson. This is of course wrong since mesons are composite particles containing a quark and an antiquark. The properties of the muon of interest here are summarized in table 1.

One finds the muon to be  $\sim 200$  times heavier than the electron and  $\sim 10$  times lighter than the proton. The finite mean life of the muon is long from the point of view of timing resolution of modern electronic circuits and poses no detection problem. The muon carries electric charge and spin. Consequently it has a magnetic dipole moment which is small compared to the moment of the electron but larger than the protonic moment. The size of its magnetic moment makes the muon an ideal probe for the relatively weak interstitial

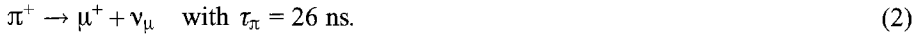
fields in materials. The Larmor precession frequency of  $S_\mu$  in the field  $B_\mu$  at the muon site is given by:

$$f_\mu = (\gamma_\mu/2\pi) \cdot B_\mu. \quad (1)$$

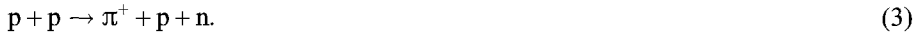
The μSR signal can typically be followed over  $5 \tau_\mu$  (i.e.,  $\sim 11 \mu\text{s}$ ). Assuming that  $S_\mu$  must make at least one half turn in this period, one obtains a minimum observable field value on the order of a mT. Good μSR spectrometers can resolve a precession period of  $2\text{--}5 \text{ ns}^{-1}$ , putting the maximum observable field in the range of  $3\text{--}5 \text{ T}$ . Similar arguments put the limits for muon spin relaxation rates between  $0.001$  and  $100 \mu\text{s}^{-1}$  under favorable conditions. It must be emphasized that the latter numbers refer to the decay rate of the muon spin polarization. In magnetism one is interested in the fluctuations of the magnetic moments in the sample which drive, *via* magnetic coupling, the muon spin depolarization. The average fluctuation period of the moments provide the *correlation time* for the local field at the muon, which causes muon spin relaxation. Observed relaxation times and the underlying correlation times need to be connected by an appropriate model. We shall discuss these aspects whenever the need arises.

### 2.3. Muon generation and decay

Muons take part in numerous elementary particle reactions. For μSR applications, the decay of pions is the source used. That means for positive muons



Pions in turn are produced in medium energy nucleon–nucleon collisions. For example:



Typically, one directs a beam of protons with a kinetic energy in the range  $0.5\text{--}1 \text{ GeV}$  onto a target of light nuclei such as Be or C.

Pion decay is mediated by the weak interaction and full parity violation comes into play. In particular, the neutrino (here  $\nu_\mu$ ) always has *left-handed chiral symmetry*, meaning that its spin  $S_\nu$  (being  $\hbar/2$  like that of the muon) is oriented in the opposite direction to its linear momentum ( $\mathbf{p}_\nu$ ). The pion has spin zero. Conservation of momentum in its decay (eq. 2) requires that the neutrino ( $\nu_\mu$ ) and the muon ( $\mu^+$ ) are ejected  $180^\circ$  apart in the rest frame of the pion. Since the orientation of  $S_\nu$  is fixed to ( $S_\nu \uparrow \downarrow \mathbf{p}_\nu$ ), the same must hold for the muon ( $S_\mu \uparrow \downarrow \mathbf{p}_\mu$ ). We thus get perfectly spin polarized muons with their spin directed opposite to their line of flight. The situation is illustrated in fig. 2. Under certain circumstances (to be discussed in the next section) the pion rest frame is identical with the laboratory frame (“surface muon” beam). The linear momentum given to the muon from pion decay at rest is  $29.8 \text{ MeV}/c$  which corresponds to a kinetic energy of  $4.1 \text{ MeV}$ .



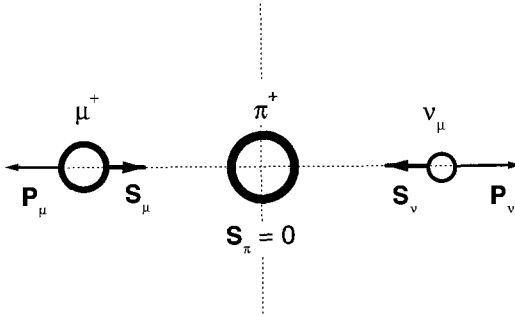


Fig. 2. Spin and momentum of decay products of the pion seen in the pion rest frame.

The decay of muons once more involves weak interactions and full parity violation. For the positive muon one has

$$\mu^+ \rightarrow e^+ + \nu_e + \bar{\nu}_\mu. \quad (4)$$

The situation here is more complex than in pion decay since there is now a three particle final state. The easily detectable signature of muon decay is the emitted positron ( $e^+$ ). As in nuclear  $\beta$ -decay (also governed by the weak interaction), the kinetic energy of the positron (electron) is distributed continuously between  $E = 0$  and  $E = E_{\max}$ , where  $E_{\max}$  is the decay energy arising from the mass difference of initial and final particles. In the case of muons,  $E_{\max} = 52.3$  MeV. The prominent effect of parity violation in muon decay is the anisotropic spatial distribution of the emitted positrons (see Commins 1973). The probability  $dP(\Theta, E, t)$  of finding a positron with energy between  $E$  and  $E + dE$  at a time between  $t$  and  $t + dt$  in solid angle  $d\Omega$ , located at the angle  $\Theta$  with respect to the muon spin at the moment of decay is given by

$$\frac{dP}{d\Omega dE dt} = C(E)e^{-t/\tau_\mu} W(E, \Theta). \quad (5)$$

$C(E)$  is the energy distribution function and  $W(E, \Theta)$  is the angular distribution function of the decay positrons. The latter can be expressed as

$$W(E, \Theta) = 1 + a_0(E) \cos \Theta, \quad (6)$$

and is the quantity essential for  $\mu$ SR. The factor  $a_0$  is called the *initial asymmetry* and is strongly dependent on positron energy. The positron detectors used in  $\mu$ SR usually are not sensitive to the energy of the particle detected and thus one integrates from energy zero to  $E_{\max}$  with  $C(E)$  as the weight function: this gives  $a_0 = \frac{1}{3}$ . In practice, the initial asymmetry is often somewhat smaller (typically  $a_0 \approx 0.2$ ) due to a number of experimental conditions. The resulting angular distribution is shown as a polar diagram in fig. 3.

Even for  $a_0 = 0.2$  one has a substantial spatial asymmetry. It means that a detector counts 40% more positrons when the muon spin is oriented in its direction compared

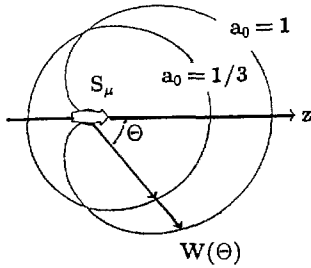


Fig. 3. Polar diagram of the angular distribution of positrons from muon decay. The pattern with  $a_0 = 1$  results if only positrons near  $E_{max}$  are counted; the pattern  $a_0 = \frac{1}{3}$  when all positron energies are sampled with equal probability. The distributions are rotationally symmetric around the muon spin direction ( $z$ -axis).

to the opposite spin direction, which is a very large effect indeed. It easily allows us to pinpoint the muon spin orientation at the moment of decay. Since the initial orientation (at  $t = 0$ , that is at the birth of the muon) is known, a measurement of the *time distribution of the decay positron rate* with a fixed detector position directly reflects the temporal development of the muon spin motion. This is what μSR is about.

In summary, parity violation in weak interactions provides an easy means to obtain a beam of perfectly polarized muons *via* pion decay and thus fixes initial muon spin orientation. In the decay of muons, parity violation comes into action for a second time in allowing the determination of the final muon spin orientation by a fairly simple counting experiment.

A modern survey on muon production and related subjects including an outlook on further developments is available from Eaton and Kilcoyne (1999).

#### 2.4. Muon implantation

The interest of the μSR physicist (or chemist) lies in determining how the muon spin moves due to its coupling to internal fields after the muon has been implanted into the material under study. One directs the beam of polarized muons onto a sample thick and large enough to stop all impinging muons. The proper selection of sample size depends on beam characteristics and will be discussed in sect. 2.5.

Implantation involves the slowing down of muons from MeV energies to thermal energies which is an intricate process not fully understood in all details. The different steps involved are reviewed by Brewer et al. (1975). We shall forgo a discussion and just point out two basic features which must be satisfied:

- (1) The perfect polarization of the muons should not be disturbed in the deceleration. This is realized in most cases, especially in metals.
- (2) The slowing down time must be very short compared to the mean life of the muon. Again this condition is well satisfied, the time span to achieve thermalization being 100 ps or less in condensed matter.

At high incoming energy the muon is slowed down by ionizing collisions with atoms. This phase is well described by the Bethe–Bloch formalism which allows, in good approximation, calculations of the range of muons in matter. The time between subsequent collisions is so short that  $S_\mu$  has no chance to precess even in a strong local field and

hence keeps its initial orientation. At energies of a few keV the positive muon forms *muonium*, the hydrogen-like bound ( $\mu^+e^-$ ) state.

As mentioned, in *semiconductors* and *insulators*, muonium may remain stable until thermal energy is reached. In such cases the  $\mu$ SR experiment is performed on the interaction of *muonium in matter*. The hyperfine coupling between muon and electron makes muonium far more sensitive to magnetic fields than a bare muon (vacuum muonium has an effective Larmor frequency of 13.9 GHz/T compared to 135.5 MHz/T for the bare muon. Muonium-like states in solids can have values as “small” as 1/2 of the vacuum value). We shall not go into a discussion of  $\mu$ SR studies involving muonium. The already mentioned reviews of  $\mu$ SR spectroscopy (especially Brewer et al. 1975, S.F.J. Cox 1987, Davis and Cox 1996) describe the situation in detail. Most recently a review on “muonium states and dynamics” has appeared (S.F.J. Cox 1999). One point needs mentioning: in paramagnetic materials, muonium-like states (if present) result in precession frequencies or muon spin depolarization rates higher than a  $\mu$ SR spectrometer can resolve (see discussion in sect. 2.2). Such signals are simply lost, meaning that they do not contribute to the initial asymmetry which, in consequence, is reduced accordingly. This is referred to as “missing fraction”. Even when muonium is stable as the stopped state, the time spent as muonium during slowing down is so small that no significant change in muon spin orientation occurs.

In *conductors* (which are the prime concern of this review) the positive charge of the muon is shielded substantially by a conduction electron cloud and muonium is not stable. In this case we end with a 100% polarized positive muon at thermal energy embedded in the sample material. Due to its positive charge, the  $\mu^+$  is repelled by atomic nuclei and usually finds the position which has a minimum of potential energy between the atoms, that is, in a crystalline lattice, an interstitial site. The site taken up by the muon in a crystal is *a priori* not known. This is not as serious as an outsider first believes. Much basic information on magnetic behavior of the sample material can be drawn from the  $\mu$ SR spectra without knowledge of the muon site. Of course, for a quantitative analysis of the strength of internal fields as well as a discussion of spin structures, the site must be known. We shall discuss in sect. 3.6 means to determine the muon stopping site.

Thermal energies may be enough to initiate muon diffusion, especially in elemental metals with simple crystal structures. That is to say, the muon hops from one interstitial site to a neighboring one on a time scale less than a  $\mu$ s. It is often trapped after some diffusional motion at a lattice imperfection. The study of muon diffusion has already been mentioned as a major application of  $\mu$ SR spectroscopy. From the point of view of magnetic studies, muon diffusion is usually an undesirable complication. It is good practice for magnetic studies to check on the mobility status of the muon, at least in the temperature regime of interest.

The muon carries charge and spin and hence is not a completely innocuous probe. The question of how much materials properties are altered by the presence of a muon appears regularly, especially in situations where  $\mu$ SR senses an unusual behavior that defies simple explanation. The positive charge of the muon will repel surrounding atomic nuclei. This results in a local distortion of lattice symmetry. It usually deepens the

interstitial potential, an effect known as “self-trapping”. The distortion may also alter the local crystalline field interaction, an effect considered, for example, by Campbell (1984). In principle, local magnetic properties sensed by the muons could be influenced *via* such a mechanism. A most pronounced feature arises from the fact that in conductors the positive muonic charge will attract a screening cloud of conduction electrons. The spin of those electrons contributes to the contact magnetic field at the muon site (see sect. 3.1) which, in consequence, is enhanced over the normal value present without a muon. The latter can in principle be measured by neutrons. The muon and the neutron result on interstitial spin densities may be different by a factor of two (see Hartmann et al. 1986). The presence of a muon may also locally change the band structure, an effect which had to be taken into consideration, for example, in connection with the  $\mu$ SR Knight shift in Sb (Lindgren et al. 1986) and for the hyperfine fields at muons implanted in ferromagnetic metals such as Fe, Co and Ni (Kanamori et al. 1981, Lindgren et al. 1987, Akai et al. 1992). Whether the presence of a muon influences and locally alters the spin structure of an ordered magnet is an open question. Such an effect is conceivable if the spin structure results from different competing interactions of nearly equal strength. The additional electric field gradient produced by the lattice distortion caused by the muon may upset this balance. There is no clear evidence of such muon-induced effects in materials with electronic magnetism, except perhaps singlet-ground state systems (sect. 5.1). In the majority of cases the muon senses the intrinsic magnetic behavior of the material studied, but it often emphasizes features not seen by other methods.

Finally a word concerning radiation damage. The muon as a rather light particle causes little damage in general. Also, the intensities of muon beams are weak from the point of view of radiation damage dosages. In a local picture, the muon comes to rest a fair distance away from the region of strong ionization, which occurs at the early part of its track. In addition, the charge recombination time in metals is very short compared to the muon life time. In good insulators or especially in molecular crystals some concern may arise as to the question of local radiolysis remaining at time scales comparable to the muon life time. Recently  $\mu$ SR measurements studying this problem have appeared (e.g., Storchak et al. 1995a,b). A recent review on the subject is available (Storchak 1999).

### 2.5. Muon beam characteristics

Muon beams used in  $\mu$ SR can be distinguished by their time structure (pulsed *vs.* continuous) and also by the muon momentum or energy (surface *vs.* decay-channel beam lines). The two differing features, time structure and muon energy, are completely independent of each other. There exist, for example, pulsed surface beams and pulsed decay-channel beams. Their different properties render the various beam types advantageous for different applications. We discuss first the time structure.

At *pulsed beam* facilities the protons hitting the muon production target are bunched into pulses. Requirements to be met are:

- (a) the pulse width must be short compared to  $\tau_\mu$ ,
- (b) the repetition period must be long compared to  $\tau_\mu$ .

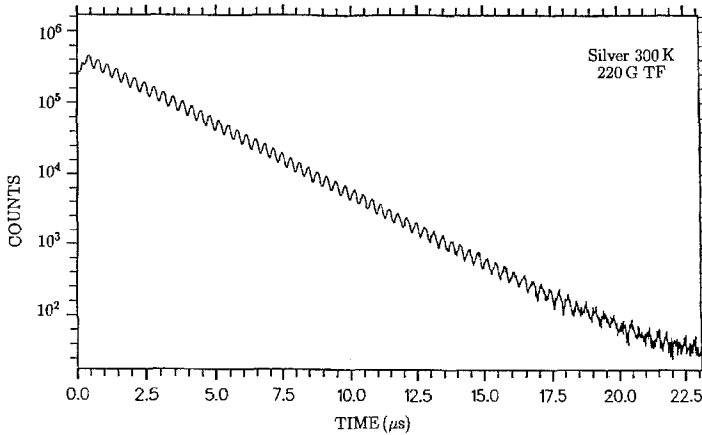


Fig. 4. Raw muon spin rotation spectrum (analogue plot) observed out to very late times on a pulsed muon beam (RAL-ISIS). Note the logarithmic vertical scale. Surface muons are stopped in pure Ag. Also visible is the distortion at early times due to the finite muon pulse width. (The data shown were taken at the time of commissioning the facility. Meanwhile, pulse structure has been improved and the time span over which distortion occurs is cut in half.)

The two pulsed muon facilities available currently (KEK in Japan and RAL in England) meet these conditions well. They have pulse widths somewhat less than 100 ns and repetition rates of 20 and 50 Hz, respectively. The pion life time ( $\tau_{\pi} = 26$  ns) is short compared to the proton beam pulse width, therefore the muon beam possesses roughly the same time structure as the proton beam. Details on these facilities can be found in Nagamine (1981), Nagamine et al. (1994), Eaton et al. (1988, 1994) and Borden et al. (1990). The RAL facility offers more intense muon beams. The advantage of a pulsed beam is a less severe restriction on muon rate (discussed in the next section) and the fact that, after the pulse has arrived, the beam line is “quiet”, that is, no further particles will impinge on the sample. The result is, the recorded muon spectrum is free of random background, which allows the extension of the measurement to very late times (approx.  $10\tau_{\mu}$ ). At this point only few muons have survived, the signal intensity is extremely weak and can be observed only against a negligible background intensity. Figure 4 depicts a muon spin precession pattern (explained in sect. 3.2) followed out to 22  $\mu$ s. The price paid for this impressive feature is the spectral distortion at early times and a limitation in time resolution of spectral features due to the muon pulse width (now about 100 ns at ISIS). In fig. 5 the  $\mu$ SR spectral response (initial asymmetry) is plotted against the spin precession frequency for the ISIS pulsed muon beam. Clearly, the upper limit is around 8 MHz. As shown by Cottrell et al. (1997), this limit can be overcome in principle by using radiofrequency fields.

In general, pulsed beam measurements will not give information on fast relaxing (depolarizing) signals or spin precession patterns with higher frequency. In addition to gaining detailed information on very slowly relaxing patterns, pulsed  $\mu$ SR allows the experimenter to apply, synchronous with the muon pulse, certain environmental

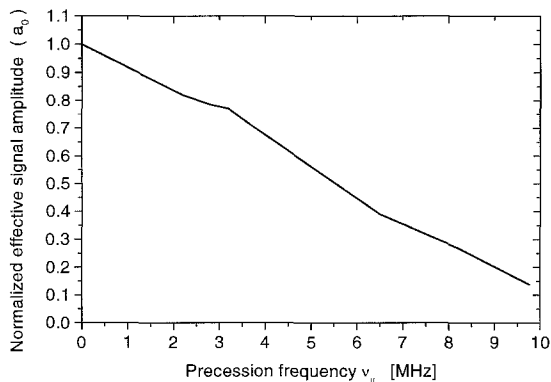


Fig. 5. Frequency response at the ISIS pulsed beam facility in single-pulse mode (pulse width  $\approx 100$  ns). The slight irregularities are due to an incomplete suppression of the second pulse in the ISIS beam structure.

conditions to the sample, which can not be kept up continuously. The most important cases are the application of RF *fields* in a muon spin resonance experiment (Nishiyama 1992, Scheuermann et al. 1997) or light, to study for example, photon excitations in semiconductors (Kadono et al. 1994). Scheuermann et al. (1997) report on the combined synchronous application of RF and illumination with light. Also, pulsed magnetic fields have been applied (Motokawa et al. 1990).

In a *continuous beam* the muons arrive at the target randomly without any dominating time structure. (The proton accelerator, typically a multiple-sector cyclotron, accelerates protons in bunches coupled to its RF-frequency, being about 50 MHz. The beam extraction techniques blur this time structure, so that usually it is hardly noticeable.) The time resolution is determined by detector construction and the electronic circuits used to verify the proper sequence of signals (muon in, positron out). It is usually around 0.5 ns. With special efforts 100 ps can be reached (Holzschuh et al. 1981). This shifts the frequency response relative to a pulsed beam (which is shown in fig. 5) by more than two orders of magnitude, into the range of 100 MHz. But the beam is always “on” and the signal to background ratio gets poor at late time in the histogram. The typical limit for the observation of a  $\mu$ SR spectrum is up to 4–5  $\tau_\mu$ , about one-half the time range available with a pulsed beam. In addition, as will be discussed in the next section, the electronic circuitry needed in case of a continuous beam limits the maximum allowed count rate of muon decay events. The two prominent  $\mu$ SR facilities featuring continuous beams are TRIUMF, Canada and PSI, Switzerland. Details on their facilities can be found in Arseneau et al. (1997) and Abela et al. (1994), respectively.

For continuous muon beam data, there is also a short time after the muon stop ( $t = 0$ ) for which the data are distorted and cannot be used. Often called “initial dead time”, this period is usually less than 30 ns, and with some care in setting up the counters and electronics can be reduced to as little as 5 ns. While often of little consequence in many  $\mu$ SR experiments, the size of the dead time limits the maximum relaxation rate that can be measured, and disordered magnetic states with rare-earth moments often generate muon relaxation times of less than 10 ns, so initial dead time is an important consideration in the experiments described in this review.

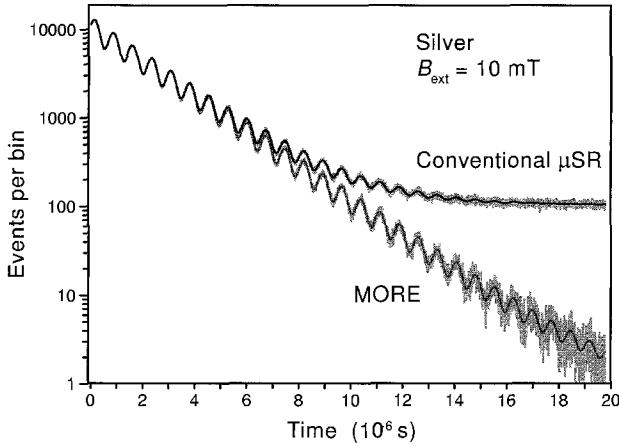


Fig. 6. Analogue plots of  $\mu$ SR spectra taken with a conventional continuous beam spectrometer and the MORE apparatus (see next section). After Abela et al. (1999).

A new design of a  $\mu$ SR facility called “MORE” (at PSI) brings to continuous beams the long time ranges of observation typical for pulsed beams (see Abela et al. 1999). The principle is briefly outlined in the next section. Figure 6 shows a comparison of spectra with the MORE function on and off (labeled “conventional”). In time range it is comparable to the spectrum shown in fig. 4. It offers, in addition, the good frequency resolution of continuous beams and is hence especially advantageous for the study of weakly depolarizing high-frequency spin precession patterns.

We now shift our attention to beams with different muon energies.

A *surface muon beam* uses pions that decay at rest in the laboratory frame. Then, as stated, the muon has the kinetic energy of  $\sim 4$  MeV and 100% spin polarization (opposite to the direction of flight). The advantage, relative to decay channel beams to be discussed further below, is that little sample material is needed to stop the muons, typically around  $100 \text{ mg/cm}^2$ . The distribution of range at 4 MeV impact energy is roughly 20% of range. In sect. 2.7.4 we shall discuss means to improve the situation further, so that even smaller samples, especially small single-crystal specimens, can be used. The surface muons emerge from pions stopped in the production target. Since the emitted slow muons are not very penetrating, they must originate from pions that have come to rest near the surface of the target hence the name: “surface” muons. Unfortunately, stopped negative pions will undergo rapid nuclear capture before they decay into muons. In consequence, surface beams are possible only for positive muons. The name does not imply that surfaces of samples can be studied with such muons. The required stopping thickness of  $200 \text{ mg/cm}^2$  means deep bulk. True surface studies require muons in the eV regime. Low-intensity “ultra-slow muon beams” are now becoming available (see sect. 2.7.5).

A surface beam is contaminated with other particles, especially positrons. Due to their lower mass the positrons are much faster than the muons at a fixed momentum. They are filtered out of the beam by a velocity separator using crossed electric and magnetic fields.

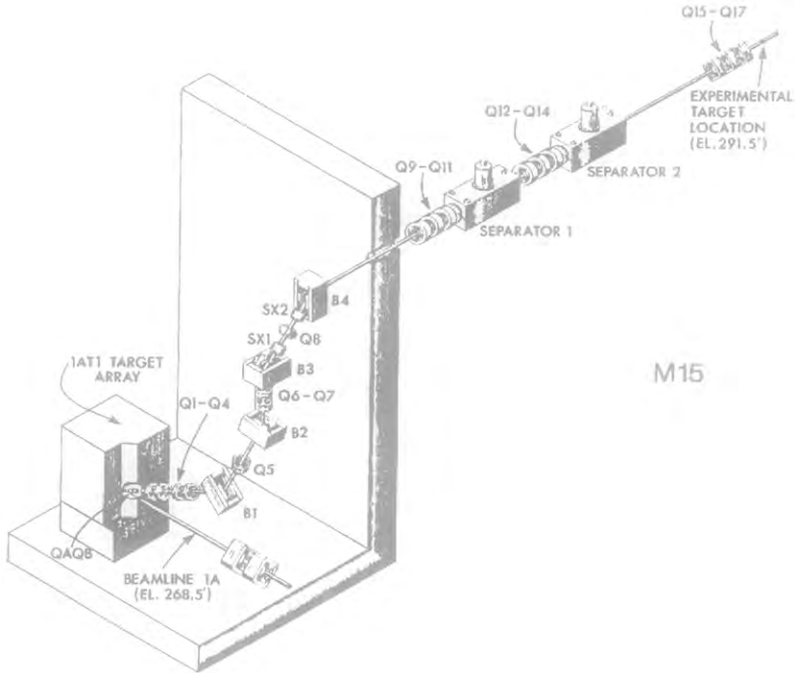


Fig. 7. Outline of a surface beam line for μSR studies (M15 beam line at TRIUMF). 1A1 is the production target. The experimental area is on a higher level than the proton beam line. Q are quadrupole; SX sextupole (normally not used); and B bending magnets. The two separators in tandem form the spin rotator. From Beveridge et al. (1986).

Increasing both fields together, the separator can also serve as a spin rotator, allowing the muon spin to be turned (prior to implantation) perpendicular to its linear momentum. Such an arrangement offers the advantage that a magnetic field applied along the beam axis is transverse with regard to  $S_{\mu}$  and induces spin precession without deflecting the beam by exerting a Lorentz force on the muons. This is a necessity if transverse fields in excess of some 10 mT are applied. A typical surface beam line is shown in fig. 7.

In a *decay channel beam*, high-momentum pions ( $\sim 200$  MeV/c, corresponding to  $E_{\pi} \approx 100$  MeV) are extracted from the production target and allowed to decay in flight. Beam line geometry collects only those muons ejected either along (forward muons) or opposite (backward muons) to the direction of the pion momentum. In both cases, the muons have a high momentum along the original flight direction of the pions in the laboratory frame. The typical muon energies are around 100 MeV (forward) and 40 MeV (backward) which is at least one order of magnitude higher than for surface muons. The stopping range for backward muons is typically 1–2 g/cm<sup>2</sup>. However, not all of this matter needs to be part of the sample. In roughly the first half of the stopping range the muons are only slowed down but rarely come to rest. Therefore, an appropriate thickness of “degrader” (e.g., polyethylene) is placed in front of the sample. The final angle of



acceptance for muons emerging from pions decaying in flight reduces the degree of muon spin polarization to  $\approx 75\%$ . This, in turn, leads to a reduction in initial asymmetry. For backward muons the spin points in the direction of flight, for forward muons in the opposite direction. Forward decay muons are rarely used nowadays for condensed matter studies, although much of the earlier work (before  $\sim 1970$ ) was successfully done on such beams. Backward muons can be used in cases where a long penetration length is tolerable or even required, as for example in high-pressure studies.

In modern facilities, the decay channel for the pions is a superconducting solenoid, about 8 m long producing a field around 5 T. This forces both the pions and the muons to helical trajectories. The decay path length in the laboratory is shortened, beam optics is improved, and beam contamination reduced. The muon momenta are much too high to construct a velocity filter (and also the degrader helps to remove positrons). Accordingly, traveling-beam spin rotation is not possible and deflection by transverse fields is comparatively small. Decay channel beams can be switched to deliver either positive or negative muons.

The standard beam spot area is  $\sim 3 \text{ cm}^2$  for both a surface or a decay channel beam. For the former roughly 0.5 g of material is needed, for the latter about 5 g to carry out a  $\mu\text{SR}$  study with ease. Special equipment and considerable experimental effort allows a reduction of the sample diameter to 0.5 cm and of the sample thickness to  $50 \text{ mg/cm}^2$  (surface beam) thus gaining nearly an order of magnitude with respect to material needed.

## 2.6. The recording of $\mu\text{SR}$ spectra

The basic layout of a  $\mu\text{SR}$  spectrometer (without electronics) is shown in fig. 8. Its performance will be discussed for the case of a (continuous) surface beam, a nonmagnetic sample and a transversely (to the beam axis) applied external field generated by a pair of Helmholtz coils. The sample may be placed inside a cryostat (or an oven, *etc.*) with appropriate windows (i.e., thin mylar) for muon transmission. The beam is collimated roughly to sample size by lead collimators. A thin transmission plastic scintillation detector, labeled "M" (for muon counter) is placed upstream of the sample. When an incoming muon passes through M, the detector delivers a signal which establishes zero time ( $t_0$ ) and starts a digital clock (TDC = time to digital converter). It is assumed that the sample is big enough to stop all impinging muons. A special technique for small samples will be discussed in sect. 2.7.4. Located downstream behind the sample is a scintillation detector for decay positrons labeled "D<sub>F</sub>" (for forward detector). When D<sub>F</sub> registers a decay event (positron), it sends a signal to the TDC which stores the elapsed time span  $t - t_0$  as a digital (time channel address) number. This procedure is repeated for a large number of incoming muons. After an appropriate time of data collection all registered decay events are stored in their appropriate time channels and then transferred into computer memory. In this fashion one obtains the *time histogram*  $N_F(t)$  of the temporal dependence of decay positron count rate in the forward counter. One uses typically  $\sim 4000$  time bins and  $N_F(t)$  can be modeled as a continuous function.

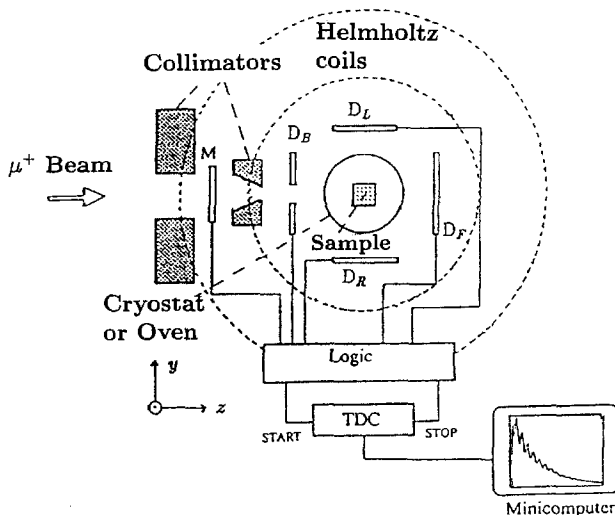


Fig. 8. Schematic of a  $\mu$ SR spectrometer. With a pulsed beam the M-counter is not needed. Collimators placed after the M counter are only suitable for decay-channel beams. Further explanation in the text.

Let us first assume that the external field is switched off. Furthermore, we have assumed that internal fields do not exist (nonmagnetic sample). Thus, no magnetic interaction works on  $S_\mu$ , which remains stationary. Under those circumstances  $N_F(t)$  simply reflects the muon decay process:

$$N_F(t) = N_0 e^{-t/\tau_\mu}.$$

Now the field is turned on. Using the coordinate system presented in fig. 8, we have  $S_\mu \parallel (-z)$  and  $B_\mu \parallel x$  (since  $B_\mu$  is assumed to be the external field only). It follows that  $S_\mu$  precesses in the  $(y, z)$ -plane. The angular distribution  $W(\Theta)$  of the emitted positrons is coupled to the motion of  $S_\mu$ . At time zero,  $S_\mu$  points away from  $D_F$  and  $N_F(t) \propto (1 - a_0)$ . Half a precession period later,  $S_\mu$  points towards  $D_F$  and  $N_F(t) \propto (1 + a_0)$ . The count rate  $N_F(t)$  will thus be modulated with the amplitude  $a_0$  and the muon spin precession frequency  $f_\mu$ . One finds

$$N_F(t) = N_0 e^{-t/\tau_\mu} [1 - a_0 G(t) \cos(2\pi f_\mu t + \Phi)]. \quad (7)$$

The phase angle  $\Phi$  takes care of a possible angle between the detector axis and the direction of initial muon spin polarization. It mostly appears when a geometrical misalignment of the detector exists. In rare cases it can have a deeper origin (i.e., a delayed formation of a magnetic state). A muon spin relaxation function  $G(t)$  has been added for completeness. It allows for a possible loss of degree of polarization with time (e.g., by incoherent spin motion). For the case under discussion ( $B_\mu = B_{app}$ ) one has  $G(t) \equiv 1$ . A time histogram, as given by eq. (7), was shown in fig. 4.

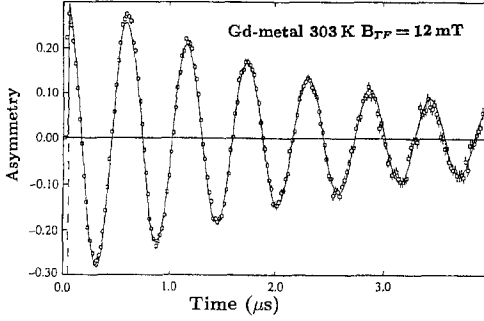


Fig. 9.  $\mu$ SR asymmetry spectrum of a simple rotation pattern. In this case  $G(t)$  is an (exponential) function of time and the oscillating term loses amplitude with time (damped rotation pattern). The sample is paramagnetic Gd metal in a transversely applied field.

In principle, we have now properly recorded a  $\mu$ SR spectrum. In practice, one often improves the situation by placing a second positron detector  $D_B$  (backward detector) upstream from the sample (with a central hole for undisturbed transmission of the beam). The same electronics as described for  $D_F$  is used for  $D_B$ . Thus one obtains

$$N_B(t) = N_0 e^{-t/\tau_\mu} [1 + a_0 G(t) \cos(2\pi f_\mu t + \Phi)], \quad (8)$$

since the precession phase is shifted by  $180^\circ$ . Forming the backward–forward ratio

$$\frac{N_B(t) - N_F(t)}{N_B(t) + N_F(t)} = \mathcal{A}(t) = a_0 G(t) \cos(2\pi f_\mu t + \Phi), \quad (9)$$

gives directly the time-dependent count rate asymmetry  $\mathcal{A}(t)$ , usually referred to as the “ $\mu$ SR asymmetry spectrum” (this is an idealized discussion; some corrections will be presented in sect. 3.5). An example is shown in fig. 9. For simplicity we shall leave out the phase constant  $\Phi$  in the future. The procedures for analyzing a  $\mu$ SR spectrum will be outlined later in sect. 3.5, after having discussed the fundamentals of the parameters which determine the spectral shape. Some researchers label the forward and backward counters oppositely, which leads to a change of sign in eq. (9).

One additional important condition must be ensured by electronic circuitry. In a continuous-beam experiment, only *one muon at a time* can be allowed in the sample to ensure a proper correlation between “start” and “stop” pulses. Since the muons arrive at random times it is possible that the M counter will be triggered a second time before a stop pulse is recorded. Such events must be rejected by an additional logical circuit called the “muon gate”. It is set by the M counter pulse and reset after  $\sim 5 \tau_\mu$  muon life times, independently whether a “stop” pulse has been recorded or not. If a recorded “stop” pulse were to reset the gate, early decay events would have a higher probability of detection and distortions in the time histogram would result. If the M counter is triggered during the time the muon gate is on, a “veto” pulse is generated which prevents the acceptance of any stop counts until the gate is reset. As a consequence, one must keep the muon beam intensity low enough that double triggers within  $5 \tau_\mu$  are rare events. Clearly, one does not want the muon gate time to be too long: it presents a true dead time of the

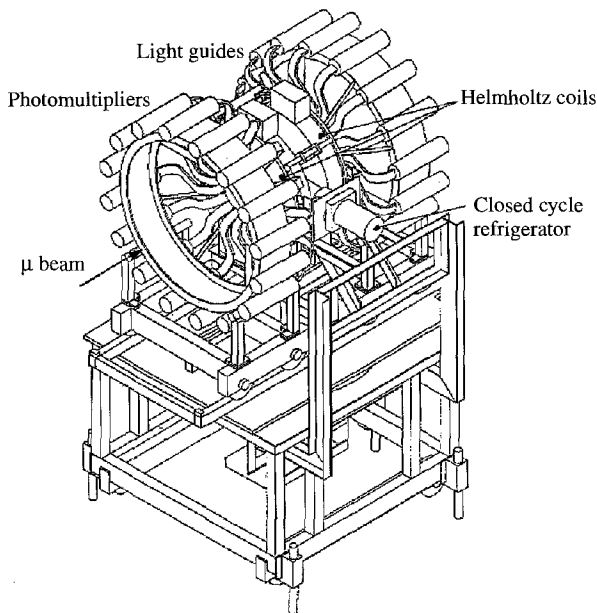


Fig. 10.  $\mu$ SR spectrometer "DIZITAL" for pulsed beam  $\mu$ SR spectroscopy as used at RAL. The multi-detector arrays are placed within the Helmholtz coils toroidally around the beam. The detector can be turned by 90 degrees in order to switch between longitudinal and transverse field geometry. It can also be moved on rails out of the beam spot position.

counting system. In conventional continuous beams it is therefore inefficient to have time histograms which extend to very late times in the histogram (more than  $10\ \mu\text{s}$ ). Also the background produced by "chance correlations" between start and stop pulses cause spectral distortion at late times (see fig. 6). Under the conditions described, one typically collects a total of 6 to 8 million decay events in time histograms per hour.

For a pulsed beam the counting logic is somewhat different and simpler. The M counter is not needed, the start signal can be derived from the proton pulse extraction. With each pulse a large number of muons (typically  $10^3$ ) enter the sample, but all at the same time (with the uncertainty of the pulse width). The TDC must accept multiple stops and record the proper time bin for each such event. After about  $10\tau_\mu$  the TDC is stopped, its contents transferred to the histogramming memory and reset. The apparatus then waits for the next muon pulse. No muon gate is needed and the spectrum can be recorded out to late times without penalty. The restriction in count rate (muon pulse intensity) is given by the maximum rate the positron detectors and their circuitry can handle. About 70% of the muons implanted by one pulse decay within the first  $2\ \mu\text{s}$ , and the counters will be overloaded if too many muons are contained in each pulse. The problem can be eased somewhat by dividing  $D_F$  and  $D_B$  into several independent detectors, each with its own pulse-handling circuit. 16 to 64 segment detectors are common. Such an apparatus is shown in fig. 10. The counts recorded by each segment must be stored separately. Final addition is done by the data analysis program. 10 to 20 million decay events per hour in the  $\mu$ SR spectrum can be obtained.

We mentioned the MORE apparatus which offers some of the features of pulsed beam data collection for continuous beams. The acronym MORE stands for Muons On REquest. Its basic feature is a fast-switching electrostatic beam deflector (for surface muons only) which extracts *one muon* out of the beam and sends it towards a  $\mu$ SR spectrometer. After  $10\tau_{\mu}$  the system is ready for the next muon to be extracted. This ensures that at any time only one muon is in the sample and the muon gate circuitry is not needed. Time resolution is not blurred by a finite pulse width when compared to a pulsed beam, but count rates are lower. The system runs parasitically on a beam line which delivers surface muons to a conventional spectrometer when the beam deflector is off (which is most of the time).

Whatever facility is used, collecting a  $\mu$ SR spectrum is not instantaneous, but requires time since the accuracy of the data is governed by the usual counting statistics. If a total of  $n$  counts has been collected in one time channel the uncertainty of that value is  $\sqrt{n}$ . With the rates quoted one needs counting times from 0.5 to 1 hour to have a satisfactory ratio between signal and statistical noise, especially at later times in the histogram. In case of weak or very complex  $\mu$ SR signals this observation time can become up to an order of magnitude larger. This discussion of spectrometer operation should make clear to the reader that the required counting time for a spectrum can not be shortened by further increasing the muon beam intensity. In order to perform a  $\mu$ SR experiment one must apply at the facility for the beam time one considers essential for the studies envisioned. Usually available beam times are oversubscribed and a peer review committee scans the applications (once or twice a year) and recommends beam time (often less than applied for). In addition, particle accelerators are complex machines and beam time losses due to equipment malfunctions occur. As a result  $\mu$ SR data sets are sometimes not as complete as one would like and  $\mu$ SR investigations often extend over long time periods.

To conclude this section we show in fig. 11 the layout of a modern (pulsed beam)  $\mu$ SR facility (ISIS). The (800 MeV, 200  $\mu$ A) pulsed (50 Hz) proton beam from the synchrotron accelerator hits first a thin muon (pion) production target ( $\sim 5$  mm carbon), then the thick (and strongly cooled) spallation neutron target (either uranium or tungsten) and is finally stopped in a beam dump. Heavy radiation shielding (not shown) is required around the experimental facilities. The neutron target is surrounded by several neutron beam lines with their instruments. They are of no interest here. Two muon beam lines are situated on both sides of the carbon target leading to the "EC MUON FACILITY" and the "RIKEN PROJECT". The "EC" beam line is a pure *surface* muon beam. Near the end of the beamline a switchyard directs muon pulses alternately to three different  $\mu$ SR beam ports (called MuSR, EMU and DEVA), which thus operate simultaneously. Located just in front of the pulse switching system is the velocity filter (separator). The "RIKEN" beam line possesses a superconducting decay channel (located just after the first bending magnet) and therefore can also deliver higher energy *decay channel* muons. Switching devices distribute the muon pulses to three different ports as well. The two muon beamlines operate independently of each other. More details on the ISIS muon facilities can be found in the article by Eaton and Kilcoyne (1999).

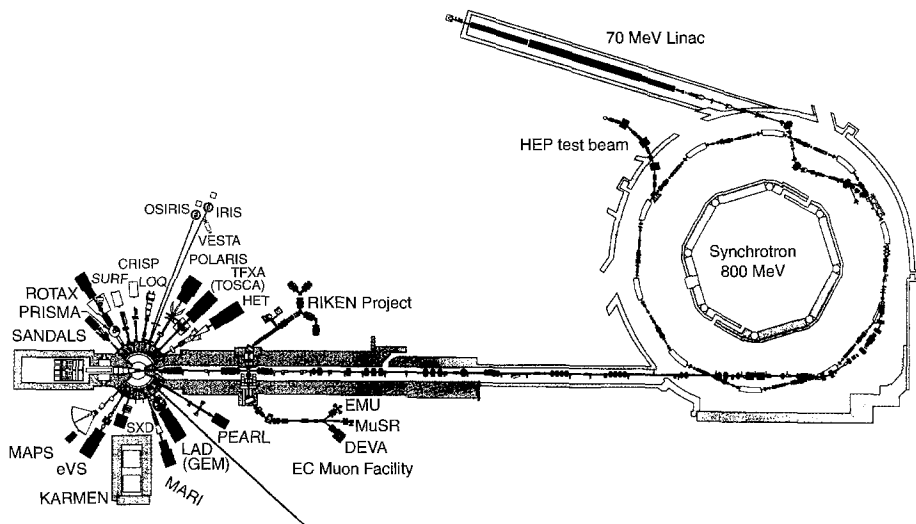


Fig. 11. A modern  $\mu$ SR facility: the setup at the ISIS neutron spallation source of RAL. This is a pulsed muon facility running parasitic on the neutron source. It is at present the most intense pulsed muon facility in operation. The neutron target with its spectrometers is at the far left side, the muon production target is more to the center of the drawing. KARMEN is a neutrino facility. For further details see text.

## 2.7. Special applications

It is the purpose of this section to show that  $\mu$ SR spectroscopy can be adapted to a wide variety of experimental conditions. We have mentioned earlier the special features offered by a pulsed muon beam, such as the synchronous applications of light and/or RF pulses. Many new adaptations of  $\mu$ SR spectroscopy are still under active development and the field becomes richer and more versatile constantly. The most exciting new prospect is probably the “ultra-slow muon beam” which will be discussed briefly in subsect. 2.7.5.

### 2.7.1. Extreme temperatures

We have already pointed out that there is no limit on sample temperature imposed by the  $\mu$ SR method *per se*. The vast majority of  $\mu$ SR experiments are carried out between 300 K and  $\sim 3$  K using conventional cryostats.

Low-temperature facilities reaching base temperatures of 10–50 mK with the use of dilution refrigerators (see Lounasmaa 1974) are also common to most  $\mu$ SR facilities. To keep beam heating low, surface muon beams are best used. A stream of  $10^5$  particles/s impinging on the sample, each particle depositing  $\sim 5$  MeV, result in a heat load of  $\sim 100$  nW. This in principle allows even lower temperatures to be reached, but no urgent need for such extreme temperatures has been seen.

High-temperature data up to  $\sim 1200$  K have been reported in connection with studies on iron above the Curie temperature (Herlach et al. 1986). These types of experiments include muon spin resonance data (Hampele et al. 1990) with a surface beam. The main

problem with incorporating a heating device is the need for thin windows (so that surface muons can enter). The system used is described by Majer et al. (1988). The relatively high Curie temperatures in perovskites and orthoferrites also demand the use of heated samples, as will be discussed in sect. 6.2. In summary, elevated temperatures to  $\sim 1000^\circ\text{C}$  pose no severe experimental problem in  $\mu\text{SR}$  studies. One must be aware, however, that at such elevated temperatures the muon is likely to diffuse, especially in metallic lattices. One also has the problem of temperature-generated vacancies which may trap diffusing muons (see for example Herlach et al. 1986).

### 2.7.2. High magnetic fields

The usual  $\mu\text{SR}$  port uses Helmholtz-like coils for the generation of static transverse or longitudinal magnetic fields. The field range is typically up to 0.4 T. As mentioned earlier, transverse fields above 0.01 T cause severe beam deflection in case of a surface muon beam, so a spin rotator is mandatory. It allows the field to be applied along the beam axis even for a transverse field measurement. For decay muon beams the restriction of field magnitude in transverse geometry is less severe. Transverse fields of about 0.8 T have been used in connection with *stroboscopic  $\mu\text{SR}$  spectroscopy* (Camani et al. 1978, Klempt et al. 1982, Schenck 1985). Those fields were generated by electromagnets and the stroboscopic methods were mainly undertaken to determine the rather minute muonic Knight shift in diamagnetic metals. The demand on field uniformity is high in transverse geometry ( $<10^{-5}$  to avoid inhomogeneous line broadening (signal damping)). Electromagnets cannot be easily configured for longitudinal geometry since this requires a bore in at least one of the pole shoes for transmitting the beam into the field region. It is difficult to analyze transverse field spectra for fields in excess of  $\sim 1$  T because the spin precession frequency approaches the spectrometer time resolution limit. Even at fields exceeding  $\sim 0.2$  T the analysis of TF spectra can turn out to be difficult. A special technique for high transverse field data using a *rotating reference frame* has been described by Riseman and Brewer (1990). Higher fields can be produced by superconducting Helmholtz coils. They are always placed longitudinal to the beam momentum. Setups for LF measurements cover the range up to 2–5 T, although time differential measurements usually become difficult above  $\sim 2$  T because of poor performance of the positron scintillation detectors. The highest fields are more useful for LCR (or ALC) measurements where only time integral counting is required (see Kiefl and Kreitzman 1992).

The highest fields in a  $\mu\text{SR}$  study have been used by Motokawa et al. (1990), employing a pulsed resistive solenoid. Clearly, this technique also calls for a pulsed muon facility. The experiments were carried out at the BOOM facility in Tsukuba, Japan. The maximum field intensity was 16 T, the pulse length 1 ms and the repetition period 2 s. The application of very high fields is of interest for the study of magnetic phase diagrams and of magnetic moment fluctuation rates in paramagnets in the fast fluctuation limit (see sect. 3.2.3). Only one very high field study on a R compound has been carried out ( $\text{PrCo}_2\text{Si}_2$  by Nojiri et al. 1992 – see sect. 5.5.2) to date. Unfortunately, the data are of very limited accuracy. The (basically very powerful) method has not been pursued further although

much more intense pulsed muon beams are now available. The field limit could certainly be increased by a factor of two. The general disturbance of surrounding electronics by the intense electromagnetic pulses poses a serious problem at general  $\mu$ SR facilities.

### 2.7.3. High pressure

The application of high pressure reduces the separation of neighboring atoms and therefore causes changes in overlap of their outer electronic orbits. Clearly, this is an important parameter in magnetism in general and in 5f magnetism in particular, where overlap strongly influences the localization of the electrons responsible for magnetic properties. High-pressure measurements have been pursued with vigor in nearly all areas of experimental condensed matter physics.

$\mu$ SR spectroscopy unfortunately can not be extended easily to high pressures. Whatever way pressure is applied, the beam must pass through a fair amount of material before reaching the sample. Only decay channel muons can be used, which, in turn, demand fairly large sample sizes. Furthermore, it is important that hydrostatic conditions prevail, since internal stress in the sample will produce lattice defects which may trap muons and also can cause wide distributions in internal fields which then cause rapid damping of the  $\mu$ SR signal (see sect. 3.2). The most widely used Bridgeman opposed anvil technique is problematic for  $\mu$ SR spectroscopy.

The easiest solution is an oil pressure cell. This has been used for the study of the volume dependence of the local field in the transition metals Fe and Ni (Butz et al. 1980). The pressure range was 0.7 GPa (7 kbar). The most serious drawback of such a setup is its limitation in temperature. Even at moderately low temperature the oil will freeze.

Rare-earth and actinide magnetism studies call for low temperatures. The solution then is a gas pressure cell. Such a system using compressed He gas as the pressure transmitting medium has been developed by Butz et al. (1986). It is now stationed at PSI with some modifications (Kratzer et al. 1994a).

The gas high-pressure system is designed for pressures up to 1.4 GPa. Helium solidifies in the low-temperature-high-pressure regime. Solid helium, fortunately, can not support significant shear forces and consequently the all important hydrostatic conditions are not seriously violated. Helium compression is achieved in two steps. First, the gas is compressed to 0.3 GPa and stored. This is followed by a pressure intensifier which is a piston system with an area ratio of 63:1, driven by a water-cooled hydraulic oil compressor. After equilibration the pressure is stable for several days. All high-pressure components are mounted inside the isolated area which is only accessible if the high pressure is released (*via* an electro-pneumatic valve).

A typical high-pressure cell made from CuBe is shown in fig. 12, top. Its central bore has 7 mm diameter and ~70 mm length. The pressure limit was 0.9 GPa, i.e., less than the design limit of the gas pressure system. The pressure cell is cooled by a closed cycle refrigerator with a base temperature ~12 K. Stammer et al. (1997) describe a new combined cryostat/furnace system which allows temperatures between 4 K and ~800 K employing a cell made from a titanium-aluminium-vanadium alloy. For applying



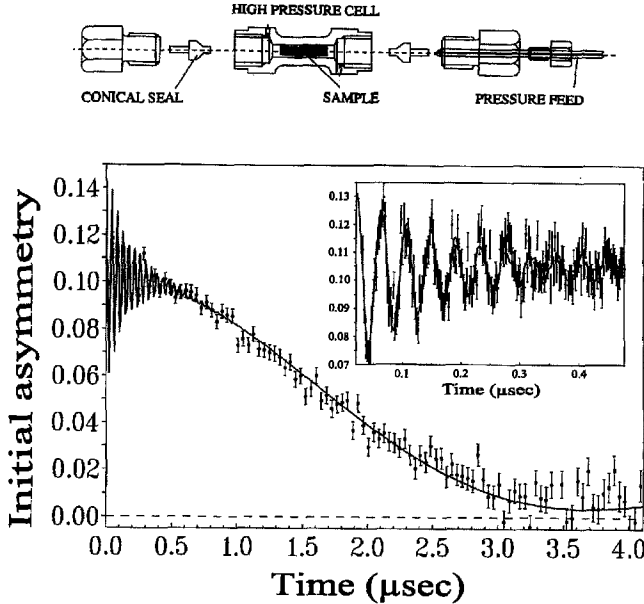


Fig. 12. Top: High-pressure cell (CuBe) used in the studies of rare-earth metals and intermetallic compounds up to 0.9 GPa (9 kbar). Bottom: ZF- $\mu$ SR spectrum of FM gadolinium metal inside the CuBe high-pressure cell. The oscillating signal (see also inset) is the spontaneous spin precession pattern of Gd. The Gaussian relaxation spectrum comes from muons stopped in the cell walls. After Schreier et al. (1997) and Kalvius et al. (2000f).

transverse fields the usual Helmholtz coil arrangement is used. Weak longitudinal fields are available from two small air coils. Even under favorable conditions, at least 50% of the  $\mu$ SR signal arises from the cell. It is thus important that the sample and cell signal can clearly be separated. In transverse field measurements this requires a noticeable Knight shift of the sample precession frequency. In zero field one either needs spontaneous spin precession from the sample (ordered magnet) or at least a fairly rapidly depolarizing signal. An example of a ZF measurement under high pressure on a FM sample (Gd metal) is shown in the lower panel of fig. 12. It demonstrates well the large background signal on which the sample signal rides. High-pressure studies with this system have been carried out on the elemental rare-earth metals and some intermetallics. They will be discussed in sects. 4 and 5. Recently, successful tests have been carried out with a small clamp-cell device which can be inserted into the standard cryostats of the  $\mu$ SR spectrometers (D. Andreica, private communication; see also Kalvius et al. 2000f). The disadvantage is that the cells must be removed for pressure changes. Higher pressures and lower temperatures than available at present should be possible.

$\mu$ SR measurements under uniaxial stress have also been reported but not for 4f or 5f materials. For example, in studies of Fe metal, Kossler et al. (1985) used a compressed air-driven piston at room temperature while Fritzsche et al. (1990) glued their sample to a

metal backing (Al or W) having markedly different thermal expansion coefficient. When cooling to low temperatures (2.7 K) strain was induced.

#### 2.7.4. Small samples

The usual beam spot diameter of  $\sim 20$  mm requires, even for a low-energy (surface) muon beam, samples of several 100 mg with the corresponding surface area. For novel materials this is often a prohibitive requirement, especially if single crystals are to be studied. Basically,  $\mu$ SR does not require single-crystalline samples, but often special features are only exhibited when single crystals are used. The  $\mu$ SR method works well with a sample consisting of a mosaic of small single crystals if these are available in corresponding numbers. The difficulty then is that the orientation of the crystalline axes must be known, at least roughly, for all the specimens.

Collimation of the beam hardly works beyond a reduction of  $\sim 50\%$  in “illuminated” area. The collimator must be placed some distance in front of the sample to avoid that forward or backward detectors pick up positrons stemming from muons stopped in the collimator. The divergence of the muon beam and especially scattering of muons by the collimator and also in the start counter, the cryostat windows *etc.* break up the collimated beam again in the case of surface muons.

One fairly simple solution is to surround the small sample with material in which implanted muons are quickly depolarized or in which muonium is formed, whose precession frequency (especially if sizable transverse fields are applied) is well beyond the time resolution of the spectrometer. Powdered high-quality  $\gamma\text{-Fe}_2\text{O}_3$  is a material of choice. Still, this leads to a poor signal/background ratio in the  $\mu$ SR spectra and hence to a severe loss in data accuracy.

It is more effective to sense muons that do not stop in the sample and to veto the corresponding events by electronic means. The basics of such a system, originally developed at TRIUMF (Kiefl et al. 1994, Arseneau et al. 1997) is shown in fig. 13.

The sample, which is considerably smaller than the bore of the beam collimator ( $\sim 10$  mm dia.), is mounted on a thin mylar foil on top of a cup-shaped scintillation detector (veto counter). The mylar is essentially transparent to the incoming muons. Thus,

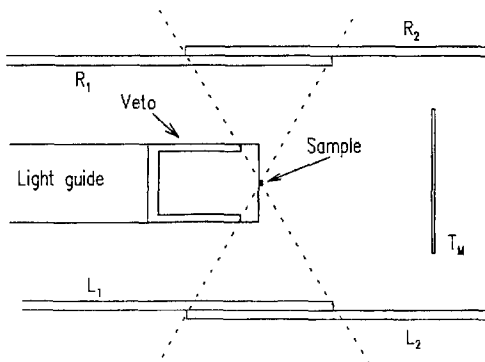


Fig. 13. “Low-background”  $\mu$ SR spectrometer for small samples. After Kiefl et al. (1994). Explanation in the text.

all muons which are not stopped in the sample will trigger the cup-shaped counter. Its detection pulse is used to veto the start pulse from the muon counter ( $T_M$ ). The positron telescopes will register decay positrons only if the two detectors  $L_1$  and  $L_2$  or  $R_1$  and  $R_2$ , respectively, are triggered in coincidence. This leads to a restricted acceptance cone as shown in fig. 13 and excludes positrons originating from muons decaying in the cup detector. The whole system (except the photomultiplier of the veto counter and the L and R telescopes) are mounted inside the exchange gas vessel of an axial cryostat. As shown the system is set up for TF measurements with left (L) and right (R) positron telescopes. It can be adjusted to ZF measurements when using a spin rotator. Since events not coming from muons stopped in the sample are altogether suppressed, the beam intensity can be increased (if possible) so that usual counting rates are achieved even for small samples and essentially background free spectra of high quality can be obtained. Kiefl et al. (1994) used a high- $T_c$  single-crystalline sample (YBCO) of only  $36 \text{ mm}^2$  and  $\sim 50 \text{ mg}$  total mass.

Arseneau et al. (1997) describe a more elaborate system mountable in a vertical cryostat. A variation of the scheme described has been used by Chakhalian et al. (1997) (denoted as " $\mu\text{SR} \times 2$ ") for simultaneous recording of Knight shift data (see sect. 3.2.1) from a sample under study and a reference material (e.g., Ag). The inside detector (S) is placed so that muons stopped in the sample trigger S and M in coincidence. An anti-coincidence trigger of S and M identifies a muon stopped in the reference material surrounding the sample. The coincidence and anti-coincidence events are routed to different sections of the histogramming memory. "Cross talk" between the two spectra is negligible and variations in Knight shift of less than 100 ppm could readily be resolved.

The ideal solution to the small sample-problem is of course a very narrow muon beam. The demands on beam optics are high and not easily fulfilled under the general conditions of primary beam and production target size. Its construction certainly would be costly.

### 2.7.5. Low-energy muons

While the method just described definitely improves the situation for comparatively thin samples as well, there are limits as to the electronic suppression of start signals triggered by muons not stopped in the material under study. If the sample is rather thin, the more proper approach is to use muons with reduced stopping length, i.e., with lower energy.

By setting the muon momentum selector magnet appropriately, a standard surface muon beam (muon momentum  $\sim 30 \text{ MeV}/c$ ) can be tuned down to about  $20 \text{ MeV}/c$  before all useful intensity is lost. This method has been used in the study of amorphous DyAg (Kalvius et al. 1986), where the sample was a sputtered film of  $50 \mu\text{m}$  thickness. By tuning to  $22 \text{ MeV}/c$  about 70% of the muons were stopped in the sample (which had a large surface area). Torikai et al. (1994) reported on measurements of magnetic MnSb/Sb multilayers using the same technique. They obtained a useful spectrum for a sample consisting of 40 layers of MnSb (1 monolayer)/Sb(49 Å), sandwiched between two 500 Å layers of Sb grown epitaxially on a polyamid surface with a beam tuned down to  $18 \text{ MeV}/c$ . The corresponding low muon energy tolerated no windows between production

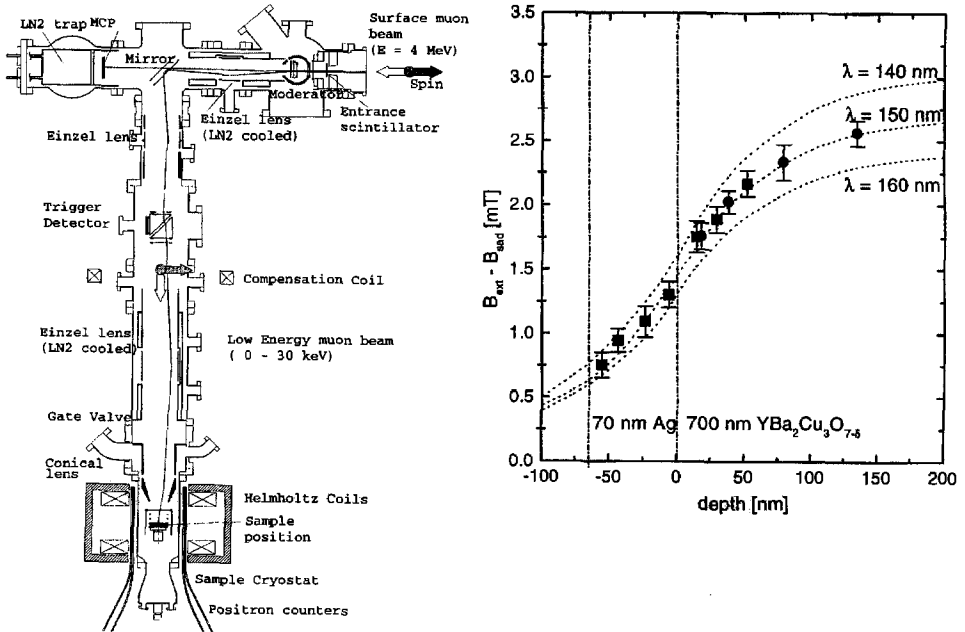


Fig. 14. Left: Apparatus for low-energy (LE)  $\mu$ SR at PSI. Normal surface muons enter from the right and are moderated by a condensed gas target. The LE muons are separated from the non-moderated muons by the electrostatic mirror. The mirror turns the linear momentum but not the spin which is now perpendicular to the line of flight. The beam passes the trigger detector, is accelerated (or decelerated) to the appropriate energy (1–30 keV) and focused onto the sample. The whole system is in ultra-high vacuum in order to maintain surface cleanliness of the moderator and the sample. Right: Depth dependence of  $B_{ext} - B_{ind}$  (see text) at 20 K in  $B_T = 10.4$  mT for a 700 nm thick film of  $YBa_2Cu_3O_{7-\delta}$ . The dotted curves are calculations based on a London model for different field penetration depths  $\lambda$ . After Morenzoni (1998) and Niedermayer et al. (1999).

target and sample. This experiment surely represents the limit for conventional muon beams, but shows that extreme situations can be handled.

Real surface, interface or thin film studies (i.e., measurements on only a few monolayers) require a beam of “ultra-slow muons”, i.e., muons with energies in the keV range. Such beams are under development at present at KEK, ISIS (both pulsed) and PSI (continuous). Two rather different approaches are used. Morenzoni et al. (1994, 1996, 1997), Morenzoni (1997, 1998) at PSI generate practically 100% polarized muons of  $\sim 10$  eV by moderating muons from a standard surface muon beam ( $\sim 4$  MeV) by a thin film ( $\sim 100$  nm) of a van der Waals gas (e.g., Ne, Ar,  $N_2$ ) condensed on a surface at cryogenic temperatures. The moderation process is fast ( $\sim 10$  ps) and preserves muon spin polarization. Efficiency, however, is still small ( $\sim 10^{-4}$ ). The moderated muons are the source of a new beam of ultra-slow muons which is transported and tuned (1–30 keV) by electric fields. An intricate technical problem is the (transmitting) muon start counter. The low-energy muon spectrometer now installed at PSI is shown in fig. 14 (left). It has recently been commissioned for scientific measurements, but beam intensity is still

low (some  $10^2\text{s}^{-1}$ ). An example of a typical measurement now possible is shown in fig. 14 (right). The study is concerned with the change of field distribution generated by the flux lattice of a type II superconductor in the Shubnikov phase near the surface (Niedermayer et al. 1999). The variation of internal field within the triangular flux lattice produces a distinctive asymmetric distribution of the field sensed by the muons. It exhibits a tail towards high fields coming from regions close to the vortex core, a cusp, which corresponds to the most probable field  $B_{\text{sad}}$  at the saddle point between adjacent vortices and a sharp cut-off on the low-field side (Riseman and Brewer 1994). One finds  $B_{\text{sad}} < B_{\text{ext}}$ . According to calculations based on a London model, the overall width of the field distribution diminishes and  $B_{\text{sad}}$  moves towards the value of the externally applied field as the sample surface is approached. By varying the muon kinetic energy between 30 and 3 keV one is able to probe layers of the sample between 135 and 18 nm. From measured TF spectra, the field distribution sensed by the implanted muons was derived by Fourier transforms. Figure 14 (right) depicts the variation of  $B_{\text{ext}} - B_{\text{sad}}$  as a function of implantation depth of the low-energy muons for a 700 nm thick film of  $\text{YBa}_2\text{Cu}_3\text{O}_{7-\delta}$  covered by 70 nm of Ag. The dotted curves are the model calculations for different values of the London penetration depth. The agreement is excellent. The data set gives a fine impression of the depth selective measurements now possible. A rather detailed survey on the PSI system, on the behavior of low-energy muons and on recent applications has been prepared by Morenzoni (1999).

A basically similar low-energy muon system is installed at ISIS. The pulsed beam circumvents the start counter problems, but beam intensity is even lower.

The group at KEK (Nagamine et al. 1995, Miyake et al. 1995, 1997) produces ultra-slow muons by first generating thermal muonium at the surface of a hot tungsten target placed in the pulsed primary proton beam. They then resonantly ionize the muonium by synchronously pulsed intense light from an UV laser. The resulting thermal  $\mu^+$  are electrostatically collected and form the pulsed ultra-slow muon beam with about 50% of muon spin polarization preserved. The  $\mu$  spin is adjusted perpendicular to the beam axis. Test spectra have been obtained for a 10 nm Au sample. Intensity is still very low.

In summary, ultra-slow muon beams are now available to the experimenter. This expands  $\mu\text{SR}$  to the acute research fields of surface-, interface- and multilayer physics. Magnetic multilayers are of course of prime interest in lanthanide magnetism.

### 3. $\mu\text{SR}$ magnetic response

#### 3.1. *The local field at the muon site*

In the standard semiclassical formulation, the magnetic influence of the material on the muon is represented by an effective field  $\mathbf{B}_\mu$  which acts on the spin  $\mathbf{S}_\mu$  of the muon at its interstitial site.  $\mathbf{B}_\mu$  can be expressed as the vector sum of various contributions, but this separation into different terms is mostly artificial and only a convenience. It must be emphasized that the muon sees only *one resultant field* independent of its sources.

First we separate  $\mathbf{B}_\mu$  into  $\mathbf{B}_{\text{app}}$  coming from outside the sample and  $\mathbf{B}_{\text{int}}$  originating from magnetic dipole moments inside the sample

$$\mathbf{B}_\mu = \mathbf{B}_{\text{app}} + \mathbf{B}_{\text{int}}. \quad (10)$$

$\mathbf{B}_{\text{app}}$  is a field usually generated by Helmholtz coils.  $\mathbf{B}_{\text{int}}$  is produced by the fields of (i) magnetic dipole moments on (paramagnetic) atoms in the magnet, (ii) nuclear dipoles, and (iii) by conduction electron spin polarization at the muon site. Of course, nuclear dipole moments are normally three orders of magnitude smaller than atomic moments and in magnets we may in general forget the nuclear fields. But under special circumstances the depolarizing influence of fields from atomic as well as nuclear moments can become comparable and then proper data analysis requires both to be taken into account (see sect. 3.4).

We separate the internal field into

$$\mathbf{B}_{\text{int}} = \mathbf{B}_{\text{con}} + \mathbf{B}_{\text{dip}}. \quad (11)$$

Both terms originate from the same set of dipoles.  $\mathbf{B}_{\text{dip}}$  is the direct dipolar field of the moments surrounding the muon. We will return to it shortly. The term  $\mathbf{B}_{\text{con}}$  is called the Fermi contact field and is produced by the net spin density of conduction electrons in contact with the muon. The spin polarization of the conduction electrons in turn is induced by the dipole moments on lattice sites. One finds

$$\mathbf{B}_{\text{con}} = -\frac{2}{3}\mu_0 \mu_e \vec{\sigma}_{\text{ce}}(n^\uparrow - n^\downarrow), \quad (12)$$

with  $\mu_e$  the electron's magnetic moment, and  $n^\uparrow$  ( $n^\downarrow$ ) the density, at the location of the muon, of conduction electrons with spin  $\vec{\sigma}_{\text{ce}}$  "up" ("down"). Spin polarization means  $n^\uparrow \neq n^\downarrow$ .  $\mathbf{B}_{\text{con}}$  is often also called the "hyperfine field", a nomenclature coming from NMR. Clearly,  $\mathbf{B}_{\text{con}}$  will be absent in non-conductors.

The *a priori* calculation of  $\mathbf{B}_{\text{con}}$  is a difficult task. In solids one must start from a band structure algorithm. As discussed in sect. 2.4 those calculations need to take the presence of the muon into account. In addition, the positive charge of the muon increases the conduction electron charge density around its site. In practice,  $\mathbf{B}_{\text{con}}$  most often is a parameter to be determined experimentally, for example by measurements of the muonic Knight shift (see sect. 3.2.1). Even then, it is not trivial to connect  $\mathbf{B}_{\text{con}}$  with the size of the atomic dipolar moments present.

The field generated by a magnetic dipole  $\vec{\mu}$  at the vector distance  $\mathbf{r}$  from the muon site is given by

$$\mathbf{B}(\mathbf{r}) = \left(\frac{\mu_0}{4\pi}\right) \frac{3\mathbf{r}(\vec{\mu} \cdot \mathbf{r}) - \vec{\mu}(\mathbf{r} \cdot \mathbf{r})}{r^5}. \quad (13)$$

The total dipolar field  $\mathbf{B}_{\text{dip}}$  felt by the muon can then in principle be calculated by carrying out the appropriate lattice sum  $\sum_j \mathbf{B}_j(\mathbf{r}_j)$  over the whole crystal. Although simple in

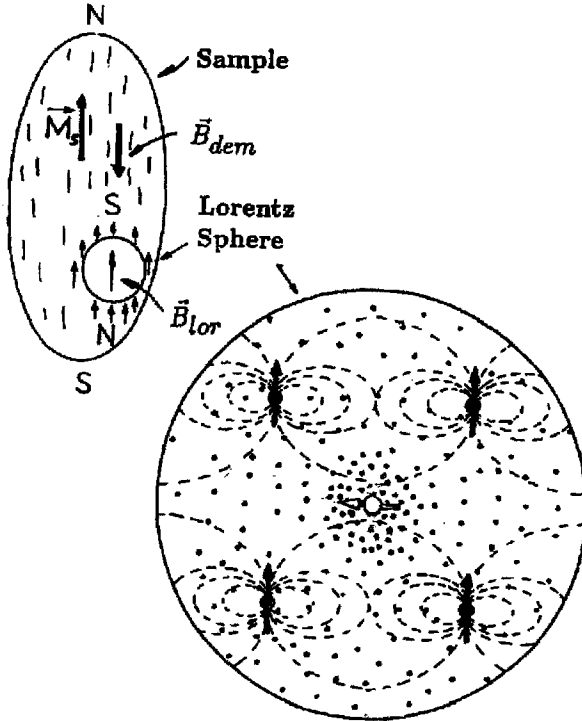


Fig. 15. The Lorentz construction. The case shown refers to a sample fully magnetized by an externally applied field. Symbols in the Lorentz sphere: solid circle and arrow, paramagnetic ion; open circle and arrow, implanted muon on interstitial site; broken lines, dipolar field lines; dots, conduction electron density.

principle, the calculation of dipolar sums often presents difficulties since they converge rather slowly. However, modern computational techniques make the direct solution of dipolar sums possible.

One often makes use of a concept developed by Lorentz instead. Most of the sample is considered a uniformly magnetized continuum. Around the point of interest a sphere (called the Lorentz sphere) is carved out of the continuum (see fig. 15). The dipolar contribution to  $B_{\mu}$  of dipoles inside the sphere (called  $B'_{\text{dip}}$ ) is calculated as a dipolar summation but the summation extends only over a rather small number of  $\vec{\mu}_j$ . A useful tensorial technique to evaluate  $B'_{\text{dip}}$  has been described by Meier et al. (1978), Meier (1984) and Seeger and Schimmele (1992). The rest of the sample is approximated by the Lorentz field  $B_{\text{lor}}$  produced by fictitious magnetic “surface charges” on the inner surface of the Lorentz sphere and by the demagnetizing field  $B_{\text{dem}}$  produced by similar charges on the outer surface of the sample. Obviously  $B_{\text{dem}}$  vanishes for a truly infinite sample. We have

$$B_{\text{dip}} = B'_{\text{dip}} + B_{\text{lor}} + B_{\text{dem}}, \quad (14)$$

and in summary for the local field:

$$B_{\mu} = B_{\text{con}} + B'_{\text{dip}} + B_{\text{lor}} + B_{\text{dem}} + B_{\text{app}}. \quad (15)$$

One finds  $\mathbf{B}_{\text{lor}} = \frac{1}{3}\mu_0\mathbf{M}_{\text{dom}}$  where  $\mathbf{M}_{\text{dom}}$  is the magnetization of the domain in which the Lorentz sphere is situated. Strictly speaking this result is true only for non-conducting compounds since in metallic ferromagnets an additional (but usually small) contribution to  $\mathbf{M}_{\text{dom}}$  arises from conduction electron polarization which is of course not part of  $\mathbf{B}_{\text{dip}}$ . The demagnetizing field can be expressed as  $\mathbf{B}_{\text{dem}} = -\mu_0\mathcal{N}\mathbf{M}_{\text{S}}$  where  $\mathcal{N}$  is the demagnetization tensor (a quantity depending on the geometrical shape of the sample) and  $\mathbf{M}_{\text{S}}$  is the total sample magnetization. For a spherical sample  $\mathcal{N} = \frac{1}{3}$ . Using such a shape and enforcing  $\mathbf{M}_{\text{dom}} = \mathbf{M}_{\text{S}}$  by fully saturating the material, magnetically reduces eq. (15) to

$$\mathbf{B}_{\mu} = \mathbf{B}'_{\text{dip}} + \mathbf{B}_{\text{con}} + \mathbf{B}_{\text{app}}, \quad (16)$$

which represents a significant simplification.

In general  $\mathbf{B}_{\text{dem}}$  is a troublesome quantity (especially for a polycrystalline sample consisting of oddly shaped grains) since it produces non-homogeneous fields which substantially increase  $\langle B_{\mu}^2 \rangle$  and hence static damping. Of course, a contribution by  $\mathbf{B}_{\text{dem}}$  can be avoided altogether by measuring in zero field. This is the standard procedure in case of ordered magnetism (see sect. 3.3). If ferro- or ferrimagnetism is present one must be sure that the sample shows no remanent magnetization. In paramagnets the magnetization is usually small for the fields used in μSR. It can be a problem, however, for Knight shift measurements in strong paramagnets such as the heavy rare earths.

The crucial point in the Lorentz construction is how to select the size of the Lorentz sphere. Its radius must be large compared to interatomic distances, otherwise the dipolar sum strongly depends on the sphere's volume. On the other hand it must be less than domain dimensions in order to have a unique definition of  $\mathbf{M}_{\text{dom}}$ . These conditions can, however, be fulfilled quite well. Finally, we point out that the Lorentz construction has originally been developed for ferromagnets. No macroscopic or domain magnetization exists in antiferromagnets under ZF conditions and both the Lorentz and the demagnetization fields are not present. An antiferromagnet, however, has a well-defined susceptibility. In consequence a magnetization develops in the presence of an external field (spin canting). Then  $\mathbf{B}_{\text{lor}}$  and  $\mathbf{B}_{\text{dem}}$  must be taken into account.

$\mathbf{B}_{\text{dip}}$  and  $\mathbf{B}_{\text{con}}$  differ in their directional dependences. While  $\mathbf{B}_{\text{con}}$  will point into (or opposite to) the direction of  $\mathbf{M}_{\text{dom}}$ , this is in general not the case for  $\mathbf{B}_{\text{dip}}$ . Symmetry arguments show that  $\mathbf{B}'_{\text{dip}}$  always vanishes if cubic symmetry exists for the location of surrounding dipoles with respect to muon site. Furthermore, any isotropic distribution of dipoles (i.e., a powder sample) leads to  $\mathbf{B}'_{\text{dip}} = 0$  when one averages over the whole crystal. One must not forget, however, that  $\mathbf{B}_{\mu} = 0$  does not imply  $\langle B_{\mu}^2 \rangle = 0$ ! In addition, due to their difference in spatial dependence, the vanishing of  $\mathbf{B}'_{\text{dip}}$  does not necessarily mean that  $\mathbf{B}_{\text{con}}$  also vanishes. We return to this problem in sect. 3.3.

One can imagine influences of the muon also on  $\mathbf{B}_{\text{dip}}$ . Firstly, the muon distorts the lattice around its position (self-trapping, small polaron). This can change the dipolar sum over the first neighbor shell. Secondly, the muon may not be that well localized at  $\mathbf{r} = 0$ , even if it does not diffuse from site to site. The muon could have an extended wave



function ranging over the whole interstitial site or it may carry out jump motions within the interstitial hole (caged diffusion). A certain averaging of  $\mathbf{B}'_{\text{dip}}(\mathbf{r})$  is the most obvious consequence (see Meier 1984). Whether an overlap of the muon wave function with the electronic wave functions of neighboring atoms can also influence the magnitude of their magnetic moment is an open question.

### 3.2. $\mu\text{SR}$ spectroscopy of dia- and paramagnets

The purpose of this and the next section is to familiarize the reader with the basic features of  $\mu\text{SR}$  spectra of magnetic materials and the parameters which determine their shape. We shall stay on very general grounds. In actual magnetic studies the situation may be considerably more complex. The discussion primarily follows the original development of  $\mu\text{SR}$  spectral theory which, as already stated, closely followed the NMR analogue. It is thus geared to interaction with nuclear moments. This is in fact the situation that prevails in diamagnets. The extension to electronic moments is not always straightforward. Paramagnets are a simple case, because in general the electronic moments can be viewed as approximately point-like, independent dipoles. One important difference is that nuclear dipoles can in most situations be considered to be static, but electronic moments are usually dynamic. Nuclear spin relaxation times are seldom shorter than  $10^{-4}$  s, so their correlation time is much longer than the muon life time. In contrast, electronic spin fluctuation frequencies in free paramagnets are beyond the GHz regime and therefore reside in the fast fluctuation limit, which will be discussed below. The extension to ordered moments is more complex and not fully solved in the more exotic cases. We shall treat the basics for ferro- and antiferromagnets in the following section and spin glass behavior in sect. 8. Special cases will be discussed as the need arises.

In a material containing dipolar moments (either electronic or nuclear) the muon at its resting place (to be discussed in sect. 3.6) experiences an effective magnetic field  $\mathbf{B}_\mu$  (either static or fluctuating in time), as discussed in the previous section. The individual members of the muon ensemble that generates the  $\mu\text{SR}$  spectrum (see sect. 2.6) do not see exactly the same field  $\mathbf{B}_\mu$ , even if all muons come to rest at one type of internal site. This is due to small changes in the local surroundings, in particular with respect to the field generated by nearby dipoles with different spatial orientation. By  $\mathbf{B}_\mu$  we denote in the following the *mean* field sensed by the muon ensemble (for clarity we no longer use the notation  $\langle \mathbf{B}_\mu \rangle$ ). We will introduce, where necessary, an appropriate parameter which describes the distribution of fields around its mean  $\mathbf{B}_\mu$ . In addition to getting information on the magnitude of  $\mathbf{B}_\mu$  and its distribution, a major objective of  $\mu\text{SR}$  in magnetic materials is the measurement of the muon spin relaxation function which then can be related to the dynamics of the spin ensemble in the sample material. We turn now in succession to  $\mu\text{SR}$  spectra obtained in the three fundamental experimental geometries, excluding muon spin resonance and level crossing data. A review on “ $\mu\text{SR}$  relaxation functions in magnetic materials” appeared recently (Uemura 1999).

### 3.2.1. Transverse field measurements (Knight shift)

“Transverse field” (TF) means that the applied field is oriented *perpendicular* to the initial muon spin polarization. As mentioned, this does not necessarily mean that the field is oriented perpendicular to the muon beam. With a surface beam, it may be oriented along the beam momentum when the muon spin has previously been turned by a spin rotator (see sect. 2.5). We restrict this discussion (except for some short remarks) to the *strong-field limit*, that is to say, we assume that the local quantization axis for muon spin and its surroundings is determined by the externally applied field alone. Then only the secular term in the Zeeman interaction of the local moments with  $\mathbf{B}_{\text{app}}$  need to be considered (details can be found, for example in Schenck 1985, chapter 2.3.1). Sensing a transverse field, the muon spin will precess in the plane perpendicular to the field axis, which generates the asymmetry spectrum

$$\mathcal{A}(t) = a_0 G_x(t) \cos(2\pi f_\mu t). \quad (17)$$

The asymmetry  $\mathcal{A}(t)$  has been defined by eq. (9). The spin precession frequency  $f_\mu$  is directly proportional to the magnitude of  $\mathbf{B}_\mu$ :

$$f_\mu = (\gamma_\mu/2\pi)B_\mu. \quad (18)$$

We shall discuss the information contained in  $f_\mu$  below.  $G_x(t)$  is the *transverse* muon spin relaxation function as indicated by the index  $x$  (the  $z$ -axis is commonly fixed parallel to the muon spin).

In the case of a dense system of randomly oriented moments, the field distribution can be assumed to have Gaussian shape. Truly random orientation is certainly fulfilled for a nuclear moment system (except at extremely low temperatures, which are out of the reach of μSR). For electronic moments it is strictly true only for a free paramagnet. This field distribution is added to  $\mathbf{B}_{\text{app}}$  and in summary  $\mathbf{B}_\mu$  is distributed. The width of this field distribution can be characterized by its second moment, the so called polycrystalline *Van Vleck moment*, originally derived for nuclear moments:

$$\sigma_{\text{VV}}^2 = \left(\frac{\mu_0}{4\pi}\right)^2 \frac{4}{15} \sum_i I(I+1) \gamma_\mu^2 \gamma_i^2 \hbar^2 r_i^{-6} \approx \left(\frac{\mu_0}{4\pi}\right)^2 \frac{4}{15} \gamma_\mu^2 \sum_i \mu_i^2 r_i^{-6}, \quad (19)$$

where  $I$  is the nuclear angular momentum,  $\gamma_i$  the corresponding gyromagnetic ratio and  $r_i$  is the distance to the  $i$ th dipole from the muon site. An analogous expression could be used for electronic moments. In general one can write

$$\sigma^2 = \gamma_\mu^2 \langle B_\mu^2 \rangle, \quad (20)$$

with  $\langle B_\mu^2 \rangle$  being the width of the (Gaussian) field distribution. This leads to the transverse field relaxation function

$$G_x(t, \tau) = \exp \left\{ -\sigma^2 \tau^2 \left[ \left( \frac{t}{\tau} \right) - 1 + \exp \left( -\frac{t}{\tau} \right) \right] \right\}, \quad (21)$$

which is commonly referred to as *Abragam relaxation*.  $1/\tau$  is the fluctuation rate of  $\mathbf{B}_\mu$ . Inherent assumptions as to the relaxation process are hidden in eq. (21). The derivation

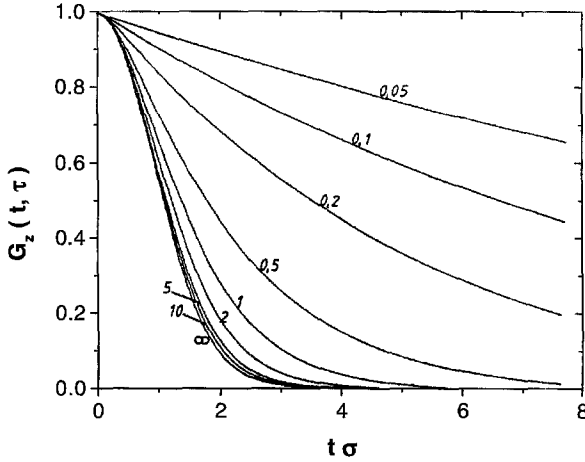


Fig. 16. Transverse field muon spin relaxation function (Abragam relaxation). The various curves are labeled by the value of  $\tau \cdot \sigma$  (in rad). They are the envelopes of the oscillatory spin precession patterns.

by Abragam (1961) is based on a Gaussian–Markovian process meaning that the field correlation function takes the form

$$\langle \mathbf{B}_\mu(t) \cdot \mathbf{B}_\mu(0) \rangle = \frac{\sigma^2}{\gamma_\mu^2} \exp\left(-\frac{t}{\tau}\right). \quad (22)$$

As seen from eq. (17), the relaxation function  $G_x(t)$  is the envelope of the spin precession pattern  $\cos(2\pi f_\mu t)$ . Its form is shown in fig. 16 for  $\tau$  as the parameter. In the static limit ( $\tau \rightarrow \infty$ ) we have pure Gaussian relaxation

$$G_x(t) = \exp\left[-\frac{1}{2}\sigma^2 t^2\right]. \quad (23)$$

In the fast fluctuation limit ( $\tau \rightarrow 0$ ), the decay of muon spin polarization becomes exponential:

$$G_x(t) = \exp[-\sigma^2 \tau t] = \exp[-\lambda t]. \quad (24)$$

According to eq. (20) one finds

$$\lambda = \sigma^2 \tau = \gamma_\mu^2 \langle B_\mu^2 \rangle \tau. \quad (25)$$

One often denotes  $\sigma$  as the *static* and  $\lambda$  as the *dynamic* relaxation rate. They are usually given in  $\mu\text{s}^{-1}$  (corresponding to  $10^6$  rad/s). One notices, especially from fig. 16, that the damping becomes weaker with rising fluctuation rate. This effect is known in NMR as *motional narrowing*. Static (Gaussian) relaxation of muon spin precession is also sometimes called inhomogeneous broadening, again borrowing from NMR. We illustrate

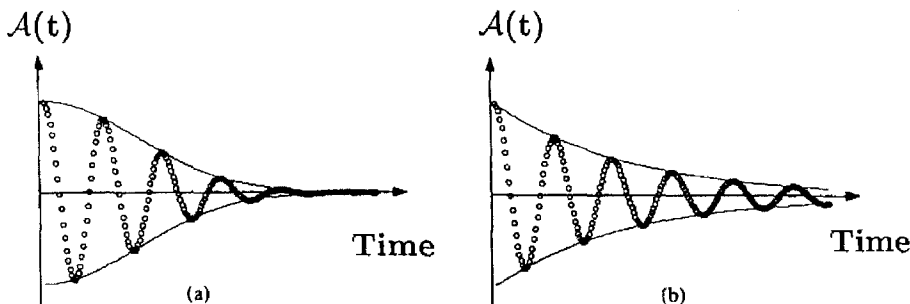


Fig. 17. Transverse field μSR spectra showing the limiting cases of (a) static (Gaussian) and (b) full dynamic (exponential) depolarization. From Karlsson (1995).

the limiting situations of static and dynamic damping with the two spectra shown in fig. 17.

According to eq. (21), transverse field measurements allow, in principle, separation of the static field width ( $\propto \sigma$ ) from the fluctuation rate ( $1/\tau$ ) in an intermediate case. In practice, this is rather difficult and the combination of zero and longitudinal field measurements are more powerful in this respect, as will be shown further below. In the static limit ( $\tau \rightarrow \infty$ ) we can extract the second moment of the field distribution (see eq. 20). In the fast fluctuation limit only the product  $\sigma^2\tau$  appears (eq. 24) and independent information on one of the two quantities is needed.

One basic assumption leading to eq. (21) was the *Gaussian* shape of the field distribution. We had stated that this requires a *dense* system of moments. In dilute systems (if less than  $\sim 10\%$  of the surrounding atoms have a moment – see Kittel and Abrahams 1953) the field distribution is close to a *Lorentzian* shape (Walstedt and Walker 1974). A Lorentzian has no second moment and the distribution width must be characterized by its half width at half maximum. It will not show motional narrowing; whether the local field is static or fluctuating, the experimenter will observe exponential relaxation, whose relaxation rate is basically insensitive to the field fluctuation rate  $1/\tau$ . In this case not much reliable information can be extracted from TF data. Dilute moment systems are therefore usually studied with ZF- and LF μSR.

We now discuss the information obtainable from the muon spin precession frequency  $f_\mu$ . The strong-field limit means that the external field is large compared to internal field contributions and  $f_\mu$  is mainly determined by  $B_{app}$ . Furthermore, for a truly random distribution of internal fields we expect their mean to be zero. The applied field, however, causes (a perhaps very weak, but still finite) magnetization of the sample and thus destroys the full randomness of moment orientation. As a result, a small internal field adds to the applied field. The resulting spin precession frequency  $\nu_\mu^{obs} = \gamma_\mu B_\mu$  is slightly shifted from the value  $\nu_\mu^0 = \gamma_\mu B_{app}$  expected if the external field alone were present. This is known as the *muonic Knight shift*. One defines the Knight shift constant

$$K = \frac{B_\mu}{B_{app}}. \tag{26}$$

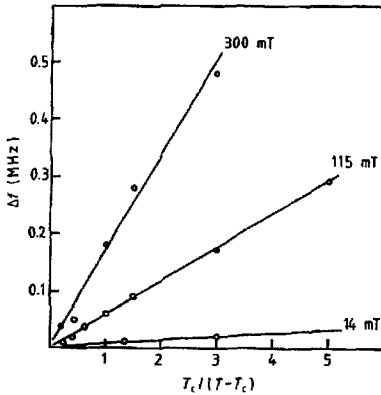


Fig. 18. Temperature dependence of the frequency shift in paramagnetic  $\text{PrAl}_2$  (polycrystalline sample) measured in a transverse field of 1 kG. The Curie-Weiss law is well reproduced ( $\Delta f_\mu \propto B_{\text{app}}/(T - T_C)$ ). From Hartmann et al. (1986).

$B_\mu$  is obtained from the  $\mu\text{SR}$  spectrum but  $B_{\text{app}}$  must be determined separately with high precision (e.g., with a NMR probe or by a  $\mu\text{SR}$  measurement on a diamagnetic material where the deviation of  $K$  from 1.0 is known to be very small). The Knight shift is a measure of the *interstitial susceptibility*. It is expected to follow the bulk susceptibility but deviations can occur under certain circumstances. As an illustration of normal behavior we show in fig. 18 the frequency shift as function of temperature for  $\text{PrAl}_2$  in the paramagnetic regime.

As discussed in sect. 3.1 the internal field has two components, the dipolar and the contact (hyperfine) field. In the polycrystalline average (and if the bulk susceptibility is isotropic), the dipolar contribution averages to zero. The Knight shift then allows a determination of the contact field magnitude. For more details on muon Knight shifts, the reader is referred to Schenck (1985) chapter 4.1, or Schenck (1999).

For single-crystalline samples, the dipolar field also contributes to the Knight shift (even in the simplest case an applied field lifts cubic symmetry), leading to an angular dependence  $K(\Theta)$ . Furthermore, the Van Vleck equation (eq. 19) is not valid in this case. One major reason is that nuclear spins  $I$  will not only feel the Zeeman interaction, but may in addition experience quadrupolar coupling if the atom (nucleus) possesses a quadrupole moment. The damping constant is then dependent on the magnitude of the applied field and on its direction with respect to the crystalline axis (Hartmann 1977). This effect, as well as measurements of  $K(\Theta)$  have been used to gain information on the muon stopping site (see also sect. 3.6).

The fact that a paramagnet in an external field shows a macroscopic magnetization means that  $B_{\text{lor}}$  and  $B_{\text{dem}}$  must be taken into account. Their contributions to  $K$  are usually of no interest and one corrects the shift for these effects in order to obtain the "true" Knight shift. These corrections are not always straightforward and can limit the accuracy of Knight shift measurements (for more details see Schenck and Gyax 1995 or Feyerherm et al. 1995).

In fig. 19 we show an example of an angularly dependent Knight shift. The sample is a single crystal of paramagnetic  $\text{CeB}_6$  (a heavy-fermion compound) which has a

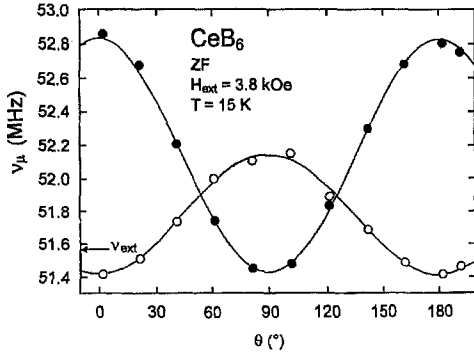


Fig. 19. Angular dependence of the muon spin precession frequency  $\nu_\mu$  of a single crystal of paramagnetic  $\text{CeB}_6$  in transverse field. Such data can be used to fix the muon stopping site (see text).  $\nu_{\text{ext}}$  is the spin precession frequency for a bare  $\mu^+$ . From Amato et al. (1997a).

cubic crystal structure and hence an isotropic susceptibility with Curie–Weiss behavior arising from the 4f electrons of Ce. The crystal was rotated around  $\langle 110 \rangle$  with the field perpendicular to this axis. The observed dependence  $K(\theta)$  is fully compatible with the muon resting on the crystallographic  $(\frac{1}{2}00)$  site, which splits magnetically into  $(00\frac{1}{2})$  and  $(\frac{1}{2}00)$ ,  $(0\frac{1}{2}0)$ , giving rise to the two signals with intensity ratio 1:2. The difference between  $\nu_{\text{ext}}$  and the average over  $\nu_\mu(\theta)$  will generate an isotropic Knight shift in a polycrystal.

Special detection schemes for small Knight shifts such as the stroboscopic (Camani et al. 1978) and the  $\mu\text{SR} \times 2$  methods (Chakhalian et al. 1997) have been developed.

### 3.2.2. Zero field measurements

In a diamagnet we have only nuclear moments (if any at all). Their effect on muon spin depolarization is analogous to that of paramagnetic moments, only that local fields of nuclear origin are usually, but not necessarily, weaker and static. We immediately turn to the more important case of a paramagnet, where, for simplicity, we assume nuclear moments to be absent for the time being. Their inclusion will be treated in sect. 3.4. Furthermore, the muon will be assumed stationary at its interstitial site.

We start out with a dense system of moments, i.e., a Gaussian field distribution. In addition we first treat the fully isotropic case, that is, each of the three spatial components of  $\mathbf{B}_\mu$  shows the same field distribution

$$P(\mathbf{B}_\mu) = P(B_x) \cdot P(B_y) \cdot P(B_z), \tag{27}$$

with

$$P(B_i) = \frac{\gamma_\mu}{\sqrt{2\pi} \cdot \Delta} \exp \left[ -\frac{\gamma_\mu^2 B_i^2}{2\Delta^2} \right]. \tag{28}$$

The assumption of isotropy is certainly valid for powders and polycrystals, on which most  $\mu\text{SR}$  experiments are performed. As is well-known, this leads to a Maxwellian distribution of field magnitude

$$P(|\mathbf{B}|) = \sqrt{\frac{2}{\pi}} \frac{\gamma_\mu^3 |\mathbf{B}|^2}{\Delta^3} \exp \left[ -\frac{\gamma_\mu^2}{2\Delta^2} \right]. \tag{29}$$

The width of the distribution of local magnetic field is  $\Delta/\gamma_\mu$ , where  $\Delta^2$  is given, if quadrupole interactions (e.g., caused by non-cubic crystalline electric field, see sect. 5.1.1) can be neglected, by

$$\Delta^2 = \left(\frac{\mu_0}{4\pi}\right) \frac{2}{3} I(I+1) \hbar^2 \gamma_I \gamma_\mu^2 \sum_i r_i^{-6}. \quad (30)$$

This is 5/2 times the Van Vleck width given in eq. (19), since both longitudinal and transverse components must be taken into account and also the strong-field limit does not apply.

The local fields acting on the muon spin are randomly oriented, which holds for a paramagnet in the absence of  $\mathbf{B}_{\text{app}}$ . In consequence, the mean vector field  $\langle \mathbf{B}_\mu \rangle$  vanishes and we will not observe a spin precession pattern and the  $\mu\text{SR}$  spectrum takes the simple form

$$\mathcal{A}(t) = a_0 G_z(t). \quad (31)$$

This does not imply that spin precession does not take place. But it is not coherent and thus will only show in a loss of signal amplitude as described by  $G_z(t)$ . The appropriate spin relaxation function  $G_z(t)$  for stationary fields was first derived by Kubo and Toyabe (1966) for NMR (where it has little practical use) and is known in  $\mu\text{SR}$  as the (static, Gaussian) Kubo–Toyabe function (Kubo 1981)

$$G_z(t) = \frac{1}{3} + \frac{2}{3}(1 - \Delta^2 t^2) \exp\left[-\frac{1}{2}\Delta^2 t^2\right]. \quad (32)$$

Its characteristic shape is presented as the solid line in fig. 20c. The polarization first drops, as time increases, from its initial value 1 to a single minimum before recovering to 1/3 at late times. As we shall see in more detail below, the “1/3 asymptote” is characteristic of ZF- $\mu\text{SR}$  in the case of static dipole moments (and a stationary muon). When everything is static, each muon sees a unique local field for its entire life and in the isotropic average 1/3 of the muon spins will be parallel to this field and not evolve in time. This is clearly expressed in the first term of eq. (32).

We have mentioned that the dilute limit calls for a Lorentzian distribution of field components

$$P(B_i) = \frac{\gamma_\mu}{\pi} \frac{a}{a^2 + \gamma_\mu^2 B_i^2}, \quad (33)$$

where  $a/\gamma_\mu$  is the field distribution’s half width at half maximum (HWHM). The corresponding static Lorentzian Kubo–Toyabe function has the shape

$$G_z(t) = \frac{1}{3} + \frac{2}{3}(1 - at) \exp[-at], \quad (34)$$

and is shown as a dashed line in fig. 20c. Differences from the Gaussian function are the exponential shape at early times and a more shallow minimum. The “1/3 asymptote”

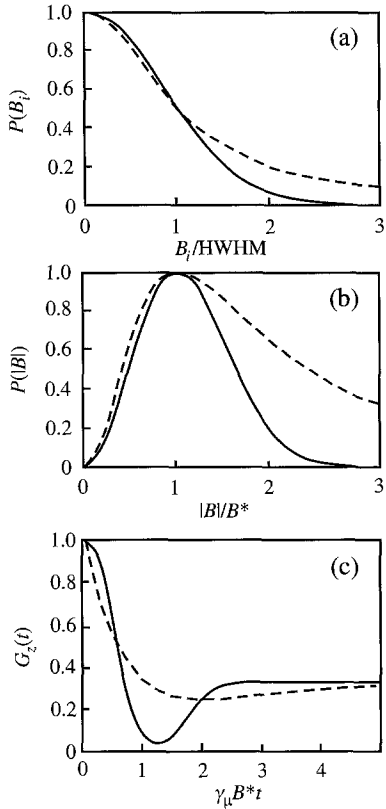


Fig. 20. Distribution of (a) field components and (b) field magnitude; (c) shows the resulting static Kubo–Toyabe functions. Solid lines refer to Gaussian, dashed lines to Lorentzian field distributions.  $B^*$  is the most probable field and HWHM the half width at half maximum of the distributions.

characteristic for a static field distribution is of course maintained. A truly Lorentzian distribution in field is a somewhat unphysical assumption since it allows the presence of arbitrarily large fields. In the real world the Lorentzian distribution must be truncated at some large finite field which might cause some deviations of the ideal Kubo–Toyabe shape.

For single-crystal samples the assumption of isotropy in field distributions is not valid and  $G_z(t)$  will change. Clearly, the long time asymptote will no longer be at  $1/3$  but will depend on the orientation of crystalline axes relative to the direction of initial muon spin orientation. The overall shape, however, does not change drastically, but depth and position (in time) of the minimum will also be affected. The general case has been treated by Turner (1986) but is mathematically very involved. The special case of uniaxial symmetry is discussed by Solt (1995). In practice the standard Kubo–Toyabe formalism has been used nearly exclusively. The real field distribution may neither be Lorentzian nor Gaussian and again the form of  $G_z(t)$  will be altered, but the non-relaxing long-time asymptote is preserved when the local fields are static. Special field distributions will be discussed as the need arises, mainly in sect. 8.



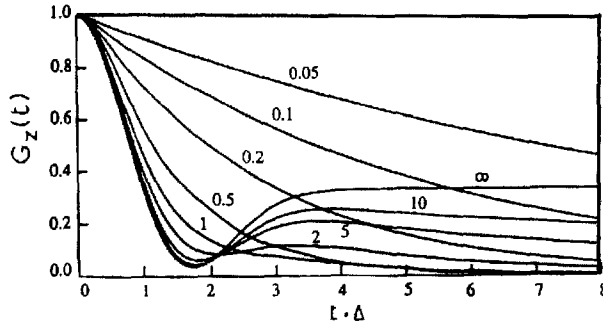


Fig. 21. Zero-field dynamic Gaussian Kubo–Toyabe functions for different field fluctuation times. The curves are labeled by the value of  $\tau \cdot \Delta$  (in rad). The calculation used the strong-collision model. In the Gaussian–Markovian approach  $G_z(t)$  decays minimally slower.

Kubo (1981) also treated the dynamic case that occurs when the muon sees a local field that fluctuates randomly with an average rate  $1/\tau$  either due to fluctuations of the field-generating moments, or to muon diffusional motion, or both. Different models for the relaxation process were assumed, for example the Gaussian–Markovian relaxation already mentioned (which is perhaps the proper model for fluctuating moments) and the strong-collision model where the Markovian feature (i.e., no memory of the previous step) is maintained but instead of using a Gaussian decay of field correlation, it changes instantaneously to the new value. This latter model is usually applied to muon diffusion where the jump time between sites is short compared to the residence time at one site. The differences in  $G_z(t, \tau)$  for the two treatments are small. A closed expression for  $G_z(t, \tau)$  is not available, but fig. 21 shows the result for a Gaussian field distribution obtained from numerical solutions. For slow fluctuations ( $\tau > 1/\Delta$ ) the main effect is that the  $1/3$  asymptote decays and the minimum gets shallower while the shape at early times is hardly altered at all. In the static case  $G_z(t)$  reflects dephasing of precessional motion due to the random field distribution. The lost polarization can be recovered by time inversion as commonly used in pulsed NMR (also see Kreitzman et al. 1988). Dynamic depolarization is a true relaxation process which can not be inverted, since spin entropy has increased. Hence the  $1/3$  asymptote can no longer be maintained at later times. For faster fluctuations ( $\tau \leq 1/\Delta$ ) the minimum vanishes altogether and the relaxation function approaches exponential shape  $G_z(t) = \exp(-\lambda t)$  with increasingly lower relaxation rates  $\lambda$ . This is again a manifestation of motional “narrowing”. The pure Lorentzian Kubo–Toyabe function will show in the dynamical situation only a loss of the  $1/3$  asymptote and with it, of the minimum as presented in fig. 22. Dilute spin glasses display Lorentzian field distributions at low temperature, yet *do* motionally decouple at high temperatures, requiring special treatment of the dynamics, as will be discussed in sect. 8.

A Gaussian field distribution (or something close to it) is the more commonly experienced situation and motional narrowing is usually observed. In the slow fluctuation limit, the decay of polarization in ZF is faster than in TF. ZF measurements for slow dynamics also allow a more unambiguous separation of static width and fluctuation rate

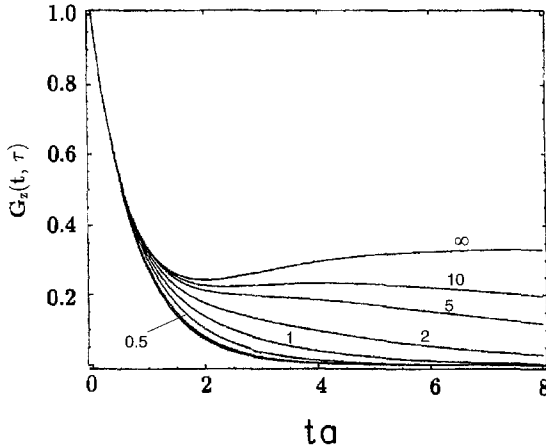


Fig. 22. Zero field strong-collision-dynamic Lorentzian Kubo–Toyabe function for different fluctuation times. The numbers are the value  $\tau \cdot a$  (in rad). Note the lack of decoupling as fluctuation rate  $\rightarrow \infty$ . After Uemura (1981).

compared to TF data (Abragam relaxation). In the fast fluctuation limit the two relaxation functions become alike and in both cases the product  $\Delta^2\tau$  or  $\sigma^2\tau$  enters, making the separation impossible. The connection between ZF and TF relaxation is discussed in detail by Hayano et al. (1979).

Let us briefly return to fig. 21. The rate  $\lambda = \gamma_\mu^2 \langle B_\mu^2 \rangle \tau$  of the exponential relaxation in the fast fluctuation regime ( $\tau \cdot \Delta < 1$ ) decreases as the fluctuations become *faster* (smaller  $\tau$ ) due to motional narrowing. In the slow limit, however, the decay of the 1/3 asymptote is the main effect and for later times one has  $G_z(t) \sim (1/3) \exp(-\lambda_{KT}t)$  with  $\lambda_{KT} = (2/3)\tau^{-1}$  (Hayano et al. 1979). Note that in this slow limit the decay rate  $\lambda_{KT}$  is independent of the width of the distribution of the local field (in contrast to the fast fluctuation case). It sometimes happens that the early part of the Kubo–Toyabe function (up to  $t \cdot \Delta \approx 5$ ) depolarizes so rapidly that it is hidden in the spectrometer dead time. All that is then visible is the Kubo–Toyabe tail decaying exponentially with  $\lambda_{KT}$  given above. In this case, the relaxation rate decreases when fluctuations become *slower*. In the static case one gets  $\lambda_{KT} = 0$ , i.e., the 1/3 asymptote. These two limits of the relaxation regimes must not be confused. The problem of fast and slow relaxation regimes is well-known in NMR (see Slichter 1978, ch. 5). In the μSR case, we shall meet this problem once more when discussing the spectral response of ordered magnets in sect. 3.3.

The actually observed relaxation function in the fast limit does not always follow strictly an exponential decay. In practice a “power exponential” relaxation is often used

$$G_z(t) = \exp[-(\lambda t)^p]. \tag{35}$$

Whether this is more than a convenient parameterization is debatable. The “stretched exponential” in eq. (35) has *no* direct relation to stretched exponential relaxation of bulk magnetization (see Campbell et al. 1994). As will be discussed in sect. 8 the only clear-cut case is the highly dilute spin glass. It was shown by Uemura et al. (1984) that above the glass transition temperature root-exponential relaxation occurs, that is  $p = 0.5$ . That

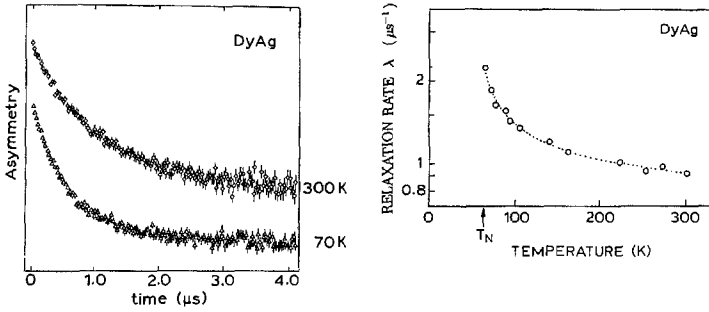


Fig. 23. Left: Zero field spectra of polycrystalline DyAg at two temperatures within the paramagnetic regime. The Néel temperature is  $\sim 60$  K. The two spectra are shifted vertically for clarity. Right: Temperature dependence of the relaxation rate  $\lambda$  derived from fits of an exponential decay of polarization to spectra of the type shown in the left hand panel. Typical is the sharp rise on approach to the magnetic transition temperature. The line is a guide to the eye, but fits to a critical power law are often possible. After Kalvius et al. (1986).

treatment does not allow a variation of  $p$  with temperature, which has occasionally been observed. Basically, power-exponential relaxation indicates the presence of a distribution in muon spin relaxation rates, but whether this reflects a similar distribution in fluctuation rates of the moments that generate the internal field, is an open question. We shall return to this point once more in sect. 8.2.1.

The typical goal of ZF studies of paramagnets is to obtain information on the temperature dependence of their spin dynamics. Of special interest is the approach to a magnetic phase transition, where slowing down of spin fluctuations often occurs. If one assumes that the field distribution (i.e.,  $\langle B_{\mu}^2 \rangle$ ) is independent of temperature (not necessarily true but a reasonable first approximation), then the change in relaxation rate  $\lambda$  is inversely proportional to the spin fluctuation rate. This further assumes that the situation remains in the fast fluctuation limit, which is the case in a typical paramagnet. As an example, fig. 23 shows ZF spectra of polycrystalline DyAg at two temperatures within the paramagnetic regime. The increase in relaxation with lower temperature is quite apparent. This is a high-moment paramagnet; in weaker paramagnets the spin fluctuations often become so fast at elevated temperatures that total motional narrowing occurs, making the damping of the  $\mu$ SR signal unmeasurably small.

### 3.2.3. Longitudinal field measurements

The term “longitudinal field” (LF) refers to an external field applied along the initial direction of muon spin (the  $z$  axis). LF measurements are most useful in cases where a Kubo–Toyabe-like relaxation function is observed in ZF. The applied LF competes with the internal field distribution, trying to hold the muon spin in its original direction (thus trying to prevent relaxation). If the longitudinal field  $B_L$  fulfills the condition

$$B_L \gg B_{\text{rms}} = \frac{\Delta}{\gamma_{\mu}}, \quad (36)$$

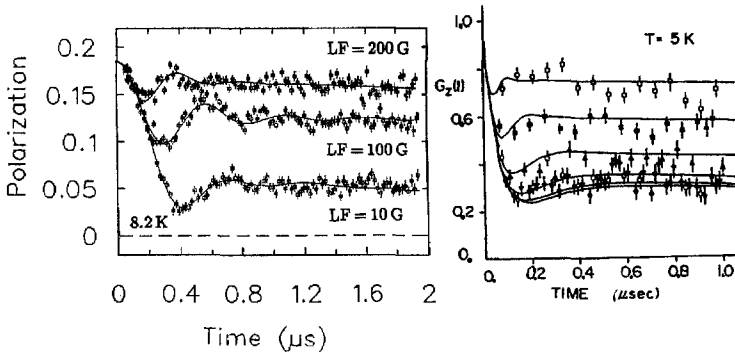


Fig. 24. Longitudinal field spectra for a Gaussian (left) and a Lorentzian (right) field distribution. The Gaussian case refers to spin freezing around 8.5 K in CePtSn, a concentrated spin system (Kalvius et al. 1995a); the Lorentzian case to a dilute Cu(Mn) spin glass below its glass transition temperature of 10.8 K. The values of the longitudinal fields are (from top to bottom): 640, 320, 160, 80, 40 and 0 G (Uemura et al. 1981). In both cases the set of spectra unambiguously proves that the spin systems are static.

and if the internal field distribution is static, then the muon spin mostly senses only the parallel-oriented  $B_L$ . Consequently, it will not evolve much in time (except for small oscillations at very early times). The shape of the static Gaussian LF Kubo–Toyabe function  $G_z(t, B_L)$  is shown in fig. 24 at left and the corresponding Lorentzian Kubo–Toyabe function at right. No algebraic expressions for the LF Kubo–Toyabe functions exist. The curves given in fig. 24 were obtained by numerical calculations.

Suppressing spin depolarization by a longitudinal field is often referred to as *longitudinal field decoupling*. The Lorentzian function is harder to decouple than the Gaussian. The dependence of the long time asymptote on  $B_L$  is a good test to distinguish between the Lorentzian and Gaussian case. (The other difference is primarily at early times and can be difficult to determine experimentally).

As already stated, in dynamic relaxation the fluctuating field increases spin entropy and the corresponding loss of polarization is irretrievable. In the slow-fluctuation limit we can still achieve partial decoupling with LF, but the long-time asymptote decays in time. In the fast-fluctuation limit,  $B_L$  will exert only a weak influence. In the most-likely case of a Gaussian field distribution, we observe exponential decay of polarization  $G_z = \exp(-\lambda t)$  and the dependence of the damping constant on  $B_L$  is given by the well-known result (see Slichter 1978, ch. 5)

$$\lambda(B_L) = \frac{\lambda(0)}{1 + (\gamma_\mu B_L \tau)^2}. \tag{37}$$

This is Lorentz-type dependence on applied field. An example is shown in fig. 117. For a 50% reduction in relaxation rate one needs a longitudinal field of strength  $B_{1/2} = 1/\gamma_\mu \tau$ . For  $\tau = 10^{-9}$  s (a fluctuation frequency of 1 GHz, which is still low for a typical paramagnet) a field of  $\sim 10$  T is required. If such measurements can resolve a change in  $\lambda$  with  $B_L$ , then they provide a value of  $\tau$  independent of  $\Delta$ . The combination with

$\lambda(0) = \gamma_\mu^2 \Delta^2 \tau$  allows determination of both  $\Delta$  and  $\tau$ . Thus there is a desire for very high fields (see sect. 2.7) which is largely unfulfilled to date.

While eq. (37) is often presented as very generally applicable, it is in fact not correct when local field distribution is Lorentzian. As noted in the previous section, standard strong-collision dynamics do not decouple a Lorentzian Kubo–Toyabe (fig. 22, *no* motional narrowing). This odd behavior requires rather special circumstances to occur (triple- $\mathbf{k}$  ordering in USb and DyAg, sect. 5.2, singlet ground state PrP, sect. 5.1.2).

Recall (above) that in ZF, fast field fluctuations in a Gaussian distribution result in muon spin relaxation at a rate determined solely by  $\Delta^2/\nu$ , so that ZF (in that limit) cannot separate the distribution width from the fluctuation rate, but LF in principle can. For a Lorentzian distribution, the ZF fast-fluctuation limit relaxation rate  $\lambda(0) \rightarrow 4a/3$  depends only on the width of the distribution. LF provides the only way to measure the local-field fluctuation rate, if the apparatus can generate a field large enough that the muon Larmor frequency in it is comparable to that fluctuation rate. Then longitudinal field does cause decoupling, but as (Noakes et al. 2000)

$$\lambda_{\text{Lor}}(B_L) = \frac{\lambda_{\text{Lor}}(0)}{\sqrt{1 + (\gamma_\mu B_L \tau)^2}}, \quad (38)$$

(see the discussion of PrP  $\mu$ SR in sect. 5.1). In fig. 25 we show the ZF and LF curves for strong-collision-dynamic relaxations of different speeds for the Gaussian and Lorentzian Kubo–Toyabe cases.

For dilute spin glasses, the field distribution is Lorentzian, but the dynamics are not of strong-collision form, because observations show that as temperature (and with it, fluctuation rate) rises, there is motional narrowing of the ZF relaxation. A special treatment of dynamics, developed by Uemura and collaborators, is used, as discussed in sect. 8.1. In this case, neither of eqs. (37) or (38) apply. Keren (1994b) has developed expressions for the non-exponential relaxation that occurs in simultaneous LF and rapid fluctuations for such dilute spin glasses.

In ending this discussion of the influence of longitudinally applied fields, it is important to point out that two very fundamental assumptions were made throughout, namely (i) the fluctuation rate  $1/\tau$  itself is not altered by the application of the field, and (ii) neither is the static field width  $\Delta$ . Both assumptions are usually fulfilled for nuclear dipoles and this is the case for which the Kubo–Toyabe formalism was developed originally. For electronic dipoles the situation is not so clear cut. Close to a magnetic phase transition, for example, spin correlations can be affected by applied fields and that would influence temporal behavior as well as the resultant local field produced at the muon site. Very little information is available on that subject. We discuss a case later in sect. 5. In general, measurements in longitudinal geometry (either ZF or LF) put a rather stringent demand on a true zero (perpendicular) field condition because very low frequency spin precession induced by a weak external field (i.e., when less than 1/4 of a period is visible within the time range of the  $\mu$ SR spectrum) is difficult to distinguish from slow relaxation. The surroundings of a beam line are not favorable to this, as stray fields are abundant. It is

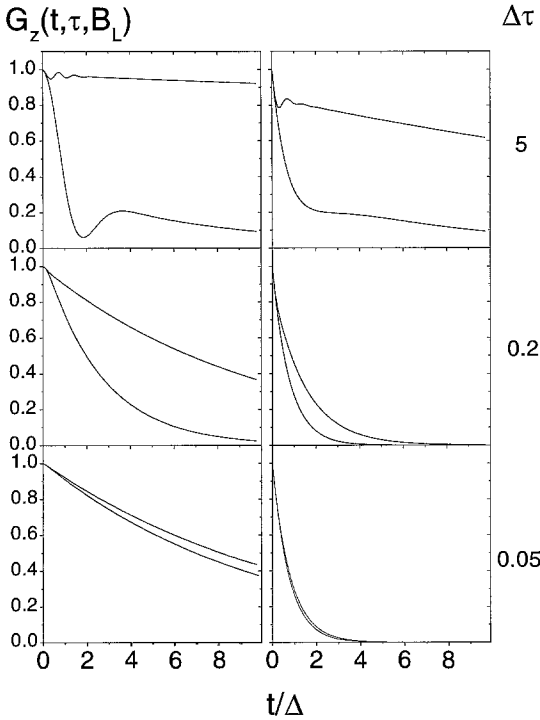


Fig. 25. Zero and longitudinal field ( $B_L = 10\Delta/\gamma_\mu$ ) Kubo-Toyabe functions for local field fluctuating increasingly faster (from top to bottom). Left: Gaussian field distribution; right: pure Lorentzian field distribution.

mandatory to have a three dimensional coil arrangement around the sample to compensate such stray fields.

### 3.3. $\mu$ SR spectroscopy of ordered magnets

The dominant feature of ordered magnetism (ferro-, antiferro- or ferrimagnetism) is the appearance of a spontaneous magnetization (in AFM, the staggered sublattice magnetization) when the temperature is lowered below the magnetic transition temperature ( $T_C$  or  $T_N$ ). The atomic dipole moments (or at least one of their spatial components) are now aligned along a crystalline direction (the easy axis). From the point of view of  $\mu$ SR this means that the moments surrounding the muon at its stopping site have preferential orientation and a resultant field  $B_\mu \neq 0$  will be felt by the full ensemble of muons implanted in the ordered magnet. (As will be discussed below there can be special-case exceptions to this rule in AFM). This resultant field will induce a spin precession pattern in a  $\mu$ SR spectrum taken in *zero applied field*. A typical example is shown in fig. 26. Details of the spectral response function will be discussed further below. For the moment we keep in mind that  $\mu$ SR studies of ordered magnets use ZF conditions

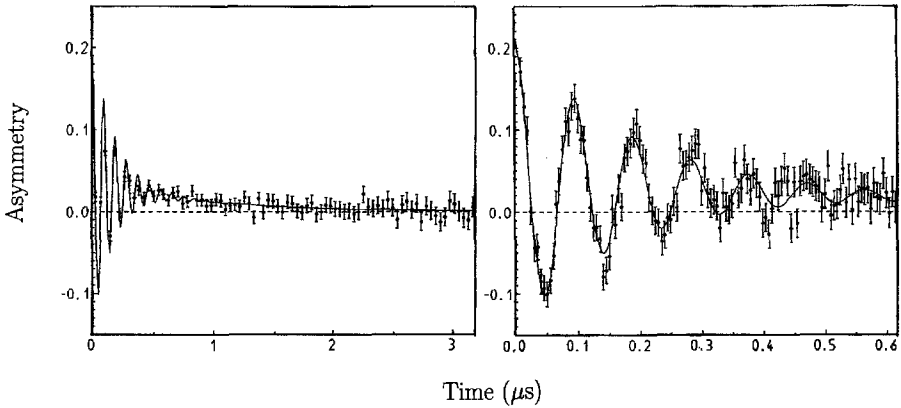


Fig. 26. ZF- $\mu$ SR spectrum of ferromagnetic Gd metal at 235 K ( $T_C = 293$  K). The solid line is a fit according to eq. (41). The oscillatory and non-oscillatory parts are clearly visible. The right-hand panel shows the rapidly damped oscillations in more detail.

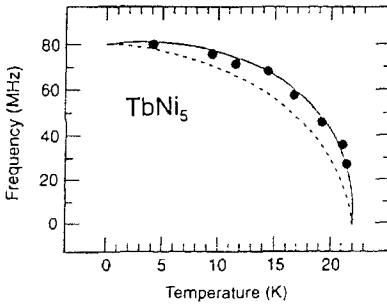


Fig. 27. Temperature dependence of the spontaneous muon spin precession frequency in single-crystalline  $\text{TbNi}_5$  with a Curie temperature of 23 K. The dashed curve is the appropriate free-ion Brillouin function. Inclusion of CEF interaction in the ground-state multiplet gives the solid curve which fits the data well. The behavior around the critical temperature is typical for a second-order magnetic phase transition. After Dalmas de Réotier et al. (1992).

almost exclusively, measuring the “spontaneous spin precession”. The sources of the field responsible for spontaneous precession are given according to eq. (15)

$$\mathbf{B}_\mu = \mathbf{B}_{\text{con}} + \mathbf{B}'_{\text{dip}} + \mathbf{B}_{\text{lor}}. \quad (39)$$

The magnitude of the spontaneous magnetization  $M$  in ordered magnets is temperature dependent due to spin wave excitations. Spin wave frequencies are so fast (THz) that they are fully motional-narrowed in  $\mu$ SR. All one will observe is the expectation value of the internal field which is coupled (but not necessarily directly proportional) to the expectation value of  $M(T)$ . For this reason one calls the  $\mathbf{B}_\mu$  of an ordered magnet a “quasistatic” field. The spontaneous precession vanishes at a second-order magnetic transition point and reaches a saturation value for  $T \rightarrow 0$ . An example is shown in fig. 27.

Thus far, we have neglected the existence of *magnetic domains*. An ordered magnet usually consists of a multitude of uniformly magnetized sub-volumes, the domains. They all have the same magnitude of magnetization (namely the temperature-dependent spontaneous magnetization) but  $\mathbf{M}_{\text{dom}}$  points in different spatial directions for different

domains. For a sample that has been cooled through its magnetic transition temperature in zero field, the sum over  $M_{\text{dom}}$  will be zero if no external field is applied (unmagnetized sample). Neighboring domains are separated by *domain walls* where moment orientation varies from one site to the next (e.g., Bloch walls). The internal field  $B_{\mu}$  within a domain wall is poorly defined and muons stopped in the walls are expected not to contribute to the spontaneous spin precession pattern. As a rule, the volume ratio of domain walls to domains proper is small and for this reason the effect of domain walls on the  $\mu$ SR spectrum is disregarded, since  $\mu$ SR, in contrast to NMR, probes the whole sample volume with equal probability. It is however a not uncommon experience that the intensity of the  $\mu$ SR signal (i.e.,  $a_0$ ) is slightly reduced when passing through the transition point to an ordered state. Another, largely unexplained, fact is the rather strong observed *static* damping of the spontaneous spin precession signal (see fig. 26 and discussion following eq. 40). Dipolar fields are of relatively long-range and the effect of domain walls might be felt as a disturbance of  $B_{\mu}$  well inside the domain. In polycrystals, domain walls tend to be linked to grain boundaries, but other disturbances such as magneto-elastic strains, lattice defects, *etc.*, might cause additional local magnetic disorder and hence contribute to the high damping rate. In effect, to the muon even a simple ferro- or antiferromagnet does not appear as a perfectly ordered spin lattice of nearly infinite size.

It should be kept in mind also that a magnetically ordered single crystal is divided into domains. In this case domains tend to be large with their magnetization pointing along the easy axis with equal parts in forward and backward direction (for an unmagnetized crystal). As will become apparent below (eq. 40), magnetizations in opposite directions lead to the same  $\mu$ SR patterns. Thus, a single-crystal FM may be viewed in rough approximation as a single-domain case, but in finer detail the so called “closure domains” oriented perpendicular to the easy axis must be taken into account. A true single-domain sample requires the application of an external field ( $B_{\text{sat}}$ ) strong enough to drive the magnet to saturation of its magnetization. Lanthanide and actinide ferromagnets have large magnetic anisotropies and hence ( $B_{\text{sat}}$ ) may easily exceed 10 T. Fields of this magnitude are not commonly available in  $\mu$ SR spectrometers.

It is also often overlooked that AFM possess domain structures as well (see Dillon 1963), so the above discussion applies to all types of ordered magnetism. In AFM, it is of course not usually possible to produce a single-domain structure with an external field. Preferred domain orientation sometimes can be achieved by application of uniaxial stress, a technique used mostly in neutron diffraction. In general, little is known about AFM domains.

At first, one might conclude that, due to the random orientation of  $M_{\text{dom}}$ , as found especially in an unmagnetized, polycrystalline magnet, a spontaneous spin precession signal is unobservable because the internal fields  $B_{\mu}$  taken over the whole sample are then randomly oriented as well. Fortunately, this is not so. We may approach the isotropic situation by assuming that exactly 1/6 of the field vectors point into each of the 6 cartesian directions (+x, -x, +y, -y, +z, -z). The 1/3 of fields oriented along  $\pm z$  will be parallel to the muon spin and do not induce precession. The 1/3 of field vectors oriented  $\pm x$  will cause precession in the (y, z) plane, one half clockwise, the other half counter clockwise.



Remember that all muons precess with the same frequency  $f_\mu = \gamma_\mu |\mathbf{B}_\mu|$ . They start together at (say) the  $+z$  direction and coincide again after one-half the precession period at the  $-z$  axis. The argument is the same for the field components along  $\pm y$ . They precess in the  $(x, z)$  plane but again coincide for  $+z$  and  $-z$ . Thus, the precession pattern can be seen *provided the positron detectors are arranged in a forward-backward ( $\pm z$ ) geometry*. A left-right detector arrangement will not observe the pattern. The combination of B-F and L-R data can prove useful in cases of complex spectra containing both magnetically ordered and paramagnetic portions. For B-F detectors we have

$$\mathcal{A}(t) = a_0 \left( \frac{2}{3} G_x(t) \cos(2\pi\nu_\mu t) + \frac{1}{3} G_z(t) \right). \quad (40)$$

The arguments just presented show that the  $\mu$ SR pattern is fundamentally the same for FM or AFM spin order.

The longitudinal relaxation function  $G_z(t)$ , related to the portion of the field pointing in the  $\pm z$  direction, is only sensitive to *dynamic* depolarization while  $G_x(t)$  involves both *static and dynamic* influences. Thus,  $G_x(t)$  usually relaxes much more quickly than  $G_z(t)$  and the net result is a strongly damped oscillatory pattern of reduced amplitude riding on a baseline given by  $G_z(t)$ , which decays more slowly with time. This is well demonstrated in the  $\mu$ SR spectrum of ferromagnetic elemental gadolinium shown in fig. 26. It is important to realize that eq. (40) allows separation of static from dynamic depolarization in ordered magnets. As mentioned, static depolarization is usually strong. In polycrystalline materials it may become so large that the oscillatory pattern is damped out within the initial dead time of the spectrometer (typically 5–10 ns) and that signal is then unobservable. All that then remains is the (more weakly damped) non-oscillatory  $G_z(t)$  pattern (“one-third signal”). It contains no information on the size of the internal field but can shed some light on spin dynamical properties in the ordered state.

In single crystals (strictly speaking in single-domain crystals) the relative magnitude of the non-oscillating term depends on the angle  $\Theta$  between initial muon spin orientation and the direction of magnetization. Eq. (40) must be replaced by

$$\mathcal{A}(t) = a_0 \left( G_x(t) \sin^2(\Theta) \cos(2\pi\nu_\mu t) + G_z(t) \cos^2(\Theta) \right). \quad (41)$$

The factor  $1/3$  in eq. (40) is just the polycrystalline average of  $\cos^2(\Theta)$ . Polycrystalline materials can exhibit texture effects and the  $2/3$  strength of the oscillating part is not sacred.

In practice one usually describes  $G_x(t)$  as well as  $G_z(t)$  by an exponential decay of polarization introducing the transverse ( $\lambda_T$ ) and the longitudinal ( $\lambda_L$ ) relaxation rates. Strictly speaking,  $G_x(t)$  should not have pure exponential form since static depolarization is at least partially involved. The longitudinal relaxation is basically the same feature as the decaying tail of a slowly dynamic Kubo–Toyabe function discussed in sect. 3.2.2. Therefore, when spin fluctuations die out in the ordered state (usually for  $T \rightarrow 0$ ), the longitudinal relaxation rate becomes smaller, reaching zero for the static limit. This is a different behavior than observed in a paramagnet where the slowing down of spin

fluctuations (i.e., in the critical regime above a phase transition – see fig. 23) causes an increase of relaxation rate. One must keep this important difference in mind.

Even when muons occupy only one particular crystallographic site in the sample, there may be magnetically different muon environments when there is a spatially fixed spontaneous magnetization. We had earlier encountered such a situation in the Knight shift data of paramagnetic  $\text{CeB}_6$  (see fig. 19). Instead of the spatially fixed magnetization we had a spatially fixed external field, leading to the same effect. Information regarding the splitting of a crystalline site into magnetic subsites can be used either to fix the muon site or the spin structure (but not both).

High crystallographic symmetry of the moments surrounding the muon site can lead to complete cancellation of the dipolar field contribution to  $\mathbf{B}_\mu$ . In a FM the unique domain magnetization will still generate  $\mathbf{B}_{\text{con}}$ , which then is the only source of  $\mathbf{B}_\mu$  if the material is unmagnetized. A well-known example is Ni metal (e.g., Denison et al. 1979). In an AFM the staggered magnetization will also force  $\mathbf{B}_{\text{con}}$  to be zero under those circumstances and spontaneous spin precession is not observed at all. This situation occurs in fcc metals or in intermetallics with simple cubic structures (e.g., NaCl, CsCl,  $\text{AuCu}_3$ ). These cases will be discussed later in detail in sect. 5.2.

As said before, even in case of a simple ferro- or antiferromagnet, the spin lattice appears faulty on a local scale and the ZF- $\mu$ SR oscillatory pattern is more or less damped. In more complicated spin structures, as found especially in AFM, the local field  $\mathbf{B}_\mu$  may have an inherent distribution width, also causing static muon spin depolarization. A pertinent example is incommensurate spin density wave ordering. It possesses a distinct broad field distribution resulting in a characteristic shape of the spontaneous spin precession pattern. This case is discussed in more detail in sect. 3.7 (see eq. 53). The extreme case is a frozen randomly oriented spin ensemble as is characteristic for a spin glass. Only decay of polarization, but no coherent spin precession signal is observed. The situation is similar to what has been discussed in sect. 3.2.2 for the static limit, i.e., a static Kubo–Toyabe pattern is seen.  $\mu$ SR response to spin glasses will be discussed in more detail in sect. 8. Between these two limiting cases one may find various degrees of spin disorder in an ordered magnet, especially in random alloy systems, meaning that the static relaxation rate  $\sigma$  of the oscillatory signal can vary over a wider range. In case  $\sigma$  has reached about the same magnitude as the precession frequency  $\nu_\mu$ , it becomes difficult to distinguish the heavily damped oscillatory pattern from a static Kubo–Toyabe function. If excessive disorder makes the rate  $\sigma$  much larger than the coherent precession frequency  $\nu_\mu$ , only a monotonic decay of muon spin polarization is seen (a situation one might call “overdamped oscillations”). Then, all one can extract from the  $\mu$ SR spectrum is the degree of disorder (*via*  $\sigma$ ); information on the ordering is lost (i.e.,  $\nu_\mu$  can not be determined). We will encounter several such cases later on. An important conclusion of the discussion in the last paragraphs is that the observation of a spontaneous spin precession pattern signals the presence of long-range magnetic order. The absence of a precession pattern, however, cannot simply be taken as proof of the absence of magnetic order.

We have stated at the beginning of this section that measurements in applied field are rarely performed for magnets in the ordered state. An external field will enter a FM

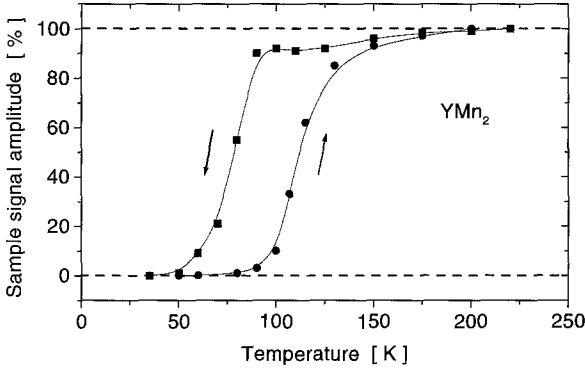


Fig. 28. Normalized (to  $T = 250$  K)  $\mu$ SR signal amplitude (= paramagnetic fraction) from TF measurements on polycrystalline  $\text{YMn}_2$ . After Weber et al. (1994a).

only if it exceeds  $B_{\text{sat}}$ , but no such restriction exists for AFM. With polycrystals the external field will randomly add to the internal field because of the random orientation of domain magnetizations and widen the field distribution. In addition  $B_{\text{dem}}$  comes into play. Both effects will cause increased static depolarization and the signal may quickly become unobservable. The situation is clearly more favorable in single crystals. The vector addition of the external field to the local field will give information on spin structure (a property which can not be extracted directly from  $\mu$ SR data) and/or muon stopping site.

When the above-mentioned loss of signal in rapid static depolarization (which, in particular, is expected for a polycrystalline sample in an external field) occurs on entering the ordered state, it allows determination of the exact magnetic transition temperature for the sample under study. An example is shown in fig. 28. The sample is  $\text{YMn}_2$ , which exhibits a first-order Néel transition with a large hysteresis. In the paramagnetic regime we observe spin precession due to an applied transverse field. The initial asymmetry  $a_0$  is a measure of the paramagnetic fraction in the material. At temperatures well above  $T_N$  it is 100% and zero well below  $T_N$ , where no oscillatory signal is observed due to excessive damping in the AFM regime. Details, especially regarding the slight loss of paramagnetic fraction just above the onset of AFM will be discussed in sect. 5.3.3.

### 3.4. Double relaxation

We have already stressed that each muon always senses *one* unique field  $B_\mu$  at its stopping site which, however, might be the vector sum of fields generated by different types of magnetic moments in its surroundings. Separate influences on the  $\mu$ SR spectrum will be visible only if these various contributions possess markedly different temporal structures. In this case one commonly approximates muon spin relaxation phenomena by using a resultant relaxation function which is the *product* of the relaxation functions appropriate for each of the field contributions.

An actual situation could be a paramagnet with both *nuclear and electronic dipoles* present (in the foregoing discussion we had assumed that no nuclear dipoles are present in the paramagnet). Barring special circumstances (to be discussed in sect. 3.7), the field

from nuclear dipoles will essentially be static while the field from electronic dipoles tends to fluctuate rapidly, as pointed out previously. The appropriate ZF relaxation function is then

$$G_{\text{total}}(t) = G_{\text{nucl}}^{\text{KT}}(t) \cdot \exp[-\lambda_{\text{el}}t], \quad (42)$$

where  $G_{\text{nucl}}^{\text{KT}}(t)$  is the Kubo–Toyabe relaxation function due to the static nuclear fields and  $\lambda_{\text{el}}$  is the relaxation rate due to the electronic fields assumed to be in rapid fluctuation. Equation (42) is strictly correct when one of the contributions is in the fast fluctuation limit. When that is not true, the relaxation will not in general be a product, but needs to be solved on a case-by-case basis. In the case described by eq. (42), the two relaxation processes can be separated easily by applying a longitudinal field:  $G_{\text{nucl}}^{\text{KT}}$  will decouple while  $\lambda_{\text{el}}$  remains practically unaffected, as outlined previously. The nuclear field width will be less than 1 mT and thus  $B_L = 10$  mT will suffice to suppress nuclear relaxation altogether and thus to obtain the electronic relaxation function separately. In magnetic studies one is primarily interested in  $\lambda_{\text{el}}(\text{T})$  and then it is often good practice to carry out the measurement on paramagnetic samples in a weak longitudinal field right away. We return to this problem in sect. 3.7.

The combination nuclear plus electronic relaxation is the most common, but not the only situation where double relaxation comes into play. In transverse field measurements on a highly susceptible (i.e., large moment) paramagnet, the applied field will produce a notable sample magnetization  $M_S$ . It, in turn, gives rise to a substantial demagnetization field  $B_{\text{dem}}$ , which being linked to  $B_{\text{app}}$  is of static nature. In contrast, the field from surrounding paramagnetic dipoles will (usually) fluctuate rapidly. The appropriate relaxation function is then

$$G_x(t) = \exp \left[ - \left( \frac{1}{2} \sigma^2 t^2 + \lambda t \right) \right]. \quad (43)$$

In this case, it is not easy to separate the two relaxation mechanisms. The only possible means are their field and their (hopefully) different temperature dependences (see Hartmann et al. 1986).

### 3.5. Data analysis

Having obtained experimental data in the form of an instrumental response as a function of time (counts  $N(t)$  or, as we will describe, asymmetry  $\mathcal{A}(t)$ ), the experimenter seeks to extract information on physical properties and processes in the sample by analyzing the data. When there are clear oscillations in the data, from either an applied transverse field or from well-defined internal fields in well-ordered magnetic states, it is often useful to transform the data into “frequency space” by Fast Fourier Transform (FFT, see e.g., Press et al. 1986), or some alternate transform algorithm (see Alves et al. 1994, Rainford and Daniell 1994). This is particularly useful if a theory that is being tested predicts response as a function of frequency. In μSR of magnetic systems, however, many of the data

observed involve relaxation (decay of polarization without clear oscillation frequencies), from which we wish to distinguish static fields from dynamics in the material (information which can be hard to extract from FFTs), so we usually prefer to compare theory to experiment by least-squares fitting (see, for example, Bevington and Robinson 1992) in the time domain.

The first task is to formulate a theoretical signal function, which we denote as  $S_{\text{th}}(t)$ , representing muon polarization as a function of time. For example, a transverse field measurement in the fast fluctuation limit should have the form

$$S_{\text{th}}(t) = a_0 \exp[-\lambda t] \cos(2\pi f_v t + \Phi). \quad (44)$$

This function must then be least-squares fit to either the single-detector response (eq. 7) in case of a forward detector,

$$N_F(t) = N_0 \exp\left(-\frac{t}{\tau_\mu}\right) (1 - S_{\text{th}}(t)), \quad (45)$$

or (preferably) to the backward–forward (respectively left–right) asymmetry (eq. 9),  $\mathcal{A}(t) = S_{\text{th}}(t)$ . The physical parameters to be returned by the fit for the example of eq. (44) would be  $a_0$ ,  $\lambda$ ,  $f_v$  and  $\Phi$ . In case of a single-telescope fit (eq. 45) the count rate normalization  $N_0$  is an additional parameter (since it is not *a priori* known). In the case of positive-muon  $\mu\text{SR}$ , the life time  $\tau_\mu$  is fixed but for negative-muon  $\mu\text{SR}$  it also becomes a variable (because of the  $Z$ -dependent nuclear capture rate).

The discussion to this point assumes an ideal world, never realized in experimental physics. Most importantly, a background count rate arising from chance coincidences between the muon and positron counters needs to be added in eq. (45). If we assume this background to be independent of time (which is reasonable but not always proven), then we have

$$N_F = N_0 \exp\left(-\frac{t}{\tau_\mu}\right) (1 - S_{\text{th}}(t)) + (N_{\text{bk}})_F. \quad (46)$$

Fortunately,  $N_{\text{bk}}$  can be determined independently and need not be fitted. This is done by collecting data *before* the muon enters the sample. Those “negative time” bins can be obtained easily by sending the positron counts through an appropriate time delay. For pulsed beams,  $N_{\text{bk}}$  can be neglected, but one needs to consider losses of counts in early channels because of high count rate load of the detectors. Turning now to an asymmetry spectrum, the data analysis program must first subtract the appropriate background counts from  $N_F(t)$  and  $N_B(t)$  before forming the backward–forward ratio according to eq. (9). Another, more serious experimental problem is that forward and backward detectors have different counting efficiencies (for many reasons which we will not discuss) and hence at any fixed time  $t$  one has  $N_F(t) \neq N_B(t)$ . One defines the parameter  $\alpha$

$$\alpha = \frac{N_F(0)}{N_B(0)}, \quad (47)$$

which should be independent of time over the course of measurements on one sample. Combining eq. (47) with eq. (9) one obtains

$$\mathcal{A}(t) = \frac{(1 - \alpha) + (1 + \alpha) \mathcal{S}_{\text{th}}(t)}{(1 + \alpha) + (1 - \alpha) \mathcal{S}_{\text{th}}(t)}. \quad (48)$$

For  $\alpha = 1$ , eq. (9) is recovered. The main effect of  $\alpha \neq 1$  is a shift of “baseline”, that is, of the value  $\mathcal{A}(t \rightarrow \infty)$ . The fit program usually least-squares fits the right hand side of eq. (48) as theory to the left hand side as data, with  $\alpha$  being a variable. The latter is unfortunately highly correlated with the initial asymmetry  $a_0$  (another fit parameter), since the value of  $a_0$  is determined as the distance from the  $\alpha$ -dependent baseline. One may obtain  $\alpha$  independently from a transverse field measurement, since in this case the baseline is easily fixed as the center between the positive and negative extremes. If so, *low* transverse fields should be used, since the detectors are affected by external fields and also one must make sure that the geometry (including the beam spot) does not change. Altogether, the “alpha problem” can sometimes be a serious limitation in the interpretation of finer details of a μSR spectrum.

There is another possible difference in the response of the two (e.g., forward and backward) ratio forming detectors. As mentioned in sect. 2.6 the initial asymmetry is dependent on positron energy. Different detectors may sample slightly different energy ranges of positrons resulting in different values of  $a_0$ . One may define, analogously to eq. (47), the parameter  $\beta$

$$\beta = \frac{(a_0)_F}{(a_0)_B}, \quad (49)$$

and include this in the formation of  $\mathcal{A}(t)$ . We do not expand further on this, because in practice  $\beta$  is usually assumed to be one. The problem of properly correcting measured asymmetry spectra for experimentally induced inaccuracies has been discussed in some detail by Riseman et al. (1994).

Often the μSR response will be a sum of theory functions

$$\mathcal{S}_{\text{th}} = \sum_i (\mathcal{S}_{\text{th}})_i, \quad (50)$$

especially if the muon occupies multiple sites. An unwanted but regularly encountered situation in this respect is a fraction of muons that stop in sample surroundings such as the sample holder, cryostat walls, *etc.* This leads to a so-called *background signal* (not to be confused with the background rate  $N_{\text{bk}}$ ). It is not always easy to disentangle background and sample signals. Usually an effort is made to have a background signal with no time dependence (e.g.,  $\lambda$  or  $\sigma = 0$ ) at any temperature. This is achieved for the muons stopped in silver. It is a recommended practice to use silver pieces in the immediate sample environment. By comparison, copper is undesirable, because it shows a substantial damping rate which varies with temperature (see Luke et al. 1990a).

$\mu$ SR least-squares fit programs are available at all muon facilities, all of which are poorly documented. Most commonly used is the MSRFIT program developed by J. Brewer at TRIUMF, which is extremely flexible and can be used either for single-telescope or asymmetry fits. Single-telescope fits are difficult if the time dependence of the signal function is slow compared to muon decay, because  $N_0$  and  $a_0$  are then strongly correlated. As mentioned, dynamic and longitudinal field Kubo–Toyabe functions can not be expressed in closed form. The TRIUMF program uses three-dimensional look-up tables for the Gaussian or Lorentzian functions  $G_z(t, \tau, B_L)$  derived from numerical calculations (see Hayano et al. 1979) which are too slow to be incorporated in a least-squares loop. Weber et al. (1994b) have developed an approximation using Fast Fourier Transforms. This makes inclusion in the loop possible. Both approaches work well.

For extracting the frequency content of a TF spectrum, the “maximum entropy” method has been described by Rainford and Daniell (1994) and Alves et al. (1994) as an improved technique compared to the usually employed Fourier transform. Aspects of the treatment of transverse field  $\mu$ SR data (with emphasis on pulsed beam measurements) have been discussed recently by Rainford (1999b). In the experimental spectra shown in this article, the solid line through the data points is the least-squares fitted theoretical function  $S_{\text{th}}(t)$ . The goodness of fit parameter is  $\chi^2$ , as usual in least-squares fitting.

### 3.6. Determination of the muon site

As outlined before, once a low-energy positive muon has been deposited in the sample of interest, it slows down to thermal velocities in a time of order  $10^{-10}$  s (for solids), with no loss of original polarization. It may emerge from “thermalization” as an apparently bare  $\mu^+$  (in metals) or in a muonium-like state (sometimes, in semiconductors and insulators). Muonium-like states will not be discussed further here. A “bare” muon in a metal is in contact hyperfine interaction with the conduction electron density at its location, which results in a muonic Knight shift (usually small in nonmagnetic materials). A “bare”  $\mu^+$  in an insulator is a diamagnetic center, and is quite likely to be bonded to the most electronegative species present.

But where exactly does the muon sit in a particular crystalline material? Knowledge of this is essential for complete understanding of the  $\mu$ SR signals observed, yet it is often difficult to determine reliably. As already mentioned, sometimes the muon does not sit still at all. Even to treat the effect of muon diffusion properly, the sites involved must be known. In some elemental metals (i.e., Al, Fe, Nb, ...) rapid diffusion is seen at all temperatures and is reasonably well understood, including quantum effects at very low temperatures (see references given in sect. 2.1), but this does not concern us here. Less is known about the situation in elemental rare-earth metals, but the lower crystal symmetry makes a stationary muon likely, at least at lower temperatures, as is also indicated by a few direct measurements on nonmagnetic hcp metals such as Sc and Be. Muon diffusion parameters in Dy metal have been extracted by Barsov et al. (1986a) using the relaxation rates observed in the helical AFM state. They show that the muon residence time is about 0.1  $\mu$ s at 125 K. It decreases by an additional factor of 3 approaching  $T_N$  around 180 K.

In compound materials, the muon is likely to be at rest at low temperatures on the  $\sim 10 \mu\text{s}$  time scale accessed by most  $\mu\text{SR}$  experiments. In general, phonon-assisted diffusional hopping is likely to occur above an onset temperature typically in the range of 200 K to 300 K. In this temperature regime care must be exercised in interpreting spectra. The effect on magnetic  $\mu\text{SR}$  response will be discussed in sect. 3.8.

In elemental metals and intermetallics, without any strong electronegative ions, the  $\mu^+$  is generally expected to be repelled (ionically) from all the ions present, and so should come to rest in the largest interstitial “holes” in the structure. Vacancy defects also qualify when present, but then  $\mu\text{SR}$  becomes a defect probe, while we are primarily interested in its use as a bulk probe. In elemental metals, which usually have high-symmetry crystal structures, the centers of the interstitial sites are also usually of high point symmetry, and can be identified by inspection of the crystal structure. It is also quite possible that the muon prefers different sites at different temperatures (site exchange), another possible complication which is not always easy to trace. Details (though mainly for transition metals) are discussed by Seeger and Schimmele (1992).

When single-crystal samples are available, the point symmetry of the muon site can be deduced from the dependence of the  $\mu\text{SR}$  signal on the orientation of the initial muon polarization with respect to the principal crystal axes. Typical parameters to be studied in such a case are either the depolarization rate (line width) or the muon Knight shift (see sect. 3.2.1, especially fig. 19). The vast majority of the “new materials” that occupy much of the forefront of pure (as opposed to applied) magnetism research, however, are compounds first available only in polycrystalline (including powder in that term) form. Consequently, the majority of  $\mu\text{SR}$  experiments on magnetic materials are on polycrystalline compound samples, for which the muon site symmetry is not measurable, and is likely to be low. On occasion, data on the position of hydrogen induced in low concentration into metallic samples is available (e.g., from neutron scattering or channeling experiments). One then infers that the muon will take the same interstitial position, a reasonable notion in many cases.

Let us consider whether muon bonding can determine the muon site in polycrystalline compound insulators. There is considerable evidence that  $\mu^+$  bonds to fluorine and oxygen to form diamagnetic centers in solid insulators. In fluorides this often results in the formation of the hydrogen-bonded  $(F\mu F)^-$  ion, generating a characteristic oscillating ZF- $\mu\text{SR}$  signal in nonmagnetic fluorides [including  $\text{YF}_3$  and  $\text{LaF}_3$  (Brewer et al. 1986, Noakes et al. 1993a,b)], that severely limits the possible muon locations in those lattices. Not much  $\mu\text{SR}$  spectroscopy, however, has been performed on magnetic rare-earth fluorides (see sect. 6.1). There are many more oxide materials of interest to the magnetism community, including the high- $T_c$  superconductors. The latter is an anomalous class, ceramic yet conducting, and related to insulating phases by differences in ion partial site occupancies. There is again considerable evidence that “diamagnetic”  $\mu^+$  sits close to  $1.0 \text{ \AA}$  away from an oxygen ion in each of these solids, including rare-earth orthoferrites (Holzschuh et al. 1983, Boekema et al. 1984) and  $\text{YBa}_2\text{Cu}_3\text{O}_{6+\delta}$  (Brewer et al. 1990). Yet even knowing this, there is debate about the  $\mu^+$  site in  $\text{YBa}_2\text{Cu}_3\text{O}_{6+\delta}$  (Boekema et al. 1994, Adams et al. 1994, Sulaiman et al. 1994a,b).



There is less information to work with in the case of a compound intermetallic where large enough single crystals are not available. To establish a draft list of muon site candidates, it is easy to write a computer program to find the local minima in the unit cell of an ionic-repulsion interaction between the  $\mu^+$  and the ions of the crystal structure (Noakes et al. 1987). There is, however, no compelling choice among several possible radial dependences of interaction outside a hard core. Different choices of interaction, and even different choices of effective ionic charge and hard-core radius for a particular interaction, will result in some variation of the detailed candidate site positions. Such a procedure only indicates generally where the holes in the structure are. At low temperatures in all but the simplest structures, different muons may stop at different local minima, because the barriers to hopping may prevent them from all finding the most desirable site.

Finally, we repeat that a unique crystalline muon site may split into multiple magnetic sites once long-range magnetic order sets in or if an external field is applied. Once the (most likely) muon site(s) has(have) been determined, modeling of the local magnetic field at that(those) site(s) can begin. Muon sites in particular materials will be discussed in the sections on those classes of material below. In conclusion we wish to stress once more: Sensitive information on magnetic properties of a material can be obtained by  $\mu$ SR *without knowledge of the muon stopping site*. It is important, however, to make sure that the muon is not hopping between different types of sites.

### 3.7. Modeling of the internal field

For a material that has a magnetic ordering (or spin freezing) transition at  $T_M$ , there are generally four regimes which might generate distinct  $\mu$ SR behavior:

- (1) the static ordered (frozen) state for  $T \ll T_M$ ;
- (2) fluctuations in the ordered state as  $T$  approaches  $T_M$  from below;
- (3) critical fluctuations and correlations in some temperature range above  $T_M$ ;
- (4) the paramagnetic limit for  $T \gg T_M$ .

There is now one class of magnetic materials known where the magnetic interactions are strong but no spin freezing or magnetic ordering occurs: “perfectly frustrated lattices”, but to date the ones studied with  $\mu$ SR involve only transition metal magnetic ions, and so fall outside the range of this review. Additionally, it is possible that “crystalline electric field” (CEF) splitting might sometimes slow lanthanide moment dynamics enough to cause observable temperature dependence in  $\mu$ SR magnetic parameters, independent of any magnetic ordering (or even in the absence of ordering). This will be discussed in sect. 5.1.

Let us consider the four regimes in the absence of those possible complications, beginning with the simplest.

*Regime 4:* The essential features of the paramagnetic limit have already been discussed in sect. 3.2. The electronic moments are fluctuating very rapidly which tends to decouple them from the muon moment (motional narrowing). This means, the depolarization of the  $\mu$ SR signal is weak and almost always of exponential shape. It may well

become unobservably small. In lanthanide compounds with strong exchange coupling one reaches the so-called Moriya limit (Moriya 1956) for  $T \gg T_M$  which causes a measurable and temperature-independent damping rate, especially in compounds with heavy rare earths where the effective magnetic moments are large (Karlsson 1990). Also Korringa relaxation needs to be considered in some cases (Hartmann et al. 1986). More details are to be found in sect. 5.3.

In sect. 3.4 the combined effect of nuclear and electronic relaxation was introduced. If one of the *nonmagnetic* constituents of a compound carries a large nuclear magnetic moment, then its dipolar field will dominate the damping of the  $\mu$ SR signal if electronic fields fluctuate rapidly enough. In its extreme limit the electronic damping can fully be neglected, and only the static Gaussian Kubo–Toyabe relaxation from nuclear moments will be observed. This situation is generally considered to be dull and usually not perused in any detail since no information can be gained about the electronic moments, except that their fluctuation rate is high.

The situation gets a bit more complex if the ion that carries the electronic magnetic moment also possesses a sizable nuclear moment. Then these two moments are not independent of each other regarding their dynamical behavior since they are coupled by the hyperfine interaction. This means the nuclear moment may not appear static on the  $\mu$ SR time scale at all temperatures. If the electronic moment fluctuates rapidly enough, as is the case for  $T \gg T_M$  then the two are decoupled again and the situation is as described in the previous paragraph. When coming closer to  $T_M$ , the electronic moment slows down and will couple to the nuclear moment, causing it to exhibit dynamical behavior as well. This situation has been observed in rare-earth systems by Noakes et al. (1987) and Weber et al. (1994a). It has been studied in detail in MnSi (Yamazaki 1990) which, however, is outside this review. The treatment of such data requires the concept of “double relaxation” as discussed in sect. 3.4. In order to separate the different depolarization mechanisms, it is important to establish that the “full paramagnetic limit”, i.e., the situation of full electron–nuclear decoupling, has been achieved. Further, it must be reached before the muon starts diffusional motion, since this again changes the relaxation shape of the  $\mu$ SR signal (see also sect. 3.8). This is not always possible and clearly requires  $T_M$  to be fairly low.

*Regime I:* In the low-temperature limit of a magnetically ordered/frozen state, a static  $\mu$ SR pattern is usually observed, for which the theoretical prediction involves specification of a (known or postulated) static structure for the magnetic moments, the knowledge (or at least a good guess) of the muon site, the choice of magnetic interaction between the ordered moments and the muon (e.g., dipolar coupling) together with a sum over the lattice, without the complication of fluctuations.

This approximation will only be valid for  $T \rightarrow 0$ , as fluctuations are often visible as the sample is warmed towards  $T_M$ . Little is understood, however, about slow spin dynamics (i.e., within the  $\mu$ SR, but below the neutron time window) in ordered magnets. A theoretical treatment of spin lattice relaxation and its relation to  $\mu$ SR for a Heisenberg ferromagnet has been given by Dalmas de Réotier and Yaouanc (1995).

The simplest calculation involves the assignment of classical point-like ionic moments leading to an effective field and its distribution at the muon site, and it often provides an

excellent approximation. The basics of deriving the local dipolar field has been treated in sect. 3.1. In the majority of cases  $\mathbf{B}_\mu$  is dominated by the dipolar field (except when it vanishes due to local symmetry).  $\mathbf{B}_{\text{con}}$ , being up to an order of magnitude smaller, is often neglected in first approximation. In any case,  $\mathbf{B}_{\text{con}}$  is isotropic and carries little information about the ordered spin structure. It can in principle be obtained independently from paramagnetic Knight shift data. Note, however, that long-range magnetic ordering of large stable (rare-earth) electronic moments is a subject where neutron scattering can measure almost everything, and  $\mu\text{SR}$  often cannot compete. On the other hand, the dipolar field at the muon site resulting from a proper summation of the fields produced by all surrounding moments is extremely sensitive to small changes in orientation of those moments. For example, in the case of a conical spin structure a small change in cone angle may markedly alter the local field sensed by the muon, while neutrons may not resolve this effect. Also, spin turning transitions are well investigated by  $\mu\text{SR}$ . Situations of this type will be discussed especially in sect. 4.

In general,  $\mu\text{SR}$  most often makes notable contributions to magnetism when the magnetism is weak or disordered in some way. When magnetism is weak, mere detection of internal magnetic fields can be significant, as is the case for a number of “correlated electron systems” (sect. 9).

Let us have a brief look at disordered magnetism which will be dealt with in more detail in sect. 8. A simple long-range ordered state generates in most cases a unique field (or a small number of discrete fields) at the muon site, usually resulting in coherent spin precession at a distinct frequency (or frequencies) in ZF- $\mu\text{SR}$  (see discussion in sect. 3.3). A static incommensurate spin-density-wave (sinusoidal amplitude modulation of the ordered moment over a long repeat length), with simplifying assumptions about coupling to the muon, should result in a field distribution of “Overhauser” form (see, for example, Peretto et al. 1981):

$$P_{\text{ISDW}}(B) = \frac{2}{\pi \sqrt{B_{\text{max}}^2 - B^2}}, \quad 0 < B < B_{\text{max}}. \quad (51)$$

This is a distribution of magnitude of field, which is what truly determines the ZF muon spin relaxation function  $G_z(t)$  for polycrystalline samples (Noakes 1991), as has been discussed in sect. 3.2.2. The equation for the ZF relaxation function for a polycrystalline sample,

$$G_z(t) = \frac{1}{3} + \frac{2}{3} \int_0^\infty P(B) \cos(\gamma_\mu B t) dB, \quad (52)$$

can be solved in this case:

$$G_{\text{ISDW}}(t) = \frac{1}{3} + \frac{2}{3} J_0(\gamma_\mu B_{\text{max}} t). \quad (53)$$

where  $J_0$  is the zero-order Bessel function. After some initial relaxation,  $G_{\text{ISDW}}(t)$  settles down to small-amplitude oscillation at frequency  $\gamma_\mu B_{\text{max}}$  (although with a phase shift of

90°). Realistic muon coupling adds some complications. For example, eq. (53) describes the spectral shape resulting from a perfect (i.e., error and distortion free) long-range ordered ISDW spin structure. Defects in the spin lattice etc. will add an additional static distribution in local field. Furthermore, there could be spin dynamics present which also depolarizes the muon spin. Therefore one uses in practice the relaxation function for a case of ISDW spin order:

$$G_{\text{ISDW}}(t) = \frac{1}{3} \exp[-\lambda_{\text{long}} t] + \frac{2}{3} J_0(\gamma_{\mu} B_{\text{max}} t) \exp[-\lambda_{\text{trans}}]. \quad (54)$$

Spectra of this kind have basically been observed in some organic conductors (Le et al. 1993) and recently, apparently in HoNi<sub>2</sub>B<sub>2</sub>C (sect. 7.1). Misfitting a spectrum of the type given by eq. (54) with an exponentially damped cosine oscillation ( $\exp[-\lambda t] \cos(f_{\mu} t + \Phi)$ ) results in a phase angle  $\Phi \approx 90^\circ$  and a poor representation of the initial decay. These features are strong indicators that an incommensurate spin structure is present, which then is better represented by the Bessel function. A pertinent example is CeAl<sub>3</sub> which will be discussed in sect. 9.3.

The other well-known class of incommensurate magnetic structures contains the helices and spirals where the ordered moment does not vary in magnitude much, but is displaced by a finite angle in orientation as one moves from moment to moment in the incommensurate direction, executing a full rotation cycle to define the incommensurate repeat length. This class has a larger phase space of possible structures, and the muon spin relaxation functions to be expected are more resistant to sweeping generalization. Individual cases in the rare-earth elements will be discussed in sect. 4 and for hard magnetic materials in sect. 6.4. Some simple computer simulations associated with the reported spiral ordering of CePtSn will be presented in sect. 9.

Static short-range magnetic ordering can occur, particularly in structurally disordered materials. In this case it is important to remember that the  $\mu^+$  is a local magnetic probe, sensing only the magnetic field at its site. This local field is likely to be dominated by the magnetic moments in the immediate vicinity, so, if the moments in the nearest couple of coordination shells are well aligned into a simple magnetic structure, and if the correlation range extends to where neutron scattering can fairly easily detect a (broad) magnetic correlation peak,  $\mu$ SR is likely to show in effect the same signal as for a fully long-range-ordered structure. If the long-range-ordered signal is a coherent oscillation, then the first indication of disorder is a static (zero slope at zero time) relaxation envelope on that oscillation). As disorder increases, the relaxation rate increases, until eventually the relaxation rate exceeds the oscillation frequency, and the signal becomes overdamped.

Spin glasses are another class of static ground state, offering, in the ideal case, a snapshot of a paramagnetic configuration, with no spin-spin correlations. In the dilute-moment spin glasses, particularly Cu(Mn),  $\mu$ SR provided useful information by detecting the distinctive Lorentzian local field distribution to be expected in such cases (Uemura et al. 1985, Pinkvos et al. 1990). This discussion will be extended in sect. 8. Unfortunately, stable-moment rare-earth spin glasses are not as well studied as transition metal spin glasses in general, and they have not been studied at all with  $\mu$ SR (and are unlikely to be

so studied in the near future, as spin glasses *per se* are no longer a popular research topic). Some spin-glass-like behavior is seen in some correlated electron systems (sect. 9).

*Regime 3:* This is the regime of critical phenomena in the paramagnetic state above the ordering temperature (we include the range above  $T_g$  in spin glasses in this, because the spins do slow down as  $T \rightarrow T_g^+$ , meaning temperature approaches  $T_g$  from above, even though there may still be some dissent about whether the freezing is a true thermodynamic transition). There is an enormous body of theory regarding power-law temperature dependences, and (because the identified “criticality classes” often group magnetic transitions with structural transitions as equivalent) many other possible probes (e.g., structural and optical methods) may be brought to bear. Meanwhile,  $\mu$ SR normally sees monotonic relaxation (this is usually a fast-fluctuation regime) yielding a generic relaxation rate that may not be simply related to a single power law with a single critical exponent. Some theoretical discussions can be found in Lovesey et al. (1990) and Dalmas de Réotier et al. (1994a). Bulk and optical measurements often work in the range of  $(T - T_M)/T_M \ll 0.1$  and to do so develop impressive temperature stability ( $\Delta T/(T - T_M) \ll 1$ ), because only very close to the transition should the simple power laws be true.  $\mu$ SR, when moving towards  $T_M$ , often sees an increase of relaxation rate far above the transition temperature (up to  $5 T_M$ ). In the already mentioned Moriya limit, the motion of each spin is separately treated as resulting from the immersion into a bath comprising all other paramagnetic spins with all spins considered equivalent. The observed rise in relaxation rate indicates that (short lived) paramagnetic correlations develop already at high temperatures well above the region usually considered the critical regime. Usually  $\mu$ SR data of this type allow a power law to be fitted to the temperature dependence of the damping constant  $\lambda(T)$  over this wide temperature range. The sensing of paramagnetic correlations far above the magnetic phase transition is a unique feature of  $\mu$ SR. The strong ionic anisotropy of CEF and magnetic interactions in most rare-earth and actinide ions leads in turn to a strong anisotropy of the paramagnetic fluctuations, the preferred axis being usually the easy axis of the magnetically ordered regime. Again, this anisotropy of spin fluctuations can be traced over a wide temperature range. Typical examples are Er (to be discussed in sect. 4.3) and  $RNi_5$  intermetallics (see sect. 5.4.3).  $\mu$ SR experimenters generally do not have apparatus capable of the temperature stability to get really close to the transition. The present limit is  $10^{-3}$  to  $10^{-4}$  in reduced temperature. To improve on that value would add substantial expense to what is already an expensive field of condensed matter research. Also the relatively large sample size renders this task difficult. Serious work toward rigorously relating  $\mu$ SR measurements to critical theory within the rare earths have focused on Gd (sect. 4.2),  $GdNi_5$  (sect. 5) and, to a lesser extent, EuO (sect. 6.1). No such work on actinides has yet appeared.

*Regime 2:* Dominant in this range are fluctuations in the ordered state as  $T \rightarrow T_M^-$  (i.e., as  $T_M$  is approached from below), which in many cases are so complicated that they defy detailed understanding by any probe. Neutron scattering finesses the problem for long-range ordered single-domain single crystals by being able to isolate and measure the elementary excitations above the ground state (magnon dispersion curves and polarizations) at low temperatures, but when only polycrystalline samples

are available, usually only qualitative conclusions can be drawn. The low-temperature limit should always be analyzed first. If a distinctive static μSR signal was observed at low temperatures, leading to some detailed understanding of the ground state, then extra relaxation as temperature is raised may well be explainable in terms of a model of fluctuations above that ground. As the relaxation becomes monotonic, however, the information extractable becomes ambiguous. Comparison with large LF-μSR may tell you what part (if any) of the relaxation is still static, but even then, many models may be consistent with the relaxation observed.

There are a number of interesting individual exceptions to the “rules” outlined in this section. They will be discussed as their classes of material appear in the sections below.

### 3.8. Muon diffusion and magnetism (site averaging)

We now lift the restriction of a *stationary* muon resting over its life time at one specific interstitial site. The simplest case is a muon hopping only between geometrically and magnetically identical sites and never leaving the domain where it was stopped (a fairly safe assumption considering typical domain volumes). In this situation muon motion will have no effect on the μSR spectrum as long as the strong-collision model holds (i.e., the change of site is sudden).

More serious is the situation when the muon travels through sites having different local fields  $\mathbf{B}_\mu$ . In the *fast diffusion limit* (meaning that the time of residence is short compared to the Larmor precession period of  $\mathbf{S}_\mu$  in  $\mathbf{B}_\mu$  of the site) the observed μSR spin precession will reflect  $\langle \mathbf{B}_\mu \rangle$ , the weighted mean of the different local fields. In the *slow hopping limit* the signal will be the overlay of the pattern produced by the different sites with some additional damping. Most complicated and not generally treatable is the *intermediate regime*. The patterns from different sites will be strongly damped and the simple approach of an overlay of the various patterns is in general not a good approximation. The additional strong static damping of the precession signal in ordered magnets (see sect. 3.3) may make this case unobservable.

An additional problem a moveable muon might create is that its diffusional path may lead to a lattice defect (most important are impurities and vacancies). Once reached, the muon is likely to be trapped and the μSR signal no longer relates to the bulk properties of the magnet. In rare-earth and actinide materials this is less of a problem than in transition element magnets where  $T_M$  tends to be high.

To this point in this section we have assumed that  $\mathbf{B}_\mu$  at each site is quasistatic (i.e., there are no spin dynamical processes within the μSR time window). This need not be the case and  $\mathbf{B}_\mu$  may fluctuate with the characteristic time  $\tau_m$  sensed by the muon. Assuming  $\tau_m$  to be in the range leading to exponential relaxation  $e^{-\lambda t}$  with the damping constant  $\lambda = \gamma_\mu^2 \langle B_\mu^2 \rangle \tau_c$  we must use

$$\frac{1}{\tau_c} = \frac{1}{\tau_m} + \frac{1}{\tau_d}, \tag{55}$$

where  $\tau_d$  is the diffusional jump time. In most cases  $\tau_d > \tau_m$  and  $1/\tau_c$  will reflect magnetic spin fluctuations in good approximation. But if  $\tau_d$  reaches the nanosecond regime then it might become comparable to  $\tau_m$ , especially in the vicinity of a magnetic phase transition. In general, this problem is far from being resolved.

The most important situation is the rather straightforward fast diffusional limit sampling different quasistatic hyperfine fields discussed above. The best known case is bcc iron metal below  $T_C$  (e.g., Yagi et al. 1984), which, though being outside the scope of this review will briefly be discussed as a pertinent example. The muon occupies the high-symmetry tetrahedral interstitial site, but due to the presence of magnetization oriented along the easy axis, the local symmetry is lowered and  $\mathbf{B}_{\text{dip}}$  will not vanish. In the FM regime one must distinguish sites where the tetragonal axis runs parallel and those where it runs perpendicular to the easy axis [001]. For those two environments  $\mathbf{B}'_{\text{dip}}$  differs by a factor of two and is of opposite sign. The sites with the lower field are twice as numerous. The muon hops quickly between those sites and the averaging leads to  $\mathbf{B}_{\text{dip}} = 0$ . The single frequency precession signal observed arises solely from the hyperfine field which, being isotropic, is insensitive to the differences in local symmetry mentioned and is therefore of unique value.

Cases exist where a single crystallographic site splits into numerous magnetic sites with fairly closely spaced local fields. An ensemble of stationary muons sees in effect a very wide distribution of fields leading to such strong static depolarization that the precession signal becomes unobservable. A fast moving muon helps in this situation because the averaging process leads in effect to a motionally narrowed single mean field and a spin precession signal is seen. Lanthanide compounds exhibiting this situation will be discussed in sect. 5.3.2.

Alexandrowicz et al. (1999) have established a case where diffusion over magnetically distinct sites could be studied in detail: singlet ground-state  $\text{PrIn}_3$  (see sect. 5.1.2) in an external field. Having identified a crystallographically unique muon site that becomes two magnetic sites with distinct frequencies if the field is applied along a symmetry axis of a single crystal, they studied deviations from simple ‘‘Markovian’’ hopping, and developed a kinematic algorithm to directly simulate the hopping process in the material.

#### 4. Elemental metals

The varied magnetic properties of the elemental lanthanide metals have attracted researchers over decades. The continuously improving purity of the materials has led to a number of revisions to ‘‘the state of our understanding’’ with time. A summary of the main crystallographic and magnetic parameters is presented in table 2. Details on bulk measurements can be found, for example, in Rhyne (1972) and McEwen (1978), neutron data in Koehler (1972) and Sinha (1978). A modern treatise on magnetic properties is given by Jensen and Mackintosh (1991). All metals contain the  $3^+$  ion except Eu and Yb which are  $2^+$ .

Table 2  
Structural and magnetic properties of lanthanide metals (after Jensen and Mackintosh 1991)

Elem.	Struc.	$a$ (Å)	$c$ (Å)	$\mu_{\text{para}}^{\text{theo}}$ ( $\mu_B$ )	$\mu_{\text{para}}^{\text{exp}}$ ( $\mu_B$ )	$g \cdot J$ ( $\mu_B$ )	$\mu_{\text{sat}}^{\text{exp}}$ ( $\mu_B$ )	$\Theta_{\text{para}}^{\parallel}$ (K)	$\Theta_{\text{para}}^{\perp}$ (K)	$T_N$ (K)	$T_C$ (K)
Ce ( $\beta$ ) <sup>a</sup>	dhcp	3.681	11.857	2.54	2.51	2.14	0.6			13.7	
Pr	dhcp	3.672	11.833	3.58	2.56	3.20	2.7				
Nd	dhcp	3.658	11.797	3.62	3.40	3.27	2.2			19.9	
Pm	dhcp	3.650	11.650	2.68		2.40					
Sm	rhom	3.629	26.207	0.85	1.74	0.71	0.13			106	
Eu	bcc	4.583	—	7.94	8.48	7.0	5.1			90.4	
Gd	hcp	3.634	5.781	7.94	7.98	7.0	7.63	317	317		293
Tb	hcp	3.606	5.697	9.72	9.77	9.0	9.34	195	239	230	220
Dy	hcp	3.592	5.650	10.65	10.83	10.0	10.33	121	169	179	89
Ho	hcp	3.578	5.618	10.61	11.20	10.0	10.34	73	88	132	20
Er	hcp	3.559	5.585	9.58	9.90	9.1	9.1	62	33	85	20
Tm	hcp	3.538	5.554	7.56	7.61	7.14	7.14	41	-17	58	32
Yb	fcc	5.485	—								

<sup>a</sup> The stable form of pure cerium below 96 K is nonmagnetic fcc.

Early μSR measurements were performed on a series of the metals (Pr, Nd, Sm, Eu, Tb, Dy, Ho, Er) by Grebinnik et al. (1979). Only TF spectra were recorded and in consequence, the data are limited to the paramagnetic regime. This work antedates the common use of longitudinal (ZF, LF) μSR spectroscopy, but the authors mention the possible utility of such experiments in magnetically ordered states. Although outdated, this work was instrumental in establishing μSR as a powerful tool in R magnetism. It showed the strong rise of muon spin relaxation rate on approach to the magnetic transition temperature and gave the correct basic interpretation that slowing down of spin fluctuations due to dynamic spin correlations must be responsible. It also pointed out the possibility of pinpointing the transition temperature *via* the loss of TF signal amplitude. Finally, it shows that the high-temperature limit of relaxation is correlated (though not simply) with the paramagnetic moment. Today it is known that other factors, especially the magnetic anisotropy and possible CEF effects (to be discussed in sect. 5.1.1) must be considered as well.

In the following we concentrate on more recent, predominantly longitudinal (and there mainly ZF) μSR measurements over wide temperature ranges (i.e., the paramagnetic and the magnetically ordered regimes) on the heavy lanthanide metals Gd, Dy, Ho and Er. For these metals, high-pressure studies were also carried out. The case of Pr is special since its electronic ground state is an isolated singlet due to CEF interactions. This causes special magnetic behavior and conventional magnetic order does not take place. We have elected to discuss this metal in sect. 5.1.2. No μSR data on elemental actinide metals are available.



One of the fundamental features of the 4f electron shell is its large orbital momentum (except for the half-filled 4f<sup>7</sup> configuration in Gd<sup>3+</sup> or Eu<sup>2+</sup> and, of course, the filled configuration 4f<sup>14</sup> in Yb<sup>2+</sup> and Lu<sup>3+</sup>). This leads not only to the substantial magnetic dipole moments of the R ions, but is also the source of large single-ion anisotropy which in turn is reflected in many magnetic parameters. In  $\mu$ SR, one of the properties affected is spin fluctuations or, more precisely, the temporal correlation functions of the local field at the muon site. These can be determined by  $\mu$ SR spectroscopy in single crystals or in strongly textured polycrystals. Since results of that type will be presented for most of the rare-earth metals to be discussed in the following, we shall begin with a brief treatment of anisotropic muon spin relaxation rates.

#### 4.1. Anisotropic spin fluctuations

Of particular interest is the situation in the paramagnetic regime, where no axis of magnetization exists on a macroscopic scale and the crystalline axes (in non-cubic systems) provide preferred orientations. The basic observables of muon relaxation above  $T_C$  or  $T_N$  in anisotropic systems like the hexagonal lanthanide metals have been discussed by Karlsson (1990, 1995)). A recent discussion of correlation functions and longitudinal relaxation rates can also be found in Dalmas de Réotier and Yaouanc (1997). As outlined earlier (and to be discussed below), the muon spin relaxation rate in the fast fluctuating limit is given by  $\lambda = \gamma_\mu^2 \langle B_\mu^2 \rangle \cdot \tau_c$  where  $\tau_c$  is the characteristic time for the fluctuations of the local field  $B_\mu$ . The temperature dependence of  $\lambda$  (or  $\tau_c$ ) can then be used, for example, to make comparisons with predictions from dynamic scaling theories, as will be discussed for the case of Gd. Single-crystal measurements that combine fixed orientations (with respect to crystalline axes) of the muon spin (at  $t = 0$ ) with definite orientations of the local fields pick up different parts of the local field correlations  $\langle B_\mu^\perp(t), B_\mu^\perp(0) \rangle$  and  $\langle B_\mu^\parallel(t), B_\mu^\parallel(0) \rangle$  at the muon site. In the present case we take the hexagonal  $c$ -axis as the main symmetry axis (parallel direction).

The muon spin relaxation rates  $\lambda_\parallel$  and  $\lambda_\perp$ , observed in ZF measurements with muons implanted with initial spin polarization parallel and perpendicular to the  $c$ -axis, are given by

$$\lambda_\parallel = \gamma_\mu^2 \int_0^\infty dt [\langle B_\mu^x(t), B_\mu^x(0) \rangle + \langle B_\mu^y(t), B_\mu^y(0) \rangle], \quad (56)$$

$$\lambda_\perp = \gamma_\mu^2 \int_0^\infty dt [\langle B_\mu^z(t), B_\mu^z(0) \rangle + \langle B_\mu^x(t), B_\mu^x(0) \rangle], \quad (57)$$

where  $z$  is the direction of the symmetry axis and  $x$  and  $y$  are the directions perpendicular to it. These are identical in case of uniaxial symmetry, which has been assumed in all the  $\mu$ SR work. There is some anisotropy within the basal planes of the hexagonal rare-earth metals (it is involved in the spin-slip structures mentioned below), but it is much smaller than the anisotropy between the  $c$ -axis and the basal plane, and unlikely to be

detectable in the relaxation rates of the equations above. By combining measurements of relaxation rates for muon spin alignments parallel and perpendicular to the  $c$ -axis a separation of fluctuations of the local field components is possible. But as eqs. (56) and (57) demonstrate, the rate  $\lambda_{\parallel}$  only contains the *perpendicular* field correlations, while  $\lambda_{\perp}$  contains both the *perpendicular and parallel* field correlation functions. Hence the evaluation of the directional dependence of field fluctuations or fluctuation times is not necessarily trivial.

The situation is more complex in transverse field experiments, where the orientation of the applied field with respect to the symmetry axis is an additional parameter. Two cases need to be considered for uniaxial symmetry:

- (a)  $\mathbf{S}_{\mu}$  points parallel to  $c$  and  $\mathbf{B}_{\text{app}}$  perpendicular to  $c$ . The correlation functions appearing in equations of the type (56) or (57) are (Karlsson 1995)

$$\begin{aligned} & \frac{1}{2} \left[ \langle B_{\mu}^{\perp}(t), B_{\mu}^{\perp}(0) \rangle + \langle B_{\mu}^{\parallel}(t), B_{\mu}^{\parallel}(0) \rangle \right] + \langle B_{\mu}^{\perp}(t), B_{\mu}^{\perp}(0) \rangle \\ & = \frac{3}{2} \langle B_{\mu}^{\perp}(t), B_{\mu}^{\perp}(0) \rangle + \frac{1}{2} \langle B_{\mu}^{\parallel}(t), B_{\mu}^{\parallel}(0) \rangle ; \end{aligned}$$

- (b)  $\mathbf{S}_{\mu}$  points perpendicular to  $c$  and  $\mathbf{B}_{\text{app}}$  parallel to  $c$ . Then one considers the correlation functions

$$\begin{aligned} & \frac{1}{2} \left[ \langle B_{\mu}^{\perp}(t), B_{\mu}^{\perp}(0) \rangle + \langle B_{\mu}^{\perp}(t), B_{\mu}^{\perp}(0) \rangle \right] + \langle B_{\mu}^{\parallel}(t), B_{\mu}^{\parallel}(0) \rangle \\ & = \langle B_{\mu}^{\perp}(t), B_{\mu}^{\perp}(0) \rangle + \langle B_{\mu}^{\parallel}(t), B_{\mu}^{\parallel}(0) \rangle . \end{aligned}$$

For uniaxial symmetry, this reduces to two distinct TF relaxation rates to be measured, as in ZF.

It is important to stress once more that μSR measures the *fluctuations of the local fields* at the muon site and *not directly the fluctuations of the spins* creating those fields. This means in essence that for a quantitative analysis (for TF as well as for ZF measurements) the exact relations between the individual components of lanthanide spin correlations  $\langle S^i(t)S^j(0) \rangle$  and the muon field correlations  $\langle B_{\mu}^i(t)B_{\mu}^j(0) \rangle$  must be worked out for each particular muon spin ↔ lanthanide crystal geometry. This step is often overlooked. The general *tensorial* relation between spin and field correlation has been given by Dalmas de Réotier et al. (1996).

Barsov et al. (1986c) directly use the short-time approximation to evaluate the field correlations. This leads to an exponential time dependence of the different components of the field correlations

$$\langle B_{\mu}^i(t'), B_{\mu}^i(t) \rangle = \langle (B_{\mu}^i)^2 \rangle \exp(-|t - t'| / \tau_c^i), \quad (58)$$

with orientationally dependent characteristic fluctuation times  $\tau_c^i$ . Here the  $\tau_c^i$  are the lifetimes of the magnetic field components  $B_{\mu}^i$ , which originate from the spin fluctuations determined by the correlation functions  $\langle S^i(t)S^j(0) \rangle$ . This means that the  $\tau_c^i$  do not directly

reflect the spin fluctuation times in different directions, since each may contain more than one directional component. Using the approximation given in eq. (58) the following expressions for the relaxation rates in uniaxial symmetry

$$\lambda_{\parallel} = 2G_{\perp} \quad \text{with } G_{\perp} = \gamma_{\mu}^2 \langle (B_{\mu}^{\perp})^2 \rangle \cdot \tau_c^{\perp},$$

$$\lambda_{\perp} = G_{\parallel} + G_{\perp} \quad \text{with } G_{\parallel} = \gamma_{\mu}^2 \langle (B_{\mu}^{\parallel})^2 \rangle \cdot \tau_c^{\parallel},$$

are obtained for the two orthogonal muon implantation geometries. Modifications of these formulae for intermediate situations, i.e., textured polycrystals, are straightforward:

$$\lambda_{\parallel} = 2G_{\perp}Y + (G_{\parallel} + G_{\perp})(1 - Y),$$

$$\lambda_{\perp} = G_{\perp}(1 - Y) + \frac{1}{2}(G_{\parallel} + G_{\perp})(1 + Y),$$

where  $Y = \langle \cos^2 \theta \rangle$  and  $\theta$  is the angle between  $S_{\mu}$  and the symmetry axis ( $c$ -axis) in a particular crystallite. In this approximation it is also easy to write down the corresponding expressions for the TF conditions.

One basic problem (which has already been pointed out in sect. 3.2.2) of the fast fluctuation limit is that a separation of  $\langle |B_{\mu}|^2 \rangle$  and  $\tau_c$  is not possible. Furthermore, since the expression (58) for the different directional components  $i$  contain different correlation times  $\tau_c^i$ , it is incorrect to express the *total* relaxation simply as  $\langle |B_{\mu}|^2 \rangle \cdot \tau_c$  in a strongly anisotropic case. Therefore, from a measurement of  $\lambda_{\parallel}$  and  $\lambda_{\perp}$  it is not trivial (among other considerations, one must know the muon interstitial site) to determine how much of the anisotropy comes from an anisotropic field distribution and how much relates to anisotropic fluctuation rates. One may hope that not too close to the magnetic transition (i.e., well inside the paramagnetic regime)  $\langle |B_{\mu}|^2 \rangle$  shows little anisotropy and that one senses the anisotropy of  $\tau_c$  in ZF. But an exact treatment of a  $\mu$ SR measurement on these terms has not been given to our knowledge.

#### 4.2. Gadolinium

Gadolinium is probably the most extensively studied elemental lanthanide metal not only in the context of bulk magnetic measurements, but equally for  $\mu$ SR spectroscopy. This is not true, however, for neutron scattering, because of the excessively high absorption cross section of natural Gd. In part, this has been overcome by selecting a neutron wavelength where absorption is much less (Cable and Wollan 1968). Also, a single crystal of the weakly absorbing isotope  $^{160}\text{Gd}$  has been produced. A review of the band structure can be found in Norman and Koelling (1993).

From a magnetic point of view, Gd is the simplest of the lanthanide metals. Exchange favors FM, while all other heavy lanthanide metals initially show AFM order. The Curie temperature ( $T_C = 293 \text{ K}$ ) is in a convenient temperature range. The  $\text{Gd}^{3+}$  ion has a half-filled 4f shell. It is thus an S state ion featuring pure (but very strong) spin magnetism.

CEF interactions vanish because of the S character (see sect. 5.1.1). The small residual anisotropy causes the moments to point along the  $c$ -axis just below  $T_C$ . About 100 K below  $T_C$ , the easy axis begins to move toward the basal plane, reaching quickly a maximum tilt angle of  $\Theta \approx 60^\circ$  at 180 K. On further lowering the temperature to  $\sim 50$  K,  $\Theta$  is reduced slowly to  $30^\circ$ , where it then stays to the lowest temperatures. It is thought that this spin turning arises from the action of a competing anisotropy having its origin in spin-orbit coupling.

The earlier  $\mu$ SR studies were concerned with the peculiar temperature dependence of the spontaneous precession frequency caused by the interplay of the isotropic contact field and the anisotropic dipolar field at the muon site. The latter is clearly dependent on the spatial alignment of the Gd spins. Also, the muon stopping site needed to be determined. These data will be discussed in sect. 4.2.2 below. Later studies included more detailed investigations of the dynamical critical behavior in the paramagnetic state (see following section).

#### 4.2.1. Paramagnetic region and critical behavior

Relaxation measurements in the paramagnetic state of Gd have been numerous. A typical example of a TF- $\mu$ SR spectrum of Gd metal above  $T_C$  has been presented in fig. 9. Such type of measurements by Wäckelgård et al. (1986, 1989) show the existence of spin correlations well above  $2T_C$ . The relaxation data can be represented by a power law of the type  $\lambda \propto (T - T_C)^{-w}$ . As can be seen from fig. 29, a crossover from  $w = 0.56$  (high-temperature value) to  $w = 0.15$  takes place at  $T - T_C \approx 10$  K. At about the same temperature the Knight shift (measured on a spherical polycrystalline sample where Lorentz and demagnetization fields cancel) changes from Curie-Weiss behavior (exponent 1) to a temperature dependence with exponent 1.25. The reason for this change of slope has to be ascribed to the onset of dipolar interactions between the Gd spins (see also discussion in the next paragraph). As described by Karlsson (1990), one consequence is a break-up of the longitudinal spin waves resulting in a reduced temperature dependence of spin fluctuation rates. Karlsson et al. (1990) discuss the influence of dynamic paramagnetic clusters on neutron and  $\mu$ SR parameters. Wäckelgård et al. (1986) also attempted an estimate of correlation lengths from their relaxation data and found  $\xi(1.2T_C) = 5 \text{ \AA}$  and  $\xi(1.5T_C) = 3 \text{ \AA}$ . The exponent  $w$  can be related (Hohenemser et al. 1982, 1989) to the correlation length exponent  $\nu$  and the dynamic scaling exponent  $z$  via  $w = \nu \cdot (z - 1.06)$ . The value of  $w$  is consistent with the mean field values  $\nu = 0.5$  and  $z = 2$ .

The paramagnetic critical region was studied later in more detail with zero field  $\mu$ SR on single crystals (Hartmann et al. 1990a). Anisotropy of the relaxation rate for muons with their spins either parallel or perpendicular to the  $c$ -axis was found (see fig. 30, left). Such orientation-dependent muon relaxation will be discussed in more detail in connection with Er and Ho. The directional differences are comparatively small in Gd because the strong single-ion anisotropy is absent. Further extensive measurements by Henneberger et al. (1997) have been compared to elaborate theoretical calculations (Dalmas de Réotier and

## Gadolinium metal

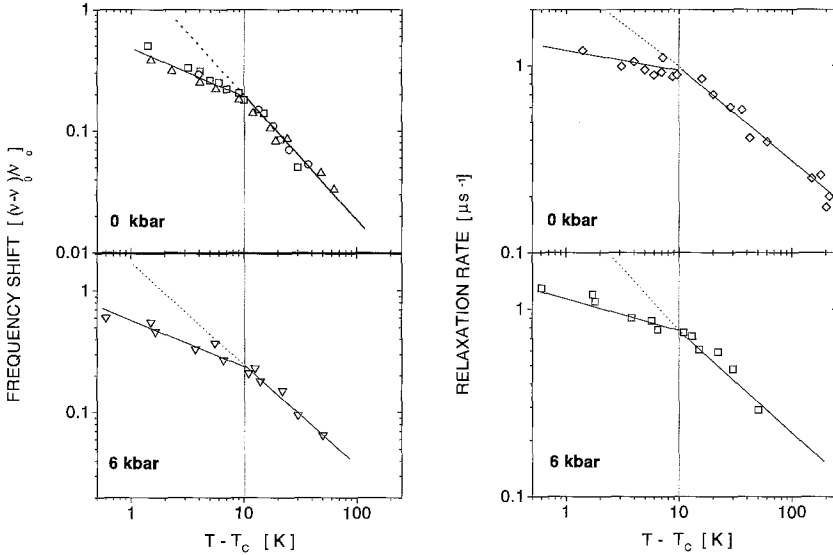


Fig. 29. Temperature dependence of the frequency shift (left) and TF relaxation rate (right) of Gd metal at ambient (top) and 6 kbar applied pressure (bottom). The measurements under ambient conditions used a polycrystalline specimen (Wäckelgård et al. 1986), the high-pressure data a single crystal (Schreier et al. 1997). The lines are power law fits as discussed in the text. The various symbols in the top-left panel refer to different values of the transverse field.

Yaouanc 1994, Dalmas de Réotier et al. 1994a, Frey et al. 1997). Henneberger et al. (1997) shows that close to  $T_C$ , not only the influence of dipolar interactions, but also the uniaxial anisotropies are of importance to reproduce precisely the critical behavior of the  $\mu$ SR relaxation rates.

A theoretical summary analysis in terms of Gd spin dynamics above  $T_C$  combining the single-crystal  $\mu$ SR results with paramagnetic fluctuation data on Gd from perturbed angular correlation and Mössbauer spectroscopies has been given by Frey et al. (1997). In applying mode-coupling theory to hexagonal lattices, and ascribing the uniaxial anisotropy to dipolar couplings only, they can indeed reproduce the major features of the observations from the three different methods. Figure 30 (right) depicts the case of perpendicular  $\mu$ SR relaxation rates from their work. The first change in the slope of muon spin relaxation rate *vs.* temperature occurs at the temperature marked  $T_D$ . This effect is also visible in the data of Wäckelgård et al. (1986) shown in fig. 29. A second change, but less pronounced, takes place at  $T_A$ . It is found that Gd behaves for  $T > T_D$  like an isotropic Heisenberg FM. Dipolar anisotropy comes into play at  $T < T_D$ . Finally, for  $T < T_A$  one must consider uniaxial anisotropy as well. The major result of the treatment by Frey et al. (1997) is that the spin dynamics of a ferromagnet with an hcp lattice (such as Gd) belongs to a new dynamic universality class (see Henneberger et al. 1999 for details). The fit of the muon data to the expected theoretical variation of  $\lambda(T)$  presented in fig. 30 raises the

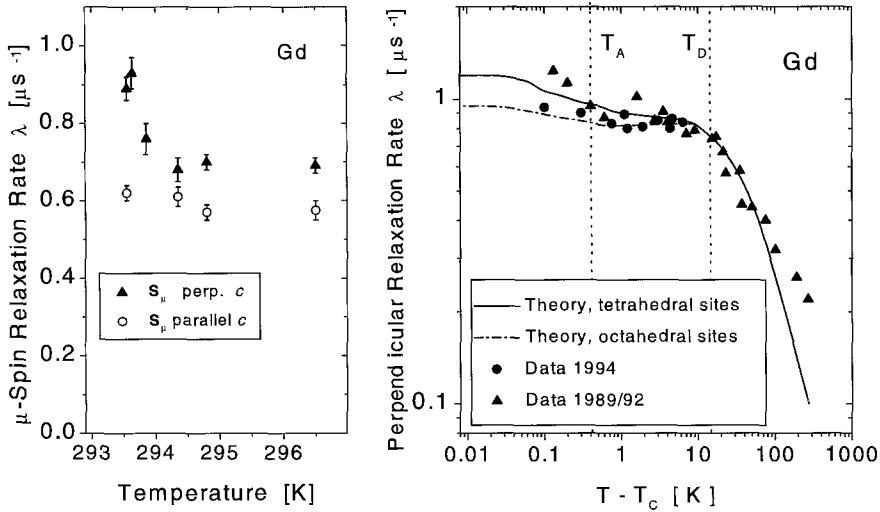


Fig. 30. Critical spin fluctuations in Gd from ZF-μSR measurements. Left: Anisotropy of the relaxation rate  $\lambda$  just above the Curie point. After Hartmann et al. (1990a). Right: Comparison of the temperature dependence of the relaxation rate measured in perpendicular geometry with the prediction of mode-coupling theory for two muon stopping sites. The rates of 1989 were re-analyzed, changing slightly their absolute values (compared to those plotted in the left-hand panel).  $T_D$  and  $T_A$  mark the points where dipolar and uniaxial anisotropies start to play a significant role. After Henneberger et al. (1997).

question whether the assignment of an octahedral muon site, which had been established in the ferromagnetic regime first by Graf et al. (1977) (see also Denison et al. 1979), should be changed to a tetrahedral site for temperatures above  $T_C$ .

#### 4.2.2. Ferromagnetic region

Studies of the spontaneous muon spin precession frequency in ferromagnetic gadolinium attracted much attention due to its peculiar behavior as function of temperature. First data by Gurevich et al. (1975) were followed by measurements of Graf et al. (1977), Nishida et al. (1978) and Hartmann et al. (1990a). The results of the various groups are quite alike. Minor differences are probably sample dependent. A characteristic ZF-μSR spectrum has been presented in fig. 26. The observed temperature dependence of the precession frequency (see the curve labeled  $p = 0$  GPa in fig. 31) shows initially the Brillouin-type rise usually seen after a second-order transition into the magnetically ordered state. Further down in temperature, marked deviations from this monotonic rise occur, which can be explained fully by the change of the dipolar field contribution to  $B_\mu$  as the Gd spins change their tilt angle with respect to the  $c$  direction. This effect is particularly noticeable in the temperature dependence of the local field in Gd because  $B_{dip}$  and  $B_{con}$  are of comparable magnitude. Using a formalism (Meier et al. 1978, Meier 1984) based on the condition of a smooth temperature dependence of the sum vector

$$\mathbf{X} = \mathbf{B}_{con} + \mathbf{B}_{lor} = \mathbf{B}_\mu - \mathbf{B}'_{dip}, \tag{59}$$

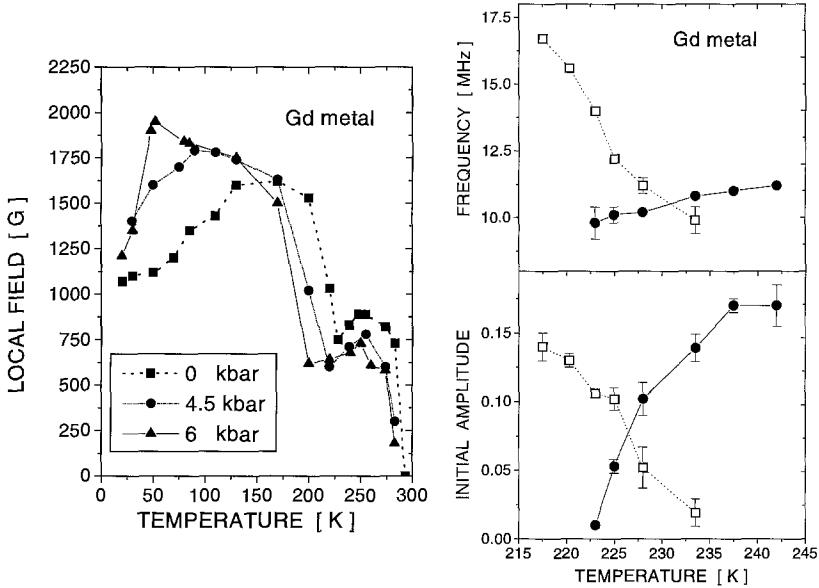


Fig. 31. Left: Temperature dependence of local magnetic field at the muon site in ferromagnetic Gd at ambient and applied pressure (Schreier et al. 1997). Right: Results of the detailed analysis of spectra in the spin turning regime. Two signals are present (open and solid symbols). Their meanings are described in the text (Hartmann et al. 1994b). The lines are guides to the eye.

allows safe separation of the contact and the dipolar contributions to the local field at the muon site, even for a polycrystalline sample (Graf et al. 1977, Denison et al. 1979). The result not only identified the muon stopping site as the octahedral interstitial position, but also allowed the extraction of the temperature dependences of the contact field contribution and the spin tilting angle  $\theta$ . The latter is found to be in excellent agreement with other determinations (Cable and Wollan 1968, Corner and Tanner 1976, Graham 1962) as demonstrated in fig. 32 (top).  $\mu$ SR gives a steeper initial rise of the tilting angle. The results shown in this figure are based on a recent evaluation of single-crystalline data (Hartmann et al. 1994b). The differences with earlier results are minor. The temperature dependence of the contact field deviates slightly from that of the bulk magnetization (Denison et al. 1979). More pronounced such deviations are seen in the 3d FM Fe and Ni. They are discussed in terms of disturbances of the local band structure by the muon (see, for example, Kanamori et al. 1981). The sign and magnitude of the contact field of  $-0.70$  T for  $T \rightarrow 0$  are in good agreement with the Knight shift measurements of Wäckelgård et al. (1986, 1989) mentioned earlier.

The single-crystal measurements by Hartmann et al. (1994b) add more details about the spin turning process. The study showed that the turning of spins does not occur uniformly and simultaneously over the whole sample. The spectra between 230 K and 220 K are best described by the sum of two subspectra. One exhibits an increase of frequency (which indicates spin turning) with decreasing temperature while the other roughly shows

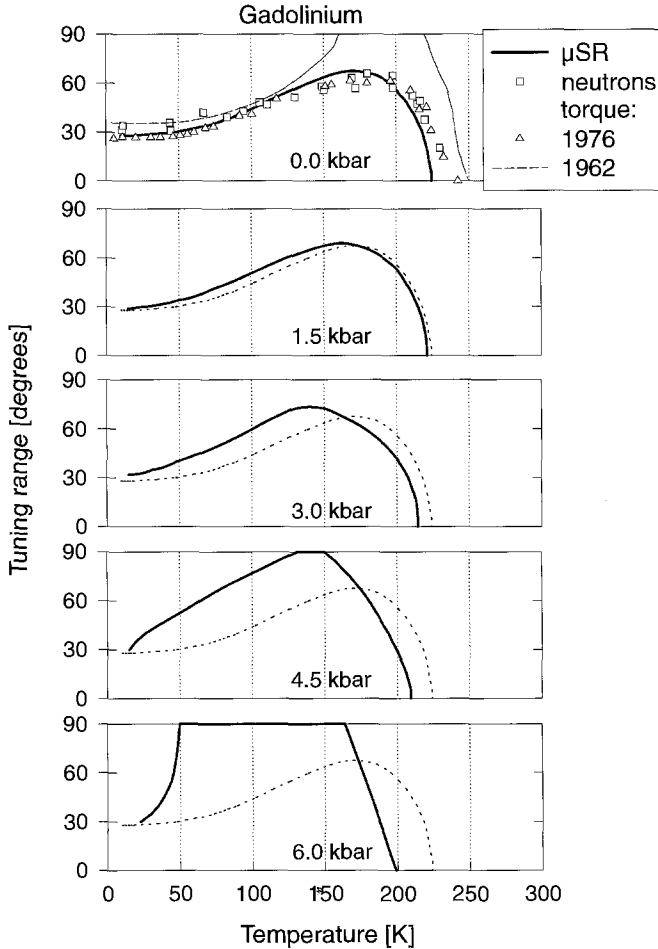


Fig. 32. Spin turning angle (with respect to the  $c$ -axis) in ferromagnetic Gd metal as a function of temperature for ambient (top) and applied pressures derived from the temperature variation of the internal field as shown in fig. 31. Results from other measurements at ambient pressure are shown for comparison. The panels depicting the results at applied pressures also contain the data for ambient pressure (dotted line) to make the differences more apparent. From Schreier (1999).

constant frequency, meaning that it reflects a portion of the sample where spins have not yet started to turn. The amplitude of the former sub-spectrum rises continuously while the amplitude of the other decreases concomitantly until it vanishes at  $\sim 220$  K, indicating that now all spins in the sample have turned (fig. 31, right).

#### 4.2.3. High-pressure measurements

High-pressure  $\mu$ SR studies (Mutzbauer et al. 1993, Kratzer et al. 1994a, Schreier et al. 1997) on Gd (a typical spectrum has been shown earlier in fig. 12) revealed that the



temperature dependence of the precession frequency (the field at the muon site) is highly sensitive to applied pressures even in the fairly low pressure range up to 0.6 GPa (6 kbar). The dominant reason is the dependence of the spin turning process on pressure. The findings are summarized in fig. 32. Under hydrostatic pressure the onset of spin-turning gradually shifts from 230 K to lower temperatures (while  $T_C$  increases slightly). In addition, the turn angles get larger with pressure below 170 K. At  $p = 0.6$  GPa it has reached  $90^\circ$  over the full temperature interval between 170 K and 50 K. It is quite remarkable that the angle then decreases again rather sharply with reduced temperature, approaching again the low-temperature limit of  $30^\circ$  as under ambient pressure. The change of tilting angle has such strong influence on the measured precession frequency that the pressure dependence of the contact field can only be evaluated above the spin-turning temperature (i.e.,  $T \gtrsim 250$  K). There the values of  $B_\mu$  are found to be lower than one would expect if only the pressure-induced shift of the ordering temperature ( $dT_C/dp = -14$  K/GPa according to Bartholin and Bloch 1968) are taken into account. The results suggest an increase of the size of the (negative) contact field with applied pressure, likely to be caused by an increase of conduction electron spin polarization as volume is reduced. The application of high pressure in the paramagnetic state (Schreier et al. 1997) has no measurable effect on the behavior of relaxation rates and frequency shifts. As fig. 29 (left) shows, the crossover behavior around  $T_C + 10$  K is still clearly present for both quantities. It can be inferred from these results that small volume reductions have no marked effect on the  $\mu$ SR magnetic parameters of Gd in the critical regime just above  $T_C$ .

### 4.3. Holmium, dysprosium and erbium

#### 4.3.1. Ambient pressure

4.3.1.1. *Holmium.* This R metal is a most impressive case demonstrating how the interplay of various magnetic and electric (CEF) interactions produces a rich variety of spin structures which are often almost continuously changing with temperature. Just below  $T_N = 132$  K, a helical AFM spin structure is stabilized. In lowering the temperature, the helix becomes distorted, as can be seen from the appearance of higher harmonics in the neutron diffraction pattern. The magnetic order runs through a series of spin-slip structures (Jensen 1996) until a second-order transition at  $T_C = 20$  K leads into a shallow-cone-shaped FM spin arrangement. The (fairly weak) magnetization points along the  $c$  axis. The helical component is commensurate, but the moments are not uniformly arranged along the helix, being bunched around the  $b$  axis. The cone angle decreases continuously towards  $80^\circ$  as  $T \rightarrow 0$ .

The original  $\mu$ SR measurements on Ho (Gurevich et al. 1976, Barsov et al. 1986b) were unable to observe spontaneous spin precession. This has, however, recently been achieved in both polycrystalline (Krivosheev et al. 1997b) and single-crystal material (Schreier et al. 2000a, Schreier 1999). The data of the two studies are quite similar in the AFM regime, but near  $T_C$  the results of Schreier et al. (2000a) are more detailed. Figure 33 shows that the overall temperature dependence of the internal field is rather smooth and Brillouin-like (as for the case of Dy). Just below  $T_N$  the data can be fitted to a critical

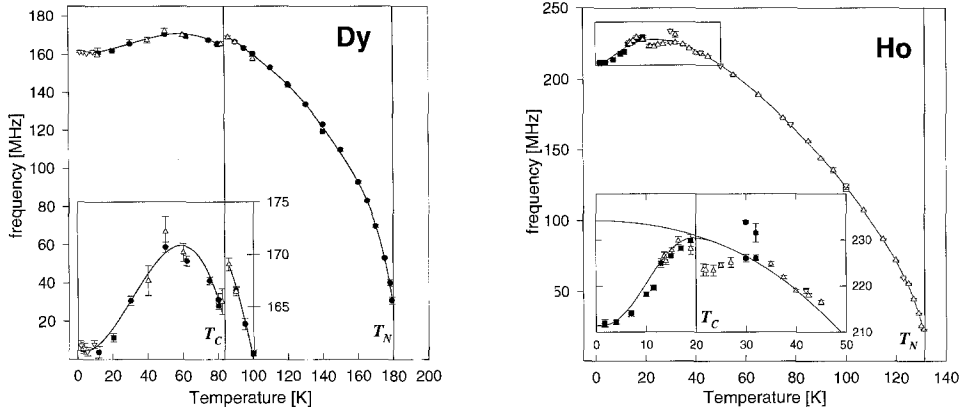


Fig. 33. Temperature dependence of the internal field in single-crystalline Dy (left) and Ho (right). The insets show the behavior at and below the Curie point with an enlarged vertical scale. The lines are guides to the eye. After Ekström et al. (1997) and Schreier et al. (2000a).

Table 3

Saturation values ( $T \rightarrow 0$ ) of the measured local magnetic field  $B_\mu$ , the calculated dipolar field and the extracted Fermi contact field for Dy, Ho and Er according to Schreier et al. (2000a); corresponding values for Gd are given for comparison<sup>a</sup>

	Saturation values ( $T \rightarrow 0$ )					$T_C$ (K)	AFM transition, $B_\mu \propto (T_N - T)^\beta$	
	$B_\mu$ (kG)		$B_{\text{dip}}, \text{ calc.}$ (kG)	$B_{\text{con}}$ (kG)			$T_N$ (K)	$\beta$
	meas.	extrap.		meas.	extrap.			
Gd	1.10(2)		8.89	-7.47		293	No AFM order	
Dy	11.86(3)	13.4	13.21	-1.35	+0.2	85	180.5(7)	0.41(1)
Ho	15.63(6)	17.3	12.44	+3.16	+4.9	20	131.2(3)	0.46(3)
Er	4.28(1)	-	10.42	-6.22	-	20	86.6(1)	0.46(1)

<sup>a</sup> The values of  $T_C$  are taken from Jensen and Mackintosh (1991).

power law  $B_\mu(T) \propto (T_N - T)^\beta$ . We stress that  $\beta$  is obtained from a fit in the ordered region, while usually we talk about critical exponents obtained in the paramagnetic regime. The fit parameters  $T_N$ ,  $\beta$  and the extrapolated saturation values of  $B_\mu(0)$  when assuming a smooth Brillouin-like behavior for  $T < T_C$  (see discussion below), as well as the actually measured field at lowest temperature are given in table 3. From dipolar sums one obtains  $B_{\text{dip}}$ . This then allows extraction of the magnitude of  $B_{\text{con}}$ . Both values are also listed, the latter for the two possibilities using either the measured or the extrapolated values of  $B_\mu(0)$ . Due to the equal distribution of magnetic domains in zero external field, ZF-μSR rotation measurements allow the determination of the frequency (magnitude of  $B_\mu$ ), but not the sense of the muon spin rotation. In consequence, two solutions for  $B_{\text{con}}$  are possible depending on the relative orientation of the measured local field  $B_\mu$  and the calculated dipolar field  $B_{\text{dip}}$ . Additional measurements in an external magnetic

field, which macroscopically magnetizes the sample, were needed. The comparison of the signals from longitudinal and transverse detectors gives the sense of spin rotation. A parallel orientation of  $\mathbf{B}_\mu$  to the sample magnetization, for an experiment carried out on Dy, excluded the choice of a strong negative contact field and thus led to the values of  $B_{\text{con}}$  listed in table 3. Therefore, the choice of a strong negative contact field was also rejected for Ho. This then produces the remarkable result that Ho seems to possess a positive contact field, while in all other heavy R metals this field is negative. This is not understood at present. Except for Gd (which is an S-state ion without orbital momentum), one finds  $B_{\text{con}}$  to be about an order of magnitude smaller than  $B_{\text{dip}}$ . The octahedral muon stopping site has been assumed, but only minor changes in values occur if the tetrahedral site is assumed.

No big irregularities are seen at the spin-slip transitions (e.g., 97, 40, 25 K) in the AFM state, except around 30 K, where the spectra are better fitted by two different precession frequencies (see inset to fig. 33, left). A study by Ponomarev et al. (2000), mainly on a textured polycrystalline sample, failed to detect any effects of spin slips. More dramatic is the irregularity that occurs (as is the case in Dy) at  $T_C$ . The field decreases slightly in the FM regime, while one should expect just the normal saturation behavior of magnetization (i.e., a precession frequency essentially independent of temperature). The cause for this behavior, which so far has only been detected by  $\mu\text{SR}$ , is not clear. One possibility would be a change in cone angle, but dipolar field model calculations cannot reproduce this behavior for any sensible parameter set (Schreier 1999). Also, Dy shows a quite similar behavior (see fig. 34, left) despite the fact that it has a simple FM spin structure (see next paragraph). It is of course most sensible to assume the same mechanism in both cases. Whether the effect is connected to special features of the contact field, or whether an additional field such as a demagnetizing field is present (meaning that spontaneous magnetization is not zero even under zero-field cooling conditions) needs further studies. Except for this irregularity, no substantial difference in the magnitude of the local field between the AFM and FM states is observed. It should also be mentioned that dipolar sum calculations show that the regular bunching of the basal moments along the  $b$ -axis produce a single value of  $\mathbf{B}_\mu$  in accordance with the experimental result.

**4.3.1.2. Dysprosium.** Large axial anisotropy confines the moments on Dy to the basal plane. Between  $T_N = 178$  K and  $T_C = 85$  K, a helical AFM spin structure is present. The helix angle decreases with lower temperature. At  $T_C$ , an orthorhombic distortion of the hcp lattice occurs and the transition into the FM state is of first order. The spins all have the same magnitude and all point along the orthorhombic  $a$  axis, so this is a simple FM structure.

The spontaneous muon spin precession frequency below  $T_N$  was observed by Hofmann et al. (1978) in polycrystalline material and more recently by Ekström et al. (1996, 1997) in a single-crystal specimen. The amplitude of the precession signal is larger in the  $\mathbf{S}_\mu \parallel c$  geometry, meaning that the local field lies predominantly in the basal plane as well. Typical data for the temperature dependence of the precession frequency are shown in fig. 33. The stopping site of the muon is not known, but calculations of the dipolar fields

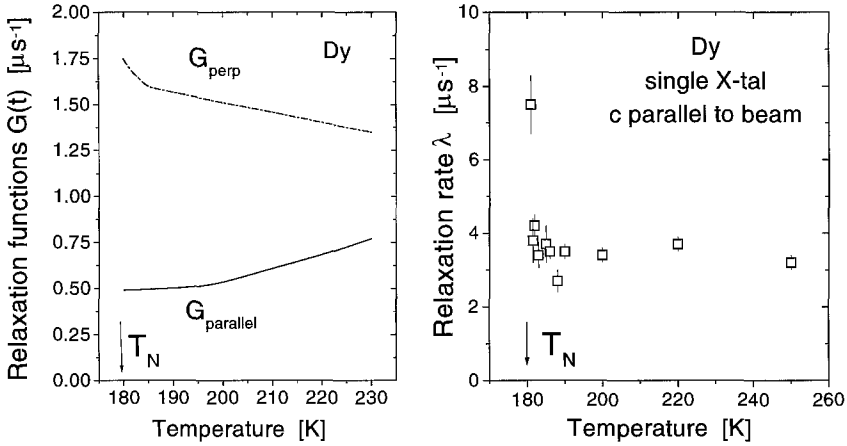


Fig. 34. Left: Temperature dependence of the correlation functions  $G_{\parallel}$  and  $G_{\perp}$  as derived from the orientational dependence of the muon spin depolarization rate of a strongly textured Dy sample in the paramagnetic regime. From Barsov et al. (1986c). Right: Temperature dependence of the relaxation rate  $\lambda_{\parallel}$  in single-crystalline Dy above  $T_N$ . From Ekström et al. (1997).

show that a small shift of the local muon field should take place at  $T_C$  if the muons occupy tetrahedral interstitial sites, but not if the site is octahedral (Denison et al. 1979). The observation of such a shift (fig. 33) indicates a tetrahedral interstitial stopping site, but the issue is not completely settled. Proceeding as discussed for Ho leads to the parameter values listed in table 3. As mentioned these calculations assumed the octahedral site, but the differences when using the tetrahedral site are minimal and of no great consequence. As in Ho, a decrease of frequency is observed in the FM state (which was not seen in the original work of Hofmann et al. 1978). As discussed above, the simple FM spin structure makes an explanation of this feature even more difficult. The case remains unsolved at this stage.

Only a few direct measurements of muon diffusion exist in hcp metals, and it would not be surprising if the muons were mobile, at least in the range from 100 K upwards. This has been examined in Dy by Barsov et al. (1986a,c). A diffusing muon would depolarize longitudinally when it experiences local fields of different orientations along its path. Since the field direction changes from layer to layer in the helical antiferromagnetic structure, muon diffusion parameters can be obtained. The result for the diffusion parameters,  $\kappa\nu_0 = 10^{8.3} \text{ s}^{-1}$  (with  $\kappa \leq 1$ ) and  $E_a = 390 \text{ K}$ , are interpreted as being due to an incoherent tunneling process, rather similar to that in the typical fcc metal Cu above 100 K (see, for example, Schenck 1985).

The relaxation rates above  $T_N$  were studied both by Barsov et al. (1986c) in a textured polycrystal, and Ekström et al. (1996, 1997) in a single-crystal sample. The muon relaxation rate is anisotropic, with larger values for  $\lambda$  if the muons are implanted parallel to the  $c$ -axis. In fig. 34 (left) we show the result by Barsov et al. (1986c) expressed in terms of the relaxation functions  $G_{\parallel}$  and  $G_{\perp}$  as introduced in sect. 4.1. It follows that

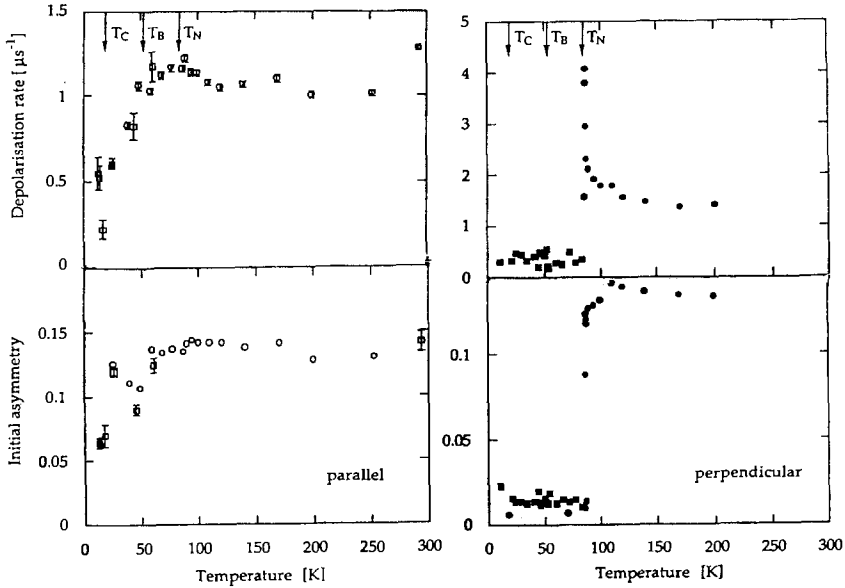


Fig. 35. Temperature dependence of signal amplitude and relaxation rate measured in ZF on a single crystal of erbium oriented with its  $c$ -axis parallel and perpendicular to the muon beam (muon spin polarization). Squares and circles refer to two different run sequences. After Wäppling et al. (1993).

the local field fluctuations occur mainly in the direction of the axis of easy magnetization (located within the basal plane). There appears to be practically no divergence at  $T_N$ , but the sample of Barsov et al. (1986b,c) has a rather wide transition temperature region which is explained by a spread of  $T_N$  through the individual grains of their sample. Ekström et al. (1997) find a narrower transition region in their single crystal and see a fairly sharp increase in relaxation rate very near  $T_N$  (fig. 34, right). The temperature dependence of  $\lambda$  definitely differs from that seen in Er (fig. 35). In comparing the two cases, one must be aware that the field geometries are reversed. In Dy the axis of sublattice magnetization just below  $T_N$  lies perpendicular to  $c$ , while in Er it is parallel to  $c$ . Thus, in Dy one expects  $\lambda_{\parallel}$  (meaning that the crystal is oriented with its  $c$ -axis in the muon beam direction) to be sensitive to critical slowing down, while in Er it is  $\lambda_{\perp}$  (as observed).

**4.3.1.3. Erbium.** The easy direction in Er is the  $c$ -axis, and below the second-order Néel transition ( $T_N = 85$  K), the moments order in a longitudinal sine-wave structure. As the temperature is lowered the sine squares up. Around  $T_B = 52$  K, a basal plane component begins to order, leading to a helical AFM structure. Finally, at  $T_C = 20$  K a first-order transition into a steep cone (opening angle  $\sim 30^\circ$ ) FM spin structure takes place. Several (first-order) spin-slip transitions occur in the helical AFM phase.

The first  $\mu$ SR studies were carried out on textured polycrystals and concentrated on the paramagnetic state (Barsov et al. 1983, 1986c). Hartmann et al. (1990c) and Wäppling et al. (1993) extended those studies to a single crystal oriented with its  $c$ -axis both

parallel and perpendicular to the muon beam (initial muon spin direction) and to the magnetically ordered regime. A summary of their ZF data is depicted in fig. 35. As can be seen immediately, Er shows a very strong anisotropy of the magnetic fluctuations up to temperatures well above the critical temperature. With the muon polarization along the  $c$ -axis of the crystal, the Er spin fluctuations cause an almost temperature-independent muon relaxation above  $T_N$ , while initial muon polarization perpendicular to the  $c$ -axis results in a strongly temperature-dependent and divergent relaxation rate. Obviously, critical behavior occurs only for those spin fluctuations that generate fluctuations of the internal field component parallel to the  $c$ -axis (the axis of easy magnetization below  $T_N$ ). Fitting  $\lambda_{\perp}(T)$  to a critical power law results in a dynamic critical exponent of  $w = 0.15$ . This is an unusually low value that is not understood at present. Henneberger et al. (1999) have pointed out recently that mode coupling theory as applied to uniaxial ferromagnets like Gd results in rather low values of the critical exponents. Whether the same can also be concluded for transition into complex AFM structures like in Er requires further theoretical studies.

In a sense, the situation for observable features is reversed in the magnetically ordered state. For the perpendicular geometry, the signal amplitude quickly collapses at  $T_N$  and stays practically at zero down to  $T_C$  (but see further below). In the parallel geometry, however, an exponentially relaxing signal can be detected in the AFM state. Since the muon spin is oriented parallel to the dominant field direction, spin precession is not observable. The signal amplitude, as well as the relaxation rate, shows irregularities at the magnetic transition temperatures  $T_N$ ,  $T_B$  and  $T_C$ . Whether the spin-slip transitions are also reflected cannot be judged reliably with the present accuracy of the data. These measurements were done at the ISIS pulsed facility with its limits on time resolution.

Recent high-precision ZF measurements (on the single crystal in perpendicular orientation on the continuous beam of PSI), resolved a strongly damped spin precession signal in the temperature range between  $T_N$  and  $T_C$  (Schreier et al. 2000a). The combination with earlier spontaneous muon spin precession data for the ferromagnetic cone state by Hartmann et al. (1997) gave the complete temperature dependence of the local field in all three magnetic states (fig. 36, left). A small break is seen in the otherwise smooth dependence of  $\nu_{\mu}(T)$  at  $T_B$ , but a dramatic 80% drop in frequency occurs at  $T_C$ , which is in sharp contrast to the behavior in Ho and Er. In Ho the basal plane component of the ordered moment is highly dominant (shallow cone angle), and in Dy no perpendicular component exists. Hence, the dipolar field components suffer little change. This is quite different in Er where the dipolar field alters both its orientation and magnitude. The FM orientation of the formerly antiferromagnetically oriented regions of four parallel axial moments each, produces a dipolar field having half the value the opposite direction compared to that in the AFM regime. The relatively small contact field experiences no change in either orientation or magnitude since it follows the (sublattice) magnetization. Its orientation, though not exactly parallel to  $\mathbf{B}_{\text{dip}}$ , further enhances the drop of the local field  $\mathbf{B}_{\mu}$ .

Two different precession frequencies with nearly equal intensities just below  $T_C$  are present in the FM regime of Er. The dependence of the frequencies on temperature is

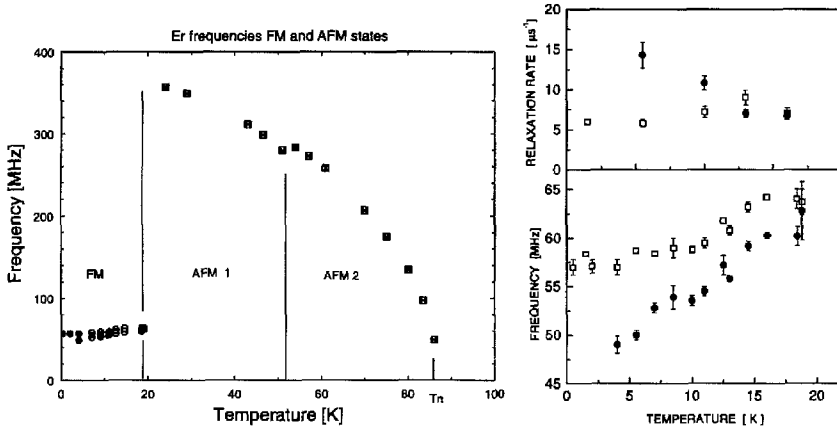


Fig. 36. ZF  $\mu$ SR data on single-crystalline Er in the magnetically ordered states. The measurements were done in the perpendicular geometry. Left: Temperature dependence of the spin precession frequencies. After Schreier et al. (2000a). Right: Temperature dependence of the two spontaneous precession frequencies (bottom) and their damping rates (top) in the FM state. Solid and open symbols distinguish the two signals. After Hartmann et al. (1997).

depicted in fig. 36 (right). The signal with lower frequency is more strongly damped (fig. 36, right) and loses amplitude as temperature is reduced. Around 4 K it becomes unobservable, presumably because of excessively rapid depolarization. Perhaps the cone opening angle varies with temperature (although no neutron data on this are available). The moments in the basal plane are subject to bunching. In a perfect cone structure, only a single muon frequency would be seen for either an octahedral or a tetrahedral stopping site. The more recently proposed spin structure models (containing the basal-plane spin bunching) would give rise to a pattern of eight precession frequencies instead of only the two strong frequencies actually observed. Also unexplained is the temperature dependence of both frequencies and why one of the components gradually decreases and finally vanishes. It should be remembered that the decrease of frequency means a decrease in local field as  $T \rightarrow 0$ . This connects with the observation in the FM state of Ho and Dy. In summary, the  $\mu$ SR data on FM erbium indicate that a revision of the spin structure derived from X-ray and neutron scattering data may be needed.

#### 4.3.2. High-pressure measurements

Preliminary data on high-pressure  $\mu$ SR measurements on Dy and Ho have recently been reported (Schreier et al. 2000b, Kalvius et al. 2000f). The pressure dependence of the spontaneous spin precession frequencies in the two metals was determined at various temperatures in their magnetically ordered states. For Ho the data are restricted to the AFM regime due to the temperature limitations of the high-pressure apparatus. Roughly linear dependences of  $\nu_\mu(p)$  were seen, leading to the pressure coefficients  $(\partial B_\mu/\partial p)_T$  of the local magnetic field (see table 4). The parameter of interest is the pressure (or volume) coefficient of the contact field as the unique quantity available from  $\mu$ SR

Table 4

Measured local field, calculated dipolar field and derived contact field together with their pressure coefficients at various temperatures for dysprosium and holmium metals<sup>a</sup> (Schreier et al. 2000b)

$T$ (K)	$B_{\mu}(T)$ (kG)	$(\partial B_{\mu}/\partial p)_T$ (kG/GPa)	$B_{\text{dip}}(T)$ (kG)	$(\partial B_{\text{dip}}/\partial p)_T$ (kG/GPa)	$B_{\text{con}}(T)$ (kG)	$(\partial B_{\text{con}}/\partial p)_T$ (kG/GPa)
<i>Dysprosium, ferromagnetic</i>						
22	+11.97(3)	+0.27(6)	+13.12	+0.31	-1.15(3)	-0.04(6)
68	+12.56(1)	+0.33(1)	+12.37	+0.28	+0.19(1)	+0.06(1)
<i>Dysprosium, antiferromagnetic</i>						
100	+11.91(7)	+0.13(15)	+11.09	+0.19	+0.82(7)	+0.06(1)
120	+10.9(1)	+0.06(29)	+10.12	+0.09	+0.76(14)	-0.03(29)
140	+9.1(2)	-0.06(4)	+8.87	-0.02	+0.21(18)	-0.04(4)
<i>Holmium, antiferromagnetic</i>						
44	+16.18(3)	+0.65(6)	+11.44	+0.21	+4.74(3)	+0.45(6)
50	+15.50(2)	+0.64(4)	+11.17	+0.18	+4.33(2)	+0.45(4)
66	+14.43(4)	+0.46(7)	+10.31	+0.10	+4.13(4)	+0.36(7)
78	+12.36(3)	+0.31(5)	+9.51	+0.01	+2.85(3)	+0.30(5)
100	+9.10(13)	+0.33(23)	+7.55	-0.20	+1.55(13)	+0.54(23)

<sup>a</sup> The errors refer to the linear regression fits to  $B_{\mu}(p)_T$  only.

data. Calculations of the dipolar field contributions to  $B_{\mu}$  as a function of pressure at different temperatures are the first step. The derivation of the contact field and its pressure coefficient is relatively straight forward in Dy and Ho since in contrast to Gd spin turning is not present (otherwise  $B_{\mu}(p)$  would not be linear). Just below the antiferromagnetic transition the main influence on  $B_{\text{dip}}(p)_T$  comes from the reduction of magnetic moment caused by the negative shift of the ordering temperatures  $\partial T_N/\partial p \approx -4.1(1)$  K/GPa for Dy and  $\partial T_N/\partial p \approx -4.8$  K/GPa for Ho (Bartholin and Bloch 1968). Below  $T/T_N < 0.7$  it is the increase of magnetization by volume reduction with the isothermal compressibility derived from the temperature dependence of the elastic constants (Palmer and Lee 1972). This leads to a change of sign in  $(\partial B_{\text{dip}}/\partial p)_T$ .

In Dy the pressure coefficients  $(\partial B_{\text{con}}/\partial p)_T$  are zero within the limits of error at all temperatures. In Ho they are comparable in size to the pressure coefficients of  $B_{\mu}$  (table 4). Theoretical calculations of the volume dependence of the interstitial conduction electron density are not available to our knowledge. The results on  $(\partial B_{\text{con}}/\partial p)$  must stand as they are at this stage. They show at least that the question of compressibility of conduction electron density is a complex one and obviously different for the otherwise rather analogous two rare-earth metals. At least in Dy the spin structure (AFM *vs.* FM) seems to have no significant influence. High-pressure data on Er are not available to date.



## 5. Intermetallics

The field of magnetism in lanthanide and actinide intermetallic compounds has been actively pursued for many decades. In consequence, the number of studies published is enormous. Also  $\mu$ SR has followed that area of magnetism quite actively. Many of the results available can also be found in the review of Schenck and Gygax (1995). Here we put the emphasis on regions of magnetic instability where short-range-ordered (SRO) magnetism often occurs and on the study of spin fluctuations, especially while approaching a magnetic transition and – if single-crystal data are available – on directional dependences. These are the fields where  $\mu$ SR shows its special strength.

The basic magnetic properties of R intermetallics were reviewed by Kirchmayr and Poldy (1979). This review is of course in part outdated by now. A more recent review is provided by Gignoux and Schmitt (1995). Gratz and Zuckermann (1982) give a compilation of transport properties of R intermetallics. The field of An intermetallics has been reviewed by Fournier and Troć (1985). A comparison of transport properties of selected R and An intermetallics is given by Fournier and Gratz (1993). Especially the Ce and U intermetallic compounds comprise the field of heavy-fermion and other strongly electron-correlated materials. Special reviews are dedicated to them, and we deal with them separately in sect. 9, where the major reviews for those compounds are listed.

The investigations by  $\mu$ SR on R and An compounds are rather broadly spread and involve examples from many series of intermetallics. The central point of these studies is to gain information on spin lattice relaxation of the 4f or 5f moments, especially in materials with pronounced magnetic anisotropy. A second important goal is to study the behavior of compounds near a magnetic instability, as found for example in materials under the influence of strong magnetic frustration. We suspect that the reader, when finished with this chapter, will be perhaps somewhat confused by the multitude of different and sometimes not directly connected data. For this reason we have attempted to give a summary of the most important aspects derived from the  $\mu$ SR studies in sect. 5.7.

### 5.1. Singlet ground state systems

#### 5.1.1. Crystalline electric field (CEF) effects

Since the majority of the readers of this review are likely to be familiar with f-electron magnetism but not so familiar with  $\mu$ SR, the introductory material of the first three sections explained how  $\mu$ SR probes magnetic properties in some detail, but assumed knowledge of those magnetic properties themselves.  $\mu$ SR experts reading this article are likely to be those familiar with magnetism in general, but they may not be acquainted with the somewhat special topic of crystalline electric field (CEF, some authors say “crystal field”) effects in lanthanide magnetism. These effects are mostly insignificant in the elemental lanthanides, and so were not mentioned in the preceding section. An exception is Pr metal, which has a CEF-induced singlet electronic ground state and will be discussed in sect. 5.1.2.1. The influence of CEF cannot be ignored in most lanthanide alloys and compounds. For readers not expert in f-electron magnetism, we present a brief

introduction to CEF effects. For a more detailed review, see Fulde and Loewenhaupt (1985).

The magnetic moments in transition metal, lanthanide and actinide magnetism reside on unpaired electrons in non-zero-angular-momentum ( $l$ ) orbitals. Each individual  $m_l$  orbital is not spherically symmetric, and so, in addition to a magnetic moment when singly occupied, it also has charge-multipole moments. In this section it will be assumed that the magnetic orbital remains localized around its particular nucleus when the ion is embedded in a crystal, and the rest of the crystal can be treated as external to it (no hybridization). This approximation fits particularly well for the heavy lanthanides (except Yb), where the  $f$  wave functions are well-buried inside the valence orbitals. It fits less well for light lanthanides, Yb and the light actinides, and is crude indeed for transition metals. CEF effects can only be identified as separate, single-ion effects to the extent the approximation (of localization) applies for the lanthanide when it is embedded in the material considered. When such a buried-moment ion sits in a crystal, the charge distribution around the ion (generated by the other ions and electrons) is also not spherical, it has the symmetry of that ion site in that crystal structure. The surrounding charge distribution creates a static electric potential  $V_{\text{CEF}}(\mathbf{r})$  with the ion's site symmetry at and around the ion site, which can be expanded in spherical harmonics  $Y_l^m(\Theta, \Phi)$ , or, more conveniently for this application, in the related strictly real basis set of "tesseral harmonics"  $Z_{l\alpha}(\Theta, \Phi)$  (Hutchings 1964).

$$V_{\text{CEF}}(\mathbf{r}) = \sum_{l\alpha} \gamma_{l\alpha} r^l Z_{l\alpha}(\Theta, \Phi), \quad (60)$$

where the coefficients  $\gamma_{l\alpha}$  are formally defined as integrals over the surrounding charge distribution. This electric potential is multiplied by the ion's local electric charge density to obtain the interaction energy (a term in the ion's electron-cloud Hamiltonian)

$$E_{\text{CEF}} = e \langle \Psi | V_{\text{CEF}} | \Psi \rangle. \quad (61)$$

For d-magnetic ions, this interaction is usually so strong that it completely lifts the orbital degeneracy (quenching the orbital moment), leaving a ground state in which only the spin degrees of freedom are available to participate in magnetic properties (see, for example, Ashcroft and Mermin 1976, p. 657). In f-ions, the interaction is not so extreme. Spin-orbit coupling makes the total angular momentum  $J$  the good quantum number, and usually makes the non-trivalent  $J$  multiplets far higher in energy than room temperature, so that only one value of  $J$  need be considered. This is usually false, however, for Ce and the magnetic light actinides, is often false for Yb and Eu, and is sometimes false for Sm. When more than one  $J$  value is accessible to a single ion by thermal fluctuations, the situation is termed "mixed valence", "valence fluctuations" or "intermediate valence" (see for details: Wohlleben 1976, Varma 1985 or Wachter 1994). As shall become apparent in sect. 9.5, this is not a topic where μSR has had much impact and, in consequence, few μSR data are available. If the excited  $J$  states have energy near the Fermi level of a

metallic system, they will hybridize to some extent with the conduction bands, leading to the “correlated electron” effects. This aspect is discussed in more detail at the beginning of sect. 9.

In the majority of lanthanide cases, with the ground  $J$  multiplet (often referred to as the Hund’s rule state) so isolated, the CEF analysis is simplified. When  $J = \text{constant}$ ,  $|\Psi\rangle = \sum a_z |j, j_z\rangle$ , and the action of each  $r^l Z_{l\alpha}$  term on any such state can be expressed as a dimensionless “Stevens factor” (Stevens 1967)  $\theta_l \equiv \alpha_j, \beta_j, \gamma_j$ , for  $l = 2, 4, 6$ , respectively (and 6 is the highest non-trivial value for 4f states), times an average of  $r^l$  over the wavefunctions of the ion, and a “Stevens operator equivalent”  $O_l^m$  involving only the total angular momentum component operators  $J_x, J_y, J_z$ . Thus,

$$H_{\text{CEF}} = \sum_{l,m} A_l^m \langle r^l \rangle \theta_l O_l^m \equiv \sum_{l,m} B_l^m O_l^m. \quad (62)$$

The  $\langle r^l \rangle$ ’s and  $\theta_l$ ’s are single-ion properties, and are tabulated in, e.g., Fulde and Loewenhaupt (1985). The coefficients  $A_l^m$  must be determined for each particular material. Formally, they can be calculated from a precise knowledge of all the ion positions and electron wave functions in the crystal. For insulators, calculation of  $\{A_l^m\}$  from assignment of point charges to the ion positions has produced good agreement with observations in a number of cases. For metals, however, the point charge model usually fails and no more sophisticated treatment has been found that is both tractable and reliable (see references cited by Fulde and Loewenhaupt 1985). The situation is then usually one of trying to deduce the coefficients from experimental data. If there is only one material (containing one particular rare earth) of interest, then usually  $B_l^m$  parameters are quoted, with units of energy, whereas, if a number of different lanthanides can reside on the same site without changing the crystal structure, creating a whole series of materials, then the  $B_l^m$  values for the different rare earths should translate into a single set of (nearly constant)  $A_l^m$ , with units energy/(length) <sup>$l$</sup> , that apply to the entire series. This is often true for heavy rare earths ( $\text{Gd} \leftrightarrow \text{Tm}$ ), but less likely for light lanthanides (where the f wavefunctions are not as well buried inside the ion). When a single set of  $A_l^m$  applies, differences in magnetic behavior for different lanthanides in the series may be due entirely to differences in single-ion anisotropy and ground-state degeneracy caused by the CEF.

The rare-earth site symmetry in the material strictly limits which coefficients in eq. (62) can be non-zero. For cubic symmetry, there are also constraints among the non-zero coefficients, so that

$$H_{\text{CEF, cub}} = B_4^0 [O_4^0 + 5O_4^4] + B_6^0 [O_4^0 - 21O_6^4], \quad (63)$$

and there are only two independent parameters to be determined. Lea et al. (1962) tabulated eigenvalues and eigenfunctions of this Hamiltonian for all standard rare-earth configurations. For successively lower and lower site symmetry, on the other hand, successively more and more  $B_l^m$  may be independently non-zero.

The effect of the CEF, acting by itself, is to split the large  $J_z$  degeneracy of the magnetic rare-earth state into a spectrum of states over an energy range. These are the so-called

CEF states or levels, characterized by their value of  $J_z$ . The energy range involved may be as small as a few tens of Kelvin to (occasionally) as large as several thousand Kelvin. If the material is measured at a temperature well below some of the excited CEF states, then those states will of course not be occupied. This will result in single-ion magnetic anisotropy, separate from any anisotropy in magnetic interactions in the material. It will also result in a reduced paramagnetic fluctuation rate among the substates, to which  $\mu$ SR is sensitive. Being a static electric effect, however, the CEF *by itself* does not cause any magnetism. For a lower-than-cubic site, the CEF states occupied often define an “easy axis”, along which the largest magnetization develops for given applied field magnitude; but without an applied magnetic field or independent magnetic interactions, all states at a particular energy have equal amplitudes of  $+j_z$  and  $-j_z$ .

When there are also magnetic interactions among the lanthanide ions in a particular material, then the importance of the CEF depends on its relative strength. If the magnetic ordering temperature is near or larger than the range of splitting of the CEF levels that would occur in the absence of magnetism (as they are in the elemental lanthanides), then the CEF effects are relatively minor. If, however, the magnetic ordering temperature is significantly lower than the overall CEF splitting, then the ordering must impose itself on the subset of CEF states still occupied at the ordering temperature, and the details of which states are still occupied can affect what ordering occurs. Even then, for cubic rare-earth sites, CEF effects are usually fairly minor, except when they cause a singlet ground state (below). For non-cubic lanthanide sites and low magnetic ordering (or freezing) temperatures, on the other hand, the outline of the CEF effects may need to be determined before the magnetic interactions can begin to be understood.

The values of the CEF parameters can be deduced from data from a number of probes (and  $\mu$ SR is not normally one of them). Optical probes are used extensively for transparent insulators, but  $\mu$ SR is not used much to study lanthanide insulators (see sect. 6), so we will not dwell on these. For metallic systems, the most useful probe is inelastic neutron scattering, which can measure the energies of transitions between CEF levels. Data from a single lanthanide material can leave ambiguities in the deduced CEF parameters, however, so either several different lanthanides in a series of materials should be measured and a single set of  $A_l^m$  parameters deduced, or, if only one material is of interest, the set of  $B_l^m$  parameters must be shown to be consistent with heat capacity or single-crystal magnetization measurements. The beginning of filling a new CEF level, as temperature rises toward the energy of the level, introduces new degrees of freedom that generate a “Schottky anomaly” in heat capacity. This is particularly obvious for excited states between 2 K and  $\sim 10$  K, a region that challenges the energy resolution normally available in neutron scattering experiments. If single crystals are available, then paramagnetic anisotropy, which is usually dominated by the CEF, can be measured directly. Other probes (Mössbauer effect, EPR) can provide specific CEF information in particular circumstances. Neutron scattering was (eventually) definitive for the CEF in  $\text{RBa}_2\text{Cu}_3\text{O}_{6+\delta}$  high-temperature superconductors (Henggeler and Furrer 1998, Whitehead et al. 1994, see sect. 7.2.2, and also below for  $\text{R}=\text{Ho}$ ). In the  $\text{RRh}_4\text{B}_4$  magnetic superconductors, where the overall splittings are smaller, the successful analysis combined

data from heat capacity, single-crystal magnetization, and Mössbauer effect (Dunlap et al. 1984).

Some points to remember about rare-earth CEF effects are:

- (1) The CEF splits half-integer-spin (“Kramers”) ion levels differently than integer-spin (“non-Kramers”) ion levels. The fermionic, antisymmetric nature of half-integer-spin states means that when all  $j_z$ ’s in a state are switched to  $-j_z$ , it must produce a different state with the same energy, even in the presence of an electric field. The CEF thus can split the states into at most “Kramers doublets”  $|\Psi_{\pm}\rangle = \sum_{-j_z, j_z} a_{\pm} |\pm j_z\rangle$ . Such a pair can still be split by a magnetic field. Meanwhile, the bosonic, symmetric nature of integer-spin states means that that switch gives back the self-same state, and does not constrain any other state relative to it. CEF splitting can then result in a singlet state at a particular energy. The exact configuration of singlets and multiplets will depend on the site symmetry.
- (2) For a single rare-earth site in an isostructural series (one set of  $A^n$ ’s), different rare earths can respond entirely differently to the CEF at that site. There are numerous cases in which the easy axis for one lanthanide can be a very hard axis for its adjacent neighbor in the periodic table. Therefore, in a series in which CEF effects are “strong” (CEF splitting  $\gg$  magnetic freezing temperatures), the alloying of two different magnetic rare earths on a site can result in bizarre magnetic behavior, due to easy-axis incompatibility.
- (3) Trivalent gadolinium is an  $l = 0$  state,  $^8S_{7/2}$ , that is, half the f states are filled with unpaired electrons so that the sum total *orbital* angular momentum for the ion is zero. The total angular momentum is entirely spin, and the ion is spherically symmetric, so it does not respond to the CEF (to first-order). Therefore, the Gd member of an isostructural series will be without the CEF anisotropy of the other members of the series. Thus it is often desirable to measure the Gd member of a series to see the effect of “turning off” the CEF. Unfortunately, Gd also has the largest thermal neutron absorption among the natural isotopic-composition elements, so it is often avoided by researchers intending to use neutron scattering.

The discussion of what  $\mu$ SR can measure in various regimes of magnetic behavior in sect. 3.7 assumed no CEF effects. When CEF effects are “strong”, there is an additional “CEF regime” in the paramagnetic state between the high-temperature paramagnetic limit and the regime of critical phenomena near any magnetic ordering temperature. The paramagnetic limit is attained for temperature far above the highest CEF level, and in it fluctuations are still governed by Moriya and Korringa terms (see discussion on  $RAI_2$  intermetallics in sect. 5.3.1.1). As temperature drops below the highest excited state, however, thermal fluctuations into that state begin to “freeze out”, and the fluctuation rate drops, due to an electric, not a magnetic, effect. For most ions the average (over all states occupied) moment remains roughly constant (except the cases discussed in the next section!), although anisotropy (pointing-axis preference) sets in. The field distribution at the muon site (in a polycrystal) should remain about the same then, and it is expected that the local field fluctuation rate should be proportional to the moment fluctuation rate (it is not clear what the constant of proportionality should be, however). This is virtually

guaranteed to be in the fast-fluctuation limit of  $\mu$ SR, so, as the moment fluctuation rate drops, the rate of monotonic relaxation of muon polarization will increase. Noakes et al. (1987) showed that the temperature dependence of spin–lattice fluctuations (see, e.g., Standley and Vaughn 1969) among the previously determined CEF levels of Sm- and  $\text{ErRh}_4\text{B}_4$  was consistent with the temperature dependence of the muon spin relaxation rate observed from below 10 K to  $\sim 200$  K (when the muon begins to hop), as mentioned in sect. 7.1. Dalmás de Réotier et al. (1996) have attempted a more sophisticated analysis of the general problem. They especially couple the  $\mu$ SR linewidth (relaxation rate) with the dynamical linewidth obtained in neutron scattering. Up to now, they have applied their formalism only to Kondo and HF systems since this allowed certain simplifications. A rigorous treatment of strong R paramagnets is not yet available. One may state in general, that in cases where the paramagnetic  $\mu$ SR rate remains temperature dependent very far above the magnetic freezing temperature of a R material, as it often does, the CEF splittings should be considered before attributing it all to an extended range of critical slowing-down. For the strongly hybridized Kondo states, the CEF interaction can have a marked influence on the spin fluctuation rates as measured by  $\mu$ SR (in contrast to analogous data obtained by neutron scattering) in the temperature range above and around the Kondo temperature (see sect. 9).

### 5.1.2. $\mu$ SR in singlet ground state systems

Following from the discussion of the previous section, if a material containing only one integer-spin lanthanide species happens to generate a CEF that makes the rare-earth ground state a singlet, and if magnetic interactions between the magnetic ions are weak enough that no magnetic ordering occurs at temperatures above the first excited state, then the situation is called “singlet ground-state magnetism”. An isolated singlet state is, by itself, nonmagnetic: it has no way to respond to an applied magnetic field. If magnetic interactions are so weak that there is no magnetic ordering, then, while at high temperatures (many CEF states occupied) the material has normal paramagnetic response, as temperature drops below the lowest excited state, the magnetic levels become depopulated, and the paramagnetic response weakens. Instead of Curie-Law divergence of susceptibility as  $T \rightarrow 0$ , the susceptibility becomes constant at low temperature, in a “Van Vleck” paramagnet (see, for example, Ashcroft and Mermin 1976, p. 653).

This weakening paramagnetic behavior as temperature drops below the first excited CEF state can lead to subtle effects not often seen in other circumstances. Because the CEF varies with position around the center of the ion site, and because vibrations move the ion charge cloud around, the CEF couples to phonons. If the coupling is strong enough, the CEF levels cease to be single-ion excitations, and participate instead in collective “vibronic” modes with dispersion relations at the very low end of the acoustic phonon range. Because the size of the magnetic moment depends in this case on which CEF state is occupied, if there are any magnetic interaction mechanisms coupling the moments attached to the vibronic states, they can lead to *magnetoelastic* effects. For example:

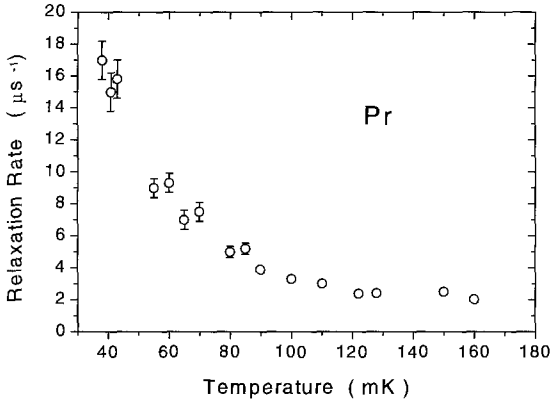


Fig. 37. Temperature dependence of the ZF relaxation rate  $\lambda$  in Pr metal (single crystal,  $b$ -axis parallel to the beam) at very low temperatures. At higher temperatures the rate is practically constant. After Rainford et al. (1996).

5.1.2.1. *Praseodymium metal.* Elemental Pr metal itself has no electronic magnetic ordering (but see further below). It does possess an unusual excitation structure (see e.g., Lindgård 1997), and magnetic ordering occurs when uniaxial pressure is applied, inducing a “softening” transition of the CEF “magnetic exciton” mode (McEwen et al. 1983, Jensen et al. 1987). To our knowledge, only a preliminary report on a  $\mu$ SR study has appeared (Rainford et al. 1996). Pr metal crystallizes in the double hexagonal structure (dhcp), which provides two non-equivalent lattice sites for the  $\text{Pr}^{3+}$  ions. One has approximately cubic (close to fcc), the other hexagonal symmetry. In both cases, the CEF interaction produces a singlet electronic ground state. This state is almost polarized by RKKY interactions for the hexagonal site, leading to an enhanced and highly anisotropic susceptibility. These features are nicely mirrored in  $\mu$ SR Knight shift data (taken in  $\text{TF} = 200$  G). The ZF relaxation rate was found to be much larger when the muons were implanted with their spin in the basal plane compared to those where the spin pointed parallel to the  $c$ -axis. For the former case in particular, a strong increase in rate was observed on approaching  $T = 45$  mK, indicating a substantial slowing down of Pr spin fluctuations (fig. 37). It had been established by neutron scattering (McEwen and Stirling 1981) that at 45 mK the hyperfine-coupled nuclear-electronic system starts to order antiferromagnetically, and specific heat (Eriksen et al. 1983) showed that a second-order phase transition occurs. This behavior is in full accordance with the  $\mu$ SR data of fig. 37. In addition the nuclear-electronic ordering produces a large pseudo-quadrupolar interaction (Abragam and Bleaney 1970, Bleaney 1973) and it has been proposed (Rainford et al. 1996) that this could well be traced by LCR (see sect. 2.1) measurement. No definite data have yet appeared, however.

A more detailed Knight shift measurement has recently been reported by Gygax et al. (1999). TF measurements in fields between 0.33 and 0.63 T were carried out on a single crystal for temperatures from 12 to 300 K. A single  $\mu$ SR signal was observed over the whole temperature range with  $\nu_{\mu} \propto \cos^2(\Theta)$  ( $\Theta =$  angle between  $B_T$  and the  $c$ -axis) and no asymmetry within the basal plane. This indicates an axially symmetric stopping site, most likely the  $e$ -site in the  $\text{P6}_3/\text{mmc}$  structure of Pr. A plot of the total Knight shift measured

parallel and perpendicular to the  $c$ -axis against their corresponding bulk susceptibilities results in linear scaling over the whole temperature range for the perpendicular case, but strong deviations for  $T < 60$  K in the parallel case. The authors discuss the loss of scaling as a consequence of a possible temperature dependence of contact interactions, or, alternatively, as resulting from an alteration of CEF parameters in the immediate vicinity of the stopped muon. The reviewers wish to point out that the scaling deviations occur at about the same temperature where the steep rise in ZF-relaxation rate occurs (see fig. 37).

5.1.2.2. *PrNi<sub>5</sub>*. The most famous CEF singlet ground-state material is  $\text{PrNi}_5$ , the active ingredient in most *adiabatic nuclear demagnetization* systems to achieve temperatures below the  $\sim 10$  mK achievable by  $^3\text{He}$  dilution refrigerators (see e.g., Pobell 1992). This is a material with no electronic-moment magnetic ordering (the nickel ions are apparently completely nonmagnetic) but the Pr ion has a strongly magnetic first excited level, so that substantial magnetization is developed in applied field at low temperature. Hyperfine coupling to the nucleus generates effective amplification of the applied field there, and significant Pr nuclear polarization is developed at  $\sim 10$  mK, enhancing greatly the cooling power (Andres and Bucher 1971). Base temperature is ultimately limited, for this system, by nuclear magnetic ordering at about 0.4 mK.

$\mu$ SR work on  $\text{PrNi}_5$  is marred by the presence of multiple signals. An early study (Kaplan et al. 1989) led to the assignment of a sizable paramagnetic moment on Ni, despite the fact that this would be detrimental to its utility as a nuclear coolant. The deeper causes for the unusual  $\mu$ SR spectra are the influences of the muon on the CEF interaction as will be discussed below. More recently, Kayzel et al. (1994) observed ZF spontaneous muon spin precession in a single crystal of  $\text{PrNi}_5$  (fig. 38) at 0.69 K, in spite of the well-established lack of electronic magnetic ordering. The oscillation is of small amplitude, and complex, indicating several frequencies in a range roughly centered on 1 MHz, corresponding to local fields  $\sim 80$  G, too large to be from nuclear moments, yet very small for any Pr magnetic ground state. Normally, ZF oscillations are interpreted to mean long-range magnetic ordering, because spin-glass-like frozen states usually generate

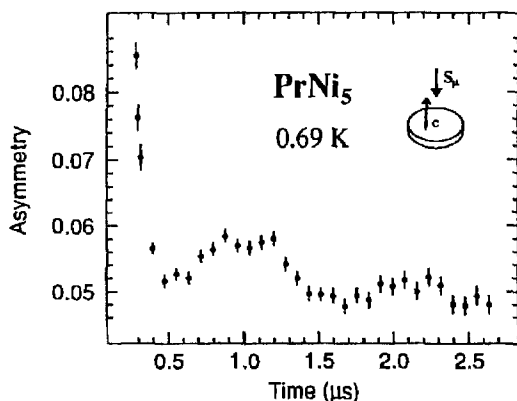


Fig. 38. ZF  $\mu$ SR asymmetry spectrum from a single crystal of singlet-ground-state  $\text{PrNi}_5$  at 0.69 K (Kayzel et al. 1994), indicating well-defined local fields at the muon sites.



Kubo–Toyabe relaxation, not oscillations. In this case, however, at this temperature and no applied field, the Pr is normally thought to have *no* moment. One is then left speculating about whether the muon magnetic moment provides an “applied” field at the nearby Pr’s to induce a magnetic polaron disturbance in the lattice around the muon, or if the muon charge disturbance, which must always push the ions around it slightly off their nominal positions, can change the CEF at the nearest Pr ions enough to cause a magnetic ground state. Both of these would be muon-induced effects, so that  $\mu$ SR would no longer be measuring properties of the muon-free host material.

Feyerherm et al. (1995) performed extensive measurements of the  $\mu^+$  Knight shift ( $K_\mu$ ) in a single crystal of  $\text{PrNi}_5$ , finding that  $K_\mu$ , a measure of the local susceptibility at the muon, is not proportional to the bulk susceptibility, having, for instance, much stronger anisotropy in the hexagonal basal plane. They determined the change in the local CEF parameters of the Pr ions nearest to the muon required to generate the observed muonic Knight shift. That change in CEF was not what would be caused by mere addition of the muon point charge in a point-charge calculation. Thus, the muon-induced effect is not simple.

5.1.2.3. *PrIn<sub>3</sub>*. Tashma et al. (1997) performed a similar single-crystal  $\mu^+$  Knight shift study of cubic singlet-ground-state  $\text{PrIn}_3$ , and again observed that the Knight shift does not scale with the bulk susceptibility. A similar nearby-Pr CEF-shift analysis produced a similar muon-induced effect on the CEF levels, as shown in fig. 39. The overall splitting of levels remains about the same, but some levels are split (by the muon reduction of the local symmetry) and pushed down by up to 20 K, resulting in increased apparent susceptibility at the muon. In a preliminary report Tashma et al. (1998) showed further that in  $\text{PrIn}_3$  (and in  $\text{PrPb}_3$ ), variations in relaxation rate and frequency shift occur for  $T > 150$  K that are attributed to the onset of muon hopping between two inequivalent magnetic sites.

The effect of muon hopping between magnetically different sites (in an applied field) has recently been studied in detail for single-crystalline  $\text{PrIn}_3$ . The case is briefly discussed in sect. 3.8.

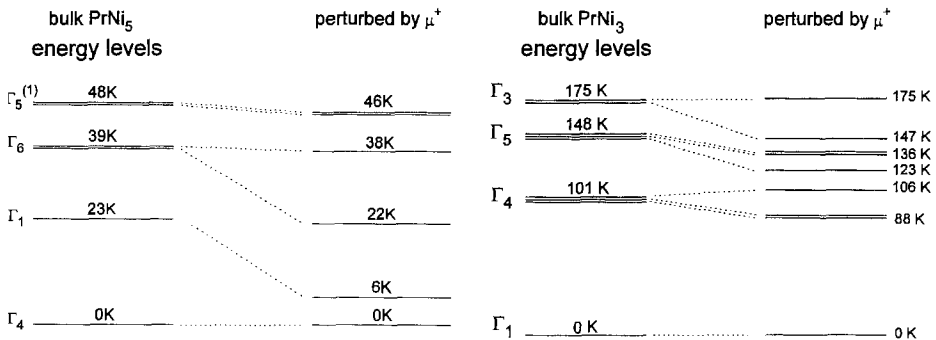


Fig. 39. Muon-induced perturbation of  $\text{Pr}^{3+}$  CEF levels deduced from  $\mu^+$  Knight shift measurements in singlet-ground-state  $\text{PrNi}_5$  (left panel, Feyerherm et al. 1995) and  $\text{PrIn}_3$  (right panel, Tashma et al. 1997).

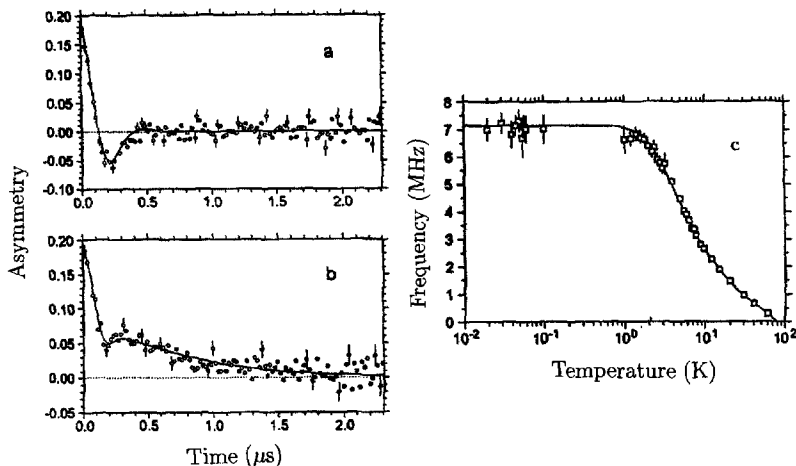


Fig. 40. Spontaneous ZF- $\mu$ SR oscillation in single-crystal PrCu<sub>2</sub>: (a) at 15 K with muon polarization along the *b*-axis; (b) similar data, but with the muon polarization along the *c*-axis; (c) temperature dependence of precession frequency (Schenck et al. 1998b).

5.1.2.4. *PrCu<sub>2</sub>*. This is a singlet ground-state compound with a Jahn–Teller distortion transition at 7.3 K (Wun and Phillips 1974), apparently induced by coupling between the Pr quadrupole moments. Only nuclear magnetic ordering occurs, at 54 mK (Andres et al. 1972, Kawarazaki and Arthur 1988). A metamagnetic transition in applied fields has been seen by Ablitz et al. (1997). Schenck et al. (1997a) report on the muon Knight shift at 12 K, which drops from the very large value of  $\sim 10\%$  for TF = 100 G to less than 1% in TF = 1 kG. This is an effect not seen in bulk susceptibility, so the authors again discuss a muon-induced effect on nearby Pr ions. Later, Schenck et al. (1998b) reported on a spontaneous spin precession in ZF (as shown in fig. 40) persisting up to 60 K. There is no change in signal near 50 mK and only a subtle change in relative strength of oscillating *vs.* monotonic signal near 7.3 K. As in PrNi<sub>5</sub> (see above) and HoBa<sub>2</sub>Cu<sub>3</sub>O<sub>7</sub> (see below), the ZF- $\mu$ SR signal suggests magnetic ordering in a singlet ground state system, when no other probe does. Schenck et al. (1998b) discuss how difficult it is to attribute the spontaneous oscillation to muon induced effects.

5.1.2.5. *PrP<sub>x</sub>*. Stoichiometric PrP is a singlet ground state material without magnetic ordering. Phosphorus-deficient PrP<sub>*x*</sub>, *x*  $\approx$  0.9 with the same crystal structure, has been reported to be a spin-glass (Hasanain et al. 1981) below 9 K. It was asserted that phosphorus vacancies adjacent to Pr ions shift the CEF levels so that the ground state becomes magnetic. Thus, moments are induced on those Pr ions that have nearest-neighbor P vacancies (Yoshizawa et al. 1983). Recent  $\mu$ SR measurements (Noakes et al. 2000) on PrP<sub>*x*</sub> samples did not show evidence of spin-glass freezing and neither did susceptibility data carried out on the same specimens. The  $\mu$ SR spectra exhibited strong-collision dynamics on Lorentzian field distributions (see the discussion of eq. (38) in

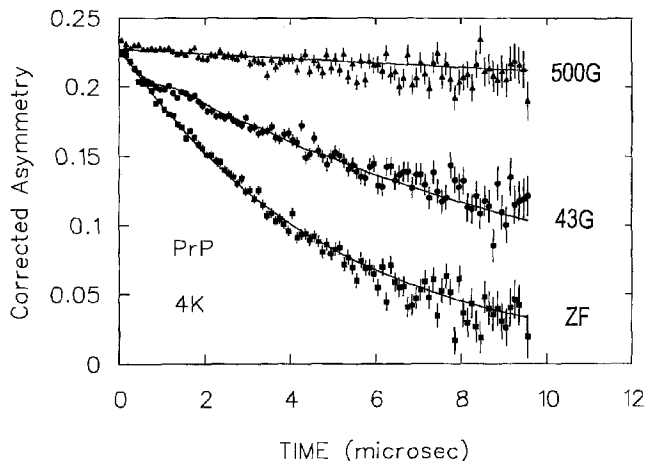


Fig. 41. ZF and LF- $\mu$ SR in nominally stoichiometric PrP at 4 K. Solid lines are fits of strong-collision-dynamic Lorentzian Kubo–Toyabe relaxation (Noakes et al. 2000).

sect. 3.2.3), even for a nominally stoichiometric sample. Figure 41 shows an example. The only other known cases of this involve high-symmetry muon sites in “triple- $k$ ” cubic antiferromagnets USb and DyAg (sect. 5.2). Here, however, the materials are paramagnetic with a tendency to spin-glassiness. The field distribution HWHM decreases smoothly as temperature rises, up to at least 50 K (the scale of the first CEF excited state of a Pr beside a P vacancy, Yoshizawa et al. 1983), while the fluctuation rate remains roughly constant. Noakes et al. (2000) have developed a model in which the dilute spins generating the Lorentzian field distribution are the fraction of  $\text{Pr}^{3+}$  ions that happen to be briefly in the (magnetic) first excited state, the majority in the singlet ground state being nonmagnetic.

5.1.2.6. *PrRu<sub>2</sub>Si<sub>2</sub>*. This non-cubic singlet ground state intermetallic (hexagonal  $\text{ThCr}_2\text{Si}_2$  structure) is characterized by a very large magnetic anisotropy (Shigeoka et al. 1992). Two different  $\mu$ SR studies have appeared. The more recent one by Mulders et al. (1997) combines single-crystal magnetization, Mössbauer spectroscopy, neutron powder diffraction and inelastic neutron scattering with  $\mu$ SR spectroscopy. The earlier work by Yaouanc et al. (1994) did not discuss the aspect of a singlet ground state but claimed that the somewhat unusual  $\mu$ SR results are an outcome of the large  $c$ -axis anisotropy without providing any theoretical analysis.

*PrRu<sub>2</sub>Si<sub>2</sub>* does not display “classic” singlet ground state behavior, mainly because the ordering temperature ( $\sim 15$  K) is slightly above the first excited CEF state (according to Mulders et al. 1997). We shall discuss this compound within the reviews on  $\mu$ SR results on other (i.e., non-singlet ground state) members of the  $\text{RT}_2\text{X}_2$  family in sect. 5.5.2.

5.1.2.7. *HoBa<sub>2</sub>Cu<sub>3</sub>O<sub>7</sub>*. By now it is clear that praseodymium is the rare earth most likely to be involved in singlet ground state magnetism, and that  $\mu$ SR can be difficult to understand in that case. The other integer-spin trivalent rare earths

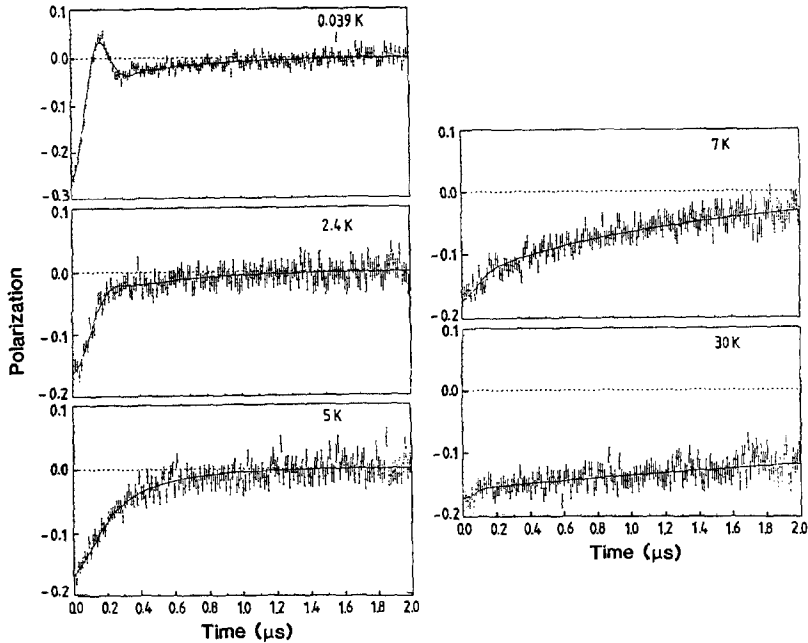


Fig. 42. ZF- $\mu$ SR asymmetry spectra from  $\text{HoBa}_2\text{Cu}_3\text{O}_7$  (Birrer et al. 1989b), showing that there is slowly freezing local field at the muon site deep inside the superconducting state ( $T_c > 90$  K) even though Ho has a singlet ground state which suppresses even short-range magnetic ordering to 0.14 K. The negative initial polarization is an artifact of the measurement geometry, and initial asymmetry is different at the lowest temperature because a different apparatus was used.

occasionally also have singlet ground states and low ordering temperatures. Among the  $T_c > 90$  K superconducting  $\text{RBa}_2\text{Cu}_3\text{O}_7$  materials discussed in sect. 7.2.2, with coexistent antiferromagnetic orderings below 2 K (except when  $R = \text{Pr}$ , which is magnetic, not singlet ground, and not superconducting at all, as discussed in that section),  $R = \text{Ho}$  has a singlet ground state, resulting in no long-range magnetic ordering down to mK temperatures. Neutron scattering sees a SRO magnetic structure beginning at 0.14 K. With ZF  $\mu$ SR, however, Birrer et al. (1989b) saw a slowly fluctuating local field distribution to temperatures above 30 K (fig. 42). They interpreted the minimum and recovery that developed below 5 K as spontaneous precession in a long-range antiferromagnetic state with 5 K as the transition temperature. Given the lack of any corroboration from any other probe, re-interpretation in terms of Kubo–Toyabe relaxation with slow dynamics may be appropriate, but even then, the persistence of a detectable local field at the muon to above 30 K is unusual (and is not seen in  $\mu$ SR of the other  $\text{RBa}_2\text{Cu}_3\text{O}_7$ 's, at full oxygenation).

### 5.1.3. Muon-induced effects

We have already pointed out the possibility of muon-induced effects in sect. 2.4, in general terms. In the last section evidence for the actual occurrence of such effects

in some lanthanide magnetic materials has been presented. Their presence is a mixed blessing for  $\mu$ SR as a field of research. It is a boon for those interested in point-defect effects, and particularly for those interested in the effects of trapped hydrogen ions on magnetism, and in the hybridization process. For these investigators, the  $\mu^+$  provides a signal from the isolated impurity itself in an otherwise pristine host. The same thing is a problem, however, for the larger number of researchers who would like  $\mu$ SR to provide information on the magnetism of the pristine host itself, as if the muon causes no disturbance. At present, the evidence is that the muon-induced effects in singlet-ground systems are amplified by the delicate magnetic balance of that state. In contrast, in strongly paramagnetic R materials such as  $\text{TbNi}_5$ , the  $\mu$ SR magnetic response can be explained fully by using the CEF level scheme determined by other methods (see fig. 27).

In general, one may state that the influence of the muon magnetic moment can be neglected, but not the influence of its charge and the resulting local field gradient and lattice distortion. Even then, one may expect trouble mainly in cases where the specific sample magnetic properties result from a near balance of electric and magnetic (exchange or dipolar) interactions. The prominent case of electric interactions is the CEF coupling as discussed above, but other types of interactions can also play a role, for example quadrupolar couplings. For the Pr singlet-ground systems of the previous section, surprising spontaneous ZF- $\mu$ SR oscillations occur for the ones with the smallest CEF first-excited state energy before the muon arrives (3 K to 5 K in  $\text{PrCu}_2$ , Ahmet et al. 1996, 23 K in  $\text{PrNi}_5$ , fig. 39), while the Knight shift studies indicated the muon moves the CEF levels of its immediate Pr neighbors up or down about 20 K. Meanwhile for Pr metal (CEF first excited  $\geq 30$  K, Lebech et al. 1975) and paramagnetic  $\text{PrP}_x$  (first excited  $\geq 50$  K) there is no spontaneous ZF oscillation.

Muon-induced effects are sometimes invoked in a number of heavy-fermion and related systems where  $\mu$ SR led to the worrisome discovery of anomalously small but non-zero magnetic moments (see sect. 9). In some instances these moments are below  $10^{-2} \mu_B$ , which makes them undetectable by other methods, except by resonant photon scattering in the light actinides. Full confirmation of small moments first detected by  $\mu$ SR occurred in cases where those moments had reached a size ( $\mu \approx 5 \cdot 10^{-2} \mu_B$ ) accessible to neutron scattering under favorable conditions. So, extremely small moment magnetism is in all likelihood an intrinsic property of many heavy-fermion compounds.

## 5.2. Simple cubic compounds

We will first discuss  $\mu$ SR studies on compounds of the form MX (where M is a R or An and X either a pnictide, a chalcogenide, or a noble metal), which crystallize either in the NaCl or CsCl cubic structures. This will be followed by an overview of  $\mu$ SR results in  $\text{MX}_3$  compounds crystallizing in the cubic  $\text{AuCu}_3$  structure. Most  $\mu$ SR data are available for the NaCl systems. The An materials are restricted to U compounds.

The compounds to be treated often exhibit quite unusual magnetic properties. One of those features is the formation of "multi- $k$ " AFM spin structure. Since they play a central role, we start out with a brief explanation of what is meant by this terminology. Multi- $k$

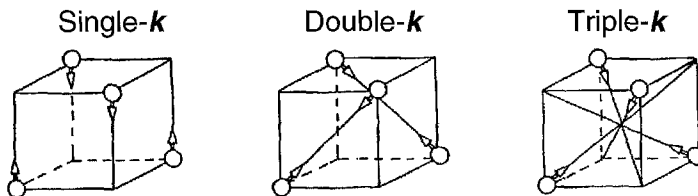


Fig. 43. Multi- $k$  spin structures for a MX compound with fcc crystal structure and type-I AFM ordering. The picture shows only the M ions (which carry the magnetic moments) in a quarter of the unit cell. Adapted from Rossat-Mignod (1987).

structures were originally proposed for transition metal compounds (Kouvel and Kasper 1963), but their breakthrough came from the neutron scattering work of J. Rossat-Mignod and his group especially on the NaCl type Ce and U compounds (see, for example, Rossat-Mignod et al. 1980a). To understand the multi- $k$  problem, one must remember that a magnetic neutron diffraction measurement gives information on the *Fourier components*  $m_k$  of the total magnetic moment  $m_n$  of the ion ( $n$ ). The moment then is obtained from the Fourier sum (for details see Rossat-Mignod et al. 1984 or Rossat-Mignod 1987)

$$m_n = \sum_k m_k \exp[-ik \cdot R_n]. \tag{64}$$

In a cubic structure one has three wave vector components  $k_1 = [k00]$ ,  $k_2 = [0k0]$  and  $k_3 = [00k]$  and the question is, over how many components  $m_k$  one must perform the sum in eq. (64). We demonstrate the situation with the help of fig. 43, depicting the basic situation in a fcc AFM of type I (propagation vector (001)).

The spin arrangement in a  $1k$  structure is collinear and the moments point along one of the cubic (100) axes. The  $2k$  and  $3k$  structures are non-collinear with the moments pointing along the face diagonals (110) in the  $2k$  and along the body diagonals (111) in the  $3k$  case. Those multi- $k$  structures exist of course for different propagation vectors, e.g., also for the type IA structure with  $(00\frac{1}{2})$ . Symmetry requires that in a crystal with only one type of magnetic ion in identical fully cubic surroundings, all Fourier components must be of the same magnitude. From a diffraction experiment that measures scattered *intensities* (like neutron diffraction), no information can be obtained on the phase factor in eq. (64). One must choose reasonable phase values that lead to a spin structure consistent with bulk data. Even more serious is the problem that neutron diffraction cannot easily differentiate between  $1k$ ,  $2k$ , or  $3k$  structures. All three cubic axes are equivalent and even in a single-crystal specimen randomly oriented due to the domain structure. A decision as to which kind of spin structure is present requires the violation of cubic symmetry which can be done either by applying a reasonably intense external field (that, however, could alter the spin arrangement) or uniaxial stress, but a single-crystalline sample is still needed. One special feature is: in a  $3k$  structure the cubic symmetry cannot be lowered by magnetostriction while the  $1k$  and  $2k$  spin lattices induce small distortions (mostly tetragonal). Jensen and Bak (1981) pointed out that the spin wave spectrum differs noticeably between  $1k$  and  $3k$  spin arrangements.

The compounds formed with the so-called “anomalous f-elements” show variation of magnetic moment with either lattice constant, or electronic structure of ligand ions, or both, as another characteristic magnetic property. This feature is, of course, not restricted to cubic compounds, but it is especially visible in this class of intermetallics and has most thoroughly been studied there. The term “anomalous f-element” refers mainly to  $R = \text{Ce, Yb}$  and  $An = \text{U, Np, Pu}$ . The anomaly is that the f orbital might not be strictly localized at the R or An ion. We have mentioned such properties already in discussing CEF effects (sect. 5.1.1). This f electron delocalization in turn weakens the orbital magnetic moment. In cases presented here, the ordered moment is known from other data (mainly neutron scattering). The  $\mu\text{SR}$  magnetic parameters then give hardly any additional insight into the degree of f electron delocalization. As mentioned in the first section,  $\mu\text{SR}$  is not a good technique to study such effects. We nevertheless briefly discuss this issue since it forms an essential part of the magnetic properties of the compounds under discussion. The fundamental mechanism responsible for f electron delocalization are either the direct overlap of f electron wave functions or hybridization of f electron states with ligand electron orbitals. The former mechanism is the basis of the so called “Hill model” (Hill 1970). It predicts a critical R–R (or An–An) separation, the “Hill limit”, below which magnetic order no longer occurs (but superconductivity may be present instead). The f electrons have fully itinerant character. Above the Hill limit the f electrons begin to localize on the R or An ion and for large separations the (standard R) fully localized picture applies, producing the free ion moment even in compounds. Characteristic is the monotonic rise of transition temperature and ordered moment with increasing R–R (An–An) separation. The most typical example of “Hill compounds” are the Laves phases  $AnX_2$  (see sect. 5.3.1). The influence of hybridization with ligand electrons cannot be described in such a simple model. For isostructural compounds with isoelectronic ligands, the lattice parameter (reflecting the bond length) is the crucial quantity. Otherwise, details of ligand electron structure can have a profound influence. Similarly, the crystal structure and even the ordered spin structure may influence the magnitude of magnetic moments. Magnetism with marked dependence on ligand electrons can be found in the NaCl compounds (next section) and in intermetallics with the  $\text{AuCu}_3$  crystal structure (see sect. 5.2.3). In conducting compounds one also observes hybridization of f electrons with the conduction electrons. This leads to Kondo-lattice and heavy-fermion behavior, which will be discussed in sect. 9.

### 5.2.1. NaCl structure

The majority of  $RX$  and  $AnX$  compounds with X being a pnictide (N, P, As, Sb, Bi) or a chalcogenide (S, Se, Te) crystallize in the NaCl fcc cubic crystal structure. The materials formed with the anomalous f-elements have played a central role in unravelling the electronic structure properties where the f-electron orbitals are partially delocalized from the R or An ion. As mentioned, hybridization with ligand electrons is the important ingredient for the NaCl compounds. Rather complex spin structures are often present despite the simple crystal structure. The latter does ease the theoretical interpretation,

especially since crystal structure parameters do not change dramatically throughout series with either different f-ions or ligands. Furthermore, isostructural pseudo-binaries are easily formed in most cases. Then the Fourier components  $m_k$  need no longer be of equal amplitude. Last but not least, the technology of growing relatively large single crystals has been perfected, including actinide compounds (Spirlet and Vogt 1984). Maintaining strict 1:1 stoichiometry can sometimes be a problem. The ease of forming pseudo-binaries allows magnetic dilution with Y, La, Lu or Th over the full concentration range. For U compounds the monochalcogenides are FM, while the monopnictides are AFM. Mixtures of these, which are likewise possible, can lead to rather complex magnetic structures. One may ask: why complicate the matter artificially? The answer is that such studies give detailed insight into the interplay of the various interactions (e.g., isotropic *vs.* anisotropic exchange, CEF interactions and direct quadrupolar couplings) to which the magnetic ion is subjected.

The most comprehensive review on bulk properties of the monopnictides and monochalcogenides has been given by Vogt and Mattenberger (1993). It compares, in particular, the properties of corresponding R and An compounds. Results on R monopnictides have been critically reviewed by Hulliger (1979). Magnetism of the An members is summarized in the already mentioned review by Fournier and Troć (1985). An overview of the theoretical approach in dealing with the compounds of anomalous f-elements has been presented by Cooper et al. (1985, see also Lam and Ellis 1985).

$\mu$ SR data are available nearly exclusively for Ce and U compounds and predominantly for the pnictides. In presenting those results we shall deviate from our usual scheme. We first discuss the U materials and among them first UAs. This allows a most direct outlay of the central problems looked at by  $\mu$ SR. Table 5 summarizes some basic magnetic parameters of the U and Ce compounds with NaCl structure studied by  $\mu$ SR. These materials are low-carrier-concentration conductors (exact numbers on specific resistance are highly sensitive to sample purity and stoichiometry). The coefficient of electronic specific heat (Sommerfeld constant  $\gamma$ ) is somewhat enhanced compared to normal metals. It becomes large when scaled to the concentration of conduction electrons. Since a large  $\gamma$  is a characteristic quantity for heavy-fermion (HF) systems, one treats these compounds on occasion as low-carrier HF systems (see sect. 9). We do not follow this scenario, especially since  $\mu$ SR has not added any relevant information on this approach.

The muon position is well-established as the  $(\frac{1}{4}, \frac{1}{4}, \frac{1}{4})$  (or equivalent) interstitial site (see fig. 46 and discussion in the paragraph on UAs). Measurement on the diamagnetic compound ThAs (Münch 1991) established a stationary muon up to  $\sim 250$  K, which makes the magnetic relaxation data reliable. The original goal of the work on NaCl compounds was to study the  $\mu$ SR response in more complex AFM structures (especially the multi- $k$  structures), since at the time little was known in this field. As it turned out, and as will be shown in the following,  $\mu$ SR gave additional information on the magnetic behavior of the NaCl-type compounds, some of which still defies understanding. It is also an extension of the Mössbauer studies on related Np compounds (see Potzel et al. 1993), because U is a poor Mössbauer candidate.



Table 5  
Important magnetic parameters of NaCl-type R and An compounds for which  $\mu$ SR data are available

Comp.	LC <sup>a</sup> (Å)	$\mu_{\text{Curie}}^b$ ( $\mu_B$ )	$T_N$ (K)	$T_C$ (K)	Propagation vector	Spin structure	Easy axis	$\mu_{\text{ord}}$ ( $\mu_B$ )
CeAs	6.078	2.82	8	–	(001)	1k,3k type I (?) <sup>c</sup>	(001)	0.7
CeSb	6.412	2.56	16	–	inc <sup>e</sup>	complex <sup>d</sup>	(001)	
			<9		(00 $\frac{1}{2}$ )	1k type IA	(001)	2.0
DySb	6.14	9.75	9.5	–	( $\frac{1}{2}, \frac{1}{2}, \frac{1}{2}$ )	1k type II	(100)	9.8
UN	4.890	2.66	53	–	(001)	1k type I	(001)	0.75
UP	5.589	3.56	122	–	(001)	1k type I	(001)	1.7
			22.5	–	(001)	2k type I	(110)	1.9
UAs	5.779	3.4	124	–	(001)	1k type I	(001)	1.9
			62	–	(00 $\frac{1}{2}$ )	2k type IA	(110)	2.25
USb	6.191	3.64	213	–	(001)	3k type I	(111)	2.85
US	5.489	2.35	–	177	0	simple ferro	(111)	1.7
UTe	6.155	2.6	–	104	0	simple ferro	(111)	2.25

<sup>a</sup> Lattice constant.

<sup>b</sup> Free ion values: 2.54(Ce<sup>3+</sup>), 10.6(Dy<sup>3+</sup>), 3.8(U<sup>3+</sup>).

<sup>c</sup> See  $\mu$ SR results.

<sup>d</sup> Several transitions into different complex structures occur sequentially.

<sup>e</sup> Several incommensurate propagation vectors.

5.2.1.1. *UAs*. Two first-order magnetic transitions take place. The first ( $T_N = 124$  K) leads into a simple collinear ( $1k$  type I), the second ( $T_I = 62$  K) into a more complex non-collinear ( $2k$  type IA) AFM spin structure (Rossat-Mignod et al. 1980b). The transitions must be coupled to tetragonal distortions with  $c/a < 1$  below  $T_N$  and  $c/a > 1$  below  $T_I$ . Slightly above  $T_N$ , inelastic neutron scattering by Sinha et al. (1981) found strongly anisotropic dynamic ISDW correlations. Before a spin-density-wave ordered state can be formed it becomes unstable and undergoes the first-order Néel transition into the type I  $1k$  state.

$\mu$ SR data in TF, ZF and LF were collected for a sample consisting of a conglomerate of non-oriented single-crystal platelets (Asch et al. 1986b, 1987, 1989, Kratzer et al. 1990). Figure 44a depicts the temperature variation of the TF muon spin relaxation rate with two step-like changes. One is at  $T_N$ , and in addition a sudden change in rate occurs at 190 K. Above this temperature the rate is low. ZF spectra show a corresponding weak Gaussian decay of muon spin polarization ( $\Delta \approx 0.1 \mu\text{s}^{-1}$ ). It can be suppressed largely by a LF = 10 G and is caused by <sup>75</sup>As nuclear dipoles. The remaining exponential relaxation is extremely weak ( $\lambda \approx 0.01 \mu\text{s}^{-1}$ ) and proves that strong motional narrowing is in effect for the U moments. One estimates  $1/\tau_f \approx 10^{13}$  Hz. These spectra mirror the free paramagnetic state. The Gaussian shape of depolarization in ZF is lost below 190 K, where also the sudden change in both the TF and ZF relaxation occurs. The new spectral shape remains practically unaltered down to  $T_N$  and is due to an increase of relaxation caused by

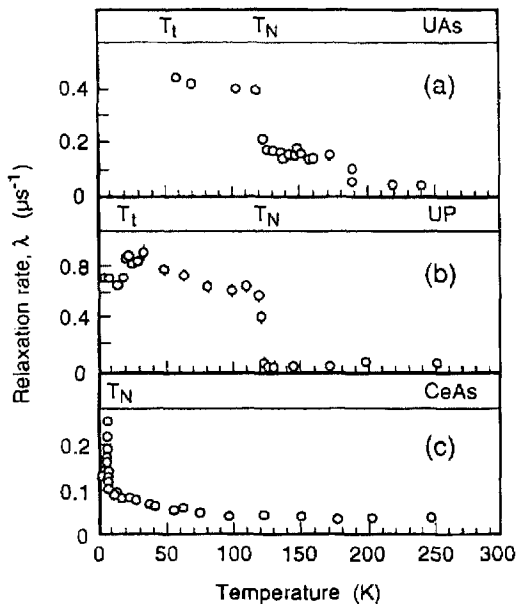


Fig. 44. Temperature dependences of TF (200 G) relaxation rates in (a) UAs, (b) UP and (c) CeAs. The magnetic transitions in UAs and UP are first-order, that in CeAs is second-order. The jump in rate in UAs at 190 K reflects the formation of a paramagnetic precursor state (see text). From Asch (1989).

the U electronic moments (while the relaxation due to nuclear moments remains constant, as expected). A paramagnetic precursor state is formed in which spin correlations slow down the fluctuation rate of U spins. μSR picks up this state already at much higher temperatures than neutron scattering. Such a sharp onset of a precursor state is unusual

The TF signal can be followed into the  $1k$  type I state without any significant loss of amplitude and with only a sudden change of frequency ( $\Delta\nu/\nu \approx 0.1\%$ ) at  $T_N$ . Furthermore, in ZF no spontaneous spin precession is seen. Clearly, the mean value of the internal field at the muon site must be zero in ZF, despite LRO of the spin system. The full cancellation of all contributions to the internal field is possible in an AFM if the muon occupies a site of high local symmetry. For MX compounds with the fcc NaCl structure, the only possible site is the  $(\frac{1}{4}, \frac{1}{4}, \frac{1}{4})$  interstitial position (and the other equivalent sites) at the center of a cube formed by four M and four X ions (see fig. 46). Such highly symmetric muon stopping sites are characteristic for fcc structures. The best known example is Ni metal. It, however, is a ferromagnet and due to the uniform spontaneous magnetization only the dipolar, but not the contact, field contribution cancels and  $B_\mu \neq 0$  (see, for example, Denison et al. 1979). To eliminate also the contact field from surrounding moments (i.e., to have  $B_\mu = 0$ ) requires the presence of the staggered magnetization of an antiferromagnet. Antiferromagnetism furthermore allows even weak external fields to enter the bulk of the sample. It can be shown that the perfect field cancellation in UAs is independent of the tetragonal distortion that must be present, but, in consequence, is not visible in μSR.

The ZF spectra of the  $1k$  type I state in UAs take the form a weakly decaying Lorentzian Kubo–Toyabe function. An example is depicted in fig. 45. LF measurements show the

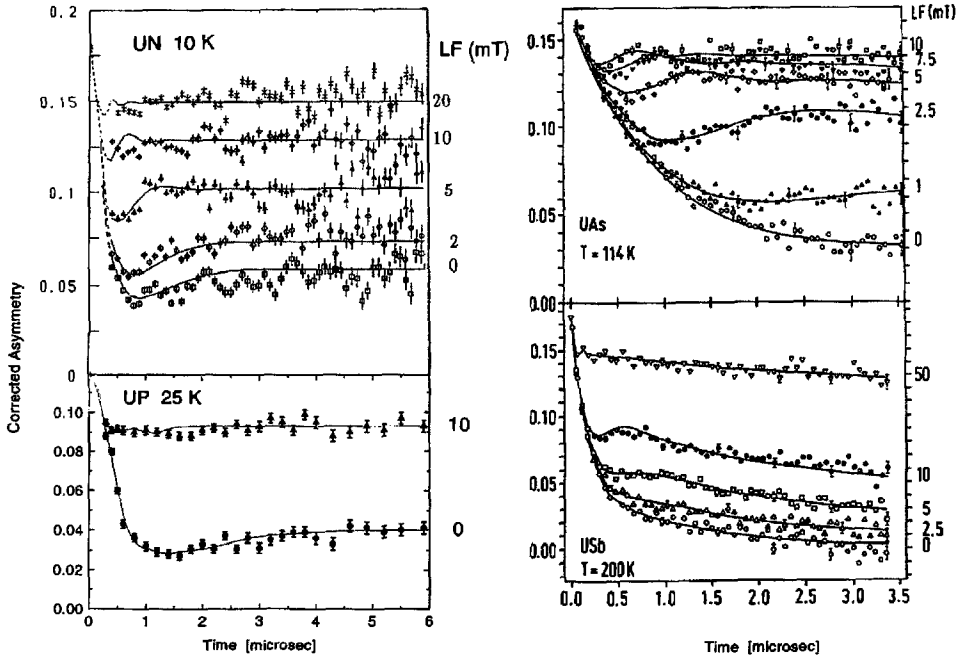


Fig. 45. ZF and LF spectra of different uranium NaCl-type compounds (UN, UP, UAs, USb) below their Néel temperatures. The fits to the data are Lorentzian Kubo–Toyabe functions (static for UN, UP and UAs, dynamic for USb (see discussion in text). Extended from Asch (1990).

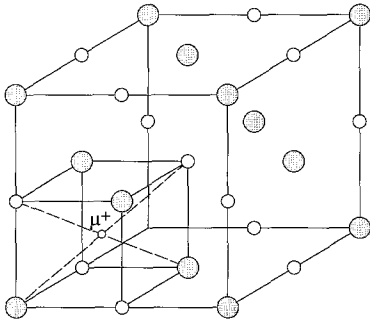


Fig. 46. Crystal structure (unit cell) and muon location for NaCl-type compounds MX. Solid circles, M atoms; open circles, X atoms.

relaxation to be essentially static down to  $T_t$ . Similarly, the field distribution width remains constant. From the presence of a Kubo–Toyabe spectral shape one concludes that a field distribution exists around the mean field  $B_\mu = 0$ . The sources of this field distribution must be dilute according to its Lorentzian shape. The proposed explanation is the presence of occasional faults in the AFM spin structure. These faults disturb the perfect cancellation of internal field contributions and hence act as dilute sources of field. We return to this spectral response in a separate paragraph further below.

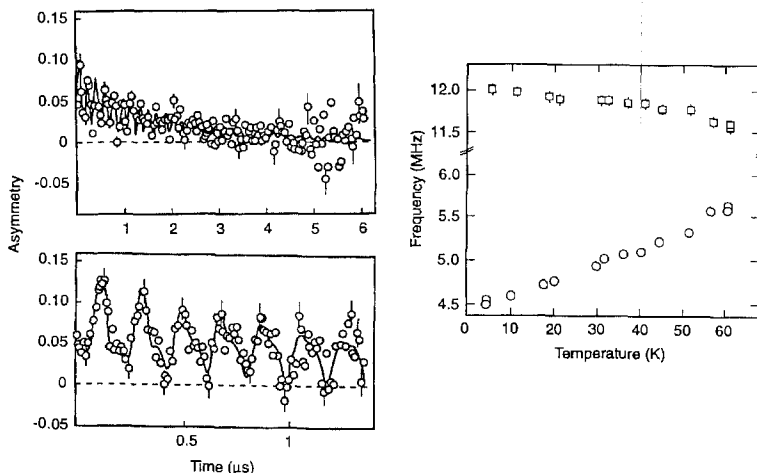


Fig. 47.  $\mu$ SR data of the  $2k$ -type IA AFM phase in UAs. Left: ZF spectrum showing two spontaneous precession frequencies and a non-precessing signal. The lower part shows the early portion of the spectrum. Right: Temperature dependences of the two precession frequencies. From Asch et al. (1987).

The situation changes dramatically at  $T_t$ . Now the spectra consist of a spontaneous spin precession signal containing two frequencies (about 5 and 12 MHz) in addition to a non-oscillating exponentially decaying signal (fig. 47, left). Taking into account that the oscillating sub-signals contribute 1/3 of their intensity to the non-oscillating pattern, one deduces the intensity ratios of 1:2:1 for the three signal components. Obviously, in the  $2k$  type IA structure, the various contributions to the local field no longer cancel. This can be verified by dipolar sum calculations which show, in addition, that the presence of a final value of  $B_{\mu}$  is strictly coupled to the presence of a tetragonal distortion.  $\mu$ SR gave the first definite evidence for the existence of the tetragonal distortion, which is required from theoretical considerations, but had eluded detection by X-ray and neutron scattering. More recently a value of  $c/a = 1.0002$  has been found using synchrotron X-rays (McWhan et al. 1990). To emphasize once more: the appearance of a local field is due to the switch from the  $1k$  to the  $2k$  arrangement together with the change in propagation vector from type I to type IA (coupled to lattice distortion). Crystallographically, only the one muon site  $(\frac{1}{4}, \frac{1}{4}, \frac{1}{4})$  exists. According to the dipolar calculations it splits into three magnetically different subsites, of which two have a final value of local dipolar field and the third no dipolar field contribution. Also, the experimentally observed intensity ratios are verified. The ratio between the two different dipolar fields is predicted to be  $\sqrt{2}$ . The experimental value of the ratio of the total internal fields is larger. This is not astonishing since the contact field contributions have been neglected. Quite astonishing is the observation of a distinct temperature dependence of the two precession frequencies (fig. 47, right). This contradicts the rigid spin lattice that is usually assumed. The most likely scenario is a small turning of spin directions from the ideal  $2k$  type IA spin alignment. A quantitative evaluation has not been given and the problem remains unsolved. One might mention that

magnetic phonon scattering (McWhan et al. 1990) sees a decrease in distance between  $+-$  spin pairs and an increase between adjacent  $++$  or  $--$  pairs in the type IA ( $++--$ ) structure *via* a charge modulation of the lattice. Still, if this modulation is the cause, then it must vary with temperature. We remind the reader of similar observations of changes of  $\mu$ SR precession frequencies in some elemental metals, most notably in the FM state of Er metal (see sect. 4), which also have defied explanation thus far.

5.2.1.2. *UN*. A single second-order transition ( $T_N=53$  K) into an antiferromagnetic  $1k$  type I state is reported (Rossat-Mignod et al. 1984). The  $\mu$ SR data (Münch et al. 1993) in the paramagnetic state reveal that the fluctuations of the moments on uranium are too fast to produce any sizable muon spin depolarization even close to  $T_N$ . A magnetic precursor state is not formed. In the AFM phase one observes in ZF a Lorentzian Kubo–Toyabe as in the corresponding state of UAs. LF data show the spin system now to be quasistatic (fig. 45). The width of the Kubo–Toyabe spectra changes little with temperature below  $T_N$ .

Bulk magnetic data under applied pressure (Fournier et al. 1980) gave strong evidence for itinerant magnetism in UN, in contrast to UAs (and UP), where f electron itinerancy is weak, if present at all. The  $\mu$ SR data for the comparable AFM structure in UAs is not fundamentally different from that of UN, which lends direct evidence to the statement made earlier that  $\mu$ SR is not particularly sensitive to 5f electron delocalization.

5.2.1.3. *UP*. A collinear  $1k$  type I AFM state is formed below the first-order Néel transition ( $T_N=122$  K), which changes at  $T_t=22.5$  K (also first-order) into the non-collinear  $2k$  type I phase. The transitions clearly appear as step-like jumps in the TF relaxation rate (Aggarwal et al. 1989) shown in fig. 44b. Full cancellation of all internal field contributions occurs for the  $2k$  state as well, since, in contrast to UAs, the magnetic propagation vector does not change. Hence one observes in ZF (and LF) a Lorentzian Kubo–Toyabe pattern (fig. 45). The spin system is again quasistatic throughout, including the transition range. The width increases slightly between  $T_N$  and  $T_t$ , as does the TF relaxation rate.

5.2.1.4. *USb*. Only one AFM state ( $3k$  type I) is formed below the second-order transition  $T_N=214$  K. The mean local field vanishes also for the non-collinear  $3k$  type I spin structure and in ZF one observes (Asch 1990, Asch et al. 1990b) again Lorentzian Kubo–Toyabe spectra below  $T_N$  (see fig. 45). The main difference in spectral response compared to the  $1k$  and  $2k$  states (UN, UP, UAs) is a distinct variation of width ( $\Delta$ ) and fluctuation rate ( $\nu$ ) with temperature as demonstrated in fig. 48. One finds a clear increase in  $\Delta$  with rising temperature leading to a maximum around 150 K. At this temperature the field fluctuation rate  $\nu$  suddenly rises dramatically on approaching  $T_N$ .  $T = 150$  K appears as a distinct temperature in various studies of USb. The electrical resistivity shows a broad maximum and likewise the slope of the temperature dependence of the Hall coefficient changes (Schoenes et al. 1984). These observations were confirmed in a carefully annealed high-purity sample (Ochiai 1996) and are thus not an impurity effect

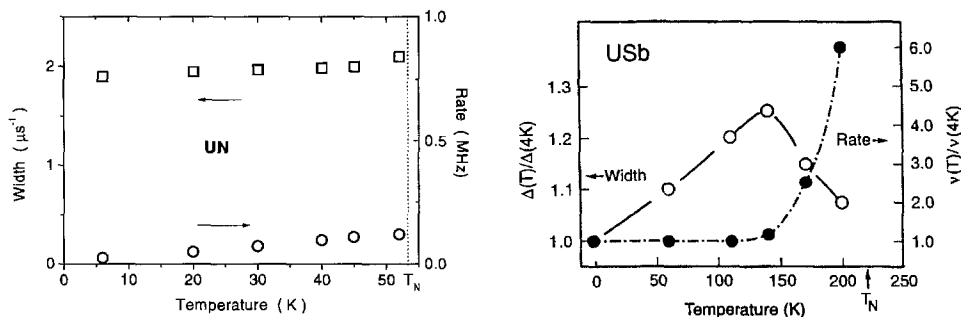


Fig. 48. Comparison of the temperature dependence of width  $\Delta$  (open symbols) and field fluctuation rate  $\nu$  (solid symbols) derived from fits to the Lorentzian Kubo–Toyabe spectra of UN (left) and USb (right). For UN the absolute values, and for USb the reduced values of parameters are plotted. At  $T \ll T_N$  width and rate for the two compounds are comparable. The lines are guides to the eye. Adapted from Münch et al. (1993) and Asch et al. (1994).

as sometimes suggested. Near 150 K neutron scattering shows a collapse of spin wave excitations into a broad peak centered at zero frequency together with a crossover from dispersive to diffusive motion (Hagen et al. 1988). Asch (1990) and Asch et al. (1994) interpret the  $\mu$ SR results as follows. At low temperatures, the phases of the Fourier components of the magnetic moment are rigidly locked to produce the  $3k$  spin lattice. As the temperature rises, excitations within the spin lattice de-lock the phases and irregularities in the AFM spin sequence occur, which produce the increase in  $\Delta$ . The disturbances propagate diffusively and the onset of this motion is reflected in the rate  $\nu$ . (The reader should be reminded that magnetic excitations such as spin waves have frequencies well beyond the  $\mu$ SR time window). Most likely, these disturbances of the spin lattice begin to propagate diffusively beyond 150 K and the onset of this motion is reflected in the rise of rate  $\nu$ . Thus, we have two fundamentally different situations concerning the effects of dynamics in the spin ensemble. At low temperatures, high-frequency spin wave excitations are present. Those *fast* spin dynamical processes are fully decoupled from the muon spin and depolarization (width  $\Delta$ ) is caused by static disorder. At higher temperatures, in the diffusive regime, spin dynamics are *slow* enough to affect the muon spin relaxation function leading to a change in effective width. The relaxation process cannot be described simply within the frame of the strong-collision model. The fact that the general Lorentzian shape is not lost means that the disturbances of the  $3k$  spin lattice by phase de-locking remain dilute up to  $T_N$ . They thus can easily escape detection by bulk techniques. The salient feature pointed out by Asch et al. (1994) is that  $\mu$ SR detects *slow propagative* motions in the spin system due to its unique time window and sensitivity at zero energy transfer. Such motions, if they exist, can lead to motional averaging and might explain why sometimes rather simple  $\mu$ SR spectra are observed in materials with complex spin structure (see discussion on hard magnetic materials in sect. 6.4).

Critical divergence of relaxation rate at the second-order Néel point (Nutall et al. 1997) has been reported. This work (which to our knowledge has not been published) mentions

that the shape of the relaxation spectra just above  $T_N$  is not exponential. Two muon sites are offered as an explanation, but the authors do not discuss the more obvious possibility of electron (U moments)–nuclear (Sb moments) double relaxation.

*5.2.1.5.  $\mu$ SR response in AFM simple cubic compounds.* From the experiments discussed thus far for the various UX compounds, we can extract a number of basic results. It will become apparent in the next two sections that these are valid not only for the NaCl compounds but for CsCl and AuCu<sub>3</sub> materials as well.

- (i) The muon stops at a place of high local symmetry (e.g., the  $(\frac{1}{4}, \frac{1}{4}, \frac{1}{4})$  interstitial position in the fcc lattice).
- (ii) At this site the mean local field is zero for collinear ( $1k$ ) and non-collinear ( $2k$  and  $3k$ ) type I structures. In a type I spin lattice this holds even in the presence of tetragonal distortions (which are required by theory for the  $1k$  and  $2k$  states).
- (iii) Dilute disturbances in the LRO spin system cause a weak field distribution of Lorentzian shape.
- (iv) This field distribution is essentially static and its HWHM is little dependent on temperature throughout the full ordered regime in case of a  $1k$  spin arrangement. In contrast, the  $3k$  structure shows an increase in both width and field fluctuation rate when approaching the transition temperature from below.

Condition (ii) can be fulfilled in other crystal structures on occasion as well. An AFM state is usually a condition, since, as mentioned, the contact field will not vanish in a FM material (but is present only in conducting compounds). The important point is that in an AFM spontaneous spin precession can be absent although LRO of the spin system exists. The strict consequence of (ii) would be a non-depolarizing  $\mu$ SR signal in ZF. But in nearly all cases the field distribution (iii) exists and Lorentzian Kubo–Toyabe patterns are seen instead. It is important to realize that the width of the Lorentzian Kubo–Toyabe patterns is not simply connected to the size of the magnetic moments: the concentration and nature of faults enters dominantly. A randomness of these faults (though probable) is not required since the muon positions would in any case be randomly distributed relative to them. We finally point out that the width of the field distribution is rather small (about 8 G for UAs) and in many cases not significantly different from that produced by nuclear dipoles. A distinction between the two can be cumbersome in some cases.

Observation (iv) (see fig. 56 for another example) can be used to distinguish between the different multi- $k$  structures which in general is a quite difficult task. The  $\mu$ SR method allows this with polycrystalline samples under field-free and stress-free conditions, a significant simplification when compared to neutron scattering where either stressed or highly magnetized single crystals are required. The features described under (iv) also point towards a novel property of  $3k$  spin structures, the de-locking of phase between the three Fourier components of magnetic moment on approach to the magnetic transition temperature, causing disorder in the spin lattice.

*5.2.1.6. CeAs.* In general, the basic magnetic properties of CeAs are considered to be understood. As we shall see, there are strong hints from the  $\mu$ SR data that the situation

may be more complex than anticipated. A neutron study of magnetic excitations (Hälg et al. 1983) deduced an isolated  $\Gamma_7$  as the electronic ground state, allowing treatment as an effective  $S = \frac{1}{2}$  AFM. A single second-order transition at  $T_N \approx 7.5$  K (the exact Néel temperature is somewhat sample dependent) is reported. A type I structure is formed, but whether it is  $1k$  or  $3k$  is under debate. Neutron diffraction puts the moments along (001) (Rossat-Mignod et al. 1983) while a  $\Gamma_7$  ground state calls for a (111) easy axis. Extending the neutron data to measurements in an applied field (Burlet et al. 1984) indicated a  $3k$  structure, which would resolve the problem of magnetic axis, but Hälg et al. (1983) and Hälg and Furrer (1986) derive a  $1k$  state from spin wave dispersion. This assignment has more recently been confirmed by high-pressure studies (Oohara et al. 1995). A theoretical evaluation (Prelovsek and Rice 1987) predicts that the  $1k$  and  $3k$  structures are nearly degenerate with a high sensitivity to random strains. Komorita et al. (1992) discuss CeAs in terms of a Kondo system.

The temperature dependence of the TF muon spin relaxation rate (measured again with an non-oriented mosaic sample) is given in fig. 44c (Asch et al. 1988b, Litterst et al. 1990). It shows the typical behavior on approaching a second-order magnetic transition. The peak value is reached at 7.6 K, which is taken as the Néel temperature of this sample. At lower temperatures the TF signal collapses. The paramagnetic frequency shift shows an analogous rise on approaching  $T_N = 7.6$  K. ZF spectra (see fig. 49) with their better resolution for small changes in relaxation behavior (particularly visible in their Fourier transforms) indicate a more complex behavior around  $T_N$ . Above 8 K the paramagnetic state is present showing Gaussian muon spin depolarization due to nuclear moments.

At  $\sim 8$  K a more rapidly depolarizing signal develops, which is interpreted as belonging to a SRO precursor phase. At 7.6 K spontaneous spin precession sets in (which is the reason for the collapse of the TF signal). This means that LRO is now present, but the SRO phase vanishes somewhat sluggishly. The Fourier spectra reveal a rather broad frequency distribution that suddenly sharpens up at 7.3 K. This indicates the sequence of two phase transitions less than 0.5 K apart. A crossover from the degenerate  $3k$ ,  $1k$  phases is a possibility. The results above 7.6 K tie in with an unusual observation made in neutron scattering. Hälg et al. (1987) found that AFM Bragg peaks appear already at 8.5 K while SRO spin fluctuations peak below (at 7.3 K).

The most unusual feature, however, is the appearance of a well defined spontaneous spin precession signal (fig. 50 gives an example) with practically full amplitude. This is not expected for either a  $3k$  or a  $1k$  structure in a type I spin sequence (see paragraph above). It is not a sample dependent effect, the measurements were repeated on an oriented single crystal (of different origin) by Klaus et al. (1997b). The precession frequency follows roughly, but not exactly, the  $S = 1/2$  Brillouin function. It agrees closely with the temperature variation of the Bragg peak intensity, except for the already mentioned peculiar disappearance of the Bragg peaks around  $T_N$  (fig. 51). The limiting ( $T \rightarrow 0$ ) value  $\nu_\mu \approx 25$  MHz corresponds to  $B_\mu = 0.18$  T. The single-crystal data also confirm the (100) orientation of magnetic moments.

There is to date no explanation of the unusual  $\mu$ SR magnetic response in CeAs. One might think that the muon (for whatever reason) takes up a site of lower symmetry. This



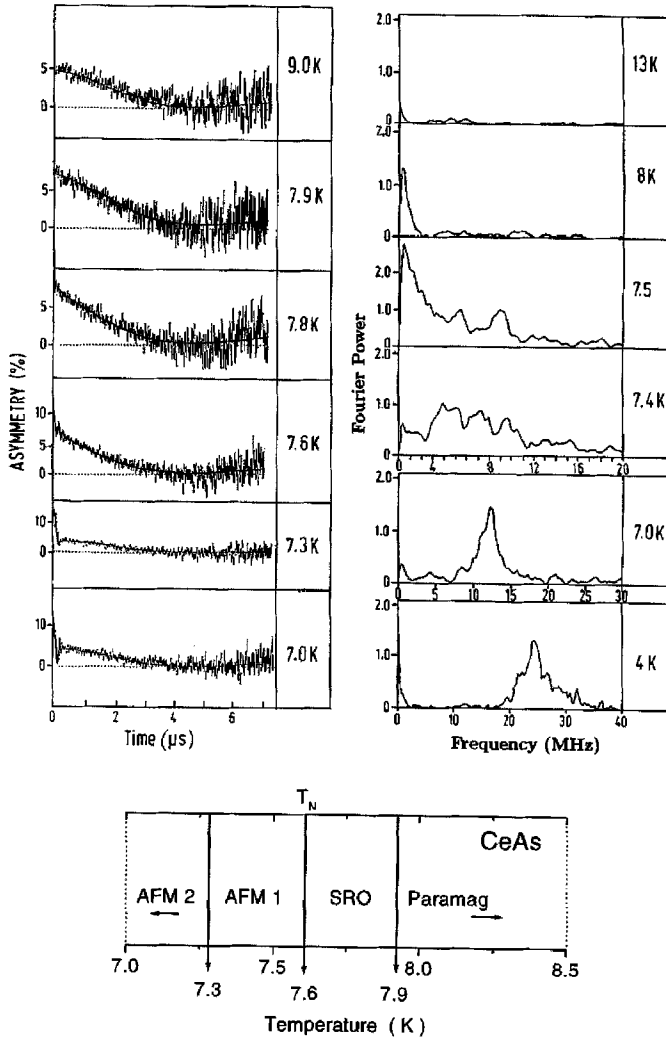


Fig. 49. ZF relaxation spectra and Fourier transforms of ZF spectra at various temperatures around the Néel point of CeAs. They lead to the bar diagram shown at the bottom, giving the various proposed magnetic phases (see text for details). Adapted from Litterst et al. (1990).

disagrees with the single-crystal data and in particular with a recent measurement of the angular dependence of the paramagnetic Knight shift (at 15 K), which is only compatible with a muon resting on the  $(\frac{1}{4}, \frac{1}{4}, \frac{1}{4})$  site (Schenck et al. 1997b). These authors report yet another (not understood) complexity. The signal in high TF (0.6 T) consists of two (closely spaced) components with opposite sign and different magnitudes (by roughly a factor of 2) of the Knight shift constants. A local field would be felt even by a muon

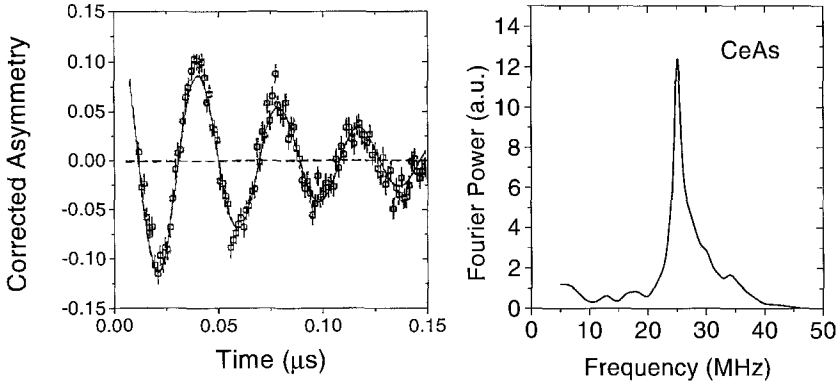


Fig. 50. ZF precession signal and its Fourier transform in CeAs at 3 K, i.e., well below the Néel temperature (Asch, unpublished).

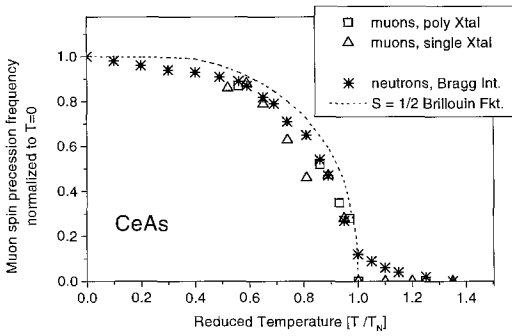


Fig. 51. Temperature dependence of ZF muon precession frequency in CeAs. The polycrystalline data are from Litterst et al. (1990), the single-crystal data from Klauß et al. (1997b). Also shown are the AFM Bragg peak intensities (Hälg et al. 1987) and the  $S = 1/2$  Brillouin function.

at the  $(\frac{1}{4}, \frac{1}{4}, \frac{1}{4})$  site if a FM component were present in the ordered state, but bulk data have not reported such an effect. It would require a canted spin structure that has not been seen by neutrons. Also, an error in propagation vector is hard to imagine. An impurity effect is equally unlikely. Firstly, because of the absence of sample dependence; secondly, because the full signal strength appears; thirdly, because of the narrow field distribution (comparatively weak damping of the oscillations). There then remains the question of a muon-induced effect. One could imagine that the muon charge locally disturbs the rather delicate balance of various interactions that determines the AFM structure (Prelovsek and Rice 1987). The well-developed weakly damped oscillations, however, speak more for a LRO bulk effect. An influence of the muon charge on the isolated  $\Gamma_7$  CEF ground state is equally unlikely. Finally, the  $\mu$ SR response in CeSb (to be discussed next) faithfully mirrors its known, rather complex, magnetic behavior. In summary, a muon-induced effect is equally unlikely and the mystery remains. Nevertheless, the  $\mu$ SR data call for a thorough re-examination of the magnetic properties of CeAs which may be more complex than generally accepted.

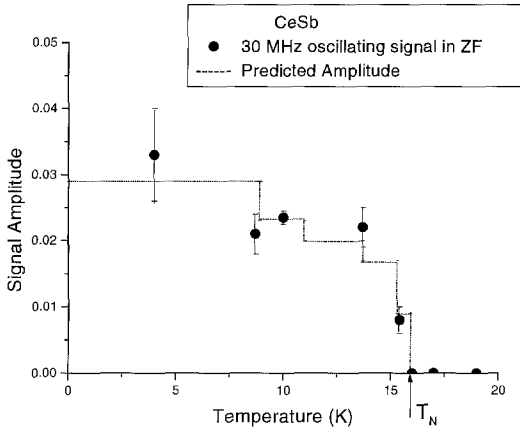


Fig. 52. Temperature dependence of the amplitude of the 30 MHz signal in CeSb measured in ZF (open circles, ZF data; solid circles, weak (5 mT) TF data). The solid line represents the predictions from dipolar sum calculations for the  $(\frac{1}{4}, \frac{1}{4}, \frac{1}{4})$  muon stopping site. After Klaub et al. (1994) as redrawn by Schenck and Gygax (1995).

5.2.1.7. *CeSb*. The magnetic phase diagram of CeSb is complicated indeed. Below  $T_N \approx 16$  K five different AFM structures appear in close sequence until the magnetic ground state ( $1k$  type IA) is reached around 9 K (Rossat-Mignod et al. 1985). The various AFM states can be described by different stacking sequences of paramagnetic and ferromagnetic [001] layers with the  $Ce^{3+}$  spins pointing along  $\pm(001)$ . All structures are commensurate and all transitions are of first-order. The  $\mu$ SR study (Klaub et al. 1994, 1995) was carried out on randomly oriented single-crystalline platelets as in most other cases of NaCl-type compounds. Dipolar field calculations were performed for all different spin structures using the  $(\frac{1}{4}, \frac{1}{4}, \frac{1}{4})$  muon stopping site. They revealed the general presence of three signals with amplitudes varying in the different magnetic states (in some structures one of the signals may have zero intensity). Two signals show spontaneous spin precession ( $\nu_1 \approx 16$  MHz;  $\nu_2 \approx 33$  MHz), the third one no spin precession. ZF and weak TF data taken as a function of temperature reproduced the calculated results quite well. Figure 52 shows an example. Instead of 33 MHz a signal with about 30 MHz is seen. The 16 MHz signal is never observed, probably due to rapid muon spin depolarization. Its amplitude was inferred from the missing fraction between the sum of amplitudes of the 30 MHz signal and the non-oscillating signal, compared to the amplitude of the paramagnetic signal. One essential point of this study is that the  $\mu$ SR spectral response follows quite well the known sequence of AFM states although some of those are surely not particularly stable. Nevertheless,  $\mu$ SR gives the expected answer and any destabilizing effect of the presence of the muon cannot be seen.

The spontaneous precession frequency remains unaltered throughout the magnetically ordered regime in accordance with the first-order nature of the phase transitions, but the non-oscillating signal shows the continuous presence of spin fluctuations even in the lowest AFM state. Above  $T_N$ , the temperature dependence of the ZF relaxation rate, together with a substantial negative Knight shift slightly above  $T_N$ , proves the existence of strong dynamic spin correlations that have also been observed by diffuse critical neutron scattering (Hälg et al. 1985). They relate to a paramagnetic precursor phase with a FM

in-plane coupling of Ce moments. This view is further consistent with the observation of a positive paramagnetic Curie temperature.

5.2.1.8. *DySb*. Below  $T_N = 9.5$  K (first-order) a MnO-like (type II) AFM structure is formed consisting of FM [111] planes with the moments pointing in the  $\pm(001)$  direction, because of strong anisotropy. Near  $T_N$ , a small tilt of moments away from the tetragonal axis has been seen (Felcher et al. 1973). Dipolar field calculations for the accepted central muon stopping position predict a single spontaneous precession frequency of 210 MHz in the AFM state. In contrast, the measured ZF spectra (Klauß et al. 1994) contained an oscillating portion ( $\nu_\mu \approx 240$  MHz) together with a non-oscillating part. Both subsignals have about the same intensity. The discrepancy with the dipolar calculation can be resolved if one assumes a CoO-like AFM structure (van Laar 1965). In this case the calculations give a 300 MHz precession signal and a non-precessing signal of equal strength. The difference between calculated and observed frequency is not serious, since the contact field has been left out. Neutron diffraction has ruled out the CoO structure with the existence of a small monoclinic distortion only. As in the case of CeSb, the spontaneous frequency is practically independent of temperature, confirming the first-order transition, and the relaxation rate of the non-oscillating signal proves it is a dynamic spin system. Similarly, the properties of the  $\mu$ SR spectra just above  $T_N$  indicate a dynamic paramagnetic precursor phase as well. If a CoO-type spin structure is accepted, this phase can be explained by the development of quadrupolar anisotropy a few degrees above  $T_N$ . Such a scenario had been proposed in an earlier structure study (Chen and Levy 1971).

5.2.1.9. *Uranium monochalcogenides*. These compounds are all simple ferromagnets. It is reasonable to assume that the muon takes up the  $(\frac{1}{4}, \frac{1}{4}, \frac{1}{4})$  interstitial position since the same crystal structure prevails and since the lattice constants are not significantly different. As pointed out above, the local field will not cancel at such a high-symmetry site for FM order. The contact field remains, pointing in the direction of spontaneous magnetization. UTe, US and the pseudo-binary system  $U_{1-x}La_xS$  were studied by  $\mu$ SR.

In the  $\mu$ SR study of UTe by Aggarwal et al. (1989) the signal was lost in TF as well as in ZF below  $T_C = 104$  K. The published data are restricted to the paramagnetic regime, especially to the temperature range close to the second-order Curie point. They yield a frequency shift that scales with susceptibility ( $\Delta f/f_0 = [(T - T_C)/T_C]^w$  with  $w = 1$ ) and a relaxation rate that rises faster than susceptibility ( $w = 1.3$ ).

The pseudo-binary system  $U_xLa_{1-x}S$  possesses some unusual magnetic properties. The lattice constant varies linearly with magnetic dilution from 5.49 to 5.87 Å, but bulk magnetic data show no simple systematic behavior (Schoenes et al. 1996). A linear decrease of the paramagnetic Curie temperature is seen, reaching negative values at high La contents. In contrast, the Curie–Weiss magnetic moment remains essentially constant.  $T_C$  first decreases linearly from 177 K for US to 95 K for  $U_{0.6}La_{0.4}S$ . In this regime the ordered moment changes little (1.7 to 1.5  $\mu_B$ ). For higher U dilutions ( $x < 0.6$ ), however, a sudden total loss of ordered magnetism seems to occur. Neutron scattering

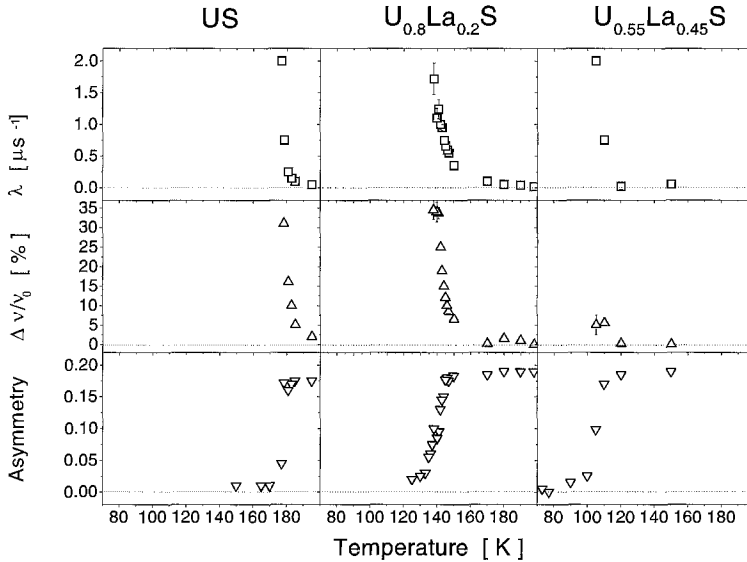


Fig. 53. TF- $\mu$ SR data for  $U_xLa_{1-x}S$  for  $x = 1, 0.8$  and  $0.55$  (left to right). From top to bottom: muon spin relaxation rate  $\lambda$ , precession frequency  $\nu_\mu$  (in TF = 50 G), initial asymmetry. After Grosse et al. (1999).

(Bourdarot et al. 1997) can no longer detect magnetic Bragg peaks and the authors conclude that the ordered moment has collapsed (at least to a value less than  $0.4\mu_B$ , which is the sensitivity limit). High-field magnetization data extrapolated to zero field gave strongly reduced moments, but the procedure is somewhat uncertain because of domain effects.  $\mu$ SR spectroscopy with its high sensitivity even in zero field offers a unique opportunity to look for the presence of weak moment magnetism in the high-dilution regime. The U moment collapse (either by pressure or alloying) in US has been modeled theoretically by Cooper and Lin (1998) using *ab initio* calculations in the local density approximation. The key scenario is that the f electron spectral density at the U ion can either be in a stable (and localized)  $f^3$  configuration for a time span long enough to initiate magnetic order, or in a rapidly fluctuating state between  $f^3$  and the nonmagnetic (delocalized)  $f^2$  configuration. This dynamic state is altogether inefficient in causing magnetism. Alloying, for instance replacing U with La, increases the fluctuating fraction. At a certain concentration the  $f^3$  component falls below a critical value necessary to sustain a local moment and magnetic ordering.

The  $\mu$ SR study by Grosse et al. (1999) used mosaics of oriented single-crystal platelets. LaS, the lower concentration limit ( $x = 0$ ), is diamagnetic. The ZF spectra are static Gaussian Kubo–Toyabe patterns originating from the nuclear moments on La. Full decoupling needs only LF = 10 G. Between 300 K and 4 K only a minute change in static width is seen, which can be accounted for by thermal contraction. These data show that effects of muon diffusion are not discernable. US, the upper concentration limit ( $x = 1$ ) is a FM ( $T_C = 177$  K and  $\mu_U = 1.7\mu_B$ ). The reduction in moment was

used by Cooper and Lin (1998) to fix a starting value for the localized and delocalized mixture of 5f configurations.  $T_C$  could easily be established by the expected rise of muon spin relaxation rate (critical slowing down), by the sharp increase of frequency shift and by the loss of signal amplitude in TF (see fig. 53). The result agrees fully with previous data (177 K). Below  $T_C$ , a spontaneous spin precession signal is seen with the limiting frequency ( $T \ll T_C$ ) of  $\nu_\mu = 63.4$  MHz (corresponding to a contact field of 0.47 T) and a damping rate of  $\sim 23 \mu\text{s}^{-1}$ . The U rich pseudo-binary with  $x = 0.8$  gave essentially the same result, but for the expected reduction in  $T_C$  (fig. 53). Again full agreement with previous data exist, showing that  $\mu$ SR senses the magnetic behavior of  $\text{U}_x\text{La}_{1-x}\text{S}$  properly. Unfortunately, a spontaneous spin precession signal could not be detected. The randomness in U configuration around the muon site increases the field distribution width, leading to relaxation rates in excess of  $100 \mu\text{s}^{-1}$ . The signal is lost in the initial dead time. This holds for all pseudo-binary samples. The higher diluted compound with  $x = 0.55$  should not show magnetic order according to the neutron study. As can be seen from fig. 53, one is able to detect a transition with  $\mu$ SR. The frequency shift has become rather small and the temperature range over which the magnetic transition occurs has widened, a trend already visible for the  $x = 0.8$  compound. The absence of a spontaneous spin precession signal calls for a different means to estimate the size of the contact field, which is expected to be (at least roughly) proportional to the U moment. The maximal value of frequency shift recorded close to the transition point offers such a possibility, since we are dealing with isostructural materials throughout. Applying this evaluation scheme results in a collapse of U moment by about an order of magnitude when comparing the  $x = 0.55$  compound with the less diluted materials ( $x \geq 0.6$ ). The  $x = 0.4$  sample gave a further reduction in  $T_C$  and moment, the latter being not dramatic here. Of particular interest is the question whether magnetism is still present in a highly diluted sample ( $x = 0.15$ ). Its ZF and LF spectra at high temperatures are very similar to those of LaS (i.e., relaxation is dominated by static nuclear dipoles), but surprisingly around 7 K muon spin relaxation generated by U moments has already become quite visible. Spin correlations have developed that cause slowing of U moment fluctuations. At 2 K relaxation by electronic moments dominates. Cooling (in a dilution refrigerator spectrometer) further reveals a weak but clearly visible rise in frequency shift and muon spin relaxation rate around 0.45 K, indicating the presence of a magnetic transition. The U moment is further reduced. The TF signal does not vanish below the peak of the frequency shift. This is in keeping with AFM order, and the negative paramagnetic Curie temperature found by Schoenes et al. (1996) at this La concentration renders further support for this interpretation. It means that the system tends toward a HF ground state with AFM order of substantially reduced moments (see also Cooper et al. 1999).

In summary, the pertinent findings of the  $\mu$ SR study are summarized in the graphs of fig. 54. A moment collapse certainly takes place for  $x < 0.6$  but not to zero magnitude. Small moments on the order between 0.3 and  $0.05\mu_B$  remain present. Despite the smallness of the moments, the compounds exhibit magnetic order, while the linear decrease of  $T_C$  with reduced U content ( $x$ ) continues down to the lowest concentration

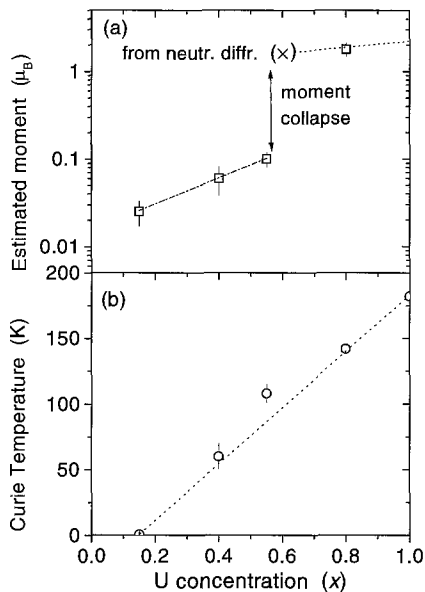


Fig. 54. Dependences of (a) the moment on U (estimated from the measured maximal frequency shift near the magnetic transition) and (b) Curie temperature (from  $\mu$ SR data) on U concentration in  $U_xLa_{1-x}S$ . Note the logarithmic scale for frequency shift. The Curie point for  $x = 0.15$  is  $0.45 \pm 0.15$  K. The lines are guides to the eye. From Grosse et al. (1999).

measured. These data are another example of the power of  $\mu$ SR in the study of small moment magnetism.

The intermediate valence monochalcogenide  $Sm_{0.9}La_{0.1}S$  has been studied by high-pressure  $\mu$ SR measurements. The findings will be presented in sect. 9.5.

### 5.2.2. CsCl structure

CsCl compounds of composition  $MX$  are known for nearly all R elements combined with noble metals (Cu, Ag, Au) but are also formed for  $X = Mg, Zn, Cd$ . Compounds of type  $AnX$  with the CsCl structure are not listed in the comprehensive review of Fournier and Troć (1985) on actinide compounds, and Sechovsky and Havela (1988) only give a brief reference on PuRu. Probably the CsCl structure is not stable for the more common lighter actinides (U and Np). The R materials have played a central role in the study of quadrupolar pair interactions in combination with magneto-elastic properties (Morin and Schmitt 1990). In several systems these types of interactions lead to quadrupolar ordering within the paramagnetic regime. Magnetic order is also regularly found and the AFM spin structures are quite often of the multi- $k$  type.  $\mu$ SR data are scarce for the CsCl type compounds formed with R, despite the sizable data set using various bulk methods. The probable reason is that  $\mu$ SR does not respond *directly* to quadrupolar interactions and thus is unlikely to give deeper insight into the microscopic mechanisms of quadrupolar ordering. The question of whether (and in which way) quadrupolar ordering affects the dynamical properties of the spin system is largely open and definitely a field to be looked at by  $\mu$ SR.

5.2.2.1.  $LaAg_{1-x}In_x$ . This pseudo-binary system is nonmagnetic but undergoes a phase transition from the cubic CsCl structure into a tetragonal structure at temperatures between 30 K and 170 K for  $x = 0.1$  to  $x = 0.4$ . A  $\mu$ SR study for  $x = 0, 0.1, 0.2, 0.3$  and  $0.4$  was carried out by Wehr et al. (1983) measuring Knight shifts with the stroboscopic method (see Klempt et al. 1982). The main result of interest (especially in view of the studies on CeAg discussed below) is the finding of a stationary muon below  $\sim 70$  K. The goal of the Knight shift studies had been to gain insight into the influence of the 5d electrons on the local contact field. This field contribution was found to be negative. It rises with increasing In content. Possible scenarios are discussed in detail. The measurements were restricted to the cubic phase except for the sample with  $x = 0.3$ . In this compound a distinct step-like discontinuity in Knight shift at the structural phase transition was observed.

5.2.2.2.  $CeAg$  and  $CeAg_{0.97}In_{0.03}$ . Several different types of couplings come together in CeAg: lattice instability of electronic origin, bilinear ferromagnetic, Kondo and quadrupolar interactions (see Morin 1988 for a detailed discussion). The quadrupolar couplings dominate the bilinear ferromagnetic interactions and enforce a ferro-quadrupolar ordering at  $T_Q \approx 15$  K. The underlying lattice instability causes a martensitic transition into a tetragonal phase. Quadrupolar ordering is followed by a second-order transition at  $T_C = 5$  K into a FM state.

ZF- and TF- $\mu$ SR measurements were carried out by Hyomi et al. (1988) on polycrystalline material. The work concentrated on the paramagnetic regime around  $T_Q$ ; the magnetically ordered phase was not investigated. The ZF data reveal an exponential decay of muon spin polarization with a relaxation rate rising below 40 K and peaking at about 25 K (but to a comparatively low value of  $0.1 \mu s^{-1}$ ). Below 25 K the depolarization is better described by a square-root exponential function and the rate decreases rapidly. Concomitantly, signal amplitude is reduced, strongly indicating the development of a fast-decaying portion that is lost in the dead time of the apparatus (pulsed beam facility at KEK). This suggests that static spin correlations start to develop around 25 K on cooling, leading to a wide spread of internal fields at the muon site. A connection with quadrupolar ordering ( $T_Q = 15$  K) and the martensitic phase transition is not obvious and the characteristic temperature of 25 K remains unexplained.

Substituting Ag partially with In raises  $T_Q$  but the nature of the structural instability is in debate here and not believed to be connected directly to quadrupolar ordering (Ihrig and Lohmann 1977, Morin 1988). The ZF  $\mu$ SR measurements in  $CeAg_{0.97}In_{0.03}$  gave results quite different from those of pure CeAg. The relaxation rate begins to rise at 25 K with the spectrum changing once more from pure exponential to root exponential shape. The rate continues its increase down to  $\sim 10$  K (the lowest temperature measured), while the signal strength remains practically constant. Obviously, the rapidly relaxing phase of pure CeAg is not formed. Figure 55 summarizes the data for both compounds. Also carried out were TF Knight shift studies. Identical results were obtained for both materials. The (negative) shift increases (in magnitude) strongly below  $\sim 20$  K following closely the temperature dependence of bulk susceptibility.



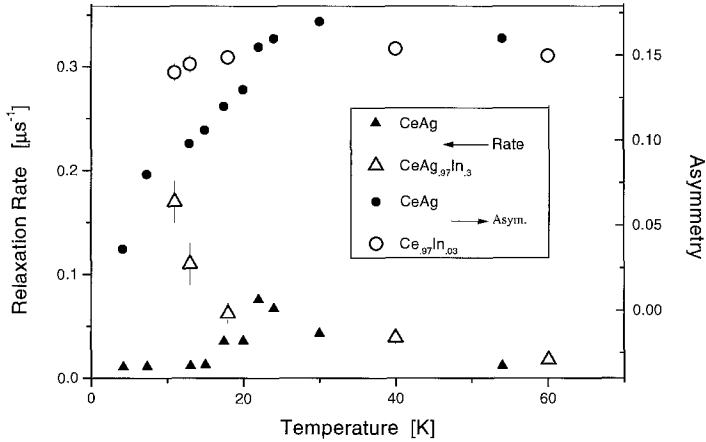


Fig. 55. ZF- $\mu$ SR data for CeAg (solid symbols) and CeAg<sub>0.97</sub>In<sub>0.03</sub> (open symbols). Shown is the asymmetry or signal amplitude (circles, right-hand scale) and the muon spin relaxation rate (triangles, left-hand scale). Adapted from Hyomi et al. (1988).

From the reviewers' point of view the results can be summarized as follows. The question of how quadrupolar ordering affects the dynamics of the spin system remains unanswered since no clear connection can be established between the temperature dependence of muon spin relaxation rate and the onset of quadrupolar ordering. It should be mentioned that the question whether quadrupolar ordering affects the  $\mu$ SR response, in particular the muon spin relaxation rate remains open. In some cases (e.g., Ce<sub>3</sub>Pd<sub>20</sub>Ge<sub>6</sub> in sect. 9.3.1) no effect was observed, but in a recent study of CeB<sub>6</sub> (also discussed in sect. 9.3.1) it was found that the slope of the temperature dependence of the relaxation rate changed at the ordering temperature. The different behavior of CeAg and CeAg<sub>0.97</sub>In<sub>0.03</sub>, where the latter keeps the dynamical nature of the spin system to much lower temperatures, may reflect the proposed difference in electronic structure connected to the mechanisms leading to the lattice instability. The changeover to a root exponential shape in the muon spin relaxation spectra points towards the development of a complex (perhaps incommensurate) spin structure as a possible magnetic precursor.

5.2.2.3. *DyAg*. Quadrupolar ordering is not reported for DyAg. This compound orders magnetically at  $T_N = 60$  K. The spin structure at low temperatures is established to be a type I,  $3k$  AFM phase. The effective moment ( $10.6\mu_B$ ) is close to the Dy<sup>3+</sup> free-ion value. The  $\mu$ SR work on DyAg (Kalvius et al. 1986) started out as an extension of preceding Mössbauer studies (Chappert et al. 1982) on polycrystalline (cr-) and thick film (50–100  $\mu\text{m}$ ) sputtered amorphous (am-) specimens of DyAg. Amorphous materials cannot support true AFM, and indeed, am-DyAg enters a FM, or more precisely, an asperomagnetic state at  $T_C = 18$  K (Boucher 1977). The designation asperomagnetic means that the spins are not strictly collinear but *randomly* distributed within a cone around the easy axis (here (111)). One of the significant findings of

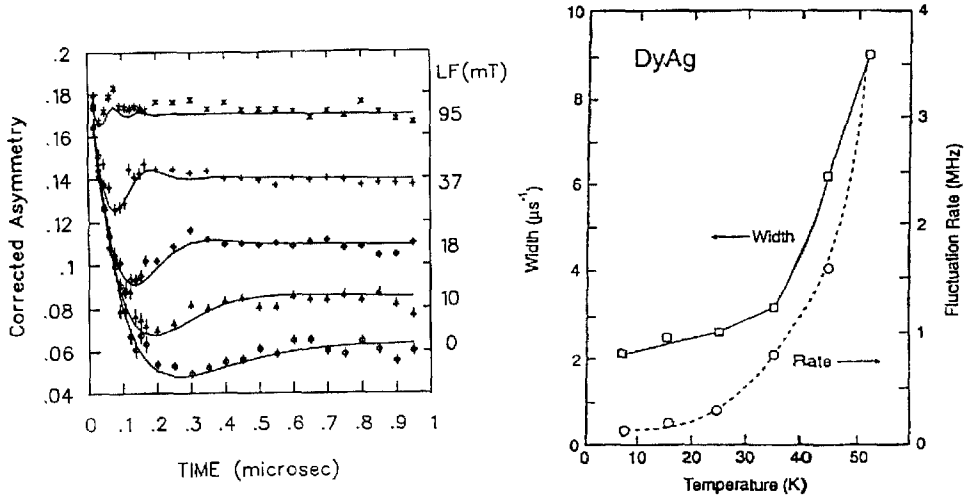


Fig. 56. Left: ZF- and LF- $\mu$ SR spectra of polycrystalline DyAg at 18 K. The solid lines are fits to a nearly static Lorentzian Kubo–Toyabe function. Right: Temperature dependence of distribution width and fluctuation rate of the field at the muon site as obtained from fits to the Lorentzian Kubo–Toyabe patterns seen in ZF data of cr-DyAg up to 51 K. From Kalvius et al. (1986, 1990)

Mössbauer spectroscopy was the distinct difference in dynamical properties of the  $\text{Dy}^{3+}$  moments in cr- and am-DyAg with the fluctuation rate being at least one order of magnitude lower in the amorphous compound. The static limit (on the Mössbauer time scale) was reached in am-DyAg well above  $T_C$ .  $\mu$ SR is a complementary technique to study spin dynamical properties with a quite different time window. It is usually possible to follow the temperature dependence of spin fluctuations deep inside the paramagnetic regime (see the examples discussed in sects. 4 and 5.3).

The distinct difference in spin dynamical properties between cr- and am-DyAg was seen in the  $\mu$ SR spectra as well and remained present up to room temperature (highest temperature measured). Another distinguishing feature was the observation that the shape of the ZF relaxation spectra is exponential in cr-DyAg throughout the paramagnetic regime, while am-DyAg shows power exponential relaxation with the power decreasing at lower temperatures. The results seen in the amorphous material will be discussed later in sect. 8.3.1. Figure 100 in that section shows the comparison of relaxation rates in the cr and am compounds.

ZF spectra of cr-DyAg had been presented as pertinent examples of  $\mu$ SR response in a paramagnet in fig. 23 in sect. 3.2.2. Cooling from room temperature results in an increase of muon spin depolarization rate characteristic for the approach to a second-order phase transition (critical slowing down). The values of rate are typical for a strong paramagnet and in keeping with the findings reported for comparable materials (see, for example  $\text{DyAl}_2$  in sect. 5.3). At low temperatures ( $T \ll T_N$ ) the  $\mu$ SR spectra in ZF and LF can fully be described by a static Lorentzian Kubo–Toyabe relaxation as shown in fig. 56 (left) (Kalvius et al. 1986, 1987, 1990). The explanation is the same as discussed in

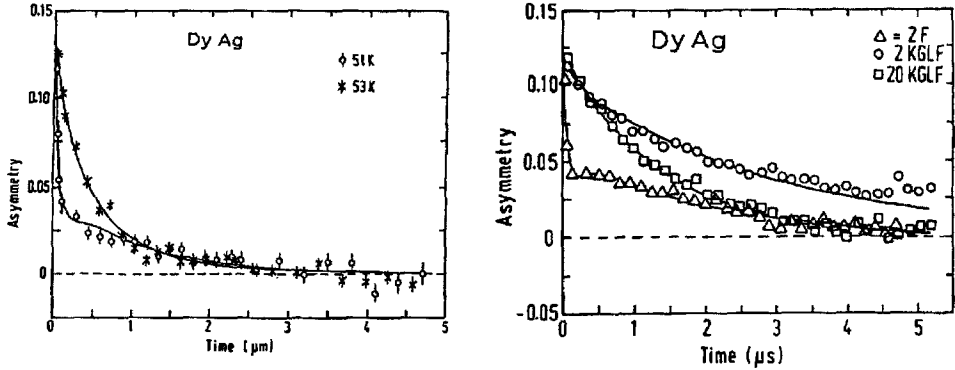


Fig. 57. Left: ZF spectra near the second magnetic phase transition at 51 K in cr-DyAg. Right: LF spectra of cr-DyAg in ZF and LF=2 and 20 kG. The fits (solid lines) are discussed in the text. After Kalvius et al. (1990)

the preceding section: the muon occupies the central interstitial site of high symmetry and in consequence all contributions to the local field cancel for a type I AFM spin structure. The remaining Lorentzian field distribution arises from dilute faults in the AFM spin lattice. Raising the temperature toward  $T_N$ , one observes the marked increase in local-field distribution width and fluctuation rate depicted in fig. 56 (right). As discussed earlier, this is the characteristic  $\mu$ SR signature of a  $3k$  spin state that reflects phase de-locking when approaching its transition temperature. At  $T_M = 51$  K a discontinuity in spectral shape occurs, followed by another change at  $T_N = 60$  K. In the regime between 51 and 60 K the ZF spectra are characterized by a power exponential decay of muon spin polarization (with  $p < 1$ ), bordered at the low-temperature side by the dynamic Lorentzian Kubo–Toyabe pattern (see fig. 57, left) and at the high-temperature side (paramagnetic regime) by the pure exponential relaxation shape. Little change in relaxation rate is seen at  $T_N$ . The type I  $3k$  AFM state is reached only *via* a state with some disordered spin structure and not directly from the paramagnetic state. Neutron diffraction (Kaneko et al. 1987) identified the spin structure just below  $T_N$  as an incommensurate sinusoidally modulated AFM structure. The two magnetic transitions were subsequently seen in bulk measurements (Morin and Schmitt 1990) as well. Values of  $T_N$  and  $T_M$  are somewhat sample dependent.

The spectral response in LF at low temperatures ( $T < 20$  K, i.e., in the static limit) is the normal decoupling behavior of a Lorentzian Kubo–Toyabe function (see fig. 56, left). Unusual features were observed, however, at higher temperatures where greater values of LF are needed to decouple the (still weakly) dynamic Kubo–Toyabe pattern. The most startling feature is shown in fig. 57 (right). The 2 kG spectrum can still be reproduced by decoupling from the ZF spectrum, albeit only with an increase of field distribution width. But the spectrum in 20 kG relaxes *faster* than the 2 kG spectrum. This is contrary to the standard decoupling formalism which should lead to a nearly complete suppression of muon spin depolarization. The fit shown in the figure is simply an exponential relaxation. The standard decoupling formalism assumes that neither the size of the moments, nor their spatial distribution, nor their fluctuation rate changes with

field. Clearly, this approximation cannot be valid in the present case. For one, the external field induces spin canting in the AFM structure with the canting angle depending on the direction of applied field with respect to the crystalline axes (spin flop transitions occur only at fields in excess of 80 kG, see Morin and Schmitt 1990). Since a powder sample was used in the  $\mu$ SR work, this effect will increase the field distribution width. Another possibility is the mixing of CEF levels which may change (slow down) the spin fluctuation rate. A detailed analysis of the high-field data is difficult for experimental reasons and has not been undertaken. The data demonstrate, however, once more the high sensitivity of  $\mu$ SR to small spatial changes in a spin structure.

### 5.2.3. $AuCu_3$ structure

The  $AuCu_3$  structure (space group  $Pm\bar{3}m$ ) is another simple cubic structure found in R and An intermetallics. Its basic atomic arrangement is shown in fig. 58 (left). As one can see, the R–R or An–An separation is given directly by the lattice constant  $a$ . Many compounds of the type  $RX_3$  or  $AnX_3$  with X being a group III or IV or a late transition element, crystallize in this structure, but by no means all. For example, the important HF materials  $CeAl_3$  and  $UPt_3$  (see sect. 9) possess a different (i.e., hexagonal) crystalline lattice. Most important among the  $AuCu_3$  intermetallics are the compounds formed with Ga, In, Sn, Pb and R = Ce and An = U, Np, Pu, since they are on the borderline of strongly correlated electron behavior. For example,  $NpSn_3$ , which has been studied extensively, was originally considered the prime example of an itinerant AFM. High-pressure Mössbauer measurements, however, showed that the Np is not strongly delocalized and that a description as an AFM–HF compound, somewhat analogous to  $CeAl_2$ , is more appropriate. (For details see Potzel et al. 1993). A compilation of magnetic and transport data for the actinide intermetallics can be found in Sechovsky and Havela (1988) and for the In and Sn compounds in particular in Fournier and Gratz (1993). In general, the 5f electrons in  $UX_3$  materials exhibit band-like behavior. The band width gets narrower the heavier X gets, one possible cause being the increase of lattice constant. Hill behavior, however, is not the dominant mechanism here. It is the hybridization with ligand p electrons that plays the important role. This model is corroborated, for example, in systematics of Mössbauer parameters in Np compounds (Potzel et al. 1993). One generally observes in the  $AnX_3$  intermetallics that group IV ligands (Si, Ge, Sn) produce weakly magnetic or even nonmagnetic compounds while group III ligands (Al, Ga, In) induce strong magnetism with AFM order.

Only two intermetallics with the  $AuCu_3$  structure containing a R ion have been studied by  $\mu$ SR. The data on  $PrIn_3$  have been discussed in sect. 5.1.2. The other material,  $CeSn_3$ , is an established HF compound. The rudimentary results available are briefly mentioned in sect. 9. More systematic  $\mu$ SR data are available for compounds formed with the light actinide uranium. The systems  $USn_3$ ,  $UIn_3$ ,  $UGa_3$  together with their pseudo-binaries  $U(Sn_{1-x}In_x)_3$  and  $U(Ge_xGa_{1-x})_3$  have been studied by Zwirner et al. (1993) and Kratzer et al. (1994b, 1997b).  $USn_3$  is an exchange-enhanced paramagnet close to a magnetic instability (Lin et al. 1985a). It exhibits Curie–Weiss susceptibility above 20 K

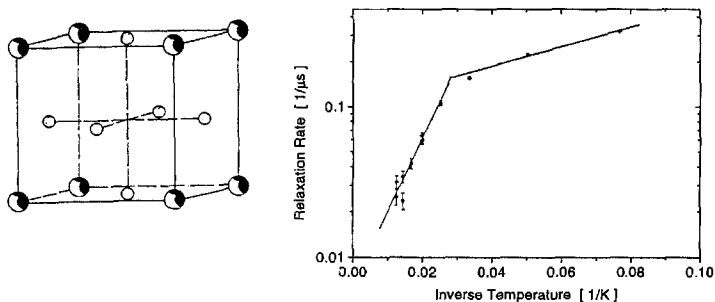


Fig. 58. Left: Atomic arrangement in the  $\text{AuCu}_3$  structure (semi-solid circles represent the R or An ions, open circles the group III or IV elements). From Sechovsky and Havela (1988). Right: Logarithmic plot of the muon spin relaxation rate of electronic origin in  $\text{U}(\text{Sn}_{0.5}\text{In}_{0.5})_3$  as a function of inverse temperature. The change in slope occurs at 30 K. From Kratzer et al. (1994b).

with  $\mu = 2.4\mu_B$ . The Sommerfeld constant is comparatively high at low temperature (2 K), with  $\gamma \approx 0.17 \text{ J}/(\text{mol K}^2)$  (van Maaren et al. 1974).  $\text{USn}_3$  is often discussed (like  $\text{UAl}_2$ ) as a spin fluctuator (Norman et al. 1986), but  $\text{UIn}_3$  shows AFM order at  $T_N = 95 \text{ K}$  with an ordered moment of  $\sim 1\mu_B$  (Buschow and van Daal 1972). Since the lattice constant changes little between  $\text{USn}_3$  (4.626 Å) and  $\text{UIn}_3$  (4.606 Å), it is assumed that the interaction with ligand electrons is responsible for magnetism. The localization of 5f electron structure when going from Sn to In is also reflected in the Sommerfeld constant, which attains a comparatively small value of  $\gamma = 0.05 \text{ J}/(\text{mol K}^2)$  (see Fournier and Troć 1985). In consequence, one observes in the pseudo-binary alloys  $\text{U}(\text{Sn}_{1-x}\text{In}_x)_3$  a continuous transition from spin fluctuator properties to AFM. Coming from the  $\text{USn}_3$  side, ordered magnetism appears around  $x = 0.55$ . Briefly before, however, the Sommerfeld constant reaches a maximum of  $\gamma \approx 0.6 \text{ J}/(\text{mol K}^2)$ . Around this point, some authors (Lin et al. 1986, Zhou et al. 1987) have proposed to discuss the system  $\text{U}(\text{Sn}_{1-x}\text{In}_x)_3$  in terms of HF behavior.

In  $\text{USn}_3$ , the  $\mu\text{SR}$  spectra show no noticeable depolarization ( $\lambda \leq 0.01 \mu\text{s}^{-1}$ ). The influence of electronic moments (on U) is fully motionally narrowed ( $1/\tau_{4f} \geq 10^{13} \text{ Hz}$ ) and nuclear dipole moments are negligible. Basically, this result agrees with that of the established spin fluctuator  $\text{UAl}_2$ , to be discussed below.

In  $\text{UIn}_3$ , the  $\mu\text{SR}$  spectra in the paramagnetic regime are dominated by the depolarizing action of the  $^{115}\text{In}$  nuclear moments. In  $LF=10 \text{ G}$  depolarization is suppressed. The value of the nuclear relaxation rate ( $\Delta = 0.16 \mu\text{s}^{-1}$ ) is in full accordance with dipolar field calculations for a muon stopping at the center of the cube formed by the U atoms (see fig. 58). This site assignment was independently determined by measurements of the angular dependence of frequency shift in a single crystal of  $\text{PrIn}_3$  (Grayevsky et al. 1997). No indication of muon diffusion could be found below  $\sim 150 \text{ K}$ . The U moments fluctuate rapidly as in  $\text{USn}_3$ . At 88 K ( $T_N$  of the sample used) the spectral shape changes to a Lorentzian Kubo–Toyabe function without loss of signal intensity. No spontaneous spin precession is observed. As expected, the internal field at the (highly symmetric) muon stopping site cancels to zero. It had been outlined in the discussion of

the NaCl compounds that the residual depolarization (i.e., the Lorentzian Kubo–Toyabe spectrum) in the AFM regime must result from dilute defects in the AFM ordered spin lattice. The relaxation rate of the Lorentzian Kubo–Toyabe is small (about  $0.2 \mu\text{s}^{-1}$ ).

Details of the magnetic spin structure of  $\text{UIn}_3$  are still under some discussion. Neutron diffraction (Murasik et al. 1973) on a polycrystal found the magnetic unit cell to be doubled in all directions with respect to the crystallographic cell suggesting a type II ( $\mathbf{q} = (\frac{1}{2} \frac{1}{2} \frac{1}{2})$ ) AFM structure. For this spin arrangement no net magnetic field should exist at the In position.  $^{119}\text{Sn}$  Mössbauer studies on 20 at% Sn-doped  $\text{UIn}_3$  (see, for example, Yuen et al. 1992), however, showed the presence of a small hyperfine field at the In position, which is taken by the Sn atoms. A  $3\mathbf{k}$  structure was suggested instead of the usually assumed  $1\mathbf{k}$  structure. This finding appeared to be in agreement with the  $\mu$ SR data, which showed on approaching  $T_N$  a behavior of relaxation rate and static width reminiscent of that of  $\text{USb}$  (Asch et al. 1994). In claiming a  $3\mathbf{k}$  spin arrangement, it was overlooked, however, that the  $\text{AuCu}_3$  structure is primitive cubic (and not fcc as in the NaCl structure of the monochalcogenides and monpnictides) and ordering along (111) results in a  $4\mathbf{k}$  rather than a  $3\mathbf{k}$  structure (see, for example, Rossat-Mignod 1987). Unfortunately, symmetry arguments do not allow a  $4\mathbf{k}$  structure for the  $(\frac{1}{2} \frac{1}{2} \frac{1}{2})$  wavevector. The absolute orientation of the U moments is not known. A  $^{111}\text{In}$ -PAC study (Cottenier et al. 1998) also found a magnetic field around 1 T at the In nuclei. A model based on canted U moments near the [001] direction was suggested. A recent theoretical APW calculation showed a [001] orientation to have the lowest energy and an induced spin density at the In site was found, which could be the origin of the hyperfine field. Thus a straight forward type II AFM structure is still a possibility for the magnetic ground state of  $\text{UIn}_3$  (M. Roots 1999, private communication). The  $\mu$ SR results mentioned above would be easier to reconcile with a *small* deviation from the [001] orientation that is static at low temperatures but becomes dynamic just below  $T_N$ , but effects of domain dynamics can not be ruled out altogether.

Samples with  $x = 0.7, 0.5, 0.4$  and  $0.3$  were measured (Kratzer et al. 1997b) within the pseudo-binaries  $\text{U}(\text{Sn}_{1-x}\text{In}_x)_3$ . The depolarization by electronic moments for  $x = 0.7$  in the paramagnetic regime is much more pronounced than in  $\text{UIn}_3$ . The signal amplitude collapses between 70 K and 60 K, where (according to bulk magnetic data) long-range order (LRO) sets in. The Lorentzian Kubo–Toyabe, which is the signature of the AFM state here, relaxes so fast that it falls within the spectrometer dead time (measurements were taken at the ISIS pulsed muon facility). This increased relaxation, both in the paramagnetic and ordered state, must be due to a substantial increase in field distribution width, a notion that is confirmed by the observation that the signal could be recovered by applying  $\text{LF} \geq 0.1$  T. The field distribution width thus derived is around 300 G, i.e., about two orders of magnitude larger than in  $\text{UIn}_3$ . The likely cause is the random spin disorder produced by dilution with nonmagnetic Sn atoms since the magnetic properties are dependent on ligand electron structure. The fairly broad magnetic transition region indicates in addition spatial inhomogeneities in the sample.

The result for  $x = 0.5$  is surprising. This material is below the concentration limit for the onset of AFM order and indeed no phase transition was seen in  $\mu$ SR, but the material

does not behave like  $\text{USn}_3$  at low temperature. Down to 50 K there is little difference compared to  $\text{USn}_3$  (weak Gaussian relaxation) but below 50 K a change in shape of the relaxation function occurs. The spectra can be fitted to a power exponential relaxation where the power  $p$  decreases towards 0.5 for  $T \sim 30$  K. Around this temperature also the slope of the temperature dependence of the relaxation rate changes (fig. 58, right) and the paramagnetic frequency shift (in  $\text{TF} = 22$  mT) rises. It is concluded that the spin system freezes into a spin-glass-like SRO state. Although the formation of a SRO state has not been claimed before, it is interesting to note that specific heat and electrical resistivity show irregularities below 30 K. These features were not explained previously (Lin et al. 1987b). Compounds with  $x = 0.4$  and  $x = 0.3$  show basically analogous behavior, but the changes in spectral shape are less pronounced and shifted to lower temperatures. In summary,  $\mu\text{SR}$  in the  $\text{U}(\text{Sn}_{1-x}\text{In}_x)_3$  series indicates that strong magnetic disorder is induced by the dilution of  $\text{UIn}_3$  (AFM) with  $\text{USn}_3$  (spin fluctuator without magnetic LRO). It leads to the development of SRO magnetism between the concentration ranges for AFM-LRO and paramagnetic spin fluctuator behavior.

The system  $\text{U}(\text{Ge}_{1-x}\text{Ga}_x)_3$  behaves quite differently. The change in lattice constant is again extremely small ( $\Delta a \approx 0.05$  Å).  $\text{UGe}_3$  has a nearly temperature-independent susceptibility together with a rather low value of the Sommerfeld constant ( $\gamma \approx 0.02$  J/(mol K<sup>2</sup>)). It is definitely no spin fluctuator, just a weakly magnetic compound. Its  $\mu\text{SR}$  spectra are dominated by the Gaussian relaxation arising from static nuclear dipoles on Ge. No significant change with temperature is observed.  $\text{UGa}_3$  is an AFM with  $T_N = 70$  K and an ordered moment of  $(0.8\text{--}0.9)\mu_B$ . The U moments are FM coupled within the [111] planes and the planes in turn are AFM coupled (Murasik et al. 1974b, Lawson et al. 1985). The  $\mu\text{SR}$  spectra are quite similar to  $\text{UIn}_3$ . No spontaneous spin precession is seen, just the changeover from Gaussian to Lorentzian shape at  $T_N$ . Again all contributions to  $\mathbf{B}_\mu$  cancel for symmetry reasons. In the ordered state the relaxation increases with decreasing temperature, in contrast to  $\text{UIn}_3$ . Most likely the spin structure still undergoes weak continuous changes below  $T_N$ . In the pseudo-binary alloy series  $\text{U}(\text{Ge}_{1-x}\text{Ga}_x)_3$  magnetism is quickly lost (at  $x \leq 0.82$ ). This is fully corroborated by the  $\mu\text{SR}$  data (Kratzer et al. 1997b). In the spectra for  $x = 0.9$  the signal vanishes below  $\sim 70$  K, over a 10 K temperature spread. Again, the additional disorder due to alloying causes a considerably increased field distribution width and magnetic inhomogeneities in the sample. The nonmagnetic samples measured ( $x = 0.75, 0.5, 0.25$ ) all show the same behavior as pure  $\text{UGe}_3$ . In particular, no evidence of enhanced magnetic correlations or even SRO were observed, in sharp contrast to the system  $\text{U}(\text{Sn}_{1-x}\text{In}_x)_3$ . This again demonstrates the sensitive influence of ligand electron structure. It appears that the special electronic structure of  $\text{USn}_3$  which leads to its spin fluctuator properties is also responsible for the formation of a SRO state at the point of magnetic instability.

### 5.3. Laves-phase compounds

In this section we discuss intermetallics of type  $\text{MX}_2$  (with  $\text{M} = \text{R}$  or  $\text{An}$  and  $\text{X} = \text{Al}$  or transition element) that crystallize in the cubic C15 Laves phase ( $\text{MgCu}_2$  structure). The

M sublattice is a diamond lattice and the point symmetry of the R (An) site belongs to the cubic  $T_d$  group. The X atoms form regular tetrahedra in the interstices between the M sites (see fig. 66). Three different interstitial sites as stopping position for the muon are possible. They are the central positions in tetrahedra formed by the M and X atoms. One finds tetrahedra with 2, 3, and 4 X atoms (and 2, 1, 0 M atoms), which are denoted as the 2-2, 3-1, and 4-0 sites. The 2-2 and 3-1 tetrahedra are slightly distorted. Measurements on single-crystalline CeAl<sub>2</sub> (see below) indicates that the 2-2 site is occupied by the muon. The measured ZF static width  $\Delta$ , however, is lower than dipolar calculations predict (see Huxley et al. 1996). Furthermore, the CeAl<sub>2</sub> data indicate that the muon is stationary in the C15 phases below ~80 K. The site assignment is corroborated by neutron scattering data of hydrogen-loaded isostructural RFe<sub>2</sub> and ZrV<sub>2</sub> compounds in the low-concentration limit (Fish et al. 1979, Didisheim et al. 1980).

### 5.3.1. *MAI<sub>2</sub>*

5.3.1.1. *RAI<sub>2</sub>*. The RAl<sub>2</sub> intermetallics have played a central role in the study of R magnetism, mainly because nearly all of them (except CeAl<sub>2</sub>) have only one (second-order) magnetic phase transition leading into a simple FM state. For surveys we refer to the reviews mentioned at the top of this chapter. Some crystalline and magnetic properties for the FM RAl<sub>2</sub> compounds are listed in table 6. CeAl<sub>2</sub> is special. It enters an AFM state, is often listed among HF materials, and also shows some intermediate valence properties. We discuss this case separately at the beginning.

CeAl<sub>2</sub> shows an enhanced Sommerfeld constant  $\gamma(T \rightarrow 0) \approx 0.135 \text{ J/mol K}^2$  which puts it into the regime of moderately heavy-fermion materials.  $T_N$  is rather sample dependent, ranging typically from 3.4 to 3.9 K. The low transition temperature allowed Hartmann et al. (1989) to determine the muon stopping site from the angular dependence of depolarization rate using a single-crystalline sample. For  $T \gg T_N$ , the influence of Ce moments is fully motional narrowed and depolarization is caused by the static fields of <sup>27</sup>Al nuclear dipoles. The measurement and a comparison with dipolar sum calculations is shown in fig. 59 (left). The 2-2 site (see discussion on interstitial positions above) fits the angular dependence data for  $T = 69 \text{ K}$ . A measurement at higher temperatures

Table 6  
Some electronic and magnetic parameters of ferromagnetic RAl<sub>2</sub> compounds studied by μSR

Compound	Lattice parameter (Å)	R <sup>3+</sup> ground state	$g_J \cdot J$	$\mu_{\text{exp}}$ ( $\mu_B$ )	$T_C$ (K)	Easy axis
PrAl <sub>2</sub>	8.025	<sup>3</sup> H <sub>4</sub>	3.2	2.88	30	[100]
NdAl <sub>2</sub>	8.000	<sup>4</sup> I <sub>9/2</sub>	3.3	2.45	78	[100]
GdAl <sub>2</sub>	7.900	<sup>8</sup> S <sub>7/2</sub>	7.0	7.10	160	
DyAl <sub>2</sub>	7.840	<sup>6</sup> H <sub>15/2</sub>	10.0	9.84	67	[100]
HoAl <sub>2</sub>	7.813	<sup>5</sup> I <sub>8</sub>	10.0	9.18	32	[100]
ErAl <sub>2</sub>	7.793	<sup>4</sup> I <sub>15/2</sub>	9.0	7.80	14	[111]
TmAl <sub>2</sub>	7.780	<sup>3</sup> H <sub>6</sub>	7.0	4.60	6	[111]



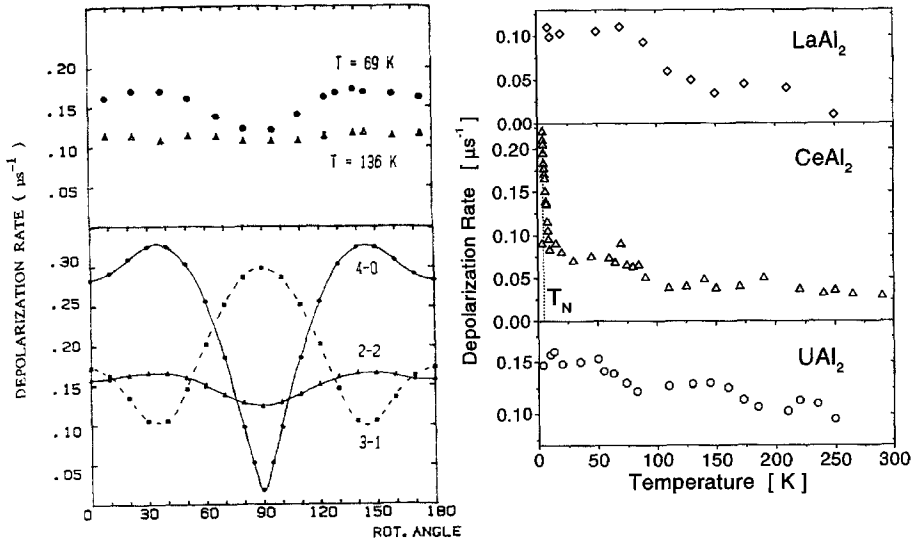


Fig. 59. Left: Angular dependence of the  $TF=0.15\text{ T } \mu\text{SR}$  depolarization rate for a single crystal of  $\text{CeAl}_2$  at temperatures well above  $T_N$  ( $\sim 3.5\text{ K}$ ). The crystal is rotated around the (110) axis. An angle of  $90^\circ$  corresponds to a field applied along (100). The top part shows the experimental result for two temperatures, the bottom part corresponding dipolar sum calculations for three different tetrahedral muon stopping sites. Right: Temperature dependence of the muon spin depolarization rate in three C15 Laves-phase compounds. The step around  $80\text{ K}$  signals the onset of muon mobility (see text). From Hartmann et al. (1989, 1990b).

shows a rate independent of crystal orientation. The result implies that the muon has become mobile. This behavior appears to be a general feature of the C15 structure, as demonstrated by the temperature dependence of the depolarization rate for paramagnetic  $\text{CeAl}_2$  and  $\text{UAl}_2$  and diamagnetic  $\text{LaAl}_2$  (fig. 59). In all cases a sudden decrease of rate is seen around  $80\text{ K}$ , signaling the onset of muon diffusion (Hartmann et al. 1990b). Another common irregularity near  $150\text{ K}$  is probably due to muon trapping–detrapping effects. Similar behavior appears to be present in  $\text{YCo}_2$  and is nicely illustrated in fig. 73.

The temperature dependence of the paramagnetic relaxation rate at low temperatures is typical for the approach to a second-order magnetic transition. In the region between  $3.2$  and  $3.8\text{ K}$ , however, a two component  $\mu\text{SR}$  spectrum is observed. One component, having a relatively slow relaxation rate ( $\lambda \approx 0.25\ \mu\text{s}^{-1}$ ) continuously decreases in strength; the other, with a rate about two orders of magnitude larger increases concomitantly as the temperature is lowered (fig. 60, left). The former signal is attributed to regions where paramagnetic spins, albeit under the influence of spin correlations (a dynamic cluster structure, as discussed for  $\text{Gd}$  metal in the preceding chapter) are still present, the latter to regions where AFM order has already occurred. A broad distribution of internal fields causes rapid loss of muon spin polarization. This set of data demonstrates that magnetic LRO does not immediately involve the whole volume of the sample (even for a single crystal), but rather, that the ordered volume fraction grows gradually over a range of  $\sim 1\text{ K}$ . One further notices that even for temperatures well below  $T_N$  a part of the sample ( $\sim 20\%$ )

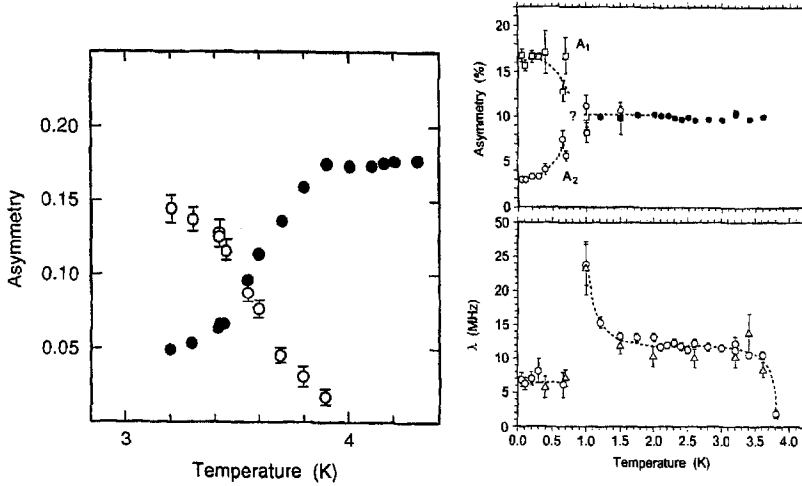


Fig. 60. Magnetism of  $CeAl_2$ . Left: Inhomogeneous transition region into the AFM state as seen in the  $\mu$ SR data of Hartmann et al. (1989). Solid symbols, slowly relaxing signal arising from the still paramagnetic volume fraction; open symbols, fast relaxing signal coming from the magnetically ordered volume fraction. Right: Change of  $\mu$ SR spectral parameters at the previously unknown transition near 1 K from the recent study of Schenck et al. (1999). Top: Temperature dependence of the amplitudes of the oscillating ( $A_1$ ) and the non-oscillating ( $A_2$ ) signals. Above 1 K one finds  $A_1 \approx A_2$  independent of temperature. Bottom: Temperature dependence of relaxation rate  $\lambda$  in  $CeAl_2$  of the non-oscillating signal. The two studies used different samples but both were single crystals.

remains in the paramagnetic state. Such a two-component magnetic structure appears in several HF compounds, most notably in  $CeAl_3$  (see sect. 9). A more recent study on a powder sample gave essentially the same result (MacLaughlin et al. 1993).

The determination of the true AFM spin structure in  $CeAl_2$  has been problematic and is still not fully solved. Neutron diffraction measurements on a high-quality single crystal (Barbara et al. 1980) revealed an incommensurate sinusoidally modulated AFM structure with  $\mu_{ord} = 0.63\mu_B$  on Ce in a single- $k$  arrangement. In contrast, Shapiro et al. (1979) pointed out that the magnetic structure must be described by a multiple- $k$  arrangement. A more recent neutron study in applied field (Forgan et al. 1990) came to the conclusion that the spin structure is a “non-chiral spiral”. In essence this means that the Ce ions in a single (0,1,1) plane can be represented by two fcc sublattices and the spirals in adjacent sublattices rotate in opposite directions.

These controversial results prompted Schenck et al. (1999) to perform a new ZF- $\mu$ SR study on a high-quality single crystal in the range between 0.1 and 4 K. These authors observe below 3.8 K a spin precession signal in addition to an exponentially relaxing non-oscillatory term. The spectra are well described by

$$\mathcal{A}(t) = A_1 \exp[-\frac{1}{2}\sigma^2 t^2] J_0(\omega t) + A_2 \exp[-\lambda t]. \quad (65)$$

The Bessel-function-type oscillations ( $J_0(\omega t)$ ) are in keeping with an incommensurate spin structure. Using dipolar sum modeling, the best agreement to the measured  $\mu$ SR

spectra was obtained for the single- $k$  structure proposed by Barbara et al. (1980). The new data reveal in addition previously unknown features. Around 1 K drastic changes occur in the spectral parameters  $A_1$ ,  $A_2$ , and  $\lambda$  as depicted in fig. 60 (right). The magnetic structure clearly undergoes some change without, however, affecting its modulated nature. There are also rapidly fluctuating field components below  $T_N$  that persist down to  $T \rightarrow 0$ . These features remain unexplained at this stage and the magnetic structure of  $\text{CeAl}_2$  still contains mysteries. A strong sample dependence is probable.

Other  $\text{RAl}_2$  intermetallics with  $\text{R} = \text{Pr, Nd, Gd, Dy, Ho, Er}$  and  $\text{Tm}$  (see table 6) were first studied by Chappert et al. (1981) and Hartmann et al. (1984, 1986) with the aim to investigate fluctuations of 4f magnetic moments in the paramagnetic regime, especially on approach to the Curie point. The TF method was used exclusively. The main features of this study were:

- (i) The signal from muons stopped in the sample vanishes below  $T_C$ .
- (ii) Above  $T_C$  the spectra are characterized by a temperature- (and field-) dependent depolarization rate that shows a divergent rise towards  $T_C$  starting at temperatures well above the critical temperature.
- (iii) A paramagnetic frequency shift is observed in nearly all compounds. It can reach values exceeding several percent close to  $T_C$ .
- (iv) The signal from muons stopped outside the sample (background signal from sample holder etc.) changes in frequency and relaxation at the critical point for the FM compounds, but not for AFM  $\text{CeAl}_2$ . The reason is the distortion of the applied field by the spontaneous bulk magnetization. This feature can be used to detect FM components in complex spin structures (see discussion on  $\text{GdMn}_2$ ).

The loss of sample signal for  $T < T_C$  comes from the fact that the 2-2 muon site divides into magnetically inequivalent sites in the presence of a local axis of magnetization, leading to several different dipolar fields (Hartmann 1989) and in turn to rapid (static) depolarization.

A typical example of temperature and field dependence of the paramagnetic depolarization rate is given in fig. 61 for  $\text{ErAl}_2$ , illustrating clearly the divergent behavior at  $T_C$ . The total relaxation rate

$$\Lambda(t) = \exp[-\sigma^2 t^2] \cdot \exp[-\lambda t], \quad (66)$$

contains the (static) inhomogeneous line broadening, which is roughly proportional to bulk susceptibility

$$\sigma = k_1 B_{\text{app}} / (T - T_C), \quad (67)$$

and the dynamic depolarization by fluctuating local fields. The latter is assumed to be field independent while its temperature dependence follows a power law:

$$\lambda = k_2 / (T - T_C)^w. \quad (68)$$

The constants  $k_1$ ,  $k_2$  and  $w$  are fit parameters. Equation (68) is a relation typical for critical behavior. The amazing result of the study by Hartmann et al. (1986) was the

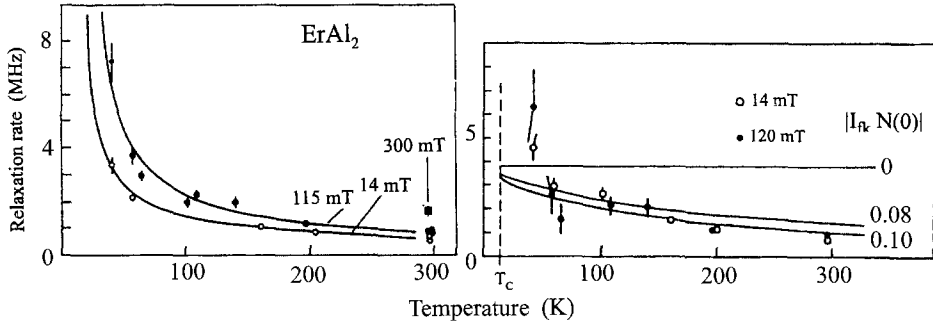


Fig. 61. Temperature dependence of the TF muon spin depolarization rate in  $\text{ErAl}_2$  for different fields. Left: Fit to the low-temperature region. Right: Fit to the high-temperature region. The fit functions are explained in the text.  $|I_{rk}N(0)|$  is a parameter of Korringa relaxation. From Hartmann et al. (1986).

observation that in many cases such a power law extends for the  $\mu\text{SR}$  relaxation over a temperature range far exceeding the usual critical regime. For example, in fig. 61 the range extends to about  $10 T_C$ . This feature has in the meantime been observed for the majority of R compounds exhibiting magnetic order (of any kind, not only FM order), especially for R ions with large orbital momenta. In the preceding chapter we have already pointed out that the relevant microscopic mechanism is the development of paramagnetic spin correlations up to the formation of dynamic magnetic clusters close to the transition point. Clearly,  $\mu\text{SR}$  already senses weak deviations from free paramagnetic spin motion.

The residual depolarization rate in the absence of spin correlations is contained in  $k_2$  of eq. (68) and determined by the RKKY (4f-4f) and Korringa (4f-ce) interactions. Starting from a treatment of the transverse NMR relaxation rate  $T_2^{-1}$  by Moriya (1956) and the common Korringa formalism (Korringa 1950) it was shown that the dynamic depolarization rate at high temperatures (when contact coupling is neglected) can be written as

$$\lambda = n \frac{4a^2}{3\hbar^2} J(J+1) \tau_J, \tag{69}$$

with

$$\tau_J = \left[ CT_C \left( \frac{3}{J(J+1)} \right)^{1/2} + \frac{\pi}{\hbar} (I_{rk}N_F(0))^2 k_B T \right]^{-1}. \tag{70}$$

The first term is the relaxation due to RKKY coupling, the second term the Korringa relaxation. The constants are  $n = 2$  for the 2-2 site and  $C = 1.477 \cdot 10^{11}$  Hz/K.  $I_{rk}$  is the 4f-ce coupling strength,  $N_F(0)$  the density of electrons at the Fermi surface for one direction of ce spin (see Loewenhaupt et al. 1983 for details and values) and  $a = (\mu_o/4\pi)(\mu_N\mu_B g_\mu g_J/d^3)$  the dipolar coupling strength between 4f moments and the muon, with  $d$  as the mean distance between  $\mu^+$  and the neighboring R ions ( $\sim 2.1 \text{ \AA}$

Table 7  
Properties of the paramagnetic state of R Laves-phase compounds from TF- $\mu$ SR<sup>a</sup>

Compound	$k_f$ (K)	$k_M \cdot M_{\text{eff}}$ (T)	$B_{\text{con}}$ (T)	$a_{\text{dip}}$ ( $10^{-7}$ eV)	$\tau_j(300)$ (ps)	$\lambda_{\text{th}}(300)$ ( $\mu\text{s}^{-1}$ )	$\lambda_{\text{exp}}(300)$ ( $\mu\text{s}^{-1}$ )
PrAl <sub>2</sub>	+0.12(1)	0.06(3)	+0.07(3)	3.8	0.39	0.09	0.05(3)
NdAl <sub>2</sub>	+0.14(5)	0.07(3)	+0.08(4)	3.5	0.19	0.04	0.02(3)
GdAl <sub>2</sub>	-0.27(5)	0.15(7)	-0.26(9)	9.6	0.09	0.11	0.38(6) <sup>b</sup>
DyAl <sub>2</sub>	+0.00(5)	sphere	0.00(2)	6.4	0.34	0.71	1.05(7)
HoAl <sub>2</sub>	+0.30(4)	0.21(9)	-0.09(11)	6.0	0.57	1.17	1.16(8)
ErAl <sub>2</sub>	+0.39(9)	0.19(9)	0.00(10) <sup>c</sup>	5.7	0.81	1.02	0.84(5)
TmAl <sub>2</sub>	-0.15(6)	0.15(8)	-0.20(10) <sup>c</sup>	5.6	0.98	0.44	0.43(4)

<sup>a</sup> Frequency shift parameter  $k_f$ , demagnetization correction  $k_M \cdot M_{\text{eff}}$  for an ellipsoidal sample with  $b/a = 1.6$ , derived contact field  $B_{\text{con}}$ , dipolar coupling strength  $a_{\text{dip}}$ , estimated  $4f$  fluctuation times (RKKY and Korringa)  $\tau_j(300)$ , calculated and measured relaxation rates  $\lambda_{\text{th}}(300)$  and  $\lambda_{\text{exp}}(300)$  at room temperature for various RAl<sub>2</sub> compounds. Errors are given in brackets. After Hartmann et al. 1986.

<sup>b</sup> Experimental values of moments were used.

<sup>c</sup> Zero field value (Kalvius et al. 1984).

for RAl<sub>2</sub> compounds). For details we refer to the original paper. One notices that the RKKY term leads to a temperature-independent relaxation rate (Moriya limit), while the Korringa term is weakly ( $1/T$ ) temperature dependent. It is, however, in many cases negligibly small and as a rule not taken into consideration, meaning that  $k_2$  in eq. (68) is taken as constant. The case of ErAl<sub>2</sub> is an example where the Korringa relaxation appears to be noticeable. The solid line in fig. 61 (right) shows theoretical calculations for different values of  $|I_{\text{fk}}N(0)|$ . In the general derivation of CEF effects on  $\mu$ SR relaxation rates by Dalmas de Réotier et al. (1996), a term appears that is not unlike the Korringa term. In practice it may not be easy to distinguish between the two contributions.

Table 7 lists calculated values of  $a_{\text{dip}}$ ,  $\tau_j$  and  $\lambda$  at 300 K together with measured rates  $\lambda(300\text{ K})$ . These values have been obtained by extrapolating to zero field the rates measured for different transverse fields. For some RAl<sub>2</sub> (most notably for GdAl<sub>2</sub>) ZF depolarization rates have been obtained by Kalvius et al. (1984). In the fast fluctuation limit the rates  $1/T_1$  (measured in ZF) and  $1/T_2$  (measured in TF and corrected for inhomogeneous line broadening) should be equal (Hayano et al. 1979). The agreement between ZF and corrected TF rates for several RAl<sub>2</sub> intermetallics is satisfactory. The same holds for the agreement between measured and calculated values of  $\lambda(300)$  if one takes into account the simplifying assumptions used. The result on  $\tau_j$  (THz region) is in keeping with inelastic neutron scattering data. One should also notice that, despite the high fluctuation rates, the heavy R ions with large orbital momenta lead to substantial depolarization rates ( $\sim 1 \mu\text{s}^{-1}$ ) in the Moriya limit. Further discussions and derivations of  $\lambda$ , especially in ZF can be found in chapter 2.3 of Schenck and Gyax (1995) and in appendix C of Dalmas de Réotier and Yaouanc (1997).

The temperature dependence of the paramagnetic frequency shift has already been shown in fig. 18 for PrAl<sub>2</sub>. The shift is given by

$$\frac{\Delta\nu}{\nu} = \frac{\mu_B g_J (J + 1)}{3k_B (T - T_C)} (k_M M_{\text{eff}} + B_{\text{con}}(T = 0)), \quad (71)$$

when using a powder sample where dipolar fields average to zero. This expression allows determination of the saturation ( $T = 0$ ) contact field. Derived values are given in table 7. The crucial parameter is the correction factor ( $k_M M_{\text{eff}}$ ) for the demagnetizing field. In the present cases it has been estimated for an ellipsoidally shaped sample with  $b/a = 1.6$ . The use of a spherical sample is advantageous (see also discussion on Gd metal). From the listed values of  $a_{\text{dip}}$  one calculates dipolar fields at the muon site on the order of 1 T. The contact fields are negligible in comparison, except for GdAl<sub>2</sub> which possesses pure spin magnetism. As discussed in sect. 3.1, the contact field can be expressed in terms of the difference in spin-up and spin-down conduction electron density at the muon site. This density is enhanced by the positive charge of the muon. Interstitial spin magnetization densities have been measured for several RAl<sub>2</sub> compounds by diffuse neutron scattering (Boucherle and Schweizer 1981). Comparison with the value of the contact field sensed by the muon gives enhancement factors around two for the conduction electron spin-polarized density induced by the muon charge. Precise theoretical estimates of this effect are not available. In summary, the work of Hartmann et al. (1986) provided the foundation for the treatment of μSR data in R intermetallics.

DyAl<sub>2</sub> has also been studied in ZF and LF by Gradwohl et al. (1986) using a single crystal. These authors found that  $\lambda$  peaks somewhat above  $T_C$ , independent of an applied LF up to 100 mT. Trapping–detrapping effects are suggested as a possible cause. This scenario is reasonable from the point of view of the temperature range involved, but it requires unusually fast diffusion rates ( $>10^{11}$  Hz). The problem remains unsolved, but Asch et al. (1986a) found that the μSR relaxation behavior of DyAl<sub>2</sub> is sample dependent. This is probably due to stoichiometry problems, a common feature in Laves-phase compounds.

The analysis of Hartmann et al. (1986) on the μSR response in RAl<sub>2</sub> intermetallics neglected any CEF effects. Deviations of the paramagnetic muon spin relaxation behavior from a smooth Curie–Weiss dependence became more evident in ZF studies of HoAl<sub>2</sub> and ErAl<sub>2</sub> (Dalmas de Réotier et al. 1990b). They were ascribed to a CEF induced temperature dependence of the 4f magnetic moment. To shift all CEF effects into a temperature-dependent magnetic moment is the simplest straightforward approach. Since the energy separation between the CEF ground and first excited state is larger in the Er than in the Ho compound, CEF effects are fairly weak in ErAl<sub>2</sub> but clearly noticeable in HoAl<sub>2</sub>. The authors also point out the strong influence of magneto-crystalline anisotropy. This aspect has been discussed in sect. 4 and is best studied with single crystals.

5.3.1.2. *AnAl<sub>2</sub>* ( $An = U, Np$ ). UAl<sub>2</sub> shows no transition into a magnetically ordered state down to temperatures below 1 K. An effective paramagnetic moment on the uranium

of  $\sim 3\mu_B$  and a paramagnetic Curie temperature  $\theta_p \approx -250$  K were derived from susceptibility data above 100 K. The somewhat enhanced low-temperature Sommerfeld constant is  $\gamma(0) = 0.09$  J/(mol K<sup>2</sup>). Below 50 K UAl<sub>2</sub> exhibits unusual temperature dependences of specific heat, magnetic susceptibility and electrical resistivity and for that reason UAl<sub>2</sub> is sometimes considered a moderate HF system. A summary of these experimental findings can be found in Fournier and Troć (1985). The low-temperature specific heat, in particular, can be expressed well in terms of spin fluctuations. Originating from this, all the unusual features of UAl<sub>2</sub> could be explained by a very narrow 5f band ( $\approx 60$ –150 K) producing a high density of states at the Fermi surface, a Stoner enhancement factor  $S \approx 4$ , and the presence of strong spin fluctuations ( $T_{SF} \approx 25$ –30 K). The latter in turn prevent the onset of magnetic order. Such systems are termed “spin fluctuators” and UAl<sub>2</sub> is the prime example. Several band structure calculations have also appeared. Boring et al. (1985) found wide 5f bands ( $\approx 500$  K) and a Stoner enhancement of  $\sim 10$  resulting in a higher spin fluctuation temperature ( $T_{SF} \geq 40$  K). In contrast, de Groot et al. (1985) calculate a low Stoner factor ( $S \approx 2$ ) and have no need for strong spin fluctuations. Both calculations explain successfully most of the low-temperature bulk properties in terms of the details of the DOS near  $E_F$ .

TF-, ZF- and LF- $\mu$ SR measurements on UAl<sub>2</sub> are reported by Asch et al. (1987) and Kratzer et al. (1986). Typical ZF and LF spectra are shown in the upper panel of fig. 62. The ZF spectra can be explained by the depolarizing action of <sup>27</sup>Al nuclear dipoles. The LF = 10 mT spectrum shows that even at low temperatures the U moments have only a weak depolarizing influence ( $\lambda \approx 0.1$   $\mu$ s<sup>-1</sup>) due to fast spin fluctuations ( $\tau_{4f} > 10^{13}$  Hz). The rate  $\lambda$  rises weakly at low temperatures, but shows no sign of critical slowing down. Similarly, the frequency shift in an applied TF remains largely independent of temperature (see lower panel of fig. 62), but shows the same irregularity (which, however, is hardly outside error limits) at low temperatures as the relaxation rate. The origin of this feature is not understood. In summary, the  $\mu$ SR data on UAl<sub>2</sub> indicate weak paramagnetic behavior down to low temperatures. The absence of ordered magnetism is in full keeping with the picture of a well-developed 4f spin fluctuator. The given limit for  $\tau_{4f}$  agrees well with neutron measurements of dynamic susceptibility (Loong et al. 1986).

Park et al. (1997a) report on a  $\mu$ SR study of spin dynamics in Gd<sub>x</sub>U<sub>1-x</sub>Al<sub>2</sub> and Gd<sub>x</sub>La<sub>1-x</sub>Al<sub>2</sub>. The magnetic LRO of GdAl<sub>2</sub> ( $x = 1$ ) is disrupted by introduction of U atoms around  $x = 0.8$  in favor of a spin glass ground state. On the other side, a strong coupling of dilute Gd moments to the rapidly fluctuating U moments in the nonmagnetic spin fluctuator UAl<sub>2</sub> leads to (spin glass) magnetism beyond  $x = 0.1$ . LaAl<sub>2</sub> is devoid of any magnetic moment. This situation is changed by doping with Gd, and spin glass magnetism develops here as well, but the concentration range where this state exists is much narrower (Ping and Coles 1982, Coles et al. 1984).

ZF- $\mu$ SR spectra for (Gd<sub>x</sub>U<sub>1-x</sub>)Al<sub>2</sub> with  $x = 0.03$  and 0.1 were measured down to 2 K. In contrast to pure UAl<sub>2</sub>, the muon relaxation in the  $x = 0.03$  alloy does not show the simple temperature-independent Gaussian shape (caused by the dominance of depolarization by Al nuclear dipoles), but rather approaches exponential shape at low temperatures. Clearly, the spin dynamics of UAl<sub>2</sub> is already affected even by this low Gd concentration and

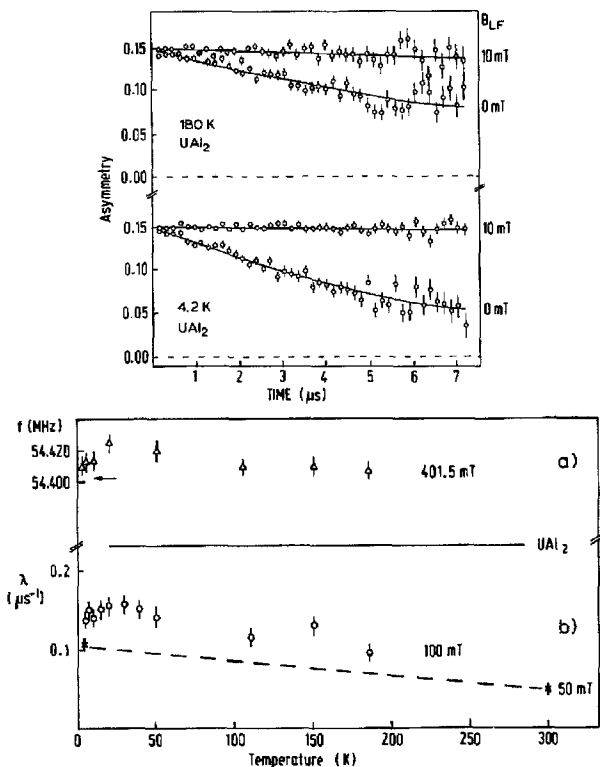


Fig. 62.  $\mu$ SR results of UAl<sub>2</sub>. Upper panel: ZF and LF = 10 mT spectra at 180 and 4.2 K. Lower panel: Temperature dependences of the precession frequency in TF = 401.5 mT ( $f_0$  for a free  $\mu^+$  is indicated by an arrow) and the electronic relaxation rate in LF = 100 mT. After Asch et al. (1987).

the spin system has left the ultra-fast limit of a spin fluctuator. The dominant feature in the spectra of the  $x = 0.1$  alloy is a gradual loss of signal amplitude with decreasing temperature below  $\sim 30$  K. In an increasing volume portion of the sample the stopped muons sense a widely distributed and fairly strong quasistatic local field. The loss of signal amplitude is complete at  $\sim 10$  K (the nominal  $T_g$ ). The whole sample has now suffered spin freezing. In magnetic fields (LF) in excess of 30 mT the signal is recovered, corroborating the picture just presented. The sample undergoes a markedly inhomogeneous spin freezing process. The shape of the decay of muon spin polarization in the non-spin-frozen portion is again not purely Gaussian, demonstrating once more the deviation in spin dynamics from the situation in pure UAl<sub>2</sub>. Gd-doped LaAl<sub>2</sub> at  $x = 0.05$  is, according to bulk data, a spin glass at low temperature. The muon spin relaxation rate as a function of temperature is peculiar and not understood. It first increases as usual down to 60 K but then decreases once more with a minimum near 20 K. A new increase follows and at 2 K the same rate is reached as before at 60 K. Disregarding this peculiarity, the  $\mu$ SR response is similar to that of (Gd<sub>0.03</sub>U<sub>0.97</sub>)Al<sub>2</sub>, meaning in particular that the signal amplitude changes little with decreasing temperature. Full spin freezing does not occur, only a moderate slowing down of spin fluctuations is observed.



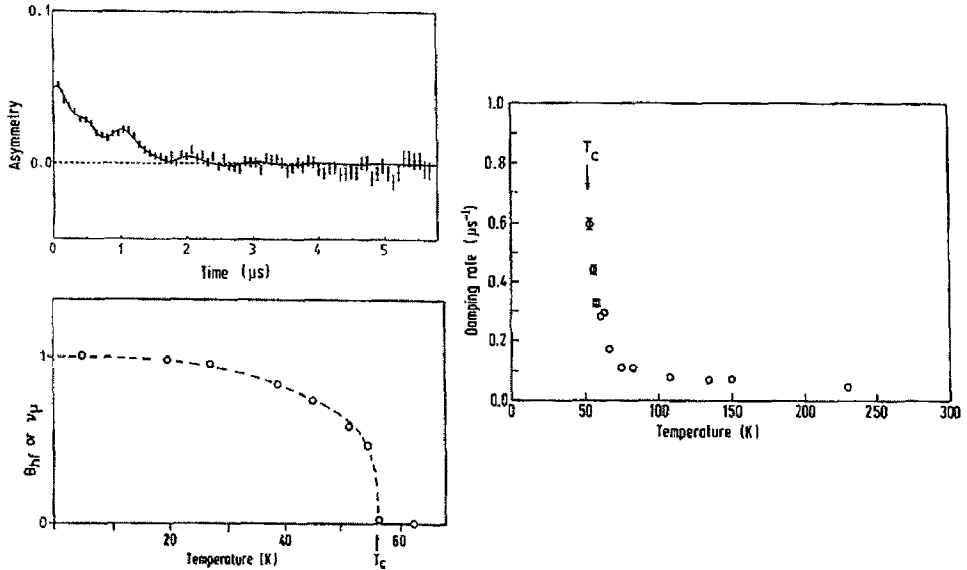


Fig. 63.  $\mu$ SR spectroscopy on  $\text{NpAl}_2$ . Top left: ZF spectrum below the Curie temperature. Bottom left: temperature variation of the normalized mean spontaneous precession frequency together with the normalized variation of the hyperfine field at the Np nucleus from Mössbauer measurements (dashed line). Right: Temperature dependence of the transverse field (20 mT) relaxation rate. After Aggarwal et al. (1990).

$\text{NpAl}_2$  (C15 Laves phase) orders ferromagnetically at  $T_C = 56\text{ K}$  with a moment  $\mu_{\text{Np}} = 1.5\mu_B$ . That value is considerably below the free-ion value (of either  $\text{Np}^{4+}$  or  $\text{Np}^{3+}$ ) and has been taken in connection with high-pressure Mössbauer data as evidence for Np moment delocalization because of 5f–5f electron overlap. A summary of bulk properties is given by Fournier and Troć (1985). The Mössbauer results are discussed in detail by Potzel et al. (1993).

The  $\mu$ SR study of  $\text{NpAl}_2$  (Aggarwal et al. 1990) was the first attempt to investigate a transuranic compound by this technique. The technical difficulties connected with the double safety encapsulation make precise measurements, especially the determination of sample signal amplitude quite difficult. The unusual result was that in ZF spontaneous spin precession is observed for  $T < T_C$  (fig. 63, top left), containing at least two different frequencies. The difficulty in nailing down the exact strength of the signal arising from muons stopped in the sample makes it impossible to decide whether the oscillating signal is the full sample signal. Indications are that this is most likely not the case. The observation of a spin precession signal is in contrast to the results in the R dialuminates where signal amplitude collapses at the magnetic transition temperature, due to the multitude of magnetic sites in the C15 Laves-phase structure (see above). One may speculate (but without any real supporting evidence) that the delocalization of the 5f magnetic moment helps in that direction, because a certain averaging of internal fields could occur. It is remarkable in this connection that a spin precession signal is seen in

one other material (CeAl<sub>2</sub>) where a not-so-well-localized f electron structure exists. In addition, Huxley et al. (1996) mention in their study of CeRu<sub>2</sub> (discussed in sect. 9) that the observed nuclear dipole width in ZF for CeAl<sub>2</sub> is distinctly smaller than the calculated one. To us, this could be another indication of the occurrence of an averaging process in this type of material.

The temperature dependence of the mean precession frequency in NpAl<sub>2</sub> (insert to fig. 63, bottom left) follows closely that of the hyperfine field ( $B_{\text{hf}}$ ) determined by Mössbauer spectroscopy. Both do not show exactly the expected Brillouin behavior. The deviations had originally been explained by Dunlap et al. (1969) with biquadratic exchange. Later, slow spin fluctuations (magnetic Mössbauer relaxation spectra) have been favored as cause (see Dunlap and Kalvius 1985). The identity of the μSR and Mössbauer results with their largely different time windows rule out the latter explanation and biquadratic exchange appears to be present. The temperature variation of relaxation rate shows the typical slowing of spin fluctuations on approach to  $T_C$  (fig. 63, right).

### 5.3.2. $MT_2$ ( $T = Fe, Co, Ni$ )

#### 5.3.2.1. $RT_2$ .

Magnetic properties of R intermetallics formed with 3d transition elements have been reviewed by Franse and Radwanski (1993). The Laves-phase compounds of type  $RT_2$  that have been studied by μSR are listed, together with the μSR references and some relevant data in table 8. In these systems (except for R = Y, Lu), two magnetic sublattices are present, one formed by the strong localized 4f electron magnetism of the  $R^{3+}$  ions (with  $\mu_R$  equal to the free (3+) ion value), the other by the weak itinerant 3d electron magnetism of the transition elements (with moments well below the free-ion value). The two sublattices order ferromagnetically at the same temperature ( $T_C$  of the compound). They are FM coupled for the light R elements (up to Sm), and

Table 8  
Ferromagnetic C15 Laves-phase compounds of type  $RT_2$  studied by μSR

Compound	Lattice constant (Å)	$T_C$ (K)	$T_{\text{comp}}$ (K)	μSR references
YFe <sub>2</sub>	7.36	535		Barth et al. (1986a)
GdFe <sub>2</sub>	7.39	810		Graf et al. (1981), Barth et al. (1986a)
GdCo <sub>2</sub>	7.26	404		Barth et al. (1986a)
ErFe <sub>2</sub>	7.28	587	486	Barth et al. (1986a)
TmFe <sub>2</sub>	7.25	599	225	Barth et al. (1986a)
LuFe <sub>2</sub>	7.23	596		Barth et al. (1986a)
GdNi <sub>2</sub>	7.20	76		Chappert et al. (1986) Dalmas de Réotier et al. (1990b)
DyNi <sub>2</sub>	7.14	22		Chappert et al. (1986) Dalmas de Réotier et al. (1990b)
HoNi <sub>2</sub>	7.14	23		Dalmas de Réotier et al. (1990b)

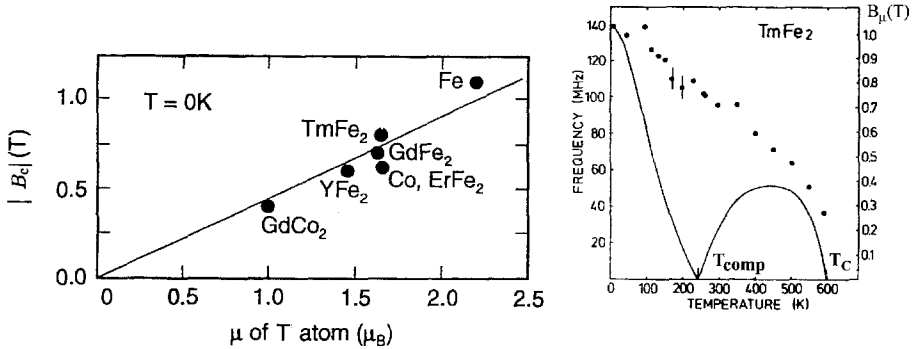


Fig. 64. Left: Contact fields for  $T \rightarrow 0$  derived from the spontaneous precession frequencies for various  $RT_2$  intermetallics. The solid line suggests a linear dependence on the magnetic moment of the 3d ligand. Also shown are the results for Fe and Co metal (Denison et al. 1979). Right: Spontaneous spin precession frequency as a function of temperature in  $TmFe_2$ . The solid line shows the temperature dependence of bulk magnetization normalized to  $\nu_\mu(0)$ . From Barth et al. (1986a).

AFM coupled for the heavy R elements. The latter coupling leads in  $TmFe_2$  and  $ErFe_2$  to a so called compensation point ( $T_{comp}$ ) where bulk magnetization goes through zero, because the magnetizations of the R and T sublattices are there of equal strength but directed oppositely.

With the exception of compounds with  $T = Ni$ , one sees that the  $T_C$ 's are located well above room temperature and thus much higher than in the di-aluminides. The contrasting result is, that in ZF a single spontaneous muon precession frequency is observed below  $T_C$ , although one expects a muon location on the 2-2 site (providing multiple local magnetic fields in the ordered state) here as well (in fact, the neutron work on hydrogen loading mentioned earlier refers specifically to  $RFe_2$  compounds). The  $\mu$ SR data shown in fig. 59 demonstrate a mobile muon above  $\sim 80$  K in the C15 structures. Hence the most likely explanation for the appearance of spontaneous muon spin precession frequency (and a single one in particular) is an averaging over the various magnetic muon stopping sites. One must remember that the differences in local field arise from the anisotropic property of dipolar fields. As the result of site averaging, the muon senses the isotropic contact field as the only microscopic contribution. Figure 64 (left) clearly demonstrates that  $B_\mu$  is given almost entirely by the moment on the transition element. For  $R = Y, La$  this is trivial. For the heavy R one could argue that the contact contribution is small (see, for example the results on  $RAI_2$  intermetallics), but the result for the Gd compounds (where a noticeable Gd contact field should exist) is not easily understood. Since only the 3d moments are responsible for the local field it is not surprising that the temperature dependence of spontaneous precession frequency does not follow that of bulk magnetization. An extreme case is depicted in fig. 64 (right). It shows that in  $TmFe_2$  the characteristic feature of a compensation point is not reflected in the behavior of  $B_\mu$  at all. Its temperature dependence follows much more closely that of the Fe sublattice magnetization as a comparison with neutron data (Bargouth and Will 1971) demonstrates. The ZF relaxation rates are

determined by both the dynamics of magnetic moments and the motional properties of the muon. The two effects are not easily separable.

Recently, the observation of the muon spin resonance signal has been reported (Lord 1998) for  $\text{YFe}_2$  at room temperature (i.e., in the FM regime). The weak, but distinct resonance is seen at 30.6 MHz in ZF with an RF-field of  $\sim 0.8$  mT. This value agrees perfectly with the result of Barth et al. (1986a). This was just a basic test of feasibility and no further discussion is given.

The  $\text{RT}_2$  intermetallics with  $T = \text{Ni}$  are, according to bulk data, much closer to the  $\text{RAl}_2$  than the  $\text{RFe}_2$  or  $\text{RCo}_2$  compounds in their magnetic properties. Their low  $T_C$ 's are but one example. Since the magnetic transitions occur below the muon localization temperature, no signal is seen in the ordered state for  $\text{GdNi}_2$ ,  $\text{DyNi}_2$  and  $\text{HoNi}_2$ , the compounds of this series studied by  $\mu$ SR. Chappert et al. (1986) compared paramagnetic fluctuation rates for the pairs  $\text{GdAl}_2/\text{GdNi}_2$  and  $\text{DyAl}_2/\text{DyNi}_2$ . In the Moriya limit the muon relaxation rate is expected to be inversely proportional to  $T_C$  and to the lattice distance  $d$  to the sixth power. When forming the ratio of rates between the Al and Ni compounds the R moments and spins should cancel. Comparing calculated and measured values show good agreement for the Gd pair but not for the Dy pair. In  $\text{DyNi}_2$  the rate is nearly an order of magnitude smaller as calculated. The authors suggest a coupling of the anisotropic (orbital) R electron distribution to the electric field gradient produced by the  $\mu^+$  (Campbell 1984), which leads to a rapid precession around the R- $\mu$  axis. This effect could lead to additional motional narrowing. It is clearly absent for  $\text{Gd}^{3+}$ .  $\text{HoNi}_2$  was studied with respect to CEF interactions (Dalmas de Réotier et al. 1990b). A behavior of  $\lambda(T)$  similar to  $\text{HoAl}_2$  was found. This is expected since CEF splittings are nearly identical.

5.3.2.2.  $\text{AnT}_2$ . All compounds  $\text{AnT}_2$  with  $\text{An} = \text{U}$  and  $\text{Np}$  possess the cubic C15 structure with the exception of  $\text{UNi}_2$  (hexagonal C14 Laves phase). To our knowledge, no  $\mu$ SR data exist for the uranium alloys. The only actinide material studied by  $\mu$ SR thus far is  $\text{NpCo}_2$ .

The  $\text{NpT}_2$  intermetallics are special with respect to their electronic structure. The Laves phases  $\text{NpX}_2$ , where X is not a 3d transition element, are prime examples (see Potzel et al. 1993) for the Hill model. In contrast, the  $\text{NpT}_2$  compounds are marked exceptions. They exhibit ordered (FM or AFM) magnetism with sizable moments ( $\sim 1\mu_B$  on Np), although their Np-Np separation is well below the Hill limit. On first thought one may suspect that ordering of the T-sublattice pulls the Np-sublattice. But  $\text{NpNi}_2$  is a dramatic counterexample ( $\mu_{\text{Np}} = 1\mu_B$ ,  $\mu_{\text{Ni}} < 0.3\mu_B$ ). The underlying cause must rather be a special electronic structure generated by 3d-5f hybridization (see, for example, Boring et al. 1985).

$\text{NpFe}_2$  and  $\text{NpNi}_2$  are established FM (with  $T_C = 492$  and 32 K). The magnetic ground state of  $\text{NpCo}_2$ , in contrast, has been under some discussion. Usually it is listed as an AFM with  $T_N = 13$  K, based on susceptibility and mainly on Mössbauer data (Aldred et al. 1975, Sanchez et al. 1992). There a Zeeman pattern appears (in the absence of an applied field) below 13 K. The spectrum shows, however, rather wide resonance lines and a clear distinction between static (distribution of internal fields) and dynamic broadening cannot

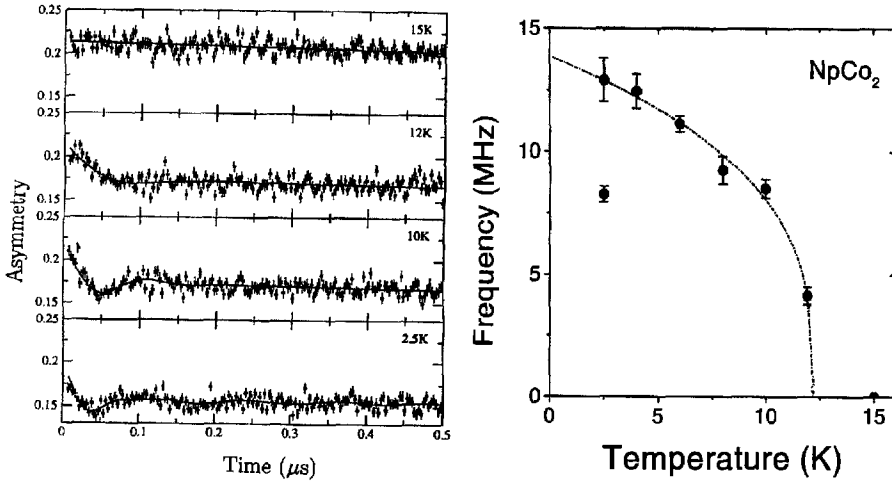


Fig. 65.  $\mu$ SR spectroscopy on  $\text{NpCo}_2$ . Left: ZF- $\mu$ SR spectra in the paramagnetic (15 K) and magnetically ordered (12, 10, 2.5 K) regimes. Right: Spontaneous spin precession frequency as a function of temperature. The line is a guide to the eye. A two-frequency fit works better at 2.5 K, suggesting a somewhat different spin structure than at higher temperatures. From Kopmann et al. (1999).

be made. Hence, an alternative explanation of the Mössbauer results would be a rather sudden slowing down of Np moment fluctuations (leading to the so called “paramagnetic hyperfine splitting” – see, for example, Dunlap and Kalvius 1985) without the presence of a magnetic phase transition. Some features of the hyperfine spectra distinctly point in that direction. Sanchez et al. (1992) also performed neutron diffraction studies. The specimen was a small single crystal. No magnetic Bragg reflections were observed. Yet, the authors point out that the conclusion of absence of long-range magnetic order can only be drawn on the basis of the (reasonable) assumption of a type I AFM spin structure. The magnitude of the magnetic hyperfine field observed by Mössbauer spectroscopy corresponds to an ordered moment of  $\mu_{\text{Np}} \approx 0.5\mu_{\text{B}}$ . Polarized neutron measurements of the magnetic form factor in an applied field of 4.6 T gave  $\mu_{\text{Co}} = 0.06\mu_{\text{B}}$  and  $\mu_{\text{Np}} = 0.21\mu_{\text{B}}$  (Wulff et al. 1990).

Recent (still preliminary) ZF- $\mu$ SR data (Kopmann et al. 1999) on  $\text{NpCo}_2$  clearly show the onset of spontaneous spin precession below 13 K (see fig. 65). The precession frequency is compatible with the quoted values for  $\mu_{\text{Np}}$ . As in  $\text{NpAl}_2$ , it is difficult to judge whether all muons stopped in the sample participate in spin precession. Again, the indication is that this is probably not the case. This, together with the strong damping of the oscillatory signal ( $\sigma > 10\mu\text{s}^{-1}$ ), points towards a more complex spin structure than type I AFM. This then is compatible with both the neutron and Mössbauer results. In any case, the AFM transition at  $T_{\text{N}} = 13$  K is safely established by  $\mu$ SR, which puts  $\text{NpCo}_2$  in line with the rest of the  $\text{NpT}_2$  materials. The spin structure of  $\text{NpCo}_2$  remains to be determined.

### 5.3.3. $MMn_2$ and related compounds

The  $RMn_2$  series exists as Laves phase for practically all rare-earth atoms. Either the cubic (C15) or the hexagonal (C14) variant is formed. Our discussion is limited to materials with the C15 structure. The special feature of this system is that the Mn atoms only carry a moment if the lattice parameter exceeds  $7.6\text{\AA}$  (or the Mn–Mn separation  $2.67\text{\AA}$ ) (Wada et al. 1987). A theoretical discussion of the problem can be found in Ballou et al. (1991). Amongst the compounds with magnetism on Mn, the material  $YMn_2$  plays a special role since in this case the R partner is not magnetic. Corresponding actinide compounds are also known (at least  $UMn_2$ ,  $NpMn_2$  and  $PuMn_2$ ). Magnetic order is definitely established only for  $NpMn_2$  (FM with  $T_C = 56\text{ K}$ ). For details see Fournier and Troć (1985).

5.3.3.1.  $YMn_2$ . The intermetallic  $YMn_2$  has been studied thoroughly with respect to its bulk magnetic properties. At high temperatures it is considered a weak itinerant-electron magnet with a moment of  $1.7\mu_B$  on Mn. Its features are well described by the self-consistent renormalization theory (SCR) of spin fluctuations (Moriya and Kawabata 1973). The corresponding strong spin fluctuations were detected by neutrons (Deportes et al. 1987). When entering the AFM state (basically a collinear type I structure) around 100 K it exhibits all features of a strong localized magnet with a moment of  $\mu_{\text{ord}} = 2.7\mu_B$ .

Since the Mn ions form a sublattice of regular tetrahedra (fig. 66, left), dominant AFM nearest-neighbor exchange leads to full geometrical frustration (see lower part of fig. 66, left). The strong longitudinal spin fluctuations in the paramagnetic regime are an outcome of frustration. In addition, such a system cannot support a collinear AFM spin structure and tends to enter a spin-glass-like state instead (Gaulin 1994).  $YMn_2$ , however, takes a different path. It combines the AFM transition with strong lattice expansion ( $\sim 5\%$  volume change) together with tetragonal distortion. Nearest-neighbor exchange is weakened and no longer independent of direction. This leads to pronounced hysteresis at  $T_N$  (fig. 66, right), establishing the first-order nature of the magnetic phase transition. In addition, a long wave ( $\sim 400\text{\AA}$ ) helical modulation of the basic collinear spin structure is present (Ballou et al. 1987). Neutron scattering also found a coexistence of para- and antiferromagnetic phases at 70 K and the persistence of strong AFM correlations up to  $6 T_N$  (Freltoft et al. 1988). In general,  $YMn_2$  and its related compounds are prime examples for the study of magnetism under heavy frustration and most of the  $\mu$ SR work is concerned with this aspect. Other materials to be mentioned in this context are the pyrochlores (see sect. 8) and the Kagomé compounds. For the latter no R or An-containing materials are known. The AFM Laves phases as well as the pyrochlores possess a three-dimensional frustrated lattice (tetrahedra) while the Kagomé materials feature a two-dimensional (corner-shared triangles) frustrated lattice.

$\mu$ SR spectroscopy in ZF, LF and TF on pure (polycrystalline)  $YMn_2$  has been reported by Cywinski et al. (1991), Weber et al. (1994a) and Kalvius (1994). The first study centered on the spin dynamics on approach to the magnetic transition, the latter two looked in addition for a spin-glass-like magnetic precursor state due to the heavy

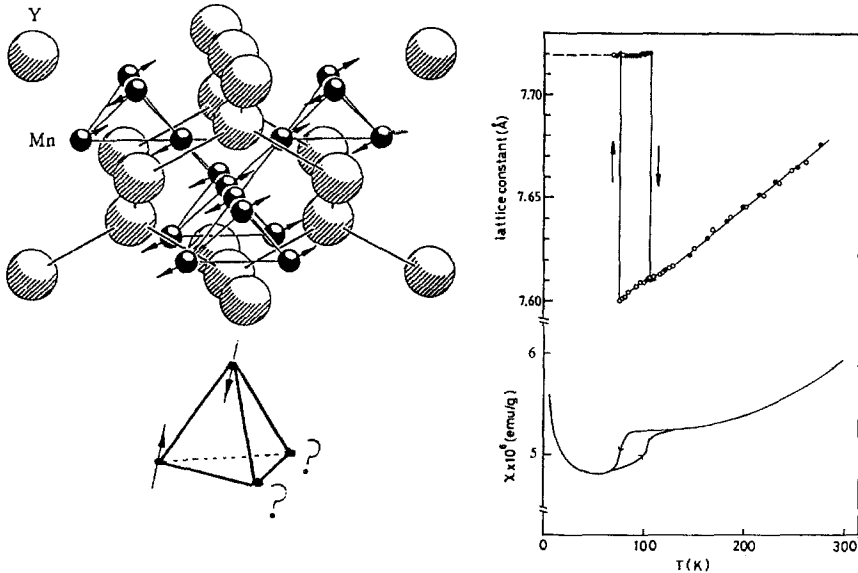


Fig. 66. Properties of  $YMn_2$ . Left: Crystalline and (basic) magnetic structure (top) and illustration of geometrical frustration in a tetrahedron (bottom). Right: Lattice expansion and hysteresis around the AFM transition (after H. Nakamura et al. 1988b), together with the temperature dependence of magnetic susceptibility (after Shiga et al. 1983).

frustration. The different works do not contain contradictory information. A  $\mu$ SR signal from the AFM-LRO phase could not be detected. A broad field distribution must cause very rapid depolarization. In the presence of AFM order the 2-2 position taken by the muon splits into 12 magnetically different sites for which dipolar sum calculations give local fields between 0.2 and 1.5 T (Weber 1992). Rapid muon depolarization is thus a natural outcome. The paramagnetic signal is characterized by electron–nuclear double relaxation. The difficulty here is that both moments are on the Mn ion and hence hyperfine coupled, meaning that also the nuclear dipole fields appear dynamic with a temperature-dependent relaxation rate. As discussed in sect. 3.4 one would need the quasistatic high-temperature limit for the nuclear depolarization in order to separate the two relaxation channels. Unfortunately, this limit is never reached in  $YMn_2$ . It is likely that the muon becomes mobile. We discuss the problem of the high-temperature relaxation further below. Weber et al. (1994a) resorted to a global fit procedure of ZF, TF and LF spectra taken under identical condition. Figure 68 gives an example of this method.

Observing the strength (initial asymmetry) of the paramagnetic signal as a function of temperature (especially in TF) directly mirrors the temperature dependence of the paramagnetic volume fraction. The typical hysteretic behavior around  $T_N$  is observed and hence also present on a local scale. We have shown this result earlier in fig. 28 in sect. 3.2.1 when discussing such types of measurements in general. Figure 28 further shows that in addition to the loss of signal when the AFM state is formed around 100 K

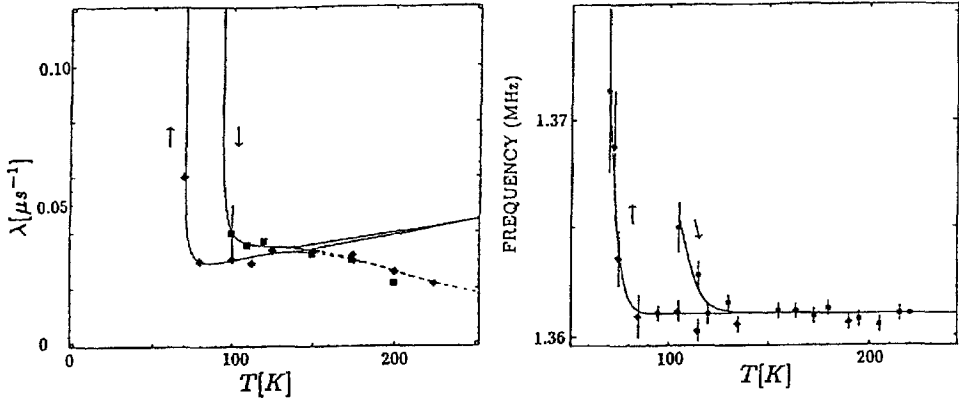


Fig. 67. Left: ZF relaxation rate  $\lambda$  of the paramagnetic signal in  $\text{YMn}_2$  as a function of temperature for a cooling and warming sequence. The solid line is a fit to the SCR model (see text), the dashed line a guide to the eye. See the text for a discussion of this deviation at higher temperatures. Right: Corresponding data for the paramagnetic frequency shift. The full line is a guide to the eye. Note the absence of temperature dependence for  $T > 130$  K. After Kalvius (1994).

(on cooling) an initial reduction of amplitude of the paramagnetic signal begins around 150 K. This drop coincides with the appearance of a rapidly damped signal. It could best be fitted by a power exponential relaxation  $\exp[-(\lambda t)^p]$  with  $p$  close to 0.5. A typical example is shown in fig. 68 (which refers to Tb-doped  $\text{YMn}_2$  where the effect is even more pronounced – see further below). LF measurements confirm the highly dynamic nature of the fast component. The relaxation rate changes little with decreasing temperature, but the signal strength increases somewhat. It is interpreted as arising from spin-glass-like clusters which begin to form above the magnetic transition when critical slowing down limits the relief of frustration by longitudinal spin fluctuations. The SRO clusters remain present throughout the region of hysteresis around  $T_N$ . In pure  $\text{YMn}_2$  their continuous presence below  $T_N$  could not be established with certainty.  $^{57}\text{Fe}$  Mössbauer spectroscopy (Przewoźnik et al. 1993) on  $\text{YMn}_2$  doped with 0.5% Fe (which substitutes for Mn atoms) showed that at 4.2 K still ~11% of the sample does not participate in the long-range AFM order. The hysteresis at  $T_N$  is also observed. The internal field at the Fe nuclei is largely temperature independent for  $T < T_N$ , as expected for a first-order transition.

The relaxation rate of the normal paramagnetic signal (separated from the spin glass signal) shows critical behavior on approaching  $T_N$  (fig. 67, left). It could be fitted up to ~150 K to the temperature dependence expected from the self-consistent-renormalization (SCR) model of Moriya and Ueda (1974) and an additional Korringa term. At higher temperatures the rate decreases again. The most straightforward explanation is the onset of muon diffusion (Kalvius 1994), but recently, pulsed  $^{55}\text{Mn}$  NMR on  $\text{YMn}_2$  (H. Nakamura et al. 1998) found a decrease of  $1/T_2$  slightly above 130 K that points towards an intrinsic irregularity of the Mn moment fluctuation rate. An explanation has not yet been given. Only the relaxation rate  $\lambda$  shows this feature in  $\mu$ SR. The paramagnetic frequency shift (fig. 67, right), which demonstrates critical



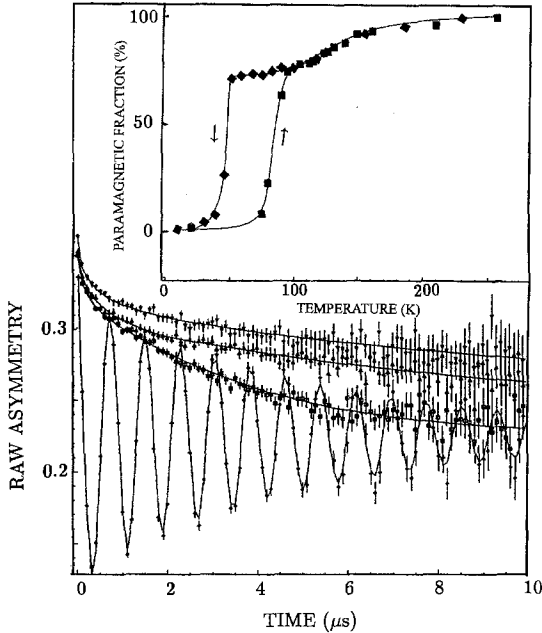


Fig. 68.  $\mu$ SR spectra of  $Y_{0.9}Tb_{0.1}Mn_2$  at 90 K (warming) taken in TF=100 G, ZF and LF=20 G and 200 G (from bottom to top). These four spectra were least squares fitted simultaneously. The inset shows the temperature variation of the paramagnetic fraction (compare with the data for pure  $YMn_2$  in fig. 28). After Kalvius (1994).

behavior as well, remains constant for  $T \gg T_N$ . From the behavior of both rate and shift on approach to  $T_N$ , it is concluded that  $YMn_2$  tries to undergo a normal second-order magnetic phase transition, but this is prevented by the pronounced frustration enforcing lattice distortion.

5.3.3.2.  $Y(Tb)Mn_2$ . Replacing Y by a few percent of Tb has two major effects. Firstly, it lowers the AFM transition temperature, but keeps the hysteretic behavior. Secondly, it suppresses the slow helical modulation of the type I spin structure (Berthier et al. 1988).  $\mu$ SR measurements were performed on  $Y_{0.9}Tb_{0.1}Mn_2$  and  $Y_{0.95}Tb_{0.05}Mn_2$  (Asch et al. 1990a, Weber et al. 1994a, Kalvius 1994). No significant difference in  $\mu$ SR response could be found for the two (polycrystalline) samples. A comparison between figs. 28 and 68 immediately demonstrates that the addition of Tb leads to a higher portion (up to  $\sim 20\%$ ) of the fast-decaying spin-glass signal at the transition temperature, as well as to an onset of this feature already at higher temperatures (although the magnetic transition temperature is lower). The fast depolarization rate is  $\sim 1.5 \mu s^{-1}$ , independent of temperature and applied LF. (The change in spectral shape in fig. 68 between LF=20 G and LF=200 G is due to the influence of field on the Mn nuclear depolarization which, due to hyperfine coupling, is dynamically driven by the electronic spin fluctuations, and thus not so easily decoupled). Furthermore, the fast depolarizing signal in the Tb-doped samples could be followed to temperatures below the hysteresis region. It appears that certain clusters in the sample do not enter the AFM ordered state, but remain spin-

glass-like. In summary, the  $\mu$ SR data demonstrate that doping  $Y\text{Mn}_2$  with a strongly paramagnetic ion such as  $\text{Tb}^{3+}$  enhances the spin glass clusters.

5.3.3.3.  $Y(\text{Sc})\text{Mn}_2$ . The AFM transition in  $Y\text{Mn}_2$  can be suppressed by the application of external pressure or *via* the lattice contraction in pseudo-binary compounds such as  $Y_{1-x}\text{Sc}_x\text{Mn}_2$ . The pressure coefficient of  $T_N$  is huge ( $\sim 35$  K/kbar) leading to a critical pressure of  $\sim 3$  kbar for the disappearance of LRO magnetism (Oomi et al. 1987, Voiron et al. 1990, Hauser et al. 1995). Neutron scattering showed that the loss of ordered magnetism is spatially inhomogeneous (Mondal et al. 1992). Furthermore, the Sommerfeld constant increases substantially with pressure, indicating an enhancement of spin fluctuations (Fisher et al. 1993). Electrical resistivity measurements to very high pressures (200 kbar) indicate that the spin fluctuations disappear above 40 kbar (Drescher and Abd-Elmeguid 1995).  $^{119}\text{Sn}$  Mössbauer spectroscopy on  $Y\text{Mn}_2$  doped with 0.5 at% Sn (Block et al. 1994) revealed the presence of a SRO magnetic state in the pressure range between the disappearances of AFM-LRO ( $\sim 3$  kbar) and spin fluctuations ( $\sim 40$  kbar).

Preliminary  $\mu$ SR high-pressure data (Schreier 1999) on  $Y_{0.9}\text{Tb}_{0.1}\text{Mn}_2$  up to 3 kbar also showed that the hysteresis of the AFM transition is shifted to lower temperatures with a coefficient of  $\sim 30$  K/kbar. They demonstrate in addition, that the breadth of the hysteresis becomes markedly narrower (i.e., from  $\Delta T \approx 30$  K at ambient pressure to  $\Delta T \approx 15$  K at 1 kbar). The spin-glass-like precursor phase appears to be unaffected.

Chemical compression in  $Y_{1-x}\text{Sc}_x\text{Mn}_2$  leads to the loss of the AFM transition for  $x \geq 0.03$  while maintaining the cubic C15 structure (H. Nakamura et al. 1988b, Shiga et al. 1993). According to NMR, magnetic order is no longer present at this concentration down to 0.07 K (H. Nakamura et al. 1988c). Again, the Sommerfeld constant is enhanced by nearly an order of magnitude compared to  $Y\text{Mn}_2$ . Its value ( $\gamma \approx 0.15$  J/mol K<sup>2</sup> for  $x = 0.03$ ) reaches the regime of medium heavy HF compounds (Wada et al. 1989). Paramagnetic neutron scattering detected strong AFM spin correlations with a strength of  $1.3\mu_B$  per ion, nearly independent of temperature (Shiga et al. 1988). Hence  $Y_{0.97}\text{Sc}_{0.03}\text{Mn}_2$  may be regarded as a dynamic AFM system with strongly correlated spin fluctuations. It exhibits the features of a quantum spin-liquid ground state due to the strong magnetic frustration (Shiga et al. 1993). It has also been inferred that the spin fluctuations caused by frustration may play the same role as the spin fluctuations resulting from the Kondo interaction in 4f and 5f HF systems (see sect. 9 for more details). From this point of view  $Y\text{Mn}_2$  exhibits the properties of a 3d itinerant electron HF compound (Lacroix and Pinettes 1995).

In general, the pseudo-binary system  $Y_{1-x}\text{Sc}_x\text{Mn}_2$  allows a more detailed study of the paramagnetic phase down to much lower temperatures in comparison to the parent compound  $Y\text{Mn}_2$ . Kalvius et al. (1996) exploited this possibility to study by TF-, ZF- and LF- $\mu$ SR the behavior of the SRO state characterized by fast (root exponential) relaxation in compounds with  $0.01 \geq x \geq 0.04$ . The sample with  $x = 0.01$  behaved much like pure  $Y\text{Mn}_2$ , only the magnetic transition is shifted to lower temperatures and has a narrower hysteresis. The SRO signal appears slightly above  $T_N$ . For  $x = 0.02$  a magnetic transition slightly below the base temperature of this study (3.5 K) cannot safely be excluded

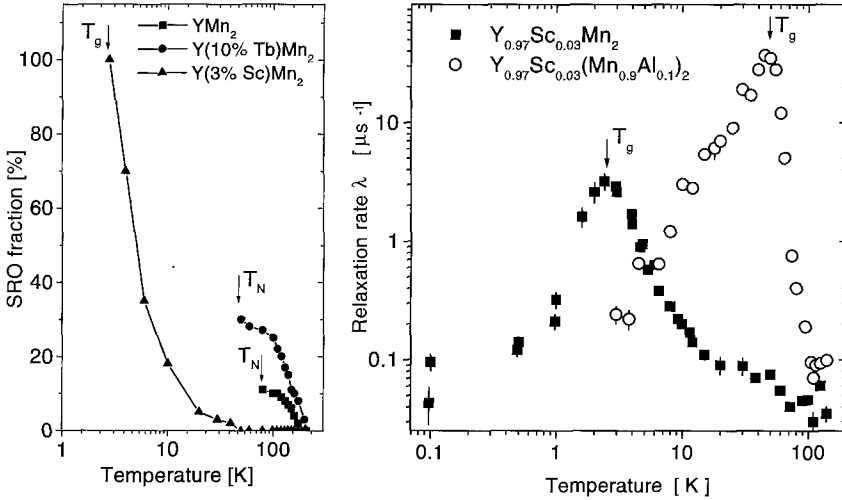


Fig. 69. Left: Comparison of the development of the volume fraction of the short-range-ordered (SRO) state in  $\text{YMn}_2$ ,  $\text{Y}_{0.9}\text{Tb}_{0.1}\text{Mn}_2$  and  $\text{Y}_{0.97}\text{Sc}_{0.03}\text{Mn}_2$ . Adapted from Kalvius et al. (1996). Right: Temperature dependence of the relaxation rate for  $\text{Y}_{0.97}\text{Sc}_{0.03}\text{Mn}_2$  (solid symbols). Also shown are analogous data for  $\text{Y}_{0.97}\text{Sc}_{0.03}(\text{Mn}_{0.9}\text{Al}_{0.1})_2$  (see discussion in sect. 5.3.3.4). The measurements were done in LF = 10 mT in order to suppress depolarization by the Mn nuclear dipoles. After Mekata et al. (1997).

because of a rise in the relaxation rate of the paramagnetic signal. In any case, the SRO signal appears around 20 K and reaches a fairly high proportion (> 50%) already at 4 K. For  $x = 0.03, 0.04$  no evidence of a magnetic transition was found, as expected. The SRO state begins to show up below ~50 K and appears to take over the whole sample volume for  $T \rightarrow 0$ . In fig. 69 (left) a comparison of the development of the SRO fraction is shown for pure  $\text{YMn}_2$ , 10%Tb-doped  $\text{YMn}_2$  and 3%Sc-doped  $\text{YMn}_2$ . In the latter material the whole volume is finally short-range-ordered.

This aspect has been studied in much more detail by Mekata et al. (1997) including results at very low temperatures. Shown in fig. 69 (right) is the temperature variation of the relaxation rate. These authors used (in contrast to Kalvius et al. 1996, who fitted their data by the sum of an exponential and a root exponential signal) a single signal fit with power exponential depolarization. The exponent decreases from 1 at high temperatures to 0.5 at low temperatures. This means of analysis reflects in essence the same situation of a steady increase of SRO volume. The relaxation rate  $\lambda$  reaches a broad maximum around 2.5 K. This is interpreted as a spin glass transition ( $T_g$ ) since the spectral shape changes to a Lorentzian Kubo–Toyabe function in the limit of slow spin dynamics. The rate  $\lambda$  plotted in fig. 69 (right) for  $T < T_g$  refers to the decay of the “1/3 tail” of the Kubo–Toyabe function. The authors remark that even for  $T \rightarrow 0$  the shallow minimum of the Lorentzian Kubo–Toyabe function is absent. Most likely the compound is magnetically inhomogeneous, which leads to a distribution of width of field distributions, analogous to the situation leading to the Gaussian-broadened Gaussian relaxation function discussed in sect. 8. Applying LF below  $T_g$  decouples the Kubo–Toyabe relaxation. From the field

dependence of initial asymmetry an internal field strength of 0.2 T was estimated for  $T = 0.1$  K.

The appearance of a *Lorentzian* Kubo–Toyabe function below  $T_g$  is surprising. It means that one deals with a dilute magnetic system. The authors make the assumption that the Mn moments in most of the tetrahedra are coupled to form a singlet. Only a small fraction of tetrahedra have uncorrelated paramagnetic Mn moments, which then freeze at  $T_g$  and the strong frustration puts the freezing point at fairly low temperatures. The problem is to create a model for the singlet formation. One possibility is the formation of a quantum spin liquid state (see sect. 9 for some discussion in this respect) which has been suggested by Shiga et al. (1993). But classical models could also be evoked. An additional ingredient is the randomness introduced by the random replacement of Y by Sc. (This complication could be avoided by studying pure  $YMn_2$  under pressure to very low temperatures; but no  $\mu$ SR data of this type are available at present). For more details we refer to the original paper and the references given therein.

5.3.3.4.  $Y(Mn,Al)_2$ . A means to reduce frustration is to substitute some of the Mn ions (e.g.,  $Y(Mn_{1-x}Al_x)_2$ ) since the strict tetrahedral exchange correlation is then partially broken. Substitution by Al also causes lattice *expansion*, which leads to some moment stabilization and in turn causes slowing down of spin fluctuations. The system enters a spin glass state at rather elevated temperatures ( $T_g \approx 50$  K) for  $x = 0.06$  and above (Motoya et al. 1991).  $\mu$ SR measurements on a sample with  $x = 0.1$  clearly confirm spin glass order below  $T_g$  and also support the notion of slowed down spin fluctuations by a more Gaussian shape of the muon spin depolarization function at  $T \ll T_g$  (Cywinski and Rainford 1994).

The strong effect of reduced frustration by substituting Mn in part by Al was convincingly demonstrated by Mekata et al. (1997) in their  $\mu$ SR study of  $Y_{0.97}Sc_{0.03}(Mn_{0.9}Al_{0.1})_2$ . Figure 69 (right) compares the temperature dependences of the relaxation rates in  $Y_{0.97}Sc_{0.03}Mn_2$  with and without Al substitution of Mn. The maximum in  $\lambda(T)$  indicating the glass transition is shifted to much higher temperatures ( $T_g = 45$  K) in the Al-containing compound. Also apparent is the much narrower temperature range over which the slowing down of spin fluctuations towards freezing occurs. The hindrance of entering even a SRO state by frustration is markedly reduced and the material behaves much more like an ordinary concentrated spin glass.

5.3.3.5.  $Y(Mn,Fe)_2$ . Substitution within the Mn lattice can also lead to lattice *contraction* and hence to a destabilization of Mn moments. An example is  $Y(Mn_{1-x}Fe_x)_2$ . A combined neutron scattering and  $\mu$ SR study was carried out by Cywinski et al. (1990). Neutrons show that already at  $x = 0.025$  the Mn moment is reduced to  $\sim 0.2\mu_B$  and the system reverts to Pauli paramagnetic behavior. They further revealed the presence of AFM correlations over a wide temperature range, but could not distinguish between static (frozen spins) or dynamic (longitudinally fluctuating spins) correlations. With the help of TF- $\mu$ SR measurements it was possible to pin down the dynamical nature of the correlations. The temperature dependence of relaxation rate followed a simple power law ( $\lambda(T) \propto T^{-w}$ )

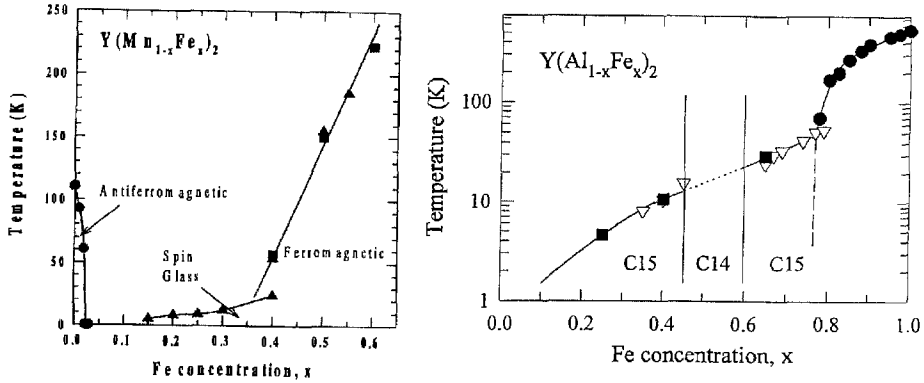


Fig. 70. Left: Magnetic transition temperatures in  $Y(Mn_{1-x}Fe_x)_2$  as a function of Fe concentration. The plot also serves as a magnetic phase diagram showing the various types of magnetic ground states present in this alloy series. From Cywinski et al. (1999). Right: Similar plot for  $Y(Al_{1-x}Fe_x)_2$ . Triangles are spin-glass transition temperatures from Mössbauer data, squares are spin-glass temperatures from  $\mu$ SR and circles are Curie temperatures. Around  $x = 0.5$  the alloy crystallizes in the hexagonal Laves phase (C14). From Telling et al. (2000).

with exponent  $w \approx 0.75$ . No paramagnetic frequency shift could be resolved in keeping with a pure Pauli paramagnet. The authors therefore exclude a move towards a magnetic transition, which is usually the origin of a power-law dependence of muon spin relaxation rate. This conclusion is also supported by the neutron results showing no temperature dependence of the nature of the spin correlations down to 5 K. The observed temperature variation of  $\lambda$  then reflects the slowing down of longitudinal spin fluctuations with decreasing temperature.

Recently, a magnetic phase diagram for the  $Y(Mn_{1-x}Fe_x)_2$  pseudo-binary series has been given by Cywinski et al. (1999). It is shown in fig. 70 (left). The substitution of Mn by only 2 at.% Fe has the same effect as 3 kbar external pressure on  $YMn_2$ , that is, a suppression of long-range AFM order. At somewhat higher Fe concentrations a spin glass state is formed with rather low freezing temperatures. The presence of the spin glass state is mainly deduced from  $\mu$ SR data. At even higher Fe concentrations one finds FM order. The  $\mu$ SR spectra in this regime show the FM state to be extremely inhomogeneous.

One might add a word of warning at this point. The Mössbauer studies of  $YMn_2$  usually use doping with Fe. Although the concentration can be kept below 1% and hence well below the critical concentration of 2%, the steep dependence of magnetic transition with Fe concentration lead to uncertainties whether the true properties of the pristine material are measured. In contrast, it is particularly rewarding that the  $\mu$ SR results on paramagnetic spin fluctuations are in full accord with the neutron inelastic line widths for  $YMn_2$  and its pseudo-binary analogues (Rainford et al. 1995b).

5.3.3.6.  $Y(Al,Fe)_2$ . Although the pseudo-binary series  $Y(Al_{1-x}Fe_x)_2$  is not a member of the  $YMn_2$  family, it is best discussed in this context. Except for a small concentration range around  $x = 0.5$ , the series forms the cubic Laves phase (C15). The geometrical

frustration leads to a spin-glass state for lower Fe concentrations. At higher Fe concentrations the FM exchange wins and the FM ground state of  $\text{YFe}_2$  (see table 8) is formed. The magnetic phase diagram derived from  $\mu$ SR and Mössbauer data is shown in fig. 70 (right) (Telling et al. 2000). The  $\mu$ SR spectra above the spin glass temperature are of varying-power exponential shape. From the variation of its parameters the authors conclude that an increasingly broad distribution of spin relaxation rates evolves as the glass temperature is approached. High-applied-field (13.5 T) Mössbauer data were interpreted in terms of a Markovian two-level-jump process. A spin-correlated state is formed after a stochastically varying time  $\tau_{\text{off}}$  and decays after  $\tau_{\text{on}}$  back to a free spin state. It was found that  $\tau_{\text{on}}$  obtained from the Mössbauer data and  $\lambda$  from the  $\mu$ SR data both follow the power law  $[(T - T_g)/T_g]^{-1}$  for Fe concentrations between  $x = 0.25$  and  $0.75$ , at least for  $T > 1.5T_g$ . This result is astonishing since the two methods probe the fluctuation of different internal fields. A final interpretation is not yet possible, but the authors indicate attempts to apply the jump process directly to the analysis of the muon spectra. This would then allow a comparison of the autocorrelation functions of the field at the (Fe) nuclear site and that of the interstitial site occupied by the muon.

5.3.3.7. *YMn<sub>2</sub> summary.* The  $\mu$ SR data presented lend strong support to the following rough picture for the magnetic behavior of  $\text{YMn}_2$  and related compounds: lattice compression (by whatever means) destabilizes the Mn moment and prevents the formation of a local moment AFM state with LRO *via* a first order transition combined with expansion and distortion of the lattice. One then is left with an itinerant-electron magnet featuring substantial geometrical frustration in the Mn magnetic lattice and in consequence huge longitudinal spin fluctuations. As mentioned, the likely magnetic ground state of such a system is a SRO glass-like state. Still, strong frustration works even against spin freezing and forces the system to stay as long as possible in the paramagnetic state where the longitudinal spin fluctuations reduce frustration. Only when these fluctuations have slowed down markedly at low temperatures does the glass transition take place. Thus, the weaker the frustration, the higher is  $T_g$ . In the limit of extreme destabilization of Mn moments, the system moves towards a Pauli paramagnet. The introduction of a 3d transition metal leads to ferromagnetic coupling and thus relieves the triangular frustration. Before the FM state is formed, the AFM frustration is sufficiently weakened to suppress the first order transition and creates a spin glass magnetic ground state with low transition temperature.

The general aspects of “spin fluctuations in itinerant magnets” have been reviewed recently by Rainford (1999a). The case of  $\text{YMn}_2$  and related systems plays a dominant role in this article. Data obtained by different methods are compared.

5.3.3.8. *RMn<sub>2</sub> with R = Gd, Tb, Dy.* Since  $\mu$ SR data are available only for the three R ions listed, and even then they are fairly rudimentary, we restrict ourselves to a brief discussion of those cases. The fact that, in contrast to  $\text{YMn}_2$ , the alloying partner is now a strongly paramagnetic 4f ion requires new aspects be taken into consideration. (i) Two magnetic sublattices will be present, both susceptible to LRO. Possible cross-exchange ( $\text{R} \leftrightarrow \text{Mn}$ )

may reduce frustration in the magnetic Mn lattice. (ii) Most of the R ions possess large orbital momenta and hence strong single-ion anisotropies. Also CEF interactions are likely to become important. Both these features also could give rise to rather complex spin structures. (iii) The lanthanide contraction reduces the lattice constant and moves the compounds containing the very heavy R ions close to and finally beyond the critical Mn–Mn separation. On the whole, much less detailed information is available for the  $\text{RMn}_2$  compounds and their magnetic behavior is considerably less understood than that of  $\text{YMn}_2$  (where the question of good understanding may be a matter of discussion as well).

One would expect  $\text{GdMn}_2$  to be a simple case. Firstly, the Mn–Mn separation (and with it the Mn moment) is about the same as in  $\text{YMn}_2$  (Wada et al. 1987). Secondly,  $\text{Gd}^{3+}$  is an S state ion devoid of single-ion anisotropy and insensitive to CEF interactions. A disadvantage is the high neutron absorption of Gd, which makes neutron scattering studies very difficult. Hence little direct information on ordered spin structures is available. A magnetic transition at  $T_N = 104$  K featuring a small volume change ( $\sim 1\%$ ), but no tetragonal distortion, is well-established. Specific heat sees a sharp peak at  $T_N$ , confirming its first order nature, and a broad anomaly around 40 K (Okamoto et al. 1987). Magnetization data (Malik and Wallace 1981) show ferromagnetic behavior below 40 K and for this reason 40 K is often referred to as the Curie point ( $T_C$ ) of  $\text{GdMn}_2$ . Two pictures of LRO magnetism were mainly discussed. Okamoto et al. (1987) assume AFM order to set in for both the Gd and Mn sublattices at  $T_N$  and interpret  $T_C$  as a spin re-orientation transition. Ibarra et al. (1993), on the basis of magnetostriction measurements, claim that two spatially separate phases exist, one which shows AFM order of Gd and Mn ions at  $T_N$ , the other remaining paramagnetic down to  $T_C$ , where only the Gd ions order ferromagnetically.

In the (preliminary)  $\mu\text{SR}$  data on  $\text{GdMn}_2$  (mainly in TF) at ambient and applied pressures (Martin 1996, Martin et al. 2000), the transition at  $T_N$  manifests itself by a complete loss of signal amplitude. This excludes a paramagnetic phase for  $T < T_N$ . The relaxation rate shows critical (second-order) behavior on approach to  $T_N$  from above, as in  $\text{YMn}_2$ . The value of  $\lambda$  close to  $T_N$  is at least an order of magnitude larger than in  $\text{YMn}_2$ , demonstrating clearly that the Gd ions with their large paramagnetic moment are involved. The Ibarra model can safely be excluded since all of the Gd and Mn ions enter a LRO state around 100 K. A similar, but not as definite, conclusion was drawn from Mössbauer spectroscopy (Przewoźnik et al. 1993). Hysteresis around  $T_N$  is absent in agreement with bulk data (Gaidukova et al. 1983). Just above  $T_N$  a slight loss of amplitude showed up (as in  $\text{YMn}_2$ ) in the TF data. This is again caused by the formation of a SRO fraction reflected in a rapidly decaying signal portion, which escapes detection in TF mode. The high-pressure data are not sensitive enough to decide on any changes in the SRO fraction with pressure. The reason is the additional signal from the high-pressure cell, which also is somewhat pressure dependent.

Under pressure a downshift of  $T_N$  occurs (fig. 71). The pressure coefficient of  $T_N$  (approximately  $-5$  K/kbar) is nearly an order of magnitude smaller than in  $\text{YMn}_2$ . This has also been seen in resistivity data (Hauser et al. 1995). It indicates that the presence of the

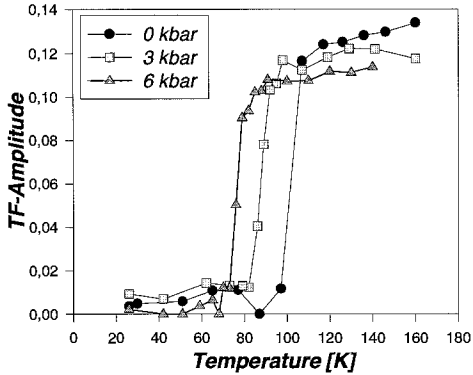


Fig. 71. Temperature dependence of TF signal amplitude of  $\text{GdMn}_2$  at different pressures. The sudden drop of amplitude indicates the magnetic transition, which is clearly pressure dependent (Martin et al. 2000).

large moment Gd magnetic sublattice reduces the effect of Mn moment destabilization. The critical behavior of  $\lambda(T)$  shows a slight increase of critical exponent  $w$  from 0.16 at 0 kbar to 0.2 at 6 kbar. The generally low value of  $w$  is not understood.

A Mössbauer study on  $\text{GdMn}_2$  using the  $^{155}\text{Gd}$  resonance up to pressures of 8 GPa (80 kbar) has appeared recently (Strecker and Wortmann 1999). At low pressures the same loss of magnetism as discussed above was observed. In the vicinity of 2 GPa the hexagonal C14 Laves phase begins to appear. The compound is fully converted to the new phase around 5 GPa. In the C14 phase the magnetic transition temperature rises again with pressure reaching  $\sim 170$  K at 8 GPa.

The loss of signal below  $T_N$  prevents a direct  $\mu$ SR study of the LRO phases. The presence of a ferromagnetic component can, however, be monitored indirectly. The strong resulting magnetization of a FM sample distorts the applied TF in its vicinity. This induces changes in the shape of the background signal stemming from muons stopped in the sample holder (an example is shown in Hartmann et al. 1986). If remanence is present, the distortion will remain even after the field is switched off. This is a sensitive test for FM. Data of this type taken down to 10 K established a FM component already below  $T_N$ , not only below  $T_C$ . But a definite change of signal occurs at  $T_C$ , meaning that the spin structure definitely changes, but still maintains a FM component. The remanent signal is also sensitive to pressure, indicating that the spin arrangement responds to volume changes. In a (rather limited) neutron study it was found that the FM component (at 2 K) is only present in an applied field (15 kG), but not in the case of ZF cooling (Ouladdiaf 1986).  $\mu$ SR needs an applied (transverse) field (which, however, can be switched on after ZF cooling) to test for a FM component. Data at 2 K do not exist, but there is no evidence at somewhat higher temperatures that ZF cooling avoids remanence. In any case, the fields involved in the  $\mu$ SR measurements are rather small, i.e., well below 1 kG. In summary, it emerges that one of the models of magnetism in  $\text{GdMn}_2$  (i.e., that of Ibarra et al. 1993) can be excluded, but also, that the details of the magnetic state and the exact meaning of the two transitions are still far from understood.

In  $\text{TbMn}_2$  the lattice constant brings the Mn–Mn distance close to (but still above) its critical value. Volume expansion of  $\sim 2\%$  and a fairly narrow hysteresis are observed



around 40 K (Gaidukova et al. 1983, Wada et al. 1987). The properties of the ordered magnetic state of  $\text{TbMn}_2$  are truly complex. There is an extreme sensitivity to external conditions such as applied field, pressure or alloying. Hysteresis effects in the low-temperature magnetic isotherms suggest metastable magnetic ordering of the Mn lattice (Ballou et al. 1992). Neutron scattering data (Brown et al. 1992) give an explanation. The spin structure is poised between two structures  $S_1$  and  $S_2$  with propagation vectors  $(\frac{1}{3} \frac{2}{3} 0)$  and  $(\frac{1}{2} \frac{1}{2} \frac{1}{2})$ , respectively. External conditions induce transitions between those structures. For example, in high magnetic fields and under pressure only  $S_2$  is present. Under ZF conditions (and one may hope that the small fields used in  $\mu\text{SR}$  of less than 25 mT still qualify as a ZF condition and hence the  $\mu\text{SR}$  data may be comparable) first *ferromagnetic* Bragg peaks appear at 45 K on cooling. They disappear at 40 K when the AFM peaks of  $S_1$  begin to rise. The  $S_2$  peaks are present at 2 K and below. In general, the question of FM components in the magnetism of  $\text{TbMn}_2$  is not clear cut as a consequence of metamagnetic behavior. It is concluded that an intricate interplay between Mn moment instability and exchange frustration is the underlying cause for the unstable magnetic behavior.

$\mu\text{SR}$  data are rather limited and restricted to the paramagnetic regime (for which hardly any neutron data exist). The TF measurements of Cywinski and Rainford (1992) showed a full collapse of signal amplitude at 45 K. The magnetic transition point is thus coupled to the appearance of the FM Bragg peaks. Power law temperature dependences were seen for the relaxation rate  $\lambda$  and the frequency shift  $\Delta\nu$ . An exponent  $w \approx 0.83$  was derived for  $\lambda(T)$  while  $\Delta\nu(T)$  varies with an exponent 1 indicating Curie–Weiss susceptibility. Kalvius (1994) briefly reports on some ZF-, LF-, and TF- $\mu\text{SR}$  measurements. Two subspectra are seen (especially in ZF) even at high temperatures (250 K), one rapidly depolarizing ( $\lambda_1 \approx 1.5 \mu\text{s}^{-1}$ ), the other slowly relaxing ( $\lambda_2 \approx 0.03 \mu\text{s}^{-1}$ ). The intensity ratio is roughly 1.5:1 and changes little with temperature. The rate of the fast signal increases by about a factor of two on approach to  $T_N$ , while the slow signal shows little change. Both signals vanish at the onset of LRO. It is tempting to consider the rapidly relaxing signal as arising from the SRO precursor state. Considering the enhanced stability of this state by alloying Tb into  $\text{YMn}_2$ , this is a definite possibility. Also, it is mentioned in Ballou et al. (1991) that  $\text{TbMn}_2$  exhibits strong SRO in its paramagnetic phase. The other subspectra would then correspond to true paramagnetic regions with very rapid spin fluctuations (nearly complete motional narrowing). On first sight, the results of Kalvius (1994) seem to be in some disagreement with those of Cywinski and Rainford (1992) who state that they fit their TF spectra with a single purely exponential relaxation function. But they also remark that their analysis may mask some more subtle features in the spectra (see the following discussion of  $\mu\text{SR}$  in  $\text{DyMn}_2$ ). Unfortunately, neither group reports on the hysteresis region and whether a FM component is originally present.

The Mn–Mn separation in  $\text{DyMn}_2$  is exactly at its critical value. In consequence, it was shown by neutron diffraction (Ritter et al. 1991) that below the Curie temperature of  $T_C = 45$  K only one out of four (of the crystallographic equivalent) Mn atoms possess a magnetic moment ( $\mu_{\text{Mn}} = 1.4\mu_B$ ). These spins are ferromagnetically ordered. The Dy sublattice forms a spin-canted FM structure with  $\mu_{\text{Dy}} = 8.8\mu_B$ . The Mn atoms that

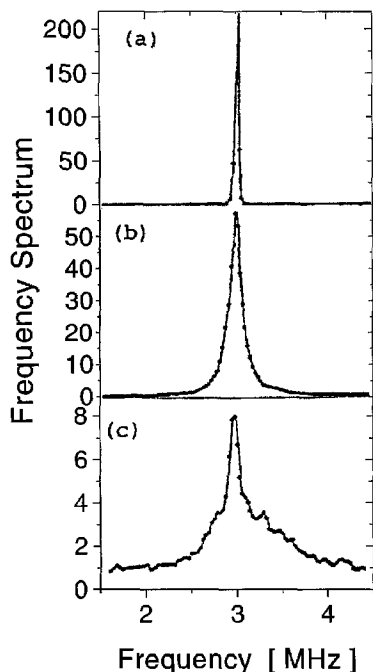


Fig. 72. Maximum Entropy Fourier analysis of  $\mu$ SR spectra taken in  $TF = 22$  mT: (a) silver at 300 K as reference; (b)  $DyMn_2$  at 300 K; (c)  $DyMn_2$  at 77 K. After Cywinski and Rainford (1992).

carry moments are those which are sandwiched between FM coupled Dy layers and thus reside in a highly polarizing environment. The other Mn atoms reside on sites with magnetic inversion symmetry.

Available  $\mu$ SR data are restricted to  $TF$  measurements in the paramagnetic range since the signal vanishes totally at  $T_C$  (Cywinski and Rainford 1992). This shows that a strong and widely distributed internal field is felt by all stopped muons (residing presumably on the 2-2 sites) even if not all Mn atoms carry a moment. As in the case of  $TbMn_2$ , the temperature dependences of  $\lambda$  and  $\Delta\nu$  are described by power laws with exponents 0.62 and 1, respectively. The signal amplitude shows a continuous decrease by  $\sim 20\%$  between 200 K and  $T_C$ . To look for more subtle effects in the  $TF$  spectral shape the authors used a Fourier transform analysis based on the maximum entropy procedure. The result (depicted in fig. 72) shows the development of a second contribution with a broad and asymmetric frequency distribution (equivalent to a rapid, not purely exponentially relaxing signal) on approach to  $T_C$ . This could again be the signature of a SRO precursor phase. The authors also mention the possibility of muons trapped at sites other than the regular 2-2 sites. This scenario is, however, not so likely.

Telling et al. (1998) recently studied the pseudo-binary system  $(Dy_{1-x}Y_x)Mn_2$  by ZF- $\mu$ SR. According to neutron scattering data by Ritter et al. (1994), this system shows for  $x > 0.75$  long-range AFM order ( $T_N$  around 100 K) similar to that of  $YMn_2$ . For  $x < 0.35$  the complex magnetic structure of  $DyMn_2$  is observed below  $\sim 45$  K. In the intermediate concentration range, LRO collapses and the indication is that a spin-glass-

like state is formed with spin freezing temperatures around 25 K. The  $\mu$ SR study employed polycrystalline specimens with  $x = 0.1, 0.55$  and  $0.7$ . The spectra for  $x = 0.1$  in the paramagnetic regime show simple exponential muon spin relaxation. The rate rises on approaching  $T_N = 45$  K in the usual fashion. Also a loss of signal amplitude is observed below 120 K, meaning that part of the sample gives rise to very high relaxation rates. Below  $T_N$  the signal collapses fully. Overall, the  $\mu$ SR response is not fundamentally different from that of pure  $\text{DyMn}_2$ . The spectra for  $x = 0.55$  and  $0.7$  are quite similar, but distinctly different from those for  $x = 0.1$ . They are better described by power exponential relaxation with a power factor decreasing continuously from  $p = 1$  at high temperatures to  $p \approx 0.3$  near  $T_g \approx 25$  K. This behavior is characteristic for concentrated spin glass systems (see, for example, Campbell et al. 1994 and sect. 8.2.1), but the Arrhenius-type temperature dependence of relaxation rate is not observed. An increasingly broad distribution of spin fluctuation rates is considered the possible cause. The initial asymmetry, which starts to decrease around 60 K, continues to do so even below the nominal spin glass temperature, meaning that the relaxation rate still increases, shifting the signal out of the spectrometer time window. (The measurements were done at the ISIS pulsed facility.) Obviously, the magnetic spin system has not reached a static limit, which prompts the authors to question whether the magnetic ground state is truly a spin glass state. They suspect that longitudinal spin fluctuations are more effective in disrupting magnetic LRO than (static) geometrical frustration alone (which would lead to spin freezing). This picture has definite similarities with the findings (discussed above) on Sc-doped  $\text{YMn}_2$  (reviewers' remark).

5.3.3.9.  $\text{YCo}_2$ . This material haunts the rare-earth magnetism community consistently because it behaves like an enhanced paramagnet only with no significant moment on Co. Various proposals for this behavior have been offered. Neutron scattering experiments point towards a spin fluctuator (see discussion on  $\text{UAl}_2$ ). For a review of the  $\text{YCo}_2$ -problem we refer to the review by Kirchmayr and Poldy (1979).

A first, rather preliminary,  $\mu$ SR study was carried out by Graham et al. (1988). More detailed results have recently been provided by Wiesinger et al. (2000). Below 1 K ZF- $\mu$ SR shows a static Gaussian Kubo–Toyabe pattern of nuclear origin. Dipolar sum calculations find reasonable agreement for the 2-2 site usually assumed in the C15 structure. As shown in fig. 73, heating leads to weakly dynamic Kubo–Toyabe spectra first with slowly rising fluctuation rates. At higher temperatures (around 70 K) the rate increases rapidly and peaks around 100 K with the still very low magnitude of approximately 1.5 MHz. It then falls quickly back to the static limit on further temperature increase, but for  $T > 200$  K dynamic behavior reappears. Concurrently the static width  $\Delta$  of the Kubo–Toyabe function changes with temperature. These features reflect muon dynamics. The muon implanted on an interstitial site first becomes mobile (and 70 K is a typical temperature for Laves-phase compounds as shown in fig. 59, right) and is then trapped. The most likely trapping sites are Co vacancies, since exact stoichiometry is a well-known problem in Laves phases of this type. It gets de-trapped when the temperature is further increased. At the trap site, the field distribution (of nuclear dipolar fields) differs

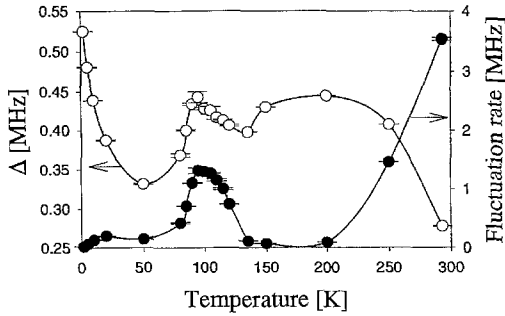


Fig. 73. Temperature dependence of the fluctuation rate and the width of the field distribution in  $\text{YCo}_2$  derived from fits to a dynamic Gaussian Kubo–Toyabe function. The data reflect muon dynamics in the C15 Laves-phase lattice (see text). From Wiesinger et al. (2000).

from the interstitial muon stopping site, which is the cause for the variation in  $\Delta$ . Again it is found by dipolar sum calculations that a muon resting on an (unoccupied) Co site sees a significantly lower width of field distribution. This is an impressive demonstration of the behavior of the muon in a C15 Laves phase. Muon stopping site and muon dynamics in this class of materials have already been discussed at the beginning of this section, especially in connection with data on  $\text{CeAl}_2$ .

An influence of electronic moments on the muon spin depolarization rate could not be detected. This is in full keeping with the notion of  $\text{YCo}_2$  being a spin fluctuator. As in the archetypal spin fluctuator  $\text{UAl}_2$  (see paragraph on  $\text{AnAl}_2$ , above) fluctuations of electronic spins are so fast even at low temperatures that full motional narrowing is in effect (reviewers' remark).

5.3.3.10.  $\text{UMn}_2$ . This is the only actinide compound within the  $\text{MMn}_2$  series studied by  $\mu$ SR. Its magnetic properties have been under some discussion. Basically,  $\text{UMn}_2$  behaves much like  $\text{UAl}_2$  (see preceding section), a well-established spin fluctuator (Fournier and Troć 1985). Anomalies in susceptibility and resistivity around 240 K are similar in appearance to the FM transition in  $\text{UFe}_2$ , which features a very small U moment ( $0.01\mu_B$ ) but a substantial Fe moment ( $0.6\mu_B$ ). The FM transition is coupled to a rhombohedral distortion and the question arose whether the 240 K anomaly in  $\text{UMn}_2$  reflects a purely structural or a coupled structural–AFM transition. Neutron diffraction, carried out together with the  $\mu$ SR study (Cywinski et al. 1994b) showed that the structural changes are more complex. Rhombohedral distortion sets in at 230 K, but below 220 K, a transition into an orthorhombic structure starts, which is then completed at 200 K.

The ZF- $\mu$ SR spectra are dominated by nuclear depolarization from  $^{55}\text{Mn}$ , which can easily be suppressed by  $\text{LF}=10\text{ mT}$ . A weak damping from fast fluctuating electronic moments remains. The situation is rather similar to that in  $\text{UAl}_2$ . The nuclear depolarization varies in accordance with the structural transitions, only a final rise below 40 K remains unexplained. In summary, the  $\mu$ SR data provide no evidence for moment localization at U or for the onset of magnetic LRO. The transitions in  $\text{UMn}_2$  are thus purely structural.

#### 5.3.4. *Other Laves phases*

Laves-phase compounds can also be formed with 4d and 5d transition elements. To our knowledge,  $\mu$ SR studies were only carried out for CeRu<sub>2</sub> (Huxley et al. 1996), which is considered a strongly correlated electron system. The case is discussed in sect. 9.3.1 ( $\mu$ SR found weak moment magnetism).

#### 5.4. *Binary compounds and alloys (other than Laves phases)*

##### 5.4.1. *MX<sub>2</sub> compounds*

This section refers to intermetallics of type MX<sub>2</sub> that do not take the Laves-phase structure. Two materials crystallizing in the orthorhombic CeCu<sub>2</sub> structure and some R-hydrides have been studied by  $\mu$ SR.

5.4.1.1. *PrCu<sub>2</sub>*. Anomalies in the field dependence of the Knight shift and an excessive ZF dipolar width in this singlet ground state system have been considered to arise from muon-induced effects (Schenck et al. 1997a). The case is presented in sect. 5.1.

5.4.1.2. *NdCu<sub>2</sub>*. This intermetallic exhibits rather complex magnetic behavior. Neutron scattering data are controversial. Arons et al. (1994) report an incommensurate AFM structure below  $T_N = 6.5$  K that changes into a commensurately modulated structure below 4.1 K. Svoboda et al. (1992) found three spin re-orientation transitions below  $T_N$  (at 5.2, 4.1, 3.2 K).  $\mu$ SR measurements with the aim of clarification of the magnetic phase diagram were carried out by Hillberg et al. (1997b). Polycrystalline and single-crystalline samples were used. Below 25 K a rapid increase of relaxation rate was observed (in 200 mT TF), which led to a disappearance of the signal around 16 K, i.e., well above  $T_N$ . The authors claim an onset of SRO spin correlations producing fast muon spin depolarization ( $\lambda > 50 \mu\text{s}^{-1}$ ). The signal reappears around 1.2 K meaning that no signal is seen around  $T_N$ . The recovered signal exhibits in ZF a spontaneous precession frequency (though with reduced signal amplitude). The precession frequency (22 MHz) is practically constant with decreasing temperature but the relaxation rate first decreases rapidly and then reaches a rather low and constant value ( $0.8 \mu\text{s}^{-1}$ ) at 0.5 K. This behavior is interpreted as resulting from the development of a square-modulated commensurate spin structure. Specific heat data (Sugawara et al. 1995) suggest the opening of a gap in the magnon excitation spectrum near 3 K. The resulting decrease in magnon excitations could be the cause for the low-temperature dependence of the muon spin relaxation rate. But a continuous re-alignment of spin orientation could be responsible as well.

5.4.1.3. *R dihydrides and dideuterides*. The  $\beta$ -phase of the RH<sub>2</sub> or RD<sub>2</sub> compounds crystallizes in the fluorite-type fcc structure with hydrogen ideally occupying all tetrahedral sites. In superstoichiometry (RH<sub>2+x</sub>) the additional hydrogen rests on octahedral interstices. Superstoichiometry profoundly changes the electronic structure

properties and can lead, for example, to metal–insulator transitions. In general, the R dihydrides are magnetic, but show a variety of transitions and ordered spin states (see Vajda 1995, for a general review).

First preliminary  $\mu$ SR studies on some members of this system have recently been reported (Gygax et al. 2000b). For  $\text{HoD}_{2.0}$ ,  $\text{HoD}_{2.12}$  and  $\text{DyD}_{2.0}$ , the results within the paramagnetic regime are straightforward. Full signal strength and a temperature dependence of relaxation rate above the critical temperatures around 5–7 K following the typical power law are seen. The exponents  $w = 0.54(2)$  for  $\text{HoD}_{2.0}$ ,  $0.66(2)$  for  $\text{HoD}_{2.12}$  and  $0.67(2)$  for  $\text{DyD}_{2.0}$  are not unusual but have not been interpreted in detail. Knight shift measurements have been performed but an evaluation in terms of possible muon sites has not yet been performed. It is mentioned that the Knight shift scales with bulk susceptibility between 200 and 300 K. Measurements below the critical temperatures suffer from a severe loss of signal amplitude and hysteretic behavior. No information on the ordered spin system has been extracted at this stage. The transition temperatures are close to those found in bulk measurements.

Puzzling are the results for  $\text{DyD}_{2.13}$ , which according to bulk data should behave like  $\text{HoD}_{2.12}$ . Above 10 K up to room temperature the  $\mu$ SR signal is reduced in amplitude, the asymmetry rising monotonically from 0.02 to 0.13. Below 10 K a spontaneous spin precession signal with  $\nu_\mu \approx 90$  MHz is found, but its intensity does not explain the reduced signal amplitude at higher temperatures. The data indicate the presence of SRO magnetism up to quite elevated temperatures, an unusual and new result if further substantiated.

#### 5.4.2. $\text{MX}_3$ compounds

To our knowledge only two, rather unrelated, intermetallics of this class were studied by  $\mu$ SR other than the cubic materials with the  $\text{AuCu}_3$  structure discussed in sect. 5.2.3.

5.4.2.1.  $\text{EuAs}_3$ . At  $T_N = 11$  K, an incommensurate structure with a strongly temperature-dependent modulation vector is formed. Lock-in to commensurability occurs at 10.3 K. The ZF  $\mu$ SR study (Chatterji and Henggeler 1998) on a single crystal oriented with the  $c$ -axis parallel to the initial muon-spin direction revealed a complex spectrum in the incommensurate phase, having four spontaneous frequencies with different temperature dependences. In the commensurate phase only an exponentially decaying signal was seen. At  $T_N$  the relaxation rate shows divergent behavior.

5.4.2.2.  $\text{UPd}_3$ . This compound crystallizes in the hexagonal  $\text{MgCd}_3$  structure and is considered a localized actinide magnet containing tetravalent ( $5f^2$ ) uranium ions on two crystallographically different sites. One (the  $a$  site) has hexagonal, the other (the  $c$  site) nearly cubic symmetry. Susceptibility shows Curie–Weiss behavior down to 100 K with a moment of  $2.8\mu_B/\text{U}$  atom, which can well be explained by the CEF interactions observed by neutron scattering (Buyers and Holden 1985). Three phase transitions are observed. All appear to be connected to the near-cubic U site. Below  $T_0 \approx 7.8$  K and  $T_Q \approx 6.5$  K

different antiferro-quadrupolar ordered states coupled to a modulated structure appear and below  $T_N \approx 4.5$  K AFM commensurate to the quadrupolar structure sets in with an ordered moment around  $0.02\mu_B/\text{U}$  atom (McEwen et al. 1998).  $\text{UPd}_3$  is also of interest as the endpoint of the pseudo-binary alloys  $\text{Y}_{1-x}\text{U}_x\text{Pd}_3$ , which are HF compounds showing non Fermi liquid behavior (see sect. 9.4).

Knight shift data were recently reported in a conference contribution (Schenck et al. 2000b). The TF signal consists of two components with amplitude ratio 2:1. The orientational dependence of the Knight shift indicates that muons rest on two axially symmetric interstitial sites.  $T_Q$  and  $T_N$  are clearly visible (but  $T_0$  less so) as a change in various spectral parameters, more pronounced in the stronger signal component. Below  $T_N$  no marked increase in relaxation rate is seen, a result difficult to explain in the context of static AFM order. The authors mention that preliminary ZF did not reveal any measurable relaxation below  $T_N$ . This would rather point towards dynamic (on the  $\mu\text{SR}$  time scale) spin order analogous to the situation in the HF compound  $\text{UPt}_3$  (see sect. 9.3.2). The temperature dependences of the Knight shifts are complex and not understood at this stage. A different magnetic response of the U atoms on the two crystallographic sites is likely to be the underlying cause.

#### 5.4.3. $\text{MX}_5$ compounds

Besides  $\text{CeCu}_5$  and  $\text{UCu}_5$  which are HF compounds (and hence discussed in sect. 9.3), only the  $\text{RNi}_5$  intermetallics have been investigated by  $\mu\text{SR}$ .  $\text{PrNi}_5$  is a singlet ground state system and has been discussed (especially in connection with muon induced effects) in sect. 5.1. The systematic studies of other members of the series were carried out with the goal of detailed insight into the dynamical properties of 4f moments, both in the *paramagnetic* and *ferromagnetic* states. Single crystals were predominantly used since anisotropies of paramagnetic spin fluctuations was another point of interest. In many aspects the work parallels that on Gd metal discussed in sect. 4. Furthermore, CEF influences play a significant role in the  $\text{RNi}_5$  compounds (for R other than Gd) and their influence on the  $\mu\text{SR}$  magnetic response has been another central theme of study.

The  $\text{RNi}_5$  materials crystallize in the hexagonal  $\text{CaCu}_5$  structure (space group P6/mmm) as does  $\text{CeCu}_5$  (but not  $\text{UCu}_5$ ).  $\mu\text{SR}$  studies are limited to compounds containing heavy R ions ( $\text{Gd}^{3+}$  and beyond). They all order ferromagnetically with  $T_C$  ranging from  $\sim 31$  K ( $\text{GdNi}_5$ ) to 0.5 K ( $\text{YbNi}_5$ ). From relaxation data on nonmagnetic  $\text{LaNi}_5$  (where only nuclear dipole fields exist) a stationary muon for  $T < 150$  K resting on the interstitial 3f site  $(\frac{1}{2}, 0, 0)$  was established (Dalmas de Réotier et al. 1990c). This site is also occupied by hydrogen in the  $\alpha$ -phase of  $\text{LaNi}_5\text{H}_x$ . The situation appears to be, however, not quite as simple as that. Data on angular scans of Knight shift for a spherical single crystal of  $\text{GdNi}_5$  (Mulders et al. 1998b, 2000) indicate that in addition to the 3f site the 6m sites  $(0.13, 0.26, \frac{1}{2})$  are occupied with the muon diffusing rapidly between the six equivalent sites of this type (see discussion below).

5.4.3.1. *GdNi<sub>5</sub>*. This intermetallic is an axial ferrimagnet (the transition temperature is  $\sim 31$  K) with FM ordered Gd moments of  $\sim 7\mu_B$ . They induce antiparallel oriented moments

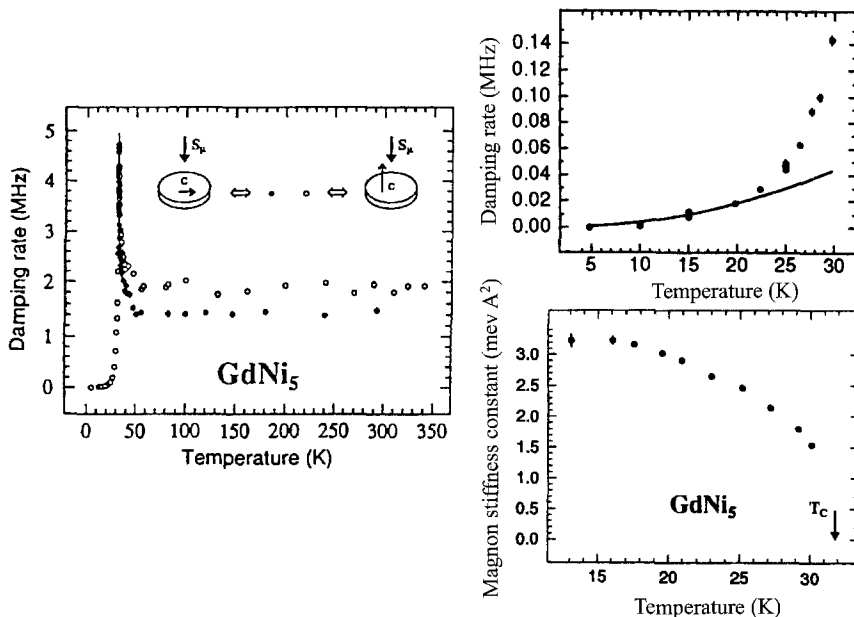


Fig. 74.  $\mu$ SR on  $GdNi_5$ . Left: Temperature dependence of the ZF muon spin depolarization rate in the para- and ferromagnetic states for the two measuring geometries indicated. The rate peaks at the Curie temperature. Right: Fit of depolarization rate in the FM state to a two magnon process (top) together with the extracted magnon stiffness constant (bottom). After Gubbens et al. (1994a) and Yaoouanc et al. (1995).

of  $0.16\mu_B$  on the Ni atoms (see Franse and Radwanski 1993). These weak moments on Ni atoms can in most cases be neglected and  $GdNi_5$  may effectively be treated as a FM. Since orbital 4f contributions are absent in Gd, only a weak magnetic anisotropy exists, which is caused by dipolar interactions between the Gd moments.

ZF- $\mu$ SR measurements by Gubbens et al. (1994a) on a single crystal established that the full muon signal can be followed continuously through the paramagnetic region into the FM state. In the latter, two spontaneous muon spin precession frequencies (with amplitude ratio 3:2) of 220.9 and 79.7 MHz, resulting from two magnetically inequivalent muon positions, were observed for the  $S_\mu \perp c$  geometry. The temperature dependence of relaxation rates for the two signals is quite similar but their absolute values differ by a factor of four (the more intense signal being more strongly damped). No oscillatory components are present for  $S_\mu \parallel c$ . These results mean that the  $c$ -axis is the easy axis in contradiction to magnetization data (Gignoux et al. 1976), but in agreement with Mössbauer data (Tomala et al. 1977).

The temperature dependence of the ZF muon spin relaxation rate beautifully demonstrates critical slowing down at  $T_C$ . As seen in fig. 74, the critical behavior of rate is not fundamentally different for the two orientations, emphasizing the weak magnetic anisotropy. In the paramagnetic regime,  $GdNi_5$  shows a temperature dependence of relaxation rate in the critical range that can well be described in terms of a dipolar



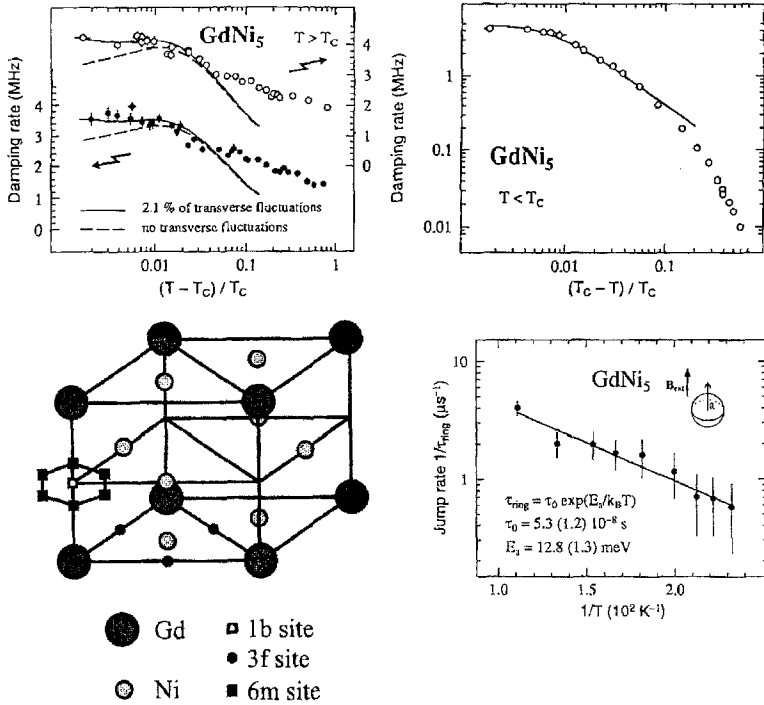


Fig. 75. Top:  $\mu$ SR studies of critical spin fluctuations in  $GdNi_5$ . Left: ZF muon spin depolarization rate in the paramagnetic critical regime as a function of reduced temperature (open circles,  $S_\mu \parallel c$ ; solid circles,  $S_\mu \perp c$ ). The lines are predictions of mode-coupling theory for a dipolar Heisenberg ferromagnet. Right: ZF muon spin depolarization rate in the ferromagnetic critical regime as a function of reduced temperature. The line is the same theoretical prediction as shown in the picture on the left. After Yaouanc et al. (1996). Bottom: Muon location and diffusion in  $GdNi_5$ . Left: Partial representation of the crystalline lattice showing the 1b, 3f and 6m interstitial sites. Right: Temperature dependence of the muon jump rate from the ring sites. The line is an Arrhenius fit. After Mulders et al. (2000).

Heisenberg ferromagnet (Yaouanc et al. 1996). In this regime the relaxation is mainly due to longitudinal fluctuations (i.e., fluctuations along the propagation vector of the FM spin structure of the Gd sublattice). Figure 75 (top left) presents a comparison of measured critical relaxation rates with theoretical predictions by mode coupling theory (see, for example Frey and Schwabl 1994) at the paramagnetic side. It is most interesting that the parameters describing those critical fluctuations are also able to reproduce the critical muon relaxation behavior in the ordered state over roughly the same temperature range of  $\Delta T = T_C - 0.1T_C$  (fig. 75, top right). This result can be understood within the frame of the dynamical scaling theory by Halperin and Hohenberg (1967).

The presence of a full  $\mu$ SR signal in the ferromagnetically ordered region allowed study of the longitudinal depolarization rate in ZF for  $T < T_C = 32 K$ . At low temperatures ( $T \leq T_C/2$ ) the temperature variation of rate can be expressed as  $\lambda(T) \propto T^2 \ln T$ . Such an expression arises when muon spin depolarization is caused by a two-magnon

scattering process (Yaouanc and Dalmas de Réotier 1991, Lovesey et al. 1992b, Dalmas de Réotier et al. 1995). Figure 74 (right) shows a fit of  $\lambda$  to the two-magnon process and the temperature dependence of the magnon stiffness constant derived from such a model (Yaouanc et al. 1995). Spin relaxation as seen by  $\mu$ SR has also been discussed by Keren (1994a) with respect to magnon processes. The possibility of (muon vibrational) excitation-assisted spin flips is mentioned. The discussion does not, however, address the R situation in particular.

The dependence of muon Knight shift on orientation of applied field relative to the  $c$ -axis has recently been studied by Mulders et al. (2000) in order to establish the muon stopping sites. The presence of two spontaneous precession frequency is indicative of two stopping sites, as already mentioned. It is concluded from an elaborate analysis of the Knight shift data that the muon sits at the 3f site  $(\frac{1}{2}, 0, 0)$  at all temperatures (see fig. 75, bottom left). Below  $\sim 70$  K the 6m site  $(0.13, 0.26, \frac{1}{2})$  also gets populated. These sites form a ring of six crystallographically equivalent positions (but not magnetically equivalent if a static magnetization axis exists) around the 1b site  $(0, 0, \frac{1}{2})$ . The muon diffuses fast between the six ring sites averaging the different internal field values, which results in a single precession frequency. Above 40 K the residence time of the muon at the ring sites becomes much shorter than the muon mean lifetime. The muon carries out a diffusional jump with rate  $1/\tau_{\text{ring}}$  to a 3f site where it usually remains until its decay. Staying on this site the muon produces the second spontaneous precession frequency observed. The temperature dependence of  $1/\tau_{\text{ring}}$  is shown in fig. 75 (bottom right). An Arrhenius law can be derived. The values of  $E_0$  and  $\tau_0$  are comparatively small and point towards quantum diffusion.

5.4.3.2.  $TbNi_5$ . Here a strong magneto-crystalline anisotropy exists and the moments point along the  $a$ -axis in the FM state. A single-frequency precession signal is observed in ZF for  $T < T_C = 23$  K (Dalmas de Réotier et al. 1992). The temperature dependence of its frequency does not follow the appropriate Brillouin function, but can satisfactorily be described using a Hamiltonian containing the sum of molecular field and CEF interactions. For the latter term, the data on CEF energies given by Gignoux and Rhyne (1986) have been used successfully. No change of CEF parameters due to the presence of the muon was required (i.e., no muon induced effect could be traced). We have presented the experimental results on the temperature variation of spontaneous frequency earlier in fig. 27. The relaxation rate in the ordered regime shows little change with decreasing temperature. For  $T > T_C$  the rate (Dalmas de Réotier et al. 1990c) reflects in part influences of CEF interactions (like  $HoAl_2$  mentioned above). A detailed analysis has not been given for either the ordered or the paramagnetic regime.

5.4.3.3.  $DyNi_5$ . The ZF data are reported to be similar to those of  $TbNi_5$  (Gubbens et al. 1994a).

5.4.3.4.  $ErNi_5$ . Strong magneto-crystalline anisotropy is present here as well. The easy axis in the FM state is the  $c$ -axis. The ZF data (Gubbens et al. 1992, 1994a) revealed marked differences in muon spin depolarization rates for the two orthogonal crystal

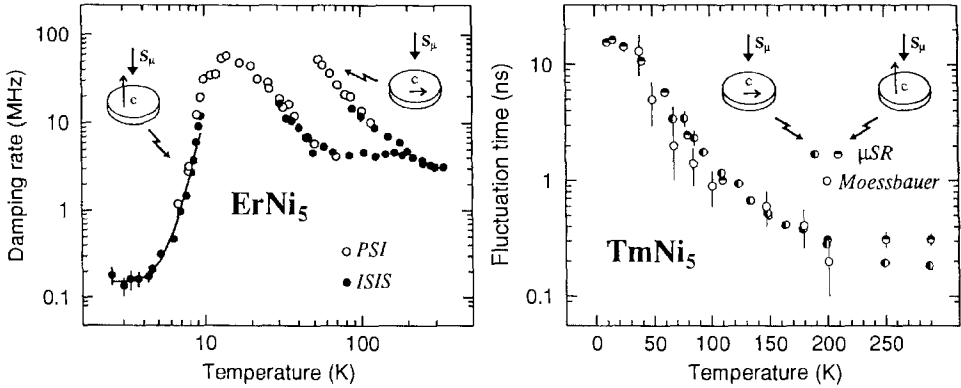


Fig. 76. Left: Temperature dependence of the ZF muon spin relaxation rate in  $\text{ErNi}_5$  for the two crystal orientations indicated. The Curie temperature is 9.2 K. The solid line is a fit of rate to phonon induced relaxation (see text). Right: Comparison of the 4f moment fluctuation times in  $\text{TmNi}_5$  as seen by  $\mu$ SR (for two sample orientations) and Mössbauer spectroscopy. The two data sets are simply normalized to each other (see text). From Gubbens et al. (1994a).

orientations up to temperatures at least ten times  $T_C = 9.2$  K (fig. 76). The rate for  $S_\mu \perp c$  increases so rapidly on approaching  $T_C$  that the signal vanishes in the instrumental dead time for  $T < 30$  K. For  $S_\mu \parallel c$  the rate is much lower. It peaks slightly above  $T_C$ . Gubbens et al. (1992) could approximately explain the high-temperature anisotropy within a mean field model amended by CEF interactions.

Below  $T_C$  a signal can only be seen for the  $S_\mu \parallel c$  geometry. No spin precession is observed; the signal consists of a single exponential decay of muon spin polarization down to  $\sim 7$  K. At lower temperatures a time independent signal appears in addition to the signal featuring exponential decay. Already at 12 K where the relaxation rate peaks, signal amplitude reduces. Perhaps static spin correlations develop in part of the sample volume. The exponential depolarization rate at low temperatures ( $T < T_C$ ) can be described by

$$\lambda(T) = a \coth\left(\frac{\Delta}{k_B T}\right) + bT^7, \quad (72)$$

with  $a = 0.15$  MHz,  $\Delta/k_B \geq 5$  K and  $b = 1.1$  Hz K $^{-7}$ . A fit of relaxation rate to this expression is shown in fig. 76 (left). It represents phonon induced relaxation (Orbach and Stapleton 1972), the first term relating to one phonon, the second term to two-phonon processes. The temperature dependence is much stronger than for the two-magnon process discussed above. The limit on the energy difference  $\Delta$  is in keeping with CEF splitting energies. The other parameters still call for a microscopic interpretation. Yaouanc et al. (1995) point out that in this system ( $\text{ErNi}_5$ ) with huge CEF anisotropy, the CEF excitations induced by phonons dominate over the magnon process, which will only be visible if CEF interactions are not present (as in  $\text{GdNi}_5$ ) or at least rather small.

5.4.3.5. *TmNi<sub>5</sub>*. Gubbens et al. (1994a) studied the paramagnetic regime ( $T > T_C = 4.5$  K) using a single crystal. The observed temperature dependence of the relaxation rate is

practically independent of sample orientation. The field persistence time  $\tau_c(T)$  (in the fast fluctuation limit) is proportional to the rate  $\lambda$ . It scales well with  $^{169}\text{Tm}$  Mössbauer results on the temperature dependence of fluctuation rate of the magnetic field at the Tm nuclei. (fig. 76, right). The two times were simply normalized to each other since the absolute value of  $\tau_c$  in  $\mu$ SR is not known. Also, the functional dependence of correlation times on temperature remains unexplained at this stage.

5.4.3.6. *YbNi<sub>5</sub>*. This compound has the lowest Curie temperature ( $\sim 0.5$  K) and has been studied by  $\mu$ SR and  $^{170}\text{Yb}$  Mössbauer spectroscopy using a polycrystalline specimen (Bonville et al. 1993). As in  $\text{TmNi}_5$ , good agreement between the temperature dependences of the  $\mu$ SR and Mössbauer field fluctuation times (in the paramagnetic regime) was established. Compared to  $\text{TmNi}_5$  the relaxation rate is much larger but shows only a weak (roughly  $1/T$ ) temperature dependence indicating that Korringa relaxation is dominant, while CEF interactions seem to have little influence.

#### 5.4.4. *RGa<sub>6</sub> compounds*

The  $\text{RGa}_6$  intermetallics exhibit different magnetic properties depending on the R atom, although they all are crystallographically isostructural with only minute changes in lattice parameters. They possess magnetic ordering temperatures between 1.7 K ( $\text{CeGa}_6$ ) and 20 K ( $\text{TbGa}_6$ ). The majority of compounds show AFM order. In the tetragonal  $\text{PuGa}_6$ -type crystal structure (space group  $\text{P4/nbm}$ ), layers of R atoms are stacked perpendicular to the  $c$ -axis with four layers of Ga atoms in between. The distance between the R layers along the  $c$ -axis is large ( $\sim 7.6$  Å) compared to the R–R separation within the  $c$ -plane (4.2 Å). In consequence, the  $\text{RGa}_6$  intermetallics can be regarded as quasi-two-dimensional magnets. Several members of the  $\text{RGa}_6$  series (R = Ce, Nd, Gd, Tb) were studied by  $\mu$ SR (together with neutron diffraction) using polycrystalline samples (Lidström et al. 1996c). Two signals are present in the paramagnetic  $\mu$ SR spectra, one relaxing much faster than the other. The fast signal dominates by a factor of 2–3. Only in  $\text{CeGa}_6$  is the presence of two spectral components not entirely clear. Most likely two muon stopping sites are involved. The weakly relaxing signal changes little when passing through  $T_N$  and keeps its amplitude. Muons producing this signal component must be located at a site where the magnetic field produced by the surrounding R moments cancels completely. For a simple AFM structure this condition is fulfilled by the  $(0\ 0\ \frac{1}{2})$  position. It is fairly removed from the R atoms, which is in keeping with its low depolarization rate. The second muon site must be much closer to the R atoms. Below  $T_N$  the amplitude of its signal is reduced to  $\sim 1/3$  (except for  $\text{TbGa}_6$  where the situation is complex). A strong internal field must be present and the likely candidate position is midway between the R atoms in the  $c$ -plane.

5.4.4.1. *CeGa<sub>6</sub>*. The relaxation rate in the paramagnetic regime between  $T_N = 1.7$  K and 12 K follows a power law  $\lambda(T) = (T - T_N)^w$  with  $w \approx -0.46$ . Above 12 K the rate decreases on warming with a steeper slope. The cause for this crossover could either be the presence of dynamic paramagnetic clusters (as discussed for Gd metal in sect. 4) at low temperatures, or the change in thermal population of the first excited CEF state

located at 43 K (Jerjini 1987). A similar behavior is present in  $\text{TbGa}_6$  (see below). The overall low relaxation rate in paramagnetic  $\text{CeGa}_6$  agrees with the low moment of  $0.4\mu_B$  found by neutrons.

5.4.4.2.  $\text{NdGa}_6$ . This compound orders at 10.4 K with a saturation moment of  $2.45\mu_B$ , forming a simple antiferromagnetic structure with adjacent ferromagnetic planes along the  $c$ -axis having their magnetizations antiparallel. The relaxation rate of the slowly depolarizing signal in the paramagnetic regime (with about 1/4 of total signal amplitude) shows weak temperature dependence and becomes constant above  $\sim 5 T_N$ . The more-strongly damped component displays the “normal” divergence in depolarization rate on approaching  $T_N$ . This is in full agreement with the muon site assignments discussed above.

Below  $T_N$ , two oscillating signals are observed (Lidström et al. 2000) arising from muons in the Nd planes. The signal from muons between the planes shows no spin precession and is only weakly relaxing. It cannot properly be separated from background signal produced by muons stopped outside the sample. Of the oscillating patterns, the lower frequency signal ( $\sim 17$  MHz for  $T \rightarrow 0$ ) comprises about 1/3 of the amplitude and shows a Brillouin-type temperature dependence. It is more strongly damped, especially close to  $T_N$ , compared to the high-frequency signal ( $\sim 55$  MHz). Its frequency decreases slightly with reduced temperature. A detailed interpretation of these contrasting features has not been given.

5.4.4.3.  $\text{GdGa}_6$ . AFM order occurs at  $T_N = 12.5$  K. The spin structure is not known. The fast-decaying signal shows a nearly temperature-independent relaxation rate of  $\lambda \approx 1.6 \mu\text{s}^{-1}$  (fig. 77, left) without distinct critical slowing down. A first-order transition can be excluded since no hysteresis is present, and also from the temperature dependence of the relaxation rate below  $T_N$  (see further down). This feature is more likely a result of the S state character of  $\text{Gd}^{3+}$ , i.e., the absence of ionic anisotropy and CEF interactions, and shows that pair correlations of paramagnetic Gd spins are small, as also observed in other Gd intermetallics. Measurements in  $\text{LF} = 200$  mT produced no change, emphasizing the dynamic nature of depolarization. The weakly depolarizing signal fraction is dominated by interactions with (static) nuclear dipole fields and naturally is nearly temperature independent.

The fast relaxing signal can be followed into the AFM state, albeit with its amplitude reduced to 1/3 and showing no oscillations. Obviously, the transverse (spin–spin) relaxation rate is high and only the longitudinal signal remains visible outside the initial dead time of the spectrometer. The temperature variation of the longitudinal (spin–lattice) relaxation rate for  $T < T_N$  reflects the behavior of 4f spin dynamics in the ordered state. The decrease in rate for  $T \rightarrow 0$  (fig. 77, left) is typical for a second-order phase transition (see the fundamental study of this problem in  $\text{CoF}_2$  by De Renzi et al. 1984).

5.4.4.4.  $\text{TbGa}_6$ . This compound displays complex magnetic order, which has been determined in the neutron work accompanying the  $\mu\text{SR}$  studies. Below  $T_N = 20$  K a modulated incommensurate AFM phase is present. There are changes in modulation

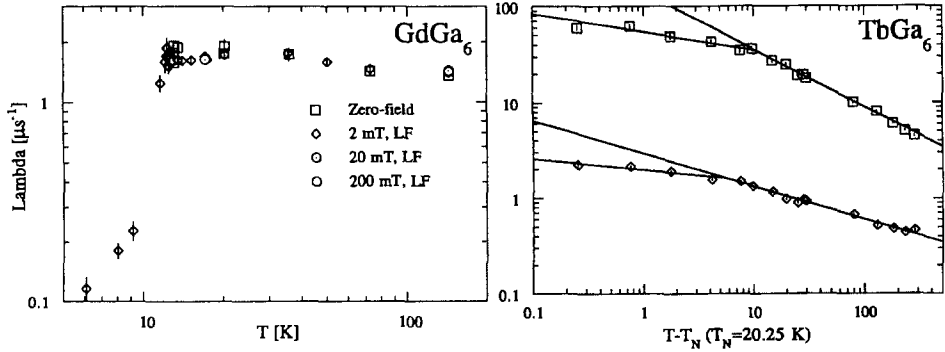


Fig. 77. μSR studies of RGa<sub>6</sub> intermetallics. Left: Temperature dependence of the fast relaxation rate in GdGa<sub>6</sub> below and above the Néel temperature (12.5 K). Right: Temperature dependences of the fast and slow relaxation rates in paramagnetic TbGa<sub>6</sub>. The solid lines are fits to a critical power law (see text) using 20.25 K as the Néel temperature. From Lidström et al. (1996c).

vector at a number of temperature points, but finally, a commensurate AFM structure is formed, in which adjacent pairs of Tb ions in the R plane have their spins coupled antiparallel. The effective Tb<sup>3+</sup> moment (9.8μ<sub>B</sub>) is practically the free-ion moment (Tagawa et al. 1986) but the saturation ordered moment derived from neutron scattering is reduced (8 μ<sub>B</sub>).

The two μSR signals in the paramagnetic regime show analogous behavior in the temperature dependences of their relaxation rates, (fig. 77, right) despite the difference in absolute value of rates by an order of magnitude. Both can be described by a critical power law with a break in slope about 10 K above T<sub>N</sub>. Close to T<sub>N</sub>, the dynamical exponent is about the same for the two signals (w ≈ 0.15). Above T<sub>N</sub> + 10 K the fast rate decreases more rapidly (w ≈ 0.6) compared to the slow rate (w ≈ 0.35). This change of slope is qualitatively similar to that of the paramagnetic signal in CeGa<sub>6</sub>, although the absolute value of that rate in CeGa<sub>6</sub> is three orders of magnitude (!) smaller. This difference in rate magnitude cannot be explained by the difference in ordered moments (0.4μ<sub>B</sub> vs. 8μ<sub>B</sub>) alone. The strong anisotropy coupled to CEF interactions in the Tb compound must contribute as well. This is also the underlying cause of the complex AFM structures just below T<sub>N</sub>. Unfortunately, the positions of the CEF levels are not known, which prevents detailed comparison with theoretical models. The formation of dynamic paramagnetic clusters close to T<sub>N</sub> is the most likely explanation of the crossover in dynamical exponent. The similarity in temperature dependences of the two signals suggest that the interplane coupling of the R layers is most pronounced here and TbGa<sub>6</sub> is thus least like a two dimensional magnet among the RGa<sub>6</sub> materials.

In the ordered state, part of the fast relaxing signal component exhibits spontaneous spin precession for T < 9 K (i.e., in the commensurate AFM state) with only moderate depolarization (λ ≈ 2 μs<sup>-1</sup>). The saturation precession frequency is ν<sub>μ</sub><sup>Tb</sup>(0) ≈ 183 MHz, corresponding to an internal field of 1.35 T. These values are of the same magnitude as those in AFM Ho and Dy metals (see fig. 33), which verifies a muon position close to

the R ions. The comparatively low depolarization rate indicates that inhomogeneous line broadening is not excessive and points towards a well-developed simple spin structure at low temperatures, in agreement with the neutron results. The temperature dependence of this depolarization rate follows the expected dynamical behavior of spins in the ordered state as previously discussed for the longitudinal signal in GdGa<sub>6</sub> (fig. 77, left).

### 5.5. Ternary compounds

#### 5.5.1. MTX

Intermetallics of this type are often labeled as 1:1:1 compounds. They exist for M=R and An, but crystallize in a large variety of structures. This leads to a broad spectrum of magnetic properties and a description on general terms is not possible. Within the R-containing compounds, the Ce intermetallics are most important. The majority of them possess heavy-fermion, or at least Kondo-lattice properties (see sect. 9 for details). Famous examples are the CeT<sub>3</sub>Sn (T=Ni, Pd, Pt) compounds, which have been studied in some detail by  $\mu$ SR (sect. 9.2). Only one (CeCuSn) of the numerous RTX compounds exhibiting more conventional magnetism has been looked at with  $\mu$ SR. This leaves the actinide members, especially the U compounds. Again, a fair number of those can be classified as HF materials (e.g., the series URhIn, UPdIn, UPtIn), but no  $\mu$ SR studies have yet appeared. An overview of their often unusual magnetic properties can be found in Sechovsky and Havela (1988). It demonstrates that HF character is not the only challenging feature. One finds series of compounds where, depending on the alloying partner, an initially localized U moment (together with AFM order) is gradually reduced (gaining more itinerant character) leading in the end to Pauli paramagnetism. These are problems well suited for  $\mu$ SR studies. As far as we could determine, data for only one compound (UNiGa) have appeared in a full (but short) publication in the literature and we must rely on several preliminary reports.

5.5.1.1. *CeCuSn*. The intermetallic has been reported (Dwight 1976) to crystallize in the CaIn<sub>2</sub> (P6<sub>3</sub>/mmc) structure which can be derived from the hexagonal AlB<sub>2</sub> structure with the Cu and Sn atoms in a zig-zag arrangement. Whether the Cu and Sn atoms form ordered sublattices is still an open question. Above 100 K, a Curie–Weiss behavior with a moment of  $2.54\mu_B$ , close to the value expected for Ce<sup>3+</sup>, and a paramagnetic Curie temperature of  $\approx -20$  K was seen (Nakotte 1994). CeCuSi and CeCuGe order ferromagnetically at 14.9 K and 10.3 K, respectively, but CeCuSn shows complex and not fully understood antiferromagnetic ordering below  $\approx 8.6$  K. The specific heat exhibits a double-peak structure featuring, apart from the peak expected at 8.6 K, a second around 7.4 K which is highly sensitive to applied magnetic fields. The bulk data were summarized in a magnetic ( $B$ – $T$ ) phase diagram (Nakotte 1994), which distinguishes three magnetically ordered phases I, II, and III, with phase III being present only at applied fields. In the limit  $B \rightarrow 0$  phase I exists between 8.6 K and 7.4 K. Below 7.4 K one finds phase II. Above 8.6 K the material is thought to be paramagnetic. Practically no information is available on the spin structure in the different magnetic phases (i.e.,

neutron diffraction data have not been reported thus far), but they were all considered to be antiferromagnetically ordered. The low-temperature Sommerfeld constant is only very slightly enhanced ( $\gamma = 32 \text{ mJ}/(\text{mol K}^2)$ ), excluding heavy-fermion behavior. In contrast, the relatively large saturation moment of  $1.48\mu_B$  per formula places CeCuSn in the regime of localized 4f magnets. CeCuSn is also of interest in connection with Cu doping of the Kondo-lattice compound CeNiSn which changes from an enhanced paramagnet to AFM behavior beyond a critical Cu concentration (see sect. 9.2). Unfortunately, CeNiSn and CeCuSn have different crystal structures and their electronic properties cannot simply be compared.

$\mu$ SR studies in zero, longitudinal and transverse fields were carried out in the temperature range between 2 K and 150 K on a polycrystalline powder sample by Kalvius et al. (2000e). The data confirm the presence of two magnetic states, but each contains differently correlated spins. A first magnetic transition commences near 11 K and extends down to 7.5 K. In this temperature range a gradual formation of a dynamic (according to LF data) short-range correlated (SRC) spin state is seen that coexist with spins keeping their paramagnetic nature. The rate of formation of the SRC state is maximal around 8.5 K, which is probably the cause for the peak seen in specific heat. The second transition observed in specific heat at 7.4 K signals, according to the  $\mu$ SR data, the long-range ordering of the remaining paramagnetic fraction (having a volume fraction of roughly 30% at all temperatures  $T < 7.4 \text{ K}$ ). The SRC state is at first unaffected by this ordering process. At lower temperatures it begins to lose its spin dynamics and ends in a spin frozen state around 3.5 K. Whether the two magnetic surroundings (short- and long-range ordered) sensed by the muons at  $T \ll 7.5 \text{ K}$  reflect a magnetically inhomogeneous material or whether a homogeneous spin structure with only partially long-range ordered spins exists (see for example the discussion on UNi<sub>4</sub>B in sect. 9.3.2) cannot be decided at this stage and calls for magnetic diffraction data.

5.5.1.2. *UNiGa*. The hexagonal ZrNiAl structure is formed. In it U–Ni and Ni–Ga layers alternate along the  $c$ -axis. This leads to a substantial magnetic anisotropy and also the 5f moment is well localized with a substantial orbital moment (Sechovsky et al. 1994). The magnetic phase diagram, established by neutron diffraction, is fairly complex (Sechovsky et al. 1995). All AFM structures (there are several) below  $T_N = 39 \text{ K}$  are based on FM order of U moments along the  $c$  direction within the basal plane. The planes are AFM coupled. This coupling is considerably weaker than the FM coupling within the planes.

$\mu$ SR spectroscopy was performed using a single crystal (Prokes et al. 1995). Several oscillatory signals were seen in ZF within the AFM state for a crystal orientation  $c \perp S_\mu$ . In contrast, spectra taken in the orientation  $c \parallel S_\mu$  showed no spin precession. This agrees with the notion that all moments point along the  $c$ -axis. The different magnetic transitions below  $T_N$  (at 34.5, 36.1, 37.2 K) are reflected by the appearance of different sets of signals (fig. 78). The signals do not reach  $\nu_\mu = 0$  exactly at the nominal Néel point, but all of them drop suddenly in frequency. A Brillouin-type behavior is not observed at all. At low temperatures the full  $\mu$ SR signal consists of two precessing components with  $\nu_\mu(0) = 47$



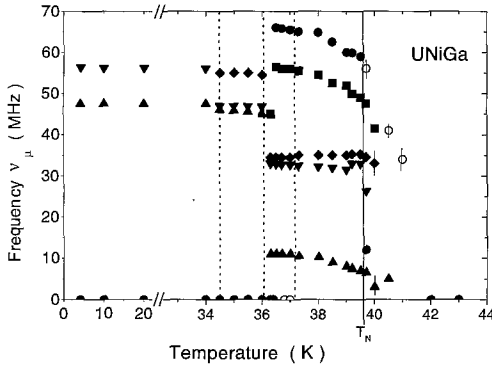


Fig. 78. Temperature dependences of spontaneous spin precession signals in AFM UNiGa (single crystal). The dotted lines indicate transitions within the AFM state, the full line represents the Néel temperature. After Prokes et al. (1995).

and 56 MHz and one monotonic-relaxing component (intensity ratio 6 : 1.5 : 3.5). The authors suggest that several muon stopping sites are involved. Knight shift measurements in the paramagnetic regime and the geometry  $\mathbf{B}_{\text{app}} \parallel c \perp \mathbf{S}_{\mu}$  revealed three distinct signals. In one the shift scales with bulk susceptibility along the  $c$ -axis, for the other two a proportionality (above 50 K) exists with respect to the basal plane susceptibility. An evaluation of the muon position requires angular dependence scans, which are reported to be under way. Clearly, for a quantitative interpretation of the  $\mu\text{SR}$  results, one needs to know the muon sites. Qualitatively, the  $\mu\text{SR}$  spectra are well in keeping with the known magnetic properties of UNiGa. In particular, they reflect quite obviously changes in spin structure at the different magnetic transitions below  $T_N$  of this unusual magnet. The data set might be considered a prime example how  $\mu\text{SR}$  can nail down transitions of spin reorientation within the ordered regime of a complex magnet.

5.5.1.3. *UNiAl*. To our knowledge, the  $\mu\text{SR}$  data for this compound can be found, oddly enough, only in two (not so recent) progress reports. UNiAl is isostructural with UNiGa and the basic notion of large anisotropy together with a sizable orbital U moment applies here as well. The spin structure in the AFM state ( $T_N = 19$  K) must, however, be different. Spontaneous muon spin precession was observed in *both* the  $c \parallel \mathbf{S}_{\mu}$  and  $c \perp \mathbf{S}_{\mu}$  geometries (Prokes et al. 1993). Hence the magnetic structure cannot be based solely on simple FM order in basal plane U layers, which confirms neutron data suggesting a modulation within the planes. The AFM  $\mu\text{SR}$  spectra consist of three fast depolarizing oscillatory signals with  $\nu_{\mu}(0) = 14, 39$  and 47 MHz. At least two muon sites must exist, one of them off the U–Ni plane. The values of precession frequencies are quite similar to those in UNiGa, suggesting that the magnitude of the U moments is about the same ( $\sim 1.4\mu_B$ ). That value is higher than that derived from either the neutron or the susceptibility data ( $0.8\mu_B$ ). The basal plane modulation could account for that difference. No indication for magnetic transitions within the AFM state was seen.

Gubbens et al. (1995b) concentrated on the behavior of relaxation rates both above and below  $T_N$  in the  $c \parallel \mathbf{S}_{\mu}$  geometry. These experiments were carried out at the ISIS pulsed facility, which precludes the observation of spontaneous spin precession patterns above the

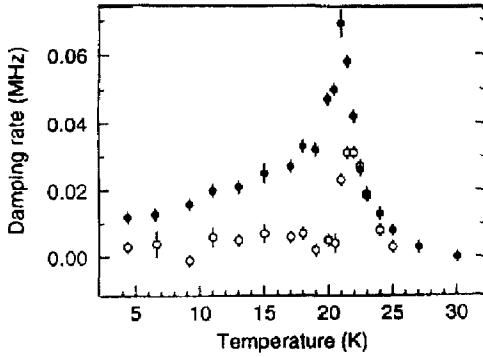


Fig. 79. Temperature dependence of muon spin relaxation rate in UNiAl in ZF (open circles) and LF (solid circles) for  $c \parallel S_{\mu}$ . After Gubbens et al. (1995b).

order of 10 MHz, and the rates below  $T_N$  refer to the non-oscillating longitudinal signal. As seen from fig. 79, the depolarization rate exhibits the typical behavior of a second-order magnetic phase transition, i.e., a maximum at  $T_N$ . In the critical paramagnetic regime it can be described by a power law, though with a rather unusual dynamic exponent of  $w \approx 1.1$ . The sensitivity of the temperature variation of rate in the ordered state to an applied LF of 200 mT is also unusual. With the field present, the rate stays at all temperatures well above the ZF value, even for  $T \rightarrow 0$ . The authors suggest that fluctuations of 5f spins are faster at sites where  $B_{\mu} \perp c$  (in ZF) than at those where  $B_{\mu} \parallel c$ . Since the internal fields are of the same order as the applied field, the latter enforces the condition  $B_{\mu} \parallel c$  throughout.

5.5.1.4. *Other UTX compounds.* A brief report on  $\mu$ SR studies in three other UTX intermetallics is given by Prokes et al. (1996). The materials studied are at the borderline of magnetism, having greatly reduced U moments due to 5f–ligand hybridization (Sechovsky and Havela 1988).

UIrGa crystallizes in the orthorhombic TiNiSi structure (related to the structure of the CeTsn Kondo metals). Specific heat and susceptibility suggest the onset of AFM order around 16 K. At 4.2 K two metamagnetic transitions are reported with  $B_c = 14$  and 19 T. Clearly, the spin structure of UIrGe is likely to be complex. ZF- $\mu$ SR spectroscopy found a very small depolarization rate of electronic origin down to 20 K. Below this temperature the rate increases markedly, indicating the development of AFM spin correlations. On passing 16 K a fast depolarizing precession signal appears with a low ( $\sim 3$  MHz) and nearly temperature-independent frequency. This result verifies a magnetic transition (of first order?) and points towards a rather small U moment.

The crystal structure of URhIn is the hexagonal ZrNiAl type structure also present in UNiGa and UNiAl. Specific heat suggests  $T_N = 6.5$  K and susceptibility peaks at 7 K. The  $\mu$ SR relaxation rate of electronic origin, however, remains low and temperature independent down to 2.6 K. This completely contradicts the bulk data and the nature of the magnetic anomaly at 6.5 K remains unsolved.

UCoAl also possesses the hexagonal ZrNiAl type crystal structure. It is considered an itinerant (5f band) metamagnet with the rather low critical field  $B_c = 0.8$  T (Havela et al. 1997). In the metamagnetic state a small moment on U ( $\sim 0.3\mu_B$ ) was found by neutrons. The moment on Co is negligibly small (Papoular and Delapalme 1994). Reproducibility of data is often poor due to nagging stoichiometry problems. The  $\mu$ SR results are similar to those of URhIn, i.e., a weak temperature-independent depolarization rate down to 2.8 K. Here, these findings are not in contradiction to bulk data. Electrical resistivity and specific heat both claim a nonmagnetic ground state below  $B_c$  (see Sechovsky and Havela 1988).

### 5.5.2. $MT_2X_2$

Compounds with the composition  $MT_2X_2$  (also often called 122 compounds) comprise a large family of R and An ternary intermetallics. Different crystal structures are found, but we limit ourselves to materials having the tetragonal  $\text{ThCr}_2\text{Si}_2$  (I4/mmm) or the closely related  $\text{CaBe}_2\text{Ge}_2$  (P4/nmm) structure, which are the most important members of the series. Basically, the M, T, X atoms are arranged in planes and the two structures differ in the sequence of planes, which is M-X-T-X-M-X-T-X-M in the former and M-T-X-T-M-X-T-X-M in the latter. Again, several members of the series are HF compounds. Particularly well-known examples are the archetypal HF materials  $\text{CeCu}_2\text{Si}_2$  and  $\text{URu}_2\text{Si}_2$ . Others studied by  $\mu$ SR are  $\text{CeRu}_2\text{Si}_2$ ,  $\text{CePt}_2\text{Si}_2$ ,  $\text{CePd}_2\text{Si}_2$  and  $\text{CeT}_2\text{Sn}_2$  (T=Cu, Pd, Pt). These results are presented in sect. 9, subsects. 9.2 and 9.3. Only those R and An materials showing more conventional magnetism will be discussed in the present section with respect to  $\mu$ SR data. They are in general characterized as strongly axial magnets, and in the U compounds the U moment is in the majority of cases rather well localized and has a substantial orbital component. The study of spin dynamical properties is the central point of  $\mu$ SR spectroscopy in the  $MT_2X_2$  intermetallics. We shall see that R and U compounds differ significantly in this respect. For the R members only compounds containing light R ions (up to Nd) have been investigated by  $\mu$ SR; the work on An compounds is restricted to U materials.

5.5.2.1. *Y and La intermetallics.*  $\mu$ SR has been used to study  $\text{YRu}_2\text{Si}_2$  (Sekine et al. 1995),  $\text{YCo}_2\text{Si}_2$  (Dalmas de Réotier et al. 1990a) and  $\text{LaNi}_2\text{Si}_2$  (Dalmas de Réotier et al. 1989). All are nonmagnetic, but possess nuclear dipole moments. The measurements were used to gain information on the muon stopping site by comparing the observed Van Vleck width with dipolar sum calculations. Eleven interstitial sites are possible candidates for the muon position (Dalmas de Réotier et al. 1990a). Unfortunately, the results from all those compounds did not provide a unique answer and the question of muon position is still open. It is also not obvious that the muon takes up the same site in all compounds of the series. The simultaneous occupancy of more than one site cannot be excluded either in some cases. The problem of muon stopping sites in  $MT_2X_2$  intermetallics is discussed in more detail in the paragraph on  $\text{CeRu}_2\text{Si}_2$  in sect. 9.3. Safely established is a stationary muon below 100–150 K.

5.5.2.2. *CeRh<sub>2</sub>Si<sub>2</sub>.* A single- $k$  AFM structure with  $\mu_{\text{Ce}} \parallel c$ -axis ( $\mathbf{q} = (\frac{1}{2} \frac{1}{2} 0)$ ) developing below  $T_N \approx 35$  K was deduced from neutron data of Quezel et al. (1984) and

Chevalier et al. (1985). Another study (Grier et al. 1984) reports two magnetic transitions  $T_{N1} = 36$  K and  $T_{N2} = 25.5$  K. At  $T_{N2}$  the propagation vector changes to  $\mathbf{q} = \frac{1}{2} \frac{1}{2} \frac{1}{2}$ . NMR measurements (Kawarazaki et al. 1995) were interpreted in terms of two structural domains with the different  $\mathbf{q}$  vectors. Recent neutron diffraction on a single crystal under applied pressure suggested a magnetic ground state of superimposed  $4\mathbf{k}$  structures (Kawarazaki et al. 2000). It has also been reported that pressure suppresses the magnetic order (Movshovich et al. 1996) and at 9 kbar superconductivity sets in at 0.35 K, probably just when magnetic order disappears.

Dalmas de Réotier et al. (1990a) reported a first μSR study using a powder sample. A strong rise in paramagnetic relaxation is observed on approach to  $T_N$ . At 22.5 K spin precession together with a simply relaxing signal exists. No change in signal amplitude occurs. The local field (at 22.5 K) amounts to only 110 G, but was explained on the basis of the neutron data by Quezel et al. (1984). Both an oscillating and non-oscillating signal were seen in the magnetic regime. This was thought to arise from two muon stopping sites, one of which produces  $\mathbf{B}_\mu = 0$ . Such types of sites exist. Detailed information on the temperature dependences of either the precession frequency or the relaxation rate were not given.

Quite recently a more detailed μSR study on CeRh<sub>2</sub>Si<sub>2</sub> has appeared (Yamamoto et al. 2000b). Polycrystalline material was used. Two signals were observed at low temperatures, one simply exponentially relaxing (amplitude  $A_1$ , relaxation rate  $\lambda$ ), the other showing spontaneous spin precession (amplitude  $A_2$ , non-relaxing). Between  $T_{N1}$  and  $T_{N2}$  only the relaxing signal is present. ZF-μSR spectra as well as the temperature dependences of signal amplitudes, relaxation rate and precession frequency are shown in fig. 80. The relaxing signal just below  $T_{N1}$  can be decoupled in a rather low LF = 50 G, meaning that a static random field of only a few Gauss strength is acting on the muons. It arises nevertheless from electronic moments. Both Rh and Si have extremely low nuclear moments and also the depolarization should be of Gaussian shape. In fact, the signal seen is considered the initial part of a Lorentzian Kubo–Toyabe relaxation which occurs in cases where the local field of an AFM cancels due to a high symmetry of the spins surrounding the muon (see Asch et al. 1989 as discussed in sect. 5.2.1). (Reviewers' remark: As can be seen from fig. 80 (right, bottom) the relaxation rate rises steadily with reduced temperature and rather sharply below ~10 K. This is incompatible with the above explanation. Some other signal must be hidden in these subspectra. Yamamoto et al. 2000b do not discuss this feature at all.) The oscillatory frequency sets in abruptly at  $T_{N2}$  and then hardly changes with temperature. Its magnitude corresponds to a local field of 125 G in fair agreement with Dalmas de Réotier et al. (1990a). In contrast to Dalmas de Réotier et al. (1990a) the authors conclude that only one muon stopping site exists. They show by dipolar sum calculations that on the basis of the  $4\mathbf{k}$  structures (or the double domain structure) a muon occupying the 4c interstitial site ( $\frac{1}{2} 0 0$ ) will produce the overall features (i.e., a non-oscillating plus an oscillating signal with the proper amplitudes) of the observed spectral shape. A Ce moment of  $1.46\mu_B$  is estimated.

We return to this data set in sect. 9.3 when discussing the evolution from the HF material CeRu<sub>2</sub>Si<sub>2</sub> to the AFM compound CeRh<sub>2</sub>Si<sub>2</sub> *via* the pseudo-binaries

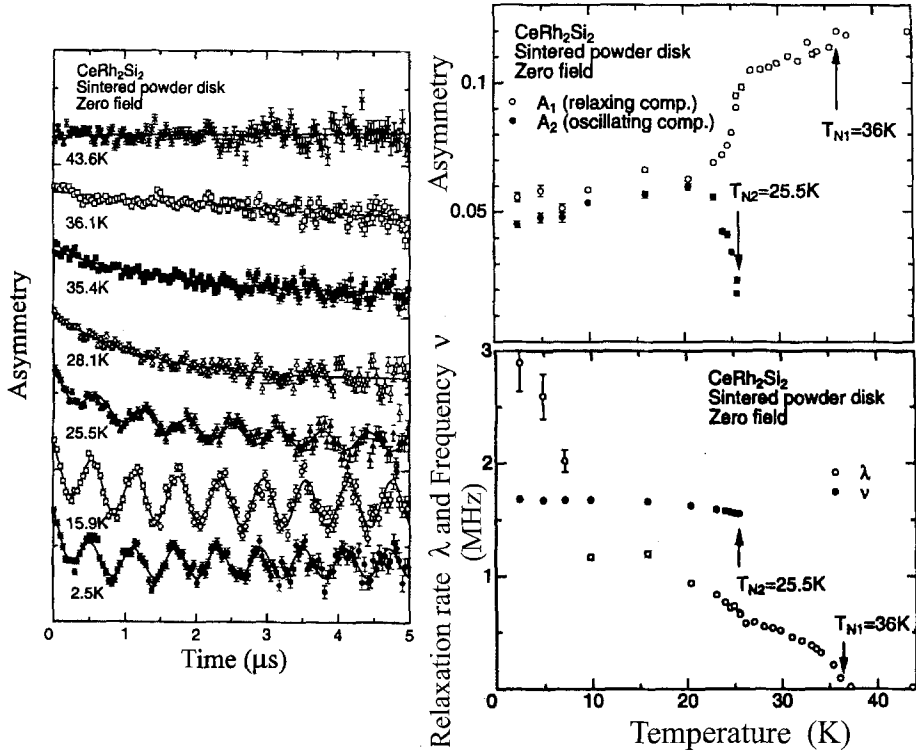


Fig. 80. Left: ZF- $\mu$ SR spectra of  $\text{CeRh}_2\text{Si}_2$  at various temperatures. Right: Temperature dependences of signal amplitudes (top); precession frequency and relaxation rate (bottom). After Yamamoto et al. (2000b).

$\text{Ce}(\text{Ru}_{1-x}\text{Rh}_x)_2\text{Si}_2$  (Murayama et al. 1993, 1997). This comparison points towards a classification of  $\text{CeRh}_2\text{Si}_2$  as a Kondo AFM.

5.5.2.3.  $\text{PrCo}_2\text{Si}_2$ . This compound probably has the most complex magnetic structure within the series. Under ZF conditions three magnetic transitions occur at 30, 17 and 9 K. These transitions are metamagnetic, meaning that changes in magnetic structure can also be induced by applied fields. At low temperatures the critical fields are 1.2, 3.8 and 12.2 T. They decrease with rising temperature. Above  $B_c = 12.2$  T, the so-called forced FM phase is formed at low temperatures which continuously changes into the normal paramagnetic phase with rising temperature. Only the  $\text{Pr}^{3+}$  ions possess magnetic moments and they are FM coupled within  $a$ - $b$  planes. Below 9 K (or 1.2 T) a simple AFM sequence of these FM planes along the  $c$ -axis is present. Between 9 and 17 K and 17 and 30 K (or 1.2 and 3.8 T and 3.8 and 12.2 T) the planes couple to two types of long period AFM sequences with propagation vectors  $\mathbf{q} = 13/14$  and  $7/9$  (Shigeoka et al. 1989).

The first  $\mu$ SR studies with a single-crystal sample were carried out by Nojiri et al. (1992) in ZF with  $\mathcal{S}_\mu \parallel c$  and in pulsed high fields (see sect. 2.7) up to 13 T with

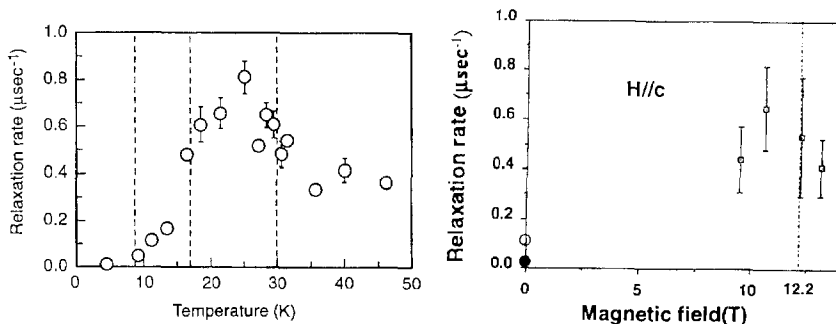


Fig. 81. μSR on single-crystal PrCo<sub>2</sub>Si<sub>2</sub> for  $B_{app} \parallel S_{\mu} \parallel c$ . Left shows the temperature dependence of relaxation rate in ZF, right the dependence of rate on strong LF at low temperature (see text). The sample is oriented with its *c*-axis parallel to the initial muon polarization. From Nojiri et al. (1992).

$B_{app} \parallel S_{\mu} \parallel c$ . In ZF the relaxation spectra between 100 and 50 K are dominated by the action of nuclear dipole fields (temperature-independent Gaussian Kubo–Toyabe functions). Above 100 K the muon starts to move. Below 50 K the depolarizing action of fluctuating atomic fields from Pr begins to be felt. These fluctuations slow down with decreasing temperature, but  $T_N$  is passed without any noticeable break in the continuous rise of relaxation rate. Oddly enough, the rate peaks about 5 K below  $T_N$  and then decreases monotonically for  $T \rightarrow 0$ , perhaps with a sharper drop around 17 K. Around 9 K, the rate has become so low that particular irregularities at the transition point are difficult to make out (fig. 81). Measurements in high LF were carried out with the sample cooled to 4.2 K. The application of the magnetic pulse, however, heats the sample to 12 K. According to the magnetic phase diagram this rise in temperature causes a downshift of  $B_c$  of only ~0.5 K and hence poses no problem. More serious are the small relaxation rates at this temperature which severely limit the resolution and, as fig. 81 shows, a definite change of rate at the 12 T transition could not be determined. But already at 8 T the rate is enhanced by an order of magnitude above its ZF value. It is not clear whether this is an experimental effect or a true sample response. Clearly, μSR measurements in ultra-high fields are still at their infancy. The 4c interstitial site is proposed as the muon stopping site in accordance with measurements on CeRh<sub>2</sub>Si<sub>2</sub> (see above).

A subsequent study by Gubbens et al. (1995a) fully verified the ZF results of Nojiri et al. (1992), especially the maximum in rate below  $T_N$ . Also carried out were measurements in the orientation ( $S_{\mu} \perp c$ ). In this case the rate does peak at  $T_N$ . A more detailed study of paramagnetic critical relaxation confirmed a power-law dependence with  $w \approx 0.87$  (Gubbens et al. 1998) in ZF. There is a dependence of relaxation rate and its temperature variation on applied LF up to 0.6 T. In this case a saturation of rate occurs below reduced temperatures of ~0.02 (fig. 82). A possible link of this effect to the hyperfine anomaly of <sup>141</sup>Pr (see sect. 5.1) could not be verified since preliminary data for NdRu<sub>2</sub>Si<sub>2</sub> show similar behavior, even more pronounced (Gubbens et al. 1998). More likely CEF effects are responsible, but a theoretical treatment is still lacking. For  $T < T_N$ , a single-frequency spontaneous precession pattern was visible together with a

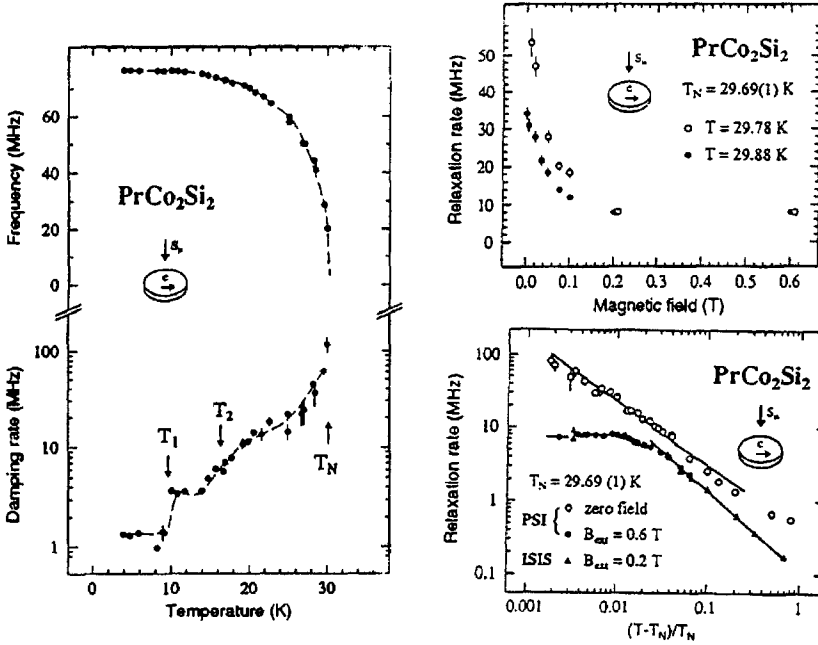


Fig. 82. Left: Temperature dependence of spontaneous muon spin precession frequency and of relaxation rate of the associated non-oscillating signal in magnetically ordered  $\text{PrCo}_2\text{Si}_2$ . Right: Field dependence of the paramagnetic relaxation rate near the Néel temperature (top) and fit to a critical law (bottom) for ZF and LF measurements as indicated. The measuring geometry is always  $S_\mu \perp c$ . After Gubbens et al. (1997a, 1998).

simply relaxing signal (Gubbens et al. 1997a) which is probably due to the occupation of a second site by the implanted muons. As shown in fig. 82, the change of frequency with temperature is smooth and Brillouin-like. The magnetic transitions are only visible in the temperature dependence of the relaxation rate of the non-oscillating signal. For the most likely muon stopping sites one calculates that the local field (if it does not altogether vanish) is parallel to the orientation of Pr magnetic moments. Under this condition, the observation that spin precession is only visible for  $S_\mu \perp c$  verifies the strict confinement of magnetic moments to the  $c$ -axis. The other observation, that only the longitudinal spin fluctuations show critical behavior (they are probed for  $c \perp S_\mu$ ) is also quite common in highly anisotropic magnets. Most unusual is the temperature behavior of transverse spin fluctuations. Generally (and we shall present some more pertinent examples in the following), they show little temperature dependence directly above the magnetic transition, but then a continuous drop below. Peaking *below* the ordering transition is (thus far) unique. An explanation has not been given, but the data show that spin dynamics must be special and unconventional in the long-range modulated magnetic structures of  $\text{PrCo}_2\text{Si}_2$ . Whether this is connected to the special electronic properties of  $\text{Pr}^{3+}$  in a strong CEF remains to be seen. As mentioned, CEF interactions could also be responsible for the peculiar field dependence of paramagnetic relaxation, especially near  $T_N$ .

5.5.2.4. *PrRu<sub>2</sub>Si<sub>2</sub>*. The compound (ThCr<sub>2</sub>Si<sub>2</sub> structure) shows giant magnetic anisotropy, corresponding to an anisotropy field of 400 T with the *c*-axis being the easy axis (Shigeoka et al. 1992). A detailed study of its magnetic properties (Mulders et al. 1997) showed that PrRu<sub>2</sub>Si<sub>2</sub> enters an axial incommensurate sine wave modulated state at  $T_N = 16$  K, followed by a first-order phase transition at  $T_C = 14$  K into an axial FM structure. The lowest CEF states are two singlets separated by 2.25 meV. The ratio of exchange energy to CEF separation of the lowest states is large enough to enable spontaneous magnetization to develop.

Two  $\mu$ SR studies exist, as already mentioned in sect. 5.1.2. They are separated by several years and treat the case differently. The reviewers are astonished that no attempt was made to reconcile the two studies, although several of the authors are identical. For this reason, the two papers will have to be reviewed separately.

At the time of the first work (Yaouanc et al. 1994) only a single magnetic phase transition into an anisotropic FM state ( $T_C = 15$  K) was known. The observation an oscillating signal below  $T_C$  (giving  $B_\mu(0) = 0.04$  T) for  $S_\mu \perp c$ , but only a monotonically relaxing one for  $S_\mu \parallel c$  is reported. Clearly, the *c*-axis is precisely the easy axis. Both signals display full initial asymmetry above and below  $T_C$ . Comparing the experimental result on  $B_\mu(0)$  with dipolar sums for the likely stopping sites lead to the conclusion that the contact field must be positive and not negligibly small (the latter in contrast to the RAl<sub>2</sub> materials, except R=Gd). Within a few Kelvin above  $T_C$  spin fluctuations become so slow that a nearly static spectral shape (Gaussian Kubo–Toyabe) results. Even at elevated temperatures (170 K), the exponential limit of motional narrowing is not yet reached. The authors argue that the Kubo–Toyabe formalism does not reproduce the spectral shape to their satisfaction, and use a description of relaxation based on temperature-dependent second moments of field distribution  $\Delta_\parallel^2$  and  $\Delta_\perp^2$  (with respect to the *c*-axis). The analysis gives about the same temperature dependences for the two second moments. In any case, the quasistatic paramagnetic spin dynamics over a large temperature range is an unusual result. It was considered to be caused by the giant anisotropy, but without a theoretical foundation of this view. The relaxation rate in the ordered regime (for  $S_\mu \parallel c$ ) shows first a rapid decrease of rate below  $T_N$  and then a smooth reduction to the limit  $\lambda = 0$  for  $T \rightarrow 0$ . A theoretical fit to phonon or magnon processes (as discussed for other members of the family) was not given.

The  $\mu$ SR spectra presented by Mulders et al. (1997) have been recorded with the *c*-axis perpendicular to  $S_\mu$ . A longitudinal field of LF=0.2 T was applied in order to suppress the depolarizing influence of <sup>141</sup>Pr nuclear dipoles. The remaining relaxation rate which arises from electronic moments shows two maxima at 14 and 16 K. This result was used to pinpoint the magnetic transition temperatures whose appearance was less clearly pronounced in the caloric data. No further discussion on  $\mu$ SR data is given, including the earlier results of Yaouanc et al. (1994). The latter clearly need to be re-analyzed in terms of a singlet ground state model with the proper CEF splittings. Mulders et al. (1997) state that the nature of the two low-lying singlet states explains the magnetic anisotropy.



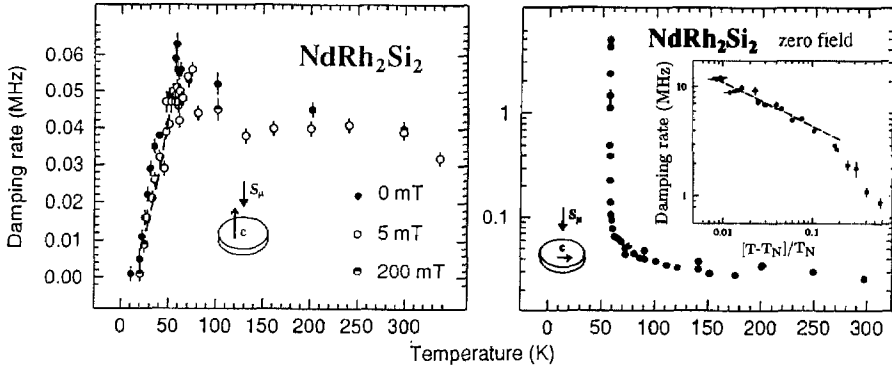


Fig. 83. Temperature dependence of the  $\mu$ SR relaxation rate in  $\text{NdRh}_2\text{Si}_2$ . Left: A single exponentially relaxing signal is seen for the  $c$ -axis parallel to muon spin polarization. The rate below the Néel temperature is fitted to a two-magnon process. Right: Critical behavior of the paramagnetic relaxation rate for the  $c$ -axis perpendicular to the muon spin polarization (longitudinal spin fluctuations). The insert shows a fit to a critical power law. After Gubbens et al. (1994b, 1997b).

5.5.2.5.  $\text{NdRh}_2\text{Si}_2$ . This is a simple AFM with a single magnetic transition at  $T_N = 57$  K. The  $\text{Nd}^{3+}$  moments are oriented parallel to the  $c$ -axis in FM [001] planes stacked in a  $+-+$  sequence along the  $c$  direction (Chevalier et al. 1985).  $\mu$ SR data were taken by Gubbens et al. (1994b). For the  $S_\mu \parallel c$  geometry hardly any critical rise in paramagnetic relaxation is seen. The exponentially relaxing signal can be followed into the ordered state without any loss of signal strength. The variation of its relaxation rate with temperature can be fitted to a quadratic dependence (fig. 83, left), meaning that two-magnon processes dominate (see discussion on  $\text{GdNi}_5$ ). A dependence on LF, other than the trivial decoupling of relaxation by nuclear moments, is not observed here.

The other measuring geometry ( $S_\mu \perp c$ ) shows (as usual) critical divergence of relaxation rate in the paramagnetic regime (fig. 83, right). A power law can be fitted to the region close to  $T_N$  giving the dynamical exponent  $w \approx 0.4$ . In the ordered state, spontaneous spin precession is present (Gubbens et al. 1997b) exhibiting a smooth, Brillouin-like temperature dependence and  $\nu_\mu(0) = 67$  MHz, corresponding to  $B_\mu(0) \approx 0.5$  T. This value is similar to that in  $\text{PrCo}_2\text{Si}_2$ , but an order of magnitude larger than in  $\text{PrRu}_2\text{Si}_2$ . It also exceeds the field in  $\text{CeRh}_2\text{Si}_2$  (0.11 T) by a substantial margin, although the ordered moment in the Ce compound is close to the free-ion moment ( $2.5\mu_B$ ) and the moment on Nd cannot exceed its free-ion moment of  $3.6\mu_B$ . Summarizing, the values of local fields found in the different compounds are at this point not explained. Different magnetic structures may be responsible in part, but no clear systematics are yet apparent.

5.5.2.6.  $\text{UT}_2\text{Si}_2$  with  $T = \text{Co}, \text{Rh}, \text{Pt}$ . Compounds of this class exhibit local moment behavior at high temperatures with sizable U moments ( $2.6\text{--}3.6\mu_B$ ). The magnetic properties at low temperatures are varied, ranging from local moment ordered magnetism to Pauli paramagnetism. The intermetallics discussed here were measured by Dalmas de

Réotier et al. (1994b), and fall into the intermediate regime between the two magnetic extremes. All three exhibit AFM order with  $T_N = 137$  K ( $\mu_{\text{ord}} = 1.96\mu_B$ ) for  $\text{URh}_2\text{Si}_2$ ,  $T_N = 85$  K ( $\mu_{\text{ord}} = 1.42\mu_B$ ) for  $\text{UCo}_2\text{Si}_2$ , and  $T_N = 35$  K ( $\mu_{\text{ord}} = 1.67\mu_B$ ) for  $\text{UPt}_2\text{Si}_2$ . Only one magnetic transition occurs and the spin structures are identical to that of  $\text{NdRh}_2\text{Si}_2$  (see above). Powder samples were used, which precluded direct measurement of effects related to the substantial magnetic anisotropy present.

In  $\text{URh}_2\text{Si}_2$  a critical divergence of paramagnetic relaxation and spontaneous spin precession below  $T_N$  with  $B_{\mu}(0) = 0.3$  T is observed. As in  $\text{NdRu}_2\text{Si}_2$ , one deduces a positive and comparatively large contact field. The relaxation of the longitudinal (1/3) signal in the AFM state is small ( $0.06\mu\text{s}^{-1}$ ) and largely temperature independent, in contrast to the findings on analogous R compounds. Again, a definite dependence on LF is seen with the result that  $\text{LF} \geq 2$  mT completely suppresses this relaxation. The authors argue (correctly) against a dominant nuclear moment contribution and conclude that a static weak moment component must be present. This latter conclusion is, however, not easily reconciled with the total signal strength. There is no reason why the observed signal is not the longitudinal component of the oscillating pattern. Then the result must mean that longitudinally only a small quasistatic internal field is present while the transverse field (the oscillating component) is by no means small. This situation is also not easy to model and finally we must conclude that this case is not yet understood.

In  $\text{UCo}_2\text{Si}_2$  the paramagnetic relaxation is dominated by nuclear depolarization throughout. The (not so small) U moments must fluctuate rapidly even near  $T_N$ . In the AFM state only the longitudinal signal is visible, the oscillating part being clearly too highly damped. No details on the temperature dependence of rates are given, but the dominance of nuclear depolarization suggests temperature independence. The paramagnetic data are used once more to gain insight into the  $\mu^+$  stopping site by comparison with calculated Van Vleck widths. The results are not different and not more convincing than the other determinations of that type discussed earlier.

In  $\text{UPt}_2\text{Si}_2$  the temperature dependence of relaxation rate (for  $T < T_N$  the rate of the longitudinal 1/3 signal) is quite similar to that of  $\text{NdRh}_2\text{Si}_2$  (see fig. 83) if one takes the proper average of data for the two measuring geometries. It is thus quite different from that of  $\text{URh}_2\text{Si}_2$ . No summary discussion on possible origins of the differences in μSR response of the three U intermetallics is given. The situation is confusing and more data would be needed to extract any form of general trend.

5.5.2.7.  $U(\text{Pd}_{1-x}\text{Fe}_x)_2\text{Ge}_2$ .  $\text{UPd}_2\text{Ge}_2$  is an AFM. Below  $T_N \approx 140$  K a longitudinal spin density wave spin structure is formed. Down to  $\sim 100$  K the sine modulation is incommensurate, at lower temperatures it is commensurate, briefly still sinusoidal and then squared (André et al. 1996). This magnetic structure is highly sensitive to doping with iron (Balagurov et al. 2000). In the range  $x = 0.01-0.02$  two phase transitions ( $T_1 \approx 50$  K and  $T_2 \approx 80$  K) below  $T_N = 140$  K are seen. The coexistence of AFM, spin glass and FM phases was discussed on the basis of bulk magnetic data (Duh et al. 1996). For  $x = 0.02$  the low-temperature magnetic structure is a collinear AFM with the U moments forming FM planes stacked antiferromagnetically along the *c*-direction

(Balagurov et al. 2000). An U moment between 2.3 and  $2.5\mu_B$  is reported. Results of a  $\mu$ SR study of magnetic  $U(\text{Pd}_{1-x}\text{Fe}_x)_2\text{Ge}_2$  for  $x = 0.01$  and  $0.02$  have been published by Pomjakushin et al. (2000) and as a shorter conference report by Rasopina et al. (2000).

The  $x = 0.02$  sample showed below  $T_N$  a single spontaneously oscillating  $\mu$ SR spectrum in ZF. The frequency first rises in the usual Brillouin-like fashion and nearly saturates around 37 MHz, but at  $T_2 \approx 80$  K it suddenly drops ( $\sim 33.5$  MHz) and then recovers to a somewhat lower saturation value (35 MHz). This is considered the signature of the transition from the SDW to the AFM state. The irregularity in  $\nu_\mu$  at  $T_2$  is accompanied by a sharp peak in muon spin relaxation rate. It is claimed that this reflects the increase of field distribution in the SDW state. [This argument is incorrect. The additional SDW field distribution is taken care of by switching from a cosine to a Bessel oscillation. The authors make this switch, initiated by the typical appearance of a  $90^\circ$  phase shift (see sect. 3.7). In any case, the relaxation rate drops to a normal level quickly on both sides of  $T_2$ . The probable cause for the peak is the sum of two signals with slightly different frequencies (to create a beat beyond the end of the spectrum's time window). This then appears in a single oscillatory fit as an increased damping. Such effects have been observed, for example, at the spin turning transition of Gd metal (Hartmann et al. 1994b).] No special effects are seen at the proposed second transition  $T_1 \approx 50$  K. The authors give no comment. They state as their salient result that no need exists for introducing a second short-range ordered phase as suggested by Duh et al. (1996). Finally, dipolar sum calculations are carried out for  $B_\mu$  in the AFM phase using the  $(0, \frac{1}{2}, \frac{1}{8})$  stopping site. Good agreement is achieved. Yet, the problem of assigning the proper muon stopping site in the  $\text{ThCr}_2\text{Si}_2$  structure is far from resolved (see discussion in sect. 9.3.1 under  $\text{CeRh}_2\text{Si}_2$ ). (The site selected by the present authors has only been suggested in one case (Yamamoto et al. 1997) and even this group has recently switched to another choice (Yamamoto et al. 2000b). It is clearly not the most favored site.) Agreement for another site  $(\frac{1}{2}, \frac{1}{2}, 0)$  can also be achieved, but needs an additional contact field contribution. (There is in fact no reason why this should be absent (see also sect. 4). Though not discussed, it is quite conceivable that the addition of a sensible contact field contribution allows several more possible muon stopping sites.)

In the  $x = 0.01$  compound a single oscillating signal was seen between  $T_N$  and  $\sim 100$  K. Below 95 K two oscillating components  $\nu_1$  and  $\nu_2$  are resolved. The temperature dependence of  $\nu_1$  is Brillouin-like from  $T_N$  down to lower temperatures. Initially it follows  $\nu(T)$  for the  $x = 0.02$  material. The other component starting around 100 K, first rises quickly but then shows a reduction in frequency around  $T_1 = 50$  K quite similar to the one of  $\nu$  at 100 K in  $x = 0.02$  material. Again dipolar sum calculations are performed for the  $(0, \frac{1}{2}, \frac{1}{8})$  stopping site using the model of superposition of a square and sine modulated SDW structure. The derived temperature dependence of the (modulated) U moments is explained by a temperature variation of the initial phase of the SDW modulation by  $\Delta\phi = 0.2$  rad.

(Reviewers' remark: As discussed, the magnetic structure of pure  $\text{UPd}_2\text{Ge}_2$  is complicated enough without Fe doping. It would have been sensible to first establish the  $\mu$ SR response in the pure material where the magnetic properties have been studied in more detail. No such  $\mu$ SR work is published to our knowledge. The final weakness of the present  $\mu$ SR paper is the uncertainty of the exact muon stopping site. The authors

present no discussion on possible mechanisms for the strong influence of small amounts of Fe on the magnetic behavior.  $\text{UFe}_2\text{Ge}_2$  appears to have no magnetic transition and Fe often has no moment when incorporated in the 122 structures. This might not be the case here because of the strong influence of Fe. This question could be settled by Mössbauer spectroscopy, but again no documentation of such a study exists to our knowledge. The samples of the  $\mu$ SR study could easily be used.)

5.6. *Other compounds*

In this section we discuss  $\mu$ SR measurements on R intermetallics and alloys that cannot easily be classified in the scheme used thus far. No additional An compounds have come to our attention.

5.6.1.  $\text{Gd}_{0.696}\text{Y}_{0.304}$

The magnetic phase diagram of  $\text{Gd}_{1-x}\text{Y}_x$  consists of three different magnetic phases labeled “Ferro I”, “Ferro II” and “helical AFM (HAF)”. Ferro II is a canted AFM phase (canting angle  $\sim 60^\circ$ ) in which the Gd spins produce a net moment along the hexagonal  $c$ -axis. In the HAF phase the moments are FM oriented in the basal plane with the net moment rotating from one layer to the next by a small turning angle. The exact nature of the Ferro I phase is still under debate. It is either a conical spin arrangement around the  $c$ -axis with additional uncorrelated moments in the basal plane (Legvold et al. 1980), or an arrangement where some spins are fixed parallel to the  $c$ -axis with the rest of the spins showing paramagnetic random orientations (Bates et al. 1987). The sample studied by  $\mu$ SR ( $x \approx 0.3$ ) orders at 215 K in Ferro I and changes at 204 K to HAF (i.e., Ferro II is not formed). A single crystal oriented  $c \parallel \mathbf{S}_\mu$  was used (Eccleston et al. 1995). Spectra showing exponential muon spin relaxation were seen at all temperatures, including the LRO regimes. At the transition temperatures distinct changes in rate and signal amplitude were found (fig. 84). The rate increases on approach to  $T_C$  in the usual fashion but jumps

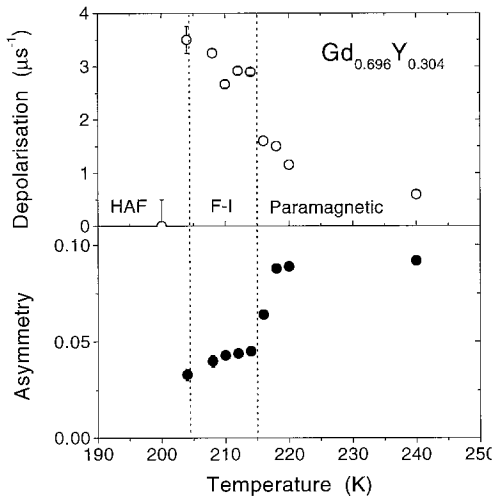


Fig. 84. Temperature dependence of depolarization rate and initial asymmetry of  $\text{Gd}_{0.696}\text{Y}_{0.304}$  measured on cooling in ZF. The lines give the boundaries of the different magnetic phases. After Eccleston et al. (1995).

at  $T_C$  to a higher value and remains practically constant throughout phase Ferro I. Signal amplitude is reduced by  $\sim 50\%$  which means a cone opening angle of  $\sim 60^\circ$ . The relaxation data demonstrate that the usual quasistatic limit of spin motions in a LRO phase is not reached for Ferro I. This interesting fact is probably coupled to the paramagnetic behavior of either a spin component or parts of the spin system, but this important distinction cannot be made with certainty. In the HAF phase the full ordering in the basal plane produces local fields of large magnitude, which puts the signal outside the time resolution of the spectrometer (ISIS pulsed source). Zero signal strength is the result.

### 5.6.2. *CeSi*, *CeGe*

Below their Néel temperatures (*CeSi*, 5 K; *CeGe*, 10.5 K), both compounds display the typical spin precession signal  $\mathcal{A} = a_0[(1/3)e^{-\lambda_1 t} + (2/3)e^{-\lambda_2 t} \cos(\omega_\mu t)]$  down to 0.1 K (Kenzelmann et al. 1998). The temperature dependence of the precession frequency (local field) in *CeSi* follows a smooth  $J = 1/2$  Brillouin function over the full temperature range. In *CeGe* a power law  $B_\mu(T) = B_\mu(0)[1 - (T/T_N)^\delta]^\beta$  provides a better description. The values of the exponents ( $\beta \approx 0.4$  and  $\delta \approx 2$ ) correspond to a 3D Heisenberg magnet and AFM magnon excitations. Neutron diffraction, however, claims for *CeSi* an incommensurately modulated AFM structure below  $T_N$ , which locks into a commensurate structure at subkelvin temperatures (Schobinger-Papamantellos and Buschow 1994). This is in disagreement with the  $\mu$ SR results. An incommensurate spin arrangement should produce a Bessel function oscillatory pattern and the locking should be visible as an anomaly in the temperature dependence of precession frequency. As it stands, the  $\mu$ SR data point towards a locally commensurate spin arrangement throughout. A similar situation has been encountered in *CePtSn* (see sect. 9.2 for a more detailed discussion and possible solutions of the problem). For *CeSi* there is an indication of random order above  $T_N$ , up to  $\sim 9.5$  K. Otherwise, critical slowing down of spin fluctuations is observed. Corresponding data for *CeGe* are not yet available.

### 5.6.3. *R<sub>2</sub>In*

The compounds with  $R = \text{Sm, Gd and Ho}$  crystallize in a hexagonal system ( $P6_3/mmc$ ). *Gd<sub>2</sub>In* becomes a FM below 200 K and then changes into an AFM at 150 K. *Sm<sub>2</sub>In* is a ferrimagnet with  $T_N = 150$  K and *Ho<sub>2</sub>In* displays two FM states with transition temperatures at 80 and 40 K, distinguished by the spin orientation relative to the  $c$ -axis.

Preliminary ZF- $\mu$ SR data were published by Ravot et al. (1997). Paramagnetic *Gd<sub>2</sub>In* shows exponential relaxation varying as  $[T - T_C]^{-w}$  with  $w = 0.56$ , a common value. At  $T_C$ , signal amplitude drops somewhat below 1/3 of the paramagnetic amplitude. Nevertheless, the observed relaxation pattern must represent the longitudinal “1/3” signal of an ordered magnet. It is also exponential in nature with the rate first dropping quickly below  $T_C$  and rising once more with reduced temperature reaching a maximum around 100 K which is well below the nominal value of  $T_N$ . A similar behavior has been seen in *PrCo<sub>2</sub>Si<sub>2</sub>* (see sect. 5.5.2). At (nominal)  $T_N$  a slight increase of amplitude is seen. The signal strength now approaches  $A_0^{\text{para}}/3$ . In ferrimagnetic *Sm<sub>2</sub>In* two relaxation rates ( $\lambda_1$

and  $\lambda_2$ ) are needed to represent the spectral shape. Rate  $\lambda_1$  follows the temperature dependence of susceptibility just below  $T_N$  (both run through a maximum), but then rises distinctly for  $T \rightarrow 0$ . This rise and the two-rate feature are not understood. No details concerning signal amplitudes or rate  $\lambda_2$  are given. In  $\text{Ho}_2\text{In}$  the  $\mu$ SR signal is lost altogether at  $T_C \approx 80$  K. No further details are reported. The depolarizing influence of  $^{115}\text{In}$  and  $^{165}\text{Ho}$  nuclear dipoles, which surely must be present, is never mentioned.

#### 5.6.4. $Y_6(\text{Mn}_{1-x}\text{Fe}_x)_{23}$

$Y_6\text{Mn}_{23}$  and  $Y_6\text{Fe}_{23}$  order magnetically at rather high temperatures ( $\sim 500$  K). In contrast, the pseudo-binaries  $Y_6(\text{Mn}_{1-x}\text{Fe}_x)_{23}$  show no LRO for  $0.2 < x < 0.7$ . Either magnetic frustration or itinerant moment collapse is responsible (Kilcoyne and Cywinski 1992).  $\mu$ SR was carried out on polycrystalline samples with  $x = 0.225, 0.45, 0.6, 0.7, 0.8$  by Kilcoyne and Telling (1995) and a magnetic phase diagram derived. It shows an extended concentration range where spin-glass-type behavior was present. The authors conclude that the loss of LRO is coupled to spin dynamical properties rather than static magnetic frustration. We remind the reader of similar findings in Sc-doped  $\text{YMn}_2$  and Y-doped  $\text{DyMn}_2$  discussed above. The data give no indication of a change in Mn moment with  $x$  in the intermediate regime.

#### 5.6.5. $\text{YMn}_{12}$

The compound  $\text{YMn}_{12}$  has the tetragonal  $\text{ThMn}_{12}$  structure (space group  $I4/mmm$ ) which contains four lattice positions denoted as 2a, 8i, 8j, and 8f. This lattice structure is quite common among rare-earth and actinide intermetallics (see sects. 5.5.2, 9.3.1, 9.3.2) and  $\text{YMn}_{12}$  is an important prototype since the 2a site is solely occupied by Y and the 8i, 8j, 8f sites all by Mn. In other intermetallics, site occupancies can be mixed (see, for example,  $\text{RFe}_6\text{Al}_6$  further below). In  $\text{YMn}_{12}$ , the Mn ions have a different magnetic moment at the 8i and 8j sites ( $0.42\mu_B$ ) than at the 8f site ( $0.14\mu_B$ ). The compound is usually discussed as an itinerant antiferromagnet with  $T_N \approx 100$  K (Deportes and Givord 1976). Yet,  $^{55}\text{Mn}$  NMR data (Yoshimura et al. 1990) could be better reproduced by a localized  $S = 1/2$  Heisenberg model than by self-consistent renormalization (SCR) theory, which has otherwise been quite successful for itinerant antiferromagnets (see, for example,  $\text{YMn}_2$  above).

$\mu$ SR data on powder samples (Kalvius et al. 2000a) showed that the ZF relaxation is largely dominated by the nuclear dipole fields of  $^{55}\text{Mn}$  above  $T_N$ . The influence of the electronic moments on Mn is only weakly felt due to motional narrowing by rapid spin fluctuations. It becomes more pronounced near  $T_N$ , when critical slowing down occurs. Below  $T_N$ , no spontaneous spin precession was observed. The ZF spectra can be described by a Lorentzian Kubo–Toyabe pattern. The overall depolarization rate remains fairly independent of temperature and also does not change dramatically at the transition temperature. The absence of muon spin precession must mean that all implanted muons occupy an interstitial site where the contributions to the local field cancel for the simple antiferromagnetic spin structure. LF measurements show further

that the antiferromagnetic spin system is essentially static (LF  $\approx$  200 G leads to complete suppression of depolarization).

A computer code (Noakes et al. 1987) to search for interstitial positions of lowest effective potential was used to gain information on possible muon stopping sites. It was found that the  $0, \frac{1}{2}, \frac{1}{4}$  (4d, 4m2) and the  $0, 0, \frac{1}{2}$  (2b, 4/mmm) sites are both likely candidates. The former site has 4 i-Mn neighbors, the latter 4 j-Mn neighbors. Dipolar sums based on the magnetic structure proposed by Deportes and Givord (1976) result indeed in full cancellation of the local field for the two sites. The basic reason is that those interstitial positions are surrounded by Mn ions of the same type and that the spin structure leads to a complete staggered AFM magnetization between neighboring spins in each sublattice separately.

#### 5.6.6. *CeAgSb<sub>2</sub>*

The compound, which belongs to general series  $RTX_2$ , crystallizes in the  $ZrCuSi_2$  structure (P4/nmm) where the R atoms occupy planes parallel to the basal plane of the unit cell. Most of the  $CeTSb_2$  intermetallics are nonmagnetic Kondo-lattice compounds, but for T = Ag fairly localized moments with a transition into FM magnetic order at 10 K are seen. At high temperatures one finds Curie–Weiss behavior with the  $Ce^{3+}$  free ion moment. The saturation ordered moment is significantly reduced ( $1.4\mu_B$ ). The reason for this is not clear, a canted AFM structure is a possibility (Houshiar et al. 1995).

Preliminary  $\mu$ SR data have been reported by Dann et al. (2000). Relaxation in the paramagnetic state is governed by nuclear dipole interactions. In low LF a weak electronic relaxation is seen; its divergence due to critical slowing down being restricted to a narrow temperature range close to  $T_M$ . In the ordered state well-developed spontaneous spin precession is observed with a  $J = 3/2$  Brillouin-like temperature dependence of frequency and a low-temperature saturation value corresponding to  $B_\mu = 170$  G. This value is in keeping with the low ordered moment. The most probable interstitial muon stopping site is the  $(\frac{3}{4}, \frac{3}{4}, 0.6)$  position.

#### 5.6.7. *RFe<sub>9,5</sub>Mo<sub>2,5</sub>*

The binary intermetallic  $RFe_{12}$  is an interesting candidate for permanent magnets. In pure form, it is crystallographically unstable and the addition of a metal such as Mo is needed to stabilize the  $ThMn_{12}$  type structure. Especially for Mo, the (itinerant) magnetism seems to be sensitive to the concentration of metal addition (Buschow 1991). A detailed study of magnetic properties of  $RFe_{9,5}Mo_{2,5}$  compounds with R = Y, Nd, Dy, Er was carried out by Ayres de Campos et al. (1996) using Mössbauer and  $\mu$ SR spectroscopies as well as magnetization. In fact, the  $\mu$ SR data primarily served to underline some of the Mössbauer results. The  $\mu$ SR spectra in the paramagnetic regime showed exponential relaxation with the typical temperature dependence on approaching a second-order magnetic transition. Below the ordering temperature only the longitudinal (1/3) signal was visible. The rather sluggish reduction of amplitude to 1/3 extended over a temperature range of  $\sim 100$  K (for ordering temperatures around 200 K). This strongly inhomogeneous behavior agrees with

Mössbauer data which see over a wide temperature range the coexistence of paramagnetic and magnetically ordered spectral types, and must be considered an inherent property of these alloys. The authors finally conclude from the combination of various data that the order–disorder transitions are dominated by the *local* magnetic properties and exclude the development of spatial clusters with ordered magnetism. The underlying reason for the distribution in local magnetic properties is the strong dependence of exchange couplings on the exact configuration of Mo atoms substituting for iron.

### 5.6.8. $RFe_6Al_6$

The intermetallics  $RFe_6Al_6$  ( $R = Tb, Ho, Er$ ) also crystallize in the  $ThMn_{12}$  structure. The 2a, 8f, 8i sites are fully occupied by R, Fe, Al, respectively, while the 8j site contains Fe and Al in random order (Schäfer et al. 1998). All three  $RFe_6Al_6$  compounds order ferrimagnetically around 340 K, forming ferromagnetic R and Fe sublattices which are antiferromagnetically coupled. Magnetic Bragg peak intensities show a sluggish increase below  $T_N$ , suggesting that the ordering process extends over a wide temperature range (see inset of fig. 85, upper left-hand panel). The likely mechanism preventing immediate full LRO is frustration of spins by the disorder on the 8j site combined with the different intra- and inter-sublattice exchange couplings (Felner and Nowik 1986).

The  $\mu$ SR data (Kalvius et al. 2000b) show for  $R = Tb$  and  $Er$  at all temperatures below  $T_N$  the spectral response typical for magnetically ordered powder samples:

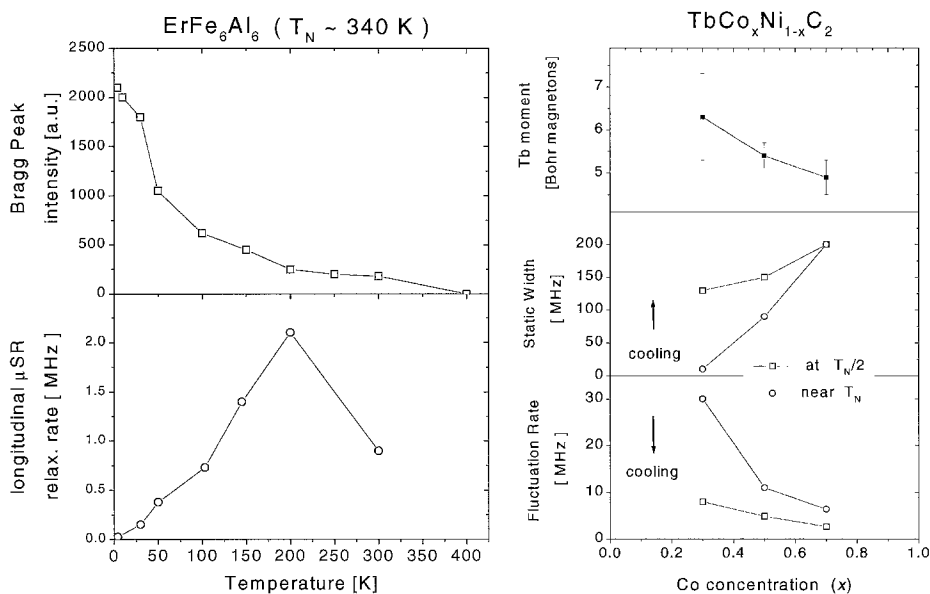


Fig. 85. Left: Temperature dependence of the intensity of the 101/200 Bragg peak (upper panel) and the longitudinal (dynamic) muon spin relaxation rate (lower panel) for  $ErFe_6Al_6$ . Right: Comparison of ZF- $\mu$ SR parameters of the modulated spin states in  $TbCo_xNi_{1-x}C_2$  near and well below the ordering temperature  $T_N$  as a function of  $x$ . (Kalvius et al. 2000b and unpublished). All lines are guides to the eye only.



$A(t) = (2A_0/3) \exp(-\Lambda_t t) \cos(\nu_\mu t) + (A_0/3) \exp(-\lambda_l t)$ . Spin-glass behavior is not observed, but it is found that  $\Lambda_t \gg \nu_\mu$ , which indicates substantial disorder in the spin lattice. The longitudinal rate  $\lambda_l$ , sensing spin dynamics alone, reveals that quasistatic LRO is attained only below  $\sim 50$  K, that is well below  $T_N$  (see fig. 85, lower left-hand panel). It is likely that this persistent spin-dynamical behavior causes the sluggish approach to saturation of Bragg peak intensity. The peak in relaxation rate around 200 K is interesting. The authors suggest that this may reflect a delayed ordering of the Fe ions on the disordered 8j site. The main effect of frustration in this system is the persistence of spin dynamics deep into the LRO state.

### 5.6.9. $RFe_4Al_8$

This compound belongs to the same class as  $RFe_6Al_6$  discussed above (and is isostructural to it); also the problems to be studied are essentially the same, mainly the competing interactions between inter- and intra-subsite magnetic couplings. Compared to  $RFe_6Al_6$ , two favorable conditions exist. Firstly, in well prepared material the Fe ions rest exclusively on the 8f positions making the study of competing interactions more direct. Secondly, the magnetic transition temperatures are lower, which allows more access to the paramagnetic state. The intermetallics  $TbFe_4Al_8$  ( $T_N = 120$  K) and  $YFe_4Al_8$  ( $T_N = 183$  K) have been studied by  $\mu$ SR and neutron diffraction by Schobinger-Papamantellos et al. (2000). The comparison of results for the two materials gives information on the additional influence of the R sublattice. The  $\mu$ SR spectra in  $TbFe_4Al_8$  above  $T_N$  show relaxation behavior that could be fitted to a power exponential form with power  $p$  ranging from 1 at high temperatures to  $1/3$  near  $T_N$ . Such behavior is typical for concentrated spin-glass-like disorder (i.e., a wide distribution of time correlations) in the spin ensemble (see sect. 8.2.1), but full spin freezing does not occur before LRO magnetic order sets in at  $T_N$ . The relaxation rate  $\lambda$  shows the typical rise towards  $T_N$  (with a peak value of  $\lambda$  around  $100 \mu s^{-1}$ ) caused by critical slowing down. The data are consistent with the simultaneous onset of LRO in both sublattices (R and Fe). Below  $T_N$  the signal is lost due to extensive damping, once more indicating strong local spin disorder as a consequence of frustration. Neutron diffraction shows a complex ordering process with two distinct order parameters, but confirms the simultaneous ordering of the sublattices. The situation is different in  $YFe_4Al_8$ . In the paramagnetic regime the ZF- $\mu$ SR spectra are governed by relaxation due to the static nuclear  $^{27}Al$  dipoles. In LF a weak purely exponential relaxation ( $\lambda \approx 0.06 \mu s^{-1}$ ) of electronic origin is seen without critical slowing down towards  $T_N$ . In the LRO state a spontaneous spin precession signal with nearly temperature-independent frequency  $\nu_\mu \approx 40$  MHz (corresponding to  $B_\mu = 2.45$  kG) and the rather small field spread (derived from the static damping) of  $\Delta B_\mu \approx 0.2$  kG. A drastic change of the amplitude of the precession signal between 90 and 140 K points towards a change in spin structure.

These results clearly show that it is the R subsystem which experience frustration by competing interactions. In the paramagnetic state this leads to spin-glass-like behavior, but frustration is not strong enough to prevent the onset of long-range magnetic order.

This is in full agreement with the data on  $RFe_6Al_6$ . In the latter case indications for the presence of frustration in the Fe system as well have been seen. The comparison with  $YFe_4Al_8$  shows that this must be due to the occupational disorder in the 8j sublattice, which has also been deduced from theory (Felner et al. 1981).

#### 5.6.10. $RTC_2$

The rare-earth (R)–transition metal (T) dicarbides have the crystallographic space group  $Amm2$ . They order ferromagnetically for  $T=Co$  and antiferromagnetically (with perpendicular easy axis) for  $T=Ni$ . One can prepare mixed systems, for example  $TbCo_xNi_{1-x}C_2$ . The competing exchange and CEF couplings lead in these materials to three magnetic states, FM, amplitude modulated, and AFM (Kockelmann et al. 1998) with the modulated state always being the magnetic ground state. The  $\mu$ SR results of Kalvius et al. (2000b) indicate strong local spin disorder and persistent spin dynamics in the different LRO magnetic states of all three compounds. Details depend on the value of  $x$  as demonstrated by fig. 85 (right). The Ni-rich material (small  $x$ ) shows more pronounced spin dynamics, the Co-rich material (large  $x$ ) enhanced spin disorder. Neutron diffraction data indicate a small effective moment in the AFM state. This is considered a consequence of the persistent (longitudinal) spin fluctuations.

#### 5.7. Summary: $\mu$ SR studies in R and An intermetallics

As mentioned at the start of this section, the results reported in the previous sections are multi-faceted and an overall picture is not easily extracted. We attempt in the following to summarize some of the results that seem to us to be of importance.

- (i) One understands the high-temperature limit of spin fluctuations as being caused by RKKY exchange acting on free paramagnetic spins (Moriya limit). Consequently, the theoretical formalism is available.
- (ii) In general, the contribution by Korringa relaxation processes (which often dominate NMR spectra), is small and can be neglected.
- (iii) CEF effects are noticeable, especially in strongly anisotropic materials. A quantitative detailed analysis of these effects is rare for the type of compounds covered in this chapter. The theoretical formalism has, however, been developed.
- (iv) In general,  $\mu$ SR senses the development of spin correlations *via* the increase of the muon spin relaxation rate in their early phase, that is, at temperatures well above (sometimes even by an order of magnitude) the magnetic transition point. This is a special power of  $\mu$ SR.
- (v) In anisotropic magnetic materials one observes distinct orientational dependences of the muon spin relaxation rate (when single crystals or textured samples are used). Again, the (unfortunately rather complex) basic formalism for treating such type of data in terms of directional components of the correlation functions of the magnetic spins is available, but a full quantitative analysis of such data is still outstanding. It should be stressed that the possibility of direct separability of components of

spin fluctuations *without applying external fields* (i.e., without disturbing the spin system) is a unique feature of  $\mu$ SR.

- (vi) The spin correlations that lead to a sharp (often called divergent) rise of muon spin depolarization rate on approaching the magnetic transition point (from temperatures above) are largely confined to *longitudinal* magnetic spin fluctuations (i.e., fluctuations along the easy magnetic axis) in strongly anisotropic materials.
- (vii) The paramagnetic muon spin relaxation rate follows a critical power law in the majority of cases. The dynamical exponents, however, vary widely and a consistent explanation of their values has, with a few exceptions, not been given. This feature of the relaxation process must be considered not understood.
- (viii) In contrast, a highly satisfactory analysis of critical fluctuations of  $\text{Gd}^{3+}$  spins in terms of mode coupling theory for a weakly anisotropic ferromagnet could be carried out.
- (ix) It has been shown that the muon spin relaxation observed in the *ordered regime* of weakly anisotropic magnetic materials can be described by *two-magnon* processes. In contrast, for strongly anisotropic materials the muon spin relaxation is more likely to be dominated by *phonon* processes.
- (x)  $\mu$ SR can sensitively trace the formation of regions with spin-glass-like SRO in highly frustrated magnets. Furthermore, the suppression of magnetic order typical for such systems was shown to be due less to the static frustration directly, but stems rather from the action of strong spin fluctuations induced by frustration.
- (xi) Additional information on open questions regarding the ordered spin structure could be obtained in several instances, but cases remain where disagreement between  $\mu$ SR and neutron scattering could not be resolved. In these compounds the necessity of a critical revision of the accepted magnetic structure is indicated.

## 6. Non-metallic compounds

There are relatively few  $\mu$ SR measurements of magnetic insulators and semiconductors in general (see Schenck and Gygax 1995), and very few indeed in non-metallic rare-earth and actinide materials. There are several practical reasons for this:

- (1) The chemistry of muons in non-metals has more direct, and complicating, effects on the  $\mu$ SR signals than in metals. A muon can capture an electron to form muonium in the solid (see sect. 2.4), a bound state that makes the muon so sensitive to magnetic fields that *nuclear* moments can cause relaxation rates too large to detect easily. In a material with electronic moments then, the polarization of muons that form muonium may simply be undetectable, generating a "missing fraction". In any particular non-conducting material, this fraction may be large, leaving little signal to measure, and it may be temperature dependent. Occasionally, there may be conversion of bare muons to muonium (or conceivably, *vice versa*) on a time scale of microseconds, which will generate slow loss of polarization (Kreitzman et al. 1986) difficult to distinguish from magnetic relaxation. Studies of nonmagnetic insulators in static *electric* fields have

shown that the muonium fraction and formation rate depend on the interaction of the stopped muon with radiolysis electrons in the muon's own stopping track (Storchak et al. 1995a,b, 1997).

- (2) The lack of a conduction band to absorb broad frequency ranges of electromagnetic radiation means that a number of electromagnetic probes (optical, NMR, EPR) are easier to observe and interpret in non-metals than in metals, and most of these probes are less expensive than  $\mu$ SR. Thus there is more competition.
- (3) Without the RKKY interaction, which is mediated by conduction electrons, lanthanide and actinide non-metal magnetic orderings tend to be low (below 10 K). This limits the likelihood of developing commercial applications for them, and so limits general interest in lanthanide non-metal magnetism. Superexchange can raise the magnetic transition temperatures again, as it does in R-garnets. The main interest in R-garnets lies in their magneto-optical properties, and there appears to be little opportunity for  $\mu$ SR to have an impact. Thus no  $\mu$ SR work has been published on these otherwise well-studied materials, with the very recent exception of Gd–Ga garnet (sect. 8.3.2).

In contrast to a good metal, where the first guess for the muon site is the largest interstitial hole in the structure (sect. 3.6), the bare muon (generating the “diamagnetic signal”) in a non-metal is often attracted to the most electronegative ion present, ending up “hydrogen bonded” to it. In oxides, this results in a muon site  $\simeq 1$  Å from an oxygen ion (as discussed below), while in fluorides, the muon can pull two fluorine ions toward itself to form an  $(F\mu F)^-$  ion (Brewer et al. 1986). When performing the first  $\mu$ SR measurements on a particular magnetic insulator material, these possibilities should be checked by measurements of depolarization by nuclear moments in the paramagnetic limit, or in a nonmagnetic analogue material, separate from  $\mu$ SR measurements of the magnetic behavior.

### 6.1. Binary oxides and halides

Given that most rare earths prefer to be trivalent in solids, it is no surprise that with oxygen the widest number of them form “sesquioxides”  $R_2O_3$ . AFM ordering temperatures, when present, are below 5 K. Research interest in the magnetism of the sesquioxides peaked in the late 1960s (Eyring 1979), long before the development of  $\mu$ SR as a solid-state probe. To our knowledge, there are no publications on  $\mu$ SR in  $R_2O_3$ .

#### 6.1.1. *EuO*

*EuO* is one of the simplest ferromagnetic systems. It has the NaCl lattice structure and the easy axes of magnetization are the [111] directions. It is considered the prime example of a Heisenberg FM. Together with the other (isostructural) monochalcogenides (*EuS*, *EuSe* and *EuTe*) it has been the subject of intense research by all available pertinent methods. In particular, Mössbauer spectroscopy under ambient and high pressure has played an important role (see Potzel et al. 1993 and references cited therein). In comparison, the existing  $\mu$ SR data are meager. Mainly, one study has been performed by Hartmann et al. (1996) concentrating on the ferromagnetic regime below  $T_C = 69.3$  K. A clear spontaneous

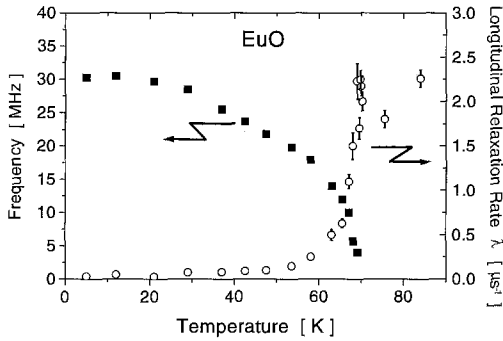


Fig. 86. Temperature dependences of the spontaneous muon spin precession frequency (in the ferromagnetic state) and the muon spin relaxation rate (both in the ferromagnetic and paramagnetic states) in EuO. The data were analyzed with an exponential decay of muon spin polarization throughout. After Hartmann et al. (1996).

muon spin precession signal is observed. The temperature dependence of the precession frequency shows the expected Brillouin-like behavior (fig. 86). The low-temperature limit  $\nu_{\mu}(0)$  corresponds to a local field  $B_{\mu} = 0.24$  T. The muon site is not known, but in simple cubic structures it is likely that the muon resides on a symmetrical interstitial site, like the center of a cube formed by 2 Eu and 2 O ions (see also sect. 5.2.1), but deviations due to muon bonding to oxygen cannot be altogether excluded. Assuming that the muon occupies the high-symmetry site, then all dipolar contributions to the local field cancel and  $B_{\mu}$  represents the contact field only. The amplitude of the precession signal was also found to be temperature dependent. Its magnitude corresponds to the contribution of all implanted muons above 60 K, but decreases significantly at lower temperatures. The reason for this behavior (which means that some of the implanted muons do not contribute any longer to the observable signal) is not understood.

Also shown in fig. 86 is the temperature dependence of the muon spin depolarization rate  $\lambda$ . Calculation of the magnitude and temperature dependence of this rate in EuO has been the subject of considerable theoretical efforts. Both the ferromagnetic state (Lovesey et al. 1992a,c) and the paramagnetic state (Lovesey et al. 1992b, Lovesey and Engdahl 1995) were treated. For the ferromagnetic regime an almost quadratic dependence of  $\lambda$  on temperature, arising from two-magnon processes, was predicted. The temperature dependence in the paramagnetic state is expected to be relatively weak outside the critical region close to  $T_C$ . The experimentally observed longitudinal relaxation rate follows the expected low power (nearly quadratic) in  $T$  only below 50 K. It then increases rapidly upon approaching  $T_C$ . Just above  $T_C$ , the value of  $\lambda$  is around  $2.0 \mu\text{s}^{-1}$  and stays practically constant up to room temperature. This value for  $\lambda$  is in fair agreement with the theoretical prediction of Lovesey and Engdahl (1995), which quotes values at  $1.3 T_C$  between  $1.5$  and  $2.1 \mu\text{s}^{-1}$ , depending on the muon position with respect to the body diagonal. A true critical study (like that in Gd, sect. 4.2) has not been carried out.

### 6.1.2. $\text{UO}_2$ and $\text{NpO}_2$

$\text{UO}_2$  and  $\text{NpO}_2$  are nearly insulating semiconductors crystallizing in the cubic  $\text{CaF}_2$  structure. The high-temperature magnetic susceptibilities are fully compatible with the  $^3\text{H}_4$  ( $5f^2$ ) and  $^4\text{I}_{9/2}$  ( $5f^3$ ) Hund's rule ground states for  $\text{U}^{4+}$  and  $\text{Np}^{4+}$ . The presence of

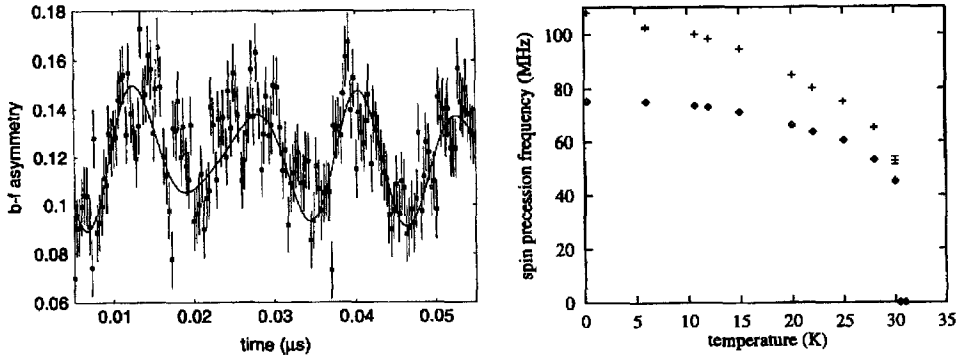


Fig. 87. ZF  $\mu$ SR spectrum of  $\text{UO}_2$  at 6.2 K (left) and temperature dependence of the spontaneous spin precession frequencies (right). From Kopmann et al. (1998).

a  $\text{Np}^{4+}$  ion in  $\text{NpO}_2$  is safely established by the Mössbauer isomer shift (Dunlap and Kalvius 1985) even at low temperatures, which rules out any discussion in terms of a non-Kramers  $\text{Np}^{3+}$  ion (Erdős et al. 1980).

In  $\text{UO}_2$  a first-order transition at 30.8 K is well-established as the Néel temperature of a  $3k$ -type I antiferromagnet with  $1.74\mu_B$  ordered moment (Burlet et al. 1986, Gianozzi and Erdős 1987).  $\mu$ SR spectroscopy has been carried out by Kopmann et al. (1998). A typical ZF- $\mu$ SR spectrum for polycrystalline antiferromagnetic  $\text{UO}_2$  is depicted in fig. 87. It consists of an oscillating and a non-oscillating portion, the latter being too intense for a “1/3 signal” only. The oscillating portion in turn consists of at least two signals with different frequencies, whose temperature dependence is also shown in fig. 87. The signal having the lower frequency is dominant. The various signals most likely arise from different muon sites and not from inhomogeneous magnetism (i.e., para- and antiferromagnetic regions) in  $\text{UO}_2$ . A detailed study of possible muon sites in the CaF structure together with the  $\mu$ SR response for those sites assuming the above mentioned spin arrangement has yet to be performed. Clearly visible in fig. 87 (right) is the sudden drop of spin precession frequency at  $T_N$ , which is characteristic for a first-order transition.

In summary, the  $\mu$ SR result on  $\text{UO}_2$  does not contain any information that would be incompatible with its known magnetic data. The study of  $\text{UO}_2$  was carried out primarily to have a data basis for comparison with the more interesting case of  $\text{NpO}_2$ .

Susceptibility, resistivity and specific heat measurements (see Amoretti et al. 1992), as well as Mössbauer spectroscopy (Friedt et al. 1985) on  $\text{NpO}_2$  establish a transition at 25 K. Its exact nature has, however, been enigmatic, especially since neither neutron (Caciuffo et al. 1987) nor Mössbauer data (see Dunlap and Kalvius 1985) could prove the existence of an ordered magnetic state. In fact, the Mössbauer spectra for  $T < 25$  K are not incompatible with the presence of magnetic order (Dunlap et al. 1968) but if so, require that the moment on the Np ion be extremely small ( $< 0.02\mu_B$ ). Friedt et al. (1985) concluded that the transition is more likely to be structural. Similarly the behavior of the

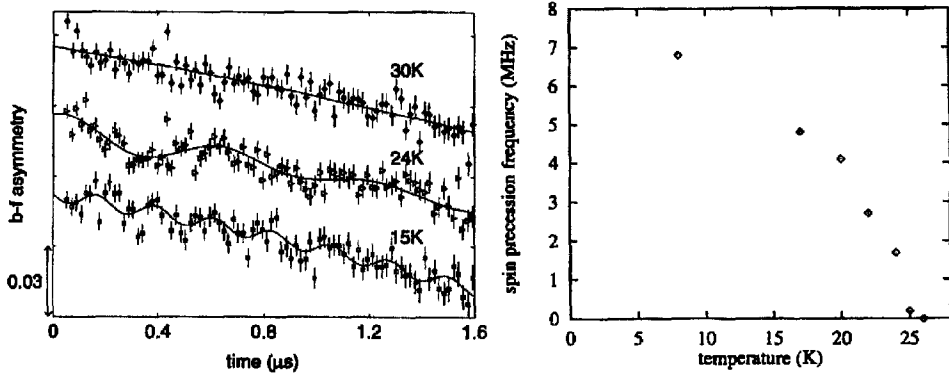


Fig. 88. Left: ZF  $\mu$ SR spectra of  $\text{NpO}_2$  above and below the 25 K transition point. (Note the difference in time scale with respect to the spectrum of  $\text{UO}_2$  in the previous figure). Right: Temperature dependence of the spin precession frequency. From Kopmann et al. (1998).

neutron inelastic cross section at low temperatures (Amoretti et al. 1992) was interpreted to result from a collective Jahn–Teller effect distortion of the oxygen sublattice.

In fig. 88 (left) ZF- $\mu$ SR spectra of  $\text{NpO}_2$  above and below the 25 K transition are shown (Kopmann et al. 1998). The appearance of an oscillating signal, in addition to a monotonically damped non-oscillating signal (as in  $\text{UO}_2$ ), is clearly visible for  $T < 25$  K. A spontaneous muon spin precession signal is a safe indicator of the presence of ordered magnetism, hence the  $\mu$ SR data prove for the first time unambiguously that the 25 K transition leads to a magnetic state, although  $\mu$ SR gives no direct information on the spin structure. One may deduce that the comparatively weak damping of the precession pattern means that a rather well defined AFM structure is present in  $\text{NpO}_2$ . For example, incommensurate spin structures usually result in a rather strong damping as does short-range magnetic order (see sect. 3.7). From the overall similarity of the magnetic  $\mu$ SR spectra in  $\text{UO}_2$  and  $\text{NpO}_2$  (though details are different) one may further draw the tentative conclusion that type I antiferromagnetic order is likely also for  $\text{NpO}_2$ . The ratio of spontaneous frequencies for  $T \rightarrow 0$  in  $\text{NpO}_2$  and  $\text{UO}_2$  should basically reflect the ratio of ordered moments on the two actinide ions. When comparing the two low-frequency components this would lead to  $\mu_{\text{Np}} \approx 0.1 \mu_{\text{B}}$  in  $\text{NpO}_2$ , which is clearly larger than the limit obtained by Mössbauer spectroscopy. The reason for this discrepancy may be differences in the details of the spin structure for  $\text{NpO}_2$ , which would mean that the here-envisaged signals for the two compounds are caused by different spin surroundings. In any case,  $\mu_{\text{Np}}$  is substantially reduced from the free ion value observed at high temperatures. CEF alone cannot account for such a reduction of ordered moment (Caciuffo et al. 1992) and the subject remains a challenge.

In fig. 88 (right) one notices that the temperature dependence of spontaneous precession frequency near the transition point is different from that of  $\text{UO}_2$ . In  $\text{NpO}_2$  we have a second-order phase transition into an (presumably) antiferromagnetic state. It must be emphasized that only  $\mu$ SR, with its extreme sensitivity to small magnetic moments, was

able to definitely establish that the transition at 25 K in  $\text{NpO}_2$  is a magnetic one. With it, a problem that had haunted the actinide community for more than three decades was finally settled. Very recently, resonant X-ray scattering was carried out on  $\text{NpO}_2$  (Mannix et al. 1999). The magnetic structure was found to be rather similar to that of  $\text{UO}_2$ , the difference being that the Np moments are oriented parallel to the magnetic wave vector and not perpendicular as is the case for the U moments. The absence of tetragonal distortion at  $T_N$  indicates a  $3k$  arrangement for  $\text{NpO}_2$  as well. The derived structure is in full keeping with the  $\mu$ SR data, but the origin of the small moment (that X-ray scattering cannot determine) remains enigmatic.

### 6.1.3. Rare-earth halides

While there have been studies of  $\mu$ SR in nonmagnetic  $\text{YF}_3$  and  $\text{LaF}_3$  (Noakes et al. 1993a) and magnetic transition metal fluorides (Noakes et al. 1993b), no magnetic rare-earth samples were involved in those studies. As for the binary oxides, when there is magnetic ordering, the transition temperatures are below 5 K.  $\text{TbF}_3$  (Joubert et al. 1987),  $\text{LiTbF}_4$  (Kötzler 1986) and  $\text{LiHoF}_4$  (W. Wu et al. 1993) are interesting for their dipole-coupled “Ising” (uniaxial) magnetic ordering.  $\text{HoF}_3$  (Jensen et al. 1995) is a singlet ground-state system that seems to achieve dipole-coupled magnetic ordering at 0.53 K. These might well be challenging systems for  $\mu$ SR studies.

The formation of muonium-like states might be a complication. This is suggested by a preliminary  $\mu$ SR study of  $\text{ErI}_3$  (Krämer et al. 1998). This has a layered form ( $\text{BiI}_3$  structure, space group R3) where neutron diffraction detected two-dimensional magnetism (two  $120^\circ$  AFM sublattices in the  $a$ - $b$  plane) below 0.3 K. No three-dimensional order was detected down to 0.018 K. The ZF  $\mu$ SR spectra between 0.03 K and 0.8 K show two exponentially relaxing signals with quite different but temperature-independent rates ( $\sim 50 \mu\text{s}^{-1}$  and  $\sim 0.02 \mu\text{s}^{-1}$ ), which were considered not to reflect the magnetic state. Additional TF data were interpreted in terms of formation of muonium-like states connected to three muon stopping sites. Many questions about this interpretation remain open, but further data would be necessary to resolve them.

### 6.2. Orthoferrites and other perovskites

This section discusses  $\mu$ SR in oxides containing both rare earths and magnetic transition metals. The combination provides opportunities for cooperation and competition between the two types of magnetic moment and their interactions, in the absence of conduction electrons (while superexchange can still act).

The structural label “perovskite” applies to an enormous number of multi-element oxides. The ideal perovskite ( $\text{CaTiO}_3$ ) structure is cubic with one formula unit per unit cell, with ions on the body center (Ca), cube corners (Ti) and face centers (O). Identification of crystal structures as distortions (tetragonal, orthorhombic, trigonal) of this has allowed extension of the class even to the wedding-cake layer structures of the high- $T_c$  superconductors (see, e.g., Phillips 1989). The properties of rare-earth perovskites (prior to the discovery of high- $T_c$ 's) are reviewed by Khattak and Wang (1979).



The rare-earth orthoferrites ( $R\text{FeO}_3$ ) have an orthorhombic perovskite structure. The iron moments interact strongly and enter ferrimagnetic states at temperatures above 600 K, the spontaneous moment being due to slight canting of the iron spins out of a planar-AFM structure. The rare-earth lattice is little affected by this, becoming magnetically ordered at only a few Kelvin. At intermediate temperatures, the ferrimagnetic structure may go through a reorientation transition, depending on the rare earth involved, a result of the steadily changing ionic radius across the R series, which is reflected in the lattice parameters. The likely mechanism is the variation in the degree of covalency by the enforced change in iron–oxygen separation.

Holzschuh and collaborators (Holzschuh et al. 1983, Denison 1984, Boekema et al. 1984) observed  $\mu\text{SR}$  in a number of rare-earth orthoferrites. These, combined with  $\mu\text{SR}$  studies of  $\alpha\text{-Fe}_2\text{O}_3$  and  $\text{Cr}_2\text{O}_3$  (Ruegg et al. 1980) established the idea that muons bond to oxygen ions in solids. In  $\text{YFeO}_3$ , with only iron moments and no reorientation transition, coherent oscillation is observed in ZF at all temperatures below  $T_N$ . At low temperature, there are three distinct frequencies (35, 41 and 53 MHz), but at 150 K and then 250 K the higher frequencies disappear and their amplitude is donated to the remaining oscillation, indicating that those frequencies were generated at metastable muon sites with energy barriers overcome at those temperatures. The low-frequency site is thus the stable one. Its frequency evolves smoothly and approximately the same way with temperature as the hyperfine field at the  $^{57}\text{Fe}$  nucleus measured by the Mössbauer effect in this material (Eibschütz et al. 1967). In  $\text{SmFeO}_3$ , with a spin reorientation around 480 K, a frequency lower than for  $R=\text{Y}$  was observed above 500 K, *no* signal was seen between 300 and 500 K, and a single frequency near 100 MHz was seen below 300 K. In  $\text{DyFeO}_3$  and  $\text{HoFeO}_3$ , with reorientations at  $\sim 30$  and  $\sim 50$  K, signals similar to  $\text{YFeO}_3$  from room-temperature down disappeared at 150 K and 110 K, respectively. In  $\text{ErFeO}_3$ , instead of disappearing at the reorientation ( $\sim 90$  K), two higher frequencies ( $\sim 70$  and  $\sim 105$  MHz) appear below 80 K. Dramatic increase in the relaxation rates of the signal above 350 K in those samples that were measured above room temperature indicate the onset of muon diffusion in that range. It appears to be the combination of a reorientation transition and muon diffusion that causes the wide temperature range of missing signal when  $R=\text{Sm}$ . Holzschuh et al. (1983) also observed the changes in frequencies with applied fields in single crystals. Their analysis achieved reasonable agreement with the data assuming muon bonding to oxygen ions and dipole magnetic couplings. Boekema et al. (1984) then argued that small remaining discrepancies are due to superexchange coupling to the muon: that is, a small polarized electron density at the muon site.

With the discovery of high- $T_c$  superconductivity in perovskite cuprates (discussed in sect. 7) and lack of understanding of the mechanism (which persists to this day), there arose research interest in other perovskite materials, whose behavior might provide clues to the mechanism the cuprates did not reveal directly. It was quickly established that in the first two classes of high- $T_c$  superconductor,  $\text{La}_{2-x}\text{Sr}_x\text{CuO}_4$  and  $\text{RBa}_2\text{Cu}_3\text{O}_{6+\delta}$ , adjustment of the off-stoichiometry parameter ( $x$  or  $\delta$ ) toward zero eventually shut off not just superconductivity, but all conductivity, in a metal–insulator transition, and once a gap opened, the materials became copper-moment antiferromagnets. Theorists began

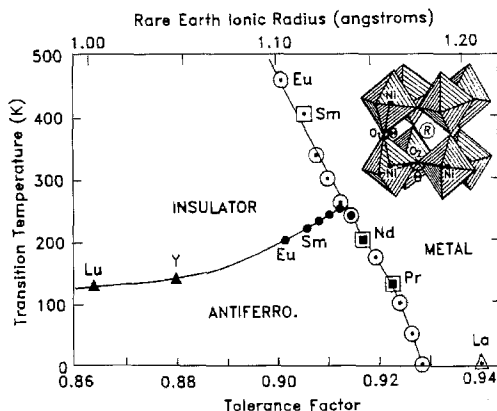


Fig. 89. Magnetic (as determined by μSR) and conducting phase diagram of RNiO<sub>3</sub> compounds as a function of rare-earth ionic radius. From Torrance et al. (1992).

to offer ideas for copper-moment magnetic-coupling superconductivity mechanisms, as alternates to the BCS mechanism. μSR has been used extensively to study the magnetism of those insulating cuprates, and that work is discussed in sect. 7.

The RNiO<sub>3</sub> materials exhibit magnetic behavior somewhat analogous to the cuprate materials, but no superconductivity. While YNiO<sub>3</sub> and LuNiO<sub>3</sub> are (orthorhombic perovskite) insulators with antiferromagnetic ordering above 100 K (Demazeau et al. 1971), LaNiO<sub>3</sub> is a (trigonal perovskite) conductor with no magnetic ordering (but also no superconductivity) to low temperature (Goodenough and Raccah 1965). Torrance et al. (1992) used μSR to establish magnetic ordering temperatures for R = Pr, Nd, Sm, and Eu, and the magnetic part of the rare-earth ion-size phase diagram shown in fig. 89. García-Muñoz et al. (1995a) related the ZF-μSR below  $T_N$  in Nd<sub>0.7</sub>La<sub>0.3</sub>NiO<sub>3</sub> to the non-trivial magnetic structure determined by neutron scattering (García-Muñoz et al. 1994).

Even closer in structure to the superconducting cuprates are the La<sub>2-x</sub>Sr<sub>x</sub>NiO<sub>4+δ</sub> nickelates. These are borderline cases for this review because to date they have only been studied without rare-earth moments: the magnetism is entirely due to the transition metal. “Stripe” magnetic order similar to that discussed for some cuprates (sect. 7.2.1) has now been observed in these materials (Tranquada et al. 1997, Tranquada 1998, Abu-Shiekah et al. 1999), making them of some general interest. μSR studies of the magnetism of these were carried out by Martinez et al. (1992), Chow et al. (1996), Jestädt et al. (1999), including a recent conference report by Klauß et al. (1999a).

### 6.3. Compounds showing giant magnetoresistance

“Giant magnetoresistance” (GMR) is the term used when in some materials the application of a static magnetic field can open and close a gap at the Fermi level, changing the resistivity of the material by orders of magnitude. The potential for commercial applications in information storage technology are obvious. Originally discovered in thin-film materials (which do not figure in this review), it was then realized that with the regular joining of metal-insulator transitions with onset of magnetism in perovskite relatives

of the high- $T_c$  superconductors, the same kind of switching can occur in some bulk perovskites. Several authors distinguish the bulk effect as “colossal magnetoresistance” (CMR, see Tokura and Tomioka 1999). Some of the most popular of these materials are  $\text{La}_{1-x}\text{Ca}_x\text{MnO}_3$  (for  $\mu\text{SR}$  on these see Heffner et al. 1996, 1997a) and  $\text{La}_{1-x}\text{Sr}_x\text{MnO}_3$  (see e.g., Louca et al. 1997).  $(\text{La,Ca})\text{MnO}_3$  is insulating when paramagnetic, and for some compositions, conducting when ferromagnetic (Ramirez et al. 1996). The tendency of perovskites to change crystal structure at such transitions in this material seems to result in “magnetic polaron” distortions (Hennion et al. 1997). Thus, there is a complicated “interplay between spin, charge and orbital degrees of freedom” (Tokura 1997).

It was only a matter of time before someone decided to substitute magnetic rare-earth ions on the lanthanum sites (e.g., Tomioka et al. 1997, Guo et al. 1997), but it is not immediately clear how useful it is to do so. The introduction of a new type of magnetic moment is as likely to introduce new effects unrelated to the GMR process as it is to provide new information on the GMR. One group (Blasco et al. 1996) has chosen to concentrate on terbium as a substituent, and have used  $\mu\text{SR}$  to help determine the magnetic phase diagram of  $(\text{La,Tb})_{2/3}\text{Ca}_{1/3}\text{MnO}_3$  (de Teresa et al. 1997).

Recently, a conference report on a  $\mu\text{SR}$  study of critical spin dynamics at the ferromagnetic ordering in the CMR material  $\text{Nd}_{1-x}\text{Sr}_x\text{MnO}_3$  with  $x = 0.5$  and  $0.55$  has appeared (Krishnamurthy et al. 2000b). Single crystals were used. This material exhibits a para- to ferromagnetic transition at  $T_C \sim 250$  K and a ferro- to antiferromagnetic transition at  $T_N = 158$  K. The paper discusses only the ZF spectra which are marred by multiple signal content. In the paramagnetic regime, starting from room temperature down, two relaxing components are distinguished, one shows exponential (amplitude  $A_1$  and rate  $\lambda_1$ ), the other root-exponential relaxation ( $A_2, \lambda_2$ ). The former is assigned to muons stopping in standard paramagnetic surroundings, the latter to muons coming to rest in spin-glass-like clusters with different volumes and spin correlation times. The intensity of the signal  $A_2$  rises on approach to  $T_C$  with the signal  $A_1$  decreasing accordingly, keeping the total signal strength ( $A_{\text{para}} = 0.22$ ) constant. About 5 K below  $T_C$ , the whole (but already slightly reduced) signal intensity is due to  $A_2$ , and  $A_1$  has vanished. On further lowering the temperature towards  $T_N$ , a fast relaxing component ( $A_3, \lambda_3$ ) emerges rapidly, reaching  $A_3 = 0.3 A_{\text{para}}$  and staying there. Signal  $A_2$  decreases in the same temperature range to the (temperature-independent) value  $A_2 = 0.1 A_{\text{para}}$ . The signal  $A_3$  is assigned to ordering of spin glass clusters. No spin precession signal is seen for  $T \leq T_C$ . The missing amplitude ( $\sim 0.6 A_{\text{para}}$ ) is not discussed. Over the whole paramagnetic range  $\lambda_1 = \lambda_2$  is found (a peculiar result, but not discussed). Both rates rise in the usual fashion on approaching  $T_C$ . Below  $T_C$  the rate  $\lambda_2$  sharply drops (signal  $A_1$  has vanished) and  $\lambda_3$  rises. No data is presented for  $T \leq T_N$ . The authors analyse  $\lambda_1$  just above  $T_C$  in terms of critical behavior. With the help of mode coupling formalism as used by Yaouanc et al. (1993b) they find a crossover from exchange-dominated to dipolar-dominated critical regimes around  $1.07 T_C$ . In the former regime the critical exponent of muon spin relaxation rate is  $w = 0.61$ , in the latter a dynamic critical exponent of  $z = 2.0$  was derived which is typical for a 3d dipolar magnet. The extraction of critical behavior appears to be the central issue of the work.

The reviewers would like to add some comments. The behavior on approach to  $T_C$  is indicative for inhomogenous spin freezing. The Curie point is only clearly visible in a change of relaxation rate  $\lambda_2$  which is, however, not sensing the free paramagnetic fraction. It is conceivable that the spin frozen state converts to long-range ordered magnetism slightly below  $T_C$ . One could take  $A_3$  as the indicator for long-range order, especially since  $\lambda_3$  shows a temperature dependence typical for the order parameter of a second-order phase transition.  $A_3$  would then simply be the tail of the full signal of the ordered state, the missing fraction having vanished in the initial spectrometer dead time (a pulsed beam was used!). This state is then governed by a very broad distribution of quasi-static local field which makes it unlikely that a simple FM spin structure has been formed. A small fraction of spin-glass-type order remains present ( $A_2 \neq 0$ ). Whether one can get reliable information on critical behavior with a “messy” phase transition is questionable. In any case, the authors do not relate their findings to the GMR properties of the material. One might point out that a connection between heterogenous cluster type magnetism and GMR is established, though in general in diluted magnetic systems (see, for example, Idzikowski et al. 1999).

Grynszpan et al. (1999) observed complicated  $\mu$ SR behavior in a  $\text{Pr}_{1/2}\text{Sr}_{1/2}\text{MnO}_3$  sample. A  $\mu$ SR study on the spin dynamics in  $\text{Pr}_{1-x}\text{Ca}_x\text{MnO}_3$  ( $x = 1/3$  and  $1/2$ ) was reported recently (Lobet et al. 2000). Again, rather complex relaxational behavior was found. Ferromagnetic correlations are dominating the temporal evolution of relaxation rate even well above  $T_N = 150$  K in the  $x = 1/3$  material. Finally,  $\mu$ SR work on another mixed manganite [ $(\text{Nd}_{0.125}\text{Sm}_{0.875})_{0.5}\text{Sr}_{0.5}\text{MnO}_3$ ] has also been briefly mentioned recently (Higemoto et al. 1999a). Systematically enhanced relaxation times above  $T_C \approx 135$  K are considered to indicate antiferromagnetic instability in the paramagnetic phase. In the metastable metallic ferromagnetic phase two magnetically inequivalent muon sites were found. The absence of temperature dependence of  $\mu$ SR response in this region together with the sudden disappearance of the two-site signal indicates the first-order nature of the phase transition.

A  $\mu$ SR study of a quite different GMR system has been carried out by Battle et al. (1996a,b, 1997). These authors have shown that  $\text{Sr}_{2-x}\text{Nd}_{1+x}\text{Mn}_2\text{O}_7$  provides counterexamples to much of the folklore that has emerged from studies of the  $(\text{R,Ca/Sr})\text{MnO}_3$  perovskites. They identify  $\text{Sr}_{2-x}\text{R}_{1+x}\text{Mn}_2\text{O}_7$  as “Ruddlesden–Popper  $n = 2$ ” (RP  $n = 2$ ) phases, where the  $(\text{R,Ca/Sr})\text{MnO}_3$  are  $n = \infty$ . While the RP  $n = 2$  phase forms for wide variety of rare earths, the GMR effect is seen only for the largest ones and is strongest for La and Nd. The La member exhibits GMR near its ferromagnetic transition at 126 K, and so conforms to the folklore.  $\text{Sr}_{2-x}\text{Nd}_{1+x}\text{Mn}_2\text{O}_7$ , however, shows GMR over a wide temperature range below 100 K, but in its antiferromagnetic state ( $T_N = 137$  K). Further, while its resistivity drops by orders of magnitude in field, it continues to show temperature dependence indicative of a gap. Thus, there does not appear to be a true metal–insulator transition.

Looked at in more detail, these phases have their own complications. The GMR Nd and Pr members have only been produced as two-phase samples, the phases differing only slightly in lattice constants, but one phase showing no long-range magnetic ordering. For

small rare earths (Gd–Er and Y), there is clearer preferential site occupation, so there is a clearer stoichiometric  $x = 0$  phase, but there is no long-range magnetic ordering and no GMR. There is spin-glass-like behavior below freezing temperatures that range from 13 K to 27 K (there is still some site disorder). In the Nd samples, the Nd moments only participate in the magnetic ordering below a transition at 28 K (Battle et al. 1996b), but  $\text{Sr}_2\text{YMn}_2\text{O}_7$  with no rare-earth moments, also shows spin-glass freezing at 20 K. The Sm and Eu members show behavior intermediate between these extremes. The Eu member has in fact been prepared in both 2-phase form, with antiferromagnetic ordering near 150 K, and single-phase form with only spin-glass freezing at 19 K.

ZF- $\mu$ SR in an array of single crystals of  $\text{Sr}_{1.6}\text{La}_{1.4}\text{Mn}_2\text{O}_7$  was studied by Heffner et al. (1998). Paramagnetic exponential relaxation, with rate increasing as temperature decreased, was observed down to near the Curie transition at  $\sim 80$  K in this sample, and spontaneous oscillation ( $>20$  MHz) was observed below 75 K. This seems like fairly ordinary magnetic ordering behavior. Somewhat more complicated behavior was seen in the details (amplitudes, relaxation shapes) at temperatures near a possible second magnetic transition at 60 K and below. ZF- $\mu$ SR in  $\text{Sr}_2\text{RMn}_2\text{O}_7$  phases with almost all the magnetic rare earths have now been reported by Bewley et al. (1999). In contrast to the La member, no spontaneous oscillations were seen. Instead, initial asymmetry decreased over a fairly wide temperature range, beginning near the nominal Néel temperature, for  $R = \text{Nd}, \text{Pr}$  and Sm. This suggests an inhomogeneous ordering process, where the ordered volume at the Néel temperature is small, but the ordered field at the muon is so large (or large and disordered, generating fast relaxation) that the frequency is lost in the initial deadtime, even in a targeted search for spontaneous oscillations at PSI. The ordered volume then grows slowly as temperature is reduced below  $T_N$ . Meanwhile, in the paramagnetic state, the ZF relaxation is exponential, or nearly so, with weak temperature dependence for Pr and Nd, and more typical behavior of rate rising as the transition is approached, for Sm. For Gd–Ho, the paramagnetic relaxation rates are large enough to cause loss of initial asymmetry in this Rutherford ISIS data well above the nominal spin-glass temperatures. The authors reasonably attribute this to the large rare-earth moments coupling to the muon. With asymmetry lost in all samples at low temperatures, however, there is little that can be said definitively about the ordered/frozen states from the  $\mu$ SR data.

Clearly, the study of CMR (GMR) systems containing rare earths has started and more work is to be expected in the near future. It has been demonstrated that  $\mu$ SR can provide important information on local aspects of the magnetic properties of these substances and in particular on the nature of phase transitions. The repeated appearance of spin freezing is noteworthy. Spin dynamical properties are another field of definite interest which is open to  $\mu$ SR. It is generally believed that the transport properties of the manganese compounds are coupled to lattice and Mn spin dynamical effects. As of yet, it is not clear how well the findings of  $\mu$ SR relate to the phenomenon of CMR (or GMR).

#### 6.4. *Hard magnetic materials*

While the vast majority of permanent magnets used in the world are iron alloys with no rare-earth content, a few rare-earth–transition-metal compounds provide better

performance (magnetization and coercivity) near room temperature, albeit at much higher cost.  $\text{SmCo}_5$  permanent magnets have been commercially available for many years. In the mid-1980s, Japanese industrial researchers (e.g., Sagawa et al. 1984) found even better permanent-magnet behavior for a combination of neodymium, iron and boron soon determined to be  $\text{Nd}_2\text{Fe}_{14}\text{B}$  (Herbst et al. 1984, Givord et al. 1984). A disadvantage is the lower magnetic transition temperature (compared to  $\text{SmCo}_5$  or iron alloys), which limits use above room temperature.

The  $\text{R}_2\text{Fe}_{14}\text{B}$  compounds crystallize in a rather complex tetragonal structure. It consists basically of various layers stacked along the  $c$ -axis. R and B atoms occupy the same layers, which are separated by three Fe-containing layers. The compounds exhibit FM for the light R ions and AFM for the heavy ones. Only the Nd material is of commercial interest. The magnetic structures are described by Onodera et al. (1987).

Yaouanc et al. (1987) observed a single spontaneous muon precession frequency in  $\text{Nd}_2\text{Fe}_{14}\text{B}$  and  $\text{Pr}_2\text{Fe}_{14}\text{B}$ , which was somewhat surprising considering the complexity of the crystal and magnetic structure. A more complete survey of  $\mu$ SR in a wide variety of  $\text{R}_2\text{Fe}_{14}\text{B}$ 's (Niedermayer et al. 1990) proposed as the muon stopping site the site occupied by hydrogen in hydrogenated  $\text{R}_2\text{Fe}_{14}\text{B}$  compounds. According to Mössbauer data (Ferreira et al. 1985), hydrogen in low concentrations is located at the tetrahedral site with two R and two Fe nearest neighbors (labeled the 4e site). There are four crystallographic equivalent 4e sites in the unit cell. They are magnetically equivalent only when the magnetization is directed parallel to the  $c$ -axis. Under these conditions, a single spontaneous precession frequency is possible.

Many of the compounds exhibit a spin reorientation transition at which the magnetization turns away from the  $c$ -axis. The amazing result of the systematic  $\mu$ SR studies is that the temperature variation of the spontaneous spin precession frequency is always proportional to the  $c$ -axis component, rather than to the total magnetization. Obviously, the muons sense only the  $c$ -component of the interstitial field. This can be understood if one assumes that each muon hops rapidly between the different 4e sites (which are now magnetically inequivalent because the magnetization no longer points along the  $c$ -axis). In this dynamical averaging process the  $c$ -component is stationary. The question of why one observes a diffusing muon at low temperatures ( $\sim 15$  K) in a material with low crystal symmetry remains unanswered. In addition, as pointed out by Asch (1990), the fact that (especially in  $\text{Ho}_2\text{Fe}_{14}\text{B}$ ) a sharp rise in muon spin depolarization rate is seen when spin reorientation sets in is difficult to reconcile with a mobile muon. It has been suggested by Asch et al. (1994), that rather than a mobile muon, one has slow propagative motions within the spin system. Such types of motion appear to exist in  $3k$  magnetic structures such as antiferromagnetic USb (see sect 5.2.1). Only  $\mu$ SR with its unique sensitivity at the low-frequency, zero-energy transfer system can detect such motions, if they exist.

A linear relation between the field  $B_\mu$  at the muon site, corrected for the (calculated) Lorentz field  $B_L$  and the magnitude of the  $c$ -component of the R magnetic moment could be established for the full series (fig. 90) of  $\text{R}_2\text{Fe}_{14}\text{B}$  compounds. Large corrections are quite apparent for the cases (Er, Tm) where the moments are oriented perpendicular to the  $c$ -axis.

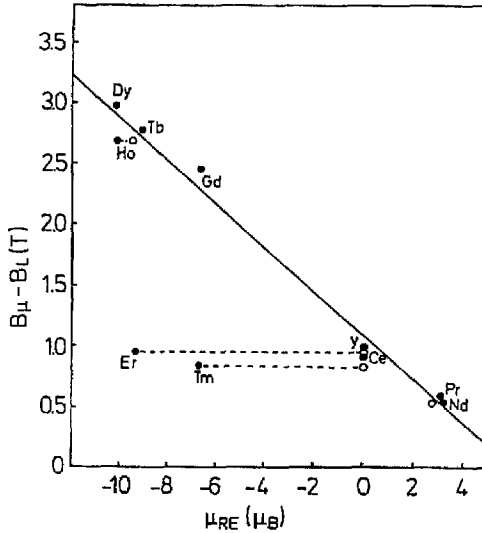


Fig. 90. Local magnetic field at the muon site (corrected for the Lorentz field) as a function of the magnetic moment of the R ion  $R_2Fe_{14}B$  compounds. Open circles represent the  $c$ -axis component of those moments. From Niedermayer et al. (1990).

Research on hard magnetic materials still continues actively today. Most of them are good conductors (e.g.,  $SmCo_5$ ). With regard to the non-conducting members (such as the Nd-Fe-B system)  $\mu$ SR can at best only contribute to the details of their magnetic phase diagrams. These, however, are now well-known and understood. In consequence, no further  $\mu$ SR studies on this class of materials have emerged recently.

## 7. Superconductors

Since 1987, two classes of superconductors are distinguished: the high- $T_c$  ones, involving copper-oxygen planes and transition temperatures up to 123 K, and the ordinary ones, with transition temperatures generally below 24 K. As stated here, the distinction leaves a few borderline cases ( $(Ba,Pb)BiO_3$ , superconducting fullerenes), but none of them involve  $f$ -electron ions, so this review can ignore them. The heavy-fermion superconductors may well be an independent class: we mention cases in sect. 9, mainly when coexistence with magnetism is found. The supercurrent carrier in an ordinary superconductor is a "Cooper pair" of conduction electrons (or holes) in an  $s$ -wave bound state of the phonon-mediated BCS interaction (see, for example, Parks 1969). The supercurrent carrier in a high- $T_c$  superconductor does appear to be a pair of the normal-state charge carriers of the material, but the pairing symmetry is still hotly debated, and no mechanism so far proposed has the endorsement of more than a small fraction of the experts in the field (Norman 1993). The literature is enormous, and book-length reviews abound (see e.g., Phillips 1989, Sheahan 1994).

We have no intention of reviewing even all papers where  $\mu$ SR is used and a rare earth appears somewhere in the high- $T_c$ 's stated composition. Since this is primarily a review of  $f$ -electron magnetism in materials, we limit our discussion of  $\mu$ SR in superconductors (and

related copper-oxide materials) to cases where unpaired f electrons are present, that is, where there is f-electron magnetism in the material. Note that this is more stringent than a limitation to “magnetic copper oxides”, because when a planar copper-oxide material has no superconductivity, there is usually copper-moment antiferromagnetism instead, independent of any f moments. Note also that the high- $T_c$  cuprates all have perovskite-type crystal structures. This review discusses copper-free perovskites in sect. 6.2.

### 7.1. Non-cuprate f-electron superconductors

Before high- $T_c$  superconductors were discovered in 1986, “magnetic superconductors” were a popular field of research. These were discovered in the course of years of study of the interaction between superconductivity, which in the Meissner state is perfectly diamagnetic, and magnetic moments, which are inherently paramagnetic. It was found in the 1960s and 70s that in elements, binary compounds, and alloys of the same, the introduction of magnetic ions rapidly reduced superconducting  $T_c$ 's, reducing them to zero before the magnetic ions were present in enough density to generate any long-range magnetic ordering. There was speculation that a spin-glass state might coexist with superconductivity in some systems, at temperatures below 1 K (Lemberger 1985) but the possible cases have never been well studied experimentally. Then, in ternary compounds that came to be called magnetic superconductors, new and interesting behaviors were discovered (for a review, see Fischer and Maple 1982). The most popular of these materials were the  $RRh_4B_4$  series and the  $RMo_6X_8$  ( $X=S$  or  $Se$ ) “Chevrel phases”. These provided the first cases of “coexistent antiferromagnetic superconductors” now considered almost unsurprising in the  $R-Ba-Cu-O$  system, and more spectacularly, the “re-entrant superconductors”  $ErRh_4B_4$  and  $HoMo_6S_8$ , in which superconductivity exists in a temperature range bounded away from absolute zero. In these, as temperature is lowered in the superconducting state to the “re-entrance” temperature,  $T_{c2}$ , the superconductivity is destroyed and replaced by (resistive) ferromagnetism, in a first-order transition.  $SnMo_6S_8$  and  $PbMo_6S_8$  offered the highest known  $H_{c2}$ 's at the time (they are now dwarfed by the best cuprate  $H_{c2}$ 's), even though the superconducting transitions for all of the magnetic superconductors were below those of a number of the A15 phases (such as  $Nb_3Sn$ , 18 K).

Magnetic superconductors became fashionable in the early 1980s, just as surface muon beams at pion factories were making it possible to study samples of a couple of grams mass (making such new and difficult-to-fabricate materials accessible). These were also the early days of ZF  $\mu$ SR (so we learned about it as we worked) and *before* the time of readily available LF  $\mu$ SR in even the kG (0.1 T) regime (so in some experiments LF simply was not done). No one tried to measure the superconducting penetration depths of these materials with  $\mu$ SR until after such measurements were demonstrated on the high- $T_c$ 's. Then, researchers went back and measured penetration depths in  $SnMo_6S_8$  and  $PbMo_6S_8$  (Birrer et al. 1990, 1993). The more complicated  $(Eu,Sn)Mo_6(S,Se)_8$  system has a unique magnetic-field-induced superconducting range in its  $(B, T)$  phase diagram completely separate from the usual low-field superconducting range (Meul et al. 1984). In it, the muon spin relaxation was completely dominated by the  $Eu^{2+}$  moments, and



penetration depth could not be measured (Birrer et al. 1988, 1989a). Since the penetration depth is a property of the superconducting state, not of f-electron magnetism, we will not discuss it in detail here. See also the recent conference report by Gygax et al. (2000a).

In the  $RRh_4B_4$  system,  $\mu$ SR measurements concentrated on the magnetic moment behavior. Crystalline electric fields (sect. 5.1.1) strongly influence the behavior of the various magnetic rare-earth ions in this structure (Noakes and Shenoy 1982, Dunlap et al. 1984), and indications of this were seen in the  $\mu$ SR.  $Gd^{3+}$  is an s-state ion unaffected by a CEF:  $\mu$ SR in  $GdRh_4B_4$  (MacLaughlin et al. 1983) exhibited almost temperature-independent ZF relaxation (at  $\sim 3 \mu s^{-1}$ , ten times the TF rate in nonmagnetic  $LuRh_4B_4$  (Boekema et al. 1982)) down to the ferromagnetic transition ( $\sim 6$  K), below which the signal suddenly was reduced in amplitude.  $Ho^{3+}$  in this structure experiences CEF splitting of its magnetic levels to temperatures ( $\sim 150$  K) much greater than  $HoRh_4B_4$ 's ferromagnetic  $T_C$  ( $\sim 7$  K). As a result it has substantial (essentially) uniaxial single-ion magnetic anisotropy. The ZF muon spin relaxation rate in  $HoRh_4B_4$  exceeds that in  $GdRh_4B_4$  for temperatures below about 150 K, rising to rates  $> 40 \mu s^{-1}$  (beyond the resolution of the apparatus) for temperatures below  $\sim 30$  K, leaving only a reduced-amplitude "tail" to be measured below that (Boekema et al. 1982). Since the moments ( $7\mu_B$  and  $10\mu_B$  "free ion") and ordering temperatures are comparable, the difference is due to the reduction in magnetic fluctuation rates by CEF splitting.  $Ho_{0.7}Lu_{0.3}Rh_4B_4$  is a ferromagnetic re-entrant superconductor like  $ErRh_4B_4$ . For it, again, only a reduced-amplitude signal can be resolved in the temperature range of the transitions, although its temperature dependence does show structure at both the superconducting  $T_c$  and at re-entrance  $T_C$  (Heffner et al. 1984). Even as little as 7%Ho in  $LuRh_4B_4$  can result in relaxation too fast to resolve with standard  $\mu$ SR apparatus (Heffner et al. 1985). In  $ErRh_4B_4$ , the CEF splittings again range up to  $\sim 150$  K, while the magnetic transition (re-entrance) is at 0.9 K. Observed ZF  $\mu$ SR was again temperature dependent up to 300 K (at least), and rates became too large (and amplitude was lost) below 30 K (Noakes et al. 1985). One lesson of this is: stable lanthanide magnetic moments can be *too large* for  $\mu$ SR in some cases.  $SmRh_4B_4$  is a coexistent antiferromagnetic superconductor. The  $Sm^{3+}$  moment is smaller ( $0.72\mu_B$ ) and the CEF splitting range is about 200 K. With the smaller moment generating smaller muon-site fields, the moment fluctuations are fast enough to completely decouple from the muon at 200 K and above, resulting in ZF (boron) nuclear Kubo–Toyabe relaxation similar to that in nonmagnetic  $YRh_4B_4$  (Noakes et al. 1987). Then, as temperature is lowered in  $SmRh_4B_4$ , coupling between the samarium electronic moments and the muon (and the boron nuclei) starts as the fluctuations slow down, eventually resulting in simple exponential decay below 10 K (see fig. 91). While the temperature dependence from 4 K up can be treated as due to CEF level splittings, the relaxation rate below 4 K increases beyond that of the CEF modeling until the relaxation becomes the sum of two exponentials sharply at  $T_N$  (0.9 K, measured several years before the first dilution refrigerator with windows suitable for  $\mu$ SR (Huang et al. 1984) and continues so below. There is no visible effect at superconducting  $T_c$ , and the rate does not increase rapidly enough as  $T \rightarrow T_N^+$  to be convincingly diverging, but some precursor behavior is clearly going on above the magnetic ordering.

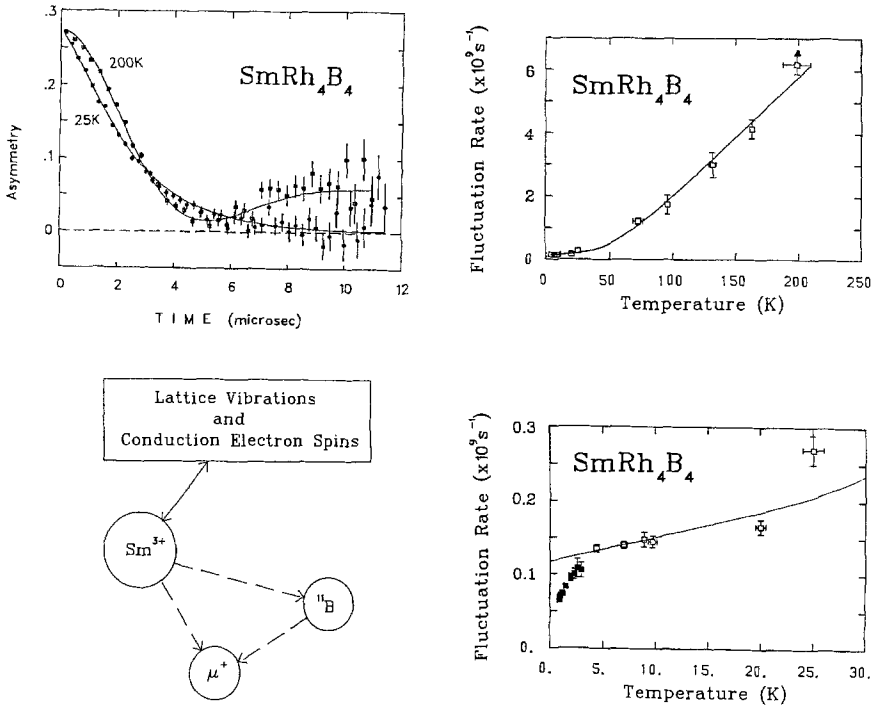


Fig. 91. ZF  $\mu$ SR spectra in  $\text{SmRh}_4\text{B}_4$ , schematic of the magnetic interaction to explain it, and the deduced local field fluctuation rate as a function of temperature with the solid line indicating the fit to a CEF model. From Noakes et al. (1987).

$\text{Y}_9\text{Co}_7$  (Ansaldò et al. 1985) is a magnetic superconductor, but a borderline case for this review, because the magnetism is likely d-band. Its unusual behavior may be due to a bizarre crystal structure (Yvon et al. 1983).

A spark of interest in non-oxide magnetic superconductors has recently been rekindled with the discovery of the quaternary “borocarbide” superconductors, with generic formula  $\text{FTr}_2\text{B}_2\text{C}$ , where  $\text{F}=\text{R}$ , Th, or U, and Tr is a transition metal (R–Pd: Adroja et al. 1994, Th–Pd: Zandbergen et al. 1994, R–Pt: Cava et al. 1994, (Th/U)–Tr: Takabatake et al. 1994).  $\mu$ SR has concentrated on the  $\text{RNi}_2\text{B}_2\text{C}$  system (Eisaki et al. 1994, but see also Suellow et al. 1994). Penetration depth has been measured in the nonmagnetic superconductor  $\text{YNi}_2\text{B}_2\text{C}$  ( $T_c=15\text{ K}$ , Cywinski et al. 1994a, S.L. Lee et al. 1994). In  $\text{HoNi}_2\text{B}_2\text{C}$ , superconductivity sets in at 7.5–8 K, but resistivity returns in a narrow range just below 5 K, reverting to superconductivity below that. Neutron scattering measurements see incommensurate spiral magnetic ordering below a  $T_{N1}$  of 6 K (single crystal) or 8 K (polycrystal), which becomes commensurate at  $T_{N2}$  in the re-entrant range. A  $\mu$ SR study of a single crystal of  $\text{HoNi}_2\text{B}_2\text{C}$  (Le et al. 1996) reports that ZF  $\mu$ SR displays a coherent oscillation below 5 K (consistent with commensurate AFM) and exhibits Bessel oscillation (eq. 53) between 5 K and 6 K (this is, however, more consistent

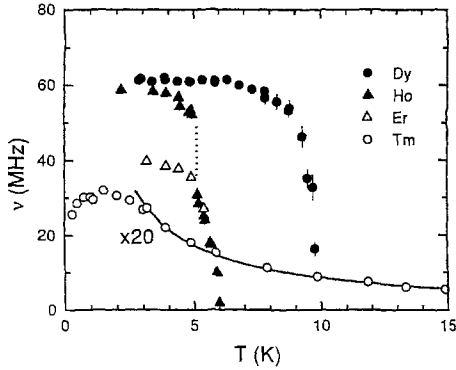


Fig. 92. Temperature dependence of ZF muon precession frequency in  $\text{RNi}_2\text{B}_2\text{C}$  for the rare earths indicated. The thulium frequencies have been multiplied by a factor of 20 to make them visible on the same scale. From Le et al. (1997).

with an amplitude-modulated ISDW than the spiral order reported by neutron scattering). Recent work has extended to  $\text{DyNi}_2\text{B}_2\text{C}$  (Le et al. 1997), as shown in fig. 92, and to more complicated compositions (Cristofolini et al. 1997).

$\text{ErNi}_2\text{B}_2\text{C}$  and  $\text{TmNi}_2\text{B}_2\text{C}$  are coexistent antiferromagnets with  $T_c \approx 10\text{--}11\text{ K}$  and lower Néel temperatures ( $\text{Er} \sim 5\text{ K}$ ,  $\text{Tm} \sim 1.5\text{ K}$ ). One brief paper (Le et al. 1995) reports a coherent oscillation in  $\text{ErNi}_2\text{B}_2\text{C}$  below 5 K, but in  $\text{TmNi}_2\text{B}_2\text{C}$  it (and another publication, Cooke et al. 1995) sees a very low frequency oscillation with relaxation rate  $\nu \sim 1/T$  up to at least 20 K. This looks qualitatively similar to the ZF  $\mu\text{SR}$  observed in singlet ground state  $\text{HoBa}_2\text{Cu}_3\text{O}_7$  (sect. 5.1.2 and below), but this material shows non-singlet ground state behavior in other probes. The ordered-state moment seen by neutrons is a substantial  $3.78\mu_B$  at 1.2 K (Chang et al. 1996), which the muons seem to be ignoring in favor of something much smaller. After an extensive study of inelastic neutron scattering and bulk probes of CEF in the  $\text{RNi}_2\text{B}_2\text{C}$  system, Gasser et al. (1996) have produced a level scheme for the thulium member with a doublet ground and first excited state near 30 K (see also Cho et al. 1995). Mulders et al. (1996) discovered that the  $^{169}\text{Tm}$  Mössbauer effect in  $\text{TmNi}_2\text{B}_2\text{C}$  is also anomalous. Eventually (Mulders et al. 1998a) they established that the Mössbauer signal is sample dependent, the fully magnetic signal spreading most magnetic peaks beyond the range of measurement but characteristically broadening the central quadrupole doublet, while in some samples an additional much-weaker-Tm-moment ( $\sim 0.1\mu_B$ ) signal generates a detectable set of hyperfine-split peaks. They attribute the weakly magnetic signal to carbon-site vacancies changing the CEF of Tm ions in their immediate vicinities to produce singlet ground states, and then suggest the anomalous muon signal (which they reproduce in their high-vacancy sample) is caused by all muons trapping at the vacancies. It is a pity that  $\mu\text{SR}$  was not measured in their low-vacancy sample (perhaps it was too small). Note also that a nearest-neighbor shell of singlet-ground state thulium ions would not be enough to shield the muon from magnetic Tm ions only slightly further away. A considerable nonmagnetic volume might need to be generated around each vacancy to keep the field at the muon that low. Finite-cluster simulations might be able to test this.

TbNi<sub>2</sub>B<sub>2</sub>C is apparently non-superconducting. It enters an antiferromagnetic state at 15 K, and then below 8 K shows weak ferromagnetism (Cho et al. 1996). Sánchez et al. (1998) studied this material with ZF and LF  $\mu$ SR. In the paramagnetic state above 15 K they observed the power-exponential relaxation usually associated with concentrated spin glasses (sect. 8.2.1), with as usual, the power decreasing from near one well above the transition to near 0.5 just above  $T_N$ . In this case, however, the transition is to long-range magnetic order: a nearly square, longitudinally polarized incommensurate spin wave (Dervenagas et al. 1996). Below  $T_N$ , the  $\mu$ SR signal amplitude abruptly dropped to  $\sim 1/3$  of that in the paramagnetic state, indicating very large local fields in the ordered state. Lack of any evidence of decoupling in LF up to 0.2 T down to 8 K indicate there are still spin dynamics, but below 8 K some LF decoupling was observed, which the authors interpret as due to freezing of a Tb spin component not involved in the 15 K ordering, to create the small ferromagnetic moment that appears at 8 K. Hillier et al. (1998) see power-exponential relaxation in the paramagnetic states of both TbNi<sub>2</sub>B<sub>2</sub>C and ErNi<sub>2</sub>B<sub>2</sub>C.

The (RC)<sub>2</sub>(NiB)<sub>2</sub> materials are related to the RNi<sub>2</sub>B<sub>2</sub>C materials above, but in this case only R = Lu has shown superconductivity ( $\sim 3$  K) to date. A first conference report on  $\mu$ SR data in these compounds has been presented recently by Klauß et al. (1999d).

### 7.2. Lanthanide magnetism in cuprates

While the vast majority of published papers on  $\mu$ SR in high- $T_c$  superconductors and related materials has nothing to do with lanthanide or actinide magnetism, the small subset of papers that do study f-electron magnetism cannot be discussed in complete isolation from that majority, so a very brief outline of  $\mu$ SR in high- $T_c$ 's is given here. Throughout this section, the reader must keep in mind that these materials are extremely, amazingly anisotropic. The copper–oxygen bond networks form two-dimensional sheets between which the many and various other ions seem to function as merely spacers and adjusters of free-carrier density, to a first approximation. All of the good conduction occurs in the Cu–O sheets in the crystallographic *ab* plane: in the *c*-axis direction, normal state conductivity and superconducting current capacity are extremely poor. Mechanically, these materials are brittle ceramics, and high-quality single crystals prefer to grow as thin flat plates, when they grow to visible size at all.

The first and most popular application of  $\mu$ SR in high- $T_c$  superconductivity is in the study of the type-II flux-penetration state with TF  $\mu$ SR, where the applied transverse field in the  $\mu$ SR apparatus serves also to create the “vortex” state. This work began with demonstration that  $\mu$ SR could in fact measure the superconducting penetration depth in polycrystalline samples when no single crystals were available, leading to the discovery of systematic correlations (Uemura et al. 1991, Schneider and Keller 1992) between the penetration depth and the transition temperature for all high- $T_c$  materials (and extending to low- $T_c$  materials). As the measurements have become more precise and sophisticated, the interpretation in terms of models for (parts of) the superconducting state has become more involved and complicated (Niedermayer et al. 1993b, Bernhard et al. 1995).

When (small, flake-like) single crystals of some of the high- $T_c$ 's became available (notably YBa<sub>2</sub>Cu<sub>3</sub>O<sub>6+ $\delta$</sub>  and “Bi2212”), the emphasis in TF  $\mu$ SR shifted away from the

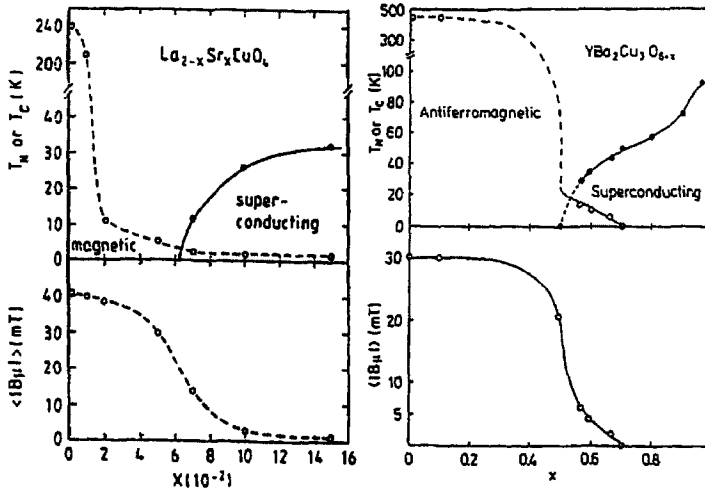


Fig. 93. Magnetic-superconducting phase diagrams as a function of hole doping for  $\text{La}_{2-x}\text{Sr}_x\text{CuO}_4$  and  $\text{YBa}_2\text{Cu}_3\text{O}_{6+x}$ . From Weidinger et al. (1989, 1990).

single penetration depth parameter toward attempts to measure the local field distribution in the vortex state in detail. These are experiments requiring high statistics whose interpretation involves debate about sample-dependent pinning strength, the systematic errors introduced by FFT's or alternate methods of deducing amplitude as a function of frequency from the data (Alves et al. 1994, Rainford and Daniell 1994), the location of the transition lines between the possible substates of the type-II flux-penetration state (vortex lattice/glass/liquid, 2D-3D "dimensional crossover", see S.L. Lee et al. 1993) in the temperature-field phase diagram, and details of the calculation of the theoretical prediction of the local field distribution (Fesenko et al. 1991, Brandt 1995).

Another area of  $\mu\text{SR}$  in cuprates has been the study of copper magnetism in "almost superconducting" materials. In particular, the first two classes of high- $T_c$  to be discovered,  $\text{La}_{2-x}\text{Sr}_x\text{CuO}_4$  and  $\text{YBa}_2\text{Cu}_3\text{O}_{6+\delta}$ , both have a continuously variable composition parameter ( $x$  and  $\delta$ , respectively) that controls the number of electrons lacking from the stoichiometric insulator state. For the compositions at which superconductivity occurs, these generate a hole conduction band, but as composition shifts to reduce the number of carriers,  $T_c$  drops until below a certain (not yet stoichiometric) composition, conductivity itself disappears, and the material becomes an antiferromagnetic insulator. With further shift toward stoichiometry, the Néel temperature rises rapidly, until the end-points,  $\text{La}_2\text{CuO}_4$  and  $\text{YBa}_2\text{Cu}_3\text{O}_6$ , have  $T_N$  well above room temperature.  $\mu\text{SR}$  contributed to the determination of alloy magnetic phase diagrams such as shown in fig. 93 and Aharony et al. (1988), Boekema et al. (1994) and Tranquada (1996). For  $\mu\text{SR}$  detection of more details within the magnetic-ordering part of these phase diagrams, see Niedermayer et al. (1998). Before 1987, the occurrence of an electronic moment on copper in materials was a rather minor topic in insulator magnetism, whereas now it is the basis for a conjectured

(and hotly debated) mechanism for the high- $T_c$  state (Norman 1993). The magnetism of the stoichiometric end points is so strong that it can be studied by many probes, and μSR has had no long term advantage in extracting information of general interest (Uemura et al. 1987, Budnick et al. 1987, but see discussions on muon site determination below). In the composition range where the Néel temperature is strongly depressed, and where there are questions of possible coexistence of the magnetism (perhaps as spin glassiness) and superconductivity (both with low transition temperatures), μSR has been useful (Harshman et al. 1988, Kitazawa et al. 1988, Kiefl et al. 1989, Weidinger et al. 1990, Watanabe et al. 1992, Kumagai et al. 1994). Of course, this is all transition-metal oxide magnetism. Cases where f-moments have been introduced are discussed below.

### 7.2.1. The “214” phases

(La,Sr)<sub>2</sub>CuO<sub>4</sub> is the material that started the high- $T_c$  field, with critical temperatures up to ~36 K (Cava et al. 1987a). As already stated, the stoichiometric end-point material La<sub>2</sub>CuO<sub>4</sub> is an antiferromagnetic insulator with  $T_N$  above room temperature. Light magnetic rare earths can be substituted for lanthanum, but as this is done, slightly different crystal structures can form. The La<sub>2</sub>CuO<sub>4</sub> structure is called T, the competing structures T' and T\*. Copper antiferromagnetic transitions remain above ~250 K for the stoichiometric R<sub>2</sub>CuO<sub>4</sub> materials, but lanthanide moment ordering typically occurs only below 10 K. This wide discrepancy in ordering temperatures indicates that each lanthanide is magnetically isolated from the Cu–O plane superexchange. The coexistence of strongly ordered Cu moments and “paramagnetic” lanthanide moments is uneasy, however, resulting in complex effects, including, in some cases, weak ferromagnetism (Thompson et al. 1989, Matsuda et al. 1990, Lynn et al. 1990, Oseroff et al. 1990, Stepanov et al. 1993).

The copper magnetism of La<sub>2</sub>CuO<sub>4</sub>, and of samples with low dopings of strontium, generates a single coherent-oscillation frequency (near 6 MHz at low temperatures) in ZF μSR in most samples, with simple temperature dependence that plausibly follows the ordered moment. This provided a fairly unambiguous local field value to use in trying to determine the muon site in the material. Work to this end has been published by experimentalists (Le et al. 1990, Hitti et al. 1990) and theorists (Saito et al. 1991, Sulaiman et al. 1994a,b), in parallel with similar efforts for oxygen-deficient Y–Ba–Cu–O described below. While there is general consensus that the muon sits about 1 Å away from an oxygen ion (and this is no surprise, the muon as a light isotope of hydrogen, being attracted to the most electronegative species, and 1 Å being the muon–oxygen bond length to be expected in general), and that there is no room for it to sit in or very near the Cu–O planes, these statements merely limit the spectrum of candidate muon sites. There is still uncertainty about the exact position.

An interesting subset of the “214” phases are the (R,Ce)<sub>2</sub>CuO<sub>4</sub> materials, where usually R = Nd or Pr. These were initially studied as the only conduction-electron high- $T_c$  superconductors (in all others, holes are the charge carriers). As usually prepared, insulating antiferromagnetic behavior is retained as cerium is added to the end-point

material out to concentrations  $\sim 15\%$ , after which there is a rapid switchover to superconductivity with  $T_c$  up to 24 K in a narrow range of Ce concentration, with no magnetic ordering. The magnetic behavior seems very sensitive to the details of the sample preparation, however (Dalichaouch et al. 1993), and a wider range of superconducting Ce concentration has recently been reported for a modified synthesis (Brinkmann et al. 1995). As with  $(\text{La,Sr})_2\text{CuO}_4$ , the copper magnetism appears to shut down when the conductivity sets in, but now there are also lanthanide moments, which remain, although they are so poorly coupled that they do not order at any appreciable temperature. This leaves large paramagnetic moments inside the superconducting material (as for R–Ba–Cu–O, below), but there appears to be no superconducting electron density at the lanthanide site, so there is almost no coupling between the two subsystems. The fact that cerium, normally associated with anomalous f-electron effects (the most anomalous being heavy-fermion superconductivity, see sect. 9) is here essential for cuprate superconductivity, was mostly ignored at first. Recently, however, specific heat measurements have begun to indicate heavy-fermion behavior (Brugger et al. 1993, Fulde et al. 1993), on which  $\mu\text{SR}$  studies have begun (Hillberg et al. 1997a, Pinkpank et al. 1997, Klaufß et al. 1999c).

Luke and collaborators (1989, 1990b) used ZF  $\mu\text{SR}$  to see magnetic reorientation transitions below  $T_N$  in pure  $\text{Nd}_2\text{CuO}_4$  and  $\text{Pr}_2\text{CuO}_4$ , and to map out the magnetic part of the  $(\text{Nd,Ce})_2\text{CuO}_4$  alloy phase diagram. The paramagnetism of the neodymium ions in superconducting  $(\text{Nd,Ce})_2\text{CuO}_4$  samples, however, caused sufficient direct muon spin relaxation to mask the effect of vortices in transverse field, preventing measurement of penetration depth (as was the case for  $(\text{Eu,Sn})\text{Mo}_6(\text{S,Se})_8$ , above). Akimitsu et al. (1994) studied  $\text{Pr}_2\text{CuO}_4$  and magnetic-ordering compositions of  $(\text{Pr,Ce})_2\text{CuO}_4$  in more detail. Rosseinsky et al. (1991) monitored the difficulty in pushing  $\text{Nd}_2\text{CuO}_4$  in the hole-doped direction by addition of strontium, with  $\mu\text{SR}$  (in the  $T'$  crystal structure). Lappas et al. (1994) studied the magnetism of  $T^*$ -structured  $\text{La}_{1.2}\text{Tb}_{0.8}\text{CuO}_4$ . For very recent work see Lappas et al. (1997), and Luke et al. (1997b).

One of the complications in the detailed properties of the cuprates is the observation in some of them of magnetic correlations in long bands or “stripes” in the Cu–O plane (see Tranquada 1996). These are apparently associated with the “1/8 effect” in 214 materials: a suppression of superconductivity and return of magnetism at substitution of 1/8 of the La ions. Most dramatically in  $\text{La}_{2-x}\text{Ba}_x\text{CuO}_4$ , it appears that the (conduction-electron) holes induced by the doping tend to congregate in stripes, suppressing the Cu magnetic moments in those stripes. At most values of  $x$ , there is considerable disorder in the positions of the stripes, and they are dynamic. At  $x \simeq 1/8$ , however, the stripes form into a static superlattice in the basal plane, allowing the stripes of magnetic Cu ions between them to establish long-range antiferromagnetic order and suppress superconductivity. In  $\text{La}_{2-x}\text{Sr}_x\text{CuO}_4$  itself, the  $x$ -range of suppression is very narrow (Kumagai et al. 1994, Borsa et al. 1995), and is thus easy to miss. In  $\text{La}_{1.6-x}\text{Nd}_{0.4}\text{Sr}_x\text{CuO}_4$ , it was found that  $T_c$  is depressed, but not to zero, so that at  $x = 1/8$ , antiferromagnetism sets in at  $\sim 30$  K and superconductivity at  $\sim 8$  K (Crawford et al. 1991, Büchner et al. 1994, Tranquada et al. 1996). These results are summarized in the (complex) phase diagrams in the introduction

of Nachumi et al. (1998), which reports  $\mu$ SR measurements on all three of these alloy series. In the Nd-doped samples they conclude that the magnetic ordering is only due to Cu moments above 5 K (the Nd moments are an unwanted complication), and that it coexists with the superconductivity. For a  $\mu$ SR study of the Nd magnetism in these alloys, see Wagener et al. (1997, 1998). Magnetic correlations at similar wavevectors to the stripe-domains are seen in neutron scattering in almost every high- $T_c$  material, although they are often interpreted as a Fermi-surface nesting effect (which would be more exciting than these charge-induced correlations, see e.g., Petit et al. 1998). Whether these magnetic correlations are part of the high- $T_c$  mechanism or, contrarily, oppose superconductivity at all times, is still debated (Aeppli et al. 1998). Recent  $\mu$ SR work was reported at the 1999 International Conference on Muon Spin Rotation (Klauss et al. 1999b, K.M. Kojima et al. 1999). See also the discussion of stripe ordering in nickelates in sect. 6.2.

Another subfield within high- $T_c$  superconductivity has been the study of the effect of zinc doping on the copper site relative to other transition metal ions. Generally, ions with magnetic moments are expected to cause stronger depression of (*s*-wave) superconductivity than nonmagnetic impurity ions, when placed in a superconducting electron or hole gas, because the magnetic moment can spin-flip scatter one member of a Cooper pair, thus breaking the (*s*-wave, total spin zero) pair. The insensitivity of the electron-carrier 214's and almost the entire "123" class of superconductors to rare-earth moments is due to space separation: the Cooper pairs move in the Cu-O planes, and have negligible density at the rare-earth site. Substitution on the copper site puts transition metal impurities in the superconducting charge-carrier gas, but strangely, in hole-doped high- $T_c$ 's, Zn causes stronger depression of  $T_c$  (and other superconducting properties) than either Co or Ni, leading to debate over whether this is evidence for *d*-wave pairing or not (there are a large number of papers on this: see, for example, Xiao et al. 1988, Alloul et al. 1991, Walstedt et al. 1993, Raffo et al. 1993, Fukuzumi et al. 1996; for  $\mu$ SR see Mendels et al. 1994, Bernhard et al. 1996, Nachumi et al. 1996). Certainly something unusual occurs when Zn is added to the hole-doped cuprates. In the electron-doped 214 superconductors, things seem more ordinary, with cobalt and nickel depressing  $T_c$  of (Nd,Ce)<sub>2</sub>CuO<sub>4</sub> much faster than zinc (Tarascon et al. 1990, Sugiyama et al. 1991). This was studied with  $\mu$ SR by Sugiyama et al. (1992).

### 7.2.2. The "123" phases

Mere months after (La,Sr)<sub>2</sub>CuO<sub>4</sub> had demonstrated the surprisingly high superconducting transition temperature of 36 K, YBa<sub>2</sub>Cu<sub>3</sub>O<sub>6+ $\delta$</sub>  broke the field wide open with  $T_c$  above 90 K (M.K. Wu et al. 1987, Cava et al. 1987b). This time the departure from stoichiometric, insulating antiferromagnetism (O<sub>6</sub>) is caused by extra oxygen (and a distortion from insulating tetragonal to conducting orthorhombic), with optimum superconducting behavior near (but not quite at) O<sub>7</sub>. At intermediate oxygen concentrations, there is a "plateau" in  $T_c$  near 60 K as shown in fig. 93, and some evidence of a slight difference in the crystal structure (see Blagojev and Wille 1993 and references cited therein) compared to the 90 K structure. Early indications of enormous  $H_{c2}$  values



accompanying the high transition temperature caused great excitement about possible revolutions in superconducting electric power transmission and high-field magnets, which was disappointed as the difficulties of brittleness, poor conduction between single-crystal grains, and weakness of flux-tube pinning emerged. These problems have persisted as  $T_c$  has been pushed higher by cuprates involving bismuth, then thallium and mercury. Today high- $T_c$  wires, and magnets made from them, are still in engineering development labs, emerging occasionally in single prototypes with interesting specifications which are nonetheless still too expensive (and/or too fragile) to be commercially viable.

Almost all lanthanides can be substituted for yttrium, with (usually) almost no effect on  $T_c$  (at fixed oxygen concentration), and typical lanthanide magnetic ordering temperatures of the order of one Kelvin or less, providing a whole range of coexistent antiferromagnetic superconductors (see e.g., Orlando et al. 1987, B.W. Lee et al. 1988). These magnetic ordering temperatures are so low that magnetic dipole coupling may be of comparable strength to the exchange coupling normally responsible for magnetic ordering (see e.g., Whitehead et al. 1994 and references cited therein). This indicates just how low the density of any conduction electrons (holes) at the lanthanide site must be. A couple of glaring exceptions to these broad generalizations are:

- (a)  $\text{CeBa}_2\text{Cu}_3\text{O}_{6+\delta}$  and  $\text{TbBa}_2\text{Cu}_3\text{O}_{6+\delta}$  do not form (see e.g., Cao et al. 1995a). Terbium can sometimes exhibit the  $3^+ \leftrightarrow 4^+$  mixed valence behavior well-known for cerium, so perhaps that tendency to tetravalence destabilizes the structure. On the other hand  $\text{EuBa}_2\text{Cu}_3\text{O}_{6+\delta}$  (Rommel et al. 1993) and  $\text{YbBa}_2\text{Cu}_3\text{O}_{6+\delta}$  (Hodges et al. 1995) do form (Ferreira et al. 1988), and europium and ytterbium appear to be stably trivalent in them.
- (b) Praseodymium also can tend to tetravalence, so the situation is made more difficult to understand by the fact that  $\text{PrBa}_2\text{Cu}_3\text{O}_{6+\delta}$  forms but is not superconducting for any composition, even  $\text{O}_{\sim 7}$ . We discuss this in more detail below.
- (c) The holmium ordering temperature in  $\text{HoBa}_2\text{Cu}_3\text{O}_{6+\delta}$  is severely depressed relative to the other lanthanide  $T_N$ 's, and there may not be true long-range holmium magnetic ordering at all. Again, see below.

Since the "123's" possess even more complicated crystal structures than the "214's", the muon sites have proved even harder to find. Most of the muon site studies have been published in the proceedings of the International Conferences on  $\mu\text{SR}$  (Oxford: Brewer et al. 1990, Nishida and Miyatake 1990, Lichti et al. 1990b, Weber et al. 1990, Dawson et al. 1990; Maui: Boekema et al. 1994, Adams et al. 1994), the exceptions being Halim et al. (1990) and Dawson et al. (1988). Some of the most popular muon sites are shown in fig. 94. Most of the experimental muon site studies used the copper-antiferromagnetic  $\text{O}_6$  materials, to again have distinct ZF frequencies. These provide evidence that at least two independent muon sites are occupied, generating low-temperature frequencies near 4.2 MHz and 18 MHz in  $\text{YBa}_2\text{Cu}_3\text{O}_6$ . It is possible that both these sites are  $\sim 1 \text{ \AA}$  away from oxygen ions. The danger of trying to extrapolate to muon sites at optimal superconducting oxygen concentration is shown by Riseman et al. (1990), where it is difficult to reconcile the ZF  $\mu\text{SR}$  signals from  $\text{PrBa}_2\text{Cu}_3\text{O}_6$  and  $\text{PrBa}_2\text{Cu}_3\text{O}_7$  (more on this below).

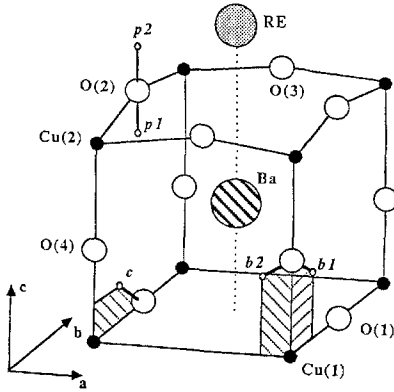


Fig. 94. Some possible muon sites in  $\text{YBa}_2\text{Cu}_3\text{O}_{6+\delta}$  (Lichti et al. 1990b, Adams et al. 1994).

7.2.2.1.  $R = \text{Gd}$ . We begin discussion of individual  $\text{R}\text{Ba}_2\text{Cu}_3\text{O}_{6+\delta}$  materials in the middle of the lanthanide series, because gadolinium is a good starting point for discussion of lanthanide magnetism. The spherical  $^8\text{S}_{7/2}$  state of  $\text{Gd}^{3+}$  makes it immune (to first-order) to the crystalline electric field effects (see sect. 5.1.1) that create single-ion anisotropies in all the other magnetic lanthanides (which means that *usually* the magnetism of the Gd member of an isostructural series will be simpler). Also, the gadolinium member of a series usually has the highest magnetic ordering temperature (e.g., in the “de Gennes rule”, Kirchmayr and Poldy 1979). This latter is true in a sense here, in that among the superconducting 123’s,  $\text{Gd}\text{Ba}_2\text{Cu}_3\text{O}_{6+\delta}$  has the highest (coexistent) Néel temperature,  $\sim 2.2$  K (see e.g., Mook et al. 1988, Meyer et al. 1987). This hardly varies with oxygen concentration over the entire range from  $\text{O}_7$ , where superconducting  $T_c$  differs little from that of  $\text{YBa}_2\text{Cu}_3\text{O}_7$  (see the table in De’Bell and Whitehead 1991), to  $\text{O}_6$ , where copper antiferromagnetic ordering at  $\sim 400$  K (e.g., Tranquada et al. 1988) differs little from that of  $\text{YBa}_2\text{Cu}_3\text{O}_6$ . In ZF  $\mu$ SR, cooling a  $\text{Gd}\text{Ba}_2\text{Cu}_3\text{O}_{\sim 6.3}$  sample through  $T_{\text{N,Cu}}$  near 300 K produced the same oscillation (from the 4 MHz site) as from an  $\text{YBa}_2\text{Cu}_3\text{O}_{\sim 6.3}$  sample down to  $\sim 100$  K, below which differences indicate the gadolinium moments slow down (Niedermayer et al. 1993a). More surprisingly, similar slowing down of moments below about 100 K was seen in  $\mu$ SR in a  $T_c \cong 60$  K superconducting sample ( $\text{O}_{\sim 6.6}$ , Golnik et al. 1987), a material for which there is no indication of long-range copper magnetism. However, no such slow magnetic fluctuations above  $T_{\text{N,Gd}}$  were seen above 2.2 K in a fully oxygenated ( $T_c > 90$  K) sample. Well below 2.2 K, the oxygen-depleted sample displayed a fast-relaxing signal with an apparent central frequency near 8 MHz, while the superconducting samples showed a strong 4.5 MHz signal and a weaker, sample-dependent  $\sim 7$  MHz signal (see also Nishida et al. 1988a).

Recently, Pinkpank et al. (1999, 2000a) studied  $\mu$ SR in a series of  $\text{Gd}\text{Ba}_2\text{Cu}_3\text{O}_{6+\delta}$  samples (and also  $R = \text{Ho}$ , below) covering the entire range of oxygen concentration from  $\delta = 0.0$  to 1.0. In the Gd-magnetically ordered state well below 2 K, they followed the relative amplitude of the two frequencies associated with the two muon sites, showing a linear dependence of the “chain” site occupancy on  $\delta$ . Above 2 K, which for some

$\delta$  is Cu-antiferromagnetic, but for others is superconducting, the muon spin relaxation is dominated by the isotropic Gd moment dynamics, which put the local fields into the fast-fluctuation limit even close to the magnetic ordering. There appears to be a critical-slowness regime of less than one Kelvin width above  $T_{M(\text{Gd})}$ , and the paramagnetic limit seems to be reached at a mere 20 K.

7.2.2.2.  $R = \text{Tb}, \text{Dy}$ . As we have said, no terbium member of this series forms.  $\text{DyBa}_2\text{Cu}_3\text{O}_{6+\delta}$  is reported to have lanthanide antiferromagnetism set in at  $\approx 1.0$  K, again without affecting superconducting or copper-antiferromagnetic ordering (De'Bell and Whitehead 1991). To our knowledge it has not been studied in detail with  $\mu\text{SR}$ .

7.2.2.3.  $R = \text{Ho}$ . The ordering temperature of the holmium member of an isostructural series is normally expected to be below the ordering of the Dy member and above that of the Er member. Instead of being between 1.0 K (Dy) and 0.6 K (Er), however, the highest reported lanthanide ordering temperature in  $\text{HoBa}_2\text{Cu}_3\text{O}_{6+\delta}$  is 0.19 K (Roessli et al. 1994), and even that is with finite correlation length along the  $c$ -axis. This suppression of magnetism is believed to be due to a CEF singlet ground state (see sect. 5.1) for the  $\text{Ho}^{3+}$  ion in this structure (see e.g., Whitehead et al. 1994). Extensive studies of CEF splittings in the  $\text{RBA}_2\text{Cu}_3\text{O}_{6+\delta}$  materials, particularly with inelastic neutron scattering, have resulted in detailed values for the CEF parameters for  $R = \text{Dy}$  (Allenspach et al. 1989a),  $\text{Ho}$  (Furrer et al. 1988) and  $\text{Er}$  (Allenspach et al. 1989b, Soderholm et al. 1992). Differences between the oxygen-deficient tetragonal and oxygen-rich orthorhombic structures have been resolved, but they do not have much effect on the holmium single-ion ground state (Staub et al. 1994). These, and a specific heat study (Ferreira et al. 1988), indicate that the  $^5\text{I}_8$  holmium ion has a singlet ground state with the first excited state at  $\sim 7$  K in the orthorhombic structure ( $\sim 14$  K for tetragonal). As discussed in sect. 5.1.2, an isolated singlet state is nonmagnetic. In a system with magnetic excited states above a singlet ground state (and no strong magnetic interactions), magnetic response and dynamics evident at temperatures above the lowest excited state begin to die out as the temperature drops below that level. Any magnetism left at temperatures well below the first excited state results from (virtual) coupling to excited states not occupied (Fauth et al. 1995) or other sources of magnetic moment (at 0.19 K, nuclear moments might contribute to the ordering). Given all this, then, it is surprising that ZF  $\mu\text{SR}$  sees nearly static internal magnetism in superconducting  $\text{HoBa}_2\text{Cu}_3\text{O}_7$  to far higher temperatures than any other probe. One group interpreted greatly increased relaxation rates below 3 K in both orthorhombic superconducting and tetragonal Cu-antiferromagnetic samples as due to Ho spin freezing (Nishida et al. 1988b, Kuno et al. 1988). A different group observed a ZF oscillation in a superconducting sample, starting near zero frequency at 5 K and rising to 1.5 MHz just above a transition near 0.1 K, at which it jumped to  $\sim 2.5$  MHz (Birrer et al. 1989b). Further, above 5 K, dynamic relaxation due to slow magnetic fluctuations was observed, and persisted to  $\sim 50$  K (see fig. 42). The transition near 0.1 K was likely the one that investigators using other probes have reported as magnetic ordering. It is tempting to interpret the higher-temperature results as due to 2D correlations as in the case of Er (below), but for Ho this is not supported by evidence from any other probe. As

discussed in sect. 5.1.2, this behavior does conform to a general trend of  $\mu$ SR in singlet ground state systems to be anomalous and difficult to explain.

Pinkpank et al. (1999) studied a set of  $\text{HoBa}_2\text{Cu}_3\text{O}_{6+\delta}$  samples with various  $\delta$ , above 2 K, in addition to the Gd samples discussed above. The CEF-induced singlet ground state and single-ion magnetic anisotropy result in temperature-dependent muon spin relaxation up to about 100 K. Below 10 K, increasing LF causes partial decoupling, indicating the local fields are no longer in the fast-fluctuation limit. In a conference contribution Pinkpank et al. (2000b) argue that a muon-induced effect (see sect. 5.1.3) is necessary to explain the details of the spontaneous oscillation observed below 190 mK.

7.2.2.4.  $R = Er$ . In  $\text{ErBa}_2\text{Cu}_3\text{O}_{6+\delta}$ , an erbium-moment ordering transition occurs near 0.6 K, but there has been disagreement about what happens in detail at and below that temperature, possibly due to dependence on the details of sample preparation. Most of the reported neutron scattering work has been on the fully oxygenated,  $T_c > 90$  K,  $\text{O}_{\sim 7}$  composition, with much less published about oxygen-deficient Cu-antiferromagnetic samples. There is universal agreement that the erbium moment correlations are strongly *ab*-plane two-dimensional, and that the correlation range in the plane diverges at the transition. Disagreement has been over whether or not long-range order develops in the *c*-axis direction, what the principal wavevectors of the ordering are (Paul et al. 1989, Chattopadhyay et al. 1989), and how much these depend on oxygen concentration (Clinton et al. 1993, Mesot et al. 1993). With ZF  $\mu$ SR, one study (Lichti et al. 1990a) of a non-superconducting  $\text{ErBa}_2\text{Cu}_3\text{O}_{6.2}$  sample saw Cu-antiferromagnetism generating two frequencies ( $\sim 5$  and  $\sim 8$  MHz), but did not get below 6 K. Apparently only one group (Maletta et al. 1990a) studied neutron diffraction in a set of samples spanning the entire range of oxygen concentration. Interestingly, while they saw 3D long-range order develop at  $\sim 0.5$  K in (orthorhombic) superconducting samples, they saw only 2D erbium correlations in (tetragonal) Cu-antiferromagnetic samples down to less than 0.1 K. This group went on to do ZF  $\mu$ SR on the same samples (Maletta et al. 1990b). In Cu-antiferromagnetic  $\text{O}_{6.11}$  and  $\text{O}_{6.34}$ , a single frequency was seen up to several hundred Kelvin, with a kink in the temperature dependence near 10 K interpreted as the start of Er-moment slowing. At  $\sim 2$  K, the frequencies were between 5 and 6 MHz. For  $\text{O}_{6.40}$  (superconducting onset  $\sim 30$  K, Maletta et al. 1989) there is much stronger relaxation (indicating more disorder), with no clear frequency above 20 K, there being instead multicomponent monotonic relaxation, which the authors call spin-glass-like. At  $\text{O}_{6.53}$  (onset  $T_c \approx 50$  K) there was only very slow relaxation down to 3 K with no evidence of copper moments. In a dilution refrigerator between 0.04 K and 1.2 K,  $\mu$ SR in an  $\text{O}_{6.20}$  sample showed no evidence of erbium moment ordering, but superconducting  $\text{O}_{6.60}$  and  $\text{O}_{7.0}$  showed a single, very low frequency (less than 100 KHz, corresponding to a local field of less than 8 G) with kinks in the temperature dependence at  $\sim 0.5$ – $0.6$  K. Whereas neutrons see 2D correlations only up to about 0.9 K (Clinton et al. 1993), the low-frequency  $\mu$ SR oscillation appears to persist to 1.2 K and above. Since frequencies greater than 4 MHz were observed below  $T_{N,\text{Gd}}$  in superconducting  $\text{GdBa}_2\text{Cu}_3\text{O}_{6+\delta}$ , interesting near-cancellation of the fields from ordered erbium moments of  $\sim 4\mu_B$  (compared to

gadolinium's  $7\mu_B$ ) would be needed at the muon site to generate such low frequencies here.

7.2.2.5.  $R = Pr$ .  $PrBa_2Cu_3O_{\sim 7}$  is the only case where the orthorhombic "123" structure forms but is not superconducting. Tetravalency may not be the source of this effect: this anomalous behavior of the Pr member differs from that of the other tetravalent-tending rare earths (Ce and Tb, as we have stated above), and direct probes of rare-earth valence have generally indicated  $Pr^{3+}$  (Radousky 1992, Hilscher et al. 1994). The other usual suspect is: the 4f wave functions, being not nearly so well hidden inside the other (closed) shells of the ion as they are in heavy rare earths, may have become involved in the bonding of the ion, or may have hybridized with band electrons near the Fermi level (see e.g., Fehrenbacher and Rice 1993, Cao et al. 1995b). In this latter case, however, one would expect  $R = Sm$  or  $Nd$  to interfere with superconductivity in the 123's in a similar way, whereas they do not. All  $PrBa_2Cu_3O_{6+\delta}$  compositions are antiferromagnetic and insulating, even though there is still a tetragonal-to-orthorhombic transition in the middle of the range. The copper ordering temperature falls from above 400 K at  $O_6$  to near room temperature at  $O_7$ . The praseodymium ordering temperatures are unusually high:  $\sim 12$  K for  $O_6$ , rising to  $\sim 17$  K for  $O_7$ . There is debate on whether the Pr ordering is long-range in the  $c$ -axis direction at all  $\delta$  values (Guillaume et al. 1994, Malik et al. 1994), and whether all copper ions participate in the high-temperature magnetism (Rosov et al. 1992, Longmore et al. 1996, Boothroyd et al. 1996). ZF  $\mu$ SR clearly sees the magnetism in these samples, but detailed interpretation is difficult. Considering the  $O_6$  end, one study (Riseman et al. 1990) saw, in the temperature range of copper ordering ( $\geq 140$  K), a strong signal of slightly less than 1 MHz, and a weak signal  $\sim 4$  MHz, compared with strong 4 MHz and weak 18 MHz in  $YBa_2Cu_3O_6$  (a different study, Dawson et al. 1991, briefly reported 2.2 and 4.7 MHz). Below 140 K, relaxation rates increased steeply (Pr moment slowing?), making detailed analysis difficult. For  $O_7$ , only one frequency is clearly deduced, but the raw data shown in Cooke et al. (1990) hints at others. This one clear frequency rises with cooling to slightly above 2 MHz just above  $T_{N,Pr}$ , below which it drops to near 1.5 MHz. There have been no reports of  $\mu$ SR in  $PrBa_2Cu_3O_{6+\delta}$  for intermediate values of  $\delta$ , so it is not clear how the sites and local fields evolve between these two end points. Instead, because partial substitution of Pr for Y in  $YBa_2Cu_3O_7$  causes similar effects to the removal of oxygen (Genossar et al. 1994), there have been  $\mu$ SR studies of  $Y_{1-x}Pr_xBa_2Cu_3O_{\sim 7}$ : Cooke et al. (1990) in the Pr-rich, magnetic region; Seaman et al. (1990) measuring penetration depth with TF in the Pr-poor superconducting region. In the latter, Pr substitution does look indistinguishable from oxygen removal.

Recently, one group (Zou et al. 1998) has reported that samples of  $PrBa_2Cu_3O_{\sim 7}$  grown by a floating-zone method have partial volumes superconducting up to as high as 80 K, and a longer  $c$ -axis length (within the same crystal structure) than insulating samples.

7.2.2.6.  $R = Nd$ . One publication (Lütgemeier et al. 1996) briefly discusses detection of magnetic ordering near room temperature in  $NdBa_2Cu_3O_{6+\delta}$ , where  $\delta = 0.5$  and  $0.6$ , as

part of many measurements indicating that the “60 K plateau” in  $T_c$  vs.  $\delta$  for R = Y is absent or squeezed to higher  $\delta$  when R = Nd.

*7.2.2.7. Other studies.* Other TF μSR studies, intended mainly to determine penetration depths, have looked at polycrystalline  $\text{EuBa}_2\text{Cu}_3\text{O}_{7-x}$  (Cooke et al. 1989) and  $\text{GdBa}_2\text{Cu}_3\text{O}_{7-x}$  (Cooke et al. 1988). The R = Eu results show no sign of europium magnetism, and are very similar to those of the many TF μSR studies of high- $T_c$ 's containing no magnetic rare earth, consistent with nonmagnetic  $\text{Eu}^{3+}$ . In the early study of R = Gd, the TF relaxation rate turns up sharply below ~20 K, but error bars are large, making detailed interpretation difficult. TF data from  $\text{ErBa}_2\text{Cu}_3\text{O}_{7-x}$  by the same group is mentioned in a demonstration of “maximum-entropy” frequency analysis as an alternative to FFT for lineshape determination (Alves et al. 1994). Features that should be sharp for single crystals are blurred in “polycrystalline averaging”, however, and this has made polycrystalline lineshape analysis unrewarding. High-quality single crystals of magnetic-R 123's large enough for μSR have not been available. Occasionally, *c*-axis oriented powders are attempted, as in De Renzi et al. (1994) for  $\text{Y}_{1-x}\text{Pr}_x\text{Ba}_2\text{Cu}_3\text{O}_{7-x}$ .

Schenck et al. (1990a) looked for *f*-moment  $\mu^+$  Knight shifts above  $T_c$  in  $\text{RBa}_2\text{Cu}_3\text{O}_{7-x}$  (R = Dy, Ho, Er). They detected no shift for Dy or Er, but two signals with opposite sign shifts for the Ho member. The latter is the ion with the singlet ground state in this structure, but at temperatures above 100 K, several magnetic states are occupied, and it should be similar in its paramagnetism to the others, so these results are hard to understand.

We note briefly that in one μSR study, the actinide thorium was involved, in  $\text{Y}_{1-2x}\text{Ca}_x\text{Th}_x\text{Ba}_2\text{Cu}_3\text{O}_{7-x}$  (Hartmann et al. 1994a). This was called “charge-neutral” doping, with equal parts  $\text{Ca}^{2+}$  and  $\text{Th}^{4+}$  substituting with an average valence 3 for  $\text{Y}^{3+}$ . Despite the fact that calcium is certainly nonmagnetic and thorium is the standard nonmagnetic analogue for uranium, this substitution depresses  $T_c$  faster than  $\text{Pr}_{2x}$ . This work has now been supplemented by a μSR study of  $\text{Nd}_{1-2x}\text{Ca}_x\text{Th}_x\text{Ba}_2\text{Cu}_3\text{O}_{7-\delta}$  (Lundqvist et al. 2000). The focus of the work again is on the depression of the superconductivity, not on magnetism.

### 7.2.3. The “2212” phase

$\text{Bi}_{1-x}\text{Sr}_{1-x}\text{Ca}_x\text{Cu}_2\text{O}_{8-x}$  is the most anisotropic high- $T_c$  material, generating its own special flux-penetration substates (see e.g., S.L. Lee et al. 1993). Effects similar to varying oxygen concentration in 123's and varying strontium concentration in 214's are here generated by exchanging trivalent rare earths for divalent calciums (Tarascon et al. 1989). Most work has been on  $\text{Bi}_{1-x}\text{Sr}_{1-x}(\text{Ca},\text{Y})\text{Cu}_2\text{O}_{8-x}$  (e.g., Oashi et al. 1989, with μSR, Weber et al. 1993) leading to the end point antiferromagnetic insulator  $\text{Bi}_{1-x}\text{Sr}_{1-x}\text{YCu}_2\text{O}_{8-x}$  with  $T_N$  well above room temperature (Nishida et al. 1988c, De Renzi et al. 1989). One μSR study (De Renzi et al. 1990) tried to assess whether “electron-doped” 2212's could be created by making samples of  $\text{Bi}_{1-x}\text{Sr}_{1-x}(\text{Nd},\text{Ce})\text{Cu}_2\text{O}_{8-x}$ . Pure  $\text{Bi}_{1-x}\text{Sr}_{1-x}\text{NdCu}_2\text{O}_{8-x}$  was, as expected, an antiferromagnetic insulator with  $T_N$  above room temperature, and alloying with cerium

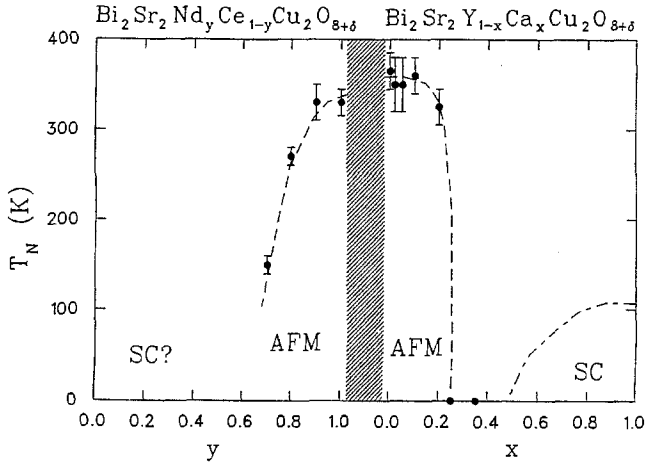


Fig. 95. Alloy magnetic phase diagram (deduced from  $\mu$ SR measurements) of  $\text{Bi}_2\text{Sr}_2(\text{Ca},\text{Y})\text{Cu}_2\text{O}_{8-\delta}$  and  $\text{Bi}_2\text{Sr}_2(\text{Nd},\text{Ce})\text{Cu}_2\text{O}_{8-\delta}$  (De Renzi et al. 1990).

depressed that ordering (see fig. 95), but beyond  $\sim 30\%$ Ce (still antiferromagnetic), only multiphase samples could be produced. One other study (de Groot et al. 1994) of  $\text{Bi}_{1-x}\text{Sr}_{2-x}(\text{Ca},\text{Gd})\text{Cu}_2\text{O}_{8-\delta}$  (Jayaram et al. 1991) concentrated on penetration depth and maximum-entropy analysis of TF spectra from the flux-penetration state, with no specific discussion of what difference the  $\text{Gd}^{3+}$  moment might be making.

#### 7.2.4. Ruthenate hybrids

$\text{RuO}_2$  layers can possess the same square-planar coordination together with rather similar bond lengths as their  $\text{CuO}_2$  counterparts. The pure ruthenate compounds (especially  $\text{Sr}_2\text{RuO}_4$ ) are at present subjects of intense studies (including  $\mu$ SR) with regard to their superconducting and giant magneto-resistance properties. They are, however, outside the scope of this review. It is also possible to construct new families of hybrid ruthenate-cuprate compounds. Recently, the 1212-type  $\text{RuSr}_2\text{GdCu}_2\text{O}_8$  system, having  $\text{CuO}_2$  bilayers and  $\text{RuO}_2$  monolayers was synthesized as single-phase material (Bauernfeind et al. 1995, 1996). It exhibits FM order ( $T_C \approx 125$  K) involving Ru moments ( $\sim 1\mu_B$ ) only (the gadolinium sublattice remains paramagnetic down to  $T_N = 2.6$  K, where it orders antiferromagnetically) and superconductivity at much lower temperatures ( $T_c = 15\text{--}40$  K, depending on preparation details). Bulk data indicated that the FM state remains essentially unaltered when superconductivity sets in. Coexistence of superconductivity and ferromagnetism is unusual (in contrast to antiferromagnetism) since it produces macroscopic magnetization which normally should break up the Cooper pairs. The pertinent question is whether this coexistence also exists on a microscopic scale or whether the material separates into magnetic and superconducting volume fractions. Clearly  $\mu$ SR is the ideal tool to shed light on this problem.

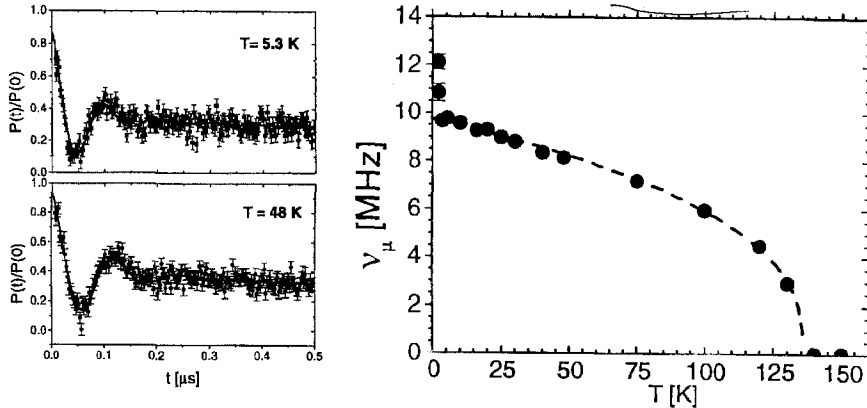


Fig. 96.  $\mu$ SR study on  $\text{RuSr}_2\text{GdCu}_2\text{O}_8$ . Left: ZF spectra in the FM state ( $T_C = 133$  K) above and below the superconducting transition ( $T_C = 16$  K). Right: Temperature dependence of the spontaneous muon spin precession frequency. The sharp rise at the low-temperature end is due to the AFM ordering of the Gd sublattice. After Bernhard et al. (1999).

$\mu$ SR studies were carried out by Bernhard et al. (1999). Bulk measurements on the same material gave  $T_C = 133$  K and  $T_C = 16$  K. Spontaneous spin precession in ZF was observed for  $T < T_C$  with a signal amplitude proving that the sample as a whole has entered the FM state. Lowering the temperature below  $T_C$  left the spectra basically unchanged. In particular, no loss of signal amplitude occurred. Furthermore, the Brillouin-like temperature dependence of the spin precession frequency shows no irregularity around  $T_C$ . The situation is illustrated in fig. 96. True coexistence of ferromagnetism and superconductivity is present in  $\text{RuSr}_2\text{GdCu}_2\text{O}_8$ , presenting a challenge to electronic structure theory in cuprate and related systems.

### 8. Disordered magnetism

In this section, we discuss what  $\mu$ SR can observe in materials in which there is some kind of transition from paramagnetism, which has rapid dynamic moment fluctuations, at higher temperatures, to a state at lower temperatures where the moments are static or at most change very slowly, yet no long-range magnetic order (that would generate magnetic Bragg peaks in neutron diffraction) occurs. Such “frozen” but disordered magnetic states can be weak in their response to bulk probes, and generate broad (and therefore weak in peak intensity) neutron diffraction signals. The muon, being a local probe, will react strongly to frozen electronic moments near it, even if there are no correlations among them. Thus,  $\mu$ SR can be a particularly useful probe of disordered magnetism.

Usually, magnetic interactions between moments in crystalline materials tend to cause long-range spin order rather than a disordered spin structure as the spin-frozen state. LRO can be prevented in particular cases by the introduction of sufficient amounts of atomic disorder (independent of the magnetic state that results at low temperature) and frustration



in the magnetic interactions. Atomic disorder can be the substitutional disorder in an alloy, or the positional disorder in an amorphous material. Frustration means that the generally pairwise magnetic interactions between spins cannot all be satisfied when considered for groups of more than two spins: the magnetic ground state becomes more degenerate as more spins are considered. Spin-glass experts (see e.g., Mydosh 1993) emphasize that neither disorder nor frustration implies the other, and that (in all systems that are felt to be understood) *both* must be present to cause spin-glass freezing.

One set of materials does indeed indicate that frustration alone need not generate a disordered frozen state. In “perfectly frustrated” lattices, the most studied of which are the Kagomé lattices, with large (strongly interacting) moments at high temperatures, no freezing at all occurs, and the moments remain dynamic to dilution-refrigerator temperatures, as has been verified with  $\mu$ SR (see sect. 8.2.2). Most such systems, however, involve transition metal moments, and will not be discussed in this article. One candidate, gadolinium gallium garnet, has not been studied with  $\mu$ SR to date (but see  $\text{CePt}_2\text{Sn}_2$  in sect. 9.3). See sect. 8.3.2 for discussion of the interesting behavior of rare-earth pyrochlores.

There is a tendency to call all disordered magnetic frozen states “spin glasses”, but there is enough variety in detailed behavior to identify several types, for some of which inclusion or exclusion from the “spin glass” category has varied between researchers. The “ideal” spin glass is one in which the microscopic (static) spin configuration is indistinguishable from an instantaneous snapshot of the high-temperature paramagnetic state, with no detectable spin–spin correlations. This ideal is difficult to realize in practice, of course, because any magnetic interactions that can cause magnetic freezing tend to cause correlations as they try to set up long-range ordered magnetism. Probably closest to the ideal are the classic dilute-alloy spin glasses, such as  $\text{Cu(Mn)}$  where magnetic ion concentration is less than 1%, discussed below, but even in those there is an indication of spin density wave (SDW) correlations (see Werner 1990). Strangely, it is not clear that the classic dilute spin-glass behavior can be reproduced in metallic lanthanide systems. Initially, it was thought that dilute lanthanides in yttrium metal,  $\text{Y(R)}$  should be spin glassy, but after several years work, neutron diffraction measurements showed that all such samples, down to very low concentrations and freezing temperatures, entered spiral magnetic ordered states (Rainford et al. 1985, Wenger et al. 1986, Caudron et al. 1988) and so the freezing temperatures were in fact Néel temperatures. No alternate possible systems, such as perhaps  $\text{La(R)}$ , have been seriously studied. We regard as unresolved the question of whether the RKKY interaction can generate a classic dilute-moment spin-glass state similar to that for the transition metal  $s$ – $d$  interaction.

As moments appear in densities higher than one per hundred of the ions present in a solid, there is in practice more tendency for local correlations among the moments to develop. It is possible then for magnetically short-range-ordered clusters to form and act as magnetic units, somewhat dynamic (the cluster moments may jump as a group between available alternate easy axes) at high temperatures, interacting with other such clusters, and then freezing into a seemingly random or poorly correlated domain structure at lower temperatures (Holden et al. 1982). Such materials continue to show spin-glass-

like response in bulk measurements (see e.g., Galazka et al. 1980, Furdyna 1987 and references cited therein), yet some would call them short-range magnets. This is not to say there are no real concentrated spin glasses, but rather there are a variety of frozen states that can all look spin-glass-like to some probes.

### 8.1. Dilute spin glasses

The dilute spin glasses are a special topic within  $\mu$ SR because they generate distinctive muon spin relaxation *via* the Lorentzian field distribution. This was discussed as a possible field distribution (eq. 33) for  $\mu$ SR in sect. 3.2.2 (the static ZF relaxation function, eq. (34), is shown in fig. 20). Whereas the Gaussian field distribution is expected (and often observed) in dense-moment systems, Walstedt and Walker (1974) predicted that the Lorentzian distribution applies in the dilute-moment limit (magnetic concentration goes to zero) of spin glasses, and Uemura and collaborators (Uemura et al. 1985, and references cited therein) observed it with  $\mu$ SR in the frozen state of dilute Cu(Mn) and Au(Fe).

While the discussion in sect. 3 indicates that Markovian dynamics cannot decouple Lorentzian Kubo–Toyabe relaxation, the dilute alloy samples generated ZF  $\mu$ SR spectra above the spin freezing that did decouple with increasing temperature. Uemura and collaborators developed a model based on the microscopics of muon positions relative to the dilute moments that showed that when the moments fluctuate, the field at any one muon can only vary in a limited range within the overall Lorentzian distribution. A muon may stop far from any magnetic moment, and if so it will see fields smaller than average at almost all times during fluctuations. Another muon that stops very near a moment will usually see fields larger than average during fluctuations throughout its life. The rate of loss of polarization for those muons that stop close to moments will be much faster than those further away, for the same moment-fluctuation rate. There are thus distinct classes of muon sites with different relaxation rates once dynamics begins. By treating the dynamic relaxation of the classes separately and then integrating them together to create the relaxation function for the sample as a whole, Uemura et al. developed detailed expressions that differ from those of “pure” Lorentzian dynamics (where each muon can access the entire Lorentzian distribution), including in the fast-fluctuation limit, “root-exponential” ZF relaxation

$$G_z(t) = \exp\left(-[4a^2\tau t]^{1/2}\right), \quad (73)$$

which *does* show fluctuation decoupling (but, again, field-distribution width,  $a/\gamma_\mu$ , cannot be separated from correlation time,  $\tau$ , in the fast-fluctuation limit). An illustrative example is shown in fig. 97. At high enough temperatures, double relaxation (sect. 3.4) with the copper nuclear moments in Cu(Mn) was seen (see e.g., Pinkvos et al. 1990). Uemura et al. used this analysis to determine moment fluctuation rates through the freezing temperature in a frequency range not accessible to other probes (see Uemura and Yamazaki 1983). A discussion on general aspects of spin dynamics in spin glasses with emphasis on  $\mu$ SR results is available from Campbell (1999).

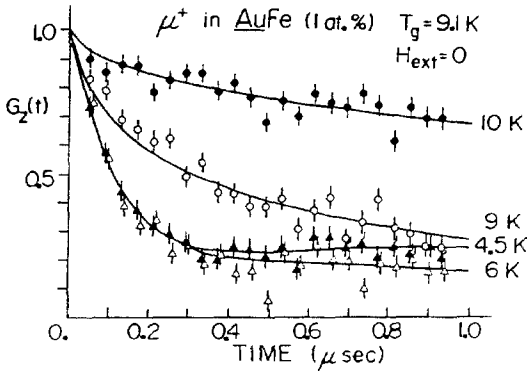


Fig. 97. Dynamic muon spin relaxation in a dilute spin glass as contrast to the behavior of the pure Lorentzian field distribution discussed in the section on longitudinal field measurements. Although a Lorentzian Kubo-Toyabe relaxation is observed in the fully spin-frozen state at lowest temperatures, motional narrowing occurs when the spins start to fluctuate. From Uemura (1981).

We have discussed this transition metal case to show what physics can be extracted when one understands the  $\mu$ SR spectra in some detail, and to provide a basis (what  $\mu$ SR sees in a nearly ideal dilute spin glass) for comparison with the other forms of behavior we will discuss. As stated above, there has been in fact no concerted study of whether this Lorentzian limit can be achieved in a dilute rare-earth alloy, with any probe. The only f-magnetic systems clearly displaying a *static* Lorentzian field distribution at the muon site that we know of are the low-temperature simple antiferromagnetic states of compounds with NaCl, CsCl or  $\text{Cu}_3\text{Au}$  structure described in sect. 5.2, where the field at the muon should sum to precisely zero, but some kind of magnetic-defect structure creates what appear to be isolated spin-lattice faults. In one isolated case, singlet-ground-state  $\text{PrP}_x$  (discussed in sect. 5.1.2), a *dynamic* Lorentzian field distribution was observed that persists to dilution refrigerator temperatures.

## 8.2. More-concentrated magnetic disorder

Even for the ideal case of completely random moment orientations, when there are more than three magnetic ions per hundred in a solid, the Lorentzian field distribution is unlikely to be even a rough approximation to the truth. Meanwhile, a Gaussian field distribution of local field is only to be expected when there are more than  $\sim 30$  magnetic ions per hundred. The local field distribution in the intermediate range has been simulated by Noakes (1991), but corresponding measurements are lacking.

The corresponding measurements of field distributions at muon sites in non-dilute disordered magnetic states are missing because the signal tends to disappear. The muon is so sensitive to magnetic fields that even about 5 magnetic ions per hundred in a frozen state can produce ZF or TF relaxation so rapid that it is lost in the initial dead time (described in sect. 2.5) of even surface muon apparatus. If the fields are close to static, this leaves in ZF- $\mu$ SR sometimes a slow-relaxing "1/3 tail" as the observable signal. As discussed in sects. 3.2.2 (on Kubo-Toyabe relaxation) and 3.3 (on spontaneous precession), such a signal provides no information on the size of the local fields involved, but indicates that the local field fluctuation rate is slow. Care must be taken to distinguish such a near-static tail from possible inhomogeneous freezing. In the latter case part of the sample has undergone

spin freezing, while another part of the sample remains unfrozen. Of course, the frozen and unfrozen portions could (and normally will) be contained in randomly distributed clusters throughout the sample. The signal arising from the spin frozen portion is fast decaying and may vanish in the dead time of the  $\mu$ SR spectrometer. The signal coming from the unfrozen portion is slowly decaying (fast spin fluctuations) and exhibits reduced asymmetry since the frozen portion has become unobservable. One indicator that one deals with the near-static “1/3-tail” relaxation of a homogeneously spin frozen sample is *reduction* of the relaxation rate as temperature is lowered and the moments become more static. In contrast, the slowly decaying signal of the unfrozen portion of an inhomogeneously spin frozen sample caused by rapid fluctuations of the local field, will depolarize faster when the dynamics of moments slows down with decreasing temperature. Also, if the initial asymmetry of the reduced-amplitude signal is greater than 1/3, then it cannot all be near-static tail. This conclusion is valid only, however, for a random polycrystal or a powder sample, since for single crystals or strongly textured samples, the amplitude of the ZF asymptote in static relaxation need not be 1/3, but will depend on the angle of the crystal axes to the initial muon polarization. Disputes concerning homogeneous *vs.* inhomogeneous spin freezing have arisen several times in  $\mu$ SR studies on classical spin glasses. We return to the problem of inhomogeneous spin freezing in sect. 8.2.4.

If a particular sample does generate only a near-static 1/3-tail with measurable relaxation rate at low temperature in ZF- $\mu$ SR, then the local field fluctuation rate is slow enough that it should be possible to partially decouple the relaxation, that is, reduce the observed relaxation rate and perhaps even increase the initial observed asymmetry, by applying longitudinal fields large enough to compete with the typical internal fields, as described in sect. 3.2.3. This would be an example of the use of LF to distinguish near-static relaxation (that will decouple in modest fields) from fast-fluctuation relaxation (which decouples very slowly, if at all, in fields available for  $\mu$ SR). In the “remnant 1/3-tail” case, however, there is no strong indication beforehand of how large the internal fields (causing the relaxation that disappears in the dead time) are, so if no effect of LF is seen, no information is gained from the LF measurement. While there are a number of cases known where asymmetry drops below a freezing temperature and an apparent 1/3-tail signal is seen at temperatures below, few measurements of the effect of LF on such remnant 1/3 tails have been published (we discuss recent work on resurrecting lost asymmetry by application of LF in rare-earth quasicrystals in sect. 8.3.3).

### 8.2.1. *Varying-power exponential relaxation*

As just described, the field distribution at the muon site in a frozen, disordered (non-dilute moment) magnetic state is often not measured, because large-asymmetry muon signals are only seen at higher temperatures, where the spins are not fully frozen, and the dynamics partially decouples the muon from the large internal fields. Interpretation of the muon relaxation in terms of the behavior of the moment system generally requires a model of both the distribution of local fields caused by the moments, and the spectrum of moment fluctuations. With no detailed information on the field distribution from the static (low-temperature) limit, there can be considerable ambiguity in interpretation.

In the paramagnetic state, well above the freezing temperature, for example, monotonic ZF relaxation is usually observed with a muon spin depolarization rate that decreases as temperature increases. We expect the paramagnetic state to generate spin fluctuations fast enough to put the system in the fast fluctuation limit. Originally it seemed reasonable to assume that there exists a fixed underlying field distribution upon which the fluctuation rate should merely be a function of temperature. The reader can refer back to sect. 3.2.2 to see that the fast fluctuation limit for a Gaussian field distribution is exponential relaxation, and to the opening of this section to see that the fast-fluctuation limit of the Lorentzian field distribution as present in a dilute spin system is “root-exponential” relaxation. Thus, the indications are that for a fixed-field distribution and simple random rapid fluctuations, the power,  $p$ , in “power-exponential” (eq. 35) relaxation should be constant for a particular sample (at least).

While there are some disordered magnetic systems that do show fixed-power paramagnetic ZF- $\mu$ SR, even some magnetically non-dilute ones (see e.g., Ansaldo et al. 1988), there are also a number of systems known in which the power changes smoothly with temperature. One of the first of these to be discovered was amorphous DyAg (sect. 8.3.1). Generally, the power is near one (simple exponential relaxation) far above the freezing temperature, but decreases smoothly toward 1/2 as temperature is lowered. An example is shown in fig. 100 further below. Visually, a power less than one in an asymmetry spectrum means that the muon spin relaxation occurs with a higher effective rate at early times and with a lower effective rate at later times when compared to pure exponential relaxation. Below the temperature at which  $p = 0.5$  is reached, even if this is well above the freezing temperature, initial asymmetry often starts to be reduced as some of the signal relaxes so quickly that it is lost in the initial dead time of the apparatus. Powers of less than 0.5 in fits to data should therefore be inspected carefully to see whether the model correctly reproduces the data at early times (yet sometimes powers less than 0.5 are properly measured: see e.g., Keren et al. 1996).

Campbell et al. (1994) argued that power-exponential ZF  $\mu$ SR should be related to “stretched exponential” relaxation observed in bulk probe measurements of spin glasses (Palmer et al. 1984, Souletie 1994, also see Ogielski 1985), but did not establish a detailed connection. The combined assumption of fixed field distribution and simple Gaussian–Markovian dynamics might no longer hold. Keren et al. (1996) analyzed ZF and LF data above the glass transition temperature for the classical spin glass AuMn(0.5 at.%) in terms of different special spin–spin autocorrelation functions. They showed that one is able to distinguish between a power law, a stretched exponential, and a cut-off power law as autocorrelation functions. Still, this is a special case (a highly dilute canonical spin glass) and as yet there is no model that can reproduce the range of variation in power (from essentially unity right down to 0.5, and perhaps below) that can be generated by single samples of various types of materials (e.g., a dense disordered spin system). These effects might also be related to the “seedy” magnetic order deduced from neutron scattering in R-based amorphous alloys (see Boucher and Chieux 1991), or to a wide distribution of moment fluctuation rates (Heffner et al. 1996).

### 8.2.2. *Kagomé dynamic relaxation*

In the Kagomé lattice  $\text{SrCr}_8\text{Ga}_4\text{O}_{19}$ , Uemura et al. (1994) observed ZF relaxation at low temperatures that was monotonic, but had rounded, Gaussian-like shape at early times. Normally, such rounded initial shape is taken as an indication of nearly static local fields, but Uemura et al. also found that there was only detectable LF decoupling in rather large applied fields, which is more definitive evidence for dynamics. They were able to reproduce this behavior with a model in which the dynamics is primarily in randomly switching the local field on and off. A muon at its site sees zero (or undetectably small) field most of the time, but occasionally a random field appears for a short time. They argued that the zero local-field state corresponds to all nearby spins paired into singlet states, while the non-zero local-field state corresponds to a nearby spin being unpaired. Although this scenario reproduces the data, the validity of its physical basis is not assured. We have briefly mentioned this case, because the same type of relaxation is (at least phenomenologically) also observed in the frustrated heavy-fermion system  $\text{CePt}_2\text{Sn}_2$  (see sect. 9.3.1), which indicates that it might be a general feature of spin systems too strongly frustrated to achieve long-range magnetic order. Characteristic is also the presence of persistent spin fluctuations in the limit  $T \rightarrow 0$ .

### 8.2.3. *Static relaxation for non-Gaussian and non-Lorentzian field distributions*

The Kubo–Toyabe relaxation functions assume a Gaussian (dense spin system) or Lorentzian (dilute spin system) distribution for the three cartesian components of the local field  $\mathbf{B}_\mu$ . Usually full isotropy of field distribution is assumed, but the non-isotropic case has been treated as well (see sect. 3.2.2).

In interesting contrast to the previous section, a small number of systems have generated ZF static *monotonic* decay of muon spin polarization (to the 1/3 asymptote), or with the minimum (in polarization before recovery to 1/3) too shallow to be fit with Gaussian or Lorentzian Kubo–Toyabe functions under any conditions. They have been found to be static by their ease of decoupling in LF, and by the fact that the long-time asymptote remains flat while increasing in amplitude as the LF is increased. The first indication of such relaxation was in data from a transition metal magnetic quasicrystal, icosahedral Al–Mn–Si (Noakes et al. 1995), but the situation there was complicated by inhomogeneous freezing (next section). Clear relaxation of this type has now been seen in the Kondo-lattice system  $\text{CeCu}_x\text{Ni}_{1-x}\text{Sn}$  (the magnetic behavior of these materials is discussed in sect. 9.2). For copper concentrations,  $x$ , large enough to cause clear spin freezing, and at temperatures well below  $T_g$ , ZF- $\mu$ SR spectra show rounded Gaussian-like initial relaxation, followed by a minimum whose depth appears to be a function of  $x$  (an example is shown in fig. 98, bottom). For  $x = 0.1$ , there is no minimum at all, only monotonic relaxation (Kalvius et al. 1997a,b). Nonetheless,  $\mu$ SR in these samples decouples rapidly in LF with flat asymptotes, so the local fields appear to be static. Similar relaxation may have been observed in  $\text{CeCu}_{5-x}\text{Ga}_x$  (Wiesinger et al. 1997).

Noakes and Kalvius (1997) have found a relaxation function that fits these shallow-minima spectra, by assuming a range of  $\Delta$  values. Instead of a single type of muon

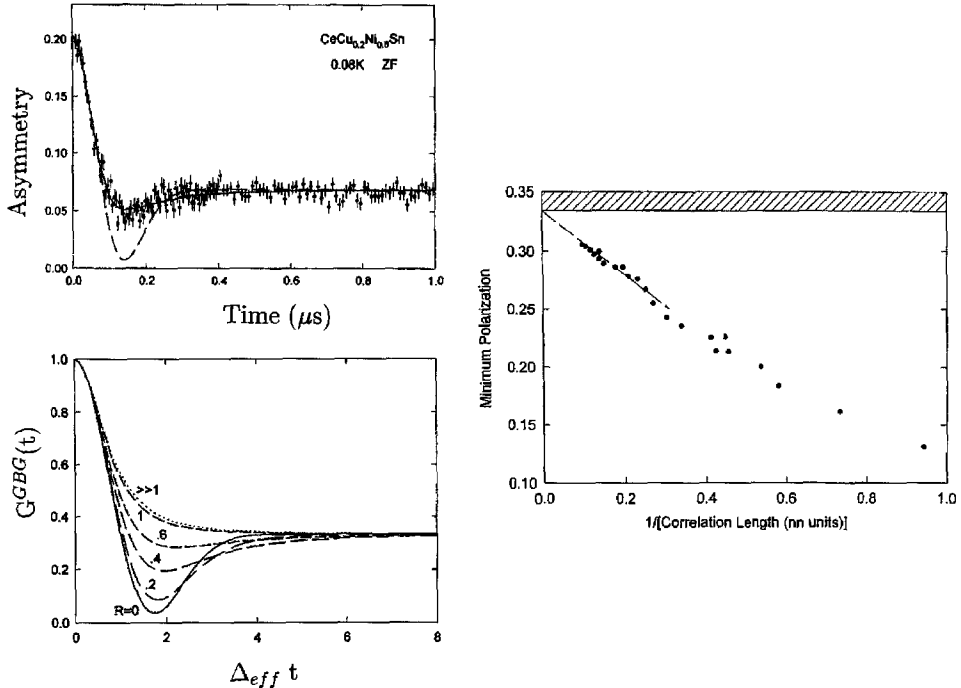


Fig. 98. Left: The “Gaussian-broadened Gaussian” relaxation function (bottom) (explanation see text). ZF  $\mu$ SR asymmetry spectrum in polycrystalline  $\text{CeCu}_{0.2}\text{Ni}_{0.8}\text{Sn}$  at 0.08 K (top). The dashed line is a fit of the static Gaussian Kubo–Toyabe relaxation function. The solid line is a fit of the static “Gaussian-broadened Gaussian” function. From Noakes and Kalvius (1997). Right: The minimum polarization achieved by the Monte Carlo RCMMV static ZF muon spin relaxation functions, as a function of the reciprocal of the moment–magnitude correlation length, in units of the magnetic-ion nearest-neighbor separation in the model lattice. The horizontal line represents the 1/3 asymptote, above which the minimum polarization cannot rise. The dashed line is a guide for the eye. From Noakes (1999).

site with a Gaussian field distribution characterized by a single width parameter,  $\Delta$ , they assumed there is a collection of muon sites with Gaussian field distributions that differ in their widths, with the probability of a particular  $\Delta$  value governed by an independent Gaussian distribution, of width  $w$ , centered on a most likely value,  $\Delta_0$ . The complete field distribution is then a convolution integral of the two Gaussians (which has no closed form solution), and the corresponding static ZF relaxation function (the “Gaussian-broadened Gaussian” Kubo–Toyabe function) is the convolution of the broadening with the single-site Kubo–Toyabe function, with closed form solution:

$$G_z^{\text{GBG}}(t) = \frac{1}{3} + \frac{2}{3} \left( \frac{1 + R^2}{1 + R^2 + R^2 \Delta_{\text{eff}}^2 t^2} \right)^{3/2} \left( 1 - \frac{\Delta_{\text{eff}}^2 t^2}{1 + R^2 + R^2 \Delta_{\text{eff}}^2 t^2} \right) \times \exp \left( \frac{-\Delta_{\text{eff}}^2 t^2}{2(1 + R^2 + R^2 \Delta_{\text{eff}}^2 t^2)} \right), \quad (74)$$

where

$$\Delta_{\text{eff}}^2 = \Delta_0^2 + w^2, \tag{75}$$

$$R = w/\Delta_0. \tag{76}$$

$\Delta_{\text{eff}}$  is the initial rate of relaxation, while the ratio  $R$  governs the depth of the minimum, which ranges from the standard Gaussian Kubo–Toyabe for  $R = 0$  (no broadening), through shallower values as  $R$  increases, until at  $R = 1$  the minimum disappears and the relaxation becomes monotonic (see fig. 98, bottom left). Figure 98 (top left) shows the fit of this function (solid line) to that data, with in this case,  $R$  near 0.5.

Note that Gaussian-broadened Gaussian relaxation was derived by mathematical manipulation, and is not based on a microscopic model of moments in a material. As such, it is phenomenological. While plausible microscopic models are easy to construct for small broadening, as  $R \rightarrow 1$  and the minimum disappears, the field-component probability distribution,  $P(B_i)$ , must diverge as  $B_i \rightarrow 0$ , an unusual requirement.

Noakes (1999) has shown, by numerical simulation, that a microscopic model involving “range-correlated moment magnitude variation” (RCMMV) can produce such shallow, static ZF relaxation functions. In most localized-moment materials, the magnitude of that moment is constant (in magnetic order, the variation of the ordered moment with temperature is a change in balance with the disordered remainder of the total single-ion moment). The RCMMV model assumes that while moment orientation is always completely random, and moment magnitude is constant within small regions, moment magnitude varies randomly (between zero and a maximum value) between regions. The typical dimension of those regions defines a correlation length. Figure 98 (right) shows the minimum polarization of the simulated ZF relaxation functions as a function of (the reciprocal of) that correlation length. Arbitrarily shallow minima can be generated as the correlation length is increased. The correspondence between this model and the  $\text{CeNi}_{1-x}\text{Cu}_x\text{Sn}$  and  $\text{Al–Mn–Si}$  quasicrystal data suggests that μSR has detected a previously unsuspected form of static moment-magnitude order/disorder distinct from the static orientational disorder of ordinary spin glassiness. In  $\text{CeCu}_{0.2}\text{Ni}_{0.8}\text{Sn}$  the minimum polarization is about 0.25. According to fig. 98 (right) this corresponds to a correlation length of ~3 nn-distances or, with an average Ce–Ce separation of roughly 4 Å (Higashi et al. 1993), to ~12 Å.

Recently, Larkin et al. (2000) have encountered (in a study of the spin-ladder system  $\text{Sr}(\text{Cu}_{1-x}\text{Zn}_x)_2\text{O}_3$ , which falls outside this review, but see sect. 8.3.4) muon spin relaxation functions with too shallow and too broad minima of polarization to be reproduced by Kubo–Toyabe functions. Again, longitudinal field data showed the spin system to be static. These authors used an approach (called Kubo golden rule, KGR), which was originally derived by Kubo (see Kubo 1981 and Yamazaki 1997) to describe their findings. For details we refer to the original papers. The KGR method allows the calculation of the muon spin relaxation function for arbitrary field distributions (if they can be described by arithmetic function). In the spin-ladder compound an exponential field distribution reproduced the data. The approach of Noakes and Kalvius (1997) can be reproduced using KGR.



Other special relaxation functions on a phenomenological basis have been given by Crook and Cywinski (1997) and K.M. Kojima et al. (1997). The treatment of dilute spin glasses based on various spin–spin autocorrelation functions (Keren et al. 1996, 2000) has been mentioned in sect. 8.2.1.

#### 8.2.4. Inhomogeneous freezing

If one has a disordered magnetic material in which the ZF  $\mu$ SR remains of large amplitude as the temperature approaches magnetic freezing from above, then one may observe inhomogeneous freezing. Consistent with the previous sections, generally the moment size must be reduced from the multiple- $\mu_B$  moments of Gd, Tb, Dy, *etc.* in order to retain detectable signal amplitude (beyond the dead time) at freezing, so many of the f-electron examples of this have been observed in Ce, Yb and U compounds variously labelled “Kondo lattices” or “heavy-fermion materials”, and discussed in sect. 9. Some discussion of inhomogeneous freezing in such materials is in Schenck (1993).

Long-range magnetic ordering transitions in high-quality samples cause the entire sample to enter the ordered state at the same temperature (for first-order transitions, when the first seed forms). In contrast, in a sample with disordered magnetic freezing the pre-existing disorder (of whatever kind) allows clusters where statistical variations have resulted in enhanced coupling (or reduced frustration) to spin-freeze at a higher temperature than other clusters elsewhere in the sample. It is then believed that the relatively sharp freezing signal that defines the glass transition temperature ( $T_g$  in bulk probes occurs at cluster percolation: at this temperature the largest cluster, formed by mergers of expanding smaller clusters, reaches “infinite” (linear) size. But it is still likely that only part of the total volume of the sample is involved and some spins remain unfrozen at  $T_g$ .  $\mu$ SR often does not see a distinctive signal at  $T_g$  but sees the inhomogeneous freezing develop instead. Often at temperatures slightly above  $T_g$  a fast-relaxing signal indicative of frozen (or very slow fluctuating) spins develops with small initial amplitude, while most of the signal remains more slowly relaxing, indicative of paramagnetism. As the clusters grow in volume, the fast-relaxing  $\mu$ SR signal increases in amplitude at the expense of the slow signal. An example is shown in fig. 99. Usually,

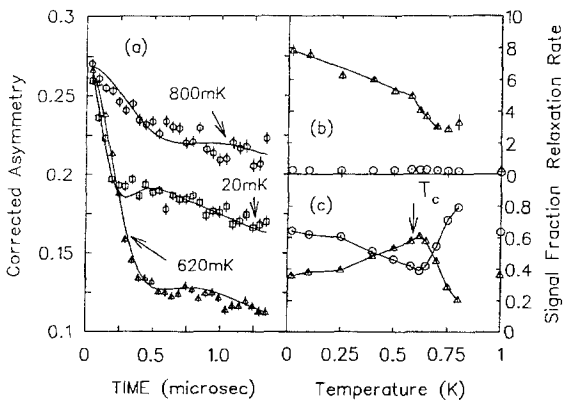


Fig. 99. An example of inhomogeneous spin freezing. The sample is  $\text{CeCu}_{2.2}\text{Si}_2$ . (a) ZF  $\mu$ SR spectra, each consisting of a fast (static) and a slow (dynamic) relaxing signal. This distinction vanishes above 1 K. (b) Relaxation rates *vs.* temperature. (c) Relative fractions of the spin-frozen (triangles) and the unfrozen (circles) parts.  $T_c$  is the superconducting transition temperature (see sect. 9.3.1.8); from Luke et al. (1994a).

at some temperature below  $T_g$  the last of the paramagnetic volume disappears, all spins are frozen, and the  $\mu$ SR becomes a single (fast) signal. In the classic dilute spin glasses, inhomogeneous freezing typically extends from about  $T = 1.1T_g$  down to several tenths of  $T_g$  below  $T_g$  (see e.g., Pinkvos et al. 1990). In fig. 99, the increase of frozen volume with decreasing temperature is halted by the onset of superconductivity at  $T_c$ .

### 8.3. Results on disordered *f*-magnetism

In this section we discuss some disordered magnetic systems that do not fit well under any of the subject headings of the other sections in this review. am-DyAg (sect. 8.3.1) is the only amorphous *f*-moment material studied with  $\mu$ SR to date, as the pyrochlores (sect. 8.3.2) are the only “perfectly frustrated” *f*-magnets studied with  $\mu$ SR. Quasicrystals (sect. 8.3.3) must stand somewhat separately because they have atomic structure that is neither amorphous nor merely disordered-crystalline. For a discussion of spin-glass-like behavior in Ce, Yb, and U strongly correlated electron materials, see sect. 9.

#### 8.3.1. Amorphous DyAg

Some time ago, Kalvius et al. (1986, 1987) compared the  $\mu$ SR behavior of a crystalline lanthanide AFM DyAg ( $T_N = 60$  K) (see sect. 5.2.2), with the amorphous material of the same composition, which would in detail be called am-Dy<sub>50</sub>Ag<sub>50</sub>. Since AFM is not possible in an amorphous compound, one finds am-DyAg to be asperomagnetic below  $T_C = 18$  K. Asperomagnetism is related to conical ferromagnetism, the difference being that the angles of spin direction with respect to the direction of magnetization are randomly distributed within the cone. For a review of the properties of amorphous magnetic materials, see Chappert (1982). Conical FM is an outcome of magnetic anisotropy and in amorphous R magnets the dominant feature is a randomness in anisotropy interaction (rather than in exchange interaction as in the amorphous 3d materials, e.g., the so-called Metglasses). There is no significant difference in effective Dy<sup>3+</sup> moment between the crystalline and amorphous materials. In both cases the moment is close to the Dy<sup>3+</sup> free ion value.

As discussed in sect. 5.2.2, the crystalline sample provided interesting results of its own, generating static Lorentzian Kubo–Toyabe relaxation in the ordered state due to near-perfect field cancellation at the muon site. In the paramagnetic state the muon spin relaxation was (ordinary) exponential, indicating a Gaussian-like field distribution when the moments are not magnetically aligned. The temperature dependence of relaxation rate is consistent with fast fluctuations of the local field with its fluctuation rate increasing with temperature in the usual fashion. In the paramagnetic state of the amorphous sample, the muon relaxation rate was much higher, rising as temperature was lowered until the signal began to be lost in the initial dead time in the vicinity of 90 K, far above the ordering temperature. We have already mentioned in sect. 8.2.1 that amorphous DyAg was the first case where varying power exponential relaxation has been observed: the relaxation spectrum is only exponential in shape at room temperature, then taking power-exponential shape with power decreasing smoothly as temperature decreases, to  $p \simeq 1/2$

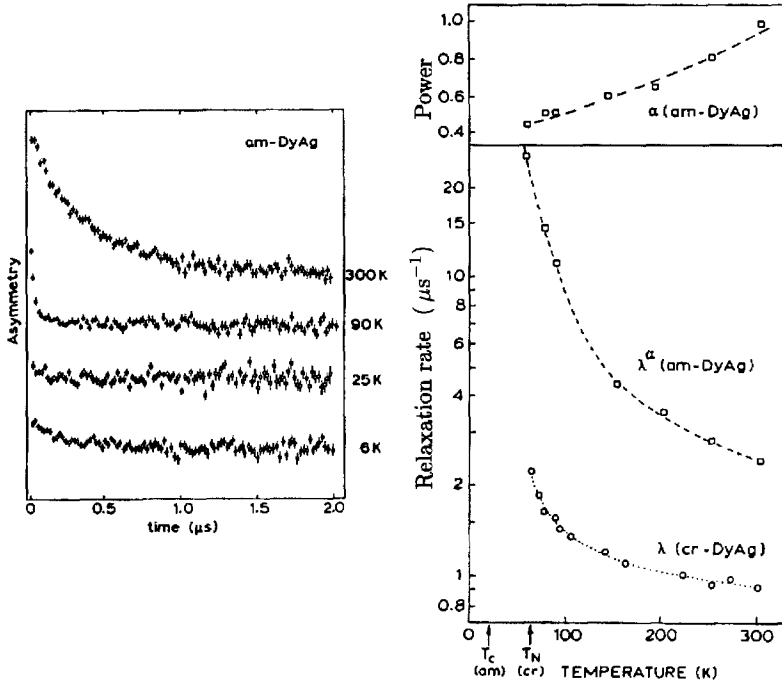


Fig. 100. ZF  $\mu$ SR spectra in amorphous DyAg (left), and temperature dependence of the relaxation rate  $\lambda^p$  (right) in comparison to the simple exponential rate in crystalline DyAg (Kalvius et al. 1986).

at 90 K, where asymmetry begins to be lost. These results are summarized in fig. 100. There had been previous indication from Mössbauer effect data that the Dy fluctuation rate was much slower in the amorphous material than in the crystalline (Chappert et al. 1982), with which the difference in muon relaxation rates between the two materials is consistent. As the likely cause, the lower symmetry of the local surroundings of the  $\text{Dy}^{3+}$  ions and its effect on CEF states has been suggested. In  $\mu$ SR the broader field distribution in the amorphous sample must be considered as well. Its presence is indicated in the low-temperature data ( $T < T_C$ ) to be discussed below. More difficult to understand is the temperature dependence of the shape of the relaxation function (as described in sect. 8.2.1). One must state at this point once more, that varying power relaxation as described appears to be a common feature in (magnetically) disordered systems, both in the magnetically dilute and concentrated ranges and is often taken as the indicator for the presence of magnetic disorder. The underlying reason for a non-exponential shape of decay of muon spin polarization in the dynamical limit is a distribution of fluctuation rates of the magnetic moments. This interpretation again is consistent with the Mössbauer result of Chappert et al. (1982) where a fit with at least two different relaxation rates was required to reproduce the spectral shape below  $\sim 140$  K.

Below  $T_C$ , a slow relaxing 1/3-tail signal appears, suggesting very slow spin fluctuations in the ordered state, in agreement with the earlier Mössbauer results (Chappert et al. 1982). The (nearly) static depolarization is obviously much faster than in the crystalline material, an outcome due to the increased width of field distribution caused by the randomness of distribution of ions on the lattice sites. No effect of LF was seen at any temperature in the amorphous sample, but at the time, fields above 0.4 T were difficult to generate at μSR spectrometers, and separately, temperatures below 3 K were not easily attained (compare to the more-advanced technology used recently for LF μSR in quasicrystals, described below).

### 8.3.2. Highly frustrated rare-earth systems

The  $R_2T_2O_7$  ( $T$  = transition metal) pyrochlore-structure materials are geometrically frustrated when crystallographically perfect. In both, the rare-earth sublattice, and separately the transition-metal sublattice, which may bear moments as well, the magnetic ions reside in connected tetrahedra over which a near-neighbor antiferromagnetic interaction (these are insulators) cannot be satisfied (see discussion on  $YMn_2$  in sect. 5.3.3). The first really interesting member to appear was  $Y_2Mo_2O_7$ , where the moment resides on the molybdenum. This material, though to all probes stoichiometric and as crystallographically perfect as can be determined, executes a spin-glass freezing at 22 K (Raju et al. 1992). This is a case then, where standard spin-glass folklore is contradicted. The material appears to have frustration but no disorder, so it would be expected to behave like a Kagomé lattice (remain paramagnetic), but instead it freezes. The Mo moment is small, so it is hard to see any magnetic effect with neutrons, but μSR sees fairly standard spin-glass freezing spectra (Dunsiger et al. 1996a, 1997), with large asymmetry retained below  $T_C$ , but only visible in the few earliest bins of the spectra (see fig. 101).

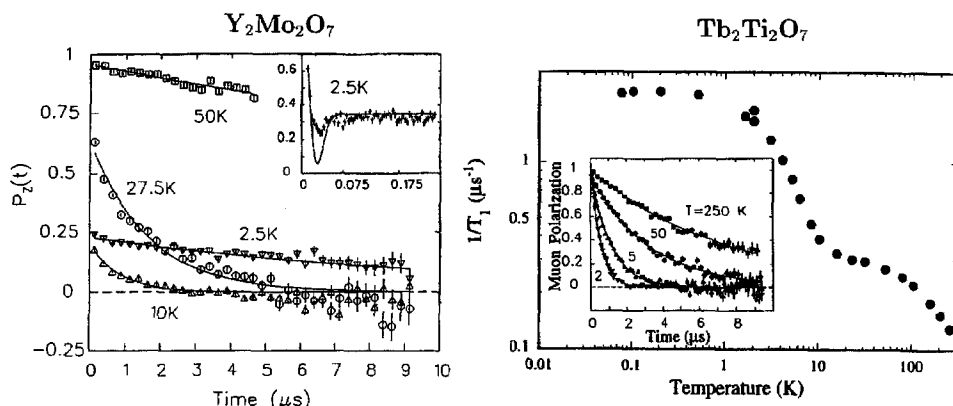


Fig. 101. Left: Near-ZF (i.e., a small LF is applied to suppress relaxation effects from nuclear moments) μSR spectra in  $Y_2Mo_2O_7$ , stated as polarization ( $A(t)$  divided by the instrumental asymmetry,  $A_0$ ), at various temperatures. The inset shows the early time behavior far below the glass transition temperature (Dunsiger et al. 1996a). Right: Near-ZF muon spin relaxation rate  $1/T_1$  as a function of temperature in  $Tb_2Ti_2O_7$ . The inset shows representative μSR spectra, all of which exhibit exponential relaxation. From Gardner et al. (1999).

Slightly unusual, however, is the shape of the nearly static spectrum well below  $T_g$ : the relaxation proceeds to the 1/3-tail through a minimum far too shallow to be fit with the Gaussian Kubo–Toyabe relaxation function to be expected for this dense-moment system. The frozen state may thus be similar to that observed in Ce(Ni,Cu)Sn (sects. 8.2.3, 9.2).

In Tb<sub>2</sub>Mo<sub>2</sub>O<sub>7</sub>, the freezing temperature is only slightly higher, 25 K, suggesting that the Mo-sublattice magnetic interactions are still dominant. With the much larger Tb moments present, short-range magnetic correlations are seen in neutron scattering (Gaulin et al. 1992). The muon spin relaxation rate is (not surprisingly) much higher, but the same qualitative temperature behavior is seen (Dunsiger et al. 1996b). In Tb<sub>2</sub>Ti<sub>2</sub>O<sub>7</sub>, where titanium does not carry a moment, there appears to be no magnetic freezing or ordering of any sort (Gaulin et al. 1998). In this material, muon spin polarization decays monotonically (compare insets to fig. 101, left and right), apparently in the fast fluctuation limit, down to at least 70 mK (Gardner et al. 1999). The saturation low-temperature relaxation rate (fig. 101, right) corresponds to a Tb<sup>3+</sup> fluctuation rate of 0.04 THz, which is a good measure of the effective exchange constant. Thus, there may be interesting information yet to be learned from these pyrochlore materials on what causes and controls spin-glass freezing in geometrically frustrated systems.

Gadolinium gallium garnet Gd<sub>3</sub>Ga<sub>5</sub>O<sub>12</sub> (GGG) has two-dimensional magnetic frustration (involving triangles of moments), whereas the pyrochlores discussed above have three-dimensional frustration (tetrahedra of moments). Used in commercial memory and switching devices operating at room temperature, high-quality single crystals of GGG have been available for some time (see e.g., Fisher et al. 1973), but the interesting low-temperature magnetic effects have only been discovered recently. In zero applied field this material appears to exhibit spin-glass freezing between 0.15 K and 0.2 K (Schiffer et al. 1995), but strangely, antiferromagnetic ordering is induced by ~1 T applied field up to near 0.4 K (Schiffer et al. 1994, Tsui et al. 1999). The entropy change in field of this material is large enough to permit continuous magnetic refrigeration to temperatures of order 1 K using it (Daudin et al. 1982).

The thermal neutron absorption of natural gadolinium is so strong that magnetic neutron scattering is only practical on samples made from isotopically tailored (to remove the difficult isotope, <sup>157</sup>Gd) starting material. One neutron diffraction study of a powder of <sup>160</sup>Gd<sub>3</sub>Ga<sub>5</sub>O<sub>12</sub> has appeared (Petrenko et al. 1998). Only zero applied field results are reported, and while a freezing is observed at 0.14 K, no more than 15% of the sample volume is frozen at 0.043 K. The authors suggest the freezing is nucleated around impurities and/or defects, such as Gd ↔ Ga site exchange.

ZF and LF-μSR has now been reported by Dunsiger et al. (2000). The ZF relaxation function is root-exponential at all temperatures down to 0.025 K, indicative of a dilute spin system with substantial dynamics. This supports the idea of isolated islands nucleated around defects, but indicates only slowed fluctuations, not full freezing. The apparent spin fluctuation rate drops starting near 1 K (where bulk probes see effects they attribute to short-range magnetic order, Schiffer et al. 1994), but does not extrapolate to zero, and shows no effect around 0.14 K. Thus μSR sees no spin-glass transition. All of this is generally consistent with the neutron diffraction results. In LF at 0.1 K, the relaxation

rate was higher at 0.2 T than at ZF, but then fell smoothly with increasing applied field, showing no effect at the reported onset of AFM at  $\sim 0.6$  T or the reported return to paramagnetism at  $\sim 1.4$  T. Thus, while  $\mu$ SR may have detected a reduction of the spin fluctuation rate in low applied field, it does not see any indication of the claimed field-induced AFM state.

### 8.3.3. Rare-earth quasicrystals

Quasicrystals are solid materials that display long-range orientational order without the translational periodicity of crystalline lattices. They generate diffraction patterns with sharply defined peaks but with axes of rotational symmetry (such as 5-fold and 10-fold) not allowed by any space group. While there are a number of review monographs concerning ongoing research and debate on their structures (see e.g., Janot 1992, Goldman and Kelton 1993), there are no reviews in print about the occurrence of magnetism in these materials. This is partly because it has been relatively rare: the vast majority of quasicrystals show no evidence of electronic magnetic moments. Fe is apparently nonmagnetic in quasicrystals (early reports of ferromagnetism were due to impurity phases). The only well-established transition-metal magnetic quasicrystal is icosahedral (i-)Al–Mn–Si (Bellisent et al. 1987, Eibschütz et al. 1988, Berger and Préjean 1990), which is spin glassy. The only actinide quasicrystal known to these authors is i-Pd–U–Si (Wong and Poon 1986, Wosnitza et al. 1988), available only in quantities too small for  $\mu$ SR.

Recently, Japanese researchers discovered the first rare-earth quasicrystals, i-R–Mg–Zn (Niiikura et al. 1994, Hattori et al. 1995a,b), where R can be Gd, Tb, Ho and Er (at least). These show bulk probe signatures of spin-glass freezing (in all cases, below 10 K). A European group, making its own samples, has reported magnetic quasilattice peaks in neutron diffraction, particularly from i-Tb–Mg–Zn, below 20 K (Charrier et al. 1997), but without any corresponding signal in bulk measurements (Charrier and Schmitt 1997). Muon spin relaxation measurements were first performed on Japanese samples by Noakes et al. (1998) and recently on independently made samples by Charrier et al. (1999).

$\mu$ SR in i-Al–Mn–Si (Noakes et al. 1995) was briefly mentioned above in sect. 8.2.3, introducing the Gaussian-broadened Gaussian static ZF relaxation function. It will be discussed in more detail now. In spite of compositions like  $\text{Al}_{75.5}\text{Mn}_{20.5}\text{Si}_4$ , with at least 20% of the ions being Mn, above  $T_g$  the samples generated ZF- $\mu$ SR spectra consistent with dilute-moment spin-glass behavior, indicating that only a fraction of the Mn ions possess electronic moments. Then, below  $T_g$ , anomalous behavior was observed, in that freezing remained inhomogeneous to the lowest temperatures ( $T \ll T_g$ ), and the frozen-region ZF signal became static monotonic relaxation to the 1/3-asymptote (see sect. 8.2.3). The  $\mu$ SR observed in i-Gd–Mg–Zn and i-Tb–Mg–Zn was, however, quite unlike that in the manganese quasicrystal. This time, with compositions  $\text{R}_8\text{Mg}_{42}\text{Zn}_{50}$ , the paramagnetic-state ZF- $\mu$ SR spectra were consistent with *dense-moment* paramagnetism, with temperature-dependent relaxation persisting to at least 200 K (fig. 102, left), and the relaxation rate increasing as temperature decreased to the point that it was “lost in

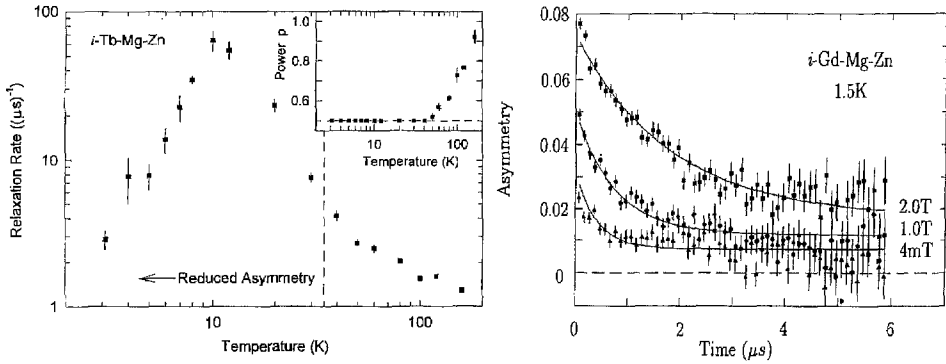


Fig. 102. Left: Temperature dependence of the near ZF muon spin relaxation rate in  $i\text{-Tb}_8\text{Mg}_{42}\text{Zn}_{50}$  on double logarithmic scales. The vertical dashed line indicates the onset of loss of asymmetry due to instrumental dead time. The inset shows the temperature dependence of power used in the power exponential fit to the relaxation spectra. The spin-glass temperature is near 8 K. Right:  $\mu\text{SR}$  asymmetry spectra of  $i\text{-Gd}_8\text{Mg}_{42}\text{Zn}_{50}$  at 1.5 K, in the applied longitudinal fields shown. The solid lines are a least-squares fit of a mildly inhomogeneous freezing model. From Noakes et al. (1998).

the initial dead time” for the Tb sample below 40 K (far above  $T_g$ ). The relaxation rate was generally lower for the Gd sample (which we attribute to non-cubic CEF effects slowing the paramagnetic fluctuation rate of the Tb moment, increasing its coupling to the muon), but strangely, the Gd–Mg–Zn paramagnetic ZF relaxation was exponential, while the faster Tb–Mg–Zn relaxation could only be fit as “power-exponential” (as described in sect. 8.2.1), with the power decreasing toward 0.5 as temperature decreased toward 40 K. This is the first case we know of where power-exponential relaxation can be turned on and off by a simple ion substitution normally thought to change only the single-ion anisotropy (by CEF) while leaving the magnetic interactions unchanged. This is as yet a mystery.

In spite of the report of magnetic quasilattice ordering near 20 K, there is no indication in the ZF- $\mu\text{SR}$  spectra of any magnetic transition in that temperature range. The reduced-asymmetry signal from the Tb sample develops indications of a near-static 1/3 tail below 12 K, consistent with the spin-glass freezing reported in bulk measurements. The Gd-sample signal retains full asymmetry down to near 3 K. Complex shape changes below 10 K and rapid increase of the overall rate of relaxation below 8 K indicate an inhomogeneous freezing process often seen in spin glasses. Below 3 K the Gd quasicrystal ZF- $\mu\text{SR}$  signal joins that of the Tb quasicrystal in being mostly lost in the dead time.

At temperatures far below  $T_g$ , where the moments may be static, and it would then be possible to measure the field distribution without the complication of spin dynamics, ZF- $\mu\text{SR}$  is of little use in these (and in many other dense-moment disordered magnetic) materials because most of the information wanted is lost in the dead time. There is then, however, some opportunity for LF- $\mu\text{SR}$ . If a significant fraction of the moments have fluctuation rates of less than a few per microsecond (and a 1/3 tail, when seen, indicates there is such a fraction), and if the longitudinal field that can be

applied approaches the characteristic width of the field distribution, then LF decoupling can increase the amount of resolved asymmetry and provide information on the field distribution. Figure 102 (right) shows the effect of 2 Tesla LF in comparison to 40 mT (which is clearly negligible relative to the internal fields operating) in i-Gd-Mg-Zn at 1.5 K. The solid lines show the fit of a model having a Gaussian field distribution with RMS field near 1 T and very slow ( $<5 \mu\text{s}^{-1}$ ) fluctuations. Similar partial decoupling spectra were observed in i-Tb-Mg-Zn at similar temperatures. This is an impressive example of the application of a strong longitudinal field to bring asymmetry back from the dead (time).

Work by Charrier et al. (1999) was carried out at the ISIS pulsed source and thus suffered more severely from losses of asymmetry in the initial dead time. The results for the Gd and Tb compounds are quite comparable to those of Noakes et al. (1998) when this limitation is taken into account. In particular, the (unexplained) two-signal spectra (rapidly and slowly relaxing) are observed as well. The study also includes measurements on the Dy and Y compounds. The former behaves much like the Tb quasicrystal, as expected. The Y material is nonmagnetic and muon spin depolarization arises solely from nuclear dipole moments. The fact that no sudden change in the rather weak depolarization rate ( $\sim 0.01 \mu\text{s}^{-1}$ ) was seen between 300 K and 10 K makes muon diffusion unlikely in this structure.

Recently published descriptions of syntheses of R-Mg-Zn quasicrystal samples by other research groups (Islam et al. 1998, Sato et al. 1998) indicate that bulk properties may depend delicately on the details of preparation. These groups were unable to reproduce by neutron diffraction the sharp quasilattice peaks reported by Charrier and Schmitt (1997), a result consistent with the  $\mu$ SR results of Noakes et al. (1998). The similarity of the data of the two  $\mu$ SR studies, which used samples of quite different origin, means that the properties measured by  $\mu$ SR are relatively insensitive to sample preparation.

#### 8.3.4. *Novel reduced-dimensionality systems*

Separate from thin films (and recently nanowires), which are like two- (or one-) dimensional surfaces (or lines) by brute force construction, it is also possible to get reduced-dimensionality magnetic behavior in otherwise 3D bulk materials by tailoring the magnetic couplings to be large in some directions and much smaller in others. This happens, for example, in intermetallics with a low lattice symmetry where the distance between neighboring magnetic ions varies greatly for different crystalline directions. A case mentioned earlier are the  $\text{RGa}_6$  compounds (sect. 5.4.4). Another approach are bond-network materials, where the dominant magnetic coupling is short-range superexchange along the bonds. The majority of such materials are transition metal oxides, but they are not always insulators: valence-imbalance alloying may produce charges free to move within the bond networks.

As said, the majority of these cases involve transition metal magnetism outside the scope of this review. Numerous classes of materials showing such behavior have been given special names and most were at least sampled by  $\mu$ SR, such as “Haldane gap” (e.g.,



K.M. Kojima et al. 1995b), “spin-Peierls transition” (e.g., Fudamoto et al. 1999, García-Muñoz et al. 1995b) and “spin chain” (e.g., Higemoto et al. 1998) compounds. Another class is “spin ladders” (spin chains connected by cross links), which includes  $\text{RCuO}_{2.5}$ . The copper is magnetic, and f-moment-free  $\text{LaCuO}_{2.5}$  was studied with  $\mu\text{SR}$  by Kadono et al. (1996). Magnetic “ordering”, which the reviewers here suspect is merely spin freezing, was deduced to occur at 125 K from the sudden loss of asymmetry in a (poor-time-resolution) pulsed-beam experiment. Recently, a conference contribution (Kakuta et al. 2000) presented data on  $(\text{Pr,Ca})\text{CuO}_{2.5}$  and  $(\text{Nd,Ca})\text{CuO}_{2.5}$ . The spin freezing temperatures are severely reduced. In this experiment there was enough time resolution to see that ZF-spectra below the transition temperature are roughly Kubo–Toyabe-like, with polarization rapidly dropping to a single minimum and then recovering, similar to what was observed in spin-ladder  $\text{Sr}_4\text{Cu}_6\text{O}_{10}$  (K.M. Kojima et al. 1995a), except that now some slow spin dynamics persist below the freezing (which may be due to the rare-earth moments not being well coupled to the frozen coppers, as in  $\text{R}_2\text{CuO}_4$  discussed in sect. 7.2.1). The authors attempt to relate the freezing behavior to theoretical predictions of the behavior of spin ladders with odd and even numbers of cross links.

## 9. Correlated electron intermetallics

### 9.1. Overview

As their name implies, strongly correlated electron systems encompass materials whose dominant physical properties are determined by the presence of strong correlations in their electronic structure, in particular between the open shell (magnetic) electrons and the charge carriers in the conduction band. The most prominent members are the high  $T_c$  superconductors and the heavy-fermion (HF) compounds. The former have already been discussed in sect. 7, the latter are the subject of this section.

Ideally, the specific heat of conduction electrons (or holes) in a metal is a linear function of temperature  $C = \gamma T$ , where  $\gamma$ , known as the Sommerfeld constant, is in the range 0.001 to 0.01 J/(mol K<sup>2</sup>) for normal materials. In HF compounds,  $\gamma$  reaches values up to 10<sup>3</sup> times larger (see tables 9, 10 and 11). In the basic theory of the specific heat of itinerant electrons (free Fermi gas),  $\gamma$  is proportional to the effective mass  $m^*$  of the charge carriers, and so the name “heavy fermions” has come to be attached to these high- $\gamma$  materials (see Stewart 1984). The linear relation between  $C$  and  $T$  is strictly fulfilled only in the limit of a free degenerate electron gas. In real materials, weak non-linearities show up that can be encompassed by, for example, allowing  $\gamma$  to be temperature dependent,  $\gamma(T)$ . The Sommerfeld “constant” of interest is then the extrapolation of  $\gamma$  for  $T \rightarrow 0$ .

The effective mass is a convenient parameterization of electron correlations. Such correlations can be generated only if there is overlap of the electron states involved, in the present case between the open shell orbits and the conduction electron (ce) band. At first sight, such a condition would seem to rule out lanthanide intermetallics, since in the

classical view the 4f states are highly localized at the lanthanide ion. The ce sea only plays the role of a medium transmitting the magnetic exchange coupling (RKKY interaction). More recently, it has become apparent that the model of highly localized 4f states is not always so rigidly fulfilled, especially in intermetallics containing elements with either a single 4f electron (Ce) or a single 4f hole state (Yb). Then one speaks of an “anomalous rare earth”. In the actinide series, 5f electron delocalization is a dominant feature of the electronic structure up to Pu, and is notable in U compounds. Known HF materials thus mostly contain either Ce, U or Yb (to a lesser extent) as the f element. A few such compounds are known for other lanthanides (Sm, Nd) and for the transuranic actinides. Whether in the latter case (especially concerning Np) this reflects just the problems in producing systematically a wide variety of intermetallics on a large scale, or whether the increased 5f electron localization drives the systems into normal magnetic states, remains open at this stage. In any case, there are no  $\mu$ SR data available even for the established HF compounds of Np (e.g., NpBe<sub>13</sub>). Similarly, the question of 3d transition element HF compounds is still under controversial debate (e.g., Coles 1996). A possible candidate is FeSi, but that subject falls outside this review.

The study of HF and related materials is a major field of present-day condensed matter research and a vast collection of data employing all available techniques and probes exists (see, for example, Grewe and Steglich 1991).  $\mu$ SR is a small but important part of this endeavor. One speciality of  $\mu$ SR, its sensitivity to very small magnetic moments and to rather low frequency fluctuations (i.e., the limit  $\omega \rightarrow 0$ ), makes it particularly useful here. Some HF intermetallics possess moments of the order of  $10^{-2}\mu_B$  or less (yet non-zero) and others show spin fluctuations in the MHz region down to mK temperatures. In addition, often a disordered magnetic state is the ground state. We have already outlined the power of  $\mu$ SR in this field (see sect. 8).

Despite the strong and broad research effort, it is as yet not possible to distill from the experimental results much in the way of detailed general systematics of HF behavior. Similarly, an all-embracing theory is missing. The basic ingredients are believed to be understood (and will briefly be outlined below) and some of the observed features can be well explained. Yet, it is, for example, still not possible to predict *a priori* the ground state of a particular HF material, among the possible choices of antiferromagnetism, superconductivity or weak paramagnetism (with enhanced Pauli susceptibility due to the large  $m^*$ ). Indeed, the enhanced mass is a parameter that describes the paramagnetism of HF materials quite well as fig. 103 demonstrates: the deviations from a constant ratio of  $\gamma$  to susceptibility (the so called *Wilson ratio*) are rather small.

Coexistence of superconductivity and AFM can occur and will be discussed. As in the preceding discussion of high- $T_c$  materials, the pure superconducting state is not a subject of this review, although  $\mu$ SR has made important contributions here as well. We refer the reader to reviews discussing  $\mu$ SR in superconducting HF compounds (e.g., Uemura and Luke 1993, Luke et al. 1994a, Heffner 1994, Amato 1995, 1997, to list just the more recent ones). Central to the study of HF superconductivity is the question whether odd parity superconductivity exists at all and if so, where is it to be found. This subject is still actively debated.

Table 9  
Cerium<sup>a</sup> heavy-fermion and related materials whose magnetism has been studied with  $\mu$ SR

Material	$\gamma$ (J/(mol K <sup>2</sup> ))	$T_N^b$ (K)	$T_c^c$ (K)	$\mu_{\text{ord}}$ ( $\mu_B$ )	$\mu_{\text{Curie}}$ ( $\mu_B$ )	$\mu$ SR references (selection)
CeNiSn <sup>d</sup>	0.040	—	—	—	2.86	Kratzer et al. (1992, 1997a) Kalvius et al. (1994)
CePdSn <sup>d</sup>		7.0	—	0.8	2.65	Kalvius et al. (1994, 1995b)
CePdSb <sup>d</sup>	0.011	17.5F	—	1.2	2.71	Neville et al. (1996)
CePtSn <sup>d</sup>	<0.2	7.5	—	0.85	~2.8	Kalvius et al. (1995a,b)
CeRhSb <sup>d</sup>	0.1	—	—	—	n/a	Rainford et al. (1995a) Lidström et al. (1997)
CeRu <sub>2</sub>	?	~40?	6.1	~10 <sup>-4</sup> ?	?	Huxley et al. (1996)
(CeSb) <sup>e</sup>		22.5*	—	2.1	2.38	Klaufß et al. (1994, 1995)
(CeAl <sub>2</sub> ) <sup>f</sup>	0.13	3.9	—	0.89	2.53	Hartmann et al. (1989)
CeAl <sub>3</sub>	1.25	0.6–0.8	—	≤0.1	2.6	Barth et al. (1987, 1989b) Amato et al. (1994b)
CePb <sub>3</sub>	~1.5	1.1	—	0.55	2.50	Uemura et al. (1986)
CeCu <sub>5</sub>	0.12	4.1	—	0.36	2.63	Wiesinger et al. (1994)
CeB <sub>6</sub>	0.26	2.4	—	0.28?	2.44	Feyerherm et al. (1994c)
CeCu <sub>6</sub>	1.6	—	—	—	~2.6	Amato et al. (1993a)
CeRuSi <sub>2</sub>	0.1	~10	?	?	1.7	Krivoshchev et al. (1997a)
CeCu <sub>2</sub> Si <sub>2</sub>	0.3–0.6	(see text)	≤0.7	~0.13	2.7	Feyerherm et al. (1997) Luke et al. (1994b) (Cu <sub>2,2</sub> ) Uemura et al. (1989)
CeRu <sub>2</sub> Si <sub>2</sub>	0.35	—	—	—	2.53	Amato et al. (1993b, 1994a) Sekine et al. (1994)
CeRu <sub>2</sub> Ge <sub>2</sub> <sup>h</sup>	~0.02	8.5	7.5	?	?	Walf et al. (1999)
CeRh <sub>2</sub> Si <sub>2</sub> <sup>h</sup>	~0.05	~37	—	~2.4	~2.5	Dalmas de Réotier et al. (1990a)
CePt <sub>2</sub> Si <sub>2</sub> <sup>i</sup>	0.086	?	—	?	~2.6	Dalmas de Réotier et al. (1997)
CeCu <sub>2</sub> Sn <sub>2</sub>	complex	1.6	—	?	2.49	Lidström et al. (1996a)
CePd <sub>2</sub> Sn <sub>2</sub>	complex	0.50	—	?	2.50	Lidström et al. (1996a)
CePt <sub>2</sub> Sn <sub>2</sub>	3.5	0.88?	—	?	2.59	Luke et al. (1995, 1997a) Lidström et al. (1996a)
CePd <sub>2</sub> Al <sub>3</sub>	0.34	≤2.8	—	0.47	2.37	Mentink et al. (1994a,b)
CeRh <sub>3</sub> B <sub>2</sub>	0.020	115F	—	0.4	1.0?	Cooke et al. (1996)
Ce <sub>3</sub> Au <sub>3</sub> Sb <sub>4</sub>	2.5	?	—	?	2.45	Amato (1995) Amato et al. (1997b)
Ce <sub>7</sub> Ni <sub>3</sub> <sup>i</sup>	~1.5	1.8	—	?	~2.6 <sup>j</sup>	Takabatake et al. (1998b)

continued on next page

Table 9, notes

- <sup>a</sup> For Cerium metal  $\gamma = 0.013 \text{ J}/(\text{mol K}^2)$ ; the free-ion moment of  $\text{Ce}^{3+}$  is  $2.14\mu_B$  and  $\mu_{\text{Curie}} = 2.54\mu_B$ .
- <sup>b</sup>  $T_N$  is the Néel temperature except for  $\text{CePdSb}$  and  $\text{CeRh}_3\text{B}_2$ , where F indicates a ferromagnetic Curie temperature.
- <sup>c</sup>  $T_c$  is the superconducting transition temperature.
- <sup>d</sup> See sect. 9.2.
- <sup>e</sup> See sect. 5.2.1.
- <sup>f</sup> See sect. 5.3.
- <sup>g</sup> Several transitions into different AFM structures follow.
- <sup>h</sup> Not truly a heavy-fermion system but used as endpoint in series of pseudo-ternary compounds.
- <sup>i</sup> See sect. 9.4.
- <sup>j</sup> Two different magnetic Ce sites with 2.61 and  $2.52\mu_B$ .

It is impossible to review the complete sweep of theory, nor all the observed HF properties and the general experimental literature in this review. We refer the reader to the numerous publications available on those subjects (e.g., Stewart 1984, Kasuya and Saso 1985, P.A. Lee et al. 1986, Ott 1987, Fulde et al. 1988, Grewe and Steglich 1991, Aeppli and Fisk 1992, Loewenhaupt and Fischer 1993, Hewson 1993, Steglich et al. 1994, Wachter 1994, Aeppli and Broholm 1994, Nieuwenhuys 1995, Fulde 1997). On the whole, we will not even be able to connect on a broad basis the μSR results with other measurements on the same material, which are often contradictory in themselves. One problem is, the HF ground state is often formed as the result of a rather intricate balance of various competing interactions, which makes it highly susceptible to variations in sample properties such as purity, internal stress, *etc.* Reproducibility is a problem and, strictly speaking, μSR spectroscopy should be performed on the *same* sample as the related measurements of other type. This, unfortunately, is too seldom the case. We shall sometimes be limited describing and explaining the μSR results on their own merit.

Without going into details of theory one may use the following basic concept of heavy-fermion behavior, in particular with respect to their magnetic properties. HF compounds are three dimensional intermetallic compounds or alloys with f transition ions in *high* concentration. This lattice of f ions is imbedded in the Fermi sea of (s, p, d) conduction electrons. Each material possesses a characteristic temperature  $T^*$ , called the “Kondo lattice temperature”. Far above  $T^*$ , the HF compound behaves like a normal lanthanide or actinide intermetallic, that is, like a free paramagnet with sizeable localized magnetic moments. Normal Curie(–Weiss) behavior is observed, the usual CEF influence being present where applicable. In this regime, coupling between f states and ce is negligible, save the RKKY interaction. This picture changes fundamentally below  $T^*$ . Then, the f–ce coupling becomes increasingly strong and the heavy charge carrier mass develops. The effective mass is proportional to the density of states (DOS) around the Fermi energy  $E_F$ , meaning that an extremely high DOS at  $E_F$  is one of the most characteristic features of HF materials. The strong correlations lead to the formation of a narrow resonance in the DOS at  $E_F$ . In this low-temperature regime one may describe the HF metal by a system of heavy itinerant electrons (fermions) generally treated within the framework of Fermi-

Table 10  
Uranium<sup>a</sup> heavy-fermion materials whose magnetism has been studied with  $\mu$ SR

Material	$\gamma$ (J/(mol K <sup>2</sup> ))	$T_N$ (K)	$T_c$ (K)	$\mu_{\text{ord}}$ ( $\mu_B$ )	$\mu_{\text{Curie}}$ ( $\mu_B$ )	$\mu$ SR references (selection)
(USb) <sup>b</sup>		247	–	2.85	3.64	Asch (1990) Asch et al. (1994)
(UAl <sub>2</sub> ) <sup>c</sup>	0.145	–	–	–	3.1	Kratzer et al. (1986)
UGe <sub>2</sub>	0.03	–	52	1.43		Yaouanc et al. (1999a)
(UIn <sub>3</sub> ) <sup>d</sup>	~0.05	88	–	1.0	3.6	Zwirner et al. (1993) Kratzer et al. (1994b, 1997b)
(USn <sub>3</sub> ) <sup>d</sup>	0.17	–	–	–	2.5	Zwirner et al. (1993) Kratzer et al. (1994b, 1997b)
UPt <sub>3</sub>	0.425	5	0.48	0.02	3.0	Dalmas de Réotier et al. (1995) Luke et al. (1993a,b) Broholm et al. (1990)
UCu <sub>5</sub>	0.086	15	–	1.55 ?	3.53	Barth et al. (1986b) Schenck et al. (1990b)
UCd <sub>11</sub>	0.25	5	–	<1.5	3.45	Barth et al. (1986c)
UBe <sub>13</sub> <sup>e</sup>	~0.8	–	0.87	–	3.5	Luke et al. (1991) Heffner et al. (1986)
U <sub>2</sub> Zn <sub>17</sub>	0.20	9.7	–	0.8	3.3	Barth et al. (1986b, 1989a) Schenck et al. (1992)
U <sub>14</sub> Au <sub>51</sub>	0.3	22	–	2.3, 1.5	3.3	Schenck et al. (1998a)
URu <sub>2</sub> Si <sub>2</sub>	0.065	17	1.3	0.03	3.51	Knetsch et al. (1993) MacLaughlin et al. (1988) Luke et al. (1994a)
URh <sub>2</sub> Ge <sub>2</sub>	0.305	–	–	–	2.98( $B \parallel c$ ) 1.25( $B \parallel a$ )	Nieuwenhuys et al. (1998)
UNi <sub>2</sub> Al <sub>3</sub>	0.12	4.6	~1	0.12	n/a	W.D. Wu et al. (1994b) Amato et al. (1992b)
UPd <sub>2</sub> Al <sub>3</sub>	<0.15	~14	~2	0.85	3.2	Feyerherm et al. (1994a,b) W.D. Wu et al. (1994b)
UNi <sub>4</sub> B	>0.4	20	–	2.2	2.9	Nieuwenhuys et al. (1995)

<sup>a</sup> For uranium metal  $\gamma = 0.012$  J/(mol K<sup>2</sup>); the free-ion moments of  $U^{3+}$  and  $U^{4+}$  are  $3.20\mu_B$  and  $3.27\mu_B$ , while the Curie law moments are near  $3.6\mu_B$  for both ions.

<sup>b</sup> See sect. 5.2.1.

<sup>c</sup> See sect. 5.3.

<sup>d</sup> See sect. 5.2.3.

<sup>e</sup> The pure material is nonmagnetic; magnetism is induced by doping with Th.

Table 11  
Other heavy-fermion materials that have been studied by μSR with respect to magnetism

Material	$\gamma$ (J/(mol K <sup>2</sup> ))	$T_N$ (K)	$T_c$ (K)	$\mu_{ord}$ ( $\mu_B$ )	$\mu_{Curie}$ ( $\mu_B$ )	μSR references
PrInAg <sub>2</sub>	6.5	—	—	—	3.63	MacLaughlin et al. (2000b)
Sm <sub>3</sub> Se <sub>4</sub>	0.79	—	—	—	?	Takagi et al. (1993b)
Sm <sub>3</sub> Te <sub>4</sub>	0.6	—	—	—	?	Amato et al. (1997b)
YbB <sub>12</sub> <sup>a</sup>	—	—	—	—	2.95	Yaouanc et al. (1997, 1999b)
YbBiPt	~8	0.4	—	0.1	—	Heffner et al. (1994) Amato et al. (1992c)
YbNiSn <sup>a</sup>	—	5.7F <sup>b</sup>	—	0.85	—	Bonville et al. (1997)
YbPdSb	3	~1(?)	—	—	~4	Bonville et al. (1997)
YbAuCu <sub>4</sub>	~0.2	0.6–1	—	1.45	4.4	Bonville et al. (1996)
Yb <sub>4</sub> As <sub>3</sub>	0.2	—	—	—	—	Amato et al. (1997b)
Yb <sub>2</sub> Cu <sub>9</sub>	0.6	—	—	—	4.22	Amato et al. (1998)

<sup>a</sup> See sect. 9.2.

<sup>b</sup> Curie temperature.

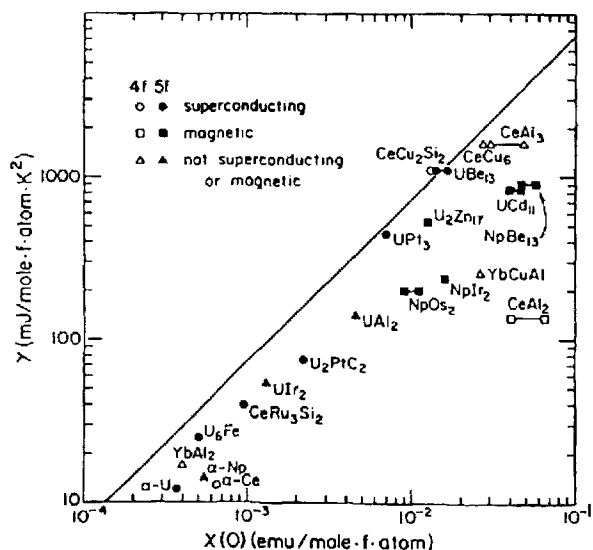


Fig. 103. Sommerfeld constant vs. susceptibility for various established heavy-fermion compounds. After P.A. Lee et al. (1986).

liquid theory, first developed by Landau (for details see the reviews on HF theory listed above).

Kondo (1964, 1969) showed that the behavior of a single magnetic impurity in a nonmagnetic metallic host at low temperatures cannot be understood in terms of the electronic states of the impurity ion alone, but must be treated as a many body phenomenon. Around the impurity a screening cloud of spin-polarized ce develops when

the temperature is lowered below a characteristic temperature  $T_K$  (the Kondo temperature) specific to the impurity system. This impurity–ce correlation tends to form a singlet ground state which, by definition, is nonmagnetic.

For a treatment of HF with their dense sub-lattice of magnetic ions this concept must be extended (the “Kondo lattice problem”) within the frame of Fermi-liquid theory. The then-resulting characteristic temperature  $T^*$  is in most cases comparable to  $T_K$  and again, for  $T < T^*$  the Kondo interaction works towards the establishment of a nonmagnetic singlet ground state. The now-relevant periodic structure in the position of magnetic ions leads at temperatures well below  $T^*$  to coherence effects (one may also define a separate Kondo coherence temperature  $T_{\text{coh}}$ ) creating a band of heavy quasiparticles with a width on the order of  $T^*$ , which is then thought to provide the charge carriers for HF superconductivity.

Magnetically, the HF materials feature the competing influence of the demagnetizing *on-site* Kondo interaction (whose strength can be expressed by  $kT^*$ ) and the magnetizing *intersite* RKKY interaction (of strength  $kT_{\text{RKKY}}$ ). It is this competition that makes the study of magnetic behavior of HF intermetallics such an interesting subject. Which of the two interactions dominates to generate either a magnetic ground state (often with significantly less than free-ion moments) or a nonmagnetic ground state depends on details of the correlated electron structure in the material.

The correlations between f and ce spins is generally described by a dimensionless coupling constant  $g$  that roughly reflects the degree of delocalization of the f electron states. One writes

$$g = N_{E_F} |\mathcal{J}|, \quad (77)$$

where  $N_{E_F}$  is the DOS of ce at  $E_F$ , and  $\mathcal{J}$  is a measure of the f-electron/conduction-band hybridization as commonly used in the Anderson impurity model (see, for example, Grewe and Steglich 1991). One finds

$$kT_{\text{RKKY}} \propto g^2 \quad \text{and} \quad kT^* \propto \exp\left(-\frac{1}{g}\right). \quad (78)$$

Clearly, for small values of  $g$  the RKKY interaction wins and a magnetic state results. Moving towards large values of  $g$  the Kondo compensation becomes more and more effective, leading to progressively weaker magnetism. One defines the critical coupling constant  $g_c$  where  $kT_{\text{RKKY}} = kT^*$ . This simple treatment is known as the “Kondo-necklace” model (Doniach 1977) and pictures of the type shown in fig. 104 are its common representation. It is a coarse, but highly useful approach. Especially in the case of actinide HF compounds, where more than one 5f electron is involved (typically  $5f^3$  and  $5f^2$  configurations) a single parameter  $g$  may not suffice. More advanced theories of the Kondo interactions like the “multi-channel” or “quadrupolar” Kondo interaction (D.L. Cox 1987, 1993) have been put forward and work successfully in certain cases.

The situation within this fundamental scenario can be summarized more generally by the graph shown in fig. 105. The range  $g \ll 1$  describes intermetallics with isolated

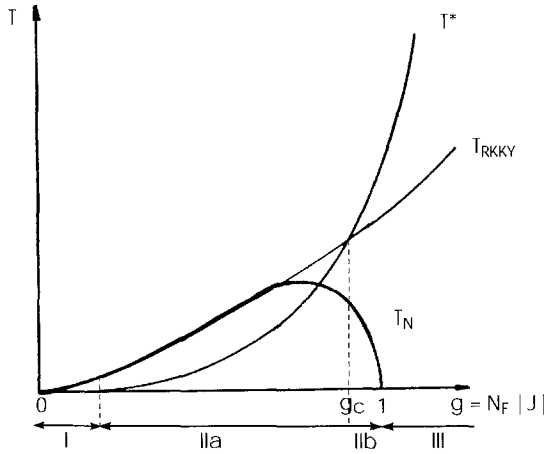


Fig. 104. The Kondo-necklace model: moving from the critical coupling constant  $g_c$  to the right strengthens the Kondo interaction ( $T^*$ ) and in consequence weakens magnetism. When moving to the left, the RKKY interaction ( $T_{RKKY}$ ) wins, leading to increasingly localized magnetism. The different regions, marked I, II and III, are explained in more detail in fig. 105. After Domiach (1977).

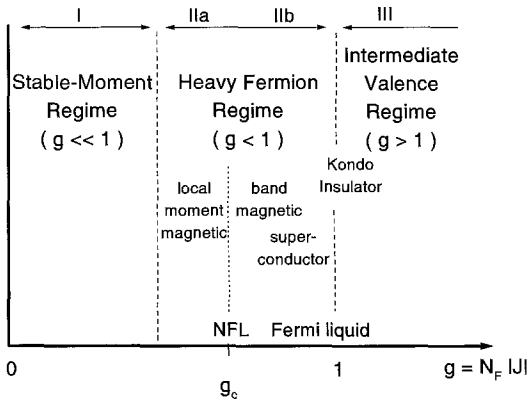


Fig. 105. Simple scheme of heavy-fermion properties (explanation in text). After Steglich et al. (1994).

f states, that is, normal stable moment f-electron magnetism. The region of somewhat larger  $g < 1$  is the HF regime. It is divided into local moment HF magnetism ( $g < g_c$ ) and (itinerant) HF band magnetism just above  $g_c$ . Further away from  $g_c$  towards  $g = 1$ , we enter the nonmagnetic regime. In the range of weak band magnetism and no magnetism one finds HF superconductivity, but not necessarily in all cases. This region is well described by Fermi-liquid theory. Slightly above  $g_c$  the Fermi-liquid description breaks down and novel phenomena appear, referred to as non-Fermi-liquid (NFL) behavior (see, for example, von Löhneysen 1996a,b, 1997) which we shall discuss later on in sect. 9.4. Finally, for  $g > 1$  one enters the intermediate valence (IV) regime. Around the borderline between HF and IV behavior one finds systems called either “Kondo semiconductors” or “Kondo semimetals” and in the extreme case “Kondo insulators”. They are characterized by the development of a hybridization gap or a pseudo-gap (which is a gap just marginally closed at  $E_F$ ) in the HF-DOS around  $E_F$  (see, for example, Fisk et al. 1995, 1996). These materials exhibit IV behavior at high temperatures as can be seen from lattice



Table 12  
Intermediate valence compounds studied by  $\mu$ SR

Material	$\gamma$ (J/(mol K <sup>2</sup> ))	$T_N$ (K)	$T_s^a$ (K)	$\mu_{\text{ord}}$ ( $\mu_B$ )	$\mu_{\text{Curie}}$ ( $\mu_B$ )	$\mu$ SR references
CeSn <sub>3</sub>	0.053	–	–	–	2.96	Wehr et al. (1982, 1984)
CePd <sub>3</sub>		–	–	–	2.5	Wehr et al. (1984)
Ce <sub>1-x</sub> Th <sub>x</sub>			~150			Wehr et al. (1981)
EuPdAs		~5	~170			Klauß et al. (1997a)
Sm <sub>0.9</sub> La <sub>0.1</sub> S						Schenck et al. (1997c)

<sup>a</sup>  $T_s$  is a crystallographic transition temperature connected to change of valence.

parameters or reduced magnetic moments. They often have comparatively low values of  $\gamma$  because the presence of a gap leads to low charge-carrier densities. The exact origin of the gap in Kondo semiconductors and insulators is still under debate, as is the precise role played by the IV properties. It appears to be a common, but not absolutely necessary ingredient. For example, YbB<sub>12</sub>, one of the most typical Kondo insulators, is of rather pure valence (Yb<sup>3+</sup>). Also, from what has been said one might naively get the impression that IV materials tend to be insulators. This is of course not the case. Many IV compounds are good metals.

A comprehensive review of  $\mu$ SR studies in HF materials has been published by Amato (1997). It discusses both the applications of  $\mu$ SR to HF superconductivity and to magnetism. As stated already, we restrict ourselves to the latter. The HF compounds to be discussed in this review are summarized in three tables. Not listed are compounds for which only recent short papers (i.e., conference abstracts or progress reports) are available. Furthermore, these tables list only the basic compounds and not the alloys derived from them, such as, for example, CeCu<sub>x</sub>Ni<sub>1-x</sub>Sn. We have subdivided into Ce, U and other compounds. The former two represent the majority of cases. The Laves-phase intermetallics CeAl<sub>2</sub> and CeRu<sub>2</sub> are borderline cases and the former has been discussed in the context of other R cubic Laves-phase materials in sect. 5.3. The cerium and uranium mono-chalcogenides like CeSb and USb are occasionally considered low-carrier-density HF compounds (Kasuya 1993, Suzuki 1993). Their value of  $\gamma$  is only moderately enhanced, but the carrier density is low, bringing ( $\gamma$ /carrier) into the HF regime. The situation is most pronounced for the Yb monopnictides (Suzuki 1993), but  $\mu$ SR data do not exist for them to our knowledge. We have elected to discuss the Ce and U monopnictides in sect. 5.2.1. Similarly, UIn<sub>3</sub>, and USn<sub>3</sub> have already been reviewed in sect. 5.2.3, although USn<sub>3</sub> in particular is often listed among HF materials. The compounds discussed elsewhere are put in brackets in the tables. U<sub>6</sub>Fe (Luke et al. 1990b) is believed to be an ordinary nonmagnetic BCS superconductor, and so will not be discussed.

We will proceed as follows. In the first subsection we present the  $\mu$ SR information on Kondo metals, *etc.*, since their behavior is somewhat different from typical HF compounds, which will be discussed in the next subsection. The sequence used is not based

on any physical properties such as band magnetism or local magnetism, since there are too many borderline or uncertain cases. We simply followed an alphabetical sequence as has been used in the tables. Ce compounds are first (see table 9), followed by uranium material (see table 10) and finally by compounds based on Sm and Yb (see table 12). The last two subsections then treat the NFL and IV cases (as listed in table 12). For both, but particularly for the latter, available  $\mu$ SR data are quite limited. Some IV materials can also be classified as low-carrier-density HF compounds and thus have been discussed in earlier sections. In general, it is not always easy to assign a compound to a certain category. Some arbitrary choices had to be made.

## 9.2. *Kondo metals, semimetals and insulators*

The distinction between Kondo metals, etc. and HF systems is fuzzy at best. As pointed out, the Kondo interaction is, among others, a basic ingredient of HF behavior. In a Kondo-lattice material one observes the effects of the Kondo interaction, for example on the magnetic properties, but very heavy quasiparticles are not formed and in consequence, the Sommerfeld constant is only slightly enhanced. That at least is the basis for a distinction we shall adopt. The hybridization between 4f and conduction electrons can lead to a hybridization gap in the density of states at the Fermi surface. The exact mechanism of gap formation is still under debate and also may vary from compound to compound. If a gap is present, one leaves the realm of Kondo metals and has, depending on the form of the gap (e.g., whether it is open in all crystallographic directions) and on its width, either a Kondo semimetal, semiconductor or insulator. The latter are certainly the most challenging class of Kondo compounds to understand.

In reviews on Kondo insulators, Fisk et al. (1995, 1996) list eleven compounds as possible candidates:

(1) CeNiSn, (2) CeRhSb, (3) Ce<sub>3</sub>Bi<sub>4</sub>Pt<sub>3</sub>, (4) Ce<sub>3</sub>Sb<sub>4</sub>Pt<sub>3</sub>, (5) Ce<sub>3</sub>Fe<sub>4</sub>P<sub>12</sub>, (6) SmB<sub>6</sub>, (7) SmS, (8) TmSe, (9) TmTe, (10) YbB<sub>12</sub>, (11) FeSi.

A recent addition is CeRhAs (Yoshii et al. 1996), which is closely related to CeRhSb. All these materials contain 4f elements that are known candidates for intermediate valence behavior and at high temperatures one finds evidence for such an electronic state in the majority of cases. Published  $\mu$ SR data exist mainly for the first two cases and also, to a more limited extent, for (10). The latter is, together with (3) and (6), a prime example of a typical Kondo insulator (Kasuya 1996), while (1) and (2) have always been classified as Kondo semiconductors instead. As better samples have become available, it has been realized that they are now better described as Kondo semimetals (Takabatake et al. 1996, 1998a). More details are provided below.

### 9.2.1. *CeTSn (T = 3d transition element)*

The series CeTSn together with CeRhSb and the related pseudo-ternary compounds crystallize in a rather complex orthorhombic structure with the non-centrosymmetric space group Pn2<sub>1</sub>a (Higashi et al. 1993). This structure, which is shown in fig. 106 (left), is closely related to the  $\epsilon$ -TiNiSi structure. It forms puckered hexagonal Ni–Sn–Ni rings

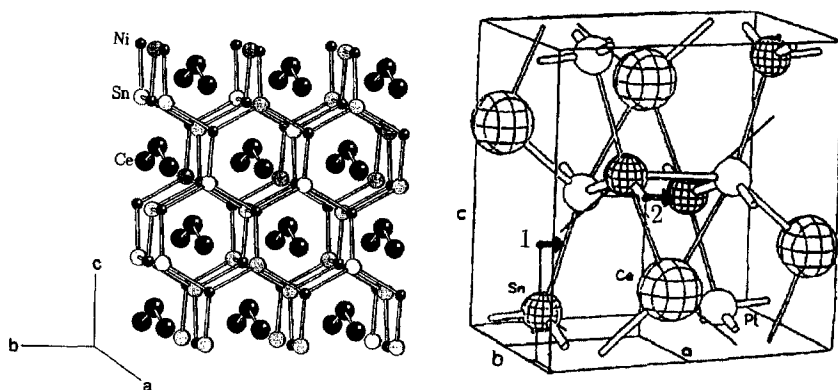


Fig. 106. Left: Crystal structure of CeTSn (after Higashi et al. 1993). Right: Calculated muon stopping sites (labeled 1 and 2) in CeTSn.

Table 13  
Lattice parameters of CeNiSn and related compounds

Compound	$a$ (Å)	$b$ (Å)	$c$ (Å)	$V$ (Å <sup>3</sup> )	$\Delta V$ (%)	$c/a$
CeNiSn	7.542	4.601	7.617	264.3	±0	1.010
Ce <sub>0.85</sub> La <sub>0.15</sub> NiSn	7.570	4.610	7.620	265.9	+0.6	1.006
CeCu <sub>0.1</sub> Ni <sub>0.9</sub> Sn <sup>a</sup>	7.562	4.621	7.637	266.9	+1	1.010
CePt <sub>0.12</sub> Ni <sub>0.88</sub> Sn	7.535	4.605	7.662	265.9	+0.6	1.017
CePt <sub>0.2</sub> Ni <sub>0.8</sub> Sn	7.526	4.607	7.697	266.9	+1	1.022
CePtSn	7.463	4.628	8.016	276.9	+5	1.074
CePdSn	7.536	4.704	7.965	282.4	+7	1.056
CeRhSb	7.420	4.619	7.859	269.4	+2	1.059
Ce <sub>0.9</sub> La <sub>0.1</sub> RhSb	7.430	4.626	7.869	270.5	+2.3	1.059

<sup>a</sup> The lattice parameters for the CeCu<sub>x</sub>Ni<sub>1-x</sub>Sn series increase linearly with  $x$  up to  $x \approx 0.5$ . Then another structure is formed.

in the  $b$ - $c$  plane with one Ce atom above and below slightly off ring center. The off-center position is reversed above and below the Ni-Sn-Ni rings. Hence the Ce atoms form zig-zag chains along the  $a$  axis. Each Ce atom has 3 Ni and 1 Sn atom as nearest neighbor within a distance of  $\sim 3.2$  Å. This is much shorter than the separation between Ce atoms (3.847 Å). The unit cell contains four formula units. The low crystal symmetry leads to pronounced anisotropies in the physical properties of single-crystal specimens, which are readily available.

Characteristic for the series, including pseudo-ternary compounds, is the change in unit cell volume when varying the T elements. Some pertinent data are summarized in table 13. This change in unit cell volume has strong effects on the electronic structure of these intermetallics. For example, CeNiSn does not order magnetically, as proven in particular by  $\mu$ SR data, while CePtSn and CePdSn show AFM order with transition temperatures

around 7 K and ordered moments around  $0.6\mu_B$ . It is argued that the volume expansion from T = Ni to T = Pt, Pd reduces the hybridization of the 4f states with the conduction electrons and thus reduces the Kondo interaction and allows the formation of local magnetic 4f moments. The weakening of hybridization is supported by photoemission data (Nohara et al. 1993).

Calculations to determine interstitial positions with lowest effective potential were performed to gain insight into possible muon stopping sites. For this, a computer program was employed (Noakes et al. 1987), which attaches hard core radii to all ions in a cluster of about 500 in the appropriate crystal structure and then looks for an interstitial site with minimal potential within the central unit cell of the cluster. For the  $Pn2_1a$  structure two possible sites were found (see fig. 106, right). Site "1" is the optimal interstitial hole. It is located in the center of a pentagon of one Ce, two Sn and two T ions in the  $z = 1/4$  ionic plane. An attempt was made to verify this choice by a measurement of the angular dependence of the muon depolarization rate for a single crystal of CePtSn well inside the paramagnetic regime. There depolarization is essentially caused by nuclear dipolar fields from  $^{195}\text{Pt}$ , the influence of electronic dipolar moments on Ce are in essence fully motionally narrowed. The low crystal symmetry makes changes of relaxation rate with crystal orientation quite small and difficult to resolve. The data (Burghart 1994) were in agreement with position "1" determined by the computer program. Most important however, is the fact that the muon is stationary at low temperatures. Data on CeRhSb suggest that the muon becomes mobile only above  $\sim 200$  K. The main interest in the study of the CeTSn and related compounds concentrates on the low-temperature regime below a few Kelvin.

9.2.1.1. *CeNiSn*. Due to its quite unusual properties, this Kondo material has been the subject of an intense research effort for over a decade, using practically all relevant physical methods. Unfortunately, transport, caloric, and bulk magnetic data are all quite sensitive to impurities. Consequently, the picture regarding the electronic structure of CeNiSn changed over the years. The original work has been reviewed extensively by Takabatake and Fujii (1993). The more recent results, based on samples of improved quality are described in Takabatake et al. (1996).

The susceptibility of CeNiSn follows a Curie-Weiss law with  $\mu_{\text{Curie}} = 2.86\mu_B$  at high temperatures. This value is larger than the free  $\text{Ce}^{3+}$  moment which, together with neutron scattering data, is taken as evidence for IV behavior (Skolozdra et al. 1984). At low temperatures the moment is reduced by Kondo interaction which is characterized by  $T^* \approx 25$  K. The original electrical resistivity data revealed semiconducting properties with a rather narrow gap ( $\sim 5$  meV) in the DOS of a heavy-fermion-like hybridized (ce-4f)-band at  $E_F$ . NMR measurements (Kyogaku et al. 1990) showed that there is a "V"-shaped pseudo-gap centered at  $E_F$ . The value of width given then refers to the HWHM. These features caused CeNiSn to be classified as a "Kondo semiconductor" which leads for  $T \rightarrow 0$  to a "Kondo insulator". Compared to other, well-established Kondo insulators such as  $\text{SmB}_6$ , the (pseudo-) gap in CeNiSn is narrower by an order of magnitude. A detailed discussion of differences in gap-related properties between CeNiSn

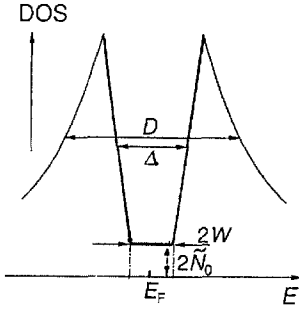


Fig. 107. Schematic representation of the electronic density of states in CeNiSn around the Fermi energy. Typical values (in K) are  $D = 58$ ,  $\Delta = 23$ ,  $W = 2$  (Izawa et al. 1998). The height  $\tilde{N}_0$  is strongly dependent on impurity content.

and more conventional Kondo semiconductors (and insulators) is presented by Takabatake et al. (1998a), which already takes into account the new results on samples of greatly improved quality.

The improved single-crystalline samples have been purified by solid state transport techniques and had an impurity content less than 0.1% (in contrast to 4% impurity of earlier materials) as well as decreased strains and defects (see Nakamoto et al. 1995 for details). They showed metallic behavior at low temperatures (albeit with a fairly high residual resistivity) and it is concluded that the pseudo-gap is strongly anisotropic and closed along the  $a$ -axis. NMR on the new samples showed at low temperatures a spin-lattice relaxation rate of the Korringa type rather than the gapped behavior previously observed (H. Nakamura et al. 1994b). Hall measurements and thermopower data made clear that a comparatively low carrier density is present. In consequence, a re-classification of CeNiSn as a “Kondo semimetal” is most appropriate. Under these circumstances, a Sommerfeld constant of  $40 \text{ mJ}/(\text{mol K}^2)$  still means that a substantial heavy quasiparticle state is formed at low temperatures.

Kagan et al. (1993) proposed the rather general idea that the most characteristic feature of CeNiSn is the presence of a low-lying CEF level embedded inside the HF band. The hybridization of the CEF state with the continuous spectrum of HF excitations allows one to understand the anomalous temperature dependences of various parameters of CeNiSn, as well as the restoration of normal HF behavior in the presence of a strong magnetic field (Takabatake et al. 1992a). Simple arguments led to the conclusion that the hybridization also produces an only partially open gap in momentum space (a pseudo-gap). Under these aspects the coexistence of normal HF behavior at very low temperatures and pseudo-gap properties at somewhat higher temperatures are a natural outcome.

Izawa et al. (1996) explained the field dependence of specific heat with the help of a modified pseudo-gap to which a residual flat DOS at  $E_F$  had been added (see fig. 107). This model also makes possible an explanation of the resistivity data for CeNiSn materials of different impurity content (Ikeda and Miyake 1996). It was found that the DOS inside the gap at  $E_F$  increases with impurity content. Furthermore, gap anisotropy could be derived from the  $k$ -dependence of the  $(ce-4f)$ -hybridization matrix element.

Neutron scattering experiments (Mason et al. 1992, Kadowaki et al. 1994a) demonstrated the formation of a gap in the magnetic excitation spectrum well below  $T^*$ . Hence,

CeNiSn is not only characterized by the pseudo-gap in the electronic DOS (charge gap) but also by a spin gap. The spin gap is highly anisotropic as well and well defined only at certain  $\mathbf{q}$  values in reciprocal space. A clear connection between those two gaps has not been established and is questionable theoretically. Furthermore, the neutron excitation spectra show pronounced peaks at 4 meV and 2 meV. The former appears at  $\mathbf{q} = (q_a, \frac{1}{2} + n, q_c)$  where  $q_a$  and  $q_c$  are arbitrary and  $n$  is an integer. This implies that the corresponding dynamical AFM correlation is quasi-one-dimensional along the  $b$ -axis and mainly polarized along the  $a$ -axis. It is interesting to note that  $\mathbf{q} = (0, \frac{1}{2}, 0)$  is close to the modulation vector of the AFM spin structure in CePtSn and CePdSn. The 2 meV excitation corresponds to Ising-like AFM correlations around  $\mathbf{q} = (001)$  and has three-dimensional character.

It is established especially by  $\mu$ SR data down to 11 mK that CeNiSn does not enter a magnetically ordered or spin frozen state. Recently, however, Umeo et al. (1999) have shown that the application of uniaxial pressure  $P$  of only  $\sim 1.5$  kbar induces magnetic order with a rather high transition temperature ( $\sim 4$  K) if  $P \parallel b$  or  $c$ , but not if  $P \parallel a$ . The authors tentatively explain this observation as due to the destruction of the quasi-trigonal symmetry of the Ce ions in CeNiSn. This symmetry is considered a prerequisite for the formation of the pseudo-gapped state. While pressure applied along the  $b$  or  $c$  direction destroys trigonal symmetry, pressure along  $a$  does not.

$\mu$ SR measurements were carried out in ZF and TF down to ultra-low temperatures (Kratzer et al. 1992, Kalvius et al. 1994, 1995c) with samples (similar to sample #2 in Takabatake et al. 1996) consisting of a mosaic of oriented single-crystalline platelets. In the TF geometry used (employing a spin rotator) the applied field was oriented along the  $a$ -axis with the initial muon spin direction perpendicular to it. The observed relaxation rates were quite small and are more easily separated from various background contributions under TF conditions. (In a dilution refrigerator, some muons are stopped at various places outside the sample volume, including at least several of: the sample holder, cryostat windows, radiation shields and the cold finger. This adds up to a complex background signal). The corrections applied are described in Kratzer et al. (1992). They affect the absolute value of the relaxation rate somewhat, but little of its temperature dependence. The smallness of relaxation rates observed did not allow the determination of the exact shape of the relaxation function. An exponential decay of muon spin polarization was fitted to the data throughout.

Typical sets of data are shown in fig. 108. They clearly demonstrate the development of spin correlations in the range of some Kelvins and below, which leads to slowing down of spin fluctuations and hence an increase of  $\lambda$ . They further show that the spin fluctuations must be strongly anisotropic. The marked dependence on the strength of the TF remains unexplained, but the muon Knight shift also exhibits some unusual field dependence (see fig. 110 and text below). The absence of spontaneous spin precession or of a sudden rise in relaxation rate excludes the formation of an (ordered) quasistatic spin structure down to 11 mK which is the lowest temperature measured (see fig. 108, right). Below  $\sim 100$  mK the relaxation rate hardly changes. A temperature-independent limit of spin fluctuations has been reached. LF measurements in this temperature range (Kalvius et al. 1995c)

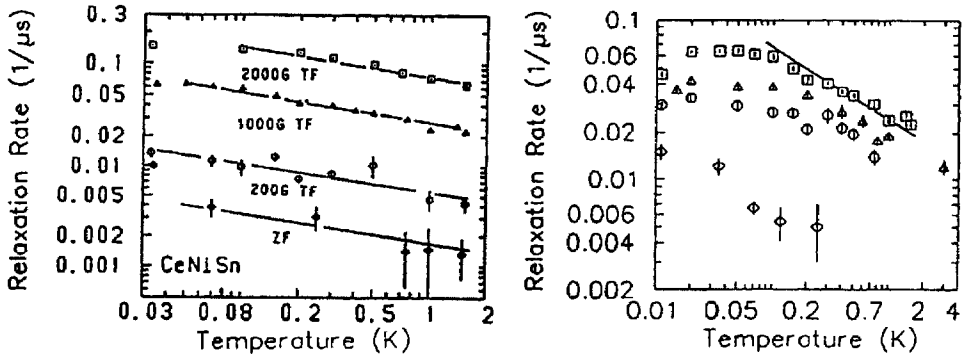


Fig. 108. Muon-spin relaxation in CeNiSn at very low temperatures. Left: Temperature dependence of relaxation rate in ZF and various TF for a single-crystalline sample with the  $a$ -axis parallel to the  $\mu$ -beam. Right: TF = 1 kG data for the  $a$ -axis (squares) and the  $c$ -axis parallel to the  $\mu$ -beam (circles). Also shown are corresponding data for polycrystalline CeNiSn (triangles) and  $\text{La}_{0.15}\text{Ce}_{0.85}\text{NiSn}$  (diamonds). The lines are guides to the eye (but see text). From Kalvius et al. (1994, 1995c).

showed that a field of  $\sim 500$  G is needed to reduce the relaxation rate  $\lambda$  by 50% from its ZF value. Using eq. (37), the relaxation time of the fluctuating electronic spin system is  $\tau_S \approx 40$  MHz. It is this persistence of dynamics in the spin correlations which keeps the material in the paramagnetic regime.

At  $T \geq 5$  K, the muon spin relaxation rate becomes unmeasurably small (i.e.,  $\lambda \leq 0.004 \mu\text{s}^{-1}$ ). Taking the high-temperature value of the moment on  $\text{Ce}^{3+}$  one arrives at a spin fluctuation rate in excess of  $10^{14}$  Hz. In particular, no effect on  $\lambda$  could be seen around 10 K where susceptibility reaches a peak. This definitely proves that this peak is not connected to any magnetic transition, but signals the onset of the AFM spin correlations seen in the neutron measurements mentioned.  $\mu\text{SR}$ , due to its different time window, responds only when the correlations have caused a substantial slowing down of spin fluctuations (i.e., at much lower temperatures).

$\mu\text{SR}$  Knight shift measurements were also carried out. The expected behavior for a free paramagnet (i.e.,  $\Delta f_{\mu} \propto B_{\text{app}}/T$ ; see, for example, fig. 18) is only found at  $T \geq 0.2$  K. Below this, deviations are substantial. Figure 110 shows typical data together with a fit to a model to be discussed below.

Returning to the low-temperature results on relaxation rates, one may ask whether the observed muon spin depolarization is due to a few large moments on impurities (of  $\text{Ce}^{3+}$  free ion size) or to small moments on *all* Ce ions in the sample. Monte Carlo calculations of spectral shape established a roughly linear dependence between the size and concentration of moments (see Kalvius et al. 1995c). The observed values of  $\lambda$  are compatible with either a concentration of  $\sim 5\%$  of large moment ( $\sim 2\mu_B$ ) impurities (which must be evenly distributed throughout the sample) or a moment on the order of  $5 \times 10^{-3} \mu_B$  on all Ce atoms. When purified (metallic) CeNiSn became available, a comparison of the relaxation behavior at low temperatures relative to the impure material was performed (Kalvius et al. 1997a, Kratzer et al. 1997a). The result, together with

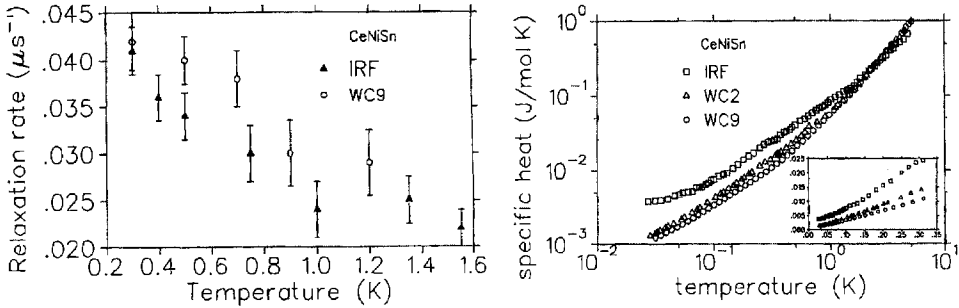


Fig. 109. Comparison of data for samples of CeNiSn with different impurity content: the temperature dependence of the transverse-field (1 kG) μSR relaxation rate (left) and of the specific heat (right) is shown for a sample having high impurity content (IRF, exhibiting semiconducting behavior in electrical resistivity) and two samples with low content (WC2 and WC9, exhibiting semimetallic behavior). The inset expands the low-temperature region of the specific heat data. After Kratzer et al. (1997a).

specific heat data taken on the same samples, is shown in fig. 109. Pure and impure samples show no difference in μSR relaxation rate, while considerable differences exist in the low-temperature dependence of specific heat. Hence, the filling of the pseudo(charge)-gap at  $E_F$  by localized impurity states (as discussed earlier) has no influence on the μSR spectral response. In fact, measurements on CePt<sub>0.12</sub>Ni<sub>0.88</sub>Sn (to be presented further below) demonstrate that even full gap closure does not affect the μSR characteristics of the Ce spin system at low temperatures. Therefore, the measured relaxation rates and their temperature and field dependences directly reflect intrinsic properties of the HF state of CeNiSn.

A simple model to explain the μSR response in CeNiSn has been offered by Kagan and Kalvius (1995). They propose that the features seen by μSR are the manifestation of a very small difference in the ground-state energy of the spin-liquid phase and a magnetically ordered phase. This results in quasicritical behavior and is equivalent to the appearance of an effective Curie temperature, which is located formally in the negative temperature region ( $-T_*$ ). Within the mean-field approximation (MFA) and for small values of  $T_*$  one finds for the static susceptibility:

$$\chi(T, B_{app}) \propto \frac{A}{(T + T_*) + C \cdot T_*^{1/3} (\mu_B B_{app})^{2/3}}, \quad (79)$$

where  $A$  is related to the Curie constant and  $C$  is needed to keep the proper dimension. The muon spin depolarization rate  $\lambda$  in the motionally narrowed regime is proportional to the electronic spin fluctuation time  $\tau_S$  (for weak non-uniform demagnetizing fields and in the absence of any dipole interaction with surrounding nuclei, as is the case in CeNiSn). The stationary muon senses local spin fluctuations and  $\tau_S$  is given by the decay in time of the spin correlation function  $\langle S^i(R=0, t) \cdot S^i(R=0, 0) \rangle$ . Within the MFA the rate  $\lambda$  can be obtained *via* the  $(\mathbf{k}, \omega)$  Fourier transform of the general magnetic susceptibility (Landau and Lifshitz 1958), resulting in  $\lambda \propto \tau_S \propto \sqrt{\chi(T)}$ . Using this approach resulted



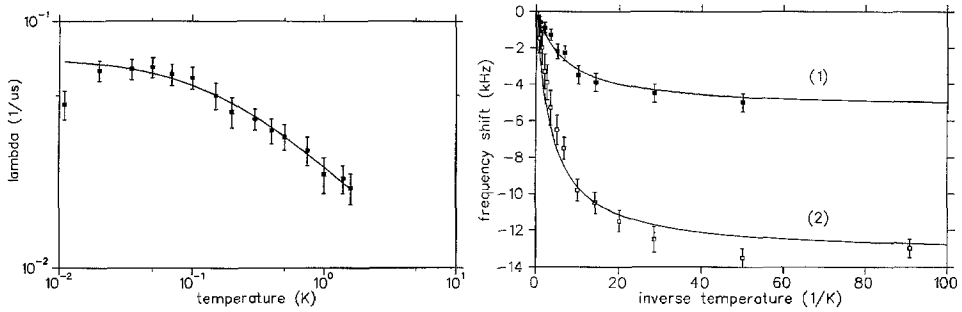


Fig. 110. Fits to some of the low-temperature  $\mu\text{SR}$  results in CeNiSn based on the model of quasicritical behavior (see text). Left: The transverse field (TF=1 kG) relaxation rate for  $a \parallel S_\mu$ . Right: The muon Knight shift in TF=0.2 (labeled 1) and 1 kG (labeled 2). After Kagan and Kalvius (1995).

in the quite satisfactory fit to  $\lambda$  shown in fig. 110 (left). It returned  $T_* = -0.15$  K. The smallness of  $T_*$ , which reflects the minute energy difference between the spin-liquid and the magnetic states, must be emphasized. It justifies in retrospect the quasicritical approach within the MFA. The muon Knight shift can be defined as  $K_\mu \propto B_{\text{app}} \chi(T)$ . Employing eq. (79), together with the values for  $T_*$  and  $A$  as obtained from the fit to  $\lambda$  also explains the temperature dependence of  $K_\mu$  quite well (fig. 110, right). The field dependence of  $K_\mu$ , however, is not so well reproduced (see Kagan and Kalvius 1995). Equation (79) predicts a  $B_{\text{app}}^{1/3}$  behavior which at least results in a strong dependence on field for small field values and a comparatively weak dependence above  $\sim 1$  kG. Clearly, the quasicritical picture discussed describes only the basic overall features, not the more intricate details.

The model by Kagan and Kalvius (1995) has been challenged by Dalmas de Réotier et al. (1996) in reference to a theoretical paper by D.L. Cox et al. (1985) which discusses the temperature dependence of the spin fluctuation rate for a system of independent Kondo ions above their characteristic temperature  $T_K$  (see also the review of  $\mu\text{SR}$  data on YbAuCu<sub>4</sub> in sect. 9.3.3). From the model by D.L. Cox et al. (1985) one derives a  $1/\sqrt{T}$  law for  $\lambda(T)$ , which indeed corresponds to the experimental result by Kalvius et al. (1994, 1995c), shown as a solid line in fig. 108 (right). This interpretation, however, is not free of problems, since it leads to an extremely low  $T_K \leq 0.1$  K and neglects all influences of the CEF, meaning that the CEF splitting energy must be equally small. Also, it provides no prediction about the Knight shift.

A brief report on an independent  $\mu\text{SR}$  measurement in ZF and LF on a CeNiSn single crystal ( $S_\mu \parallel a$ ) of different origin has been given recently (Yaouanc et al. 2000a). Using the ISIS pulsed beam facility it followed the decrease of relaxation rate with increasing temperatures up to  $\sim 5$  K. It found somewhat lower rates than Kalvius et al. (1994, 1995c) and significantly slower spin fluctuation rates (at 45 mK) from LF decoupling. Whether this reflects a sample dependence is an open question. According to the model of Kagan and Kalvius (1995) the fluctuation rate would critically depend on the effective (negative) Curie temperature  $T_*$  which could easily depend on sample

properties (reviewers' remark). Yaouanc et al. (1999b) also remark that they cannot distinguish whether the observed relaxation rate is of nuclear or electronic origin. The temperature dependence speaks against nuclear origin, since it is hard to see how a relaxation by nuclear fields is temperature dependent in the subkelvin regime in a material like CeNiSn. The data on isostructural CePtSn show that the muon is stationary to well above 100 K. The authors state in addition that their spectra can be better fitted by exponential relaxation than by a Kubo–Toyabe function, which also points towards relaxation by electronic moments (reviewers' remarks).

9.2.1.2. *CePtSn and CePdSn*. As mentioned, both these intermetallics order magnetically (they are Kondo antiferromagnets) due to the weakening of the (ce–4f)-hybridization caused by lattice expansion. For CePdSn, the transition temperature is  $T_N \approx 7$  K (Malik et al. 1989). From single-crystal neutron diffraction data, Kadowaki et al. (1994b) proposed a  $1k$  magnetic structure with an incommensurate modulation vector  $\mathbf{k} = (0, \frac{1}{2} - \delta, 0)$  ( $\delta \ll 1$ ) along the crystalline  $b$ -axis. Clearly, there is some connection to the 4 meV dynamic AFM spin correlations in CeNiSn at  $(k_a \frac{1}{2} k_c)$ , but this fact has not yet been followed up in detail. The mean ordered moment is  $\sim 0.8\mu_B$ , which represents a substantial reduction from the high-temperature Curie–Weiss moment (about the  $Ce^{3+}$  free ion moment of  $2.5\mu_B$ ). The Kondo interaction, whose strength ( $T^* \approx 10$  K) is of the same magnitude as  $T_{RKKY} \approx T_N$ , is primarily responsible.

ZF-μSR spectra for  $T < T_N$  on polycrystalline material (Kalvius et al. 1994, 1995b) revealed a rather well defined (i.e., comparatively weakly damped) spontaneous muon spin precession pattern containing two distinct frequencies (fig. 111, left). The variation of the precession frequencies with temperature is in agreement with a second-order phase transition at  $T_N$  (fig. 111, right). But why two well-defined frequencies are observed, when the spin structure is allegedly incommensurate, is a serious problem. We return to this issue below within the discussion of CePtSn.

The magnetic behavior of CePtSn is more complex.  $T_N$  is listed as 7.5 K (Sakurai et al. 1990). A second transition into another AFM state occurs at  $T_1 = 5$  K. Both transition temperatures appear to be somewhat sample dependent. The upper transition ( $T_N$ ) is considered to be second order, the lower ( $T_1$ ) of first order. Both AFM states are

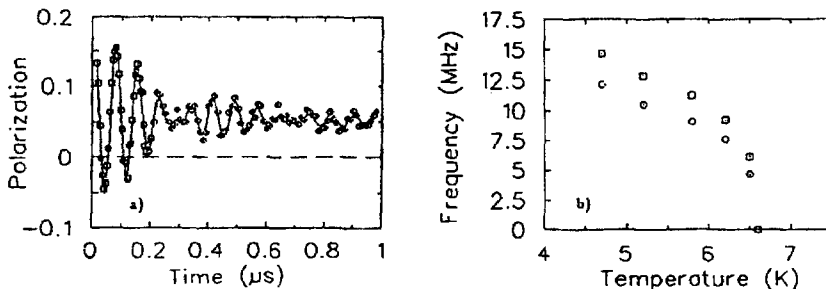


Fig. 111. μSR spectroscopy of CePdSn in the AFM regime: (a) ZF spectrum containing two spontaneous spin precession frequencies; (b) temperature dependence of those frequencies. After Kalvius et al. (1995c).

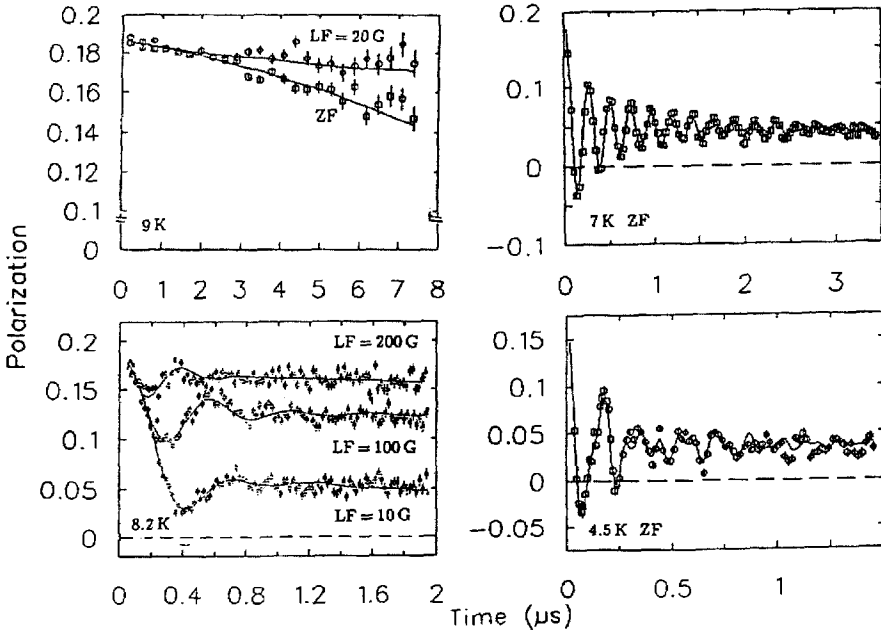


Fig. 112. ZF and LF spectra in CePtSn around the magnetic ordering temperatures: paramagnetic (top left), spin frozen (bottom left), intermediate-T AFM (top right), low-T AFM (bottom right). Note the different time scales. After Kalvius et al. (1994).

incommensurately modulated spin structures according to neutron studies by Kadowaki et al. (1993). The modulation vector changes at  $T_1$  (and differs also from that of CePdSn), but is always directed along the  $b$ -axis. The mean moment is around  $0.6\mu_B$  in the upper and around  $0.85\mu_B$  in the lower AFM state. Clearly, Kondo compensation is as effective here as in CePdSn.

The ZF- and LF- $\mu$ SR studies of Kalvius et al. (1995a,b) displayed rather unexpected behavior, especially in the vicinity of  $T_N$ . The measurements were carried out on polycrystalline materials, but a later check with a single-crystalline sample at selected temperatures showed no essential difference. A set of characteristic spectra is presented in fig. 112. At 9 K CePtSn is still paramagnetic. Depolarization is weak and, as demonstrated by the LF=20 G data, mainly caused by the action of the static nuclear dipole fields of  $^{195}\text{Pt}$ . The moments on Ce still fluctuate so rapidly that full motional narrowing is in effect. At 8.2 K the spectral shape has changed completely.  $\mu$ SR now sees a Gaussian Kubo–Toyabe relaxation function arising from *quasistatic randomly oriented electronic dipoles*. The width of the resulting field distribution is  $\sim 45$  G which leads to an estimate of  $\mu_{\text{Ce}} \approx 0.05\mu_B$ . At 7 K a spontaneous muon spin precession pattern is seen, signaling that CePtSn has now entered a long-range ordered AFM state. In contrast to CePdSn, the spin precession spectrum contains only a single frequency. Depolarization is even weaker than in CePdSn, meaning that the muon sees an even more narrowly distributed

distinct interstitial field. At 4.5 K (i.e., below  $T_1$ ) the spectral shape has changed once more. One still observes a spontaneous precession pattern, but it is more complex. The analysis shows that at least 3 different frequencies are present, having different amplitudes and now somewhat wider distributions.

The behavior seen around  $T_1$  is consistent with a first-order transition. The features around  $T_N$ , however, make this transition not a simple second-order case. The μSR data establish a precursor spin-glass-like magnetic state that persists for a range of about 1 K above  $T_N$ . It appears that the fluctuation rate of the paramagnetic spins suddenly slows down by orders of magnitude into the MHz range. The cause for this is not known. The depopulation of a CEF state is unlikely, since inelastic neutron scattering data (Kohgi et al. 1993) places the first excited CEF doublet at 23.6 meV. Magnetic frustration due to the near equality of  $T^*$  and  $T_{\text{RKKY}}$  is a possibility. In the case of the geometrically frustrated Laves phases of type  $\text{RMn}_2$  (see sect. 5.3), μSR sees a SRO precursor phase above the (first-order) Néel transition, but only part of the sample volume is involved. The paramagnetic to spin glass (around 8.7 K) and spin glass to AFM (around 7.5 K) transitions are not sharp, but smeared out over at least 0.3 K. These magnetic features observed by μSR also offer an explanation for the broad peak seen in specific heat around  $T_N$ , which is quite different in appearance from the much sharper peak at  $T_1$  (Takabatake et al. 1993).

The rather well-defined spin precession frequencies in CePdSn and CePtSn (especially the single frequency in the upper AFM state of CePtSn) are inconsistent with an incommensurately modulated spin structure. Dipolar sum calculations were carried out for the muon stopping site mentioned earlier and the spin structure of the upper AFM state of CePtSn as derived by Kadowaki et al. (1993), in order to elucidate the problem somewhat further (Kalvius et al. 1995b). The calculations generated four field distributions of the type discussed in sect. 3.7 (see eq. 51):

$$P_I(|\mathbf{B}_\mu|) = \frac{2}{\pi} \frac{B}{\sqrt{(B_{\text{max}}^2 - B^2)(B^2 - B_{\text{min}}^2)}}, \quad B_{\text{min}} < B < B_{\text{max}}. \quad (80)$$

They lead to Bessel function-type relaxation.  $B_{\text{min}}$  and  $B_{\text{max}}$  are roughly between 200 G and 1 kG. The upper field value ties in nicely with the observed precession frequency. Any simplification of those structures while retaining incommensurability can reduce the number of magnetic sites, but keeps the general form of the distribution. Only commensurate ordering produces a small number of isolated muon oscillation frequencies in the calculation, and only the simplest of those (ferromagnetic ordering in a plane, opposing spin directions in adjacent planes [ $\mathbf{k} = 1/2$ ]) produces a single precession frequency. Similar arguments should apply to the low-temperature spin structures of CePtSn and CePdSn, although no model predicting the precise set of observed multiple frequencies is available at this stage.

The neutron scattering observation of (long-range) magnetic incommensurability and the μSR observation of local magnetic commensuration are reconcilable in a spin-slip model, as has been developed for the magnetic ordering of holmium and erbium (see, for

example, Cowley and Bates 1988). In these metals, the long-range exchange interaction, favoring incommensurate helical or cycloidal ordering, must compete with single-ion CEF anisotropy that makes only a limited number of crystalline directions magnetically easy. This is incompatible with incommensurability: at times a compromise is reached in which the order is a locally commensurate helix or cycloid, but it is interrupted by spin-slip defects that make the larger-scale structure incommensurate. In CePtSn and CePdSn, substantial CEF splittings have been found (Kohgi et al. 1993), and the marked paramagnetic anisotropy caused by them has been observed (Takabatake et al. 1993). Kadowaki (1998) has re-analyzed the neutron diffraction data of CePtSn and CePdSn and deduced several possible spin-slip structures that can locally be extrapolated to a commensurate structure with  $k = 1/2$  along the  $b$ -axis. In turn, Noakes and Kalvius (2000) have shown by numerical modeling that, given a simple incommensurate ordering mechanism, represented by a spiraling effective field at the cerium sites, the known Ce crystalline electric field in CePtSn will generate that kind of spin-slip structure. Further numerical modeling shows that such CEF spin-slip structures generate magnetic field distributions at the muon sites with sharp peaks generally consistent with the coherent oscillations observed in the  $\mu$ SR data of CePtSn. CePdSn is likely to behave in a similar manner.

### 9.2.2. Pseudo-ternary compounds of type CeTSn

Contrasting the magnetic properties of CeNiSn to those of CePdSn and CePtSn demonstrates how long-range magnetic order can be induced by expansion of the lattice. As shown in table 13, one may achieve a controlled widening of the unit cell by forming pseudo-ternary compounds, that is, replacing either Ce or Ni by related elements. When Ce is replaced by La or Ni by Cu, however, a change in density of valence electrons occurs as well. It is of special interest to study those two effects in some detail and to determine their relative significance.

9.2.2.1.  $La_xCe_{1-x}NiSn$ . A theoretical treatment (Doniach and Fazekas 1992) suggested that doping a Kondo insulator with small amounts of La might produce a dilute heavy-hole gas. Hole-hole exchange coupling would then lead to an AFM ground state. Transverse field (TF = 1 kG) measurements were carried out for polycrystalline  $La_{0.15}Ce_{0.85}NiSn$ . Muon spin depolarization is very weak and could be resolved only for  $T < 0.3$  K. Figure 108 depicts the results in comparison with equivalent data on CeNiSn. The doping of CeNiSn with 15% La is considered optimal because at this concentration transport measurements indicate gap closure (Aliev et al. 1990). No spontaneous spin precession or even sudden increase of relaxation rate as indicators of AFM ordering were found down to 11 mK. Instead, a weakening of magnetic correlations with respect to pure CeNiSn was observed, as is typical for a R paramagnet diluted with La (Flaschin et al. 1996).

9.2.2.2.  $U_xCe_{1-x}NiSn$ . UNiSn is an AFM, but has a different crystal structure. Alloying CeNiSn with moderate amounts of U preserves the original orthorhombic structure.

Resistivity, magnetization and thermopower studies on  $U_xCe_{1-x}NiSn$  (Park et al. 1994a,b) showed that around  $x = 0.2$  the ground state of the system changes to a magnetic one, albeit a very weak one. ZF- and LF- $\mu$ SR studies were performed to elucidate the situation in more detail (Park et al. 1997b). Polycrystalline samples were used throughout. The temperature range was limited to  $T \geq 2$  K, i.e., data at ultra-low temperatures are not available.

No significant difference from pure CeNiSn was observed for  $x = 0.05$ , that is, depolarization was very weak and nearly temperature independent. At  $x = 0.1$  depolarization increased below 6 K, implying that spin correlations have increased and in turn the effect of electronic moments becomes observable. Also seen is a slight loss of signal amplitude at low temperatures, which means that a certain portion of the compound has left the paramagnetic regime. Since the measurements were done at the ISIS pulsed muon facility, even moderately fast depolarizing signals cannot be observed. Full amplitude could be restored with  $LF \leq 1$  kG. The probable situation is the partial formation of a spin-glass-like state with moments in the range of  $0.1\mu_B$  (from a comparison with the  $\mu$ SR results for the spin glass precursor state in CePtSn (fig. 112). Clearly, the Kubo–Toyabe relaxation would then be beyond the time resolution of the present study). The spectra were fitted to power-exponential relaxation but the power deviated little from one in this case. When  $x$  is increased to 0.2, all features just described become more enhanced. The amplitude of the paramagnetic signal decreases by 30% between 6 K and 2 K. The LF needed to restore full signal amplitude has increased to 1.5 kG. The power in the paramagnetic power-exponential relaxation varies from 1.6 at 50 K to 0.7 at 10 K as is often the case in compounds approaching a highly disordered state (see discussions in sect. 8). The temperature at which strong loss of amplitude is seen agrees with the onset of a magnetic state from bulk measurements.

In conclusion, the partial replacement of Ce by U leads to moment localization (in contrast to the replacement by La). The resulting magnetic behavior is strongly inhomogeneous. Only parts of the sample enter into a quasistatic (presumably spin frozen) magnetic state while the rest remains paramagnetic, though with enhanced spin correlations.

9.2.2.3. *CePt<sub>x</sub>Ni<sub>1-x</sub>Sn*. Specific heat measurements by Nishigori et al. (1993) show that  $C/T$  at low temperatures increases markedly with rising Pt content, suggesting the recovery of DOS at the Fermi level. Gap closure is achieved around  $x = 0.1$ . The increase of the magnetic part of  $C/T$  with  $x$  in CePt<sub>x</sub>Ni<sub>1-x</sub>Sn has been explained by the presence of isolated Kondo impurities having  $T_K = 25$  K. The crossover between the weakly paramagnetic Kondo semimetal CeNiSn and the Kondo AFM CePtSn in the alloy system CePt<sub>x</sub>Ni<sub>1-x</sub>Sn has been studied in detail by Adroja et al. (1996). Susceptibility data for  $1.0 \geq x \geq 0.7$  show the presence of the two magnetic transitions of CePtSn, nearly independent of concentration. At  $x = 0.5$  and 0.4 only a single transition is seen and for  $x \leq 0.3$  the compounds remain paramagnetic down to 2 K. The data could well be explained within the Kondo necklace model of competing Kondo and RKKY interactions. Also, the well-defined CEF excitations seen in CePtSn broaden out with

decreasing Pt content, leading continuously to the inelastic neutron spectrum of CeNiSn, which is devoid of distinct CEF features (Kohgi et al. 1992).

$\mu$ SR spectroscopy on  $\text{CePt}_x\text{Ni}_{1-x}\text{Sn}$  for  $x = 0.12$  and  $0.2$  has been reported by Flaschin et al. (1996) and Kalvius et al. (2000c). No difference in the temperature dependence of the muon spin relaxation in  $\text{CePt}_{0.12}\text{Ni}_{0.88}\text{Sn}$  and pure CeNiSn could be observed. This result has already been quoted as proof for the insensitivity of the  $\mu$ SR relaxation parameters to gap properties. It also demonstrates that the spin-lattice relaxation time  $T_1$  as it appears in  $\mu$ SR spectroscopy and which senses the temporal behavior of the interstitial dipolar field contains different information than  $T_1$  measured by ( $^{119}\text{Sn}$ ) NMR, which reflects the dynamics of the contact field at the nucleus.

Raising the Pt content to 20% still does not induce short- or long-range ordered magnetism. This agrees with the bulk measurements (Nishigori et al. 1993, Adroja et al. 1996) but extends the temperature range down to 40 mK. At 26% and 33% Pt a sudden rise in relaxation rate is seen around 1.5 K, respectively 2 K (Kalvius et al. 2000c and unpublished) signaling the onset of some kind of ordered magnetism or at least spin freezing. The spectral shape in both cases is a monotonic decay of muon spin relaxation of the type we shall discuss further below for the  $\text{CeCu}_x\text{Ni}_{1-x}\text{Sn}$  system. Also, the difference in critical concentration for the onset of magnetism is of importance (see fig. 114, left) as will be discussed below.

Longitudinal field measurements were performed for  $\text{CePt}_{0.2}\text{Ni}_{0.8}\text{Sn}$ . If we assume that the depolarization rate of  $\sim 0.07 \mu\text{s}^{-1}$  observed at 0.045 K in ZF is solely due to static interactions with surrounding electronic dipoles, then  $\text{LF} = 10$  G should suffice to suppress muon spin relaxation altogether. Actually, a longitudinal field of 35 G is needed to reduce the relaxation rate by 50%. This leads to  $1/\tau_S \approx 3$  MHz. The spin system remains dynamic, but its fluctuation frequency is reduced by roughly an order of magnitude when compared to pure CeNiSn. Clearly, doping with Pt moves CeNiSn towards static magnetism, but up to  $\sim 23\%$  Pt content, the lattice expansion is not enough to reduce (ce-4f)-hybridization sufficiently to have the RKKY interaction overcome the Kondo effect. The dynamic nature of the spin system persists (weakly) to the lowest temperatures.

**9.2.2.4.  $\text{CeCu}_x\text{Ni}_{1-x}\text{Sn}$ .** In general, the results of specific heat, bulk magnetic and electrical resistivity measurements (Takabatake et al. 1987, 1988) on  $\text{CeCu}_x\text{Ni}_{1-x}\text{Sn}$  are not fundamentally different from those in  $\text{CePt}_x\text{Ni}_{1-x}\text{Sn}$ . Gap closure occurs near  $x = 0.1$  and for  $x = 0.13$  the onset of long-range magnetic order at 2.5 K is inferred. The ordering temperature rises first sharply, then rather slowly with increasing Cu content and reaches 6 K for  $x = 0.5$ , the maximum concentration where the crystal structure of CeNiSn is still maintained. Pure CeCuSn is an antiferromagnet with rather complex magnetic properties. The results of a  $\mu$ SR study can be found in sect. 5.5.1.

Based on low-temperature specific heat data, Takabatake et al. (1988) suggest that a HF regime is formed after gap closure and before magnetic order sets in. The strong reduction of the paramagnetic Curie-Weiss temperature ( $\Theta_p = -187$  K) of CeNiSn with increasing Cu content is thought to reflect a decrease in Kondo temperature. The negative values of  $\Theta_p$  indicate AFM correlations throughout.

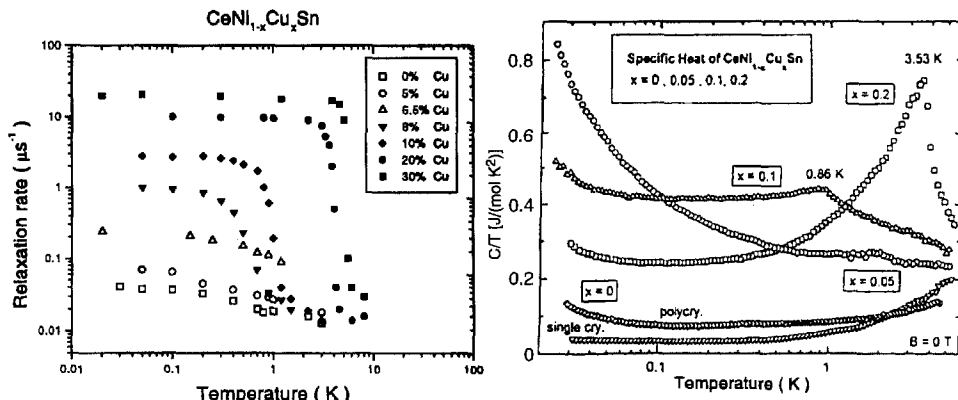


Fig. 113. Left: Summary of low-temperature muon-spin relaxation data in  $\text{CeCu}_x\text{Ni}_{1-x}\text{Sn}$  (for details see text). Right: Low-temperature specific heat divided by temperature for  $\text{CeCu}_x\text{Ni}_{1-x}\text{Sn}$ . The same samples were used in  $\mu\text{SR}$  and specific-heat measurements. After Kalvius et al. (1997b).

The ZF- and LF- $\mu\text{SR}$  data (Flaschin et al. 1996, Kalvius et al. 1997a,b, 2000c) for  $\text{CeCu}_x\text{Ni}_{1-x}\text{Sn}$  in the concentration range  $0 \leq x \leq 0.3$  provide a slightly different picture. One of the reasons is that these measurements extend to much lower temperatures than the original bulk data. Polycrystalline samples were mostly used. A summary of relaxation data is presented in fig. 113 (left). The shape of the temperature dependence of relaxation rate is distinctly different for  $x \leq 0.07$  when compared to  $x \geq 0.08$ . In the lower concentration range, only a moderate increase of relaxation rate relative to pure  $\text{CeNiSn}$  is seen, meaning that spin correlations are somewhat enhanced but the sample remains weakly paramagnetic down to lowest temperatures ( $\approx 30\text{mK}$ ). The situation is quite comparable to  $\text{CePt}_{0.2}\text{Ni}_{0.8}\text{Sn}$ . We shall briefly return to the  $x = 0.05$  case later on. In the higher concentration range, one finds that a sharp rise in relaxation rate is seen at a particular temperature  $T_M$  in all cases. As already stated, such behavior is considered the indicator for the development of a quasistatic magnetic state. In fact, LF data for  $T < T_M$  definitely establish the quasistatic nature of the electronic spin system ( $1/\tau_S < 1\text{MHz}$ ). The fact that  $\text{CeCu}_{0.08}\text{Ni}_{0.92}\text{Sn}$  orders magnetically is corroborated (including the transition temperature) by susceptibility measurements on a single-crystalline specimen (Vollmer et al. 2000).

A plot of magnetic transition temperatures  $T_M$  as extracted from the relaxation data (fig. 114, left) establishes  $x_{\text{cr}}^{\text{Cu}} \approx 0.07$  (corresponding to a volume increase of 7%) as the critical concentration for the onset of quasistatic magnetism in the case of doping  $\text{CeNiSn}$  with Cu. This result is in full agreement with NMR data (K. Nakamura et al. 1996) where the signal is lost because of extreme line broadening at about the same Cu concentration. In contrast, a roughly 23% replacement of Ni by Pt (corresponding to a volume increase of 12%) is needed to induce magnetism.

The salient result is that the filling of d-electron states is an equally important mechanism for inducing magnetism as the reduction of (ce-4f)-hybridization by volume



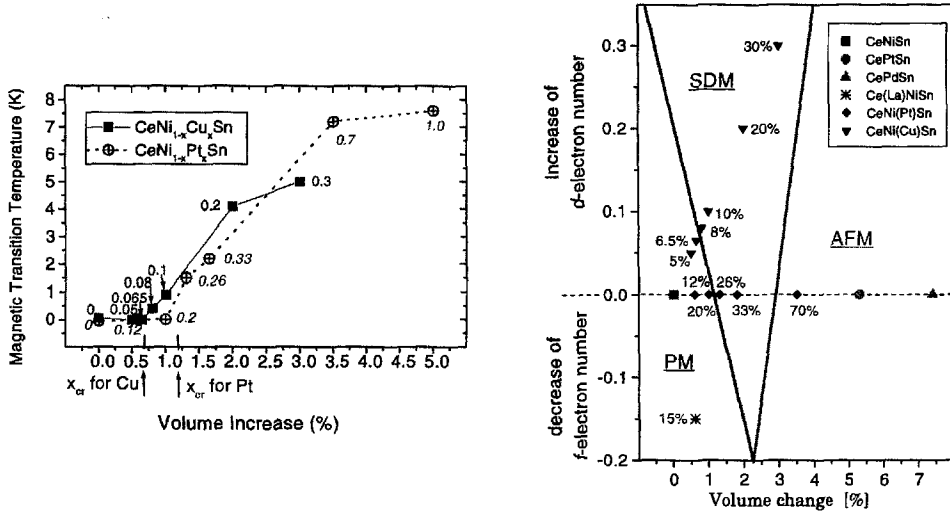


Fig. 114. Left: Variation of the magnetic transition temperature (temperature where the sharp rise in relaxation rate occurs) with volume increase in  $\text{CeCu}_x\text{Ni}_{1-x}\text{Sn}$  and  $\text{CePt}_x\text{Ni}_{1-x}\text{Sn}$ . The numbers at the data points indicate the values of  $x$  (italics refer the Pt series). The point for  $\text{CeNi}_{0.3}\text{Pt}_{0.7}\text{Sn}$  is from bulk data (Adroja et al. 1996). Right: Provisional magnetic phase diagram for the CeTSn system as derived from  $\mu\text{SR}$  results. AFM, antiferromagnetism; PM, paramagnetism; SDM, strongly disordered magnetism (spin-glass-like). After Kalvius et al. (2000c) and unpublished.

expansion. There is other evidence for the coupling of d states to magnetic properties of  $\text{CeNiSn}$ . A polarized neutron study (Hiess et al. 1997) of the magnetization density within the unit cell induced by an external field (4.6 T along the  $b$ -axis) revealed that some density is present also at the Ni site in pure  $\text{CeNiSn}$ . This implies that the Ni-3d band cannot be fully filled. This important result is further corroborated by photoemission studies on  $\text{CeNiSn}$  (Nohara et al. 1993) which show that the Ni-3d band is located close to  $E_F$  and hybridizes with the unoccupied Sn-5p states.

Spontaneous spin precession was not observed in any of the pseudo-ternary samples. Also, within experimental accuracy, no loss of signal amplitude was found when passing through  $T_M$ . Standard Gaussian Kubo–Toyabe relaxation is not seen either. This means that neither a simple spin-frozen state like the precursor state in  $\text{CePtSn}$  nor its long-range ordered AFM state is present. For  $x = 0.08$  and  $0.1$ , the  $\mu\text{SR}$  spectra for  $T < T_M$  show monotonic decrease of muon spin polarization to the asymptotic value of  $a_0(\infty) = a_0(0)/3$  (characteristic for static internal fields) with roughly Gaussian shape. For  $x = 0.2$  and  $0.3$  the decay of polarization at early times remains Gaussian, but the minimum (characteristic for a Gaussian Kubo–Toyabe function) is too shallow. The spectrum of  $\text{CeCu}_{0.2}\text{Ni}_{0.8}\text{Sn}$  at 80 mK has been used in sect. 8.2.3 as a pertinent example for the application of the “Gaussian-broadened Gaussian” relaxation function  $G_z^{\text{GBG}}(t)$  (see eq. 74 and fig. 98).

In summary, the  $\mu\text{SR}$  spectral shape reveals that a strongly disordered magnetic state has been formed. In contrast, Echizen et al. (2000) have concluded from bulk magnetic,

thermal and transport measurements on a single crystal with  $x = 0.18$  that this compound enters long-range AFM order at 3.5 K. The transition temperature agrees well with the μSR relaxation data for  $x = 0.2$ . Whether magnetic order is long-range or short-range, the μSR data cannot definitely answer. They just emphasize the presence of considerable spin disorder. Echizen et al. (2000) compare favorably their results with the magnetic properties of antiferromagnetic CePtSn, but μSR, as stated, does not see the magnetic response observed for that material. This type of discrepancy in magnetic response had already arisen earlier. Schröder et al. (1997) reported for a single crystal with  $x = 0.13$  the observation below  $T_N = 1.4$  K of AFM Bragg peaks located at the commensurate  $\mathbf{q} = (0 \frac{1}{2} 0)$  position of the 4 meV quasielastic peak in CeNiSn. A low Ce moment was estimated ( $0.2\mu_B$ ). A test of the same crystal by μSR gave results basically identical to those obtained earlier for the 10% polycrystalline material (Kratzer 1997). Visual inspection of a crack surface of the crystal revealed that the sample consisted of numerous small crystallites. A possible explanation is, that neutron scattering picked out some properly oriented crystallites showing AFM order, while μSR, integrating over all crystallites of the sample, reveals disordered magnetism. Echizen et al. (2000) find that the jump in specific heat at  $T_N$  is only 0.7 J/(mol K), much smaller than the expected value of  $\sim 12.5$  J/(mol K). They state: “This indicates that only a small portion of Ce magnetic moment takes part in the magnetic order”. They do not elaborate (and probably cannot decide on the basis of their type of data) whether this means that all Ce ions order with a small moment or whether only a portion of Ce ions order with full moment. In the latter case one calculates an AFM volume fraction around 6%. The μSR signal of such a small AFM ordered volume might have escaped detection. In this connection, it should be pointed out the appearance of a GBG relaxation function strictly requires local inhomogeneities in the magnetic behavior *in addition* to randomness of spin orientations. A completely random distribution of moment magnitudes, for example, is not sufficient. Recently, Noakes (1999) was able to show *via* Monte Carlo simulations that spatial inhomogeneity of regions with different sizes of moments generates the field distribution needed for GBG relaxation (see sect. 8.2.3 and fig. 98). Figure 115 depicts the GBG parameter  $R$  (which is a measure for the Gaussian distribution of static width of local field distribution) as a function of temperature in CeCu<sub>0.2</sub>Ni<sub>0.8</sub>Sn. One notices the strong increase when approaching the transition temperature, meaning that the inhomogeneity is largest at the onset of magnetic freezing. The origin of the inhomogeneity remains in the dark. It should be remarked that the μSR studies were carried out on polycrystalline samples.

In the paramagnetic regime ( $T > T_M$ ), the spectra in a weak LF (needed to suppress the depolarization by Cu nuclear dipoles) for  $x \geq 0.08$  were most easily fitted to a power exponential ( $\exp[-(\lambda t)^p]$ ) relaxation. Hence the summary label “relaxation rate” in fig. 113 (left) refers to the static width  $\Delta_{\text{eff}}$  (see eq. 74) for  $T < T_M$  and to the dynamic rate  $\lambda$  for  $T > T_M$ . The variation of power  $p$  was studied in some detail for the 10% sample. A decrease from  $p \approx 1$  at high temperatures to  $p \approx 0.6$  close to  $T_M$  was found. This is another indication that a disordered spin-glass-like state is approached and  $T_M$  might best be considered a spin freezing temperature. This spin-glass-like state, however,

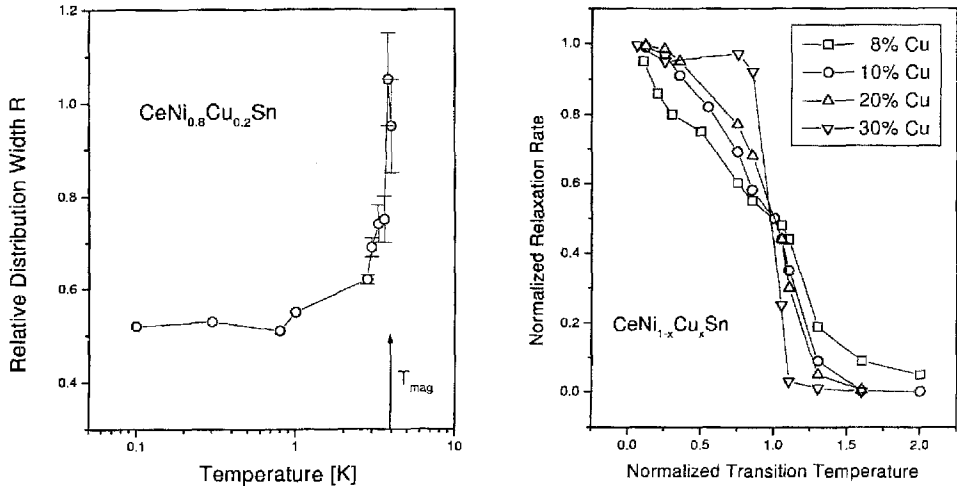


Fig. 115. Left: Temperature dependence of the parameter  $R$  of the GBG spectral shape (see sect. 8.2.3). It describes inhomogeneities in the disordered magnetic state of  $\text{CeCu}_{0.2}\text{Ni}_{0.8}\text{Sn}$  which become larger near the transition (or spin freezing) temperature  $T_M$ . Right: Normalized (to the value  $T \rightarrow 0$ ) relaxation rate as function of  $T/T_M$  showing the increase of sharpness of magnetic transition with rising Cu concentration (Kalvius et al. unpublished).

must be fundamentally different from that of a classical spin glass such as  $\text{Cu}(\text{Mn})$ . There, magnetic impurities (Mn) are introduced into a diamagnetic host (Cu). In the present case we start out with a paramagnetic host lattice ( $\text{Ce}^{3+}$ ). At low temperatures its moments are suppressed by the Kondo interaction. Introducing a nonmagnetic impurity (Cu) changes, either locally or over the bulk of the material, the electronic structure, and moments reappear at the  $\text{Ce}^{3+}$  ions. This situation is reminiscent of the “induced-moment spin glass” model proposed for under-stoichiometric PrP (Hasanain et al. 1981, Yoshizawa et al. 1983). In stoichiometric PrP, CEF interactions produce an isolated (nonmagnetic) singlet as the ground state (as discussed in sect. 5.1.2) of the  $\text{Pr}^{3+}$  ions. Disturbance of the local symmetry by vacancies near some of the Pr ions in the under-stoichiometric compound alters the CEF interaction and brings a magnetic excited state energetically close to the ground state. A moment on those Pr ions appears *via* Van Vleck interaction. In the present case it is doubtful that CEF interactions are important, although the local symmetry is surely influenced by the replacement of a nearest neighbor Ni by Cu. Yet, the point symmetry of the  $\text{CeTSn}$  structure is very low to begin with and a further distortion will probably have little influence. It should be kept in mind, however, that Kagan et al. (1993) explain the unusual features of  $\text{CeNiSn}$  by the presence of a low-lying CEF level embedded in the heavy-fermion band.  $\mu\text{SR}$  on  $\text{PrP}_x$  should be a test for this model. The results obtained (discussed in sect. 5.1.2) are entirely unlike those in  $\text{CeCu}_x\text{Ni}_{1-x}\text{Sn}$ . The  $\text{PrP}_x$  samples used in the  $\mu\text{SR}$  study failed to exhibit any spin freezing.

Whether this spin-glass-like state will evolve into normal long-range ordered AFM for values of  $x$  exceeding 0.3 remains an open question. In fig. 115 (right) one observes that

$T_M$  becomes better defined with rising Cu content. This is fully supported by the specific heat data shown in fig. 113 (right). The magnetic peak is more pronounced in the 20% Cu sample than in the 10% Cu compound. The transition temperatures are in excellent agreement with μSR. The sharpening of the magnetic transition may indeed point towards the development of a fully long-range ordered AFM state for  $x > 0.3$ . Figure 114 (left) confirms the observation made in bulk measurements that the transition temperature rises at first quickly, and then rather slowly with  $x$ . The initial filling of the d-band seems to have the most profound effect in inducing static magnetism.

We return briefly to the case  $x = 0.05$  where the μSR data showed the strengthening of paramagnetic correlations, but no magnetic transition (fig. 113, left). The  $Ce^{3+}$  moments remain in a fluctuating state down to temperatures around 30 mK. The low-temperature specific heat (fig. 113, right), measured on the same polycrystalline material used for μSR is clearly enhanced when compared to CeNiSn. This finding, in combination with susceptibility data, was interpreted by Brückl et al. (1997) as a consequence of the destruction of the high coherence of the AFM spin fluctuations in the HF state of pure CeNiSn by the induced disorder when small amounts of Cu are alloyed into the system. The notion that the system  $CeCu_xNi_{1-x}Sn$  moves from a coherent spin-fluctuator state through an incoherent HF state into a magnetic Kondo material with rising  $x$  is fully consistent with the μSR and specific heat results.

$CeCu_{0.05}Ni_{0.85}Sn$  is close to the critical concentration for the onset of static magnetism ( $x_{cr}^{Cu} = 0.07$ ) and thus might well be in a region of magnetic instability and could, in consequence, exhibit non-Fermi liquid (NFL) behavior (see sect. 9.4). Recently, Vollmer et al. (2000) have measured the low-temperature specific heat of a single crystal with  $x = 0.5$  in ZF and an applied field of 6 T (along the  $a$ -axis). A strong upturn of  $C/T$  is seen in zero applied field for  $T \rightarrow 0$  (which had also been present in the polycrystalline sample of Brückl et al. 1997). This upturn follows roughly, but not precisely a logarithmic dependence as expected for metal with NFL properties. A better description is an algebraic temperature dependence  $C/T \propto T^{-\alpha}$  with  $\alpha = 0.29$ . This type of behavior was predicted for magnetically strongly disordered systems near a magnetic instability within the frame of a Griffiths phase scenario (Castro Neto et al. 1998), originally developed for spin glasses. The value of the exponent  $\lambda = 1 - \alpha = 0.71$  is within the expected range. The upturn in  $C/T$  is largely suppressed by the applied magnetic field of 6 T. This finding agrees well with corresponding observations near the magnetic instability in  $CeCu_{6-x}Au_x$ , which is one of the best documented examples of NFL properties connected to a quantum critical point (see sect. 9.4). In summary, there is good evidence that quantum critical behavior governs the onset of magnetism in the vicinity of  $x_{crit} = 0.7$  for  $CeNi_{1-x}Cu_xSn$ .

The μSR data can be summarized by the provisional magnetic phase diagram presented in fig. 114 (right). It emphasizes once more that doping with 3d electrons strengthens the magnetic (RKKY) interaction. These findings show that CeNiSn cannot fully be described by the Kondo necklace model which is based on the variation of (ce-4f)-hybridization as induced, for example, by lattice expansion. The magnetic state reached (at least for  $x \leq 0.3$ ) is not a simple long-range ordered AFM state, but rather a magnetically inhomogeneous, highly disordered (spin-glass-like) state. The creation

of 4f holes by partial replacement of Ce with La does not lead to AFM *via* hole-hole exchange. In contrast, it weakens the magnetic correlations. Replacing Ce by U produced inhomogeneous, weak-moment, disordered magnetism for concentrations exceeding  $\sim 10\%$  (not included in fig. 114, right). Assuming that the U ions are in the 4+ ( $4f^2$ ) configuration, one might deduce that magnetism can also be induced by an increase of 4f electron density. It is possible to create 3d holes by alloying CeNiSn with Co. Bulk measurements by Adroja et al. (1995) show that this produces an increasing trend towards IV behavior leading to a valence phase transition at  $\text{CeCo}_{0.38}\text{Ni}_{0.62}\text{Sn}$ . These, and NMR data (K. Nakamura et al. 1996), give no indication of any magnetic transition. Alloying with Co also decreases the unit cell volume. This effect, combined with the reduction of 3d electron density, works against the formation of a magnetic state. For this reason, a  $\mu\text{SR}$  study has not been undertaken. Also, as will be discussed in sect. 9.5,  $\mu\text{SR}$  is not a good technique to study IV properties.

### 9.2.3. *CeRhSb* and *La<sub>x</sub>Ce<sub>1-x</sub>RhSb*

CeRhSb not only possesses the same crystal structure as CeNiSn, but also the electronic structures of the two materials are quite similar. One may hence classify CeRhSb as another Kondo semimetal (Takabatake et al. 1996) with a V-shaped anisotropic pseudo-gap. The main differences are a twice as large gap-width (H. Nakamura et al. 1994b) and a 2% increase in unit cell volume (Malik et al. 1995, see also table 13). Problems regarding the sensitivity of transport data to impurity content exist here as well. Localized impurity states fill the pseudo-gap at its center (i.e., at  $E_F$ ). It has not been possible to produce samples showing the same full metallic character as CeNiSn. Whether this is an intrinsic property, or, whether CeRhSb cannot be purified to the same extent as CeNiSn, has not finally been decided. In general, CeRhSb has been less thoroughly studied than CeNiSn.

$\mu\text{SR}$  investigations on polycrystalline material were reported by Rainford et al. (1995a) and Lidström et al. (1997). Technically the main difference from corresponding measurements on CeNiSn is the pronounced depolarization effect caused by the nuclear dipoles of  $^{121,123}\text{Sb}$ . This dominates the muon spin relaxation at high temperatures, and must be taken into account even at ultra-low temperatures. Its presence limits the accuracy to which relaxation parameters can be determined. Of interest is only the relaxation behavior due to electronic dipole moments on the Ce ions. It is assumed that pure exponential decay ( $\exp[-\lambda t]$ ) of muon spin polarization occurs in this relaxation channel.

The left-hand panel of fig. 116 shows the relevant relaxation results. Both the magnitude of  $\lambda$  and its variation with temperature are quite similar to the corresponding data from CeNiSn. Perhaps the increase in rate  $\lambda$  starts at slightly higher temperatures and its low-temperature saturation is reached somewhat earlier. Electronic and nuclear depolarization cannot be separated by the application of LF since they both decouple in roughly the same weak fields. This does mean that the small moments (estimated to be  $\mu_{\text{Ce}} \approx 10^{-3}\mu_B$ ) are more static ( $1/\tau_S \approx 1\text{ MHz}$ ) than their counterparts in CeNiSn. The more static behavior

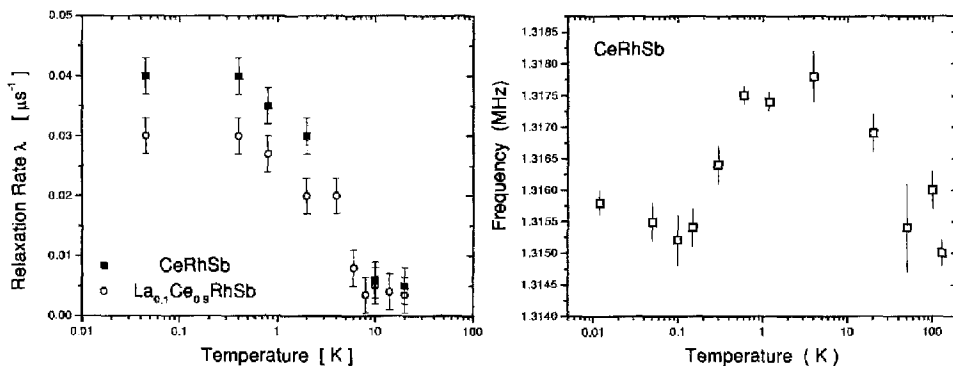


Fig. 116. Left: Temperature dependence of the rate  $\lambda$  of muon-spin depolarization caused by electronic dipole moments on the Ce ions of CeRhSb (squares) and  $\text{La}_{0.1}\text{Ce}_{0.9}\text{RhSb}$  (circles). Right: Transverse field (10 mT) muon spin precession frequency of CeRhSb as a function of temperature. From Lidström et al. (1997).

is not astonishing in view of the widened crystal lattice. A similar result was obtained, for example, in  $\text{CePt}_{0.2}\text{Ni}_{0.8}\text{Sn}$ . The main results in CeRhSb are (a) enhanced spin correlations in the sub-Kelvin range, (b) the persistence of paramagnetism down to lowest temperatures (40 mK), (c) highly Kondo-compensated moments on  $\text{Ce}^{3+}$ . Overall,  $\mu$ SR cannot find any significant difference between CeRhSb and CeNiSn.

The right-hand panel of fig. 116 presents Knight shift data for CeRhSb. Around 10 K a peak in shift occurs which correlates to a similar peak in bulk susceptibility. It had originally been thought to arise from a small amount of static  $\text{Ce}^{3+}$  ions (Malik and Adroja 1991a). If so, then the muon spin relaxation rate should show an irregularity in this temperature range, which is not the case. Also, new bulk magnetic studies on a purified single crystal (Takabatake et al. 1996) still show this peak in  $\chi_a$  but not in  $\chi_b$  nor  $\chi_c$ . This is similar to corresponding data on CeNiSn, where it has been interpreted as arising from the onset of the dynamic AFM spin correlations seen by quasielastic neutron scattering. Just recently, those spin excitations have directly been measured in CeRhSb as well (Ohoyama et al. 1999). It was found that marked differences exist in the excitation spectra of CeNiSn and CeRhSb, the latter being more typical for a valence fluctuator. These differences are not apparent in susceptibility or resistivity data and neither in the  $\mu$ SR results. We have also pointed out earlier that the spin correlations in question must fluctuate quite rapidly when they are formed. Only on slowing down with decreasing temperature do they make their presence felt in the muon spin relaxation rate. Below 100 mK the  $\mu$ -shift rises once more. Bulk susceptibility data are not available in this temperature range. Most likely the rise is due to the approach of the static limit (which, however, is never reached) by the AFM spin correlations.

The left-hand panel of fig. 116 shows in addition the relaxation data for CeRhSb doped with 10% La. They are quite in keeping with the results for CeNiSn doped with 15% La. There is no evidence for the formation of hole-hole correlations leading to an AFM state. The spin correlations of CeRhSb are merely weakened by the dilution of 4f electron

density. Furthermore, these data confirm once more that gap closure (which occurs around 10% La content) basically does not affect the muon spin relaxation behavior.

#### 9.2.4. The Kondo insulator $\text{YbB}_{12}$

As stated, this intermetallic is considered an archetypal Kondo insulator, although it is the only Yb compound in this class of strongly electron correlated materials. At high temperature it is metallic and its Curie–Weiss moment ( $2.95\mu_B$ ) is close to the  $\text{Yb}^{3+}$  free ion moment. Hence  $\text{YbB}_{12}$  is particularly special in that mixed valence is not an important ingredient. It possesses a much wider gap in the DOS at  $E_F$  than  $\text{CeNiSn}$  (see Takabatake et al. 1998a for a detailed comparison) and, in consequence, shows strong semiconducting properties at lower temperatures, leading to an insulating ground state. Magnetic and transport properties can be found in Kasaya et al. (1983, 1985), specific heat in Iga et al. (1988). Moiseenko and Odintsov (1979) point out that the RKKY interaction must be considered very weak ( $T_{\text{RKKY}} \approx 1$  K), while the Kondo coupling is strong (as demonstrated by the highly negative paramagnetic Curie temperature  $\Theta_p = -135$  K). Rather complex magnetic excitation spectra have been found by inelastic neutron scattering (Bouvet et al. 1998).

Two  $\mu\text{SR}$  studies are available. The original work (Yaouanc et al. 1999b, an earlier brief account is given in Yaouanc et al. 1997) concerns ZF and LF spectra taken between 0.05 and 50 K on a polycrystalline sample of  $\text{YbB}_{12}$ . The ZF-data were fitted over the whole temperature range using nuclear-electronic double relaxation with a weakly dynamic Gaussian Kubo–Toyabe function ( $\Delta \approx 0.5\mu\text{s}^{-1}$ ) for the nuclear part and an exponential relaxation for the electronic part. A reason for the unusual (dynamic) nuclear function (constant fluctuation rate of  $\sim 0.25$  MHz) is not given. The nuclear depolarization is suppressed by the application of a longitudinal field of 20 mT. The remaining very weak depolarization exhibits the marked temperature dependence shown in fig. 117 (left). The fit (solid line) to the data between 20 and 2 K reflects a quadratic dependence of rate on

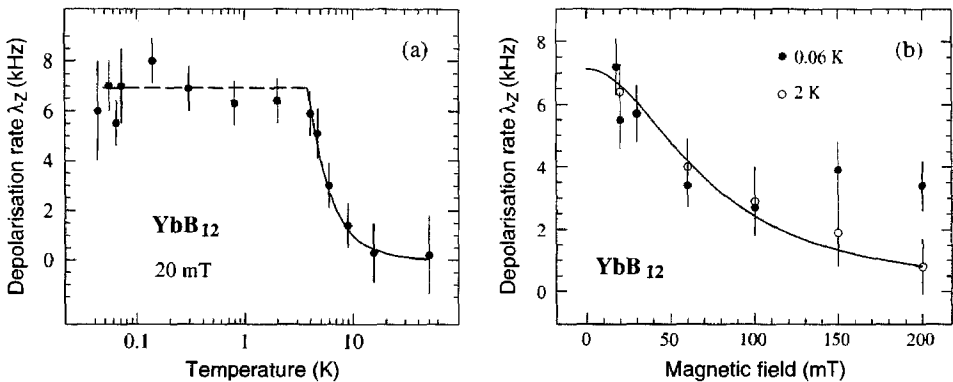


Fig. 117.  $\mu\text{SR}$  spectroscopy on  $\text{YbB}_{12}$ . Left: Temperature dependence of the longitudinal muon-spin depolarization rate. Right: Dependence of  $\lambda_z$  on applied longitudinal field. The fit uses eq. (37). Note that the rates are given in kHz (or  $\text{ms}^{-1}$ ) and not in the usual MHz (or  $\mu\text{s}^{-1}$ ). From Yaouanc et al. (1999b).

temperature. Below 2 K the rate becomes independent of temperature. It is remarkable that the electronic depolarization rate also responds to (albeit much stronger) LF as depicted in fig. 117 (right). This means that the low value of  $\lambda$  is not due to extreme motional narrowing of the depolarizing action of large moments. The authors deduce the presence of a weak (i.e., highly Kondo compensated) Yb moment of  $\sim 10^{-2}\mu_B$  fluctuating down to  $T \rightarrow 0$  with the low frequency of  $\sim 60$  MHz.

$^{170}\text{Yb}$  Mössbauer studies were also performed using the  $\beta$ -decay parent  $^{170}\text{TmB}_{12}$  as the source in conjunction with a single resonance line absorber. No change in resonance line width was found between 0.03 K and 4.2 K. The constant width had the value expected from the excited state lifetime under consideration of instrumental factors. This means that any local field (if present at all) must be less than 10 kG, corresponding to  $\mu_{\text{Yb}} \approx 0.1\mu_B$  in good agreement with the  $\mu$ SR data.

In summary, the work of Yaouanc et al. (1999b) finds no magnetic phase transition, only comparatively slow paramagnetic spin fluctuations persisting down to 40 mK coupled to a strongly reduced Yb moment.

Quite recently Kalvius et al. (2001) performed  $\mu$ SR spectroscopy on high-purity single-crystalline samples of  $\text{Yb}_{1-x}\text{Lu}_x\text{B}_{12}$  with  $x = 0, 0.125, 0.5, 1$  between 1.8 and 300 K. The original aim of this work was to get additional information on local magnetic properties as a function of gap closure which is induced by the partial replacement of Yb by Lu (Iga et al. 1999). The new  $\mu$ SR data, however, raised serious questions concerning the conclusions reached by Yaouanc et al. (1999b) with respect to the magnetic properties of  $\text{YbB}_{12}$  on the basis of the following observations. (1) Significant changes in ZF spectral shape occur with temperature in pure  $\text{YbB}_{12}$  predominantly at  $\sim 20$  K,  $\sim 100$  K and  $\sim 150$  K. This contradicts the interpretation of ZF spectra as a single-site nuclear Kubo–Toyabe relaxation with  $\Delta \approx 0.5 \mu\text{s}^{-1}$ . (2) This single-site parameter set was not able to reproduce the spectra in low LF (5 to 50 G) where nuclear Kubo–Toyabe relaxation is only partially decoupled. (3) The drop in LF = 100 (or 200) G relaxation rate near 10 K was not confirmed. In contrast, it was found that the LF relaxation rate suddenly peaks sharply at 150 K (see fig. 118, left). Confirmed, on the other hand, is the observation that for LF  $\geq 1000$  G the relaxation rate is close to zero at all temperatures which means, one truly deals with comparatively slow dynamical effects. (4) No systematic differences with Yb content could be detected in the spectra of the various  $\text{Yb}_{1-x}\text{Lu}_x\text{B}_{12}$  compounds. For example, roughly the same temperature dependence of the relaxation rate in LF = 100 G was seen for the different  $\text{Yb}_{1-x}\text{Lu}_x\text{B}_{12}$  compounds (fig. 118, left). This, together with observation (3), excludes magnetic correlations as its origin. The ZF and low LF spectra were difficult to fit precisely. Below  $\sim 100$  K, best results were obtained with a sum of two (nuclear) Gaussian Kubo–Toyabe functions ( $\Delta_1 \approx 0.55 \mu\text{s}^{-1}$  and  $\Delta_2 \approx 0.13 \mu\text{s}^{-1}$ ) each including the dynamics observed in medium strong LF. The intensities  $a_1$  and  $a_2$  of the two signal components showed a distinct temperature (but not field) dependence (see fig. 118, right top). Above  $\sim 100$  K a single-site static Kubo–Toyabe function with roughly the weighted average of widths at 100 K (reaching  $\Delta_0 = 0.22 \mu\text{s}^{-1}$  for  $T > 200$  K) fits the spectra well (see fig. 118, right bottom). The probable explanation is fast motional narrowing between the two muon surroundings leading to a single



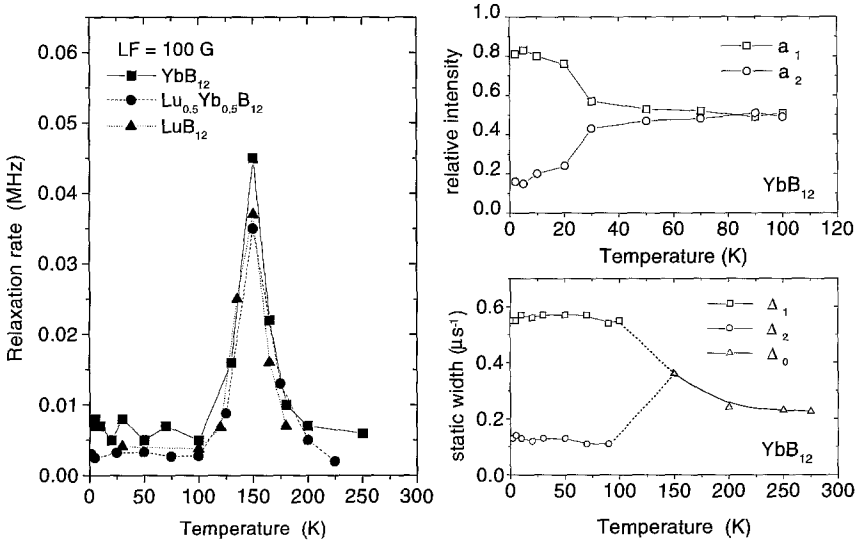


Fig. 118.  $\mu$ SR spectroscopy on  $\text{Yb}_{1-x}\text{Lu}_x\text{B}_{12}$ . Left: Temperature dependence of the LF=100 G relaxation rate in  $\text{Yb}_{1-x}\text{Lu}_x\text{B}_{12}$ . Right: Temperature dependence of the relative intensities  $a_1$  and  $a_2$  (top) together with their Kubo–Toyabe widths  $\Delta_1$ , and  $\Delta_2$  of the two spectral components in the ZF spectra of  $\text{YbB}_{12}$  below 100 K (bottom). Also shown is the Kubo–Toyabe width  $\Delta_0$  above 100 K where the spectral form has changed into a single-component pattern. See the text for details.

quasistatic relaxation function. A site change may be another scenario which cannot be excluded. It could be initiated by molecular rearrangement which would explain the peak in low LF relaxation rate.

In summary, the new data suggest that the features of the  $\mu$ SR spectra of  $\text{Yb}_{1-x}\text{Lu}_x\text{B}_{12}$  arise mainly from molecular dynamics (probably within the  $\text{B}_{12}$  clusters). This is supported by recent  $^{171}\text{Yb}$  NMR measurements (Ikushima et al. 2000) where a minimum of  $1/T_1$  was seen around 15 K which ties in with the temperature dependence of ZF- $\mu$ SR spectral shape. The NMR results on the  $^{171}\text{Yb}$  sites differs from those at the  $^{11}\text{B}$  sites requiring an additional relaxation process for the B ions. There is no compelling evidence that Yb carries a moment. The exact magnetic properties of  $\text{YbB}_{12}$  in its Kondo state remain an open question.

### 9.2.5. Other Kondo metals

**9.2.5.1. CePdSb.** Kondo lattice behavior in transport properties together with a FM ground state ( $T_C = 17.5$  K), is seen in CePdSb (Malik and Adroja 1991b). The findings of specific heat are unusual since they show no anomaly at  $T_C$ , only a broad Schottky-type peak around 10 K (Trovarelli et al. 1994).  $\mu$ SR spectra were recorded by Neville et al. (1996). At high temperatures ( $T \gg T_C$ ) they are governed by depolarization from nuclear dipole fields, which can be suppressed by the application of LF=50 G. The residual slow relaxation rate in weak LF ( $\lambda \approx 0.09 \mu\text{s}^{-1}$ ), which is of electronic origin,

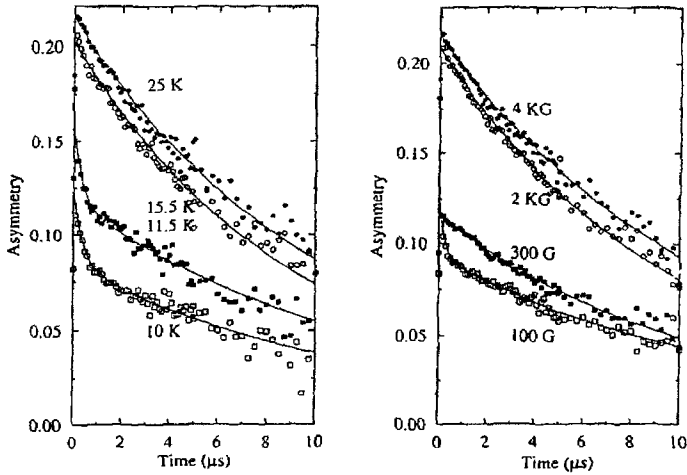


Fig. 119. Longitudinal  $\mu$ SR spectra of CePdSb. Left: LF=50 G spectra at different temperatures. Right: Dependence of spectral shape at 10 K for different LF. From Neville et al. (1996).

stays constant with decreasing temperature, even when passing through  $T_C$ . Directly at  $T_C$  there is no sudden loss of signal amplitude, but the apparent signal strength decreases continuously when the temperature is lowered towards 10 K. It is, however, possible to recover the full signal amplitude in stronger LF. The most pronounced of these features are shown in fig. 119.

The authors give no explanation for their peculiar  $\mu$ SR findings. It is certainly remarkable that in an FM state one of the usual situations is not observed: either spontaneous spin precession, or a total loss of signal due to rapid depolarization. Even if the muon occupies a site of high local symmetry only the dipolar field cancels, but not the isotropic contact field (see, for example, the discussion on US in sect. 5.2.1). Thus, one concludes in the present case, that the distribution of local field is broad enough to prevent the development of a spin precession pattern but still enables the observation of a monotonically decaying signal (overdamped oscillations). In consequence, the spin arrangement is not likely a simple FM structure. Also, one clearly has a weak FM if an external field of LF=100 G can penetrate the sample (see fig. 119). The observed field dependence of the low-temperature spectra is compatible with the coexistence of a quasistatic and a fluctuating portion of local fields.

The same study (Neville et al. 1996) also reports on inelastic neutron scattering measurements. They show spin wave excitation at low temperatures which, however, collapse into a diffusive response at 10 K (see in this connection also the discussion on USb). The 10 K point is clearly a special temperature but its exact nature remains enigmatic. But without doubt, this Kondo material exhibits most unusual spin dynamical properties. Further studies are called for.

9.2.5.2. *YbNiSn*. This intermetallic also possesses the orthorhombic structure and therefore displays strong anisotropies in many physical properties. It also exhibits some rather unusual features (Bonville et al. 1992a). For example

- (a) It is, like CePdSb, a FM (with  $T_C = 5.7$  K);
- (b) The interplay between exchange and magnetocrystalline anisotropy causes the  $\text{Yb}^{3+}$  moments to be directed along the (orthorhombic)  $c$ -axis in the FM state, whereas the easy paramagnetic axis is the  $a$ -axis;
- (c) The ordered moment ( $\mu_{\text{ord}} = 0.85\mu_B$ ) is strongly reduced compared to the free ion value, presumably due to Kondo interaction.

$\mu$ SR measurements (Bonville 1997) resolved a spontaneous spin precession below  $T_C$ . The temperature variation of  $\nu_\mu$  follows the mean field prediction for a  $\text{Yb}^{3+}$  Kramers doublet ground state. For  $T \rightarrow 0$  a value  $\nu_\mu \approx 8$  MHz is found, corresponding to an internal field of  $\sim 600$  G. ZF- $\mu$ SR relaxation in the paramagnetic regime shows the sharp increase on approaching  $T_C$ , as expected for a second-order phase transition. Usually the paramagnetic spin fluctuations are always in the fast fluctuation limit from the  $\mu$ SR point of view (except perhaps very close to the transition temperature) and hence not affected by the application of a longitudinal field (in the range of some kG). Here, in contrast, it was observed that longitudinal fields of the order of 100 G already suppress the peaking of the relaxation rate near  $T_C$ . In fact, the data revealed a relaxation rate practically independent of temperatures for  $B_L \geq 100$  G, keeping the high-temperature value of  $\lambda_0 = 0.013 \mu\text{s}^{-1}$  throughout. The author tentatively suggests that the relaxation rate in ZF is composed of two fractions. One ( $\lambda_0$ ) is caused by rapidly fluctuating localized paramagnetic moments and not affected by longitudinal fields. The other, which is field and temperature dependent, arises from nearly static moments. It supposedly reflects properties of a delocalized, i.e., hybridized, 4f electron configuration. These electrons are subjected to the Kondo interaction. The temperature dependence of their relaxation rate can be approximated by a  $\sqrt{T}$  law for  $T > T_C$ , which is predicted by some models (see Dalmas de Réotier et al. 1996 for more details). There is no hard evidence for these proposed separate 4f states and it is not easy to see how they come about in a lattice with one unique site (when paramagnetic) for the R element. Recently, Yaouanc et al. (1999a) discussed the anomalous dependence on longitudinal fields of the paramagnetic muon spin relaxation rate near the magnetic transition as an outcome of the presence of a quasielastic low-energy magnetic excitation, supposedly a unique feature of correlated electron systems (see paragraph on  $\text{CeRu}_2\text{Si}_2$  in the following section).

9.2.5.3. *Yb(Cu<sub>1-x</sub>Ni<sub>x</sub>)<sub>2</sub>Si<sub>2</sub>*. A crossover from intermediate valence to magnetic Kondo-lattice behavior is found in this pseudo-ternary system that crystallizes in the tetragonal  $\text{ThCr}_2\text{Si}_2$  structure. Pure  $\text{YbCu}_2\text{Si}_2$  is nonmagnetic, but magnetism can be induced by external pressure  $P \geq 8$  GPa (Alami-Yadri 1997). Transport data show that the same effect can be created by a partial replacement of Cu by Ni beyond the critical concentration of  $x_c = 0.125$  (Andreica et al. 2000). Since the lattice constant decreases (almost linearly) with rising Ni concentration, it is inferred that chemical pressure is responsible.

Andreica et al. (1999) also present preliminary  $\mu$ SR data for the alloy system. It is found that the appearance of quasistatic magnetic correlations is primarily related to a critical number  $N_c$  of nearest Ni neighbors around Yb. Even for  $x < x_c$  one finds that part of the sample exhibits magnetic order. Assuming purely random distribution of Ni atoms leads to  $N_c = 2$ . It might be pointed out that this behavior is different from that of the system  $\text{CeNi}_{1-x}\text{Cu}_x\text{Sn}$ , where  $\mu$ SR had shown that the onset of magnetism occurs over the whole sample volume at a distinct value of  $x$ , giving once more support to the notion that in the latter system electronic structure changes are more effective than volume changes.

9.2.5.4. *UCu<sub>2</sub>Sn*. Several members of the  $\text{UT}_2\text{X}$  system (T=transition element, X=metalloid) are characterized by hybridization between the local 5f electrons and delocalized ligand electrons.  $\text{UCu}_2\text{Sn}$  shows Kondo-lattice properties, but does not develop a HF state ( $\gamma = 0.06 \text{ J}/(\text{mol K}^2)$ ). It crystallizes in the hexagonal  $\text{ZrPt}_2\text{Al}$ -type structure where the constituents are arranged in layers perpendicular to the  $c$ -axis in the sequence Sn, Cu, U, Cu. Within the U layers the atoms form a triangular lattice. Specific heat, resistivity and susceptibility suggested an AFM phase transition at 16 K (Takabatake et al. 1992b), but neutron diffraction (Takabatake et al. 1998c), Mössbauer spectroscopy (Wiese et al. 1997) and NMR (K. Kojima et al. 1999) failed to detect magnetic ordering. The NMR result indicated that a complex magnetic state might be present at low temperatures.

Higemoto et al. (2000b) performed a  $\mu$ SR study in order to get further information on the curious behavior of  $\text{UCu}_2\text{Sn}$ . Again, no change in spectral response (nuclear Kubo–Toyabe relaxation combined with exponential relaxation from electronic U moments) was found at 16 K. At 10 K, however, the electronic relaxation changed in a manner suggesting short-range magnetic order. LF data at 1.9 K reveal that spin dynamics persist, meaning that the spin ensemble is not entirely frozen. The authors suggest that the magnetic ground state of  $\text{UCu}_2\text{Sn}$  is a spin-glass-like state due to geometrical frustration. This assignment is basically in keeping with the NMR results. What exactly happens at 16 K (quadrupolar ordering?) is not yet clear.

### 9.3. Heavy-fermion compounds

The review of HF compounds is divided into three subsections (Ce-, U- and other materials). At the end of each paragraph dealing with a certain compound or series of compounds we give a short summary of the main impact of  $\mu$ SR data. Compounds where magnetic instability leads to non-Fermi-liquid behavior are discussed in the following extra section.

#### 9.3.1. *Ce intermetallics*

9.3.1.1. *CeRu<sub>2</sub>*. The compound (cubic Laves phase) was originally used as a nonmagnetic host for R doping in early studies of the interaction of magnetism and superconductivity (see for example Matthias et al. 1958, Hillenbrand and Wilhelm 1972). In recent years, it has been established that the superconducting properties of  $\text{CeRu}_2$  itself are most unusual,

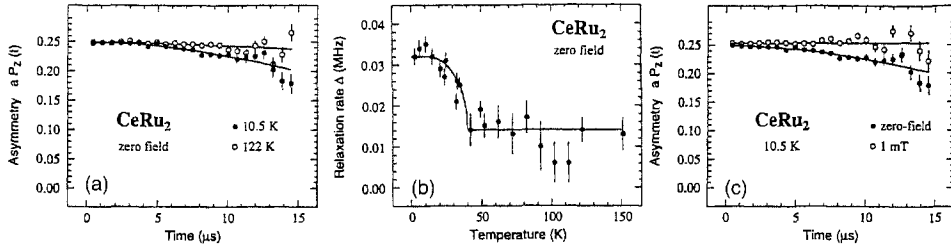


Fig. 120. ZF and LF spectra of  $\text{CeRu}_2$ . (a) Spectral shape at temperatures above and below the claimed magnetic transition at  $\sim 40$  K. (b) Temperature variation of ZF relaxation rate. (c) Comparison of ZF and LF data at low temperatures (i.e., in the magnetic state). The fits are based on Gaussian depolarization. Note the extension of the asymmetry spectra to late times (pulsed muons). After Huxley et al. (1996).

beginning with the recognition that  $T_c$  for  $\text{CeRu}_2$  is higher than for  $\text{LaRu}_2$  and more recently with discoveries (see Roy et al. 1996 and references therein) of anomalies in the type-II superconducting vortex state near  $B_{C2}$  (especially concerning the hysteresis loop). In most cases,  $\text{CeRu}_2$  is treated as a strongly correlated, superconducting electron system, but magnetism was not involved. The non-uniform superconducting state found had been predicted previously by Fulde and Ferrell (1964) and Larkin and Ovchinnikov (1965) and is known today as the FFLO state. Research on its features, especially in  $\text{CeRu}_2$ , is still active, but the problem lies outside this review. For some recent work, see Kadowaki et al. (1996), Goshima et al. (1996), Dilley et al. (1996), and Yamashita et al. (1997).

A single  $\mu\text{SR}$  study was carried out by Huxley et al. (1996). They found a small but significant increase in ZF muon spin depolarization rate below  $T_M \approx 40$  K. The difference in depolarization rate between the ZF spectra well above and well below  $T_M$  is clearly visible in fig. 120a. A small longitudinal field suppresses the increased relaxation below  $T_M$  (see fig. 120c). AC susceptibility measurements performed by the same authors found irregularities in the range of 40–60 K. Comparable magnetization data are reported by Nakama et al. (1995).

Depolarization by nuclear moments is extremely low in  $\text{CeRu}_2$  and the increased depolarization emerging at  $\sim 40$  K is considered to be of electronic origin. Its small value ( $\sim 0.02 \mu\text{s}^{-1}$ ) is quite similar to  $\text{CeRu}_2\text{Si}_2$  (see discussion there) and also the conclusions drawn are the same: a disordered static arrangement of extremely low Ce moments ( $\sim 10^{-3} \mu_B$ ) is formed. The authors conclude that at least 15% of sample volume must contain the static moments and no impurity content of that magnitude could be detected. The weak magnetic state is thus considered an intrinsic property. No details about the coexistence of superconductivity and magnetism are available at this stage. In their general review Dalmas de Réotier and Yaouanc (1997) mention that the extremely small value of the Ce moment points towards itinerant magnetism (the same is claimed for  $\text{CeRu}_2\text{Si}_2$ ). This conclusion is not obvious. Furthermore, they quote high-energy neutron scattering studies on  $\text{CeNi}_2$  (a compound which they claim has the same magnetic characteristics as  $\text{CeRu}_2$ ), which demonstrate strong inelastic paramagnetic response of the Ce ion with a large Kondo temperature (Murani and Eccleston 1996). The combination of the  $\mu\text{SR}$

data with these neutron results is taken as an indication that in  $\text{CeRu}_2$  a two-component 4f electronic system exists: a weakly polarized itinerant and a localized paramagnetic system.

*Summary:* The  $\mu$ SR results on  $\text{CeRu}_2$  forces its re-classification as a HF, intermetallic, superconducting compound with freezing of extremely small moments well above its superconducting transition. Similarities to  $\text{CeRu}_2\text{Si}_2$  exist, in particular the possibility of a double 4f configuration, having an itinerant as well as a localized subsystem.

9.3.1.2. *CeAl<sub>3</sub>*.  $\text{CeAl}_3$  is one of the first established HF compounds (a Sommerfeld constant of  $\gamma \approx 1.6\text{J}/(\text{molK}^2)$  was found by Andres et al. 1975), but its ground state properties, especially with respect to magnetic behavior, are not fully solved even today. The crystal structure is hexagonal ( $P6_3/mmc$ ) and strong anisotropies of physical properties are seen (Jaccard et al. 1987). On the basis of numerous bulk magnetic and transport data (e.g., Flouquet et al. 1982)  $\text{CeAl}_3$  was considered a representative example of a HF compound with a paramagnetic ground state. Neutron diffraction as well did not observe any magnetic order (Murani et al. 1980). The same result was obtained by  $^{27}\text{Al}$  NMR, but these studies claimed the “development of magnetic correlations” below  $\sim 2\text{K}$  (Lysak and MacLaughlin 1985, Gavrilano et al. 1994, 1995). The outcome of the  $\mu$ SR investigation by Barth et al. (1987) was a big surprise then, as spontaneous spin precession was clearly observed in ZF below  $\sim 0.7\text{K}$ , unambiguously demonstrating the presence of static magnetic order. Sample quality was initially questioned, but repetition of the  $\mu$ SR studies with a well characterized polycrystalline sample of high purity (Amato et al. 1994b) gave essentially the same result and thus showed that the occurrence of static magnetism at very low temperatures is intrinsic.

The exact interpretation of the  $\mu$ SR spectrum shown in fig. 121 (top) however, turned out to be difficult. The main reason is the rapid loss of polarization within the first 200 ns. Originally, the presence of a fast depolarizing signal in addition to the slower depolarizing oscillatory pattern was claimed. Later, it was speculated (Amato et al. 1994b) that the rapid-decaying signal arises from a precursor state that quickly changes into the state susceptible to the static magnetic field. This analysis led to a quite unrealistic phase shift of the oscillating signal. This phase shift delivered the clue to a more straightforward explanation (Amato 1997). Such phase shifts vanish (as became known in the meantime) if the depolarization of the oscillating signal is described by a  $J_0$  Bessel function. It also reproduces the initial rapid decay of polarization so that an additional fast signal is not needed. An analysis of this kind, however, implies that the internal field is distributed widely (as it would be in a SDW state: for more details see sect. 3.7). Since the data were taken with a powder sample the non-oscillating “1/3 signal” must be included in the fit. The fact that it also decays (albeit more weakly) shows that spin dynamics is still active even at these low temperatures. The fit required, furthermore, the addition of a weakly Gaussian-damped signal. This implies that not all of the sample volume enters into an ordered magnetic state. A certain fraction remains paramagnetic even as  $T \rightarrow 0$ . The depolarization of this paramagnetic signal is caused by the action of static  $^{27}\text{Al}$  nuclear

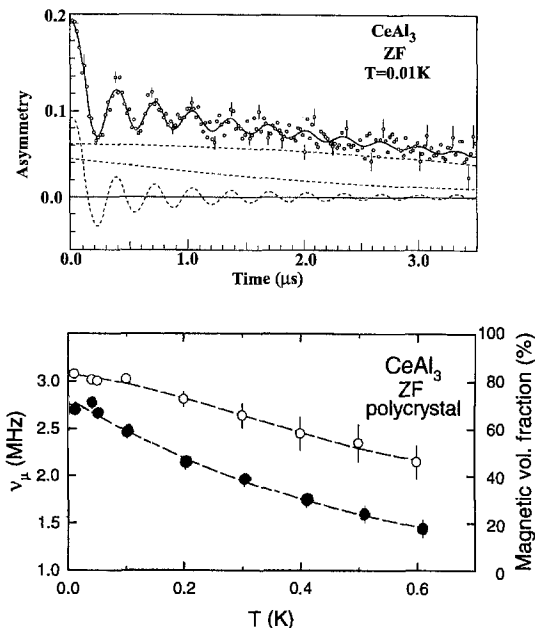


Fig. 121. Top: ZF- $\mu$ SR spectrum of  $\text{CeAl}_3$  at 10 mK. The broken lines show the decomposition of the fit (solid line) to the spectrum into 3 subspectra (the Bessel-damped oscillatory pattern and the exponentially damped “1/3 signal” from the magnetic fraction together with the weakly Gaussian-damped spectrum of the paramagnetic fraction). Bottom: Temperature dependence of the maximum frequency in the oscillatory signal of  $\text{CeAl}_3$  (open circles, left-hand scale) and of the magnetic volume fraction (solid circles, right-hand scale). The lines are guides to the eye. After Amato (1997).

dipoles ( $\Delta \approx 0.2 \mu\text{s}^{-1}$ ). The Ce electronic moments in this fraction must fluctuate very rapidly, causing total motional narrowing.

When cooling, a loss of  $\mu$ SR signal strength begins around 2 K, suggesting that a small portion enters the magnetic state. The field distribution is too wide to produce spontaneous spin precession. Spin precession becomes visible at  $\sim 0.7$  K and below, where also the magnetic volume rises rapidly. As mentioned, it never reaches 100%. The observation of a first onset of magnetism at  $\sim 2$  K is in agreement with NMR data (H. Nakamura et al. 1988a). In fig. 121 (bottom) the temperature dependence of the magnetic fraction is plotted. Also shown is the maximum spontaneous frequency (within the wide field distribution) as a function of temperature. Its variation is small and not typical for a second-order transition. A first-order transition cannot be excluded.

The maximum field of the field distribution seen by the muon is around 20 mT for  $T \rightarrow 0$ . Unfortunately, the muon stopping site in  $\text{CeAl}_3$  is not known and the  $\text{Ce}^{3+}$  moment can only be roughly estimated to be  $0.1\text{--}0.5 \mu_B/\text{Ce}$ , which should be detectable by neutrons. These findings must be reconciled with bulk data and other pertinent measurements, which so far have not indicated the presence of a magnetic state. The last word on the magnetic properties of  $\text{CeAl}_3$  is not yet in.

*Summary:* The  $\mu$ SR results at low temperatures show:

- (a) The ground state of  $\text{CeAl}_3$  is magnetic with static magnetic order setting in at  $\sim 2$  K. It is fully developed below  $\sim 0.7$  K.

- (b) A wide field distribution is present in the magnetic state, excluding a simple AFM spin structure. An incommensurate spin density wave as suggested from NMR data is a possibility.
- (c) The moment on Ce is small ( $\sim 0.1-0.5\mu_B$ ), but not below detection limits by standard magnetic techniques.
- (d) The transition into magnetic order is sluggish and inhomogeneous with the magnetic state never extending to the whole sample volume. A wide first-order transition could be the cause. Details are sample dependent.

In part, these results have yet to be reconciled with bulk magnetic and neutron diffraction measurements.

9.3.1.3. *CePb<sub>3</sub>*. This HF compound has the AuCu<sub>3</sub> structure (see sect. 5.2.3). Neutron scattering (Vettier et al. 1986) found a Néel transition around 1 K into an incommensurate spin-density-wave structure, with peculiarly, the propagation direction not locked to any symmetry axis of the crystal. CePb<sub>3</sub> is not superconducting, but Lin et al. (1985b) reported field-induced superconductivity in a polycrystal, a strange result if true, and not seen later in single crystals (Welp et al. 1987). Most likely there are spin-flop transitions in single crystals in applied field (McDonough and Julian 1996). For bulk magnetic and thermal data see Dürkop et al. (1986), Fortune et al. (1987) and Lin et al. (1987a).

Only rudimentary μSR data on an early polycrystalline sample, which may not have been of high quality, are available (Uemura et al. 1986). We report them for completeness. Muon Knight shift was studied above 2 K. The TF spectra are complex: at least four different signals were resolved (which is quite unusual considering μSR data on other AuCu<sub>3</sub>-structure materials, reported in sect. 5.2.3), two with positive shifts, two with negative. The measurements predated both the availability of dilution refrigerators for μSR, and the discovery of the magnetic transition in the material.

9.3.1.4. *CeCu<sub>5</sub>*, *CeCu<sub>5-x</sub>Al<sub>x</sub>*, *CeCu<sub>5-x</sub>Ga<sub>x</sub>*. This system crystallizes in the same hexagonal (P6/mmm) structure as CePd<sub>2</sub>Al<sub>3</sub>. Neutron scattering sees simple AFM order below  $T_N \approx 4$  K with  $\mathbf{q} = (00 \frac{1}{2})$  (Bauer et al. 1994). The moments of  $\sim 0.36\mu_B$  are perpendicular to the basal plane (in *c*-direction) in contrast to other members of this structure (e.g., CePd<sub>2</sub>Al<sub>3</sub>) where they are aligned within the basal plane. The CEF interaction puts the  $|\pm \frac{1}{2}\rangle$  state lowest. It should be followed by the  $|\pm 3/2\rangle$  doublet, but inelastic neutron scattering sees only one transition. Several explanations have been discussed: see Goremychkin et al. (1987) and Gignoux et al. (1990). The orientation of  $\mu_{\text{ord}}$  along the *c*-axis is also surprising for a  $|\pm \frac{1}{2}\rangle$  state and points toward strong anisotropic exchange. Detailed susceptibility and specific heat data are also available (Bauer et al. 1987a,b). Single crystals are difficult to grow and most studies use polycrystalline samples.

μSR data on CeCu<sub>5</sub> are available from Wiesinger et al. (1994). Below  $T_N$  one observes in ZF a spontaneous precession frequency which shows a temperature dependence as expected for a second-order magnetic phase transition (see fig. 122, left). The fairly low frequency (corresponding to  $B_\mu \approx 50$  mT) is in keeping with the low moment value. The problem with the ZF spectra for  $T < T_N$  is a substantial non-oscillating fraction



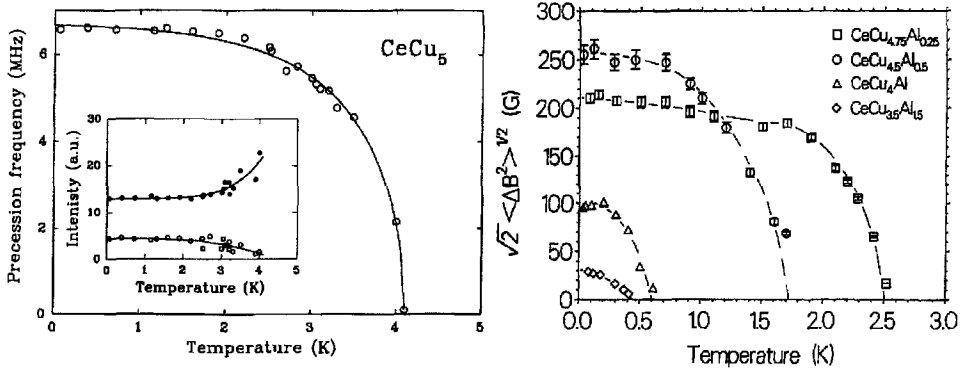


Fig. 122. Left: Temperature dependence of the spontaneous spin precession frequency for CeCu<sub>5</sub> in the AFM state. The inset gives the initial asymmetries (amplitudes) of the oscillating (lower curve) and non-oscillating (upper curve) sub-signals. The value for the oscillating signal is multiplied by 1.5 and thus represents the total amplitude of the magnetic signal, including the non-oscillating 1/3 part. Right: Temperature dependence of the rms field at the muon site for different Al concentrations in CeCu<sub>5-x</sub>Al<sub>x</sub>. The lines are guides to the eye. After Wiesinger et al. (1994, 1995, 1997).

whose intensity (see inset to fig. 122, left) is at least twice that of the oscillating part (including in the latter already the “1/3” non-oscillating fraction expected to be present for a polycrystalline sample). A detailed interpretation of this finding needs the knowledge of the muon stopping site, which is not available with certainty. The spectrum above  $T_N$  can be fitted to a Kubo–Toyabe relaxation with  $\Delta = 0.16 \mu\text{s}^{-1}$ . This value is compatible with a stopping site around the  $(0, 0, \frac{1}{2})$  lattice position. There are three such sites available, labeled  $b$ ,  $k$  or  $m$  (for more information, see Amato 1997).  $B_\mu$  would cancel for symmetry reasons for the simple AFM structure given by Bauer et al. (1994), if the muon occupies the  $b$  position. Wiesinger et al. (1994) propose a more complex structure consisting of 2 up–2 down ordered moments along the  $c$ -direction and FM order within the basal plane. Then, only every second site would see  $B_\mu = 0$  and the combination of oscillating and non-oscillating fractions could be understood. All  $k$  and  $m$  sites see the same  $B_\mu \neq 0$  (and  $B_\mu \approx 50 \text{ mT}$  is quite sensible) for the simple AFM spin structure. But then, the non-oscillating fraction cannot be explained. At this point one cannot decide between three scenarios:

- (1) the muons occupy the  $b$  site only but the AFM spin structure is more complex than the one deduced by Bauer et al. (1994);
- (2) The muon stops at both the  $b$  and  $k$  (and/or  $m$ ) sites. Then the spin structure can be that given by Bauer et al. (1994). In cases (1) and (2), the whole sample volume experiences long-range AFM order;
- (3) The muon occupies the  $k$  and/or  $m$  site (but not the  $b$  site) with the simple AFM spin structure of Bauer et al. (1994) prevailing. But then only a portion of the sample can undergo long-range order.

More data are needed to resolve this question. It would be particularly useful to measure a single-crystal specimen.

$\mu$ SR studies have also been carried out on the pseudo-binaries  $\text{CeCu}_{5-x}\text{Al}_x$  (Wiesinger et al. 1995) and  $\text{CeCu}_{5-x}\text{Ga}_x$  (Wiesinger et al. 1997). In these materials, the crystal structure remains unchanged for  $x \leq 2$ . Al or Ga atoms exclusively occupy (in random order) one particular site (the 3g site) in the  $\text{CaCu}_5$  lattice (Kim et al. 1991) and enlargement of the  $c/a$  ratio with  $x$  is a consequence. With increasing  $x$ , the Kondo interaction becomes more dominant and weakens the influence of the RKKY coupling. By  $x = 0.25$ , the magnetic transition temperature is reduced by 50% and at  $x = 2$ , magnetic order is altogether absent. The Sommerfeld constant has increased to about  $3 \text{ J}/(\text{mol K}^2)$ , making the material a strong HF compound. In the region  $0.25 \leq x \leq 2$  neither caloric nor bulk magnetic measurements could unambiguously establish long-range order, although some sort of magnetism prevails as long as  $x = 2$  is not reached (Bauer 1991).

ZF  $\mu$ SR spectroscopy on the Al and Ga pseudo-binaries for  $0.25 \leq x \leq 1.8$  down to very low temperatures found no spontaneous spin precession (in contrast to pure  $\text{CeCu}_5$ ). All samples did show a rise in relaxation rate at a specific temperature  $T_M$ , depending on  $x$ . The spectra for  $T < T_M$  could roughly, but not precisely, be represented by a nearly static Gaussian Kubo–Toyabe function. The *rms* field derived from the width of the initial Gaussian decay of muon spin polarization is presented as a function of temperature for  $\text{CeCu}_{5-x}\text{Al}_x$  in fig. 122 (right). While  $T_M$  decreases monotonically with rising  $x$  from 2.5 K to 0.4 K,  $B_{\text{rms}}$  shows some irregularity. It is larger for  $x = 0.5$  than for both neighbouring values ( $x = 0.25$  and  $x = 1$ ). The estimated values of  $\mu_{\text{ord}}$  range from  $\sim 0.1\mu_B$  to  $\sim 0.01\mu_B$ . It is suggested that the irregularities could be due to incomplete randomness of moment orientation.

Coarsely seen, the results for the Ga pseudo-binaries are quite similar to those of the Al materials, but irregularities are more pronounced. An increase of both  $T_M$  and  $B_{\text{rms}}$  is observed at  $x = 1.5$ , followed by a dramatic decrease for larger Ga concentrations. This looks more like a sudden strengthening of RKKY interaction at a certain concentration and a possible cause could be that the Fermi wave vector has reached a critical value.

For some samples  $\mu$ SR Knight shifts have been obtained between 5 K and 300 K (i.e., in the paramagnetic regime) in  $\text{TF} = 0.6 \text{ T}$ . The Knight shifts scale well with bulk susceptibility for all concentrations and over the whole temperature range covered. The slope of the curves (which is proportional to the hyperfine coupling constant) decreases systematically with increasing  $x$ . The authors suggest this to be due to a variation in phase of the RKKY oscillations. Again, the results for the Ga-containing samples are somewhat different in detail. The lattice constants at similar Al and Ga concentrations almost coincide. This then points toward finer differences in the electronic structure in the two series of intermetallics.

*Summary:* The existence of long-range AFM order in  $\text{CeCu}_5$  is verified by  $\mu$ SR, but the spectra are not easy to understand in terms of the spin structure proposed by neutron investigators. The final decision about whether the magnetic structure must be modified rests with the determination of the muon stopping site (which requires measurement of a single-crystal specimen). Replacing Cu in part by Al or Ga weakens magnetism, as expected. Not only is the magnetic transition temperature reduced, but it leads now to

a disordered (short-range correlated?) magnetic state. The distribution width of internal field also gets smaller with increased doping. Differences in detail of the  $\mu$ SR response for the Al and Ga doped materials suggest that the induced change of lattice parameter is not the sole cause for the variation in magnetic behavior. The electronic structure of the dopant also enters, albeit much less pronounced.

9.3.1.5. *CeB<sub>6</sub>*. *CeB<sub>6</sub>* is considered a prime example of a Ce-based band-magnetic HF compound. It has a cubic (Pm3m) crystal structure. Single crystals can be rather readily obtained and are used in most measurements. The magnetic phase diagram has been established in detail (Kawakami et al. 1980, Effantin et al. 1985, Hart et al. 1994). Under ambient conditions antiferro-quadrupolar ordering occurs at  $T_Q = 3.2$  K and antiferromagnetic order sets in at  $T_N = 2.4$  K. For RB<sub>6</sub> compounds in general, large CEF-strain interactions have been proposed (S. Nakamura et al. 1994), but they have not been studied intensively (see also Segawa et al. 1992). Neutron diffraction (Effantin et al. 1985) gives the  $\mathbf{q}$ -vector at 1.3 K as  $(\frac{1}{4} \frac{1}{4} \frac{1}{2})$  and a relatively small moment of  $\mu_{\text{ord}} = 0.28\mu_B/\text{Ce}$  (superceding an earlier result of  $0.65\mu_B$  by Horn et al. 1981). The absorption by boron makes neutron scattering experiments difficult in this material, and the temperature dependence of the Bragg intensity (local magnetization) was not measured. In contrast, <sup>11</sup>B-NMR (e.g., Tagikawa et al. 1983) rather suggests a fairly complex triple  $\mathbf{k}$  spin structure. Inelastic neutron scattering observes a single CEF transition appropriate for the cubic structure (Zirngiebl et al. 1984). Detailed transport and bulk magnetic data are available, as are papers dealing with the possible band structure of *CeB<sub>6</sub>*. We refer the interested reader to one of the general reviews on HF systems, for example Grewe and Steglich (1991).

$\mu$ SR studies of *CeB<sub>6</sub>* have rather added to the confusion about its magnetic state. The single muon stopping site is known from the angular dependence of the  $\mu$ SR Knight shift (Amato et al. 1997a). We have used this measurement earlier as a pertinent example in sect. 3.2.1 and refer to fig. 19 in particular. Based on the known  $\mu^+$  site together with the AFM spin structure derived by Effantin et al. (1985), one finds from dipolar sum calculations that the ZF- $\mu$ SR spectrum should contain three spontaneous precession frequencies. The measured spectrum, however is much more complex (Feyerherm et al. 1994c). It has been analyzed in terms of 8 distinct frequencies ranging roughly from 2 to 80 MHz. As can be seen from fig. 123, the temperature dependence of some of the frequencies does not follow the usual magnetization behavior (Brillouin curve) and also the relative intensities of the various components show a strange temperature behavior. The authors suggest a gradual change of spin structure. Whether one accepts in detail this rather involved analysis of the ZF- $\mu$ SR spectra in the AFM regime of *CeB<sub>6</sub>* is less important than the conclusion that *CeB<sub>6</sub>* is another case where neutron diffraction and  $\mu$ SR results are incompatible. If taken at face value, local and long-range order must differ. In such situations one quickly tends to evoke “muon-induced effects”. This is not likely the case here, because there is no indication of a delicate balance of various interactions that could lead to magnetic instabilities. Also, another local probe (NMR) gives results that contradict the neutron data, as mentioned above.

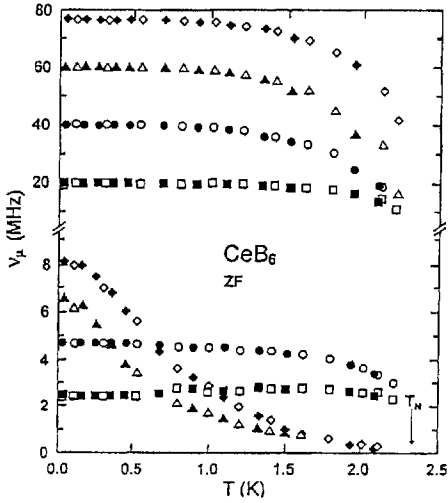


Fig. 123. Temperature dependence of the spontaneous spin precession frequencies in the ZF spectra of magnetic CeB<sub>6</sub>. Solid and open symbols refer to different runs. From Feyrerherm et al. (1994c).

For CeB<sub>6</sub>, however, even two local probes of magnetism (μSR and NMR) differ in their results. Feyrerherm et al. (1994c) and Amato (1997) point out that μSR Knight shift data for  $T_N \leq T \leq T_Q$  appear to be incompatible with NMR Knight shifts under comparable conditions (in particular under comparable applied fields). The quadrupolar ordering in combination with possible CEF–strain interactions are certainly a severe complication. But the question of whether the differences in spin structure are sample dependent or an intrinsic property, as well as the question of which spin structure μSR actually sees, remain open at this point. Further studies by different methods are clearly indicated.

*Summary:* The muon stopping site in CeB<sub>6</sub> is known. The long-range AFM order below  $T_N = 2.4$  K is confirmed by μSR, but the observed local fields cannot be reconciled with the simple AFM structure found by neutron scattering. The difference between long-range magnetism (neutrons) and local magnetism (μSR) is not understood. Sample problems cannot be ruled out entirely, but the indication is of a more complex, perhaps temperature-dependent, spin structure.

Papers discussed above established the muon site in CeB<sub>6</sub> as  $(\frac{1}{2}, 0, 0)$  from muon Knight shift studies, and described multiple spontaneous frequencies in the AFM state below  $T_N = 2.4$  K, but resolved little in the antiferroquadrupolar state for  $T_N < T < T_Q = 3.2$  K. Kadono et al. (2000b) studied ZF and low-LF μSR in a polycrystalline sample of CeB<sub>6</sub>. Over a wide temperature range above  $T_N$ , the ZF relaxation function is a static nuclear Kubo–Toyabe multiplied by an exponential indicating rapidly fluctuating electronic moments. From the width of the nuclear field distribution, they confirm the site selection. The nuclear KT decouples completely in 10 mT LF (as it should), leaving the exponential. The exponential relaxation rate rises smoothly as temperature is decreased, with a change in slope at  $T_Q$ . Thus μSR has detected the quadrupole transition, but does not say much about the form of the ordering that occurs.

9.3.1.6. *CeCu<sub>6</sub>*. This intermetallic, which crystallizes in an orthorhombic (Pnma) structure, is the best established example of a HF system with a paramagnetic ground state without superconductivity being present (Ōnuki et al. 1984, Stewart et al. 1984, Ott et al. 1985a). Its Fermi-liquid behavior with  $T^* \approx 5$  K is well documented. In  $\mu$ SR studies on a single-crystalline specimen, the  $\mu^+$  stopping site  $(0, 0, \frac{1}{2})$  was determined from the angular dependence of the Knight shift (Amato et al. 1997a), analogously to the example of CeB<sub>6</sub> discussed above. ZF and LF data showed a temperature-independent (down to 40 mK) static, Gaussian Kubo–Toyabe relaxation, which is due to the nuclear dipole fields of <sup>63,65</sup>Cu (Amato et al. 1993a). The observed static width  $\Delta = 0.23 \mu\text{s}^{-1}$  can be fully accounted for by a dipolar summation for the established  $\mu^+$  site meaning that the depolarizing action of electronic Ce moments is fully motionally narrowed. Quasistatic magnetic correlations do not develop. Also, no indication of spontaneous spin precession was detected, which excludes long-range order.

We take this example for a brief discussion on the sensitivity of  $\mu$ SR for small electronic moments in the presence of sizeable nuclear moments. In the case of fast fluctuating Ce moments ( $\mu_{\text{Ce}}$ ) their influence on muon spin depolarization can be separated from that of nuclear moments ( $\mu_{\text{nucl}}$ ) by applying the proper LF as discussed in sect. 3.4. The question of detection limit is then the closeness to complete motional narrowing. If  $\mu_{\text{Ce}}$  is small, the limit of observability ( $\lambda \leq 0.005 \mu\text{s}^{-1}$ ) is reached already at quite moderate fluctuation frequencies (the finer details depending on the geometric arrangement of the moments around the muon). In the static limit, the effect of a small  $\mu_{\text{Ce}}$  will not be seen if  $\mu_{\text{Ce}} < \mu_{\text{nucl}}$ . Then LF spectroscopy will not help either, since both the electronic and the nuclear relaxation function will decouple quite the same way. An experimental search for temperature dependence of ZF spectra may find some change in relaxation function if the  $\mu_{\text{Ce}}$  become dynamic at some temperature, while the  $\mu_{\text{nucl}}$  will remain quasistatic. If  $\mu_{\text{Ce}}$  is much smaller than  $\mu_{\text{nucl}}$  however, this effect will be unmeasurably small. Hence, if a detectable  $\mu_{\text{nucl}}$  is present, then it becomes a rough lower limit on the *static*  $\mu_{\text{Ce}}$  that can be resolved. In the case of CeCu<sub>6</sub>, such estimates give  $\mu_{\text{Ce}} \leq 2 \cdot 10^{-3} \mu_{\text{B}}$  if  $\mu_{\text{Ce}}$  is static. In the dynamic situation no proper upper limit on  $\mu_{\text{Ce}}$  can be given from the  $\mu$ SR data by themselves as long as independent information on its fluctuation rate is not available. Good Fermi liquid behavior, however, means that the bulk susceptibility can be accounted for by the Pauli susceptibility of the heavy quasiparticles. Using this with the appropriate error estimates gives an upper limit on  $\mu_{\text{Ce}}$  about one order of magnitude larger than the static limit quoted above.

In spite of the absence of any quasistatic moment formation, CeCe<sub>6</sub> must be considered not far from magnetic ordering. Neutron data (Regnault et al. 1987) found dynamic short-range AFM correlations below  $\sim 10$  K. Since no effect is seen on the  $\mu$ SR relaxation rate, the fluctuations of the moments must remain in the fast dynamical limit. Similarly magneto-resistance (Ōnuki et al. 1985) and thermoelectric power (Amato et al. 1987) show anomalies at low temperature that point towards incipient magnetism. The possibility of magnetic order below 5 mK has been pointed out (Schuberth et al. 1995, Pollack et al. 1995).

As we shall discuss in sect. 9.4, a magnetic ground state develops when Cu is replaced in part by Au or Ag (von Löhneysen et al. 1994). NFL behavior concomitantly appears in the nonmagnetic  $\rightarrow$  magnetic transition region.

*Summary:* The  $\mu$ SR data on  $\text{CeCu}_6$  fully confirm its nonmagnetic ground state to an extreme limit (no quasistatic  $\mu_{\text{Ce}} \geq 10^{-3} \mu_{\text{B}}$ ). For dynamic moments, the limit is an order of magnitude larger.

9.3.1.7. *CeRuSi<sub>2</sub>*. The Sommerfeld constant of  $\text{CeRuSi}_2$  is enhanced ( $\gamma \approx 0.1 \text{ J}/(\text{mol K}^2)$ ) but still on the low side for a HF material. The crystal structure is monoclinic ( $P2_1/m$ ) and differs from other members of the  $\text{CeTX}_2$  series. Curie–Weiss behavior is observed above  $\sim 60 \text{ K}$  but with an effective moment of only  $1.7 \mu_{\text{B}}$  which is considerably lower than the  $\text{Ce}^{3+}$  free ion value (Nikiforov et al. 1993). A sharp upturn in  $\chi(T)$  around  $10 \text{ K}$ , together with a  $\lambda$ -like behavior in specific heat, indicates a magnetic transition (Velikhovskii and Nikiforov 1993).

A  $\mu$ SR study on polycrystalline material between  $4.2 \text{ K}$  and  $300 \text{ K}$  was undertaken by Krivosheev et al. (1997a). The depolarization rate as function of temperature is presented in fig. 124b. The onset of magnetism at  $T_{\text{M}} \approx 12 \text{ K}$  is confirmed. Above  $T_{\text{M}}$  the  $\mu$ SR spectrum can be fitted to a single exponential decay, below  $T_{\text{M}}$  a fast relaxing “2/3 signal” and a slowly relaxing “1/3 signal” is seen which is the expected behavior in case of long-range magnetic order (fig. 124a). Both signals were fitted with exponential relaxation. No spontaneous spin precession was visible at any temperature as long as strict ZF conditions were maintained at all times. This means that the distribution width of internal fields must be of the same order as the mean field value.

LF measurements in the magnetic state shown that a field of  $\sim 150 \text{ G}$  is needed to suppress the fast relaxing part. This is a much higher field value than the one expected for static depolarization and consequently, the field distribution below  $T_{\text{M}}$  must be slightly dynamic with a fluctuation rate on the order of MHz. This weakly dynamic property also explains why an exponential (and not a Gaussian) damping is observed. Above  $T_{\text{M}}$  the relaxation rate is quickly reduced for small values of  $B_{\text{L}}$  reflecting the decoupling of

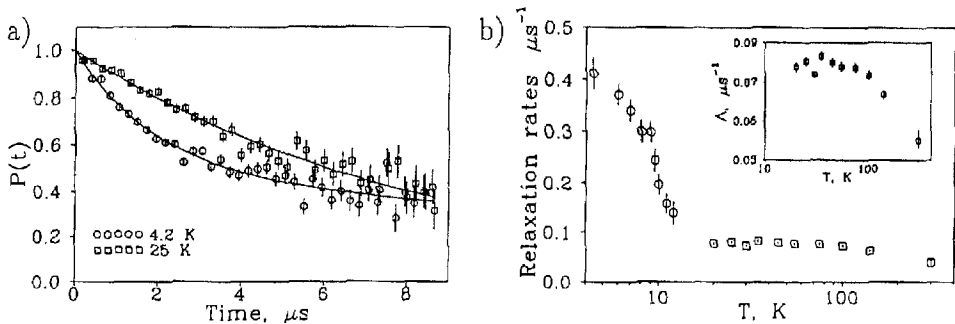


Fig. 124. ZF- $\mu$ SR results on polycrystalline  $\text{CeRuSi}_2$ . (a) Spectra at  $25 \text{ K}$  and  $4 \text{ K}$  when strict ZF conditions are constantly maintained. (b) Temperature dependence of the muon spin depolarization rate. Below the magnetic transition only the rate of the fast depolarizing “2/3 signal” is plotted. From Krivosheev et al. (1997a).

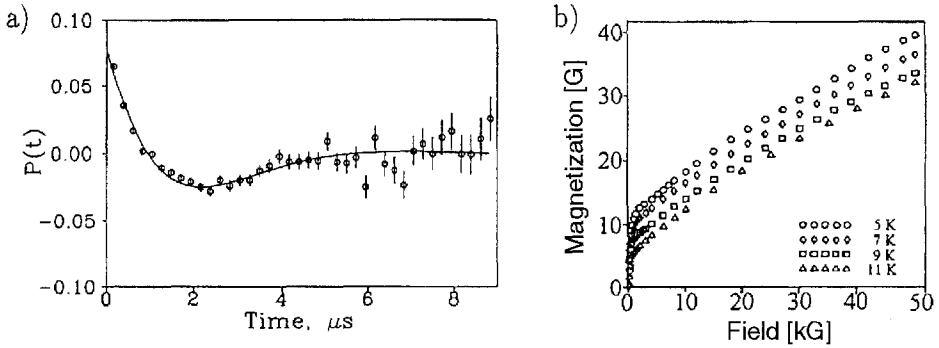


Fig. 125. (a) ZF- $\mu$ SR spectra of polycrystalline CeRuSi<sub>2</sub> after having the sample exposed to a transverse field of 0.5 T. (b) Field dependence of magnetization below the magnetic transition. From Krivosheev et al. (1997a).

depolarization by nuclear moments. A remaining rate ( $\sim 0.03 \mu\text{s}^{-1}$ ) is not affected by even larger fields (400 G). This is the depolarization caused by moderately rapid fluctuating paramagnetic Ce moments. One estimates  $1/\tau_{4f} > 100 \text{ MHz}$ .

Data taken in strong applied fields (especially TF up to 0.5 T) demonstrated the presence of hysteresis effects and remanence. For example, after applying a transverse field of 0.5 T the ZF- $\mu$ SR spectrum shown in fig. 125b was recorded. It clearly differs from the corresponding spectrum taken without previously exposing the sample to an external field (fig. 124a), and was analyzed as a spin precession pattern with nearly critical damping ( $\lambda \approx \omega$ ) in addition to a Lorentzian Kubo–Toyabe term. These findings are in keeping with the field dependence (fig. 125b) and the hysteresis loop observed for the magnetization below  $T_M$  (Nikiforov et al. 1993). Although ferromagnetic response is observed, it cannot be a simple FM spin structure. That would produce spontaneous muon spin precession even for a nonmagnetized sample. In unmagnetized CeRuSi<sub>2</sub>, muons see highly disordered and slowly fluctuating magnetism below  $\sim 12 \text{ K}$ . A weak ferromagnetic component could already be present but need not be. A possibility is a complex canted spin structure (remarks by the reviewers, the authors do not speculate as to the actual type of magnetic ordering).

A ferromagnetic ground state is not expected for a HF material with competing RKKY and Kondo interactions in the “Kondo necklace” model. More recently, however, several HF compounds exhibiting such a ground state have been found. Pertinent examples are URu<sub>2-x</sub>Re<sub>x</sub>Si<sub>2</sub> for  $x > 0.4$  (Dalichaouch et al. 1989) or CePd<sub>2</sub>Ga<sub>3</sub> (Bauer et al. 1993). The debate as to the proper theoretical model for this feature is still active. CeRuSi<sub>2</sub> is without doubt an interesting specimen and altogether more  $\mu$ SR data on ferromagnetic HF materials would be highly desirable.

*Summary:*  $\mu$ SR verifies that the transition at 12 K leads into a magnetically frozen (with slow dynamics) state. The spectra are sensitive to the pre-history of applied magnetic fields and hysteresis-like effects, including remanence, appear. A ferromagnetic component in the spin structure is indicated, but the distribution of local field is too large for a simple FM spin structure.

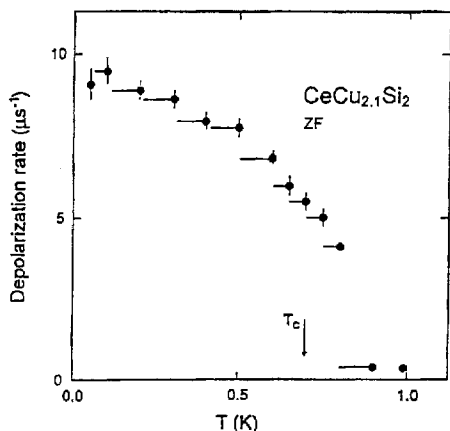


Fig. 126. Temperature dependence of the muon spin depolarization rate in ZF for polycrystalline  $\text{CeCu}_{2.1}\text{Si}_2$ . The superconducting transition temperature of this sample is indicated and falls well within the region of static magnetism. From Uemura et al. (1988).

9.3.1.8. *CeCu<sub>2</sub>Si<sub>2</sub> and related compounds.* This tetragonal ( $I4/mmm$ ,  $\text{ThCr}_2\text{Si}_2$  structure) intermetallic was the first HF superconductor discovered (Steglich et al. 1979). Progress in understanding its properties was severely hampered by problems of irreproducibility of results for different samples. The main problem appears to be the copper stoichiometry. Copper deficient samples ( $\text{CeCu}_{1.9}\text{Si}_2$ ) are not superconducting, while excess Cu (e.g.,  $\text{CeCu}_{2.2}\text{Si}_2$ ) produces the comparatively highest  $T_c$ 's. Which lattice sites the excess Cu occupies remains enigmatic (see for example Ishikawa et al. 1983, Braun and Jorda 1985). A detailed discussion of the sample problem can also be found in Grewe and Steglich (1991). Recently, Gegenwart et al. (1998) have come up with a magnetic phase diagram that has magnetic ordering at higher temperatures on one side of stoichiometry and superconductivity at higher temperatures on the other. They claim in particular that the diagram has a quantum critical point, which is one of the possible conditions for NFL behavior (see sect. 9.4).

$\mu$ SR studies concentrated on the observation that superconductivity occurs within a magnetic phase. The latter was discovered by ZF- $\mu$ SR measurements (Uemura et al. 1988, 1989) and also seen in NMR studies (H. Nakamura et al. 1988a) and magneto-resistance data (Rauchschwalbe et al. 1987). The original  $\mu$ SR result on a  $\text{CeCu}_{2.1}\text{Si}_2$  sample is presented in fig. 126 and shows a definite rise in depolarization rate below  $\sim 0.9$  K, which is significantly above the superconducting transition temperature of 0.65 K found for the same sample. LF measurements proved that *static* magnetic correlations of moments on the order of  $0.1\mu_B/\text{Ce}$  are responsible. The absence of a spontaneous precession pattern indicates a freezing of randomly oriented Ce moments.

Recently, more detailed  $\mu$ SR studies have been reported (Luke et al. 1994b, Amato 1994 and Feyerherm et al. 1997). Basically the same results were obtained by the various groups. Differences in detail arise from sample dependences. It was found that the  $\mu$ SR signal below 1 K consists of two portions, a fast and slow relaxing one. Above 1 K the two signals are indistinguishable, the relaxation rate being dominated by relaxation due to static Cu nuclear moments. The depolarization rate of the fast relaxing signal



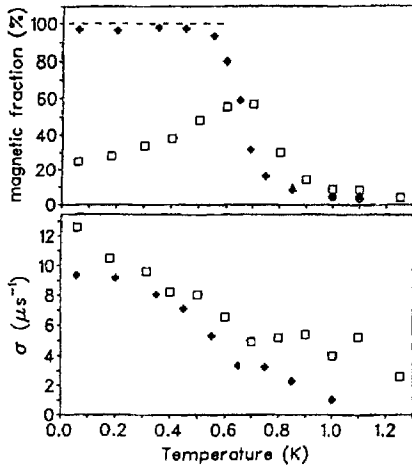


Fig. 127. Temperature dependences of the magnetic volume fraction (fast relaxing component) (top) and its relaxation rate (bottom). Open squares refer to a superconducting sample with composition  $\text{CeCu}_{2.05}\text{Si}_2$ , solid diamonds to a  $\text{CeCu}_{2.04}\text{Si}_2$  sample that exhibits no bulk superconductivity. After Feyerherm et al. (1997).

increases steadily with decreasing temperature, reaching  $\sim 8 \mu\text{s}^{-1}$  for  $T \rightarrow 0$ . It must be of electronic origin. This rise in rate is in overall agreement with the earlier findings of Uemura et al. (1988). The relaxation rate of the weakly depolarizing signal changes little with temperature and remains at the high-temperature value ( $\sim 0.15 \mu\text{s}^{-1}$ ). In principle one could use this value for a comparison with calculated Van Vleck widths for various interstitial sites to gain information on the stopping place of the muon. In the present case, unfortunately, all likely sites give about the same value and a distinction cannot be made (Feyerherm et al. 1997). This is, however, without consequences for the basic deduction to be drawn from the  $\mu\text{SR}$  data.

The presence of two signals, both definitely from the sample, means that the magnetic properties of  $\text{CeCu}_2\text{Si}_2$  are inhomogeneous. One portion of the sample has undergone spin freezing (fast depolarization), the other remains paramagnetic. We have used the results of Luke et al. (1994b) as an example of *inhomogeneous spin freezing* in sect. 8.2.3 and plots of the spectra and their pertinent parameters were presented there in fig. 99. The variation in amplitude of the two signals directly reflects the volume fractions of the two portions. We present the situation once more in fig. 127 for two samples studied by Feyerherm et al. (1997). We shall first discuss the results for superconducting  $\text{CeCu}_{2.05}\text{Si}_2$ , which are quite similar to the data for the  $\text{CeCu}_{2.2}\text{Si}_2$  compound obtained by Luke et al. (1994b) and presented in fig. 99. After the onset of spin freezing the magnetic volume fraction rises sharply, reaching 60–70% at  $T_c$ . The formation of the superconducting state suppresses magnetism and the spin-frozen volume decreases again with further decrease in temperature. But for  $T \rightarrow 0$ , 30–40% of the sample still remains in the spin-frozen state. Feyerherm et al. (1997) analyse the magnetic fraction with a dynamic Kubo–Toyabe function and obtain a fluctuation rate around 3 MHz, which from the point of view of paramagnetic spin fluctuations is essentially static. Their main reason for this approach is the too-shallow minimum seen in the Kubo–Toyabe pattern. But as has been argued in sect. 8.2.3, there can be other causes for such an effect, especially in magnetically

inhomogeneous states. In the paramagnetic fraction, the fluctuation of Ce moments must always be very fast and full motional narrowing is achieved.

Feyerherm et al. (1997) also show results for samples with different Cu content (from 1.95 to 2.2). It is interesting that one sample (2.04) does not exhibit bulk superconductivity. As seen in fig. 127, the magnetic volume fraction in it rapidly reaches nearly 100% and maintains this value down to  $T \rightarrow 0$ . In contrast, all superconducting samples show the maximum in magnetic volume fraction at  $T_c$ , but with varying percentage. The temperature dependence of relaxation rates is, however, roughly the same for all samples, except for the difference in onset temperature (see fig. 127).

These  $\mu$ SR results provide clear evidence against true coexistence of superconductivity and magnetism on a microscopic scale. The data rather suggest that competition between the two ordering phenomena exists with a tendency to avoid coexistence. Feyerherm et al. (1997) point out that the superconducting state is first formed in the paramagnetic fraction, which means that a nonmagnetic ground state is a prerequisite for the appearance of superconductivity. Later on, the two ordering interactions are in competition for the *same set of quasiparticles* in the formation of the HF ground state. Luke et al. (1994b) speculate about a collapse of RKKY coupling once the superconducting state is established. This scenario is in sharp contrast to the existence of *two sets of quasiparticles*, one superconducting, one magnetic, which has been established for some uranium HF materials by the confirmation of microscopic coexistence of superconductivity and magnetism (see next section). Whether this fundamental difference is based on the difference in spatial extent of the 4f and 5f electron wave functions is an open question at this stage.

Koda et al. (2000) recently studied by  $\mu$ SR a sample of  $\text{Ce}_{0.99}\text{Cu}_{2.02}\text{Si}_2$  (polycrystal) that is magnetic (A-phase) but shows no bulk superconductivity. Below  $T_M \approx 0.8$  K a two component signal (more rapid and very slow Gaussian relaxation) is observed in ZF in accordance with previous results (e.g., Feyerherm et al. 1997). Short-range magnetic order is suggested. The authors interpret the LF decoupling data differently by relating the comparatively large fields needed to suppress muon spin relaxation to large randomly oriented *static* fields ( $\sim 200$  G) rather than to spin fluctuations (of  $\sim 3$  MHz), the explanation other authors favored. The disordered frozen spin state (called spin-glass-like magnetic ordering) is discussed in terms of a recent theoretical study by Kohno et al. (1999) that points out the possibility of nucleation of staggered moments around disorder centers such as Ce vacancies.

Subsequently, Kadono et al. (2000a) studied the  $\mu$ SR spectra of  $\text{Ce}_{0.99}\text{Cu}_{2.02}\text{Si}_2$  in the magnetic A-phase in conjunction with  $\text{Sr}_{2.5}\text{Ca}_{11.5}\text{Cu}_{24}\text{O}_{41}$  in its magnetic state. The latter compound is related to the Kagomé systems discussed briefly in sect. 8.2.2. It was found that these two basically quite different systems share common features in their  $\mu$ SR spectra. Of special interest is the observation that the magnitude of the local magnetic field estimated from the ZF relaxation rate is much smaller than suggested by decoupling in LF. Such findings were reported earlier for Kagomé lattices (Uemura et al. 1994) and also for  $\text{CePt}_2\text{Sn}_2$  (Luke et al. 1997a and Kalvius et al. 2000d). Particularly the Kagomé data led to a model where it was assumed that a random local field acts on the muon only for

a fraction of the mean spin-fluctuation period (termed “sporadic paramagnetism”). This scenario explained another common unusual feature, the discrepancy between the initial Gaussian shape of the relaxation function (pointing towards a static field distribution) and the decay of the “1/3 tail” at late times (typical for spin dynamics). Concentrating (unfortunately, from the point of view of this review) on the case of  $\text{Sr}_{2.5}\text{Ca}_{11.5}\text{Cu}_{24}\text{O}_{41}$ , Kadono et al. (2000a) found that the formalism of “sporadic paramagnetism” will not convincingly reproduce the spectra measured in ZF and LF. The authors question whether the abnormal  $\mu\text{SR}$  response reflects bulk properties of the material and proceed to develop a local model based on the partial shielding of a *static* internal field sensed by the muons. In effect they introduce a reduced gyromagnetic ratio  $\tilde{\gamma}_\mu$ . The absence of a spin precession signal requires that the field distribution width  $\sigma$  must obey the condition  $\sigma/\tilde{\gamma}_\mu \approx B_\mu$ . It should be emphasized that this differs substantially from a Gaussian random field distribution with  $\langle B_\mu \rangle = 0$ . They continue to propose as the cause of the shielding effect the magnetic instability of a frustrated spin system near a quantum critical point (see sect. 9.4 for details on the latter subject) which is greatly enhanced by the presence of the muon. A clear connection to the case of  $\text{Ce}_{0.99}\text{Cu}_{2.02}\text{Si}_2$  is not made. It is remarked that this material is magnetically unstable (due to sensitivity to stoichiometry) like  $\text{CePt}_2\text{Sn}_2$  (sensitivity to tetragonal distortion, see sect. 9.3.1). Also, frustration is expected in both cases since Kondo and RKKY interactions are about of equal strength. In any case, both recent papers on the A-phase of  $\text{CeCu}_2\text{Si}_2$  stress the static nature of the internal field. They also make clear that one deals with a complex magnetic phase strongly responding to details of crystal structure.

Finally, a  $\mu\text{SR}$  study on  $\text{CeCu}_2(\text{Si}_{1-x}\text{Ge}_x)_2$  was undertaken by Higemoto et al. (1999b) in another attempt to gain information on the magnetic phase (the so-called “A-phase”) of  $\text{CeCu}_2\text{Si}_2$ . Substituting Ge for Si is equivalent to applying pressure to the system, which influences the superconductivity and magnetic properties (Trovarelli et al. 1997). It was found that the A-phase persists for  $x = 0.02$  and  $0.05$ . A study of the magnetic properties with  $\mu\text{SR}$  is underway.

*Summary:* The occurrence of spin freezing in  $\text{CeCu}_2\text{Si}_2$  involving moments  $\mu_{\text{Ce}} \approx 0.1\mu_{\text{B}}$  above the superconducting transition temperature is definitely established by  $\mu\text{SR}$ . The spin freezing process is inhomogeneous, meaning that different parts exhibit either magnetism *or* superconductivity. It appears that the two features are mutually exclusive in the same volume fraction: there is no coexistence on a microscopic scale. Details of the  $\mu\text{SR}$  response are strongly sample dependent and influenced especially by the Cu stoichiometry (as are bulk properties).

9.3.1.9. *CeCu<sub>2</sub>Ge<sub>2</sub>*. In the HF system  $\text{CeCu}_2\text{Ge}_2$  the Kondo and RKKY interaction strength are considered to be of roughly equal strength. According to the Kondo necklace diagram by Doniach (see fig. 104) this means that the compound is close to a magnetic instability.  $\text{CeCu}_2\text{Ge}_2$  shows incommensurate AFM order below  $T_{\text{N}} \approx 4.2\text{K}$ , but the application of pressure, which increases the 5f-conduction-electron hybridization, rapidly suppresses magnetic order (Steglich et al. 1996). Similarly,  $\text{CeNi}_2\text{Ge}_2$ , which has a smaller

unit cell volume is nonmagnetic.  $\mu$ SR spectroscopy on a single crystal of  $\text{CeCu}_2\text{Ge}_2$  has been reported in a conference contribution by Klauß et al. (1999d). A strongly damped oscillatory pattern with markedly reduced asymmetry is seen below  $T_N$ . A rapid increase of relaxation rate masks the signal below 3.5 K. Strong anisotropy of the static internal field distribution with a doubling of relaxation rate for  $\mathcal{S}_\mu \perp c$  compared to  $\mathcal{S}_\mu \parallel c$  (i.e., parallel to the easy axis) is considered to originate from the incommensurate spin structure. Down to 2 K no indications for a second magnetic transition, as proposed by thermal expansion and susceptibility data, were found. Two signals were seen in Knight shift measurements for  $\mathcal{S}_\mu \parallel c$ . The shift did not linearly scale with susceptibility in either direction.

*Summary:* This preliminary work already indicates that  $\text{CeCu}_2\text{Ge}_2$  possesses rather complex magnetic properties. More work is in progress, especially the deduction of the muon stopping site from the dipolar coupling tensor derived from angular dependent Knight shift data. Measurements on the pseudo-binary system  $\text{Ce}(\text{Cu}_{1-x}\text{Ni}_x)_2\text{Ge}_2$  will be discussed in sect. 9.4 in connection with NFL behavior. These data show that  $\text{CeCu}_2\text{Ge}_2$  is indeed close to a magnetic instability.

9.3.1.10.  $\text{CeRu}_2\text{Si}_2$ ,  $\text{Ce}_{1-x}\text{La}_x\text{Ru}_2\text{Si}_2$ ,  $\text{Ce}(\text{Ru}_{1-x}\text{Rh}_x)_2\text{Si}_2$ . This series of intermetallics also crystallizes in the tetragonal I4/mmm ( $\text{ThCr}_2\text{Si}_2$ ) structure. A review of the bulk properties of  $\text{CeRu}_2\text{Si}_2$  has been published by Flouquet et al. (1995).  $\text{CeRu}_2\text{Si}_2$  is another case where the notion of a Fermi-liquid paramagnetic ground state must be questioned because of  $\mu$ SR data. The work of Amato et al. (1993b) on single-crystalline  $\text{CeRu}_2\text{Si}_2$  clearly showed the presence of some type of weak, quasistatic magnetism below  $\sim 2$  K (see fig. 128).

Several attempts have been made to determine the  $\mu^+$  stopping site. Most use data for para- or diamagnetic isostructural compounds and compare the (Kubo–Toyabe type) muon spin depolarization caused by the nuclear moments (i.e.,  $^{29}\text{Si}$ ,  $^{99,101}\text{Ru}$ ) with dipolar sum calculations of the Van Vleck width. There are 11 possible interstitial sites in the  $\text{ThCr}_2\text{Si}_2$  structure. Unfortunately, the nuclear relaxation rates are small and differ only little for some of the possible sites. Sekine et al. (1995) use  $\text{YRu}_2\text{Si}_2$  and deduce the  $(\frac{1}{8}, \frac{1}{2}, \frac{3}{32})$  site, although the distinction of this site is not outstanding. Yamamoto et al. (1997) measured  $\text{Ce}_{0.95}\text{La}_{0.05}\text{Ru}_2\text{Si}_2$  and select the  $(0, \frac{1}{2}, \frac{1}{8})$  position. Dalmas de Réotier et al. (1990a) propose the  $(\frac{1}{2}, 0, 0)$  or the  $(\frac{1}{2}, \frac{1}{4}, 0)$  sites from data on  $\text{YCo}_2\text{Si}_2$ . In contrast, Amato et al. (1997a) performed measurements of the temperature dependence of the muonic Knight shift on a single crystal with the muon spin oriented parallel and perpendicular to the  $c$ -axis. The Knight shifts scale linearly with the contribution of  $f$  electrons to the bulk susceptibility between 300 K and 10 K. The extracted value of the dipolar coupling constant was compared to dipolar sum calculations and suggested the  $(\frac{1}{2}, \frac{1}{2}, 0)$  site. This site, however gives too small a value of the nuclear Van Vleck width and is incompatible with the data of Sekine et al. (1995). A recent study by Yamamoto et al. (2000b) (discussed in detail in sect. 5.5.2) compares the ZF spectra of antiferromagnetic  $\text{CeRh}_2\text{Si}_2$  with calculated dipolar fields and concludes that the  $4c$   $(\frac{1}{2}, 0, 0)$  site is occupied. A similar

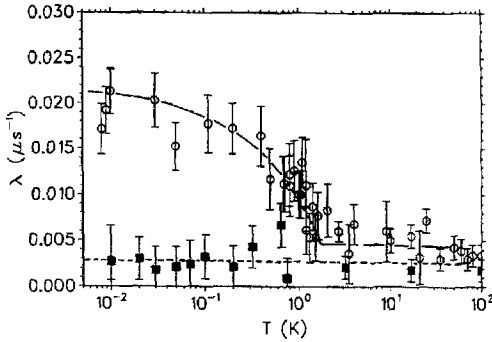


Fig. 128. Muon spin relaxation rate in ZF (open circles) and LF=0.6 T (solid squares) in a single crystal of  $\text{CeRu}_2\text{Si}_2$ . The initial muon spin direction is along the  $c$ -axis. The lines are guides to the eye. From Amato et al. (1993b).

result was obtained for  $\text{PrCo}_2\text{Si}_2$  (Nojiri et al. 1992). If one makes the reasonable, but not guaranteed, assumption that the muon stopping site is unique for the  $\text{ThCr}_2\text{Si}_2$  structure, then at present a clear picture does not exist. The 4c site seems to be the most convincing choice. The knowledge of the muon site is not essential for the basic features to be discussed next. It would help, however, in extracting more quantitative results as to the exact size of moments and would provide more details on spin structures. It is important that all studies do show clear evidence for a stationary muon up to  $\sim 180$  K. Only at higher temperatures does muon diffusion become noticeable.

As pointed out, Amato et al. (1993b, 1994a) found an increase of relaxation rate (fig. 128) below 2–3 K (slightly sample dependent) in ZF with a temperature dependence typical for a second-order magnetic transition. Application of LF suppresses this additional relaxation showing that the field sensed by the muons is essentially static. The overall features are quite reminiscent of the findings by Uemura et al. (1989) in  $\text{CeCu}_{2.02}\text{Si}_2$ , but the maximum relaxation rate ( $T \rightarrow 0$ ) is more than two orders of magnitude lower ( $\sim 0.02 \mu\text{s}^{-1}$ ), meaning that the magnetic moments involved are correspondingly smaller. It is of course true that the size of relaxation rate seen in  $\text{CeRu}_2\text{Si}_2$  falls well inside the range of depolarization by nuclear moments, but there is no scenario that would explain the rise in depolarization by nuclear moments if one excludes muon hopping between different lattice sites, which is fully justified. The interpretation is then that the additional relaxation comes from a highly disordered array of static electronic moments on Ce with a magnitude  $\sim 10^{-3} \mu_B$ .

Bulk data had led to the classification of  $\text{CeRu}_2\text{Si}_2$  as an “almost ordered” compound. For example, neutron studies have shown that doping of  $\text{CeRu}_2\text{Si}_2$  with La in excess of  $\sim 7\%$  induces incommensurate spin density wave (ISDW) ordering (Quezel et al. 1988) whereas pure  $\text{CeRu}_2\text{Si}_2$  only exhibits ISDW-type spin correlations (Regnault et al. 1988). It is thought that the lattice expansion induced by La doping leads to the formation of the ISDW ordered state. In any case, the absence of spontaneous spin precession in the  $\mu\text{SR}$  spectra of  $\text{CeRu}_2\text{Si}_2$  below 2 K points towards a highly disordered magnetic state. Further support for this assignment comes from  $\mu\text{SR}$  data on the pseudo-ternary compounds  $\text{Ce}_{1-x}\text{La}_x\text{Ru}_2\text{Si}_2$  and  $\text{Ce}(\text{Ru}_{1-x}\text{Rh}_x)_2\text{Si}_2$ , which will be discussed below. The smallness of the moment precludes any direct measurement of spin structure.

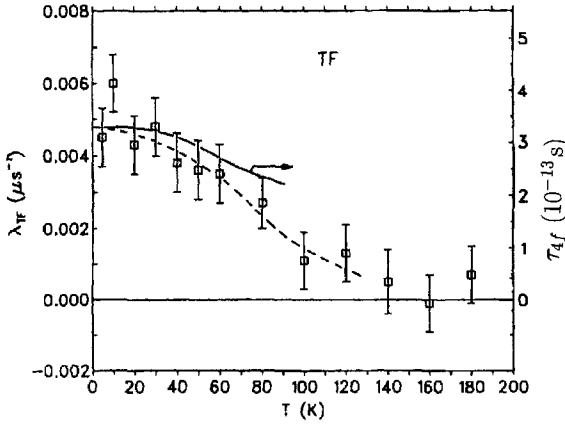


Fig. 129. Exponential (dynamic) relaxation rate in paramagnetic  $\text{CeRu}_2\text{Si}_2$  measured in  $TF = 7.4 \text{ mT}$  applied parallel to the  $c$ -axis (left-hand scale). The fluctuation rate  $\tau_{4f}$  from neutron scattering (see text) is plotted as a solid line (right-hand scale). From Amato et al. (1993b).

Low TF ( $7.4 \text{ mT} \parallel c$ ) measurements between 6–180 K (i.e., well above the onset of magnetism) were also carried out by Amato et al. (1993b, 1994a). The analysis of data used the double relaxation formalism for a Gaussian relaxation due to static nuclear moments and an exponential relaxation due to fluctuating electronic moments on Ce. For the latter, one can use  $\lambda_{TF} = 2\Delta^2 \tau_{4f}$ , where  $\Delta^2$  is the second moment of the field arising from Ce dipoles and  $1/\tau_{4f}$  is their single-site (ss) fluctuation rate. The values of  $\lambda_{TF}$  were compared to the neutron quasielastic linewidth  $\Gamma_{ss} = \hbar/\tau_{4f}$  (Regnault et al. 1988) after correction for inter-site fluctuations. Combining the two data sets (see fig. 129) results in a paramagnetic moment on the Ce atoms of  $\sim 0.6\mu_B$  in the temperature range covered. This moment is greatly reduced relative to the high-temperature Curie moment ( $\sim 2.53\mu_B$ ), emphasizing the pronounced influence of Kondo interaction on the quasiparticles.

Finally, high-field (600 mT) LF data demonstrate that the relaxation rate in field is strongly reduced but not zero at all temperatures, including the magnetic range  $T < 2 \text{ K}$  (see fig. 128). This means that the quasistatic structure of small moments coexists with the fluctuating larger moments, a picture that requires the presence of two subsets of electrons in the HF ground state. As mentioned before, such a model has been put forward for some uranium HF compounds (see sect. 9.3.2).

Another  $\mu\text{SR}$  study of  $\text{CeRu}_2\text{Si}_2$  was carried out by Sekine et al. (1994, 1995). Their work covers only the paramagnetic regime and gives essentially the same result as the TF studies by Amato et al. (1993b, 1994a), that is, the presence of fast fluctuating ( $\tau_{4f} \approx 10^{-13} \text{ s}$ ) Ce moments on the order of  $1\mu_B$ . The similarity of  $\lambda_{TF}$  and  $\lambda_{ZF}$  is additional proof that the fast fluctuation limit is reached. Sekine et al. (1994) point out that their value of  $1/\tau_{4f}$  leads to  $T_{sf} = \hbar/k_B \tau_{4f} = 38 \text{ K}$  for the (4f–ce) coupling strength. This number is close to  $T_K \approx 25 \text{ K}$  from bulk data.

A recent brief report by Yaouanc et al. (1999a) points out that the temperature and longitudinal field dependence of the muon spin relaxation rate near the transition temperature is anomalous in the intermetallics  $\text{CeRu}_2\text{Si}_2$ ,  $\text{UGe}_2$  and  $\text{YbNiSn}$ . We had

already mentioned in the preceding section the suppression in fairly low longitudinal fields of the typical rise of rate when approaching the magnetic transition from the paramagnetic side for the case of YbNiSn. The authors claim that all three compounds have an anomalous spectral weight of magnetic excitations in the energy range of 10 meV, despite the fact that their electronic ground states are quite different. UGe<sub>2</sub> is listed as a HF-ferromagnet (Önuki 1993), YbNiSn is a ferromagnetic Kondo-lattice system, while CeRu<sub>2</sub>Si<sub>2</sub> exhibits weak quasistatic (antiferro-) magnetism. It is further stated that the quasielastic low-energy magnetic excitation is not caused by the dual f electron structure discussed for CeRu<sub>2</sub>Si<sub>2</sub> and YbNiSn (see above), but is rather considered to be a basic feature of correlated electron systems. Theoretical details on this scenario are not given and neither is a derivation of the quasielastic excitations presented. The significance of the model cannot be judged at this point.

It has already been mentioned that in Ce<sub>1-x</sub>La<sub>x</sub>Ru<sub>2</sub>Si<sub>2</sub>, magnetic order of the ISDW type is stabilized for  $x > 0.07$ . In this concentration range sinusoidal modulation is observed. It squares up with the same wave vector  $\mathbf{q} = (0.39, 0, 0)$  beyond  $x = 0.2$ . Yamamoto et al. (1997) report on ZF- $\mu$ SR measurements on single-crystalline samples with  $x = 0.05$  (paramagnetic),  $x = 0.13$  (sinusoidal modulated) and  $x = 0.25$  (squarely modulated). The spectra for the paramagnetic ( $x = 0.05$ ) material were analysed once again in terms of double relaxation combining Gaussian depolarization from nuclear and exponential depolarization from (presumably) electronic moments. The Gaussian relaxation is temperature independent, as expected. Also, the exponential rate becomes smaller with rising temperature, as in the pure compound. The authors make the disturbing remark, however, that the exponential relaxation can be eliminated by small longitudinal fields ( $\sim 10$  G), which would mean that the electronic moments are static as well but give rise to a *Lorentzian* field distribution. This is an entirely different picture than the fast-fluctuating Ce moments in the pure compound and hard to understand. The authors give no further explanation.

The  $x = 0.13$  sample has  $T_N = 4.2$  K. Below this temperature, a fast (Lorentzian) Kubo–Toyabe relaxation is seen (see fig. 130, left), but no spontaneous spin precession. The authors use a field distribution based on the known ISDW magnetic structure calculated by dipolar sums for the  $(0, \frac{1}{2}, \frac{1}{8})$  stopping site they prefer. This theoretical depolarization function is shown in fig. 130 (left) and agrees roughly (but not in detail) with the measured spectrum (the discrepancy becomes worse at lower temperatures), and supports the notion of ISDW magnetism.

For  $x = 0.25$  the relaxation rate for  $T < T_N = 6.2$  K has further increased. Most of the signal is lost in the initial dead time (of the BOOM pulsed muon facility). No further details are given.

Another means to induce long-range magnetic order in the CeRu<sub>2</sub>Si<sub>2</sub> system is to replace Ru by Rh. The end point of the pseudo-ternary series Ce(Ru<sub>1-x</sub>Rh<sub>x</sub>)<sub>2</sub>Si<sub>2</sub>, i.e., pure CeRh<sub>2</sub>Si<sub>2</sub>, is an antiferromagnet with the highest transition temperature ( $T_N \approx 37$  K) of all CeT<sub>2</sub>Si<sub>2</sub> intermetallics. This, together with a fairly substantial ordered moment, makes CeRh<sub>2</sub>Si<sub>2</sub> more likely a weak Kondo AFM than a HF compound.  $\mu$ SR spectroscopy on CeRh<sub>2</sub>Si<sub>2</sub> has been discussed in sect. 5.5.2. The rather complex AFM spin structure leads

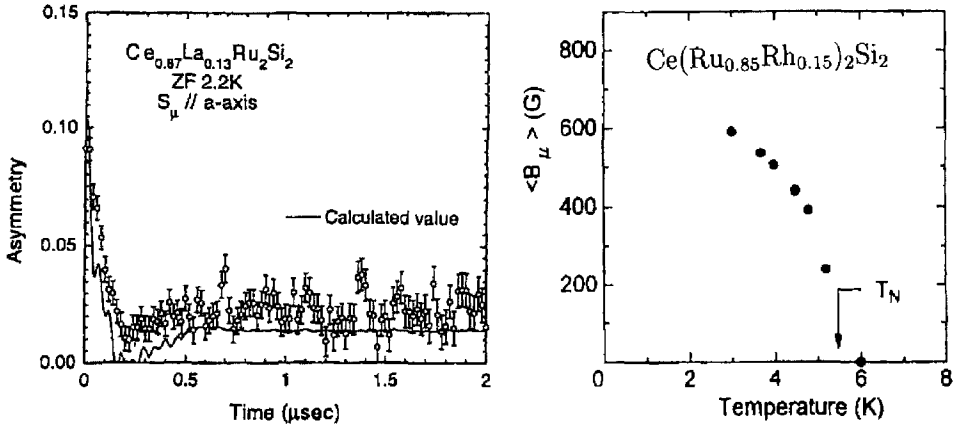


Fig. 130. Left: ZF  $\mu$ SR spectrum of  $\text{Ce}_{0.87}\text{La}_{0.13}\text{Ru}_2\text{Si}_2$  together with the theoretical depolarization function based on incommensurate sinusoidally modulated spin wave magnetic order (see text for details). From Yamamoto et al. (1997). Right: Temperature dependence of the mean field seen by muons in magnetic  $\text{Ce}(\text{Ru}_{0.85}\text{Rh}_{0.15})_2\text{Si}_2$ . A single crystal oriented with the  $c$ -axis perpendicular to the muon beam was used. From Murayama et al. (1997).

to a two-component  $\mu$ SR spectrum, one oscillating, the other just relaxing. A rather small local field (125 G) is present at the low-temperature limit.

The pseudo-ternary compound  $\text{Ce}(\text{Ru}_{0.85}\text{Rh}_{0.15})_2\text{Si}_2$  was studied by Murayama et al. (1993, 1997). This material exhibits incommensurate sinusoidal spin modulation with a magnetic moment of  $0.65\mu_B$  along the  $c$ -axis below  $T_N \approx 5.5$  K (Kawarazaki et al. 1995). Correspondingly, a strong rise in ZF relaxation rate sets in below  $T_N$ , but again without spontaneous spin precession. The signal vanishes in the dead time of the BOOM facility below  $\sim 3$  K. The spectra in the magnetic regime have been analyzed using a Gaussian decay ( $\exp[-\sigma^2 t^2/2]$ ) from which the mean field  $\langle B_\mu \rangle = \sigma/\gamma_\mu$  was deduced. Its temperature dependence is depicted in fig. 130 (right) and clearly indicates a second-order phase transition. The extraction of  $\langle B_\mu \rangle$  as described assumes a static field distribution, which was verified by LF measurements. An attempt was made to obtain the field distribution function  $P(|B_\mu|)$  via FFT. The authors conclude that the results are in keeping with ISDW ordering. Coexisting with this ordered state are fluctuating Ce moments as has been previously postulated for pure  $\text{CeRu}_2\text{Si}_2$ . The relaxation rates are not markedly different in the pure and alloyed samples.

More recently, Yamamoto et al. (2000a) have briefly reported on a  $\mu$ SR study of the more dilute Rh-doped pseudo-ternary  $\text{Ce}(\text{Ru}_{0.95}\text{Rh}_{0.05})_2\text{Si}_2$  using a single-crystalline sample. This compound is close to the lower concentration limit of Rh for the formation of the ISDW ordered state. The ZF- $\mu$ SR data for  $S_\mu \parallel c$  and  $S_\mu \parallel a$  show exponential relaxation down to  $\sim 0.2$  K, reflecting fast fluctuations of the 4f moments (as confirmed by additional LF data). Below this temperature, which is interpreted as the magnetic transition point  $T_N$ , a two component pattern is seen. One component is a fast relaxing signal of Gaussian form, the other a slowly relaxing signal of exponential shape. The



Gaussian signal is soon lost in the instrumental dead time when cooling below  $T_N$ . Muons generating this signal see a broad distribution of local field, much broader than usually encountered in ISDW states. Especially in view of the comparatively small ordered moment, this means that strong additional disorder must be present in the ISDW spin lattice. The exponentially relaxing signal loses amplitude continuously on cooling but still has not vanished at the base temperature (0.3 K). While the basic features of the  $\mu$ SR signal for  $T < T_N$  are independent of sample orientation, the spectral parameters such as relaxation rates and sub-signal amplitudes are not. These anisotropies are roughly in keeping with the notion that the ordered moment is predominantly aligned along the  $c$ -axis, as deduced from neutron data.

The exponentially relaxing single paramagnetic signal exhibits critical slowing down on approach to  $T_N$ , which was analyzed in terms of SCR theory (Ishigaki and Moriya 1996). Good agreement for AFM spin fluctuations was achieved for  $\mathbf{S}_\mu \parallel c$ , but for  $\mathbf{S}_\mu \parallel a$  FM fluctuations gave the better result. Although the authors speculate on a  $q$ -dependence of spin fluctuations, the reason for this behavior remains enigmatic. The reviewers would like to stress that this experiment provides a direct observation of two signals (one related to ISDW order, the other to persistent spin fluctuations) below  $T_N$ , which lends strong support to the picture of two electronic subsets in  $\text{CeRu}_2\text{Si}_2$ , which was introduced above.

*Summary:* The  $\mu$ SR studies on  $\text{CeRu}_2\text{Si}_2$  and its related compounds suggest that the magnetic ISDW ordering observed in  $\text{Ce}_{1-x}\text{La}_x\text{Ru}_2\text{Si}_2$  and  $\text{Ce}(\text{Ru}_{1-x}\text{Rh}_x)_2\text{Si}_2$  does not altogether vanish for  $x = 0$ . Below  $\sim 2$  K such a magnetic state is likely to exist in pure  $\text{CeRu}_2\text{Si}_2$  although with an extremely low ordered moment ( $10^{-2}$ – $10^{-3}\mu_B$ ). This ordered state coexists with much larger, fluctuating Ce moments ( $\sim 1\mu_B$ ) suggesting the existence of two subsets of electrons in the ground state of this HF material. It is so far the only Ce compound for which this feature has been found with some reliance (but see also  $\text{CeRu}_2$ ).

9.3.1.11.  $\text{CeRu}_2\text{Ge}_2$ ,  $\text{Ce}(\text{Ru}_{1-x}\text{Fe}_x)_2\text{Ge}_2$ . These intermetallics crystallize in the same tetragonal  $\text{ThCr}_2\text{Si}_2$  structure as  $\text{CeRu}_2\text{Si}_2$ .  $\text{CeRu}_2\text{Ge}_2$  shows, in contrast to  $\text{CeRu}_2\text{Si}_2$ , hardly any HF properties. The Sommerfeld constant is little enhanced ( $0.02 \text{ J}/(\text{mol K}^2)$ ). Via magnetization, two magnetic transitions ( $T_N = 8.5 \text{ K}$  and  $T_C = 7.5 \text{ K}$ ) are established (see, for example, Böhm et al. 1988). The spin state below  $T_N$  has only recently been confirmed by neutrons (Raymond et al. 1998) to be a commensurate AFM structure.

ZF- $\mu$ SR spectra (Walf et al. 1999) show spontaneous spin precession below  $T_N = 8.5 \text{ K}$ . In the AFM regime two precession frequencies are present, in the FM regime only one. This result is in basic agreement with the assignment of a commensurate AFM and a collinear FM structure. The temperature dependence of the precession frequencies is presented in fig. 131 (left). It shows a most unusual feature. The two frequencies in the AFM state first rise (roughly in parallel) when lowering the temperature in a normal fashion. But at  $T_C$  a sudden collapse of frequency to  $\nu_\mu(T_C) = 0$  is seen, followed again by a rise of frequency below  $T_C$ . All LRO magnetism appears to be lost in the

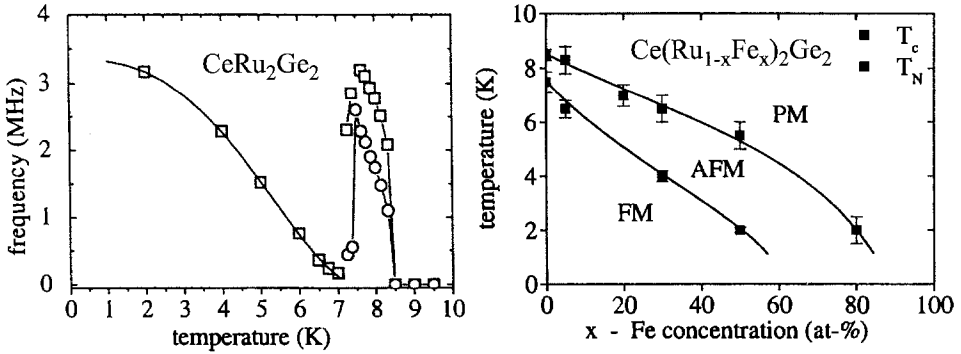


Fig. 131. Left: Temperature dependence of spontaneous precession frequencies in magnetically ordered  $\text{CeRu}_2\text{Ge}_2$ . Right: Magnetic phase diagram for  $\text{Ce}(\text{Ru}_{1-x}\text{Fe}_x)_2\text{Ge}_2$  derived from  $\mu$ SR data. From Walf et al. (1999).

crossover from the AFM to the FM state, a novel behavior. Inside the FM regime one finds a temperature dependence  $\nu_\mu(T)$  that is not of the simple Brillouin type seen for the bulk magnetization. Furthermore, the saturation frequency ( $\nu_\mu(2\text{K}) = 3.2\text{ MHz}$ ) is significantly lower than the value calculated by dipolar sums ( $\nu_{\text{dip}}(0) = 5.2\text{ MHz}$ ). The  $(0, \frac{1}{2}, \frac{1}{8})$  interstitial position has been assumed as the muon stopping site together with a moment of  $2\mu_B$  aligned along the  $c$ -axis. The authors study the effect of moment tilting and find that such a model reproduces the asymmetric frequency distribution obtained by FFT of the precession signal. It fails, however, to lower the value of  $\nu_\mu(0)$ .

$\text{CeFe}_2\text{Ge}_2$  is a moderate HF compound with a nonmagnetic ground state. A substitution of Ru by Fe increases the 4f hybridization and one expects a continuous decrease of  $T_N$  with rising Fe concentration within the Kondo necklace model. Figure 131 (right) shows the magnetic phase diagram derived from  $\mu$ SR data. The reduction of  $T_C$  is in good agreement with corresponding data for the isostructural pseudo-binary system  $\text{CeRu}_2(\text{Ge}_{1-x}\text{Si}_x)_2$ . The monotonic decrease in  $T_N$  with Fe concentration, however, though in agreement with the Doniach model, is different from the behavior of  $T_N(x)$  seen by magnetization in  $\text{CeRu}_2(\text{Ge}_{1-x}\text{Si}_x)_2$  where it passes through a weak maximum (Haen et al. 1996). Walf et al. (1999) suggest different hybridization mechanisms to be the underlying cause. While the change of unit cell volume is effective for the Ge–Si replacement, the change in 4f hybridization by Ru–Fe replacement is thought to come primarily from the increase of itinerant 3d electron density. All magnetism vanishes near the Fe concentration  $x = 0.9$ , which might establish a quantum critical point.

**Summary:**  $\mu$ SR spectroscopy on  $\text{CeRu}_2\text{Ge}_2$  reveals an unusual loss of magnetism at the transition from the AFM to the FM state ( $T_C = 7.5\text{ K}$ ). The data below  $T_C$  are not in good agreement with FM spins aligned along the  $c$ -axis and moment tilting is a possibility. The variation of  $T_N$  with increasing replacement of Ru by Fe follows the expectations of the Doniach necklace model, but is significantly different from corresponding data in  $\text{CeRu}_2(\text{Ge}_{1-x}\text{Si}_x)_2$ , which points towards an influence of increasing 3d electron density.

9.3.1.12.  $CeT_2Sn_2$  ( $T = Cu, Pd, Pt$ ). This series of ternary Ce intermetallics has attracted considerable interest because it provides a good testing ground for the study of the interplay between Kondo and RKKY interaction within the frame of the Kondo necklace model.  $CeCu_2Sn_2$  and  $CePd_2Sn_2$  are well established AFM (Beyermann et al. 1991a).  $CePt_2Sn_2$  develops a very large Sommerfeld constant ( $\gamma > 3 \text{ J}/(\text{mol K}^2)$ ) below 5 K and exhibits unusual magnetic properties, which will be discussed below. All compounds crystallize in the tetragonal  $P4/nmm$  ( $CaBe_2Si_2$ ) structure, but in  $CePt_2Sn_2$  some minor deviations can occur (see below). They show strong anisotropy in their physical parameters. We shall first discuss the Pt compound since it is the most unusual, and more detailed  $\mu$ SR data are available for it.

Beyermann et al. (1991b) reported that polycrystalline  $CePt_2Sn_2$  can possess a small monoclinic distortion and undergoes magnetic order at  $T_N = 0.88 \text{ K}$  as revealed by a peak in the specific heat. Inelastic neutron scattering gave a value for the quasielastic linewidth consistent with the large Sommerfeld constant. It also determined the Kondo temperature ( $T^* \approx 1 \text{ K}$ ) to be rather close to  $T_N$  (Mignot et al. 1993), which shows that RKKY and Kondo interactions are indeed of comparable strength. Shigeoka et al. (1993) have studied single-crystalline samples by specific heat, magnetic susceptibility and electrical resistivity and found that magnetic order was apparently absent (above 0.45 K). The difference in behavior is ascribed to the monoclinic distortion present only in polycrystalline material.

Luke et al. (1995) studied a single crystal of  $CePt_2Sn_2$  with ZF- and LF- $\mu$ SR between 0.02 and 200 K with the muon spin aligned initially along the  $a$ -axis. The variation of the relaxation rate with temperature is shown in fig. 132 together with analogous data for a polycrystalline sample (Luke et al. 1997a). At this point we shall concentrate on the single-crystal data, the comparison with the polycrystal will be made later on. At all temperatures the relaxation in the single-crystal specimen is well described by a power-exponential decay ( $\exp[-(\lambda t)^p]$ ). The variation of power  $p$  with temperature is depicted in fig. 133. At higher temperatures ( $T > 0.7 \text{ K}$ ) pure exponential ( $p = 1$ ) decay of polarization is seen. Only at very low temperatures does the power gradually rise toward  $p = 2$ , that is, Gaussian relaxation. The exponential relaxation is largely insensitive to a longitudinal field of 1 kG and hence rapidly fluctuating (electronic) moments must be responsible.

The first increase of relaxation rate on cooling from room temperature reflects the formation of the heavy-fermion state where the  $Ce^{3+}$  begin to be Kondo-screened and their fluctuation rate slows down. This corresponds to the narrowing of the quasielastic linewidth seen by neutrons (see also the discussion of analogous data for  $CeRu_2Si_2$ ). One may take the temperature at which this relaxation process saturates as an estimate of  $T^*$ . The resulting value of  $\sim 20 \text{ K}$  is considerably larger than the neutron value quoted earlier and the reaching of a plateau may just be an indication of a crossover between the Kondo mechanism and another mechanism for 4f spin fluctuations. Specific heat shows a Schottky anomaly around 30 K and susceptibility data as well indicate that this is roughly the position of the first CEF level (Shigeoka et al. 1993). One might then relate the temperature variation of relaxation rate also to the depopulation of the excited

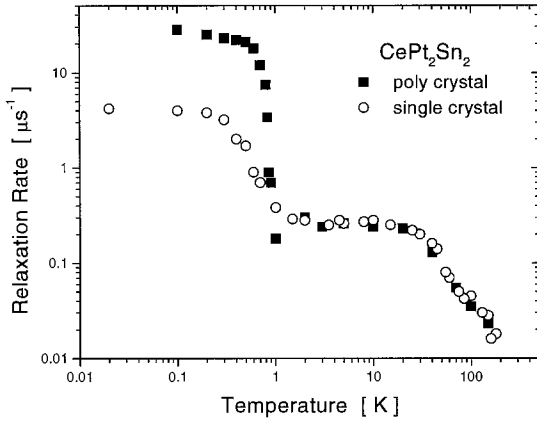


Fig. 132. ZF relaxation rate as a function of temperature in single-crystalline and poly-crystalline samples of  $\text{CePt}_2\text{Sn}_2$ . Below 1 K the relaxation rates have different meaning in the two cases (see text), but above this temperature are directly comparable.

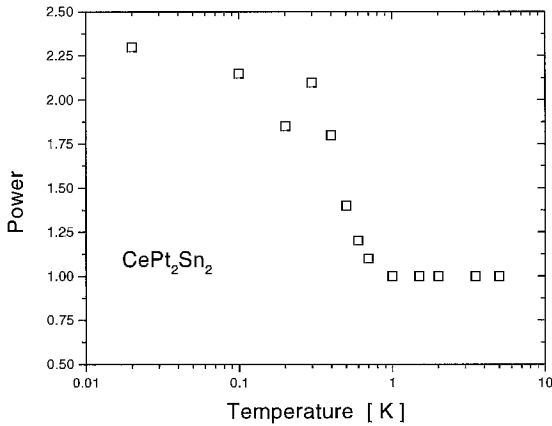


Fig. 133. Temperature dependence of the power in the power-exponential relaxation fit to the ZF spectra of single-crystalline  $\text{CePt}_2\text{Sn}_2$ . From Luke et al. (1997a).

CEF levels of  $\text{Ce}^{3+}$  (see sect. 5.1.1). Dalmás de Réotier et al. (1996) discuss in general the connection between CEF and Kondo interactions. They point out that the difference in  $T^*$  between the neutron and  $\mu$ SR measurements in  $\text{CePt}_2\text{Sn}_2$  could be a straightforward result of CEF interactions. The absence of information on the full CEF level scheme does not allow a quantitative discussion of this aspect (for some more details, see the discussion of the HF compound  $\text{YbAuCu}_4$ ).

The rise in relaxation rate below 1 K is considered an indication of the attempt of the largely compensated moments to order magnetically. This is not achieved, however. The longitudinal field data of fig. 134 (left) demonstrate clearly that the fluctuations of the  $\text{Ce}^{3+}$  moments never die out, even at 20 mK. Strong fields can now affect the relaxation process more than at high temperatures, but the 5 kG pattern is very convincingly dynamic. In short, slowing down of fluctuations by the formation of magnetic correlations has occurred, but the quasistatic situation of long-range order is not realised. The likely block to magnetic order is geometric frustration.

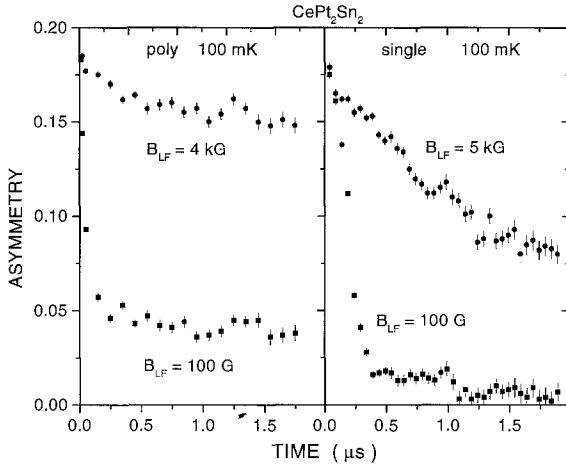


Fig. 134. Longitudinal field decoupling at 100 mK measured in  $\text{CePt}_2\text{Sn}_2$  single crystal and polycrystal. The LF data of the polycrystal prove the spin system to be static, while it remains clearly dynamic in the single-crystalline material. Adapted from Luke et al. (1997a).

The data for a polycrystalline sample by Luke et al. (1997a) follow the results of the single-crystal specimen above  $\sim 1$  K. Though expected, since in this temperature region magnetic order is not in question, the agreement is satisfying. The temperature dependence of the dynamics of Ce moments is similar in the two samples, so the same mechanisms are at work. The data below 1 K, however, differ significantly from that of the single crystal. The relaxation rate rises more sharply and reaches values about one order of magnitude higher for  $T \rightarrow 0$ . The LF studies shown in fig. 134 (right) prove that now there are quasistatic moments. The appearance of the (slowly decaying) “1/3 tail” is important in establishing this. The freezing occurs around 0.85 K in excellent agreement with the specific heat data of Beyermann et al. (1991b). A spontaneous precession signal is not observed. The local field must be widely distributed, meaning that a highly disordered magnetic state has been entered.

A word of caution about fig. 132: the relaxation rate below 1 K has a completely different meaning for the single crystal relative to the polycrystalline samples. In the former, the dynamic situation prevails and the variation of relaxation rate reflects changes in the fluctuation rate of 4f moments. It rises as moment fluctuations slow down at lower temperatures. In the latter, depolarization is close to static and the rate more directly relates to the field distribution width, which increases in proportion to the rise of magnetization in an ordered magnet when temperature is reduced.

The likely explanation for the fundamental difference in magnetic behavior between the single crystal and the polycrystalline sample is the relief of frustration by the monoclinic distortion in the latter. Different preparation methods resulting in changes in stoichiometry or impurity content may be important. Internal strain in the sample can play a role as well. It should be mentioned that whether distortion is present or not is not necessarily connected to the polycrystalline *vs.* single-crystal form (see the results of Lidström et al. 1996a discussed below).

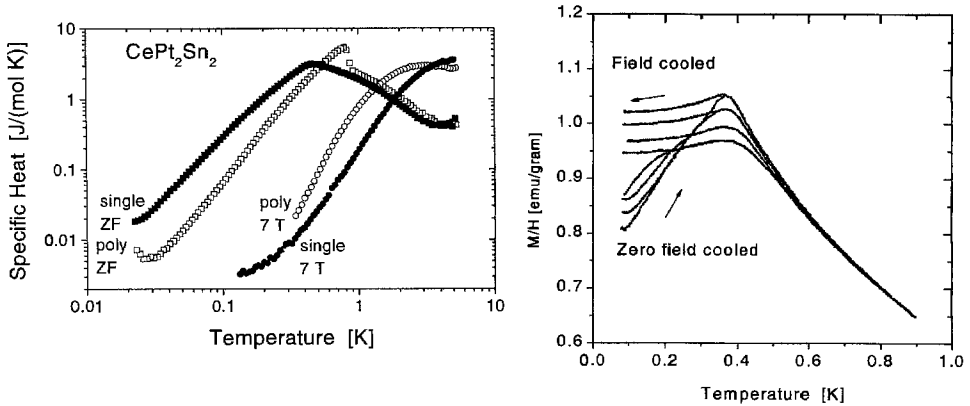


Fig. 135. Left: temperature dependence of specific heat for the single-crystalline (solid symbols) and polycrystalline (open symbols) specimen of  $\text{CePt}_2\text{Sn}_2$  used in the  $\mu$ SR studies by Luke et al. (1995, 1997a) in zero and 7 T applied fields. Right: dc susceptibility in 31, 80, 227 and 474 G (top to bottom) for the single-crystalline sample (Kalvius et al. 2000d).

In fig. 135 left, low-temperature specific heat data are presented measured on the *same samples* as used in the  $\mu$ SR study (Kalvius et al. 2000d). The presence (absence) of a magnetic transition in the polycrystalline (single-crystalline) sample is quite visible. Remarkably, under strong applied fields ( $B \geq 3$  T), the magnetic transition in the polycrystal appears to be suppressed (or at least smeared out) and the shape of the  $C(T)$  curve approaches that of the single-crystal sample. The dc susceptibility (fig. 135 right) indicates the formation of a spin-glass-like state below 0.4 K. The zero-field specific heat data agree with those published by Takeda et al. (1996). These authors also present ac susceptibility data for both polycrystalline and single-crystal materials. The latter exhibit a sharp, field-dependent cusp near 0.4 K, which is interpreted as a spin-glass transition. The validity of this conclusion is questionable, since no irregularity is apparent at this temperature in the  $\mu$ SR parameters and true spin freezing does not occur. The (well-developed) spin correlations remain dynamic and the system is better described as a dynamically short-range-correlated magnet. (See also the discussion of data by Lidström et al. 1996a further below.)

Finally, a word concerning the atypical form of the  $\mu$ SR spectrum in the single-crystal sample at low temperatures. It is Gaussian at early times, a feature characteristic for a static spin system, but both the missing “1/3 tail” and the LF behavior prove it to be dynamic. Such an unusual spectral shape has been seen in a number of geometrically frustrated systems, most notably in Kagomé lattices (Uemura et al. 1994). It signals the breakdown of Markovian spin dynamics. The situation in Kagomé lattices is successfully described by the assumption that a local field  $B_\mu$  of significant magnitude exists at each muon site only sporadically, i.e., it is present only during a fraction  $f$  (with  $f \ll 1$ ) of the residence time of the muon. Otherwise  $B_\mu = 0$ . The likely explanation of this zero-field time span is the formation of local spin-singlet pairs. Some spins, however, remain

unpaired and migrate through the lattice, producing a substantial value of  $B_{\mu}$  when passing close to a muon site.

$\mu$ SR results for a powder sample of  $\text{CePt}_2\text{Sn}_2$  have also been published by Lidström et al. (1996a) in the course of a general study of the  $\text{CeT}_2\text{Sn}_2$  system. Their data on  $\text{CePt}_2\text{Sn}_2$  are remarkable in the sense that their features are close to those of Luke et al. (1995) for single-crystalline material. It must be concluded that the powder material of Lidström et al. (1996a) does not possess the monoclinic distortion discussed earlier for polycrystalline materials. As stated above, the question of the presence of distortion is perhaps more strictly connected to the preparation process. In fact, Lidström et al. (1996b) argue that the presence of monoclinic distortion in the polycrystals is a misinterpretation of the diffraction pattern. One should also consider that the samples of Lidström et al. (1996a,b) contain  $\sim 15\%$  of nonmagnetic PtSn and deviate from perfect stoichiometry, as mentioned by the authors.

Despite the fact that the data of Lidström et al. (1996a) closely resemble those of Luke et al. (1995) for a single-crystalline specimen, the former authors choose a quite different interpretation. They take the change from Lorentzian to Gaussian initial slope, occurring around 0.4 K (see also fig. 133), as an indicator for the onset of long-range AFM order. The spectra above this temperature are fitted with a Kubo–Toyabe (static Pt nuclear dipoles) plus exponential (fluctuating Ce moments) double relaxation. Below 0.4 K they use a combination of an oscillating signal with  $2/3$  amplitude and Lorentzian–Gaussian double relaxation (meaning that a wide static field distribution causes dephasing while relaxation is still present due to spin dynamics) and a non-oscillating “ $1/3$  signal” exhibiting only dynamic depolarization (with the same rate as seen in dynamic contribution to the damping of the “ $2/3$  signal”). Yet, explicit spin precession is not observed in the spectra: that requires the dephasing rate to be significantly larger than the precession frequency (the fit gives a factor of  $\sim 2.5$ ). This is a rather involved fitting procedure for spectra that show little in the way of distinct features. The facts that no sudden changes in spectral shape occur around 0.4 K, and that no change in total signal amplitude is seen, in contrast to the results for  $\text{CePd}_2\text{Sn}_2$  and  $\text{CeCu}_2\text{Sn}_2$  (see below), argue against this interpretation. In the polycrystalline sample of Luke et al. (1995) (with an established AFM transition around 0.9 K) the relaxation rate rises sharply to significantly larger values (see fig. 132). For a pulsed beam this would have resulted in signal loss. Furthermore, with long-range order one expects the dynamic portion of the relaxation rate to decrease again as the critical region is left. This is not observed. The likely explanation is the one used by Luke et al. (1995) for their results on the single-crystalline sample, namely an increase of spin correlations which, however, remain dynamic. In consequence, the fascinating result is that a polycrystalline sample can also show frustration, most likely because monoclinic distortion has not occurred, or is too weak.

In  $\text{CePd}_2\text{Sn}_2$  an AFM transition with  $T_N \approx 0.5$  K has been established by Beyermann et al. (1991a,b) for polycrystalline material. The  $\mu$ SR data by Lidström et al. (1996a) are fully compatible with this view. Since there is no significant nuclear depolarization in the Pd compound, the temperature variation of (exponential) relaxation rate  $\lambda$  directly reflects the dynamics of Ce moments. For  $T > T_N$  one observes a critical power

law  $\lambda \propto (T - T_N)^{-0.4}$  over a wide temperature range. This is the typical behavior for a magnetic rare-earth compound. Below  $T_N$  the sample signal is practically lost. Relaxation now exceeds the initial dead time of the (pulsed muon) spectrometer.

In  $CeCu_2Sn_2$  a magnetic transition occurs at  $T_N = 1.6$  K. The analysis of the μSR data (Lidström et al. 1996a) in the paramagnetic regime is more difficult since relaxation is dominated by the static Cu nuclear dipoles. Using the electron–nuclear double relaxation formalism, a result similar to  $CePd_2Sn_2$  was obtained, but with considerably less accuracy. At  $T_N$ , the signal amplitude begins to decrease but only gradually. This indicates that the transition temperature is distributed over the sample. Variation in local stoichiometry is the likely cause.

*Summary:* In  $CePt_2Sn_2$ , a significant difference occurs in the magnetic response (especially for μSR) between samples having the “correct” tetragonal structure and those with an additional monoclinic distortion. In the former, strong spin correlations develop below ~1 K but remain *dynamic* even for  $T \rightarrow 0$ . This is likely due to frustration and prevents long-range magnetic order. If lattice distortion is present, the quasistatic limit of correlations is reached and a disordered magnetic state is formed around 0.85 K. The temperature dependence of the relaxation rate at higher temperatures is identical in both samples and reflects the formation of the HF state. The μSR data on  $CePd_2Sn_2$  and  $CeCu_2Sn_2$  confirm their classification as Kondo AFM.

9.3.1.13.  $CePd_2Al_3$ . This compound crystallizes in an hexagonal (P6/mmm) structure. Polycrystalline  $CePd_2Al_3$  (well annealed) shows a transition at  $T_N = 2.7$  K into long-range ordered AFM according to neutron diffraction data by Kitazawa et al. (1992). The Ce moments are aligned within the basal plane with  $q = (00 \frac{1}{2})$ . μSR data taken on similar samples exhibit a strong rise in ZF depolarization rate at  $T_N$ , with a temperature dependence resembling the typical magnetization curve (fig. 136, Mentink et al. 1994a,b).

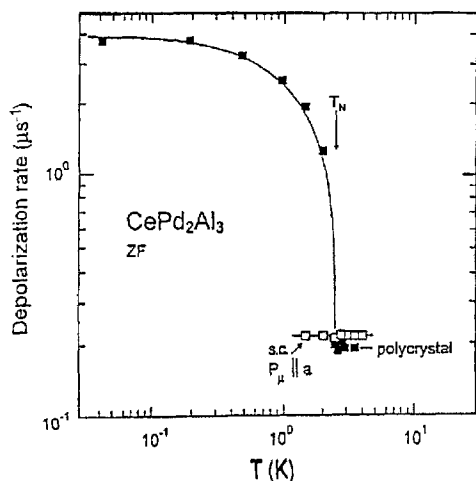


Fig. 136. Temperature dependence of the ZF depolarization rate in  $CePd_2Al_3$  for a polycrystalline and a single-crystalline (sc) specimen (beam parallel to the  $a$ -axis). After Mentink et al. (1994b).



The static Ce moment determined by neutrons is  $\sim 0.4\mu_B$ , much lower than the moment calculated for the expected  $|\pm 1/2\rangle$  CEF doublet ( $1.28\mu_B$ ). Mentink et al. (1994b) invoke a large exchange constant  $\mathcal{J}$  and Kondo temperature  $T^*$  to explain this substantial moment reduction. Surprisingly, single-crystalline samples do not exhibit any magnetic transition down to at least 0.3 K. It is thought that magnetic ordering depends on the perfection of the Al sub-lattice which perhaps is disturbed by the single-crystal growing procedure (Mentink et al. 1994a). An early neutron diffraction study (Mitsuda et al. 1992) reported incommensurate magnetic ordering in a narrow range above 2.8 K, but a later study disagrees (Dönni et al. 1994). In any case, one is forced to conclude that  $\text{CePd}_2\text{Al}_3$  is magnetically unstable and close to the boundary between a magnetic and a nonmagnetic ground state. This may be the underlying cause for the sample dependence of its magnetic properties. Additional support for this picture comes from the fact that isoelectronic and isostructural  $\text{CeNi}_2\text{Al}_3$  has a smaller lattice constant, leading to a lower magnetic transition temperature and the clear presence of IV behavior.

The  $\mu\text{SR}$  spectra of polycrystalline  $\text{CePd}_2\text{Al}_3$  having the 2.7 K magnetic transition show no spontaneous spin precession below  $T_N$ . The spectra are well reproduced by Kubo–Toyabe relaxation with a Brillouin type increase of depolarization rate on cooling. Bulk properties (on the same sample), in contrast, show no obvious anomalies around 2.7 K. This indicates that only very short-ranged static magnetic order can be present which only shows in a sensitive microscopic technique as  $\mu\text{SR}$ . Taking the value  $\mu_{\text{Ce}} \approx 0.4\mu_B$  from neutron scattering, the observed  $\mu\text{SR}$  depolarization rate for  $T \rightarrow 0$  corresponds to a completely random orientation of frozen moments. Of course, it can not be guaranteed that the neutron data, which were taken on a different sample are applicable to the material used in the  $\mu\text{SR}$  study.

*Summary:* A magnetic  $\mu\text{SR}$  response at the established (by neutrons) Néel temperature of 2.7 K is observed only in polycrystalline, but not in single-crystalline samples. Where present, the magnetic  $\mu\text{SR}$  spectra indicate short-range order in contrast to the findings of neutron diffraction, which established simple, long-range AFM order. Whether this difference is based on sample dependence (which is pronounced in this system) cannot be decided at this point.

9.3.1.14. *CeRh<sub>3</sub>B<sub>2</sub>*. The value of its Sommerfeld constant hardly classifies this intermetallic, which crystallizes in the hexagonal  $\text{CeCo}_3\text{B}_2$  structure, as a HF compound, but  $\gamma$  is clearly enhanced and electron correlations must be present. Because of its several unusual properties, it might be considered a class by itself. It has the highest magnetic ordering temperature ( $T_c = 115$  K) of any Ce compound devoid of other magnetic constituents and enters a FM state. This ordering is at a higher temperature than  $\text{GdRh}_3\text{B}_2$  (90 K), emphasizing that its f-electron structure is anomalous since, for example, it violates grossly the de Gennes systematics. The ordered moment is reduced ( $0.84\mu_B$ ), but so is the Curie–Weiss effective moment (Maple et al. 1985) around room temperature ( $\sim 1\mu_B$ ). It has been suggested that anomalous d-band magnetism rather than anomalous f-band magnetism is acting in  $\text{CeRh}_3\text{B}_2$  (Malik et al. 1985, Shaheen et al.

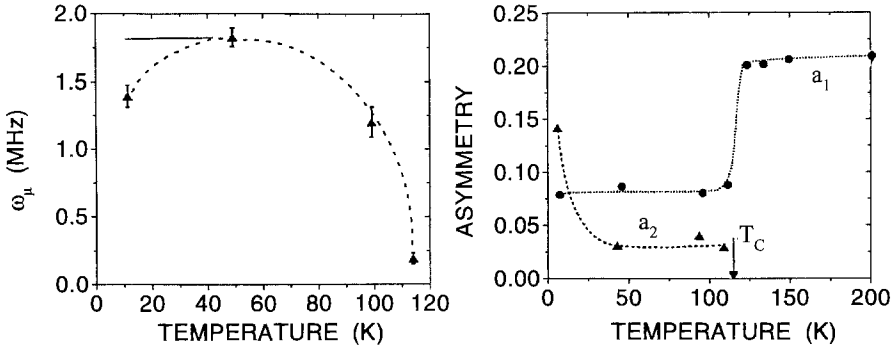


Fig. 137.  $\mu$ SR results for  $\text{CeRh}_3\text{B}_2$ . Left: Temperature dependence of spontaneous precession frequency. The dashed line is a guide to the eye, the full line indicates the expected behavior at low temperatures for simple ferromagnetic order. Right: Temperature dependences of the amplitudes (initial asymmetry) of the oscillating ( $a_2$ ) and non-oscillating ( $a_1$ ) signals. The errors are less than the symbol size. Lines are guides to the eye. From Cooke et al. (1996).

1985). Lawson et al. (1986) concluded from neutron diffraction data that no long-range order of the local magnetic moments exist in ZF, but that the application of a small field ( $\sim 150$  mT) induces order.

A ZF- $\mu$ SR study was undertaken by Cooke et al. (1996) but only rudimentary results are reported. Well above  $T_C$  the signal experiences relaxation that can be fully explained by the action of the nuclear moments on  $^{11}\text{B}$ , the influence of Ce electronic moments being altogether suppressed by motional narrowing. On approaching  $T_C$  from above, the critical slowing down of Ce moments causes strongly increased relaxation, the typical behavior of a R ferromagnet. Below  $T_C$  spontaneous spin precession is observed but in addition to a substantial non-oscillating signal. Figure 137 shows the temperature dependences of the spontaneous frequency (left) and relative amplitudes of the two signals (right). It should be noted that the sum of the two amplitudes ( $a_1 + a_2$ ) in the temperature range  $40\text{ K} \leq T \leq T_C$  does not account for the full signal strength (given by  $a_1$  at  $T \geq T_C$ ). Below  $T_C$  a third (unobserved) signal with extremely rapid depolarization must be present. Interestingly enough, the amplitude of the oscillating signal rises sharply below  $\sim 40$  K and near 10 K the full signal strength is contained in the sum of  $a_1$  and  $a_2$ . (Oddly, the authors do not comment on the behavior of signal strength at all). At low temperatures one might well conclude that unique magnetic order has been established throughout the sample since the ratio  $a_2 : a_1$  is about 2 : 1, meaning  $a_1$  represents now the expected “1/3 signal”. In fact,  $a_1$  below  $T_C$  could always be a “1/3 signal” if one assumes that the muons producing the unobserved signal also sense long-range order but with a much wider static field distribution at the muon site than compared to the site producing the observable spin precession. It is further found that the relaxation rate of the non-oscillating signal ( $a_1$ ) diverges critically at  $T_C$ . This supports the notion (in the reviewers’ view) that  $a_1$  is always the 1/3 signal, which by definition is only sensitive to dynamic depolarization. Relaxation of the oscillating signal is one order of magnitude

larger than that of the “ $a_1$ -signal”, showing the dominance of the static field distribution. This static rate rises rapidly at lower temperatures. The maximum precession frequency (near 50 K) corresponds to  $B_\mu = 13$  mT (see fig. 137, left), a rather low value, but in keeping with a moment around  $1\mu_B$ .

The authors suggest that the drop in  $B_\mu$  below  $\sim 40$  K is due to antiferromagnetic (with respect to the Ce moments) ordering of Rh moments (which are expected to be about one order of magnitude smaller than the Ce moments). They do not explain how this picture can account for the variation in signal amplitude shown in fig. 137 (right). To the reviewers, a change in magnetic structure without involving ordering of additional ions is an equally likely scenario.

In any case, either picture means that the magnetic state of  $\text{CeRh}_3\text{B}_3$  is not a simple ferromagnetic one. Also, the authors state their data show that long-range order occurs in ZF in contrast to the findings of Lawson et al. (1986). This is true, but again, it neglects the details of the signal amplitudes. From those one extracts that below  $T_C$ , but above 40 K, only 20–25% of the sample is magnetically ordered in a simple FM structure. The rest is likely to be in a highly disordered magnetic state. The FM fraction might be sample and field dependent. Unfortunately, no data with applied fields in the range of 150 mT are reported.

*Summary:* The  $\mu\text{SR}$  data available are rather incomplete, but are not compatible with the standard picture of a simple FM structure at all temperatures below  $T_C$ . Metamagnetism is a definite possibility. A change in magnetic structure around 40 K is shown to exist, but its exact nature is unknown. One suggestion is ordering of the Rh sub-lattice but no safe evidence is available. Additional  $\mu\text{SR}$  data, and also neutron scattering from single crystals (G.H. Lander, private communication), if available, are badly needed.

9.3.1.15.  $\text{Ce}_3\text{Au}_3\text{Sb}_4$ . This compound belongs to the class of “low-carrier-density” HF systems, which have recently attracted much interest, mainly due to the work of Kasuya and his group (see, for example, Kasuya et al. 1993b). For these materials, the non-4f reference compounds are semimetals or narrow gap semiconductors and the related 4f containing compounds are characterized by a low carrier density on the order of  $10^{-2}/(4f\text{-atom})$ . Despite the small number of conduction electrons available to form a correlated state with the local 4f moments one observes typical HF behavior such as a substantially enhanced Sommerfeld constant.

Cubic (space group  $I\bar{4}3d$ )  $\text{Ce}_3\text{Au}_3\text{Sb}_4$  exhibits semiconducting resistivity down to at least 0.15 K. The Ce atoms are fully in the ionic  $4f^1$  state. Inelastic neutron scattering sees three CEF levels appropriate for  $\text{Ce}^{3+}$  in tetragonal symmetry (the local symmetry of the Ce site). A huge peak in susceptibility and specific heat around 3 K has been attributed to a Kondo resonance within the narrow band gap (Kasaya et al. 1991, 1994).

$\mu\text{SR}$  studies have been undertaken by Amato (1995) and Amato et al. (1997b). The ZF- $\mu\text{SR}$  spectra are characterized by a Gaussian decay of polarization at all temperatures. From room temperature down to  $T_M \approx 2.54$  K, the depolarization rate ( $\sigma \approx 0.3 \mu\text{s}^{-1}$ ) is small and practically temperature independent. It can fully be accounted by the action of the static nuclear moments of  $^{121,123}\text{Sb}$ . Electronic Ce moments clearly fluctuate

rapidly. Below  $T_M$  the depolarization rate rises quickly and reaches  $\sigma \approx 3 \mu\text{s}^{-1}$  for  $T \rightarrow 0$ . Now the Ce moments have become effective. If they were fully frozen, the spectrum should be of the Kubo–Toyabe type with its typical “1/3 tail”. This tail is not observed, however, and the authors conclude that slow moment fluctuations must still be present. No detailed analysis is given. There is no trace of spontaneous spin precession.

The  $\mu$ SR data are compatible with either dense spin glass freezing or with the sudden condensation of a coherent Kondo state (for a discussion see, for example, Grewe and Steglich 1991) with slow, but dynamic spin correlations at  $\sim 2.5$  K. The latter interpretation ties in with the specific heat data, especially in applied fields. The former could be explained in terms of the magnetic polaron model formulated by Kasuya et al. (1993a,b).

*Summary:* ZF- $\mu$ SR sees a rise in relaxation rate below 2.5 K. Two explanations have been put forward: either the formation of a “nearly” frozen spin state or the sudden condensation into a coherent Kondo state. A fully static limit of spin correlations is not reached.

9.3.1.16.  $Ce_3Pd_{20}Si_6$  and  $Ce_3Pd_{20}Ge_6$ . These materials are among the heaviest HF compounds known, with  $\gamma \approx 8 \text{ J}/(\text{mol K}^2)$ . They crystallize in a cubic phase with the  $Cr_{23}C_6$  superstructure where the Ce atoms occupy two crystallographic different sites denoted Ce-1 and Ce-2 (Takeda et al. 1995). Brief conference reports on  $\mu$ SR studies on the two materials were recently presented.

Duginov et al. (2000) observed in the Si compound a marked increase of relaxation rate below 0.5 K indicating a magnetic transition point. Spontaneous spin precession is absent, the signal just shows a monotonic Gaussian decay of muon spin polarization, which remained unaffected by the application of LF up to 5 kG, meaning that spin dynamics remain present. A remanent local field of 2 G was observed after a field (4 kG) had been applied. These data are discussed in terms of superparamagnetic cubes of eight Ce-2 atoms which order ferromagnetically.

Specific heat on the Ge compound shows a sharp peak at 0.7 K and a broad peak at 2.1 K. The sharp peak is considered to signal AFM order, the broad peak is attributed to antiferro-quadrupolar ordering. The  $\mu$ SR measurements by Krishnamurthy et al. (1999c) on a single-crystal specimen ( $S_\mu \parallel [110]$ ) confirm the magnetic transition at 0.7 K. Below this temperature they observe spontaneous spin precession with a Brillouin-like temperature dependence of frequency. The saturation field ( $T \rightarrow 0$ ) is  $B_\mu \approx 500$  G. The spin lattice relaxation shows no irregularity at 2.1 K. The absence of a  $\mu$ SR response at the onset of quadrupolar ordering has been observed in other cases (see CeAg in sect. 5.2.2), but a change of slope in the temperature dependence of the muon spin relaxation rate has been reported in  $CeB_6$  (see sect. 9.3.1).

It is apparent from these sets of data that the magnetic behavior (spin structure) is substantially different in  $Ce_3Pd_{20}Si_6$  and  $Ce_3Pd_{20}Ge_6$ , which still calls for an explanation.

### 9.3.2. *U intermetallics*

9.3.2.1. *UGe<sub>2</sub>*. This intermetallic is a strongly anisotropic FM with  $T_C = 52$  K. The Sommerfeld constant is only slightly enhanced ( $\gamma \approx 0.03$  J/(molK<sup>2</sup>)), nevertheless UGe<sub>2</sub> is usually listed among HF compounds. Ōnuki (1993) argues on the basis of magnetoresistance and de Haas–van Alphen data that the 5f electrons in UGe<sub>2</sub> are itinerant but strongly correlated. Also present are strong spin fluctuations. Based on these features a calculation of the Fermi surface was carried out (Yamagami and Hasegawa 1993). The result reproduces the electronic structure properties of UGe<sub>2</sub> well.

$\mu$ SR studies are mentioned within the context of a brief report by Yaouanc et al. (1999a) discussing “quasielastic magnetic excitations in strongly correlated compounds” (see paragraph on CeRu<sub>2</sub>Si<sub>2</sub> above). Only data for the paramagnetic regime are mentioned. The temperature dependence of muon spin relaxation rate on approaching the magnetic transition is shown, but not commented on, except for the fact that its critical rise within the range  $0.001 \leq (T - T_C)/T_C \leq 0.01$  could be reproduced well by the model of Yaouanc et al. (1993a) for a ferromagnet with dipolar forces present. Most unusual is the strong dependence of the critical fluctuations on comparatively low longitudinal fields. A LF = 150 mT nearly fully suppresses the critical rise of relaxation rate. It is this feature (that is also observed in CeRu<sub>2</sub>Si<sub>2</sub> and YbNiSn) that leads the authors to introduce their scenario of quasielastic magnetic excitations. A direct connection to the known electronic structure of UGe<sub>2</sub> is not made.

*Summary:*  $\mu$ SR on UGe<sub>2</sub> shows an anomalous dependence on applied field of critical fluctuations above the Curie point. The presence of quasielastic magnetic excitations in the 10 meV transfer energy range is claimed.

9.3.2.2. *UPt<sub>3</sub>, U<sub>1-x</sub>Th<sub>x</sub>Pt<sub>3</sub>, U(Pd<sub>x</sub>Pt<sub>1-x</sub>)<sub>3</sub>*. UPt<sub>3</sub> is probably the most thoroughly studied HF compound. The properties of UPt<sub>3</sub> are rather sensitive to impurities and crystal imperfections, as is the case for the majority of archetypal HF materials. Thus, as better and purer single-crystalline samples became available, the features exhibited by UPt<sub>3</sub> changed and became much richer in detail. UPt<sub>3</sub> is still the best candidate for unconventional (odd pairing) superconductivity. There is mounting evidence for this, but a final conclusion has not yet been reached. Also, UPt<sub>3</sub> is a prime (and early) example of coexistence of magnetism and superconductivity as found in several Fermi-liquid systems with a superconducting ground state. Well below its Kondo temperature  $T^* = 80$  K but also markedly above its superconducting transition ( $T_C \approx 0.5$  K) UPt<sub>3</sub> enters into a weak AFM state ( $T_N \approx 5$  K). This was first established by the  $\mu$ SR study of Cooke et al. (1986). In that study, a small rise in relaxation rate was found, indicating as in comparable cases (such as CeRu<sub>2</sub>Si<sub>2</sub>, CeRu<sub>2</sub>), the development of a magnetic state characterized by extremely low ( $10^{-2}$ – $10^{-3}$   $\mu_B$ ) nearly frozen moments that most likely are fairly itinerant. Application of LF largely suppresses this rise of rate, demonstrating the quasistatic nature of the spin system. Itinerant magnetism was considered essential for the coexistence with superconductivity until the discovery of UPd<sub>2</sub>Al<sub>3</sub> (and, to a lesser extent, UNi<sub>2</sub>Al<sub>3</sub>). These two materials establish that also strong, localized AFM can coexist

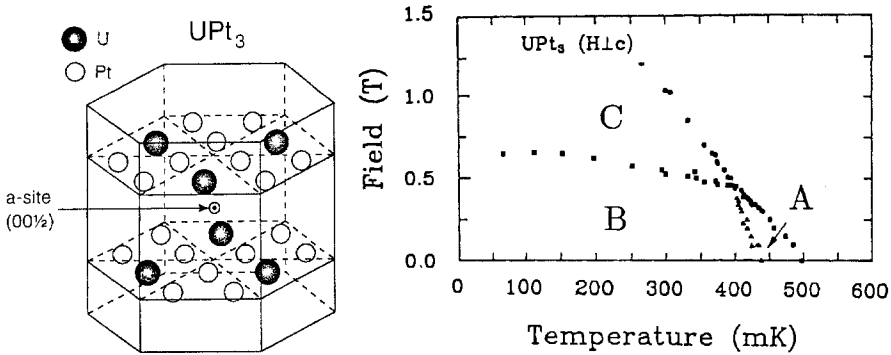


Fig. 138. Left: Hexagonal structure of  $UPt_3$ . A prominent interstitial site is indicated. Right: Magnetic field-temperature phase diagram of single-crystalline  $UPt_3$  with the field applied in the basal plane. The three superconducting phases (A, B, C) are indicated. The diagram was derived from sound velocity data. Adapted from Taillefer (1994).

(homogeneously) with superconductivity. As will be pointed out below, the presence of magnetism is a fundamental ingredient in several theoretical models addressing the peculiar superconducting properties of  $UPt_3$ .

It would be futile to try to list the complete literature of bulk measurements here. Reviews to be consulted are given, for example, by Sauls (1994), von Löhneysen (1994) and Taillefer (1994). Ultrasound and uniaxial stress data can be found in Adenwalla et al. (1990) and Boukhny et al. (1994a,b,c). They indicate a triplet superconducting-order parameter.

The crystal structure of  $UPt_3$  is hexagonal (see fig. 138, left) which gives rise to strong anisotropy of physical parameters (Shivaram et al. 1986, Zhao et al. 1991, Keller et al. 1994, Lussier et al. 1994, Fledderjohann and Hirschfeld 1995). Direct detection of the vortex flux lattice by neutrons was reported by Kleiman et al. (1992). Magnetic neutron scattering and related work will be mentioned in context below.

The salient result of more recent work is the establishment of three superconducting phases (A, B and C) with a single tetracritical point, with a kink in critical field *vs.* temperature at this point. As an example we show fig. 138 (right), for fields applied perpendicular to the *c*-axis. The parallel orientation gives basically the same result (three phases with a tetracritical point). These features have become more pronounced the purer the compound and the more perfect the crystal. This is in contrast to  $U_{1-x}Th_xBe_{13}$  where impurities are essential (to be discussed in sect. 9.3.2.5). For ZF the phase diagram predicts two closely spaced superconducting transitions between 0.4 and 0.5 K. This is observed in good samples as can be seen in fig. 139 (left).

Extensive neutron studies (Aeppli et al. 1988, 1989), which were instigated by the  $\mu$ SR results of Cooke et al. (1986), revealed that static AFM correlations set in at  $T_N = 5$  K, with finite correlation range and a moment of  $\sim 0.02\mu_B$ . The finite correlation length could be the reason that  $\mu$ SR does not observe explicit spin precession. The magnetic order parameter grows as  $(T_N - T)^{1/2}$  for  $T_c < T < T_N$ , after which it ceases

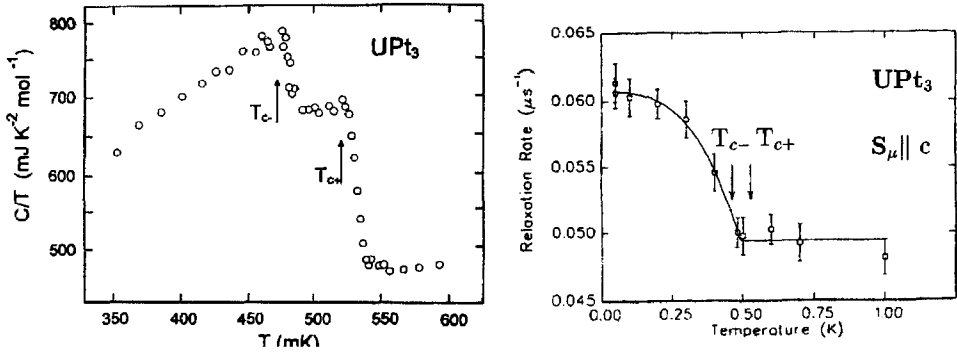


Fig. 139. Left: Specific heat of  $UPt_3$  near the superconducting transition for a high-purity sample showing the double transitions  $T_{c+}$  and  $T_{c-}$ . The precise positions of  $T_{c+}$  and  $T_{c-}$  are sample dependent, but typically between 0.35 and 0.55 K. After data by Dalmas de Réotier et al. (1995) as shown in Amato (1997). Right: Depolarization rate  $\lambda$  due to electronic dipole moments on U in  $UPt_3$  (for details see text) in the vicinity of the double superconducting transitions. The positions of  $T_{c+} = 545$  mK and  $T_{c-} = 488$  mK for this sample are indicated. After Luke et al. (1993b).

to evolve. This is taken as direct evidence that superconducting and magnetic order parameters are strongly coupled and that hence the same 5f electrons are responsible for superconductivity and magnetism. Several theoretical scenarios addressing the occurrence of the three superconducting phases (e.g., Joynt 1988, Machida and Ozuki 1989, 1991) use the presence of a symmetry breaking field to generate the splitting of  $T_c$  (see fig. 139, left). Hayden et al. (1992) and von Löhneysen et al. (1992) argue that the weak AFM below 5 K provides such a field. Hence the magnetism may be an important fundamental property of  $UPt_3$ .

The connection between order parameters raises the question of whether the magnetic structure is affected by the onset of superconductivity. In neutron scattering (Aeppli et al. 1989), a reduced  $(\frac{1}{2} 0 1)$  Bragg intensity (by about 5%) is seen below  $T_c$ . This study used a sample with a broad single peak transition. In ZF- $\mu$ SR an additional rise in relaxation rate was observed by Luke et al. (1993a,b) connected with the superconducting transition. This study used single-crystalline samples with a well-split transition temperature ( $T_{c-}$  and  $T_{c+}$ ). The ZF data were analysed by double electron- ( $e^{-\lambda t}$ ) nuclear (static Gaussian Kubo-Toyabe) relaxation. In fig. 139 (right) the electronic relaxation rate  $\lambda$  is plotted against temperature in the range of onset of superconductivity. The data connect this additional rise, which is larger than that occurring at  $T_N$  (not shown), definitely to  $T_{c-}$ , that is, to the B-phase. The authors offer two possible explanations. Firstly, a reorientation of the AFM spins may have occurred. Such an effect had been suggested (Blount et al. 1990) as an explanation for the reduced Bragg intensity. Secondly, the lower superconducting phase may be a state with broken time-reversal symmetry that needs the presence of a corresponding symmetry-breaking field. It is this field that causes the faster muon spin depolarization. Using magnetic X-ray diffraction, Isaacs et al. (1995) find that a suppression of the antiferromagnetic scattering intensity in the superconducting phase is

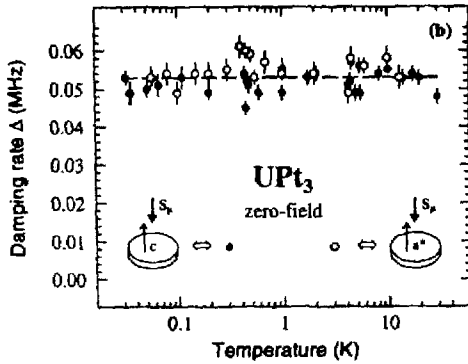


Fig. 140. Temperature dependence of the static Kubo–Toyabe relaxation rate in a high-purity single crystal of  $UPt_3$  for two orientations. Note that no change in relaxation occurs at either the magnetic ( $\sim 5$  K) or superconducting ( $\sim 0.5$  K) transition temperatures. From Dalmas de Réotier et al. (1995).

due to a reduction in magnitude of the ordered moment with no change in symmetry. In their data no definite correlation to the split superconducting transition could be established, but they rule out the first of the explanations given by Luke et al. (1993b) (i.e., spin reorientation) for the source of the additional  $\mu$ SR line broadening. Note here that magnetic X-ray scattering is very surface-sensitive. Isaacs et al. (1995) also report comparative neutron data and conclude that no significant difference between bulk and surface regions exist regarding the AFM spin structure. The presence of AFM in  $UPt_3$  with  $T_N \approx 5$  K has been asserted by neutron scattering for samples of different quality without exception. Recently, Schuberth et al. (1992) reported large anomalies around 18 mK in the bulk data of two single-crystalline samples. The authors conclude that these anomalies indicate additional forms of order within the heavy-quasiparticle system. Susceptibility measurements show that the sample remains superconducting below 18 mK. Although some possible modifications within the superconducting state are discussed, the exact nature of the specific heat anomaly remains enigmatic. No other data exist in that temperature regime.

The development of AFM around 5 K is not always coupled to the observation of a change in  $\mu$ SR relaxation rate in the best samples. Dalmas de Réotier et al. (1995) measured a single-crystalline sample of high quality (as documented by the very well resolved double peak structure for  $T_c$  shown in fig. 139 and an extremely low residual resistivity) and found in ZF- $\mu$ SR a low, temperature-independent relaxation rate (compatible to the action of  $^{195}\text{Pt}$  nuclear dipoles) from 30 K on downwards. Any rise in relaxation rate around  $T_N$  or  $T_c$  is absent within the accuracy of data for different orientations of the sample (see fig. 140). Neutron scattering performed later on the same sample (see Dalmas de Réotier and Yaouanc 1997) confirmed the usual AFM transition at 5 K. In addition, the presence of the magnetic transition could be seen by Knight shift measurements (Dalmas de Réotier et al. 1998a, 2000b). The presence of two magnetically independent regions (or domains) up to at least 115 K is claimed.

More recently, Higemoto et al. (2000a) have repeated the ZF-relaxation study on a single crystal of  $UPt_3$  (with  $S_\mu \parallel c$ ) from 10 K down to 20.8 mK. The spectra exhibited no significant change throughout this temperature range, meaning that neither any indication



for spontaneous magnetization in the B phase, nor a precursor of long-range magnetic order (as suggested by the specific heat data of Schuberth et al. 1992) could be observed. To pin down the latter state even lower temperatures will be needed.

The absence of any change in the  $\mu$ SR signal around 6 K where the onset of (weak) magnetism is verified by neutron data, leaves two explanations open. Either the muon occupies a site of high local symmetry where all contributions to the local field cancel (a likely candidate is the (0,0,0) site) or the AFM spins remain dynamic. Fluctuations in the range of 10–100 MHz would fully motional narrow any depolarization by the small uranium moments. The second scenario is now considered to be more likely since it also explains the absence of any signature of the magnetic state in NMR experiments (Kohori et al. 1990, Tou et al. 1996). Such slowly fluctuating moments would appear static in neutron scattering. The question of whether a slowly fluctuating field can also be the agent for symmetry breaking has not been addressed in detail to our knowledge.

It remains a mystery in either scenario why the earlier (impure) samples showed the effect of spontaneous magnetization in the B phase. In the first case, distortions or disturbances of the hexagonal crystal lattice, which interfere with the perfect cancelation of field contributions from U neighbors surrounding the stopped muon, could be responsible. In view of the strong anisotropy of  $\text{UPt}_3$ , this is a real possibility. It is also possible that only in a perfect crystal is the (0,0,0) site the muon stopping site (see also discussion on alloyed samples below). In the second case, impurities might slow down the fluctuation rate. A combination of both cases cannot be excluded. Be that as it may, these results show that one cannot always take the absence of increase in ZF- $\mu$ SR relaxation as an indicator for the absence of AFM. (TF data are less conclusive in a superconductor, since the vortex lattice will cause additional relaxation below  $T_c$ ). Dalmas de Réotier and Yaouanc (1997) argued that the newer  $\mu$ SR data on  $\text{UPt}_3$  do not support models predicting a triplet Cooper pair. They also question the assertion by Luke et al. (1993b) that their observation of increased relaxation at  $T_{c-}$  mirrors the symmetry breaking magnetic field. The problem is not resolved.

In addition to the ZF- $\mu$ SR data on  $\text{UPt}_3$  described there exist a large number of TF measurements under varying conditions that explore the superconducting vortex state. The main question of interest is the parity of the Cooper pairing. This subject is outside this review and we refer the interested reader to the articles by Schenck (1993), Uemura and Luke (1993), Heffner (1994), Luke et al. (1994a) and especially Amato (1997). We mention here that the data all support the notion that magnetism and superconductivity both have their origin in the 5f electron structure, meaning that the 3d electrons are not directly involved.

A study of muon Knight shifts (in a minimum of 0.6 T) in single crystals of  $\text{UPt}_3$  was performed by Yaouanc et al. (2000b). Two signals with different Knight shifts are seen. The two signals are of comparable amplitude except in the range of  $2 < T < 10$  K, where the higher-shift signal becomes more prominent, peaking in amplitude near 6 K. This is near the weak-AFM ordering temperature, which is not seen in low-field  $\mu$ SR of these samples. Additionally, the shift of the larger-shift signal increases significantly as temperature drops below 6 K. The interpretation of the existence of two sites in such

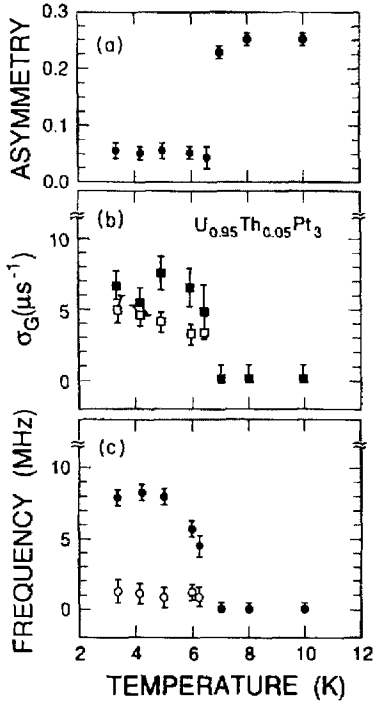


Fig. 141. Temperature dependence of ZF- $\mu$ SR spectral parameters of  $U_{0.95}Th_{0.05}Pt_3$ . (a) Signal amplitude; (b) relaxation rates; (c) spontaneous spin precession frequencies. In (b) and (c) the solid symbols refer to the high-frequency signal, the open symbols to the low-frequency signal. Above  $T_N = 6.5$  K only one weakly damped signal is seen. From Heffner et al. (1989).

applied fields is not clear, but the authors suggest  $UPt_3$  is magnetically inhomogeneous, at least in applied fields.

Although the three-region phase diagram of superconductivity and the AFM transition in  $UPt_3$  are not a consequence of impurity doping (as is the case in  $UBe_{13}$ ), the ground state of  $UPt_3$  is nevertheless quite sensitive to alloying with impurities. A Fermi surface instability is found in  $U_{1-x}Th_xPt_3$  for  $0.01 \leq x \leq 0.1$  at 6.5 K which results in a commensurate AFM structure with an enhanced moment of order  $0.5\mu_B$  (Ramirez et al. 1986, Goldman et al. 1986, Frings et al. 1987).

Heffner et al. (1989) studied polycrystalline  $U_{1-x}Th_xPt_3$  for  $x = 0.01$  and 0.05 by  $\mu$ SR. The data for  $x = 0.01$  in the range of 4 to 22 K are consistent with those of pure  $UPt_3$  although the lack of data for  $T \leq 4$  K does not allow a definite conclusion as to an increase of relaxation rate below 5 K. The situation is markedly different for  $x = 0.05$ . There, two spontaneous frequencies are observed below 6.5 K coupled to a substantial loss in asymmetry. The results are summarized in fig. 141. The spectra are considered to contain three signals. One is not directly visible since it experiences relaxation in excess of spectrometer dead time ( $\sim 25$  ns). This signal refers to the majority of stopped muons ( $\sim 80\%$ ). The higher of the two visible precession frequencies exhibits a temperature dependence that mirrors the growth of magnetic order parameter in a typical magnet. The saturation frequency ( $\sim 8$  MHz) is quite in keeping with an ordered moment of  $\sim 0.5\mu_B$ . The relaxation rate is of the same order as the precession frequency indicating

a very broad distribution of local field which is not easily conceived for a commensurate AFM spin structure. The authors suspect defect-induced perturbations. The low-frequency signal exhibits basically similar features. Clearly, more than one muon stopping site is likely to be involved, in contrast to the conclusion reached from the data by Dalmas de Réotier et al. (2000b) for pure  $\text{UPt}_3$ . This is a strong hint that impurities may affect the interstitial position at which the implanted muon comes finally to rest. The unusual strong damping of the 8 MHz signal gives evidence that, in addition, imperfections can have a strong influence on the width of the field distribution, that is, they may well disturb the spin structure. All these features render support for the earlier discussion on the observed variations in  $\mu\text{SR}$  depolarization rates of pure  $\text{UPt}_3$  as being impurity related.

Bulk properties of the system  $\text{U}(\text{Pt}_{1-x}\text{Pd}_x)_3$  were first investigated by de Visser et al. (1987). The results of more detailed studies in the range of low Pd concentration are given by Graf et al. (1999) for high-quality polycrystals. The upper superconducting transition (normal  $\leftrightarrow$  A) temperature decreases with Pd concentration, but the lower transition (A  $\leftrightarrow$  B) is depressed more rapidly, leading to a larger separation between the two phase transitions. In consequence, for  $0.004 < x < 0.006$  only the A-phase is present. Superconductivity vanishes altogether at  $x = 0.006$ . Neutron diffraction on single crystals showed that around the Pd concentration where superconductivity is destroyed ( $x = 0.006$ ) a crossover from small moment AFM (as in pure  $\text{UPt}_3$  with  $\mu_{\text{U}} \approx 0.02\mu_{\text{B}}$  and  $T_{\text{N}} = 6\text{ K}$ ) to larger moment AFM occurs (de Visser et al. 1997a). The latter state is restricted to  $x \leq 0.1$ . The moments rise with Pd concentration ( $\mu_{\text{U}} = 0.11, 0.35, 0.62\mu_{\text{B}}$  for  $x = 0.01, 0.02, 0.05$ ). The concentration dependence of the magnetic transition temperatures is shown in fig. 142. The small moment state has its transition near 6 K, as in pure  $\text{UPt}_3$ . The transition into the large moment state is concentration dependent and peaks at  $x = 0.05$ , where it reaches the same value ( $\sim 6\text{ K}$ ) as the low moment transition. At Pd concentrations above  $x = 0.01$  but below  $x \approx 0.05$ , both phases are reached consecutively as is demonstrated clearly by the  $\mu\text{SR}$  data to be discussed below. Near  $x = 0.05$  the existence of the low-moment phase can no longer be detected. As stated, superconductivity and large-moment AFM are mutually exclusive. In a recent review, de Visser et al. (1998a) point out that the combination of specific heat and neutron diffraction data for  $\text{U}(\text{Pt}_{1-x}\text{Pd}_x)_3$  renders strong evidence for a Ginzburg–Landau model leading to the double superconducting transition of  $\text{UPt}_3$  by the action of a symmetry breaking field for which the weak AFM exchange is the probable candidate.

ZF- $\mu\text{SR}$  studies on polycrystalline material with  $x = 0, 0.002, 0.01, 0.02$  and  $0.05$  were performed by de Visser et al. (1997b, 1998b) and Keizer et al. (1999). The samples with  $x < 0.005$ , where only the small-moment AFM state (SMAF) exists, showed ZF- $\mu\text{SR}$  spectra analogous to those of Dalmas de Réotier et al. (1995) and Higemoto et al. (2000a) in high-purity  $\text{UPt}_3$ , i.e., no change in relaxation rate around 6 K and a depolarization rate consistent with  $^{195}\text{Pt}$  nuclear dipole relaxation ( $\Delta \approx 0.07\mu\text{s}^{-1}$ ). For  $0.01 \leq x \leq 0.05$ , where the large-moment state (LMAF) comes into play, the ZF- $\mu\text{SR}$  spectra in the ordered state consist of two terms of equal amplitude: an exponentially damped spontaneous spin precession signal (including the non-oscillating “1/3-term”) and a static Lorentzian Kubo–

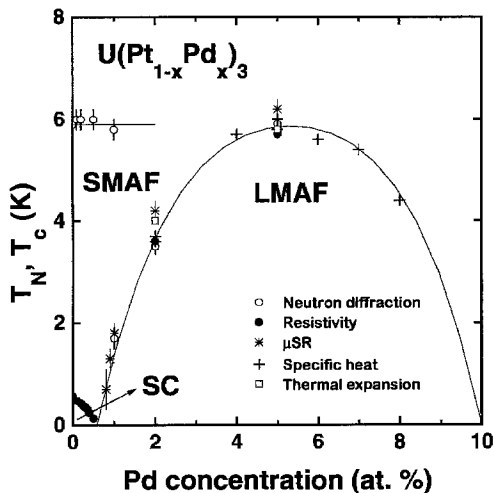


Fig. 142. Magnetic transition temperatures of the small moment antiferromagnetic state (SMAF) and the large moment antiferromagnetic state (LMAF) as a function of Pd concentration in  $U(Pt_{1-x}Pd_x)_3$ . Also shown is the superconducting (SC) transition temperature. After de Visser et al. (1997a).

Toyabe function. This analysis supersedes an earlier attempt described in de Visser et al. (1997b). A typical spectrum is shown in the top panel of fig. 143.

The transition temperatures agree well with the results plotted in fig. 142. The variation of spontaneous precession frequencies with temperature is shown in the left lower panel of fig. 143. The right lower panel shows the corresponding plot for the (static) Lorentzian Kubo–Toyabe relaxation rate (denoted here as  $\lambda_{KL}$ , which corresponds to the HWHM denoted as  $a$  in sect. 3.2.2). These results are curious: while  $\lambda_{KL}$  roughly scales with the magnitude of ordered uranium moment as derived by neutron diffraction, the precession frequencies do not. The authors do not rule out problems with the data analysis, but in general this feature is not understood. In the paramagnetic state the ZF spectra are not significantly different from those of pure  $UPT_3$ .

The two-signal analysis in the ordered state suggests two magnetically (but not necessarily crystallographically) different muon stopping sites, one with high local symmetry so that the various field contributions cancels. Knight shift measurements were carried out on a spherical single crystal of  $U(Pt_{0.95}Pd_{0.05})_3$  for  $10\text{ K} \leq T \leq 250\text{ K}$  in  $TF = 6\text{ kG}$  (see also Schenck et al. 2000c). Two (closely spaced in frequency) signals originating from the sample were observed for  $B_{ext} \parallel a$ , but only one for  $B_{ext} \parallel c$ . The angular dependence of shift measured at 10 K shows that the muon stopping site must have axial symmetry. As the most likely site, the (0,0,0) position (2a site) is suggested in accordance with the findings for pure  $UPT_3$ . The two-signal spectrum is attributed to two spatially distinct regions of different magnetic response as already mentioned above for the case of pure  $UPT_3$ . A comparison with bulk susceptibilities shows strong deviations from a linear behavior. Above  $\sim 115\text{ K}$  slow muon hopping sets in.

Unfortunately, the exact spin structure of the LMAF state is not known, but neutron diffraction demonstrates that the SMAF and the LMAF states are not closely related. The fluctuating nature is seen in the  $\mu$ SR data for the SMAF state, which contrasts with the

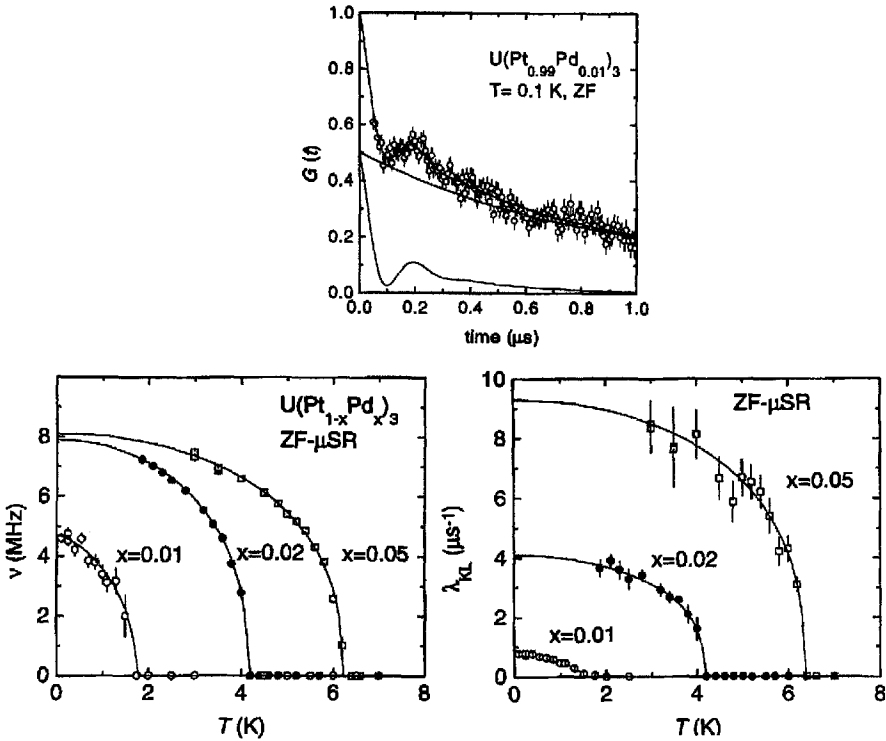


Fig. 143. ZF- $\mu$ SR results for  $U(Pt_{1-x}Pd_x)_3$ . Top:  $\mu$ SR spectrum at 0.1 K. The two signals used in the fit (see text) are indicated. Only the initial part of the Lorentzian Kubo–Toyabe function is visible due to the short time window displayed. Bottom: Temperature variation of the spontaneous precession frequency (left) and the width  $\lambda_{KL}$  of the Kubo–Toyabe function for  $x = 0.1, 0.2, 0.5$  (right). From Keizer et al. (1999).

quasistatic  $\mu$ SR response in the LMAF state, and suggests to the authors that the formation of the SMAF state is not a true phase transition but rather a crossover phenomenon. The order parameter for the LMAF state is conventional.

De Visser et al. (2000) have used TF- $\mu$ SR in the PSI dilution refrigerator to more carefully study the region near  $x = 0.006$  of the  $U(Pd_xPt_{1-x})_3$  phase diagram (see fig. 142) where the superconductivity disappears and the LMAF state appears. They follow the reduction of LMAF  $T_N$  as concentration is reduced from 0.01, showing excellent agreement with straight-line depression extrapolating to zero near  $x = 0.006$ , exactly where superconducting  $T_c$  goes to zero as  $x$  increases from smaller values. Thus, the concentration where  $T_c = T_N = 0$  appears to be a quantum critical point where superconductivity switches over to LMAF. This is consistent with the LMAF interaction being responsible for the depression of  $T_c$  as Pd is added to  $UPt_3$ , and allows the possibility that the SMAF state is not antagonistic to superconductivity, and might even be involved in generating it, as suggested by spin-fluctuation-mediated superconductivity models.

Although there are some similarities between the  $\mu$ SR data for the Pd and the Th-doped samples (in both cases larger-moment magnetism is induced and multi-component spectra are observed in the ordered state), distinct differences exist in details. Part of this is due to the fact that the Th-containing samples predated the availability of “high-quality”  $\text{UPt}_3$  as the starting material. It would be desirable to repeat the study of Th-doped  $\text{UPt}_3$  with high-quality samples in order to draw a more direct comparison.

*Summary:*  $\text{UPt}_3$  is the classic example where  $\mu$ SR first discovered weak moment AFM which then was put on a firm basis by neutron diffraction, which showed it was of limited correlation length. Details of the shape of the magnetic  $\mu$ SR signal appear to be impurity related. The magnetic phase appears to be connected to the lower superconducting phase (B-phase). It is proposed that the internal magnetic field in the B-phase provides the symmetry breaking field required in some models of unconventional (odd parity) superconductivity, for which  $\text{UPt}_3$  is the prime candidate. Samples of improved quality did not show the weak magnetic  $\mu$ SR response originally observed, but neutron diffraction verifies the existence of the magnetic state in these samples. It is probable that the uranium spins are slowly fluctuating. From muon Knight shift data it is concluded that two magnetically independent regions are present. The (0,0,0) interstitial site is the most likely muon stopping place. Muon hopping occurs for  $T > 115$  K.  $\mu$ SR data on pseudo-binary samples like  $(\text{U,Th})\text{Pt}_3$  and  $\text{U}(\text{Pt,Pd})_3$  confirm the formation of larger-moment AFM in certain ranges of doping. The larger-moment magnetic state is conventional, but its spin structure has not been determined. It is suggested that the formation of the low-moment state (i.e., in pure  $\text{UPt}_3$ ) is not a true phase transition but a crossover phenomenon. Clearly, the nature of the magnetism in  $\text{UPt}_3$  and related compounds is complex and not yet solved.

9.3.2.3.  $\text{UCu}_5$ . This material, which crystallizes in the face-centered ( $\text{F}\bar{4}3\text{m}$ ) structure, exhibits a quite unusual property. Based on results from neutron diffraction (Murasik et al. 1974a) one would classify  $\text{UCu}_5$  as a typical 5f AFM with  $T_N = 15$  K and a sizeable localized U moment. Yet, caloric and transport measurements (Ott et al. 1985b) clearly show that a HF state develops well *below*  $T_N$ . This is hard to comprehend within the generally accepted model for the formation of a HF state, since the all-important Kondo effect relies on fluctuations of the f moments to generate the heavy quasiparticles. Quasistatic ordered magnetism with a fairly large local moment seems inimical to that mechanism. The issue is not resolved.

Neutron data show that the U sub-lattice orders ferromagnetically in the [111] planes, which are stacked antiferromagnetically. The ordered moments are aligned along the (111) direction. Murasik et al. (1974a) report  $\mu_{\text{ord}} = 0.9\mu_B$ , while Schenck et al. (1990b) give  $\mu_{\text{ord}} = 1.55\mu_B$ . In any case, one deals with a substantial and typical uranium 5f moment. It was pointed out by H. Nakamura et al. (1990), that the spin structure derived from the neutron data is not unique. The data set is also compatible with a  $4k$  arrangement (see Rossat-Mignod 1987 for an introduction to multi- $k$  structures).

Specific heat and electrical resistivity results (Ott et al. 1985b, Lopez de la Torre et al. 1995) not only show the formation of the HF state well below  $T_N$ , but also establish a

second phase transition around 1 K. This transition is hysteretic but possesses no latent heat. Resistivity increases dramatically. It is only present in samples declared to be of “high quality”. Neutrons see no change at 1 K (Schenck et al. 1990b, Metoki et al. 1995). In contrast,  $^{63,65}\text{Cu}$  NMR frequencies change (H. Nakamura et al. 1994a, 1995). Because of the polarization-direction ambiguities in powder magnetic neutron diffraction a spin-reorientation transition is suggested. For example, a change from  $4\mathbf{k}$  to  $1\mathbf{k}$  (but see the  $\mu\text{SR}$  results below).

Barth et al. (1986b) first studied polycrystalline  $\text{UCu}_5$  by  $\mu\text{SR}$ . Their sample did not exhibit the 1 K transition. Well above  $T_N = 15$  K relaxation is dominated by the static field of Cu nuclear dipoles. The U moments fluctuate rapidly. On approaching  $T_N$  the moments slow down, their depolarizing effect comes into play and the relaxation rate increases drastically, as is usual in strong paramagnets. It peaks at  $T_N$  and then decreases again. At  $\sim 10$  K, relaxation (for all three signals mentioned below) is low again ( $\sim 0.5\mu^{-1}$ ) and shows no further temperature dependence.

Below  $T_N$  three signals are seen in ZF:

- (1) a spontaneous spin precession with  $\nu_1(T \rightarrow 0) = 19.8$  MHz ( $B_\mu = 1.46$  kG); relative amplitude  $\sim 57\%$ ;
- (2) a spontaneous spin precession with  $\nu_2(T \rightarrow 0) = 13.6$  MHz ( $B_\mu = 1$  kG); relative amplitude  $\sim 17\%$ ;
- (3) a non-oscillating signal with relative amplitude of 26%.

There is no interstitial site that would give rise to the three signals for either spin structure proposed. Sites with  $B_\mu = 0$  exists, but then the two oscillating patterns remain unexplained. Oddly enough, a non-oscillating “1/3 signal” (which should be present in a magnetically ordered polycrystal) is never discussed. It is proposed that the muon occupies more than one site but the  $\nu_2$ -signal is still difficult to account for and so are the relative intensities.

Also carried out were Knight shift measurements in TF = 0.3 T. It was found that the  $\mu\text{SR}$  shift  $K_\mu$  scales perfectly with the bulk susceptibility  $\chi$ . The linear relation  $K_\mu$  vs.  $\chi$  however, shows a drastic change in slope at 20 K, which remains unexplained.

A second experiment (Schenck et al. 1990c) used a polycrystalline sample exhibiting the 1 K anomaly. The same three signals as observed by Barth et al. (1986b) were found. Figure 144 (left) displays the temperature dependence of the two spontaneous frequencies. Overlaid is the variation of ordered U moment as derived from neutron diffraction. Neutrons give only one unique moment and it is disturbing that  $\nu_1$  follows its temperature dependence well, but not  $\nu_2$ . This problem also has no explanation to date. The most amazing finding is, however, that neither frequency ( $\nu_1, \nu_2$ ) changes within the limits of error around 1 K. This makes the assignment as a spin-reorientation transition extremely unlikely.  $\mu\text{SR}$  is highly sensitive to even minute changes in spin structure and the data imply that no variation in magnetic structure occurs.

The 1 K transition is, however, noticeable in the  $\mu\text{SR}$  data. It manifests itself as a sudden increase of depolarization and a changeover from Gaussian to Lorentzian shape (see fig. 144, right). Interestingly, the non-oscillating signal also changes. Seen by itself, it resembles the onset of weak random magnetism observed in some originally nonmagnetic

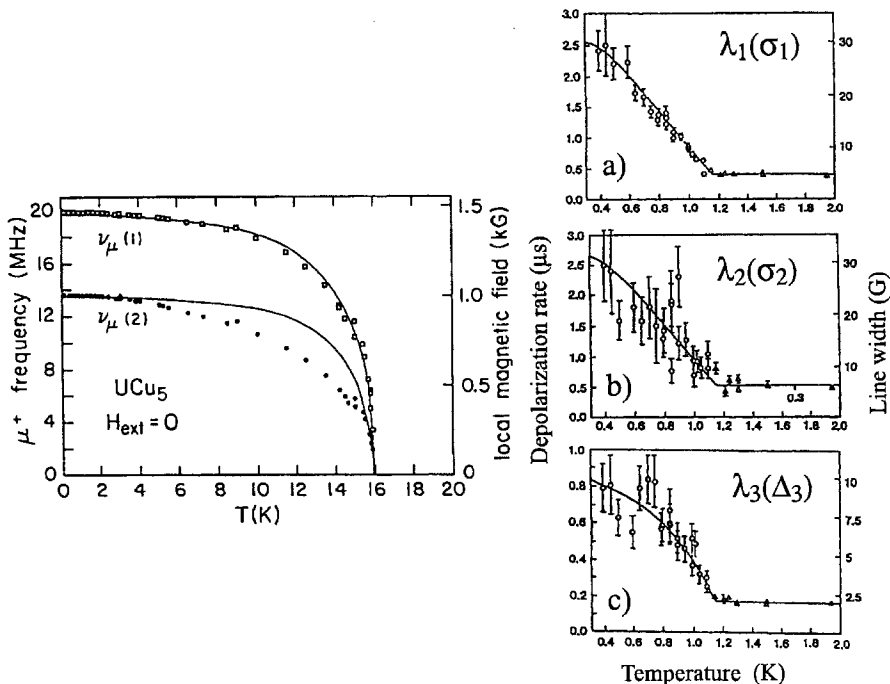


Fig. 144.  $\mu$ SR studies on  $UCu_5$ . Left: Temperature dependence of the two spontaneous  $\mu$ SR frequencies (data points). The solid line represents the variation of ordered U moment as measured by neutrons scaled to the  $\mu$ SR data. From Schenck (1993). Right: Temperature dependence of muon spin depolarization in  $UCu_5$  around and below 1 K. (a) Signal  $\nu_1$ ; (b) signal  $\nu_2$ ; (c) non-oscillating signal. Above 1.15 K relaxation is of Gaussian shape, below 1.15 K it attains Lorentzian shape. From Schenck et al. (1990c). The original figure included a fourth relaxation. Its intensity is weak and associated with  $\nu_1$  and considered to reflect muons at grain boundaries, etc.

HF compounds (e.g.,  $CeRu_2Si_2$ ). The authors suggest that signal 3 is due to the presence of an electronic subsystem that develops first into the Fermi-liquid quasiparticle state (nonmagnetic) and then produces the weak random magnetic order, while a second electronic subsystem produces localized AFM order at much higher temperatures. The notion of two different, largely uncoupled f-electron subsystems has been discussed for some Ce compounds and appears even more likely for some U compounds. Yet, this picture is not easy to conceive in the present case. Why does the onset of order of weak moments (the estimate is  $\sim 0.01\mu_B$ ) so strongly influence the well established local AFM reflected in signals 1 and 2? Why is Lorentzian relaxation observed? Unfortunately, the absence of LF data does not allow determination of whether the Lorentzian shape is due to spin dynamics or to a special field distribution. At the present time, the situation in  $UCu_5$  must simply be labeled as “not understood”. This is true for the 1 K transition in particular but also for its magnetic and HF properties in general.

*Summary:* In general, the electronic structure properties of  $UCu_5$  are still poorly understood and  $\mu$ SR has helped only in a limited way. The presence of long-range



magnetic order is seen in the  $\mu$ SR spectra, but their shape cannot be reproduced on the basis of the proposed magnetic structure. The  $\mu$ SR data rule out a spin re-orientation as the cause of the mysterious 1 K transition and are suggestive of two 4f subsystems, of which one remains paramagnetic at  $T_N$  but develops low-moment magnetism at 1 K. This scenario, though tempting, is not free of inconsistencies, even within the  $\mu$ SR data set.

9.3.2.4. *UCd<sub>11</sub>*. This cubic compound orders (antiferro-) magnetically around 5 K. The spin structure is not known. Neutron scattering is difficult (because of the high absorption by Cd) and only an upper limit of  $1.5\mu_B$  for the U ordered moment could be given (Thompson et al. 1988). Specific heat and susceptibility data (Fisk et al. 1984) established UCd<sub>11</sub> as a moderate HF material (the Sommerfeld constant, for example, is  $0.25 \text{ J}/(\text{mol K}^2)$ ) within the regime of magnetic order.

The only direct information on the magnetic phase transition at  $T_N = 5 \text{ K}$  comes from a  $\mu$ SR study on polycrystalline material (Barth et al. 1986c) in TF, ZF and LF. A sudden loss of signal amplitude is observed at  $T_N$ . Obviously, within the magnetic regime the muons are quickly depolarized due to a wide distribution of local fields. The crystal structure (BaHg<sub>11</sub>), though cubic, is complex and provides a large number of magnetically inequivalent sites. The authors argue that the moment on U must be around  $1\mu_B$  in order to produce the required spread of field.

The relaxation on approaching  $T_N$  from above exhibits a power-law dependence, which means that the 5f spin fluctuation rate  $(1/\tau)_{5f}$  behaves like

$$(1/\tau)_{5f} \propto (T - T_N)^{-x},$$

with  $x = 0.4 \pm 0.1$ . This result is interpreted as a dependence

$$(1/\tau)_{5f} \propto \sqrt{T} \quad \text{for } T > T_N,$$

which corresponds to a prediction of spin fluctuation rate dependence within the Fermi-liquid state given by D.L. Cox et al. (1985). Applying LF up to 4 kG had no influence on the relaxation rate, which puts  $(1/\tau)_{5f}$  in the range of 10 GHz or above.

*Summary:*  $\mu$ SR establishes a magnetic phase transition at 5 K, but the spin structure is not known. The U moment is around  $1\mu_B$ . Paramagnetic relaxation mirrors the formation of the HF state.

9.3.2.5. *UBe<sub>13</sub>, U<sub>1-x</sub>Th<sub>x</sub>Be<sub>13</sub>, U<sub>1-x</sub>Th<sub>x</sub>Be<sub>13-y</sub>By*. Cubic (space group Fm3c) UBe<sub>13</sub> is one of the few HF compounds that possesses a pure superconducting ground state (another example is U<sub>6</sub>Fe, see Luke et al. 1990c).  $\mu$ SR studies on polycrystalline material ruled out the presence of any magnetically ordered state with  $\mu_{\text{ord}} > 10^{-3}\mu_B$  (Heffner et al. 1990, Luke et al. 1991). A recent single-crystal study (Dalmas de Réotier et al. 2000a) confirms this result. In ZF, a temperature-independent Kubo–Toyabe-type relaxation is observed down to 50 mK whose static width  $\Delta \approx 0.24 \mu\text{s}^{-1}$  (e.g., fig. 146, right) can fully be accounted for by  $^9\text{Be}$  nuclear dipole fields for the most probable muon stopping

site (the so called “d” site, see Amato 1997). This, and other bulk measurements, put to rest the suggestion of a possible magnetic transition at 8.8 K (Kleiman et al. 1990). For more recent bulk measurements see de Visser et al. (1992).

Knight shift measurements were reported by Sonier et al. (2000a). The muon stopping site is the  $(0, 0, \frac{1}{4})$  position half way between two neighboring U ions. This site splits in applied magnetic field into two magnetically inequivalent sites. The peculiar result is that below the superconducting transition temperature, the shift increases for one site and decreases for the other, as temperature is reduced. This result is explained with the assumption that the effective exchange interaction between the muon and the uranium moments becomes temperature dependent and anisotropic below ~6 K. As a possible interpretation for this behavior, the authors suggest that the Kondo screening alters the contact interaction with the muon.

UBe<sub>13</sub> is another candidate for unconventional superconductivity ( $T_c \approx 0.87$  K). Results from TF-μSR measurements support such a claim. There is a remarkable absence of any increase in TF depolarization when superconductivity sets in, meaning that the magnetic penetration depth exceeds  $10^4$  Å (Luke et al. 1991). The new single-crystal study gives  $\lambda = 12100$  Å. Earlier, Einzel et al. (1986) had shown by magnetic induction, that the penetration depth varies as  $T^2$ . These results strongly point towards odd parity pairing. (The method used by Einzel et al. (1986) could be an interesting competitor for μSR measurements of the penetration depth, but its general applicability has not been established.)

Novel and unusual features develop when U is partially substituted by Th. First  $T_c$  begins to decrease with rising Th concentration, which is the expected behavior. Then, in the region  $0.019 \leq x \leq 0.043$ , the superconducting state splits into two phases with an upper ( $T_{c+}$ ) and a lower ( $T_{c-}$ ) transition temperature. The situation is somewhat reminiscent of pure UPt<sub>3</sub> but a tetracritical point does not exist. Beyond  $x = 0.043$ , only a single superconducting phase is present again. Figure 145 shows the phase diagram established by several bulk methods (see Heffner and Norman 1996 and references cited therein). ZF-μSR studies by Heffner et al. (1990) established that

- (a) an increase of relaxation, which indicates (as usual) the presence of weak magnetism, is only present in the two-phase region (fig. 146, left);
- (b) the onset of weak magnetism is coupled to  $T_{c-}$  (fig. 146, right);
- (c) the additional electronic contribution to the relaxation rate below  $T_{c-}$  increases less than linearly with Th concentration;
- (d) the depolarization rates outside  $0.019 \leq x \leq 0.043$  are practically the same as those for pure UBe<sub>13</sub>, meaning they are independent of temperature (for  $0.05 \text{ K} \leq T \leq 10 \text{ K}$ ) and their sole source is the <sup>9</sup>Be nuclear moments.

Findings (c) and (d) in particular rule out the formation of local moments on Th or the formation of large moments on U atoms close to an Th impurity atom. The temperature dependence of the electronic depolarization rate reflects the behavior of a magnetic order parameter following a second-order phase transition. Since this holds also for the superconducting phase, the two parameters are coupled, as already discussed for UPt<sub>3</sub>. The magnetic moments involved are estimated to be  $\sim 3 \cdot 10^{-3} \mu_B$  per U ion.

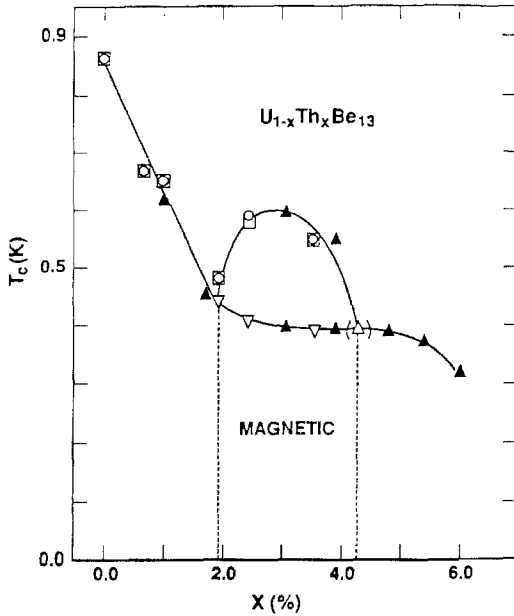


Fig. 145. Phase diagram of  $U_{1-x}Th_xBe_{13}$ . The upper line indicates the superconducting transition, the lower line the transition into the second superconducting state (whose existence is restricted to a certain concentration range). Magnetism only occurs below the lower line. The different symbols refer to susceptibility, specific heat and ac-susceptibility measurements. After Hefner and Norman (1996).

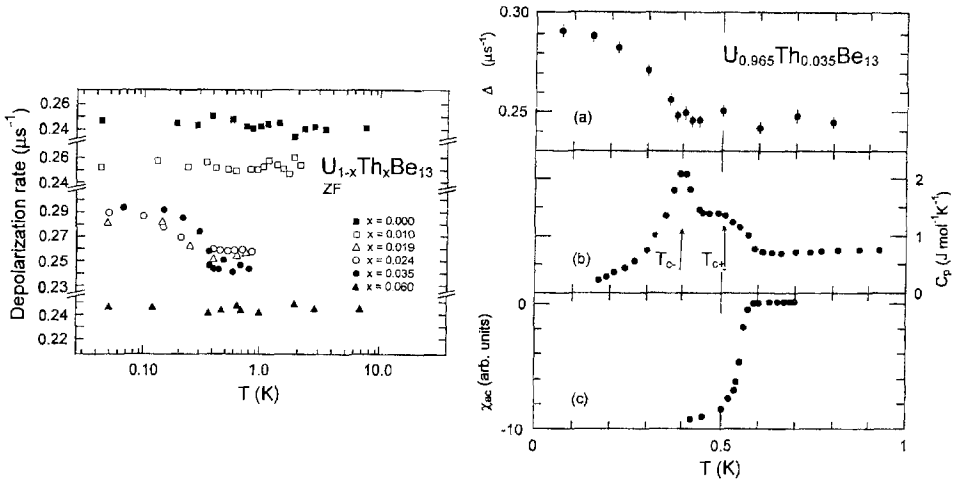


Fig. 146. ZF- $\mu$ SR spectroscopy in  $U_{1-x}Th_xBe_{13}$ . Left: Temperature dependence of depolarization rate for samples with different Th concentrations. Note the breaks in the y-axis scales. Right: Comparison of temperature dependences (from top to bottom) of muon spin depolarization rate  $\Delta$ , specific heat  $C_p$  and ac-susceptibility  $\chi_{ac}$  for  $x = 0.035$ . The superconducting transitions are  $T_{c+} \approx 0.5$  K and  $T_{c-} \approx 0.4$  K. From Hefner et al. (1990).

The strong response of the  $UBe_{13}$  system to impurity doping prompted Felder et al. (1989) to look into the behavior of the pseudo-binary compounds  $UBe_{13-y}B_y$ . This study was later extended by Beyermann et al. (1995). A weak reduction of  $T_c$  with

B concentration emerged together with an unusual rise in the jump of specific heat at  $T_c$  having a maximum around  $y = 0.03$ . No evidence for a split of superconducting transition was found. One possible cause for the increased jump in specific heat could be the development of magnetic order together with superconductivity. This scenario was ruled out by  $\mu$ SR measurements on  $UBe_{12.97}B_{0.03}$  (Heffner et al. 1991) that resulted in a temperature-independent ZF relaxation rate indistinguishable from that of pure  $UBe_{13}$ . The  $\mu$ SR work was extended to  $U_{0.981}Th_{0.019}Be_{12.97}B_{0.03}$ . There, the same rise of depolarization rate around  $T_c$  as in  $U_{0.981}Th_{0.019}Be_{13}$  was observed. Doping with boron appears to have no influence on the magnetic behavior of  $UBe_{13}$  and also does not in any way affect the magnetism induced by Th doping. This weak magnetism hence is strictly coupled to the lower superconducting phase in the two-phase region of  $U_{1-x}Th_xBe_{13}$ . The coupling to  $T_{c-}$  is reminiscent of the findings of Luke et al. (1993b) in  $UPt_3$ . But there, magnetism had set in already at much higher temperatures, only an additional, but unexplained change occurred at  $T_{c-}$ . In  $U_{1-x}Th_xBe_{13}$ , the question arises whether the boundary line  $T_{c-}$  (see fig. 145) is just the onset of magnetic order within the already formed superconducting phase or whether it represents the transition into a different superconducting phase that has magnetism as a fundamental ingredient. The substantial specific heat connected with  $T_{c-}$  (Ott et al. 1984b) (as apparent in fig. 146, right), favors the latter scenario. The entropy of any order in a spin system with moments less than  $10^{-2}\mu_B$  is just too small. One might use a similar approach as in  $UPt_3$ , concentrating on the weak AFM as provider of a symmetry breaking field. Other models work with a SDW transition, producing, for example, a loss of Fermi surface. We refer the reader to the review by Heffner and Norman (1996). Finally, we mention a recent measurement of muonic Knight shift in superconducting  $UBe_{12.91}B_{0.09}$  by Heffner et al. (1997b). The results are interpreted as indicating the possible alignment of spin and orbital magnetic moments associated with the unconventional superconductivity in this system.

Sonier et al. (2000b) extended their Knight shift study on pure  $UBe_{13}$  (Sonier et al. 2000a) to  $U_{0.965}Th_{0.035}Be_{13}$ , in the composition region of the mysterious second transition within the superconducting state (see fig. 145). This time the analysis is extended to deduction of anomalous behavior of the (local) susceptibility: it drops steeply as temperature decreases through  $T_{c1}$ , as it should, but then levels off below  $T_{c2}$ , instead of going to zero. Unfortunately, the corresponding behavior in pure  $UBe_{13}$ , which does not have the second transition, is not clearly displayed or described.

*Summary:*  $\mu$ SR proved that pure  $UBe_{13}$  possesses no magnetic phase with moments  $>10^{-3}\mu_B$  in its superconducting ground state. It then first saw the formation of weak static magnetism ( $\mu_{ord} \approx 3 \cdot 10^{-3}\mu_B$ ) in the two phase regime of  $U_{1-x}Th_xBe_{13}$ . The magnetic state is concomitant with the lower superconducting phase and similar arguments as for  $UPt_3$  have been put forward regarding a symmetry-breaking field. A partial replacement of Be by B has no influence on magnetic properties, for pure  $UBe_{13}$  as well as for  $U_{1-x}Th_xBe_{13}$ .

9.3.2.6.  $U_2Zn_{17}$ . This material, having a rhombohedral (trigonal) crystal structure (space group  $R\bar{3}m$ ) is another example of a well-established HF compound (Ott et al. 1984a)

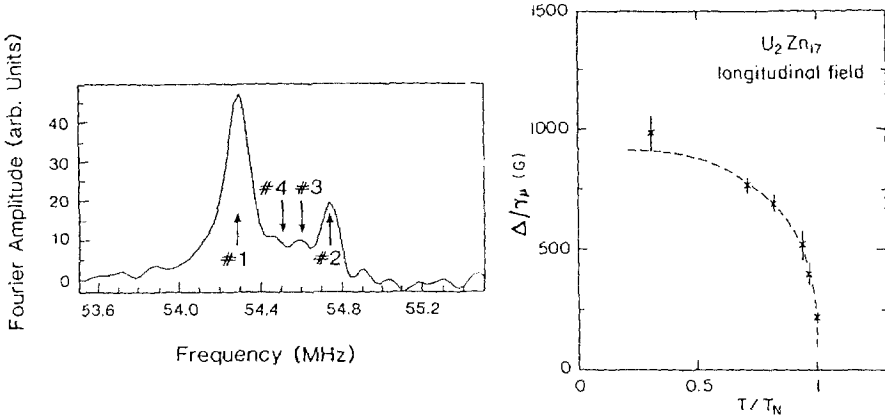


Fig. 147. Left: Fourier spectrum of the TF=4 kG data in paramagnetic ( $T = 9.8$  K)  $U_2Zn_{17}$ . The field is applied roughly parallel to the  $c$ -axis. Right: Temperature dependence of field width of the  $\mu$ SR signal not observable under ZF conditions in antiferromagnetic  $U_2Zn_{17}$  as deduced from LF data (see discussion in text). From Schenck (1993).

with an AFM ground state. Superconductivity is not present. The magnetic transition temperature of  $T_N = 9.7$  K, the spin structure consisting of antiferromagnetically coupled (along the  $c$ -axis) ferromagnetic (110) planes as well as the ordered U moment of  $\mu_{\text{ord}} = 0.8\mu_B$  (aligned in the (111) planes), were all determined by neutron diffraction (D.E. Cox et al. 1986).

The crystal structure of  $U_2Zn_{17}$  offers three possible  $\mu^+$  stopping sites, all resulting in  $B_\mu = 0$  for the above mentioned spin structure (see Schenck 1993). Hence, one expected rather straightforward results in the  $\mu$ SR study. Polycrystalline (Barth et al. 1986b) as well as single-crystalline (Barth et al. 1989a) samples were studied. They both gave similar results, but lead to a considerably more complex, as yet not understood, picture regarding the magnetic properties.

At first glance, the ZF spectra for  $T < T_N$  show the result expected for stopping sites where the contributions to the local field from neighboring moments cancel: One observes a monotonic (basically exponential) depolarization without the presence of spontaneous spin precession. The problem is the signal amplitude. About 30% of the stopped muons produce no observable  $\mu$ SR pattern. Those muons must experience a rather wide field distribution, which causes the loss of their spin polarization in a time shorter than the initial dead time of the spectrometer ( $\approx 20$  ns). A closer inspection of the features of the observable magnetic  $\mu$ SR spectrum indicates unusual properties there as well. We shall return to these problems after discussing the  $\mu$ SR response in the paramagnetic regime.

Spectra taken in TF = 4 kG for  $T > T_N$  reveal four signals with different frequencies (fig. 147, left). Signal #1 comes mainly from muons stopped outside the sample but a small sample signal is likely to be contained within. Little can be said about the properties of this sample signal, however, since a separation from the background signal could not be achieved under any experimental condition. Signal #2 shows an angular dependence

of frequency shift that is consistent with dipolar interaction by U moments aligned along the applied field. This is expected for the probable stopping sites. In contrast, signals #3 and #4, which make up about 30% of the total signal strength, have paramagnetic frequency shifts with quite unusual angular dependence. It is usual to express this angular dependence as a sum over directional cosines. For signals #3 and #4 terms up to the eighth order are required. The dipolar coupling of the muon to surrounding moments for any interstitial site cannot produce terms of such high order. The authors conclude that an additional interaction must be present. One might consider a bond between the muon and the Zn ions, but for the time being this feature is simply termed “unexplained” in the literature. From the strength of signals #3 and #4, one concludes that they comprise the portion of the signal that is lost in the magnetically ordered state. It has been stated that a wide field distribution seen by the muons must be the underlying cause. For  $T \rightarrow 0$  one expects the field distribution to be static. In this case one expects a recovery of signal for  $B_L \geq 5\Delta/\gamma_\mu$  as discussed in sect. 3.2.3. Longitudinal field data showed this indeed to happen. From the dependence of signal amplitude on LF (up to 4.5 T) and temperature (in the range between 9.5 K and 3 K) the variation of the width of the field distribution with temperature was deduced. It is shown in fig. 147 (right). A field spread of  $\sim 1000$  G for  $T \ll T_N$  is found. This result cannot be reconciled with the spin structure together with the ordered moment magnitude derived by neutrons and the possible muon stopping sites mentioned above.

We finally turn to the observable  $\mu$ SR signal below  $T_N$  once more. It allows TF measurements since it arises from muon sites with  $B_\mu = 0$  in an antiferromagnet (no bulk magnetization). The major contribution to this signal comes from the sub-signal #2. One finds that the angular dependence of frequency is unaltered when the temperature is lowered below  $T_N$ . As stated, this angular dependence is consistent with a local field aligned by the applied field, which is the expected behavior in the paramagnetic regime, but contradictory to long-range AFM order, where a sub-lattice magnetization along the easy axis is present. The obvious conclusion is that signal #2 is associated with muons stopped in paramagnetic domains even below  $T_N$ . Neutron diffraction may not be able to pinpoint the volume fraction that produces the Bragg pattern and hence may not be contradictory to the  $\mu$ SR result, but why even a single crystal should divide into an ordered and a paramagnetic portion is difficult to understand. This leaves the sample signal hidden under the background signal (#1) as the only one displaying the expected magnetic response. But its intensity is low and, as stated, its properties are not known in any detail.

*Summary:* The  $\mu$ SR results remain largely unexplained. They suggest that at best a small portion of the stopped muons produce a signal in agreement with the magnetism detected by neutrons. The dominant  $\mu$ SR signal in the ordered regime is suggestive of inhomogeneous magnetism with coexistence of magnetically ordered and paramagnetic domains, even in single-crystal specimens. Furthermore, a part of the stopped muons experience a coupling of higher order than dipolar to their surroundings. This feature is also as yet not understood. Which of those astonishing details reflect truly intrinsic

magnetic properties remains to be seen, but a sample dependence was not found. The  $\mu$ SR results point toward the presence of more complex magnetism in  $U_2Zn_{17}$  than generally accepted on the basis of bulk measurements and neutron data, and call for additional studies.

9.3.2.7.  $U_{14}Au_{51}$ . This is a hexagonal (space group P6/m) HF compound ( $\gamma = 0.3$  J/mol(U)K<sup>2</sup>) with a magnetic transition  $T_N = 22$  K. It has been investigated several times by neutron diffraction. The more recent study (Brown et al. 1997) found a considerably more complex AFM structure than the original one (Dommann et al. 1990). Both agree, however, that different moments are present on the three distinguishable U lattice sites (U1, U2, U3). The U3 site carries no moment at all, the other two have 2.28 (U1) and 1.48 $\mu_B$  (U2), respectively.

A recent study by Schenck et al. (1998a) reports on  $\mu$ SR measurements in both the paramagnetic and AFM phases. In the paramagnetic regime four components are seen in the TF spectra with different Knight shifts. From the angular dependence of shift two different muon stopping sites are deduced, one between two U3 ions (producing a single TF signal), the other near the center of a triangle between three U1 ions. The paramagnetic  $\mu$ SR data indicate that the U3 ions are nearly, but not completely nonmagnetic. The temperature dependences of the Knight shifts follow Curie–Weiss laws but need different Curie–Weiss temperatures, which do not agree with the values obtained by bulk susceptibility. The authors exclude a muon induced effect but argue that the  $\mu$ SR spectra do not weight the magnetically different U ions the same way as bulk susceptibility.

In the AFM state below  $T_N = 22$  K two different spontaneous spin precession frequencies are observed. Both show the usual (Brillouin-like) dependence on temperature, but have significantly different  $T \rightarrow 0$  saturation values (4.4 MHz or  $B_\mu = 0.32$  kG and 28.5 MHz or  $B_\mu = 2.1$  kG). The two frequencies correspond to the two different muon sites. The  $\mu$ SR spectral response in the AFM state could be fully explained on the basis of the spin structure derived by Brown et al. (1997), but not with the simpler one proposed by Dommann et al. (1990). If the improved neutron data on spin structure had not been available, this would have been another case of discrepancy between neutron and  $\mu$ SR data. The work is a good indication that final agreement must always be obtained if the spin structure is truly understood. The data on  $U_{14}Au_{51}$  give additional weight to the notion that the spin structure of  $U_2Zn_{17}$  is more complex than generally considered.

*Summary:* The  $\mu$ SR data confirm a more complex spin structure recently derived by neutron diffraction. They also show that the U3 uranium site is not completely nonmagnetic but weakly magnetic.

9.3.2.8.  $URu_2Si_2$ ,  $URh_2Si_2$  and related compounds. This series forms in the tetragonal  $ThCr_2Si_2$  structure with space group I4/mmm (like  $CeCu_2Si_2$ ). In  $URu_2Si_2$  the development of superconductivity (at  $T_c = 1.3$  K) within an AFM state ( $T_N = 17.5$  K) was observed for the first time in a HF material (Palstra et al. 1985, Maple et al. 1986,

Schlabitz et al. 1986, de Visser et al. 1986a,b). The broad interest in  $\text{URu}_2\text{Si}_2$  is also due to neutron diffraction (Broholm et al. 1987) finding a rather small ordered moment ( $\sim 0.02\mu_B$ ) while the loss of entropy at  $T_N$  is large, a problem that remains unsolved.

Both polycrystalline and single-crystalline samples have been prepared successfully. The study of  $\text{URu}_2\text{Si}_2$  is, however, plagued by sample-dependent inconsistencies. The most extensive study on the influence of sample quality on magnetic properties was carried out by Fåk et al. (1996) using neutron scattering, specific heat, electrical resistivity and magnetic susceptibility measurements. One of the most striking findings of this work was the sample dependence of the temperature dependence of ordered magnetic moment as reflected by the integrated Bragg-peak intensity (see discussion below and fig. 148, right). Also, the original findings of Broholm et al. (1987) that the AFM of  $\text{URu}_2\text{Si}_2$  is characterized by a sluggish onset around  $T_N$  and a reduced correlation length are in part a sample problem. These features are much less pronounced in high-quality single crystals (Mason et al. 1990, Fåk et al. 1996), but the Néel temperature, the weak saturation ( $T \rightarrow 0$ ) moment and the basic AFM spin structure seem to be intrinsic properties shown by all samples investigated.

Broholm et al. (1987) and subsequently Mason et al. (1990) (neutron scattering) as well as Isaacs et al. (1990) (resonant photon scattering) showed the AFM spin structure to be of type I with a propagation vector  $\mathbf{q} = (001)$  and the moments aligned along the  $c$ -axis. The ordered moment is given by Mason et al. (1990) to be  $0.037\mu_B$ , while the others give  $0.02\mu_B$ . Additional neutron studies (Buyers et al. 1994, Mason et al. 1995, Walker et al. 1993, 1994) have largely been used to disprove most of an equally numerous variety of theoretical explanations of the system (see, for example, Agterberg and Walker 1994, Santini and Amoretti 1994, Monachesi and Continenza 1995, Brison et al. 1995, Sikkema et al. 1996). A clear and definite picture has not yet evolved.

The simple AFM structure revealed by neutron scattering indicates that ZF- $\mu$ SR should see a well-developed spontaneous spin precession signal below  $T_N$ , but this was not observed. The original work by MacLaughlin et al. (1988) on a polycrystalline specimen only found a moderate rise in depolarization rate around  $T_N$  together with a monotonic Gaussian decay of muon spin polarization. A later, more extensive study on good single crystals by Knetsch et al. (1993) gave essentially the same result (see fig. 148, left), but the rise at  $T_N$  is sharper here than in MacLaughlin et al. (1988). There, the relaxation rate started to increase slowly somewhat above  $T_N$ . It has been suggested, mainly because of discrepancies between neutron and caloric data (see, for example, Fåk et al. 1996) that the magnetic transition is actually a double transition, one around 17 K the other closer to 14 K. The  $\mu$ SR data, in particular those of Knetsch et al. (1993), give no indication of such a property. More extensive single-crystal data have recently been reported by Dalmas de Réotier et al. (1998b). The dependence of relaxation rate below  $T_N$  on crystal orientation, already apparent in fig. 148, is even more pronounced. The authors conclude that a temperature dependence of field distribution must exist that is markedly anisotropic. The width of the component along the  $c$ -axis rises faster as  $T$  decreases than the perpendicular component. This points towards a complex spin structure.



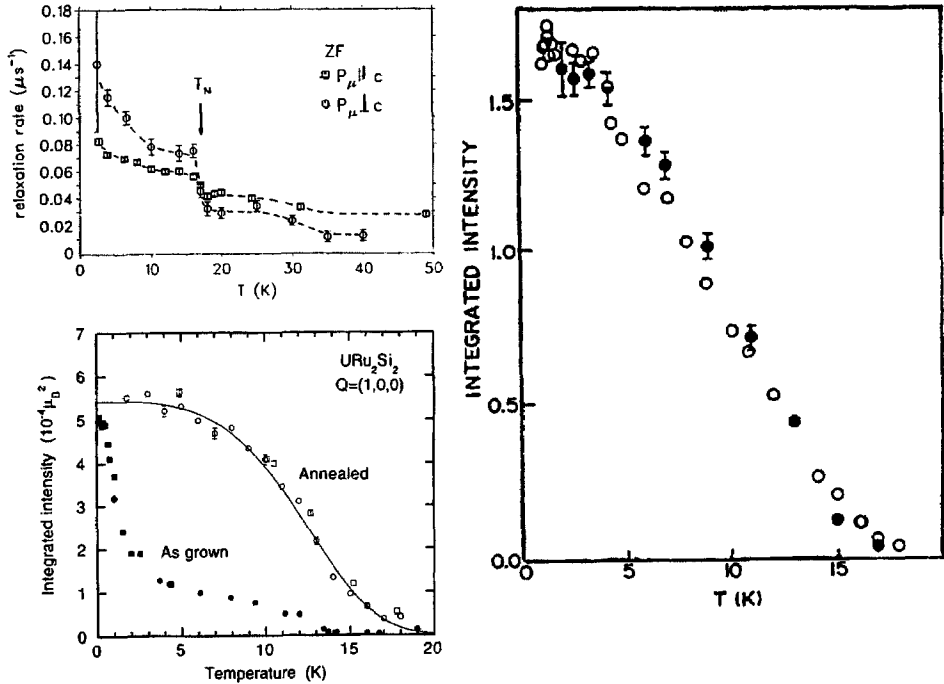


Fig. 148. Top left: Temperature dependence of the ZF relaxation rate (using exponential decay of polarization) in single-crystalline  $\text{URu}_2\text{Si}_2$  for two crystal orientations. From Knetsch et al. (1993). Right: Temperature dependence of the integrated intensity of the (111) magnetic Bragg peak in a single crystal of  $\text{URu}_2\text{Si}_2$ . Solid circles refer to neutron data, open circles to X-ray scattering. From Mason et al. (1990). Bottom left: corresponding data (on the (100) peak), showing differences due to sample treatment. By Fåk et al. (1996).

Remarkably, the temperature dependence of the relaxation rate does not follow a Brillouin-type dependence but increases monotonically as temperature decreases. This ties in with the result of Mason et al. (1990) and Isaacs et al. (1990) that the magnetic Bragg intensity grows linearly with decreasing temperature down to  $\sim 3$  K where it saturates (fig. 148, right). The dependence seen by Fåk et al. (1996) (see fig. 148, bottom left) in the annealed sample is not observed in  $\mu\text{SR}$ . No change in relaxation rate can be detected at the superconducting transition temperature ( $T_c = 1.3$  K, which agrees with neutron and photon scattering data), thereby excluding a change in long-range AFM order.

The salient difficulty with the  $\mu\text{SR}$  data is the absence of spontaneous spin precession. A first suggestion proposes that the muon occupies a site  $(\frac{1}{4}, \frac{1}{4}, \frac{1}{4})$  where  $B_{\mu} = 0$  and the observed relaxation only comes from local distortions of the perfect site symmetry. Such an argument has also been discussed in the case of  $\text{UPt}_3$ , but is seriously questioned nowadays. Here, it is fairly unlikely as well in view of the  $\mu\text{SR}$  results for  $\text{URh}_2\text{Si}_2$  (Dalmas de Réotier et al. 1994b). This isostructural compound is a localized-moment AFM with  $T_N = 131$  K and  $\mu_{\text{ord}} = 1.95\mu_B$  (Ptasiewicz-Bak et al. 1981). Below  $T_N$ ,

a single-frequency spontaneous spin-precession signal with  $\nu_\mu(T \rightarrow 0) \approx 41$  MHz (corresponding to  $B_\mu = 3$  kG) is seen, which excludes the  $(\frac{1}{4}, \frac{1}{4}, \frac{1}{4})$  muon site. The change of relaxation rate on approaching  $T_N$  from above shows typical power-law critical behavior. MacLaughlin et al. (1988) mention the possibility that the charged muon quenches the 5f moment in URu<sub>2</sub>Si<sub>2</sub> on the nearest neighbor uranium sites. Invocation of muon-induced effects is always possible in desperation, but this idea seems unlikely. Note, for example, that the μSR results on URh<sub>2</sub>Si<sub>2</sub> are fully compatible with the known (from neutron scattering) AFM spin structure. That neutron and photon scattering in URu<sub>2</sub>Si<sub>2</sub> have not correctly determined the magnetic structure is equally unlikely. Another argument is that locally the AFM structure is disturbed but over long correlation lengths it is maintained. In other words, there exists a certain random (perhaps weakly dynamic) disordered magnetic component in addition to the quasistatic ordered moment. With this argument, however, it is difficult to explain the smallness of the relaxation rate. Precise weak-LF data which could shed additional light on this problem have not been reported. Inelastic neutron scattering work mentions an anomalous damping of magnetic excitations with a component of momentum transfer along the *c*-axis as an intrinsic (i.e., not sample dependent) property (Mason et al. 1990).

It is worthwhile to point briefly to a quite curious result obtained by Luke et al. (1994b). In their ZF-μSR study on a single-crystal specimen they saw a definite two-component structure of the signal in the magnetic phase. The predominant component, comprising ~90% of signal strength, showed a behavior similar to that seen in the other μSR studies discussed (i.e., only a moderate increase of depolarization rate). The weak component showed spontaneous spin precession with  $\nu_\mu(T \rightarrow 0) \approx 8$  MHz. The amplitude of this portion rises with decreasing temperature but does not exceed ~15% of muons stopped in the sample. The essential point is that this result implies inhomogeneous coexistence of superconductivity and magnetism (as definitely established in CeCu<sub>2</sub>Si<sub>2</sub>, with which it shares the crystal structure). All other work rather point towards a homogeneous coexistence (as, for example, in UPt<sub>3</sub>) but the general consensus is that even then the coupling between magnetic order and superconductivity is weak (in contrast to UPt<sub>3</sub>). A final conclusion cannot be drawn at this stage.

We briefly mention the Knight shift study in the paramagnetic regime by Knetsch et al. (1993), mainly for a field applied parallel to the *c*-axis. Scaling with bulk susceptibility is found down to 50 K, but below, this feature is lost. At 50 K the susceptibility exhibits a broad peak, usually ascribed to a CEF splitting of the <sup>3</sup>H<sub>4</sub> Hund's rule ground state. Several scenarios for this loss of scaling are offered (we refer to the original paper and to Amato 1997), none of which are very convincing.

Since URu<sub>2</sub>Si<sub>2</sub> is a weak AFM but URh<sub>2</sub>Si<sub>2</sub> is a strong local moment AFM, it is tempting to study the series of pseudo-ternary compounds U(Ru<sub>1-x</sub>Rh<sub>x</sub>)<sub>2</sub>Si<sub>2</sub>. Dalmas de Réotier et al. (1990a) looked at a powder sample with  $x = 0.35$  by ZF-μSR at the ISIS pulsed muon facility. As shown in fig. 149 (left) they found around 40 K a drop in signal amplitude (asymmetry) down to 1/3 of the high-temperature value and a peak in relaxation rate. This shows that this material has  $T_N \approx 42$  K (derived from the peak in relaxation rate) and most likely forms long-range AFM order (but the data

give no definite indication of the type of spin structure). Probably spontaneous spin precession develops for  $T < T_N$  but is at a frequency beyond the detection range of the pulsed facility. The signal seen below  $T_N$  is the “1/3 signal” then expected for a powder sample in the magnetically ordered state. The relaxation rate shows the typical critical behavior. Noticeable from the temperature dependence of the signal amplitude is the wide temperature range over which the drop in intensity occurs, indicating that magnetic order develops in a spatially inhomogeneous way. The corresponding behavior of pure  $URh_2Si_2$  is different. The drop in amplitude is sudden at  $T_N$  (but the relaxation rate does not peak as sharply). Yet, as we have seen,  $URu_2Si_2$  is also plagued by a (sample-dependent) temperature range over which magnetism sets in.

Partial replacement of the magnetic ion is also possible. Cywinski et al. (1995) report on ZF- $\mu$ SR studies of  $U_{1-x}La_xRu_2Si_2$  (with  $x = 0.25$ ) and  $U_{1-x}Y_xRu_2Si_2$  (with  $x = 0.05$ ). The spectra for the La-doped sample can be described at all temperatures by weak Gaussian depolarization. There is a drop in initial asymmetry between 30 and 15 K, down to 1/3. Again, this is taken as a sluggish entry into a magnetically ordered state. The magnetic signal is not resolved, only the 1/3 fraction is seen. The Y-doped material behaves differently. In addition to the weak Gaussian depolarization (of nuclear origin) a much faster relaxing signal develops below  $\sim 17$  K, which indicates the presence of static random fields arising from 5f magnetic moments. Even for  $T \rightarrow 0$ , however, this magnetic signal never comprises more than  $\sim 65\%$  of total signal strength. Obviously, this material exhibits inhomogeneous magnetic behavior. From the static width of the magnetic signal, the frozen 5f moments are estimated to be  $\sim 0.01\mu_B$ , that is, quite comparable to pure  $URu_2Si_2$  (and so is the transition temperature). LF data definitely prove the static character of the depolarizing fields. The data are summarized in fig. 149 (right).

Park et al. (1996) extended the study to  $x = 0.05$  for La doping and  $x = 0.5$  for Y doping. The 5% La sample showed muon spin depolarization behavior similar to the 5% Y material. The onset of magnetic order occurs at 10 K (5% La) and 14 K (50% Y), respectively. The magnetic order parameter does not saturate down to 5 K (the lowest temperature measured), which is quite similar to the behavior of pure  $URu_2Si_2$ .

*Summary:* The  $URu_2Si_2$  system appears to be especially sensitive to impurities and/or crystal imperfections in the details of its magnetic behavior. This holds not only for the  $\mu$ SR response but for other methods as well. It is difficult to distill the true intrinsic properties and the material is not too well understood at this stage. In general, the  $\mu$ SR results are in agreement with neutron data on comparable samples as far as entering into the magnetic state and the development of sub-lattice magnetization are concerned.  $\mu$ SR, however, sees considerably stronger local magnetic inhomogeneities than expected from the simple AFM spin structure given by neutron or photon scattering. Studies of mixed systems such as  $U(Ru,Rh)_2Si_2$  and  $(U,Y)Ru_2Si_2$  strongly support the picture that impurities are primarily the cause of inhomogeneous magnetism. In contrast, the  $\mu$ SR response of the local moment AFM  $URh_2Si_2$  follows the expectations derived from the established magnetic structure and the second-order phase transition leading into it.

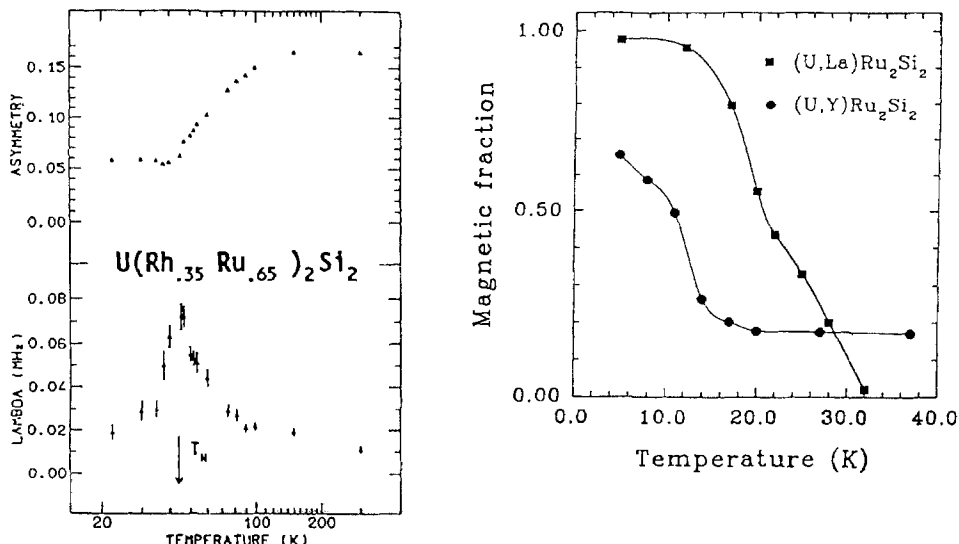


Fig. 149. Left: Signal amplitude (top) and relaxation rate (bottom) as a function of temperature from ZF-μSR data in  $U(Rh_{0.35}Ru_{0.65})_2Si_2$ . Below the Néel point of  $\approx 42$  K the rate refers to the “1/3 signal”. After Dalmás de Réotier et al. (1990a). Right: Temperature dependence of the fractional volume showing magnetic order (or spin freezing) in  $U_{0.75}La_{0.25}Ru_2Si_2$  and  $U_{0.95}Y_{0.05}Ru_2Si_2$  as derived from ZF-μSR spectra. From Cywinski et al. (1995).

9.3.2.9.  $URh_2Ge_2$ . This moderately heavy ( $\gamma = 0.3 \text{ J}/(\text{mol K}^2)$ ) HF compound crystallizes in a hexagonal structure, but a decision on whether the  $ThCr_2Si_2$  structure, with randomly distributed Rh and Ge atoms, or a  $CaBe_2Ge_2$  structure is present could not be made (Dirkmaat et al. 1990).  $URh_2Ge_2$  shows strong anisotropy in its bulk parameters. It exhibits unusual magnetic properties that deviate markedly from those found in most other members of the uranium-122 series (simple AF stacking, see Nieuwenhuys 1995). While magnetic susceptibility displays a distinct maximum at 8 K, neutron scattering did not detect any magnetic ordering (Ptasiewicz-Bak et al. 1981, 1985), and also in specific heat only a shallow maximum around 10 K is seen. Dirkmaat et al. (1990) concluded from the combination of various bulk data that there is no magnetic order, no superconductivity and no coherent state present down to 35 mK.

A brief report of a μSR study using a single crystal “as cast” (Nieuwenhuys et al. 1998) describes the observation of a substantial rise of depolarization rate around 15 K, but no spontaneous spin precession pattern below this temperature. The increased relaxation rate was fully suppressed by a LF=0.2 T. At all temperatures the shape of the ZF spectra could be reproduced by a power-exponential decay of polarization. The power decreases from  $p \approx 1$  at 30 K and above, to  $p \approx 0.5$  at 15 K and below. The authors conclude that  $URh_2Ge_2$  enters a highly disordered, spin-glass-like magnetic state at the spin freezing temperature of  $\sim 13$  K. This spin-frozen state produces a widely distributed, static interstitial field. The compound is termed a “random bond” spin glass.

Neutron diffraction on the same crystal (Suellow et al. 1997) showed the development of dynamic magnetic correlations around 16 K. The magnetic reflections are aligned along the  $c$ -axis, as is common for the 122 materials.  $\mu$ SR, in contrast, could not detect any differences in the behavior of relaxation rates parallel and perpendicular to the  $c$ -axis. The  $(\frac{1}{2}, 0, 0.1)$  position was deduced as the muon stopping site from recent Knight shift measurements on the single-crystalline sample (Nieuwenhuys et al. 2000). Simulations of the  $\mu$ SR signal for random and Ising (moments aligned along the  $c$ -axis) spin-glass states show that the isotropic behavior requires random anisotropy for the U moments.

The magnetic properties of  $\text{URh}_2\text{Ge}_2$  have also been discussed by Mydosh (1999) in terms of disorder and magnetic frustration. He points out that the system could be close to a  $T = 0$  quantum critical point (see sect. 9.4).

*Summary:*  $\mu$ SR shows that  $\text{URh}_2\text{Ge}_2$  undergoes spin freezing at 13 K and enters a highly disordered spin-glass-like state. This result is in keeping with neutron diffraction, which failed to detect long-range magnetic order, but sees the development of magnetic correlations below 16 K.  $\mu$ SR, in contrast to the neutron result, suggests random anisotropy for the short-range correlated U moments.

9.3.2.10.  $\text{UNi}_2\text{Al}_3$  and  $\text{UPd}_2\text{Al}_3$ . These materials share a hexagonal crystal structure (space group  $P6/mmm$ ). They are special in the respect that they show coexistence of superconductivity and fairly large local moment (on the order of  $1\mu_B$ ) AFM. The discovery of these materials (Geibel et al. 1991b) contradicted the notion that small moments are a prerequisite for coexistence of superconductivity and AFM (as is the case in  $\text{UPt}_3$ ). Startlingly, the superconducting transition temperature of  $\text{UPd}_2\text{Al}_3$  is the highest of all known HF compounds (around 2 K) despite the fact that the material enters the magnetically ordered state at much higher temperature ( $T_N \approx 14$  K). The same situation prevails in  $\text{UNi}_2\text{Al}_3$  but is less extreme ( $T_c \approx 1$  K,  $T_N \approx 5$  K).

We first discuss  $\text{UPd}_2\text{Al}_3$  as the more straightforward case. Susceptibility and specific heat have been presented by Geibel et al. (1991b) and also by Caspary et al. (1993). Superconducting properties were specifically measured by Dalichaouch et al. (1992). Non-uniform superconductivity of FFLO type (see discussion on  $\text{CeRu}_2$  in sect. 9.3.1.1) has been suggested (Gloos et al. 1993) but is still under debate (Haga et al. 1996). Anisotropy of susceptibility and  $H_{c2}$  for single-crystalline specimens are discussed by Sato et al. (1997). Neutron diffraction (Krimmel et al. 1993) sees simple commensurate AFM order with a propagation vector  $\mathbf{q} = (00\frac{1}{2})$ . A following study by resonant magnetic phonon scattering (Gaulin et al. 1994) showed a distinct anomaly in the order parameter at 11.8 K, i.e., below  $T_N = 14.5$  K. This result was interpreted as indicative for at least two AFM phases sharing a *common periodicity* (of the same  $\mathbf{q}$ ) as determined by neutrons. In addition, the correlation length was found to be long ( $\sim 1500$  Å), in contrast to the results (less than 500 Å) for  $\text{URu}_2\text{Si}_2$  or  $\text{UPt}_3$ . Bulk magnetic data (Grauel et al. 1992) also identified three magnetic phases, but only in the presence of a sizeable field (0.4 T) applied within the  $a - b$  plane. These authors developed a CEF model based on a stable  $\text{U}^{4+}$  configuration that is in agreement with specific heat, the single-

crystal susceptibility and the incoherent inelastic neutron scattering data (Krimmel et al. 1996, Bernhoeft et al. 1998). This, as well as the inelastic magnetic neutron scattering studies of Metoki et al. (1998) and Sato et al. (1996), reports a gap at  $T_c$ , giving strong support for a “two component” model of coexistence of superconductivity and magnetism. In any case, the presence of an AFM state below  $T_N = 14.5$  K that exhibits a sizeable  $\mu_{\text{ord}}$  is well-established by various methods, but details of the magnetic state, its formation and structure are still under some debate. Gaulin et al. (1995) remark that sample inhomogeneities could be responsible and point out the fact that magnetic photon scattering has the advantage of response to a single microcrystal which is likely to be perfect. Yet, one also must keep in mind that this method preferentially samples the layers close to the surface. In their original neutron work, Krimmel et al. (1993) report reduced Bragg peak intensities below  $T_c$ . This result was contradicted by Kita et al. (1994). Also Gaulin et al. (1995) see no change in AFM order parameter to within 2% when entering the superconducting phase, and Petersen et al. (1994) see no effect on the magnon spectrum in crossing  $T_c$ .

The  $\mu$ SR study on polycrystalline material by Amato et al. (1992a,b) detected no spontaneous spin precession. Above and below  $T_N$  a non-oscillating, moderately relaxing signal was seen. An example of a spectrum for  $T \ll T_N$  is shown in fig. 150. The muon must occupy a site of high symmetry where the local field produced by surrounding U moments cancels. The remaining relaxation rate exceeds the value expected from nuclear dipole fields of  $^{27}\text{Al}$  and reflects defects in the AFM structure as discussed for UAs (see sect. 5.2.1). For this reason, the  $\mu$ SR data will not give information on a possible second transition *if periodicity is maintained*. In general, a full cancelation of internal field is possible only for simple AFM spin structures. Above  $T_N$ , the relaxation becomes weaker and the depolarizing influence of  $^{27}\text{Al}$  nuclear fields dominates. An appropriate muon stopping site is the interstitial position (the b site) between two U atoms along the  $c$  axis (see inset to fig. 150). TF measurements on a single crystal confirmed this assignment *via* the angular dependence of Knight shift (see Amato et al. 1997a).

Between 0.08 K and 2.5 K the muon spin relaxation rate ( $\lambda = 0.42 \mu\text{s}^{-1}$ ) is temperature independent, meaning that the onset of superconductivity has no detectable influence here as well. In TF data the situation is different. A first increase in depolarization rate (together with a change from Gaussian to Lorentzian shape) is observed at  $T_N$ , but another sharp increase occurs at  $T_c$  (Feyerherm et al. 1994b, W.D. Wu et al. 1994b). The latter reflects the enhancement of internal magnetic field distribution due to the formation of the flux-vortex lattice. The data confirm that all muons stopped in the sample are subject to the increased relaxation, meaning that the coexistence of superconductivity and ordered local magnetism extends uniformly over the sample as a whole, in contrast to the situation in  $\text{CeCu}_2\text{Si}_2$ .

Feyerherm (1995) studied the angular dependence of the (nuclear) muon spin depolarization rate at high temperatures (295 K) in ZF. The simple cosine dependence observed indicates that the muon occupies the interstitial b site (insert to fig. 150). In order to reproduce the amplitude of the angular dependence one has to know the direction of the electric field gradient (EFG) at the site occupied by the  $^{27}\text{Al}$  nuclei. Neither a

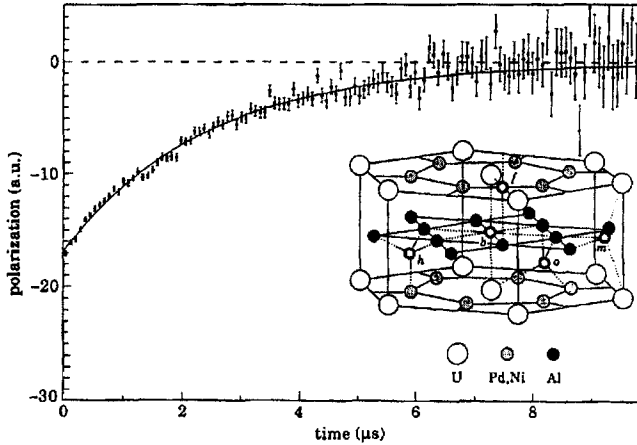


Fig. 150. ZF- $\mu$ SR spectrum of  $\text{UPd}_2\text{Al}_3$  at 80 mK, fitted to an exponential decay of muon spin polarization. The negative initial polarization is an artifact of measurement geometry. The inset shows the unit cell with prominent interstitial sites. The muon occupies the b site. From Amato et al. (1992b).

radial gradient directed towards the muon nor an axial gradient parallel to the crystalline  $c$  direction gave a fully convincing result. A combined action of axial and radial gradients is needed. This problem will be taken up once more within the paragraph on isostructural  $\text{UNi}_2\text{Al}_3$ .

An AFM has no macroscopic magnetization and even small fields can enter the sample. In addition, corrections for demagnetizing fields are small. Furthermore, in the present case, the implanted muons do not sense a residual field from the ordered U moments. These facts allow the measurement of Knight shifts below  $T_N$ . The  $\mu$ SR frequency shift is then a measure of the local susceptibility of 5f electrons. Figure 151 shows such data around and below  $T_c$ . One notices that  $K_{\parallel}$  is positive while  $K_{\perp}$  is negative. In both cases, however, the shift is *reduced in absolute value* in the superconducting state. The diamagnetic shift due to partial flux expulsion is estimated to be much smaller and should be negative, independent of field orientation. The authors relate the observed change in shift for  $T < T_c$  to the singlet pairing of f electrons in the superconducting state. In consequence, this change in shift is practically isotropic. The remaining shift, which is strongly anisotropic, must be ascribed to the 5f electrons giving rise to the local antiferromagnetism which, according to the ZF data, is unaffected in the superconducting state. In short, the results of frequency shift data in the ordered state provide strong evidence for the existence of two distinct 5f electron subsystems, a notion later supported by inelastic neutron scattering data (see above). The isotropic portion reflects an itinerant electron state creating the heavy-quasiparticle system that finally enters the superconducting state. The anisotropic portion is correlated to localized electron states, which leads to the local moment magnetism. Theoretical models concerning the existence of duality in the 5f electron system have been put forward by Kuramoto and

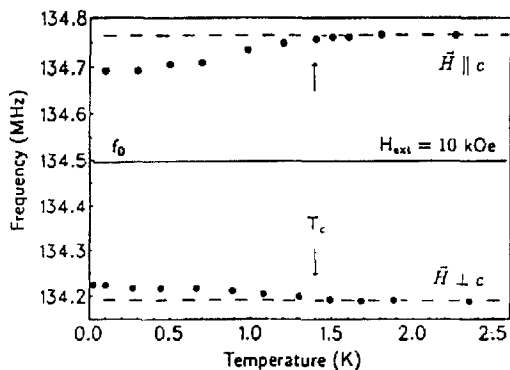


Fig. 151. Temperature dependence of the  $\mu$ SR frequency in  $UPd_2Al_3$  in an external field of 1 T applied in two directions near and below the superconducting transition (i.e., always in the magnetically ordered state). The line  $f_0$  marks the frequency of a free muon. The dashed lines give the general Knight shift in the magnetic state. Note that changes in shift occur at the superconducting transition temperature ( $T_c$ ) whose sign depends on field orientation. From Feyerherm et al. (1994a).

Miyake (1990) and Caspary et al. (1993). In general, this picture, though tempting, should still be regarded as provisional.

Further results from TF- $\mu$ SR studies on  $UPd_2Al_3$  concern superconducting properties that are outside this review. We mention the approximately isotropic London penetration depth ( $\approx 5000\text{\AA}$ ) and the ratio  $T_c/T_F \approx 10^{-2}$  ( $T_F$  being the Fermi temperature) which is one order of magnitude larger than that for simple metallic BCS superconductors (W.D. Wu et al. 1994b).

Isostructural  $UNi_2Al_3$  has lower magnetic and superconducting transition temperatures ( $T_N \approx 5\text{ K}$ ,  $T_c \approx 1\text{ K}$ ) and exhibits a considerably more complex AFM structure. Susceptibility deviates from Curie-Weiss behavior up to 300 K (Geibel et al. 1991a). Other references given for measured bulk properties of  $UPd_2Al_3$  contain results for the Ni compound as well. Single-crystal susceptibility and specific heat are also presented by Mihalik et al. (1997). Single-crystal neutron diffraction (Schröder et al. 1994b) finds incommensurate AFM order below 4.6 K and 5.2 K (sample dependent) with a small ordered moment ( $\mu_{ord} \approx 0.2\mu_B$ ). This is consistent with the failure to detect magnetic order by neutron diffraction of powder samples (Krimmel et al. 1995).

ZF- $\mu$ SR both on single-crystalline (W.D. Wu et al. 1994b) and polycrystalline (Amato et al. 1992b) material showed the presence of spontaneous spin precession below  $\sim 5\text{ K}$ . W.D. Wu et al. (1994b) noted that the spectral shape resembles that seen in the incommensurate SDW system  $(TMTSF)_2PF_6$  (Le et al. 1991) suggesting an incommensurate spin arrangement, which since has been confirmed by the neutron data of Schröder et al. (1994b). This result prompted Amato (1997) to attempt a fit to the magnetic  $\mu$ SR spectrum of  $UNi_2Al_3$  with Bessel function oscillations as appropriate for incommensurate spin structures. The fit, shown in fig. 152 (left), needs two Bessel functions with amplitude ratio 2/1 and respective cutoff frequencies  $\nu_1(T \rightarrow 0) \approx 2.78\text{ MHz}$  and  $\nu_2(T \rightarrow 0) \approx 0.62\text{ MHz}$ , in addition to a relaxing “1/3 signal”. These frequencies show a temperature dependence expected for a normal magnetic transition (see fig. 152, right).

Measurements of the angular dependence of paramagnetic Knight shift together with the dipolar field calculations for the proposed orientation of U moments along the  $a$  axis



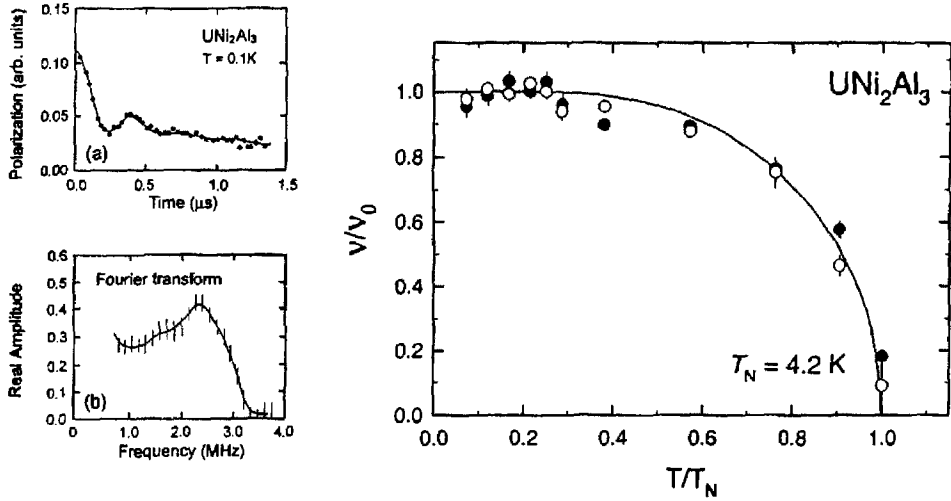


Fig. 152. Left: ZF- $\mu$ SR spectrum of polycrystalline  $\text{UNi}_2\text{Al}_3$  below  $T_N$ . The solid curve refers to a fit explained in the text. Also shown is the Fourier transform of this spectrum, demonstrating the wide distribution in local field. Right: Temperature dependence of the two cut-off frequencies  $\nu_1$  (solid symbols) and  $\nu_2$  (open symbols) obtained from fits to spectra of the type shown on the right side. Both frequencies are normalized to their values at  $T \rightarrow 0$  (2.78 and 0.62 MHz). From Amato (1997).

(Schröder et al. 1994b) implies that the muon rests on the interstitial site with coordinates  $(x, x, \frac{1}{2})$  for  $x \approx 0.08$ . This is a position close to the b site ( $x = 0$ ) occupied in  $\text{UPdAl}_3$  (see fig. 150.) More recently, Schenck et al. (2000a) have determined the local susceptibility tensor from Knight shift measurements on a single crystal. Comparison with bulk data shows agreement above  $\sim 150$  K but marked deviations below this temperature in the basal plane. A disturbance by the muon is claimed for this behavior. The data could be reproduced by muon influence on the CEF Hamiltonian. The calculations are based on the assumption of a highly localized 5f wave function for a  $\text{U}^{4+}$  ion and on the determination of the muon site from TF relaxation rates. As an improvement to the earlier site determination, it was found that about 30% of the implanted muons occupy the d site at low temperatures but none if  $T > 200$  K. The majority of muons were found to be in a tunneling state involving six m sites around the b site, which is the muon stopping site in isostructural  $\text{UPd}_2\text{Al}_3$ . It is suggested that zero point motion prevents the localization of the muon at any single m or k site. Hence, one has to consider a muon wave function which extends over several neighboring sites. It should be pointed out that a similar ring diffusion exists in  $\text{GdNi}_5$  (see sect. 5.4.3). Long-range muon diffusion appears to be absent up to room temperature.

Amato et al. (2000) return to the question of the EFG acting on the  $^{27}\text{Al}$  nuclei which had been discussed by Feyerherm (1995) for  $\text{UPd}_2\text{Al}_3$  (see above). They find that a fit to the relaxation rates of  $\text{UNi}_2\text{Al}_3$  in lower transverse fields (0.01 to 0.1 T) requires the additive combination of  $F_0$ , the (known) inherent EFG possessing the local symmetry of the Al site and of  $F_\mu$ , a muon generated EFG for nuclei close to the muon stopping

site. The total EFG thus has neither the Al site symmetry nor the cylindrical symmetry of  $F_{\mu}$  expected for a point charge calculation. A satisfactory reproduction of the field dependence of relaxation rate for different crystal orientations could be achieved with an appropriate tensor representation.

The complex magnetic spectra of  $\text{UNi}_2\text{Al}_3$  prevent muon studies of the superconducting state similar to those performed for  $\text{UPd}_2\text{Al}_3$ . Thus  $\mu$ SR is restricted to the properties of the magnetic state. It confirms the incommensurate ordering of relatively small U moments. Clearly, the 5f electrons in  $\text{UNi}_2\text{Al}_3$  are considerably less localized than those in  $\text{UPd}_2\text{Al}_3$ , a result in keeping with the deviation from Curie–Weiss behavior already mentioned. The likely cause is the reduction in unit cell volume when Pd is replaced by Ni. This increases the (5f–ce) hybridization as discussed earlier for the CeTsn system.

*Summary:* Information from ZF- $\mu$ SR data on the magnetic properties of  $\text{UPd}_2\text{Al}_3$  is fairly limited, because the internal field cancels at the muon stopping site due to high local symmetry. No change in  $\mu$ SR magnetic response is seen on entering the superconducting phase, in accordance with other data. Measurements in TF definitely prove the *homogeneous* coexistence of magnetism and superconductivity over the whole sample volume. In addition, the  $\mu$ -Knight shift gives strong support for the model of a dual 5f electron structure, i.e., the presence of an itinerant (superconducting) and a localized (magnetic) subsystem everywhere. Inelastic neutron scattering data also support a two-component model (Krimmel et al. 1993). For  $\text{UNi}_2\text{Al}_3$  the magnetic  $\mu$ SR data fully agree with the proposed incommensurate AFM spin structure. They also support the notion of a less-localized 5f magnetic moment when compared to the Pd compound.

9.3.2.11.  $\text{UNi}_4\text{B}$ . This HF compound has the same hexagonal crystal structure ( $\text{CeCo}_4\text{B}$ , of  $\text{CaCu}_5$  type) as  $\text{UNi}_2\text{Al}_3$  and  $\text{UPd}_2\text{Al}_3$ . It does not exhibit coexistence of superconductivity and AFM, but just possesses an AFM ground state with a fairly high transition temperature of  $T_N = 20$  K. Its spin structure is quite anomalous. According to neutron data (Mentink et al. 1994c) only 2/3 of the uranium moments order and form a hexagonal structure in the basal plane. The moments' directions are within this plane and the planes are ferromagnetically stacked in the  $c$  direction. The moment size is fairly large ( $2.2\mu_B$ ). The remaining 1/3 of the moments remain disordered, probably due to frustration. The situation is illustrated in fig. 153. The U sites labeled (1) and (2) carry the disordered moments. Magnetic and transport data are reported by Mentink et al. (1995, 1996) especially in view of the complex magnetic structure. Specific heat results can be found in Mentink et al. (1997) and the field-temperature phase diagram in Mentink et al. (1995). It is interesting that the Kondo temperature  $T^* = 7$  K is well below  $T_N$ . Thus, the magnetic state is well-developed and stable. Nevertheless, Mydosh (1999) argues that the behavior of  $\text{UNi}_4\text{B}$  might be the result of the system being close to a  $T = 0$  quantum critical point (see sect. 9.4) in combination with geometric frustration.

The ZF  $\mu$ SR study by Nieuwenhuys et al. (1995) on a single-crystal specimen provided no surprises. When orienting the sample with its  $b$  axis parallel to the muon beam (parallel to the initial muon spin orientation) no spontaneous spin precession signal

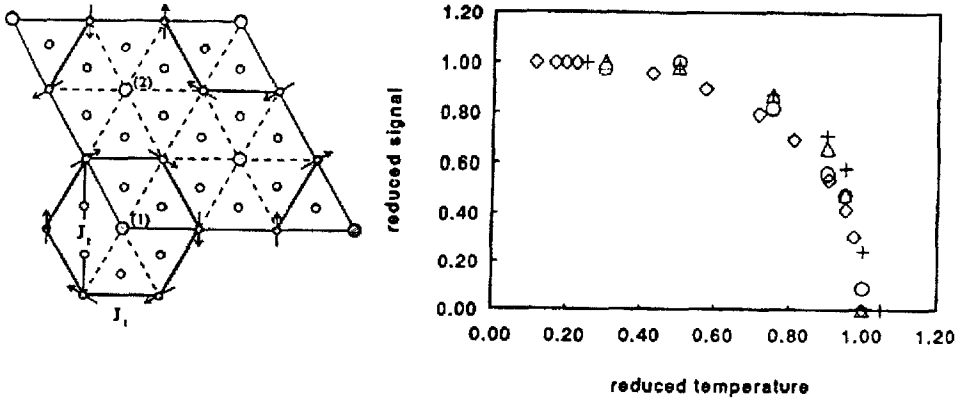


Fig. 153. Left: Magnetic structure of  $\text{UNi}_2\text{B}$  projected onto the basal plane. The magnetic layers are ferromagnetically stacked along the  $c$ -axis. (1) and (2) refer to the disordered U moments. The thin solid lines represent the magnetic unit cell.  $J_1$  and  $J_2$  are the nearest and next-nearest neighbor coupling constants. From Mentink et al. (1995). Right: Reduced values of the spontaneous precession frequency (triangles), the relaxation rate of the non-oscillating signal (circles), both for the  $c$ -axis parallel to the beam; the relaxation rate for the  $b$ -axis parallel to the beam (crosses) and the ordered U moment from neutron diffraction (diamonds) against reduced temperature. From Nieuwenhuys et al. (1995).

was seen. This verifies that all ordered spins are oriented fully within the basal plane. Turning the  $c$  axis into the beam produced a weakly damped spontaneous spin precession signal having  $\nu_\mu(T \rightarrow 0) \approx 5$  MHz together with a rapidly depolarizing non-oscillating signal. In fig. 153 (right), several reduced magnetic parameters are plotted against reduced temperature. The agreement between precession frequency, depolarization rates and ordered moment is impressive.

The stopping site of the muon is not known. The most probable site is the so-called 3f site  $(\frac{1}{2}, 0, 0)$  surrounding the disordered U moment inside the hexagonal structure. A dipolar field calculation gave approximately the observed spontaneous precession frequency. Other possible sites give much higher frequencies.

TF measurements were also performed for  $T > T_N$ . The 3f site is not highly symmetric with respect to the U magnetic structure. The low symmetry was verified but a precise site determination was not possible. The Knight shift is negative and roughly proportional to the bulk susceptibility. Finally, the ZF- $\mu$ SR data showed no irregularities around 10 K where magnetic susceptibility exhibits a second maximum. This is in agreement with neutron data and rules out an extra magnetic phase transition or spin reorientation.

*Summary:* The  $\mu$ SR data are fully consistent with the spin structure established by neutrons, even though it is very complex. No change in magnetic structure (as suggested by susceptibility) occurs around 10 K.

### 9.3.3. Other heavy-fermion compounds

9.3.3.1. *PrInAg<sub>2</sub>*. Specific heat, magnetic susceptibility and neutron scattering (Galera et al. 1984) carried out on this Kondo-lattice material indicate a non-Kramers doublet ( $\Gamma_3$ ,

which is nonmagnetic) as the CEF ground state. On the other hand, the large Sommerfeld constant of  $\gamma \approx 6.5 \text{ J}/(\text{mol K}^2)$  and a specific heat anomaly around 1 K prompted Yatskar et al. (1996) to suggest that  $\text{PrInAg}_2$  may be a system with an unusual nonmagnetic path to heavy-fermion behavior.

The  $\mu$ SR study by MacLaughlin et al. (2000b) revealed a muon spin relaxation rate independent of temperature between 0.1 K and 10 K. This rules out a magnetic origin (spin freezing or a conventional Kondo effect) for the specific heat anomaly. The observed relaxation rate can fully be explained by  $^{115}\text{In}$  and hyperfine enhanced (Andres and Bucher 1971)  $^{141}\text{Pr}$  nuclear moments. These findings provide strong evidence against the presence of any  $\text{Pr}^{3+}$  moment in the CEF ground state, which was an essential ingredient of the model used by Yatskar et al. (1996). The  $\mu$ SR data indicate, however, the presence of an indirect exchange coupling between neighboring  $\text{Pr}^{3+}$  ions with a strength corresponding to 0.2 K. The authors point out that this coupling needs to be taken into account for a complete theory of a nonmagnetic Kondo effect in  $\text{PrInAg}_2$ .

9.3.3.2. *Sm<sub>3</sub>Se<sub>4</sub> (and Sm<sub>2</sub>Se<sub>3</sub>)*. The  $\text{Sm}_3\text{X}_4$  series ( $X = \text{S, Se, Te}$ ) forms in the cubic  $\text{Th}_3\text{P}_4$  structure (space group  $\text{I}\bar{4}3\text{d}$ ) and shows semiconducting behavior with charge gaps on the order of some eV. It has been thoroughly studied in the context of valence fluctuations (see Holtzberg 1980 for details). All Sm sites are crystallographically equivalent but randomly occupied by either  $\text{Sm}^{3+}$  ( $4f^5$ ;  $J = 5/2$ ) or  $\text{Sm}^{2+}$  ( $4f^6$ ;  $J = 0$ ) ions, in the overall ratio of 2:1. No crystallographic transition and no charge ordering transition occurs (meaning that no  $\text{Sm}^{3+}/\text{Sm}^{2+}$  superlattice is created). The two charge states hop or tunnel between sites with a strongly temperature-dependent rate.

The relatively large Sommerfeld constant ( $0.79 \text{ J}/(\text{mol K}^2)$ ) of  $\text{Sm}_3\text{Se}_4$  points towards the formation of heavy quasiparticles and, despite the fact that all  $\text{Sm}_3\text{X}_4$  compounds are non-metallic, they have been discussed as low-carrier-density HF systems. Optical measurements on  $\text{Sm}_3\text{Se}_4$  (Batlogg et al. 1976) placed the 4f level inside the gap ( $\sim 4 \text{ eV}$  width) about 0.7 eV below the bottom of the conduction band. Hence, conduction electrons do not play an essential role in the valence fluctuations.

The DC-susceptibility of  $\text{Sm}_3\text{Se}_4$  (Fraas et al. 1992) shows a cusp around 0.7 K and a dependence on magnetic history at low temperatures. The authors discuss their findings in terms of the Kondo effect. Unfortunately, the  $^{77}\text{Se}$  NMR signal becomes unobservable below  $\sim 125 \text{ K}$  because of increasingly fast relaxation (Takagi et al. 1993a). The time window is more favorable for  $\mu$ SR (Takagi et al. 1993b, 1997).

The left-hand panel of fig. 154 presents the basic  $\mu$ SR results in ZF. Above  $\sim 20 \text{ K}$  one observes exponential relaxation that is little affected by strong longitudinal fields. It must be of electronic origin, the nuclear contributions from  $^{77}\text{Se}$  and  $^{147,149}\text{Sm}$  being rather small. In consequence, moments on  $\text{Sm}^{3+}$  ions ( $\text{Sm}^{2+}$  is diamagnetic) with moderately fast dynamics must be the source. Possibly this reflects the charge hopping process. Below 10 K the signal is analyzed in terms of two components, one showing exponential relaxation with little change in rate, the other Gaussian relaxation whose rate rises rapidly with decreasing temperature. The volume portion (signal amplitude) of the latter increases

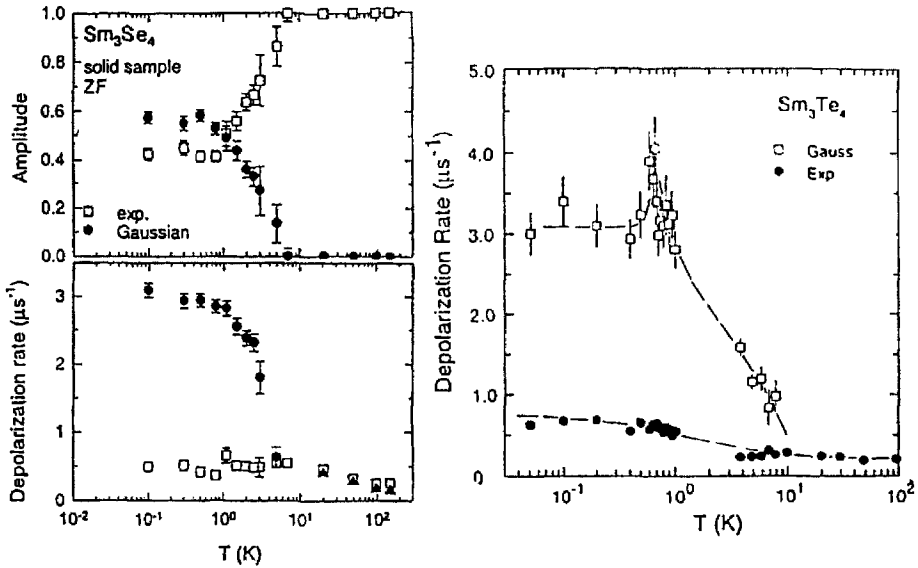


Fig. 154. Left: Temperature dependence of signal amplitudes and depolarization rates in  $\text{Sm}_3\text{Se}_4$ . The  $\mu\text{SR}$  spectrum is analyzed in terms of a two component signal below 10 K (see text for details). The data for  $T > 10$  K are from a powder sample (which at low temperatures gives analogous results to the solid sample shown). The data points ( $T > 20$  K) represented by solid triangles refer to a measurement in LF = 6 kG. After Takagi et al. (1997). Right: Temperature dependence of the depolarization rate for  $\text{Sm}_3\text{Te}_4$ . The same two-component analysis was used. The broken lines are guides to the eye only. From Amato et al. (1997b).

together with its rate but saturates between 50–60% for  $T \rightarrow 0$ . The exponentially relaxing portion is correspondingly reduced.

The Gaussian shape of the additional relaxation indicates the development of a strongly disordered magnetic state with moments around  $0.03\mu_B$ . The authors note that the onset of this relaxation corresponds to the appearance of a broad and sizeable anomaly in specific heat (Furuno et al. 1988) and to the development of the dependence of  $\chi$  on magnetic history.

Considering the possibility that dense spin-glass-like magnetism has formed, the linear dependence of  $C(T)$  and its rather large slope could be explained as being due to magnon-type excitations below the spin freezing transition as discussed in general by Maletta and Zinn (1989). This view then generates doubts as to the presence of the Kondo interaction and the formation of a HF state.

There are unexplained inconsistencies in the  $\mu\text{SR}$  data. Firstly, no effect is seen around 0.7 K where susceptibility sees a cusp. Secondly, the spin-glass fraction is temperature dependent and never reaches 100% of sample volume. Around 40% of the sample remains in the paramagnetic state it had occupied as a whole above 10 K. It is true that only 2/3 of the Sm ions (i.e., the  $\text{Sm}^{3+}$  ions) contribute to muon spin depolarization, but since charge order does not take place, they are randomly distributed throughout the sample. Hence, temperature-dependent, inhomogeneous magnetism must be present. The

authors do not comment on that feature. Two different samples were measured, one was a pressed powder, the other solid, polycrystalline material. No fundamental difference between the two was observed. The powder sample showed a somewhat more sluggish rise in (Gaussian) depolarization rate and a slightly smaller volume fraction of the spin-glass-like state. But no clear evidence for a connection to sample quality could be found.

For comparison a brief study of  $\text{Sm}_2\text{Se}_3$  was carried out. This compound is isostructural to  $\text{Sm}_3\text{Se}_4$  and also semiconducting, but all Sm ions are in the  $3+$  state (and  $1/9$  of the sites vacant). No spin-glass-like rise in relaxation rate was seen. The depolarization function retained exponential shape down to lowest temperature ( $\sim 0.1$  K) and also saturates (for  $T \rightarrow 0$ ) at a rather low rate ( $0.65 \mu\text{s}^{-1}$ ). LF data confirm that most of the depolarization is due to dynamic  $\text{Sm}^{3+}$  moments. Overall, the data for  $\text{Sm}_2\text{Se}_3$  correspond to the high-temperature behavior in  $\text{Sm}_3\text{Se}_4$ . It appears that valence fluctuations help induce the formation of a (strongly disordered) magnetic state.

*Summary:* The formation of a spin-glass-like state is observed for a part of the sample. The cause for this inhomogeneous magnetism remains unknown. The presence of spin glassy magnetism allows the interpretation of the low-temperature behavior of  $\text{Sm}_3\text{Se}_4$  in terms of magnon-type excitations in contrast to the HF scenario. A final resolution has not been achieved.

9.3.3.3.  $\text{Sm}_3\text{Te}_4$ . This compound (which has many properties in common with  $\text{Sm}_3\text{Se}_4$ ) has also been discussed as a low-charge-carrier-density HF system (Ahlheim et al. 1992). In ZF- $\mu$ SR (Amato et al. 1997b), again two-component spectra are observed below  $\sim 10$  K (a weak, nearly temperature-independent exponential plus a strong, temperature-dependent Gaussian relaxation). The relative amplitude of the Gaussian signal, which here as well is taken as an indicator for the formation of a highly disordered magnetic state, reaches only about 25% at very low temperatures. No explanation is suggested. The rate for  $T \rightarrow 0$  is about the same as in  $\text{Sm}_3\text{Se}_4$  and hence the size of the quasistatic moment must be similar ( $0.03$ – $0.04\mu_B$ ), but, in contrast to  $\text{Sm}_3\text{Se}_4$ , it shows a small but distinct peak at  $\sim 1$  K (see fig. 154, right). In this temperature regime, specific heat sees two sharp maxima, originally interpreted as magnetic in origin (Ahlheim et al. 1992). Yet, in  $\mu$ SR there is no additional rise in rate below the peak and it is unlikely that any well-developed magnetic structure is now present. It is thus concluded that the 1 K anomalies do not involve charge ordering.

*Summary:* The  $\mu$ SR properties of  $\text{Sm}_3\text{Te}_4$  are roughly, but not in detail, similar to those of  $\text{Sm}_3\text{Se}_4$ , meaning in particular that an inhomogeneous spin-glass-like state is formed. Thus, the notion of HF-like behavior is put into question on the same grounds as for  $\text{Sm}_3\text{Se}_4$ . The transition around 1 K does not involve charge ordering, but otherwise remains unexplained.

9.3.3.4.  $\text{Yb}_4\text{As}_3$ . This material is metallic, albeit with a low density of conduction electrons. This makes the system more likely a low-carrier-density HF compound, as is suggested by specific heat and resistivity data (Ochiai et al. 1993, Kadowaki and Woods

1986). It crystallizes in the inverse  $\text{Th}_3\text{P}_4$  structure (same space group,  $\bar{1}\bar{4}3d$ , as the normal  $\text{Th}_3\text{P}_4$  structure) with a 1:3 ratio of randomly distributed, dynamic  $\text{Yb}^{3+}$  and  $\text{Yb}^{2+}$  ions at high temperatures. Only the former ion carries a magnetic moment, while the latter has a closed 4f shell. At 290 K a first-order charge transition is found.

A single-component relaxation is observed in the preliminary ZF- $\mu\text{SR}$  data of Amato et al. (1997b). Spin precession is absent and the spectrum can be described at all temperatures by nuclear- (Gaussian Kubo–Toyabe) electronic (exponential) double relaxation. The electronic rate exhibits a sharp rise around 2 K from the high-temperature value of  $\sim 0.03 \mu\text{s}^{-1}$  to the  $T \rightarrow 0$  saturation value of  $0.14 \mu\text{s}^{-1}$ . This ties in with a distinct rise in  $\chi$  below 2 K, originally attributed to isolated  $\text{Yb}^{3+}$  impurity atoms (Ochiai et al. 1993), but later shown by Mössbauer spectroscopy to be intrinsic (Bonville et al. 1994) and connected to the presence of local magnetization which remains constant down to lowest temperatures. Thus, some magnetic state develops, presumably connected to small moments and substantial spin disorder. The  $\mu\text{SR}$  data indicate that magnetism in  $\text{Yb}_4\text{As}_3$  is weak compared to  $\text{Sm}_3\text{X}_4$  ( $X = \text{Se}, \text{Te}$ ), which excludes a discussion of the linear term in specific heat in terms of magnon-type excitations. An association with a heavy-quasiparticle state is more likely here. If so, with low charge carrier density, the mass enhancement would be enormous.

*Summary:*  $\mu\text{SR}$  shows the formation of a weak magnetic state below 2 K. The data are not adverse to the scenario of a low-charge-carrier-density HF system. In general, the issues concerning this class of HF materials are still largely unexplored and certainly more detailed  $\mu\text{SR}$  data are needed.

9.3.3.5. *YbBiPt and  $\text{Y}_{0.5}\text{Yb}_{0.5}\text{BiPt}$ .* This (complex) cubic (space group  $\bar{F}43m$ ) system has a remarkably high Sommerfeld constant of  $\sim 8 \text{ J}/(\text{mol K}^2)$  below 0.2 K. AC-susceptibility points towards some form of magnetic order around 0.4 K and specific heat peaks near that temperature as well (Fisk et al. 1991). An Yb moment of  $\sim 3\mu_B$  was deduced from susceptibility below 10 K.

$\mu\text{SR}$  investigations were first carried out on a powder sample (Amato et al. 1992c) and later on a specimen made from a mosaic of small crystals, together with a similar sample of  $\text{Y}_{0.5}\text{Yb}_{0.5}\text{BiPt}$  (Amato et al. 1993c). Small differences were seen between the two samples of pure YbBiPt. The  $\mu\text{SR}$  spectra revealed no spin precession over the temperature range of interest. The spectra could be fully described by a relaxation function containing a fast (f) and a slowly (s) decaying component:

$$G(t) = A_f G_f(t) + A_s \exp[-\lambda_s t] \quad \text{with} \quad \begin{cases} G_f(t) = \exp[-\lambda_f t] & \text{for } T > 0.4 \text{ K,} \\ G_f(t) = \exp[-\sigma_f^2 t^2] & \text{for } T \leq 0.4 \text{ K.} \end{cases}$$

As indicated, the fast component changes shape at the critical temperature of 0.4 K established by susceptibility. In addition the rate  $\sigma_f$  increases substantially when going to lower temperatures (see fig. 155) in keeping with the notion that a magnetic state is formed. The amplitudes  $A_f$  and  $A_s$  are temperature dependent as well. This is also shown

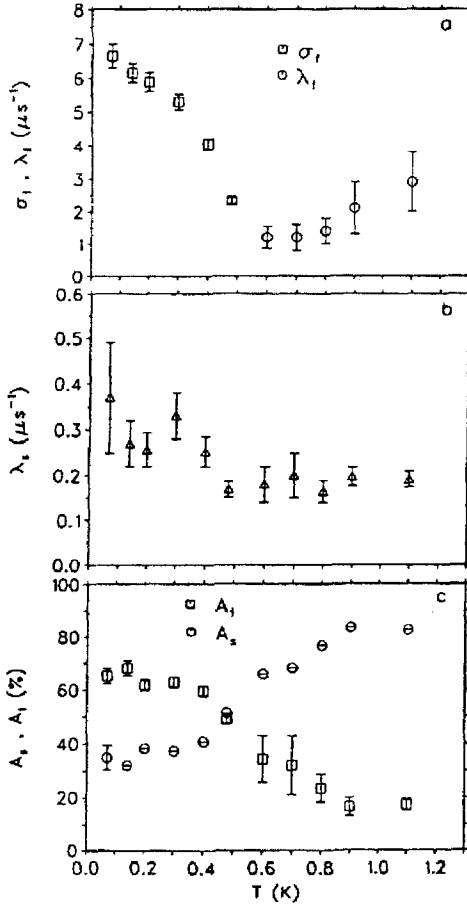


Fig. 155. Temperature dependences of the relaxation rates of (a) the "fast" and (b) the "slow" component and (c) of the corresponding signal amplitudes of the ZF- $\mu$ SR spectra of YbBiPt (for explanation see text). From Amato et al. (1993c).

in fig. 155. Above  $\sim 0.9$  K the slow component dominates, but below the fast component rises in proportion reaching roughly 2/3 amplitude.

Originally (Amato et al. 1993c), these results were interpreted as the development of dense spin-glass-like domains interspersed between domains that keep their paramagnetic state down to lowest temperatures. The suspected cause for this inhomogeneous behavior was marked magnetic frustration. In a subsequent publication (Heffner et al. 1994) the authors point out that the  $\mu$ SR spectrum could also be understood in terms of an ISDW spin structure throughout the sample. They base this interpretation on the example of  $\text{Cr}_{.85}\text{Mo}_{.15}$  (Telling et al. 1994), which shows comparable behavior. The rather sluggish rise of  $\sigma_f$  would be in keeping with such an interpretation. A final decision as to the precise nature of the magnetic state cannot be made. Multiple stopping sites as the cause for the two-component relaxation were ruled out by TF measurements (see Amato et al. 1997a). Using the model of randomly oriented moments a value of  $\mu_{\text{ord}} = 0.1\mu_B$  was



estimated, a substantial reduction from the moment derived from  $\chi$  at higher temperatures, showing the action of the Kondo effect. This size of moment is also in keeping with the results from neutron scattering, which puts a limit of  $\mu_{\text{ord}} \leq 0.25\mu_{\text{B}}$  (Robinson et al. 1994). Unfortunately, that small magnitude of Yb moment has thus far precluded any definite determination of spin structure.

Above  $T_{\text{M}} = 0.4$  K the (exponential) relaxation rates are still comparatively large. The authors point out that this means unusually long Yb-spin correlation times (on the order of  $10^3 (kT_{\text{M}}/\hbar)^{-1}$ ). The expression  $(kT_{\text{M}}/\hbar)^{-1}$  is a common estimate for the spin-correlation time in a conventional magnet.

The results for  $\text{Y}_{0.5}\text{Yb}_{0.5}\text{BiPt}$  are only marginally different from those of the pure sample. The transition temperature  $T_{\text{M}}$  is slightly lower and so is the saturation (Gaussian) relaxation rate. Both effects can well be explained by the dilution of magnetic ions and mean that  $\mu_{\text{ord}}$  has not been affected. More unusual is the fact that the relative amplitude  $A_{\text{f}}$  is essentially temperature independent below 1 K at 45%. This is not commented upon but clearly means that the magnetic state is not the same in detail.

*Summary:*  $\mu\text{SR}$  results agree with the notion that  $\text{YbBiPt}$  enters a magnetic state around 0.4 K. Whether one deals with an inhomogeneous spin-glass-like state or with a homogeneous ISDW spin structure is not clear at this stage. The ordered moment involved is comparatively small ( $0.1\mu_{\text{B}}$ ) making a definite decision on spin structure difficult. Dilution of the magnetic ion with 50% Y changes neither the formation of a magnetic state nor the ordered moment involved, but details of the spin order appear to be different.

9.3.3.6. *YbPdSb.* Transport, bulk magnetic and caloric measurements (Le Bras et al. 1995, Suzuki et al. 1995, Bonville et al. 1997) clearly show that cubic  $\text{YbPdSb}$  is a Kondo-lattice compound. CEF interaction puts a  $\Gamma_8$  quartet lowest on which the Kondo coupling acts with a strength of  $T^* \approx 7$  K.

It also exhibits at low temperatures a substantial Sommerfeld constant ( $\sim 3 \text{ J}/(\text{mol K}^2)$ ), which puts the material definitely into the HF regime. The magnetic behavior is less clear cut and strongly sample dependent. Some specimens show a first-order AFM transition around  $T_{\text{N}} = 1$  K. In others, long-range spin order is absent altogether, but strong magnetic correlations are present at low temperatures (determined, for example, by inelastic neutron scattering (Suzuki et al. 1995)). From Mössbauer spectroscopy on a sample that underwent magnetic order, the strength of the exchange coupling was deduced to be  $T_{\text{RKKY}} \approx 6$  K (Le Bras et al. 1995). Hence, one is faced with the situation  $T^* \approx T_{\text{RKKY}}$ . In the frame of the Kondo necklace model this puts the material just at the borderline between the magnetically ordered and the spin-liquid (i.e., Pauli paramagnetic) phases. Magnetic instability is no surprise in this context. In the spin-liquid state dynamically coupled AFM spin pairs are formed by the Kondo interaction, meaning that the pair-bond fluctuates at random through the lattice. Dynamic spin correlations are then definitely expected. The Mössbauer hyperfine field allows estimation of the  $\text{Yb}^{3+}$  moment involved:  $\sim 1.3\mu_{\text{B}}$ .

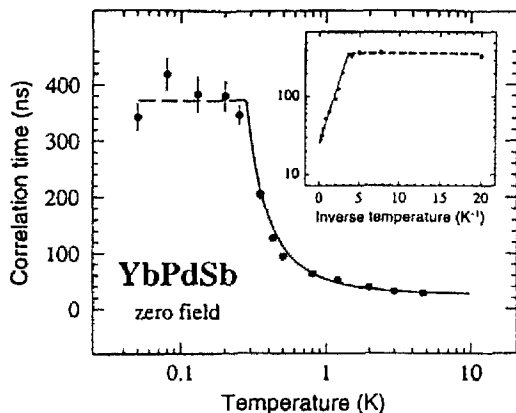


Fig. 156. Temperature variation of the fluctuation time  $\tau$  of the local field at the muon site in a YbPdSb sample that does not magnetically order. The inset shows the same data as a function of inverse temperature, demonstrating that at  $\sim 0.3$  K a crossover from an activation law (solid line) to independence from temperature (broken line) occurs. Further details in text. From Bonville (1997).

$\mu$ SR measurements were performed down to 50 mK on a sample not showing a transition into an AFM state. This allows study of the dynamics of magnetic correlations down to  $T \rightarrow 0$ , the declared aim of the study by Bonville et al. (1997). At high temperatures (100 K and above) the spectra are of the static Gaussian Kubo–Toyabe type. The field distribution width  $\Delta/\gamma_\mu = 0.19$  mT is typical for nuclear dipolar fields as the cause for depolarization. The effect of electronic Yb<sup>3+</sup> moments is negligible due to motional narrowing. The muon stopping site is not definitely known. A most likely candidate is the  $(\frac{1}{2}, \frac{1}{2}, \frac{1}{2})$  interstitial site. Dipolar field sums based on this site give  $\Delta/\gamma_\mu \approx 0.14$  mT for the nuclear moments involved, which compares favorably with the experimental result.

At low temperatures the depolarization rate rises sharply and could satisfactorily be reproduced by a dynamic Gaussian Kubo–Toyabe function down to lowest temperatures. At 50 mK values of  $\Delta/\gamma_\mu = 4.9$  mT and  $1/\tau \approx 3$  MHz were found. The magnitude of  $\Delta/\gamma_\mu$  definitely proves that now electronic moments are the depolarizing agent. The correlation time  $\tau$  increases with cooling below a few Kelvin and reaches saturation around 0.3 K. Figure 156 depicts the situation in detail. The initial rise of  $\tau$  can be well described by an activation law with  $E_A/kT = 0.75$  K. It is speculated that this barrier might represent the energy needed to break a pair of AFM-coupled Yb<sup>3+</sup> spins (Bonville 1997).

One expects a field distribution width of  $\Delta/\gamma_\mu \approx 100$  mT for a moment of  $1.3\mu_B$  on the Yb ions. This is more than an order of magnitude larger than the value observed. To resolve this discrepancy, the authors invoke the model first used by Uemura et al. (1994) which has previously been discussed in this review in the context of the low-temperature spectra of CePt<sub>2</sub>Sn<sub>2</sub>. It assumes that the local field acts on the muon only during a fraction  $f < 1$  of the time. If simple scaling holds (which is by no means clear) then the ratio of observed to expected field width results in  $f = 0.05$  and in an actual value of  $1/\tau = 60$  MHz in the low-temperature limit. This rate is interpreted as arising from local field fluctuations induced by the dynamic bonding of AFM spin pairs well inside the spin-liquid state. One might assume that this state is formed around 1 K where  $\tau$  starts to increase substantially. It is interesting to note that this is about the temperature where

other samples enter into the quasistatic ordered AFM spin state. As in CeNiSn one might suspect that the persistence of spin fluctuations for  $T \rightarrow 0$  which, on account of their independence from temperature are likely to be quantum fluctuations, are the underlying reason that AFM order does not set in.

*Summary:* YbPdSb is magnetically unstable. The  $\mu$ SR data on a sample that does not develop long-range AFM order show that the material enters a spin-liquid state instead. This state is characterized by dynamic short-range correlations whose fluctuation rate becomes temperature independent below 0.3 K at the comparatively low value of 60 MHz. Probably one deals with quantum fluctuations that are interpreted here as local moment fluctuations induced by the dynamics of fluctuating bonds of Kondo spin pairs.

9.3.3.7. *YbAuCu<sub>4</sub>*. In this cubic (fcc, space group  $F\bar{4}3m$ ) intermetallic, the  $\text{Yb}^{3+}$  sublattice orders magnetically near 0.6 K according to specific heat (Rossel et al. 1987) and around 1 K according to  $^{170}\text{Yb}$  Mössbauer spectroscopy (Bonville et al. 1992b). An AFM structure is commonly assumed since  $\Theta_p = -11$  K, but its exact nature is not known. The Curie moment for  $T > 100$  K is  $4.4\mu_B$ , close to the  $\text{Yb}^{3+}$  free ion value. The Mössbauer data give  $\mu_{\text{ord}} = 1.47\mu_B$  for  $T \rightarrow 0$ . The cubic CEF interaction splits the  $J=7/2$  multiplet into a  $\Gamma_7$  doublet as ground state, followed by a  $\Gamma_8$  quartet and a  $\Gamma_6$  doublet. Inelastic neutron scattering puts the  $\Gamma_8$  at 45 K and the  $\Gamma_6$  at 80 K above the  $\Gamma_7$ . The pure  $\Gamma_7$  moment is  $1.0\mu_B$ , and thus  $\mu_{\text{ord}}$  is reduced by Kondo interaction.

$\mu$ SR spectroscopy was performed on a polycrystalline ingot that had 10% metallic Cu as impurity phase (Bonville et al. 1996). The ZF spectra for  $T < 2$  K showed simple exponential decay ( $\exp[-\lambda_z t]$ ) of muon spin polarization. Spontaneous spin precession was not observed.  $\lambda_z$  rises sharply below  $\sim 0.7$  K and peaks at 0.4 K. Around this temperature the signal amplitude begins to drop down to roughly 1/3 of its high-temperature value. All these findings are in keeping with the notion of a magnetic transition into an ordered state around 0.5 K. The measurements were carried out at the ISIS pulsed muon facility and suffer from the usual restrictions of pulsed beam temporal resolution, which may well have prevented the observation of spontaneous spin precession. No specific information as to the nature of the AFM state can be drawn from the  $\mu$ SR data available. A simple AFM spin structure is possible. Supplementary measurements with LF = 20 mT resulted in no visible change of  $\lambda_z$ . Depolarizing action in this temperature range is clearly dominated by fluctuating  $\text{Yb}^{3+}$  moments, which also show the expected critical slowing down on approach to  $T_N$ . Because of the limitations in spectral resolution, the authors rather concentrate on the temperature regime above  $T^* \approx 20$  K where the Kondo lattice state is formed. There the ZF spectra are governed by electron-nuclear double relaxation. Of interest is the electronic part ( $\lambda_z$ ) which can be obtained separately in LF = 20 mT. The authors define a  $\mu$ SR dynamical width  $\Gamma_{\mu\text{SR}}$  by

$$\lambda_z = 2\Delta_e^2 \Gamma_{\mu\text{SR}}^{-1},$$

where  $\Delta_e$  is the muon-4f coupling matrix, which reduces to a scalar in cubic symmetry. It depends, of course, on the muon stopping site which is not known. Theoretically

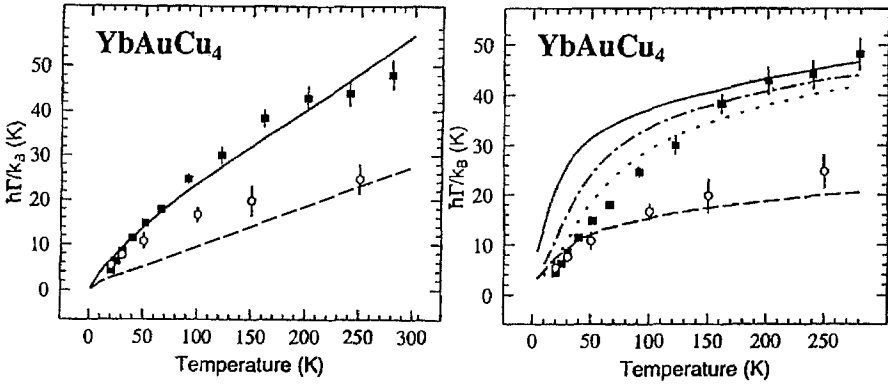


Fig. 157. Comparison of the temperature dependence of experimental values of  $\Gamma_{\mu\text{SR}}$  (solid symbols) and  $\Gamma_Q$  (open symbols) for  $\text{YbAuCu}_4$  with model calculations. Left: Predictions based on the Korringa interaction (k-f exchange) only with a coupling strength of  $|J_{\text{kf}}n(E_F)| = 0.37$  (solid and broken lines). Cubic CEF splitting is taken into account. Right: Predictions of the NCA formalism of Kondo interaction with a Kondo scale of 20 K and cubic symmetry for the Yb site (solid and broken lines). The dash-dotted and the dotted lines assume a trigonal distortion of the Yb site due to the presence of a stopped  $\mu^+$  with a  $B_2^0$  term of  $-1.75$  and  $-2.35$ , respectively. The muon-4f coupling constant  $\Delta_e$  was set to 208 MHz in all cases corresponding to the calculated value for the “4d” interstitial stopping site. After Bonville et al. (1996).

the “4d” site with coordinates  $(\frac{3}{4}, \frac{3}{4}, \frac{3}{4})$  is the most likely candidate. For this site one finds  $\Delta_e = 208$  MHz.  $\Gamma_{\mu\text{SR}}$  is equal to the neutron quasielastic linewidth  $\Gamma_Q$  in case of a Lorentzian shaped excitation spectrum (a common assumption) and in the absence of CEF splittings of the  $J$  multiplet. The CEF interaction affects  $\Gamma_{\mu\text{SR}}$ , which is to be modified using the appropriate Curie and Van Vleck susceptibilities in a summation over the CEF levels (Dalmas de Réotier et al. 1996).

$\Gamma_Q$  depends linearly on temperature if spin dynamics are solely determined by k-f exchange between the conduction and 4f electrons. This is the well-known Korringa relaxation.  $\Gamma_{\mu\text{SR}}$  will exhibit deviations from strict linearity if the CEF interaction is taken into account. The comparison between measured values of  $\Gamma_{\mu\text{SR}}$  and  $\Gamma_Q$  (from Severing et al. 1990) and the Korringa model is depicted in fig. 157 (left). The agreement for  $\Gamma_Q$  is poor, especially at low temperatures. For  $\Gamma_{\mu\text{SR}}$  deviations are also present but less severe. A second set of calculations included the Kondo interaction within the Non-Crossing-Approximation (NCA) developed by D.L. Cox et al. (1985). It leads, as mentioned already on another occasion, to a  $\sqrt{T}$  dependence. The comparison with this model is shown in fig. 157 (right) as the solid and broken lines.  $\Gamma_Q$  is well reproduced, but  $\Gamma_{\mu\text{SR}}$  deviates badly, except at rather high temperatures. The calculations used cubic symmetry for the  $\text{Yb}^{3+}$  site. A stopped  $\mu^+$  in the vicinity is known to cause lattice distortions. The NCA calculations were repeated for tetragonal site distortions of different strengths (dash-dotted and dotted lines in fig. 157, right). Now the agreement with the experimental values of  $\Gamma_{\mu\text{SR}}$  is much better, but still not perfect. In any case, this result demonstrates the importance of lattice distortions by the muon for parameters that depend crucially on local symmetry, such as the CEF splitting.

Whether the NCA model is a proper description of Kondo interaction in the present case could be questioned since Kondo temperature and CEF splittings are roughly equal. In addition, magnetic correlations have been completely neglected. It is true that the discussion is of a temperature range far above  $T_N$ , but on the other hand, it is known (see, for example sect. 5.3) that  $\mu$ SR senses such correlations far into the paramagnetic regime.

In conclusion, we mention that comparisons between  $\mu$ SR relaxation rates and neutron quasielastic linewidths have also been made (though less elaborate) for  $\text{CeRu}_2\text{Si}_2$  and  $\text{CePt}_2\text{Sn}_2$  as discussed earlier.

*Summary:* The available  $\mu$ SR data show the presence of a magnetic transition around 0.5 K, but give no additional insight into the nature of the magnetic state, which is not precisely known. A thorough comparison of  $\mu$ SR relaxation rates and neutron quasielastic widths with theoretical calculations including the Kondo coupling and CEF interaction were made. The  $\mu$ SR data needed the inclusion of local lattice distortion by the stopped muon. Residual deviations of experimental data point towards the need for extension of the model for the Kondo coupling.

9.3.3.8.  $\text{Yb}_2\text{Cu}_9$ . This compound has a complex cubic structure (AuB<sub>5</sub> type) and one of the largest Sommerfeld constants ( $\gamma = 0.6 \text{ J}/(\text{mol}(\text{Yb})\text{K}^2)$ ) found in HF compounds of Yb (Jaccard et al. 1980). It is suspected to be close to a magnetic instability. At ambient conditions it is nonmagnetic, but high-pressure resistivity data point towards a possible magnetic ground state (Spendeler et al. 1994). Superconductivity has not been found.

A preliminary report (Amato et al. 1998) presents ZF- and LF- $\mu$ SR data down to 0.1 K. The ZF spectra are characterized by nuclear–electronic double relaxation. The nuclear part can be suppressed in LF = 20 G. No magnetic transition was observed. Below  $\sim 10$  K, the electronic relaxation rate increases monotonically with decreasing temperature. Application of LF = 200 G also suppresses electronic relaxation, indicating rather slow dynamics of the spin system. From the field dependence of relaxation rate the spin fluctuation frequency was found to be  $\nu_{4f}(T \rightarrow 0) \approx 2.7 \text{ MHz}$ . It appears that this is another case where spin correlations develop at low temperatures, but persistent slow spin dynamics prevent the formation of an ordered magnetic state (see CeNiSn in sect. 9.2 for comparison).

*Summary:*  $\mu$ SR data indicate the formation of spin correlations at low temperatures which, however, remain dynamic on approach to  $T \rightarrow 0$ . A magnetically ordered state is thus not reached.

#### 9.3.4. Conclusions: heavy fermions

The main impact of  $\mu$ SR studies on HF materials is the realization that a pure Fermi-liquid ground state with only Pauli paramagnetism is the exception rather than the rule, even when superconductivity is present. Many systems form weak magnetic states at low temperatures, which in the majority of cases could only be detected by  $\mu$ SR. This weak magnetic state consists of quasistatic moments on the 4f or 5f ion having extremely low

magnitude ( $10^{-2}$ – $10^{-3}\mu_B$ ) and being randomly oriented (or at least exhibiting a highly disordered spin structure). It should be emphasized that the small moments are not a “muon induced effect”. In cases where  $\mu$ SR first detected a moderately low moment (some  $10^{-2}\mu_B$ ), neutron diffraction later confirmed these findings.

Another strength of  $\mu$ SR is that it can easily and reliably measure volume fractions when more than one (magnetic) state is present. This feature has been instrumental in demonstrating that both, homogeneous and inhomogeneous coexistence of superconductivity and magnetism can be present. The former requires the combined existence of a more itinerant and a more localized portion of the f electron structure. This feature appears to be more pronounced in the 5f systems. A firm theoretical basis is missing at this stage.

It is often found that the magnetic  $\mu$ SR signal is not compatible with the spin structure derived by neutron or photon scattering. In some cases improved neutron data or data analysis relieved the discrepancies. It must especially be kept in mind that  $\mu$ SR responds to very short magnetic correlation lengths which are not easy to detect by neutrons. Also, it appears that in a fair number of cases the local symmetry of spin arrangement differs from the long-range features. In other words, additional disorder not detected by the scattering data is present. On the whole the differences between neutron and  $\mu$ SR point towards more complex magnetic properties than otherwise anticipated. This holds even for compounds with strong local magnetism.

$\mu$ SR also demonstrates that cases exist where strong paramagnetic spin correlations are formed and they remain dynamic even in the limit  $T \rightarrow 0$ . This behavior in turn suppresses the development of long-range magnetic order. It may well have its origin in magnetic frustration.

Important contributions have also been made by  $\mu$ SR in elucidating the superconducting properties of HF materials. This aspect is not covered in this review. We just point out that the weak magnetic state may be a fundamental ingredient for unconventional superconductivity, one of the most exciting aspects of HF behavior.

## 9.4. *Non-Fermi-liquid behavior*

### 9.4.1. *General considerations*

Archetypal properties of the Fermi-liquid (FL) state in HF systems are a large Sommerfeld constant  $\gamma$  of low-temperature specific heat together with a correspondingly enhanced Pauli susceptibility (see fig. 103), both being only weakly dependent on temperature. Furthermore, the FL contribution to the electrical resistivity has the form  $\Delta\rho \propto T^2$  (see Grewe and Steglich 1991 for more details). In recent years, several examples of HF materials have been discovered that show rather dramatic deviations from those established FL properties. A first survey was given by Maple et al. (1994). For example, in some materials there is a logarithmic divergence of  $C/T = \gamma$  for  $T \rightarrow 0$  and a linear dependence of  $\Delta\rho$  with  $T$ . The microscopic origin of this NFL behavior is still not uniquely solved and in fact it is not obvious that in all cases the same mechanism is at work. On the whole, this special field of HF compounds is still in its infancy.

One possible scenario for NFL behavior has been put forward by D.L. Cox (1987, 1993). It evokes the *single-ion* two-channel Kondo effect which, under certain conditions of local symmetry (a twofold degeneracy apart from Kramers degeneracy), applies to  $Ce^{3+}$  materials. In U compounds the quadrupolar Kondo effect may be present due to the large ionic quadrupole moment of the  $U^{4+}$  ion, which is the generally present ionic state. A recent summary on the multichannel Kondo mechanism and its connection to NFL behavior has been given by D.L. Cox and Jarrell (1996). This model describes in effect an anomalous screening of magnetic moments. Andraka and Tsvetik (1991) as well as von Löhneysen et al. (1994) and von Löhneysen (1996a,b), relate NFL behavior to a *collective* property of the magnetic lattice: the near degeneracy of a magnetic and nonmagnetic ground state. This occurs when the Kondo interaction is just slightly larger than the RKKY interaction, i.e., somewhat below the critical hybridization strength  $g_c$ , (see fig. 105). In this situation, there will be a  $T = 0$  critical point that separates the magnetically ordered state from one with no long-range order. Quantum fluctuations around this critical point are responsible for creating NFL properties. Bhatt and Fisher (1994) as well as Dobrosavljević et al. (1992) pointed out that disorder in the lattice of magnetic ions may cause a distribution  $P(T_K)$  of Kondo temperatures, which in turn may produce NFL properties. This scenario is known as “Kondo disorder” and its implication on transport and magnetic properties of a HF material has recently been discussed in detail by Miranda et al. (1996). Such a disorder is, however, not present in all cases.

NFL behavior appears in transport and bulk magnetic parameters and is not directly revealed to  $\mu$ SR, but the underlying magnetic instability makes NFL materials an interesting class for  $\mu$ SR studies. These instabilities can be initiated by either driving an originally nonmagnetic HF compound into the weak magnetic regime by alloying, or vice versa an originally magnetic HF material into the nonmagnetic regime. An alternate to alloying is the application of hydrostatic pressure. Thus far, few systems have been studied by  $\mu$ SR and the results must largely be considered preliminary. Further work is still in progress.

#### 9.4.2. *Non-Fermi-liquid materials*

The compounds to be dealt with in this section are:

- |                      |                              |                  |
|----------------------|------------------------------|------------------|
| (1) $CeCu_{6-x}Au_x$ | (4) $Ce(Cu_{1-x}Ni_x)_2Ge_2$ | (7) $CePt_2Si_2$ |
| (2) $UCu_{5-x}Pd_x$  | (5) $CeCo(Ge_{3-x}Si_x)$     | (8) $U_2Pt_2In$  |
| (3) $Y_{1-x}U_xPd_3$ | (6) $Ce_7Ni_3$               |                  |

The first 5 materials are pseudo-binary or ternary compounds based on established HF or Kondo-lattice materials. The last 3 are independent intermetallics on their own for which NFL behavior has been claimed.

9.4.2.1. *CeCu<sub>6-x</sub>Au<sub>x</sub>*. The parent compound  $CeCu_6$  is a HF material with FL properties and a nonmagnetic, non-superconducting ground state (see previous section). It is close to a magnetic instability and replacing Cu in part by a related ion with larger radius (e.g., Au, Ag) drives  $CeCu_6$  towards magnetism *via* lattice expansion (von Löhneysen 1995).

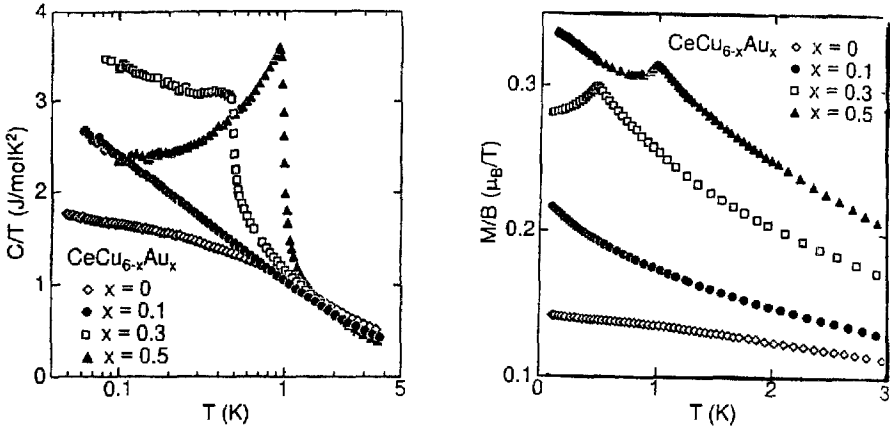


Fig. 158. The onset of magnetism in  $\text{CeCu}_{6-x}\text{Au}_x$ : Temperature dependence of specific heat  $C/T$  (left), and of bulk susceptibility  $M/B$  (right) for various Au concentrations. After von Löhneysen (1996a).

In fig. 158, the temperature dependences of  $C/T$  ( $=\gamma$ ) and the low field (0.1 T) magnetization over field ( $M/B = \chi$ ) are shown for  $0 \leq x \leq 0.5$ . Figure 159 (left) presents the corresponding variation of  $T_N$ . The critical concentration for the onset of magnetism is  $x_c \approx 0.1$ . As has been discussed for  $\text{CeCu}_x\text{Ni}_{1-x}\text{Sn}$ , lattice expansion by alloying reduces the 4f–ce hybridization and with it the hybridization strength  $g$  (see fig. 105), thereby stabilizing magnetic moments, which then interact *via* the RKKY exchange. In fig. 158, the NFL behavior at the critical concentration (a logarithmic dependence of  $\gamma$ ) is clearly visible for  $C/T$ , as is the presence of magnetism for  $x \geq 0.3$ . Neutron scattering (Schröder et al. 1994a, Stockert et al. 1997) finds incommensurate sinusoidal modulation of the Ce moments in  $\text{CeCu}_{6-x}\text{Cu}_x$ . The wave vector changes from  $\mathbf{q} = (100)$  for  $x = 0$  and 0.1, where only short-range correlations exist, through  $(0.79\ 0\ 0)$  for  $x = 0.2$ , to  $(0.5\ 0\ 0)$  for  $x = 0.5$ , where long-range order has set in. The ordered moment rises from  $0.02\mu_B$  at  $x = 0.2$  to  $0.5\text{--}1\mu_B$  at  $x = 0.5$ . There is strong similarity in behavior with  $\text{CeNi}_{1-x}\text{Cu}_x\text{Sn}$  around its critical concentration that is apparent from a comparison of fig. 158 (left) and fig. 113 (right).

The fundamental importance of lattice expansion as the initiator of magnetism in  $\text{CeCu}_{6-x}\text{Au}_x$  has been proven by Bogenberger and von Löhneysen (1995) *via* pressure measurements. They applied hydrostatic pressure to  $\text{CeCu}_{5.7}\text{Au}_{0.3}$ , thereby reducing its magnetic transition temperature. The data give  $T_M \rightarrow 0$  for  $p \approx 8$  kbar. Around this critical pressure NFL behavior is observed (see fig. 159, right).

Amato et al. (1995b) studied  $\text{CeCu}_5\text{Au}$  ( $x = 1$ ) and  $\text{CeCu}_{5.9}\text{Au}_{0.1}$  ( $x = 0.1$ , the critical concentration) by  $\mu$ SR using single-crystalline specimens. In the former material, the ZF spectra clearly establish the AFM transition at  $T_N \approx 2.3$  K by the appearance of spontaneous muon spin precession (see fig. 160). The depolarization of the spontaneous precession signal can well be described by a  $J_0$  Bessel function. As discussed in sect. 3.7, (see eq. 53) this spectral shape is typical for incommensurate magnetic order. The ordered



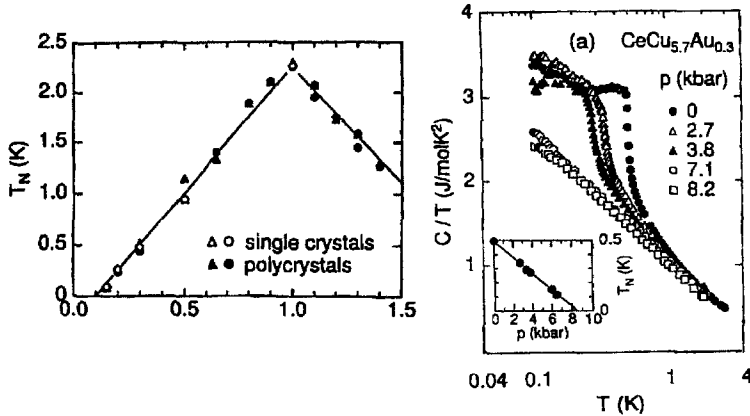


Fig. 159. Left: Néel temperature *vs.* Au concentration  $x$  for  $\text{CeCu}_{6-x}\text{Au}_x$  as derived from specific heat (triangles) and susceptibility (circles). Right: Temperature dependence of specific heat  $C/T$  of  $\text{CeCu}_{5.7}\text{Au}_{0.3}$  at different applied pressures. The inset shows the decrease of Néel temperature with pressure. From von Löhneysen (1996a) and von Löhneysen et al. (1997).

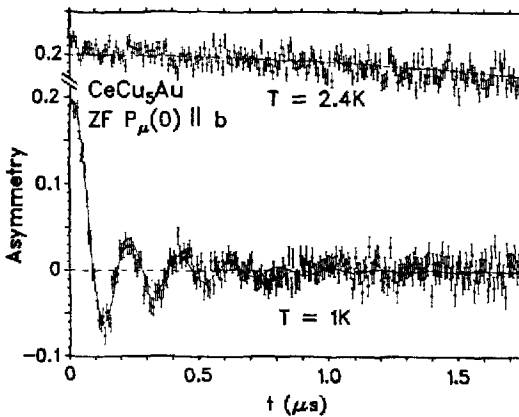


Fig. 160. ZF spectra of  $\text{CeCu}_5\text{Au}$  above (top) and below (bottom) the Néel temperature (2.3 K). The initial muon polarization is parallel to the  $b$  axis (Amato et al. 1995b).

moment deduced is  $\mu_{\text{ord}} \approx 0.8\mu_{\text{B}}/\text{Ce}$ . The  $\mu\text{SR}$  and neutron data are thus in full agreement. FL behavior is more or less re-established in the limit  $x \rightarrow 1$  and hence  $\text{CeCu}_5\text{Au}$  may be considered a separate HF compound with a magnetic ground state exhibiting a sizeable magnetic moment.

For  $x = 0.1$ , no difference in the ZF spectra could be detected when compared to the data of pure  $\text{CeCu}_6$  down to 20 mK. As shown in fig. 161, the magnitude of the static width  $\Delta$  is indistinguishable for the two compounds, a finding that excludes the occurrence of a magnetic transition or even markedly enhanced correlations between  $\mu_{\text{Ce}}$ . This result is fully supported by the neutron data of Stockert et al. (1997). For  $x \leq x_c \approx 0.1$ , one would have expected that even the purely nuclear damping changes when Cu is replaced by Au which has a considerably smaller nuclear moment. It is known, however, that for

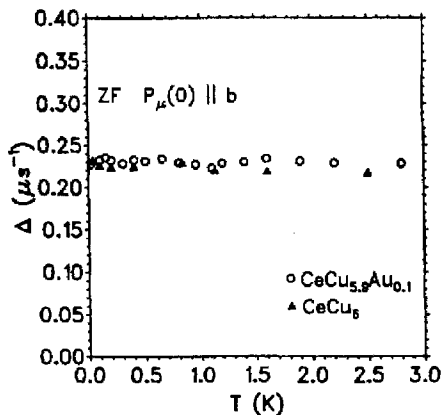


Fig. 161. Temperature dependence of the static width  $\Delta$  (from a fit of a Kubo–Toyabe function to the ZF data) for  $\text{CeCu}_6$  and  $\text{CeCu}_{5.9}\text{Au}_{0.1}$ . The experimental error is less than the size of the data points (Amato et al. 1995b).

small concentration the Au ions only occupy specific Cu sites (Ruck et al. 1993) that are not in the nearest surroundings of the stopped  $\mu^+$ . Using the established  $\mu^+$  stopping site (Amato et al. 1997a), a dipolar sum calculation gives a decrease of  $\Delta$  of 0.4% for  $\text{CeCu}_{5.9}\text{Au}_{0.1}$  including the effect of lattice expansion. This is beyond experimental resolution.

The compound  $\text{CeCu}_{5.5}\text{Au}_{0.5}$  (i.e.,  $x = 0.5$ ) was studied with ZF- $\mu\text{SR}$  by Chattopadhyay et al. (1995) down to 50 mK. The sample consisted of a mosaic of arbitrarily oriented single-crystalline platelets. A magnetic transition was observed at  $T_N = 0.95$  K. Below this temperature the  $\mu\text{SR}$  signal consisted of a very rapidly and a slowly depolarizing part. The former is interpreted as a heavily damped spontaneous spin-precession signal with a depolarization rate so large that not even the first full oscillatory cycle is visible, but the fits give a consistent variation in frequency with temperature (see fig. 162). For  $T \rightarrow 0$  the values are  $\nu_\mu \approx 1.5$  MHz and  $\lambda \approx 5 \mu\text{s}^{-1}$ . The measurements were performed at the ISIS pulsed muon facility and hence suffer from limitations in temporal resolution. It is quite possible that the true signal is also a  $J_0$  Bessel function damped spin precession as seen in  $\text{CeCu}_5\text{Au}$ . In any case the high depolarization rate points towards a wide distribution of internal field as expected for the incommensurate spin structure derived from neutron scattering. The  $\mu\text{SR}$  and neutron data can be considered to be in agreement. At temperatures somewhat above  $T_N$  only the weakly damped signal reflecting the effect of nuclear dipoles is seen. This corresponds to pure  $\text{CeCu}_6$  and shows that the Ce moments fluctuate with a very high rate. As stated, these fluctuations should be different in the two materials because the neutron data indicate that the (wave vector of the) ordering is different. Unfortunately,  $\mu\text{SR}$  cannot give any information because of full motional narrowing.

The two-channel Kondo effect can be ruled out as the source for NFL behavior for  $\text{CeCu}_{6-x}\text{Au}_x$  because of symmetry arguments (D.L. Cox 1993). A distribution of  $T_K$  is a possibility in systems with structural disorder, even when, as in the present case, the 4f ion lattice remains undisturbed. An indicator of Kondo disorder is a local variation of susceptibility  $\chi$  (Miranda et al. 1996). A test for its occurrence is a measurement of

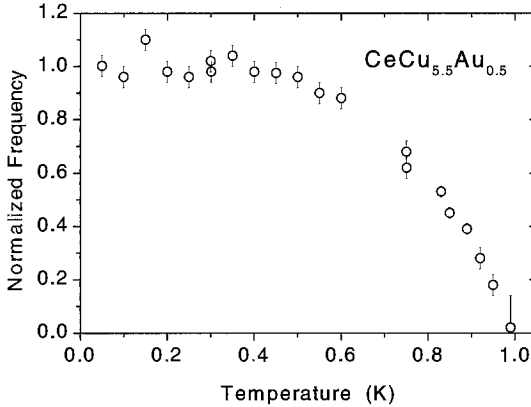


Fig. 162. Normalized spontaneous spin precession frequency as function of temperature for  $\text{CeCu}_{5.5}\text{Au}_{0.5}$ . From Chattopadhyay et al. (1995).

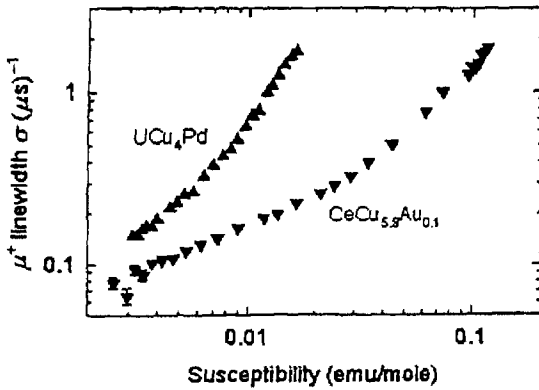


Fig. 163. Transverse field damping constant ( $\mu^+$  linewidth)  $\sigma$  vs. bulk molar susceptibility in  $\text{CeCu}_{6-x}\text{Au}_x$  ( $x = 0.1$ ) and  $\text{UCu}_{5-x}\text{Pd}_x$  (with  $x = 1$ ). Temperature is an implicit parameter and decreases towards the right. After Amato et al. (1995a).

the static TF- $\mu$ SR relaxation rate  $\sigma$  ( $\mu^+$  linewidth) as function of temperature, which is then plotted vs. the bulk susceptibility. In the case of uniform  $\chi$ , one expects  $\sigma$  to be proportional to  $\chi$ . The result of such a study is presented in fig. 163 for  $\text{CeCu}_{5.9}\text{Au}_{0.1}$  together with corresponding data for  $\text{UCu}_4\text{Pd}$ . As will be discussed in the paragraph on  $\text{UCu}_{5-x}\text{Pd}_x$ , the data for  $\text{UCu}_4\text{Pd}$  show that the disordered susceptibility is characterized by short-range correlations. It supports the notion that Kondo disorder is instrumental in the NFL behavior of that system. In  $\text{CeCu}_{5.9}\text{Au}_{0.1}$  the non-proportionality between  $\sigma$  and  $\chi$ , the absolute value of  $\sigma$ , and its temperature dependence are much weaker than for  $\text{UCu}_4\text{Pd}$ . Substantial Kondo disorder can only be inferred if the spatial correlation is of long range. Such a feature is, however, not indicated by any other property of the alloy. Hence, a distribution of Kondo temperatures is not likely to be the mechanism of NFL behavior in the  $\text{CeCu}_{6-x}\text{Au}_x$  system (Bernal et al. 1996), which leaves the  $T \rightarrow 0$  quantum phase transition as the most probable cause (von Löhneysen 1996a,b, 1997).

9.4.2.2.  $\text{UCu}_{5-x}\text{Pd}_x$ . The path to NFL behavior in  $\text{UCu}_{5-x}\text{Pd}_x$  is opposite that of  $\text{CeCu}_{6-x}\text{Au}_x$ . Here, the parent compound  $\text{UCu}_5$  is a HF system with an established, strong

AFM ground state (but with some unusual and ill-understood features). We have already discussed its properties and  $\mu$ SR data in the previous section. Replacing Cu in part by Pd quickly destroys the AFM ground state (which is stable only for  $x < 0.75$ ) together with promoting NFL behavior (Andraka and Stewart 1993). Bernal et al. (1995) argued in connection with NMR results that the temperature dependence of the specific heat and susceptibility in  $UCu_{5-x}Pd_x$  can be explained consistently by “Kondo disorder”, i.e., a sizeable distribution  $P(T_K)$  of Kondo temperatures (Miranda et al. 1996).  $\mu$ SR studies have been reported for  $x = 1.0$  and  $1.5$  (Bernal et al. 1995, 1996, MacLaughlin et al. 1997, 1998). In ZF a static Gaussian Kubo–Toyabe relaxation is observed for both samples. They show practically the same static width of  $\Delta = 0.23 \pm 0.03 \mu s^{-1}$  over the temperature range from  $\sim 50$  K to  $\sim 3$  K. No signs of spontaneous spin precession could be found. The width  $\Delta$  can fully be explained by the field of nuclear moments on Cu. The data put an upper bound of  $\sim 0.01 \mu_B$  on any *static* moment of U. Since the other magnetic data show the presence of sizeable moments on U, the  $\mu$ SR result means that these moments must fluctuate rapidly (rate  $> 10^{12} s^{-1}$ ) to lose all depolarizing influence.

Transverse field  $\mu$ SR was performed on two samples of  $UCu_4Pd$  in  $B_T = 5$  kG between 4 and 300 K. They gave identical results. The data from one of the samples has already been presented as a plot of transverse-field Gaussian damping rate  $\sigma$  ( $\mu^+$  linewidth) vs. bulk susceptibility  $\chi$  in fig. 163. The  $\mu^+$  linewidth reflects the static distribution of local fields. As discussed for the case of  $CeCu_{5.9}Au_{0.1}$  one expects  $\sigma$  to be proportional to  $\chi$  if  $\chi$  were uniform throughout the material. A detailed analysis performed both for the limit of long-range correlations and short-range correlations confirms that a distribution of  $\chi$  dominates the  $\mu^+$  linewidth in  $UCu_4Pd$ . The extremely low limit on the static U moment from ZF- $\mu$ SR further proves that the observed NMR linewidth of Cu must arise from a distribution of Knight shifts. Combination of NMR and  $\mu$ SR linewidth data were in satisfactory agreement in the short-range correlation limit, but not for the long-range limit. In conclusion, the results for  $UCu_4Pd$  indicate considerable susceptibility inhomogeneity characterized by a correlation length of the order of the lattice constant. Two possible scenarios are suggested by MacLaughlin et al. (1998). Either crystalline disorder (e.g., site exchange between Cu and Pd) or a periodical modulation of local U moment susceptibility. The latter feature has never been observed in the absence of spin-modulated long-range magnetic order. This is excluded by the ZF- $\mu$ SR data, but the authors point out that no argument exists against *local susceptibility modulation in the absence of long-range magnetic order* in principle. Crystalline disorder faces the difficulty that recent neutron data (Chau et al. 1998, taken on one of the samples also used for  $\mu$ SR) have been interpreted as consistent with crystalline order. MacLaughlin et al. (1998) lean toward an interpretation in terms of *residual* crystalline disorder (i.e., disorder below the detection limit of the neutron scattering result). The system is then characterized as a nominally ordered compound with disorder-driven NFL behavior.  $\mu$ SR spectroscopy is highly sensitive to the resulting small local magnetic disorder.

A recent publication (MacLaughlin et al. 2000a) stresses that the inhomogeneity of the U-ion susceptibility in  $UCu_4Pd$  as derived from TF- $\mu$ SR data is in good agreement with disorder-driven NFL mechanisms. The inhomogeneity is remarkably independent of the

exact amount of structural disorder. LF measurements lead to values of  $1/T_1$  an order of magnitude faster than those derived from the single-ion Kondo-disorder model and thus suggest a cooperative NFL phenomenon, which can be treated in terms of a Griffiths phase model of correlated spin clusters (Castro Neto et al. 1998). It is further found that no more than a few percent of uranium spins can be in a spin frozen state above 0.1 K in  $\text{UCu}_4\text{Pd}$ .

The situation concerning the local susceptibility is not fundamentally different in  $\text{UCu}_{3.5}\text{Pd}_{1.5}$ . The agreement with NMR in the short-range correlation limit is not as good as for  $\text{UCu}_4\text{Pd}$ , but still much better than for long-range correlations. In this material considerable crystalline disorder should be present and the result is more straightforward.

In a moderately short review paper, Bernal (2000) briefly discusses TF- $\mu\text{SR}$  combination with NMR as a probe of NFL behavior in  $\text{UCu}_4\text{Pd}$ . This covers the same ground, but in less depth, as MacLaughlin et al.'s (1996) review. Much more detail on the  $\mu\text{SR}$  is found in MacLaughlin et al. (2000b).

In summary, the  $\mu\text{SR}$  results together with the NMR data imply that a broad distribution of Kondo temperatures is present in  $\text{UCu}_{5-x}\text{Pd}_x$  supporting a disorder-driven NFL state. This need not be connected to marked crystalline disorder. A cooperative rather than a single-ion mechanism appears to be present. Only a small portion of moments is spin frozen in  $\text{UCu}_4\text{Pd}$ , if at all.

9.4.2.3.  $Y_{1-x}U_x\text{Pd}_3$ . The compound  $Y_{0.8}U_{0.2}\text{Pd}_3$  within this series was the first material on which the typical NFL properties were established (Seaman et al. 1991, 1992, Andraka and Tsvetik 1991). The alloy system  $Y_{1-x}U_x\text{Pd}_3$  differs from the ones discussed before since the f element lattice is now disordered. The two-channel quadrupolar Kondo effect has been promoted as the source of its NFL behavior (Seaman et al. 1991, Maple et al. 1995), because of the large ionic quadrupole moment of U. On the other hand, the  $\mu\text{SR}$  data (W.D. Wu et al. 1994a) prove in particular that magnetic instability is a major ingredient in this series as well and may be instrumental in producing NFL properties. In particular, Andraka and Tsvetik (1991) argue that the behavior of the system is inconsistent with any single-impurity interpretation and that the system has a quantum phase transition at  $T = 0$ . A contrasting view is put forward by Maple et al. (1996), who favor single-ion effects. The experimental problem with this alloy series is the possibility of macroscopic concentration fluctuations. Long-range magnetic order for  $x = 0.45$  is claimed from neutron data by Dai et al. (1995). Bull et al. (1998) give an overview of the neutron work on this system. Their interpretation is devoid of any discussion on the influence of disorder but they provide evidence for collective NFL behavior.

ZF- and LF- $\mu\text{SR}$  studies by W.D. Wu et al. (1994a) cover polycrystalline materials with  $x = 0.1, 0.2, 0.4$  and  $\text{UPd}_4$ . The latter might be considered the case of  $x = 0.75$ , if one assumes that  $Y_{0.25}$  is replaced by a vacancy concentration of 0.25, which is reasonable since the cubic  $\text{Pm}\bar{3}\text{m}$  ( $\text{Cu}_3\text{Au}$ ) structure is maintained. The compound  $\text{UPd}_3$  ( $x = 1$ ) has the hexagonal ( $\text{P6}_3/\text{mmc}$ ) structure and is a localized f-moment magnet (see sect. 5.4.2).

For  $x = 0.75$  and 0.4, spin glass (SG) type magnetism was found. The  $\mu\text{SR}$  relaxation function at low temperatures is of the Kubo–Toyabe type with the typical recovery to  $a_0/3$

Table 14  
μSR results for  $Y_{1-x}U_xPd_3$  compounds (W.D. Wu et al. 1994a)

Compound	HWHM ( $a_s$ ) ( $\mu s^{-1}$ )	$T_g$ (K)	$\alpha$	Spin glass fraction (%)
UPd <sub>4</sub>	41	12.5±1	1.6	~90
Y <sub>0.6</sub> U <sub>0.4</sub> Pd <sub>3</sub>	22	11.0±0.5	1.6	~90
Y <sub>0.8</sub> U <sub>0.2</sub> Pd <sub>3</sub>	0.5	1.0±0.5	1	39±5
Y <sub>0.9</sub> U <sub>0.1</sub> Pd <sub>3</sub>	~0.1	0	~1	<10

at late times. Decoupling can be achieved in LF. Nuclear moments cannot account for the observed strong depolarization rate and the correspondingly large decoupling fields. The μSR spectra thus prove the existence of a frozen electronic spin system. A concentrated spin glass leads for  $T \ll T_g$  to a static *Gaussian* Kubo–Toyabe function while a dilute spin glass is characterized by a *Lorentzian* Kubo–Toyabe relaxation (see sect. 8). The system  $Y_{1-x}U_xPd_3$  lies between these limiting situations and W.D. Wu et al. (1994a) have used a phenomenological intermediate relaxation function of the form

$$G_z(a_s, \alpha, \lambda, p, t) = \left[ \frac{1}{3} + \frac{2}{3}(1 - (a_s t)^\alpha) \exp(-(a_s t)^\alpha / \alpha) \right] \exp[-(\lambda t)^p], \tag{81}$$

where  $a_s$  is the HWHM of the distribution of the static random field and  $\lambda$  is the dynamic relaxation rate if the full static limit is not reached. A spin glass with Gaussian field distribution corresponds to  $\alpha = 2$  and  $p = 1$ , with Lorentzian distribution to  $\alpha = 1$  and  $p = 1/2$ . W.D. Wu et al. (1994a) claim that eq. (81) can be derived for a mixed Gaussian/Lorentzian field distribution on a microscopic basis, but their proof to our knowledge has not been published. Crook and Cywinski (1997) have provided numerical simulations supporting the claim. The values of  $a_s$  and  $T_g$  derived from those fits are summarized in table 14.

Also listed in the table is the spin glass fraction. In UPd<sub>4</sub> a drop in  $a_0$  was seen and interpreted in accordance with magnetization data as arising from the development of long-range magnetic order in roughly 10% of sample volume. The spin glass signal (eq. 81) in Y<sub>0.8</sub>U<sub>0.2</sub>Pd<sub>3</sub> well below  $T_g$  has only ~40% of the signal amplitude seen at  $T \gg T_g$ . In this alloy a sizeable volume fraction remains in the paramagnetic state without spin freezing. This effect is even more pronounced in Y<sub>0.9</sub>U<sub>0.1</sub>Pd<sub>3</sub>, where the spin glass signal is hardly discernable at all, even at temperatures as low as 0.02 K. Also, the width of field distribution ( $a_s$ ) drops rapidly for  $x = 0.2$  and 0.1. For these concentrations NFL behavior was established.

In summary, the tendency towards magnetic ordering diminishes quickly for a decreasing uranium concentration, simultaneously promoting NFL properties. W.D. Wu et al. (1994a) discuss their results on the weakening of magnetic properties *via* partial spin glass order in terms of a competition between exchange coupling and CEF splitting  $\Delta_{CEF}$ . A well-developed CEF will produce a nonmagnetic ground state ( $\Gamma_3$ ) followed by a magnetic excited state. If  $\Delta_{CEF}$  is small, the two states will mix and an induced-moment

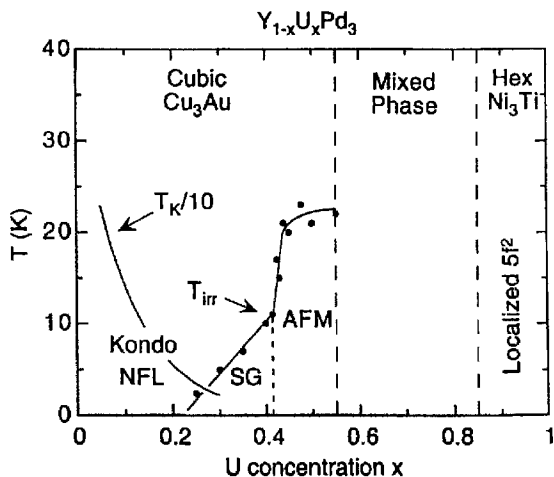


Fig. 164. Magnetic phase diagram of  $Y_{1-x}U_xPd_3$  system. From Maple et al. (1995).

spin glass of the type seen in PrP results (see discussion in sect. 9.2 on this subject). The theory of Sherrington (1979) holds quantitatively for  $UPd_4$ .

Maple et al. (1995) summarized the information available for  $Y_{1-x}U_xPd_3$  in the magnetic phase diagram shown in fig. 164.

9.4.2.4.  $Ce(Cu_{1-x}Ni_x)_2Ge_2$ .  $CeCu_2Ge_2$  shows incommensurate AFM order below  $T_N \approx 4.2$  K, while  $CeNi_2Ge_2$ , which has a smaller unit cell volume, is nonmagnetic with typical Fermi liquid properties. The considered mechanism for the suppression of magnetism is the increased hybridization between 5f and conduction electrons due to volume reduction. The pseudo-ternary system  $Ce(Cu_{1-x}Ni_x)_2Ge_2$  offers the possibility to trace the crossover from local AFM via HF band magnetism to nonmagnetic behavior. NFL behavior has been reported for higher Ni concentrations (i.e., in the concentration range where magnetism vanishes). Details of the magnetic phase diagram derived from bulk data can be found in Steglich et al. (1996).  $\mu$ SR data on the “master HF compound”  $CeCu_2Ge_2$  whose Néel temperature drops sharply with pressure have briefly been reviewed in sect. 9.3.1.

Preliminary  $\mu$ SR data on  $Ce(Cu_{1-x}Ni_x)_2Ge_2$  are contained in two recent conference report (Klauff et al. 1999e, Krishnamurthy et al. 1999b). The former authors studied single-crystalline samples with  $x = 0.1, 0.2, 0.5, 0.8, 0.9$ . For the low Ni concentrations ( $x = 0.1, 0.2$ ) a reduction in  $T_N$  was observed (3.1 K and 1.5 K, respectively). The  $x = 0.5$  sample showed relaxation behavior below 3.1 K, which points towards a spin-glass-like state. The highly doped compounds ( $x = 0.8$  and  $0.9$ ) showed no sign of magnetic order down to 0.02 K. Krishnamurthy et al. (1999b) measured samples with  $x = 0.5, 0.7, 0.8$ . Their results are fundamentally similar to those of Klauff et al. (1999e), except that somewhat different magnetic transition temperatures are given. For  $x = 0.5$  no spontaneous spin precession is observed for  $T < T_N$ , which corresponds to the failure of neutron diffraction to observe magnetic reflections and indicates a spin structure

generating a broad distribution in internal field. Decoupling data lead to a static field at the muon site of the order of 0.05 T (at 2 K). Weak magnetic order was still seen for  $x = 0.7$  ( $T_N \approx 2.2$  K). The sample with  $x = 0.8$  showed only temperature-independent weak relaxation ( $\lambda \approx 0.05 \mu\text{s}^{-1}$ ) of nuclear origin. The μSR data of both studies exclude any form of magnetism (strong or weak, LRO or SRO) for  $x \geq 0.8$ . The generation of NFL behavior in this concentration range due to the presence of a quantum critical point is a realistic possibility.

9.4.2.5. *CeCoGe<sub>3-x</sub>Si<sub>x</sub>*. CeCoGe<sub>3</sub> crystallizes in the tetragonal BaNiSn<sub>3</sub> structure where two Ce sites can be distinguished. It is an AFM with  $T_N = 21$  K. Ordered magnetism can be suppressed by replacing Ge with Si (see Millis 1993 and Eom et al. 1998 for details). Around the critical Si concentration for the disappearance of magnetism ( $x_c \approx 1$ ) one also observes NFL behavior. Kondo disorder is considered the main cause for the NFL features, but the weakening of RKKY interaction is thought to be important as well.

μSR spectroscopy was performed on powder samples of CeCoGe<sub>3-x</sub>Si<sub>x</sub> for  $x = 1.1$ , 1.2 and 1.5 (Krishnamurthy et al. 1999a, 2000a), i.e., near the critical concentration. Relaxation spectra taken in ZF for all compounds in the temperature range between 1 K and 0.034 K were fitted to a two-term relaxation function. Each term contains a static Kubo–Toyabe function of nuclear origin (<sup>59</sup>Co) double relaxing with an exponential relaxation of electronic origin (Ce ions). The parameters of the spectrum are the amplitudes  $A_1$  and  $A_2$ , the field widths  $\Delta_1$  and  $\Delta_2$  and the relaxation rates  $\lambda_1$  and  $\lambda_2$ . The two terms are thought to arise from two different muon stopping sites. For the  $x = 1.1$  compound the amplitudes  $A_1$  and  $A_2$  are found to be independent of temperature down to ~1.2 K where a loss of signal strength occurs on further cooling. Similarly, the rates  $\lambda_1$  and  $\lambda_2$  are constant in temperature down to ~1.2 K. Below,  $\lambda_1$  rises sharply and  $\lambda_2$ , after a brief rise slightly above 1.2 K, decreases monotonically. The electronic relaxation  $\lambda_1$  could be decoupled in strong LF (~0.1 T) pointing towards a broadly distributed quasistatic internal field from Ce ions at site 1 around 0.03 T, which is considered an indicator for AFM with  $T_N = 1.2$  K. The local field at site 2 is significantly lower. Both relaxation rates ( $\lambda_1$  and  $\lambda_2$ ) show a linear temperature dependence below  $T_N$ , the former rising, the latter decreasing. These observations are discussed in terms of ingrowing disorder in the AFM state ( $\lambda_1$ ) and Korringa type relaxation ( $\lambda_2$ ). No magnetic transition was observed for the  $x = 1.5$  compound down to 34 mK. A logarithmic dependence of muon spin-lattice relaxation is seen below 1.5 K and it is suggested that this feature can be considered the signature of NFL behavior. There is no documentation for such a conclusion to the reviewers' knowledge, and the authors give no reference. Sengupta and Georges (1995) have derived power-law dependences of spin-lattice relaxation rates for comparable conditions.

9.4.2.6. *Ce<sub>7</sub>Ni<sub>3</sub>*. This intermetallic, in contrast to the NFL materials discussed thus far, is a stoichiometric compound. It exhibits HF properties with  $\gamma \approx 1.5$  J/(mol K<sup>2</sup>) and an AFM ground state ( $T_N = 1.9$  K, Sereni et al. 1994). In its hexagonal Th<sub>7</sub>Fe<sub>3</sub> crystal structure, with space group P6<sub>3</sub>mc, three different Ce sites, labeled Ce<sub>1</sub> (one atom/unit cell, with



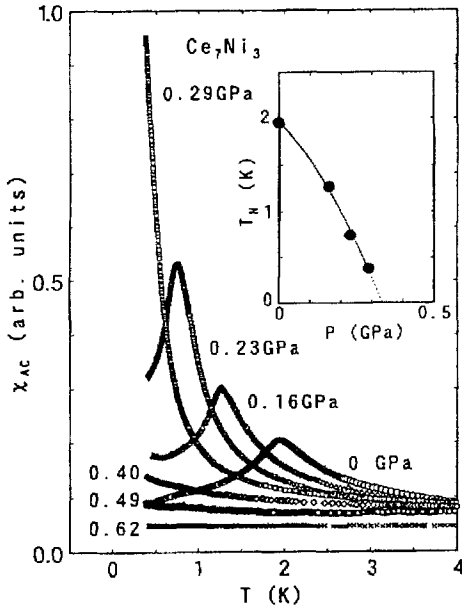


Fig. 165. Temperature dependence of the AC susceptibility of  $\text{Ce}_7\text{Ni}_3$  at various pressures. The insert shows the pressure dependence of Néel temperature. From Umeo et al. (1996a).

trigonal symmetry),  $\text{Ce}_{\text{II}}$  and  $\text{Ce}_{\text{III}}$  (both three atoms, monoclinic) can be distinguished (Roof et al. 1961). Under applied pressure  $T_N$  is rapidly reduced (Umeo et al. 1996a,b). AFM vanishes at  $P_c \approx 0.32$  GPa and NFL behavior appears around 0.46 GPa (see fig. 165). Beyond  $\sim 0.62$  GPa, FL behavior is restored. The measured bulk properties were found to be in agreement with the predictions of the self-consistent renormalization theory of spin fluctuations for HF systems near an AFM instability (Moriya and Takimoto 1995, Umeo et al. 1996b).

The electronic structure of  $\text{Ce}_7\text{Ni}_3$  is challenging even at ambient pressure. The competition between RKKY and Kondo interactions suggests a phenomenological two-component model of the kind first applied to  $\text{CeAl}_2$  (Bredl et al. 1978). Trovarelli et al. (1995) suggested that  $\text{Ce}_I$  is responsible for AFM order,  $\text{Ce}_{\text{II}}$  for the HF behavior and  $\text{Ce}_{\text{III}}$  for the IV contributions. Very recent neutron data (Kadowaki et al. 2000) show a single- $k$ -type magnetic structure with an incommensurate modulation vector below 1.8 K involving all three Ce sites, but with largely different moments (0.46, 0.7 and  $0.1\mu_B$ , respectively). Below a second transition at 0.7 K commensurate ordering appears in addition to the incommensurate structure. Metamagnetism is observed in an applied field.

$\mu\text{SR}$  studies of this compound are mainly available as brief preliminary reports (Takabatake et al. 1998b, Kratzer et al. 1999, 2001). Single-crystal specimens were used with measurements being carried out in different crystalline orientations. All data are fully consistent with a magnetic transition at  $T_N = 1.85$  K. The ZF relaxation rate for  $T > T_N$  (fig. 166, left top) shows critical behavior (i.e., follows a critical power law) typical for a second order transition. The critical exponent was found to be  $w \approx 1$ . One further notices a distinct dependence of relaxation rate on crystal orientation, meaning that magnetic

anisotropy persists, leading to non-isotropic paramagnetic spin fluctuations in the vicinity of  $T_N$ . Knight shift studies were carried out between 3 K and 300 K in a transverse field of 6 kG (Schenck et al. 2001). Two signals, one with positive, the other with negative Knight shift were observed. Both show a simple cosine angular dependence but with opposite phases (see fig. 166, left bottom). These results were interpreted in terms of two muon stopping sites. Both are tetrahedrally coordinated b sites. Their nearest neighbor shells are identical (1 Ce<sub>I</sub> and 3 Ce<sub>III</sub> ions), but the next nearest neighbor shell (3 Ni ions *vs.* 3 Ce<sub>II</sub> ions) are different. The relative occupation of the two sites by the muon varies with temperature and, surprisingly, depends also on the orientation of the crystalline axes with respect to the applied field  $\mathbf{B}_{\text{app}}$ . Below 80 K the muon Knight shifts follow a Curie–Weiss behavior down to 3 K which is in striking contrast to bulk susceptibility. This behavior is not understood, yet above 100 K the Knight shifts scale with bulk susceptibility. There is indication that muon dynamics set in around 60 K probably starting out with jumps between the two b sites. Measurements of the Knight shifts (in a lower transverse field of 250 G) close to  $T_N$  showed the presence of critical divergence below  $\sim 3$  K. The relative separation between the two frequencies (as shown, for example, in fig. 166, left bottom) increases from 20% at 3 K to 37% at 2 K.

Below  $T_N$  heavily damped oscillatory muon spin precession signals are seen for  $c \perp \mathcal{S}_\mu$  (see fig. 166, right top). A fit with a single Bessel-type oscillatory signal (in accordance with the incommensurate spin structure) was unsatisfactory. A phase shift near  $180^\circ$  remained. The fit shown in fig. 166 (right top) includes a monotonically decaying fast Gaussian relaxation which, however, has no theoretical base. The likely conclusion is that a more complex spin arrangement than a simple incommensurate modulation exists. The two muon stopping sites are an additional complication, but as stated, their immediate neighborhood of magnetic ions is identical and differences are expected to be small. Independent of these problems one easily derives the temperature dependence of the precession frequency (fig. 166, right bottom). It reflects the order parameter of a second-order phase transition. The saturation field is roughly 0.15 T, a low value, but in agreement with the comparatively small Ce moments detected by neutrons. No significant change in spectral shape was seen around  $T_M = 0.7$  K. If this second transition exists at all, then the spatial arrangement of Ce spins around the muon changes only very little. The inset to fig. 166 (right top) reveals that spontaneous spin precession is not seen for  $c \parallel \mathcal{S}_\mu$  and the spectrum can be fitted to a simple exponential decay of muon spin polarization. This confirms that the moments are oriented predominantly in the  $c$  direction.

In summary, the  $\mu$ SR results indicate a more complex spin structure at ambient pressure than that derived from neutron scattering data. Spin disorder is substantial and exceeds what one would expect from the known magnetic structures. Even the  $\mu$ SR results in the paramagnetic regime are not fully understood. Strong anisotropies in spin dynamical properties are present. A study of local magnetic properties near the pressure-induced magnetic instability (where also NFL behavior is observed) needs high-pressure  $\mu$ SR data below 2 K. These temperatures are outside the operating range of the existing high-pressure spectrometers.

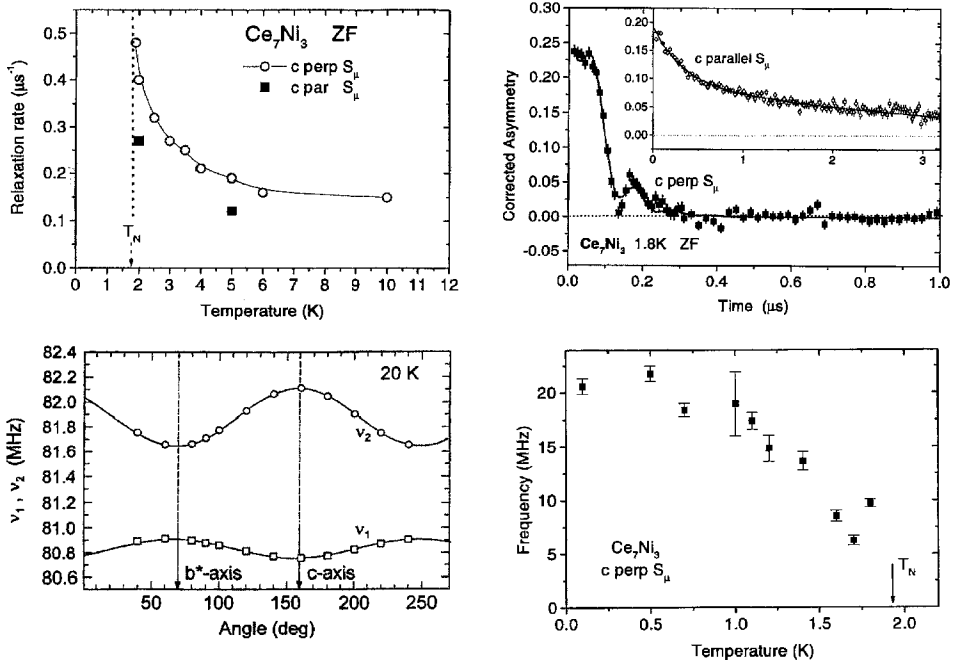


Fig. 166.  $\mu$ SR data on single-crystalline  $\text{Ce}_7\text{Ni}_3$ . Left: Measurements above  $T_N$ . Top: Temperature dependence of the ZF-relaxation rate for two orientations. Bottom: Angular dependence of the muon spin precession frequencies (two signals are seen) at 20 K in a transverse field of 6 kG. The marks refer to crystalline orientations parallel to the applied field. Right: Measurements below  $T_N$ . Top: ZF spectra at 1.8 K for  $c \perp S_\mu$  and  $c \parallel S_\mu$  (inset). The fits are explained in text. Bottom: Temperature dependence of the spontaneous muon spin precession frequency. (Bottom left: Schenck et al. 2001; all others: Kratzer et al. 2001.)

9.4.2.7.  $\text{CePt}_2\text{Si}_2$ . The specific heat ( $C(T)$ ) and electrical resistivity ( $\rho(T)$ ) of this tetragonal compound (space group  $P4/nmm$ ) show Fermi-liquid behavior between 10 K and 4 K with a Kondo temperature  $T^* = 70$  K (Ayache et al. 1987, Gignoux et al. 1988). At low temperatures, however, these quantities show temperature dependences more typical for NFL behavior. Since the formation of a NFL state is quite often coupled to magnetic instabilities, it was suggested that a possible collapse of magnetic susceptibility in the  $c$ -plane below 4 K (visible only after serious background corrections) is indicative of some metamagnetic behavior (Gignoux et al. 1988).

ZF- $\mu$ SR measurements (Dalmas de Réotier et al. 1997) on a single crystal oriented with the  $c$ -axis parallel and perpendicular to the beam only showed a weak, temperature-independent depolarization rate down to 50 mK, arising from nuclear dipolar fields. Since no electronic relaxation signal is discernible, the proposed metamagnetic behavior is not an intrinsic property and must be ruled out as the source of NFL behavior of  $C(T)$  and  $\rho(T)$  at low temperatures. In fact, no tendency towards magnetic order has been found and one may question whether  $\text{CePt}_2\text{Si}_2$  is a NFL system in the first place. The observed characteristics in  $C(T)$  and  $\rho(T)$  may then have a different, as yet unknown, origin.

9.4.2.8.  $U_2Pt_2In$ . This intermetallic crystallizes in a structure related to the tetragonal  $U_3Si_2$  type (showing a superstructure which leads to the space group  $P4_2/mnm$ ). It is a Pauli paramagnet with strongly enhanced electronic specific heat ( $\gamma \approx 0.4 \text{ J}/(\text{mol K}^2)$ ) at low temperatures. Tracing the ordering temperatures across the 2:2:1 series in relation to the Kondo necklace model led Nakotte (1994) to suggest that  $U_2Pt_2In$  lies close to the magnetic/nonmagnetic border and hence is likely to exhibit NFL behavior. Recent caloric and transport data (Estrela et al. 1999) established indeed NFL behavior for the temperature range between 0.1 K and 6 K. These authors also report briefly on  $\mu$ SR measurements on a single-crystalline specimen. The ZF spectra could be fitted to a combination of Gaussian (from static In nuclear moments) and exponential (from fluctuating U moments) relaxation. Above 10 K only 1/4 of the expected signal amplitude was observed. No comments are made concerning the missing fraction. Below 10 K the signal amplitude rises and approaches the expected magnitude at low temperatures. Also seen is a rise in relaxation rate indicating the slowing down of U spin fluctuations. Around 10 K susceptibility (for  $B \parallel c$ ) exhibits a weak maximum. No indication for the formation of (even weak moment) static magnetic order is present in the ZF- $\mu$ SR data down to lowest temperatures (0.3 K). The authors point out, however, that no information on the muon stopping site is available and hence the possibility that the muon rests at a position where all local field contributions cancel cannot safely be excluded.

*Summary:*  $U_2Pt_2In$  is an intermetallic close to a magnetic instability. It exhibits NFL behavior below  $\sim 8$  K.  $\mu$ SR sees no evidence for static magnetic order (for  $T \geq 0.3$  K), even in the low moment limit. The  $\mu$ SR spectra are not understood in detail, especially at higher temperatures ( $>10$  K). The absence of static magnetism suggests a quantum critical point as the likely cause for NFL behavior.

#### 9.4.3. *Summary: NFL compounds*

The question of what drives a HF system into NFL behavior remains unsolved at this stage. The two most fundamental approaches are the proximity to a quantum critical point and a disorder-based distribution of Kondo temperatures (Kondo interaction strengths). They are not mutually exclusive in alloyed compounds.  $\mu$ SR can make important contributions to both scenarios. It is well suited to track down the conditions where the quantum critical point occurs, especially if one deals with a spin freezing transition (spin glass behavior) rather than a true magnetic phase transition. The former then evokes advanced models like the Griffiths phase scenario.  $\mu$ SR is also perhaps the best method to get information on the behavior of spin dynamics on approach to a quantum critical point. If carefully analyzed it may help to decide whether a multi-channel Kondo effect is present (another ingredient which can in principle lead to NFL properties). Regarding disorder-driven NFL behavior,  $\mu$ SR offers the possibility of measuring the local (interstitial) susceptibility, which, when compared to the bulk susceptibility, renders information on the all important *local* spin disorder. The field is certainly still wide open.

### 9.5. Intermediate valence

The theory of intermediate valence (IV) forms the starting point for the treatment of HF materials. IV represents the limiting situation of a very strong coupling parameter  $g$  in strongly correlated electron materials, as can be seen from fig. 105. Kondo insulators in particular possess IV behavior at high temperatures as an essential ingredient. They form a borderline case. We have discussed them earlier as a separate class of materials.

Few  $\mu$ SR studies on the subject of intermediate valence exist, although IV is a common phenomenon in lanthanide intermetallics, especially for lanthanides positioned at the beginning (Ce), in the middle (Sm, Eu), and at the end (Tm, Yb) of the series. The likely reason is that charge properties *by themselves* are not reflected in the  $\mu$ SR signal (although the corresponding change of magnetic moment is). Also, a rather good understanding of this class of materials had already been developed by the time modern  $\mu$ SR spectroscopy became truly effective. Without doubt, other local probes, especially Mössbauer spectroscopy (see Potzel et al. 1993 and references cited therein) are much better suited for studies of microscopic properties of IV states in lanthanides and actinides.

Very early work (Wehr et al. 1981, 1984) deals with Knight shift measurements on a few well-established IV systems. Recently, a (still preliminary) study with the declared goal to test the  $\mu$ SR response in a properly classified IV compound (EuPdAs) has appeared (Klauß et al. 1997a).

A compound that is often considered a good case of IV and which has been studied by  $\mu$ SR is  $\text{Sm}_3\text{Se}_4$ . Because of its distinct Kondo properties (Takagi et al. 1993a,b, 1997), the authors rather view  $\text{Sm}_3\text{Se}_4$  as a low-carrier-density HF material. The same holds for  $\text{Yb}_4\text{As}_3$ . We have thus included these compounds in the section on HF materials (see also table 11).

9.5.1. *CeSn<sub>3</sub> (and LaSn<sub>3</sub>), CePd<sub>3</sub>*. The compounds have the cubic  $\text{AuCu}_3$  structure, for which the basic  $\mu$ SR properties have been discussed in sect. 5.2.3. The study by Wehr et al. (1984) is solely concerned with Knight shift measurements performed with the stroboscopic method. The observed Knight shifts  $K_\mu = B_\mu/B_{\text{app}}$  (see sect. 3.2.1) are on the order of 100 ppm, that is quite small.  $\text{CeIn}_3$  is a localized 4f paramagnet containing the trivalent ion and serves as a standard for comparison. Its shift follows quite closely the Curie–Weiss-like bulk susceptibility  $\chi$ , as expected. The same is true for  $\text{CeSn}_3$  above  $\sim 200$  K. Buschow et al. (1979) report for  $\text{CeSn}_3$  an effective moment from susceptibility larger than the free-ion moment of  $\text{Ce}^{3+}$ . Below 200 K, the susceptibility drops, which is considered the signature of IV behavior. For  $T < 200$  K the proportionality between  $K_\mu$  and  $\chi$  is no longer maintained; the reduction in  $K_\mu$  being stronger (see fig. 167). One possible explanation is the appearance of an additional negative shift related to the IV state. A similar anomaly occurs in the NMR Knight shift, but the difference in  $\chi$  has the opposite sign (Malik et al. 1975, MacLaughlin 1981). In the susceptibility data presented by Tsang et al. (1984) a sharp rise is seen (for a discussion, see also Liu 1993), which is not reproduced by  $K_\mu$ . Recently, Kim and Cox (1998) have attempted to give a theoretical

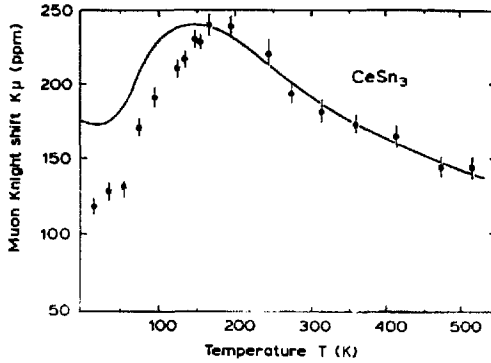


Fig. 167. Temperature dependence of the muon Knight shift of  $\text{CeSn}_3$ . The solid line represents the variation of bulk susceptibility with temperature. After Wehr et al. (1984).

explanation of the muonic Knight shift in  $\text{CeSn}_3$  together with some anomalous NMR Knight shifts. We refer the reader to the original paper for details.

The behavior of  $K_\mu$  for  $\text{CePd}_3$ , which is considered to be in the IV state already at room temperature, is somewhat different. The shift is *negative* and much smaller. Within the limits of error no temperature dependence is noticeable. The authors propose that the anomalous reduction in  $K_\mu$  and its negative sign arise from an enhanced d character of the conduction electrons in the  $e_g$  sub-band (Liu et al. 1981). This effect might also be the cause of the too-small Knight shift in  $\text{CeSn}_3$  below 200 K when compared to bulk susceptibility.

9.5.2.  $\text{Ce}_{1-x}\text{Th}_x$ . This system crystallizes in the fcc structure and undergoes an isomorphous phase transition around  $T_s = 150$  K (Shapiro et al. 1977). The transition involves a reduction in unit cell volume of 16% and is of first order for  $x < 0.26$  and of second order otherwise. For  $T > T_s$  one observes Curie-type susceptibility. At  $T_s$  the magnitude of  $\chi$  drops by 60% and  $\chi$  then remains essentially independent of temperature (Lawrence et al. 1975).

$\mu$ SR Knight shift measurements were carried out between 300 K and  $\sim 60$  K by Wehr et al. (1981), again employing the stroboscopic method in applied fields of 0.7 T for a polycrystalline sample with  $x = 0.26$ . Also measured was  $\text{La}_{0.74}\text{Th}_{0.26}$  for comparison.  $K_\mu$  is positive in  $\text{Ce}_{0.74}\text{Th}_{0.26}$  and follows  $\chi$  at all temperatures, that is, through the transition. Notably, no anomaly like that in  $\text{CeSn}_3$  (see above) is apparent in the IV regime. The shift in the La material is independent of temperature and close to zero.

The behavior of the transverse field relaxation rate  $\lambda$  (see fig. 168) is quite interesting. It rises sharply when  $T_s$  is approached from above and drops markedly at  $T_s$ . It then remains about constant. The La compound exhibits a temperature-independent small relaxation rate which has its origin in the nuclear dipole fields of  $^{139}\text{La}$  ( $\sim 100\%$  abundant). The variation of rate in  $\text{Ce}_{0.74}\text{Th}_{0.26}$  mirrors the behavior of the dynamics of the local field produced by moments on Ce. Close to  $T_s$  critical slowing down occurs (for  $T > T_s$ ), but motional narrowing again becomes effective for  $T < T_s$ . The microscopic origin of those fluctuations cannot be extracted from the  $\mu$ SR data. The authors discuss normal

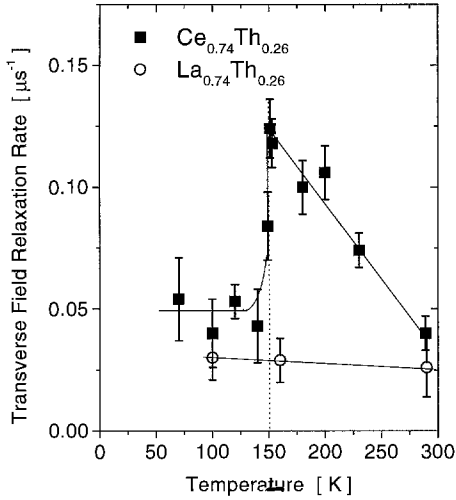


Fig. 168. Temperature dependence of the transverse muon spin relaxation rate in  $\text{Ce}_{0.74}\text{Th}_{0.26}$  and  $\text{La}_{0.74}\text{Th}_{0.26}$ . The lines are guides to the eye. From Wehr et al. (1981).

paramagnetic fluctuations of the 4f moment and charge fluctuations connected with the IV behavior. They consider the latter more likely and use ultrasonic measurements that were also carried out for support. Those measurements show a behavior of fluctuation rates around  $T_s$  quite similar to those extracted from the  $\mu\text{SR}$  data.

**9.5.3. *EuPdAs* (and *NdPdAs*).** The metallic compound *EuPdAs* crystallizes in the hexagonal  $\text{Ni}_2\text{In}$  structure. The Eu mean valence changes in a first-order transition at  $\sim 170$  K from +2.15 around 300 K to +2.35 below 100 K. Mössbauer spectroscopy established a very low valence fluctuation rate  $\nu_{\text{VF}} \leq 100$  MHz (Michels et al. 1992, 1995) over the whole temperature range. Around 5 K a magnetic transition occurs.  $\text{Eu}^{2+}$  has the same  $4f^7$  configuration as  $\text{Gd}^{3+}$ . It is an S-state ion with a large effective spin moment of  $\sim 7.9\mu_{\text{B}}$ . For  $\text{Eu}^{3+}$  the moment vanishes due to its  $J = 0$  state. This extreme difference in magnetic moments is expected to lead to a distribution of the magnetic coupling to the muon *via* dipolar and contact interaction. From model calculations, Klaufß et al. (1997a) first deduced a most probable muon site and then (using dipolar summation) the presence of a resolvable difference in Knight shift (about 1% in  $\text{TF} = 0.1$  T applied along the *c*-axis) above and below the 170 K transition. If the two charge states were static one would observe a  $\mu\text{SR}$  spectrum containing two precession frequencies  $\nu_{\mu}$ . In the dynamic case ( $\nu_{\text{VF}} \geq \nu_{\mu}$ ) only a single precession frequency would be seen but with a broadened linewidth in the limit of not-too-fast relaxation rates. The time window for such dynamic effects extends down into the MHz range for TF- $\mu\text{SR}$  and probes a range not accessible to Mössbauer spectroscopy.

As a reference system, isostructural *NdPdAs* was also investigated. This compound contains  $\text{Nd}^{3+}$  ions which lead to Curie-Weiss behavior with  $\mu_{\text{Curie}} = 3.47\mu_{\text{B}}$ , close to the free ion value. A transition into a FM state takes place at  $\sim 15$  K.

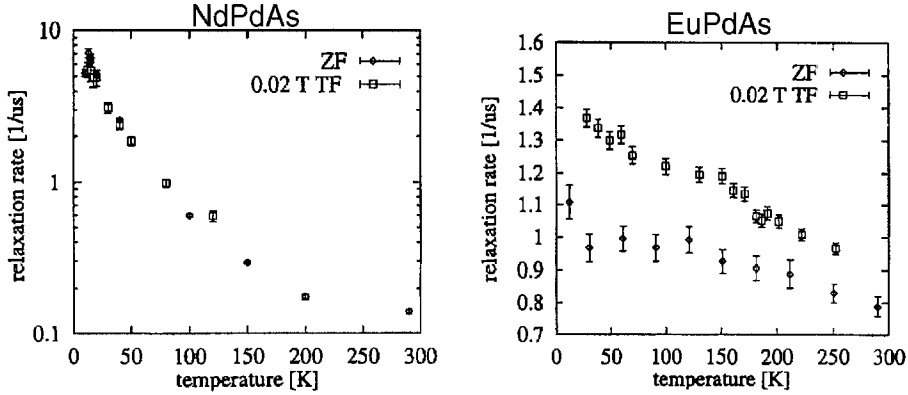


Fig. 169. Temperature dependence of the ZF and TF relaxation rates for NdPdAs (left, semi-logarithmic plot) and EuPdAs (right, linear plot). More detailed data are available for EuPdAs below 20 K but not shown in this figure. From Klaus et al. (1997a).

An overview of the temperature dependence of depolarization rates in ZF and TF (0.02 T) for both the Nd and the Eu compounds is presented in fig. 169. The Nd material itself shows some usual behavior: the relaxation rate in it begins to rise at 200 K due to the approach to a magnetic phase transition (although depopulation of CEF levels may play a role). The magnetic state was not explored. The fact that the depolarization rate in TF is virtually the same proves that the local fields are in the fast-fluctuation limit.

In EuPdAs the ZF depolarization rate around room temperature is considerably larger than in NdEuAs. This is mostly due to the larger moment on Eu. The rate shows little variation with temperature except below  $\sim 10$  K when the 5 K magnetic transition is approached. The difference in the temperature range where the rise of relaxation rate on moving towards a magnetic transition takes place is typical for a non-S-state and a S-state ion. Compounds containing the  $Gd^{3+}$  ion also tend to exhibit a nearly constant relaxation rate in the paramagnetic regime until rather close to the transition. This difference most likely has its roots in the strong single-ion anisotropy of non-S-state 4f ions.

In TF a single precession frequency was observed. The signal is strongly damped, mainly due to inhomogeneous line broadening since a polycrystalline sample was used. This severely restricts the evaluation of the Knight shift. It could well be that a two-frequency pattern is simply not resolved. At the first-order transition a slight irregularity in TF relaxation rate is observed, presumably coupled to the change in unit cell volume. The variation of relaxation rate with the strength of the applied TF (measured up to 0.7 T) at 200 K showed the quadratic dependence expected from the valence fluctuation modeling. The initial slope, however, is too low for dominant dipolar coupling and the isotropic Fermi contact interaction is probably substantial. This then makes comparisons to model calculations using dipolar sums (as discussed above) much less reliable. A quadratic fit to the field dependence of the relaxation rate returned a valence fluctuation rate of  $\nu_{VF} \approx 0.8 \mu s^{-1}$ . The authors consider this an estimate, but the value is in agreement with the Mössbauer data and reflects at least the order of magnitude.



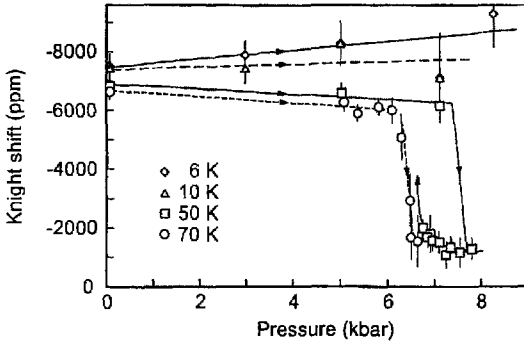


Fig. 170. Pressure dependence of the muon Knight shift in  $\text{Sm}_{0.9}\text{La}_{0.1}\text{S}$  for various temperatures. The lines are guides to the eye. Note the hysteresis at 50 K. From Schenck et al. (1997c).

9.5.4.  $\text{Sm}_{0.9}\text{La}_{0.1}\text{S}$ . This pseudo-binary cubic (NaCl) compound of intermediate valence is metallic in its ground state, but turns into an insulator under moderate pressure at low temperatures (Wachter et al. 1995). The metal–insulator transition is thought to arise *via* a condensation of excitons formed by 4f holes and conduction electrons. One consequence of this type of exciton formation should be a strong suppression of paramagnetism leading essentially to diamagnetism. While such a scenario could definitely be established for the corresponding compound  $\text{Tm}_{0.45}\text{Te}_{0.55}$  (Wachter and Jung 1994), bulk magnetic measurements on  $\text{Sm}_{0.9}\text{La}_{0.1}\text{S}$  turned out to be difficult due to its extremely small paramagnetic moment. For this reason, a  $\mu\text{SR}$  measurement was undertaken (Schenck et al. 1997c), concentrating on the variation of Knight shift with applied pressure.

A mosaic sample of small single crystals was used, which were oriented for measurements under ambient conditions, but not for those under high pressure. Over the temperature range from 300 to 6 K pressures up to 8 kbar in a transverse field of 0.6 T were applied. An angular scan of Knight shift at 30 K under ambient pressure verified the  $(\frac{1}{4}, \frac{1}{4}, \frac{1}{4})$  muon stopping position typical for NaCl-type compounds (see sect. 5.2.1). For this position, the Knight shift is solely due to the isotropic contact field, even for a single-crystalline sample. The Knight shift scales with bulk susceptibility only for  $T > 100$  K. Under pressure a collapse of shift is seen around 7 kbar for  $T > 30$  K (see fig. 170) and hence *not restricted* to the insulating phase as demanded by theory. Schenck et al. (1997c) are doubtful whether this collapse reflects the behavior of bulk magnetic response. They argue that it may rather be caused by a severe weakening of the RKKY interaction between 4f and conduction electrons for Sm atoms close to the muon stopping site, when volume reduction exceeds a critical, temperature-dependent value.

## 10. Conclusions

We hope to have demonstrated to the readers that  $\mu\text{SR}$  has developed into a major tool for microscopic studies of magnetism and that its application to 4f- and 5f-magnetic materials is broad and multifaceted. In fact, the amount of data revealed by our literature search surprised us. This is even more astonishing when considering that we have not discussed

the many important studies of superconducting properties of high  $T_c$  and HF compounds. In this field the search for unconventional superconductivity has become a major focus of recent  $\mu$ SR research.

In general, the prime impacts of  $\mu$ SR on lanthanide and actinide magnetism have been fivefold:

- (1) The muon senses small variations (i.e., minor spin canting) even in otherwise well-established spin structures. It is mandatory that the  $\mu$ SR magnetic parameters and their temperature and/or pressure dependences be consistent with the findings of other methods, in particular with neutron scattering data. This task is far from completed in a number of systems studied thus far, and the  $\mu$ SR results indicate in these cases that the magnetic structure is not understood in all details.
- (2)  $\mu$ SR spectroscopy has a high sensitivity to small moment magnetism. It can detect quasistatic magnetism caused by moments as low as  $10^{-3}\mu_B$  or less. This has been seminal in Kondo-lattice and HF systems, showing that magnetism is often present where it was not expected. It appears that pure nonmagnetic ground states are the exception in these materials, even when they exhibit superconductivity.
- (3) The muon is a highly local probe. Hence  $\mu$ SR is a technique particularly well suited for detecting and studying short-range-ordered magnetism. Typical applications are the magnetic properties of strongly frustrated magnetic systems and spin freezing in combination with the low-moment magnetism mentioned above. The latter feature is a new aspect revealed by  $\mu$ SR in the field of strongly correlated electron systems.
- (4) The muon samples the volume of the material studied uniformly. This gives microscopic insight into systems exhibiting simultaneously more than one cooperative state. The prime example is the coexistence of magnetism and superconductivity. Here, the pertinent question is, whether these two states coexist on a microscopic scale or whether the material splits into different volume fractions, each showing only one of the two states. Two findings are especially important. Firstly, the cuprate superconductors (e.g., the "1 2 3" compounds) move from localized AFM to superconductivity through a coexistence regime (with short-range-ordered magnetism) when varying the carrier concentration. Secondly, in some HF materials (most notably  $UPt_3$ ) superconductivity and small moment magnetism coexist on a microscopic level and the internal magnetic field generated by the magnetic state is considered a decisive ingredient in several models of unconventional superconductivity.
- (5)  $\mu$ SR possesses a unique time window for spin dynamical processes and is also sensitive to spin excitations with very low energy transfer. The frequency range of spin fluctuations monitored by  $\mu$ SR extends to comparatively low values (i.e., 1 MHz or less under favorable conditions). One important outcome is that  $\mu$ SR is able to connect the absence of magnetic order in various highly correlated electron systems to the presence of persisting spin fluctuations even as the temperature approaches zero. Either frustration or Kondo interactions (or both) are likely the driving forces. Furthermore,  $\mu$ SR can make the important distinction between static and dynamic spin-glass-order, and, in combination with its high sensitivity to very short-ranged magnetic correlations, is a prime tool to detect inhomogeneous spin

freezing. The muon spin relaxation rate responds strongly to the development of spin correlations, particularly in the realm of critical slowing down near a second-order phase transition.  $\mu$ SR was able to show, especially in strongly anisotropic magnets, that spin correlations persist very far (often up to  $5 \cdot T_M$ ) above the transition temperature. It also has become a tool to study *longitudinal* spin fluctuations in the true critical regime and has given new insight into various universality classes of phase transitions. The field of slow spin dynamics in ordered spin systems is not yet fully explored at this stage and new insights will surely emerge as time passes.

As has been said at the beginning,  $\mu$ SR is not a good technique to detect the delocalization of f electrons in anomalous lanthanide and actinide materials. Yet, the formation of small-moment magnetism is clearly connected to a hybridization of f-electron states and in that sense  $\mu$ SR detects magnetic non-localized electron states with high sensitivity.

In summary, we believe it is fair to say that  $\mu$ SR, especially within the last decade or so, has helped to shape our understanding of the many facets of magnetism involving rare-earth and actinide ions. New features have emerged and we are fully convinced that this will continue in the future. One particularly promising aspect is the commissioning of the new low-energy muon facilities which allow thin films and multi-layers to be probed by  $\mu$ SR. We are looking forward to this.

## Acknowledgements

It is a pleasure to thank many of our colleagues for helpful discussions and clarification of special problems. One of us (GMK) expresses his gratitude to Dr. A. Amato (PSI) for making available an advance copy of his review on HF systems. We are indebted to Dr. L. Asch (TU Munich) and to Professor C.E. Stronach (Virginia State University) for critical readings of the manuscript. Last and not least, we thank the editors for their patience and good advice.

## References

- Abela, R., C. Baines, X. Donath, D. Herlach, D. Maden, I.D. Reid, D. Renker, G. Solt and U. Zimmermann, 1994, *Hyperfine Interactions* **87**, 1105.
- Abela, R., A. Amato, C. Baines, X. Donath, R. Erne, D.C. George, D. Herlach, G. Irminger, I.D. Reid, D. Reukev, G. Solt, D. Suki, M. Werner and U. Zimmermann, 1999, *Hyperfine Interactions* **120–121**, 575.
- Ablitz, M., R. Settai, P. Ahmet, D. Aoki, K. Sugiyama and Y. Ōnuki, 1997, *Philos. Mag. B* **75**, 443.
- Abragam, A., 1961, *The Principles of Nuclear Magnetism* (Oxford University Press, London).
- Abragam, A., and B. Bleaney, 1970, *Electron Paramagnetic Resonance of Transition Ions* (Clarendon Press, Oxford).
- Abu-Shiekah, I.M., O.O. Bernal, A.A. Menovsky, H.B. Brom and J. Zaanen, 1999, *Phys. Rev. Lett.* **83**, 3309.
- Adams, T.R., R.L. Lichti and T.L. Gibson, 1994, *Hyperfine Interactions* **86**, 561.
- Adenwalla, S., S.W. Lin, Q.Z. Rau, Z. Zhao,

- J.B. Ketterson, J.A. Sauls, L. Taillefer, D.G. Hinks, M. Levy and B.K. Sarma, 1990, *Phys. Rev. Lett.* **65**, 2298.
- Adroja, D.T., B.D. Rainford, A.V. Volkozub and P.A.J. de Groot, 1994, *Physica C* **229**, 193.
- Adroja, D.T., B.D. Rainford, J.M. de Teresa, A. del Moral, M.R. Ibarra and K.S. Knight, 1995, *Phys. Rev. B* **52**, 12790.
- Adroja, D.T., B.D. Rainford, A.J. Neville, P. Mandal and A.G.M. Jansen, 1996, *J. Magn. Magn. Mater.* **161**, 157.
- Aeppli, G., and C. Broholm, 1994, in: *Handbook on the Physics and Chemistry of Rare Earths*, Vol. 19, eds K.A. Gschneidner Jr and L. Eyring (North-Holland, Amsterdam) p. 123.
- Aeppli, G., and Z. Fisk, 1992, *Comm. Condens. Matter Phys.* **16**, 155.
- Aeppli, G., E. Bucher, C. Broholm, J.K. Kjems, J. Baumann and J. Hufnagl, 1988, *Phys. Rev. Lett.* **60**, 615.
- Aeppli, G., D.J. Bishop, C. Broholm, E. Bucher, K. Siemensmeyer, M. Steiner and N. Stüsser, 1989, *Phys. Rev. Lett.* **63**, 676.
- Aeppli, G., T.E. Mason, S.M. Hayden, H.A. Mook and J. Kulda, 1998, *Science* **278**, 1432.
- Aggarwal, K., L. Asch, F.N. Gygax, O. Hartmann, G.M. Kalvius, A. Kratzer, F.J. Litterst, K. Mattenberger, A. Schenck and O. Vogt, 1989, *Hyperfine Interactions* **51**, 935.
- Aggarwal, K., L. Asch, S. Fredo, J. Gal, F.N. Gygax, B. Hitti, G.M. Kalvius, A. Kratzer, F.J. Litterst, K.H. Münch and A. Schenck, 1990, *Hyperfine Interactions* **64**, 401.
- Agterberg, D.F., and M.B. Walker, 1994, *Phys. Rev. B* **50**, 563.
- Aharony, A., R.J. Birgeneau, A. Coniglio, M.A. Kastner and H.E. Stanley, 1988, *Phys. Rev. Lett.* **60**, 1330.
- Ahlheim, U., K. Fraas, P.H.P. Reinders, F. Steglich, O. Nakamura, T. Suzuki and T. Kasuya, 1992, *J. Magn. Magn. Mater.* **108**, 213.
- Ahmet, P., M. Ablitz, R. Settai, K. Sugiyama, Y. Ōnuki, T. Takeuchi, K. Kindo and S. Takayanagi, 1996, *J. Phys. Soc. Japan* **65**, 1077.
- Akai, H., K. Terakura and J. Kanamori, 1992, in: *Perspectives of Meson Science*, eds T. Yamazaki, K. Nakai and K. Nagamine (North-Holland, Amsterdam) p. 161.
- Akimitsu, J., J. Amano, M. Yoshinari, M. Kokubun, T. Iwasaki, S. Okuma, N. Nishida, K. Nishiyama and N. Mori, 1994, *Hyperfine Interactions* **85**, 187.
- Alami-Yadri, K., 1997, Ph.D. Thesis (University of Geneva).
- Aldred, A.T., D.J. Lam, A.R. Harvey and B.D. Dunlap, 1975, *Phys. Rev. B* **11**, 1169.
- Alexandrowicz, G., T. Tashma, M. Socolovsky, A. Amato, A. Grayevsky, F.N. Gygax, M. Pinkpank, A. Schenck and N. Kaplan, 1999, *Phys. Rev. Lett.* **82**, 1028.
- Aliev, F.G., V. Moshchal'kov, M.K. Zalyalyutdinov, G.I. Pak, R.V. Skolozdra, P.A. Aleksev, V.N. Lazukov and I.P. Sadikov, 1990, *Physica B* **163**, 358.
- Allenspach, P., A. Furrer and P. Unternährer, 1989a, *Phys. Rev. B* **39**, 2226.
- Allenspach, P., A. Furrer, B. Rupp and H. Blank, 1989b, *Physica C* **161**, 671.
- Alloul, H., P. Mendels, H. Casalta, J.F. Marucco and J. Arabski, 1991, *Phys. Rev. Lett.* **67**, 3140.
- Alves, S., C. Boekema, C.H. Halim, G.C. Lam, E. Wang, D.W. Cooke and M. Leon, 1994, *Phys. Rev. B* **49**, 12396.
- Amato, A., 1994, *Physica B* **199–200**, 91.
- Amato, A., 1995, *Physica B* **206&207**, 49.
- Amato, A., 1997, *Rev. Mod. Phys.* **69**, 1119.
- Amato, A., D. Jaccard, J. Flouquet, F. Lapiere, J.L. Tholence, R.A. Fisher, S.E. Lacy, J.A. Olsen and N.E. Phillips, 1987, *J. Low Temp. Phys.* **68**, 371.
- Amato, A., R. Feyerherm, F.N. Gygax, A. Schenck, M. Weber, R. Caspary, P. Hellmann, C. Schank, C. Geibel, F. Steglich, D.E. MacLaughlin, E.A. Knetsch and R.H. Heffner, 1992a, *Europhys. Lett.* **19**, 127.
- Amato, A., C. Geibel, F.N. Gygax, R.H. Heffner, E.A. Knetsch, D.E. MacLaughlin, C. Schank, A. Schenck, F. Steglich and M. Weber, 1992b, *Z. Phys. B* **86**, 159.
- Amato, A., P.C. Canfield, R. Feyerherm, Z. Fisk, F.N. Gygax, R.H. Heffner, D.E. MacLaughlin, H.R. Ott, A. Schenck and J.D. Thompson, 1992c, *Phys. Rev. B* **46**, 3153.
- Amato, A., R. Feyerherm, F.N. Gygax, D. Jaccard, A. Schenck, J. Sierro, E. Walker and U. Zimmermann, 1993a, *Physica B* **186–188**, 273.
- Amato, A., C. Baines, R. Feyerherm, J. Flouquet, F.N. Gygax, P. Lejay, A. Schenck and U. Zimmermann, 1993b, *Physica B* **186–188**, 276.
- Amato, A., P.C. Canfield, R. Feyerherm, Z. Fisk, F.N. Gygax, R.H. Heffner, E.A. Knetsch, D.E. MacLaughlin, H.R. Ott, A. Schenck, J.D. Thompson and U. Zimmermann, 1993c, *Physica B* **186–188**, 615.

- Amato, A., R. Feyerherm, F.N. Gygax, A. Schenck, J. Flouquet and P. Lejay, 1994a, *Phys. Rev. B* **50**, 619.
- Amato, A., R. Feyerherm, F.N. Gygax, A. Schenck and D. Jaccard, 1994b, *Hyperfine Interactions* **85**, 369.
- Amato, A., B. Andracka, O.O. Bernal, R. Feyerherm, F.N. Gygax, R.H. Heffner, L.P. Le, H. von Löhneysen, D.E. MacLaughlin, G.J. Nieuwenhuys, H.R. Ott and A. Schenck, 1995a, *Nuclear and Particle Physics Newsletter* (Paul Scherrer Institute, Villigen, unpublished) p. 77.
- Amato, A., R. Feyerherm, F.N. Gygax, A. Schenck, H. von Löhneysen and H.G. Schlager, 1995b, *Phys. Rev. B* **52**, 54.
- Amato, A., R. Feyerherm, F.N. Gygax and A. Schenck, 1997a, *Hyperfine Interactions* **104**, 115.
- Amato, A., R. Feyerherm, F.N. Gygax, A. Schenck, M. Kasaya, T. Suzuki, S. Takagi and A. Ochiai, 1997b, *Hyperfine Interactions* **104**, 165.
- Amato, A., D. Andreica, F.N. Gygax, D. Jaccard, M. Pinkpank and A. Schenck, 1998, *Annual Report 1997/Annex 1* (Paul Scherrer Institute, Villigen, unpublished) p. 34.
- Amato, A., D. Andreica, F.N. Gygax, M. Pinkpank, N. Sato, A. Schenck and G. Solt, 2000, *Physica B* **289–290**, 447.
- Amoretti, G., A. Blaise, R. Caciuffo, D. Di Cola, J.M. Fournier, M.T. Hutchings, G.H. Lander, R. Osborn, A. Severing and A.D. Taylor, 1992, *J. Phys.: Condens. Matter* **4**, 3459.
- Andracka, B., and G.R. Stewart, 1993, *Phys. Rev. B* **47**, 3208.
- Andracka, B., and A.M. Tsvetlik, 1991, *Phys. Rev. Lett.* **67**, 2886.
- André, G., F. Bourée, A. Oleś, W. Sikora, B. Penc, A. Szytuła and Z. Tomkowicz, 1996, *Solid State Commun.* **97**, 923.
- Andreica, D., K. Alami-Yadri, D. Jaccard, A. Amato and A. Schenck, 1999, *Physica B* **259–261**, 144.
- Andreica, D., A. Amato, F.N. Gygax, M. Pinkpank and A. Schenck, 2000, *Physica B* **289–290**, 24.
- Andres, K., and E. Bucher, 1971, *J. Appl. Phys.* **42**, 1522.
- Andres, K., E. Bucher, J.P. Maita and A.S. Cooper, 1972, *Phys. Rev. Lett.* **28**, 1652.
- Andres, K., J.E. Graebner and H.R. Ott, 1975, *Phys. Rev. Lett.* **35**, 1779.
- Ansaldò, E.J., D.R. Noakes, J.H. Brewer, R. Keitel, D.R. Harshman, M. Senba, C.Y. Huang and B.V.B. Sarkissian, 1985, *Solid State Commun.* **55**, 193.
- Ansaldò, E.J., D.R. Noakes, J.H. Brewer, S.R. Kreitzman and J.K. Furdyna, 1988, *Phys. Rev. B* **38**, 1183.
- Arons, R.R., M. Loewenhaupt, T. Reif and E. Gratz, 1994, *J. Phys.: Condens. Matter* **6**, 6789.
- Arseneau, D.J., B. Hitti, S.R. Kreitzman and E. Whidden, 1997, *Hyperfine Interactions* **106**, 277.
- Asch, L., 1989, *Physica B* **161**, 299.
- Asch, L., 1990, *Hyperfine Interactions* **64**, 351.
- Asch, L., G.M. Kalvius, A. Kratzer, F.J. Litterst, U. Potzel, R. Keitel, D.R. Noakes, E.J. Ansaldò, O. Hartmann, E. Karlsson, R. Wäppling, J. Chappert and A. Yaouanc, 1986a, *Hyperfine Interactions* **31**, 337.
- Asch, L., S. Barth, F.N. Gygax, G.M. Kalvius, A. Kratzer, F.J. Litterst, K. Mattenberger, W. Potzel, A. Schenck and O. Vogt, 1986b, *Hyperfine Interactions* **31**, 443.
- Asch, L., S. Barth, F.N. Gygax, G.M. Kalvius, A. Kratzer, F.J. Litterst, K. Mattenberger, W. Potzel, A. Schenck, J.C. Spirlet and O. Vogt, 1987, *J. Magn. Magn. Mater.* **63&64**, 169.
- Asch, L., G.M. Kalvius and J. Chappert, 1988a, *Hyperfine Interactions* **40**, 1133 and 1137.
- Asch, L., F.J. Litterst, A. Kratzer, K. Aggarwal, W. Potzel, G.M. Kalvius, F.N. Gygax, B. Hitti, A. Schenck, S. Barth, O. Vogt and K. Mattenberger, 1988b, *J. Phys. Paris* **49**, C8-495.
- Asch, L., G.M. Kalvius, A. Kratzer, F.J. Litterst, A. Schenck, B. Hitti, F.N. Gygax, C.A. Scott, K. Mattenberger and O. Vogt, 1989, *Europhys. Lett.* **10**, 673.
- Asch, L., G.M. Kalvius, F.J. Litterst, M. Weber, K.H. Münch, A. Kratzer, K. Aggarwal, A. Schenck, F.N. Gygax, R. Ballou, J. Deportes and J. Chappert, 1990a, *Hyperfine Interactions* **64**, 435.
- Asch, L., G.M. Kalvius, A. Kratzer, F.J. Litterst, F.N. Gygax, A. Schenck, K. Mattenberger and O. Vogt, 1990b, *Hyperfine Interactions* **64**, 453.
- Asch, L., G.M. Kalvius, A. Kratzer and F.J. Litterst, 1994, *Hyperfine Interactions* **85**, 193.
- Ashcroft, N.W., and N.D. Mermin, 1976, *Solid State Physics* (Holt, Rinehart and Winston, New York).
- Ayache, C., J. Beille, E. Bonjour, R. Calemczuk, G. Creuset, D. Gignoux, A. Najik, D. Schmitt, J. Voiron and M. Zerguine, 1987, *J. Magn. Magn. Mater.* **63&64**, 329.
- Ayres de Campos, J., J.M. Gil, P.J. Mendes, L.P. Ferreira, I.C. Ferreira, N. Ayres de Campos, P. Estrela, M. Godinho, M. Bououdina, A. Collomb, D. Fruchart, J.L. Soubeyroux, S. Takele, J. Pelloth

- and R.A. Brand, 1996, *J. Magn. Magn. Mater.* **164**, 305.
- Balagurov, A.M., E.V. Raspopina, V.V. Sikolenko, I.S. Lyubutin, A.S. Stepin, A.V. Gribov, G. Andre, F. Bourée and H.M. Duh, 2000, *J. Magn. Magn. Mat.* **210**, 225.
- Ballou, R., J. Deportes, R. Lemaire, Y. Nakamura and B. Ouladdiaf, 1987, *J. Magn. Magn. Mater.* **70**, 129.
- Ballou, R., C. Lacroix and M.D. Nunez Regueiro, 1991, *Phys. Rev. Lett.* **66**, 1910.
- Ballou, R., P.J. Brown, J. Deportes, A.S. Markosyan and B. Ouladdiaf, 1992, *J. Magn. Magn. Mater.* **104-107**, 935.
- Barbara, B., M.F. Rossignol, J.X. Boucherle and C. Vettier, 1980, *Phys. Rev. Lett.* **45**, 938.
- Bargouth, M.O., and G. Will, 1971, *J. Phys. C* **1**, 675.
- Barsov, S.G., A.L. Getalov, V.G. Grebinnik, V.A. Gordeev, I.I. Gurevich, V.A. Zhukov, A.I. Klimov, S.P. Kruglov, L.A. Kuzmin, A.B. Lazarev, S.M. Mikirtychyants, N.I. Moreva, V.A. Morozova, B.A. Nikolskii, A.V. Pirogov, V.I. Selivanov, V.A. Suetin, S.V. Formichev and G.V. Shcherbakov, 1983, *Sov. Phys. JETP* **57**, 1105.
- Barsov, S.G., A.L. Getalov, V.G. Grebinnik, I.I. Gurevich, B.F. Kirilov, I.G. Ivanter, A.I. Klimov, S.P. Kruglov, L.A. Kuzmin, A.B. Lazarev, S.M. Mikirtychyants, N.I. Moreva, B.A. Nikolskii, A.V. Pirogov, A.N. Ponomarev, V.I. Selivanov, G.V. Shcherbakov, S.N. Shilov, V.A. Suetin and V.A. Zhukov, 1986a, *Hyperfine Interactions* **31**, 255.
- Barsov, S.G., A.L. Getalov, V.G. Grebinnik, I.I. Gurevich, B.F. Kirilov, A.I. Klimov, S.P. Kruglov, L.A. Kuzmin, A.B. Lazarev, S.M. Mikirtychyants, N.I. Moreva, B.A. Nikolskii, A.V. Pirogov, A.N. Ponomarev, V.I. Selivanov, G.V. Shcherbakov, S.N. Shilov, V.A. Suetin and V.A. Zhukov, 1986b, *Hyperfine Interactions* **31**, 339.
- Barsov, S.G., A.L. Getalov, V.G. Grebinnik, I.I. Gurevich, V.A. Zhukov, I.G. Ivanter, B.F. Kirilov, A.I. Klimov, S.P. Kruglov, L.A. Kuzmin, A.B. Lazarev, S.M. Mikirtychyants, N.I. Moreva, B.A. Nikolskii, A.V. Pirogov, A.N. Ponomarev, V.A. Suetin, S.N. Shilov and G.V. Shcherbakov, 1986c, *Sov. Phys. JETP* **64**, 174.
- Barth, S., E. Albert, G. Heiduk, A. Möslang, A. Weidinger, E. Recknagel and K.H.J. Buschow, 1986a, *Phys. Rev. B* **33**, 430.
- Barth, S., H.R. Ott, F.N. Gygax, A. Schenck, T.M. Rice and Z. Fisk, 1986b, *Hyperfine Interactions* **31**, 397.
- Barth, S., H.R. Ott, F. Hulliger, F.N. Gygax, A. Schenck and T.M. Rice, 1986c, *Hyperfine Interactions* **31**, 403.
- Barth, S., H.R. Ott, F.N. Gygax, B. Hitti, E. Lippelt, A. Schenck, C. Baines, B. van den Brandt, T. Konter and S. Mango, 1987, *Phys. Rev. Lett.* **59**, 2991.
- Barth, S., H.R. Ott, F.N. Gygax, B. Hitti, E. Lippelt, A. Schenck and Z. Fisk, 1989a, *Hyperfine Interactions* **50**, 711.
- Barth, S., H.R. Ott, F.N. Gygax, B. Hitti, E. Lippelt, A. Schenck and C. Baines, 1989b, *Phys. Rev. B* **39**, 11695.
- Bartholin, H., and D. Bloch, 1968, *J. Phys. Chem. Solids* **29**, 1063.
- Bates, S., G.J. McIntyre, S.B. Palmer and J.B. Sousa, 1987, *J. Phys. F* **17**, 1973.
- Batlogg, B., E. Kaldis, A. Schlegl, G. von Schulthess and P. Wachter, 1976, *Solid State Commun.* **19**, 673.
- Battle, P.D., S.J. Blundell, M.A. Green, W. Hayes, M. Honold, A.K. Klehe, N.S. Laskey, J.E. Millburn, L. Murphy, M.J. Rosseinsky, N.A. Samarin, J. Singleton, N.E. Sluchanko, S.P. Sullivan and J.F. Vente, 1996a, *J. Phys.: Condens. Matter* **8**, L427.
- Battle, P.D., M.A. Green, N.S. Laskey, J.E. Millburn, P.G. Radaelli, M.J. Rosseinsky, S.P. Sullivan and J.F. Vente, 1996b, *Phys. Rev. B* **54**, 15967.
- Battle, P.D., M.A. Green, N.S. Laskey, N. Kasmir, J.E. Millburn, L.E. Spring, S.P. Sullivan, M.J. Rosseinsky and J.F. Vente, 1997, *J. Mater. Chem.* **7**, 977.
- Bauer, E., 1991, *Adv. Phys.* **40**, 417.
- Bauer, E., E. Gratz and C. Schmitzer, 1987a, *J. Magn. Magn. Mater.* **63&64**, 37.
- Bauer, E., D. Gignoux, D. Schmitt and K. Winzer, 1987b, *J. Magn. Magn. Mater.* **69**, 158.
- Bauer, E., R. Hauser, E. Gratz, G. Schandy, M. Rotter, A. Lindenbauer, D. Gignoux and D. Schmitt, 1993, *Z. Phys. B* **92**, 411.
- Bauer, E., M. Rotter, L. Keller, P. Fischer, M. Ellerby and K.A. McEwen, 1994, *J. Phys.: Condens. Matter* **6**, 5533.
- Bauernfeind, L., W. Widder and H.F. Braun, 1995, *Physica C* **254**, 151.
- Bauernfeind, L., W. Widder and H.F. Braun, 1996, *J. Low Temp. Phys.* **105**, 1605.
- Bellissent, R., F. Hippert, P. Monod and F. Vigneron, 1987, *Phys. Rev. B* **36**, 5540.
- Berger, C., and J.J. Préjean, 1990, *Phys. Rev. Lett.* **64**, 1769.

- Bernal, O.O., 2000, *Phys. Status Solidi b* **220**, 335.
- Bernal, O.O., D.E. MacLaughlin, H.G. Lukefahr and B. Andraka, 1995, *Phys. Rev. Lett.* **75**, 2023.
- Bernal, O.O., D.E. MacLaughlin, A. Amato, R. Feyrherm, F.N. Gygax, A. Schenck, R.H. Heffner, L.P. Le, G.J. Nieuwenhuys, B. Andraka, H. von Löhneysen, O. Stockert and H.R. Ott, 1996, *Phys. Rev. B* **54**, 1300.
- Bernhard, C., C. Niedermayer, U. Binniger, A. Hofer, C. Wenger, J.L. Tallon, G.V.M. Williams, E.J. Ansaldo, J.I. Budnick, C.E. Stronach, D.R. Noakes and M.A. Blankson-Mills, 1995, *Phys. Rev. B* **52**, 10488.
- Bernhard, C., J.L. Tallon, C. Bucci, R. De Renzi, G. Guidi, G.V.M. Williams and C. Niedermayer, 1996, *Phys. Rev. Lett.* **77**, 2304.
- Bernhard, C., J.L. Tallon, C. Niedermayer, T. Blasius, A. Golnik, E. Brücher, R.K. Kremer, D.R. Noakes, C.E. Stronach and E.J. Ansaldo, 1999, *Phys. Rev. B* **59**, 14099.
- Bernhoeft, N., N. Sato, B. Roesli, N. Aso, A. Hiess, G.H. Lander, Y. Endoh and T. Komatsubara, 1998, *Phys. Rev. Lett.* **81**, 4244.
- Berthier, Y., J. Deportes, M. Horvatic and P. Rouault, 1988, *J. Phys. Paris* **49**, C8-261.
- Beveridge, J.L., J. Doornbos and G.M. Garner, 1986, *Hyperfine Interactions* **32**, 907.
- Bevington, P.R., and D.K. Robinson, 1992, *Data Reduction and Error Analysis for the Physical Sciences*, 2nd Ed. (McGraw-Hill, New York).
- Bewley, R.I., S.J. Blundell, B.W. Lovett, T. Jestädt, F.L. Pratt, K.H. Chow, W. Hayes, P.D. Battle, M.A. Green, J.E. Millburn, M.J. Rosseinsky, L.E. Spring and J.F. Vente, 1999, *Phys. Rev. B* **60**, 12286.
- Beyermann, W.P., M.F. Hundley, P.C. Canfield, J.D. Thompson, M. Selsane, C. Godart and M. Latroche, 1991a, *Phys. Rev. Lett.* **66**, 3289.
- Beyermann, W.P., M.F. Hundley, P.C. Canfield, J.D. Thompson, M. Latroche, C. Godart, M. Selsane, Z. Fisk and J.L. Smith, 1991b, *Phys. Rev. B* **43**, 13130.
- Beyermann, W.P., R.H. Heffner, J.L. Smith, M.F. Hundley, P.C. Canfield and J.D. Thompson, 1995, *Phys. Rev. B* **51**, 404.
- Bhatt, R.N., and D.S. Fisher, 1994, *Phys. Rev. Lett.* **68**, 3072.
- Birrer, P., F.N. Gygax, B. Hitti, E. Lippelt, A. Schenck, D. Cattani, J. Cors, M. Decroux, Ø. Fischer and S. Barth, 1988, *Physica C* **153–155**, 751.
- Birrer, P., F.N. Gygax, B. Hitti, E. Lippelt, A. Schenck, D. Cattani, J. Cors, M. Decroux, Ø. Fischer and S. Barth, 1989a, *Hyperfine Interactions* **50**, 503.
- Birrer, P., F.N. Gygax, B. Hitti, E. Lippelt, A. Schenck, M. Weber, S. Barth, F. Hulliger and H.R. Ott, 1989b, *Phys. Rev. B* **39**, 11449.
- Birrer, P., D. Cattani, J. Cors, M. Decroux, Ø. Fischer, F.N. Gygax, B. Hitti, E. Lippelt, A. Schenck and M. Weber, 1990, *Hyperfine Interactions* **63**, 103.
- Birrer, P., F.N. Gygax, B. Hitti, E. Lippelt, A. Schenck, M. Weber, D. Cattani, J. Cors, M. Decroux and Ø. Fischer, 1993, *Phys. Rev. B* **48**, 16589.
- Blagoev, K.B., and L.T. Wille, 1993, *Phys. Rev. B* **48**, 6588.
- Blasco, J., J. García, J.M. de Teresa, P.A. Algarabel and C. Marquina, 1996, *J. Phys.: Condens. Matter* **8**, 7427.
- Bleaney, B., 1973, *Physica B* **69**, 317.
- Block, A., M.M. Abd-Elmeguid and H. Micklitz, 1994, *Phys. Rev. B* **49**, 12365.
- Blount, E.L., C.M. Varma and G. Aeppli, 1990, *Phys. Rev. Lett.* **64**, 3074.
- Boekema, C., R.H. Heffner, R.L. Hutson, M. Leon, M.E. Schillaci, J.L. Smith, S.A. Dodds and D.E. MacLaughlin, 1982, *J. Appl. Phys.* **53**, 2625.
- Boekema, C., R.L. Lichti and K.J. Rugg, 1984, *Phys. Rev. B* **30**, 6766.
- Boekema, C., W.K. Dawson and D.W. Cooke, 1994, *Hyperfine Interactions* **86**, 519.
- Bogenberger, B., and H. von Löhneysen, 1995, *Phys. Rev. Lett.* **74**, 1016.
- Böhm, H., R. Caspary, U. Habel, L. Pawlak, A. Zuber, F. Steglich and A. Loidl, 1988, *J. Magn. Magn. Mater.* **76&77**, 150.
- Bonville, P., 1997, in: *Proc. XXXII Zakopane School of Physics (Condensed Matter Studies by Nuclear Methods)*, eds E.A. Görlich and K. Latka (Jagiellonian University Press, Krakov). See also: *ISIS Annual Report 1994*, A111.
- Bonville, P., P. Bellot, J.A. Hodges, P. Imbert, G. Jéhanno, G. Le Bras, J. Hammann, L. Leylejian, G. Chevrier, P. Thuéry, L. D'Onofrio, A. Hamzic and A. Barthélémy, 1992a, *Physica B* **182**, 105.
- Bonville, P., B. Canaud, J. Hammann, J.A. Hodges, P. Imbert, G. Jéhanno, A. Severing and Z. Fisk, 1992b, *J. Phys. I France* **2**, 459.
- Bonville, P., J.A. Hodges, P. Imbert, G. Le Bras, P. Pari, P. Dalmas de Réotier, A. Yaouanc and P.C.M. Gubbens, 1993, contribution to  $\mu$ SR 1993, Maui, Hawaii, USA, unpublished. Also quoted by Gubbens et al. (1994a) and Schenck and Gygax (1995).

- Bonville, P., A. Ochiai, T. Suzuki and E. Vincent, 1994, *J. Phys. I France* **4**, 595.
- Bonville, P., P. Dalmas de Réotier, A. Yaouanc, G. Polatsck, P.C.M. Gubbens and A.M. Mulders, 1996, *J. Phys.: Condens. Matter* **8**, 7755.
- Bonville, P., G. Le Bras, P. Dalmas de Réotier, A. Yaouanc, R. Calemczuk, C. Paulsen, M. Kasuya and F.G. Aliev, 1997, *Physica B* **230–232**, 266.
- Boothroyd, A.T., A. Longmore, N.H. Anderson, E. Brecht and T. Wolf, 1996, *Phys. Rev. Lett.* **78**, 130.
- Borden, A.I., A. Carne, M. Clarke-Gayther, G.H. Eaton, H.J. Jones, G. Thomas, O. Hartmann and T. Sundquist, 1990, *Nucl. Instrum. Methods A* **292**, 21.
- Boring, A.M., R.C. Albers, G.R. Stewart and D.D. Koelling, 1985, *Phys. Rev. B* **31**, 3251.
- Borsa, F., P. Caretta, J.N. Cho, F.C. Chou, Q. Nu, D.C. Johnston, A. Lascialfari, D.R. Torgeson, R.J. Gooding, N.M. Salem and K.J.E. Vos, 1995, *Phys. Rev. B* **52**, 7334.
- Boucher, B., 1977, *IEEE Trans. Magn.* **MAG-13**, 1601.
- Boucher, B., and P. Chieux, 1991, *J. Phys.: Condens. Matter* **3**, 2207.
- Boucherle, J.X., and J. Schweizer, 1981, *J. Magn. Magn. Mater.* **24**, 308.
- Boukhny, M., G.L. Bullock, B.S. Shivaram and D.G. Hinks, 1994a, *Philos. Mag. Lett.* **69**, 319.
- Boukhny, M., G.L. Bullock, B.S. Shivaram and D.G. Hinks, 1994b, *Phys. Rev. Lett.* **73**, 1707.
- Boukhny, M., G.L. Bullock and B.S. Shivaram, 1994c, *Phys. Rev. B* **50**, 8985.
- Bourdarot, F., P. Burlet, R. Calemczuk, F. Lapierre, K. Mattenberger and O. Vogt, 1997, presented at 27me Journées des Actinides, Dijon, France (unpublished).
- Bouvet, A., T. Kasuya, M. Bonnet, L.P. Regnault, J. Rossat-Mignod, F. Iga, B. Fåk and A. Severing, 1998, *J. Phys.: Condens. Matter* **10**, 5667.
- Brandt, E.H., 1995, *Rep. Prog. Phys.* **58**, 1465.
- Braun, H.F., and J.L. Jorda, 1985, *Physica B* **135**, 72.
- Bredl, C.D., F. Steglich and K.D. Schotte, 1978, *Z. Phys. B* **29**, 327.
- Brewer, J.H., K.M. Crowe, F.N. Gyax and A. Schenck, 1975, in: *Muon Physics*, eds V.W. Hughes and C.S. Wu (Academic Press, New York).
- Brewer, J.H., S.R. Kreitzman, D.R. Noakes, E.J. Ansaldo, D.R. Harshman and R. Keitel, 1986, *Phys. Rev. B* **33**, 7813.
- Brewer, J.H., R.F. Kiefl, J.F. Carolan, P. Dosanjh, W.N. Hardy, S.R. Kreitzman, Q. Li, T.M. Riseman, P. Schleger, H. Zhou, E.J. Ansaldo, D.R. Noakes, L.P. Le, G.M. Luke, Y.J. Uemura, K. Hepburn-Wiley and C.E. Stronach, 1990, *Hyperfine Interactions* **63**, 177.
- Brinkmann, M., T. Rex, H. Bach and K. Westerholt, 1995, *Phys. Rev. Lett.* **74**, 4927.
- Brisson, J.P., N. Keller, A. Vernière, P. Lejay, L. Schmidt, A.I. Buzdin, J. Flouquet, S.R. Julian and G.G. Lonzarich, 1995, *Physica C* **250**, 128.
- Broholm, C., J.K. Kjems, W.J.L. Buyers, P. Matthews, T.T.M. Palstra, A.A. Menovsky and J.A. Mydosh, 1987, *Phys. Rev. Lett.* **58**, 1467.
- Broholm, C., G. Aeppli, R.N. Kleiman, D.R. Harshman, D.J. Bishop, E. Bucher, D.L. Williams, E.J. Ansaldo and R.H. Heffner, 1990, *Phys. Rev. Lett.* **65**, 2062.
- Brown, P.J., B. Ouladdiaf, R. Ballou, J. Deportes and A.S. Markosyan, 1992, *J. Phys.: Condens. Matter* **4**, 1103.
- Brown, P.J., J. Crangle, K.U. Neumann, J.G. Smith and K.R.A. Ziebeck, 1997, *J. Phys.: Condens. Matter* **9**, 4729.
- Brückl, A., K. Neumaier, Ch. Probst, K. Andres, S.J. Flaschin, A. Kratzer, G.M. Kalvius and T. Takabatake, 1997, *Physica B* **240**, 199.
- Brugger, T., T. Schreiner, G. Roth, P. Adelmann and G. Czjzek, 1993, *Phys. Rev. Lett.* **71**, 2481.
- Büchner, B., M. Breuer, A. Freimuth and A.P. Kampf, 1994, *Phys. Rev. Lett.* **73**, 1841.
- Budnick, J.I., A. Golnik, C. Niedermayer, E. Recknagel, M. Rossmannith, A. Weidinger, B. Chamberland, M. Filipkowski and D.P. Yang, 1987, *Phys. Lett.* **124A**, 103.
- Bull, M.J., K.A. McEwen and R.S. Eccleston, 1998, *Phys. Rev. B* **57**, 3850.
- Burghart, F.J., 1994, Diplom Thesis (Physics Department, TU Munich) unpublished. See also ISIS Annual Report 1996, A138.
- Burlet, P., S. Quezel, J. Rossat-Mignod and O. Vogt, 1984, presented at Symp. on Neutron Scattering, Pub: HMI-B411 (Hahn-Meitner Institut, Berlin).
- Burlet, P., J. Rossat-Mignod, S. Quezel, O. Vogt, J.C. Spirlet and J. Rebizant, 1986, *J. Less-Common Met.* **121**, 121.
- Buschow, K.H.J., 1991, *J. Magn. Magn. Mater.* **100**, 79.
- Buschow, K.H.J., and H.J. van Daal, 1972, *AIP Conf. Proc.* **5**, 1464.
- Buschow, K.H.J., U. Goebel and E. Dormann, 1979, *Phys. Status Solidi b* **93**, 607.



- Butz, T., J. Chappert, J.F. Dufresne, O. Hartmann, E. Karlsson, B. Lindgren, L.O. Norlin, P. Podini and A. Yaouanc, 1980, *Phys. Lett.* **75A**, 321.
- Butz, T., G.M. Kalvius, B. Lindgren, O. Hartmann, R. Wäppling and E. Karlsson, 1986, *Hyperfine Interactions* **32**, 881.
- Buyers, W.J.L., and T.M. Holden, 1985, in: *Handbook on the Physics and Chemistry of the Actinides*, Vol. 2, eds A.J. Freeman and G.H. Lander (North-Holland, Amsterdam), p. 239.
- Buyers, W.J.L., Z. Tun, T. Petersen, T.E. Mason, J.G. Lussier, B.D. Gaulin and A.A. Menovsky, 1994, *Physica B* **199&200**, 95.
- Cable, J.W., and E.O. Wollan, 1968, *Phys. Rev.* **165**, 733.
- Caciuffo, R., G.H. Lander, J.C. Spirlet, J.M. Fournier and W.F. Kuhs, 1987, *Solid State Commun.* **64**, 149.
- Caciuffo, R., G. Amoretti, A. Blaise, J.M. Fournier, M.T. Hutchings, G.H. Lander, R. Osborn, A. Severing and A.D. Taylor, 1992, *Physica B* **180&181**, 149.
- Camani, M., F.N. Gyax, E. Klempt, W. Ruegg, A. Schenck, R. Schulze and H. Wolf, 1978, *Phys. Lett.* **77B**, 326.
- Campbell, I.A., 1984, *J. Phys. France Lett.* **45**, L27.
- Campbell, I.A., 1999, in: *Muon Science*, eds S.L. Lee, S.H. Kilcoyne and R. Cywinski (Institute of Physics Publishing, Bristol) p. 137.
- Campbell, I.A., A. Amato, F.N. Gyax, D. Herlach, A. Schenck, R. Cywinski and S.H. Kilcoyne, 1994, *Phys. Rev. Lett.* **72**, 1291.
- Cao, G., S. McCall, F. Freibert, M. Shepard, P. Henning, J.E. Crow and B. Andraka, 1995a, *Phys. Rev. B* **52**, 71.
- Cao, G., Y. Qian, Z. Chen and Y. Zhang, 1995b, *J. Phys. Chem. Solids* **56**, 981.
- Caspary, R., P. Hellmann, M. Keller, G. Sparn, C. Wassilev, R. Köhler, C. Geibel, C. Schank, F. Steglich and N.E. Phillips, 1993, *Phys. Rev. Lett.* **71**, 2146.
- Castro Neto, A.H., G. Castilla and B.A. Jones, 1998, *Phys. Rev. Lett.* **81**, 3531.
- Caudron, R., H. Bouchiat, P.J. Brown, P. Monod and J.L. Tholence, 1988, *J. Phys. Paris* **49**, C8-363.
- Cava, R.J., R.B. van Dover, B. Batlogg and E.A. Reitman, 1987a, *Phys. Rev. Lett.* **58**, 408.
- Cava, R.J., B. Batlogg, R.B. van Dover, D.W. Murphy, S. Sunshine, T. Siegrist, J.P. Remeika, E.A. Reitman, S. Zahurak and G.P. Espinosa, 1987b, *Phys. Rev. Lett.* **58**, 1676.
- Cava, R.J., B. Batlogg, T. Siegrist, J.J. Krajewski, W.F. Peck Jr, S. Carter, R.J. Felder, H. Takagi and R.B. van Dover, 1994, *Phys. Rev. B* **49**, 12384.
- Chakhalian, J.A., S.R. Dunsiger, R.F. Kiefl, W.A. MacFarlane, J.E. Sonier, B. Hitti and J. Fischer, 1997, *Hyperfine Interactions* **106**, 245.
- Chang, L.J., C.V. Tomy, D.M. Paul and C. Ritter, 1996, *Phys. Rev. B* **54**, 9031.
- Chappert, J., 1982, in: *Magnetism of Metals and Alloys*, ed. M. Cyrot (North-Holland, Amsterdam) p. 487.
- Chappert, J., 1984, in: *Muons and Pions in Materials Research*, eds J. Chappert and R.I. Grynszpan (North-Holland, Amsterdam) p. 35.
- Chappert, J., G.M. Kalvius, L. Asch, A. Yaouanc, O. Hartmann, L.O. Norlin and E. Karlsson, 1981, *Hyperfine Interactions* **9**, 595.
- Chappert, J., L. Asch, M. Bogé, G.M. Kalvius and B. Boucher, 1982, *J. Magn. Magn. Mater.* **28**, 124.
- Chappert, J., A. Yaouanc, O. Hartmann, E. Karlsson, E. Wäckelgård, R. Wäppling, L. Asch and G.M. Kalvius, 1986, *Hyperfine interactions* **31**, 331.
- Charrier, B., and D. Schmitt, 1997, *J. Magn. Magn. Mater.* **171**, 106.
- Charrier, B., B. Ouladdiaf and D. Schmitt, 1997, *Phys. Rev. Lett.* **78**, 4637.
- Charrier, B., S.P. Cottrell and D. Schmitt, 1999, *Physica B* **266**, 165.
- Chatterji, T., and W. Henggeler, 1998, *Annual Report 1997, Annex 1* (Paul Scherrer Institute, Villigen, unpublished) p. 41.
- Chattopadhyay, T., P.J. Brown, B.C. Sales, L.A. Boatner, H.A. Mook and H. Maletta, 1989, *Phys. Rev. B* **40**, 2624.
- Chattopadhyay, T., C.A. Scott and H. von Löhneysen, 1995, *J. Magn. Magn. Mater.* **140-144**, 1259.
- Chau, R., M.B. Maple and R.A. Robinson, 1998, *Phys. Rev. B* **58**, 139.
- Chen, H.H., and P.M. Levy, 1971, *Phys. Rev. Lett.* **27**, 1383, 1385.
- Chevalier, B., J. Etourneau, P. Hagenmuller, S. Quezel and J. Rossat-Mignod, 1985, *J. Less-Common Met.* **111**, 161.
- Cho, B.K., M. Xu, P.C. Canfield, L.L. Miller and D.C. Johnston, 1995, *Phys. Rev. B* **52**, 3676.
- Cho, B.K., P.C. Canfield and D.C. Johnston, 1996, *Phys. Rev. B* **53**, 8499.
- Chow, K.H., R.F. Kiefl, W.A. MacFarlane, J.W. Schneider, D.W. Cooke, M. Leon, M. Paciotti, T.L. Estle, B. Hitti, R.L. Lichti, S.F.J. Cox, C. Schwab,

- E.A. Davis, A. Morrobel-Sosa and L. Zavich, 1995, *Phys. Rev. B* **51**, 14762.
- Chow, K.H., P.A. Pattenden, S.J. Blundell, W. Hayes, F.L. Pratt, T. Jestädt, M.A. Green, J.E. Millburn, M.J. Rosseinsky, B. Hitti, S.R. Dunsiger, R.F. Kiefl, C.H. Chen and A.J.S. Chowdhury, 1996, *Phys. Rev. B* **53**, R14725.
- Clinton, T.W., J.W. Lynn, J.Z. Liu, Y.X. Jia and R.N. Shelton, 1993, *Physica C* **217**, 53.
- Coles, B.R., 1996, *Physica B* **223&224**, 260.
- Coles, B.R., J.Y. Ping and M.H. Bennet, 1984, *Philos. Mag.* **B 52**, 1.
- Commings, E.D., 1973, *Weak Interactions* (McGraw-Hill, New York).
- Cooke, D.W., R.H. Heffner, R.L. Hutson, M.E. Schillaci, J.L. Smith, J.O. Willis, D.E. MacLaughlin, C. Boekema, R.L. Lichti, A.B. Denison and J. Oostens, 1986, *Hyperfine Interactions* **31**, 425.
- Cooke, D.W., R.L. Hutson, R.S. Kwok, M. Maez, H.D. Rempp, M.E. Schillaci, J.L. Smith, J.O. Willis, R.L. Lichti, K.C.B. Chan, C. Boekema, S.P. Weathersby, J.A. Flint and J. Oostens, 1988, *Phys. Rev. B* **37**, 9401.
- Cooke, D.W., R.L. Hutson, R.S. Kwok, M. Maez, H.D. Rempp, M.E. Schillaci, J.L. Smith, J.O. Willis, R.L. Lichti, K.C.B. Chan, C. Boekema, S.P. Weathersby and J. Oostens, 1989, *Phys. Rev. B* **39**, 2748.
- Cooke, D.W., R.S. Kwok, R.L. Lichti, T.R. Adams, C. Boekema, W.K. Dawson, A. Kebede, J. Schwegler, J.E. Crow and T. Mihalisin, 1990, *Phys. Rev. B* **41**, 4801.
- Cooke, D.W., J.L. Smith, S.J. Blundell, K.H. Chow, P.A. Pattenden, F.L. Pratt, S.F.J. Cox, S.R. Brown, A. Morrobel-Sosa, R.L. Lichti, L.C. Gupta, R. Nagarajan, Z. Hossain, C. Mazumdar and C. Godart, 1995, *Phys. Rev. B* **52**, R3864.
- Cooke, D.W., B.L. Bennett, A.C. Lawson, J.G. Huber, J. Oostens, C. Boekema, J.A. Flint and R.L. Lichti, 1996, *Philos. Mag. B* **74**, 259.
- Cooper, B.R., and Y.-L. Lin, 1998, *J. Appl. Phys.* **83**, 6432.
- Cooper, B.R., R. Siemann, D. Yang, P. Thayamballi and A. Bannerjea, 1985, in: *Handbook on the Physics and Chemistry of the Actinides*, Vol. 2, eds A.J. Freeman and G.H. Lander (North-Holland, Amsterdam) p. 435.
- Cooper, B.R., O. Vogt, Q.-G. Sheng and Y.-L. Lin, 1999, *Philos. Mag. B* **79**, 683.
- Corner, W.D., and B.K. Tanner, 1976, *J. Phys. C* **9**, 627.
- Cottenier, S., S. Demuyne, D. Kaczorowski, J.C. Spirlet and M. Rots, 1998, *J. Phys.: Condens. Matter* **10**, 8381.
- Cottrell, S.P., C.A. Scott and B. Hitti, 1997, *Hyperfine Interactions* **106**, 251.
- Cowley, R.A., and S. Bates, 1988, *J. Phys. C* **21**, 4113.
- Cox, D.E., G. Shirane, S.M. Shapiro, G. Aeppli, Z. Fisk, J.L. Smith, J.K. Kjems and H.R. Ott, 1986, *Phys. Rev. B* **33**, 3614.
- Cox, D.L., 1987, *Phys. Rev. Lett.* **59**, 1240.
- Cox, D.L., 1993, *Physica B* **186-188**, 312.
- Cox, D.L., and M. Jarrell, 1996, *J. Phys.: Condens. Matter* **8**, 9825.
- Cox, D.L., N.E. Bickers and J.W. Wilkins, 1985, *J. Appl. Phys.* **57**, 3166.
- Cox, S.F.J., 1987, *J. Phys.: Condens. Matter* **20**, 3187.
- Cox, S.F.J., 1999, in: *Muon Science*, eds S.L. Lee, S.H. Kilcoyne and R. Cywinski (Institute of Physics Publishing, Bristol) p. 239.
- Cox, S.F.J., and M.C.R. Symons, 1986, *Hyperfine Interactions* **32**, 689.
- Crawford, M.K., R.L. Harlow, E.M. McCarron, W.E. Farneth, J.D. Axe, H. Chou and Q. Huang, 1991, *Phys. Rev. B* **44**, 7749.
- Cristofolini, L., A. Lappas, K. Prassides, K. Vavekis and M. Buchgeister, 1997, *Hyperfine Interactions* **104**, 61.
- Crook, M.R., and R. Cywinski, 1997, *J. Phys.: Condens. Matter* **9**, 1449.
- Cywinski, R., and B.D. Rainford, 1992, *J. Magn. Magn. Mater.* **104-107**, 1424.
- Cywinski, R., and B.D. Rainford, 1994, *Hyperfine Interactions* **85**, 215.
- Cywinski, R., S.H. Kilcoyne, S.F.J. Cox, C.A. Cox and O. Schärpf, 1990, *Hyperfine Interactions* **64**, 427.
- Cywinski, R., S.H. Kilcoyne and C.A. Scott, 1991, *J. Phys.: Condens. Matter* **3**, 6473.
- Cywinski, R., Z.P. Han, R.I. Bewley, R. Cubitt, M.T. Wylie, E.M. Forgan, S.L. Lee, M. Warden and S.H. Kilcoyne, 1994a, *Physica C* **233**, 273.
- Cywinski, R., S.H. Kilcoyne, T. Holubar and G. Hilscher, 1994b, *Hyperfine Interactions* **85**, 221.
- Cywinski, R., B.R. Coles, S.H. Kilcoyne and J.G. Park, 1995, *Physica B* **206&207**, 412.
- Cywinski, R., P.M. Bentley, A.D. Brisford and J.S. Lord, 1999, *ISIS Annual Report 1998*, RB10274.
- Dai, P., H.A. Mook, C.L. Seaman, M.B. Maple and J.P. Koster, 1995, *Phys. Rev. Lett.* **75**, 1202.
- Dalichaouch, Y., M.B. Maple, M.S. Torikachvili and A.L. Giorgi, 1989, *Phys. Rev. B* **39**, 2433.

- Dalichaouch, Y., M.C. de Andrade and M.B. Maple, 1992, *Phys. Rev. B* **46**, 8671.
- Dalichaouch, Y., M.C. de Andrade and M.B. Maple, 1993, *Physica C* **218**, 309.
- Dalmas de Réotier, P., and A. Yaouanc, 1994, *Phys. Rev. Lett.* **72**, 290.
- Dalmas de Réotier, P., and A. Yaouanc, 1995, *Phys. Rev. B* **52**, 9155.
- Dalmas de Réotier, P., and A. Yaouanc, 1997, *J. Phys.: Condens. Matter* **9**, 9113.
- Dalmas de Réotier, P., B. Licciardi, A. Yaouanc, B. Chevalier, P. Chaudouët, R. Madar and J.P. Sanchez, 1989, preprint (unpublished).
- Dalmas de Réotier, P., J.P. Sanchez, A. Yaouanc, B. Chevalier, P. Chaudouët and R. Madar, 1990a, *Hyperfine Interactions* **64**, 457.
- Dalmas de Réotier, P., J.P. Sanchez, A. Yaouanc, S.W. Harris, O. Hartmann, E. Karlsson, R. Wäppling, B. Barbara and P. L'Héritier, 1990b, *Hyperfine Interactions* **64**, 383.
- Dalmas de Réotier, P., J.P. Sanchez, A. Yaouanc, S.W. Harris, O. Hartmann, E. Karlsson, R. Wäppling, D. Gignoux, B. Gorges, D. Schmitt, P. L'Héritier, A. Weidinger and P.C.M. Gubbens, 1990c, *Hyperfine Interactions* **64**, 389.
- Dalmas de Réotier, P., A. Yaouanc, P.C.M. Gubbens, D. Gignoux, B. Gorges, D. Schmitt, O. Hartmann, R. Wäppling and A. Weidinger, 1992, *J. Magn. Magn. Mater.* **104–107**, 1267.
- Dalmas de Réotier, P., A. Yaouanc and E. Frey, 1994a, *Phys. Rev. B* **50**, 3033.
- Dalmas de Réotier, P., A. Yaouanc, P.C.M. Gubbens and B. Chevalier, 1994b, *Hyperfine Interactions* **85**, 227.
- Dalmas de Réotier, P., A.D. Huxley, A. Yaouanc, J. Flouquet, P. Bonville, P. Imbert, P. Pari, P.C.M. Gubbens and A.M. Mulders, 1995, *Phys. Lett. A* **205**, 239.
- Dalmas de Réotier, P., A. Yaouanc and P. Bonville, 1996, *J. Phys.: Condens. Matter* **8**, 5113.
- Dalmas de Réotier, P., A. Yaouanc, R. Calemczuk, A.D. Huxley, C. Marcenat, P. Bonville, P. Lejay, P.C.M. Gubbens and A.M. Mulders, 1997, *Phys. Rev. B* **55**, 2737.
- Dalmas de Réotier, P., A.D. Huxley, A. Yaouanc, J. Flouquet, C.T. Kaiser, A.M. Mulders, P.C.M. Gubbens, A. Amato, F.N. Gygax, M. Pinkpank and A. Schenck, 1998a, Annual Report 1997, Annex 1 (Paul Scherrer Institute, Villigen, unpublished) p. 39.
- Dalmas de Réotier, P., A. Yaouanc, P.C.M. Gubbens and C.T. Kaiser, 1998b, ISIS Annual Report 1998, RB 364.
- Dalmas de Réotier, P., A. Yaouanc, R.H. Heffner, J.L. Smith, P.C.M. Gubbens and C.T. Kaiser, 2000a, *Phys. Rev. B* **61**, 6377.
- Dalmas de Réotier, P., A. Yaouanc, P.C.M. Gubbens, C.T. Kaiser, A.M. Mulders, F.N. Gygax, A. Schenck, A. Amato, C. Baines, A. de Visser, R.J. Keiser, P. Bonville, P.J.C. King, A.D. Huxley and A.A. Menovsky, 2000b, *Physica B* **289–290**, 10.
- Dann, J.A., A.D. Hillier, J.G.M. Armitage and R. Cywinski, 2000, *Physica B* **289–290**, 38.
- Dattagupta, S., 1989, *Hyperfine Interactions* **49**, 253.
- Daudin, B., R. Langier and B. Salce, 1982, *J. Magn. Magn. Mater.* **27**, 315.
- Davis, E.A., and S.F.J. Cox, 1996, *Protons and Muons in Materials Science* (Taylor and Francis, London).
- Dawson, W.K., K. Tibbs, S.P. Weathersby, C. Boekema and K.C.B. Chan, 1988, *J. Appl. Phys.* **64**, 5809.
- Dawson, W.K., C.H. Halim, S.P. Weathersby, J.A. Flint, J.C. Lam, T.J. Hoffman, C. Boekema, K.C.B. Chan, R.L. Lichti, D.W. Cooke, M.S. Jahan and J.E. Crow, 1990, *Hyperfine Interactions* **63**, 219.
- Dawson, W.K., J.C. Lam, C. Boekema, R.L. Lichti, D.W. Cooke and J.E. Crow, 1991, *J. Appl. Phys.* **69**, 5385.
- de Groot, P.A.J., R.A. Rose and B.D. Rainford, 1994, *Hyperfine Interactions* **69**, 591.
- de Groot, R.A., D.D. Koelling and M. Weger, 1985, *Phys. Rev. B* **32**, 2659.
- De Renzi, R., 1999, in: *Muon Science*, eds S.L. Lee, S.H. Kilcoyne and R. Cywinski (Institute of Physics Publishing, Bristol) p. 211.
- De Renzi, R., G. Guidi, C. Bucci, P. Podini, R. Tedeschi and S.F.J. Cox, 1984, *Hyperfine Interactions* **17–19**, 479.
- De Renzi, R., G. Guidi, P. Carretta, G. Calestani and S.F.J. Cox, 1989, *Phys. Lett. A* **135**, 132.
- De Renzi, R., G. Guidi, C. Bucci, R. Tedeschi and G. Calestani, 1990, *Hyperfine Interactions* **63**, 295.
- De Renzi, R., G. Guidi, C. Bucci, R. Tedeschi and F.C. Maccotta, 1994, *Physica C* **235–240**, 1847.
- de Teresa, J.M., C. Ritter, M.R. Ibarra, P.A. Algarabel, J.L. García-Muñoz, J. Blasco, J. García and C. Marquina, 1997, *Phys. Rev. B* **56**, 3317.
- de Visser, A., J.C.P. Klaasse, M. van Sprang, J.J.M. Franse, A.A. Menovsky and T.T.M. Palstra, 1986a, *J. Magn. Magn. Mater.* **54–57**, 375.

- de Visser, A., F.E. Kayzel, A.A. Menovsky, J.J.M. Franse, J. van den Berg and G.J. Nieuwenhuys, 1986b, *Phys. Rev. B* **34**, 8168.
- de Visser, A., A.A. Menovsky and J.J.M. Franse, 1987, *Physica B* **147**, 81.
- de Visser, A., N.H. van Dijk, J.J.M. Franse, A. Lacerda, J. Flouquet, Z. Fisk and J.L. Smith, 1992, *J. Magn. Magn. Mater.* **108**, 56.
- de Visser, A., R.J. Keizer, A.A. Menovsky, M. Mihalik, F.S. Tautz, J.J.M. Franse, B. Fåk, N.H. van Dijk, J. Flouquet, J. Bossy and S. Pujol, 1997a, *Physica B* **230–232**, 49.
- de Visser, A., R.J. Keizer, R. van Harrevelt, A.A. Menovsky, J.J.M. Franse, A. Amato, F.N. Gygax, M. Pinkpank and A. Schenck, 1997b, *Physica B* **230–232**, 53.
- de Visser, A., R.J. Keizer, M.J. Graf, A.A. Menovsky and J.J.M. Franse, 1998a, *J. Magn. Magn. Mater.* **177–181**, 287.
- de Visser, A., R.J. Keizer, R. van Harrevelt, A.A. Menovsky, J.J.M. Franse, A. Amato, F.N. Gygax, M. Pinkpank and A. Schenck, 1998b, *J. Magn. Magn. Mater.* **177–181**, 435.
- de Visser, A., M.J. Graf, P. Estrela, A. Amato, C. Baines, D. Andreica, F.N. Gygax and A. Schenck, 2000, *Phys. Rev. Lett.* **85**, 3005.
- De'Bell, K., and J.P. Whitehead, 1991, *J. Phys.: Condens. Matter* **3**, 2431.
- Demazeau, G., A. Marbeuf, M. Pouchard and P. Hagenmuller, 1971, *J. Solid State Chem.* **3**, 582.
- Denison, A.B., 1984, *J. Appl. Phys.* **55**, 2278.
- Denison, A.B., H. Graf, W. Kündig and P.F. Meier, 1979, *Helv. Phys. Acta* **52**, 460.
- Deportes, J., and D. Givord, 1976, *Solid State Commun.* **19**, 845.
- Deportes, J., B. Ouladdiaf and K.R.A. Ziebeck, 1987, *J. Phys. Paris* **48**, 1029.
- Dervenagas, P., J. Zaretsky, C. Stassis, A.I. Goldman, P.C. Canfield and B.K. Cho, 1996, *Phys. Rev. B* **53**, 8506.
- Didisheim, F.F., K. Yvon, P. Fischer and D. Shaltiel, 1980, *J. Less-Common Met.* **73**, 355.
- Dilley, N.R., J. Herrmann, S.H. Han, M.B. Maple, S. Spagna, J. Diederichs and R.E. Sager, 1996, *Physica C* **265**, 150.
- Dillon Jr, J.F., 1963, in: *Magnetism*, Vol. III, eds G.T. Rado and H. Suhl (Academic Press, New York).
- Dirkmaat, A.J., T. Endstra, E.A. Knetsch, A.A. Menovsky, G.J. Nieuwenhuys and J.A. Mydosh, 1990, *Europhys. Lett.* **11**, 275.
- Dobrosavljević, V., T.R. Kirkpatrick and G. Kotliar, 1992, *Phys. Rev. Lett.* **69**, 1113.
- Dommann, A., H.R. Ott, F. Hulliger and P. Fischer, 1990, *J. Less-Common Met.* **160**, 171.
- Doniach, S., 1977, *Physica B* **91**, 231.
- Doniach, S., and P. Fazekas, 1992, *Philos. Mag.* **65**, 1171.
- Dönni, A., P. Fischer, B. Roessli and H. Kitazawa, 1994, *Z. Phys. B* **93**, 449.
- Drescher, K., and M.M. Abd-Elmeguid, 1995, *Physica B* **206&207**, 14.
- Duginov, V.N., K.I. Gritsaj, A. Amato, C. Baines, D. Herlach, V.Yu. Pomjakushin, U. Zimmermann, A.N. Ponomarev, I.A. Krivosheev, A.A. Neshivov, A.V. Gribanov, A.V. Nikiforov and Yu.D. Seropegin, 2000, *Physica B* **289–290**, 43.
- Duh, H.M., I.S. Lyubutin, I.M. Jiang, G.H. Hwang and K.D. Lain, 1996, *J. Magn. Magn. Mater.* **153**, 86.
- Dunlap, B.D., and G.M. Kalvius, 1985, in: *Handbook on the Physics and Chemistry of the Actinides*, Vol. 2, eds A.J. Freeman and G.H. Lander (North-Holland, Amsterdam) p. 329.
- Dunlap, B.D., G.M. Kalvius, D.J. Lam and M.B. Brodsky, 1968, *J. Phys. Chem. Solids* **29**, 1365.
- Dunlap, B.D., M.B. Brodsky, G.M. Kalvius, G.K. Shenoy and D.J. Lani, 1969, *J. Appl. Phys.* **40**, 1495.
- Dunlap, B.D., L.N. Hall, F. Behroozi, G.W. Crabtree and D.G. Niarchos, 1984, *Phys. Rev. B* **29**, 6244.
- Dunsiger, S.R., R.F. Kiefl, K.H. Chow, B.D. Gaulin, M.J.P. Gingras, J.E. Greedan, A. Keren, K.M. Kojima, G.M. Luke, W.A. MacFarlane, N.P. Raju, J.E. Sonier, Y.J. Uemura and W.D. Wu, 1996a, *J. Appl. Phys.* **79**, 6636.
- Dunsiger, S.R., R.F. Kiefl, K.H. Chow, B.D. Gaulin, M.J.P. Gingras, J.E. Greedan, A. Keren, K.M. Kojima, G.M. Luke, W.A. MacFarlane, N.P. Raju, J.E. Sonier, Y.J. Uemura and W.D. Wu, 1996b, *Phys. Rev. B* **54**, 9019.
- Dunsiger, S.R., R.F. Kiefl, K.H. Chow, B.D. Gaulin, M.J.P. Gingras, J.E. Greedan, A. Keren, K.M. Kojima, G.M. Luke, W.A. MacFarlane, N.P. Raju, J.E. Sonier, Y.J. Uemura and W.D. Wu, 1997, *Hyperfine Interactions* **104**, 275.
- Dunsiger, S.R., J.S. Gardner, J.A. Chakhalian, A.L. Cornelius, M. Jaime, R.F. Kiefl, R. Movshovich, W.A. MacFarlane, R.I. Miller, J.E. Sonier and B.D. Gaulin, 2000, *Phys. Rev. Lett.* **85**, 3504.
- Dürkop, D., E. Braun, B. Politt, H. Schmidt, B. Roden and D. Wohlleben, 1986, *Z. Phys. B* **63**, 55.

- Dwight, A.E., 1976, in: Proc. 12th Rare Earth Research Conf., ed. C.E. Lundin (Denver Research Institute, Denver, CO) p. 480.
- Eaton, G.H., and S.H. Kilcoyne, 1999, in: Muon Science, eds S.L. Lee, S.H. Kilcoyne and R. Cywinski (Institute of Physics Publishing, Bristol) p. 11.
- Eaton, G.H., A. Carne, S.F.J. Cox, J.D. Davis, R. De Renzi, O. Hartmann, A. Kratzer, C. Ristori, C.A. Scott, G.C. Stirling and T. Sundquist, 1988, Nucl. Instrum. Methods **A296**, 463.
- Eaton, G.H., C.A. Scott and W.G. Williams, 1994, Hyperfine Interactions **87**, 1099.
- Eccleston, R.S., S.R. Brown and S.B. Palmer, 1995, J. Magn. Magn. Mater. **140–144**, 745.
- Echizen, Y., K. Umeo, S. Hamashimi, T. Fujita, T. Takabatake, N. Kobayashi and I. Oguro, 2000, Solid State Commun. **115**, 587.
- Effantin, J.M., J. Rossat-Mignod, P. Burlet, H. Bartholin, S. Kunii and T. Kasuya, 1985, J. Magn. Magn. Mater. **47&48**, 145.
- Eibschütz, M., S. Shtrikman and D. Treves, 1967, Phys. Rev. **156**, 562.
- Eibschütz, M., M.E. Lines, H.S. Chen and J.V. Waszczak, 1988, Phys. Rev. B **38**, 10038.
- Einzel, D., P.J. Hirschfeld, F. Gross, B.S. Chandrasekhar, K. Andres, H.R. Ott, J. Beuers, Z. Fisk and J.L. Smith, 1986, Phys. Rev. Lett. **56**, 2513.
- Eisaki, H., H. Takagi, R.J. Cava, B. Batlogg, J.J. Krajewski, W.F. Peck Jr, K. Mizuhashi, J.O. Lee and S. Uchida, 1994, Phys. Rev. B **50**, 647.
- Ekström, M., O. Hartmann, A. Marelius, R. Wäppling, E. Schreier, S. Henneberger, A. Kratzer and G.M. Kalvius, 1996, Hyperfine Interactions **C1**, 57.
- Ekström, M., O. Hartmann, A. Marelius, R. Wäppling, E. Schreier, S. Henneberger, A. Kratzer and G.M. Kalvius, 1997, Hyperfine Interactions **104**, 281.
- Eom, D.H., M. Ishikawa, J. Kitagawa and N. Takeda, 1998, J. Phys. Soc. Japan **67**, 2495.
- Erdős, P., G. Solt, Z. Zolnierak, A. Blaise and J.M. Fourmier, 1980, Physica B **120**, 164.
- Eriksen, M., E.M. Forgan, C.M. Muirhead and R.C. Young, 1983, J. Phys. F **13**, 929.
- Estrela, P., A. de Visser, F.R. de Boer, G.J. Nieuwenhuys, L.C.P. Pereira and M. Almeida, 1999, Physica B **259–261**, 409.
- Eyring, L., 1979, in: Handbook on the Physics and Chemistry of Rare Earths, Vol. 3, eds K.A. Gschneidner Jr and L. Eyring (North-Holland, Amsterdam) p. 337.
- Fåk, B., C. Vettier, J. Flouquet, F. Bourdarot, S. Raymond, A. Vernière, P. Lejay, P. Boutrouille, N. Bernhoeft, S.T. Bramwell, R.A. Fischer and N.E. Phillips, 1996, J. Magn. Magn. Mater. **154**, 339.
- Fauth, F., U. Staub, M. Guillaume, J. Mesot, A. Furrer, P. Dosanjh, H. Zhou and P. Vorderwisch, 1995, J. Phys.: Condens. Matter **7**, 4215.
- Fehrenbacher, R., and T.M. Rice, 1993, Phys. Rev. Lett. **70**, 3471.
- Felcher, G.P., T.O. Brun, R.J. Gambino and M. Kuzniec, 1973, Phys. Rev. B **8**, 260.
- Felder, E., A. Bernasconi, H.R. Ott, Z. Fisk and J.L. Smith, 1989, Physica C **162–164**, 429.
- Felner, I., and I. Nowik, 1986, J. Magn. Magn. Mater. **58**, 169.
- Felner, I., M. Sch, M. Rakavy and I. Nowik, 1981, J. Phys. Chem. Solids **42**, 369.
- Ferreira, J.M., B.W. Lee, Y. Dalichaouch, M.S. Torikachvili, K.N. Yang and M.B. Maple, 1988, Phys. Rev. B **37**, 1580.
- Ferreira, L.P., R. Guillen, P. Vulliet, A. Yaouanc, D. Fruchart, P. Wolfers, P.L. Heritier and R. Fruchart, 1985, J. Magn. Magn. Mater. **53**, 145.
- Fesenko, V.I., V.N. Gorbunov and V.P. Smilga, 1991, Physica C **176**, 551.
- Feyerherm, R., 1995, Ph.D. Thesis (ETH Zurich).
- Feyerherm, R., A. Amato, C. Geibel, F.N. Gygax, T. Komatsubara, N. Sato, A. Schenck and F. Steglich, 1994a, Physica B **199**, 103.
- Feyerherm, R., A. Amato, F.N. Gygax, A. Schenck, C. Geibel, F. Steglich, N. Sato and T. Komatsubara, 1994b, Phys. Rev. Lett. **73**, 1849.
- Feyerherm, R., A. Amato, F.N. Gygax, A. Schenck, Y. Ōnuki and N. Sato, 1994c, Physica B **194**, 357.
- Feyerherm, R., A. Amato, A. Grayevsky, F.N. Gygax, N. Kaplan and A. Schenck, 1995, Z. Phys. B **99**, 3.
- Feyerherm, R., A. Amato, C. Geibel, F.N. Gygax, P. Hellmann, R.H. Heffner, D.E. MacLaughlin, R. Müller-Reisener, G.J. Nieuwenhuys, A. Schenck and F. Steglich, 1997, Phys. Rev. B **56**, 699.
- Fischer, H., 1984, Hyperfine Interactions **17–19**, 751.
- Fischer, Ø., and M.B. Maple, eds, 1982, Superconductivity in Ternary Compounds, 2 volumes (Springer, Berlin).
- Fish, G.E., J.J. Rhyne, S.G. Sonkar and W.E. Wallace, 1979, J. Appl. Phys. **50**, 2003.
- Fisher, R.A., G.E. Brodale, E.W. Hornung and W.F. Giaque, 1973, J. Chem. Phys. **59**, 4652.

- Fisher, R.A., R. Ballou, J.P. Emerson, E. Lelièvre-Berna and N.E. Phillips, 1993, *Int. J. Mod. Phys. B* **7**, 830.
- Fisk, Z., G.R. Stewart, J.O. Willis, H.R. Ott and F. Hulliger, 1984, *Phys. Rev. B* **30**, 6360.
- Fisk, Z., P.C. Canfield, W.P. Beyermann, J.D. Thompson, M.F. Hundley, H.R. Ott, E. Felder, M.B. Maple, M.A. Lopez de la Torre, P. Visani and C.L. Seaman, 1991, *Phys. Rev. Lett.* **67**, 3310.
- Fisk, Z., J.L. Sarrao, J.D. Thompson, D. Mandrus, M.F. Hundley, A. Migliori, B. Bucher, Z. Schlessinger, G. Aeppli, E. Bucher, J.F. DiTusa, C.S. Oglesby, H.R. Ott, P.C. Canfield and S.E. Brown, 1995, *Physica B* **206&207**, 798.
- Fisk, Z., J.L. Sarrao, S.L. Cooper, P. Nyhus, G.S. Boebinger, A. Passner and P.C. Canfield, 1996, *Physica B* **223&224**, 409.
- Flaschin, S.J., A. Kratzer, F.J. Burghart, G.M. Kalvius, R. Wäppling, D.R. Noakes, R. Kadono, I. Watanabe, T. Takabatake, K. Kobayashi, G. Nakamoto and H. Fujii, 1996, *J. Phys.: Condens. Matter* **8**, 6967.
- Fledderjohann, A., and P.J. Hirschfeld, 1995, *Solid State Commun.* **94**, 163.
- Fleming, D.G., and M. Senba, 1992, in: *Perspectives of Meson Science*, eds T. Yamazaki, K. Nakai and K. Nagamine (North-Holland, Amsterdam) p. 219.
- Flouquet, J., J.C. Lasjournias, J. Peyrard and M. Ribault, 1982, *J. Appl. Phys.* **53**, 2117.
- Flouquet, J., S. Kambe, L.P. Regnault, P. Haen, J.P. Brison, F. Lapiere and P. Lejay, 1995, *Physica B* **215**, 77.
- Forgan, E.M., B.D. Rainford, S.L. Lee, J.S. Abell and Y. Bi, 1990, *J. Phys.: Condens. Matter* **2**, 10211.
- Fortune, N.A., G.M. Schmiedeshoff, J.S. Brooks, C.L. Lin, J.E. Crow, T. Mihalisin and G.R. Stewart, 1987, *Jpn. J. Appl. Phys.* **26**(Suppl. 3), 541.
- Fournier, J.M., and E. Gratz, 1993, in: *Handbook on the Physics and Chemistry of Rare Earths*, Vol. 17, eds K.A. Gschneidner Jr and L. Eyring (North-Holland, Amsterdam) p. 409.
- Fournier, J.M., and R. Troc, 1985, in: *Handbook on the Physics and Chemistry of the Actinides*, Vol. 2, eds A.J. Freeman and G.H. Lander (North-Holland, Amsterdam) p. 29.
- Fournier, J.M., J. Beille, A. Boef, C. Vettier and A. Wedgwood, 1980, *Physica B* **102**, 282.
- Fraas, K., U. Ahlheim, P.H.P. Reinders, C. Schank, R. Caspary, F. Steglich, A. Oichai, T. Suzuki and T. Kasuya, 1992, *J. Magn. Magn. Mater.* **108**, 220.
- Fransé, J.J.M., and R.J. Radwanski, 1993, in: *Handbook of Magnetic Materials*, Vol. 7, ed. K.H.J. Buschow (Elsevier, Amsterdam) p. 307.
- Freltoft, T., P. Böni, G. Shirane and K. Motoya, 1988, *Phys. Rev. B* **37**, 3454.
- Frey, E., and F. Schwabl, 1994, *Adv. Phys.* **43**, 577.
- Frey, E., F. Schwabl, S. Henneberger, O. Hartmann, R. Wäppling, A. Kratzer and G.M. Kalvius, 1997, *Phys. Rev. Lett.* **79**, 5142.
- Friedt, J.M., F.J. Litterst and J. Rebizant, 1985, *Phys. Rev. B* **32**, 257.
- Frings, P., R. Renker and C. Vettier, 1987, *J. Magn. Magn. Mater.* **63&64**, 202.
- Fritzsche, A., M. Hampele, D. Herlach, K. Maier, J. Major, L. Schimmele, A. Seeger, W. Staiger, W. Templ and C. Baines, 1990, *Hyperfine Interactions* **64**, 691.
- Fudamoto, Y., K.M. Kojima, M. Larkin, G.M. Luke, J. Merrin, B. Nachumi, Y.J. Uemura, M. Isobe and Y. Ueda, 1999, *Phys. Rev. Lett.* **83**, 3301.
- Fukuzumi, Y., K. Mizuhashi, K. Kanetada and S. Uchida, 1996, *Phys. Rev. Lett.* **76**, 684.
- Fulde, P., 1997, *Physica B* **230-232**, 1.
- Fulde, P., and R.A. Ferrell, 1964, *Phys. Rev. A* **135**, 550.
- Fulde, P., and M. Loewenhaupt, 1985, *Adv. Phys.* **34**, 589.
- Fulde, P., J. Keller and G. Zwicky, 1988, in: *Solid State Physics*, Vol. 41, eds F. Seitz, D. Turnbull and H. Ehrenreich (Academic Press, New York) p. 1.
- Fulde, P., V. Zevin and G. Zwicky, 1993, *Z. Phys. B* **92**, 133.
- Furdyna, J.K., 1987, *J. Appl. Phys.* **61**, 3526.
- Furrer, A., P. Brüesch and P. Unternährer, 1988, *Phys. Rev. B* **38**, 4616.
- Furuno, T., K. Ando, S. Kunii, A. Ochiai, H. Suzuki, M. Fujioka, T. Suzuki, W. Sasaki and T. Kasuya, 1988, *J. Magn. Magn. Mater.* **76&77**, 117.
- Gaidukova, I.Yu., S.B. Kruglyashov, A.S. Markosyan, R.Z. Levitin, Yu.G. Pastushenkov and V.V. Snegirev, 1983, *Sov. Phys. JETP* **57**, 1083.
- Galazka, R.R., S. Nagata and P.H. Keesom, 1980, *Phys. Rev. B* **22**, 3344.
- Galera, R.M., J. Pierre, E. Siant and A.P. Murani, 1984, *J. Less-Common Met.* **97**, 151.
- García-Muñoz, J.L., J. Rodríguez-Carvajal and P. Lacorre, 1994, *Phys. Rev. B* **50**, 978.
- García-Muñoz, J.L., P. Lacorre and R. Cywinski, 1995a, *Phys. Rev. B* **51**, 15197.
- García-Muñoz, J.L., M. Suaadi and B. Martinez, 1995b, *Phys. Rev. B* **52**, 4288.

- Gardner, J.S., S.R. Dunsiger, B.D. Gaulin, M.J.P. Gingras, J.E. Greedan, R.F. Kiefl, M.D. Lumsden, W.A. MacFarlane, N.P. Raju, J.E. Sonier, I. Swainson and Z. Tun, 1999, *Phys. Rev. Lett.* **82**, 1012.
- Gasser, U., P. Allenspach, F. Fauth, W. Henggeler, J. Mesot, A. Furrer, S. Rosenkranz, P. Vorderwisch and M. Buchgeister, 1996, *Z. Phys. B* **101** 345.
- Gaulin, B.D., 1994, *Hyperfine Interactions* **85**, 159.
- Gaulin, B.D., J.N. Reimers, T.E. Mason, J.E. Greedan and Z. Tun, 1992, *Phys. Rev. Lett.* **69**, 3244.
- Gaulin, B.D., D. Gibbs, E.D. Isaacs, J.G. Lussier, J.N. Reimers, A. Schröder, L. Taillefer and P. Zschack, 1994, *Phys. Rev. Lett.* **73**, 890.
- Gaulin, B.D., D. Gibbs, E.D. Isaacs, J.G. Lussier, J.N. Reimers, A. Schröder, L. Taillefer and P. Zschack, 1995, *Phys. Rev. Lett.* **73**, 890.
- Gaulin, B.D., J.S. Gardner, S.R. Dunsiger, Z. Tun, M.D. Lumsden, R.F. Kiefl, N.P. Raju, J.N. Reimers and J.E. Greedan, 1998, *Physica B* **241–243**, 511.
- Gavrilano, J.L., J. Hunziker and H.R. Ott, 1994, *Physica B* **194–196**, 195.
- Gavrilano, J.L., J. Hunziker and H.R. Ott, 1995, *Phys. Rev. B* **52**, R13106.
- Gegenwart, P., C. Langhammer, C. Geibel, R. Helfrich, M. Lang, G. Sparn, F. Steglich, R. Horn, L. Donnevert, A. Link and W. Assmus, 1998, *Phys. Rev. Lett.* **81**, 1501.
- Geibel, C., S. Thies, D. Kaczorowski, A. Mehner, A. Grauel, B. Seidel, U. Ahlheim, R. Helfrich, K. Petersen, C.D. Bredl and F. Steglich, 1991a, *Z. Phys. B* **83**, 305.
- Geibel, C., C. Schank, S. Thies, H. Kitazawa, C.D. Bredl, A. Böhm, M. Rau, A. Grauel, R. Caspary, R. Helfrich, U. Ahlheim, G. Weber and F. Steglich, 1991b, *Z. Phys. B* **84**, 1.
- Genossar, J., S. Israelit, B. Fischer, C. Kuper, L. Patlagan and G.M. Reisner, 1994, *Physica C* **235–240**, 305.
- Gianozzi, P., and P. Erdős, 1987, *J. Magn. Magn. Mater.* **67**, 75.
- Gignoux, D., and J.J. Rhyne, 1986, *J. Magn. Magn. Mater.* **54–57**, 1179.
- Gignoux, D., and D. Schmitt, 1995, in: *Handbook on the Physics and Chemistry of Rare Earths*, Vol. 20, eds K.A. Gschneidner Jr and L. Eyring (North-Holland, Amsterdam) p. 293.
- Gignoux, D., D. Givord and A. del Moral, 1976, *Solid State Commun.* **19**, 891.
- Gignoux, D., D. Schmitt and M. Zerguine, 1988, *Phys. Rev. B* **37**, 9882.
- Gignoux, D., D. Schmitt, E. Bauer and A.P. Murani, 1990, *J. Magn. Magn. Mater.* **88**, 63.
- Givord, D., H.S. Li and J.M. Moreau, 1984, *Solid State Commun.* **50**, 4176.
- Gloos, K., R. Modler, H. Schimanski, C.D. Bredl, C. Geibel, F. Steglich, A.I. Buzdin, N. Sato and T. Komatsubara, 1993, *Phys. Rev. Lett.* **70**, 501.
- Goldman, A.I., and R.F. Kelton, 1993, *Rev. Mod. Phys.* **65**, 213.
- Goldman, A.I., G. Shirane, G. Aeppli, B. Batlogg and E. Bucher, 1986, *Phys. Rev. B* **34**, 6564.
- Golnik, A., C. Niedermayer, E. Recknagel, M. Rossmannith, A. Weidinger, J.I. Budnick, B. Chamberland, M. Filipkowski, Y. Zhang, D.P. Yang, L.L. Lynds, F.A. Otter and C. Baines, 1987, *Phys. Lett. A* **125**, 71.
- Goodenough, J.B., and P.M. Raccah, 1965, *J. Appl. Phys.* **36**, 1031.
- Goremeychkin, E.A., I. Natkaniec, E. Mühler, H. Müller and P. Frach, 1987, *Solid State Commun.* **64**, 1473.
- Goshima, H., T. Suzuki, T. Fujita, R. Settai, H. Sugawara and Y. Ōnuki, 1996, *Physica B* **223&224**, 172.
- Gradwohl, B.A., A. Grayevsky, N. Kaplan, F.N. Gygax, A. Schenck and A.J. van der Wal, 1986, *Hyperfine Interactions* **31**, 319.
- Graf, H., W. Hofmann, W. Kündig, P.F. Meier, B.D. Patterson and W. Reichart, 1977, *Solid State Commun.* **23**, 653.
- Graf, H., G. Balzer, T. Möslang, E. Recknagel, A. Weidinger and K.H.J. Buschow, 1981, *Hyperfine Interactions* **8**, 605.
- Graf, M.H., R.J. Keizer, A. de Visser and J.J.M. Franse, 1999, *Physica B* **259–261**, 666.
- Graham Jr, C.D., 1962, *J. Phys. Soc. Japan* **17**, 1310.
- Graham, R.G., J.G.M. Armitage, P.C. Reidi, S.F.J. Cox and C.A. Scott, 1988, in: *IOP Short Meeting Series*, No. 22, ed. S.F.J. Cox (Institute of Physics, Bristol) p. 41.
- Gratz, E., and M.J. Zuckermann, 1982, in: *Handbook on the Physics and Chemistry of Rare Earths*, Vol. 5, eds K.A. Gschneidner Jr and L. Eyring (North-Holland, Amsterdam) p. 117.
- Grauel, A., A. Böhm, H. Fischer, C. Geibel, R. Köhler, R. Modler, C. Schank, F. Steglich, G. Weber, T. Komatsubara and N. Sato, 1992, *Phys. Rev. B* **46**, 5818.
- Grayevsky, A., I. Felner, T. Tashma, N. Kaplan, F.N. Gygax, A. Amato, M. Pinkpank and A. Schenck, 1997, *Hyperfine Interactions* **104**, 73.

- Grebinnik, V.G., I.I. Gurevich, V.A. Zhukov, A.P. Manych, B.A. Nikolskii, V.I. Selivanov and V.A. Suetin, 1979, *Sov. Phys. JETP* **49**, 1100.
- Grewe, N., and F. Steglich, 1991, in: *Handbook on the Physics and Chemistry of Rare Earths*, Vol. 14, eds K.A. Gschneidner Jr and L. Eyring (North-Holland, Amsterdam) p. 343.
- Grier, B.H., J.M. Lawrence, V. Murgai and R.D. Parks, 1984, *Phys. Rev. B* **29**, 2664.
- Grosse, G., G.M. Kalvius, A. Kratzer, E. Schreier, F.J. Burghart, K. Mattenberger and O. Vogt, 1999, *J. Magn. Magn. Mater.* **205**, 79.
- Grynszpan, R.I., I.M. Savic, S. Romer, X. Wan, J. Fenichel, C.M. Aegerter, H. Keller, D.R. Noakes, C.E. Stronach, A. Maignan, C. Martin and B. Raveau, 1999, *Physica B* **259–261**, 824.
- Gubbens, P.C.M., P. Dalmas de Réotier, J.P. Sanchez, A. Yaouanc, C.E. Snel, R. Verhoef, F.E. Kayzel, J. Song-Quan and J.J.M. Franse, 1992, *J. Magn. Magn. Mater.* **104–107**, 1269.
- Gubbens, P.C.M., A.A. Moolenaar, P. Dalmas de Réotier, A. Yaouanc, F.E. Kayzel, J.J.M. Franse, K. Prokes, C.E. Snel, P. Bonville, J.A. Hodges, P. Imbert and P. Pari, 1994a, *Hyperfine Interactions* **85**, 239.
- Gubbens, P.C.M., P. Dalmas de Réotier, A. Yaouanc, A.A. Menovsky, K. Prokes and C.E. Snel, 1994b, *Hyperfine Interactions* **85**, 245.
- Gubbens, P.C.M., A.A. Moolenaar, P. Dalmas de Réotier, A. Yaouanc, A.A. Menovsky, K. Prokes and C.E. Snel, 1995a, *J. Magn. Magn. Mater.* **140–144**, 1993.
- Gubbens, P.C.M., K. Prokes, A.M. Mulders, P. Dalmas de Réotier, A. Yaouanc, P. Bonville and E. Brück, 1995b, *ISIS Annual Report 1994–95*, A145.
- Gubbens, P.C.M., C.T. Kaiser, A.M. Mulders, P. Dalmas de Réotier, A. Yaouanc and A.A. Menovsky, 1997a, *Annual Report 1996*, Annex 1 (Paul Scherrer Institute, Villigen, unpublished) p. 45.
- Gubbens, P.C.M., A.M. Mulders, P. Dalmas de Réotier, A. Yaouanc, A.A. Menovsky and K. Prokes, 1997b, *Annual Report 1996*, Annex 1 (Paul Scherrer Institute, Villigen, unpublished) p. 44.
- Gubbens, P.C.M., C.T. Kaiser, P. Dalmas de Réotier, A. Yaouanc and A.A. Menovsky, 1998, *Annual Report 1997*, Annex 1 (Paul Scherrer Institute, Villigen, unpublished) p. 42.
- Guillaume, M., P. Fischer, B. Roessli, A. Podlesnyak, J. Schefer and A. Furrer, 1994, *J. Appl. Phys.* **75**, 6331.
- Guo, Z.B., H. Huang, W.P. Ding and Y.W. Du, 1997, *Phys. Rev. B* **56**, 10789.
- Gurevich, I.I., A.I. Klimov, V.N. Maiorov, E.A. Meleshko, B.A. Nikolskii, V.I. Selivanov and V.A. Suetin, 1975, *Sov. Phys. JETP* **42**, 222.
- Gurevich, I.I., A.I. Klimov, V.N. Maiorov, B.A. Nikolskii, V.S. Roganov, V.I. Selivanov and V.A. Suetin, 1976, *JETP Lett.* **23**, 310.
- Gygax, F.N., A. Amato, D. Andreica, M. Pinkpank and A. Schenck, 1999, *Book of abstracts*, 8th Int. Conf. on Muon Spin Rotation, Relaxation and Resonance, Les Diablerets, Switzerland, August/September 1999, unpublished.
- Gygax, F.N., M. Pinkpank, A. Schenck, M. Decroux and Ø. Fischer, 2000a, *Physica B* **289–290**, 381.
- Gygax, F.N., P. Vajda, D. Andreica, M. Pinkpank and A. Schenck, 2000b, *Physica B* **289–290**, 273.
- Haen, P., F. Mallmann, M.J. Besnus, J.P. Kappler, F. Boudarot, P. Burllet and T. Fukuhara, 1996, *J. Phys. Soc. Japan* **65**(Suppl. B), 16.
- Haga, Y., E. Yamamoto, Y. Inada, D. Aoki, K. Tenya, M. Ikeda, T. Sakakibara and Y. Ōnuki, 1996, *J. Phys. Soc. Japan* **65**, 3646.
- Hagen, M., W.G. Stirling and G.H. Lander, 1988, *Phys. Rev. B* **37**, 1846.
- Hälg, B., and A. Furrer, 1986, *Phys. Rev. B* **34**, 6258.
- Hälg, B., A. Furrer, J.K. Kjems and O. Vogt, 1983, *Phys. Rev. Lett.* **50**, 1085.
- Hälg, B., A. Furrer and O. Vogt, 1985, *Phys. Rev. Lett.* **54**, 1388.
- Hälg, B., A. Furrer and J.K. Kjems, 1987, *Phys. Rev. Lett.* **59**, 1034.
- Halim, C.H., W.K. Dawson, W.A. Baldwin and C. Boekema, 1990, *Physica B* **163**, 453.
- Halperin, B.I., and P.C. Hohenberg, 1967, *Phys. Rev. Lett.* **19**, 700.
- Hampele, M., D. Herlach, A. Kratzer, G. Majer, J. Major, H.-P. Raich, R. Roth, C.A. Scott, A. Seeger, W. Templ, M. Blanz, S.F.J. Cox and K. Fürderer, 1990, *Hyperfine Interactions* **65**, 1081.
- Hannon, J.P., G.T. Tremell, M. Blune and D. Gibbs, 1989, *Phys. Rev. Lett.* **62**, 167.
- Harshman, D.R., G. Aeppli, G.P. Espinosa, A.S. Cooper, J.P. Remeika, E.J. Ansaldo, T.M. Riseman, D.L. Williams, D.R. Noakes, B. Ellman and T.F. Rosenbaum, 1988, *Phys. Rev. B* **38**, 852. The data in this paper are good, but eq. (1) is completely wrong.
- Hart, I., P. Meeson, P.A. Probst and M. Springford, 1994, *Physica B* **199&200**, 20.
- Hartmann, O., 1977, *Phys. Rev. Lett.* **39**, 832.



- Hartmann, O., 1989, *Hyperfine Interactions* **49**, 61.
- Hartmann, O., E. Karlsson, R. Wäppling, J. Chappert, A. Yaouanc, L. Asch and G.M. Kalvius, 1984, *Hyperfine Interactions* **17–19**, 491.
- Hartmann, O., E. Karlsson, R. Wäppling, J. Chappert, A. Yaouanc, L. Asch and G.M. Kalvius, 1986, *J. Phys. F* **16**, 1593.
- Hartmann, O., R. Wäppling, A. Yaouanc, P. Dalmas de Réotier, B. Barbara, K. Aggarwal, L. Asch, A. Kratzer, G.M. Kalvius, F.J. Litterst, F.N. Gygax, B. Hitti, E. Lippelt and A. Schenck, 1989, *Hyperfine Interactions* **51**, 955.
- Hartmann, O., R. Wäppling, E. Karlsson, G.M. Kalvius, L. Asch, F.J. Litterst, K. Aggarwal, K.H. Münch, F.N. Gygax and A. Schenck, 1990a, *Hyperfine Interactions* **64**, 369.
- Hartmann, O., R. Wäppling, K. Aggarwal, L. Asch, A. Kratzer, G.M. Kalvius, F.J. Litterst, A. Yaouanc, P. Dalmas de Réotier, B. Barbara, F.N. Gygax, B. Hitti, E. Lippelt and A. Schenck, 1990b, *Hyperfine Interactions* **64**, 711.
- Hartmann, O., S.W. Harris, R. Wäppling, G.M. Kalvius, L. Asch, P. Dalmas de Réotier and A. Yaouanc, 1990c, *Hyperfine Interactions* **64**, 381.
- Hartmann, O., E. Karlsson, E. Lidström, R. Wäppling, P. Lundqvist, Z. Hegedus and O. Rapp, 1994a, *Physica C* **235–240**, 1695.
- Hartmann, O., E. Karlsson, R. Wäppling, L. Asch, S. Henneberger, G.M. Kalvius, A. Kratzer, H.H. Klauß, F.J. Litterst and M.A.C. de Melo, 1994b, *Hyperfine Interactions* **85**, 251.
- Hartmann, O., R. Wäppling, G.M. Kalvius, A. Kratzer and H.H. Klauß, 1996,  $\mu$ SR 96, Nikko, Japan, Book of Abstracts (unpublished) Abstract 1PA10.
- Hartmann, O., E. Lidström, M. Ekström, R. Wäppling, L. Asch and G.M. Kalvius, 1997, *Hyperfine Interactions* **104**, 293.
- Hasanain, S.K., R.P. Guertin, K. Westerholt, M. Guyot and S. Foner, 1981, *Phys. Rev. B* **24**, 5165.
- Hattori, Y., A. Niikura, A.P. Tsai, A. Inoue, T. Matsumoto, K. Fukamichi, H. Aruga-Katori and T. Goto, 1995a, *J. Phys.: Condens. Matter* **7**, 2313.
- Hattori, Y., K. Fukamichi, K. Suzuki, A. Niikura, A.P. Tsai, A. Inoue and T. Matsumoto, 1995b, *J. Phys.: Condens. Matter* **7**, 4183.
- Hauser, R., A. Indinger, E. Bauer and E. Gratz, 1995, *J. Magn. Magn. Mater.* **140–144**, 799.
- Havela, L., A.V. Andreev, V. Sechovsky, I.K. Kozlovskaya, K. Prokes, P. Javorsky, M.I. Bartashevich, T. Goto and K. Kamishima, 1997, *Physica B* **230–232**, 98.
- Hayano, R.S., Y.J. Uemura, J. Imazato, N. Nishida, T. Yamazaki and R. Kubo, 1979, *Phys. Rev. B* **20**, 850.
- Hayden, S.M., L. Taillefer, C. Vettier and J. Flouquet, 1992, *Phys. Rev. B* **46**, 8675.
- Heffner, R.H., 1994, *J. Alloys Compounds* **213**, 232.
- Heffner, R.H., and M.R. Norman, 1996, *Comm. Condens. Matter Phys.* **17**, 361.
- Heffner, R.H., D.W. Cooke, R.L. Hutson, M. Leon, M.E. Schillaci, J.L. Smith, A. Yaouanc, S.A. Dodds, L.C. Gupta, D.E. MacLaughlin and C. Boekema, 1984, *J. Appl. Phys.* **55**, 2007.
- Heffner, R.H., D.W. Cooke, R.L. Hutson, M.E. Schillaci, J.L. Smith, P.M. Richards, D.E. MacLaughlin, S.A. Dodds and J. Oostens, 1985, *J. Appl. Phys.* **57**, 3107.
- Heffner, R.H., D.W. Cooke, Z. Fisk, R.L. Hutson, M.E. Schillaci, J.L. Smith, J.O. Willis, D.E. MacLaughlin, C. Boekema, R.L. Lichti, A.B. Denison and J. Oostens, 1986, *Phys. Rev. Lett.* **57**, 1255.
- Heffner, R.H., D.W. Cooke, A.L. Giorgi, R.L. Hutson, M.E. Schillaci, H.D. Rempp, J.L. Smith, J.O. Willis, D.E. MacLaughlin, C. Boekema, R.L. Lichti, J. Oostens and A.B. Denison, 1989, *Phys. Rev. B* **39**, 11345.
- Heffner, R.H., J.L. Smith, J.O. Willis, P. Birrer, C. Baines, F.N. Gygax, B. Hitti, E. Lippelt, H.R. Ott, A. Schenck, E.A. Knetsch, J.A. Mydosh and D.E. MacLaughlin, 1990, *Phys. Rev. Lett.* **65**, 2816.
- Heffner, R.H., W.P. Beyermann, M.F. Hundley, J.D. Thompson, J.L. Smith, Z. Fisk, K. Bedell, P. Birrer, C. Baines, F.N. Gygax, B. Hitti, E. Lippelt, H.R. Ott, A. Schenck and D.E. MacLaughlin, 1991, *J. Appl. Phys.* **69**, 5481.
- Heffner, R.H., A. Amato, P.C. Canfield, R. Feyerherm, Z. Fisk, F.N. Gygax, D.E. MacLaughlin, A. Schenck, J.D. Thompson and H.R. Ott, 1994, *Physica B* **199&200**, 113.
- Heffner, R.H., L.P. Le, M.F. Hundley, J.J. Neumeier, G.M. Luke, K.M. Kojima, B. Nachumi, Y.J. Uemura, D.E. MacLaughlin and S.W. Cheong, 1996, *Phys. Rev. Lett.* **77**, 1869.
- Heffner, R.H., L.P. Le, D.E. MacLaughlin, G.M. Luke, K.M. Kojima, B. Nachumi, Y.J. Uemura, G.J. Nieuwenhuys and S.W. Cheong, 1997a, *Physica B* **230–232**, 759.
- Heffner, R.H., L.P. Le, G.J. Nieuwenhuys, D.E. MacLaughlin, A. Amato, F.N. Gygax, A. Schenck, J.S. Kim, G.R. Stewart and H.R. Ott, 1997b, *Physica B* **230–232**, 398.

- Heffner, R.H., D.E. MacLaughlin, G.J. Nieuwenhuys, T. Kimura, G.M. Luke, Y. Tokura and Y.J. Uemura, 1998, *Phys. Rev. Lett.* **81**, 1706.
- Heming, M., E. Roduner and B.D. Patterson, 1986, *Hyperfine Interactions* **32**, 727.
- Henggeler, W., and A. Furrer, 1998, *J. Phys.: Condens. Matter* **10**, 2579.
- Henneberger, S., E. Schreier, A. Kratzer, L. Asch, G.M. Kalvius, E. Frey, F. Schwabl, O. Hartmann, M. Ekström, R. Wäppling, F.J. Litterst and H.H. Klauß, 1997, *Hyperfine Interactions* **104**, 301.
- Henneberger, S., E. Frey, P.G. Maier, F. Schwabl and G.M. Kalvius, 1999, *Phys. Rev. B* **60**, 9630.
- Hennion, M., F. Mousa, J. Rodriguez-Carvajal, L. Pinsard and A. Revcolevschi, 1997, *Phys. Rev. B* **56**, R497.
- Herbst, J.F., J.J. Croat, F.E. Pinkerton and W.B. Yelon, 1984, *Phys. Rev. B* **29**, 4176.
- Herlach, D., K. Fürderer, M. Fähnle and L. Schimmele, 1986, *Hyperfine Interactions* **31**, 287.
- Hewson, A.C., 1993, *The Kondo Problem to Heavy Fermions* (Cambridge University Press, Cambridge).
- Hiess, A., I. Zokkalo, M. Bonnet, J. Schweizer, E. Lelièvre-Berna, F. Tasset, Y. Isikawa and G.H. Lander, 1997, *Physica B* **230–232**, 687.
- Higashi, I., K. Kobayashi, T. Takabatake and M. Kasaya, 1993, *J. Alloys Compounds* **193**, 300.
- Higemoto, W., H. Tanaka, I. Watanabe and K. Nagamine, 1998, *Phys. Lett. A* **243**, 80.
- Higemoto, W., K. Nishiyama, I. Watanabe, K. Nagamine, A. Asamitsu, H. Kuwahara and Y. Tokura, 1999a, *Physica B* **259–261**, 822.
- Higemoto, W., A. Koda, R. Kadono, K. Ishida, Y. Kawasaki, Y. Kitaoka, C. Geibel and F. Steglich, 1999b, *Book of abstracts, 8th Int. Conf. on Muon Spin Rotation, Relaxation and Resonance, Les Diablerets, Switzerland, August/September 1999*, unpublished.
- Higemoto, W., K. Satoh, N. Nishida, A. Koda, K. Nagamine, Y. Haga, E. Yamamoto, N. Kimura and Y. Ōnuki, 2000a, *Physica B* **281&282**, 984.
- Higemoto, W., A. Koda, R. Kadono, Y. Echizen and T. Takabatake, 2000b, *Physica B* **281&282**, 234.
- Hill, H.H., 1970, in: *Plutonium 1970 and other Actinides*, ed. W.H. Miner, Vol. 17 of AIME Nuclear Metallurgy Series (AIME, New York) p. 2.
- Hillberg, M., M.A.C. de Melo, H.H. Klauß, W. Wagener, F.J. Litterst, P. Adelman and G. Czjzek, 1997a, *Hyperfine Interactions* **104**, 221.
- Hillberg, M., W. Wagner, M.A.C. de Melo, H.H. Klauß, F.J. Litterst and W. Löwenhaupt, 1997b, *Hyperfine Interactions* **104**, 307.
- Hillenbrand, B., and M. Wilhelm, 1972, *Phys. Lett.* **40A**, 387; **41A**, 419.
- Hillier, A.D., J.R. Stewart, M.T.F. Telling, R.I. Bewley, Z.P. Han, S.L. Lee and R. Cywinski, 1998, *J. Magn. Magn. Mater.* **177–181**, 1111.
- Hilscher, G., E. Holland-Moritz, T. Holubar, H.D. Jostarndt, V. Nekvasil, G. Schaudy, U. Walter and G. Fillion, 1994, *Phys. Rev. B* **49**, 535.
- Hitti, B., P. Birrer, K.H. Fischer, F.N. Gygax, E. Lippelt, H. Maletta, A. Schenck and M. Weber, 1990, *Hyperfine Interactions* **63**, 287.
- Hodges, J.A., P. Bonville, P. Imbert and A. Pinatel-Phillipot, 1995, *J. Phys. I France* **5**, 501.
- Hofmann, W., W. Kündig, P.F. Maier, B.D. Patterson, K.J. Ruegg, O. Echt, H. Graf, E. Recknagel, A. Weidinger and T. Wiechert, 1978, *Phys. Lett.* **65A**, 343.
- Hohenemser, C., L. Chow and R.M. Sutter, 1982, *Phys. Rev. B* **26**, 5056.
- Hohenemser, C., N. Rosov and A. Kleinhammes, 1989, *Hyperfine Interactions* **49**, 267.
- Holden, T.M., G. Dolling, V.F. Sears, J.K. Furdyna and W. Giritat, 1982, *Phys. Rev. B* **26**, 5074.
- Holtzberg, F., 1980, *Philos. Mag. B* **42**, 491.
- Holzschuh, E., W. Kündig and B.D. Patterson, 1981, *Helv. Phys. Acta* **54**, 552.
- Holzschuh, E., A.B. Denison, W. Kündig, P.F. Meier and B.D. Patterson, 1983, *Phys. Rev. B* **27**, 5294.
- Horn, S., F. Steglich, M. Loewenhaupt, H. Scheuer, W. Felsch and K. Winzer, 1981, *Z. Phys. B* **42**, 125.
- Houshiar, M., D.T. Adroja and B.D. Rainford, 1995, *J. Magn. Magn. Mater.* **140–144**, 4321.
- Huang, C.Y., E.J. Ansaldo, J.H. Brewer, D.R. Harshman, K.M. Crowe, S.S. Rosenblum, C.W. Clawson, Z. Fisk, S.E. Lambert, M.S. Torikachvili and M.B. Maple, 1984, *Hyperfine Interactions* **17–19**, 509.
- Hulliger, F., 1979, in: *Handbook on the Physics and Chemistry of Rare Earths*, Vol. 4, eds K.A. Gschneidner Jr and L. Eyring (North-Holland, Amsterdam) p. 153.
- Hutchings, M.T., 1964, in: *Solid State Physics*, Vol. 16, eds F. Seitz and B. Turnbull (Academic Press, New York) p. 227.
- Huxley, A.D., P. Dalmas de Réotier, A. Yaouanc, D. Caplan, M. Couach, P. Lejay, P.C.M. Gubbens and A.M. Mulders, 1996, *Phys. Rev. B* **54**, R9666.
- Hyomi, K., H. Amitsuka, T. Nishioka, S. Marayama, Y. Myako, K. Nishiyama, K. Nagamine, T. Yamazaki

- and P. Morin, 1988, *J. Magn. Magn. Mater.* **76&77**, 462.
- Ibarra, M.R., C. Marquina, L. Garcia-Orza, Z. Arnold and A. del Moral, 1993, *J. Magn. Magn. Mater.* **128**, L249.
- Idzikowski, B., V.K. Rössler, D. Eckert, K. Nenkov and K.H. Müller, 1999, *Europhys. Lett.* **45**, 714.
- Iga, F., M. Kasaya and T. Kasuya, 1988, *J. Magn. Magn. Mater.* **76&77**, 156.
- Iga, F., S. Hiura, J. Klijn, N. Shimizu, T. Takabatake, M. Ito, Y. Matsumoto, F. Masaki, T. Suzuki and T. Fujita, 1999, *Physica B* **259–261**, 312.
- Ihrig, H., and W. Lohmann, 1977, *J. Phys. F* **7**, 1957.
- Ikeda, H., and K. Miyake, 1996, *J. Phys. Soc. Japan* **65**, 1796.
- Ikushima, K., Y. Kato, M. Takigawa, F. Iga, S. Hiura and T. Takabatake, 2000, *Physica B* **281&282**, 274.
- Isaacs, E.D., D.B. McWhan, C. Peters, G.E. Ice, D.P. Siddons, J.B. Hastings, C. Veltier and O. Vogt, 1989, *Phys. Rev. Lett.* **62**, 1671.
- Isaacs, E.D., D.B. McWhan, R.N. Kleiman, D.J. Bishop, G.E. Ice, P. Zschack, B.D. Gaulin, T.E. Mason, J.D. Garrett and W.J.L. Buyers, 1990, *Phys. Rev. Lett.* **65**, 3185.
- Isaacs, E.D., P. Zschack, C. Broholm, C.A. Burns, G. Aeppli, A.P. Ramirez, T.T.M. Palstra, R. Erwin, N. Stücheli and E. Buchev, 1995, *Phys. Rev. Lett.* **75**, 1178.
- Ishigaki, A., and T. Moriya, 1996, *J. Phys. Soc. Japan* **65**, 3402.
- Ishikawa, M., H.F. Braun and J.L. Jorda, 1983, *Phys. Rev. B* **27**, 3092.
- Islam, Z., I.R. Fischer, J. Zaretsky, P.C. Canfield, C. Stassis and A.I. Goldman, 1998, *Phys. Rev. B* **57**, R11047.
- Izawa, K., T. Suzuki, M. Kitamura, T. Fujita, T. Takabatake, G. Nakamoto, H. Fujii and K. Maezawa, 1996, *J. Phys. Soc. Japan* **65**, 3119.
- Izawa, K., T. Suzuki, T. Fujita, T. Takabatake, G. Nakamoto, H. Fujii and K. Maezawa, 1998, *J. Magn. Magn. Mater.* **177&178**, 395.
- Jaccard, D., A. Junod and J. Sierro, 1980, *Helv. Phys. Acta* **53**, 585.
- Jaccard, D., R. Cibin, J.L. Jorda and J. Flouquet, 1987, *Jpn. J. Appl. Phys.* **26**(Suppl. 3), 517.
- Janot, C., 1992, *Quasicrystals, A Primer* (Oxford University Press, London).
- Jayaram, B., P.C. Lanchester and M.T. Weller, 1991, *Phys. Rev. B* **43**, 5444.
- Jensen, J., 1996, *Phys. Rev. B* **54**, 4021.
- Jensen, J., and P. Bak, 1981, *Phys. Rev. B* **23**, 6180.
- Jensen, J., and A.R. Mackintosh, 1991, *Rare Earth Magnetism* (Clarendon Press, Oxford).
- Jensen, J., K.A. McEwen and W.G. Stirling, 1987, *Phys. Rev. B* **35**, 3327.
- Jensen, J., M.J.M. Leask, M.R. Wells, R.C.C. Ward, S.M. Hayden and A.P. Ramirez, 1995, *J. Magn. Magn. Mater.* **140–144**, 1191.
- Jerjini, M., 1987, *Doctoral Thesis* (University of Grenoble, unpublished).
- Jestädt, T., K.H. Chow, S.J. Blundell, W. Hayes, F.L. Pratt, B.W. Lovett, M.A. Green, J.E. Millburn and M.J. Rosseinsky, 1999, *Phys. Rev. B* **59**, 3775.
- Joubert, M.F., B. Jacquier and R.L. Cone, 1987, *Phys. Rev. B* **35**, 8322.
- Joynt, R., 1988, *Supercond. Sci. Technol.* **1**, 210.
- Kadono, R., 1990, *Hyperfine Interactions* **64**, 615.
- Kadono, R., A. Matsushita, R.M. Macrae, K. Nishiyama and K. Nagamine, 1994, *Phys. Rev. Lett.* **73**, 2724.
- Kadono, R., K. Okajima, A. Yamashita, K. Ishii, T. Yokoo, J. Akimitsu, N. Kobayashi, Z. Hiroi, M. Tanaka and K. Nagamine, 1996, *Phys. Rev. B* **54**, R9628.
- Kadono, R., A. Koda, W. Higemoto, K. Ohishi, K. Kakuta, J. Akimitsu, K. Ishida, Y. Kitaoka, C. Geibel and F. Steglich, 2000a, *Physica B* **289–290**, 322.
- Kadono, R., W. Higemoto, A. Koda, K. Kakuta, K. Ohishi, H. Takagiwa, T. Yokoo and J. Akimitsu, 2000b, *J. Phys. Soc. Japan* **69**, 3189.
- Kadowaki, H., 1998, *J. Phys. Soc. Japan* **67**, 3261.
- Kadowaki, H., T. Ekino, H. Iwasaki, T. Takabatake, H. Fujii and J. Sakurai, 1993, *J. Phys. Soc. Japan* **62**, 4426.
- Kadowaki, H., T. Sato, H. Yoshizawa, T. Ekino, T. Takabatake, H. Fujii, L.P. Regnault and Y. Isikawa, 1994a, *J. Phys. Soc. Japan* **63**, 2074.
- Kadowaki, H., M. Kohgi, K. Ohoyama and M. Kasaya, 1994b, *J. Phys. Soc. Japan* **63**, 2337.
- Kadowaki, H., K. Motoya, T. Kawasaki, T. Osakabe, H. Okumura, K. Kakurai, K. Umeo and T. Takabatake, 2000, *J. Phys. Soc. Japan* **69**, 2269.
- Kadowaki, K., and S.B. Woods, 1986, *Solid State Commun.* **58**, 507.
- Kadowaki, K., H. Takeya and K. Hirata, 1996, *Phys. Rev. B* **54**, 462.
- Kagan, Yu., and G.M. Kalvius, 1995, *JETP Lett.* **61**, 758.
- Kagan, Yu., K.A. Kikoin and N.V. Prokof'ev, 1993, *JETP Lett.* **57**, 600.

- Kakuta, K., K. Ohishi, S. Furuya, W. Higemoto, R. Kadono and J. Akimitsu, 2000, *Physica B* **289–290**, 168.
- Kalvius, G.M., 1994, *Hyperfine Interactions* **84**, 249.
- Kalvius, G.M., K. Nishiyama, K. Nagamine, T. Yamazaki, J. Chappert, O. Hartmann, E. Karlsson, R. Wäppling, A. Yaouanc and L. Asch, 1984, *Hyperfine Interactions* **17–19**, 497.
- Kalvius, G.M., L. Asch, D.R. Noakes, R. Keitel, J.H. Brewer, E.J. Ansaldo, F.J. Litterst, B. Boucher, J. Chappert, A. Yaouanc, T. Yamazaki, K. Nagamine, K. Nishiyama, O. Hartmann and R. Wäppling, 1986, *Hyperfine Interactions* **31**, 303.
- Kalvius, G.M., L. Asch, D.R. Noakes, R. Keitel, J.H. Brewer, E.J. Ansaldo, F.J. Litterst, B. Boucher, J. Chappert, A. Yaouanc, T. Yamazaki, K. Nagamine, K. Nishiyama, O. Hartmann and R. Wäppling, 1987, *J. Magn. Magn. Mater.* **70**, 285.
- Kalvius, G.M., L. Asch, F.J. Litterst, D.R. Noakes, J.H. Brewer, E.J. Ansaldo, J. Chappert, P. Morin, K. Nishiyama, O. Hartmann and R. Wäppling, 1990, *Hyperfine Interactions* **64**, 439.
- Kalvius, G.M., A. Kratzer, K.H. Münch, T. Takabatake, G. Nakamoto, H. Fujii, R. Wäppling, H.H. Klauß, R.F. Kiefl, S.R. Kreitzman and D.R. Noakes, 1994, *Hyperfine Interactions* **85**, 411.
- Kalvius, G.M., A. Kratzer, D.R. Noakes, K.H. Münch, R. Wäppling, H. Tanaka, T. Takabatake and R.F. Kiefl, 1995a, *Europhys. Lett.* **29**, 501.
- Kalvius, G.M., D.R. Noakes, A. Kratzer, K.H. Münch, R. Wäppling, H. Tanaka, T. Takabatake and R.F. Kiefl, 1995b, *Physica B* **206&207**, 205.
- Kalvius, G.M., A. Kratzer, R. Wäppling, T. Takabatake, G. Nakamoto, H. Fujii, R.F. Kiefl and S.R. Kreitzman, 1995c, *Physica B* **206&207**, 807.
- Kalvius, G.M., M. Weber, A. Kratzer, E. Schreier, R. Ballou, J. Deportes, R. Wäppling, J. Chappert and F.J. Litterst, 1996, in: *Proc. Int. Conf. HFI 1995*, *Hyperfine Interactions C* **1**, 135.
- Kalvius, G.M., T. Takabatake, A. Kratzer, R. Wäppling, D.R. Noakes, S.J. Flaschin, F.J. Burghart, R. Kadono, I. Watanabe, A. Brückl, K. Neumaier, K. Andres, K. Kobayashi, G. Nakamoto and H. Fujii, 1997a, *Hyperfine Interactions* **104**, 157.
- Kalvius, G.M., S.J. Flaschin, T. Takabatake, A. Kratzer, R. Wäppling, D.R. Noakes, F.J. Burghart, A. Brückl, K. Neumaier, K. Andres, R. Kadono, I. Watanabe, K. Kobayashi, G. Nakamoto and H. Fujii, 1997b, *Physica B* **230–232**, 655.
- Kalvius, G.M., K.H. Münch, A. Kratzer, R. Wäppling, D.R. Noakes, J. Deportes and R. Ballou, 2000a, *Physica B* **289–290**, 261.
- Kalvius, G.M., D.R. Noakes, G. Grosse, W. Schäfer, W. Kockelmann, J.K. Yakinthos, P.A. Kostanides, S. Fredo, I. Halevy and J. Gal, 2000b, *Physica B* **289–290**, 225.
- Kalvius, G.M., A. Kratzer, G. Grosse, D.R. Noakes, R. Wäppling, H. von Löhneysen, T. Takabatake and Y. Echizen, 2000c, *Physica B* **289–290**, 256.
- Kalvius, G.M., K.M. Kojima, M. Larkin, G.M. Luke, J. Merrin, B. Nachumi, Y.J. Uemura, A. Brückl, K. Neumaier, K. Andres, C. Paulsen, G. Nakamoto and T. Takabatake, 2000d, *Physica B* **281&282**, 66.
- Kalvius, G.M., A. Kratzer, H. Nakotte, D.R. Noakes, C.E. Stronach and R. Wäppling, 2000e, *Physica B* **289–290**, 252.
- Kalvius, G.M., E. Schreier, M. Ekström, O. Hartmann, S. Henneberger, A. Kratzer, R. Wäppling, E.M. Martin, F.J. Burghart, R. Ballou, J. Deportes and C. Niedermayer, 2000f, *Hyperfine Interactions* **128**, 275.
- Kalvius, G.M., E. Schreier, A. Kratzer, D.R. Noakes, R. Wäppling, F. Iga, T. Takabatake and H. von Löhneysen, 2001, to be published. See also: *PSI – Scientific Report 2000*, Vol. I: *Particles and Matter* (Paul Scherrer Institute, Villigen, 2001).
- Kanamori, J., H. Yoshida and K. Terakura, 1981, *Hyperfine Interactions* **8**, 573.
- Kaneko, T., H. Yoshida, M. Ohashi and S. Abe, 1987, *J. Magn. Magn. Mater.* **70**, 277.
- Kaplan, N., A. Grayevsky, P. Birrer, F.N. Gygax, B. Hitti, E. Lippelt and A. Schenck, 1989, *Phys. Rev. Lett.* **62**, 2732.
- Karlsson, E., 1982, *Phys. Rep.* **82**, 272.
- Karlsson, E., 1990, *Hyperfine Interactions* **64**, 331.
- Karlsson, E., 1995, *Solid State Phenomena as seen by Muons, Protons and Excited Nuclei* (Oxford University Press, London).
- Karlsson, E., 1996, *Hyperfine Interactions* **97&98**, 287.
- Karlsson, E., C.A. Chatzidimitriou-Dreismann and E.J. Brändas, 1990, *Hyperfine Interactions* **64**, 373.
- Kasaya, M., F. Iga, K. Negishi, S. Nakai and T. Kasuya, 1983, *J. Magn. Magn. Mater.* **31–34**, 437.
- Kasaya, M., F. Iga, M. Takigawa and T. Kasuya, 1985, *J. Magn. Magn. Mater.* **47&48**, 429.
- Kasaya, M., K. Katoh and K. Takegahara, 1991, *Solid State Commun.* **78**, 797.
- Kasaya, M., K. Katoh, M. Kohgi, T. Osakabe and N. Sato, 1994, *Physica B* **199&200**, 534.

- Kasuya, T., 1993, *Jpn. J. Appl. Phys. Ser. B* **8**, 3.
- Kasuya, T., 1996, *Physica B* **223&224**, 402.
- Kasuya, T., and T. Saso, eds, 1985, *Theory of Heavy Fermions and Valence Fluctuations* (Springer, Berlin).
- Kasuya, T., T. Suzuki and Y. Haga, 1993a, *J. Phys. Soc. Japan* **62**, 2549.
- Kasuya, T., Y. Haga, Y.S. Kwon and T. Suzuki, 1993b, *Physica B* **186-188**, 9.
- Kawakami, M., S. Kunii, T. Komatsubara and T. Kasuya, 1980, *Solid State Commun.* **36**, 435.
- Kawarazaki, S., and J. Arthur, 1988, *J. Phys. Soc. Japan* **57**, 1077.
- Kawarazaki, S., Y. Kobashi, J.A. Fernandez-Baca, S. Murayama, Y. Ōnuki and Y. Miyako, 1995, *Physica B* **206&207**, 298.
- Kawarazaki, S., M. Sato, Y. Miyako, N. Chigusa, K. Watanabe, N. Metoki, Y. Koike and M. Nishi, 2000, *Phys. Rev. B* **61**, 4167.
- Kayzel, F.E., J.J.M. Franse, P.C.M. Gubbens, A.A. Moolenaar, P. Dalmas de Réotier, A. Yaouanc, P. Bonville, P. Imbert and P. Pari, 1994, *Hyperfine Interactions* **85**, 275.
- Kehr, K.W., D. Richter, J.M. Welter, O. Hartmann, E. Karlsson, L.O. Norlin, T.O. Niinikoski and A. Yaouanc, 1982, *Phys. Rev. B* **26**, 567.
- Keizer, R.J., A. de Visser, A.A. Menovsky, J.J.M. Franse, A. Amato, F.N. Gygax, M. Pinkpank and A. Schenck, 1999, *J. Phys.: Condens. Matter* **11**, 8591.
- Keller, N., J.L. Tholence, A.D. Huxley and J. Flouquet, 1994, *Phys. Rev. Lett.* **73**, 2364.
- Kenzelmann, M., P. Schobinger-Papamantellos, F.N. Gygax, M. Pinkpank and A. Schenck, 1998, *Annual Report 1997, Annex 1* (Paul Scherrer Institute, Villigen, unpublished) p. 40.
- Keren, A., 1994a, *Hyperfine Interactions* **85**, 281.
- Keren, A., 1994b, *Phys. Rev. B* **50**, 10039.
- Keren, A., P. Mendels, I.A. Campbell and J. Lord, 1996, *Phys. Rev. Lett.* **77**, 1386.
- Keren, A., J.G. Bazalitsky, P. Mendels, I.A. Campbell and J. Lord, 2000, *Physica B* **289-290**, 202.
- Khattak, C.P., and F.F.Y. Wang, 1979, in: *Handbook on the Physics and Chemistry of Rare Earths*, Vol. 3, eds K.A. Gschneidner Jr and L. Eyring (North-Holland, Amsterdam) p. 525.
- Kiefl, R.F., 1986, *Hyperfine Interactions* **32**, 707.
- Kiefl, R.F., and S.R. Kreitzman, 1992, in: *Perspectives of Meson Science*, eds T. Yamazaki, K. Nakai and K. Nagamine (North-Holland, Amsterdam) p. 265.
- Kiefl, R.F., J.H. Brewer, J.F. Carolan, P. Dosanjh, W.N. Hardy, P. Schleger, B.X. Yang, H. Zhou, G.M. Luke, B.J. Sternlieb, Y.J. Uemura, W.J. Kossler, X.H. Yu, E.J. Ansaldo, H. Takagi, S. Uchida and C.L. Seaman, 1989, *Phys. Rev. Lett.* **63**, 2136.
- Kiefl, R.F., J.E. Sonier, D.A. Bonn, J.H. Brewer, J.F. Carolan, K.H. Chow, P. Dosanjh, W.N. Hardy, R.X. Liang, W.A. MacFarlane, P. Mendels, G.D. Morris, T.M. Riseman and J.W. Schneider, 1994, *Hyperfine Interactions* **86**, 537.
- Kilcoyne, S.H., and R. Cywinski, 1992, *J. Magn. Magn. Mater.* **104-107**, 1959.
- Kilcoyne, S.H., and M.T.F. Telling, 1995, *J. Magn. Magn. Mater.* **140-144**, 871.
- Kim, E., and D.L. Cox, 1998, *Phys. Rev. B* **58**, 3313.
- Kim, S.M., W.J.L. Buyers, H. Lin and E. Bauer, 1991, *Z. Phys. B* **84**, 201.
- Kirchmayr, H.R., and C.A. Poldy, 1979, in: *Handbook on the Physics and Chemistry of Rare Earths*, Vol. 2, eds K.A. Gschneidner Jr and L. Eyring (North-Holland, Amsterdam) p. 55.
- Kita, H., A. Dönni, Y. Endoh, K. Kakurai, N. Sato and T. Komatsubara, 1994, *J. Phys. Soc. Japan* **63**, 726.
- Kitaoka, Y., M. Takigawa, H. Yasuoka, M. Itoh, S. Tagaki, Y. Kuno, K. Nishiyama, R.S. Hayano, Y.J. Uemura, J. Imazato, H. Nakayama, K. Nagamine and T. Yamazaki, 1982, *Hyperfine Interactions* **12**, 51.
- Kitazawa, H., K. Katsumata, E. Torikai and K. Nagamine, 1988, *Solid State Commun.* **67**, 1191.
- Kitazawa, H., C. Schank, S. Thies, B. Seidel, C. Geibel and F. Steglich, 1992, *J. Phys. Soc. Japan* **61**, 1461.
- Kittel, C., and A. Abrahams, 1953, *Phys. Rev.* **90**, 238.
- Klauß, H.H., F.J. Litterst, L. Asch, A. Kratzer, S. Henneberger, G.M. Kalvius, K. Mattenberger and F. Hulliger, 1994, *Hyperfine Interactions* **85**, 293.
- Klauß, H.H., M.A.C. de Melo, M. Hillberg, F.J. Litterst, L. Asch, A. Kratzer, G.M. Kalvius, K. Mattenberger and O. Vogt, 1995, *J. Magn. Magn. Mater.* **140-144**, 1163.
- Klauß, H.H., M. Hillberg, W. Wagner, M.A.C. de Melo, F.J. Litterst, E. Schreier, W. Schlabbitz and G. Michels, 1997a, *Hyperfine Interactions* **104**, 171.
- Klauß, H.H., M. Hillberg, W. Wagner, M. Burke, F.J. Litterst, E. Schreier, A. Kratzer, G.M. Kalvius, Y. Haga and T. Suzuki, 1997b, *Hyperfine Interactions* **104**, 177.
- Klauß, H.H., D. Baabe, W. Kopmann, W. Wägener, H. Walf, M. Birke, H. Luetkens, F.J. Litterst,

- O. Fried, M. Hücker and B. Büchner, 1999a, Book of abstracts, 8th Int. Conf. on Muon Spin Rotation, Relaxation and Resonance, Les Diablerets, Switzerland, August/September 1999, unpublished.
- Klauß, H.H., W. Wagener, M. Hillberg, W. Kopmann, M. Birke, H. Luetkens, D. Baabe, D. Mienert, F.J. Litterst, M. Hücker and B. Büchner, 1999b, Book of abstracts, 8th Int. Conf. on Muon Spin Rotation, Relaxation and Resonance, Les Diablerets, Switzerland, August/September 1999, unpublished.
- Klauß, H.H., M. Hillberg, D. Baabe, W. Wagener, W. Kopmann, M. Birke, H. Luetkens, F.J. Litterst, P. Adelmann, E. Maiser, G. Czjzek and H. Berg, 1999c, Book of abstracts, 8th Int. Conf. on Muon Spin Rotation, Relaxation and Resonance, Les Diablerets, Switzerland, August/September 1999, unpublished.
- Klauß, H.H., W. Kopmann, H. Walf, D. Mainert, D. Baabe, M. Birke, H. Luetkens, M. Hillberg, F.J. Litterst, M. Fontes, E. Baggio-Saitovich and M.A.C. de Melo, 1999d, Book of abstracts, 8th Int. Conf. on Muon Spin Rotation, Relaxation and Resonance, Les Diablerets, Switzerland, August/September 1999, unpublished.
- Klauß, H.H., H. Walf, D. Mainert, D. Baabe, W. Kopmann, M. Birke, F.J. Litterst, S. Süllow, C. Geibel and M.A.C. de Melo, 1999e, Book of abstracts, 8th Int. Conf. on Muon Spin Rotation, Relaxation and Resonance, Les Diablerets, Switzerland, August/September 1999, unpublished.
- Kleiman, R.N., D.J. Bishop, H.R. Ott, Z. Fisk and J.L. Smith, 1990, *Phys. Rev. Lett.* **64**, 1975.
- Kleiman, R.N., C. Broholm, G. Aeppli, E. Bucher, N. Stücheli, D.J. Bishop, K.N. Clausen, K. Mortensen, J.S. Pedersen and B. Howard, 1992, *Phys. Rev. Lett.* **69**, 3120.
- Klempt, E., R. Schulze, H. Wolf, M. Camani, F.N. Gygax, W. Ruegg, A. Schenck and H. Schilling, 1982, *Phys. Rev. D* **25**, 652.
- Knetsch, E.A., A.A. Menovsky, G.J. Nieuwenhuys, J.A. Mydosh, A. Amato, R. Feyherm, F.N. Gygax, A. Schenck, R.H. Heffner and D.E. MacLaughlin, 1993, *Physica B* **188**, 300.
- Kockelmann, W., W. Schäfer, J.K. Yakinthos and P.A. Kotsanides, 1998, *J. Magn. Magn. Mater.* **177–181**, 792.
- Koda, A., W. Higemoto, R. Kadono, K. Ishida, Y. Kitaoka, C. Geibel and F. Steglich, 2000, *Physica B* **281&282**, 16.
- Koehler, W.C., 1972, in: *Magnetic Properties of Rare Earth Metals*, ed. R.J. Elliot (Plenum Press, London) p. 81.
- Kohgi, M., K. Ohoyama, T. Osakabe and M. Kasaya, 1992, *J. Magn. Magn. Mater.* **187–189**, 187.
- Kohgi, M., K. Ohoyama, T. Osakabe, M. Kasaya, T. Takabatake and H. Fujii, 1993, *Physica B* **186–188**, 409.
- Kohno, H., H. Fukuyama and M. Sigrist, 1999, *J. Phys. Soc. Japan* **68**, 1500.
- Kohori, Y., M. Kyogaku, T. Kohara, K. Asayama, H. Amitsuka and Y. Miyako, 1990, *J. Magn. Magn. Mater.* **90–91**, 15.
- Kojima, K., A. Harada, T. Takabatake, S. Ogura and K. Hiraoka, 1999, *Physica B* **269**, 249.
- Kojima, K.M., A. Keren, G.M. Luke, B. Nachumi, W.D. Wu, Y.J. Uemura, M. Azuma and M. Takano, 1995a, *Phys. Rev. Lett.* **74**, 2812.
- Kojima, K.M., A. Keren, L.P. Le, G.M. Luke, B. Nachumi, W.D. Wu, Y.J. Uemura, K. Kiyono, S. Miyasaki, H. Takagi and S. Uchida, 1995b, *Phys. Rev. Lett.* **74**, 3471.
- Kojima, K.M., Y. Fudamoto, M. Larkin, G.M. Luke, J. Merrin, B. Nachumi, Y.J. Uemura, M. Hase, Y. Sasago, K. Uchinokura, Y. Ajiro, A. Revcolevschi and J.P. Renard, 1997, *Phys. Rev. Lett.* **79**, 503.
- Kojima, K.M., H. Eisaki, S. Uchida, Y. Fudamoto, I.M. Gat, A. Kinkhabwala, M. Larkin, G.M. Luke and Y.J. Uemura, 1999, Book of abstracts, 8th Int. Conf. on Muon Spin Rotation, Relaxation and Resonance, Les Diablerets, Switzerland, August/September 1999, unpublished.
- Komorita, K., G. Kido, Y. Nakagawa, Y.S. Kwon and T. Suzuki, 1992, *J. Magn. Magn. Mater.* **104–107**, 1241.
- Kondo, J., 1964, *Prog. Theor. Phys. Kyoto* **32**, 37.
- Kondo, J., 1969, in: *Solid State Physics*, Vol. 23, eds F. Seitz, D. Turnbull and H. Ehrenreich (Academic Press, New York) p. 183.
- Kondo, J., 1986, *Hyperfine Interactions* **31**, 171.
- Kopmann, W., F.J. Litterst, H.H. Klauß, M. Hillberg, W. Wagner, G.M. Kalvius, E. Schreier, F.J. Burghart, G.H. Lander, J. Rebizant and J.C. Spirlet, 1998, *J. Alloys Compounds* **271–273**, 463.
- Kopmann, W., F.J. Litterst, W. Wagner, M. Hillberg, H. Walf, H.H. Klauß, G.M. Kalvius, F.J. Burghart, E. Schreier, G.H. Lander and J. Rebizant, 1999, Book of abstracts, 8th Int. Conf. on Muon Spin Rotation, Relaxation and Resonance, Les Diablerets, Switzerland, August/September 1999, unpublished.

- Korringa, J., 1950, *Physica* **16**, 601.
- Kossler, W.J., M. Namkung, B. Hitti, Y. Li, J.R. Kempton, C.E. Stronach, L.R. Goode Jr, W.F. Lankford, B.D. Patterson, W. Kündig and R.I. Grynszpan, 1985, *Phys. Rev. B* **32**, 293.
- Kötzler, J., 1986, *J. Magn. Magn. Mater.* **54–57**, 649.
- Kouvel, J.S., and J.S. Kasper, 1963, *J. Phys. Chem. Solids* **24**, 529.
- Krämer, K., H.U. Güdel, F.N. Gygax, M. Pinkpank and A. Schenck, 1998, Annual Report 1977, Annex 1 (Paul Scherrer Institute, Villigen, unpublished) p. 45.
- Kratzer, A., 1997, private communication.
- Kratzer, A., F.J. Litterst, F.N. Gygax, L. Asch, A. Schenck, G.M. Kalvius, S. Barth, W. Potzel and J.C. Spirlet, 1986, *Hyperfine Interactions* **31**, 309.
- Kratzer, A., G.M. Kalvius, L. Asch, F.J. Litterst, F.N. Gygax, B. Hitti, A. Schenck, K. Mattenberger and O. Vogt, 1990, *Hyperfine Interactions* **64**, 449.
- Kratzer, A., G.M. Kalvius, T. Takabatake, G. Nakamoto, H. Fujii and S.R. Kreitzman, 1992, *Europhys. Lett.* **19**, 649.
- Kratzer, A., K. Hutzbauer, S. Henneberger, G.M. Kalvius, O. Hartmann, R. Wäppling, H.H. Klauf, M.A.C. de Melo, F.J. Litterst and Th. Stammeler, 1994a, *Hyperfine Interactions* **87**, 1055.
- Kratzer, A., H.H. Klauf, S. Zwirner, G.M. Kalvius and J.C. Spirlet, 1994b, *Hyperfine Interactions* **86**, 431.
- Kratzer, A., G.M. Kalvius, S.J. Flaschin, D.R. Noakes, R. Wäppling, A. Brückl, K. Neumaier, K. Andres, T. Takabatake, K. Kobayashi, G. Nakamoto and H. Fujii, 1997a, *Physica B* **230–232**, 661.
- Kratzer, A., C. Schopf, G.M. Kalvius, H.H. Klauf, S. Zwirner and J.C. Spirlet, 1997b, *Hyperfine Interactions* **104**, 181.
- Kratzer, A., G.M. Kalvius, T. Takabatake, K. Umeo, D.T. Adroja, Y. Echizen, I. Watanabe, R. Wäppling, D.R. Noakes, C.U. Jackson and C.E. Stronach, 1999, Progress Report (Paul Scherrer Institute, Villigen, unpublished).
- Kratzer, A., D.R. Noakes, G.M. Kalvius, E. Schreier, R. Wäppling, K. Umeo, T. Takabatake and H. von Löhneysen, 2001, to be published. See also PSI – Scientific Report 2000, Vol. I: Particles and Matter (Paul Scherrer Institute, Villigen, 2001).
- Kreitzman, S.R., 1986, *Hyperfine Interactions* **32**, 13.
- Kreitzman, S.R., 1990, *Hyperfine Interactions* **65**, 1055.
- Kreitzman, S.R., R.F. Kiefl, D.R. Noakes, J.H. Brewer and E.J. Ansaldo, 1986, *Hyperfine Interactions* **32**, 521.
- Kreitzman, S.R., D.L. Williams, N. Kaplan, J.R. Kempton and J.H. Brewer, 1988, *Phys. Rev. Lett.* **25**, 2890.
- Kreitzman, S.R., T.L. Estle, B. Hitti, J.W. Schneider, K.H. Chow and R.L. Lichti, 1994, *Hyperfine Interactions* **87**, 1063.
- Krimmel, A., A. Loidl, P. Fischer, B. Roessli, A. Dönni, H. Kita, N. Sato, Y. Endoh, T. Komatsubara, C. Geibel and F. Steglich, 1993, *Solid State Commun.* **87**, 829.
- Krimmel, A., P. Fischer, B. Roessli, C. Geibel, F. Steglich and A. Loidl, 1995, *J. Magn. Magn. Mater.* **149**, 380.
- Krimmel, A., A. Loidl, R.S. Eccleston, C. Geibel and F. Steglich, 1996, *J. Phys.: Condens. Matter* **8**, 1677.
- Krishnamurthy, V.V., I. Watanabe, S. Ohira, K. Nishiyama, K. Nagamine, M. Ishikawa, D.H. Eom and N. Takeda, 1999a, *Physica B* **259–261**, 374.
- Krishnamurthy, V.V., I. Watanabe, K. Nagamine, C. Geibel, G. Sparn and F. Steglich, 1999b, *Hyperfine Interactions* **120/121**, 607.
- Krishnamurthy, V.V., I. Watanabe, K. Nagamine, J. Kitagawa, M. Ishikawa and M. Komatsubara, 1999c, Book of abstracts, 8th Int. Conf. on Muon Spin Rotation, Relaxation and Resonance, Les Diablerets, Switzerland, August/September 1999, unpublished.
- Krishnamurthy, V.V., K. Nagamine, I. Watanabe, K. Nishiyama, S. Ohira, M. Ishikawa, D.H. Eom and T. Ishikawa, 2000a, *Physica B* **289–290**, 47.
- Krishnamurthy, V.V., I. Watanabe, K. Nagamine, H. Kuwahara and Y. Tokura, 2000b, *Physica B* **289–290**, 56.
- Krivoshchev, I.A., V.N. Duginov, V.G. Grebinnik, K.I. Gritsaj, T.N. Mamedov, V.N. Nikiforov, V.G. Olshevsky, V.Yu. Pomjakushin, A.N. Ponomarev, Yu.D. Seropegin, V.A. Zhukov, M. Baran and H. Szymczak, 1997a, *Hyperfine Interactions* **104**, 187.
- Krivoshchev, I.A., A.A. Nezhivoy, B.A. Nikolskii, A.N. Ponomarev, V.N. Duginov, V.G. Olshevsky and V.Yu. Pomjakushin, 1997b, *JETP Let.* **65**, 81.
- Kubo, R., 1981, *Hyperfine Interactions* **8**, 731.
- Kubo, R., and T. Toyabe, 1966, in: *Magnetic Resonance and Relaxation*, ed. R. Blinc (North-Holland, Amsterdam) p. 810.
- Kumagai, K., K. Kawano, I. Watanabe, K. Nishiyama and K. Nagamine, 1994, *Hyperfine Interactions* **86**, 473.

- Kuno, Y., N. Nishida, H. Miyatake, S. Okuma, Y. Watanabe, T. Yamazaki, M. Ishikawa, T. Takabatake, Y. Nakazawa, J.H. Brewer, S.R. Kreitzman and T.M. Riseman, 1988, *Phys. Rev. B* **38**, 9276.
- Kuramoto, Y., and K. Miyake, 1990, *J. Phys. Soc. Japan* **59**, 2831.
- Kyogaku, M., Y. Kitaoka, H. Nakamura, K. Asayama, T. Takabatake, F. Teshima and H. Fujii, 1990, *J. Phys. Soc. Japan* **59**, 1728.
- Lacroix, C., and C. Pinettes, 1995, *Physica B* **206&207**, 11.
- Lam, D.J., and D.E. Ellis, 1985, *Physica B* **130**, 541.
- Landau, L.D., and E.M. Lifshitz, 1958, *Statistical Physics* (Pergamon Press, Oxford).
- Lappas, A., K. Prassides, A. Amato, R. Feyerherm, F.N. Gygax and A. Schenck, 1994, *Hyperfine Interactions* **86**, 555.
- Lappas, A., L. Cristofolini, K. Prassides, K. Vavakis, A. Amato, F.N. Gygax, M. Pinkpank and A. Schenck, 1997, *Hyperfine Interactions* **105**, 101.
- Larkin, A.I., and Y.N. Ovchinnikov, 1965, *Sov. Phys. JETP* **20**, 762.
- Larkin, M., Y. Fudamoto, I.M. Gat, A. Kinkhabwala, K.M. Kojima, G.M. Luke, J. Merrin, B. Nachumi, Y.J. Uemura, M. Azuma and M. Takano, 2000, *Physica B* **289-290**, 153.
- Lawrence, J.M., M.C. Croft and R.D. Parks, 1975, *Phys. Rev. Lett.* **35**, 289.
- Lawson, A.C., A. Williams, J.L. Smith, P.A. Seeger, J.A. Goldstone, J.A. O'Rourke and Z. Fisk, 1985, *J. Magn. Magn. Mater.* **50**, 83.
- Lawson, A.C., A. Williams and J.G. Huber, 1986, *J. Less-Common Met.* **120**, 147.
- Le, L.P., G.M. Luke, B.J. Sternlieb, Y.J. Uemura, J.H. Brewer, T.M. Riseman, D.C. Johnston, L.L. Miller, Y. Hidaka and H. Murakami, 1990, *Hyperfine Interactions* **63**, 279.
- Le, L.P., G.M. Luke, B.J. Sternlieb, W.D. Wu, Y.J. Uemura, J.H. Brewer, R.V. Upasani, L.Y. Chiang and P.M. Chaikin, 1991, *Europhys. Lett.* **15**, 547.
- Le, L.P., A. Keren, G.M. Luke, B.J. Sternlieb, W.D. Wu, Y.J. Uemura, J.H. Brewer, T.M. Riseman, R.V. Upasani, L.Y. Chiang, W. Kang, P.M. Chaikin, T. Csiba and G. Grüner, 1993, *Phys. Rev. B* **48**, 7284.
- Le, L.P., R.H. Heffner, G.J. Nieuwenhuys, P.C. Canfield, B.K. Cho, A. Amato, R. Feyerherm, F.N. Gygax, D.E. MacLaughlin and A. Schenck, 1995, *Physica B* **206&207**, 552.
- Le, L.P., R.H. Heffner, J.D. Thompson, D.E. MacLaughlin, G.J. Nieuwenhuys, A. Amato, R. Feyerherm, F.N. Gygax, A. Schenck, P.C. Canfield and B.K. Cho, 1996, *Phys. Rev. B* **53**, R510.
- Le, L.P., R.H. Heffner, J.D. Thompson, G.J. Nieuwenhuys, D.E. MacLaughlin, P.C. Canfield, B.K. Cho, A. Amato, R. Feyerherm, F.N. Gygax and A. Schenck, 1997, *Hyperfine Interactions* **104**, 49.
- Le Bras, G., P. Bonville, M.J. Besnus, P. Haen, P. Imbert, G. Polatsek and F.G. Aliev, 1995, *Physica B* **206&207**, 388.
- Lea, K.R., M.J.M. Leask and W.P. Wolf, 1962, *J. Phys. Chem. Solids* **23**, 1381.
- Lebech, B., K.A. McEwen and P.A. Lindgård, 1975, *J. Phys. C* **8**, 1684.
- Lee, B.W., J.M. Ferreira, Y. Dalichaouch, M.S. Torikachvili, K.N. Yang and M.B. Maple, 1988, *Phys. Rev. B* **37**, 2368.
- Lee, P.A., T.M. Rice, J.W. Serene, L.J. Sham and J.W. Wilkins, 1986, *Comm. Condens. Matter Phys.* **12**, 99.
- Lee, S.L., 1999, in: *Muon Science*, eds S.L. Lee, S.H. Kilcoyne and R. Cywinski (Institute of Physics Publishing, Bristol) p. 149.
- Lee, S.L., P. Zimmerman, H. Keller, M. Warden, I.M. Savic, R. Schauwecker, D. Zech, R. Cubitt, E.M. Forgan, P.H. Kes, T.W. Li, A.A. Menovsky and Z. Tarnawski, 1993, *Phys. Rev. Lett.* **71**, 3862.
- Lee, S.L., M. Brunner, H. Keller, M. Warden, D. Zech, R.I. Bewley, R. Cywinski, Z.P. Han, R. Cubitt, E.M. Forgan, M.T. Wylie and S.H. Kilcoyne, 1994, *Physica C* **235-240**, 2535.
- Lee, S.L., S.H. Kilcoyne and R. Cywinski, eds, 1999, *Muon Science* (Institute of Physics Publishing, Bristol).
- Lee, T.D., 1994, *Hyperfine Interactions* **86**, 439.
- Legvold, S., T. Ito and B.J. Beaudry, 1980, *Phys. Rev. Lett.* **45**, 1275.
- Lemberger, T.R., 1985, *Phys. Rev. B* **31**, 3131.
- Leon, M., 1994, *Hyperfine Interactions* **87**, 1994.
- Lichti, R.L., K.C.B. Chan, T.R. Adams, C. Boekema, W.K. Dawson, J.A. Flint, D.W. Cooke, R.S. Kwok and J.O. Willis, 1990a, *J. Appl. Phys.* **67**, 5055.
- Lichti, R.L., T.R. Adams and T.L. Gibson, 1990b, *Hyperfine Interactions* **63**, 199.
- Lidström, E., R. Wäppling and O. Hartmann, 1996a, *Physica Scripta* **54**, 210.
- Lidström, E., A.M. Ghandour, L. Häggström and Y. Andersson, 1996b, *J. Alloys Compounds* **232**, 95.
- Lidström, E., R. Wäppling, O. Hartmann, M. Ekström and G.M. Kalvius, 1996c, *J. Phys.: Condens. Matter* **8**, 6281.



- Lidström, E., R. Wäppling, S.J. Flaschin, G.M. Kalvius, A. Kratzer, D.T. Adroja, B.D. Rainford and A.J. Neville, 1997, *Hyperfine Interactions* **104**, 193.
- Lidström, E., M. Ekström, R. Wäppling, O. Hartmann and G.M. Kalvius, 2000, *Physica B* **289–290**, 269.
- Lin, C.L., L.W. Zhou, J.E. Crow and R.P. Guertin, 1985a, *J. Appl. Phys.* **57**, 3146.
- Lin, C.L., J. Teter, J.E. Crow, T. Mihalisin, J.S. Brooks, A.I. Abou-Aly and G.R. Stewart, 1985b, *Phys. Rev. Lett.* **54**, 2541.
- Lin, C.L., L.W. Zhou, J.E. Crow, R.P. Guertin and G.R. Stewart, 1986, *J. Magn. Magn. Mater.* **54–57**, 391.
- Lin, C.L., A. Wallash, J.E. Crow, T. Mihalisin and P. Schlottmann, 1987a, *Phys. Rev. Lett.* **58**, 1232.
- Lin, C.L., L.W. Zhou, C.S. Jee, A. Wallash and J.E. Crow, 1987b, *J. Phys.: Condens. Matter* **133**, 67.
- Lindgård, P.A., 1997, *Phys. Rev. Lett.* **78**, 4641.
- Lindgren, B., O. Hartmann, E. Karlsson, R. Wäppling, T. Butz and G.M. Kalvius, 1986, *Hyperfine Interactions* **31**, 439.
- Lindgren, B., O. Hartmann, E. Karlsson, R. Wäppling, A. Yaouanc, T. Butz, L. Asch and G.M. Kalvius, 1987, *J. Magn. Magn. Mater.* **67**, 130.
- Litterst, F.J., L. Asch, G.M. Kalvius, A. Kratzer, A. Schenck, F.N. Gyax, B. Hitti, K. Mattenberger and O. Vogt, 1990, *Hyperfine Interactions* **64**, 443.
- Liu, S.H., 1993, in: *Handbook on the Physics and Chemistry of Rare Earths*, Vol. 17, eds K.A. Gschneidner Jr and L. Eyring (North-Holland, Amsterdam) p. 87.
- Liu, S.H., C. Stassis and K.A. Gschneidner Jr, 1981, in: *Valence Fluctuations in Solids*, eds L.M. Falicov, W. Hanke and M.B. Maple (North-Holland, Amsterdam).
- Llobet, A., J.L. García-Muñoz, C. Frontera, M. Respaud, H. Rakoto and J. Lord, 2000, *Physica B* **289–290**, 73.
- Loewenhaupt, M., and K.H. Fischer, 1993, in: *Handbook of Magnetic Materials*, Vol. 7, ed. K.H.J. Buschow (Elsevier, Amsterdam) p. 503.
- Loewenhaupt, M., B. Frick, U. Walter and E. Holland-Moritz, 1983, *J. Magn. Magn. Mater.* **31–34**, 187.
- Longmore, A., A.T. Boothroyd, C. Changkang, H. Yongle, M.P. Nutley, N.H. Andersen, H. Casalta, P. Schleger and A.N. Christensen, 1996, *Phys. Rev. B* **53**, 9382.
- Loong, C.K., M. Loewenhaupt and M.L. Vrtis, 1986, *Physica B* **136**, 413.
- Lopez de la Torre, M.A., K.A. McEwen, M. Ellerby, C. Haworth and M. Springford, 1995, *J. Phys.: Condens. Matter* **7**, 9235.
- Lord, J.S., 1998, *J. Magn. Magn. Mater.* **177–181**, 1470.
- Louca, D., T. Egami, E.L. Brosha, H. Röder and A.R. Bishop, 1997, *Phys. Rev. B* **56**, R8475.
- Lounasmaa, O.V., 1974, *Experimental Principles and Methods below 1 K* (Academic Press, New York).
- Lovesey, S.W., and E. Engdahl, 1995, *J. Phys.: Condens. Matter* **7**, 769.
- Lovesey, S.W., A. Cuccolli and V. Tagnetti, 1990, *Hyperfine Interactions* **64**, 321.
- Lovesey, S.W., K.N. Trohidou and E. Karlsson, 1992a, *J. Phys.: Condens. Matter* **4**, 2061.
- Lovesey, S.W., E. Karlsson and K.N. Trohidou, 1992b, *J. Phys. C* **4**, 2043. Erratum: Lovesey et al. 1992c.
- Lovesey, S.W., K.N. Trohidou and E. Karlsson, 1992c, *J. Phys.: Condens. Matter* **4**, 9489. Erratum.
- Luke, G.M., B.J. Sternlieb, Y.J. Uemura, J.H. Brewer, R. Kadono, R.F. Kiefl, S.R. Kreitzman, T.M. Riseman, J. Gopalakrishnan, A.W. Sleight, M.A. Subramanian, S. Uchida, H. Takagi and Y. Tokura, 1989, *Nature* **338**, 49.
- Luke, G.M., J.H. Brewer, S.R. Kreitzman, D.R. Noakes, M. Celio, R. Kadono and E.J. Ansaldo, 1990a, *Hyperfine Interactions* **64**, 721.
- Luke, G.M., L.P. Le, B.J. Sternlieb, Y.J. Uemura, J.H. Brewer, R. Kadono, R.F. Kiefl, S.R. Kreitzman, T.M. Riseman, C.E. Stronach, M.R. Davis, S. Uchida, H. Takagi, Y. Tokura, Y. Hidaki, T. Murakami, J. Gopalakrishnan, A.W. Sleight, M.A. Subramanian, E.A. Early, J.T. Markert, M.B. Maple and C.L. Seaman, 1990b, *Phys. Rev. B* **42**, 7981.
- Luke, G.M., L.P. Le, B.J. Sternlieb, Y.J. Uemura, J.H. Brewer, R. Kadono, R.F. Kiefl, S.R. Kreitzman, T.M. Riseman, C.L. Seaman, Y. Dalichaouch, M.B. Maple and J.D. Garrett, 1990c, *Hyperfine Interactions* **64**, 517.
- Luke, G.M., L.P. Le, B.J. Sternlieb, W.D. Wu, Y.J. Uemura, J.H. Brewer, R. Kadono, R.F. Kiefl, S.R. Kreitzman, T.M. Riseman, Y. Dalichaouch, B.W. Lee, M.B. Maple, C.L. Seaman, P.E. Armstrong, R.W. Ellis, Z. Fisk and J.L. Smith, 1991, *Phys. Lett. A* **157**, 173.
- Luke, G.M., A. Keren, L.P. Le, W.D. Wu, Y.J. Uemura, D.A. Bonn, L. Taillefer and J.D. Garrett, 1993a, *Physica B* **188**, 264.

- Luke, G.M., A. Keren, L.P. Le, W.D. Wu, Y.J. Uemura, D.A. Bonn, L. Taillefer and J.D. Garrett, 1993b, *Phys. Rev. Lett.* **71**, 1466.
- Luke, G.M., A. Keren, L.P. Le, Y.J. Uemura, W.D. Wu, D.A. Bonn, L. Taillefer, J.D. Garrett and Y. Ōnuki, 1994a, *Hyperfine Interactions* **85**, 397.
- Luke, G.M., A. Keren, K.M. Kojima, L.P. Le, B.J. Sternlieb, W.D. Wu, Y.J. Uemura, Y. Ōnuki and T. Komatsubara, 1994b, *Phys. Rev. Lett.* **73**, 1853.
- Luke, G.M., A. Keren, K.M. Kojima, L.P. Le, G.M. Kalvius, A. Kratzer, G. Nakamoto, T. Takabatake and M. Ishikawa, 1995, *Physica B* **206&207**, 222.
- Luke, G.M., K.M. Kojima, M. Larkin, J. Merrin, B. Nachumi, Y.J. Uemura, G.M. Kalvius, A. Brückl, K. Neumaier, K. Andres, G. Nakamoto, M. Sirasi, H. Tanaka, T. Takabatake, H. Fujii and M. Ishikawa, 1997a, *Hyperfine Interactions* **104**, 199.
- Luke, G.M., K.M. Kojima, M. Larkin, J. Merrin, B. Nachumi, Y.J. Uemura, Y. Nakamura, S. Uchida and M.K. Crawford, 1997b, *Hyperfine Interactions* **105**, 113.
- Lundqvist, P., O. Rapp, O. Hartmann, E. Karlsson and R. Wäppling, 2000, *Physica C* **338**, 263.
- Lussier, B., B. Ellman and L. Taillefer, 1994, *Phys. Rev. Lett.* **73**, 3294.
- Lütgemeier, H., S. Schmenn, P. Meuffels, O. Storz, R. Schöllhorn, C. Niedermayer, I. Heinmaa and Y. Baikov, 1996, *Physica C* **267**, 191.
- Lynn, J.W., I.W. Sumarlin, S. Skanthakumar, W.H. Li, R.N. Shelton, J.L. Peng, Z. Fisk and S.W. Cheong, 1990, *Phys. Rev. B* **41**, 2569.
- Lysak, M.J., and D.E. MacLaughlin, 1985, *Phys. Rev. B* **31**, 6963.
- Machida, K., and M. Ozuki, 1989, *J. Phys. Soc. Japan* **58**, 2244.
- Machida, K., and M. Ozuki, 1991, *Phys. Rev. Lett.* **66**, 3293.
- MacLaughlin, D.E., 1981, in: *Valence Fluctuations in Solids*, eds L.M. Falicov, W. Hanke and M.B. Maple (North-Holland, Amsterdam) p. 321.
- MacLaughlin, D.E., S.A. Dodds, C. Boekema, R.H. Heffner, R.L. Hutson, M. Leon, M.E. Schillaci and J.L. Smith, 1983, *J. Magn. Magn. Mater.* **31–34**, 497.
- MacLaughlin, D.E., D.W. Cooke, R.H. Heffner, R.L. Hutson, M.W. McElfresh, M.E. Schillaci, H.D. Rempp, J.L. Smith, J.O. Willis, E. Zirngiebl, C. Boekema, R.L. Lichti and J. Oostens, 1988, *Phys. Rev. B* **37**, 3153.
- MacLaughlin, D.E., et al., 1993, unpublished. Quoted as private communication by Amato (1997). The same data are quoted as Ott et al., 1993, private communication, by Schenck and Gygax (1995).
- MacLaughlin, D.E., O.O. Bernal and H.G. Lukefahr, 1996, *J. Phys.: Condens. Matter* **8**, 9855.
- MacLaughlin, D.E., O.O. Bernal, A. Amato, R. Feyherm, F.N. Gygax, A. Schenck, R.H. Heffner, L.P. Le, G.J. Nieuwenhuys, B. Andraka, H. von Löhneysen, O. Stockert and H.R. Ott, 1997, *Physica B* **230–232**, 606.
- MacLaughlin, D.E., R.H. Heffner, G.J. Nieuwenhuys, G.M. Luke, Y. Fudamoto, Y.J. Uemura, R. Chau, M.B. Maple and B. Andraka, 1998, *Phys. Rev. B* **58**, R11849.
- MacLaughlin, D.E., R.H. Heffner, J.E. Sonier, G.J. Nieuwenhuys, R. Chau, M.B. Maple, B. Andraka, G.M. Luke, Y. Fudamoto, Y.J. Uemura, A. Amato and C. Baines, 2000a, *Physica B* **289–290**, 15.
- MacLaughlin, D.E., R.H. Heffner, G.J. Nieuwenhuys, P.C. Canfield, A. Amato, C. Baines, A. Schenck, G.M. Luke, Y. Fudamoto and Y.J. Uemura, 2000b, *Phys. Rev. B* **61**, 555.
- Majer, G., R. Messer, A. Seeger, W. Templ, K. Fürderer, M. Gladisch and D. Herlach, 1988, *Philos. Mag. Lett.* **57**, 57.
- Maletta, H., and W. Zinn, 1989, in: *Handbook on the Physics and Chemistry of Rare Earths*, Vol. 12, eds K.A. Gschneidner Jr and L. Eyring (North-Holland, Amsterdam) p. 213.
- Maletta, H., E. Pörschke, B. Rupp and P. Meuffels, 1989, *Z. Phys. B* **77**, 181.
- Maletta, H., E. Pörschke, T. Chattopadhyay and P.J. Brown, 1990a, *Physica C* **166**, 9.
- Maletta, H., P. Birrer, F.N. Gygax, B. Hitti, E. Lippelt, A. Schenck and M. Weber, 1990b, *Hyperfine Interactions* **63**, 235.
- Malik, S.K., and D.T. Adroja, 1991a, *Phys. Rev. B* **43**, 6277.
- Malik, S.K., and D.T. Adroja, 1991b, *Phys. Rev. B* **43**, 6295.
- Malik, S.K., and W.E. Wallace, 1981, *J. Magn. Magn. Mater.* **24**, 23.
- Malik, S.K., R. Vijayaraghavan, S.K. Garg and R.J. Ripmeester, 1975, *Phys. Status Solidi B* **68**, 399.
- Malik, S.K., A.M. Umarji, G.K. Shenoy, P.A. Montano and M.E. Reeves, 1985, *Phys. Rev. B* **31**, 4728.
- Malik, S.K., D.T. Adroja, S.K. Dhar, R. Vijayaraghavan and B.D. Padalia, 1989, *Phys. Rev. B* **40**, 2414.
- Malik, S.K., W.B. Yelon, J.J. Rhyné, W.J. James, R. Prasad, K. Adhikary and N.C. Soni, 1994, *Solid State Commun.* **89**, 383.

- Malik, S.K., L. Menon, K. Gosh and S. Ramakrishnan, 1995, *Phys. Rev. B* **51**, 399.
- Mannix, D., G.H. Lander, J. Rebizant, R. Caciuffo, N. Bernhoeft, E. Lidström and C. Vettier, 1999, *Phys. Rev. B* **60**, 15187.
- Maple, M.B., S.E. Lambert, M.S. Torikachvili, K.N. Yang, J.W. Allen, B.B. Pate and L. Lindau, 1985, *J. Less-Common Met.* **111**, 239.
- Maple, M.B., J.W. Chen, Y. Dalichaouch, T. Kohara, C. Rossel, M.S. Torikachvili, M.W. McElfresh and J.D. Thompson, 1986, *Phys. Rev. Lett.* **56**, 185.
- Maple, M.B., C.L. Seaman, D.A. Gajewski, Y. Dalichaouch, V.B. Barbeta, M.C. de Andrade, H.A. Mook, H.G. Lukefahr, O.O. Bernal and D.E. MacLaughlin, 1994, *J. Low Temp. Phys.* **95**, 225.
- Maple, M.B., M.C. de Andrade, J. Herrmann, Y. Dalichaouch, D.A. Gajewski, C.L. Seaman, R. Chan, R. Movshovich, A.C. Aronson and R. Osborn, 1995, *J. Low Temp. Phys.* **99**, 223.
- Maple, M.B., R.P. Dickey, J. Herrmann, M.C. de Andrade, E.J. Freeman, D.A. Gajewski and R. Chan, 1996, *J. Phys.: Condens. Matter* **8**, 9773.
- Martin, E.M., 1996, Diplom Thesis (Physics Department, Technical University Munich, Germany, unpublished).
- Martin, E.M., E. Schreier, G.M. Kalvius, A. Kratzer, O. Hartmann, R. Wäppling, D.R. Noakes, K. Krop, R. Ballou and J. Deportes, 2000, *Physica B* **289–290**, 265.
- Martinez, B., X. Obradors, E.J. Ansaldo, C. Niedermayer, D.R. Noakes, M.J. Sayagués, M. Vallet and J. González-Calbet, 1992, *J. Magn. Magn. Mater.* **104–107**, 941.
- Mason, T.E., B.D. Gaulin, J.D. Garrett, Z. Tun, W.J.L. Buyers and E.D. Isaacs, 1990, *Phys. Rev. Lett.* **65**, 3189.
- Mason, T.E., G. Aeppli, A.P. Ramirez, K.N. Clausen, C. Broholm, N. Stücheli, E. Bucher and T.T.M. Palstra, 1992, *Phys. Rev. Lett.* **69**, 490.
- Mason, T.E., W.J.L. Buyers, T. Petersen, A.A. Menovsky and J.D. Garrett, 1995, *J. Phys.: Condens. Matter* **7**, 5089.
- Matsuda, M., K. Yamada, K. Kakurai, H. Kadowaki, T.R. Thurston, Y. Endoh, Y. Hidaka, R.J. Birgeneau, M.A. Kastner, P.M. Gehring, A.H. Moudden and G. Shirane, 1990, *Phys. Rev. B* **42**, 10098.
- Matthias, B.T., H. Suhl and E. Corenzwit, 1958, *Phys. Rev. Lett.* **1**, 449.
- McDonough, J., and S.R. Julian, 1996, *Phys. Rev. B* **53**, 14411.
- McEwen, K.A., 1978, in: *Handbook on the Physics and Chemistry of Rare Earths*, Vol. 1, eds K.A. Gschneidner Jr and L. Eyring (North-Holland, Amsterdam) p. 411.
- McEwen, K.A., and W.G. Stirling, 1981, *J. Phys. C* **14**, 157.
- McEwen, K.A., W.G. Stirling and C. Vettier, 1983, *Physica B* **120**, 152.
- McEwen, K.A., U. Steigenberger, K.N. Clausen, J. Kulda, J.G. Park and M.B. Walker, 1998, *J. Magn. Magn. Mater.* **177–181**, 37.
- McWhan, D.B., C. Vettier, E.D. Isaacs, G.E. Ice, D.P. Siddons, J.B. Hastings, C. Peters and O. Vogt, 1990, *Phys. Rev. B* **42**, 6007.
- Meier, P.F., 1984, in: *Muons and Pions in Materials Research*, eds J. Chappert and R.I. Grynspan (North-Holland, Amsterdam) p. 77.
- Meier, P.F., W. Kündig, B.D. Patterson and K.J. Rugg, 1978, *Hyperfine Interactions* **5**, 311.
- Mekata, M., T. Asano, H. Nakamura, M. Shiga, K.M. Kojima, G.M. Luke, A. Keren, W.D. Wu, Y.J. Uemura, S.R. Dunsiger and M.J.P. Gingras, 1997, *Hyperfine Interactions* **104**, 337.
- Mendels, P., H. Alloul, J.H. Brewer, G.D. Morris, T.L. Duty, S. Johnston, E.J. Ansaldo, G. Collin, J.F. Marucco, C. Niedermayer, D.R. Noakes and C.E. Stronach, 1994, *Phys. Rev. B* **49**, 10035.
- Mentink, S.A.M., G.J. Nieuwenhuys, A.A. Menovsky, J.A. Mydosh, A. Drost, E. Frikkee, Y. Bando, T. Takabatake, P. Böni, P. Fischer, A. Furrer, A. Amato and A. Schenck, 1994a, *Physica B* **199**, 143.
- Mentink, S.A.M., G.J. Nieuwenhuys, A.A. Menovsky, J.A. Mydosh, H. Tou and Y. Kitaoka, 1994b, *Phys. Rev. B* **49**, 15759.
- Mentink, S.A.M., A. Drost, G.J. Nieuwenhuys, E. Frikkee, A.A. Menovsky and J.A. Mydosh, 1994c, *Phys. Rev. Lett.* **73**, 1031.
- Mentink, S.A.M., G.J. Nieuwenhuys, H. Nakotte, A.A. Menovsky, A. Drost, E. Frikkee and J.A. Mydosh, 1995, *Phys. Rev. B* **51**, 11567.
- Mentink, S.A.M., T.E. Mason, A. Drost, E. Frikkee, B. Becker, A.A. Menovsky and J.A. Mydosh, 1996, *Physica B* **223&224**, 237.
- Mentink, S.A.M., H. Amitsuka, A. de Visser, Z. Slanič, D.P. Belanger, J.J. Neumeier, J.D. Thompson, A.A. Menovsky, J.A. Mydosh and T.E. Mason, 1997, *Physica B* **230–232**, 108.
- Mesot, J., P. Allenspach, U. Staub, A. Furrer, H. Mutka, R. Osborn and A.D. Taylor, 1993, *Phys. Rev. B* **47**, 6027.

- Metoki, N., T. Osakabe, Y. Morii, Y. Ōnuki and M. Date, 1995, *J. Phys. Soc. Japan* **64**, 4491.
- Metoki, N., Y. Haga, Y. Kochi and Y. Ōnuki, 1998, *Phys. Rev. Lett.* **80**, 5417.
- Meul, H.W., C. Rossel, M. Decroux, Ø. Fischer, G. Remenyi and A. Briggs, 1984, *Phys. Rev. Lett.* **53**, 497.
- Meyer, C., H.J. Bornemann, H. Schmidt, R. Ahrens, D. Ewert, B. Renker and G. Czjzek, 1987, *J. Phys. F* **17**, L345.
- Michels, G., S. Junk, N. Lossau, W. Schlabit, D. Wollleben, D. Johrendt, A. Mewis, Ch. Sauer and Th. Woike, 1992, *Z. Phys. B* **74**, 227.
- Michels, G., C. Huhnt, W. Scharbrodt, W. Schlabit, E. Holland-Moritz, M.M. Abd-Elmeguid, M. Micklitz, D. Johrendt, V. Keimes and A. Mewis, 1995, *Z. Phys. B* **98**, 75.
- Mignot, J.M., R. Kahn, M.J. Besnus, J.P. Kappler and C. Godart, 1993, *Physica B* **186–188**, 475.
- Mihalik, M., F.E. Kayzel, T. Yoshida, K. Kuwahara, H. Amitsuka, T. Sakakibara, A.A. Menovsky, J.A. Mydosh and J.J.M. Franse, 1997, *Physica B* **230–232**, 364.
- Millis, A.J., 1993, *Phys. Rev. B* **48**, 9887.
- Miranda, E., V. Dobrosavljević and G. Kotliar, 1996, *J. Phys.: Condens. Matter* **8**, 9871.
- Mitsuda, S., T. Wada, K. Hosoya, H. Yoshizawa and H. Kitazawa, 1992, *J. Phys. Soc. Japan* **61**, 4667.
- Miyake, Y., J.P. Marangos, K. Shimomura, P. Birrer and K. Nagamine, 1995, *Nucl. Instrum. Methods B* **95**, 265.
- Miyake, Y., K. Shimomura, A.P. Mills and K. Nagamine, 1997, *Hyperfine Interactions* **106**, 237.
- Moiseenko, L.L., and V.V. Odintsov, 1979, *J. Less-Common Met.* **67**, 237.
- Monachesi, P., and A. Continenza, 1995, *J. Magn. Magn. Mater.* **140–144**, 1401.
- Mondal, S., R. Cywinski, S.H. Kilcoyne, B.D. Rainford and C. Ritter, 1992, *Physica B* **180&181**, 108.
- Mook, H.A., D.M. Paul, B.C. Sales, L.A. Boatner and L. Cussen, 1988, *Phys. Rev. B* **38**, 12008.
- Morenzoni, E., 1997, *Appl. Magn. Res.* **13**, 219.
- Morenzoni, E., 1998, Report PSI-PR-98-23 (Paul Scherrer Institute, Villigen).
- Morenzoni, E., 1999, in: *Muon Science*, eds S.L. Lee, S.H. Kilcoyne and R. Cywinski (Institute of Physics Publishing, Bristol) p. 343.
- Morenzoni, E., F. Kottmann, D. Maden, B. Matthias, M. Meyberg, T. Proschka, Th. Wutzke and U. Zimmermann, 1994, *Phys. Rev. Lett.* **72**, 2793.
- Morenzoni, E., M. Birke, A. Hofer, F. Kottmann, F.J. Litterst, B. Matthias, M. Meyberg, C. Niedermayer, T. Proschka, G. Schatz and Th. Wutzke, 1996, *Hyperfine Interactions* **97&98**, 395.
- Morenzoni, E., M. Birke, H. Glücklichler, A. Hofer, F.J. Litterst, M. Meyberg, C. Niedermayer, T. Proschka, G. Schatz and Th. Wutzke, 1997, *Hyperfine Interactions* **106**, 229.
- Morin, P., 1988, *J. Magn. Magn. Mater.* **71**, 151.
- Morin, P., and D. Schmitt, 1990, in: *Ferromagnetic Materials*, Vol. 5, eds K.H.J. Buschow and E.P. Wohlfarth (North-Holland, Amsterdam) p. 1.
- Moriya, T., 1956, *Prog. Theor. Phys.* **16**, 41.
- Moriya, T., and A. Kawabata, 1973, *J. Phys. Soc. Japan* **34**, 639; **35**, 669.
- Moriya, T., and T. Takimoto, 1995, *J. Phys. Soc. Japan* **64**, 960.
- Moriya, T., and K. Ueda, 1974, *Solid State Commun.* **15**, 169.
- Motokawa, M., H. Nojiri, M. Uchi, S. Watamura, K. Nishiyama and K. Nagamine, 1990, *Hyperfine Interactions* **65**, 1089.
- Motoya, K., S.M. Shapiro, L. Rebersky and M.S. Torikachvili, 1991, *Phys. Rev. B* **44**, 183.
- Movshovich, R., T. Graf, D. Mandrus, J.D. Thompson, J.L. Smith and Z. Fisk, 1996, *Phys. Rev. B* **53**, 8241.
- Mulders, A.M., P.C.M. Gubbens and K.H.J. Buschow, 1996, *Phys. Rev. B* **54**, 14963.
- Mulders, A.M., A. Yaouanc, P. Dalmas de Réotier, P.C.M. Gubbens, A.A. Moolenaar, B. Fåk, E. Ressouche, K. Prokes, A.A. Menovsky and K.H.J. Buschow, 1997, *Phys. Rev. B* **56**, 8752.
- Mulders, A.M., P.C.M. Gubbens, U. Gasser, C. Baines and K.H.J. Buschow, 1998a, *Phys. Rev. B* **57**, 10320.
- Mulders, A.M., P.C.M. Gubbens, C.T. Kaiser, A. Amato, R. Feyerherm, F.N. Gyax, A. Schenck, P. Dalmas de Réotier, A. Yaouanc, F.E. Kayzel and J.J.M. Franse, 1998b, Annual Report 1997, Annex 1 (Paul Scherrer Institute, Villigen, unpublished) p. 68.
- Mulders, A.M., C.T. Kaiser, P.C.M. Gubbens, A. Amato, F.N. Gyax, M. Pinkpank, A. Schenck, P. Dalmas de Réotier, A. Yaouanc, K.H.J. Buschow, F.E. Kayzel and A.A. Menovsky, 2000, *Physica B* **289–290**, 451.
- Münch, K.H., 1991, Diplom Thesis (Physics Department, TU Munich, unpublished).

- Münch, K.H., A. Kratzer, G.M. Kalvius, L. Asch, F.J. Litterst and K. Richter, 1993, *Hyperfine Interactions* **78**, 435.
- Murani, A.P., and R.S. Eccleston, 1996, *Phys. Rev. B* **53**, 48.
- Murani, A.P., K. Knorr, K.H.J. Buschow, A. Benoit and J. Flouquet, 1980, *Solid State Commun.* **36**, 523.
- Murasik, A., J. Leciejewicz, S. Ligenza and A. Misiuk, 1973, *Phys. Status Solidi* **a 20**, 395.
- Murasik, A., S. Ligenza and A. Zygmunt, 1974a, *Phys. Status Solidi* **a 23**, K163.
- Murasik, A., J. Leciejewicz, S. Ligenza and A. Misiuk, 1974b, *Phys. Status Solidi* **a 23**, K147.
- Murayama, S., C. Sekine, H. Takano, K. Hoshi, K. Nishiyama and K. Nagamine, 1993, *Physica B* **188**, 500.
- Murayama, S., C. Sekine, A. Yokoyanagi, Y. Asakura, K. Hoshi, K. Nishiyama, K. Nagamine and Y. Ōnuki, 1997, *Hyperfine Interactions* **104**, 205.
- Mutzbauer, K., O. Hartmann, R. Wäppling, A. Kratzer, S. Henneberger, H.H. Klauß, F.J. Litterst and G.M. Kalvius, 1993, *Physica B* **190**, 40.
- Mydosh, J.A., 1993, *Spin Glasses: An Experimental Introduction* (Taylor and Francis, London).
- Mydosh, J.A., 1999, *Physica B* **259–261**, 882.
- Nachumi, B., A. Keren, K.M. Kojima, M. Larkin, G.M. Luke, J. Merrin, O. Tchernyshyov, Y.J. Uemura, N. Ichikawa, M. Goto and S. Uchida, 1996, *Phys. Rev. Lett.* **77**, 5421.
- Nachumi, B., Y. Fudamoto, A. Keren, K.M. Kojima, M. Larkin, G.M. Luke, J. Merrin, O. Tchernyshyov, Y.J. Uemura, N. Ichikawa, M. Goto, H. Takagi, S. Uchida, M.K. Crawford, E.M. McCarron, D.E. MacLaughlin and R.H. Heffner, 1998, *Phys. Rev. B* **58**, 8760.
- Nagamine, K., 1981, *Hyperfine Interactions* **8**, 787.
- Nagamine, K., 1999, in: *Muon Science*, eds S.L. Lee, S.H. Kilcoyne and R. Cywinski (Institute of Physics Publishing, Bristol) p. 313.
- Nagamine, K., T. Matsuzaki, K. Ishida, I. Watanabe, R. Kadono, G.H. Eaton, H.J. Jones and W.G. Williams, 1994, *Hyperfine Interactions* **87**, 1091.
- Nagamine, K., Y. Miyake, K. Shimomura, P. Birrer, J.P. Marangos, M. Iwasaki, P. Strasser and T. Kuga, 1995, *Phys. Rev. Lett.* **74**, 4811.
- Nakama, T., M. Hedo, T. Mackawa, M. Higa, R. Resel, H. Sugawara, R. Settai, Y. Ōnuki and K. Yagasaki, 1995, *J. Phys. Soc. Japan* **64**, 1471.
- Nakamoto, G., T. Takabatake, Y. Bando, H. Fujii, K. Izawa, T. Suzuki, T. Fujita, A. Minami, I. Oguro, L.T. Tai and A.A. Menovsky, 1995, *Physica B* **206&207**, 840.
- Nakamura, H., Y. Kitaoka, K. Asayama and J. Flouquet, 1988a, *J. Phys. Soc. Japan* **57**, 2644.
- Nakamura, H., Y. Kitaoka, K. Yoshimura, Y. Kohori, K. Asayama, M. Shiga and Y. Nakamura, 1988b, *J. Phys. Paris* **49**, C8-257.
- Nakamura, H., H. Wada, K. Yoshimura, M. Shiga, Y. Nakamura, J. Sakurai and Y. Komura, 1988c, *J. Phys. F* **18**, 98.
- Nakamura, H., Y. Kitaoka, I. Inoue, K. Asayama and Y. Ōnuki, 1990, *J. Magn. Magn. Mater.* **90&91**, 459.
- Nakamura, H., Y. Kitaoka, K. Asayama, Y. Ōnuki and M. Shiga, 1994a, *J. Phys.: Condens. Matter* **6**, 10567.
- Nakamura, H., Y. Kitaoka, K. Asayama, T. Takabatake, H. Tanaka and H. Fujii, 1994b, *J. Phys. Soc. Japan* **63**, 433.
- Nakamura, H., Y. Kitaoka, K. Asayama, M. Shiga and Y. Ōnuki, 1995, *Physica B* **206&207**, 444.
- Nakamura, H., F. Takayanagi and M. Shiga, 1998, *J. Magn. Magn. Mater.* **177–181**, 595.
- Nakamura, K., Y. Kitaoka, K. Asayama, T. Takabatake, G. Nakamoto, H. Tanaka and H. Fujii, 1996, *Phys. Rev. B* **53**, 6385.
- Nakamura, S., T. Goto, S. Kunii, K. Iwashita and A. Tamaki, 1994, *J. Phys. Soc. Japan* **63**, 623.
- Nakotte, H., 1994, Ph.D. Thesis (University of Amsterdam).
- Neddermeyer, S.H., and C.D. Anderson, 1938, *Phys. Rev.* **54**, 88.
- Neville, A.J., B.D. Rainford, D.T. Adroja and H. Schober, 1996, *Physica B* **223&224**, 271.
- Niedermayer, C., A. Golnik, E. Recknagel, A. Weidinger, A. Yaouanc, P. L'Héritier, D. Fruchart, J.I. Budnick and K.H.J. Buschow, 1990, *Hyperfine Interactions* **64**, 405.
- Niedermayer, C., H. Glückler, A. Golnik, U. Binninger, M. Rauer, E. Recknagel, J.I. Budnick and A. Weidinger, 1993a, *Phys. Rev. B* **47**, 3427.
- Niedermayer, C., C. Bernhard, U. Binninger, H. Glückler, J.L. Tallon, E.J. Ansaldo and J.I. Budnick, 1993b, *Phys. Rev. Lett.* **71**, 1764.
- Niedermayer, C., C. Bernhard, T. Blasius, A. Golnik, A. Moodenbaugh and J.I. Budnick, 1998, *Phys. Rev. Lett.* **80**, 3843.
- Niedermayer, C., E.M. Forgan, H. Glückler, A. Hofer, E. Morenzoni, M. Plaines, T. Proschka, T.M. Riseman, M. Birke, T.J. Jackson, F.J. Litterst, M.W. Long, H. Luetkens, A. Schatz and G. Schatz,

- 1999, Report PSI-PR-99-20 (Paul Scherrer Institute, Villigen).
- Nieuwenhuys, G.J., 1995, in: *Handbook of Magnetic Materials*, Vol. 9, ed. K.H.J. Buschow (Elsevier, Amsterdam) p. 1.
- Nieuwenhuys, G.J., S.A.M. Mentink, A.A. Menovsky, A. Amato, R. Feyerherm, F.N. Gygax, R.H. Heffner, L.P. Le, D.E. MacLaughlin and A. Schenck, 1995, *Physica B* **206–207**, 470.
- Nieuwenhuys, G.J., S. Suellow, A.A. Menovsky, J.A. Mydosh, R.H. Heffner, L.P. Le, D.E. MacLaughlin, O.O. Bernal and A. Schenck, 1998, *J. Magn. Magn. Mater.* **177–181**, 803.
- Nieuwenhuys, G.J., N.G. Patil, H. Noijons, D.G. Tomuta, D.E. MacLaughlin, R.H. Heffner and A. Amato, 2000, *Physica B* **289–290**, 228.
- Niikura, A., A.P. Tsai, A. Inoue and T. Matsumoto, 1994, *Philos. Mag. Lett.* **69**, 351.
- Nikiforov, V.N., V. Kovacik, I.O. Grishenko, A.A. Velikhovskii, J. Mirkovic, B.I. Shapiev, O.I. Bodak and Yu.D. Scropegin, 1993, *Physica B* **186–188**, 514.
- Nishida, N., 1992, in: *Perspectives of Meson Science*, eds T. Yamazaki, K. Nakai and K. Nagamine (North-Holland, Amsterdam) p. 45.
- Nishida, N., and H. Miyatake, 1990, *Hyperfine Interactions* **63**, 183.
- Nishida, N., K. Nagamine, R.S. Hayano, Y.J. Uemura, J. Imazato, T. Yamazaki, D.G. Fleming, R.A. Duncan, J.H. Brewer, A. Ahktar and H. Yasuoka, 1978, *J. Phys. Soc. Japan* **44**, 1131.
- Nishida, N., H. Miyatake, S. Okuma, Y. Kuno, Y. Watanabe, T. Yamazaki, S. Hikami, I. Ishikawa, T. Takabatake, Y. Nakazawa, S.R. Kreitzman, J.H. Brewer and C.Y. Huang, 1988a, *Jpn. J. Appl. Phys.* **27**, L94.
- Nishida, N., H. Miyatake, D. Shimada, S. Okuma, T. Yamazaki, Y. Watanabe, Y. Kuno, M. Ishikawa, T. Takabatake, K. Nagamine, K. Nishiyama, J.H. Brewer and S.R. Kreitzman, 1988b, *Physica C* **153–155**, 761.
- Nishida, N., H. Miyatake, S. Okuma, T. Tamegai, Y. Iye, R. Yoshizaki, K. Nishiyama and K. Nagamine, 1988c, *Physica C* **156**, 625.
- Nishigori, S., H. Goshima, T. Suzuki, T. Fujita, G. Nakamoto, T. Takabatake, H. Fujii and J. Sakurai, 1993, *Physica B* **186–188**, 406.
- Nishiyama, K., 1992, in: *Perspectives of Meson Science*, eds T. Yamazaki, K. Nakai and K. Nagamine (North-Holland, Amsterdam) p. 199.
- Noakes, D.R., 1991, *Phys. Rev. B* **44**, 5064.
- Noakes, D.R., 1999, *J. Phys.: Condens. Matter* **11**, 1589.
- Noakes, D.R., and G.M. Kalvius, 1997, *Phys. Rev. B* **56**, 2352.
- Noakes, D.R., and G.M. Kalvius, 2000, *Physica B* **289–290**, 248.
- Noakes, D.R., and G.K. Shenoy, 1982, *Phys. Lett.* **91A**, 35.
- Noakes, D.R., E.J. Ansaldo, J.H. Brewer, D.R. Harshman, C.Y. Huang, M.S. Torikachvili, S.E. Lambert and M.B. Maple, 1985, *J. Appl. Phys.* **57**, 3197.
- Noakes, D.R., J.H. Brewer, D.R. Harshman, E.J. Ansaldo and C.Y. Huang, 1987, *Phys. Rev. B* **35**, 6597.
- Noakes, D.R., E.J. Ansaldo, S.R. Kreitzman and G.M. Luke, 1993a, *J. Phys. Chem. Solids* **54**, 785.
- Noakes, D.R., E.J. Ansaldo and G.M. Luke, 1993b, *J. Appl. Phys.* **73**, 5666.
- Noakes, D.R., A. Ismail, E.J. Ansaldo, J.H. Brewer, G.M. Luke, P. Mendels and S.J. Poon, 1995, *Phys. Lett. A* **199**, 107.
- Noakes, D.R., G.M. Kalvius, R. Wäppling, C.E. Stronach, M.F. White Jr, H. Saito and K. Fukamichi, 1998, *Phys. Lett. A* **238**, 197.
- Noakes, D.R., R. Wäppling, G.M. Kalvius, Y. Andersson, A. Broddefalk, M.F. White Jr and C.E. Stronach, 2000, *Physica B* **289–290**, 303.
- Nohara, S., H. Namatame, A. Fujimori and T. Takabatake, 1993, *Phys. Rev. B* **47**, 1754.
- Nojiri, H., M. Motokawa, K. Nishiyama, K. Nagamine and T. Shigeoka, 1992, *J. Magn. Magn. Mater.* **104–107**, 1399.
- Norman, M.R., 1993, *J. Phys. Chem. Solids* **54**, 1165.
- Norman, M.R., and D.D. Koelling, 1993, in: *Handbook on the Physics and Chemistry of Rare Earths*, Vol. 17, eds K.A. Gschneidner Jr and L. Eyring (North-Holland, Amsterdam) p. 1.
- Norman, M.R., S.D. Bader and H.A. Kierstead, 1986, *Phys. Rev. B* **33**, 8035.
- Nutall, J.W., S.C. Perry, W.G. Stirling, S.H. Kilcoyne and R. Cywinski, 1997, preprint.
- Oashi, T., K. Kumagai, Y. Nakajima, T. Tomita and T. Fujita, 1989, *Physica C* **157**, 315.
- Ochiai, A., 1996, private communication.
- Ochiai, A., D.X. Li, Y. Haga, O. Nakamura and T. Suzuki, 1993, *Physica B* **186–188**, 437.
- Ogielski, A.T., 1985, *Phys. Rev. B* **32**, 7384.
- Ohoyama, K., M. Kohgi, T. Yoshino, T. Takabatake, W. Hahn and R.S. Eccleston, 1999, *Physica B* **259–261**, 283.

- Okamoto, T., H. Nagata, H. Fujii and Y. Makihara, 1987, *J. Magn. Magn. Mater.* **70**, 139.
- Onodera, M., H. Yamauchi, M. Yamada, H. Yamamoto, S. Sagawa and S. Hirose, 1987, *J. Magn. Magn. Mater.* **68**, 15.
- Ōnuki, Y., 1993, *Physica B* **186–188**, 92.
- Ōnuki, Y., Y. Shimizu and T. Komatsubara, 1984, *J. Phys. Soc. Japan* **53**, 1210.
- Ōnuki, Y., Y. Shimizu and T. Komatsubara, 1985, *J. Phys. Soc. Japan* **54**, 304.
- Oohara, Y., Y. Okayama, H. Takahashi, H. Yoshizawa, N. Mori, S. Mitsuda, Y. Haga and T. Suzuki, 1995, *J. Phys. Soc. Japan* **64**, 4363.
- Oomi, G., T. Tereda, M. Shiga and Y. Nakamura, 1987, *J. Magn. Magn. Mater.* **70**, 137.
- Orbach, R., and H.J. Stapleton, 1972, in: *Electron Paramagnetic Resonance*, ed. S. Gschwind (Plenum Press, New York).
- Orlando, T.P., A. Delin, S. Foner, E.J. McNiff, J.M. Tarascon, L.H. Greene, W.R. McKinnon and G.W. Hill, 1987, *Phys. Rev. B* **36**, 2394.
- Oseroff, S.B., D. Rao, F. Wright, D.C. Vier, S. Schultz, J.D. Thompson, Z. Fisk, S.W. Cheong, M.F. Hundley and M. Tovar, 1990, *Phys. Rev. B* **41**, 1934.
- Ott, H.R., 1987, *Prog. Low Temp. Phys.* **11**, 216.
- Ott, H.R., H. Rudiger, P. Delsing and Z. Fisk, 1984a, *Phys. Rev. Lett.* **52**, 1551.
- Ott, H.R., H. Rudiger, T.M. Rice, K. Ueda, Z. Fisk and J.L. Smith, 1984b, *Phys. Rev. Lett.* **52**, 1915.
- Ott, H.R., H. Rudiger, Z. Fisk, J.O. Willis and G.R. Stewart, 1985a, *Solid State Commun.* **53**, 235.
- Ott, H.R., H. Rudiger, E. Felder, Z. Fisk and B. Batlogg, 1985b, *Phys. Rev. Lett.* **55**, 1595.
- Ouladdiaf, B., 1986, Doctoral Thesis (University of Grenoble, unpublished).
- Palmer, R.G., D.L. Stein, E. Abrahams and P.W. Anderson, 1984, *Phys. Rev. Lett.* **53**, 958.
- Palmer, S.B., and E.W. Lee, 1972, *Proc. R. Soc. A* **327**, 519.
- Palstra, T.T.M., A.A. Menovsky, J. van den Berg, A.J. Dirkmaat, P.H. Kes, G.J. Nieuwenhuys and J.A. Mydosh, 1985, *Phys. Rev. Lett.* **55**, 2727.
- Papoular, R.J., and A. Delapalme, 1994, *Phys. Rev. Lett.* **72**, 1486.
- Park, J.G., B.R. Coles and B.V.B. Sarkissian, 1994a, *Physica B* **199&200**, 475.
- Park, J.G., M. Ocko and B.R. Coles, 1994b, *J. Phys.: Condens. Matter* **6**, L781.
- Park, J.G., B.R. Coles, C.A. Scott and R. Cywinski, 1996, *Physica B* **223&224**, 189.
- Park, J.G., B.R. Coles, S.P. Cottrell and K.A. McEwen, 1997a, *Physica B* **230–232**, 92.
- Park, J.G., C.A. Scott, K.A. McEwen and R. Cywinski, 1997b, *Physica B* **230–232**, 673.
- Parks, R.D., ed., 1969, *Superconductivity*, 2 volumes (Dekker, New York).
- Paul, D.M., H.A. Mook, L.A. Boatner, B.C. Sales, J.O. Ramey and L. Cussen, 1989, *Phys. Rev. B* **39**, 4291.
- Peretto, P., R. Venegas and G.N. Rao, 1981, *Phys. Rev. B* **23**, 6544.
- Petersen, T., T.E. Mason, G. Aeppli, A.P. Ramirez, E. Bucher and R.N. Kleiman, 1994, *Physica B* **199&200**, 151.
- Petit, S., A.H. Moudden, B. Hennion, A. Vietkin and A. Revcolevschi, 1998, *Eur. Phys. J. B* **3**, 163.
- Petrenko, O.A., C. Ritter, M. Yethiraj and D.M. Paul, 1998, *Phys. Rev. Lett.* **80**, 4570.
- Phillips, J.C., 1989, *Physics of High- $T_c$  Superconductors* (Academic Press, New York).
- Ping, J.Y., and B.R. Coles, 1982, *J. Magn. Magn. Mater.* **29**, 209.
- Pinkpank, M., A. Amato, F.N. Gygax, A. Schenck, W. Henggeler and P. Fischer, 1997, *Hyperfine Interactions* **105**, 145.
- Pinkpank, M., A. Amato, D. Andreica, F.N. Gygax, H.R. Ott and A. Schenck, 1999, *Physica C* **317–318**, 299.
- Pinkpank, M., A. Amato, D. Andreica, F.N. Gygax, H.R. Ott and A. Schenck, 2000a, *Physica B* **289–290**, 295.
- Pinkpank, M., A. Amato, D. Andreica, F.N. Gygax, H.R. Ott and A. Schenck, 2000b, *Physica B* **289–290**, 316.
- Pinkvos, H., A. Kalk and C. Schwink, 1990, *Phys. Rev. B* **41**, 590.
- Pobell, F., 1992, *Matter and Methods at Low Temperatures* (Springer, Berlin).
- Pollack, L., M.J.R. Hoch, C. Jin, E.N. Smith, J.M. Parpia, D.L. Hawthorne, D.A. Geller, D.M. Lee, R.C. Richardson, D.G. Hinks and E. Bucher, 1995, *Phys. Rev. B* **52**, R15707.
- Pomjakushin, V.Yu., A.M. Balagurov, E.V. Raspopina, V.V. Sikolenko, A.V. Gribanov, A. Schenck, A. Amato, U. Zimmermann and I.S. Lyubutin, 2000, *J. Phys.: Condens. Matter* **12**, 7969.
- Ponomarev, A.N., I.G. Ivanter, I.A. Krivosheev, A.A. Nezhivov, B.A. Nikolskii, V.N. Duginov, K.I. Gritsaj, V.G. Olshevsky, D. Herlach, V.Yu. Pomjakushin and U. Zimmermann, 2000, *Physica B* **289–290**, 236.

- Potzel, W., G.M. Kalvius and J. Gal, 1993, in: Handbook on the Physics and Chemistry of Rare Earths, Vol. 17, eds K.A. Gschneidner Jr and L. Eyring (North-Holland, Amsterdam) p. 539.
- Prelovsek, P., and T.M. Rice, 1987, Phys. Rev. Lett. **59**, 1248.
- Press, W.H., B.P. Flannery, S.A. Teukolsky and W.T. Vetterling, 1986, Numerical Recipes (Cambridge University Press, Cambridge).
- Prokes, K., V. Sechovsky, P. Svoboda, A. Amato, R. Feyerherm, F.N. Gygax, A. Schenck and H. Maletta, 1993, Nuclear and Particle Physics Newsletter (Paul Scherrer Institute, Villigen, unpublished) p. 95.
- Prokes, K., P. Svoboda, V. Sechovsky, E. Brück, A. Amato, R. Feyerherm, F.N. Gygax, A. Schenck, H. Maletta and F.R. de Boer, 1995, J. Magn. Magn. Mater. **140–144**, 1381.
- Prokes, K., V. Sechovsky, P. Svoboda, H. Nakotte, E. Brück and F.R. de Boer, 1996, Annual Report 1995, Annex 1 (Paul Scherrer Institute, Villigen, unpublished).
- Prokof'ev, N.V., 1994, Hyperfine Interactions **85–87**, 3.
- Przewoźnik, J., J. Zukrowski and K. Krop, 1993, J. Magn. Magn. Mater. **119**, 150.
- Ptasiewicz-Bak, H., J. Leciejewicz and A. Zygmont, 1981, J. Phys. F **11**, 1225.
- Ptasiewicz-Bak, H., J. Leciejewicz and A. Zygmont, 1985, Solid State Commun. **55**, 601.
- Quezel, S., J. Rossat-Mignod, B. Chevalier, P. Lejay and J. Etourneau, 1984, Solid State Commun. **49**, 685.
- Quezel, S., P. Burlet, J.L. Jacoud, L.P. Regnault, J. Rossat-Mignod, C. Vettier, P. Lejay and J. Flouquet, 1988, J. Magn. Magn. Mater. **76–77**, 403.
- Radousky, H.B., 1992, J. Mater. Res. **7**, 1917.
- Raffo, L., F. Licci and A. Migliori, 1993, Phys. Rev. B **48**, 1192.
- Rainford, B.D., 1999a, in: Muon Science, eds S.L. Lee, S.H. Kilcoyne and R. Cywinski (Institute of Physics Publishing, Bristol) p. 115.
- Rainford, B.D., 1999b, in: Muon Science, eds S.L. Lee, S.H. Kilcoyne and R. Cywinski (Institute of Physics Publishing, Bristol) p. 463.
- Rainford, B.D., and G.J. Daniell, 1994, Hyperfine Interactions **87**, 1129.
- Rainford, B.D., H.B. Stanley and B.V.B. Sarkissian, 1985, Physica B **130**, 388.
- Rainford, B.D., D.T. Adroja, R. Wäppling, G.M. Kalvius and A. Kratzer, 1995a, Physica B **206&207**, 202.
- Rainford, B.D., R. Cywinski and S.J. Dakin, 1995b, J. Magn. Magn. Mater. **140–144**, 805.
- Rainford, B.D., T. Forgan, D. Watson and G. Bowden, 1996, ISIS Annual Report 1995–96, A136.
- Raju, N.P., E. Gmelin and R.K. Kremer, 1992, Phys. Rev. B **46**, 5405.
- Ramirez, A.P., B. Batlogg, E. Bucher and A.S. Cooper, 1986, Phys. Rev. Lett. **57**, 1072.
- Ramirez, A.P., P. Schiffer, S.W. Cheong, C.H. Chen, W. Bao, T.T.M. Palstra, P.L. Gammel, D.J. Bishop and B. Zegarski, 1996, Phys. Rev. Lett. **76**, 3188.
- Raspopina, E.V., A.M. Balagurov, V.Yu. Pomjakushin, V.V. Sikolenko, A.V. Gribanov, A. Amato and A. Schenck, 2000, Physica B **289–290**, 282.
- Rauchschwalbe, U., F. Steglich, A. de Visser and J.J.M. Franse, 1987, J. Magn. Magn. Mater. **63&64**, 347.
- Ravot, D., M. Latroche and A. Percheron-Guegan, 1997, Physica B **234–236**, 647.
- Raymond, S., et al., 1998, quoted as private communication by Walf et al. (1999).
- Regnault, L.P., W.A.C. Erkelens, J. Rossat-Mignod, J. Flouquet, E. Walker, D. Jaccard, A. Amato and B. Hennion, 1987, J. Magn. Magn. Mater. **63&64**, 289.
- Regnault, L.P., W.A.C. Erkelens, J. Rossat-Mignod, P. Lejay and J. Flouquet, 1988, Phys. Rev. B **38**, 4481.
- Rimmel, J., O. Meyer, J. Geerk, J. Reiner, G. Linker, A. Erb and G. Müller-Vogt, 1993, Phys. Rev. B **48**, 16168.
- Rhyne, J.J., 1972, in: Magnetic Properties of Rare Earth Metals, ed. R.J. Elliot (Plenum Press, London) p. 129.
- Riseman, T.M., and J.H. Brewer, 1990, Hyperfine Interactions **65**, 1107.
- Riseman, T.M., and J.H. Brewer, 1994, Hyperfine Interactions **86**, 597.
- Riseman, T.M., J.H. Brewer, E.J. Ansaldo, P.M. Grant, M.E. Lopez-Morales and B.J. Sternlieb, 1990, Hyperfine Interactions **63**, 249.
- Riseman, T.M., J.H. Brewer and D.J. Arsenau, 1994, Hyperfine Interactions **87**, 1135.
- Ritter, C., S.H. Kilcoyne and R. Cywinski, 1991, J. Phys.: Condens. Matter **3**, 727.
- Ritter, C., R. Cywinski, S.H. Kilcoyne, S. Mondal and B.D. Rainford, 1994, Phys. Rev. B **50**, 9894.
- Robinson, R.A., A. Purwanto, M. Kohgi, P.C. Canfield, T. Kamiyama, T. Ishigaki, J.W. Lynn, R. Erwin, E. Peterson and M. Movshovich, 1994, Phys. Rev. Lett. **50**, 9595.
- Roduner, E., 1990, Hyperfine Interactions **65**, 857.



- Roduner, E., 1999, in: *Muon Science*, eds S.L. Lee, S.H. Kilcoyne and R. Cywinski (Institute of Physics Publishing, Bristol) p. 173.
- Roduner, E., A. Schenck and G. Solt, eds, 2000, *Proc. 8th Int. Conf. on Muon Spin Rotation, Relaxation and Resonance*, *Physica B* **289–290**.
- Roessli, B., P. Fischer, U. Staub, M. Zolliker and A. Furrer, 1994, *J. Appl. Phys.* **75**, 6337.
- Roof Jr, R.B., A.C. Larson and D.T. Cromer, 1961, *Acta Crystallogr.* **14**, 1084.
- Rosov, N., J.W. Lynn, G. Cao, J.W. O'Reilly, P. Pernambuco-Wise and J.E. Crow, 1992, *Physica C* **204**, 171.
- Rossat-Mignod, J., 1987, in: *Methods of Experimental Physics*, Vol. 23C, eds K. Sköld and D.L. Price (Academic Press, New York) p. 69.
- Rossat-Mignod, J., P. Burlet, S. Quezel and O. Vogt, 1980a, *Physica B* **102**, 237.
- Rossat-Mignod, J., P. Burlet, H. Bartholin, R. Tschapoutiou, O. Vogt, C. Vettier and R. Lagnier, 1980b, *Physica B* **102**, 177.
- Rossat-Mignod, J., S. Quezel, J.M. Effantin, P. Delacote, H. Bartholin, O. Vogt and D. Ravot, 1983, *J. Magn. Magn. Mater.* **31–34**, 398.
- Rossat-Mignod, J., G.H. Lander and P. Burlet, 1984, in: *Handbook on the Physics and Chemistry of the Actinides*, Vol. 1, eds A.J. Freeman and G.H. Lander (North-Holland, Amsterdam) p. 415.
- Rossat-Mignod, J., J.M. Effantin, P. Burlet, T. Chattertopadhyay, L.P. Regnault, H. Bartholin, C. Vettier, O. Vogt, D. Ravot and J.C. Achard, 1985, *J. Magn. Magn. Mater.* **52**, 111.
- Rosseinsky, M.J., K. Prassides and C.A. Scott, 1991, *Inorg. Chem.* **30**, 3367.
- Rossel, C., K.N. Yang, M.B. Maple, Z. Fisk, E. Zirngiebl and J.D. Thompson, 1987, *Phys. Rev. B* **35**, 1914.
- Roy, S.B., A.K. Pradhan and P. Chaddah, 1996, *Physica C* **271**, 181.
- Ruck, M., G. Portisch, H.G. Schlager and H. von Löhneysen, 1993, *Acta Crystallogr. B* **49**, 936.
- Ruegg, K.J., C. Boekema, A.B. Denison, W. Hofmann and W. Kündig, 1980, *J. Magn. Magn. Mater.* **15–18**, 669.
- Sagawa, M., S. Fujimura, N. Togawa, H. Yamamoto and Y. Matsuura, 1984, *J. Appl. Phys.* **55**, 2083.
- Saito, R., H. Kamimura and K. Nagamine, 1991, *Physica C* **185**, 1217.
- Sakurai, J., Y. Yamaguchi, S. Nishigori, T. Suzuki and T. Fujita, 1990, *J. Magn. Magn. Mater.* **90&91**, 422.
- Sánchez, D.R., M.A.C. de Melo, M. Fontes, S.L. Bud'ko, E. Baggio-Saitovich, M. Hillberg, W. Wagener, H.H. Klauff, H. Walf and F.J. Litterst, 1998, *Phys. Rev. B* **57**, 10268.
- Sanchez, J.P., B. Lebech, M. Wulff, G.H. Lander, K. Tomala, K. Mattenberger, O. Vogt, A. Blaise, J. Rebizant, J.C. Spirlet and P.J. Brown, 1992, *J. Phys.: Condens. Matter* **4**, 9423.
- Santini, P., and G. Amoretti, 1994, *Phys. Rev. Lett.* **73**, 1027.
- Sato, N., N. Aso, K. Hirota, T. Komatsubara, Y. Endoh, S.M. Shapiro, G.H. Lander and K. Kakurai, 1996, *Phys. Rev. B* **53**, 14043.
- Sato, N., N. Aso, N. Tateiwa, N. Koga, T. Komatsubara and N. Metoki, 1997, *Physica B* **230–232**, 367.
- Sato, T., H. Takakura, A.P. Tsai and K. Shibata, 1998, *Phys. Rev. Lett.* **81** 2364.
- Sauls, J.A., 1994, *Adv. Phys.* **43**, 113.
- Schäfer, W., W. Kockelmann, S. Fredo, I. Halevy and J. Gal, 1998, *J. Magn. Magn. Mater.* **177–181**, 808.
- Schatz, G., and A. Weidinger, 1992, *Nukleare Festkörperphysik*, 2nd Ed. (Teubner, Stuttgart). English translation: 1996, *Nuclear Condensed Matter Physics* (Wiley, New York).
- Schenck, A., 1985, *Muon Spin Rotation Spectroscopy* (Adam Hilger, Bristol).
- Schenck, A., 1993, in: *Frontiers in Solid State Science*, Vol. 2, eds L.C. Gupta and M.S. Multani (World Scientific, Singapore) p. 269.
- Schenck, A., 1999, in: *Muon Science*, eds S.L. Lee, S.H. Kilcoyne and R. Cywinski (Institute of Physics Publishing, Bristol) p. 39.
- Schenck, A., and F.N. Gygax, 1995, in: *Handbook of Magnetic Materials*, Vol. 9, ed. K.H.J. Buschow (Elsevier, Amsterdam) p. 57.
- Schenck, A., P. Birrer, F.N. Gygax, B. Hitti, E. Lippelt, H. Maletta and M. Weber, 1990a, *Hyperfine Interactions* **63**, 227.
- Schenck, A., P. Birrer, F.N. Gygax, B. Hitti, E. Lippelt, M. Weber, P. Böni, P. Fischer, H.R. Ott and Z. Fisk, 1990b, *Phys. Rev. Lett.* **65**, 2454.
- Schenck, A., P. Birrer, F.N. Gygax, B. Hitti, E. Lippelt, H.R. Ott and M. Weber, 1990c, *Hyperfine Interactions* **63**, 511.
- Schenck, A., P. Birrer, F.N. Gygax, B. Hitti, E. Lippelt, S. Barth, H.R. Ott and Z. Fisk, 1992, *J. Magn. Magn. Mater.* **108**, 97.
- Schenck, A., A. Amato, F.N. Gygax, M. Pinkpank, P. Ahmet, M. Ablitz, R. Settai and Y. Ōnuki, 1997a, *Hyperfine Interactions* **104**, 105.

- Schenck, A., A. Amato, F.N. Gygax, M. Pinkpank and H.R. Ott, 1997b, *Hyperfine Interactions* **104**, 215.
- Schenck, A., A. Amato, F.N. Gygax, M. Pinkpank, A. Jung, P. Wachter, J. Major, Th. Stammeler and R. Scheuermann, 1997c, *Hyperfine Interactions* **104**, 209.
- Schenck, A., M. Pinkpank, F.N. Gygax, K.U. Neumann, K.R.A. Ziebeck and A. Amato, 1998a, *J. Phys.: Condens. Matter* **10**, 8059.
- Schenck, A., D. Andreica, F.N. Gygax, M. Pinkpank, Y. Önuki, P. Ahmet, M. Ablitz, R. Settai, A. Amato and N. Kaplan, 1998b, *Phys. Rev. B* **58**, 5205.
- Schenck, A., D. Andreica, M. Pinkpank, F.N. Gygax, H.R. Ott, A. Amato, R.H. Heffner, D.E. MacLaughlin and G.J. Nieuwenhuys, 1999, *Physica B* **259–261**, 14.
- Schenck, A., N. Sato, G. Solt, D. Andreica, F.N. Gygax, M. Pinkpank and A. Amato, 2000a, *Eur. Phys. J. B* **13**, 245.
- Schenck, A., D. Andreica, F.N. Gygax, M. Pinkpank, K.A. McEwen and A. Amato, 2000b, *Physica B* **289–290**, 311.
- Schenck, A., R.J. Keiser, A. de Visser, A. Amato, D. Andreica, F.N. Gygax, M. Pinkpank, P. Estrela, M.J. Graf, A.A. Menovsky and J.J.M. Franse, 2000c, *Physica B* **289–290**, 455.
- Schenck, A., D. Andreica, F.N. Gygax, K. Umeo, T. Takabatake, E. Schreier, A. Kratzer and G.M. Kalvius, 2001, *J. Phys.: Condens. Matter* **13**, 4277.
- Scheuermann, R., J. Schmidt, A. Seeger, Th. Stammeler, D. Herlach and J. Major, 1997, *Hyperfine Interactions* **106**, 295.
- Schiffer, P., A.P. Ramirez, D.A. Huse and A.J. Valentino, 1994, *Phys. Rev. Lett.* **73**, 2500.
- Schiffer, P., A.P. Ramirez, D.A. Huse, P.L. Gammel, U. Yaron, D.J. Bishop and A.J. Valentino, 1995, *Phys. Rev. Lett.* **74**, 2379.
- Schlabitz, W., J. Baumann, B. Politt, U. Rauchschwalbe, M.H. Mayer, A. Ahlheim and C.D. Bredl, 1986, *Z. Phys. B* **62**, 171.
- Schneider, T., and H. Keller, 1992, *Phys. Rev. Lett.* **69**, 3374.
- Schobinger-Papamantellos, P., and K.H.J. Buschow, 1994, *J. Magn. Magn. Mater.* **130**, 242.
- Schobinger-Papamantellos, P., N.P. Duong, K.H.J. Buschow, D. Andreica, F.N. Gygax, M. Pinkpank and A. Schenck, 2000, *Physica B* **289–290**, 277.
- Schoenes, J., B. Frick and O. Vogt, 1984, *Phys. Rev. B* **30**, 6578.
- Schoenes, J., O. Vogt, J. Löhle, F. Hulliger and K. Mattenberger, 1996, *Phys. Rev. B* **53**, 14987.
- Schreier, E., 1999, Doctoral Thesis (Physics Department, Technical University Munich, Germany, unpublished).
- Schreier, E., S. Henneberger, F.J. Burghart, A. Kratzer, G.M. Kalvius, O. Hartmann, M. Ekström and R. Wäppling, 1997, *Hyperfine Interactions* **104**, 311.
- Schreier, E., M. Ekström, O. Hartmann, R. Wäppling, G.M. Kalvius, F.J. Burghart, S. Henneberger, A. Marelius and A. Kratzer, 2000a, *Physica B* **289–290**, 240.
- Schreier, E., M. Ekström, O. Hartmann, R. Wäppling, G.M. Kalvius, F.J. Burghart, A. Kratzer, L. Asch and F.J. Litterst, 2000b, *Physica B* **289–290**, 244.
- Schröder, A., J.W. Lynn, R.E. Ewin, M. Loewenhaupt and H. von Löhneysen, 1994a, *Physica B* **199&200**, 47.
- Schröder, A., J.G. Lussier, B.D. Gaulin, J.D. Garrett, W.J.L. Buyers, L. Rebersky and S.M. Shapiro, 1994b, *Phys. Rev. Lett.* **72**, 136.
- Schröder, A., G. Aeppli, T.E. Mason and E. Bucher, 1997, *Physica B* **234–236**, 861.
- Schuberth, E.A., B. Strikler and K. Andres, 1992, *Phys. Rev. Lett.* **68**, 117.
- Schuberth, E.A., J. Schupp, R. Freese and K. Andres, 1995, *Phys. Rev. B* **51**, 12892.
- Seaman, C.L., J.J. Neumeier, M.B. Maple, L.P. Le, G.M. Luke, B.J. Sternlieb, Y.J. Uemura, J.H. Brewer, R. Kadono, R.F. Kiefl, S.R. Kreitzman and T.R. Riseman, 1990, *Phys. Rev. B* **42**, 6801.
- Seaman, C.L., M.B. Maple, B.W. Lee, S. Ghamati, M.S. Torikachvili, J.S. Kang, L.Z. Liu, J.W. Allen and D.L. Cox, 1991, *Phys. Rev. Lett.* **67**, 2882.
- Seaman, C.L., M.B. Maple, B.W. Lee, S. Ghamati, M.S. Torikachvili, J.S. Kang, L.Z. Liu, J.W. Allen and D.L. Cox, 1992, *J. Alloys Compounds* **181**, 327.
- Sechovsky, V., and L. Havela, 1988, in: *Ferromagnetic Materials*, Vol. 4, eds E.P. Wohlfahrt and K.H.J. Buschow (Elsevier, Amsterdam) p. 309.
- Sechovsky, V., L. Havela, H. Nakotte, F.R. de Boer and E. Brück, 1994, *J. Alloys Compounds* **206/207**, 221.
- Sechovsky, V., L. Havela, P. Svoboda, A.V. Andreev, P. Burel, K. Prokes, H. Nakotte, F.R. de Boer, R.A. Robinson and H. Maletta, 1995, *J. Magn. Magn. Mater.* **140–144**, 1379.
- Seeger, A., and L. Schimmele, 1992, in: *Perspectives of Meson Science*, eds T. Yamazaki, K. Nakai and K. Nagamine (North-Holland, Amsterdam) p. 293.

- Segawa, K., A. Tomita, K. Iwashita, M. Kasuya, T. Suzuki and S. Kunii, 1992, *J. Magn. Magn. Mater.* **104–107**, 1233.
- Sekine, C., S. Murayama, H. Takano, K. Hoshi, K. Nishiyama, K. Nagamine and Y. Ōnuki, 1994, *Hyperfine Interactions* **85**, 419.
- Sekine, C., H. Sakamoto, S. Murayama, H. Takano, K. Hoshi, K. Nishiyama, K. Nagamine and Y. Ōnuki, 1995, *Physica B* **206&207**, 307.
- Sengupta, A.M., and A. Georges, 1995, *Phys. Rev. B* **52**, 10295.
- Sereni, J.G., O. Trovarelli, J.P. Kappler, C. Paschke, T. Trappmann and H. von Löhneysen, 1994, *Physica B* **199&200**, 567.
- Severing, A., A.P. Murani, J.D. Thompson, Z. Fisk and C.K. Loong, 1990, *Phys. Rev. B* **41**, 1317.
- Shaheen, S.A., J.S. Schilling and R.N. Shelton, 1985, *Phys. Rev. B* **31**, 656.
- Shapiro, S.M., J.D. Axe, R.J. Birgeneau, J.M. Lawrence and R.D. Parks, 1977, *Phys. Rev. B* **16**, 2225.
- Shapiro, S.M., E. Gurewitz, R.D. Parks and L.C. Kupferberg, 1979, *Phys. Rev. Lett.* **43**, 1748.
- Sheaen, T.P., 1994, *Introduction to High-Temperature Superconductivity* (Plenum, New York).
- Sherrington, D., 1979, *J. Phys. C* **12**, L929.
- Shiga, M., H. Wada and J. Nakamura, 1983, *J. Magn. Magn. Mater.* **31–34**, 119, 829.
- Shiga, M., H. Wada, Y. Nakamura, J. Deportes and K.R.A. Ziebeck, 1988, *J. Phys. Soc. Japan* **57**, 3141.
- Shiga, M., K. Fujisawa and H. Wada, 1993, *J. Phys. Soc. Japan* **62**, 1329.
- Shigeoka, T., N. Iwata, Y. Hashimoto, Y. Andoh and H. Fujii, 1989, *Physica B* **156–157**, 741.
- Shigeoka, T., N. Iwata and H. Fujii, 1992, *J. Magn. Magn. Mater.* **104–107**, 1229.
- Shigeoka, T., K. Hirota, M. Ishikawa, T. Takabatake and H. Fujii, 1993, *Physica B* **186–188**, 469.
- Shivaram, B.S., T.F. Rosenbaum and D.G. Hinks, 1986, *Phys. Rev. Lett.* **57**, 1259.
- Sikkema, A.E., W.J.L. Buyers, I. Affleck and J. Gan, 1996, *Phys. Rev. B* **54**, 9322.
- Sinha, S.K., 1978, in: *Handbook on the Physics and Chemistry of Rare Earths*, Vol. 1, eds K.A. Gschneidner Jr and L. Eyring (North-Holland, Amsterdam) p. 489.
- Sinha, S.K., G.H. Lander, S.H. Shapiro and O. Vogt, 1981, *Phys. Rev. B* **23**, 4556.
- Skolozdra, R.V., O.E. Koretskaya and Yu.K. Gorelenko, 1984, *Inorg. Mater.* **20**, 604.
- Slichter, C.P., 1978, *Principles of Magnetic Resonance* (Springer, Berlin/New York).
- Soderholm, L., C.K. Loong and S. Kern, 1992, *Phys. Rev. B* **45**, 10062.
- Solt, G., 1995, *Hyperfine Interactions* **96**, 167.
- Sonier, J.E., R.H. Heffner, D.E. MacLaughlin, J.L. Smith, J. Cooley and G.J. Nieuwenhuys, 2000a, *Physica B* **289–290**, 20.
- Sonier, J.E., R.H. Heffner, D.E. MacLaughlin, G.J. Nieuwenhuys, O.O. Bernal, R. Movshovich, P.G. Pagliuso, J. Cooley, J.L. Smith and J.D. Thompson, 2000b, *Phys. Rev. Lett.* **85**, 2821.
- Souletie, J., 1994, *J. Appl. Phys.* **75**, 5512.
- Spendler, L., D. Jaccard, J. Sierro, M. François, A.A. Stepanov and J. Voiron, 1994, *J. Low Temp. Phys.* **94**, 585.
- Spirlet, J.C., and O. Vogt, 1984, in: *Handbook on the Physics and Chemistry of the Actinides*, Vol. 1, eds A.J. Freeman and G.H. Lander (North-Holland, Amsterdam) p. 301.
- Stammler, Th., E. Gmelin, K.-H. Greubel, M. Hampele, J. Major and R. Scheuermann, 1997, *Hyperfine Interactions* **106**, 307.
- Standley, K.J., and R.A. Vaughn, 1969, *Electron Spin Relaxation Phenomena in Solids* (Hilger, London).
- Staub, U., J. Mesot, M. Guillaume, P. Allenspach, A. Furrer, H. Mutka, Z. Bowden and A.D. Taylor, 1994, *Phys. Rev. B* **50**, 4068.
- Steglich, F., J. Aarts, C.D. Bredl, W. Lieke, D. Meschede, W. Franz and H. Schäfer, 1979, *Phys. Rev. Lett.* **43**, 1892.
- Steglich, F., C. Geibel, K. Gloos, G. Olesch, C. Schank, C. Wassilev, A. Loidl, A. Krimmel and G.R. Stewart, 1994, *J. Low Temp. Phys.* **95**, 3.
- Steglich, F., P. Gegenwart, C. Geibel, R. Helfrich, P. Hellmann, M. Lang, A. Link, R. Modler, G. Sparn, N. Büttgen and A. Loidl, 1996, *Physica B* **223&224**, 1.
- Stepanov, A.A., P. Wyder, T. Chattopadhyay, P.J. Brown, I.M. Vitebsky, A. Deville, B. Gaillard, S.N. Barilo and D.I. Zhigunov, 1993, *Phys. Rev. B* **48**, 12979.
- Stevens, K.W.H., 1967, *Rep. Prog. Phys.* **30**, 189.
- Stewart, G.R., 1984, *Rev. Mod. Phys.* **56**, 755.
- Stewart, G.R., Z. Fisk and M.S. Wire, 1984, *Phys. Rev. B* **30**, 482.
- Stockert, O., H. von Löhneysen, A. Schröder, M. Loewenhaupt, N. Pyka, P.L. Gammel and U. Yaron, 1997, *Physica B* **230–232**, 247.

- Storchak, V., 1999, in: *Muon Science*, eds S.L. Lee, S.H. Kilcoyne and R. Cywinski (Institute of Physics Publishing, Bristol) p. 287.
- Storchak, V., J.H. Brewer and G.D. Morris, 1995a, *Phys. Rev. Lett.* **75**, 2384.
- Storchak, V., J.H. Brewer and G.D. Morris, 1995b, *Philos. Mag.* **72**, 241.
- Storchak, V., J.H. Brewer and G.D. Morris, 1996, *Hyperfine Interactions* **97&98**, 323.
- Storchak, V., S.F.J. Cox, S.P. Cottrell, J.H. Brewer, G.D. Morris, D.J. Arsenneau and B. Hitti, 1997, *Phys. Rev. Lett.* **78**, 2835.
- Strecker, M., and G. Wortmann, 1999, *Hyperfine Interactions* **120–121**, 187.
- Suellow, S., R.W.A. Hendriks, T.J. Gortemulder, G.J. Nieuwenhuys, A.A. Menovsky, A. Schenck and J.A. Mydosh, 1994, *Physica C* **233**, 138.
- Suellow, S., G.J. Nieuwenhuys, A.A. Menovsky, J.A. Mydosh, S.A.M. Mentink, T.E. Mason and W.J.L. Buyers, 1997, *Phys. Rev. Lett.* **78**, 354.
- Sugawara, H., P. Svoboda, Y. Aoki, H. Sato, R. Settai, Y. Ōnuki, K. Sugiyama and S. Takayamaki, 1995, *J. Phys. Soc. Japan* **64**, 4889.
- Sugiyama, J., S. Tokuono, S. Koriyama, H. Yamauchi and S. Tanaka, 1991, *Phys. Rev. B* **43**, 10489.
- Sugiyama, J., J.H. Brewer, G.D. Morris, C. Niedermayer, T.M. Riseman, I. Shinkoda, H. Zhou, E.J. Ansaldo, H. Glückler, H. Yamauchi and S. Tanaka, 1992, *Physica C* **193**, 449.
- Sulaiman, S.B., S. Srinivas, N. Sahoo, F. Hagelberg, T.P. Das, E. Torikai and K. Nagamine, 1994a, *Phys. Rev. B* **49**, 9879.
- Sulaiman, S.B., N. Sahoo, S. Srinivas, F. Hagelberg, T.P. Das, E. Torikai and K. Nagamine, 1994b, *Hyperfine Interactions* **84**, 87.
- Suzuki, H., M. Kasaya, M. Kohgi, A. Dönni, P. Fischer, G. Le Bras and P. Bonville, 1995, *Physica B* **206&207**, 341.
- Suzuki, T., 1993, *Jpn. J. Appl. Phys. Series* **8**, 267.
- Svoboda, P., M. Divis, A.V. Andreev, N.V. Baranov, M.I. Bartashevich and P.E. Markin, 1992, *J. Magn. Magn. Mater.* **104–107**, 1329.
- Tagawa, Y., J. Sakurai, Y. Komura and T. Ishimasa, 1986, *Solid State Commun.* **82**, 111.
- Tagikawa, M., H. Yasuoka, T. Tanaka and Y. Ishizawa, 1983, *J. Phys. Soc. Japan* **52**, 728.
- Taillefer, L., 1994, *Hyperfine Interactions* **85**, 379.
- Takabatake, T., and H. Fujii, 1993, *Jpn. J. Appl. Phys. Series* **8**, 254.
- Takabatake, T., Y. Nakazawa and M. Ishikawa, 1987, *Jpn. J. Appl. Phys.* **26**(Suppl. 26-3), 547.
- Takabatake, T., Y. Nakazawa, M. Ishikawa, T. Sakakibara and K. Koga, 1988, *J. Magn. Magn. Mater.* **76&77**, 87.
- Takabatake, T., M. Nagasawa, H. Fujii, G. Kido, M. Nohara, S. Nishigori, T. Suzuki, T. Fujita, R. Helfrich, U. Ahlheim, K. Fraas, C. Geibel and F. Steglich, 1992a, *Phys. Rev. B* **45**, 5740.
- Takabatake, T., H. Iwasaki, H. Fujii, S. Ikeda, S. Nishigori, Y. Aoki, T. Suzuki and T. Fujita, 1992b, *J. Phys. Soc. Japan* **61**, 778.
- Takabatake, T., H. Iwasaki, G. Nakamoto, H. Fujii, H. Nakotte, F.R. de Boer and V. Sechovsky, 1993, *Physica B* **183**, 108.
- Takabatake, T., Y. Maeda, T. Konishi and H. Fujii, 1994, *J. Phys. Soc. Japan* **63**, 2853.
- Takabatake, T., G. Nakamoto, T. Yoshino, H. Fujii, K. Izawa, S. Nishigori, H. Goshima, T. Suzuki, T. Fujita, K. Maezawa, T. Hiraoka, Y. Okayama, I. Oguro, A.A. Menovsky, K. Neumaier, A. Brückl and K. Andres, 1996, *Physica B* **223&224**, 413.
- Takabatake, T., F. Iga, T. Yoshino, Y. Echizen, K. Kobayashi, M. Higa, K. Katoh, N. Shimizu, Y. Bando, G. Nakamoto, H. Fujii, K. Izawa, T. Suzuki, T. Fujita, M. Serac, M. Hiroi, K. Maezawa, S. Mock, H. von Löhneysen, A. Brückl, K. Neumaier and K. Andres, 1998a, *J. Magn. Magn. Mater.* **177–181**, 277.
- Takabatake, T., K. Umeo, R. Kadono, I. Watanabe, G.M. Kalvius and A. Kratzer, 1998b, *RIKEN Accel. Prog. Rep.* **31**.
- Takabatake, T., M. Shirasse, K. Katoh, Y. Echizen, K. Sugiyama and T. Osakabe, 1998c, *J. Magn. Magn. Mater.* **177–181**, 53.
- Takagi, S., H. Suzuki, A. Ochiai and T. Suzuki, 1993a, *J. Phys. Soc. Japan* **63**, 2891.
- Takagi, S., H. Suzuki, A. Ochiai, T. Suzuki, A. Amato, R. Feyerherm, F.N. Gygax and A. Schenck, 1993b, *Physica B* **186–188**, 422.
- Takagi, S., T. Suzuki, A. Amato, F.N. Gygax, A. Schenck and A. Ochiai, 1997, *Hyperfine Interactions* **104**, 151.
- Takeda, N., J. Kitagawa and M. Ishikawa, 1995, *J. Phys. Soc. Japan* **64**, 387.
- Takeda, N., M. Ishikawa, T. Takabatake and T. Shiogeoka, 1996, *J. Phys. Soc. Japan* **63**, 1186.
- Tarascon, J.M., P. Barboux, G.W. Hull Jr, R. Ramesh, L.H. Greene, M. Giroud, M.S. Hegde and W.R. McKinnon, 1989, *Phys. Rev. B* **39**, 4316.
- Tarascon, J.M., E. Wang, S. Kivelson, B.G. Bagley, G.W. Hull Jr and R. Ramesh, 1990, *Phys. Rev. B* **42**, 218.

- Tashma, T., A. Amato, A. Grayevsky, F.N. Gygax, M. Pinkpank, A. Schenck and N. Kaplan, 1997, *Phys. Rev. B* **56**, 9397.
- Tashma, T., A. Grayevsky, N. Kaplan, F.N. Gygax, A. Amato, M. Pinkpank and A. Schenck, 1998, Annual Report 1997, Annex 1 (Paul Scherrer Institute, Villigen, unpublished) p. 67.
- Telling, M.T.F., S.H. Kilcoyne and R. Cywinski, 1994, *Hyperfine Interactions* **85**, 209.
- Telling, M.T.F., C. Ritter and R. Cywinski, 1998, *J. Magn. Magn. Mater.* **177–181**, 1480.
- Telling, M.T.F., J.A. Dann, R. Cywinski, J. Bogner, M. Reissner and W. Steiner, 2000, *Physica B* **289–290**, 213.
- Thompson, J.D., A.C. Lawson, M.W. McElfresh, A.P. Sattelberger and Z. Fisk, 1988, *J. Magn. Magn. Mater.* **76&77**, 437.
- Thompson, J.D., S.W. Cheong, S.E. Brown, Z. Fisk, S.B. Oseroff, M. Tovar, D.C. Vier and S. Schultz, 1989, *Phys. Rev. B* **39**, 6660.
- Tokura, Y., 1997, *Physica B* **237&238**, 1.
- Tokura, Y., and Y. Tomioka, 1999, *J. Magn. Magn. Mater.* **200**, 1.
- Tomala, K., G. Czjzek, J. Fink and H. Schmidt, 1977, *Solid State Commun.* **24**, 857.
- Tomioka, Y., A. Asamitsu, H. Kuwahara, Y. Moritomo, M. Kasai, R. Kumai and Y. Tokura, 1997, *Physica B* **237&238**, 6.
- Torikai, E., E. Hirose, P. Birrer, K. Nagamine and T. Shinjo, 1994, *Hyperfine Interactions* **85**, 151.
- Torrance, J.B., P. Lacorre, A.I. Nazzari, E.J. Ansaldo and C. Niedermayer, 1992, *Phys. Rev. B* **45**, 8209.
- Tou, H., Y. Kitaoka, K. Asayama, N. Kimura, Y. Ōnuki, E. Yamamoto and K. Maezawa, 1996, *Phys. Rev. Lett.* **77**, 1374.
- Tranquada, J.M., 1996, *Neutron News* **7**, 17.
- Tranquada, J.M., 1998, *J. Phys. Chem. Solids* **59**, 2190.
- Tranquada, J.M., D.E. Cox, W. Kunmann, A.H. Moudden, G. Shirane, M. Suenaga and P. Zolliker, 1988, *Phys. Rev. Lett.* **60**, 156.
- Tranquada, J.M., J.D. Axe, N. Ichikawa, Y. Nakamura, S. Uchida and B. Nachumi, 1996, *Phys. Rev. B* **54**, 7489.
- Tranquada, J.M., P. Wochner and D.J. Buttrey, 1997, *Phys. Rev. Lett.* **79**, 2133.
- Trovarelli, O., J.G. Sereni, G. Schmerber and J.P. Kappler, 1994, *Phys. Rev. B* **49**, 15179.
- Trovarelli, O., J.G. Sereni, G. Schmerber and J.P. Kappler, 1995, *Physica B* **206&207**, 243.
- Trovarelli, O., M. Weiden, R. Müller-Reisener, M. Gomez-Berisso, P. Gegenwart, M. Deppe, C. Geibel, J.G. Sereni and F. Steglich, 1997, *Phys. Rev. B* **56**, 678.
- Tsang, T., K.A. Gschneidner Jr, O.D. McMasters, R.J. Stiermann and S.K. Dhar, 1984, *Phys. Rev. B* **29**, 4185.
- Tsui, Y.K., C.A. Burns, J. Snyder and P. Schiffer, 1999, *Phys. Rev. Lett.* **82**, 3532.
- Turner, E., 1986, *Hyperfine Interactions* **30**, 17.
- Uemura, Y.J., 1981, Ph.D. Thesis (University of Tokyo). UT-MSL Report 20.
- Uemura, Y.J., 1989, *Hyperfine Interactions* **49**, 205.
- Uemura, Y.J., 1992, in: *Perspectives of Meson Science*, eds T. Yamazaki, K. Nakai and K. Nagamine (North-Holland, Amsterdam) p. 87.
- Uemura, Y.J., 1997, *Hyperfine Interactions* **105**, 35.
- Uemura, Y.J., 1999, in: *Muon Science*, eds S.L. Lee, S.H. Kilcoyne and R. Cywinski (Institute of Physics Publishing, Bristol) p. 85.
- Uemura, Y.J., and R. Cywinski, 1999, in: *Muon Science*, eds S.L. Lee, S.H. Kilcoyne and R. Cywinski (Institute of Physics Publishing, Bristol) p. 165.
- Uemura, Y.J., and G.M. Luke, 1993, *Physica B* **188**, 223.
- Uemura, Y.J., and T. Yamazaki, 1983, *J. Magn. Magn. Mater.* **31–34**, 1359.
- Uemura, Y.J., K. Nishiyama, T. Yamazaki and R. Nakai, 1981, *Solid State Commun.* **39**, 461.
- Uemura, Y.J., D.R. Harshman, M. Senba, E.J. Ansaldo and A.P. Murani, 1984, *Phys. Rev. B* **30**, 1606.
- Uemura, Y.J., T. Yamazaki, D.R. Harshman, M. Senba and E.J. Ansaldo, 1985, *Phys. Rev. B* **31**, 546.
- Uemura, Y.J., W.J. Kossler, B. Hitti, J.R. Kempton, H.E. Schone, X.H. Yu, C.E. Stronach, W.F. Lankford, D.R. Noakes, R. Keitel, M. Senba, J.H. Brewer, E.J. Ansaldo, Y. Ōnuki, T. Komatsubara, G. Acpli, E. Bucher and J.E. Crow, 1986, *Hyperfine Interactions* **31**, 413.
- Uemura, Y.J., W.J. Kossler, X.H. Yu, J.R. Kempton, H.E. Schone, D. Opie, C.E. Stronach, D.C. Johnston, M.S. Alvarez and D.P. Goshorn, 1987, *Phys. Rev. Lett.* **59**, 1045.
- Uemura, Y.J., W.J. Kossler, X.H. Yu, H.E. Schone, J.R. Kempton, C.E. Stronach, S. Barth, F.N. Gygax, B. Hitti, A. Schenck, C. Baines, W.F. Lankford, Y. Ōnuki and T. Komatsubara, 1988, *Physica C* **153–155**, 455.
- Uemura, Y.J., W.J. Kossler, X.H. Yu, H.E. Schone, J.R. Kempton, C.E. Stronach, S. Barth, F.N. Gygax,

- B. Hitti, A. Schenck, C. Baines, W.F. Lankford, Y. Ōnuki and T. Komatsubara, 1989, *Phys. Rev. B* **39**, 4726.
- Uemura, Y.J., L.P. Le, G.M. Luke, B.J. Sternlieb, W.D. Wu, J.H. Brewer, T.M. Riseman, C.L. Seaman, M.B. Maple, M. Ishikawa, D.G. Hinks, J.D. Jorgensen, G. Saito and H. Yamochi, 1991, *Phys. Rev. Lett.* **66**, 2665.
- Uemura, Y.J., A. Keren, K.M. Kojima, L.P. Le, G.M. Luke, W.D. Wu, Y. Ajiro, T. Asano, Y. Kuriyama, M. Mekata, H. Kikuchi and K. Kakurai, 1994, *Phys. Rev. Lett.* **73**, 3306.
- Umeo, K., H. Kadomatsu and T. Takabatake, 1996a, *Phys. Rev. B* **54**, 1194.
- Umeo, K., H. Kadomatsu and T. Takabatake, 1996b, *J. Phys.: Condens. Matter* **8**, 9743.
- Umeo, K., T. Igaue, H. Chyono, Y. Echizen, T. Takabatake, M. Kosaka and Y. Uwatoko, 1999, *Phys. Rev. B* **60**, 6957.
- Vajda, P., 1995, in: *Handbook on the Physics and Chemistry of Rare Earths*, Vol. 20, eds K.A. Gschneidner Jr and L. Eyring (North-Holland, Amsterdam) p. 207.
- van Laar, B., 1965, *Phys. Rev.* **138**, A584.
- van Maaren, M.H., H.J. van Daal and K.H.J. Buschow, 1974, *Solid State Commun.* **14**, 145.
- Varma, C.M., 1985, *Comm. Solid State Phys.* **11**, 221.
- Velikhovskii, A.A., and V.N. Nikiforov, 1993, *IEEE Trans. Magn.* **MAG-30**, 1208.
- Vettier, C., P. Morin and J. Flouquet, 1986, *Phys. Rev. Lett.* **56**, 1980.
- Vogt, O., and K. Mattenberger, 1993, in: *Handbook on the Physics and Chemistry of Rare Earths*, Vol. 17, eds K.A. Gschneidner Jr and L. Eyring (North-Holland, Amsterdam) p. 301.
- Voiron, J., R. Ballou, J. Deportes, R.M. Galera and E. Lelièvre, 1990, *J. Appl. Phys.* **69**, 5678.
- Vollmer, R., T. Miokovic, A. Schröder, H. von Löhneysen, G.M. Kalvius, Y. Echizen and T. Takabatake, 2000, *Phys. Rev. B* **291**, 307.
- von Löhneysen, H., 1994, *Physica B* **197**, 551.
- von Löhneysen, H., 1995, *Physica B* **206&207**, 101.
- von Löhneysen, H., 1996a, *J. Magn. Magn. Mater.* **157&158**, 601.
- von Löhneysen, H., 1996b, *J. Phys.: Condens. Matter* **8**, 9689.
- von Löhneysen, H., 1997, *Hyperfine Interactions* **104**, 127.
- von Löhneysen, H., T. Trappmann and L. Taillefer, 1992, *J. Magn. Magn. Mater.* **108**, 49.
- von Löhneysen, H., T. Pietrus, G. Portisch, H.G. Schlager, A. Schröder, M. Sieck and T. Trappmann, 1994, *Phys. Rev. Lett.* **72**, 3262.
- von Löhneysen, H., F. Huster, S. Mock, A. Neubert, T. Pietrus, M. Sieck, O. Stockert and M. Waffenschmidt, 1997, *Physica B* **230–232**, 550.
- Wachter, P., 1994, in: *Handbook on the Physics and Chemistry of Rare Earths*, Vol. 19, eds K.A. Gschneidner Jr and L. Eyring (North-Holland, Amsterdam) p. 177.
- Wachter, P., and A. Jung, 1994, *IEEE Trans. Magn.* **MAG-30**, 954.
- Wachter, P., A. Jung and P. Steiner, 1995, *Phys. Rev. B* **51**, 5542.
- Wäckelgård, E., O. Hartmann, E. Karlsson, R. Wäppling, L. Asch, G.M. Kalvius, J. Chappert and A. Yaouanc, 1986, *Hyperfine Interactions* **31**, 325.
- Wäckelgård, E., O. Hartmann, E. Karlsson, R. Wäppling, L. Asch, G.M. Kalvius, J. Chappert and A. Yaouanc, 1989, *Hyperfine Interactions* **50**, 781.
- Wada, H., H. Nakamura, K. Yoshimura, M. Shiga and Y. Nakamura, 1987, *J. Magn. Magn. Mater.* **70**, 134.
- Wada, H., M. Shiga and Y. Nakamura, 1989, *Physica B* **161**, 197.
- Wagener, W., H.H. Klauß, M. Hillberg, M.A.C. de Melo, M. Birke, F.J. Litterst, B. Büchner and H. Micklitz, 1997, *Phys. Rev. B* **55**, R14761.
- Wagener, W., H.H. Klauß, M. Hillberg, M.A.C. de Melo, W. Kopmann, M. Birke, F.J. Litterst, B. Büchner and H. Micklitz, 1998, *J. Magn. Magn. Mater.* **177**, 545.
- Walf, H., D. Mienert, W. Wagner, W. Kopmann, M. Hillberg, H.H. Klauß, F.J. Litterst, M. Fontes, S.L. Bud'ko and E. Baggio-Saitovich, 1999, *Hyperfine Interactions* **120–121**, 629.
- Walker, D.C., 1983, *Muon and Muonium Chemistry* (Cambridge University Press, Cambridge).
- Walker, M.B., W.J.L. Buyers, Z. Tun, W. Que, A.A. Menovsky and J.D. Garrett, 1993, *Phys. Rev. Lett.* **71**, 2630.
- Walker, M.B., Z. Tun, W.J.L. Buyers, A.A. Menovsky and W. Que, 1994, *Physica B* **199&200**, 165.
- Walstedt, R.E., and L.R. Walker, 1974, *Phys. Rev. B* **9**, 4857.
- Walstedt, R.E., R.F. Bell, L.F. Schneemeyer, J.V. Waszczak, W.W. Warren, R. Dupree and A. Gencten, 1993, *Phys. Rev. B* **48**, 10646.
- Wäppling, R., O. Hartmann, S.W. Harris, E. Karlsson, G.M. Kalvius, L. Asch, A. Kratzer, P. Dalmas de

- Réotier and A. Yaouanc, 1993, *J. Magn. Magn. Mater.* **119**, 123.
- Watanabe, I., K. Kawano, K. Kumagai, K. Nishiyama and K. Nagamine, 1992, *J. Phys. Soc. Japan* **61**, 3058.
- Weber, M., 1992, Ph.D. Thesis (Physics Department, Technical University Munich, unpublished).
- Weber, M., P. Birrer, F.N. Gygax, B. Hitti, E. Lippelt, H. Maletta and A. Schenck, 1990, *Hyperfine Interactions* **63**, 207.
- Weber, M., A. Amato, F.N. Gygax, A. Schenck, H. Maletta, V.N. Duginov, V.G. Grebinnik, A.B. Lazarev, V.G. Olshevsky, V.Yu. Pomjakushin, S.N. Shilov, V.A. Zhukov, B.F. Kirilov, A.V. Pirogov, A.N. Ponomarev, V. Storchak, S. Kapusta and J. Bock, 1993, *Phys. Rev. B* **48**, 13022.
- Weber, M., L. Asch, A. Kratzer, G.M. Kalvius, K.H. Münch, R. Ballou, J. Deportes, R. Wäppling, F.J. Litterst, H.H. Klauß, C. Niedermayer and J. Chappert, 1994a, *Hyperfine Interactions* **85**, 265.
- Weber, M., A. Kratzer and G.M. Kalvius, 1994b, *Hyperfine Interactions* **87**, 1197.
- Wehr, H., K. Knorr, R. Schulze, F.N. Gygax, A. Hintermann, W. Ruegg, A. Schenck and W. Studer, 1981, *Hyperfine Interactions* **8**, 495.
- Wehr, H., K. Knorr, F.N. Gygax, A. Schenck and W. Studer, 1982, in: *Valence Instabilities*, eds P. Wachter and H. Boppart (North-Holland, Amsterdam) p. 485.
- Wehr, H., K. Knorr, F.N. Gygax, A. Hintermann, A. Schenck and W. Studer, 1983, *J. Phys. F* **13**, 885.
- Wehr, H., K. Knorr, F.N. Gygax, A. Schenck and W. Studer, 1984, *Phys. Rev. B* **29**, 6381.
- Weidinger, A., C. Niedermayer, A. Golnik, R. Simon, E. Recknagel, J.I. Budnick, B. Chamberland and C. Baines, 1989, *Phys. Rev. Lett.* **62**, 102.
- Weidinger, A., C. Niedermayer, H. Glückler, A. Golnik, G. Nowitzke, E. Recknagel, H. Eickenbusch, W. Paulus, R. Schöllhorn and J.I. Budnick, 1990, *Hyperfine Interactions* **63**, 147.
- Welp, U., P. Haen, G. Bruls, G. Remenyi, J. Flouquet, P. Morin, A. Briggs, G. Cors and M. Karkut, 1987, *J. Magn. Magn. Mater.* **63&64**, 28.
- Wenger, L.E., G.W. Hunter, J.A. Mydosh, J.A. Gotaas and J.J. Rhyne, 1986, *Phys. Rev. Lett.* **56**, 1090.
- Werner, S.A., 1990, *Comm. Condens. Matter Phys.* **15**, 55.
- Whitehead, J.P., K. De'Bell and D.R. Noakes, 1994, *Phys. Rev. B* **49**, 12341.
- Wiese, S., E. Gamper, H. Winkelmann, B. Bücher, M.M. Abd-Elmeguid, H. Micklitz and T. Takabatake, 1997, *Physica B* **230–232**, 95.
- Wiesinger, G., E. Bauer, A. Amato, R. Feyerherm, F.N. Gygax and A. Schenck, 1994, *Physica B* **199**, 52.
- Wiesinger, G., E. Bauer, T. Häufner, A. Amato, R. Feyerherm, F.N. Gygax and A. Schenck, 1995, *Physica B* **206&207**, 1995.
- Wiesinger, G., R. Hatzl, E. Bauer, A. Amato, R. Feyerherm, F.N. Gygax and A. Schenck, 1997, *Physica B* **230–232**, 243.
- Wiesinger, G., C. Reichl, E. Gratz, P. Mietniowski and H. Figel, 2000, *Physica B* **289–290**, 307.
- Wohlleben, D., 1976, *J. Phys. Paris* **C4**, 231.
- Wong, K.M., and S.J. Poon, 1986, *Phys. Rev. B* **34**, 7371.
- Wosnitza, J., R. van den Berg and H. von Löhneysen, 1988, *Z. Phys. B* **70**, 31.
- Wu, M.K., J.R. Ashburn, C.J. Torng, P.H. Hor, R.L. Meng, L. Gao, Z.J. Huang, Y.Q. Wang and C.W. Chu, 1987, *Phys. Rev. Lett.* **58**, 908.
- Wu, W., D. Bitko, T.F. Rosenbaum and G. Aeppli, 1993, *Phys. Rev. Lett.* **71**, 1919.
- Wu, W.D., A. Keren, L.P. Le, G.M. Luke, B.J. Sternlieb, Y.J. Uemura, C.L. Seaman, Y. Dalichaouch and M.B. Maple, 1994a, *Phys. Rev. Lett.* **72**, 3722.
- Wu, W.D., A. Keren, L.P. Le, G.M. Luke, B.J. Sternlieb, Y.J. Uemura, N. Sato, T. Komatsubara and G.P. Meisner, 1994b, *Hyperfine Interactions* **85**, 425.
- Wulff, M., O. Eriksson, B. Johansson, B. Lebeck, M.S.S. Brooks, G.H. Lander, J. Rebizant, J.C. Spirlet and P.J. Brown, 1990, *Europhys. Lett.* **11**, 269.
- Wun, M., and N.E. Phillips, 1974, *Phys. Lett.* **50A**, 195.
- Xiao, G., M.Z. Cieplak, A. Gavrin, F.H. Streitz, A. Bakhshai and C.L. Chien, 1988, *Phys. Rev. Lett.* **60**, 1446.
- Yagi, E., G. Flik, K. Fürderer, N. Haas, D. Herlach, J. Major, A. Seeger, W. Jacobs, M. Krause, M. Krauth, H.J. Munding and H. Orth, 1984, *Phys. Rev. B* **30**, 441.
- Yamagami, H., and A. Hasegawa, 1993, *Physica B* **186–188**, 182.
- Yamamoto, Y., K. Marumoto, Y. Miyako, K. Nishiyama and K. Nagamine, 1997, *Hyperfine Interactions* **104**, 227.
- Yamamoto, Y., Y. Miyako, T. Takeuchi, M. Ocio, P. Pari, J. Hammann, I. Watanabe and K. Nagamine, 2000a, *Physica B* **281–282**, 351.

- Yamamoto, Y., S. Kawarazaki, Y. Miyako, K. Nishiyama and K. Nagamine, 2000b, *Physica B* **289–290**, 32.
- Yamashita, A., K. Ishii, T. Yokoo, J. Akimitsu, M. Hedo, Y. Inada, Y. Onuki, E. Yamamoto, Y. Haga and R. Kadono, 1997, *Phys. Rev. Lett.* **79**, 3771.
- Yamazaki, T., 1990, *Hyperfine Interactions* **65**, 757.
- Yamazaki, T., 1997, *Hyperfine Interactions* **104**, 3.
- Yaouanc, A., and P. Dalmas de Réotier, 1991, *J. Phys.: Condens. Matter* **3**, 6195.
- Yaouanc, A., J.I. Budnick, E. Albert, M. Hamma, A. Weidinger, R. Fruchart, P. L'Héritier, D. Fruchart and P. Wolfers, 1987, *J. Magn. Magn. Mater.* **67**, L286.
- Yaouanc, A., P. Dalmas de Réotier and E. Frey, 1993a, *Europhys. Lett.* **21**, 93.
- Yaouanc, A., P. Dalmas de Réotier and E. Frey, 1993b, *Phys. Rev. B* **47**, 796.
- Yaouanc, A., P. Dalmas de Réotier, P.C.M. Gubbens, A.A. Moolenaar, A.A. Menovsky and C.E. Snel, 1994, *Hyperfine Interactions* **85**, 351.
- Yaouanc, A., P. Dalmas de Réotier, P.C.M. Gubbens, F.E. Kayzel, P. Bonville, J.J.M. Franse and A.M. Mulders, 1995, *J. Magn. Magn. Mater.* **140–144**, 1949.
- Yaouanc, A., P. Dalmas de Réotier, P.C.M. Gubbens, A.M. Mulders, F.E. Kayzel and J.J.M. Franse, 1996, *Phys. Rev. B* **53**, 350.
- Yaouanc, A., P. Dalmas de Réotier, A.D. Huxley, P. Bonville, P.C.M. Gubbens, A.M. Mulders, P. Lejay and S. Kunii, 1997, *Physica B* **230–232**, 269.
- Yaouanc, A., P. Dalmas de Réotier, P.C.M. Gubbens, C.T. Kaiser, P. Bonville, J.A. Hodges, A. Amato, A. Schenck, P. Lejay, A.A. Menovsky and M. Mihalik, 1999a, *Physica B* **259–261**, 126.
- Yaouanc, A., P. Dalmas de Réotier, P. Bonville, G. Le Bras, P.C.M. Gubbens, A.M. Mulders and S. Kunii, 1999b, *Europhys. Lett.* **47**, 247.
- Yaouanc, A., P. Dalmas de Réotier, P.C.M. Gubbens, A.M. Mulders and Y. Ishikawa, 2000a, *Physica B* **289–290**, 28.
- Yaouanc, A., P. Dalmas de Réotier, F.N. Gyax, A. Schenck, A. Amato, C. Baines, P.C.M. Gubbens, C.T. Kaiser, A. de Visser, R.J. Keizer, A.D. Huxley and A.A. Menovsky, 2000b, *Phys. Rev. Lett.* **84**, 2702.
- Yatskar, A., W.P. Beyermann, R. Movshovich and P.C. Canfield, 1996, *Phys. Rev. Lett.* **77**, 3637.
- Yoshii, S., M. Kasaya, H. Takahashi and N. Mori, 1996, *Physica B* **223&224**, 421.
- Yoshimura, K., H. Yasuoka and Y. Nakamura, 1990, *J. Magn. Magn. Mater.* **90&91**, 706.
- Yoshizawa, H., S.M. Shapiro, S.K. Hasanain and R.P. Guertin, 1983, *Phys. Rev. B* **27**, 448.
- Yuen, T., C.L. Lin, J.E. Crow and N. Bykowitz, 1992, *J. Magn. Magn. Mater.* **109**, 98.
- Yvon, K., H.F. Braun and E. Gratz, 1983, *J. Phys. F* **13**, L131.
- Zandbergen, H.W., T.J. Gortenmulder, J.L. Sarrao, J.C. Harrison, M.C. de Andrade, J. Herrmann, S.H. Han, Z. Fisk, M.B. Maple and R.J. Cava, 1994, *Physica C* **232**, 328.
- Zhao, Z., F. Behroozi, S. Adenwalla, Y. Guan, J.B. Ketterson, B.K. Sarma and D.G. Hinks, 1991, *Phys. Rev. B* **43**, 13720.
- Zhou, L.W., C.S. Jee, C.L. Lin, J.E. Crow, S. Bloom and R.P. Guertin, 1987, *J. Appl. Phys.* **61**, 3377.
- Zirngiebl, E., B. Hillenbrand, S. Blumenröder, G. Güntherodt, M. Loewenhaupt, J.M. Carpenter, K. Winzer and Z. Fisk, 1984, *Phys. Rev. B* **30**, 4052.
- Zou, Z., J. Ye, K. Oka and Y. Nishihara, 1998, *Phys. Rev. Lett.* **80**, 1074.
- Zwirner, S., J.C. Spirlet, K.H. Münch, A. Kratzer, L. Asch and G.M. Kalvius, 1993, *Physica B* **186–188**, 798.



## Chapter 207

# STRUCTURE-PROPERTY RELATIONS OF TERNARY EQUIATOMIC YbTX INTERMETALLICS

Rainer PÖTTGEN

Department Chemie, Ludwig-Maximilians-Universität München,  
Butenandtstraße 5-13 (Haus D), 81377 München, Germany;  
E-mail: rapch@cup.uni-muenchen.de

Dirk JOHRENDT

Institut für Anorganische Chemie und Strukturchemie II,  
Heinrich-Heine-Universität Düsseldorf, Universitätsstraße 1,  
40225 Düsseldorf, Germany; E-mail: johrendt@uni-duesseldorf.de

Dirk KUSSMANN

SAP AG, IBU Retail&CP (SXT-Gebäude), Neuwirtstraße 16,  
69190 Walldorf, Germany; E-mail: dirk.kussmann@sap.com

---

## Contents

Symbols and abbreviations	453	3.11. Intermetallic magnesium and zinc compounds YbTMg and YbTZn	485
1. Introduction	454	3.12. Some general remarks	486
2. Syntheses	455	4. Chemical and physical properties	487
3. Crystal chemistry and chemical bonding	456	4.1. Chemical properties	487
3.1. Equiatomic aluminides YbTAl	456	4.2. Magnetic properties	487
3.2. Equiatomic gallides YbTGa	463	4.3. Electrical properties	495
3.3. Indium and thallium compounds YbTIn and YbTTl	464	4.4. Mössbauer spectroscopy	497
3.4. YbCoC and the silicides YbTSi	466	4.5. Specific-heat data	500
3.5. Equiatomic germanides YbTGe	471	4.6. High-pressure investigations	502
3.6. Equiatomic stannides YbTSn	474	4.7. Thermoelectric power	503
3.7. The plumbides YbTPb	478	4.8. XAS, neutron scattering and photoemission	504
3.8. The phosphides and arsenides YbTP and YbTAs	479	5. Conclusion	505
3.9. Ternary antimonides YbTSb	481	Acknowledgments	506
3.10. Equiatomic bismuthides YbTBi	483	References	506

---

## Symbols and abbreviations

AF	antiferromagnetism	DOS	density of states
$B_C$	critical magnetic field	$\Delta E_Q$	quadrupole splitting parameter
COHP	crystal orbital Hamilton population	EFG	electric field gradient
COOP	crystal orbital overlap population	ELF	electron localization function

EPR	electron paramagnetic resonance	$T_C$	magnetic Curie temperature
F	ferromagnetism	TEP	thermoelectric power
HP	high pressure	TIP	temperature-independent paramagnetism
HT	high temperature	$T_N$	magnetic Néel temperature
ICF	interconfiguration fluctuation	$T_{SF}$	magnetic spin-fluctuation temperature
IV	intermediate valence	VF	valence fluctuation
LAPW	linearized augmented plane-wave	$X$	element of 3rd, 4th or 5th main group
LMTO	linear muffin-tin orbital	XAS	X-ray absorption spectroscopy
LSD	local spin density	$\Gamma$	experimental linewidth
LSDA	local spin-density approximation	$\gamma$	electronic specific-heat coefficient
LT	low temperature	$\delta$	isomer shift
MM	metamagnetism	$\Theta$	paramagnetic Curie temperature (Weiss constant)
NP	normal pressure	$\mu_B$	Bohr magneton
P	paramagnetism	$\mu_{sm(exp)}$	experimental magnetic saturation magnetization
R	residual	$\chi$	magnetic susceptibility; absolute electronegativity
SG	space group		
SIC	self-interaction correction		
$T$	transition metal		
TB-LMTO-	tight-binding linear muffin-tin orbital		
ASA	atomic sphere approximation		

---

## 1. Introduction

Equiatomic intermetallic compounds  $RTX$  ( $R$  = rare earth or actinide metal;  $T$  = transition metal;  $X$  = element of the 3rd or 4th main group) have attracted considerable interest in the last two decades due to their greatly varying physical properties (Parthé and Chabot 1984, Szytuła and Leciejewicz 1989, 1994, Szytuła 1991, 1998, Gignoux and Schmitt 1997). Today more than 1000  $RTX$  compounds are known (Villars and Calvert 1991). They crystallize in more than 40 different structure types (Fornasini and Merlo 1995).

With the actinides as  $R$  component the compounds with uranium have most intensively been investigated (Sechovsky and Havela 1988, Fournier 1985, Fournier and Tróć 1985). Here, the various magnetic properties strongly depend on the energy of the uranium 5f electrons with respect to the Fermi level as well as the strength of hybridization of the uranium 5f states with the conduction electrons. Within the series of rare-earth  $RTX$  compounds those with cerium, europium, and ytterbium display the largest variety of physical properties. Due to their peculiar electron configuration, these compounds are possible candidates when searching for mixed valence, i.e.  $Ce^{3+} [Xe]4f^1$  vs.  $Ce^{4+} [Xe]4f^0$ ,  $Eu^{2+} [Xe]4f^7$  vs.  $Eu^{3+} [Xe]4f^6$ , and  $Yb^{2+} [Xe]4f^{14}$  vs.  $Yb^{3+} [Xe]4f^{13}$ . The cerium compounds have most intensively been investigated in the past and their various magnetic and electrical properties have been summarized in detail in several papers (Fujita et al. 1992, Takabatake et al. 1990, Endstra et al. 1993). Most  $EuTX$  europium compounds have been studied in the last decade and these results have recently been reviewed (Pöttgen and Johrendt 2000).

In this chapter we focus on the ytterbium-based compounds. Besides mixed valency ( $\text{Yb}^{2+}$  or  $\text{Yb}^{3+}$ ), these ytterbium intermetallics can also display heavy-fermion or Kondo-like behavior. Structural phase transitions accompanied by a valence change ( $\text{Yb}^{3+}$  in the low-temperature and  $\text{Yb}^{2+}$  in the high-temperature modification) have recently been observed for  $\alpha$ - and  $\beta$ -YbPdSn (Kumann et al. 1998a) and  $\alpha$ - and  $\beta$ -YbAgGa<sub>2</sub> (Grin et al. 1995), while stable trivalent ytterbium occurs in the ZrNiAl-type compounds YbNiAl (Schank et al. 1995) and YbPtSn (Katoh et al. 1997, Pttgen et al. 1999a, Kaczorowski et al. 1999) which order antiferromagnetically below  $T_N = 2.9$  and 3.5 K, respectively.

The crystal chemistry of the YbTX compounds and the various physical properties and spectroscopic data (magnetism, electrical conductivity, specific heat,  $L_{\text{III}}$  spectra, Mssbauer spectroscopy) are critically reviewed in the present article. Additionally we comment on the synthesis conditions and the chemical bonding within the YbTX compounds. We have written this article from the viewpoint of a solid-state chemist who is interested in the interdisciplinary field of inorganic and physical chemistry, elucidating structure-property relations of intermetallic compounds.

## 2. Syntheses

The synthesis conditions for ternary intermetallic ytterbium compounds mostly resemble those discussed earlier for the EuTX intermetallics (Pttgen and Johrendt 2000). We therefore give only some technical details in this chapter and refer to the original literature for additional information. The main problem for the synthesis arises from the low boiling temperature (1466 K) of ytterbium which is the by far lowest in the rare-earth series. In a quasi open system like an arc-melting furnace (Pttgen et al. 1999b), significant evaporation can irreversibly affect the synthesis conditions. To give an example: for the synthesis of YbPtSn (Katoh et al. 1997, Pttgen et al. 1999a, Kaczorowski et al. 1999) by arc melting, ytterbium would evaporate (b.p. 1466 K) before platinum melts (m.p. 2045 K). Such difficulties can be overcome if the elements are reacted in sealed inert, refractory metal tubes, e.g. niobium, tantalum or molybdenum in a high-frequency furnace (Pttgen et al. 1999a). Such container materials, namely tantalum, have been reviewed by Corbett (1983). An effective method is the reaction of pre-reacted transition metal alloys with ytterbium. This technique was recently utilized for the synthesis of YbPtSn (Pttgen et al. 1999a). In a first step, a relatively low-melting PtSn alloy was prepared by arc melting and subsequently this alloy was reacted with ytterbium in a sealed tantalum tube resulting in a single phase YbPtSn sample.

In some cases it is also possible to react the elements in glassy carbon crucibles in a water-cooled sample chamber in a high-frequency furnace. This method has been described in detail by Kumann et al. (1998b). An advantage of this preparative technique is the direct observability of the reaction through an observation window.

The techniques described above have mainly been used for compounds with the X = element from the third and fourth main group. For the synthesis of pnictides some other techniques can also be applied. Phosphides (von Schnering and Hnle 1994),

arsenides, and bismuthides can be synthesized directly from the elemental components in evacuated sealed silica tubes. In order to avoid side reactions with the silica tube, an aluminium oxide container can be used as inner crucible material. In this way YbPtP (Wenski and Mewis 1986a) was prepared. This solid-state synthesis can sometimes lead to inhomogeneous products, if reaction layers form an unreacted material and prevent diffusion. In such cases, repeated grinding, pressing and reannealing is necessary.

Another method is the reaction of the elemental components in fluxes (Jolibois 1910, Vigouroux 1905, Kaner et al. 1977, and ref. therein). Such fluxes may be low-melting metals (Cu, Bi, Sn, Pb) or halide mixtures (low-melting eutectics). In any case, a possible incorporation of silicon from the silica tube should be kept in mind.

An important problem for the synthesis of intermetallic ytterbium compounds is certainly the purity of the elements. Today, ytterbium is commercially available in pure form as sublimed ingots. It is desirable to use only larger metal pieces in order to reduce surface contaminations. The use of ytterbium powders (too large surface) should be avoided. The main experimental difficulties may arise from a contamination with the sesquioxide  $\text{Yb}_2\text{O}_3$  (Bonrath et al. 1966) which exhibits paramagnetic behavior down to 3 K. The contamination of diamagnetic or Pauli-paramagnetic samples with  $\text{Yb}_2\text{O}_3$  could irreversibly affect the magnetic measurements, as discussed in detail for YbAuIn (Zell et al. 1981).

### 3. Crystal chemistry and chemical bonding

In the present section we focus on the crystal chemistry of the various  $\text{YbTX}$  compounds. These results are summarized in separate groups for the different  $X$  components, i.e. aluminides, gallides, indides etc. The basic crystallographic data, i.e. lattice parameters and residuals, are listed in the various tables. For the atomic parameters of those compounds where the crystal structures have been refined, we refer to the original literature. Some compounds have the transition-metal site occupied by lithium or another element of the third, fourth or fifth main group; these equiatomic compounds have also been included in the present review, since they exhibit similar structural features. Besides the crystal chemistry we also focus on the chemical bonding in these interesting materials. We review the results presented in the literature, but we have also performed new calculations on some selected compounds using the TB-LMTO-ASA method. Details about the computational methodology have been given by Andersen (1975), Andersen and Jepsen (1984) and Andersen et al. (1985), and computational details for the compounds are given in the respective subsections.

#### 3.1. *Equiatomic aluminides YbTAl*

So far, nine equiatomic ytterbium aluminides have been reported (table 1). In the pseudobinary system  $\text{YbGa}_2\text{--YbAl}_2$  (Beck and Girgis 1985, Iandelli 1987) equiatomic YbGaAl occurs with the  $\text{CaIn}_2$  structure, where the gallium and aluminium atoms

Table 1  
Lattice parameters and residuals for YbTAl ( $T = \text{Ga, Co, Ni, Cu, Rh, Pd, Ag, Pt, Au}$ )

Compound	Type	SG	$a$ (pm)	$b$ (pm)	$c$ (pm)	$V$ (nm <sup>3</sup> )	$R$ -value	Ref.
YbGaAl	MgCu <sub>2</sub>	$Fd\bar{3}m$	786.5	$a$	$a$	0.4865	–	1
YbGaAl	CaIn <sub>2</sub>	$P6_3/mmc$	451	$a$	714.5	0.1259	–	1,2
YbCoAl	MgZn <sub>2</sub>	$P6_3/mmc$	529.8	$a$	846.6	0.2058	–	3
NP-YbNiAl	ZrNiAl	$P\bar{6}2m$	695.2	$a$	376.9	0.1578	–	4
NP-YbNiAl	ZrNiAl	$P\bar{6}2m$	694.9	$a$	377.1	0.1577	–	5
HP-YbNiAl	MgZn <sub>2</sub>	$P6_3/mmc$	529.3	$a$	851.8	0.2067	–	6,7
NP-YbCuAl	ZrNiAl	$P\bar{6}2m$	692.6(3)	$a$	398.6(1)	0.1656	–	9
HP-YbCuAl	MgCu <sub>2</sub>	$Fd\bar{3}m$	766.0	$a$	$a$	0.4495	–	6,8
NP-YbCuAl	ZrNiAl	$P\bar{6}2m$	692.2	$a$	399.3	0.1657	–	10
YbRhAl	TiNiSi	$Pnma$	676.1(1)	412.6(1)	789.3(2)	0.2202	0.0164	11
YbPdAl	TiNiSi	$Pnma$	681.9(2)	435.0(1)	780.1(2)	0.2314	0.025	12
YbPdAl	TiNiSi	$Pnma$	680.79(3)	434.73(2)	778.89(3)	0.2305	–	13
YbPdAl	TiNiSi	$Pnma$	681.8	435.0	779.5	0.2312	–	14
YbAgAl	MgZn <sub>2</sub>	$P6_3/mmc$	566.3(1)	$a$	908.7(3)	0.2524	0.027	15
YbPtAl	TiNiSi	$Pnma$	676.7	434.8	770.5	0.2267	–	5
YbPtAl	TiNiSi	$Pnma$	676.9(2)	434.8(1)	769.0(2)	0.2263	–	16
YbPtAl	TiNiSi	$Pnma$	675.11(5)	433.84(3)	767.36(5)	0.2248	–	13
YbAuAl	TiNiSi	$Pnma$	719.67(7)	447.94(4)	771.35(6)	0.2487	–	17
YbAuAl	TiNiSi	$Pnma$	721.0(2)	448.8(1)	773.2(2)	0.2502	0.053	18
YbAuAl	TiNiSi	$Pnma$	719.8	447.8	771.6	0.2487	–	14

#### References

1. Beck and Girgis (1985)
2. Iandelli (1987)
3. Oesterreicher (1971a)
4. Rossi et al. (1983b)
5. Schank et al. (1995)
6. Tsvyashchenko and Fomicheva (1987a)
7. Tsvyashchenko and Fomicheva (1987b)
8. Tsvyashchenko and Fomicheva (1987c)
9. Dwight et al. (1968)
10. Mattens et al. (1980a,b)
11. Cardoso Gil et al. (1999)
12. Cordier and Henseleit (1993a)
13. Hulliger (1995)
14. Schank et al. (1994)
15. Fornasini et al. (2000)
16. Cordier et al. (1993)
17. Hulliger (1993)
18. Cordier and Henseleit (1993b)

statistically occupy the indium positions of the CaIn<sub>2</sub> type (space group  $P6_3/mmc$ ). No long-range ordering has been observed during X-ray experiments. The gallium and aluminium atoms form puckered hexagonal layers with stronger intralayer and weaker interlayer bonding. The ytterbium atoms are located between the puckered layers. In fig. 1 we present the LiGaGe-type structure of YbCuGe as an example of an ordered variant of the CaIn<sub>2</sub> type. Besides the CaIn<sub>2</sub>-type phase, a MgCu<sub>2</sub>-type (fig. 2) phase YbGaAl has also been observed. In the YbGa<sub>2-x</sub>Al<sub>x</sub> system, the hexagonal CaIn<sub>2</sub> phase exists in the range  $0 \leq x \leq 0.87$ , while the cubic MgCu<sub>2</sub>-type phase (space group  $Fd\bar{3}m$ ) is stable in the range  $1.47 \leq x \leq 2.0$ . Both phases coexist in the range  $0.87 \leq x \leq 1.47$ . The CaIn<sub>2</sub> phase

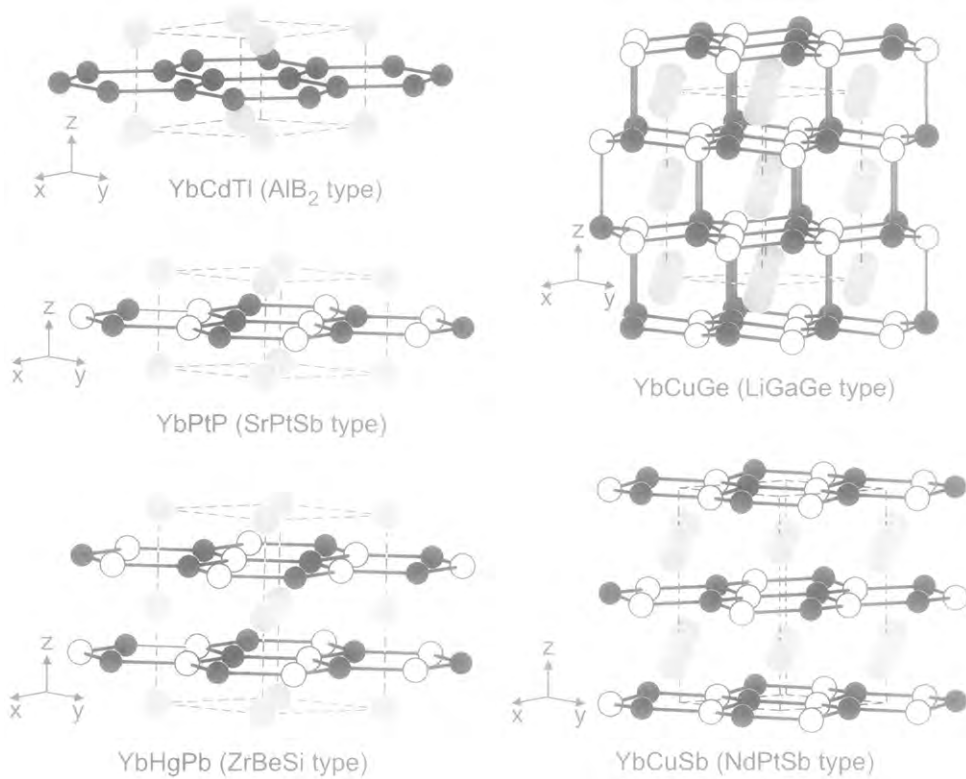


Fig. 1. Crystal structures of YbCdTi, YbPtP, YbHgPb, YbCuGe, and YbCuSb. The ytterbium, transition-metal and p-group-element atoms are drawn as large grey, solid, and open circles, respectively, throughout the chapter. The two- and three-dimensional  $[TX]$  polyanions are emphasized.

has two formula units ( $Z$ ) YbGaAl per unit cell, while  $Z = 8$  for the cubic phase. The cell volume per formula unit of  $63 \text{ \AA}^3$  for the hexagonal phase is slightly larger than that for the cubic phase ( $61 \text{ \AA}^3$ ). This is most likely due to small homogeneity ranges or a partial change of the ytterbium valence.

The ordering of the gallium and aluminium atoms in the cubic  $\text{MgCu}_2$ -type phase was not studied. This is also the case for HP-YbCuAl discussed below. In the cubic YbGaAl structure the gallium and aluminium atoms form a three-dimensional tetrahedral network in which the ytterbium atoms fill cages. Chemical bonding in  $\text{MgCu}_2$ -related intermetallic phases was investigated recently on the basis of extended Hückel calculations (Johnston and Hoffmann 1992, Burdett 1995).

The aluminides with nickel and copper as transition-metal component show a very interesting behavior. At normal pressure conditions, YbNiAl (Schank et al. 1995, Rossi et al. 1983a,b) and YbCuAl (Mattens et al. 1982) crystallize with the hexagonal ZrNiAl type (Krypyakevich et al. 1967, Jacob et al. 1987, Zumdick et al. 1999) (fig. 3), a ternary ordered version of the  $\text{Fe}_2\text{P}$  structure (Rundqvist and Jellinek 1959) (space group  $P\bar{6}2m$ ).

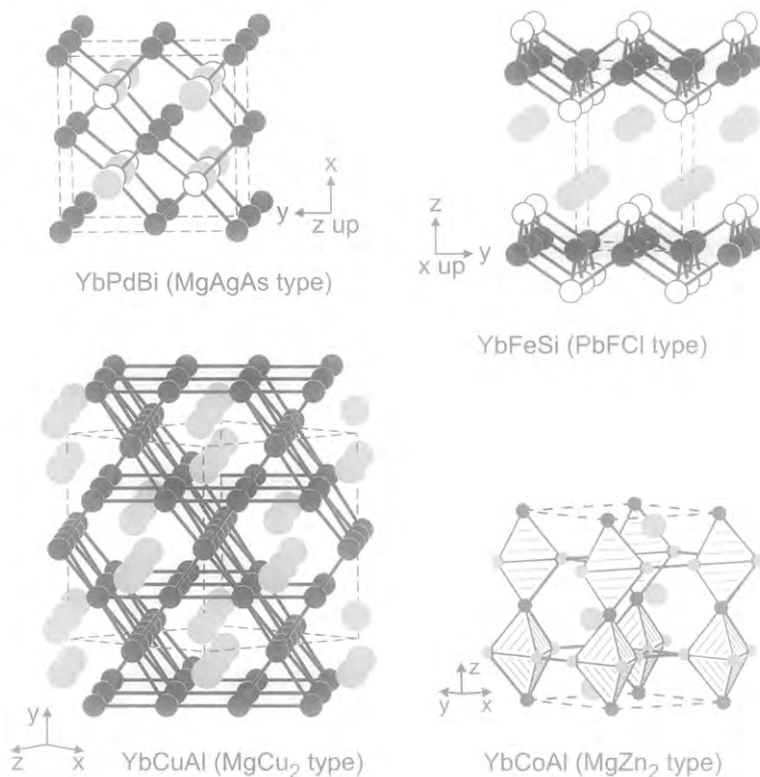


Fig. 2. Crystal structures of YbPdBi, HP-YbCuAl, YbFeSi, and YbCoAl. The two- and three-dimensional [YbX] polyanions are emphasized.

The crystal chemistry of the ZrNiAl-type ytterbium compounds is discussed in more detail in sect. 3.6 for the respective stannides, since most of them have been investigated by single-crystal techniques. Both YbNiAl and YbCuAl undergo a reconstructive phase transition under an applied constant pressure of 7.7 GPa (Tsvyashchenko and Fomicheva 1987a–c). HP-YbNiAl crystallizes with the structure of the hexagonal Laves phase MgZn<sub>2</sub> (fig. 2) which is more dense than the ZrNiAl type. This is readily visible from the cell volumes per formula unit of 52.6 Å<sup>3</sup> (NP-YbNiAl) and 51.7 Å<sup>3</sup> (HP-YbNiAl). HP-YbCuAl (56.2 Å<sup>3</sup>) adopts the structure of the cubic Laves phase MgCu<sub>2</sub>. Interestingly, HP-YbCuAl has a larger cell volume than HP-TmCuAl (Tsvyashchenko and Fomicheva 1987a), indicating that the ytterbium valence is smaller than three. This is also evident from the smaller volume of 55.2 Å<sup>3</sup> per formula unit for NP-YbCuAl.

Mattens et al. (1977, 1980a,b) assumed the Fe<sub>2</sub>P-type structure for NP-YbCuAl, while Dwight et al. (1968) indicated the ZrNiAl type, assuming an ordering of the copper and aluminium atoms on the iron and phosphorous sites. At this point it is worthwhile to note that such an ordering is only evident from small changes of the intensities in the X-ray

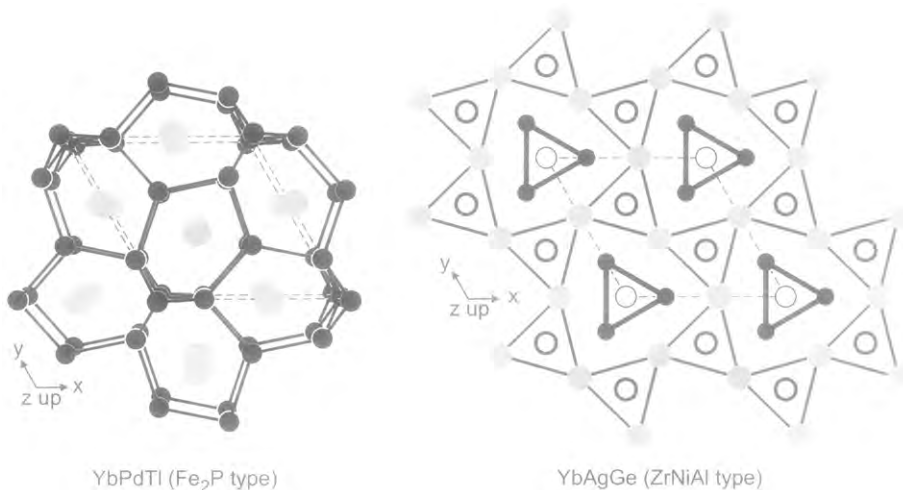


Fig. 3. Crystal structures of YbPdTi ( $\text{Fe}_2\text{P}$  type) and YbAgGe (ZrNiAl type). The three-dimensional [PdTi] polyanion is outlined at the left-hand side while the trigonal prisms around the germanium atoms are emphasized at the right-hand side for YbAgGe.

powder patterns. The lattice parameters of YbCuAl were determined as a function of temperature (Mattens et al. 1980a,b) in order to investigate the influence of the ytterbium valence on the structure. Furthermore, thermal expansion measurements show that the thermal expansion coefficient of YbCuAl is a linear function of temperature with a very large negative coefficient (Pott et al. 1981). An anomaly occurs with a maximum at 22 K, most likely due to a temperature-driven valence change.

The aluminide with the lowest electron count, YbCoAl, crystallizes with the  $\text{MgZn}_2$  structure (Oesterreicher 1971a) (space group  $P6_3/mmc$ ). Also, the cell volume of YbCoAl is larger than that of TmCoAl, indicating partially divalent ytterbium. In the YbCoAl structure we observe a tetrahedral network of cobalt and aluminium atoms. The large cages formed by this three-dimensional [CoAl] network are filled with the ytterbium atoms (fig. 2). With iron as the transition metal a product of unknown structure occurs (Oesterreicher 1971b).

The four aluminides YbPdAl (Schank et al. 1994, Cordier and Henseleit 1993a, Hulliger 1995), YbRhAl (Cardoso Gil et al. 1999), YbPtAl (Schank et al. 1995, Hulliger 1995, Cordier et al. 1993) and YbAuAl (Schank et al. 1994, Cordier and Henseleit 1993b, Hulliger 1993) adopt the orthorhombic TiNiSi structure (Shoemaker and Shoemaker 1965) (space group  $Pnma$ ), a ternary ordered version of the  $\text{KHg}_2$  ( $\text{CeCu}_2$ ) type (Duwell and Baenziger 1955, Larson and Cromer 1961). The  $\text{KHg}_2$  type is frequently designated also as  $\text{CeCu}_2$  type, mainly in the physics literature. The  $\text{CeCu}_2$  structure has been described in a setting which is different from that of the earlier reported  $\text{KHg}_2$  structure. Parthé and Gelato (1984) have shown that the two structures are identical. As an example we present in fig. 4 the YbPdAl structure. The palladium and aluminium atoms build



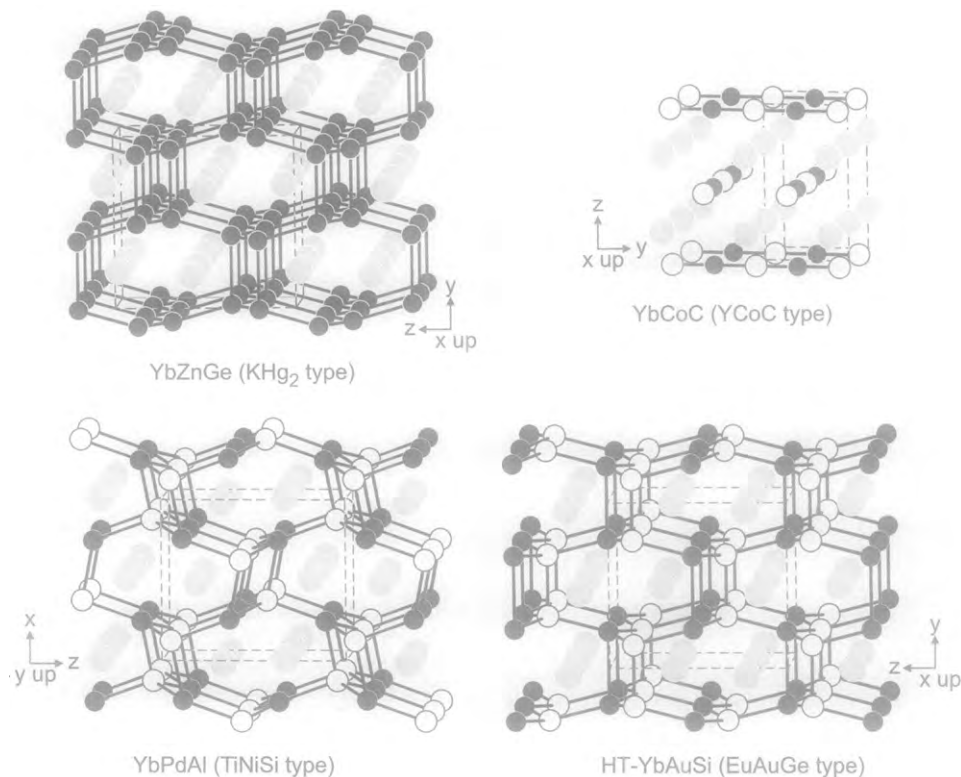


Fig. 4. Crystal structures of YbZnGe, YbPdAl, YbCoC, and HT-YbAuSi. The linear  $-CoC-$  chains of YbCoC and the three-dimensional  $[TX]$  polyanions are emphasized.

a three-dimensional  $[PdAl]$  polyanionic network which consists of puckered  $Pd_3Al_3$  hexagons. The Pd–Al distances within and between these hexagons vary from 256 to 286 pm. The shortest contacts are only slightly longer than the sum of Pauling's single bond radii of 253 pm (Pauling 1960) for palladium and aluminium, indicating a significant degree of covalent Pd–Al bonding. The shortest Al–Al contacts between the  $Pd_3Al_3$  hexagons of 304 pm are already 18 pm longer than in fcc aluminium (Donohue 1974), where each aluminium atom has twelve neighbours at 286 pm. Between the puckered  $Pd_3Al_3$  hexagons we observe  $Pd_2Al_2$  parallelograms in which the more electronegative palladium atoms ( $\chi_{Pd} = 4.45$  eV;  $\chi_{Al} = 3.23$  eV, Pearson 1988) show a maximal separation (fig. 4). The ytterbium atoms fill the large channels within the  $[PdAl]$  network.

Chemical bonding in TiNiSi-related intermetallic compounds was investigated in recent years (Nuspl et al. 1996, Landrum et al. 1998, Hoffmann and Pöttgen 2000) on the basis of extended Hückel calculations. The influence of the electron count was discussed in detail by Nuspl et al. (1996). The theoretical results are confirmed by single-crystal refinements on various TiNiSi-type compounds (Nuspl et al. 1996, Hoffmann and Pöttgen 2000, Dasoulidou-Gritner and Schuster 1994, Pöttgen 1996a).

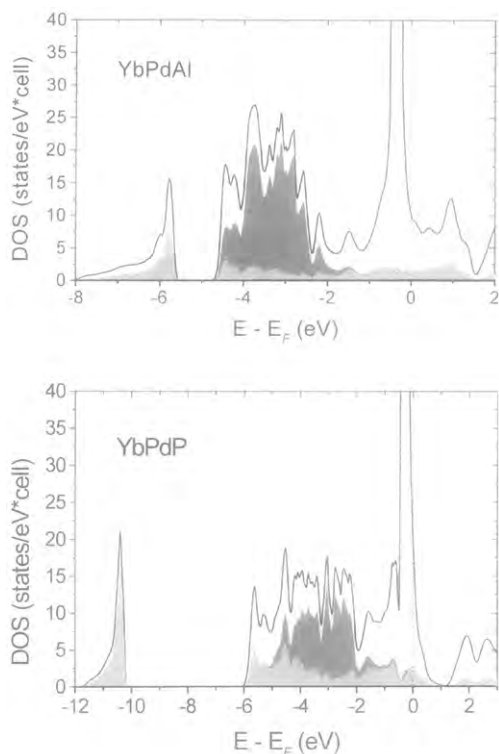


Fig. 5. Electronic density of states (DOS) diagrams for (top) YbPdAl and (bottom) YbPdP. Solid lines: total DOS; dark gray shaded areas: Pd contributions; light gray shaded areas: Al or P contributions. The energy zeros are taken at the Fermi level.

The electronic structure of EuPdGa with TiNiSi-type structure was investigated by the TB-LMTO-ASA technique (Pöttgen and Johrendt 2000). The results reported for the EuTX compounds may safely be applied to the ytterbium compounds. Main features are strong covalent bonds within the  $[TX]^\delta-$  polyanions and rather electrostatic interactions between the positively polarized Yb and the  $T/X$  atoms. This requires the Yb atoms to be the most electropositive component in order to provide electrons to the  $T-X$  bonds in the sense of an extended Zintl concept. With regard to the electropositive character of aluminium in YbPdAl, the question arises whether the formulation of a  $[PdAl]^\delta-$  polyanion is justified. To elucidate this, we have performed first-principles LMTO (Andersen 1975, Andersen and Jepsen 1984, Andersen et al. 1985) calculations, and in the following we compare briefly the electronic structures of YbPdAl and YbPdP (sect. 3.8), both adopting the TiNiSi structure. Their electronic density-of-states (DOS) plots are shown in fig. 5. The total DOS curves are quite similar, and also their decompositions in contributions of Pd (dark grey area) and Al/P (light grey area) reveal no fundamental differences. The orbital energy orderings are essentially the same: low-lying 3s states of P and Al, followed by the 3p states in the same energy range as the palladium 4d levels. In the vicinity of the Fermi energy the DOS is dominated by the 4f and partially occupied 5d states of ytterbium in both cases. The higher electronegativity of phosphorus becomes

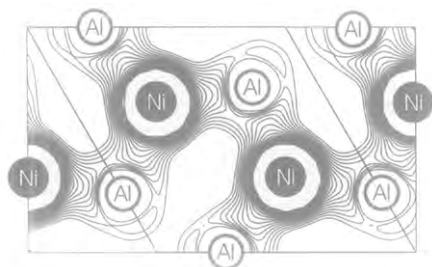


Fig. 6. Calculated valence electron charge density of YbNiAl (hexagonal ZrNiAl structure) within the (001) plane. The hexagonal unit cell is indicated.

apparent in the DOS of YbPdP by the larger energy range ( $-12$  eV) compared with YbPdAl ( $-8$  eV) and a higher contribution of P 3p states to the valence band. From the P and Al partial DOS curves in fig. 5 it is clear that almost all P 3p (bonding) states are filled and phosphorous is nearly  $P^{3-}$  in YbPdP, whereas the Al 3p states are filled to a smaller extent, but sufficiently to form negatively polarized aluminium in YbPdAl. In both compounds the Pd and Al/P levels form the valence bands and the Yb states are only partially filled, consequently the formulation  $Yb^{\delta+}[PdX]^{\delta-}$  remains valid for  $X = Al$ .

The evidence for covalent  $T-Al$  bonding can also be visualized in real space by the valence charge density distribution; as an example, this is shown for YbNiAl with hexagonal ZrNiAl structure in fig. 6. The accumulation of charge is clearly discernible between Al and Ni with the charge density shifted to the more electronegative nickel atoms.

YbAgAl (Fornasini et al. 2000) was studied by single-crystal techniques. This aluminide crystallizes with the hexagonal  $MgZn_2$ -type structure, as does YbCoAl. No long-range ordering was evident from the X-ray data, although a large degree of short-range ordering might be expected. Such mixed occupancies are frequently observed for similar intermetallic silver compounds (Pöttgen and Johrendt 2000), and the nature of this phenomenon is not yet known. Finally we should consider the electron count of YbAgAl which is the same as for the gold compound. Furthermore, the metallic radii of silver and gold are almost the same. The gold compound, however, crystallizes with the orthorhombic TiNiSi type.

### 3.2. Equiatomic gallides YbTGa

So far, eight YbTGa gallides have been reported. They all crystallize with orthorhombic structures. For YbNiGa the  $CeCu_2$ - ( $KHg_2$ )-type structure with a statistical occupancy of nickel and gallium atoms at the copper (mercury) position was initially reported (Debray 1973). In a recent paper (Trovarelli et al. 2000), however, the ordering of the nickel and gallium atoms was established on the basis of a precise single-crystal investigation. YbNiGa adopts the TiNiSi-type structure. The same holds true for the gallides YbRhGa (Hulliger 1996), YbPdGa (Rossi et al. 1983a) and YbPtGa (Adroja et al. 1994, Hovestreydt et al. 1982). The crystal chemistry and chemical bonding in these gallides is comparable to the aluminides discussed above.

The gallides YbCuGa, YbAgGa, and YbAuGa have repeatedly been reported (Adroja et al. 1997, 1990, Malik et al. 1987a,b), however, only with respect to their physical

Table 2  
Lattice parameters and residuals for YbTGa ( $T = \text{Ni, Cu, Zn, Rh, Pd, Ag, Pt, Au}$ )

Compound	Type	SG	$a$ (pm)	$b$ (pm)	$c$ (pm)	$V$ (nm <sup>3</sup> )	$R$ -value	Ref.
YbNiGa	TiNiSi	<i>Pnma</i>	671.9(8)	422.8(5)	727.8(8)	0.2068	–	1
YbNiGa	TiNiSi	<i>Pnma</i>	672.8(1)	423.4(1)	721.2(1)	0.2054	0.028	2
YbNiGa	KHg <sub>2</sub>	<i>Imma</i>	425	676	733	0.2106	–	3
YbCuGa	KHg <sub>2</sub>	<i>Imma</i>	432.44(3)	687.72(6)	740.68(6)	0.2203	–	4
YbZnGa	KHg <sub>2</sub>	<i>Imma</i>	448.88(5)	718.66(7)	769.59(8)	0.2483	–	4
YbRhGa	TiNiSi	<i>Pnma</i>	669.85(5)	420.09(3)	774.16(5)	0.2178	–	5
YbPdGa	TiNiSi	<i>Pnma</i>	685.8	439.2	761.6	0.2294	–	6
YbAgGa	KHg <sub>2</sub>	<i>Imma</i>	457.29(5)	721.16(7)	782.11(9)	0.2579	–	4
YbPtGa	TiNiSi	<i>Pnma</i>	675.0(4)	436.7(3)	757.6(5)	0.2233	–	7
YbPtGa	TiNiSi	<i>Pnma</i>	673.028(6)	434.511(4)	758.4440(7)	0.2218	0.0379	8
YbAuGa	KHg <sub>2</sub>	<i>Imma</i>	711.31(4)	899.84(6)	1541.10(9)	0.9864	–	4

#### References

- |                             |                         |                              |
|-----------------------------|-------------------------|------------------------------|
| 1. Yarmolyuk et al. (1979)  | 4. Grin et al. (2000)   | 7. Hovestreydt et al. (1982) |
| 2. Trovarelli et al. (2000) | 5. Hulliger (1996)      | 8. Adroja et al. (1994)      |
| 3. Debray (1973)            | 6. Rossi et al. (1983a) |                              |

properties. No lattice parameters are available in the literature. We have thus started a more detailed study of the crystal structures of these three compounds. The refined lattice parameters of these gallides are listed in table 2. Single-crystal X-ray studies are still in progress. YbAuGa adopts a complex superstructure of the KHg<sub>2</sub> type. The unit cell is four times larger than the KHg<sub>2</sub>-type subcell with the setting  $a' = b(\text{KHg}_2)$ ;  $b' = 2a(\text{KHg}_2)$ , and  $c' = 2c(\text{KHg}_2)$  (Grin et al. 2000).

During our recent studies we have also obtained the new gallide YbZnGa (Grin et al. 2000) with KHg<sub>2</sub>-type structure (fig. 4). YbZnGa represents the gallide with the highest electron count observed to date. Since zinc and gallium differ only by one valence electron, the ordering between these atoms could not be established on the basis of the X-ray data.

### 3.3. Indium and thallium compounds YbTIn and YbTTl

The indides crystallize with two different structure types. YbZnIn (Mazzone et al. 1982) and YbCdIn (Rossi et al. 1981) adopt the CaIn<sub>2</sub>-type structure (fig. 1), a puckered version of the AIB<sub>2</sub> type. According to X-ray powder data, no long-range ordering of the zinc (cadmium) and indium atoms was evident. Consequently these atoms are randomly distributed on the indium network of the CaIn<sub>2</sub> type, although a large degree of short-range order can be expected. In the case of YbCdIn, it is nearly impossible to distinguish between cadmium and indium, since both elements differ only by one electron. One possibility for ordering of the zinc (cadmium) and indium atoms is the NdPtSb structure (Wenski and Mewis 1986a) (fig. 1) which crystallizes in space group *P6<sub>3</sub>mc*. Since this is a *translationengleiche* subgroup of *P6<sub>3</sub>/mmc* (CaIn<sub>2</sub> type), the ordering expresses itself

only in a change of the subcell intensities. This procedure has been described in detail by Pöttgen et al. (1996) and Pöttgen and Hoffmann (2000).

The structure of YbZnIn was revised by Dhar et al. (1995). According to their X-ray powder data, this indide adopts the orthorhombic  $KHg_2$  type. The cell volume reported in this paper is twice that reported by (Mazzone et al. 1982).

With palladium (Ferro et al. 1974a, Cirafici et al. 1985), platinum (Trovarelli et al. 2000, Kaczorowski et al. 2000b) and gold (Rossi et al. 1977, Pöttgen and Grin 1997) as transition-metal components, the YbTIn indides crystallize with the hexagonal ZrNiAl-type structure (fig. 3). The ordering of the transition-metal and indium atoms was evident from the X-ray data. We note that a significant homogeneity range was observed for the intermediate-valent system YbAuIn (Zell et al. 1981, Pöttgen and Grin 1997). A solid solution YbAu<sub>1+x</sub>In<sub>1-x</sub> up to YbAu<sub>1.27</sub>In<sub>0.73</sub> was evident from X-ray powder and single-crystal data (Pöttgen and Grin 1997, Pöttgen et al. 2000c). With increasing gold content it is possible to partially oxidize the ytterbium atoms in YbAu<sub>1.27</sub>In<sub>0.73</sub> with respect to YbAuIn. As a consequence, the absolute susceptibility values and the ytterbium valence increase (Pöttgen et al. 2000c).

So far, only the two thallides YbPdTl (Ferro et al. 1974b) and YbCdTl (Rossi et al. 1990) have been reported. A severe problem with these compounds is certainly the rather strong hydrolyzability in contrast to the indium compounds. In the case of europium, not even equiatomic thallides are known (Pöttgen and Johrendt 2000). YbPdTl (Ferro et al. 1974b) crystallizes with the ZrNiAl type as most indides do. The intensity distribution of the X-ray powder pattern confirmed an ordering between the palladium and thallium atoms. Due to the larger thallium atoms we observe a larger *a* lattice parameter for YbPdTl when compared with isotopic YbPdIn (see tables 3 and 4).

Table 3  
Lattice parameters and residuals for the indium compounds YbTIn (*T* = Zn, Pd, Cd, Pt, Au)

Compound	Type	SG	<i>a</i> (pm)	<i>b</i> (pm)	<i>c</i> (pm)	<i>V</i> (nm <sup>3</sup> )	<i>R</i> -value	Ref.
YbZnIn	CaIn <sub>2</sub>	<i>P6<sub>3</sub>/mmc</i>	472.5(3)	<i>a</i>	738.2(5)	0.1427	–	1
YbZnIn	KHg <sub>2</sub>	<i>Imma</i>	473.4	737.0	819.1	0.2858	–	2
YbPdIn	Fe <sub>2</sub> P	<i>P6<sub>2</sub>m</i>	757.4	<i>a</i>	393.2	0.1953	–	3
YbPdIn	ZrNiAl	<i>P6<sub>2</sub>m</i>	757.3	<i>a</i>	393.3	0.1953	–	4
YbCdIn	CaIn <sub>2</sub>	<i>P6<sub>3</sub>/mmc</i>	494.8(3)	<i>a</i>	730.2(5)	0.1548	–	5
YbPtIn	ZrNiAl	<i>P6<sub>2</sub>m</i>	754.8(1)	<i>a</i>	376.6(1)	0.1858	0.019	6
YbPtIn	ZrNiAl	<i>P6<sub>2</sub>m</i>	753.5(2)	<i>a</i>	376.3(1)	0.1850	0.0517	7
YbAuIn	Fe <sub>2</sub> P	<i>P6<sub>2</sub>m</i>	770.8	<i>a</i>	402.7	0.2072	–	8
YbAuIn	ZrNiAl	<i>P6<sub>2</sub>m</i>	769.8(1)	<i>a</i>	402.7(1)	0.2067	0.1308	9
YbAu <sub>1.27</sub> In <sub>0.73</sub>	ZrNiAl	<i>P6<sub>2</sub>m</i>	772.3(3)	<i>a</i>	394.7(1)	0.2039	0.0645	9

#### References

- Mazzone et al. (1982)
- Dhar et al. (1995)
- Ferro et al. (1974a)
- Cirafici et al. (1985)
- Rossi et al. (1981)
- Trovarelli et al. (2000)
- Kaczorowski et al. (2000b)
- Rossi et al. (1977)
- Pöttgen and Grin (1997)

Table 4  
Lattice parameters and structure types for the thallides YbTl ( $T = \text{Pd, Cd}$ )

Compound	Type	SG	$a$ (pm)	$b$ (pm)	$c$ (pm)	$V(\text{nm}^3)$	Ref.
YbPdTl	ZrNiAl	$P\bar{6}2m$	771.9(2)	$a$	389.9(1)	0.2012	1
YbCdTl	$\text{AlB}_2$	$P6/mmm$	496.7	$a$	367.3	0.0785	2

#### References

1. Ferro et al. (1974b)

2. Rossi et al. (1990)

For YbCdTl (Rossi et al. 1990) the  $\text{AlB}_2$ -type structure occurs. The cadmium and thallium atoms show a random distribution on the boron network. In view of the different chemical potentials of cadmium and thallium, however, a large degree of short-range order can be expected. Such an ordering is realized in the SrPtSb type (Wenski and Mewis 1986b), space group  $P\bar{6}m2$ . The latter is a *translationengleiche* subgroup of  $P6/mmm$  ( $\text{AlB}_2$  type) and consequently, also for this compound, the ordering can be detected only from a careful investigation of the subcell intensities.

#### 3.4. YbCoC and the silicides YbTSi

With carbon as the electronegative component, so far, only the equiatomic carbide YbCoC (Danebrock et al. 1995) with YCoC-type structure (Gerß and Jeitschko 1986, Tsokol' et al. 1989) has been synthesized (table 5). In this complex carbide the cobalt and carbon atoms form infinite linear  $[\text{CoC}]^{3-}$  polyanionic chains (fig. 4) with Co–C distances of 181 pm. From a geometrical point of view, the YbCoC structure may be described as a carbon-filled YbCo host lattice with a tetragonally distorted CsCl-type structure. Only one third of the compressed octahedral voids is filled, and the linear  $[\text{CoC}]$  chains are rotated by  $90^\circ$  in every other layer. Within the chains we observe strong covalent Co–C bonding which was investigated by extended Hückel band structure calculations (Hoffmann et al. 1987) for the prototype YCoC. This model of chemical bonding may safely be applied also to YbCoC. Since ytterbium is trivalent in YbCoC (there is no anomaly in the plot of the cell volumes; ytterbium fits perfectly between thulium and lutetium), the formula may, to first approximation, be written as  $\text{Yb}^{3+}[\text{CoC}]^{3-}$ , emphasizing the polyanionic character of the linear chains. The extended Hückel calculations for an isolated  $\text{CoC}^{3-}$  chain of YCoC by Hoffmann et al. (1987) resulted in a half-filled  $\pi^*$ -band generated by Co 3d orbitals. Since the crystal structure of YCoC shows no Peierls distortion, they suggested the chain is likely magnetic. But according to susceptibility measurements YCoC is Pauli-paramagnetic, as is the isostructural nitride CaNiN. The absence of a structural distortion in YCoC-type compounds was later attributed to weak interactions between neighbouring chains, shown by self-consistent band-structure calculations on CaNiN (Massidda et al. 1991). However, magnetic Co–C chains cannot be ruled out for YbCoC, which contains one valence electron less than the nitride. Since no susceptibility data are available for YbCoC, we have performed a spin-polarized LMTO calculation in order to look theoretically for a magnetic ground state. This was not obtained, and a

Table 5

Lattice parameters and residuals for the carbide YbCoC and the silicides YbT<sub>2</sub>Si ( $T = \text{Mg, Fe, Cu, Pd, Ag, Pt, Au}$ ). The R-value marked with an asterisk results from a Rietveld refinement (Bragg residual)

Compound	Type	SG	$a$ (pm)	$b$ (pm)	$c$ (pm)	$\beta$ (°)	$V$ (nm <sup>3</sup> )	R-value	Ref.
YbCoC	YCoC	$P4_2/mmc$	362.6(1)	$a$	662.5(2)	–	0.0871	–	1
YbMgSi	TiNiSi	$Pnma$	741.7(2)	440.8(2)	826.2(2)	–	0.2701	–	2
YbFeSi	Cu <sub>2</sub> Sb	$P4/nmm$	397.2(3)	$a$	678.4(5)	–	0.1070	–	3
YbCuSi	Ni <sub>2</sub> In	$P6_3/mmc$	413.0(2)	$a$	715.0(5)	–	0.1056	–	4
YbPdSi	TiNiSi	$Pnma$	681.3(1)	426.1(1)	736.2(1)	–	0.2137	0.0312*	5
YbPdSi	TiNiSi	$Pnma$	687.68	443.5	671.7	–	0.2049	–	6,7
YbPdSi	YPdSi	$Pmmm$	426.8(1)	1364.4(4)	737.7(2)	–	0.4296	–	8
YbAgSi	ZrNiAl	$P\bar{6}2m$	693.2(2)	$a$	411.8(2)	–	0.1714	–	9
YbPtSi	TiNiSi	$Pnma$	684.4	431.4	741.0	–	0.2188	–	10
LT-YbAuSi	SrAgGe	$C2/m$	1038.5(2)	436.4(1)	1319.8(3)	98.71(2)	0.5912	–	11
LT-YbAuSi	SrAgGe	$C2/m$	1042.0(3)	435.7(1)	1319.0(3)	98.53(2)	0.5922	–	11
LT-YbAuSi	SrAgGe	$C2/m$	1044.6(3)	437.2(1)	1319.7(3)	98.54(1)	0.5960	–	11
HT-YbAuSi	EuAuGe	$Imm2$	439.7(1)	702.3(1)	757.2(1)	–	0.2338	0.030	11
YbAu <sub>0.63</sub> Si <sub>1.37</sub>	AlB <sub>2</sub>	$P6/mmm$	416.3(2)	$a$	400.9(2)	–	0.0602	0.022	11
YbAu <sub>0.88</sub> Si <sub>1.12</sub>	AlB <sub>2</sub>	$P6/mmm$	418.2(1)	$a$	396.2(2)	–	0.0600	0.042	11
YbAu <sub>1.25</sub> Si <sub>0.75</sub>	KHg <sub>2</sub>	$Imma$	443.1(1)	701.8(1)	763.1(1)	–	0.2373	0.049	11

## References

- Danebrock et al. (1995)
- Merlo et al. (1993)
- Bodak et al. (1970)
- Iandelli (1983)
- Sendlinger (1993)
- Nikiforov et al. (1994)
- Borisenko et al. (1995)
- Prots' et al. (1998)
- Merlo et al. (1996)
- Rossi et al. (1983a)
- Pani et al. (1999)

look at the band dispersions shows that the relevant  $\pi^*$ -band is only scarcely occupied in YbCoC. Thus, the precondition for an electronic instability is not given on the basis of self-consistent calculations where the complete structure is taken into account.

Equiatomic silicides have been observed with Fe, Cu, Pd, Ag, Pt, and Au as transition-metal component (table 5). In YbMgSi (Merlo et al. 1993) the transition-metal position is occupied by magnesium atoms. YbMgSi and YbPtSi crystallize with the orthorhombic TiNiSi-type structure. So far, no detailed structural data are available for these silicides. Chemical bonding in these compounds is similar to the gallides and calcium compounds discussed in detail (Pöttgen and Johrendt 2000, Nuspl et al. 1996, Landrum et al. 1998, Hoffmann and Pöttgen 2000). In this context we should note that YbMgSi may be understood with an extended Zintl formulation. Assuming that two valence electrons of ytterbium and magnesium have been transferred to the silicon atoms we may write  $\text{Yb}^{2+}\text{Mg}^{2+}\text{Si}^{4-}$ , in agreement with the isolated silicon atoms observed in the structure.

The palladium-based silicide was investigated by three different groups (Sendlinger 1993, Prots' et al. 1998, Nikiforov et al. 1994, Borisenko et al. 1995). While

Sendlinger (1993), Nikiforov et al. (1994) and Borisenko et al. (1995) assigned the TiNiSi type, a superstructure (YPdSi type) with a doubled *b*-axis was reported recently (Prots' et al. 1998). This superstructure (fig. 7) results from a peculiar type of ordering between the palladium and silicon atoms. Like in the TiNiSi type we observe orthorhombically distorted, puckered Pd<sub>3</sub>Si<sub>3</sub> hexagons, but these layers are stacked in a different way, resulting in Pd–Si as well as Pd–Pd and Si–Si interlayer interactions, while only Pd–Si interlayer interactions would occur in TiNiSi-type YbPdSi. Both ordering variants are superstructures of the KHg<sub>2</sub> type, but different sets of weak superstructure reflections occur. Thus, only a careful investigation by X-ray powder and single-crystal data clearly manifests which superstructure is formed. It is most likely that some weak superstructure reflections have been overlooked in the previous investigations, and that the YPdSi type (Prots' et al. 1998) is indeed the correct structure for YbPdSi.

With iron as transition-metal component the tetragonal PbFCI type (space group *P4/nmm*), a ternary ordered version of the Cu<sub>2</sub>Sb structure (Villars and Calvert 1991) (fig. 2) was observed. The iron and silicon atoms show an ordering on the two crystallographically different copper sites, while the ytterbium atoms are located on the antimony position. The iron and silicon atoms together form a two-dimensional infinite [FeSi] network of edge-sharing FeSi<sub>4/4</sub> tetrahedra. The [FeSi] layers are separated from each other via two layers of ytterbium atoms. These different layers are connected to each other by Yb–Si contacts along the *c*-axis. This tetragonal structure type occurs only for YbFeSi in the ytterbium series and for EuRhGa (Pöttgen and Johrendt 2000) in the europium series, i.e. for compounds with a relatively low electron count of 14 valence electrons per formula unit.

The Ni<sub>2</sub>In structure (Villars and Calvert 1991) with space group *P6<sub>3</sub>/mmc* was reported for YbCuSi (Iandelli 1983). Based on the X-ray powder data, the ordering between the copper and silicon atoms was not exactly determined; however, the doubling of the *c* lattice parameter was clearly detected. An ordered variant of the Ni<sub>2</sub>In type was presented in fig. 1 for YbHgPb (ZrBeSi type, Villars and Calvert 1991). This structural arrangement most likely also occurs for YbCuSi. The copper and silicon atoms form planar Cu<sub>3</sub>Si<sub>3</sub> hexagons which are rotated by 60° with respect to each other in every other layer. The ytterbium atoms are located between these layers. Thus each ytterbium atom has a sandwich-like coordination of two Cu<sub>3</sub>Si<sub>3</sub> hexagons. A single-crystal study would elucidate the degree of ordering and puckering of the Cu<sub>3</sub>Si<sub>3</sub> hexagons.

The silver silicide (Iandelli 1985) shows an ordering between the silver and silicon atoms. It crystallizes with the ZrNiAl type. This is one of the rare cases where the silver atoms show no random distribution within the polyanion.

A special situation occurs with gold as transition-metal component (Pani et al. 1999). For the equiatomic composition two phases were observed: HT-YbAuSi with orthorhombic EuAuGe-type structure (Pöttgen 1995, Müllmann et al. 1997) and LT-YbAuSi with the monoclinic SrAgGe type (Merlo et al. 1996). In the high-temperature modification the gold and silicon atoms form puckered Au<sub>3</sub>Si<sub>3</sub> hexagons. The puckering is realized in such a way that the gold and silicon atoms from adjacent layers form weak Au–Au and Si–Si contacts (see fig. 4). The Au–Au distance is 312 pm, and therefore considerable



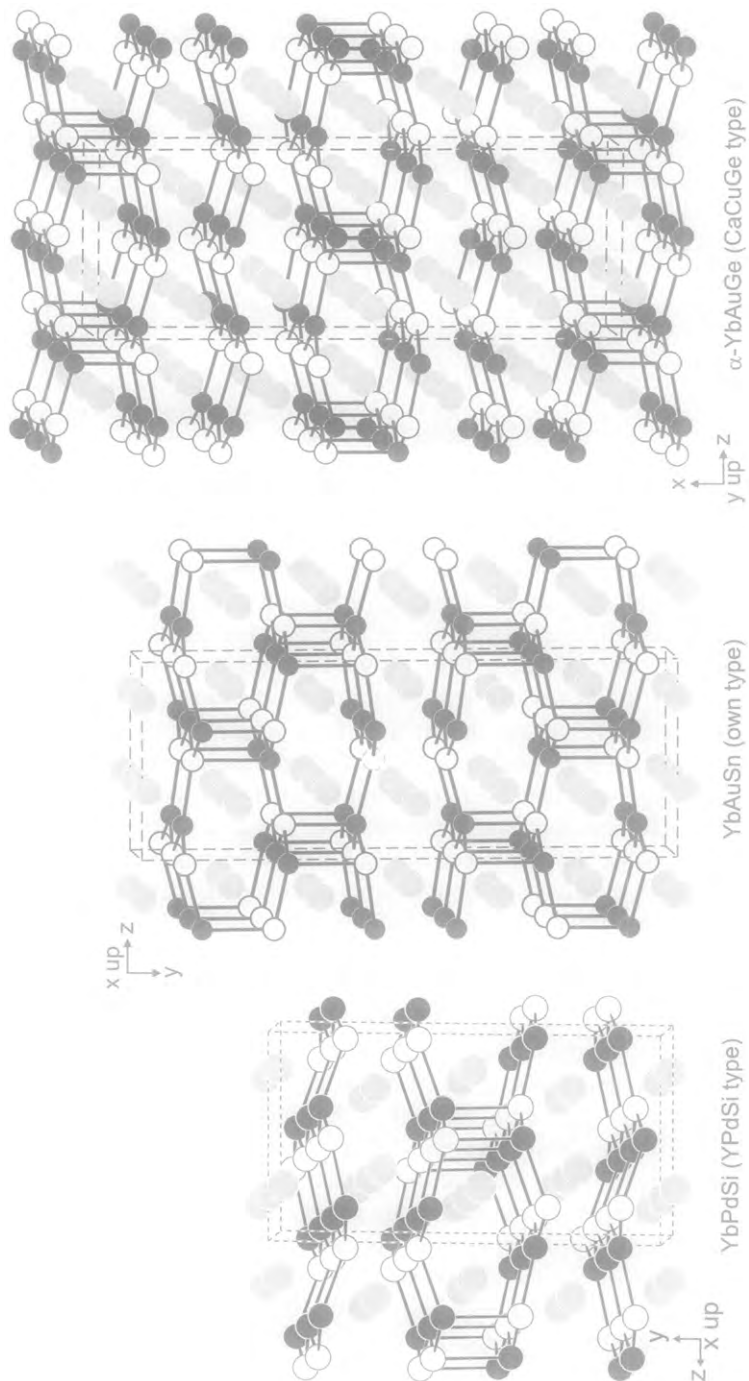


Fig. 7. Crystal structures of YbPdSi, YbAuSn, and  $\alpha$ -YbAuGe. The puckered  $T_3X_3$  layers and some relevant interlayer  $T-X$  contacts are outlined.

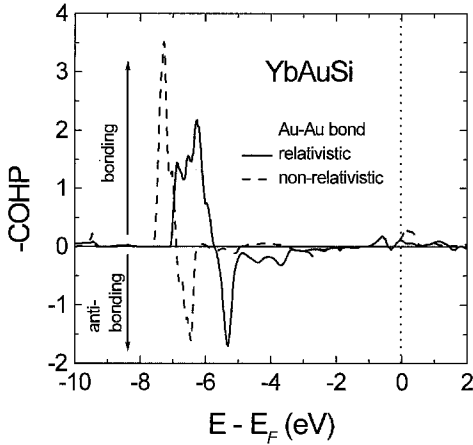


Fig. 8. COHP diagram of the Au–Au interactions in HT-YbAuSi. Solid line: relativistic effects included, dashed line: relativistic effects neglected.

interactions are expected. This is an interesting variant within the  $\text{YbTX}$  structural family where short distances between the transition-metal atoms seem to be favorably avoided. Such Au–Au contacts show the exceptional tendency of gold to form homonuclear bonds despite the equivalent electrical charge ( $\text{Au}^{1+}$ ) and the supposed closed-shell electronic configuration. This effect was observed frequently in gold coordination chemistry and was denoted as *aurophilicity* (Schmidbauer 1990, 1999). One important factor for the affinity between Au atoms is the relativistic effect exerting on the electrons due to the high nuclear charge (Schmidbauer 1990). As an example for a solid-state compound, we illustrate this effect in HT-YbAuSi by comparing the COHP (Dronskowski and Blöchl 1993) of the Au–Au bond (fig. 8) calculated with and without relativistic terms (spin–orbit coupling not included). COHP represents an energy-resolved bonding description based on an energy-partitioning scheme, in contrast to the well-known crystal orbital overlap population, COOP, which is an electron-partitioning scheme. Negative values for COHP indicate bonding, positive values antibonding contributions for a specified bond. To make the COHP diagrams similar to the COOP, we plot  $-\text{COHP}$  vs. energy.

The COHP diagram for the Au–Au bond in HT-YbAuSi is shown in fig. 8. The peaks between  $-7.5$  and  $-5$  eV correspond mainly to the Au 5d states which are completely filled and split into a bonding part at lower (more negative) energies and an antibonding part at higher (less negative) energies. A bonding effect results from mixing of the 5d with 6s and 6p orbitals (Mehrotra and Hoffmann 1978). This depends strongly on the energy separation between the sp and d-levels and increases when the energy difference between sp and d decreases – this is exactly what the relativistic effect does. 6s and – to a smaller extent – 6p go down, while 5d expands and goes up in energy. Consequently the mixing is enhanced and leads to stronger Au–Au bonding. This mechanism is nicely reflected by the COHP diagrams in fig. 8. Without the relativistic effect (dashed line) the 5d orbitals are contracted as seen by the sharp peaks at  $-7.5$  and  $-6.5$  eV. The sp–d mixing is low and the bonding peak is almost neutralized by the antibonding one. When the relativistic terms are switched on (solid line), the situation changes significantly. Because of the enhanced

mixing the bonding peak at  $-6\text{ eV}$  gets much larger than the antibonding part and an attractive Au–Au interaction results. The calculated bonding energy (integration of the COHP up to the Fermi level) increases by about 50% due to the relativistic effect.

For LT-YbAuSi the monoclinic SrAgGe type (Merlo et al. 1996) was assigned on the basis of X-ray powder data. The SrAgGe structure, however, still shows some sites with mixed Ag/Ge occupancy. Although superstructure reflections enlarging the subcell have been observed, the correct ordering has not yet been determined. In several recent papers concerning  $\text{KHg}_2$  superstructures (Kußmann et al. 1998b, Pöttgen et al. 1997a, Niepmann et al. 2000b) it was shown that they all adopt orthorhombic unit cells. The  $\text{KHg}_2$  type has four formula units per cell while the SrAgGe type has ten. It is highly questionable whether or not this factor of 2.5 is correct. Based on a  $\text{KHg}_2$ -type subcell, it is only possible to observe superstructures with  $4n$  formula units per cell where  $n$  is an integral number. We therefore do not discuss the LT-YbAuSi structure any further and we recommend a reinvestigation. SrAgGe and LT-YbAuSi most likely crystallize with the CaAuSn- or EuAuSn-type structure, respectively (Pöttgen and Hoffmann 2000). Furthermore, three different sets of unit-cell parameters were reported for LT-YbAuSi, already indicating a small homogeneity range.

The latter has indeed a large extension and it was investigated in detail by single-crystal X-ray data. Both the binary phases  $\text{YbAu}_2$  (Villars and Calvert 1991) with  $\text{KHg}_2$ -type structure and  $\text{YbSi}_2$  (Villars and Calvert 1991) with  $\text{AlB}_2$  structure are known. The solid solution is observed for the silicon-rich silicides  $\text{YbAu}_{0.63}\text{Si}_{1.37}$  and  $\text{YbAu}_{0.88}\text{Si}_{1.12}$  with  $\text{AlB}_2$  structure as well as a gold-rich compound  $\text{YbAu}_{1.25}\text{Si}_{0.75}$  with  $\text{KHg}_2$  type. The degree of gold substitution in the silicide network can significantly influence the valence of the ytterbium atoms. Thus it would be of interest to determine the magnetic properties of the whole series of compounds within the solid solutions  $\text{YbAu}_{1+x}\text{Si}_{1-x}$  and  $\text{YbAu}_{1-x}\text{Si}_{1+x}$ . Susceptibility measurements of the equiatomic compound showed essentially divalent ytterbium.

### 3.5. Equiatomic germanides $\text{YbTGe}$

Most structural information is available for the germanides and stannides. In both series twelve different intermetallic compounds are known. Interestingly, the transition-metal site can be also occupied by lithium and magnesium atoms.  $\text{YbLiGe}$  (Grund et al. 1986) adopts the  $\text{ZrNiAl}$  type with an ordered arrangement of the lithium and germanium atoms. In the structure we observe no Ge–Ge contacts, and we can consequently assume a  $\text{Ge}^{4-}$  species within an extended Zintl formulation. The charge balance would then be achieved with the  $\text{Li}^+$  and  $\text{Yb}^{3+}$  cations. According to this formulation  $\text{YbLiGe}$  would be paramagnetic, and indeed the magnetic moment derived from the susceptibility measurements clearly revealed trivalent ytterbium (Grund et al. 1986).

When lithium occupies the transition-metal site, the question arises whether the formulation of a  $[\text{LiGe}]^{3-}$  polyanion is still appropriate. As shown in sect. 3.1 for the aluminides, no fundamental difference appears in the electronic structure and the bonding model when an electropositive element is introduced. Also the calculated DOS of  $\text{YbLiGe}$

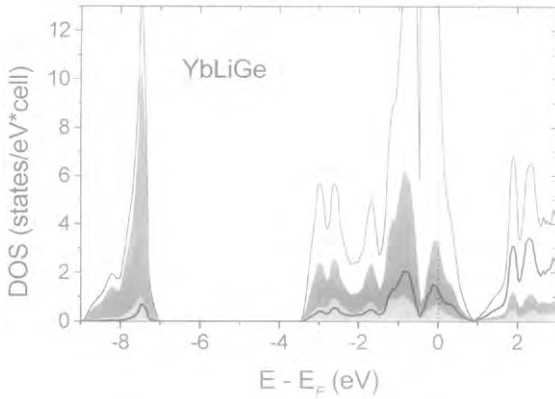


Fig. 9. Electronic density of states of YbLiGe. Outline: total DOS; dark grey area: Ge contribution; light grey area: Li contribution; bold line: Yb-5d contribution.

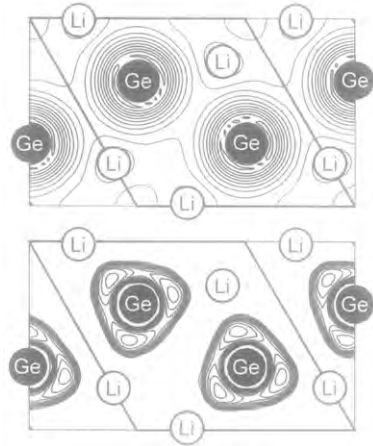


Fig. 10. (top) Charge density and (bottom) electron localization function ELF for the [001] plane in YbLiGe. The hexagonal unit cell is indicated.

reveals noticeable occupation of Li 2s and 2p states, approximately to the same extent as the Yb 5d states (fig. 9). We illustrate the character of the Li–Ge bonds in YbLiGe by the charge density and the electron localization function ELF (Savin et al. 1997, Fässler and Savin 1997), shown in fig. 10. Values of ELF are defined between 0 and 1. Large values ( $>0.7$ ) mean a high probability of paired electron spins, i.e., regions of either covalent bonds or lone pairs of electrons. The almost spherical charge distribution around the Ge atoms and practically no charge near the Li atoms looks like ionic bonding (fig. 10, top). However, the electron localization function ELF (fig. 10, bottom) shows no spherical distribution of paired electrons (as expected for ionic interactions), but maxima near the Ge atoms pointing towards the Li atoms as is typical for covalent bonds.

Based on these results we can safely apply the bonding model of a negatively charged  $[\text{LiGe}]^{\delta-}$  polyanion for YbLiGe and also for related magnesium compounds like YbMgSi or YbMgSn. In these compounds, lithium and magnesium show a certain degree of covalency, emphasizing their special performance in the group of the alkali and alkaline-earth elements. Due to their diagonal relation lithium and magnesium show similar behavior also in the series of YbTX compounds.

An extended Zintl formulation is also possible for  $\text{Yb}^{2+}\text{Mg}^{2+}\text{Ge}^{4-}$  (Merlo et al. 1993) with TiNiSi-type structure. In contrast to YbLiGe, the ytterbium atoms in YbMgGe should not carry a magnetic moment and one should expect Pauli paramagnetism or small temperature-independent paramagnetism (TIP). In view of the missing magnetic data, this remains an open question.

The structure of the cobalt germanide YbCoGe (Dzyanyi et al. 1995a) is still unknown. Dzyanyi and coworkers reported an orthorhombic unit cell with a cell volume of  $0.2550 \text{ nm}^3$ . This corresponds to approximately five formula units of YbCoGe.

YbNiGe, YbRhGe, and YbPtGe (Borisenko et al. 1994) adopt the orthorhombic TiNiSi type. The structural features and chemical bonding of related compounds have already been described in sects. 3.1 and 3.2. The TiNiSi type was also reported for YbPdGe (Sendlinger 1993), based on X-ray powder data. The disordered KHg<sub>2</sub> type was assigned by Nikiforov et al. (1994) and Seropegin et al. (1994). A recent reinvestigation of the YbPdGe structure by single-crystal X-ray film data (Pöttgen and Niepmann 2000), however, showed weak superstructure reflections which significantly enlarge the unit cell. The precise structure determination is still in progress.

The structure of YbCuGe has been investigated independently by Iandelli (1993) and by Dzyanyi et al. (1995a). Both groups assigned the CaIn<sub>2</sub> type, however, significantly different lattice parameters were reported (table 6). This is indicative for a solid solution YbCu<sub>1+x</sub>Ge<sub>1-x</sub> or YbCu<sub>1-x</sub>Ge<sub>1+x</sub>, similar to the europium-based system (Pöttgen and Johrendt 2000). In both investigations the ordering of copper and germanium was not studied.

Zinc-germanium long-range ordering was also not observed for YbZnGe (Merlo et al. 1991). The KHg<sub>2</sub> type structure (fig. 4) was assigned for this germanide with a statistical distribution of the zinc and germanium atoms on the mercury site. This is also the case for the related stannide EuZnSn; however, a recent reinvestigation (Pöttgen 1996a) clearly revealed an ordering between zinc and tin. In view of the significantly different chemical potentials of zinc and germanium, an ordering of these elements is very probable.

YbAgGe (Gibson et al. 1996, Pöttgen et al. 1997b, Zanicchi et al. 1983) and YbCdGe (Merlo et al. 1991) crystallize with the ZrNiAl type. The ordering of the silver and germanium atoms in YbAgGe was studied by single-crystal X-ray data. It is obvious that most silver compounds with ZrNiAl-type structure (YbAgSi and YbAgGe) show Ag/X ordering, while those with KHg<sub>2</sub> related structures show at least partial Ag/X order.

The most interesting compound in the germanide series is YbAuGe (Merlo et al. 1998). Three different modifications occur, depending on the thermal treatment of the sample.  $\gamma$ -YbAuGe with KHg<sub>2</sub>-type structure crystallizes above 1308 K. In this modification the gold and germanium atoms show no long-range order. Below 1308 K a tripling of the subcell *b*-axis ( $3b$ ,  $a$ ,  $-c$  setting) occurs and the gold and germanium atoms show some ordering ( $\beta$ -YbAuGe), however, some sites show still mixed gold/germanium occupancies. Finally at low temperature (below 1003 K) a completely ordered version occurs.  $\alpha$ -YbAuGe crystallizes with the CaCuGe-type structure (Kußmann et al. 1998b), space group *Pnma*.  $\beta$ -YbAuGe can then be described as a site-occupancy variant of the CaCuGe type. In the first investigation (Rossi et al. 1992) YbAuGe was reported to be isotypic with the hexagonal LiGaGe type. Here, some weak reflections have most likely been overlooked. The orthorhombic (o) KHg<sub>2</sub> and hexagonal (h) LiGaGe unit cells have the following relation:  $a_o = a_h$ ;  $b_o = c_h$ , and  $c_o = \sqrt{3}a_h$ . As in the case of the silicide system, YbAuGe also shows a significant homogeneity range. In the germanium-rich part, YbAu<sub>0.67</sub>Ge<sub>1.33</sub> with AlB<sub>2</sub> structure forms. Here, the gold and germanium atoms show a random distribution. A partial ordering occurs in the gold-rich phase YbAu<sub>1.24</sub>Ge<sub>0.76</sub> with EuAuGe structure. Susceptibility measurements of YbAuGe

Table 6

Lattice parameters and residuals for the germanides YbTGe ( $T = \text{Li, Mg, Co, Ni, Cu, Zn, Rh, Pd, Ag, Cd, Pt, Au}$ ). The  $R$ -values marked with an asterisk result from Rietveld refinements (Bragg residuals)

Compound	Type	SG	$a$ (pm)	$b$ (pm)	$c$ (pm)	$V$ (nm <sup>3</sup> )	$R$ -value	Ref.
YbLiGe	ZrNiAl	$P\bar{6}2m$	694.4(1)	$a$	419.0(1)	0.1750	0.095	1
YbMgGe	TiNiSi	$Pnma$	747.4(1)	443.6(1)	834.3(1)	0.2766	0.027	2
YbCoGe	?	?	413.1	1559.6	395.8	0.2550	–	3
YbNiGe	TiNiSi	$Pnma$	674.0(4)	416.2(2)	721.7(3)	0.2025	–	4,5
YbCuGe	CaIn <sub>2</sub>	$P6_3/mmc$	418.60(3)	$a$	698.80(5)	0.1060	0.12*	6
YbCuGe	CaIn <sub>2</sub>	$P6_3/mmc$	421.3(1)	$a$	703.6(2)	0.1082	–	7
YbZnGe	KHg <sub>2</sub>	$Imma$	436.6(1)	728.8(1)	764.0(1)	0.2431	–	8
YbRhGe	TiNiSi	$Pnma$	675.84(9)	422.88(5)	748.5(1)	0.2139	0.056	9
YbPdGe	TiNiSi	$Pnma$	682.7(1)	432.8(1)	752.1(1)	0.2222	0.0268*	10
YbPdGe	KHg <sub>2</sub>	$Imma$	434.4	683.9	752.2	0.2235	–	11
YbPdGe	KHg <sub>2</sub>	$Imma$	434.4(3)	683.9(2)	752.2(3)	0.2235	–	12
YbAgGe	ZrNiAl	$P\bar{6}2m$	705.9	$a$	414.7	0.1790	–	13
YbAgGe	ZrNiAl	$P\bar{6}2m$	705.2(1)	$a$	413.87(8)	0.1783	0.014	14
YbCdGe	ZrNiAl	$P\bar{6}2m$	728.1(1)	$a$	444.1(1)	0.2039	–	8
YbPtGe	TiNiSi	$Pnma$	689.7	432.5	754.2	0.2250	–	11,15
$\alpha$ -YbAuGe	CaCuGe	$Pnma$	2133.2(2)	448.5(1)	770.8(1)	0.7375	0.050	16
$\beta$ -YbAuGe	$\beta$ -YbAuGe	$Pnma$	2131.1(3)	448.1(1)	770.4(1)	0.7357	0.055	16
$\gamma$ -YbAuGe	KHg <sub>2</sub>	$Imma$	446.6(1)	712.3(2)	770.7(2)	0.2452	0.026	16
YbAu <sub>1.24</sub> Ge <sub>0.76</sub>	EuAuGe	$Imm2$	451.0(1)	706.7(1)	778.6(1)	0.2482	0.035	16
YbAu <sub>0.67</sub> Ge <sub>1.33</sub>	AlB <sub>2</sub>	$P6/mmm$	432.3(2)	$a$	393.6(2)	0.0637	0.024	16
YbAuGe	LiGaGe	$P6_3mc$	447.5(3)	$a$	716.3(3)	0.1242	–	17

### References

- Grund et al. (1986)
- Merlo et al. (1993)
- Dzyanyi et al. (1995a)
- Gorelenko et al. (1984)
- Dzyanyi et al. (1995b)
- Dzyanyi et al. (1995c)
- Iandelli (1993)
- Merlo et al. (1991)
- Gladyshevskii and Parthé (1992)
- Sendlinger (1993)
- Nikiforov et al. (1994)
- Seropegin et al. (1994)
- Zanicchi et al. (1983)
- Pöttgen et al. (1997b)
- Seropegin et al. (2000)
- Merlo et al. (1998)
- Rossi et al. (1992)

indicated divalent ytterbium. A simple assignment of oxidation numbers is thus not possible.

### 3.6. Equiatomic stannides YbT<sub>2</sub>Sn

The series of equiatomic ytterbium transition-metal stannides has most intensively been investigated. Today twelve stannides with a variety of six different crystal structures are

known, see table 7. The Zintl phase YbMgSn (Merlo et al. 1993) adopts the hexagonal ZrNiAl-type structure (fig. 3), where the smaller magnesium atoms are located in the trigonal prisms which are formed by the ytterbium and tin atoms. Apart from this purely geometrical view, we can also describe the YbMgSn structure with a three-dimensional [MgSn] network in which the ytterbium atoms fill distorted hexagonal channels. The formula of YbMgSn may be described as  $\text{Yb}^{2+}\text{Mg}^{2+}\text{Sn}^{4-}$ . In view of the missing magnetic data the valence state of the ytterbium atoms remains an open question.

The same structure type is also adopted by the stannides YbRhSn (Kaczorowski et al. 1999, Trovarelli et al. 2000, Dwight et al. 1973, Katoh et al. 1999),  $\alpha$ -YbPdSn (Kußmann et al. 1998a, Sendlinger 1993), YbCdSn (Merlo et al. 1991), and YbPtSn (Katoh et al. 1997, Pöttgen et al. 1999a, Kaczorowski et al. 1999, Dwight et al. 1973). Of these compounds only the structures of  $\alpha$ -YbPdSn and YbPtSn have been refined from single-crystal X-ray data, while all other ZrNiAl-type stannides were characterized on the basis of powder-diffraction data. An important result of the single-crystal investigation was the enlarged displacement parameter  $U_{33}$  of the palladium and platinum atoms within the trigonal ytterbium prisms, indicating small structural distortions. If these structural distortions become larger, a superstructure results, as was investigated in detail for the prototype HfRhSn (Zumnick and Pöttgen 1999) and some other stannides and gallides (Zumnick et al. 1999). The formation of the superstructure seems to depend on the  $c/a$  ratio of the cell parameters (Zumnick et al. 1999).

The structures of the other stannides are superstructures which are all derived from the aristotype  $\text{AlB}_2$ . The transition-metal and tin atoms are ordered in the boron network. The resulting  $T_3X_3$  hexagons are distorted and puckered in different ways. In the LiGaGe-type stannides YbZnSn (Kaczorowski et al. 1999, Merlo et al. 1991, Pöttgen et al. 1999c) and YbHgSn (Merlo et al. 1993), the  $\text{Zn}_3\text{Sn}_3$  and  $\text{Hg}_3\text{Sn}_3$  layers are rotated by  $60^\circ$  around the  $c$ -axis in every other layer (fig. 1). In this way, each zinc and mercury atom obtains a distorted tetrahedral tin coordination with shorter  $T$ -Sn intralayer and longer  $T$ -Sn interlayer distances. These stannides may again be interpreted as Zintl phases by the formulae  $\text{Yb}^{2+}\text{Zn}^{2+}\text{Sn}^{4-}$  and  $\text{Yb}^{2+}\text{Hg}^{2+}\text{Sn}^{4-}$ .

Hexagonal  $\text{Ag}_3\text{Sn}_3$  layers also occur in the silver stannide YbAgSn (Katoh et al. 1997, Kaczorowski et al. 1999, Merlo et al. 1996, Pöttgen et al. 1999c, Mazzone et al. 1981). X-ray powder data of YbAgSn were first reported in 1981 by Mazzone et al. (1981). They assumed the  $\text{CaIn}_2$ -type structure with a statistical occupancy of silver and tin atoms on the indium site. All subsequent X-ray powder investigations (Katoh et al. 1997, Kaczorowski et al. 1999, Merlo et al. 1996, Pöttgen et al. 1999c), however, clearly showed that the YbAgSn unit cell is larger. It consists of three different  $\text{AlB}_2$ -related subcells which are stacked along the  $c$ -axis in the sequence ABC (fig. 11). Although silver and tin differ only by three electrons (i.e. they have a similar scattering power for X-rays), a recent single-crystal investigation (Pöttgen et al. 1999c) unambiguously revealed the silver-tin ordering in this stannide. It is isotypic with YbAgPb (Merlo et al. 1996). One  $\text{Ag}_3\text{Sn}_3$  layer is planar, while the other two  $\text{Ag}_3\text{Sn}_3$  layers are puckered in such a way that the tin atoms form pairs with Sn-Sn distances of 318 pm between these layers. This structural model is strongly supported by  $^{119}\text{Sn}$  Mössbauer experiments (see sect. 4.4).

Table 7

Lattice parameters and residuals for the orthorhombic stannides YbT<sub>2</sub>Sn (*T* = Mg, Ni, Cu, Zn, Rh, Pd, Ag, Cd, Ir, Pt, Au, Hg). The *R*-values marked with an asterisk result from Rietveld refinements (Bragg residuals)

Compound	Type	SG	<i>a</i> (pm)	<i>b</i> (pm)	<i>c</i> (pm)	<i>V</i> (nm <sup>3</sup> )	<i>R</i> -value	Ref.
YbMgSn	ZrNiAl	<i>P</i> $\bar{6}2m$	763.7(1)	<i>a</i>	468.4(2)	0.2366	0.044	1
YbNiSn	TiNiSi	<i>Pnma</i>	697.3	441.4	762.7	0.2348	–	2
YbNiSn	TiNiSi	<i>Pnma</i>	698.3	442.6	761.6	0.2354	–	3
YbNiSn	TiNiSi	<i>Pnma</i>	696.0(3)	439.6(2)	759.7(2)	0.2324	–	4
YbNiSn	TiNiSi	<i>Pnma</i>	696.0(2)	441.0(1)	760.7(2)	0.2335	0.07	5
YbNiSn	TiNiSi	<i>Pnma</i>	697.0(5)	441.2(4)	759.0(6)	0.2334	–	6
YbNiSn	TiNiSi	<i>Pnma</i>	697.1	441.2	759.0	0.2334	–	7
YbNiSn	KHg <sub>2</sub>	<i>Imma</i>	441.4	697.3	762.7	0.2348	–	8
YbCuSn	KHg <sub>2</sub>	<i>Imma</i>	455.5(1)	727.4(3)	781.2(3)	0.2588	0.057	9
YbCuSn	TiNiSi	<i>Pnma</i>	729.4	456.4	783.1	0.2607	–	10
YbZnSn	LiGaGe	<i>P</i> 6 <sub>3</sub> <i>mc</i>	465.14(4)	<i>a</i>	747.32(1)	0.1400	–	11
YbZnSn	LiGaGe	<i>P</i> 6 <sub>3</sub> <i>mc</i>	464.9(1)	<i>a</i>	747.6(1)	0.1399	0.030	12
YbZnSn	LiGaGe	<i>P</i> 6 <sub>3</sub> <i>mc</i>	464.7(1)	<i>a</i>	747.7(2)	0.1398	–	13
YbRhSn	Fe <sub>2</sub> P	<i>P</i> $\bar{6}2m$	753.8(1)	<i>a</i>	366.86(8)	0.1805	–	11
YbRhSn	ZrNiAl	<i>P</i> $\bar{6}2m$	753.1(3)	<i>a</i>	366.6(6)	0.1801	–	14
YbRhSn	Fe <sub>2</sub> P	<i>P</i> $\bar{6}2m$	752	<i>a</i>	367	0.1797	–	15
YbRhSn	ZrNiAl	<i>P</i> $\bar{6}2m$	753.3	<i>a</i>	366.3	0.1800	–	16
$\alpha$ -YbPdSn	ZrNiAl	<i>P</i> $\bar{6}2m$	755.6(1)	<i>a</i>	380.3(1)	0.1880	0.0570	17
$\alpha$ -YbPdSn	ZrNiAl	<i>P</i> $\bar{6}2m$	759.0(2)	<i>a</i>	376.98(9)	0.1881	0.0287	18
$\beta$ -YbPdSn	TiNiSi	<i>Pnma</i>	719.5(1)	458.5(1)	796.6(1)	0.2628	0.0288	17
$\beta$ -YbPdSn	TiNiSi	<i>Pnma</i>	718.7(1)	458.3(1)	796.1(1)	0.2622	0.0505	18
YbPdSn	TiNiSi	<i>Pnma</i>	715.4	458.6	788.5	0.2587	–	19
YbAgSn	CaIn <sub>2</sub>	<i>P</i> 6 <sub>3</sub> / <i>mmc</i>	479.1	<i>a</i>	725.6	0.1442	–	20
YbAgSn	CaLiSn	<i>P</i> 3 <i>m</i> 1	478.8(1)	<i>a</i>	1087.0(1)	0.2158	–	21
YbAgSn	CaLiSn	<i>P</i> 3 <i>m</i> 1	479.0	<i>a</i>	1088.7	0.2163	–	10
YbAgSn	CaLiSn	<i>P</i> 3 <i>m</i> 1	478.91(8)	<i>a</i>	1087.7(4)	0.2160	–	11
YbAgSn	YbAgPb	<i>P</i> $\bar{6}m$ 2	479.2(2)	<i>a</i>	1087.3(3)	0.2162	0.033	13
YbCdSn	ZrNiAl	<i>P</i> $\bar{6}2m$	759.4(1)	<i>a</i>	467.9(1)	0.2337	–	12
YbIrSn	Fe <sub>2</sub> P	<i>P</i> $\bar{6}2m$	749	<i>a</i>	373	0.1812	–	15
YbIrSn	ZrNiAl	<i>P</i> $\bar{6}2m$	746.3	<i>a</i>	375.0	0.1809	–	16
YbPtSn	ZrNiAl	<i>P</i> $\bar{6}2m$	738.2	<i>a</i>	393.3	0.1856	–	10
YbPtSn	Fe <sub>2</sub> P	<i>P</i> $\bar{6}2m$	738.6(2)	<i>a</i>	392.13(6)	0.1853	0.074*	11
YbPtSn	Fe <sub>2</sub> P	<i>P</i> $\bar{6}2m$	737.9(1)	<i>a</i>	393.3(1)	0.1855	–	15
YbPtSn	ZrNiAl	<i>P</i> $\bar{6}2m$	737.8(3)	<i>a</i>	393.1(2)	0.1853	0.0213	20
YbAuSn	TiNiSi	<i>Pnma</i>	730.3(2)	470.82(9)	812.3(4)	0.2793	–	11
YbAuSn	TiNiSi	<i>Pnma</i>	731.2	471.6	813.9	0.2807	–	10
YbAuSn	YbAuSn	<i>Imm</i> 2	469.9(2)	2191.4(5)	812.9(2)	0.8371	0.049	22
YbHgSn	LiGaGe	<i>P</i> 6 <sub>3</sub> <i>mc</i>	479.5(1)	<i>a</i>	768.3(2)	0.1530	–	1

continued on next page



Table 7, notes

## References

- |                            |                               |                             |
|----------------------------|-------------------------------|-----------------------------|
| 1. Merlo et al. (1993)     | 9. Zanicchi et al. (1999)     | 17. Sendlinger (1993)       |
| 2. Rossi et al. (1985)     | 10. Katoh et al. (1997)       | 18. Kußmann et al. (1998a)  |
| 3. Dwight (1983)           | 11. Kaczorowski et al. (1999) | 19. Adroja and Malik (1992) |
| 4. Skolozdra et al. (1984) | 12. Merlo et al. (1991)       | 20. Mazzone et al. (1981)   |
| 5. Bonville et al. (1992)  | 13. Pöttgen et al. (1999c)    | 21. Merlo et al. (1996)     |
| 6. Adroja et al. (1998)    | 14. Trovarelli et al. (2000)  | 22. Hoffmann et al. (2001)  |
| 7. Kasaya et al. (1991)    | 15. Dwight et al. (1973)      |                             |
| 8. Rossi et al. (1983a,b)  | 16. Katoh et al. (1999)       |                             |

Chemical bonding in YbAgSn was studied in detail by TB-LMTO-ASA band structure calculations (Pöttgen et al. 1999c). These theoretical investigations clearly revealed strong covalent Ag–Sn intralayer interactions both in the planar and in the puckered networks. A theoretically calculated charge density underlines the interlayer Sn–Sn bonding between the puckered  $\text{Ag}_3\text{Sn}_3$  networks.

The remaining stannides, i.e. YbNiSn (Skolozdra et al. 1984, Dwight 1983, Rossi et al. 1983a,b, 1985, Bonville et al. 1992, Adroja et al. 1998, Kasaya et al. 1991), YbCuSn (Katoh et al. 1997, Zanicchi et al. 1999),  $\beta$ -YbPdSn (Kußmann et al. 1998a, Sendlinger 1993) and YbAuSn (Katoh et al. 1997, Kaczorowski et al. 1999, Hoffmann et al. 2001), were reported to be isotypic with TiNiSi. Also in these structures, the transition-metal and tin atoms form orthorhombically distorted puckered  $T_3\text{Sn}_3$  hexagons which are rotated by about  $60^\circ$  with respect to each other in every other layer. The TiNiSi type has already been discussed in detail for YbPdAl in sect. 3.1 (fig. 4). The TiNiSi type definitely does not occur for YbAuSn. The powder patterns of this stannide clearly show a  $\text{KHg}_2$ -type subcell (Katoh et al. 1997, Kaczorowski et al. 1999); however, precise single-crystal

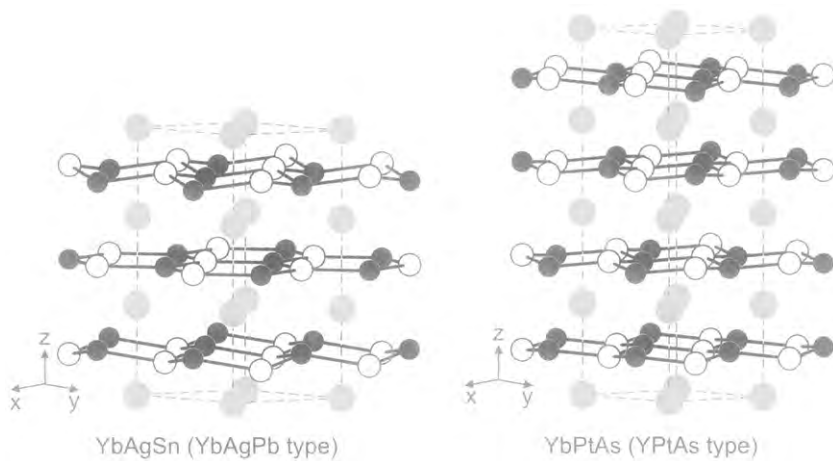


Fig. 11. Crystal structures of YbAgSn and YbPtAs. The slightly puckered  $\text{Ag}_3\text{Sn}_3$  and  $\text{Pt}_3\text{As}_3$  hexagons are emphasized.

data indicate a tripling of the subcell *b*-axis (Hoffmann et al. 2001) and a complex twinning mechanism.

The YbAuSn superstructure (fig. 7) results from a different stacking sequence of the puckered Au<sub>3</sub>Sn<sub>3</sub> networks. In this peculiar structure type we observe strong intralayer Au–Sn bonding besides weak interlayer Au–Sn, Sn–Sn and Au–Au bonding. Such structural features have recently also been observed in the superstructures of CaAuSn (Kußmann et al. 1998b) and EuAuSn (Pöttgen et al. 1997a). Also in YbAuSn the relativistic nature of the gold atoms (Schmidbauer 1999) might account for the formation of the superstructure.

The most striking stannide is certainly YbPdSn (Kußmann et al. 1998a, Sendlinger 1993, Adroja and Malik 1992), which shows a structural phase transition.  $\beta$ -YbPdSn with orthorhombic TiNiSi-type structure crystallizes from the melt and transforms to  $\alpha$ -YbPdSn with hexagonal ZrNiAl-type structure upon annealing at 970 K. This phase transition is of a reconstructive type as demonstrated by a group–subgroup scheme (Bärnighausen 1980, Kußmann et al. 1998a). The change in crystal structure is paralleled by a change of the ytterbium valence, i.e. essentially trivalent ytterbium in the low-temperature phase and essentially divalent ytterbium in  $\beta$ -YbPdSn. The physical properties will be discussed in detail in section 4.

### 3.7. The plumbides YbTPb

Most plumbides are available only in the form of microcrystalline powders. In contrast to the situation for stannides, it is difficult to grow small single crystals suitable for X-ray investigation. Furthermore the plumbides do not resist the humidity of the air and must therefore be kept under inert conditions. This chemical behavior is similar to the europium-based plumbides (Pöttgen and Johrendt 2000). The structural details of the YbTPb phases are given in table 8.

YbMgPb (Merlo et al. 1993), YbPdPb (Sendlinger 1993, Iandelli 1994, Marazza et al. 1995) and YbCdPb (Merlo et al. 1991) adopt the ZrNiAl structure. The magnesium- and cadmium-containing compounds are Zintl phases according to the formulations Yb<sup>2+</sup>Mg<sup>2+</sup>Pb<sup>4-</sup> and Yb<sup>2+</sup>Cd<sup>2+</sup>Pb<sup>4-</sup>. Such a simple assignment of oxidation numbers is not possible for the palladium plumbide. In this compound the palladium atoms are the most electronegative component. Furthermore, Sendlinger (1993) reported a second phase of composition Yb(Pd,Pb) with CsCl structure in the palladium system.

The structures of the other plumbides are all hexagonal. They are derived from the AlB<sub>2</sub> type. YbCuPb (Mazzone et al. 1982) was described with the CaIn<sub>2</sub> type with a random distribution of the copper and lead atoms. Nevertheless, in view of the difference in size between copper and lead, ordering is highly probable, the more because zinc–lead ordering was established for YbZnPb (Merlo et al. 1991) with LiGaGe structure (fig. 1). Since no single-crystal data are available for YbZnPb, the degree of puckering of the Zn<sub>3</sub>Pb<sub>3</sub> network is unknown. According to Dhar et al. (1995), the existence of YbCuPb is highly questionable. This is most likely due to a misprint between YbCuPb and YCuPb in the paper by Mazzone et al. (1982).

Table 8

Lattice parameters and residuals for the plumbides YbTPb ( $T = \text{Mg, Cu, Zn, Pd, Ag, Cd, Hg}$ ). The asterisk indicates the result of a Rietveld refinement (Bragg residual)

Compound	Type	SG	$a$ (pm)	$b$ (pm)	$c$ (pm)	$V$ (nm <sup>3</sup> )	$R$ -value	Ref.
YbMgPb	ZrNiAl	$P\bar{6}2m$	771.9(1)	$a$	472.8(1)	0.2440	–	1
YbCuPb	CaIn <sub>2</sub>	$P6_3/mmc$	455.7(3)	$a$	733.1(5)	0.1318	–	2
YbZnPb	LiGaGe	$P6_3mc$	471.6(1)	$a$	762.5(1)	0.1469	–	3
YbPdPb	ZrNiAl	$P\bar{6}2m$	784.5	$a$	380.5	0.2028	–	4
YbPdPb	ZrNiAl	$P\bar{6}2m$	781.9(1)	$a$	379.9(1)	0.2011	0.0347*	5
YbPdPb	ZrNiAl	$P\bar{6}2m$	784.6(1)	$a$	380.2(2)	0.2027	–	6
Yb(Pd,Pb)	CsCl	$Pm\bar{3}m$	333.9	$a$	$a$	0.0372	–	5
YbAgPb	CaIn <sub>2</sub>	$P6_3/mmc$	489	$a$	723	0.1497	–	7
YbAgPb	YbAgPb	$P\bar{6}m2$	487.3(1)	$a$	1101.7(3)	0.2266	0.068	8
YbCdPb	ZrNiAl	$P\bar{6}2m$	770.4(1)	$a$	471.9(1)	0.2426	–	3
YbHgPb	ZrBeSi	$P6_3/mmc$	492.2(2)	$a$	723.1(5)	0.1517	–	1

#### References

1. Merlo et al. (1993)
2. Mazzone et al. (1982)
3. Merlo et al. (1991)
4. Marazza et al. (1995)
5. Sendlinger (1993)
6. Iandelli (1994)
7. Mazzone et al. (1983)
8. Merlo et al. (1996)

The silver plumbide was first reported with CaIn<sub>2</sub>-type structure with a statistical Ag/Pb occupancy (Mazzone et al. 1983). Recent single-crystal data, however, have revealed that the unit cell is tripled and not doubled. YbAgPb crystallizes with its own structure type (Merlo et al. 1996), space group  $P\bar{6}2m$  (fig. 11). It contains planar and puckered Ag<sub>3</sub>Pb<sub>3</sub> layers. This structure was already discussed in sect. 3.6 for isotypic YbAgSn.

Exclusively planar Hg<sub>3</sub>Pb<sub>3</sub> layers occur in YbHgPb (Merlo et al. 1993) with ZrBeSi structure, space group  $P6_3/mmc$  (fig. 1). In every other layer the Hg<sub>3</sub>Pb<sub>3</sub> hexagons are rotated by 60° with respect to each other around the  $c$ -axis. The intralayer Hg–Pb distance of 284 pm is directly available from the lattice parameters. This distance is significantly smaller than the sum of Pauling's single-bond radii of 298 pm, indicating strong Hg–Pb bonding within the layers.

### 3.8. The phosphides and arsenides YbTP and YbTAs

The ternary ytterbium phosphides (table 9) and arsenides (table 10) have only scarcely been investigated. So far only YbPdP (Johrendt and Mewis 1992), with orthorhombic TiNiSi structure, and YbPtP (Wenski and Mewis 1986b), with hexagonal SrPtP-type structure, are known. In both phosphides the palladium (platinum) and phosphorous atoms are ordered. The [PdP] polyanion is three-dimensional and it consists of puckered Pd<sub>3</sub>P<sub>3</sub> hexagons, while YbPtP contains a planar [PtP] polyanion. Thus, we observe a 3+1 (elongated tetrahedron) coordination for the palladium atoms and a trigonal planar coordination for the platinum atoms. This is quite unexpected from the viewpoint of atomic sizes. Structures with planar coordination of the transition metal are generally

Table 9  
Lattice parameters, structure types and residuals for the phosphides YbTP ( $T = \text{Pd, Pt}$ )

Compound	Type	SG	$a$ (pm)	$b$ (pm)	$c$ (pm)	$V$ (nm <sup>3</sup> )	$R$ -value	Ref.
YbPdP	TiNiSi	$Pnma$	677.6(1)	393.7(1)	767.0(1)	0.2046	–	1
YbPtP	SrPtSb	$P\bar{6}m2$	407.7(1)	$a$	377.7(1)	0.0544	0.050	2

References

1. Johrendt and Mewis (1990)
2. Wenski and Mewis (1986b)

Table 10  
Lattice parameters, structure types and residuals for the arsenides YbTAs ( $T = \text{Li, Pd, Pt}$ ). The  $R$ -value for YbLiAs results from a Rietveld refinement

Compound	Type	SG	$a$ (pm)	$b$ (pm)	$c$ (pm)	$V$ (nm <sup>3</sup> )	$R$ -value	Ref.
YbLiAs	TiNiSi	$Pnma$	723.0(1)	432.8(1)	788.1(1)	0.2466	0.005*	1,2
YbPdAs	Fe <sub>2</sub> P	$P\bar{6}2m$	699.7(1)	$a$	391.3(1)	0.1659	0.022	3
YbPtAs	YPtAs	$P6_3/mmc$	423.4(1)	$a$	1485.1(3)	0.2306	–	4

References

1. Albering (1993)
2. Albering et al. (1997)
3. Johrendt and Mewis (1992)
4. Wenski and Mewis (1986b)

observed for  $ATX$  ( $A = \text{base metal component}$ ) compounds with larger values of the quotient  $r_A/r_{TX}$  ( $r_A = \text{metallic radius of } A$ ;  $r_{TX} = \text{mean covalent radius of } T \text{ and } X$ ). Smaller  $A$  components like Yb favour the formation of structures with tetrahedral or distorted tetrahedral coordination of the transition metal. This trend is obvious from the compounds reviewed here, where representatives with  $\text{AlB}_2$  or  $\text{ZrBeSi}$  structures (planar  $T_3X_3$  hexagons) are scarce, but occur frequently in  $\text{EuTX}$  compounds due to the larger europium atoms (Pöttgen and Johrendt 2000).

We have performed LMTO band structure calculations on orthorhombic YbPdP and hexagonal YbPtP, and could not find apparent electronic differences. In order to compare Pt–P and Pd–P bonds we have calculated the COHP for hexagonal YbPtP and hypothetical YbPdP with the same geometry. Surprisingly, the Pt–P bonding energy is found to be about 20% larger than the Pd–P bonding energy. A reason for this may be the relativistic effect of platinum which changes the orbital energies of 6sp and 5d as mentioned for Au in sect. 3.4. When the relativistic effect is neglected in our calculations we get almost the same bonding energy for Pt–P as for Pd–P bonds. These results points to an outstanding stability of trigonal–planar Pt–P bonds. In order to understand the preference of platinum to form  $\text{AlB}_2$ -related structures rather than the TiNiSi type a more detailed analysis of the electronic structures is recommended.

So far only three YbTAs arsenides are known (table 10). YbLiAs (Albering 1993, Albering et al. 1997) crystallizes with the TiNiSi type structure. In this arsenide, the lithium atoms occupy the typical transition-metal site and we observe puckered  $\text{Li}_3\text{As}_3$  networks.

YbPdAs adopts the ZrNiAl-type structure. According to the structure refinements (Johrendt and Mewis 1992) relatively short (261–269 pm) Pd–As distances are indicative for strongly bonding Pd–As interactions. A peculiar structure occurs for YbPtAs. This arsenide crystallizes with the YPtAs-type structure (Wenski and Mewis 1986b), a superstructure of the AlB<sub>2</sub> type. Four different puckered Pt<sub>3</sub>As<sub>3</sub> networks are stacked along the *c*-axis (fig. 11). According to the short Pt–As contacts we assume strongly bonding Pt–As intralayer interactions. Since the puckering of the Pt<sub>3</sub>As<sub>3</sub> networks is not very pronounced, we observe no bonding interactions between the layers. This structure type has so far only been observed for the arsenides *R*PtAs (*R* = Y, Sm, Gd–Lu), for CaGaGe, CaGaSn, SrGaGe, SrGaSn, BaGaGe (Czybulka et al. 1989), and for the uranium germanide UAuGe (Gibson et al. 2001). In UAuGe the puckering is stronger when compared with YbPtAs, most likely due to the smaller uranium atoms. We therefore observe significant Au–Au interlayer bonding at Au–Au distances of 327 pm. Chemical bonding in UAuGe was investigated on the basis of TB-LMTO-ASA calculations (Gibson et al. 2001). Calculated charge densities underline the strong intralayer Au–Ge and weaker interlayer Au–Au interactions.

### 3.9. Ternary antimonides YbT<sub>2</sub>Sb

The seven antimonides crystallize with three different structure types. YbLiSb (Albering 1993, Albering et al. 1997) and YbAgSb (Katoh et al. 1997, Merlo et al. 1990, Flandorfer et al. 1997) adopt the orthorhombic TiNiSi type structure. According to the magnetic data (sect. 4.2), the ytterbium atoms are divalent and the formulae may be written as Yb<sup>2+</sup>Li<sup>+</sup>Sb<sup>3-</sup> and Yb<sup>2+</sup>Ag<sup>+</sup>Sb<sup>3-</sup>. At this point it is important to note that the lattice parameters of YbAgSb given by Katoh et al. (1997) differ significantly from those reported by Merlo et al. (1990) and Flandorfer et al. (1997). This discrepancy may be due to a homogeneity range or erroneous indexing of the X-ray powder data.

YbCuSb and YbAuSb (Katoh et al. 1997, Merlo et al. 1990, Flandorfer et al. 1997) have hexagonal structures. The copper (gold) and antimony atoms form slightly puckered Cu<sub>3</sub>Sb<sub>3</sub> (Au<sub>3</sub>Sb<sub>3</sub>) hexagons resulting in a NdPtSb-type structure (fig. 1). The original structure refinements of YbCuSb and YbAuSb were performed from X-ray single-crystal data (Merlo et al. 1990). These data clearly revealed an ordering of the copper (gold) and antimony atoms as well as a puckering of the hexagons. The X-ray powder data presented later by Flandorfer et al. (1997) do not reveal the puckering in the case of YbCuSb.

Also, for YbCuSb and YbAuSb a discrepancy occurs for the lattice parameters (Katoh et al. 1997, Merlo et al. 1990, Flandorfer et al. 1997), whatever the reason for this difference might be. Finally it is worthwhile to note that the three antimonides Yb(Cu,Ag,Au)Sb have the same electron count, but crystallize in two different structure types. Magnetic investigations (sect. 4.2) of these antimonides showed essentially divalent ytterbium, leading to the descriptions Yb<sup>2+</sup>Cu<sup>+</sup>Sb<sup>3-</sup> etc.

The isoelectronic antimonides YbNiSb (Le Bras et al. 1995a,b, Dwight 1974, Skolozdra et al. 1997, Larson et al. 1999), YbPdSb (Marazza et al. 1980a,b, Aliev et al. 1989a, Dhar et al. 1988), and YbPtSb (Dwight 1974) crystallize with the non-centrosymmetric cubic MgAgAs-type structure (Villars and Calvert 1991), space group *F*4̄3*m* as presented

in fig. 2 for isotypic YbPdBi. Both the transition-metal and antimony atoms have a tetrahedral  $TSb_{4/4}$  and  $SbT_{4/4}$  coordination, resulting in a three-dimensional infinite network of edge-sharing tetrahedra. The ytterbium atoms are located in cages within this network. A simple assignment of oxidation numbers is not possible for these antimonides since the nickel, palladium, and platinum atoms have electronegativities (Pauling scale: Ni 1.91, Pd 2.20, Pt 2.28, Sb 2.05) comparable to that of antimony. Finally we should point out that the MgAgAs-type structure seems to be favorable for sufficiently high electron counts. The influence of the electron count on the formation of such structures was theoretically investigated by Lee (1991).

A peculiarity occurs for YbNiSb (Skolozdra et al. 1997). This antimonide shows a small nickel deficiency resulting in an exact composition  $YbNi_{0.9}Sb$ . The deficiency has a drastic influence on the properties (see sect. 4.2). The experimental magnetic moments presented by Le Bras et al. (1995a,b) and Skolozdra et al. (1997) differ significantly. Furthermore we should keep in mind that also the lattice parameters for this antimonide differ considerably (see table 11).

Table 11

Lattice parameters, structure types and residuals for the antimonides  $YbTSb$  ( $T = Li, Ni, Cu, Pd, Ag, Pt, Au$ ). The asterisk indicates the result of a Rietveld refinement (Bragg residual)

Compound	Type	SG	<i>a</i> (pm)	<i>b</i> (pm)	<i>c</i> (pm)	<i>V</i> (nm <sup>3</sup> )	<i>R</i> -value	Ref.
YbLiSb	TiNiSi	<i>Pnma</i>	755.3(2)	464.3(1)	820.0(1)	0.2876	0.045*	1,2
YbNiSb	MgAgAs	$F\bar{4}3m$	623.8	<i>a</i>	<i>a</i>	0.2427	–	3,4
YbNiSb	MgAgAs	$F\bar{4}3m$	624.23(1)	<i>a</i>	<i>a</i>	0.2432	–	5
YbNiSb	MgAgAs	$F\bar{4}3m$	624.2	<i>a</i>	<i>a</i>	0.2432	–	6
YbCuSb	Ni <sub>2</sub> In	<i>P6<sub>3</sub>/mmc</i>	445.6(1)	<i>a</i>	800.6(2)	0.1377	0.036*	7
YbCuSb	NdPtSb	<i>P6<sub>3</sub>mc</i>	445.2(1)	<i>a</i>	799.5(1)	0.1372	0.044	8
YbCuSb	NdPtSb	<i>P6<sub>3</sub>mc</i>	444.8	<i>a</i>	791.6	0.1356	–	9
YbPdSb	MgAgAs	$F\bar{4}3m$	647.1	<i>a</i>	<i>a</i>	0.2710	–	10
YbPdSb	MgAgAs	$F\bar{4}3m$	646.5(2)	<i>a</i>	<i>a</i>	0.2702	–	11
YbPdSb	MgAgAs	$F\bar{4}3m$	646.2	<i>a</i>	<i>a</i>	0.2698	–	12
YbAgSb	TiNiSi	<i>Pnma</i>	770.1	469.6	818.5	0.2960	–	9
YbAgSb	TiNiSi	<i>Pnma</i>	766.8(2)	459.6(1)	835.3(2)	0.2944	–	8
YbAgSb	TiNiSi	<i>Pnma</i>	766.8(3)	459.2(1)	837.8(4)	0.2950	0.054*	7
YbPtSb	MgAgAs	$F\bar{4}3m$	647.3	<i>a</i>	<i>a</i>	0.2712	–	3
YbAuSb	NdPtSb	<i>P6<sub>3</sub>mc</i>	461.9	<i>a</i>	776.8	0.1435	–	9
YbAuSb	NdPtSb	<i>P6<sub>3</sub>mc</i>	463.9(1)	<i>a</i>	772.2(3)	0.1439	0.038*	7
YbAuSb	NdPtSb	<i>P6<sub>3</sub>mc</i>	463.5(1)	<i>a</i>	776.5(1)	0.1445	0.055	8

#### References

- |                            |                             |                              |
|----------------------------|-----------------------------|------------------------------|
| 1. Albering (1993)         | 5. Le Bras et al. (1995a,b) | 9. Katoh et al. (1997)       |
| 2. Albering et al. (1997)  | 6. Larson et al. (1999)     | 10. Marazza et al. (1980a,b) |
| 3. Dwight (1974)           | 7. Flandorfer et al. (1997) | 11. Aliev et al. (1989a)     |
| 4. Skolozdra et al. (1997) | 8. Merlo et al. (1990)      | 12. Dhar et al. (1988)       |

Chemical bonding in YbNiSb was recently investigated on the basis of LMTO (Solanki et al. 1994, Sportouch et al. 1999) and LAPW (Larson et al. 1999) calculations. The aim of these works was to understand the transport properties of  $RNiSb$  ( $R=Ho-Yb, Y$ ) compounds in view of potential thermoelectric materials. The cubic MgAgAs-type compounds with trivalent rare-earth elements are narrow-gap semiconductors according to the calculations and the experimental data. This agrees with an electron-precise formulation  $Ln^{3+}Ni^0Sb^{3-}$ . We note that band gaps calculated by density-functional methods are always too small, and often underestimated by more than 50%. The origin of the band gaps is discussed and mainly attributed to the interaction of Ni 3d with the 5d-orbitals of the rare-earth atoms. But in YbNiSb the ytterbium tends to be divalent and the material is a metallic mixed-valence heavy-fermion system. The calculations place the 4f states very close to the Fermi energy, resulting in a high density of states with large 4f contribution. The adequacy of the calculation method in describing these very narrow 4f bands is critically examined.

### 3.10. *Equiatomic bismuthides YbTBi*

Six bismuthides have been reported. They crystallize in three different structure types. YbLiBi (Albering 1993, Albering et al. 1997) adopts the orthorhombic TiNiSi type as do YbLiAs and YbLiSb. Since the ytterbium atoms are divalent (see sect. 4.2) we can write  $Yb^{2+}Li^+Bi^{3-}$ , in agreement with a Zintl formulation. In a previous paper by Grund et al. (1986), the hexagonal YLiSn type was assigned to YbLiBi. This structure would have twice the cell volume of the TiNiSi type (table 12). Since the experimental X-ray intensities given by Albering (1993) match the TiNiSi model very well, we assume that the TiNiSi type is correct for YbLiBi.

YbCuBi and YbAgBi (Kaczorowski et al. 1999, Merlo et al. 1990) crystallize with the hexagonal LiGaGe structure. This is also the case for the high-temperature modification of YbAuBi (Merlo et al. 1990), however, this bismuthide transforms to the cubic MgAgAs type upon annealing at 730 K. The main difference between these two structure types is the stacking sequence of the puckered  $Au_3Bi_3$  hexagonal layers: ABC in the cubic modification, and AB in the hexagonal one. This, however, is a purely geometrical description. Both modifications have different cell content: two formula units in  $\beta$ -YbAuBi and four in  $\alpha$ -YbAuBi. The phase transition also has a drastic effect on the volumes per formula unit: 75.9 and 80.2  $\text{\AA}^3$  for  $\beta$ -YbAuBi and  $\alpha$ -YbAuBi, respectively. The low-temperature phase has the larger volume and, we assume, also the higher content of divalent ytterbium. This is consistent with the magnetic properties given by Kaczorowski et al. (1999). The magnetic behavior of the high-temperature phase, however, has not been studied.

The bismuthides with palladium and platinum also crystallize with the cubic MgAgAs type with an ordering of the palladium (platinum) and bismuth atoms. YbPdBi has been studied most intensively, and six different lattice parameters have been reported (table 12) ranging from 654.7 pm to 661.25 pm. This variation has a drastic effect on the cell volume and we attribute this different behavior to palladium/bismuth mixing or a homogeneity range within the tetrahedral network. A severe problem with this mixing arises certainly for the physical properties, which will strongly depend on composition.

Table 12

Lattice parameters, structure types and residuals for the bismuthides YbT<sub>2</sub>Bi (*T* = Li, Cu, Pd, Ag, Pt, Au). The asterisk indicates the result of a Rietveld refinement (Bragg residual)

Compound	Type	SG	<i>a</i> (pm)	<i>b</i> (pm)	<i>c</i> (pm)	<i>V</i> (nm <sup>3</sup> )	<i>R</i> -value	Ref.
YbLiBi	TiNiSi	<i>Pnma</i>	769.2(1)	473.3(1)	837.4(1)	0.3049	–	1,2
YbLiBi	YLiSn	<i>P6<sub>3</sub>mc</i>	959.5(2)	<i>a</i>	763.5(4)	0.6087	–	3
YbCuBi	LiGaGe	<i>P6<sub>3</sub>mc</i>	458.29(9)	<i>a</i>	785.4(3)	0.1429	–	4
YbCuBi	LiGaGe	<i>P6<sub>3</sub>mc</i>	457.2(1)	<i>a</i>	786.0(1)	0.1423	–	5
YbPdBi	MgAgAs	<i>F<math>\bar{4}3m</math></i>	659.34(3)	<i>a</i>	<i>a</i>	0.2866	0.0699*	4
YbPdBi	MgAgAs	<i>F<math>\bar{4}3m</math></i>	654.7(3)	<i>a</i>	<i>a</i>	0.2806	–	6
YbPdBi	MgAgAs	<i>F<math>\bar{4}3m</math></i>	659	<i>a</i>	<i>a</i>	0.2862	–	7
YbPdBi	MgAgAs	<i>F<math>\bar{4}3m</math></i>	661.25(8)	<i>a</i>	<i>a</i>	0.2891	–	8
YbPdBi	MgAgAs	<i>F<math>\bar{4}3m</math></i>	659.2(2)	<i>a</i>	<i>a</i>	0.2865	–	9
YbPdBi	MgAgAs	<i>F<math>\bar{4}3m</math></i>	659.75(5)	<i>a</i>	<i>a</i>	0.2872	–	10
YbAgBi	LiGaGe	<i>P6<sub>3</sub>mc</i>	481.18(4)	<i>a</i>	777.7(2)	0.1559	–	4
YbAgBi	LiGaGe	<i>P6<sub>3</sub>mc</i>	480.3(1)	<i>a</i>	777.7(1)	0.1554	–	5
YbPtBi	MgAgAs	<i>F<math>\bar{4}3m</math></i>	660.0	<i>a</i>	<i>a</i>	0.2875	–	11
YbPtBi	MgAgAs	<i>F<math>\bar{4}3m</math></i>	659.53(1)	<i>a</i>	<i>a</i>	0.2869	–	12
YbAuBi	MgAgAs	<i>F<math>\bar{4}3m</math></i>	684.8(1)	<i>a</i>	<i>a</i>	0.3211	–	4
$\beta$ -YbAuBi	LiGaGe	<i>P6<sub>3</sub>mc</i>	473.4(1)	<i>a</i>	781.4(1)	0.1517	–	5
$\alpha$ -YbAuBi	MgAgAs	<i>F<math>\bar{4}3m</math></i>	684.6(1)	<i>a</i>	<i>a</i>	0.3209	–	5

#### References

- |                              |                         |                              |
|------------------------------|-------------------------|------------------------------|
| 1. Albering (1993)           | 5. Merlo et al. (1990)  | 9. Marazza et al. (1980a,b)  |
| 2. Albering et al. (1997)    | 6. Aliev et al. (1989a) | 10. Le Bras et al. (1995a,b) |
| 3. Grund et al. (1986)       | 7. Dhar et al. (1988)   | 11. Hundley et al. (1997)    |
| 4. Kaczorowski et al. (1999) | 8. Block (1988)         | 12. Robinson et al. (1994)   |

At low temperatures, forbidden splittings at 1 and 2 meV are observed in the inelastic neutron scattering spectra (see below). Since this might be indicative for a structural phase transition at low temperatures, the YbPtBi structure was investigated by high-resolution neutron powder diffraction down to 0.45 K (Robinson et al. 1994, 1999). No splittings or broadenings of reflections were observed and there is no hint for a symmetry reduction in going to the space groups *I $\bar{4}2m$*  or *R3m*.

From the neutron diffraction study the site occupancies of the ytterbium, platinum, and bismuth atoms are clear (Robinson et al. 1994). Since these heavy atoms differ only by few electrons, it is difficult to assign the correct sites only on the basis of X-ray powder diffraction data. Another important feature concerns the wet chemical analysis. Since all crystals of YbPtBi were grown from a bismuth flux, elemental bismuth occurs as an impurity phase in all samples. An amount of 8.1 wt.% was detected in a neutron diffraction experiment. In view of this impurity, the absolute values of all physical property measurements should be discussed with caution.



Chemical bonding in YbPtBi and other binary ytterbium compounds has recently been investigated by using the self-interaction correction (SIC) and local-spin-density (LSD) approximation (Temmermann et al. 1999). The calculations predict that YbPtBi should be semimetallic between divalent and trivalent, albeit weakly trivalent. The various resistivity measurements (see sect. 4.3) are in agreement with the calculations. The SIC calculations showed that a change in valency is associated with a partial f-electron delocalization, i.e. part of the f-shell experiences a stronger tendency to localize, resulting in bands with little dispersion, while other f-derived states are delocalized and have more dispersion.

Independent electronic structure calculations on YbPtBi were performed by Oppeneer et al. (1997) on the basis of density-functional theory in the local-spin-density approximation (LSDA), generalized with additional intra-atomic Coulomb correlations between 4f electrons. These calculations show that the Yb 4f<sup>14</sup> level is pinned at the Fermi energy. This pinning is a generic property. Furthermore the hybridized 4f level is split into two van Hove-like side maxima.

Eriksson et al. (1992) also compared the electronic structures of semiconducting YPtBi and metallic YbPtBi. Their calculations showed that the smaller volume in YbPtBi results in broader ytterbium d and platinum d bands and a closing of the semiconducting gap. This closing is partly a relativistic effect. In semiconducting YPtBi the valence band is dominated by the platinum d states and the conduction band by the yttrium d states.

### 3.11. Intermetallic magnesium and zinc compounds YbTMg and YbTZn

In this section we focus on the typical intermetallic compounds YbAuMg (Pöttgen et al. 2000b), YbCuZn and YbAgZn (Fornasini et al. 2000). Although these compounds have exclusively metallic components, their structures are similar to those of the Zintl phases described above. YbAuMg adopts the TiNiSi type. Full ordering between gold and magnesium was observed. In contrast, YbCuZn and YbAgZn crystallize with the KHg<sub>2</sub> type with a statistical occupancy of the copper (silver) and zinc atoms. In the case of YbAuMg the difference in electronegativity between gold (2.54 on the Pauling scale) and magnesium (1.31) is large enough to enable the formation of a TiNiSi-related three-dimensional [AuMg] polyanion which is closely related to the indide structures, e.g. the structure of EuAuIn (Pöttgen 1996a). The crystallographic data are given in table 13.

Table 13  
Lattice parameters, structure types and residuals for YbAuMg, YbCuZn, and YbAgZn

Compound	Type	SG	<i>a</i> (pm)	<i>b</i> (pm)	<i>c</i> (pm)	<i>V</i> (nm <sup>3</sup> )	<i>R</i> -value	Ref.
YbAuMg	TiNiSi	<i>Pnma</i>	738.4(1)	436.2(1)	864.6(2)	0.2785	0.0251	1
YbCuZn	KHg <sub>2</sub>	<i>Imma</i>	443.2(2)	708.8(3)	750.1(3)	0.2356	–	2
YbAgZn	KHg <sub>2</sub>	<i>Imma</i>	461.8(2)	728.6(2)	785.4(3)	0.2643	0.013	2

#### References

1. Pöttgen et al. (2000a)

2. Fornasini et al. (2000)

YbAuMg (Pöttgen et al. 2000b), YbCuZn and YbAgZn (Fornasini et al. 2000) are first examples for ytterbium intermetallics, where the site typically occupied by an element of the 3rd, 4th or 5th main group is now occupied by a zinc or magnesium atom (table 13). Recent investigations (Niepmann et al. 2000a, Pöttgen et al. 2000b, Mishra et al. 2001) showed that even cadmium can take this position. It is worthwhile to further investigate these really intermetallic compounds, since they might exhibit a variety of interesting physical properties.

### 3.12. *Some general remarks*

In the preceding eleven subsections we have listed all the YbTX compounds presently known, and we have described their various crystal structures and peculiarities in chemical bonding. The diverse YbTX compounds crystallize with 23 different structure types. It is interesting to note that some structure types which occur for the equiatomic europium compounds (Pöttgen and Johrendt 2000), i.e. the cubic LaIrSi type for EuPdSi, EuPtSi, EuPtGe, and EuIrP, the tetragonal LaPtSi type for EuAlGe, the orthorhombic EuAuSn type, the La<sub>2</sub>Sb type for EuScGe, and the monoclinic EuNiGe type for EuNiGe and EuPdGe, do not occur in the ytterbium-based systems. This is most likely due to the larger size of the europium atoms.

From the drawings of the different crystal structures (figs. 1, 2, 3, 4, 7, and 11) it is evident that most structures are closely related and belong to larger structural families. Most of these structure types consist of planar, tilted, or puckered  $T_3X_3$  hexagons which are readily related to the well-known AlB<sub>2</sub> structure. A detailed description of these AlB<sub>2</sub> superstructures has been given by Pöttgen and Hoffmann (2000) on the basis of group-subgroup schemes.

The structures formed by the various YbTX compounds do not simply depend on the electron count. This is nicely reflected by the series of isoelectronic compounds YbAuSn (own type)–YbCuGe (CaIn<sub>2</sub> type)–YbAgSn (YbAgPb type)–YbAuSi (EuAuGe type)–YbAgGe (ZrNiAl type)– $\alpha$ -YbAuGe (CaCuGe type). Besides the electron count we certainly have to consider the size of the atoms forming the [TX] polyanion and the electronic nature of the transition metals. Small differences in the electronic structures cause differences in the local atomic coordinations. The compounds can thus fulfil their specific electronic requirements by different small structural distortions.

Throughout this section we have repeatedly discussed the ordering between the transition-metal and p-group element atoms within the [TX] polyanions. In view of the differences in chemical potential we assume that indeed most compounds should be ordered. Reliable statements about the ordering can only be made from precise single-crystal X-ray data, and we suggest that redeterminations of the disordered structures are necessary to verify the ordering or disordering of these atoms. In some cases superstructure reflections might be weak and they can be overlooked in powder patterns with poor resolution. Nevertheless, in some cases even the single-crystal data gave no evidence for  $T$ – $X$  ordering (Pöttgen and Johrendt 2000, Pöttgen 1996c). In those compounds, however, a considerable degree of short-range order can be assumed. In the

case of most  $\text{KHg}_2$ -type compounds (Pöttgen and Johrendt 2000, Pöttgen 1996c and references therein), the larger  $U_{22}$  displacement parameter of the randomly occupied  $T/X$  position already indicates short-range order. High-resolution electron microscopy might also be a powerful tool for the investigation of  $T-X$  ordering in such intermetallic compounds.

#### 4. Chemical and physical properties

In the present section we focus on the various chemical and physical properties of the equiatomic YbTX compounds; especially the physical properties, which have been intensively investigated in the last two decades. Besides detailed magnetic susceptibility and electrical resistivity measurements, various other techniques have been used to get deeper insight into the peculiar properties of these intermetallics:  $^{119}\text{Sn}$  and  $^{170}\text{Yb}$  Mössbauer spectroscopy, specific-heat data, thermopower measurements, solid-state NMR, photoemission studies, neutron diffraction, muon spin relaxation, and a variety of high-pressure experiments. The diverse data are summarized in the following subsections.

##### 4.1. Chemical properties

The equiatomic YbTX compounds are typical intermetallic compounds. Most of them are light gray in polycrystalline form, while ground powders are dark gray. Single crystals are silvery with metallic lustre.

The stability of the YbTX compounds in moist air varies significantly. If  $X$  is a heavy element of the third, fourth or fifth main group, i.e. thallium, lead or bismuth, the compounds are quite sensitive to moisture. They completely deteriorate in moist air within a few days. Most aluminides, gallides, indides, silicides, germanides, and stannides are stable in moist air over weeks. The mercury-containing phases, however, show a rapid deterioration in moist air. Some compounds have a remarkable chemical stability. Polished surfaces can easily be etched with  $\text{HCl}/\text{HNO}_3$  solutions. In general, perfectly shaped single crystals of the YbTX compounds show a larger stability than ground powders due to the much larger surface of the powder. The mechanical stability of the YbTX compounds, however, is not very high. Most samples are extremely brittle. They can easily be ground to powder in an agate mortar.

##### 4.2. Magnetic properties

Trivalent intermetallic  $[\text{Xe}]4f^{13}$  ytterbium compounds are particularly important for comparison with cerium compounds, since they exhibit the f-hole analog of  $[\text{Xe}]4f^1$  cerium. In principle, the Kondo effect should be symmetrical between electrons and holes. The main mechanism determining the ground-state behavior in cerium and ytterbium intermetallics is the interaction between the 4f electrons and s, p and d electrons of neighbouring ligands. This so-called f-sp $d$  hybridization tends to reduce the 4f-level

occupation and thus destabilize the magnetic state of cerium or the nonmagnetic state of ytterbium. We can therefore expect a variety of ytterbium intermetallics whose low-temperature electronic properties show the same range of behavior as those of the known cerium compounds. Furthermore it should be possible to find ytterbium-based heavy-fermion compounds (Fisk and Maple 1992). Besides the trivalent state, ytterbium can also be divalent,  $[\text{Xe}]4f^{14}$ , or it can exhibit static mixed- or intermediate-valent behavior. A powerful tool for the examination of these phenomena is the measurement of the temperature dependence of the magnetic susceptibility.

Depending on the valence state of the ytterbium atoms, we can observe a variety of different magnetic phenomena. Those intermetallics with essentially divalent ytterbium show Pauli paramagnetism or weak temperature-independent paramagnetism (TIP). Compounds with stable trivalent ytterbium show Curie–Weiss behavior and sometimes antiferromagnetic (AF) or ferromagnetic (F) ordering at low temperatures. Among the antiferromagnets, so far only three metamagnets (field-induced ferromagnetism; antiparallel to parallel spin alignment) have been observed in the ytterbium series. Metamagnetism is more frequently observed for the  $\text{EuTX}$  compounds (Pöttgen and Johrendt 2000, Pöttgen 1996b). Where the ytterbium valence state is in between trivalency ( $4f^{13}$ ) and divalency ( $4f^{14}$ ), mixed-valence behavior occurs. The magnetic data of the  $\text{YbTX}$  intermetallics are listed in table 14.

A small, almost temperature-independent susceptibility of  $239 \times 10^{-6}$  emu/mol was determined for  $\text{YbAuAl}$ , compatible with a ytterbium valence near +2 (Schank et al. 1994, Cordier et al. 1993, Hulliger 1993). For  $\text{YbPdAl}$  (Schank et al. 1994) a weakly temperature-dependent susceptibility with a maximum near 180 K occurs. According to the Klaasse formula, the ytterbium valence is about +2.9, indicating mixed valency of the ytterbium atoms (Cordier et al. 1993). This behavior is similar to  $\text{YbZnIn}$  (Dhar et al. 1995). Pauli paramagnetism is also reported for  $\text{YbAuSb}$  (Suzuki et al. 1993).

The silicide  $\text{YbAuSi}$  (Pani et al. 1999) shows a room-temperature susceptibility of  $550 \times 10^{-6}$  emu/mol. This is in agreement with essentially divalent ytterbium. Also the room temperature susceptibility of  $\alpha\text{-YbAuGe}$  (Merlo et al. 1998) of  $150 \times 10^{-6}$  emu/mol suggests divalent ytterbium, however, the susceptibilities are affected by a small degree of paramagnetic  $\text{Yb}_2\text{O}_3$ . After subtracting the impurity contribution, a room-temperature susceptibility of  $48 \times 10^{-6}$  emu/mol is obtained for  $\alpha\text{-YbAuGe}$ , indicating Pauli paramagnetism and a low density of states at the Fermi level.  $\gamma\text{-YbAuGe}$  shows similar behavior.

For  $\text{Ni}_2\text{In}$ -type  $\text{YbCuSi}$  (Iandelli 1983), the ytterbium valence is +3 in the temperature range 80–300 K, leading to a formulation  $\text{Yb}^{3+}\text{Cu}^+\text{Si}^{4-}$ . The same holds true for  $\text{YbAgSi}$  with  $\text{ZrNiAl}$  type structure (Iandelli 1985).

$\text{YbNiAl}$  is a heavy-fermion antiferromagnet (Schank et al. 1995), and three successive antiferromagnetic phase transitions at  $T_N = 5.8, 2.9,$  and  $1.3$  K were observed for  $\text{YbPtAl}$  (Drescher et al. 1998). The Néel temperature of this aluminide shows a pressure dependence.  $T_N$  is almost pressure independent in an extended range up to about 11 GPa (5.6–5.2 K) and then increases rapidly, reaching  $T_N = 7.2$  K at 26.2 GPa (Drescher et al. 1998). Both aluminides show metamagnetic transitions at critical fields of 2 T ( $\text{YbNiAl}$ )

Table 14  
Magnetic properties of ternary YbTX compounds<sup>a</sup>

Compound	Order	$T_{\text{Order}}^{\dagger}$ [K]	$\chi_0 \times 10^{-3}$ emu/mol	$\mu_{\text{exp}}$ [ $\mu_{\text{B}}$ ]	$\Theta$ [K]	$\mu_{\text{sm(exp)}}$ [ $\mu_{\text{B}}$ ]	$B_{\text{C}}$ [T]	Ref.
<b>Aluminides</b>								
YbNiAl	AF	$T_{\text{N}}=2.9$	–	4.4	–	–	–	1
YbNiAl	AF	$T_{\text{N}}=2.8$	–	4.4	–35	1.2	2	2
YbCuAl	IV	–	–	4.35	34	1.8	–	3
YbCuAl	IV	–	–	4.33	33	–	–	4
YbPtAl	MM	$T_{\text{N}}=5.8$	–	4.5	–60	2.5	0.3	2
YbPtAl	AF	$T_{\text{N}}=5.8; 2.9; 1.3$	–	4.5	–	–	–	5
YbPtAl	AF	$T_{\text{N}}=5.9$	–	4.5	–	–	–	1
<b>Gallides</b>								
YbNiGa	AF	$T_{\text{N}}=1.7; 1.9$	–	4.4	–30	2.2	–	6
YbPtGa	MM	$T_{\text{N}}=3.8$	–	3.95	–23	1.55	<0.2	7
<b>Indides</b>								
YbPtIn	AF	$T_{\text{N}}=3.1$	–	4.21	–16	1.6	–	8,9
YbPtIn	AF	$T_{\text{N}}=1.4; 3.4$	–	4.4	–30	–	–	6
YbZnIn	TIP	–	2	0.24	–	–	–	10
<b>Silicides</b>								
YbPdSi	P	–	–	4.2(2)	–	–	–	11
<b>Germanides</b>								
YbLiGe	P	–	–	4.0–4.5	–	–	–	12
YbNiGe	P	–	–	4.31	3	–	–	13
YbPdGe	F	$T_{\text{C}}=11.4$	–	–	–	0.95	–	14
YbPdGe	P	–	–	4.3(2)	–	–	–	11
YbPtGe	F	$T_{\text{C}}=4.7$	–	–	–	0.68	–	14
<b>Stannides</b>								
YbNiSn	P	–	–	4.57	–65	–	–	15
YbNiSn	F	$T_{\text{C}}=5.65$	–	–	–	0.85	–	16,17
YbNiSn	F	$T_{\text{C}}=5.5$	–	4.3	–43	–	–	18
YbCuSn	TIP	–	0.42	0.2	–4.4	–	–	19
YbZnSn	TIP	–	–	0.7	–	–	–	20
YbZnSn	TIP	–	0.007	–	–2.1(6)	–	–	21
YbRhSn	AF?	$T_{\text{N}}=2$	–	4.51(3)	–7(1)	1.7(1)	–	21
YbRhSn	AF	$T_{\text{N}}=1.4; 1.85$	–	4.3	–20	–	–	6
YbRhSn	P	–	–	4.5	–4.6	2.35	–	22
$\alpha$ -YbPdSn	P	–	–	4.2(1)	–75(2)	–	–	23
$\beta$ -YbPdSn	P	–	0.24	1.6(1)	–5(1)	–	–	23
$\beta$ -YbPdSn	P	–	0.51	1.43	–4	–	–	24

continued on next page

Table 14, *continued*

Compound	Order	$T_{\text{Order}}$ [K]	$\chi_0 \times 10^{-3}$ emu/mol	$\mu_{\text{exp}}$ [ $\mu_{\text{B}}$ ]	$\Theta$ [K]	$\mu_{\text{sm(exp)}}$ [ $\mu_{\text{B}}$ ]	$B_{\text{C}}$ [T]	Ref.
YbAgSn	TIP	–	–0.01	0.2	–4.5	–	–	19
YbAgSn	TIP	–	2.09	–	–2.7(7)	–	–	21
YbAgSn	TIP	–	–	0.9	–	–	–	20
YbIrSn	AF	$T_{\text{N}}=3.2$	–	4.3	–17.7	1.95	–	22
YbPtSn	MM	$T_{\text{N}}=3.5$	–	4.46	0.4	2.31	0.3	19
YbPtSn	MM	$T_{\text{N}}=3.5(4)$	–	4.27(2)	9.2(8)	2.12(2)	0.5	21
YbAuSn	TIP	–	–0.03	0.1	–3.5	–	–	19
YbAuSn	TIP	–	–0.002	–	–4.4(8)	–	–	21
<b>Phosphides</b>								
YbPtP	P	–	–	4.4	–23	–	–	25
<b>Arsenides</b>								
YbLiAs	TIP	–	–	0.9	–8(3)	–	–	26
YbPtAs	VF	–	–	3.9	–45	–	–	25
<b>Antimonides</b>								
YbLiSb	TIP	–	–	0.7	–8(3)	–	–	26
YbNiSb	P	–	–	4.6	13	–	–	27
YbNiSb	VF	$T_{\text{SF}}=15$	–	4.09	–8.5	1.6	–	28
YbNiSb	P	–	–	4.6	–13	–	–	29
YbCuSb	TIP	–	0.07	–	–	–	–	30
YbCuSb	TIP	–	0.14	0.5	–35.8	–	–	19
YbPdSb	P	–	–	4.39	–9	–	–	31
YbPdSb	P	–	–	4.3	–7.2	–	–	32
YbPdSb	P	–	–	4	–3.5	–	–	33
YbAgSb	TIP	–	0.06	–	–	–	–	30
YbAgSb	TIP	–	–0.08	0.1	–4.4	–	–	19
YbPtSb	P	–	–	4.4	–5.3	–	–	32
YbAuSb	TIP	–	0.49	1.0	9.8	–	–	30
YbAuSb	TIP	–	–0.08	0.2	–4.4	–	–	19
<b>Bismuthides</b>								
YbLiBi	TIP	–	–	1.0	–13(3)	–	–	26
YbLiBi	TIP	–	–	0.9–1.3	–	–	–	12
YbCuBi	TIP	–	0.16	–	–1.5(7)	–	–	21
YbPdBi	AF?	$T_{\text{N}}=1$	–	4.11(5)	–3.9(8)	–	–	21
YbPdBi	AF/F?	$T_{\text{N}}=1$	–	4.2	6	–	–	27
YbPdBi	P	–	–	4.04	–9	–	–	31
YbAgBi	TIP	–	0.01	–	–1.1(8)	–	–	21

*continued on next page*

Table 14, *continued*

Compound	Order	$T_{\text{Order}}$ [K]	$\chi_0 \times 10^{-3}$ emu/mol	$\mu_{\text{exp}}$ [ $\mu_{\text{B}}$ ]	$\Theta$ [K]	$\mu_{\text{sm(exp)}}$ [ $\mu_{\text{B}}$ ]	$B_{\text{C}}$ [T]	Ref.
YbPtBi	AF	$T_{\text{N}} = 0.4$	–	4.2	2	–	–	34
YbPtBi	AF	$T_{\text{N}} \leq 0.3$	–	4.22	–1.4	–	–	35
YbAuBi	TIP	–	0.17	–	0.8(5)	–	–	21

<sup>a</sup> Symbols:

P, paramagnetism;

AF, antiferromagnetism;

F, ferromagnetism;

MM, metamagnetism;

$\mu_{\text{exp}}$ , experimental magnetic moment;

$T_{\text{Order}}$ , ordering temperature:  $T_{\text{C}}$ ,  $T_{\text{N}}$  or  $T_{\text{SF}}$ ;

$T_{\text{C}}$ , Curie temperature;

$T_{\text{N}}$ , Néel temperature;

$T_{\text{SF}}$ , spin fluctuation temperature;

$\Theta$ , paramagnetic Curie temperature;

$B_{\text{C}}$ , critical field;

VF, valence fluctuation;

TIP, temperature-independent paramagnetism;

$\mu_{\text{sm(exp)}}$ , experimental saturation magnetic moment;

IV, intermediate valence

#### References

- Schank et al. (1995)
- Dichl et al. (1995)
- Mattens et al. (1977)
- Tien et al. (1993)
- Drescher et al. (1998)
- Trovarelli et al. (2000)
- Adroja et al. (1994)
- Kaczorowski et al. (2000a)
- Kaczorowski et al. (2000b)
- Dhar et al. (1995)
- Sendlinger (1993)
- Grund et al. (1986)
- Gorelenko et al. (1984)
- Itoh and Kadomatsu (1998)
- Skolozdra et al. (1984)
- Bonville et al. (1992)
- Bonville et al. (1993)
- Kasaya et al. (1988)
- Katoh et al. (1997)
- Pöttgen et al. (1999c)
- Kaczorowski et al. (1999)
- Katoh et al. (1999)
- Kußmann et al. (1998a)
- Adroja and Malik (1992)
- Kuss et al. (1987)
- Ebel (1995)
- Le Bras et al. (1995a,b)
- Skolozdra et al. (1997)
- Dhar et al. (1993)
- Flandorfer et al. (1997)
- Dhar et al. (1988)
- Kasaya et al. (1992a,b)
- Bonville et al. (1997a)
- Fisk et al. (1991)
- Canfield et al. (1991)

and 0.3 T (YbPtAl). The inflection points, however, are not very pronounced. While the magnetization of YbPtAl tends towards saturation at 7 T, YbNiAl still shows a steep increase at 6 T.

The incommensurate magnetic structure of YbPtAl was determined by neutron diffraction experiments. The wave vector is  $\mathbf{k} = [0.30\ 0\ 0]$ . The presence of  $(000) \pm$  satellites shows that the directions of the magnetic moments are not parallel to the propagation direction  $a$  (Bonville et al. 2000a,b).

The antiferromagnetic spin structure of YbNiAl was determined by neutron diffraction experiments. Below  $T_{\text{N}} = 2.9$  K a sinusoidal modulated structure with an amplitude of  $\mu = 1.9(2)\mu_{\text{B}}$  is observed (Ehlers et al. 1997). The magnetic propagation vector is  $\mathbf{k}_{\text{m}} = [0.779(1)\ 0\ 0]$ , and the ytterbium magnetic moments lie perpendicular to the hexagonal  $c$ -axis. These investigations are paralleled by a detailed study of  $^{27}\text{Al}$  nuclear spin–lattice relaxation measurements (Fay et al. 1997).

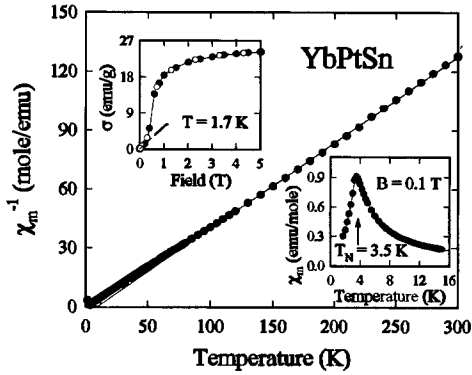


Fig. 12. Temperature dependence of the inverse magnetic susceptibility of YbPtSn. The right-hand inset shows the low-temperature magnetic susceptibility, while the magnetization behavior is presented in the upper inset. From Kaczorowski et al. (1999).

Susceptibility measurements on a YbRhGa sample show a Néel temperature of 2.6 K, indicating trivalent ytterbium, in agreement with the observed lattice parameters of the ytterbium compound relative to the corresponding  $RRhGa$  samples for  $R=Tm$  and  $Lu$  (Hulliger 1996). A reduction of the magnetic moment to  $3.95\mu_B/Yb$  was observed for the metamagnet YbPtGa. This peculiar behavior was attributed to a large value of overall crystal-field splitting (Adroja et al. 1994).

Antiferromagnetic ordering was detected for YbPtSn below 3.5 K (Katoh et al. 1997, Kaczorowski et al. 1999) through a sharp maximum in the  $\chi$  vs  $T$  plot (fig. 12). YbPtSn shows a metamagnetic transition (antiparallel to parallel spin alignment) at a critical field strength of 0.5 T (inset of fig. 12). The saturation magnetic moment at 1.7 K and 5 T is  $2.12(2)\mu_B/Yb$ , significantly reduced from the theoretical  $gJ$  maximal value of  $4.0\mu_B/Yb$  (Szytuła and Leciejewicz 1989), and is most likely due to crystal-field splitting. This is also the case for YbRhGa (Adroja et al. 1994).

Two different antiferromagnetic transitions occur at low temperatures for YbNiGa, YbRhSn and YbPtIn (Trovarelli et al. 2000, Kaczorowski et al. 2000b), indicating a competition between single-ion anisotropy and frustration of the magnetic interactions due to the topology of the underlying crystal structure. The magnetic behavior of YbPtIn was also investigated for a single crystal (Trovarelli et al. 2000).

Various low-temperature susceptibility measurements of YbPtBi (Heffner et al. 1994, Canfield et al. 1991) have shown anomalies at 120 mK and 400 mK, respectively. Precise low-frequency magnetic susceptibility measurements, however, clearly showed that only the 400 mK antiferromagnetic transition is an intrinsic property of YbPtBi (Bremer et al. 1995). The 120 mK transition is most likely due to the superconductive transition of a surface impurity  $Bi_2Pt$ . Furthermore positive-muon ( $\mu^+$ ) spin-relaxation experiments have been performed to elucidate the low-temperature magnetism in YbPtBi in more detail (Amato et al. 1992). They give strong evidence for a highly frustrated spin system with anomalously long correlation times compared to the observed freezing temperatures (Amato et al. 1993). Dilution of ytterbium by 50% yttrium produces the expected reduction in the zero-temperature frozen-spin linewidth but little reduction in the spin-freezing temperature. The investigations on YbPtBi have



been extended to the whole series of  $R\text{PtBi}$  compounds (Canfield et al. 1991). An interesting result of these studies is an apparently discontinuous drop of the  $a$  lattice parameter between gadolinium and ytterbium. So far no explanation was found for this peculiar behavior.

$\text{YbPdSi}$ ,  $\text{YbPdGe}$ , and  $\text{YbPtGe}$  show metallic behavior (Nikiforov et al. 1994, Seropegin et al. 1994). Anomalies at low temperatures are indicative for magnetic ordering. More detailed measurements were performed recently (Itoh and Kadomatsu 1998). Ferromagnetic ordering was detected at  $T_C=11.4$  and  $4.7$  K for  $\text{YbPdGe}$  and  $\text{YbPtGe}$ , respectively.

The magnetic behavior of  $\text{YbNiSn}$  has intensively been investigated for powdered (Kasaya et al. 1988) and single-crystalline samples (Bonville et al. 1992, Kasaya et al. 1992a,b, Bellot et al. 1992). Susceptibility and neutron-diffraction measurements clearly show that  $\text{YbNiSn}$  behaves like a ferromagnetic Kondo lattice. The  $\text{Yb}^{3+}$  magnetic moments lie along the orthorhombic  $c$ -axis of the  $\text{TiNiSi}$ -type structure. The influence of the crystal electric field anisotropy at low temperatures is discussed in detail. Due to hybridization of the ytterbium  $4f$  electrons with band electrons the saturated ferromagnetic moment of  $0.85\mu_B$  is reduced by about 20% with respect to the value expected from the known crystal electric field splitting.  $\text{YbNiSn}$  is a weak ferromagnet due to canting of the antiferromagnetic sublattice within the  $ab$  plane (Kasaya et al. 1991, 1992a,b). The magnetization behavior along the  $a$ -axis shows the anomalies at external fields  $H_{C1}$ ,  $H_{C2}$  and  $H_{C3}$ , characteristic for spin-flipping transitions (Kasaya et al. 1991, 1992a,b). Muon spin relaxation measurements of  $\text{YbNiSn}$  show that this stannide exhibits an anomalous quasi-elastic spectral weight of magnetic excitations in the transfer energy range of  $10$  neV (Yaouanc et al. 1999).

The pressure and temperature dependence of the magnetic susceptibility of  $\text{YbCuAl}$ ,  $\text{YbPdIn}$  and  $\text{YbAuIn}$  (Zell et al. 1981, Mattens et al. 1980a,b) was also investigated. Mixed valence was observed for  $\text{YbCuAl}$  (Klaasse et al. 1977) with a rather high value of the susceptibility at liquid-helium temperature. The mixed valency of ytterbium was also evident from  $L_{III}$  absorption spectra (Bauchspiess et al. 1981). Time-of-flight neutron scattering experiments were used to establish the dynamical susceptibility of  $\text{YbCuAl}$ . A non-Korringa behavior of the quasi-elastic linewidth has been observed (Mattens et al. 1980a,b). Far-infrared optical measurements of  $\text{YbCuAl}$  at photon energies between  $3$  and  $40$  meV and temperatures between  $4.2$  and  $150$  K showed no anomalies (Pinkerton et al. 1984).

Exact high- and low-temperature results for the Coqblin-Schrieffer model with application to intermediate-valent  $\text{YbCuAl}$  have been reported (Hewson et al. 1983, 1985, Hewson and Rasul 1983). This theoretical work allows an explanation of the susceptibility, specific-heat, and magnetization data for  $\text{YbCuAl}$ . A reasonable agreement with the experimental data is observed. Similar calculations were also performed by Lustfeld and Bringer (1978). Their theory for strong mixed-valent substances describes the susceptibility, magnetization, and electronic specific-heat coefficient satisfactorily, but it overestimates the electronic specific heat of  $\text{YbCuAl}$  in the cross-over region. Lustfeld and Bringer attributed this behavior to the fact that  $\text{YbCuAl}$  is on the borderline of a weak

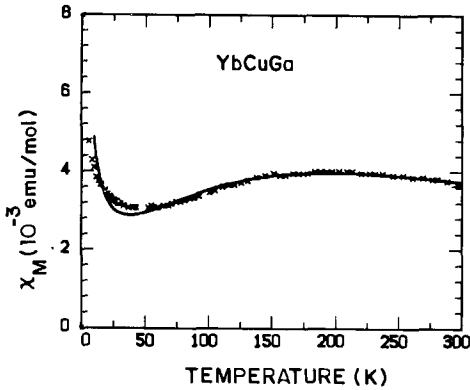


Fig. 13. Temperature dependence of the (symbols) experimental and (solid line) theoretical magnetic susceptibility of YbCuGa. From Adroja et al. (1990).

mixed valency. The dynamics of the 4f electrons in YbCuAl was also explained with a simple microscopic theory presented by Kuramoto and Müller-Hartmann (1981).

The influence of yttrium doping in YbCuAl was investigated by van Kalker et al. (1985). According to these experiments, the intermediate-valent (IV) state remains unchanged up to  $\text{Yb}_{1-x}\text{Y}_x\text{CuAl}$  with  $x=0.7$ . Based on these results it is concluded that a single-ion description of the IV state is appropriate. Also, chemical pressure effects in scandium-substituted YbCuAl were investigated (Jaccard and Sierro 1982). EPR studies of gadolinium-doped YbCuAl show a large positive  $g$ -shift and a strong temperature dependence of linewidth (Larica and Coles 1985). EPR spectra of pure YbCuAl have been observed between 4 and 77 K (Tien et al. 1993), although the nature of the signal is not entirely understood. Enormous  $g$ -shifts occur below 10 K. The properties of EPR spectra in YbCuAl can be qualitatively described by the  $s$ - $f$  mixing model. Future EPR measurements might be a powerful tool for the study of mixed-valent and heavy-fermion materials.

Also YbPdIn shows the typical behavior of an intermediate-valent compound. The magnetic susceptibility was measured up to about 1000 K (Cirafici et al. 1985). The intermediate-valent behavior is also evident from the temperature dependence of the lattice parameters. A significant anomaly is detected only for the  $c$  parameter, while  $a$  increases linearly.

The susceptibility of the two modifications of YbPdSn was investigated in the temperature range 100 to 750 K (Sendlinger 1993). The ytterbium valence in HT-YbPdSn with TiNiSi-type structure continuously increases from +2.05 at 100 K to +2.10 at 300 K and then to +2.40 at about 750 K. The degree of trivalent ytterbium increases with temperature for both modifications. For LT-YbPdSn a saturation at about +2.6 occurs at about 600 K.

The gallide YbCuGa (Adroja et al. 1990, Malik et al. 1987a,b) shows a susceptibility behavior typical for an intermediate-valent compound (fig. 13). This behavior can be understood in terms of the ionic-configuration-fluctuation (ICF) model (Sales and Wohlleben 1975). A fit according to this model results in a temperature-independent

part of the susceptibility of  $\chi_0 = 4.4 \times 10^{-5}$  emu/mol and a spin-fluctuation temperature  $T_{SF} = 141$  K (Adroja et al. 1990). Susceptibility measurements were also reported for YbPdGa and YbPtGa (Malik et al. 1987b), indicating a mixed-valent state for the palladium and a nearly divalent state for the platinum gallide, respectively.

#### 4.3. Electrical properties

Depending on the magnetic ground state of the ytterbium atoms we observe a variety of different transport properties. Several of the YbTX intermetallics behave like classical metals. In those cases where the ytterbium 4f electrons interact with the conduction electrons we observe Kondo-lattice behavior at low temperatures. The onset of magnetic ordering expresses itself as a drop at low temperatures due to a decrease of spin disorder scattering.

The resistivity curve of YbPtGa shows single Kondo impurities in the presence of crystal field effects (Adroja et al. 1994, 1997) (fig. 14). At 8 K a sharp drop is detected. This can be attributed to either a substantial degree of magnetic short-range order or to the onset of coherence among the ytterbium magnetic moments. Such a behavior was also observed for the germanides YbPdGe and YbPtGe (Itoh and Kadomatsu 1998). The presence of crystal-field effects is also observed for YbPdSi, however, this silicide shows no Kondo anomaly. A small but not pronounced decrease of the specific resistivity is observed at low temperature, possibly due to the onset of magnetic ordering (Borisenko et al. 1995).

The specific resistivity of ferromagnetic YbNiSn was investigated for a single crystal (Bonville et al. 1992). From these measurements it is evident that the specific resistivity is the highest in the *c*-direction (fig. 15), where the ferromagnetic moments lie. Also the Kondo minimum and the crystal electric field effects are pronounced in this direction.

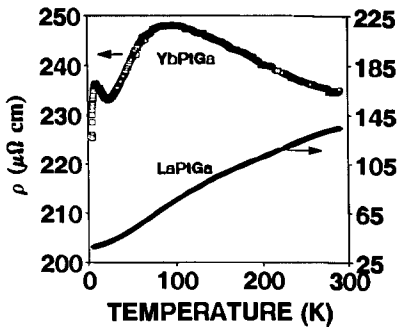


Fig. 14. Temperature dependence of the specific resistivity of YbPtGa and LaPtGa (for comparison). From Adroja et al. (1994).

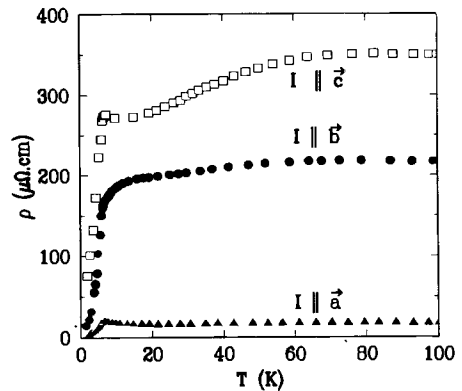


Fig. 15. Temperature dependence of the specific resistivity of YbNiSn when the current flows along the three orthorhombic directions *a*, *b* and *c*. From Bonville et al. (1992).

Detailed magnetoresistance measurements were performed for YbNiSn (Adroja et al. 1998, D'Onofrio et al. 1991), emphasizing the influence of the Kondo interactions.

YbZnSn (Pöttgen et al. 1999c), Yb(Cu,Ag,Au)Sn and Yb(Cu,Ag,Pt,Au)Sb are metallic conductors (Kato et al. 1997, Pöttgen et al. 1999c). No pronounced anomalies are observed down to low temperatures.

The temperature-dependent behavior of the specific resistivities of YbRhSn and YbPtSn (Kaczorowski et al. 1999) was analyzed quantitatively with respect to the Matthiessen rule and a modified Bloch–Grüneisen expression. Above 5 K these stannides behave in a Kondo-like manner. At low temperatures the magnetic contribution to the specific resistivity exhibits a Fermi-liquid-type behavior and can be expressed by a  $T^2$  dependence. Finally it is worthwhile to note that the resistivity behavior reported for YbPtSn by Kato et al. (1997) and Kaczorowski et al. (1999) is slightly different. Magnetoresistance measurements of YbPtSn imply the presence of strong ferromagnetic correlations, while the magnetoresistance of YbRhSn exhibits a single-impurity Kondo scaling (Pietri et al. 2000, Andracka et al. 2000).

For YbPtIn (Trovarelli et al. 2000, Kaczorowski et al. 2000b), YbPdSb and YbPdBi (Aliev et al. 1988, 1989a), the resistivity behavior is similar to YbPtSn. Furthermore, YbPtIn shows a negative and rather large magnetoresistivity (Kaczorowski et al. 2000b). Fermi-liquid behavior was also observed for the gallides YbCuGa, YbAgGa and YbAuGa (Adroja et al. 1990, 1997, Malik et al. 1987a). Due to the Kondo effect, a spin-liquid phase can be stabilized in YbPdSb, as established from muon spin relaxation measurements (Bonville et al. 1997a,b).

A phonon contribution with an additional cubic term can be used to analyze the resistivity behavior of the metallic bismuthides YbAgBi and YbAuBi (Merlo et al. 1995). An anomaly occurs in the temperature dependence of the resistivity of YbCuBi at about 375 K, most likely resulting from a structural phase transition from the high-temperature ZrBeSi to the low-temperature NdPtSb modification. The anomaly in the resistivity is paralleled by a drop of the  $c/a$  ratio of the lattice parameters in the same temperature range.

YbPtAl, YbNiGa, and YbPtIn are metallic conductors. The three compounds show Kondo-like minima in the specific resistivity and steep decreases at low temperature resulting from the onset of magnetic ordering (Trovarelli et al. 2000, Diehl et al. 1995). Such a steep decrease also occurs for YbNiAl, however, crystal-field effects dominate the resistivity behavior in the high-temperature region (Diehl et al. 1995).

Resistivity measurements for YbPtBi show a relatively large and monotonic decrease with decreasing temperature without Kondo anomaly (Hundley et al. 1997). Magnetic-field-dependent Hall measurements show that hole-like carriers dominate the electronic transport in YbPtBi. This is also evident from the positive sign of the thermoelectric power. According to these data, YbPtBi may be classified as a semimetallic heavy-fermion system. Detailed resistivity and specific-heat measurements at low temperature indicate a magnetic phase transition at  $T_N = 0.45$  K (Canfield et al. 1994, Movshovich et al. 1994a). The anisotropy in the resistivity can be associated with some combination of the formation of either a SDW or a superzone gap and a Jahn–Teller distortion. Resistivity measurements

under hydrostatic pressures of up to 6 kbar have been presented by Movshovich et al. (1994a,b).

YbNiSb shows metallic behavior with a room-temperature specific resistivity of 3.6 m $\Omega$ cm (Dhar et al. 1993), about one order of magnitude larger than that of isotypic YbPtBi. Since the sample appeared devoid of any cracks, the high value of the resistivity arises most likely from a low carrier density.

Intermediate-valent YbCuAl shows the well-known nonlinear temperature dependence (above 50 K) with a strong saturation. The temperature dependence of the Hall coefficient shows a discontinuity at around 40 K. This peculiar behavior is attributed to an extraordinary contribution to the Hall coefficient (Cattaneo 1985, 1986). High-pressure resistivity measurements were also performed on this material (Mignot and Wittig 1981, 1982).

The aluminides YbAuAl and YbPdAl (Schank et al. 1994, Cordier et al. 1993) are metallic conductors. Due to the mixed-valent character of the ytterbium atoms in YbPdAl, a *bump* is observed around 100 K in the resistivity curve. YbAuAl,  $\gamma$ -YbAuGe (Merlo et al. 1998) and YbPtSb (Kasaya et al. 1992a,b) show no anomaly in the temperature dependencies of their resistivities.

#### 4.4. Mössbauer spectroscopy

So far only  $^{119}\text{Sn}$  and  $^{170}\text{Yb}$  Mössbauer spectroscopic experiments have been performed on the YbTX compounds. The  $^{170}\text{Yb}$  data give direct information on the oxidation state of the ytterbium atoms. At low temperatures magnetic hyperfine field splitting may be observed. The  $^{119}\text{Sn}$  spectra give information about the environment around the tin species in the respective stannides.

YbNiSn was intensively investigated by  $^{170}\text{Yb}$  Mössbauer spectroscopy in the paramagnetic and in the ferromagnetically ordered state (Bonville et al. 1992, Bellot et al. 1992). The 1.48 K spectrum shows hyperfine field splitting with five well-resolved lines with an experimental linewidth of about 3 mm/s (fig. 16). Due to the non-cubic ytterbium site, a quadrupolar hyperfine term with an electric field gradient is observed. In the paramagnetic phase (6 K measurement) the spectrum shows two resolved lines which result from quadrupole splitting.

Magnetic ordering in YbPdBi was studied by low-temperature susceptibility, specific heat ( $\lambda$  anomaly at 1 K), and in detail by  $^{170}\text{Yb}$  Mössbauer spectroscopy (Le Bras et al. 1995a,b). Above 1 K the spectra show a three-line structure in a ratio 2 : 1 : 2. Above 20 K the spectra become less resolved and consist of a broad line. The intensity ratio and the line splitting are characteristic for  $^{170}\text{Yb}$ , and these spectra may be interpreted as due to the presence of a non-zero electric field gradient tensor at the ytterbium site. At 0.035 K, well below the magnetic ordering temperature, a five-line spectrum is detected, resulting from magnetic hyperfine interactions superposed on the quadrupolar hyperfine interaction, similar to the  $^{170}\text{Yb}$  Mössbauer data of YbNiSn.

The  $^{170}\text{Yb}$  Mössbauer spectra of YbPtAl in the magnetically ordered state at 1.8 K can be approximated by two components with relatively high magnetic hyperfine fields  $B_1 = 156(3)\text{ T}$  and  $B_2 = 110(5)\text{ T}$  (Drescher et al. 1998) which correspond to magnetic moments of  $\mu_{\text{Yb}}(1) = 1.53(3)\mu_{\text{B}}$  and  $\mu_{\text{Yb}}(2) = 1.08(5)\mu_{\text{B}}$  (Drescher et al. 1998). Most

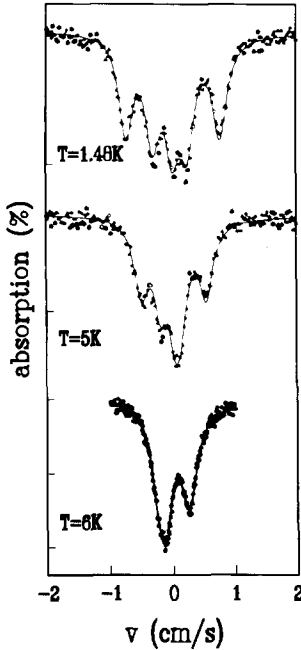


Fig. 16. Experimental and simulated  $^{170}\text{Yb}$  Mössbauer spectra of  $\text{YbNiSn}$  in the ferromagnetic (1.48 and 5 K) and in the paramagnetic (6 K) phase. From Bonville et al. (1992).

recent measurements of spectra down to 0.025 K show evidence for a non-square modulation of the magnetic moment, incommensurate with the lattice spacings (Bonville et al. 2000a,b), in agreement with neutron diffraction data (see sect. 4.2).  $\text{YbPtAl}$  is the first clear example of a Kramers local moment ytterbium-based system where the Kondo-singlet ground state allows a modulated magnetic structure to persist down to 0 K.

Besides the isomer shift, the experimental linewidth and the electric field gradient, information about the crystal-field anisotropy can also be obtained from  $^{170}\text{Yb}$  Mössbauer spectroscopy, as shown by Bonville et al. (1990) and Bonville and Hodges (1985) for  $\text{YbCuAl}$ . Furthermore,  $\text{YbCuAl}$  was investigated by  $^{170}\text{Yb}$  Mössbauer spectroscopy at pressures up to 130 kbar. The data give strong evidence for a valence transition towards the  $4f^{13}$  ( $\text{Yb}^{3+}$ ) configuration. At 4.2 K the transition is completed at about 50 kbar (Schöppner et al. 1986). This behavior is paralleled by the pressure-dependent susceptibility measurements (Klaasse et al. 1977).

Since susceptibility data ( $\Theta = -9$  K) of  $\text{YbPdSb}$  indicated antiferromagnetic interactions, detailed  $^{170}\text{Yb}$ -Mössbauer spectroscopic, neutron diffraction, electrical resistivity, thermoelectric power, and specific-heat measurements were performed down to 0.1 K (Suzuki et al. 1995, Le Bras et al. 1994, 1995a,b, Aliev et al. 1989a, 1994). The presence of a hyperfine field in the Mössbauer spectra indicates spatial correlations of  $\text{Yb}^{3+}$  moments up to 5 K. These correlations correspond to a magnetic moment of  $1.3\mu_B$  at 0.07 K. Above 1 K these moments are of dynamic nature. Neutron diffraction experiments also reveal short-range magnetic order in the range 4.2 to 1 K.

Table 15  
 $^{119}\text{Sn}$  Mössbauer spectroscopic data of ternary YbTX compounds<sup>a</sup>

Compound	$T$ [K]	$\delta$ [mm/s]	EFG [mm/s]	$\Gamma$ [mm/s]	$\Delta E_Q$ [mm/s]	Ref.
YbZnSn	300	1.85(1)	–	0.91(2)	–	1
$\alpha$ -YbPdSn	78	1.84(2)	–	1.07(7)	0.73(4)	2
$\beta$ -YbPdSn	78	1.96(4)	–	0.98(4)	0.97(5)	2
YbAgSn	78	1.94(1)	–0.43(1)	0.77(2)	–	1
YbAgSn	78	1.99(1)	–	0.84(3)	1.35(1)	1
YbPtSn	78	1.75(1)	–	1.05(5)	0.59(5)	3
YbPtSn	4	1.75(1)	–	1.22(5)	0.59(5)	3

<sup>a</sup> Symbols:

$T$ , temperature of the measurement;

$\delta$ , isomer shift;

EFG, electrical field gradient;

$\Gamma$ , experimental linewidth;

$\Delta E_Q$ , quadrupole splitting parameter

References

1. Pöttgen et al. (1999c)

2. Kußmann et al. (1998a)

3. Pöttgen et al. (1999a)

So far, only four stannides have been investigated by  $^{119}\text{Sn}$  Mössbauer spectroscopy. These Mössbauer spectroscopic data are summarized in table 15. Some peculiar features of these spectra are discussed in more detail.

A slightly increased linewidth is observed for the  $^{119}\text{Sn}$  spectrum of YbPtSn at 4.2 K (Pöttgen et al. 1999a). This is probably due to a small transferred hyperfine field resulting from magnetic fluctuations of the ytterbium atoms.

The different tin sites in YbZnSn and YbAgSn can be distinguished by  $^{119}\text{Sn}$  Mössbauer spectroscopy (Pöttgen et al. 1999c). YbZnSn has only one tin site and consequently we observe only one Mössbauer signal. In contrast, two tin sites occur in YbAgSn (sect. 3.6) and two signals with a ratio of 2:1 can be distinguished in the spectrum (fig. 17 and

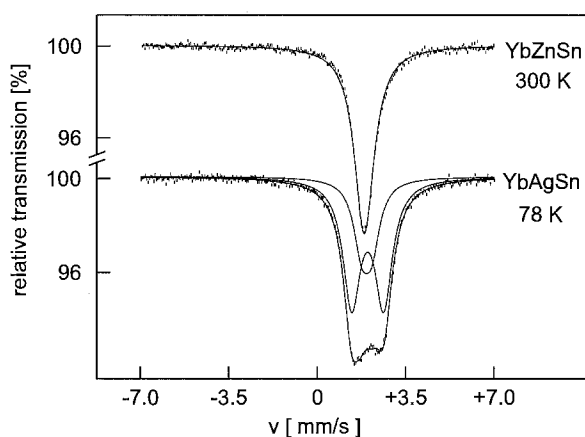


Fig. 17. Experimental and simulated  $^{119}\text{Sn}$  Mössbauer spectra of YbZnSn (300 K) and YbAgSn (78 K). From Pöttgen et al. (1999c).

table 15). The superimposed singlet and doublet account for the different site symmetries of these crystallographically different tin atoms.

#### 4.5. Specific-heat data

While magnetic measurements give direct macroscopic information about the magnetic properties of a compound, indirect but useful information may be obtained from the measurement of transport properties. In this subsection we especially focus on the specific-heat data.

In most cases the low-temperature specific heat (at temperatures much lower than the Debye temperature) can be described by  $C_p = \gamma T + \beta T^3$ , where  $\gamma T$  is the so-called linear term due to the excitations of the conduction electrons, and  $\beta T^3$  is the low-temperature approximation of the specific heat of the lattice. For normal conductors,  $\gamma$  is of the order of 1–10 mJ/(mol K<sup>2</sup>), while heavy fermions show  $\gamma$ -values up to 1000 mJ/(mol K<sup>2</sup>). Details about cerium- and uranium-based heavy-fermion materials have been reviewed by Grewe and Steglich (1991), Sereni (1991), Loewenhaupt and Fischer (1993), Fournier and Gratz (1993), Wachter (1994), Nieuwenhuys (1995), Ōnuki and Hasegawa (1995) and Arko et al. (1999).

A  $\lambda$ -type anomaly for YbPtGa occurs in the heat-capacity measurement (Adroja et al. 1994) at 3.8 K, in agreement with the Néel temperature. As an example we present a  $C/T$  vs.  $T$  plot in fig. 18.

The determination of the  $\gamma$ -values is important for the classification of YbTX intermetallics as heavy-fermion systems which exhibit significantly enlarged  $\gamma$ -values. The source of the large  $\gamma$ -values arises from the compensation of the magnetic moment associated with a nearly localized electron state, generally of f character, by the spins of the conduction electrons in the metallic material.

The value of  $C/T$  for YbNiSb extrapolated to 0 K is 150 mJ/mol K<sup>2</sup>. Together with the high value of the specific resistivity, YbNiSb may be classified as a low-carrier heavy-fermion compound (Dhar et al. 1993).

A discrepancy occurs for the specific-heat data of YbPtSn. Suzuki et al. (1999) report a  $\gamma$ -value of 2.5 mJ/K<sup>2</sup>, while Kaczorowski et al. (1999) give  $\gamma = 370$  mJ/K<sup>2</sup>. Similar discrepancies occur for the  $\gamma$ -values of YbRhSn and YbPdBi (table 16). We should keep in mind that the  $\gamma$ -value significantly influences one's opinion on whether or not YbPtSn is considered to be a heavy-electron compound.

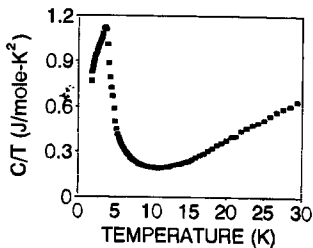


Fig. 18. Heat capacity of YbPtGa plotted as  $C/T$  vs  $T$ . From Adroja et al. (1994).



Table 16  
Electronic specific heat coefficients  $\gamma$  [mJ/K<sup>2</sup>mol] for various YbTX compounds

Compound	$\gamma$	Ref.	Compound	$\gamma$	Ref.
YbNiAl	350	1	YbRhSn	80	9
YbCuAl	260	2	YbRhSn	1200±200	10
YbCuAl	220±20	3	YbRhSn	360	5
YbCuAl	267	4	YbPtSn	370±20	9
YbPtAl	200±50	1	YbPtSn	2.5	11
YbNiGa	450	5	YbPtSn	100	12
YbPtGa	107	6	YbPdSb	240	13
YbPtIn	430	5	YbPdBi	470	13
YbPtIn	740	7	YbPdBi	1200±100	10
YbNiSn	300	8	YbPtBi	8000	14

#### References

- Schank et al. (1995)
- Mattens et al. (1977)
- Bleckwedel et al. (1981)
- Pott et al. (1981)
- Trovarelli et al. (2000)
- Adroja et al. (1994)
- Kaczorowski et al. (2000a,b)
- Kasaya et al. (1991)
- Kaczorowski et al. (1999)
- Pietri et al. (2000)
- Suzuki et al. (1999)
- Andraka et al. (2000)
- Dhar et al. (1988)
- Fisk et al. (1991)

The specific heat of valence-fluctuating YbCuAl was measured under pressures up to 10 kbar (Bleckwedel et al. 1981, Bleckwedel and Eichler 1981). The electronic specific-heat coefficient increases dramatically from 220±20 mJ/mol K<sup>2</sup> at 0 kbar to 340±15 mJ/mol K<sup>2</sup> at 10.6 kbar without a change in crystal structure. This behavior is without parallel in the series of ytterbium intermetallics. Furthermore, the specific-heat anomaly of YbCuAl contains nearly the full entropy expected from a gradual freezing out of the degrees of freedom of the 4f<sup>14</sup> and 4f<sup>13</sup> configurations of the ytterbium ion (Pott et al. 1981).

Heat-capacity measurements of YbPdIn were also used to determine the energy for the oxidation reaction  $\text{Yb}^{2+} \rightarrow \text{Yb}^{3+} + e^-$ . A value of 0.11 eV was derived from the temperature-dependent  $C_P$  data (Cirafici et al. 1985).

The so far highest  $\gamma$ -value of 8000 mJ/K<sup>2</sup> was observed for YbPtBi (Fisk et al. 1991, Thompson et al. 1993). This bismuthide can be classified as a *very* heavy-electron system. The heavy-mass state in YbPtBi is unconventional in that it develops from Bloch states in an electron subsystem with a low carrier concentration (Hundley et al. 1997, Fisk et al. 1991).

Crystal electric field parameters for YbPtBi have been derived from neutron scattering data (Robinson et al. 1993, 1995) and are interpreted in terms of strongly broadened crystal-field levels. The ground state is six-fold degenerate, consisting of a doublet ( $\Gamma_7$ ) and a quartet ( $\Gamma_8$ ). Integration of the levels is in agreement with the experimentally derived linear specific-heat coefficient within an accuracy of ±20%. Furthermore, <sup>209</sup>Bi NMR

data of this bismuthide showed a transferred hyperfine coupling which was attributed to ytterbium f moments (Reyes et al. 1995).

The effect of chemical pressure on YbPtBi single crystals was studied by heat-capacity measurements on yttrium- and lutetium-doped samples (Lacerda et al. 1993). According to these measurements, the heavy-fermion state of this compound seems to be unchangeable by a relatively large amount of nonmagnetic doping (yttrium or lutetium). Furthermore, the heat capacity measurements reveal only a small pressure dependence when compared with other heavy-fermion materials.

#### 4.6. High-pressure investigations

Investigations of YbTX compounds under high pressure conditions are of particular interest with respect to the influence on the crystal structure and the physical properties. From a structural point of view, divalent ytterbium compounds might show a structural phase transition under pressure, resulting in a modification with trivalent ytterbium. The pressure-induced magnetization of Yb<sup>2+</sup> should then be the mirror image of the demagnetization of Ce<sup>3+</sup>.

The ground-state properties of Kondo-lattice systems, for example, are expected to be very sensitive to external pressure. The latter may modify the strength of the exchange interaction  $J$  between the localized 4f and the conduction electrons and thereby the competition between the intersite (RKKY) and intrasite (Kondo) interactions. The balance between these effects has been theoretically described by Doniach (1977) for a magnetic phase diagram depending on the exchange parameter  $J$ .

The influence of hydrostatic pressure on the Curie temperature of YbNiSn was investigated by ac susceptibility and resistivity measurements. The ordering temperature first increases at a rate of 2 K/GPa, passes through a maximum at 7.7 K, and then decreases (fig. 19) (Cornelius et al. 1995, Drescher et al. 1996a,b, Abd-Elmeguid 1998, Sparn et al. 1992). The asymmetry in this diagram is opposite to that observed in

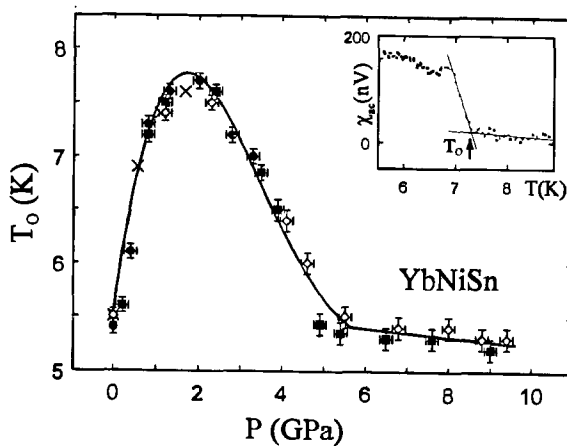


Fig. 19. Pressure dependence of the Curie temperature of YbNiSn (from Cornelius et al. 1995). Inset: experimental ac-susceptibility signal in units of nanovolts at 0.8 GPa after subtraction of a temperature-dependent background.

related cerium intermetallics. This has to do with the fact that the Kondo temperature increases with pressure for cerium compounds, but decreases for ytterbium compounds as is readily evident from Doniach's (1997) diagram. The lattice parameters of YbNiSn were also investigated under high-pressure conditions (Drescher et al. 1996a). A smooth decrease of the lattice parameters is observed. No structural phase transition is obvious up to 26.4 GPa. This pressure dependence of  $T_C$  was also studied by  $^{170}\text{Yb}$  Mössbauer spectroscopy (Drescher et al. 1996b). The complete high-pressure Mössbauer and resistivity data of YbNiSn and the aluminide YbPtAl have recently been summarized in a micro-review by Abd-Elmeguid (1998).

The pressure dependence of the electrical resistivity of YbCuAl was investigated (Alami-Yadri et al. 1998, 1999a,b) up to 8 GPa. The resistivity at 300 K decreases with increasing pressure. At 8 GPa a  $T^2$  dependence occurs at low temperature (Fermi-liquid behavior), and the Kondo temperature decreases with increasing pressure. The experimental setup for these measurements was presented by Jaccard et al. (1998). Furthermore, point-contact spectroscopy was used to measure the interconfigurational excitation energies and conduction-electron lifetime width of valence-fluctuating YbCuAl (Bussian et al. 1982).

The strong correlation between the valence and the ionic volume of the lanthanides is one of the best known features of mixed-valent lanthanide systems. In contrast to cerium and europium intermetallics, divalent ytterbium intermetallics show a negative volume effect under applied hydrostatic pressure. Häfner (1985) determined values of  $-\partial\chi/\partial p$  and  $2\partial V/\partial H^2$  of  $-7.1 \times 10^{-13}$  and  $-1.5 \times 10^{-12}$  for YbCuAl (Zieglowski et al. 1986).

#### 4.7. Thermoelectric power

Thermoelectric power (TEP) measurements are useful for obtaining more detailed information about the influence of the Kondo effect on the ground-state properties. In general, the thermoelectric power of heavy-fermion compounds shows much larger values than normal metals. This is a consequence of the enhancement of the density of states at the Fermi level. For YbPtIn, the thermoelectric power reaches  $-9 \mu\text{V/K}$  at 150 K (Trovarelli et al. 2000). Measurements of YbNiSb, YbPdSb and YbPdBi yielded  $S = +26 \mu\text{V/K}$ ,  $+25 \mu\text{V/K}$  and  $-4 \mu\text{V/K}$ , respectively (Aliev et al. 1988, 1989b, Skolozdra et al. 1997). The positive sign of the thermoelectric power of YbPtBi suggests that holes are the predominant carriers in this bismuthide (Hundley et al. 1997).

Intermediate-valent YbCuGa shows a TEP of  $-4 \mu\text{V/K}$  at room temperature as is observed in most ytterbium-based mixed valent systems. This suggests that the majority carriers in YbCuGa are electrons (Adroja et al. 1990).

TEP measurements of YbPdGe and YbPtGe yielded maximum values of  $-6 \mu\text{V/K}$  at 120 K for YbPdGe and  $+6 \mu\text{V/K}$  at 30 K for the platinum germanide (Itoh and Kadomatsu 1998). The variation of TEP is significantly different for the isotopic cerium compounds. Nevertheless, a common feature of these compounds is that the conduction bands do not consist of 5d6s states of Yb and Ce, but of Pd and Pt states.

The TEP of YbNiSn exhibits a broad minimum at 100 K ( $-18 \mu\text{V/K}$ ), a maximum at 17 K ( $-0.5 \mu\text{V/K}$ ), and a sharp peak at 7.5 K, followed by a sign change from negative to positive below 5 K (Adroja et al. 1998). This behavior can be understood on the basis of crystal-field and Kondo-type interactions. A more detailed discussion of TEP results for YbCuAl and YbNiSn was given by Alami-Yadri et al. (1999a,b) in a broader context, together with the heavy-fermion compounds YbSi and YbCu<sub>2</sub>Si<sub>2</sub>.

TEP experiments on YbCuAl were performed down to low temperatures. By analogy with transition metals, the low-temperature TEP of 4f instability compounds was interpreted in a crude two-band model of a heavy band and a broad d band according to the Mott formula (Mott 1936). Analysis of the YbCuAl data above 1 K in the two-band model clearly reveals the electron-hole symmetry in comparison with cerium compounds (Jaccard et al. 1985, Jaccard and Sierro 1982).

#### 4.8. XAS, neutron scattering and photoemission

L<sub>III</sub> absorption edge measurements of the Yb(Cu,Ag,Au)Sb antimonides (fig. 20) show two different peaks around  $\sim 8937 \text{ eV}$  and  $\sim 8943 \text{ eV}$ , which correspond to the  $4f^{14}$  and  $4f^{13}$  configurations of Yb<sup>2+</sup> and Yb<sup>3+</sup>, respectively (Flandorfer et al. 1997). These studies show that the ytterbium atoms might be in a non-integral valence state in the respective antimonides. The corresponding valences are  $2.08 \pm 0.02$ ,  $2.06 \pm 0.02$  and  $2.14 \pm 0.02$  for YbCuSb, YbAgSb and YbAuSb, respectively. Nevertheless, one should keep in mind that such small amounts of trivalent ytterbium might also arise from small amounts of a Yb<sub>2</sub>O<sub>3</sub> impurity.

A L<sub>III</sub> XANES spectrum in the ytterbium region of YbCuGa exhibits two distinct peaks separated by 7 eV (Adroja et al. 1990), indicating an intermediate-valence state of the ytterbium atoms. This is in agreement with the magnetic behavior.

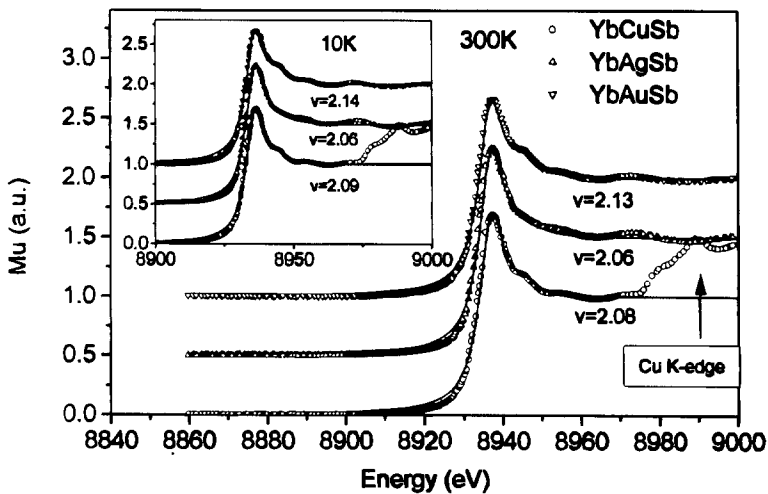


Fig. 20. XAS spectra for Yb(Cu,Ag,Au)Sb at 300 K. From Flandorfer et al. (1997).

The gallides YbCuGa, YbPdGa, and YbPtGa were investigated by inelastic neutron scattering (Adroja et al. 1997). The spectrum of YbPtGa shows three well-defined crystal-field excitations, while that of the copper compound shows a broad inelastic excitation around 17.7 meV. YbPdGa shows two broad excitations besides a weak crystal-field excitation. The three peaks of YbPtGa correspond to transitions between the ground-state doublet and the three excited doublets of the crystal-field-split  $J = 7/2$  multiplet of the  $\text{Yb}^{3+}$  ion.

Two well-defined crystal-field excitations at 12.2 and 18.1 meV and a quasi-elastic excitation centered at zero energy were derived from inelastic neutron scattering experiments of ferromagnetic YbNiSn. A crystal-field potential based on a superposition model was presented in that work (Adroja et al. 1998).

High-resolution photoemission studies were performed for YbPdAl, YbPtAl, and YbAuAl (Reinert et al. 1999). For these intermediate-valent and Kondo compounds a clear correlation of the linewidths, the binding energies and the spectral-weight distributions of the 4f spectra with the characteristic temperature  $T_{\text{max}}$  of the maximum in the magnetic susceptibility is observed.

Inelastic neutron scattering experiments on intermediate-valent YbCuAl at low temperatures reveal well-defined inelastic magnetic-response peaks superposed on a broad quasielastic-scattering spectrum (Murani et al. 1985). The peaks are clearly magnetic in origin. This observation correlates with NMR Knight shift measurements.  $^{27}\text{Al}$  NMR shifts and spin-lattice relaxation time measurements were performed to further elucidate the spin-fluctuation behavior in YbCuAl (MacLaughlin et al. 1979). Relaxation data show a 4f spin fluctuation rate which decreases by a factor of about 2 between  $T_{\text{max}}$  and 100 K. Also, quadrupole splitting of the  $^{27}\text{Al}$  NMR spectrum was investigated as a function of temperature (Lysak et al. 1987, MacLaughlin 1981). The results suggest a considerable temperature dependence of the ytterbium electronic structure, which is apparently an important contributor to the electric field gradient at the aluminium sites. The electric field gradient appears to reflect the breakup of the intermediate-valent ground state with increasing temperature.

## 5. Conclusion

Summing up, the crystal chemistry of 84 equiatomic YbTX compounds has been reviewed. These intermetallics crystallize in 20 different structure types. The  $T$  components are mostly transition metals from the iron to the zinc group and  $X$  is an element of main group III, IV or V. The electron count of the YbTX compounds can effectively be varied through a substitution of the  $T$  and  $X$  components. The electronic structure of some compounds was investigated by LMTO band-structure calculations. Chemical bonding is governed by strong covalent  $T-X$  interactions within the polyanions and rather ionic Yb- $T(X)$  bonds.

In addition to the crystal chemistry, the greatly varying magnetic and electrical properties are reviewed. Besides simple temperature-independent paramagnets (TIP), antiferromagnetic or ferromagnetic ground states occur. Some YbTX compounds are

characterized as intermediate-valence systems. The magnetic investigations have been paralleled by  $^{170}\text{Yb}$  Mössbauer spectroscopy and  $L_{\text{III}}$  X-ray absorption experiments in order to investigate the valence behavior of the ytterbium atoms. Several  $\text{YbTX}$  compounds show Kondo or heavy-fermion behavior. These ground-state properties were further characterized by specific-heat and thermopower measurements. We have finally tried to compare the X-ray crystallographic results with physical property measurements in order to figure out structure–property relations for several compounds.

The most outstanding  $\text{YbTX}$  compounds are ferromagnetic  $\text{YbNiSn}$ , intermediate-valent  $\text{YbCuAl}$ , and the bismuthide  $\text{YbPtBi}$  with an extremely large linear coefficient of the specific heat  $\gamma = 8 \text{ J/mol K}^2$ . More than 85 publications have been devoted to these three peculiar materials in recent years.

Although numerous investigations of  $\text{YbTX}$  compounds have already been performed, this interesting family of intermetallics still has a large potential for future studies. One strategy might certainly be a more detailed examination of the structures and properties under high-pressure conditions.

### Acknowledgments

We are indebted to Professors Eckert, Grin, Jeitschko, Mewis, and Simon for their interest in this work and for many fruitful discussions. Special thanks go to all our coworkers and colleagues mentioned in the references. Financial support by the Deutsche Forschungsgemeinschaft, the Fonds der Chemischen Industrie, and the Bundesministerium für Bildung, Wissenschaft, Forschung und Technologie is gratefully acknowledged.

### References

- Abd-Elmeguid, M.M., 1998, *Hyperfine Interactions* **113**, 111.
- Adroja, D.T., and S.K. Malik, 1992, *Phys. Rev. B* **45**, 779.
- Adroja, D.T., S.K. Malik, B.D. Padalia, S.N. Bhatia, R. Walia and R. Vijayaraghavan, 1990, *Phys. Rev. B* **42**, 2700.
- Adroja, D.T., B.D. Rainford, S.K. Malik, M. Gailloux and K.A. Gschneidner Jr, 1994, *Phys. Rev. B* **50**, 248.
- Adroja, D.T., B.D. Rainford, L.E. Miller and S.K. Malik, 1997, *Physica B* **230–232**, 282.
- Adroja, D.T., B.D. Rainford and T. Takabatake, 1998, *Physica B* **253**, 269.
- Alami-Yadri, K., H. Wilhelm and D. Jaccard, 1998, *Solid State Commun.* **108**, 279.
- Alami-Yadri, K., H. Wilhelm and D. Jaccard, 1999a, *Physica B* **259–261**, 157.
- Alami-Yadri, K., D. Jaccard and D. Andreica, 1999b, *J. Low Temp. Phys.* **114**, 135.
- Albering, J.H., 1993, *Struktur und Eigenschaften ternärer Actinoid–Übergangsmetall-Phosphide und ähnlicher Verbindungen*, Dissertation (Universität Münster, Germany).
- Albering, J.H., Th. Ebel and W. Jeitschko, 1997, *Z. Kristallogr. Suppl.* **12**, 242.
- Aliev, F.G., V.V. Moshchalkov, V.V. Kozyrkov, M.K. Zalyalyutdinov, V.V. Pryadun and R.V. Skolozdra, 1988, *J. Magn. Magn. Mater.* **76–77**, 295.
- Aliev, F.G., G.I. Pak and T.M. Shkatova, 1989a, *Sov. Phys. Solid State* **31**, 1615.
- Aliev, F.G., G.I. Pak and T.M. Shkatova, 1989b, *Fiz. Tverd. Tela* **31**, 244.
- Aliev, F.G., S. Vieira, R. Viirar, M. Kasaia, H. Sutsuki and R. Vonvibe, 1994, *Pis'ma Zh. Eksp. Teor. Fiz.* **60**, 714.

- Amato, A., P.C. Canfield, R. Feyherherm, Z. Fisk, F.N. Gyax, R.H. Heffner, D.E. MacLaughlin, H.R. Ott, A. Schenck and J.D. Thompson, 1992, *Phys. Rev. B* **46**, 3151.
- Amato, A., P.C. Canfield, R. Feyherherm, Z. Fisk, F.N. Gyax, R.H. Heffner, E.A. Knetsch, D.E. MacLaughlin, H.R. Ott, A. Schenck, J.D. Thompson and U. Zimmermann, 1993, *Physica B* **186-188**, 615.
- Andersen, O.K., 1975, *Phys. Rev. B* **12**, 3060.
- Andersen, O.K., and O. Jepsen, 1984, *Phys. Rev. Lett.* **53**, 2571.
- Andersen, O.K., O. Jepsen and D. Götzel, 1985, in: *Highlights of Condensed-Matter Theory*, eds F. Bassani, F. Furi and M.P. Tosi (North-Holland, New York).
- Andraka, B., R. Pietri, D. Kaczorowski, A. Leithe-Jasper and P. Rogl, 2000, *J. Appl. Phys.* **87**, 5149.
- Arko, A.J., P.S. Riseborough, A.B. Andrews, J.J. Joyce, A.N. Tahvildhar-Zadeh and M. Jarrell, 1999, *Photoelectron spectroscopy in heavy fermion systems: emphasis on single crystals*, in: *Handbook on the Physics and Chemistry of Rare Earths*, Vol. 26, eds K.A. Gschneidner Jr and L. Eyring (North-Holland, Amsterdam) ch. 172.
- Bärnighausen, H., 1980, *Commun. Math. Chem.* **9**, 139.
- Bauchspiess, K.R., W. Boksich, E. Holland-Moritz, H. Launois, R. Pott and D. Wohlleben, 1981, in: *Valence Fluctuations in Solids*, St. Barbara Inst. Theor. Phys. Conf., eds L.M. Falicov, W. Hanke and M.B. Maple (North-Holland, Amsterdam) p. 417.
- Beck, L., and K. Girgis, 1985, *J. Less-Common Met.* **109**, 275.
- Bellot, P., P. Bonville, J. Hammann, J.A. Hodges, P. Imbert, G. Jéhanno, L. Leylekian and L. D'Onofrio, 1992, *J. Magn. Magn. Mater.* **108**, 141.
- Bleckwedel, A., and A. Eichler, 1981, in: *Proc. Int. Symp. on the Physics of Solids at High Pressure* (North-Holland, Amsterdam) p. 323.
- Bleckwedel, A., A. Eichler and R. Pott, 1981, *Physica B* **107**, 93.
- Block, H., 1988, *Antimonide und Wismutide von Titan, Zirkonium, Hafnium und anderen Nebengruppen-elementen*, Dissertation (Universität Münster, Germany).
- Bodak, O.I., E.I. Gladyshevskii and P.I. Kripyakevich, 1970, *J. Struct. Chem., Zh. Struct. Khim.* **11**, 283.
- Bonrath, H., K.H. Hellwege, K. Nicolay and G. Weber, 1966, *Phys. Kond. Mater.* **4**, 382.
- Bonville, P., and J.A. Hodges, 1985, *J. Magn. Magn. Mater.* **47-48**, 152.
- Bonville, P., J.A. Hodges, P. Imbert, D. Jaccard, J. Sierro, M.J. Besnus and A. Meyer, 1990, *Physica B* **163**, 347.
- Bonville, P., P. Bellot, J.A. Hodges, P. Imbert, G. Jéhanno, G. Le Bras, J. Hammann, L. Leylekian, G. Chevrier, P. Thuéry, L. D'Onofrio, A. Hamzic and A. Barthélémy, 1992, *Physica B* **182**, 105.
- Bonville, P., G. Polatsck, J.A. Hodges, P. Imbert and G. Le Bras, 1993, *Physica B* **186-188**, 254.
- Bonville, P., G. Le Bras, P. Dalmas de Réotier, A. Yaouanc, R. Calemczuk, C. Paulsen, M. Kasaya and F.G. Aliev, 1997a, *Physica B* **230-232**, 266.
- Bonville, P., J.A. Hodges, P. Dalmas de Réotier and A. Yaouanc, 1997b, *Positive muon spectroscopy in Yb-based Kondo lattices*, in: *Proc. XXXII Zakopane School of Physics, Condensed Matter Studies by Nuclear Methods*, eds E.A. Görlich and K. Łątka (Wydawnictwo Uniwersytetu Jagiellońskiego, Kraków) p. 297.
- Bonville, P., B. Malaman, E. Ressouche, J.P. Sanchez, M. Abd-Elmeguid, C. Geibel and O. Trovarelli, 2000a, *Europhys. Lett.*, in press.
- Bonville, P., M. Abd-Elmeguid, B. Malaman, E. Ressouche, J.P. Sanchez, C. Geibel and O. Trovarelli, 2000b, *Physica B* **281-282**, 144.
- Borisenko, O.L., O.I. Bodak and Yu.D. Seropegin, 1994, *Moscow University Chemistry Bulletin*. Translated from: *Vestn. Mosk. Univ. Khim.* **49(1)**, 103.
- Borisenko, O.L., O.I. Bodak, Yu.D. Seropegin, V.N. Nikiforov, M.V. Kovachikova and Yu.V. Kochetkov, 1995, *Metally* **2**, 167.
- Bremer, J., D.A. Sergatskov, J.S. Xia, G.E. Granroth, P.J.C. Signore, G.G. Ihas, M.W. Meisel, P.C. Canfield, R. Movshovich, A. Lacerda and Z. Fisk, 1995, *Physica B* **206-207**, 336.
- Burdett, J.K., ed., 1995, *Chemical Bonding in Solids* (Oxford University Press, New York).
- Bussian, B., I. Frankowski and D. Wohlleben, 1982, *Phys. Rev. Lett.* **49**, 1026.
- Canfield, P.C., J.D. Thompson, W.P. Beyermann, A. Lacerda, M.F. Hundley, E. Peterson, Z. Fisk and H.R. Ott, 1991, *J. Appl. Phys.* **70**, 5800.
- Canfield, P.C., R. Movshovich, R.A. Robinson, J.D. Thompson, Z. Fisk, W.P. Beyermann, A. Lacerda, M.F. Hundley, R.H. Heffner, D.E. MacLaughlin, F. Trouw and H.R. Ott, 1994, *Physica B* **197**, 101.
- Cardoso Gil, R.H., O. Trovarelli, C. Geibel and Yu. Grin, 1999, *Z. Kristallogr. - New Crystal Structures* **214**, 459.

- Cattaneo, E., 1985, *J. Magn. Magn. Mater.* **47–48**, 529.
- Cattaneo, E., 1986, *Z. Phys. Condens. Matter* **64**, 317.
- Cirafici, S., A. Palenzona and F. Canepa, 1985, *J. Less-Common Met.* **107**, 179.
- Corbett, J.D., 1983, *Inorg. Synth.* **22**, 15.
- Cordier, G., and R. Henseleit, 1993a, *Z. Kristallogr.* **203**, 144.
- Cordier, G., and R. Henseleit, 1993b, *Z. Kristallogr.* **203**, 142.
- Cordier, G., T. Friedrich, R. Henseleit, A. Grauel, U. Tegel, C. Schank and C. Geibel, 1993, *J. Alloys Compd.* **201**, 197.
- Cornelius, A.L., J.S. Schilling, D. Mandrus and J.D. Thompson, 1995, *Phys. Rev. B* **52**, R15699.
- Czybulka, A., B. Pinger and H.-U. Schuster, 1989, *Z. Anorg. Allg. Chem.* **579**, 151.
- Danebrock, M.E., W. Jeitschko, A.M. Witte and R. Pöttgen, 1995, *J. Phys. Chem. Solids* **56**, 807.
- Dascolidou-Gritner, K., and H.-U. Schuster, 1994, *Z. Anorg. Allg. Chem.* **620**, 1151.
- Debray, D., 1973, *J. Less-Common Met.* **30**, 23.
- Dhar, S.K., N. Nambudripad and R. Vijayaraghavan, 1988, *J. Phys. F* **18**, L41.
- Dhar, S.K., K.A. Gschneidner Jr and R. Vijayaraghavan, 1993, *Physica B* **186–188**, 463.
- Dhar, S.K., P. Manfrinetti and A. Palenzona, 1995, *Phys. Rev. B* **51**, 12464.
- Diehl, J., H. Davideit, S. Klimm, U. Tegel, C. Geibel, F. Steglich and S. Horn, 1995, *Physica B* **206–207**, 344.
- Doniach, S., 1977, *Physica B* **91**, 231.
- Doniach, S., 1997, in: *Valence Instabilities and Related Narrow Band Phenomena*, ed. R.D. Park (Plenum Press, New York).
- D'Onofrio, L., A. Hamzić and A. Fert, 1991, *Physica B* **171**, 266.
- Donohue, J., 1974, *The Structures of the Elements* (Wiley, New York).
- Drescher, K., M.M. Abd-Elmeguid, J.P. Sanchez and C. Meyer, 1996a, *J. Phys.: Condens. Matter* **8**, L65.
- Drescher, K., M.M. Abd-Elmeguid, H. Micklitz and J.P. Sanchez, 1996b, *Phys. Rev. Lett.* **77**, 3228.
- Drescher, K., M.M. Abd-Elmeguid, H. Micklitz, J.P. Sanchez, C. Geibel and F. Steglich, 1998, *J. Magn. Mater.* **182**, L275.
- Dronskowski, R., and P.E. Blöchl, 1993, *J. Phys. Chem.* **97**, 8617.
- Duwell, E.J., and N.C. Baenziger, 1955, *Acta Crystallogr.* **8**, 705.
- Dwight, A.E., 1974, in: *Proc. 11th Rare Earth Research Conf., Michigan*, 1974, Vol. 2, p. 642.
- Dwight, A.E., 1983, *J. Less-Common Met.* **93**, 411.
- Dwight, A.E., M.H. Mueller, R.A. Conner Jr, J.W. Downey and H. Knott, 1968, *Trans. AIME* **242**, 2075.
- Dwight, A.E., W.C. Harper and C.W. Kimball, 1973, *J. Less-Common Met.* **30**, 1.
- Dzyani, R.B., O.I. Bodak and L.G. Aksel'rud, 1995a, *Inorg. Mater.* **31**, 913.
- Dzyani, R.B., O.I. Bodak and V.V. Pavlyuk, 1995b, *Metally* **4**, 172.
- Dzyani, R.B., O.I. Bodak and V.V. Pavlyuk, 1995c, *Inorg. Mater.* **31**, 908.
- Ebel, Th., 1995, *Magnetische Eigenschaften ternärer Uran- und Seltenerd-Übergangsmetall-Aluminide, -Carbide und -Phosphide und ähnlicher Verbindungen*, Dissertation (Universität Münster, Germany).
- Ehlers, G., C. Geibel, F. Steglich and H. Maletta, 1997, *Z. Phys. B* **104**, 393.
- Endstra, T., S.A.M. Mentink, G.J. Nieuwenhuys and J.A. Mydosh, 1993, in: *Frontiers in Solid State Sciences*, Vol. 2, eds L.C. Gupta and M.S. Multani (World Scientific, Singapore) pp. 167.
- Eriksson, O., J.M. Wills and A.M. Boring, 1992, *J. Alloys Compounds* **185**, 145.
- Fässler, T.F., and A. Savin, 1997, *Chem. Unserer Zeit* **31**, 110.
- Fay, D., D.-R. Gutsch, M.W. Pieper, C. Geibel, C. Schank and F. Steglich, 1997, *Z. Phys. B* **104**, 247.
- Ferro, R., R. Marazza and G. Rambaldi, 1974a, *Z. Metallkd.* **65**, 37.
- Ferro, R., R. Marazza and G. Rambaldi, 1974b, *Z. Metallkd.* **65**, 40.
- Fisk, Z., and M.B. Maple, 1992, *J. Alloys Compounds* **183**, 303.
- Fisk, Z., P.C. Canfield, W.P. Beyermann, J.D. Thompson, M.F. Hundley, H.R. Ott, E. Felder, M.B. Maple, M.A. Lopez de la Torre, P. Visani and C.L. Seaman, 1991, *Phys. Rev. Lett.* **67**, 3310.
- Flandorfer, H., K. Hiebl, C. Godart, P. Rogl, A. Saccone and R. Ferro, 1997, *J. Alloys Compounds* **256**, 170.
- Fornasini, M.L., and F. Merlo, 1995, *J. Alloys Compounds* **219**, 63.
- Fornasini, M.L., A. Iandelli, F. Merlo and M. Pani, 2000, *Intermetallics* **8**, 239.
- Fournier, J.M., 1985, *Struct. Bonding* **59–60**, 127.



- Fournier, J.M., and E. Gratz, 1993, Transport properties of rare earth and actinide intermetallics, in: *Handbook on the Physics and Chemistry of Rare Earths*, Vol. 17, eds K.A. Gschneidner Jr and L. Eyring (North-Holland, Amsterdam) ch. 115.
- Fournier, J.M., and R. Troć, 1985, in: *Handbook on the Physics and Chemistry of the Actinides*, Vol. 2, eds A.J. Freeman and G.H. Lander (North-Holland, Amsterdam) pp. 29–73.
- Fujita, T., T. Suzuki, S. Nishigori, T. Takabatake, H. Fujii and J. Sakurai, 1992, *J. Magn. Magn. Mater.* **108**, 35.
- Gerß, M.H., and W. Jeitschko, 1986, *Z. Naturforsch.* **41b**, 946.
- Gibson, B., R. Pöttgen, R.K. Kremer, A. Simon and K.R.A. Ziebeck, 1996, *J. Alloys Compounds* **239**, 34.
- Gibson, B., R.K. Kremer, O. Jepsen, J.D. Garrett, R.-D. Hoffmann and R. Pöttgen, 2001, *J. Phys. C* **13**, 3123.
- Gignoux, D., and D. Schmitt, 1997, in: *Handbook of Magnetic Materials*, Vol. 10, ed. K.H.J. Buschow (Elsevier, Amsterdam) ch. 2, p. 239.
- Gladysheskii, R.E., and E. Parthé, 1992, *Z. Kristallogr.* **198**, 175.
- Gorelenko, Yu.K., P.K. Starodub, V.A. Bruskov, R.V. Skolozdra, V.I. Yarovets, O.I. Bodak and V.K. Pecharsky, 1984, *Ukr. Fiz. Zh.* **29**, 867.
- Grewe, N., and F. Steglich, 1991, Heavy fermions, in: *Handbook on the Physics and Chemistry of Rare Earths*, Vol. 14, eds K.A. Gschneidner Jr and L. Eyring (North-Holland, Amsterdam) ch. 97.
- Grin, Yu., M. Ellner, K. Hiebl, B. Baumgartner and P. Rogl, 1995, *J. Alloys Compounds* **221**, 125.
- Grin, Yu., R. Mishra and R. Pöttgen, 2000, unpublished results.
- Grund, I., G. Zwiener and H.-U. Schuster, 1986, *Z. Anorg. Allg. Chem.* **535**, 7.
- Häfner, H.U., 1985, *J. Magn. Magn. Mater.* **47–48**, 299.
- Heffner, R.H., A. Amato, P.C. Canfield, R. Feyerherm, Z. Fisk, F.N. Gygax, D.E. MacLaughlin, A. Schenck, J.D. Thompson and H.R. Ott, 1994, *Physica B* **199–200**, 113.
- Hewson, A.C., and J.W. Rasul, 1983, *J. Phys. C* **16**, 6799.
- Hewson, A.C., J.W. Rasul and D.M. Newns, 1983, *Solid State Commun.* **47**, 59.
- Hewson, A.C., D.M. Newns, J.W. Rasul and N. Read, 1985, *J. Magn. Magn. Mater.* **47–48**, 354.
- Hoffmann, R., J. Li and R.A. Wheeler, 1987, *J. Am. Chem. Soc.* **109**, 6600.
- Hoffmann, R.-D., and R. Pöttgen, 2000, *Z. Anorg. Allg. Chem.* **626**, 28.
- Hoffmann, R.-D., R. Pöttgen, D. Kußmann, R. Müllmann and B.D. Mosel, 2001, *Chem. Mater.*, in press.
- Hovestreydt, E., N. Engel, K. Klepp, B. Chabot and E. Parthé, 1982, *J. Less-Common Met.* **85**, 247.
- Hulliger, F., 1993, *J. Alloys Compounds* **200**, 75.
- Hulliger, F., 1995, *J. Alloys Compounds* **218**, 44.
- Hulliger, F., 1996, *J. Alloys Compounds* **239**, 131.
- Hundley, M.F., J.D. Thompson, P.C. Canfield and Z. Fisk, 1997, *Phys. Rev. B* **56**, 8098.
- Iandelli, A., 1983, *J. Less-Common Met.* **90**, 121.
- Iandelli, A., 1985, *J. Less-Common Met.* **113**, L25.
- Iandelli, A., 1987, *J. Less-Common Met.* **135**, 195.
- Iandelli, A., 1993, *J. Alloys Compounds* **198**, 141.
- Iandelli, A., 1994, *J. Alloys Compounds* **203**, 137.
- Itoh, Y., and H. Kadomatsu, 1998, *J. Alloys Compounds* **280**, 39.
- Jaccard, D., and J. Sierro, 1982, in: *Proc. Int. Symp. on Valence Instabilities* (North-Holland, Amsterdam) p. 409.
- Jaccard, D., J. Flouquet and J. Sierro, 1985, *J. Appl. Phys.* **57**, 3084.
- Jaccard, D., E. Vargoz, K. Alami-Yadri and H. Wilhelm, 1998, *Rev. High Pressure Sci. Technol.* **7**, 412.
- Jacob, I., M. Fisher and Z. Hadari, 1987, *J. Less-Common Met.* **130**, 503.
- Johnston, R.L., and R. Hoffmann, 1992, *Z. Anorg. Allg. Chem.* **616**, 105.
- Johrendt, D., and A. Mewis, 1990, *Z. Naturforsch.* **45b**, 1262.
- Johrendt, D., and A. Mewis, 1992, *J. Alloys Compounds* **183**, 210.
- Jolibois, P., 1910, *C.R. Acad. Sci.* **150**, 106.
- Kaczorowski, D., A. Leithe-Jasper, P. Rogl, H. Flandorfer, T. Cichorek, R. Pietri and B. Andraka, 1999, *Phys. Rev. B* **60**, 422.
- Kaczorowski, D., B. Andraka, R. Pietri, T. Cichorek and V.I. Zaremba, 2000a, *Phys. Rev. B* **61**, 15255.
- Kaczorowski, D., B. Andraka, V.I. Zaremba and Cz. Marucha, 2000b, *Physica B* **281–282**, 44.
- Kaner, R., C.A. Castro, R.P. Gruska and A. Wold, 1977, *Mater. Res. Bull.* **12**, 1143.
- Kasaya, M., T. Tani, F. Iga and T. Kasuya, 1988, *J. Magn. Magn. Mater.* **76–77**, 278.

- Kasaya, M., T. Tani, K. Kawate, T. Mizushima, Y. Isikawa and K. Sato, 1991, *J. Phys. Soc. Jpn.* **60**, 3145.
- Kasaya, M., T. Tani, K. Ohoyama, M. Kohgi and Y. Isikawa, 1992a, *J. Magn. Magn. Mater.* **104–107**, 665.
- Kasaya, M., H. Suzuki, T. Yamaguchi and K. Katoh, 1992b, *J. Phys. Soc. Jpn.* **61**, 4187.
- Katoh, K., T. Takabatake, A. Minami, I. Oguro and H. Sawa, 1997, *J. Alloys Compounds* **261**, 32.
- Katoh, K., G. Terui, Y. Niide, H. Aoki and A. Ochiai, 1999, *Physica B* **259–261**, 161.
- Klaasse, J.C.P., W.C.M. Mattens, F.R. de Boer and P.F. de Châtel, 1977, *Physica B* **86–88**, 234.
- Krypyakevich, P.I., V.Ya. Markiv and Ya. Melnyk, 1967, *Dopov. Akad. Nauk. Ukr. RSR, Ser. A*, p. 750.
- Kußmann, D., R. Pöttgen, B. Künnen, G. Kotzyba, R. Müllmann and B.D. Mosel, 1998a, *Z. Kristallogr.* **213**, 356.
- Kußmann, D., R.-D. Hoffmann and R. Pöttgen, 1998b, *Z. Anorg. Allg. Chem.* **624**, 1727.
- Kuramoto, Y., and E. Müller-Hartmann, 1981, in: *Valence Fluctuations in Solids*, St. Barbara Inst. Theor. Phys. Conf., eds L.M. Falicov, W. Hanke and M.B. Maple (North-Holland, Amsterdam) p. 139.
- Kuss, M., G. Wenski, A. Mewis and H.-U. Schuster, 1987, *Z. Anorg. Allg. Chem.* **553**, 156.
- Lacerda, A., R. Movshovich, M.F. Hundley, P.C. Canfield, D. Arms, G. Sparr, J.D. Thompson, Z. Fisk, R.A. Fisher, N.E. Phillips and H.R. Ott, 1993, *J. Appl. Phys.* **73**, 5415.
- Landrum, G.A., R. Hoffmann, J. Evers and H. Boysen, 1998, *Inorg. Chem.* **37**, 5754.
- Larica, C., and B.R. Coles, 1985, *Philos. Mag. B* **52**, 1097.
- Larson, A.C., and D.T. Cromer, 1961, *Acta Crystallogr.* **14**, 73.
- Larson, P., S.D. Mahanti, S. Sportouch and M.G. Kanatzidis, 1999, *Phys. Rev. B* **59**, 15660.
- Le Bras, G., P. Bonville, P. Imbert, G. Polatsek, M.J. Besnus, P. Haen and V. Moshchal'kov, 1994, *Physica B* **199–200**, 542.
- Le Bras, G., P. Bonville, J.A. Hodges, J. Hammann, M.J. Besnus, G. Schmerber, S.K. Dhar, F.G. Aliev and G. André, 1995a, *J. Phys.: Condens. Matter.* **7**, 5665.
- Le Bras, G., P. Bonville, M.J. Besnus, P. Haen, P. Imbert, G. Polatsek and F.G. Aliev, 1995b, *Physica B* **206–207**, 338.
- Lee, S., 1991, *J. Am. Chem. Soc.* **113**, 101.
- Loewenhaupt, M., and K.H. Fischer, 1993, Valence-fluctuation and heavy-fermion 4f systems, in: *Handbook on the Physics and Chemistry of Rare Earths*, Vol. 16, eds K.A. Gschneidner Jr and L. Eyring (North-Holland, Amsterdam) ch. 105.
- Lustfeld, H., and A. Bringer, 1978, *Solid State Commun.* **28**, 119.
- Lysak, M., A.P. Reyes, Ch. Tien, G. Van Kalkeren, D.E. MacLaughlin and F.R. de Boer, 1987, *J. Appl. Phys.* **61**, 3186.
- MacLaughlin, D.E., 1981, in: *Valence Fluctuation in Solids*, St. Barbara Inst. Theor. Phys. Conf., eds L.M. Falicov, W. Hanke and M.B. Maple (North-Holland, Amsterdam) p. 321.
- MacLaughlin, D.E., F.R. de Boer, J. Bijvoet, P.F. de Châtel and W.C.M. Mattens, 1979, *J. Appl. Phys.* **50**, 2094.
- Malik, S.K., D.T. Adroja, B.D. Padalia and R. Vijayaraghavan, 1987a, in: *Theoretical and Experimental Aspects of Valence Fluctuations and Heavy Fermions*, eds L.C. Gupta and S.K. Malik (Plenum, New York) p. 463.
- Malik, S.K., D.T. Adroja, B.D. Padalia and R. Vijayaraghavan, 1987b, *Jpn. J. Appl. Phys. Suppl.* **26–3**, 553.
- Marazza, R., D. Rossi and R. Ferro, 1980a, *J. Less-Common Met.* **75**, P25.
- Marazza, R., D. Rossi and R. Ferro, 1980b, *Gazz. Chim. Ital.* **110**, 357.
- Marazza, R., D. Mazzone, P. Riani and G. Zanicchi, 1995, *J. Alloys Compounds* **220**, 241.
- Massidda, S., W.E. Pickett and M. Posternak, 1991, *Phys. Rev. B* **44**, 1258.
- Mattens, W.C.M., R.A. Elenbaas and F.R. de Boer, 1977, *Commun. Phys.* **2**, 147.
- Mattens, W.C.M., F.R. de Boer, A.P. Murani and G.H. Lander, 1980a, *J. Magn. Magn. Mater.* **15–18**, 973.
- Mattens, W.C.M., H. Hölscher, G.J.M. Tuin, A.C. Moleman and F.R. de Boer, 1980b, *J. Magn. Magn. Mater.* **15–18**, 982.
- Mattens, W.C.M., J. Aarts, A.C. Moleman, I. Rachman and F.R. de Boer, 1982, in: *Proc. Int. Symp. on Valence Instabilities* (North-Holland, Amsterdam) p. 211.
- Mazzone, D., D. Rossi, R. Marazza and R. Ferro, 1981, *J. Less-Common Met.* **80**, P47.
- Mazzone, D., D. Rossi, R. Marazza and R. Ferro, 1982, *J. Less-Common Met.* **84**, 301.
- Mazzone, D., G. Borzone, D. Rossi and R. Ferro, 1983, *J. Less-Common Met.* **94**, L5.

- Mehrotra, P.K., and R. Hoffmann, 1978, *Inorg. Chem.* **17**, 2187.
- Merlo, F., M. Pani and M.L. Fornasini, 1990, *J. Less-Common Met.* **166**, 319.
- Merlo, F., M. Pani and M.L. Fornasini, 1991, *J. Less-Common Met.* **171**, 329.
- Merlo, F., M. Pani and M.L. Fornasini, 1993, *J. Alloys Compounds* **196**, 145.
- Merlo, F., M. Pani and M.L. Fornasini, 1995, *J. Alloys Compounds* **221**, 280.
- Merlo, F., M. Pani and M.L. Fornasini, 1996, *J. Alloys Compounds* **232**, 289.
- Merlo, F., M. Pani, F. Capena and M.L. Fornasini, 1998, *J. Alloys Compounds* **264**, 82.
- Mignot, J.M., and J. Wittig, 1981, in: *Proc. Int. Symp. on the Physics of Solids at High Pressure* (North-Holland, Amsterdam) p. 311.
- Mignot, J.M., and J. Wittig, 1982, in: *Proc. Int. Symp. on Valence Instabilities* (North-Holland, Amsterdam) p. 203.
- Mishra, R., R. Pöttgen, R.-D. Hoffmann, D. Kaczorowski, H. Piotrowski, P. Mayr, C. Rosenhahn and B.D. Mosel, 2001, *Z. Anorg. Allg. Chem.* **627**, 1283.
- Mott, N.F., 1936, *Proc. R. Soc. London Ser. A* **156**, 368.
- Movshovich, R., A. Lacerda, P.C. Canfield, D. Arms, J.D. Thompson and Z. Fisk, 1994a, *Physica B* **199&200**, 67.
- Movshovich, R., A. Lacerda, P.C. Canfield, J.D. Thompson and Z. Fisk, 1994b, *Phys. Rev. Lett.* **73**, 492.
- Müllmann, R., B.D. Mosel, H. Eckert, R. Pöttgen and R.K. Kremer, 1997, *Hyperfine Interactions* **108**, 389.
- Murani, A.P., W.C.M. Mattens, F.R. de Boer and G.H. Lander, 1985, *Phys. Rev. B* **31**, 52.
- Niepmann, D., R. Pöttgen, G. Kotzyba and B. Künnen, 2000a, *J. Solid State Chem.* **150**, 139.
- Niepmann, D., Yu.M. Prots', R. Pöttgen and W. Jeitschko, 2000b, *J. Solid State Chem.* **154**, 329.
- Nieuwenhuys, G.J., 1995, Heavy fermions and related compounds, in: *Handbook of Magnetic Materials*, Vol. 9, ed. K.H.J. Buschow (Elsevier, Amsterdam) ch. 1.
- Nikiforov, V.N., M.V. Kovachikova, A.A. Velikhovskii, Yu.V. Kochetkov, J. Mirkovic, O.M. Borisenko and Yu.D. Seropegin, 1994, *Mosk. Gos. Univ., Moscow, Russia, Fiz. Tverd. Tela (S.-Petersburg)* **36**, 471.
- Nuspl, G., K. Polborn, J. Evers, G.A. Landrum and R. Hoffmann, 1996, *Inorg. Chem.* **35**, 6922.
- Oesterreicher, H., 1971a, *J. Less-Common Met.* **25**, 228.
- Oesterreicher, H., 1971b, *J. Less-Common Met.* **25**, 341.
- Ōnuki, Y., and A. Hasegawa, 1995, Fermi surfaces of intermetallic compounds, in: *Handbook on the Physics and Chemistry of Rare Earths*, Vol. 20, eds K.A. Gschneidner Jr and L. Eyring (North-Holland, Amsterdam) ch. 135.
- Oppeneer, P.M., V.N. Antonov, A.N. Yaresko, A.Ya. Perlov and H. Eschrig, 1997, *Phys. Rev. Lett.* **78**, 4079.
- Pani, M., F. Merlo and M.L. Fornasini, 1999, *Z. Kristallogr.* **214**, 108.
- Parthé, E., and B. Chabot, 1984, in: *Handbook on the Physics and Chemistry of Rare Earths*, Vol. 6, eds K.A. Gschneidner Jr and L. Eyring (North-Holland, Amsterdam) p. 235.
- Parthé, E., and L.M. Gelato, 1984, *Acta Crystallogr. A* **40**, 169.
- Pauling, L., 1960, *The Nature of the Chemical Bond and the Structure of Molecules and Crystals* (Cornell University Press, Ithaca, NY).
- Pearson, R.G., 1988, *Inorg. Chem.* **27**, 734.
- Pietri, R., B. Andraka, D. Kaczorowski, A. Leithe-Jasper and P. Rogl, 2000, *Phys. Rev. B* **61**, 12169.
- Pinkerton, F.E., A.J. Sievers, M.B. Maple and B.C. Sales, 1984, *Phys. Rev. B* **29**, 609.
- Pott, R., R. Schefzyk, D. Wohlleben and A. Junod, 1981, *Z. Phys. B* **44**, 17.
- Pöttgen, R., 1995, *J. Mater. Chem.* **5**, 505.
- Pöttgen, R., 1996a, *Z. Kristallogr.* **211**, 884.
- Pöttgen, R., 1996b, *J. Mater. Chem.* **6**, 63.
- Pöttgen, R., 1996c, *J. Alloys Compounds* **243**, L1.
- Pöttgen, R., and Y. Grin, 1997, *Z. Kristallogr. Suppl.* **12**, 136.
- Pöttgen, R., and R.-D. Hoffmann, 2000, *Z. Kristallogr.* **216**, 127.
- Pöttgen, R., and D. Johrendt, 2000, *Chem. Mater.* **12**, 875.
- Pöttgen, R., and D. Niepmann, 2000, unpublished results.
- Pöttgen, R., H. Borrmann, C. Felser, O. Jepsen, R. Henn, R.K. Kremer and A. Simon, 1996, *J. Alloys Compounds* **235**, 170.
- Pöttgen, R., R.-D. Hoffmann, R. Müllmann, B.D. Mosel and G. Kotzyba, 1997a, *Chem. Eur. J.* **3**, 1852.

- Pöttgen, R., B. Gibson and R.K. Kremer, 1997b, *Z. Kristallogr.* **212**, 58.
- Pöttgen, R., A. Lang, R.-D. Hoffmann, B. Künnen, G. Kotzyba, R. Müllmann, B.D. Mosel and C. Rosenhahn, 1999a, *Z. Kristallogr.* **214**, 143.
- Pöttgen, R., Th. Gulden and A. Simon, 1999b, *GIT Fachz. Lab.* **43**, 133.
- Pöttgen, R., P.E. Arpe, C. Felser, D. Kußmann, R. Müllmann, B.D. Mosel, B. Künnen and G. Kotzyba, 1999c, *J. Solid State Chem.* **145**, 668.
- Pöttgen, R., R.-D. Hoffmann, J. Renger, U.Ch. Rodewald and M.H. Möller, 2000a, *Z. Anorg. Allg. Chem.* **626**, 2257.
- Pöttgen, R., A. Fugmann, R.-D. Hoffmann, U.Ch. Rodewald and D. Niepmann, 2000b, *Z. Naturforsch.* **55b**, 155.
- Pöttgen, R., Yu. Grin, R.K. Kremer and F.E. Wagner, 2000c, unpublished results.
- Prots', Yu.M., R. Pöttgen and W. Jeitschko, 1998, *Z. Anorg. Allg. Chem.* **624**, 425.
- Reinert, F., R. Claessen, C. Geibel and S. Hüfner, 1999, *Physica B* **259–261**, 1128.
- Reyes, A.P., L.P. Le, R.H. Heffner, E.T. Ahrens, Z. Fisk and P.C. Canfield, 1995, *Physica B* **206–207**, 332.
- Robinson, R.A., M. Kohgi, T. Osakabe, P.C. Canfield, T. Kamiyama, T. Nakane, Z. Fisk and J.D. Thompson, 1993, *Physica B* **186–188**, 550.
- Robinson, R.A., A. Purwanto, M. Kohgi, P.C. Canfield, T. Kamiyama, T. Ishigaki, J.W. Lynn, R. Erwin, E. Peterson and R. Movshovich, 1994, *Phys. Rev. B* **50**, 9595.
- Robinson, R.A., M. Kohgi, T. Osakabe, F. Trouw, J.W. Lynn, P.C. Canfield, J.D. Thompson, Z. Fisk and W.P. Beyermann, 1995, *Phys. Rev. Lett.* **75**, 1194.
- Robinson, R.A., A. Christianson, H. Nakotte, W.P. Beyermann and P.C. Canfield, 1999, *Physica B* **259–261**, 138.
- Rossi, D., R. Ferro, V. Contardi and R. Marazza, 1977, *Z. Metallkd.* **68**, 493.
- Rossi, D., R. Marazza, D. Mazzone and R. Ferro, 1981, *J. Less-Common Met.* **78**, P1.
- Rossi, D., D. Mazzone, R. Marazza and R. Ferro, 1983a, *Z. Anorg. Allg. Chem.* **507**, 235.
- Rossi, D., V. Contardi, R. Marazza, D. Mazzone and G. Zanicchi, 1983b, in: 16th Congr. Naz. Chim. Inorg., Ferrara, Italy, p. 240.
- Rossi, D., R. Marazza and R. Ferro, 1985, *J. Less-Common Met.* **107**, 99.
- Rossi, D., R. Marazza, G. Zanicchi and R. Ferro, 1990, *J. Less-Common Met.* **158**, L37.
- Rossi, D., R. Marazza and R. Ferro, 1992, *J. Alloys Compounds* **187**, 267.
- Rundqvist, S., and F. Jellinek, 1959, *Acta Chem. Scand.* **13**, 425.
- Sales, B.C., and D.K. Wohlleben, 1975, *Phys. Rev. Lett.* **35**, 1240.
- Savin, A., R. Nesper, S. Wengert and T.F. Fässler, 1997, *Angew. Chem.* **109**, 1893.
- Schank, C., U. Tegel, R. Henseleit, A. Grauel, G. Olesch, C. Geibel, G. Cordier, R. Kniep and F. Steglich, 1994, *J. Alloys Compounds* **207/208**, 333.
- Schank, C., G. Olesch, J. Köhler, U. Tegel, U. Klinger, J. Diehl, S. Klimm, G. Sparr, S. Horn, C. Geibel and F. Steglich, 1995, *J. Magn. Magn. Mater.* **140–144**, 1237.
- Schmidbaur, H., 1990, *Gold Bull.* **23(1)**, 11.
- Schmidbaur, H., ed., 1999, *Gold – Progress in Chemistry, Biochemistry and Technology* (Wiley, Chichester).
- Schöppner, M., J. Moser, A. Kratzer, U. Potzel, J.M. Mignot and G.M. Kalvius, 1986, *Z. Phys. B* **63**, 25.
- Sechovsky, V., and L. Havela, 1988, *Intermetallic compounds of actinides*, in: *Ferromagnetic Materials*, Vol. 4, eds E.P. Wohlfahrt and K.H.J. Buschow (Elsevier, Amsterdam) p. 309.
- Sendlinger, B., 1993, *Hochdruckuntersuchungen an den ambivalenten Verbindungen MTX (M = Yb, Ca, Eu, Sr, Ba; T = Pd, Pt; X = Si, Ge, Sn, Pb)*, Dissertation (Ludwig-Maximilians-Universität, München).
- Sereni, J.G., 1991, *Low-temperature behaviour of cerium compounds*, in: *Handbook on the Physics and Chemistry of Rare Earths*, Vol. 15, eds K.A. Gschneidner Jr and L. Eyring (North-Holland, Amsterdam) ch. 98.
- Seropegin, Yu.D., O.L. Borisenko, O.I. Bodak, V.N. Nikiforov, M.V. Kovachikova and Yu.V. Kochetkov, 1994, *J. Alloys Compounds* **216**, 259.
- Seropegin, Yu.D., O.L. Shepelyuk, J.M. Kurenbaeva, A.V. Griboan and O.I. Bodak, 2000, *J. Alloys Compounds* **299**, 241.
- Shoemaker, C.B., and D.P. Shoemaker, 1965, *Acta Crystallogr.* **18**, 900.
- Skolozdra, R.V., O.É. Koretskaya and Yu.K. Gorenko, 1984, *Izv. Akad. Nauk SSSR, Neorg. Mater.* **20**, 604.
- Skolozdra, R.V., A. Guzik, A.M. Goryn and J. Pierre, 1997, *Acta Phys. Pol. A* **92**, 343.
- Solanki, A.K., A. Kashyap, S. Auluck and M.S.S. Brooks, 1994, *J. Appl. Phys.* **75**, 6301.

- Sparn, G., J.D. Thompson and A. Hamzic, 1992, *J. Alloys Compounds* **181**, 197.
- Sportouch, S., P. Larson, M. Bastea, P. Brazis, J. Ireland, C.R. Kannewurf, S.D. Mahanti, C. Uher and M.G. Kanatzidis, 1999, *Mater. Res. Soc. Symp. Proc.*, East Lansing, MI, p. 421.
- Suzuki, H., T. Yamaguchi, K. Katoh and M. Kasaya, 1993, *Physica B* **186-188**, 390.
- Suzuki, H., M. Kasaya, M. Kohgi, A. Dönni, P. Fischer, G. Le Bras and P. Bonville, 1995, *Physica B* **206&207**, 341.
- Suzuki, T., Y. Matsumoto, F. Masaki, K. Izawa, M. Ito, K. Katoh, T. Takabatake and T. Fujita, 1999, *Physica B* **259-261**, 146.
- Szytuła, A., 1991, in: *Handbook of Magnetic Materials*, Vol. 6, ed. K.H.J. Buschow (North-Holland, Amsterdam) ch. 2, p. 85.
- Szytuła, A., 1998, *Crystal Structures and Magnetic Properties of RTX Rare Earth Intermetallics* (Wydawnictwo Uniwersytetu Jagiellońskiego, Krakow).
- Szytuła, A., and J. Leciejewicz, 1989, in: *Handbook on the Physics and Chemistry of Rare Earths*, Vol. 12, eds K.A. Gschneidner Jr and L. Eyring (North-Holland, Amsterdam) p. 133.
- Szytuła, A., and J. Leciejewicz, 1994, *Handbook of Crystal Structures and Magnetic Properties of Rare Earth Intermetallics* (CRC Press, Boca Raton, FL).
- Takabatake, T., F. Teshima, H. Fujii, S. Nishigori, T. Suzuki, T. Fujita, Y. Yamaguchi and J. Sakurai, 1990, *J. Magn. Magn. Mater.* **90&91**, 474.
- Temmermann, W.M., Z. Szotek, A. Svane, P. Strange, H. Winter, A. Delin, B. Johansson, O. Eriksson, L. Fast and J.M. Wills, 1999, *Phys. Rev. Lett.* **83**, 3900.
- Thompson, J.D., P.C. Canfield, A. Lacerda, M.F. Hundley, Z. Fisk, H.R. Ott, E. Felder, M. Chernikov, M.B. Maple, P. Visani, C.L. Seaman, M.A. Lopez de la Torre and G. Aeppli, 1993, *Physica B* **186-188**, 355.
- Tien, Ch., J.T. Yu and H.-M. Duh, 1993, *Jpn. J. Appl. Phys.* **32**, 2658.
- Trovarelli, O., C. Geibel, R. Cardoso Gil, S. Mederle, R. Borth, B. Buschinger, F.M. Grosche, Y. Grin, G. Sparn and F. Steglich, 2000, *Phys. Rev. B* **61**, 9467.
- Tsokol', A.O., O.I. Bodak and E.P. Marusin, 1989, *Sov. Phys. Crystallogr.* **34**, 612.
- Tsvyashchenko, A.V., and L.N. Fomicheva, 1987a, *Inorg. Mater.* **23**, 1024.
- Tsvyashchenko, A.V., and L.N. Fomicheva, 1987b, *J. Less-Common Met.* **134**, L13.
- Tsvyashchenko, A.V., and L.N. Fomicheva, 1987c, *J. Less-Common Met.* **135**, L9.
- van Kalkeren, G., H. Van Nassou and F.R. de Boer, 1985, *J. Magn. Magn. Mater.* **47-48**, 105.
- Vigouroux, 1905, *C.R. Acad. Sci.* **144**, 639, 712.
- Villars, P., and L.D. Calvert, 1991, *Pearson's Handbook of Crystallographic Data for Intermetallic Compounds*, 2nd Ed. (American Society for Metals, Materials Park, OH). Desk edition, 1997.
- von Schnering, H.G., and W. Hönlle, 1994, *Phosphides: solid state chemistry*, in: *Encyclopedia of Inorganic Chemistry*, ed. R.B. King (Wiley, London).
- Wachter, P., 1994, *Intermediate valence and heavy fermions*, in: *Handbook on the Physics and Chemistry of Rare Earths*, Vol. 19, eds K.A. Gschneidner Jr and L. Eyring (North-Holland, Amsterdam) ch. 132.
- Wenski, G., and A. Mewis, 1986a, *Z. Kristallogr.* **176**, 125.
- Wenski, G., and A. Mewis, 1986b, *Z. Anorg. Allg. Chem.* **535**, 110.
- Yaouanc, A., P. Dalmas de Réotier, P.C.M. Gubbens, C.T. Kaiser, P. Bonville, J.A. Hodges, A. Amato, A. Schenck, P. Lejay, A.A. Menovsky and M. Mihalik, 1999, *Physica B* **259-261**, 126.
- Yarmolyuk, Ya.P., Yu.N. Grin and E.I. Gladyshevskii, 1979, *Dopov. Akad. Nauk URSR A* **41**, 772.
- Zanicchi, G., D. Mazzone, V. Contardi, R. Marazza, G. Rambaldi and D. Rossi, 1983, *Gazz. Chim. Ital.* **113**, 257.
- Zanicchi, G., D. Mazzone, M.L. Fornasini, P. Riani, R. Marazza and R. Ferro, 1999, *Intermetallics* **7**, 957.
- Zell, W., R. Pott, B. Roden and D. Wohlleben, 1981, *Solid State Commun.* **40**, 751.
- Ziegłowski, J., H. Häfner and D. Wohlleben, 1986, *Phys. Rev. Lett.* **56**, 193.
- Zumdick, M.F., and R. Pöttgen, 1999, *Z. Kristallogr.* **214**, 90.
- Zumdick, M.F., R.-D. Hoffmann and R. Pöttgen, 1999, *Z. Naturforsch.* **54b**, 45.

## Chapter 208

### PERMANENT MAGNETS

Kurima KOBAYASHI<sup>1</sup> and Satoshi HIROSAWA<sup>2</sup>

<sup>1</sup> Department of Materials Science, Shizuoka Institute of Science and Technology, 2200-2 Toyosawa, Fukuroi 437-8555, Japan; <sup>2</sup> Fundamental Research Section, Research and Development Division, Sumitomo Special Metals Industry Co., Ltd., 2-15-17 Egawa, Shimamoto-cho, Mishima-gun, Osaka-fu 618-0013, Japan

#### Contents

Acronyms and symbols	515	4.4. Reaction velocity	547
Introduction	516	5. Relation between corrosion and coercivity	548
1. Some aspects of fundamental research on rare-earth permanent magnetic materials	517	5.1. Improvement of coercivity and corrosion resistance in Nd <sub>2</sub> Fe <sub>14</sub> B-based magnets	548
1.1. General remarks	517	5.2. Some aspects of the corrosion mechanism in rare-earth magnets	552
1.2. Magneto-volume effects	520	6. Other preparation methods of industrial magnets	555
1.3. Band structure near the Fermi level	524	6.1. Hot-working and casting methods	555
2. Sintered magnets	526	6.2. Bonded magnets	556
3. HDDR process	530	7. Some typical studies using micromagnetic approaches	558
4. Nanocomposite permanent magnetic materials	537	References	561
4.1. Rapid solidification	538		
4.2. Mechanical alloying	540		
4.3. Exchange-coupled magnets	540		

#### Acronyms and symbols

AEI	Atomic exchange interaction (model)	LMTO	Linear muffin-tin orbital (method)
$(BH)_{\max}$	Energy production maximum of magnets	LSDF	Local spin-density functional (method)
$B_r$	Remanence (residual magnetization)	MQP-B	Melt-quenched powder (type B) (trademarked name)
CIP	Cold isostatic pressing	MRI	Magnetic resonance imaging
DOS	Density of states	SADP	Selected-area diffraction pattern
EDX	Energy dispersion X-ray (analysis)	TEM	Transmission electron microscope
EV	Electrical vehicle	3D-APM	Three-dimensional atom probe microanalysis
FEM	Finite-elements method	TM	Transition metals
$H_a$	Anisotropy fields	VCM	Voice-coil motor
$H_{cJ}$	Coercivity in $H$ - $J$ curves ( $J$ , polarization)	XMCD	X-ray magnetic circular dichroism
HD	Hydrogenation-disproportionation		
HDDR	Hydrogenation disproportionation desorption recombination		

## Introduction

Rare-earth permanent magnets are mainly composed of rare-earth and transition-metal elements. The first industrial rare-earth magnets of SmCo<sub>5</sub>-type were proposed and investigated at the end of the 1960s, and the production on industrial scale started in the early 1970s (Strnat 1976, 1988). These magnets are produced by a metallurgical method: powder production, compaction, sintering, post-sintering heat treatment, and machining.

Following this, the next industrially successful rare-earth magnet, the "2-17" type, was developed from the same Sm-Co system (Strnat 1988). There are several good review papers on these magnets (Kumar 1984, Strnat and Strnat 1991).

In the early 1980s, the new Nd<sub>2</sub>Fe<sub>14</sub>B-type magnet was invented by two groups (Croat et al. 1984, Sagawa et al. 1984a). This magnet was initially prepared in the following two ways: sintering of powders by metallurgical techniques, and melt-spinning and/or liquid quenching. The crystal structure of this magnet appears only in the B(boron)-Nd-Fe ternary system, and is never observed in the pure Nd-Fe binary system. These initial, different methods of preparation were separately developed, and resulted in the fruitful development of high-energy sintered magnets and nanostructural magnetic materials.

Other interesting materials in the rare-earth family of magnets have Th<sub>2</sub>Zn<sub>17</sub>- and ThMn<sub>12</sub>-type structures (Coey and Sun 1990, Fujii et al. 1992, de Mooij and Buschow 1988). These materials contain nitrogen (e.g. Sm<sub>2</sub>Fe<sub>17</sub>N<sub>3</sub>, Nd(Fe,Ti)<sub>12</sub>N) and/or carbon (e.g. Sm<sub>2</sub>Fe<sub>17</sub>C<sub>x</sub>) in their structures. Review papers about these interstitially modified materials have appeared in many scientific magazines and books (Fujii and Sun 1995).

In this review, we will point out some basic aspects which are of great relevance to the understanding of the effects of the third elements in these materials, such as B in Nd-Fe-B magnets and N and/or C in Sm<sub>2</sub>Fe<sub>17</sub>N<sub>3</sub> and Sm<sub>2</sub>Fe<sub>17</sub>C<sub>x</sub> magnets.

Various methods of preparation of the magnets have been developed, such as ordinary powder-metallurgical sintering, melt spinning, mechanical alloying, hot working, and the hydrogenation disproportionation desorption recombination (HDDR) process. In each method of preparation, the development of magnetic properties is achieved by changing the microstructure, grain boundary structure and intrinsic magnetic properties of the materials. For example, the SmFe<sub>7</sub>-N<sub>x</sub> phase can be stabilized in the intermediate steps of the reactions by mechanical alloying and/or melt spinning (Yamamoto et al. 1996, Sakurada et al. 1997). Therefore this phase has been the subject of much interest in fundamental and application studies.

The methods of preparation revealed many interesting points in terms of materials science. The development in each method will be summarized and some future tasks will be pointed out in this review.

As is the case for the Sm-Co system (Strnat 1988), some additives, such as Co, Ga, Zr, and the heavy lanthanide elements, strongly affect the magnetic properties of Nd-Fe-B and Sm-Fe-N or Sm-Fe-C magnets. The effects come from changes in intrinsic magnetic properties such as magnetic anisotropy, polarization, Curie temperature; microstructural changes such as depression of grain growth; and formation of secondary phases at grain boundaries. Analysis of the effects yields a deeper understanding of the

magnetic properties of rare-earth magnets (Fidler et al. 1994). The studies of the effects of additives, therefore, are important research tasks which will be discussed in this review.

Another interesting development is the appearance of exchange-coupled magnets, which are composed of fine hard and soft magnetic phases of some 10 nanometers (nm) in diameter. The idea underlying this magnet is the quantum-mechanical interaction between nanometer-size magnetic phases (Kneller and Hawig 1991). In the Nd-Fe-B system, the interactions between the  $\text{Nd}_2\text{Fe}_{14}\text{B}$  phase and the  $\text{Fe}_3\text{B}$  phase (Coehoorn et al. 1988) or the  $\alpha$ -Fe phase (Manaf et al. 1991) were investigated. For  $\text{Sm}_2\text{Fe}_{17}\text{N}_x$ , the interaction between the  $\text{Sm}_2\text{Fe}_{17}\text{N}_x$  phase and  $\alpha$ -Fe was initially studied by Ding et al. (1993). A more recent study based on  $\text{Sm}_2\text{Fe}_{15}\text{Ga}_2\text{C}_x$  magnets has fundamentally the same direction of motivation (van Lier et al. 1999).

These exchange-coupled magnets which are based on long-range quantum effects, are of interest as mesoscopic phenomena in a number of physicochemical fields. The principle of these magnets merits further fundamental and applied studies on the appearance of a new type of long-range order in ferromagnetic materials.

In this review, we will discuss some aspects in each active field of research on these magnets. Our intention is to summarize the fundamental ideas of the development of research in each field mentioned above, and to point out some important results which were recently obtained.

## **1. Some aspects of fundamental research on rare-earth permanent magnetic materials**

### *1.1. General remarks*

The most obvious characteristic of the rare-earth magnets is that these compounds are fundamentally metallic alloys between rare earths and transition metals. A recent trend in the development of rare-earth permanent magnets is the use of a third element, such as B in  $\text{Nd}_2\text{Fe}_{14}\text{B}$  and N in  $\text{Sm}_2\text{Fe}_{17}\text{N}_3$ .

After the invention of  $\text{Nd}_2\text{Fe}_{14}\text{B}$ , some researchers theoretically studied the relation between electronic and magnetic structures of the material. They used the point-charge model (Cadogan and Coey 1984, Yamada et al. 1987), simplified empirical methods for calculation of the density of states (DOS) (Inoue and Shimizu 1986), and first-principles band-structure calculation (Gu and Ching 1987). They tried to explain spin reorientation and other magnetic properties of the  $\text{Nd}_2\text{Fe}_{14}\text{B}$  magnet. More recently, the fundamental understanding of the magnetic properties of the alloys and compounds was extended by the use of the local spin-density functional (LSDF) method and the linear muffin-tin orbital (LMTO) method (Kanamori 1990, Coehoorn 1991, Jaswal 1992). The role of the third element, however, has not been fully explained by the theoretical analyses of the band structure of the magnetic compounds. Some aspects concerning this point will be discussed in the present section.

Franse and Radwanski (1996) have reviewed the experimental efforts towards understanding the fundamental properties of the rare-earth transition-metal compounds.

The rare-earth permanent magnets were born by combining the high magnetization of the transition-metal sublattice with the high crystalline anisotropy of the lanthanide



sublattice. The characteristics of these sublattices, however, are obviously different. The properties of transition metals, especially magnetic properties, mainly come from 3d-band electrons directly contributing to the band structure near the Fermi level, with 4s and 4p electrons in the conduction bands: for example the sp and/or spd bands.

On the other hand, the magnetic properties of the lanthanide sublattice are governed by 4f electrons in the inner orbitals. The 4f electrons have little effect on the band structure of the crystals, since their narrow width,  $\sim 0.1$  eV, means their interaction with the neighboring atoms is weak.

Since some properties of each sublattice, especially the anisotropy of the lanthanide sublattice, as experimentally established, govern the behavior of the whole crystal of the magnet, the magnetic properties of the lanthanide sublattice will affect the sublattice of the transition metals, i.e., interactions between sublattices exist. The 4f electrons, however, have almost no direct bonds with the 3d electrons of the transition-metal sublattice, so the anisotropy of the 4f electrons initially transfers to the outer orbitals of 6s, 5d and/or 6p electrons of the lanthanide atoms, and these in turn interact with 4s and/or 4d electrons of the transition-metal sublattice, which is composed of sp and/or spd bands with the transition metal's 3d electrons. The interactions between the 4f and 3d electrons, therefore, are indirect. Figure 1a schematically shows the band structure in the lanthanide-transition-metal compounds.

From a theoretical point of view, the 3d electrons and the 4f electrons independently show some important characteristics, such as the Kondo effect and heavy-fermion behavior. The properties of the electrons have been studied by many researchers. A theoretical analysis of the electrons, however, in a physical sense, is still insufficient for explaining the magnetic properties of lanthanide-transition-metal magnets. The difficulties mainly come from the complexity of the mixture of the 3d and 4f electrons and of the interactions among them in these materials.

As mentioned above, recent developments in permanent magnets are due to the use of third elements for controlling the magnetic properties of the alloys. The third elements, such as B in  $\text{Nd}_2\text{Fe}_{14}\text{B}$ , and N and/or C in  $\text{Sm}_2\text{Fe}_{17}\text{N}_x(-\text{C}_y)$  are used to modify the magnetic properties of the compounds, through the appearance of a new phase in  $\text{Nd}_2\text{Fe}_{14}\text{B}$  (Herbst et al. 1984), and mainly through lattice expansion of the starting structure of the  $\text{Th}_2\text{Zn}_{17}$ -type phase, without structural change upon introduction of the third element, in  $\text{Sm}_2\text{Fe}_{17}\text{N}_x$  and  $\text{Sm}_2\text{Fe}_{17}\text{C}_y$ .

We present a summary of the resulting compounds containing a third element, and their simplified characteristics as the materials for permanent magnets, in table 1. We also show, in fig. 1b, a schematic representation of the band structure of lanthanide-transition-metal alloys containing a third element.

The roles of B in  $\text{Nd}_2\text{Fe}_{14}\text{B}$  magnets and N in  $\text{Sm}_2\text{Fe}_{17}\text{N}_x$  magnets have been understood from two main points of view. The first point is the modification of the band structure by the formation of bands between 2p electrons of the third element and the 4s, 3d and/or 4p electrons of the transition metal, as shown in fig. 1b. Concerning this point, we show in fig. 2 a schematic representation of the relation between energy ( $E$ ) and density of states (DOS) in  $\text{Y}_2\text{Fe}_{17}(-\text{N}_3)$  systems, which was initially calculated and then presented

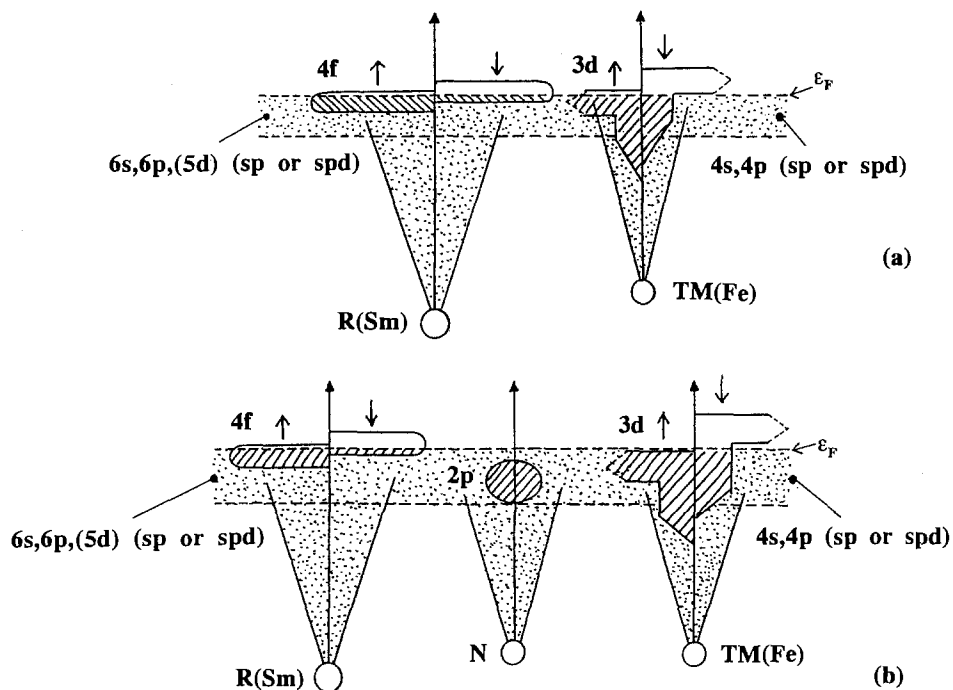


Fig. 1. Schematic presentation of band structures of (a) lanthanide-transition-metal (3d-4f) compounds, and (b) compounds including light elements having 2p electrons.

Table 1  
Materials for rare-earth permanent magnets and their typical properties

Alloy	H	B	C	N	O
SmCo <sub>5</sub> , Sm <sub>2</sub> Co <sub>17</sub>	Sm <sub>2</sub> Fe <sub>17</sub> H <sub>x</sub>	Nd <sub>2</sub> Fe <sub>14</sub> B, Pr <sub>2</sub> Fe <sub>14</sub> B	Sm <sub>2</sub> Fe <sub>17</sub> C <sub>y</sub>	Sm <sub>2</sub> Fe <sub>17</sub> N <sub>z</sub>	Ferrites
Sinterable	<550 K(?)	Sinterable	Sinterable(?)	<800 K(?)	Sinterable
Metallic (+additives)	x: 0-6 (?) Interstitial	B=1 New phase (+additives)	y=1 (SSR) <sup>a</sup> y > 1 (Gas R) <sup>b</sup> Interstitial	z: 0-4 (?) z=3 (stable?) Interstitial	Oxide

<sup>a</sup> SSR, Solid state reaction.

<sup>b</sup> Gas R, Gas reaction.

by Jaswal et al. (1991) as an explanation for the effects of the 2p electrons of the third element on the band structure of the material. The change of band structure and DOS near the Fermi level is the origin of the enhancement of magnetization and Curie temperature.

The second point is the magneto-volume effect. The volume of the unit cell is expanded by the insertion of a third element, and the expansion yields an increase of the interatomic

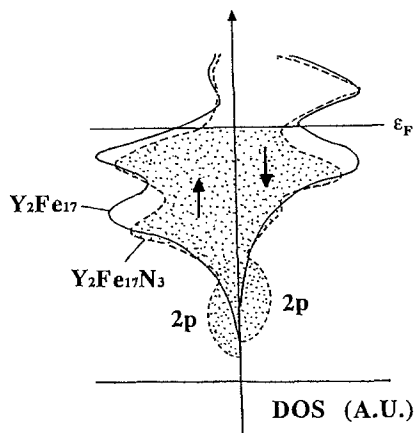


Fig. 2. Schematic presentation of the density of states (DOS) of the  $Y_2Fe_{17}$  and  $Y_2Fe_{17}N_3$  compounds (Jaswal et al. 1991).

distances of Fe–Fe pairs. These structural changes also affect the band structure of the materials. This effect is also included in the calculation of DOS vs.  $E$  shown in fig. 2.

Magnets based on the Nd–Fe–B system are basically metallic, and they are prepared by metallurgical techniques. The technique for introducing boron atoms into the structure is basically that of alloy making. Except for second-phase formation, the boron atoms naturally find their sites in the crystal structure during the formation of the 2-14-1 phase as a result of thermodynamic stability.

The magnets of Sm–Fe–X ( $X=C, N$ ) compounds having  $Th_2Zn_{17}$  crystal structure, however, are prepared by gas–solid reactions. The third element is gradually introduced into specific sites in the crystal by a bulk diffusion process. In the 2-17 structure, when hydrogen ( $X=H$ ) is introduced, the H atoms exist in both interstitial 9e and 18g sites in the structure; in the cases of C and N, the atoms mainly occupy the 9e site, with a small fraction in the 18g site as shown in some neutron diffraction studies (Jaswal 1992, Isnard et al. 1992, Kajitani et al. 1993).

In the  $Sm_2Fe_{17}N_x(-C_y)$  compounds, the situation for theoretical and experimental investigations of the effects of the third element are simpler than in the case of  $Nd_2Fe_{14}B$ . This simplicity stems from the fact that the basic structure of  $Sm_2Fe_{17}$  is stable, which makes it possible to compare the electronic and magnetic properties of the parent phase with those of the nitrogen- and/or carbon-doped hard magnetic phase (Jaswal et al. 1991, Jaswal 1992).

Many important conclusions of the calculations can be found in the original papers quoted. In the following sections, therefore, we will discuss a few interesting points concerning the effects of the third element on the magnetic properties of the lanthanide–transition-metal magnets.

### 1.2. Magneto-volume effects

The crystal structures of Sm–Co and Sm–Fe–X ( $X=N, C$ ) compounds of the lanthanide permanent magnets are based on the  $CaCu_5$  structure.  $SmCo_5$  has this structure, and the

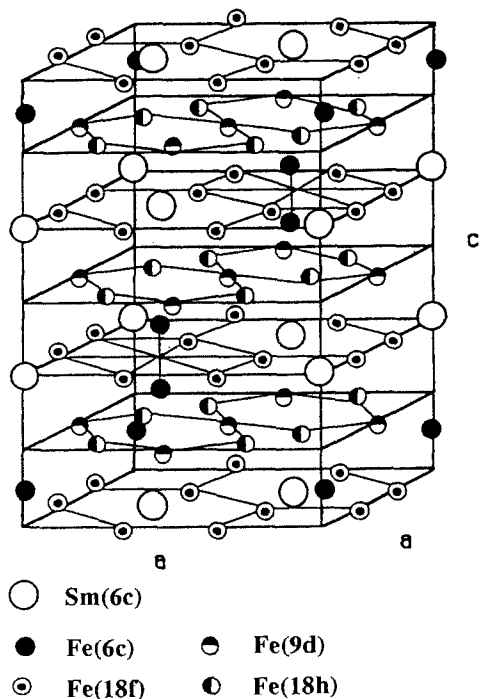


Fig. 3. Schematic presentation of  $\text{Th}_2\text{Fe}_{17}$  crystal structure (Coe 1996).

2-17-type structures in Sm–Co and Sm–Fe–X systems, which can be categorized into  $\text{Th}_2\text{Zn}_{17}$  and  $\text{Th}_2\text{Ni}_{17}$  structures, have a structure in which a half of the lanthanide sites are substituted by so-called Fe–Fe dumbbell pairs. The structure of  $\text{Sm}_2\text{Fe}_{17}\text{N}_x$  ( $x=0-3$ ) compounds is also of this type (Buschow et al. 1990, Miraglia et al. 1991).

Figure 3 schematically shows the  $\text{Th}_2\text{Zn}_{17}$  crystal structure (Coe 1996). The unit cell of this structure consists of 3 units of  $\text{Sm}_2\text{Fe}_{17}\text{N}_3$  composition ( $Z=3$ ). There is only one site, 6c, for the Sm atoms; and 4 sites, 6c, 9d, 18f and 18h, for the Fe atoms.

The structure is composed of 2 types of planes perpendicular to the  $c$ -axis. One plane is composed of Sm, Fe, and the nitrogens in 9e sites. The 9e sites lie between the 6-fold local structure of Fe atoms in this plane. The second plane is composed only of Fe atoms. If nitrogen occupies the 18g sites, it exists in this plane. The results of neutron diffraction studies revealed that only 5–10% of the nitrogen atoms occupy these 18g sites (Miraglia et al. 1991, Jaswal 1992, Isnard et al. 1992, Kajitani et al. 1993).

As to the origin of the enhancement of the magnetic properties in  $\text{Sm}_2\text{Fe}_{17}\text{N}_3$  compared to  $\text{Sm}_2\text{Fe}_{17}$ , magneto-volume effects, i.e. changing Fe–Fe interatomic distances, are thought to be the main reason. Magneto-volume effects have been theoretically explained, for Fe by Moruzzi et al. (1986), and for other compounds, including the 2-17 structure, by Coehoorn (1991).

Figure 4a shows the calculated dependence of magnetic moments on Wigner–Seitz cell volume in bcc-Fe (Moruzzi et al. 1986); the cross (×) denotes the moment at

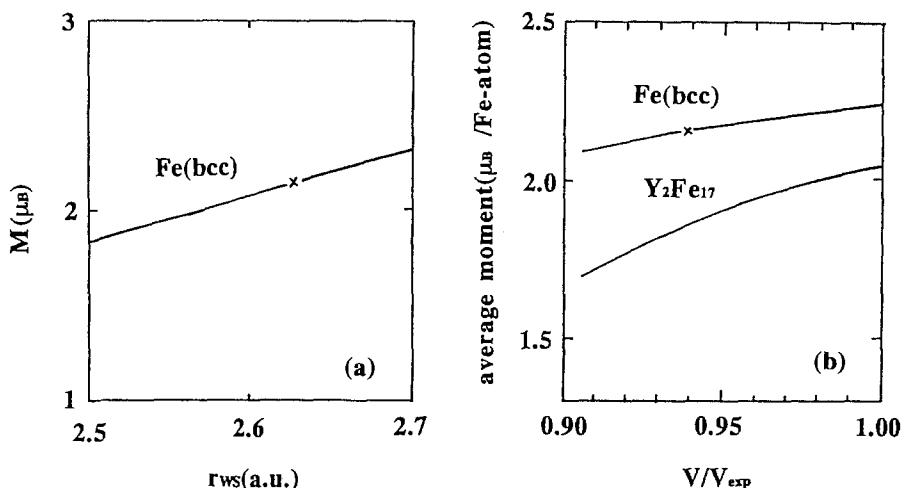


Fig. 4. Relations between magnetic moments and Wigner-Seitz radius for bcc-Fe (Moruzzi et al. 1986), and specific volumes of bcc-Fe and  $Y_2Fe_{17}$  compounds (Coehoorn 1991).

zero pressure. It is obvious that the moment increases with increasing cell volume. The local-spin-density approximation was used in the calculation.

Coehoorn (1991) used a similar method to calculate electronic structures of rare-earth-transition-metal compounds. Figure 4b shows schematic representations of his calculation of the dependence of the average magnetic moment on cell volume in bcc-Fe and  $Y_2Fe_{17}$ . In the case of yttrium-iron compounds, we can estimate the volume dependence of the magnetic properties of the Fe sublattice because of the lack of 4f electrons at rare-earth sites. The cross denotes the moment at the equilibrium volume.

These calculations reveal that the magneto-volume effect exists in bcc-Fe and in the  $Y_2Fe_{17}$  structure, which can be used as an adequate model for the  $Sm_2Fe_{17}$  phase. Since there is a volume expansion of about 7% after nitrogenation of the starting  $Sm_2Fe_{17}$  alloy, the magneto-volume effect should be the origin of the enhancement of the magnetic properties by introduction of a third element into lanthanide-transition-metal systems.

We also estimate that the volume effect directly corresponds to changing Fe-Fe interatomic distances in the structures. When we examine the details of crystal structure analyses of the systems, however, it is not always true that the Fe-Fe interatomic distances increase upon introduction of a third element into the structures.

In the case of  $Sm_2Fe_{17}N_3$ , it is obvious that introduction of nitrogens into 9e sites results in an increase of cell volume. According to the neutron diffraction study by Koyama et al. (1997), however, the interatomic distances between the Fe(6c) and Fe(18f) sites *decrease* with increasing nitrogen concentration in the case of nitrogenation of  $Y_2Fe_{17}$  and  $Y_2Fe_{17}N_3$ . They obtained lattice constants  $a = 8.5003(1) \text{ \AA}$  and  $c = 12.4294(1) \text{ \AA}$  for the  $Y_2Fe_{17}$  phase, and  $a = 8.6710(3) \text{ \AA}$  and  $c = 12.7241(4) \text{ \AA}$  for the  $Y_2Fe_{17}N_3$  phase. These lattice parameters are similar to the values reported for  $Sm_2Fe_{17}$  and  $Sm_2Fe_{17}N_3$ . They

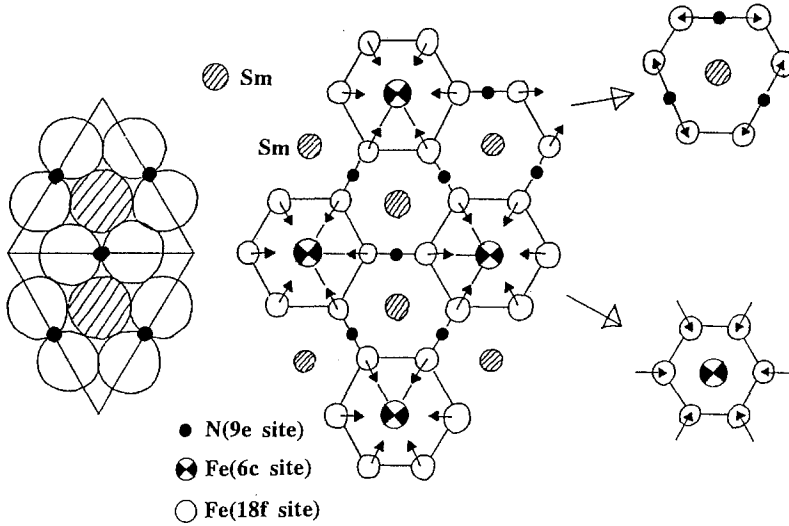


Fig. 5. Schematic presentation of local shrinkage and expansion in the *c*-plane of  $\text{Th}_2\text{Fe}_{17}$  crystal structure with introduction of nitrogen atoms.

also calculated the distances between Fe(6c) (dumbbell) and Fe(18f), which are neighbors of the nitrogen atoms introduced into 9e sites. The following results were obtained:

$$d(6c-18f) = \begin{cases} 2.7801 \text{ \AA} & \text{for } \text{Y}_2\text{Fe}_{17}, \\ 2.7349 \text{ \AA} & \text{for } \text{Y}_2\text{Fe}_{17}\text{N}_3. \end{cases}$$

The distances between Fe(18f) sites are

$$d(18f-18f)_a = \begin{cases} 2.5110 \text{ \AA} & \text{for } \text{Y}_2\text{Fe}_{17}, \\ 2.4539 \text{ \AA} & \text{for } \text{Y}_2\text{Fe}_{17}\text{N}_3, \end{cases} \quad d(18f-18f)_b = \begin{cases} 3.4765 \text{ \AA} & \text{for } \text{Y}_2\text{Fe}_{17}, \\ 3.7648 \text{ \AA} & \text{for } \text{Y}_2\text{Fe}_{17}\text{N}_3. \end{cases}$$

After introduction of nitrogen into 9e sites, there are two different distances between Fe(18f) sites. The former distance is shorter than the latter, where the nitrogen atom occupies a site between the Fe atoms. As shown, some iron interatomic distances shrink by the introduction of nitrogen into 9e sites, and this can be physically understood by examination of fig. 5. The distances between Fe(6c) and Fe(9d), and also between Fe(6c) and Fe(18h), increase:

$$d(6c-9d) = \begin{cases} 2.6072 \text{ \AA} & \text{for } \text{Y}_2\text{Fe}_{17}, \\ 2.6653 \text{ \AA} & \text{for } \text{Y}_2\text{Fe}_{17}\text{N}_3, \end{cases} \quad d(6c-18h) = \begin{cases} 2.6394 \text{ \AA} & \text{for } (\text{Y}_2\text{Fe}_{17}), \\ 2.6816 \text{ \AA} & \text{for } (\text{Y}_2\text{Fe}_{17}\text{N}_3) \end{cases}$$

With these results, we can image a kind of Wigner-Seitz (W-S) cell which has Fe(6c) at its center surrounded by six Fe(18f), one Fe(6c), three Fe(9d) and three Fe(18h), as shown in fig. 6a.

The volume change of the W-S cell by the nitrogenation can be calculated from the interatomic distances given in the paper by Koyama et al. (1997) using the model

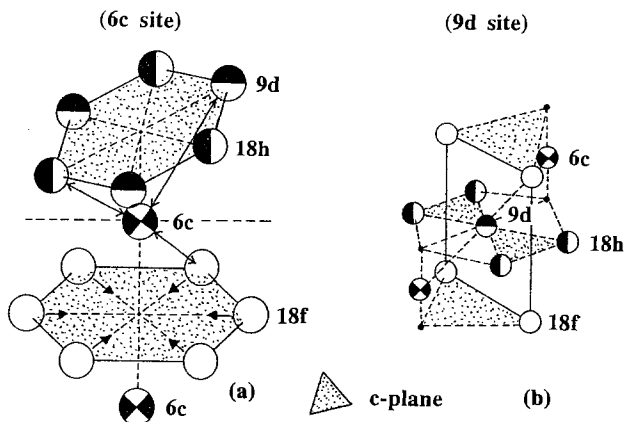


Fig. 6. Simplified Wigner-Seitz cells for (a) Fe(6c) site and (b) Fe(9d) site.

presented in fig. 6a. The volume of the W-S sphere after nitrogen introduction is slightly larger than that of the W-S cell before, because the shrinkage of the Fe-Fe distances in the  $c$ -plane is compensated for by the expansion in the  $c$ -axis direction, i.e.  $\Delta V = 0.76\%$ . This value is smaller than that,  $\Delta V > 4\%$ , for a similar W-S sphere with the Fe(9d) atom at the center, surrounded by the Fe(18h), Fe(18f) and Fe(6c) atoms, as shown in fig. 6b.

On the other hand, the magnetic moments determined by neutron diffraction at 10 K (Koyama et al. 1997) show a 28.2% increase of the moment at the 6c sites [ $2.23(5)\mu_B$  ( $Y_2Fe_{17}$ ) to  $2.86(5)\mu_B$  ( $Y_2Fe_{17}N_3$ )] and a 12.8% increase at the 9d sites [ $1.88(6)\mu_B$  ( $Y_2Fe_{17}$ ) to  $2.12(8)\mu_B$  ( $Y_2Fe_{17}N_3$ )].

With respect to the other two sites in the structure, it is difficult to evaluate the effects which come from nitrogen atoms occupying the nearest-neighbor sites: Fe(18h) and Fe(18f). However, we can conclude that it is difficult to explain the increase in the magnetic moments at the Fe(6c) and Fe(9d) sites by magneto-volume effects.

To investigate the details of the phenomena mentioned above, we must refer to another discussion, based on the change of band structure induced by the existence of a third element in the structure, for example, by Kanamori (1990).

### 1.3. Band structure near the Fermi level

The discussion in this subsection will be based on the band structure of the lanthanide-transition-metal compounds as shown schematically in figs. 1a,b. If we think about the effect of the anisotropy of the inner 4f electrons of the lanthanides (Sm or Nd) on the Fe sublattices, the 4f electrons should initially transfer their characteristics to 5d, 6s and 6p band electrons of the lanthanide atom, which in turn will transfer the information to 4s, 4p and 3d electrons of the Fe atoms, finally affecting the magnetic properties, for example the crystalline anisotropy, of the entire crystal.

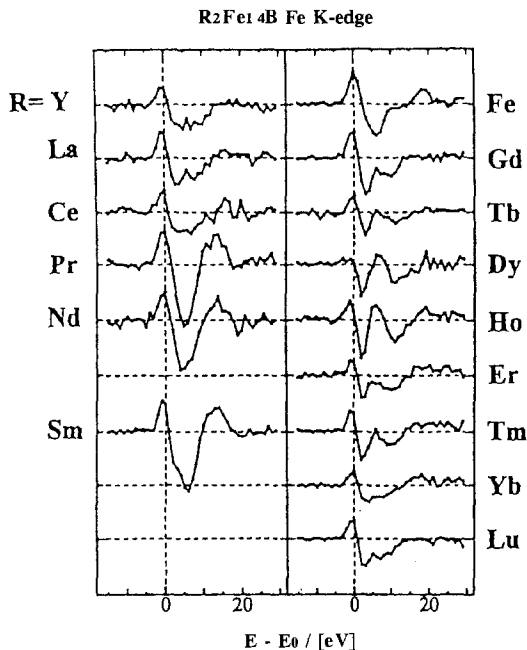


Fig. 7. Fe K-edge XMCD spectrum in the  $R_2Fe_{14}B$  compounds compared with Fe metal (Chaboy et al. 1997).

When nitrogen atoms are introduced into the structure, the 2p electrons of nitrogen generate new states in the band structure of the newly prepared phase of  $Sm_2Fe_{17}N_3$  composition, as shown in fig. 2. The nitrogens form bands with Fe sublattices, causing the shape of the density of states (DOS) to change from the so-called weak ferromagnetic type to the strong ferromagnetic type.

This point was experimentally studied in the band structure of  $Nd_2Fe_{14}B$ . Recently, Chaboy et al. (1997) and Maruyama (1998) investigated and discussed the band structures of the  $R_2Fe_{14}B$  series of compounds using X-ray magnetic circular dichroism (XMCD), see the data presented in figs. 7 and 8. They used Fe K-edge absorption, and determined the band structures near the Fermi level in the  $R_2Fe_{14}B$  series of compounds.

Figure 7 presents the Fe K-edge absorption spectra of the series of  $R_2Fe_{14}B$  compounds. The absorption corresponds to the  $E1$  spectrum of the  $Fe(1s) \rightarrow Fe(4p)$  transition. Maruyama (1998) was interested in the peaks at  $(E - E_0)$  of about 6 eV, and noted the following points: (1) in the cases of  $R = Y, La, Ce, Yb$  and  $Lu$ , the XMCD spectra are fundamentally the same as for pure Fe; (2) for  $R = Pr, Nd$  and  $Sm$ , the spectra largely increase toward the negative direction; and (3) for  $R = Gd, Tb, Dy, Ho, Er$  and  $Tm$ , the spectra shift in the positive direction.

The variation in the spectra from different lanthanide elements corresponds to the difference in the polarization of the 4p-conduction bands of Fe in the structures. The authors treated the spectra by subtracting the spectrum of the  $Y_2Fe_{14}B$  compound [which should correspond to the direct contribution from only the Fe sublattice] from the observed



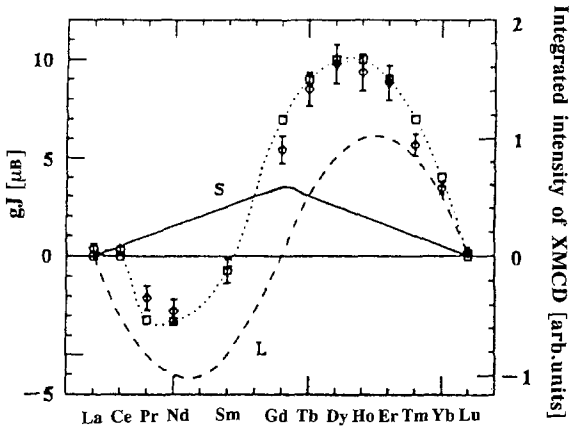


Fig. 8. Comparison between R 4f magnetic moments (open squares) and Fe K-edge integrated XMCD signal (diamonds) for  $R_2Fe_{14}B$  compounds (Maruyama 1998).

individual  $R_2Fe_{14}B$  spectra. As a conclusion, they found that the shape of Fe K-edge integrated XMCD signals, in arbitrary units, almost agrees with the 4f-electron magnetic moments of the rare-earth elements, as shown in fig. 8.

They suggest that a strong correlation exists between the 4p electrons in Fe and the 4f electrons in the lanthanide. The relation should emerge from the interaction  $4p(Fe) \rightarrow 5d(R) \rightarrow 4f(R)$ .

They also studied the lanthanide L-edge absorption, which corresponds to the E1 transition of  $R(2p) \rightarrow R(5d)$  in the lanthanide elements, to examine the 5d bands in the  $R_2Fe_{14}B$  compounds. The results were complex due to ferro- or antiferromagnetic alignment ( $L$ - $S$  coupling of the  $R \leftrightarrow Fe$  moments) of the magnetic moments of the lanthanide elements in the structure (Chaboy et al. 1997). This complexity was explained by a shrinkage of the wave functions of the 5d orbitals (König et al. 1994). Thus, we are now ready to discuss the observed spectra concerning the interaction of  $4p(Fe) \leftrightarrow 5d(R) \leftrightarrow 4f(R)$  electrons.

Experimental studies of the band structure in lanthanide permanent magnets, therefore, must be continued, and should help to solve the complex interactions of the 3d and 4f electrons through other bands. A clearer understanding of the physics of lanthanide magnets should be achieved by these studies.

## 2. Sintered magnets

Sintered magnets based on the  $Nd_2Fe_{14}B$  phase are the most important material for industrial magnetic applications. The most important applications are voice-coil motors (VCM) for hard disk drives, CD/MD pick-up systems, magnetic resonance imaging (MRI), and more recently motors for the electrical vehicle (EV) (Hirosawa and Kaneko 1998).

Sagawa et al. (1987) prepared the first high-energy-product magnets using  $Nd_2Fe_{14}B$  phase, which had a  $(BH)_{max}$  of  $405 \text{ kJ/m}^3$ . They controlled mainly the oxygen content of the sintered magnets to be less than 1500 ppm. Otsuki et al. (1990) developed a technique of mixing stoichiometric  $Nd_2Fe_{14}B$  powder with a Nd-rich alloy powder prepared by

melt spinning, and achieved  $416 \text{ kJ/m}^3$ . Kaneko and Ishigaki (1994) found that the size distribution of the starting powders and the method of applying the aligning magnetic field were important, and succeeded in preparing a magnet with an energy product of  $431 \text{ kJ/m}^3$ . Kaneko et al. (1999) achieved the latest record of  $444 \text{ kJ/m}^3$ , by preparing particles of about  $5 \mu\text{m}$  average grain size by a sophisticated pulverization method, surface treatment of the starting powder, and an increase of the orientation up to about 98% using a cold isostatic pressing (CIP) technique.

For higher energy products, the volume fraction of main phase of  $\text{Nd}_2\text{Fe}_{14}\text{B}$  ( $\phi$ ) in the sintered bodies should be as large as possible. The Nd-rich phase, however, is necessary for liquid-phase sintering which is important in order to realize high density magnets. It surrounds the main  $\phi$ -phase in the sintering process, and appears to have a strong correlation with the coercivity in the magnets (Sagawa et al. 1984b, Fidler et al. 1991).

The Nd-rich phase is highly reactive with oxygen which is introduced during processing of the magnets. The amount of Nd-rich phase necessary for sintering of the higher-density magnets, therefore, has a clear relation with the amount of  $\text{Nd}_2\text{O}_3$  phase formed after the sintering process. An important factor for the preparation of high energy products exceeding  $400 \text{ kJ/m}^3$ , which have recently been realized, is the development of a distribution method for the Nd-rich phase in the magnets (Otsuki et al. 1990).

Other important factors for the preparation of high-energy sintered magnets are particle-size distribution and alignment of the particles in sintered bodies. The effects of the former factor were clearly indicated by Kaneko and Ishigaki (1994) and Kaneko et al. (1999), and the development of the latter factor was discussed, including new methods of alignment, by Endoh and Shindoh (1994) and Sagawa and Nagata (1993).

As to intrinsic properties of the  $\text{Nd}_2\text{Fe}_{14}\text{B}$  phase, important issues are improvement of the Curie temperature of 586 K, and of the corrosion resistance. Another important task for industrial applications is controlling the coercivity. These problems are gradually being solved by the use of additives to the magnets. The relation between corrosion resistance and coercivity will be discussed in sect. 6.

For raising the Curie temperature, Co is added to substitute partially for Fe (Sagawa et al. 1984b). Cobalt, however, reacts with Nd to form a paramagnetic Nd-Co ( $\text{Nd}_3\text{Co}$ ) phase at grain boundaries, which deteriorates the obtainable maximum flux density. However, the addition of Co does increase the corrosion resistance of the magnets (Fidler et al. 1991, 1994).

Another important additive is Dy, which partially substitutes for Nd. Dy increases the intrinsic magnetic anisotropy of  $\text{Nd}_2\text{Fe}_{14}\text{B}$ , which means increasing the coercivity. However, since the magnetic moments of Dy are anti-parallel with those of Nd, the magnetization of the  $\phi$ -phase decreases with increasing Dy content.

As is the case for Sm-Co magnets, there are some other additives for improving magnetic properties of the magnets: Cu, Nb, Ga, V, Mo and so on. The role of each additive was discussed, for example, by Fidler et al. (1991, 1994). They distinguished two groups of dopants as follows:

Type 1 : Al, Cu, Zn, Ga, Ge, Sn;      Type 2 : Ti, Zr, V, Mo, Nb, W.

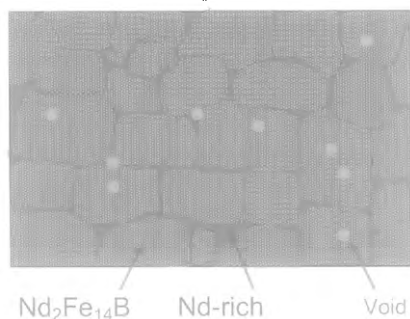


Fig. 9. Schematic of the microstructure of a real sintered Nd-Fe-B magnet: large grains create large stray fields; incomplete magnetic separation by grain boundaries.

Type-1 additives (M1) form binary M1-Nd phases and ternary M1-Fe-Nd phases, i.e.  $\text{Nd}_3(\text{Ga,Fe})$ ,  $\text{Nd}_5(\text{Ga,Fe})_3$ ,  $\text{NdCu}$ ,  $\text{NdCu}_2$ , and  $\text{Nd}_6\text{Fe}_3\text{M1}$ , where  $\text{M1} = \text{Al, Ga, Cu}$ . These additives mainly form intermetallic compounds with Nd at the grain boundaries; magnetically, the phases yield better separation and decoupling of the grains which leads to an enhancement of the coercivity of the magnets, and also an improvement of the corrosion resistance.

Type-2 additives (M2) have low-solubility in the hard magnetic phase, and form precipitates in the main phase and at grain boundaries. For example, they form  $(\text{V,Fe})_3\text{B}_2$ ,  $(\text{Mo,Fe})_3\text{B}_2$ ,  $\text{NbFeB}$  and  $\text{WFeB}$  phases. These phases also improve corrosion resistance.

Here, we will discuss two cases to show the effects of additives. When V are added to the  $\text{Nd}_2(\text{Fe,Co})_{14}\text{B}$  phase, the alloying agent reduces grain growth, and the average grain size is about half of that in normal sintered bodies without additives. They cause the disappearance of the  $\text{Nd}_{1.1}\text{Fe}_4\text{B}_4$  phase by the formation of  $(\text{Fe,M2})_3\text{B}_2$  (Hirosawa 1992). These borides appear at grain boundaries, which reduce the grain growth of the main phase. As a result of the V and Mo additions, the Co content in the magnets can be increased up to about 5 at. %.

Fidler et al. (1991, 1994) discussed the combined effects of type-1 and type-2 additives, such as (Ga,Nb)- and (Cu,Nb)- dopants, on the magnetic properties. A small amount of Cu and/or Ga addition is effective in increasing the coercivity (Kim and Camp 1996). However, these additives assist in the formation of the  $\alpha$ -Fe phase. On the other hand, Nb prevents the formation of the  $\alpha$ -Fe phase. The combinations, therefore, yield an attractive microstructure as sintered magnets.

The effects of additives on the properties of sintered Nd-Fe-B magnets, and ideas for optimizing the magnetic properties, are discussed next.

In fig. 9 we show schematically the microstructure of a typical sintered Nd-Fe-B permanent magnet, which consists of the main  $[\text{Nd}_2\text{Fe}_{14}\text{B} (\phi)]$  phase, the grain-boundary phase (a Nd-rich phase), and microstructural defects such as voids. The  $\phi$ -phase mainly gives rise to the magnetization and determines Curie temperature of the magnets. The effects of additives on the intrinsic properties of the  $\phi$ -phase is obvious. Co substitution for Fe raises the Curie temperature. The saturation magnetization, however, does not increase, although that would be expected from our general knowledge about the Slater-Pauling curve for Fe-Co alloys.

Moreover, from an industrial view point, the amount of Co addition is limited to about 5 at.%, because if the Co concentration exceeds this value, the coercivity of the magnet decreases, even if other alloying agents such as V and Mo are added.

Another important and obvious additive is Dy, which results in an increase of anisotropy (i.e. coercivity) by replacing Nd and enhancing  $H_{cJ}$ . However, the magnetization of the magnets decreases with increasing Dy content. Commercially, the cost-performance of Dy addition is limited by the high price of Dy metal.

The grain size of the  $\phi$ -phase in the sintered magnets is normally about 10  $\mu\text{m}$ . As generally known, decreasing the grain size of the  $\phi$ -phase increases the coercivity of the magnets. The cause of this effect is not completely obvious. However, it is thought that intergranular interaction through a dipole or magnetostatic interaction is lowered, and the possibility of the existence of a nucleation center for magnetic reversal in low applied field in a grain also decreases with decreasing grain size.

For the reduction of grain growth in sintered magnets it is effective to add Nb, V, and Mo, for example. These metals form borides at grain boundaries, which should retard the intergranular diffusion of elements, i.e. the mobility of the grain boundary. The negative effect of this addition is to enhance the formation of the  $\alpha$ -Fe phase.

Another important factor in the sintering process is the role of the grain-boundary phase, which is a Nd-rich phase in the sintered bulk material without additives. The Nd-rich phase behaves as the source of the liquid phase, which helps in the diffusion of the elements and/or grain growth during the sintering. It appears that the Nd-rich phase, Nd-Co, Nd-Ga, and Nd-Cu alloys in the various cases of sintering also have the so-called "magnetic cleaning effect", i.e., wetting of the grain surface by reducing surface oxidized layers, and the disappearance of magnetic defects in the  $\phi$ -phase, such as micro-cracks, small secondary phases, and local shape smoothing which corresponds to the reduction of the local demagnetizing factors.

The additives always show both positive and negative effects as mentioned above. Efforts to increase  $(BH)_{\text{max}}$  of the sintered magnets, for example, can be realized by enhancing the intrinsic properties, increasing the content and alignment of the  $\phi$ -phase with the minimum amount of grain boundary phases, which can be accomplished by magnetic cleaning and increasing sinterability of the magnets.

Figure 10 schematically shows the ideal microstructure of sintered  $\text{Nd}_2\text{Fe}_{14}\text{B}$  magnets. The simulations in figs. 9 and 10 can be readily related to the real observations of the microstructures of sintered magnets represented in figs. 11 and 12. In fig. 12 we show a newly developed high-energy-product magnet (444  $\text{kJ/m}^3$ ) which consists of a Nd-rich phase, the  $\text{Nd}_{1.1}\text{Fe}_4\text{B}_4$  phase, and the main  $\phi$ -phase with homogeneous grains of about 5  $\mu\text{m}$  in diameter, except for small voids (black) which are introduced during the polishing process by removal of the grain-boundary phases. The magnetic hysteresis curve of this magnet is shown in fig. 13 (Kaneko et al. 1999). This magnet has a remanence of 1.5 T with a density of 99%, a volume fraction of main  $\phi$ -phase of 97.5%, and a grain orientation of about 98%. All these values are nearly the maximum values found in commercial permanent Nd-Fe-B magnets (Kaneko et al. 1999).

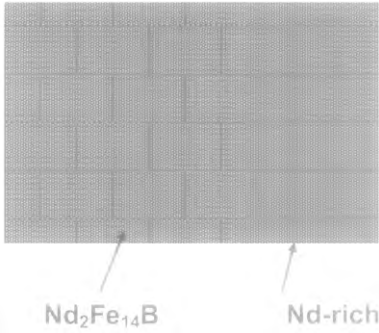


Fig. 10. Idealized microstructure of sintered Nd-Fe-B magnets: the magnet is divided into uniform grains; grain boundaries consist of a nonmagnetic Nd-rich liquid-forming phase of monolayer thickness.

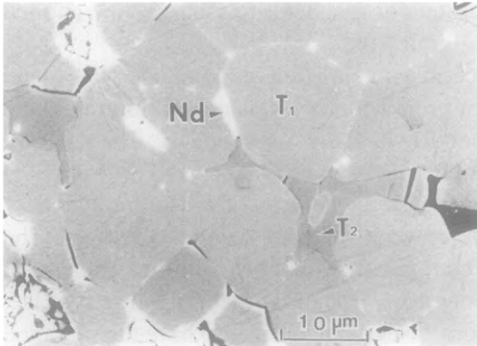


Fig. 11. Microstructure of a sintered Nd-Fe-B magnet:  $T_1$ , main  $\text{Nd}_2\text{Fe}_{14}\text{B}$  phase;  $T_2$ ,  $\text{Nd}_{11}\text{Fe}_4\text{B}_4$  phase; Nd, Nd-rich phase.

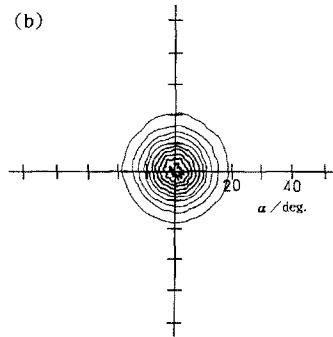
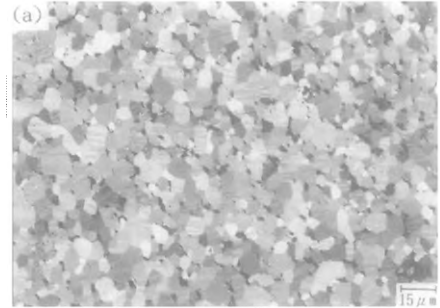


Fig. 12. (a) Microstructure and (b) distribution of grain orientations observed by X-ray diffraction in a Nd-Fe-B sintered magnet with  $(BH)_{\text{max}} = 444 \text{ kJ/m}^3$ .

### 3. HDDR process

Hydrogen disproportionation desorption recombination (HDDR) for the preparation of unique microstructures for  $\text{Nd}_2\text{Fe}_{14}\text{B}$  and  $\text{Sm}_2\text{Fe}_{17}$  is one of the most interesting techniques in the field of preparing permanent magnets. This method has been developed from the hydrogen decipitation technique (Harris et al. 1985), and the extension of this method by Takeshita and Nakayama (1989), and McGuinness et al. (1990) who reported on a newly developed recombination technique from disproportionated phases.

The most obvious and important feature of this method is the microstructural change in the treated alloys, in which the starting cast/homogenized phase with an average grain

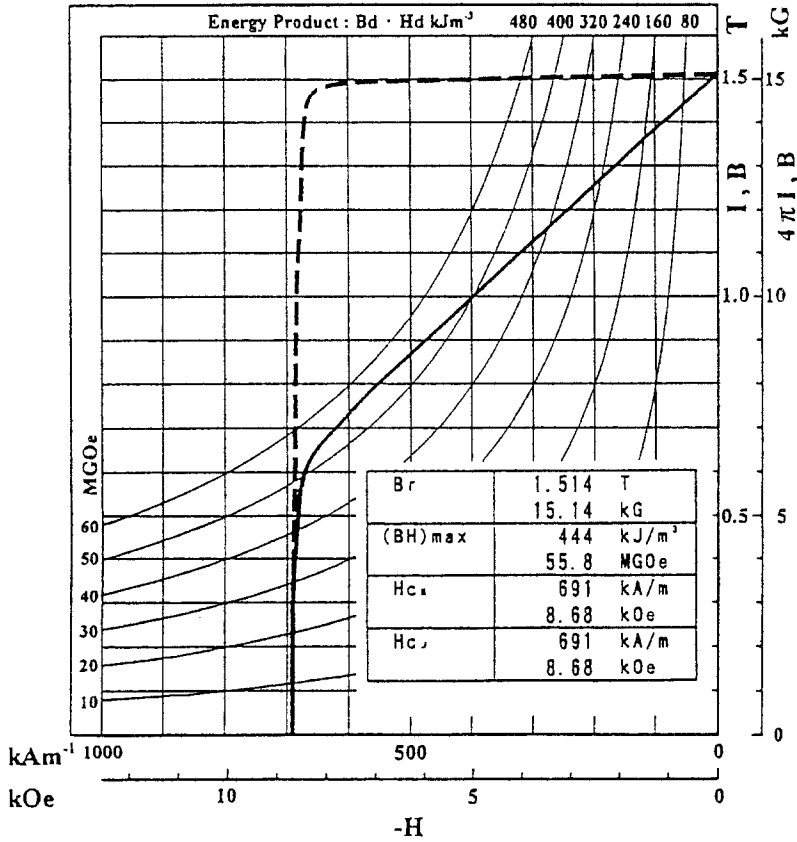


Fig. 13. Demagnetization curve of a Nd-Fe-B sintered magnet with  $(BH)_{max} = 444 \text{ kJ/m}^3$  in the 2nd quadrant of the magnetic hysteresis curve.

size of about  $100 \mu\text{m}$  was reduced in the treated phase to fine grains of sub-micron size. The merits of the resultant microstructures will be discussed in the following.

The coercivity of the magnets is expected to be enlarged by the fine grain sizes, and when an anisotropic HDDR powder can be prepared, the powder should have industrial cost-performance values comparable with those of anisotropic powders produced via die-upset forging and crushing (Gutfleisch and Harris 1998).

Another characteristic of the prepared powders is that the average sub-micron grain size is intermediate between that of sintered magnets and that of nanocrystalline magnets obtained by mechanical alloying or melt-spun methods. For industrial applications, therefore, the grain sizes should correspond to the single-domain particle size of rare-earth permanent magnets.

Relative to the HDDR method, the hydrogen absorption of magnetic alloys were initially reported. Harris et al. (1985) studied and reported the existence of a hydrogen

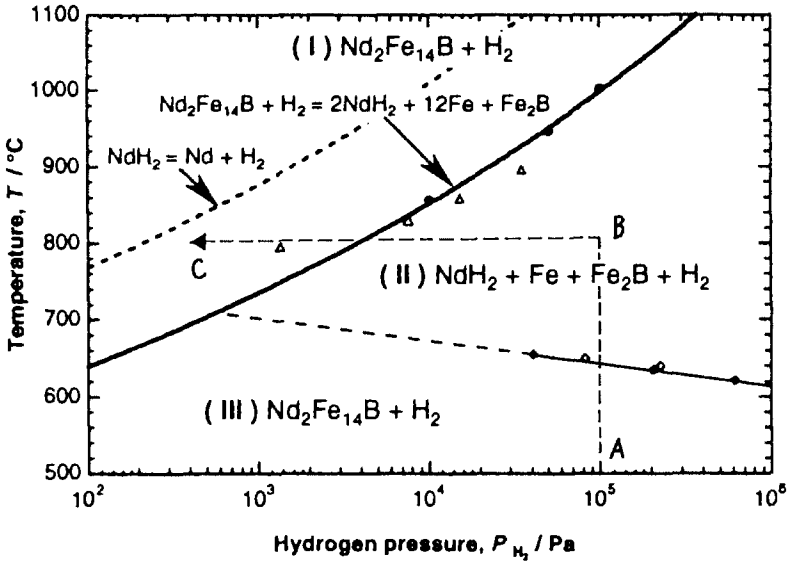
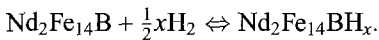


Fig. 14. Phase relation in  $\text{Nd}_2\text{Fe}_{14}\text{B}-\text{H}_2$  system (Nakamura et al. 1998). Dotted line (A  $\rightarrow$  B  $\rightarrow$  C) shows a typical treatment conditions during hydrogenation, disproportionation, and desorption processes.

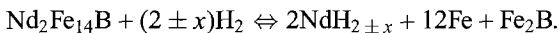
pressure plateau for  $\text{SmCo}_5$ , which means the alloy has a maximum amount of hydrogen it can absorb. Hydrogenation of  $\text{Nd}_2\text{Fe}_{14}\text{B}$  resulted in about a 4.8% volume expansion (Oesterreicher and Oesterreicher 1984) and that in  $\text{Sm}_2\text{Fe}_{17}$  of about 3.4% (Christodoulou and Takeshita 1993).

The hydrogenation in  $\text{Nd}_2\text{Fe}_{14}\text{B}$  occurs as follows:



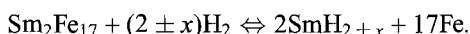
The absorbed hydrogen gradually forms the  $\text{NdH}_{2 \pm x}$  phase at grain boundaries surrounding the  $\text{Nd}_2\text{Fe}_{14}\text{B}$  main phase in overstoichiometric (Nd-rich) alloys (Oesterreicher and Oesterreicher 1984). The hydrogen desorption is initiated by the different expansion rates in the  $\text{NdH}_{2 \pm x}$  phase and the  $\text{Nd}_2\text{Fe}_{14}\text{B}$  main phase (McGuinness et al. 1990). This kind of mechanism was also pointed out by Takeshita (1995) concerning the anisotropic desorption phenomenon.

The most important reactions in the HDDR method are presented in fig. 14 (Nakamura et al. 1999). In the case of  $\text{Nd}_2\text{Fe}_{14}\text{B}$ , hydrogen absorption starts at around 923 K (Sugimoto et al. 1997). This is the start of the disproportionation process which occurs according to the following relation (Book and Harris 1995):



If the hydrogen partial pressure is less than  $10^2$  Pa, the reaction is not observed in this system (Sugimoto et al. 1997, Book and Harris 1995).

The disproportionation in  $\text{Sm}_2\text{Fe}_{17}$  was given by Christodoulou and Takeshita (1993) as



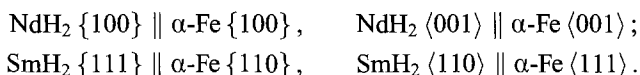
The most obvious difference between this and the case of  $\text{Nd}_2\text{Fe}_{14}\text{B}$  is that there is no  $\text{Fe}_2\text{B}$  phase in the disproportionated sample. In both alloys, the disproportionation starts at the grain boundaries, and the matrix phase is gradually hydrogenated into  $\text{RH}_{2 \pm x}$  ( $\text{R} = \text{Nd}, \text{Sm}$ ) which is surrounded by Fe in both cases, and/or  $\text{Fe}_2\text{B}$  phase in the  $\text{Nd}_2\text{Fe}_{14}\text{B}$  case (McGuinness et al. 1990).

The most important point concerning the HDDR method, in both fundamental and industrial sense, is the formation of an anisotropic powder. This phenomenon has a strong impact on the evaluation of the disproportionated phase. Takeshita and Nakayama (1992) described the effects of additives, such as Co, Ga and Zr, on the development of magnetic properties of HDDR Nd–Fe–B.

The appearance of anisotropy in the powder was initially thought to be related to the effects of the additives on hydrogen absorption and desorption mechanisms. The amount of hydrogen absorption, for example, decreases with increasing additive content in the  $\text{Nd}_2\text{Fe}_{14}\text{B}$  phase. This phenomenon suggests that the disproportionation reaction into  $\text{NdH}_{2 \pm x}$ ,  $\text{Fe}_2\text{B}$  and Fe phases should be incomplete in the alloyed  $\text{Nd}_2\text{Fe}_{14}\text{B}$  material (Nakamura et al. 1995, Fujita and Harris 1994). The amount of unreacted  $\text{Nd}_2\text{Fe}_{14}\text{B}$  can be estimated from the residual un-decomposed  $\text{Nd}_2\text{Fe}_{14}\text{B}$  and/or  $(\text{Nd}, \text{Zr})_2(\text{Fe}, \text{Co}, \text{Ga})_{14}\text{B}$  regions, which keep their original orientation. The additives also reduce the explosive grain growth which occurs in un-alloyed  $\text{Nd}_2\text{Fe}_{14}\text{B}$  during the recombination step.

Buschow (1994) analyzed these effects thermodynamically using the van 't Hoff relation. The  $(\text{Nd}, \text{Zr})_2\text{Fe}_{14}\text{B}$  and/or Co- and Zr-containing regions have the higher equilibrium hydrogen partial pressure ( $P_{\text{H}_2}$ ), which means that in the phases with additives the completion of the disproportionation process becomes difficult, and also the recombination process should be accelerated under the same conditions. The recombination reaction depends on thermally activated bulk diffusion which increases with temperature (McGuinness et al. 1990).

Gutfleisch et al. (1995) and Gutfleisch and Harris (1998) have discussed the importance of the orientations of the  $\text{NdH}_{2 \pm x}$  and  $\alpha\text{-Fe}$  phases. McGuinness et al. (1990) pointed out a similar relation in the disproportionated phase in  $\text{Sm}_2\text{Fe}_{16}\text{Ga}$ . The relationships are as follows:



The disproportionated phase can be prepared by another route. Nakamura et al. (1998, 1999) initially heated the starting alloy to 1023–1123 K in vacuum, and hydrogenation started at the same temperature by introducing  $\text{H}_2$  gas into the system.

They found that this treatment gave a disproportionated phase with a coarse lamellar structure. They believed that the appearance of anisotropy after HDDR processing via this reaction path should relate to this anisotropic microstructure.



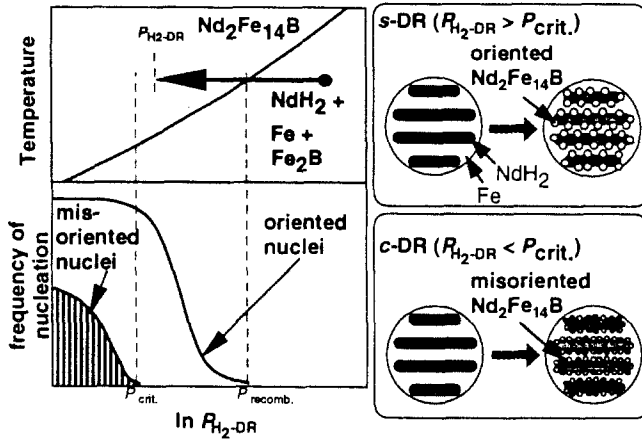


Fig. 15. Schematic diagram of the relationship between the  $H_2$  pressure during recombination,  $P_{H_2-DR}$ , and number of nuclei, and schematic illustration of the microstructural changes during c-DR or s-DR treatments, where c-DR and s-DR are the recombination reactions in an apparatus at ordinary exhaust gas rate, and at a comparatively smaller rate under higher gas pressure, respectively (Nakamura et al. 1999).

Recently, Nakamura et al. (1999) discussed the details of the origin of the anisotropy, and emphasized the importance of hydrogen partial pressure during recombination reaction. As shown in fig. 15, when the partial pressure is comparatively high, the oriented nuclei of the  $Nd_2Fe_{14}B$  phase mainly form in a lamellar structure formed by  $NdH_2$  and Fe phases. Inversely, the mis-oriented nuclei of the main phase increase with a low partial pressure of hydrogen. They believe, therefore, that the origin of the anisotropy should be the residual strain which yields oriented main-phase regions in the lamellar structure during the HDDR process.

Tomida et al. (1999) also studied the origin of the anisotropy. They paid much attention to the role of the tetragonal  $Fe_3B$  phase probably saturated with hydrogen, which appears in the initial stage of disproportionation, co-existing with the lamellar structure mentioned above. In this metastable  $Fe_3B$  phase, the  $Nd_2Fe_{14}B$  main phase has the following crystal orientation relationship:

$$(001)_{t-Fe_3B} \parallel (001)_{Nd_2Fe_{14}B}$$

This point can be directly observed by TEM as shown in fig. 16. As the hydrogenation–disproportionation (HD) process develops, the main phase is changed into a lamellar structure of  $NdH_2$  and  $\alpha$ -Fe phases. At the front of the lamellar structure formation, there is the t- $Fe_3B$  phase, which contains the spherical  $NdH_2$  and  $Nd_2Fe_{14}B$  phases. The t- $Fe_3B$  phase is decomposed into  $Fe_2B$  and  $\alpha$ -Fe phases as the HD process develops.

Figures 17 and 18 show the morphology of the spherical regions in the  $Fe_2B$  matrix phases, and the chemical compositions of the spherical grains by EDX analysis. As shown in fig. 19, Tomida et al. (1999) think that the origin of the anisotropy is in the spherical  $Nd_2Fe_{14}B$  ( $\phi$ ) phases within the  $Fe_3B$  phase, which is obviously different from the idea

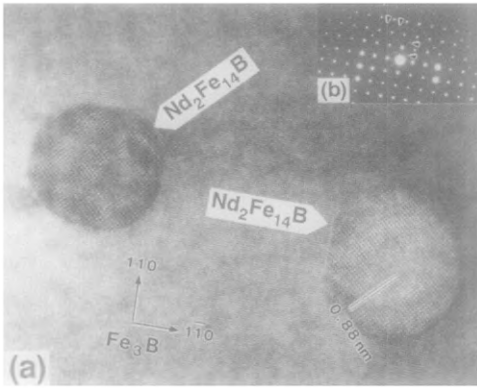


Fig. 16. High-resolution TEM micrograph of  $t\text{-Fe}_3\text{B}$  with embedded  $\text{Nd}_2\text{Fe}_{14}\text{B}$  particles and (b) its SADP (selected-area diffraction pattern) of the  $[001]$  zone for both phases. The arrowheads in (b) indicate some weak diffraction spots from the particles. The sample was hydrided at  $1123\text{ K}$  for  $30\text{ min}$  (Tomida et al. 1999).

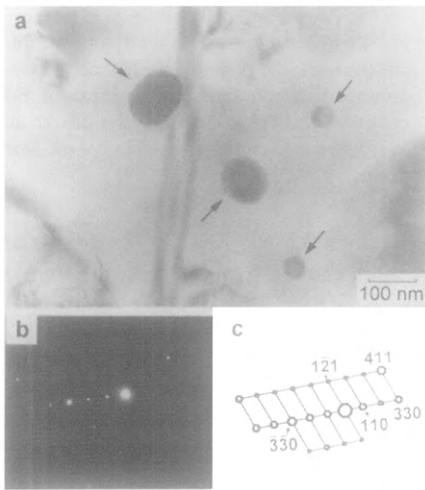


Fig. 17. Crystallographically aligned  $\text{Nd}_2\text{Fe}_{14}\text{B}$  particles (arrows) in a  $\text{Fe}_2\text{B}$  grain in the disproportionation stage: (a) bright-field image; (b) selected-area diffraction pattern; (c) its schematic representation. The powder was hydrided at  $1123\text{ K}$  for  $120\text{ min}$  (Hirosawa et al. 1997).

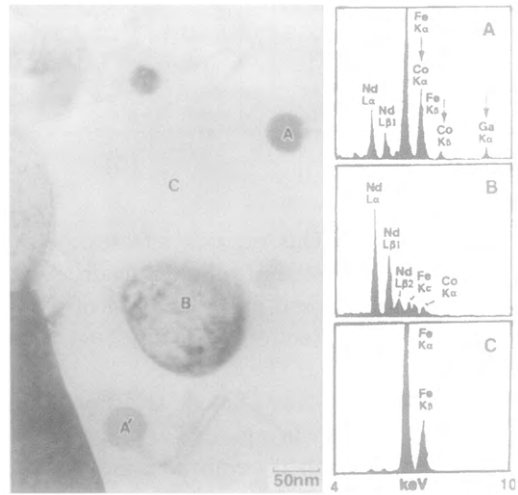


Fig. 18. Bright-field image of fine particles in a  $\text{Fe}_2\text{B}$  matrix and the corresponding EDS spectra for the particles (indexed as A and B) and matrix (indexed as C). Particle B is  $\text{NdH}_2$ , and particle A' has shown an EDS spectrum similar to that for particle A (Tomida et al. 1996).

proposed by Nakamura et al. (1999). Tomida et al. believe that the disproportionation reaction of the HDDR process starts along grain boundaries where hydrogen diffusion is fast. Because of the fast kinetics allowed by short diffusion distances, a lamellar decomposition of  $\text{Nd}_2\text{Fe}_{14}\text{BH}_x$  into  $\text{NdH}_2$  and Fe takes place in the initial stage, creating a B-enriched region in the un-decomposed  $\text{Nd}_2\text{Fe}_{14}\text{BH}_x$  matrix near the reaction front (fig. 19a). As the excess B builds up in the matrix, the reaction kinetics of the lamellar decomposition are retarded, and the B-enriched regions decompose into  $t\text{-Fe}_3\text{B}$  and

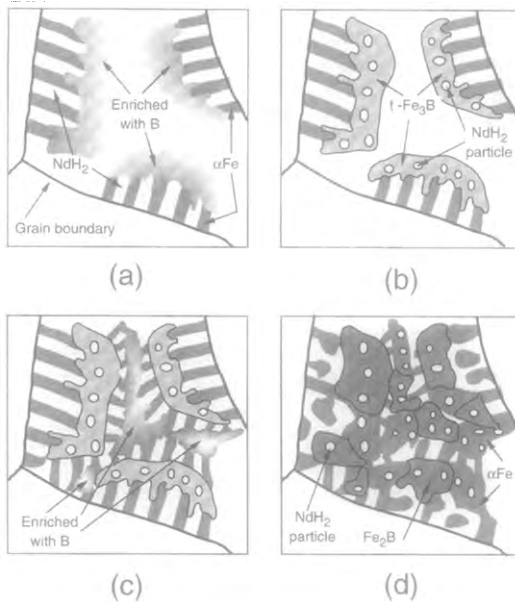


Fig. 19. Schematic diagram illustrating the microstructural change during the hydrogenation–disproportionation (HD) process, except for embedded  $\text{Nd}_2\text{Fe}_{14}\text{B}$  particles (Tomida et al. 1999). See the text for a discussion of the four parts.

$\text{NdH}_2$  (fig. 19b). This reaction releases the excess B from the  $\text{Nd}_2\text{Fe}_{14}\text{BH}_x$  matrix, and lamellar decomposition is allowed again. After repeating these two processes, the whole matrix is decomposed into a mixture of two regions: the Fe/ $\text{NdH}_2$  lamellar region and the  $\text{Fe}_3\text{B}/\text{NdH}_2$  mixture region (fig. 19c). Finally, t- $\text{Fe}_3\text{B}$  decomposes into  $\text{Fe}_2\text{B}$  and Fe (fig. 19d).

This model involves a kinetic selection of phases which appear when the reaction front moves at a velocity in a particular range. The t- $\text{Fe}_3\text{B}$  has crystallographic coherence with  $\text{Nd}_2\text{Fe}_{14}\text{B}$  microspheres embedded in the  $\text{Fe}_3\text{B}$ . These residual  $\text{Nd}_2\text{Fe}_{14}\text{B}$  microspheres survive through the entire HDDR process and carry the orientational information.

From the discussion by Tomida et al. (1999), it is naturally concluded that HDDR processing of lanthanide–transition-metal alloys without boron, such as  $\text{Sm}_2\text{Fe}_{17}$ , should always yield isotropic materials because of the absence of the Fe–B phases, in which the nuclei of the main phase continuously exist during HDDR process without changing their initial crystal orientations.

As a conclusion of the above-mentioned discussions, clearly more work needs to be done in the future concerning the origin of the anisotropy in lanthanide permanent magnets during HDDR processing.

Concerning the industrial application of the HDDR method, Ikegami et al. (1998) studied the thermal properties of Nd–Fe–B magnets prepared by this method. Figure 20 shows the effect of Dy additions on the temperature dependence of coercivity with optimum concentrations of Co, Ga, and Zr additives. The temperature coefficient of coercivity of anisotropic  $\text{Nd}_2\text{Fe}_{14}\text{B}$ -based magnets is typically about  $-0.5\%/K$ . They also prepared samples of various coercivities, and found that the flux loss after treatment

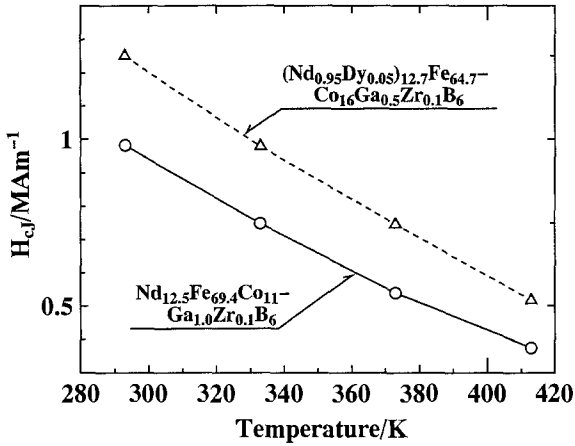


Fig. 20. The effect of Dy addition on the temperature dependence of coercivities in Nd-Fe-Co-Ga-Zr-B magnets prepared by the HDDR process (Ikegami et al. 1998).

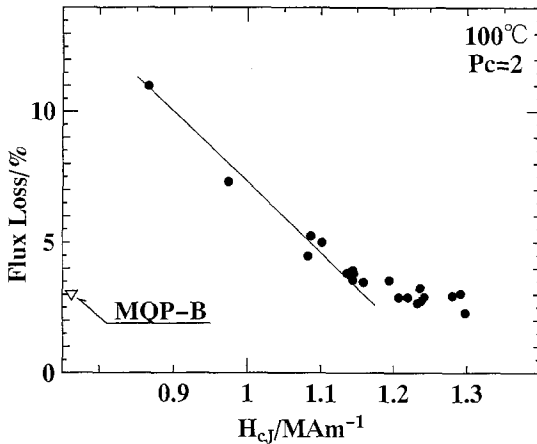


Fig. 21. Comparison of flux losses in MQP-B and HDDR magnets with various initial coercivities (Ikegami et al. 1998).

at 373 K for a certain duration reached an almost constant value of  $\sim 3\%$ , when the coercivity was more than 11.1 MA/m as shown in fig. 21. This value corresponds to the flux loss in MQP-B powder with a coercivity of about 0.75 MA/m (fig. 21), in which the temperature coefficient of coercivity,  $\beta$ , is about  $-0.4\%/K$ .

#### 4. Nanocomposite permanent magnetic materials

Nanocomposites or mesoscopic materials are of interest in many fields of materials science, solid-state physics and solid-state chemistry. This is also true in the research of magnets: much effort has been spent on these kind of materials. The most recent development is that of exchange-coupled magnets, in which hard and soft magnetic fine

grains and/or regions interact on quantum-mechanical scale, i.e.  $\sim 10$  nm. This size also corresponds to the width of domain walls in magnetic materials.

The study of these materials started with the formation of nanometer-size grains with an agglomerated microstructure, by melt-spinning and mechanical alloying methods. In this section, we will initially discuss the development of both methods, and also explain recent studies of nanocomposite materials in the sense mentioned above.

#### 4.1. *Rapid solidification*

At the time of the discovery of the  $\text{Nd}_2\text{Fe}_{14}\text{B}$  magnets, Croat et al. (1984) used a technique in which alloys melted at high temperature are fed onto a spinning roll made of metal, such as Cu, and are rapidly solidified. The method is called “melt-quenching”, “rapid quenching” or “melt-spinning”.

The microstructures of the ribbon-like specimen can be changed by changing the speed of rotation of the spinning roll, from very fine amorphous grain sizes to crystallized grains of some 10 nm in diameter. For example, a  $\text{Nd}_{13.5}\text{Fe}_{81.0}\text{B}_{5.5}$  thin flake (or ribbon) sample, which was prepared under optimum conditions for the magnetic properties, showed a microstructure composed of  $\text{Nd}_2\text{Fe}_{14}\text{B}$  grains of 20–30 nm in diameter surrounded by an amorphous phase 1–2 nm in thickness (Mishra 1986). The composition of the amorphous phase was analyzed as  $\text{Nd}_{70}\text{B}_{30}$  (Hutten and Haasen 1989).

The microstructure of the ribbon gives some characteristic properties to the samples. First, deterioration of the magnetic properties by pulverization into fine particles is small. This character is a result of the separation of the hard magnetic grains by grain boundaries and/or by intergranular phases. Second, the grain-boundary phases can be eliminated, for example, by Si addition to the  $\text{Nd}_2\text{Fe}_{14}\text{B}$  phase. These Nd–(Fe,Si)–B magnets also show very fine grain sizes, and the corrosion resistance is also high because of the elimination of the Nd-rich phase at grain boundaries (Matsuura et al. 1988, Clemente et al. 1988). It was also pointed out that Si additions produce the remanence-enhancement “phenomenon”. This point will be discussed more precisely below.

The third characteristic is that samples prepared by the melt-spinning method can be substituted by a large amount of Co compared with the sintered magnets. The temperature dependence of the magnetic properties and the corrosion resistance, therefore, is improved by the addition of Co (Li and Graham 1990).

The fourth characteristic is that the grain sizes in the microstructure are initially already small enough for the preparation of magnets, and the pulverization process does not affect the magnetic properties, especially the coercivity.

For industrial applications of the powders, the following three methods were proposed by Lee (1985) and Lee et al. (1985):

- (1) The resultant powders are mixed with resin to prepare bonded magnets. This type of magnet is called MQ-1, and is magnetically isotropic. They have been used in a wide variety of industrial applications, and still have a large market.
- (2) The second type of permanent magnets (MQ-2) results from hot-pressing of the powders under about 0.1 GPa at about 973 K. The resultant magnets show a magnetic

orientation parallel to the direction of compression, which results in an improvement of the magnetic properties over MQ-1.

- (3) The third type of powders (MQ-3) is prepared by the introduction of plastic deformation, by a certain pressure at around 973 K, to MQ-2-type magnets with about 100% bulk density. This treatment increases the anisotropy of MQ-2-type magnets, and yields magnets with a polarization of 1.35 T, and  $(BH)_{\max}$  of 318 kJ/m<sup>3</sup> (Lee et al. 1985). The maximum  $(BH)_{\max}$  can be raised to 358 kJ/m<sup>3</sup> by refining the method.

The rapid-quenching method can also be applied to materials based on Th<sub>2</sub>Zn<sub>17</sub>, Th<sub>2</sub>Ni<sub>17</sub> and TbCu<sub>7</sub> structures. Katter et al. (1991) prepared Sm-Fe-N magnets by rapid quenching followed by annealing and nitrogenation. They obtained the best hard magnetic properties for an isotropic TbCu<sub>7</sub>-type material, (Sm<sub>10.6</sub>Fe<sub>89.4</sub>)<sub>1-x</sub>N<sub>x</sub>, with a coercivity of  $H_{cJ} = 490$  kA/m, a remanence  $J_r = 0.86$  T, and a  $(BH)_{\max}$  of 69.6 kJ/m<sup>3</sup>. They also prepared a slightly Sm-rich material of Th<sub>2</sub>Zn<sub>17</sub>-type structure, and the magnetic properties of this material, especially the coercivity, were greatly enhanced. The  $(BH)_{\max}$ , however, was not different from that of the former material.

Pinkerton and Fuerst (1992) obtained a coercivity of 1.78 MA/m by nitriding melt-spun Sm-Fe ribbons followed by pulverization to powder with grain sizes of <25 μm. Their material showed the TbCu<sub>7</sub>-type structure.

More recently, Sakurada et al. (1996) studied the nitrogenation of (R,Zr)(Fe,Co)<sub>x</sub> (R = Nd, Sm) materials prepared by rapid solidification. They believed that the substitution of Zr into rare-earth sites resulted in a higher magnetization because of the high Fe content and because of elongation of the *c*-axis, i.e. the *c/a* ratio increased. The main phase of their materials also has the TbCu<sub>7</sub>-type structure. Yamamoto et al. (1996) studied nanocomposite magnets of Sm-Zr-Fe-N + α-Fe which were prepared by nitrogenation following the heat treatment of rapidly quenched alloys. They also used the rapid-quenching method for the preparation of the Sm-Fe-M (M = Zr, Nb, Si, Al, Ti, B) phases. The main phase of the prepared powders has TbCu<sub>7</sub>-type structure. Since their materials are exchange-coupled magnets, we will discuss this magnet in more detail in sect. 5.3.

Concerning Sm-Fe-C materials, Shen et al. (1993) discovered that Ga additions can stabilize the Th<sub>2</sub>Zn<sub>17</sub>-type structure up to about 1000 K. van Lier et al. (1998, 1999) studied Ga-substituted Sm<sub>2</sub>(Fe,Ga)<sub>17</sub> carbides prepared by the melt-spinning technique. They optimized the Sm content and the annealing conditions of the ribbons, and were able to prepare a powder with a coercivity of  $\mu_0 H_c = 2.18$  T. Their as-quenched ribbon flakes consist of amorphous and TbCu<sub>7</sub>-type related phases, and annealing at higher temperatures yields a Th<sub>2</sub>Zn<sub>17</sub>-type structure. The Curie temperature of the material was improved by the appearance of the Th<sub>2</sub>Zn<sub>17</sub>-type structure.

In Sm-Fe-based materials prepared by rapid solidification methods, the important and interesting point is that the structure of the main phase in the materials has either the TbCu<sub>7</sub>- or the Th<sub>2</sub>Zn<sub>17</sub>-structure depending on preparation method and conditions. This point has been investigated by Katter et al. (1991), Wendhausen et al. (1994), and recently by Teresiak et al. (1998).

#### 4.2. Mechanical alloying

Mechanical alloying method is a dry ball-milling technique to form alloys from a mixture of metals. Schultz et al. (1987, 1988) and Heisz and Schultz (1988) applied this technique to the Nd–Fe–B system, and obtained a layered structure of Nd–Fe, in which there are distributed boron regions. A microstructure composed of fine grains of Nd<sub>2</sub>Fe<sub>14</sub>B was acquired when the samples were heated at about 873 K for 1 hour. These Nd<sub>2</sub>Fe<sub>14</sub>B magnet samples had magnetic properties similar to those produced by the melt-quenching technique.

Schnitzke et al. (1990) produced Sm<sub>2</sub>Fe<sub>17</sub>N<sub>3</sub> with a coercivity of 2.4 MA/m by this method. The bulk of their isotropic magnets had a remanence of 0.75 T, which corresponds to approximately half the saturated magnetization of the material. Ding et al. (1992) prepared isotropic Sm<sub>2</sub>Fe<sub>17</sub>N<sub>3</sub> powders by mechanical alloying, and studied the magnetization as a function of maximum applied magnetic field. Their powders have comparatively low magnetization, less than 1 kG, and high coercivity, about 2.8 MA/m, when magnetized under an applied field of 12 T. Kuhrt et al. (1992) prepared microcrystalline Sm<sub>2</sub>Fe<sub>17</sub>C<sub>x</sub> ( $x \approx 2$ ) powders by mechanical alloying, and a subsequent solid–gas reaction in acetylene atmosphere. Their powders showed a room-temperature coercivity of about 1.85 MA/m, and a maximum energy product of about 60 kJ/m<sup>3</sup>. Ding et al. (1994) studied Sm<sub>2</sub>(Fe,Ga)<sub>17</sub>C<sub>2</sub> material prepared by mechanical alloying, and found that the powder, which had the 2:17-type structure, showed a coercivity of about 1.3 MA/m.

Materials prepared by this technique have comparable magnetic properties as those obtained by the melt-quench technique. This method, however, has been mainly used for the preparation of fine microstructures in which exchange-coupled effects can be expected.

#### 4.3. Exchange-coupled magnets

The early study of exchange-coupled magnets was based on the reports of remanence enhancement by the Philips group (Buschow 1987, Coehoorn et al. 1988). Both melt-spinning and mechanical-alloying methods have been used to prepare this type of magnets. Coehoorn et al. (1988) prepared amorphous ribbons by the melt-spinning method, followed by a heat-treatment at 943 K for 30 minutes, and obtained flakes of Nd<sub>4</sub>Fe<sub>80</sub>B<sub>20</sub>–Nd<sub>3.8</sub>Fe<sub>77</sub>B<sub>19.2</sub>. These samples consisted of Fe<sub>3</sub>B (73%), Nd<sub>2</sub>Fe<sub>14</sub>B (15%) and  $\alpha$ -Fe (12%), and had  $J_s = 1.6$  T,  $J_r = 1.2$  T and  $H_{cJ} = 240$  kA/m in the bulk. The microstructure of the magnet shows that the Fe<sub>3</sub>B phase has a grain size of about 30 nm and the Nd<sub>2</sub>Fe<sub>14</sub>B phase of about 10 nm.

Ding et al. (1993) investigated the remanence enhancement in a two-phase mixture of Sm<sub>2</sub>Fe<sub>17</sub>N<sub>3</sub> and  $\alpha$ -Fe prepared by mechanical alloying. After nitrogenation, their powder had  $J_r = 1.4$  T,  $H_{cJ} = 310$  kA/m, and  $(BH)_{\max} = 205$  kJ/m<sup>3</sup>.

The microstructure of the magnets in which remanence enhancement can be observed is composed of fine grains about 10 nm in diameter, which is three times smaller than that of normal melt-quenched powders. The grain size can be controlled by additives such as Si, V, Cu, Ga and Zr. The  $(BH)_{\max}$  gradually increases with decreasing grain size,

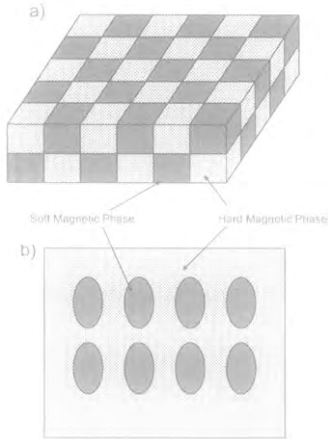


Fig. 22. Schematic representation of the concept of a nanocomposite magnet (Hirosawa 1999).

from  $130 \text{ kJ/m}^3$  to more than  $160 \text{ kJ/m}^3$  in the case of  $\text{Nd}_2\text{Fe}_{14}\text{B}$  magnets (Davies et al. 1996). The size of the grains in these magnets is the origin of the name “nanocomposite magnets”.

An idealized schematic representation of exchange-coupled magnets is shown in fig. 22.

Kneller and Hawig (1991) have proposed an interesting idea to explain the origin of the remanence-enhancement phenomenon. They analyzed exchange interactions between hard and soft magnetic phases, and concluded that magnets composed of exchange-coupled (two-phase) fine grains should show a reversible change in magnetization in the second quadrant of their hysteresis curves. This is the phenomenon that the once reversed magnetizations (in the soft-phase regions by the applied magnetic field) recover their original direction by the interaction between the soft magnetic phase and the hard magnetic phase in which the magnetization is always in the original direction even under applied field. They called this type of magnet “exchange-spring-magnets”. In fig. 23 we show an example of the exchange-spring phenomenon of such a magnet as compared to the hysteresis curve of an MQP-B ( $\text{Nd}_2\text{Fe}_{14}\text{B}$ ) magnet for comparison.

Skomski and Coey (1993) have pointed out more attractive possibilities for this type of magnet. They proposed a microstructure consisting of distributed spherical soft magnetic phases in an oriented hard magnetic matrix with an aligned mixture of plate-like regions of soft and hard magnetic phases in a specific direction. Their calculations showed that a multi-layer composite of the  $\text{Sm}_2\text{Fe}_{17}\text{N}_3$  phase with thickness 2.4 nm and the  $\text{Fe}_{65}\text{Co}_{35}$  phase with thickness 9 nm should have a  $(BH)_{\text{max}}$  of more than  $1 \text{ MJ/m}^3$  (120 MGOe).

In real exchange-coupled magnets, it is difficult to align the orientations of the hard magnetic phases. The realization of the proposed microstructures in bulk magnets may be difficult because of the technical difficulties in aligning both phase regions in the desired way. Multilayer thin films, however, should allow one to prepare a two-dimensional ideal microstructure, if combined with the strong tendency of thin films to form texture during film growth.



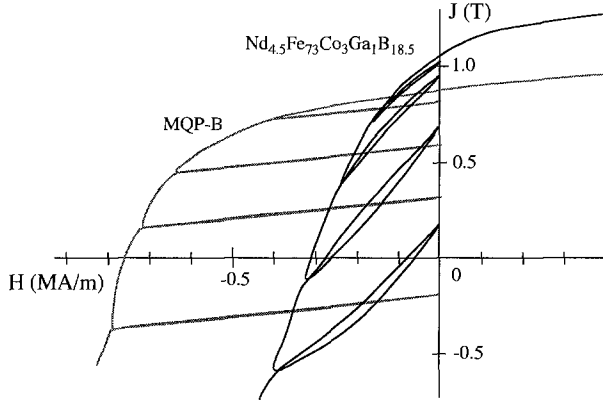


Fig. 23. Comparison between recoil hysteresis curves of a  $\text{Fe}_3\text{B}/\text{Nd}_2\text{Fe}_{14}\text{B}$  nanocomposite magnet and an ordinary "single-phase"  $\text{Nd}_2\text{Fe}_{14}\text{B}$  magnet (MQP-B) (Hirosawa 1999).

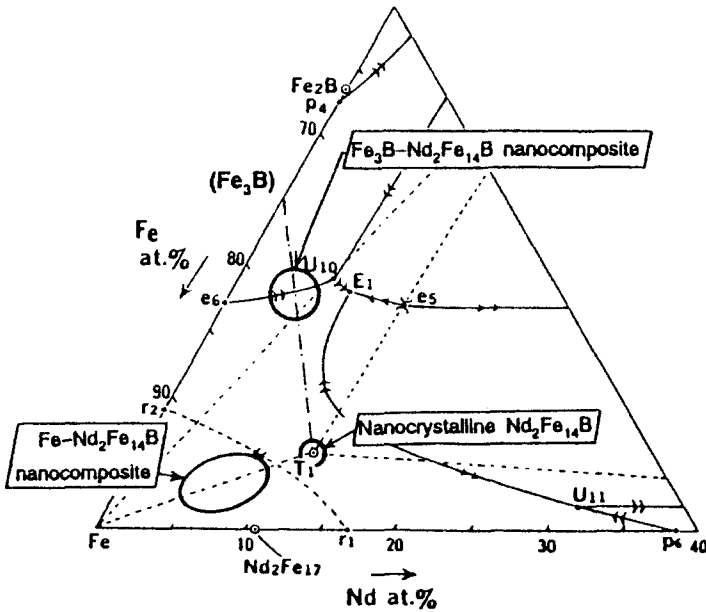


Fig. 24. Three types of nanostructure Nd-Fe-B magnets and their typical compositions (Hirosawa and Kanekiyo 1995).

As shown in fig. 24, the compositions of nanocrystalline magnets in the Nd-Fe-B system can be categorized into three regions (Hirosawa and Kanekiyo 1995): The first region is  $\text{Nd}_2\text{Fe}_{14}\text{B}$  itself, and a large remanence enhancement can be expected by exchange coupling at the grain interfaces (Manaf et al. 1993). The second region lies on the tie line of the Fe- $\text{Nd}_2\text{Fe}_{14}\text{B}$  phases, i.e. a mixture of  $\alpha$ -Fe and  $\text{Nd}_2\text{Fe}_{14}\text{B}$

phases. The third type of material are the nanocomposites of  $\text{Fe}_3\text{B}$ – $\text{Nd}_2\text{Fe}_{14}\text{B}$  mixtures (Buschow 1987, Coehoorn et al. 1988). In this region,  $\text{Fe}_3\text{B}$  is a metastable phase, and the thermodynamically stable phase is  $\text{Fe}_2\text{B}$ .

Since 1987 many exchange-coupled rare-earth–transition-metal magnets have been developed. Examples of exchange-coupled magnets are listed in table 2.

Hadjipanayis et al. (1995), Neu et al. (1996) and Miao et al. (1996) have studied the formation of  $\text{Nd}_2\text{Fe}_{14}\text{B} + \alpha\text{-Fe}$  nanocomposites, which are equilibrium mixtures on the  $\text{Fe}$ – $\text{Nd}_2\text{Fe}_{14}\text{B}$  tie line. They observed remanence enhancement in samples with average grain sizes around 20–30 nm. Coercivity, for example, was about 360 kA/m in the sample of  $\text{Nd}_{3.5}\text{Fe}_{91}\text{Nb}_2\text{B}_{3.5}$  composition (Hadjipanayis et al. 1995).

In the  $\text{Fe}_3\text{B}$ – $\text{Nd}_2\text{Fe}_{14}\text{B}$  region, mixed nanostructures are prepared from the  $\text{Nd}_4\text{Fe}_{77}\text{B}_{19}$  composition by the melt-quench method. The  $\text{Fe}_3\text{B}$  phase initially forms from an amorphous phase followed by crystallization of  $\text{Nd}_2\text{Fe}_{14}\text{B}$  phase. Buschow et al. (1986) studied phase compositions in this region. When the Nd content is higher than about 5 at.%, metastable  $\text{Nd}_2\text{Fe}_{23}\text{B}_3$  and  $\text{NdFe}_{12}\text{B}_6$  phases are also formed. However, these two phases have lower Curie temperatures and magnetizations than the  $\text{Fe}_3\text{B}$  phase (Hirosawa and Kanekiyo 1995). To obtain better magnetic properties of the  $\text{Fe}_3\text{B}$ – $\text{Nd}_2\text{Fe}_{14}\text{B}$  mixed nanostructures, the composition should have <5 at.% Nd, and  $19 \pm 2$  at.% B (Hirosawa and Kanekiyo 1995).

The present most challenging problem of nanocomposite materials is their comparatively low coercivity. Recent values of the coercivities of isotropic magnets are presented in fig. 25. As seen, most of these magnets have coercivities less than 400 kA/m, except for some of the recently developed high-coercive powders. The values of coercivity are still comparatively small for industrial applications. Substitution of Dy or Tb for Nd is one way to increase the magnetic anisotropy of the main phase, and that has been tried by some groups (Coehoorn et al. 1989, Kanekiyo et al. 1993). These improvements, however, are at the expense of the magnetization and loop squareness.

Another approach to increase coercivity is to diminish the grain size. Some additives are effective in reducing grain growth. For example, Ga attracted interest as a candidate for this purpose (Hirosawa and Kanekiyo 1993). A  $\text{Nd}_{4.5}\text{Fe}_{73}\text{Ga}_1\text{Co}_3\text{B}_{18.5}$  amorphous composite containing Ga prepared by melt-spinning shows crystallization of the  $\text{Fe}_3\text{B}$  phase around 850 K, followed by crystallization of the  $\text{Nd}_2\text{Fe}_{14}\text{B}$  phase as in the ternary Coehoorn alloy (Coehoorn et al. 1988). Ga in the initial amorphous phase has an inclination to stay in the amorphous phase as the  $\text{Fe}_3\text{B}$  and  $\text{Nd}_2\text{Fe}_{14}\text{B}$  phases crystallize step by step with increasing temperature from the amorphous phase. Ga, however, does not exist as Ga metal, but remains in the grain-boundary region and/or substitutes into the Fe sites in  $\text{Nd}_2\text{Fe}_{14}\text{B}$ . Recently, however, it has been assumed that the main effect of the Ga addition is to increase the volume fraction of  $\text{Nd}_2\text{Fe}_{14}\text{B}$  phase, which yields better magnetic properties.

Similar effects and behavior have been observed with Al, Si, Cu, Ag, and Au additives.

For reducing grain growth, Cr additions were also effective. For example, in  $\text{Nd}_{4.5}(\text{Fe}_{1-x}\text{Cr}_x)_{77}\text{B}_{18.5}$  nanocomposite material, Cr substitutes for Fe in the  $\text{Fe}$ – $\text{B}$  phases, and not in the  $\text{Nd}_2\text{Fe}_{14}\text{B}$  main phase (Kanekiyo et al. 1993). The optimum Nd content

Table 2  
Composition and magnetic properties of exchange-coupled multi-phase permanent magnet flakes and powders<sup>a</sup>

Composition	Magnetic phases (soft/hard)	Volume % soft phase	Preparation method <sup>b</sup>	$J_s$ (T)	$B_i$ (T)	$H_{c,d}$ (kA/m)	$(BH)_{max}$ (kJ/m <sup>3</sup> )	Reference
Nd <sub>4</sub> Fe <sub>80</sub> B <sub>20</sub>	Fe <sub>3</sub> B-Fe/Nd <sub>2</sub> Fe <sub>14</sub> B	85%	RS+A	1.6	1.20	191	93.1	Coehoorn et al. (1988)
Nd <sub>4.5</sub> Fe <sub>37</sub> Co <sub>3</sub> Ga <sub>1</sub> B <sub>18.5</sub>	Fe <sub>3</sub> B-Fe/Nd <sub>2</sub> Fe <sub>14</sub> B		RS+A	1.42	1.21	340	128	Hirosawa and Kanekiyo (1994)
Nd <sub>3.5</sub> DyFe <sub>73</sub> Co <sub>3</sub> GaB <sub>18.5</sub>	Fe <sub>3</sub> B-Fe/Nd <sub>2</sub> Fe <sub>14</sub> B		RS+A	1.37	1.18	390	136	Hirosawa and Kanekiyo (1994)
Nd <sub>4.5</sub> Fe <sub>66</sub> Cr <sub>3</sub> Co <sub>3</sub> B <sub>18.5</sub>	Fe <sub>2</sub> B-Fe/Nd <sub>2</sub> Fe <sub>14</sub> B		RS+A	1.06	0.86	610	96.6	Hirosawa and Kanekiyo (1994)
Nd <sub>4.5</sub> Fe <sub>91</sub> Nb <sub>2</sub> B <sub>3.5</sub>	Fe/Nd <sub>2</sub> Fe <sub>14</sub> B		RS+A	1.84	1.45	215	115	Hadjipanayis et al. (1995)
Nd <sub>9</sub> Fe <sub>85</sub> B <sub>6</sub>	Fe/Nd <sub>2</sub> Fe <sub>14</sub> B	25%	RS+A		1.09	326	93.1	Chan and Hsing (1996)
Nd <sub>9</sub> Fe <sub>85</sub> B <sub>6</sub>	Fe/Nd <sub>2</sub> Fe <sub>14</sub> B		RS+A		1.10	485	158	Manaf et al. (1993)
Nd <sub>8</sub> Fe <sub>86</sub> B <sub>6</sub>	Fe/Nd <sub>2</sub> Fe <sub>14</sub> B		RS+A		1.12	458	157	Manaf et al. (1993)
Nd <sub>7.5</sub> Fe <sub>87</sub> B <sub>3.5</sub>	Fe/Nd <sub>2</sub> Fe <sub>14</sub> B		RS+A		1.01	340	99.5	Panchanathan (1995)
Nd <sub>7</sub> Fe <sub>89</sub> B <sub>4</sub>	Amo <sup>c</sup> -Fe/Nd <sub>2</sub> Fe <sub>14</sub> B		RS+A		1.28	252	146	Inoue et al. (1995)
Sm <sub>7</sub> Fe <sub>93</sub> N <sub>x</sub>	Fe/Sm <sub>12</sub> Fe <sub>17</sub> N <sub>x</sub>		MA+A		1.127	310	205 <sup>d</sup>	Ding et al. (1993)
Sm <sub>8</sub> Zr <sub>3</sub> Fe <sub>85</sub> Co <sub>4</sub> N <sub>x</sub>	Fe/SmFe <sub>7</sub> N <sub>x</sub>		RS+A		0.94	764	118	Yoneyama et al. (1995)
Nd <sub>9.7</sub> Fe <sub>84</sub> Mo <sub>6.3</sub>	Fe/Nd(Fe,Mo) <sub>12</sub> N <sub>x</sub>		MA+A		1.12	207	48	Paviprasad et al. (1995)
Nd <sub>7.2</sub> Fe <sub>85</sub> Mo <sub>7.8</sub> N <sub>x</sub>	Fe <sub>85</sub> Mo <sub>7.8</sub> N <sub>x</sub>	40%	MA+A		1.37	281		Jurcyk (1996)
SM <sub>11.67</sub> Co <sub>38.33</sub> Fe <sub>50</sub>	Fe/SmCo <sub>5</sub>		MA+A		0.97	600	101.1	Majima et al. (1996)
SmCo <sub>10</sub>	Co/Sm <sub>2</sub> Co <sub>17</sub>	12%	MA+A		0.94	318	81.2	Chen et al. (1996)

<sup>a</sup> Full density is assumed. No demagnetization corrections were performed except where indicated. From Hiroswawa and Tomizawa (1997).

<sup>b</sup> Abbreviations: RS, rapid solidification; MA, mechanical alloying; A, annealing.

<sup>c</sup> Amo, amorphous phase.

<sup>d</sup> This value involves an uncertainty resulting from a demagnetization field correction (demagnetization coefficient not reported).

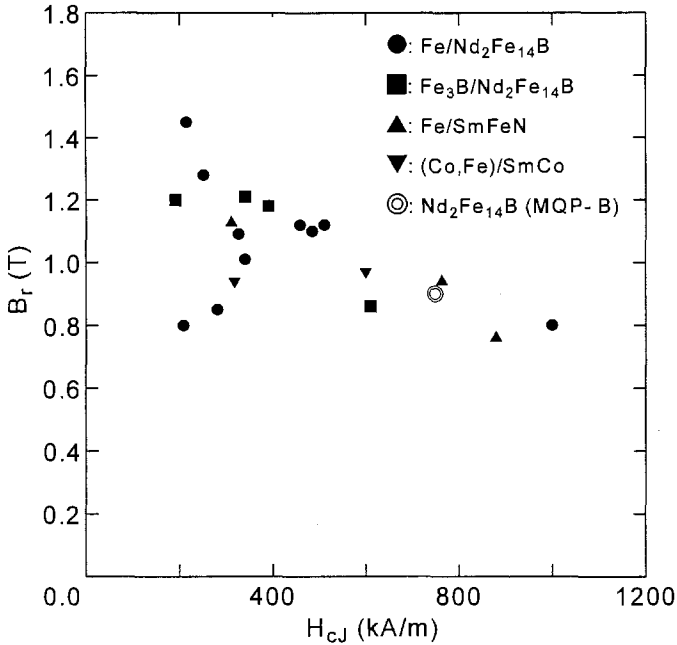


Fig. 25. The remanence vs. coercivity of rare-earth isotropic nanocomposite magnets (Hirosawa 1999).

increases slightly with increasing Cr content. The grain sizes of the Cr-free Nd<sub>2</sub>Fe<sub>14</sub>B nanocomposites are 20–50 nm, while the average grain size is about 20 nm in composites to which Cr has been added (Kanekiyo et al. 1993). This reduction of grain size is one of the reasons for the enhanced coercivity in the samples. Another reason is the increase in the volume fraction of Nd<sub>2</sub>Fe<sub>14</sub>B with increasing Nd content.

Other effects of Cr additions are as follows. First, the crystallized phases change with increasing Cr content in the sample. Cr-free samples are composed of a mixture of Fe<sub>3</sub>B and Nd<sub>2</sub>Fe<sub>14</sub>B phases, but with increasing Cr content the amount of  $\alpha$ -Fe phase gradually increases, and finally the sample consists of Nd<sub>2</sub>Fe<sub>14</sub>B and Fe<sub>2</sub>B +  $\alpha$ -Fe when the Cr content reaches 10–20 at.%. Second, the Curie temperature of the samples decreases with increasing Cr content (Hirosawa et al. 1993, Hirosawa and Kanekiyo 1996).

Except for the lowering of the Curie temperature, Cr addition improves the magnetic properties of the permanent magnets.

The Sumitomo Special Metal Co., Ltd. research team has been able to control the magnetic properties of Nd–Fe–B nanocomposite magnets by using some of the additives mentioned above. The relation between  $B_r$  and  $H_{cJ}$  of the magnets is shown in fig. 26. These values are quite good for industrial applications.

Smith et al. (1998) studied Nd–Tb–Fe–Cr–B nanocomposite materials produced by the mechanical milling technique. They investigated the phase relationships of the Nd<sub>2</sub>Fe<sub>14</sub>B phase and Fe<sub>3</sub>B, Fe<sub>2</sub>B and  $\alpha$ -Fe phases, and the strength of exchange coupling. They

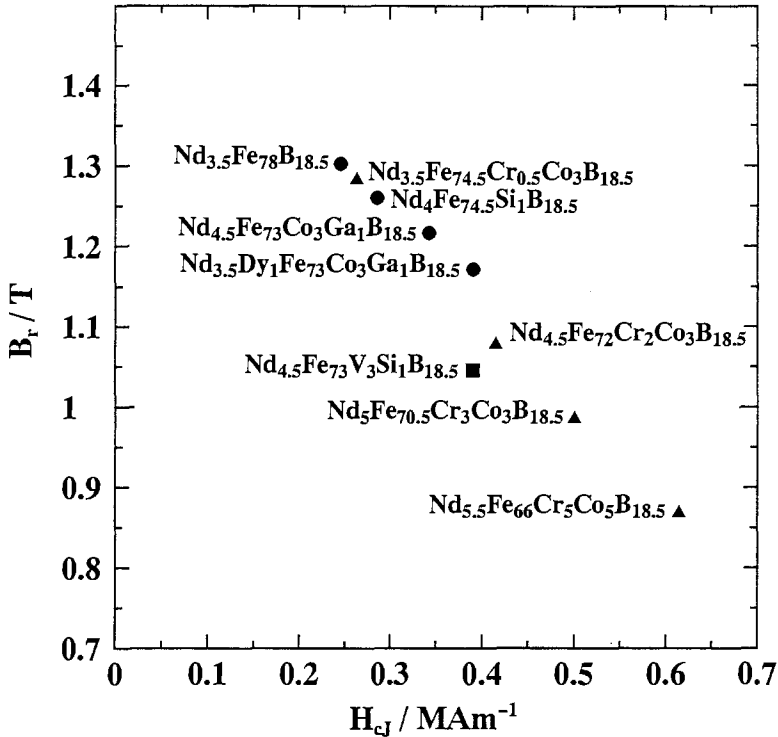


Fig. 26. The remanence vs. coercivity of some industrial nanocomposite magnets (Hirosawa and Kanekiyo 1994).

found that a Cr content up to 3 at.% or more leads to increased stability of  $(\text{Nd}, \text{Tb})_2\text{Fe}_{14}\text{B}$ , and the Cr itself is concentrated in the  $\text{Fe}_2\text{B}$  phase. They concluded that the phenomena mentioned above, in turn, decrease both the strength of exchange coupling and the spontaneous magnetization in the soft magnetic phase. The increase in coercivity of the bulk magnet can also be explained by the phenomena.

Ping et al. (1999) studied the correlation between microstructure and magnetic properties of melt-spun ribbons of  $\text{Nd}_{4.5}\text{Fe}_{77}\text{B}_{18.5}$ ,  $\text{Nd}_{4.5}\text{Fe}_{76}\text{B}_{18.5}\text{Nb}_{1.0}$ ,  $\text{Nd}_{4.5}\text{Fe}_{76.8}\text{B}_{18.5}\text{Cu}_{0.2}$  and  $\text{Nd}_{4.5}\text{Fe}_{75.8}\text{B}_{18.5}\text{Cu}_{0.1}\text{Nb}_{1.0}$ , which were crystallized by annealing. The crystallization process in the ternary ribbons consists of two reactions; crystallization of the  $\text{Fe}_3\text{B}$ , starting at 874 K, and  $\text{Nd}_2\text{Fe}_{14}\text{B}$ , at 898 K, for a heating rate of 20 K/min. Addition of Nb raised the onset temperatures of both crystallization reactions by about 20–40 K. Cu, on the other hand, favors the crystallization reaction. Three-dimensional atom-probe microanalysis (3D-APM) indicated that Cu addition causes formation of high-density ( $10^{24} \text{ m}^{-3}$ ) atomic clusters in which both Cu and Nd are enriched and B is excluded at temperatures much lower than the crystallization temperature. 3D-APM also revealed that  $\text{Fe}_3\text{B}$  crystallizes in the region next to these atomic clusters where Fe and B are enriched. Therefore, the kinetics enhancement by Cu addition is of chemical origin.

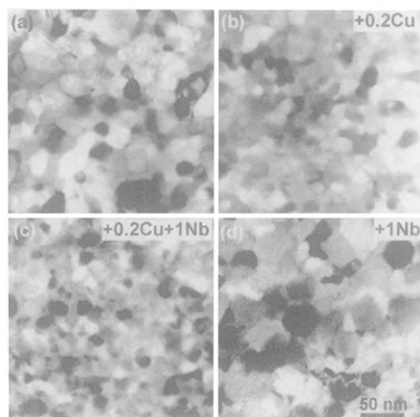


Fig. 27. TEM bright-field micrographs of (a)  $\text{Nd}_{4.5}\text{Fe}_{77}\text{B}_{18.5}$ , (b)  $\text{Nd}_{4.5}\text{Fe}_{76.8}\text{B}_{18.5}\text{Cu}_{0.2}$ , (c)  $\text{Nd}_{4.5}\text{Fe}_{75.8}\text{B}_{18.5}\text{Cu}_{0.1}\text{Nb}_{1.0}$ , and (d)  $\text{Nd}_{4.5}\text{Fe}_{76.0}\text{B}_{18.5}\text{Nb}_{1.0}$  melt-spun ribbons which were crystallized at 933 K for 10 min. The average grain size is about 30, 17, 12, and 43 nm, respectively.

Niobium was found to cause formation of the  $\text{Fe}_{23}\text{B}_6$  at the second stage of crystallization in these ribbons. 3D-APM indicated that Nb dissolves in this phase (in which almost no Cu was detected) when the  $\text{Nd}_{4.5}\text{Fe}_{75.8}\text{B}_{18.5}\text{Cu}_{0.1}\text{Nb}_{1.0}$  ribbon is annealed at the optimum temperature of 933 K. Since two phases crystallize from the amorphous phases surrounding the  $\text{Fe}_3\text{B}$  primary crystallites, a finer microstructure is achieved in comparison to the case in which Cu is added (fig. 27).

The investigation of a method for obtaining a sufficient coercivity for industrial applications is still an important task in the research on the exchange-coupled magnets. With optimization of preparation conditions, exchange-coupled magnets based on  $\text{Nd}_2\text{Fe}_{14}\text{B}$  are currently in the initial stage of industrialization. The commercial value of exchange-coupled magnets, however, does not seem to be in the high energy product, but in the good cost–performance ratio due to the high Fe content which means a low cost of production.

On the other hand, the industrialization of Sm–Fe-based nanocomposite magnets will be realized by the manufacturing activities of Sumitomo Metal Mining Co., Ltd., TDK Co., Ltd., Hitachi Metal Ind. Co., Ltd., Toshiba Co., Ltd. and other companies in Japan.

#### 4.4. Reaction velocity

Reaction velocity, or the kinetics of reactions, is an important fundamental point in mechanical alloying and rapid solidification. For example, in the early stage of solidification of a cast alloy, and/or of the rapid solidification in Nd–Fe–B materials, the elements Nd and Fe are homogeneously mixed. In these cases, the final phases obtained are largely dependent on the velocity of the cooling of the solution. The temperature of the solution needs to be sufficiently high, for a suitable time, for atomic diffusion of the elements to complete the equilibrium reactions.

Figure 28 shows a schematic presentation of the microstructure of the alloys obtained by conventional casting. The microstructure is composed of three phases: Nd-rich,  $\text{Nd}_2\text{Fe}_{14}\text{B}$ , and  $\alpha$ -Fe dendritic phases which appear via phase transitions from the original  $\gamma$ -Fe dendritic phases.

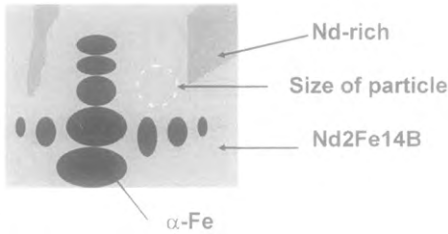


Fig. 28. Schematic representation of the microstructure of solidified Nd-Fe-B before annealing (Hirosawa 1999).

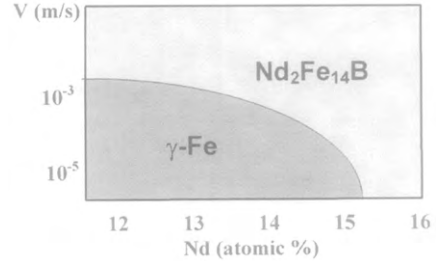


Fig. 29. Relationship between the velocity of the solidification front and the Nd concentration in Nd-Fe-B system (Umeda et al. 1996).

In general, the peritectic formation of the  $\text{Nd}_2\text{Fe}_{14}\text{B}$  phase is preferred to that of the  $\gamma\text{-Fe}$  phase under the higher cooling rate in the rapid solidification method. This phenomenon can be understood from the fact that the formation of the  $\gamma\text{-Fe}$  phase requires a long diffusion distance for Fe atoms, which naturally requires that the materials be kept at sufficiently high temperature during the development of the microstructure.

Umeda et al. (1996) studied the relationship between the velocity of the solidification fronts and the Nd content in the starting mixtures during the cooling process. Their study also revealed the relationship between the  $\gamma\text{-Fe}$  and  $\text{Nd}_2\text{Fe}_{14}\text{B}$  phases under the rapid solidification conditions. The results are summarized in fig. 29. At a higher velocity of the solidification fronts, the  $\text{Nd}_2\text{Fe}_{14}\text{B}$  phase is more stable than the  $\gamma\text{-Fe}$  phase, which should be the stable phase in the equilibrium state.

We conclude that the cooling velocity in the rapid solidification process has a strong relationship with the reaction velocity and/or the velocity of the movement of solidification fronts, which decides the stable phase under the given conditions. More attention, therefore, should be paid to the reaction velocity of phase formation for controlling the microstructures of the rare-earth permanent magnets.

## 5. Relation between corrosion and coercivity

### 5.1. Improvement of coercivity and corrosion resistance in $\text{Nd}_2\text{Fe}_{14}\text{B}$ -based magnets

Even at the present time, the obvious features of Sm-Co magnets are the high Curie temperatures, which means better magnetic properties at higher temperatures, and better corrosion resistance than the Nd-Fe-B materials. Except for increasing the energy product, the most important tasks for research on  $\text{Nd}_2\text{Fe}_{14}\text{B}$ -phase magnets and also other newly developed permanent-magnet materials, therefore, is to improve the corrosion resistance and raise the Curie temperature.

In early studies, Sagawa et al. (1984a,b) already pointed out the effects of additives such as Co and Dy on improvements of the magnetic properties, especially the Curie temperature ( $T_C$ ) and coercivity ( $H_{cJ}$ ), respectively, of Nd-Fe-B sintered magnets. Dy addition increases the intrinsic anisotropy field, which results in an increase of coercivity. The disadvantage of Dy addition, however, is the high cost of dysprosium.

Ohashi et al. (1987) studied the addition of Co to improve the corrosion resistance. As mentioned above, cobalt substitution was also known to increase the Curie temperature. Even though the anisotropy field of materials doped with less than 3 at.% Co is almost constant, the coercivity of the doped magnets decreases drastically (Grössinger et al. 1987).

With our present knowledge, the co-addition of Dy and Co to Nd-Fe-B-based magnets is a standard technique for commercial magnets. The reduction of the Dy content and the recovery of the coercivity by decreasing the amount of Co addition, however, are vital research tasks for Nd-Fe-B-based magnets.

The effects of other elements, such as Mo (Grössinger et al. 1984, Sagawa et al. 1988), (Nb, Ti, Zr) (Kou et al. 1989, Nakamura et al. 1989), Al (Sagawa et al. 1988), Cr (Higgins and Oesterreicher 1987), and V (Sagawa et al. 1990), on the magnetic properties of the magnets have been investigated.

Phenomenologically, some metal oxides, such as  $\text{Cr}_2\text{O}_3$ ,  $\text{Y}_2\text{O}_3$ ,  $\text{V}_2\text{O}_3$  and  $\text{Al}_2\text{O}_3$ , are effective for increasing the corrosion resistance of the magnets (Takeshita and Watanabe 1989). Limited contents of oxygen, carbon and/or nitrogen are also effective in stabilizing the magnets in corrosive environments (Narasimhan et al. 1986, Kim et al. 1990). The optimum contents of these elements are, O: 0.06–0.12%, C: 0.06–0.14%, and N: 0.05–0.10% (Kim et al. 1990), depending on Nd content.

Concerning the composition of corrosion-resistant Nd-Fe-B-based magnets, Shimotomai et al. (1990, 1994) and Fukuda and Shimotomai (1994) proposed an interesting magnet of composition  $\text{Nd}-(\text{Fe}_{1-x-y}\text{Co}_x\text{Ni}_y)\text{-B}$ ;  $0.2 \leq x \leq 0.45$ ,  $0.05 \leq y \leq 0.25$ , and a trace of Ti ( $\text{Ti}_{0.015}$ ). Their magnets show good corrosion resistance, which is due to the stabilization of the grain-boundary phases of  $\text{Nd}(\text{Ni},\text{Fe})$  and/or  $\text{Nd}(\text{Co},\text{Fe})$  compounds. The grain-boundary phase corresponds to  $\text{Nd}_3\text{Co}$  for Nd-Fe-Co-B magnets, which is more corrosion resistant than the normal Nd-rich phase in the undoped alloy (Sagawa et al. 1984a,b). The Ti additive was thought to form a  $\text{TiB}_2$  precipitated phase at grain boundary, which inhibited grain growth during sintering.

They also added Ga and Dy to their magnets. The Ga addition was thought to lower the Curie temperature of the harmful impurity phase  $\text{Nd}(\text{Fe},\text{Co},\text{Ni})_2$ , while the effect of the Dy addition has been discussed earlier in this section (see also sect. 2).

The microstructure of sintered Nd-Fe-B magnets is mainly composed of the  $\text{Nd}_2\text{Fe}_{14}\text{B}$  phase, the  $\text{Nd}_{1.1}\text{Fe}_4\text{B}_4$  phase, and the Nd-rich phase at grain boundaries. The corrosion mechanism of the sintered body has been discussed in several papers. Nakamura et al. (1989) revealed that the Nd-rich phase has a more negative electric potential than the matrix  $\text{Nd}_2\text{Fe}_{14}\text{B}$  phase, the  $\text{Nd}_{1.1}\text{Fe}_4\text{B}_4$  phase and, if it exists, the Fe-B phase. They also pointed out that the Nd-rich phase is easily dissolved in water.

Kim and Jacobson (1987), Jacobson and Kim (1987) and Kim (1989) studied and discussed the corrosion of Nd-Fe-B magnets in a number of solutions such as  $\text{H}_2\text{CrO}_4$ , HF,  $\text{H}_3\text{PO}_4$ , and in an autoclave at high temperature. They indicated that the oxidation of the magnets shows parabolic weight gain in dry and humid air at temperatures between room temperature and 423 K, and that the oxidation rate at 423 K is smaller than that at room temperature. This reduction can be explained by the fact that the formation of



Fe oxides takes place at around room temperature but is limited above 373 K, where the main phase formed by oxidation is a Nd oxide. Naturally, the formation of Nd oxides should reduce the formation of Fe oxides. This is also consistent with the above-mentioned results that the oxidation rate is reduced with increasing Nd content of the magnets.

Oxidation in heated water vapor results in the formation of  $\text{Nd}(\text{OH})_3$  which is formed by a selective attack of the grain-boundary Nd-rich phase by the water vapor.

They also found that combined surface treatment with  $\text{H}_2\text{CrO}_4$ , HF, and  $\text{H}_3\text{PO}_4$  improved the corrosion resistance of the magnets in both the water and autoclave environments. They thought that this improvement comes from (a) the removal of nucleation sites for corrosion by chromic acid, and (b) the formation of a protective film at the surface by chromate conversion.

They insisted that the chloride ion, which is introduced mainly by the handling of magnets, remarkably deteriorates the corrosion resistance of the magnets, and pointed out that Dy and Al additions reduce the oxidation rate (Kim and Jacobson 1987).

In practice, surface coating methods are a standard technique for increasing the corrosion resistance of the magnets. The coatings used include resin (William and Narasimhan 1987), Al-ion plating (Hirosawa et al. 1991a), and Ni plating (Minowa et al. 1989).

Surface coating techniques can also be applied to other magnets, such as  $\text{Sm}_2\text{Fe}_{17}\text{N}_3$  powders. Machida et al. (1995), Izumi et al. (1996), and Noguchi et al. (1998) studied the surface coating of powders with Zn metal derived from  $\text{Zn}(\text{C}_2\text{H}_5)_2$ , and were able to prepare highly corrosion-resistant powders for magnets. Recently, they improved their methods to apply alloy films composed of effective metallic elements: Zn, In, and Cu (Noguchi et al. 1998).

The corrosion mechanism for Nd-Fe-B-based magnets has been studied in detail. Chin et al. (1988) investigated passivating currents of Nd-Fe-B-based magnets in various aqueous solutions, and found that the current density between a Nd-Fe-B sintered magnet and a Ni-Cr reference electrode alloy was more than double that of Sm-Co magnets.

Fukuda and Shimotomai (1994) measured the electrochemical potentials between grain-boundary phases and the Nd-Fe-B and Nd-(Fe,Co,Ni)-B main phases, and concluded that the potential difference between the Nd-rich grain-boundary phase and the main phase is about 7 times larger in the Nd-Fe-B-based magnet than in the Nd-(Fe,Co,Ni)-B magnet.

It is concluded that the corrosion of Nd-Fe-B-based magnets proceeds mainly in the grain-boundary phase, especially the Nd-rich phase. Increasing the corrosion resistance of the grain-boundary Nd-rich phase is probably the most effective approach for the preparation of corrosion-resistant Nd-Fe-B magnets.

Concerning the oxidation of the grain-boundary phase, Steyaert et al. (1996) studied the kinetics of oxidation of  $\text{Nd}_2\text{Fe}_{14}\text{B}$  magnets by Mössbauer spectroscopy. They prepared powders of different average particle sizes, and exposed the powders in ambient air at temperatures between 423 and 573 K. They concluded that the oxidation started from the intergranular region of the particles, and then proceeded into the center portion of the particles by a bulk diffusion process when the intergranular portions were already

sufficiently oxidized. They calculated an activation energy of 110 kJ/mol and a diffusivity pre-exponential factor of  $2.4 \text{ mm}^2/\text{s}$  using a simple single-particle analysis model (Jander's model). The obtained value of the activation energy is close to the value for the oxidation of pure Fe.

Edgley et al. (1993) studied the oxidation at around 373 K, and concluded that the oxidation rate increases with temperature.

Blank and Adler (1987) studied the oxidation behavior of Nd-Fe-B and (Nd,Dy)-Fe-B magnets in the high-temperature region of 673–873 K, and they obtained parabolic oxidation rates. The observed microstructures of the oxidized samples using scanning electron microscopy (SEM), however, showed a clear interface between the oxidized surface region and the undamaged bulk, on the order of  $1 \mu\text{m}$  in thickness. In their experiments, there was no evidence of intergranular diffusion.

The experiments of Blank and Adler (1987), however, were done at too high temperatures to be useful in analyzing the oxidation of Nd-Fe-B magnets in common usage. For example, the humidity ( $\text{H}_2\text{O}$ ) in ambient air near room temperature, which contributes to the formation of  $\text{Nd}(\text{OH})_3$  in the initial stage of corrosion, needs to be considered. The initial oxidation of the magnets, therefore, is expected to start from the grain-boundary region where the Nd-rich phase normally exists.

The enhancement of corrosion resistance of the grain-boundary phase has therefore been studied by many researchers. As mentioned before, Co addition, for example, forms the  $\text{Nd}_3\text{Co}$  phase at grain boundaries when the Co content is less than 5%, and this phase shows better corrosion resistance than the pure Nd-rich phase. Hirosawa et al. (1991a) studied this phase using TEM, and from EDX analysis clearly proved that the phase is  $\text{Nd}_3\text{Co}$ . The existence of this phase was shown in studies on Nd-(Fe,Co,Ni)-B-based magnets by Kim and Jacobson (1987) and Fukuda and Shimotomai (1994).

Other additives, such as Mo and V, should form  $(\text{V},\text{Mo})_2\text{FeB}_2$  phases and/or other B-containing phases at the grain boundary. The Mo and V are finely distributed in the materials, and suppress the grain growth during sintering (Sagawa et al. 1990). It is thought that a certain amount of Nd is released to form some anti-corrosive phases at grain boundaries as a result of the reaction, and that the borides thus formed suppress grain growth. However, the effectiveness of the Mo additive should have a strong relationship with the B content of the material (Rodewald and Schrey 1989, Hirosawa et al. 1991b). Tenaud et al. (1990) reported high-coercivity magnets with  $H_{cJ} \approx 17 \text{ kOe}$  prepared with only Co and V additives without Mo.

As Sagawa et al. (1990) discussed, the following three points should be important to obtain high coercivity, at least, in the sintered magnets:

- (a) Small grain size.
- (b) Good magnetic insulation among grains.
- (c) No soft magnetic impurity phases, or no direct contact of these phases with the main phase.

Of course, the second and third points should be carefully considered for nanocomposite materials. However, improvements in coercivity and corrosion resistance of Nd-Fe-B-based sintered magnets have been achieved by using these guidelines up to now.

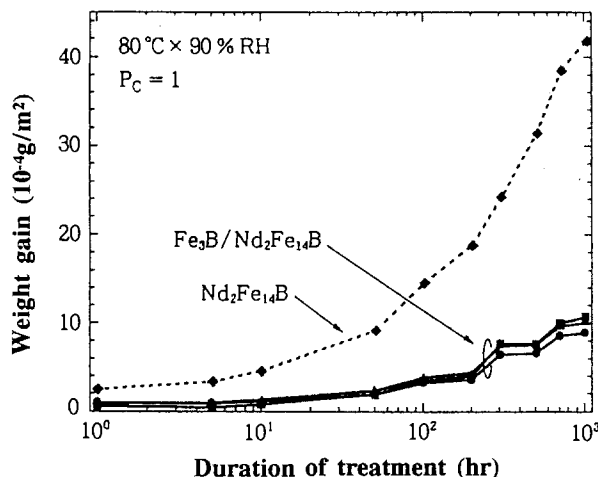


Fig. 30. Relation between weight gain and duration of treatment of a  $\text{Nd}_2\text{Fe}_{14}\text{B}$  sintered magnet and a  $\text{Fe}_3\text{B}/\text{Nd}_2\text{Fe}_{14}\text{B}$  nanocomposite magnet.

The corrosion and/or oxidation of nanocomposite magnets seems to be a more complicated phenomenon compared to the case of sintered magnets. Figure 30 shows a comparison between the oxidation in an ordinary sintered  $\text{Nd}_2\text{Fe}_{14}\text{B}$  magnet and that in a  $\text{Fe}_3\text{B}/\text{Nd}_2\text{Fe}_{14}\text{B}$  nanocomposite magnet. The nanocomposite magnet indicates better corrosion resistance. However, the analysis of the mechanism of the oxidation, and the relation between magnetic properties and oxidation behavior, are just starting to be studied in some research groups.

### 5.2. Some aspects of the corrosion mechanism in rare-earth magnets

Kim and Jacobson (1987) and Blank and Adler (1987) have pointed out that the oxidation mechanism of Nd–Fe–B-based magnets obeys a parabolic law. The parabolic law of oxidation in metals was explained theoretically by Wagner (1933). His explanation can be summarized as follows:

The increase of the thickness of a surface oxidized thin layer is governed by flux flow,  $j$  ( $j$  may be oxygen and/or metal diffusion), which is inversely proportional to the thickness of the layer,  $x$ :

$$j = c \frac{dx}{dt} = \frac{k}{x}, \text{ where } t \text{ is time, and } k \text{ is a constant.}$$

The results obtained by Blank and Adler (1987), especially their photographs of the oxidized layer, seem to be a typical case of this parabolic-law oxidation, showing the formation of an oxidized layer on the surface of metal of homogeneous thickness. The oxidation mechanisms discussed in this section, however, are not so simple in the case in which the grain-boundary Nd-rich phase is oxidized selectively. This point has been schematically illustrated in fig. 31. The relationship between the oxidation mechanisms of the grain-boundary Nd-rich phase (fig. 31a) and of the growth of the thickness of the oxidized layer (fig. 31b) should be important considerations in the oxidation of Nd–Fe–B magnets. We will return to this in more detail in the discussion of the oxidation mechanism of the magnets.

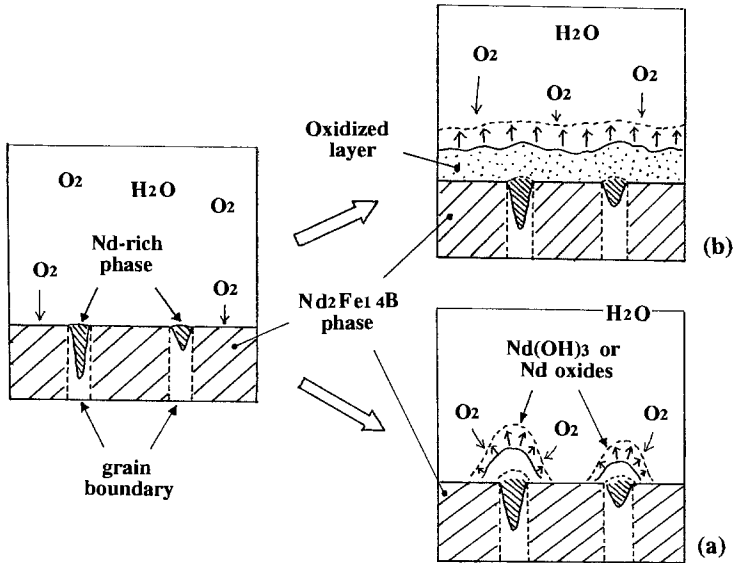


Fig. 31. Schematic representation of the oxidation mechanism in Nd-Fe-B magnets.

In general, metal surfaces are covered by a thin oxide film of around 10 nm thickness. Kobayashi et al. (1993) showed that the oxidized surface layer was about 10 nm thick for  $\text{Sm}_2\text{Fe}_{17}\text{N}_3$  magnetic particles. This thin oxidized layer should exist as well in other magnet materials, such as Sm-Co and Nd-Fe-B based magnets; however, this thin layer is thought to have no obvious effects on the coercivity and other magnetic properties, except for a slight decrease in saturation magnetization, which decreases with increasing volume fraction of the oxidized layer.

If the magnets are oxidized, and some oxidized phases appear at grain boundaries as in the case of Nd-Fe-B magnets, it is an important question what effects should be expected, for example, on the magnetic reversal mechanism in the magnets.

Kobayashi et al. (1995) proposed a phenomenological model which deeply concerns this question.  $\text{Sm}_2\text{Fe}_{17}\text{N}_3$  powders of initial coercivity 6.3 kOe in samples of aligned particles, were exposed to ambient air at 373–473 K for certain durations between 60 and 3600 seconds. The sample powders showed a weight gain which corresponded to the increase in oxygen content, as shown in fig. 32.

The weight gain always results in a decrease in saturation magnetization under an applied field of  $\mu_0 H_{\text{appl.}} = 1.5 \text{ T}$  after pulse magnetization in a magnetic field of  $\mu_0 H_{\text{appl.}} = 5 \text{ T}$  (see fig. 33). It was determined that almost all of the oxygen pick-up formed an oxidized non-magnetic phase, which was not identified (Kobayashi et al. 1996).

The dependence on oxidation time at various temperatures is shown for coercivity and magnetization in figs. 34 and 35, respectively. These measurements were made on aligned powders in a field of about 0.5 T, and following pulse magnetization of about 5 T. The dependences follow a logarithmic law. When a logarithmic dependence of the increase in

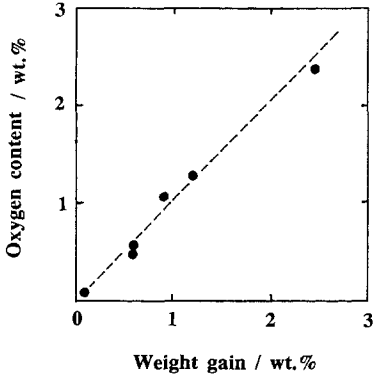


Fig. 32. Relationship between the weight gain and the oxygen contents of  $\text{Sm}_2\text{Fe}_{17}\text{N}_3$  oxidized powders.

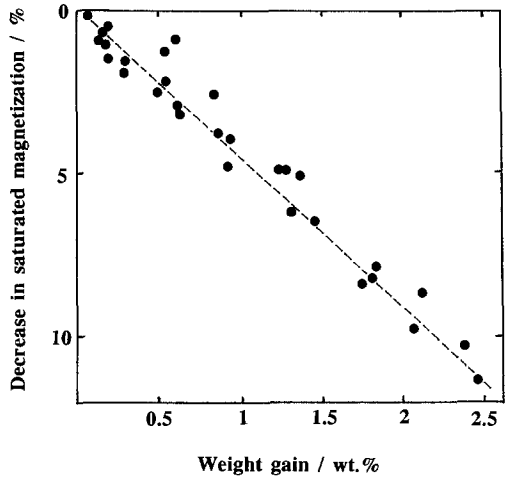


Fig. 33. Relationship between the saturated magnetization and the weight gain of oxidized  $\text{Sm}_2\text{Fe}_{17}\text{N}_3$  powders.

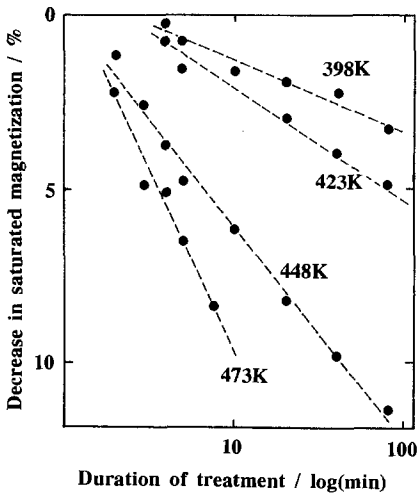


Fig. 34. Time dependence,  $\log(t/\text{min})$ , of the decrease in saturated magnetization at various temperatures.

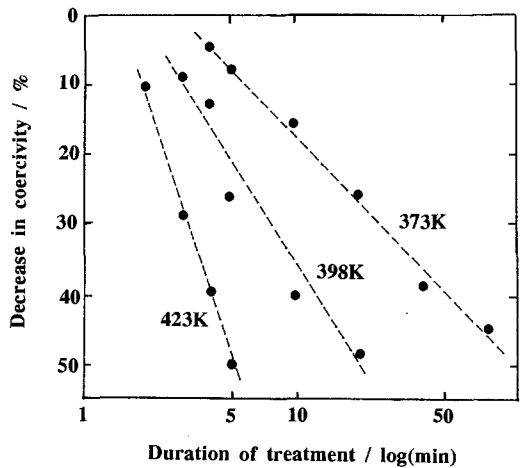


Fig. 35. Time dependence,  $\log(t/\text{min})$ , of the decrease in coercivity at various temperatures.

thickness of the oxidized layer, i.e. the decrease in saturation magnetization, is observed, the growth of the layer can be explained by the long-range quantum-tunneling oxidation mechanism proposed by Cabrera and Mott (1948).

In  $\text{Sm}_2\text{Fe}_{17}\text{N}_3$  magnetic particles, the microstructure of the particles is simply composed of the main 2-17 phase and a trace of a Sm-rich phase, which does not play an

important role in the formation of the microstructure as compared with the Nd-rich phase in Nd–Fe–B magnets. The oxidation of the main phase is expected to become as indicated in fig. 34. The relationship between the formation of the oxidized surface phase and the deterioration in coercivity, shown in fig. 35, has not been clarified up to the present time.

In conclusion, the use of industrialized magnets in harsh environmental conditions has been made possible by the improvement of the corrosion resistance and coercivity of the materials themselves through controlling the compositions using additives, and by protective techniques such as surface coating. A fundamental analysis of the oxidation and/or corrosion mechanisms, and the origin of the deterioration of the magnetic properties are future tasks in the researches on permanent magnets.

## 6. Other preparation methods of industrial magnets

There are a few other methods for preparing industrial magnets. In this section, some of the methods, except sintering which was discussed in sect. 3, will be briefly reviewed. The methods can be roughly categorized into two types: first, the methods using metallurgical techniques, such as casting and hot-plastic working; and second, a method which is known as the “bonded magnets” technique, which uses different types of resins for the binder.

### 6.1. Hot-working and casting methods

Lee et al. (1985) showed that hot-plastic working gives anisotropy to an initially isotropical Nd–Fe–B bulk magnet. This anisotropy comes from crystal grain growth in a certain direction under applied pressure. The original method was unidirectional pressing; later, a back-extrusion technique was applied. The grains align perpendicular to the plastic flow.

This technique has been developed to prepare the so-called “radial anisotropic ring magnets”, in which magnetic grains are aligned in the radial direction in bulk ring magnets (Yoshikawa et al. 1994). In another application of the technique, Saito et al. obtained a Nd–Fe–B magnet with  $(BH)_{\max} = 430 \text{ kJ/m}^3$  by hot deformation of an amorphous bulk precursor prepared using shock compaction.

A variation of the hot-working technique, a hot-pressing and plasma-activating process, was used to prepare high-density isotropic Nd–Fe–Co–B magnets for motor applications (Wada and Yamashita 1990). The main features of the obtained magnets are: (1) high density (nearly 100%), and (2) high coercivity which is mainly due to the starting powder composition. They prepared a magnet with a  $(BH)_{\max}$  of 15 MGOe and a coercivity of 1.36 MA/m. The temperature coefficients of magnetization and coercivity are comparatively better than those of the sintered Nd–Fe–B magnets.

Shimoda et al. (1988) succeeded in preparing cast  $\text{Pr}_2\text{Fe}_{14}\text{B}$  magnets. The anisotropy of these cast Pr–Fe–B magnets can be enhanced by hot-working, in which the deformation comes from the rotation of the Pr–Fe–B-phase grains, which are pulverized during deformation, in a praseodymium-rich liquid phase under pressure (Yuri and Ohki 1994). The mechanism is different from ordinary plastic deformation of metals which is caused by the appearance of dislocations in microstructure.

The casting method can also be applied to Nd-Fe-B and Nd-Fe-C systems (Eisses et al. 1991). Since the magnetic properties and the shape homogeneity of small and thin magnets, however, are better in sintered magnets, the industrialization of the cast magnets has not been yet realized.

## 6.2. Bonded magnets

The basic idea of a bonded magnet is the mixture of a magnetic powder and a binder. The most obvious features of bonded magnets are: (1) high degree of freedom in the shape of the magnets, which means that thin and long magnets can be prepared, (2) high shape accuracy without secondary machining, such as cutting and grinding, (3) high toughness without breaking and cracking, and (4) suitability for mass production.

Almost all rare-earth magnets, except the sintered Nd-Fe-B magnets, can be prepared as bonded magnets. The magnetic powders are prepared by melt-quenching, such as the MQ types, by the HDDR technique, and by mechanical alloying. Exchange-coupled magnetic powders are also used for bonded magnets. Improvement in the preparation methods for bonded magnets, therefore, is an important task for future researches on permanent-magnet materials.

Bonded magnets can be categorized into four types according to fabrication techniques: (a) calendaring type using a flexible binder, (b) extrusion type using a thermoplastic resin, (c) injection type also using a thermoplastic resin, and (d) compression type thermoset resin. Figure 36 summarizes the types of bonded magnets.

Calendaring methods are normally used in the production of ordinary magnets used in daily life. Some ideas exist about the use of a thin sheet of a mixture of rubber or resin and the magnetic powder, such as for radially oriented magnets by rolling the sheets. However, scientific papers about the fundamental points of the techniques generally do not appear in ordinary technical magazines.

The extrusion technique has been applied to Nd-Fe-B-based magnets. Sakata et al. (1992) reported on preparing magnets with 72 vol.% magnetic powder. The volume fraction has been increased to 78 vol.% using this technique (Akioka 1996). This value is nearly the same as for compression-molded magnets.

Injection molding magnets can be easily prepared in complex shapes with high mass productivity by using automatic injection molding machines. The maximum content of magnetic powder can be raised up to about 67 vol.% by optimization of the bonding conditions, i.e. selection of the resin and the pre-treatment reagent for the powders. Anisotropic magnets can also be produced using magnetically anisotropic powders, by the application of magnetic fields during injection molding. For an anisotropic bonded Sm-Fe-N magnet, Sumitomo Metal Mining Co.Ltd. has achieved a  $(BH)_{\max}$  of about  $100 \text{ kJ/m}^3$ . The injection-molding method has another advantage in that the magnets are without voids in bulk microstructure, which is advantageous for the prevention of the deterioration of magnetic properties by oxidation and/or by humidity (Claude et al. 1993).

Compression molding realizes high densities of magnetic powders. In laboratory-scale experiments, it is possible to prepare magnets with more than 80 vol.% magnetic powder.

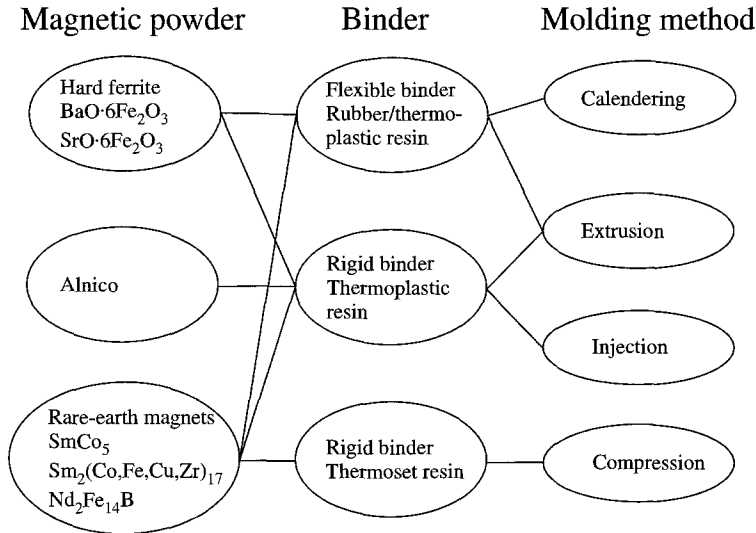


Fig. 36. Relations among constituent technologies relevant to the fabrication of bonded permanent magnets (Hirosawa and Tomizawa 1997).

Since the compression technique needs comparatively high pressure, more than 600 MPa in ordinary cases, mass production is comparatively difficult except when rotary press machines can be used. The two main difficulties are in the powder feeding and in the wear and fatigue of dies for molding, which is also a problem in injection molding.

Matsunaga et al. (1996) developed a method using a binder of low melting viscosity, and achieved a high volume fraction of highly oriented HDDR Nd–Fe–B magnetic powder. Their magnets also have the advantage of a low void fraction in the microstructure, which prevents or reduces the deterioration of the magnetic properties by hydrogen attack (Claude et al. 1993).

The relationship between the magnetic flux loss and the volume fraction of voids in injection/compression-molding bonded magnets after treatment under the same conditions is represented in fig. 37 (Mino and Hirosawa 1999). It is clear that the magnetic flux losses proportionally decrease with increasing volume fraction of voids.

The total world-wide market for rare-earth bonded magnets is estimated to be 200 million dollars at present. There are some promising bonded magnets for future applications. Magnets using isotropic nanocomposite magnetic materials will be used for small-size rotors, such as stepping motors with multi-pole magnetization. For higher-temperature applications, Cr-doped Fe–Fe<sub>2</sub>B–Nd<sub>2</sub>Fe<sub>14</sub>B nanocomposite bonded magnets should be useful.

The most promising bonded magnet, however, is the anisotropic nanocomposite and/or metastable-phase magnet which potentially can achieve a  $(BH)_{\text{max}}$  of more than 300 kJ/m<sup>3</sup> with a sophistication of the current preparation techniques (Schrefl et al. 1994a).



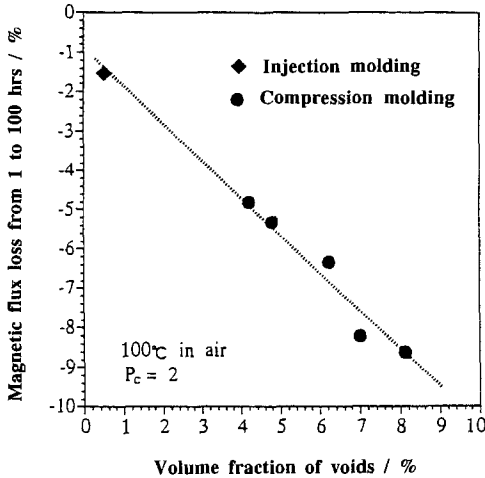


Fig. 37. Relationship between the volume fraction of voids (%) and the magnetic flux losses in typical injection and compression molding bonded magnets (Mino and Hirose 1999).

## 7. Some typical studies using micromagnetic approaches

Micromagnetism was introduced in the studies of magnetism by Brown (1962, 1963). In this section, we briefly summarize the present stage of this active field of research. With the development of greatly increased computing power, the calculation using, for example, the finite elements method (FEM), it is now possible to simulate the details of the magnetic reversal mechanisms and/or interactions between grains in complex microstructures, i.e. those found in nanocomposite magnets.

The important reasons for recent developments of this type of simulation are the following. First, the specific coherent length ( $L$ ), represented as

$$L \approx \sqrt{\frac{A}{K}},$$

where  $A$  is the exchange stiffness coefficient, and  $K$  is the anisotropy constant, is comparable with the typical grain size in nanocomposite materials. This size is also about the same as the size of the activation volume,  $v$ , in magnetic after-effects, which means the nucleation region in the magnetic reversal. The width of domain walls in hard magnetic materials is about 10 nm, which is of the same order as the length  $L$ .

All these sizes can be treated as a unit of magnetic moment in micromagnetic calculations, for example, see Fukunaga and Kanai (1998). The interactions among them can also be evaluated in the simulations.

Second, the real microstructure of the magnetic materials can be observed directly by TEM, and this information can also be used directly in the simulations as the morphological information needed in the calculations for the models.

Therefore, the most obvious ability of the micromagnetic approaches appears to be in the simulation of systems in which complex interactions between finite regions strongly

influence the properties of the whole system. In this sense, nanocomposites and/or exchange-coupled magnets are suitable materials for the micromagnetic approach.

The principles of the simulation method may be found in the introductions of papers quoted in this section. Four independent factors are important: (a) the exchange energy between the magnetization units, such as the Heisenberg model, (b) the magnetostatic energy of the magnetization in an external field, (c) the magnetocrystalline anisotropy energy coming from uniaxial magnetic anisotropy, and (d) the stray field.

For example, Schrefl et al. (1994b) analyzed the remanence enhancement in some magnets,  $\text{Nd}_2\text{Fe}_{14}\text{B}$ ,  $\text{SmCo}_5$ , and  $\text{Sm}_2(\text{Fe}_{0.8}\text{Co}_{0.2})_{17}\text{N}_{2.8}$ . They predicted (a) more than 40% of remanence enhancement is due to exchange interactions, (b) hardening of the soft magnetic phase which preserves a sufficiently high coercivity by exchange coupling, and (c) average grain sizes in the microstructure of the magnets comparable with the exchange length.

Kronmüller et al. (1994, 1996) and Bachmann et al. (1998) have been continuously developing micromagnetics-based methods. They studied the coercivity of rare-earth magnets by calculations in which each parameter was evaluated by following the well-known Stoner–Wohlfarth coherent rotation equation (Stoner and Wohlfarth 1948):

$$\mu_0 H_c = \alpha \frac{2K_1}{M_s} - N_{\text{eff}} \mu_0 M_s,$$

where  $\mu_0$  is the magnetic permeability of vacuum,  $H_c$  is the coercive field, and  $K_1$  and  $M_s$  are the first anisotropy constant and the saturated magnetization, respectively. The parameters  $\alpha$  and  $N_{\text{eff}}$  are important characteristic values of each material:  $\alpha$  characterizes the intrinsic character of the coherent magnetic reversal, and  $N_{\text{eff}}$  is a demagnetizing factor including the local parameters in the real shape of the sample, respectively.

They also applied their technique to nanocrystalline magnets, and discussed the difference between the “Nucleation Model” and the “Nucleation Expansion Model”. Their conclusion was that the difference between the models, if it exists, corresponds to a very small energy, and has almost no meaning in real magnets.

They also pointed out that the finite-elements method, in which the material is divided into elemental units, may fail to represent the exchange energy in systems containing strong inhomogeneities in magnetization distributions. For these cases, they proposed the use of the atomic-exchange-interaction (AEI) model based on the Heisenberg model in the limited volume of discontinuous local regions. Unfortunately the AEI model requires extremely powerful computers if applied to a realistic system. For real applications, they proposed a combined FEM–AEI method.

The group at the Laboratoire de Magnétisme Louis Néel has also been developing simulation methods based on micromagnetism. Recently, Toussaint et al. (1998) studied magnetization reversal in thin films, such as Sm–Co/Co–Zr/Sm–Co multilayer films, and films and an array of particles in W/Fe/W samples. They concluded that the magnetic reversal in the former case is governed by the propagation of a wall which is already

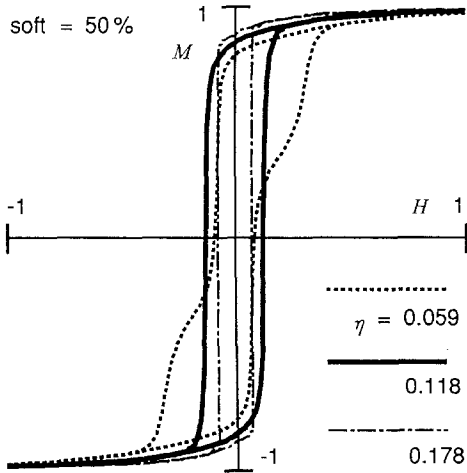


Fig. 38. Simulated effect of strength of interaction between hard and soft regions. Reduced  $M$ - $H$  curves are calculated under the assumption that the soft and hard grains have the same saturation magnetization (Fukunaga 1995).

present in the soft magnetic phase; and that the considerable reduction of the coercivity in the latter materials, compared with coherent rotation model (S-W model) is due to the emergence of large nonsaturated volumes at the edges of the particle.

The general contributions from the group are mainly concerned with the coercivity problems, which were summarized along with important contributions from other groups in an article by Givord and Rossignol (1996).

Fukunaga (1995) and Fukunaga and Kanai (1998) have been developing simulations in nanocomposite magnetic materials using a model based on interactions between cubic regions. Their method is an original approach in which each cubic region in the model corresponds to a hard or a soft magnetic phase region, and an interaction parameter  $\eta$  at the surface of the two cubic regions, which is given by

$$\eta = \frac{SJ_e}{6K_uV},$$

where  $J_e$  corresponds to the exchange constant for a unit surface area of a cubic region, and  $K_u$  corresponds to the anisotropy constant in the hard phase, and  $S$  is the surface area where the interaction appears, and  $V$  is the volume of a cubic region. They used an average grain size of about 10 nm for the hard and soft phases, and calculated the magnetic properties of the magnets as a function of the exchange-interaction parameter. Figure 38 is an example of their simulation, in which the volume fractions of the hard and soft regions were both 50%, and the interaction parameter between them was varied:  $\eta = 0.059$ , 0.118 and 0.178. The optimum hysteresis curve was obtained for  $\eta = 0.118$  in this calculation.

They improved their method by using finer magnetic elements, and developed a representation for the local demagnetizing field (Fukunaga and Kanai 1998). They concluded that a magnet composed of 60% soft and 40% hard grains with a grain size around 20 nm should be the best nanocomposite microstructure for the Nd-Fe-B system.

Other groups are also investigating the magnetic properties of rare-earth magnets using micromagnetic approaches. The magnetic properties of nanocomposite materials include

complex problems which are difficult to treat by either classical continuum models or quantum statics of distributed spin clusters alone. Combining these and other approaches, therefore, should be helpful for understanding the properties of these important magnetic materials, and should lead to a more powerful technique in the near future.

## References

- Akioka, K., 1996, in: Proc. Magnet-Seminar of Japan Electronic Materials Industry Association, February 21, Tokyo, pp. 3–14. In Japanese.
- Bachmann, M., R. Fisher and H. Kronmüller, 1998, in: Proc. 10th Int. Symp. on Magnetic Anisotropy and Coercivity in RE–TM Alloys, Dresden, eds L. Schultz and K.-H. Müller (Werkstoff-Informationsgesellschaft, Frankfurt) pp. 217–236.
- Blank, R., and E. Adler, 1987, in: Proc. 9th Int. Workshop on RE magnets and their Applications, Bad Soden, Germany, eds C. Herget and P. Poerschke (Deutsche Physikalische Gesellschaft, Bad Honnef) pp. 537–544.
- Book, D., and I.R. Harris, 1995, *J. Alloys Compounds* **221**, 187.
- Brown Jr, W.F., 1962, *Magnetostatic Principles in Ferromagnetism* (North-Holland, Amsterdam).
- Brown Jr, W.F., 1963, *Micromagnetics* (Interscience, New York).
- Buschow, K.H.J., 1987, in: Proc. 9th Int. Workshop on RE Magnets and their Applications, Bad Soden, Germany, eds C. Herget and P. Poerschke (Deutsche Physikalische Gesellschaft, Bad Honnef) p. 453.
- Buschow, K.H.J., 1994, *IEEE Trans. Magn.* **30**(2), 565.
- Buschow, K.H.J., D.B. de Mooij and H.M. van Noort, 1986, *J. Less-Common Met.* **125**, 135.
- Buschow, K.H.J., R. Coehoorn, D.B. de Mooij, C. de Waard and T.H. Jacobs, 1990, *J. Magn. Magn. Mater.* **92**, 135.
- Cabrera, N., and N.F. Mott, 1948, *Rep. Progr. Phys.* **12**, 163.
- Cadogan, J.M., and J.M.D. Coey, 1984, *Phys. Rev. B* **30**, 7326.
- Chaboy, J., L.M. Garcia, F. Bartolome, J. Bartolome, H. Maruyama, K. Kobayashi, N. Kawamura, A. Marcelli and L. Bozukov, 1997, *J. Phys. IV Paris* **7**, C2-449.
- Chan, W.C., and D.M. Hsing, 1996, *J. Appl. Phys.* **79**, 843.
- Chen, S.K., J.L. Tsai and T.S. Chin, 1996, *J. Appl. Phys.* **79**, 5964.
- Chin, T.S., R.T. Chang, W.T. Tsai and M.P. Hung, 1988, *IEEE Trans. Magn.* **24**, 1927.
- Christodoulou, C.N., and T. Takeshita, 1993, *J. Alloys Compounds* **194**, 113.
- Claude, E., S. Ram, I. Gimenez, P. Chaudouet, D. Boursier and J.C. Joubert, 1993, *IEEE Trans. Magn.* **29**(6), 2767.
- Clemente, G.B., J.E. Keem and J.P. Brandley, 1988, *J. Appl. Phys.* **64**, 5299.
- Coehoorn, R., 1991, in: *Supermagnets, Hard Magnetic Materials*, eds G.J. Long and F. Grandjean (Kluwer Academic Publishers, Dordrecht) pp. 133–170.
- Coehoorn, R., D.B. de Mooij, J.P.W.B. Duchateau and K.H.J. Buschow, 1988, *J. Phys. Paris* **49**, C8-669.
- Coehoorn, R., D.B. de Mooij and C. de Waard, 1989, *J. Magn. Magn. Mater.* **80**, 101.
- Coey, J.M.D., 1996, in: *Rare-earth Iron Permanent Magnets*, ed. J.M.D. Coey (Clarendon Press, Oxford) ch. 1, pp. 1–57.
- Coey, J.M.D., and H. Sun, 1990, *J. Magn. Magn. Mater.* **87**, L251.
- Croat, J.J., J.F. Herbst, R.W. Lee and F.E. Pinkerton, 1984, *J. Appl. Phys.* **55**, 2078.
- Davies, H.A., J. Liu and G. Medoza, 1996, in: Proc. 9th Int. Symp. on Magnetic Anisotropy and Coercivity in RE Transition metal Alloys, Bad Soden, eds C. Herget and P. Poerschke (Deutsche Physikalische Gesellschaft, Bad Honnef) p. 251.
- de Mooij, D.B., and K.H.J. Buschow, 1988, *J. Less-common Met.* **142**, 349.
- Ding, J., R. Street and P.G. McCormick, 1992, in: Proc. 7th Int. Symp. on Magnetic Anisotropy & Coercivity in RE–TM Alloys (University of Western Australia, Perth, WA, Australia) pp. 130–136.
- Ding, J., P.G. McCormick and R. Street, 1993, *J. Magn. Magn. Mater.* **124**, L1–L4.
- Ding, J., P.G. McCormick and R. Street, 1994, in: Proc. 13th Int. Workshop on RE Magnets and their Applications, Birmingham, eds C.A.F. Manwaring,

- D.G.R. Jones, A.J. Williams and I.R. Harris (REMXIII Committee) pp. 787–793.
- Edgley, D.S., J.M. Le Breton, D. Lemarchand, I.R. Harris and J. Teillet, 1993, *J. Magn. Magn. Mater.* **128**, L1.
- Eisses, J., D.B. de Mooij, K.H.J. Buschow and G. Martinek, 1991, *J. Less-Common Met.* **171**, 17.
- Endoh, M., and M. Shindoh, 1994, in: Proc. 13th Int. Workshop on RE Magnets and their Applications, Birmingham, eds C.A.F. Manwaring, D.G.R. Jones, A.J. Williams and I.R. Harris, pp. 397–404.
- Fidler, J., J. Bernardi, T. Schrefl and H. Kronmüller, 1991, *Mater. Res. Soc. Symp. Proc.* **232**, eds M. Doyama, S. Somiya, R.P.H. Chang, M. Homma and Y. Imaoka, pp. 275–288.
- Fidler, J., J. Bernardi, T. Schrefl and H. Kronmüller, 1994, in: Proc. 8th Int. Symposium on Magnetic Anisotropy and Coercivity in RE–TM Alloys, Birmingham, eds C.A.F. Manwaring, D.G.R. Jones, A.J. Williams, and I.R. Harris (REMXIII Committee) pp. 385–404.
- Fransé, J.J.M., and R.J. Radwanski, 1996, in: Rare-earth Iron Permanent Magnets, ed. J.M.D. Coey (Oxford Science Publications) ch. 2, pp. 58–158.
- Fujii, H., and H. Sun, 1995, in: Handbook of Magnetic Materials, Vol. 9, ed. K.H.J. Buschow (North-Holland, Amsterdam) pp. 303–404.
- Fujii, H., K. Tatami, M. Akayama and K. Yamamoto, 1992, in: Proc. 6th Int. Conf. on Ferrites, ICF6, Tokyo/Kyoto, Japan (Japan Society of Powder and Powder Metallurgy, Tokyo) p. 1081.
- Fujita, A., and I.R. Harris, 1994, *IEEE Trans. Magn.* **30**(2), 860.
- Fukuda, Y., and M. Shimotomai, 1994, *Trans. Mater. Res. Soc. Japan* **14B**, 1021.
- Fukunaga, H., 1995, *J. Magn. Soc. Japan* **19**, 791. In Japanese.
- Fukunaga, H., and Y. Kanai, 1998, in: Proc. 10th Int. Symp. on Magnetic Anisotropy and Coercivity in RE–TM Alloys, Dresden, eds L. Schultz and K.-H. Muller (Werkstoff-Informationsgesellschaft, Frankfurt) pp. 237–250.
- Givord, D., and M.F. Rossignol, 1996, Coercivity, in: Rare-earth Iron Permanent Magnets, ed. J.M.D. Coey (Clarendon Press, Oxford) ch. 5, pp. 218–285.
- Grössinger, R., P. Obitsch, X.K. Sun, R. Eibler and H.R. Kirchmayr, 1984, *Mater. Lett.* **2**, 539.
- Grössinger, R., A. Keresztes, H. Harada and Z. Shongong, 1987, in: Proc. 9th Int. Workshop on RE Magnets and their Applications, Bad Soden, Germany, eds C. Herget and P. Poerschke (Deutsche Physikalische Gesellschaft, Bad Honnef) p. 593.
- Gu, Z.-Q., and W.Y. Ching, 1987, *Phys. Rev. B* **36**(16), 8530.
- Gutfleisch, O., and I.R. Harris, 1998, in: Proc. 15th Int. Workshop on RE Magnets and their Applications, Dresden, Germany, eds L. Schultz and K.-H. Muller (Werkstoff-Informationsgesellschaft) pp. 487–506.
- Gutfleisch, O., M. Matzinger, J. Fidler and I.R. Harris, 1995, *J. Magn. Magn. Mater.* **147**, 320.
- Hadjipanayis, G.C., L. Withanawasam and R.F. Krause, 1995, *IEEE Trans. Magn.* **31**(6), 3596.
- Harris, I.R., C. Noble and T. Bailey, 1985, *J. Less-Common Met.* **106**, L1.
- Heisz, W., and L. Schultz, 1988, *Appl. Phys. Lett.* **53**, 342.
- Herbst, J.F., J.J. Croat, F.E. Pinkerton and W.B. Yelon, 1984, *Phys. Rev. B* **29**, 4176.
- Higgins, B.E., and H. Oesterreicher, 1987, *IEEE Trans. Magn.* **MAG-23**, 92.
- Hirosawa, S., 1992, Development of Nd–Fe–B magnets, 1. In Japanese.
- Hirosawa, S., 1999, *Met. Technol.* (August), 24 [AGNE publishing, Inc.]
- Hirosawa, S., and H. Kanekiyo, 1993, *IEEE Trans. Magn.* **29**(6), 2863.
- Hirosawa, S., and H. Kanekiyo, 1994, *Proc. Magn. Soc. Japan 85-2*, hand-out. In Japanese.
- Hirosawa, S., and H. Kanekiyo, 1995, in: Textbook for 91st Topical Symp., Magn. Soc. of Japan, p. 91-5. In Japanese.
- Hirosawa, S., and H. Kanekiyo, 1996, *Mater. Sci. Eng. A* **217/218**, 367.
- Hirosawa, S., and Y. Kaneko, 1998, in: Proc. 15th Int. Workshop on RE Magnets and their Applications, Dresden, eds L. Schultz and K.-H. Muller (Werkstoff-Informationsgesellschaft, Frankfurt) pp. 215–224.
- Hirosawa, S., and H. Tomizawa, 1997, *J. Magn. Soc. Japan* **21**(4), 160.
- Hirosawa, S., S. Mino and H. Tomozawa, 1991a, *J. Appl. Phys.* **69**(8), 5844.
- Hirosawa, S., K. Tokuhara, S. Mino, T. Matui, K. Morii and Y. Nakayama, 1991b, *Mater. Res. Soc. Symp. Proc.* **232**, eds M. Doyama, S. Somiya, R.P.H. Chang, M. Homma and Y. Imaoka, p. 275.
- Hirosawa, S., H. Kanekiyo and S. Uehara, 1993, *J. Appl. Phys.* **73**, 6488.
- Hirosawa, S., M. Uehara, S. Mino, N. Ishigaki and T. Tomida, 1997, *J. Appl. Phys.* **81**(8), 4821.

- Hutten, A., and P. Haasen, 1989, *J. Phys. Paris* **C8**, 337.
- Ikegami, T., M. Uehara and S. Hirose, 1998, *J. Alloys Compounds* **281**, 64.
- Inoue, A., A. Takeuchi, A. Makino and T. Masumoto, 1995, *IEEE Trans. Magn.* **31**, 3626.
- Inoue, J., and M. Shimizu, 1986, *J. Phys. F* **16**, 1051; L157.
- Isnard, O., S. Miraglia, J.L. Soubeyroux, D. Fruchart and J. Pannetier, 1992, *Phys. Rev. B* **45**, 2920.
- Izumi, H., K. Machida, A. Siomi, M. Iguchi and G. Adachi, 1996, *Jpn. J. Appl. Phys.* **35**, L894.
- Jacobson, J., and A. Kim, 1987, *J. Appl. Phys.* **61**(8), 3763.
- Jaswal, S.S., 1992, *IEEE Trans. Magn.* **28**(5), 2322.
- Jaswal, S.S., W.B. Yelon, G.C. Hadjipanayis, Y.Z. Wang and D.J. Sellmyer, 1991, *Phys. Rev. Lett.* **67**(5), 644.
- Jurczyk, M., 1996, *J. Alloys Compounds* **235**, 232.
- Kajitani, T., Y. Morri, S. Funahashi, T. Iriyama, K. Kobayashi, H. Kato, Y. Nakagawa and K. Hiraya, 1993, *J. Appl. Phys.* **73**, 6032.
- Kanamori, J., 1990, *Prog. Theor. Phys. Suppl.* **101**, 1.
- Kanekiyo, H., M. Uehara and S. Hirose, 1993, *IEEE Trans. Magn.* **29**, 2863.
- Kaneko, Y., and N. Ishigaki, 1994, *J. Mater. Eng. & Perform.* **3**, 228.
- Kaneko, Y., Y. Sasakawa, S. Kohara, K. Tokuhara and S. Kidowaki, 1999, *Materia Japan* **38**(7), 248. In Japanese.
- Katter, M., J. Wecker and L. Schultz, 1991, *J. Appl. Phys.* **70**(6), 3188.
- Kim, A.S., 1989, *J. Mater. Eng.* **11**(1), 95.
- Kim, A.S., and F.E. Camp, 1996, *J. Appl. Phys.* **79**, 5035.
- Kim, A.S., and J. Jacobson, 1987, *IEEE Trans. Magn.* **MAG-23**, 2509.
- Kim, A.S., F.E. Camp and E.J. Dulis, 1990, *IEEE Trans. Magn.* **26**, 1936.
- Kneller, E.F., and R. Hawig, 1991, *IEEE Trans. Magn.* **27**, 3588.
- Kobayashi, K., T. Iriyama, T. Yamaguchi, H. Kato and Y. Nakagawa, 1993, *J. Alloys Compounds* **193**, 235.
- Kobayashi, K., Q. Qi and J.M.D. Coey, 1995, *J. Magn. Mater.* **140-144**, 1077.
- Kobayashi, K., X.L. Rao, J.M.D. Coey and D. Givord, 1996, *J. Appl. Phys.* **80**(11), 6385.
- König, H., X. Wang, B.N. Harmon and P. Carra, 1994, *J. Appl. Phys.* **66**, 337.
- Kou, X.C., X.K. Sun, Y.C. Chuang, T.S. Zhao, R. Grossinger and H.R. Kirchmayr, 1989, *J. Magn. Mater.* **82**, 327.
- Koyama, K., T. Kajitani, Y. Morri, H. Fujii and M. Akayama, 1997, *Phys. Rev. B* **55**, 11414.
- Kronmüller, H., T. Schrefl, R. Fischer and J. Fidler, 1994, in: *Proc. 8th Int. Symp. on Magnetic Anisotropy and Coercivity in RE-TM Alloys*, Birmingham, eds C.A.F. Manwaring, D.G.R. Jones, A.J. Williams and I.R. Harris, pp. 1-24.
- Kronmüller, H., M. Becher, M. Seeger and A. Zern, 1996, in: *Proc. 9th Int. Symp. on Magnetic Anisotropy and Coercivity in RE-TM Alloys*, São Paulo, eds F.P. Missel, V. Villa-Boas, H.R. Rechenberg and F.J.G. Landgraf (World Scientific, Singapore) pp. 1-20.
- Kuhr, C., M. Katter, J. Wecker, K. Schmitzke and L. Schultz, 1992, *Appl. Phys. Lett.* **60**(16), 2029.
- Kumar, K., 1984, *J. Appl. Phys.* **63**(6), R13-R57.
- Lee, R.W., 1985, *Appl. Phys. Lett.* **46**, 790.
- Lee, R.W., E.G. Brewer and N.A. Schaffel, 1985, *IEEE Trans. Magn.* **MAG-21**, 1958.
- Li, L., and C.D. Graham Jr, 1990, *J. Appl. Phys.* **67**, 4756.
- Machida, K., A. Shiomi, H. Izumi and G. Adachi, 1995, *Jpn. J. Appl. Phys.* **34**, L741.
- Majima, K., M. Itou, T. Umamoto, S. Katsuyama and H. Nagai, 1996, *Funtai oyobi Funmatsu-yakin* **43**, 629. In Japanese.
- Manaf, A., R.A. Buckley, H.A. Davies and M. Leonowicz, 1991, *J. Magn. Mater.* **101**, 6366.
- Manaf, A., R.A. Buckley and H.A. Davies, 1993, *J. Magn. Mater.* **128**, 302.
- Maruyama, H., 1998, *J. Magn. Soc. Japan* **22**, 1369 [also in: Master thesis of I. Inoue (Okayama University)]. In Japanese.
- Matsunaga, H., M. Ohkita, M. Asano and N. Ishigaki, 1996, *J. Magn. Soc. Japan* **20**, 217. In Japanese.
- Matsuura, F., H. Sakamoto, M. Koyama and M. Fujikura, 1988, *J. Appl. Phys.* **63**, 3507.
- McGuinness, P.J., X.J. Zhang, X.J. Yin and I.R. Harris, 1990, *J. Less-Common Met.* **158**, 379.
- Miao, W.F., J. Ding, P.G. McCormick and R. Street, 1996, *J. Appl. Phys.* **79**, 2079.
- Mino, S., and S. Hirose, 1999, *Mater. Technol.* **17**(2), 46. In Japanese.
- Minowa, T., M. Yoshikawa and M. Honshima, 1989, *IEEE Trans. Magn.* **MAG-25**, 3776.

- Miraglia, M., J.L. Soubeyroux, C. Kolbeck, O. Isnard, D. Fruchart and M. Guillot, 1991, *J. Less-Common Met.* **171**, 51.
- Mishra, R., 1986, *J. Magn. Magn. Mater.* **54–57**, 450.
- Moruzzi, V.L., P.M. Marcus, K. Schwarz and P. Mohn, 1986, *Phys. Rev. B* **34**, 1784.
- Nakamura, H., A. Fukuno and T. Yoneyama, 1989, in: *Proc. 10th Int. Workshop on RE magnets and their Applications, Kyoto (The Society of Non-traditional Technology, Tokyo) Part II*, p. 315.
- Nakamura, H., S. Sugimoto, T. Tanaka, M. Okada and M. Homma, 1995, *J. Alloys Compounds* **222**, 136.
- Nakamura, H., K. Kato, D. Book, S. Sugimoto, M. Okada and M. Homma, 1998, in: *Proc. 15th Int. Workshop on RE Magnets and their Applications, Dresden*, eds L. Schultz and K.-H. Müller (Werkstoff-Informationsgesellschaft, Frankfurt) pp. 507–516.
- Nakamura, H., K. Kato, D. Book, S. Sugimoto, M. Okada and M. Homma, 1999, *Trans. IEE Japan* **119-A(6)**, 808. In Japanese.
- Narasimhan, K., C. Willman and E.J. Dulis, 1986, US Patent No. 458839.
- Neu, V., U. Klement, R. Schafle, J. Eckert and L. Schultz, 1996, *Mater. Lett.* **26**, 167.
- Noguchi, K., K. Machida, M. Nishimura and G. Adachi, 1998, in: *Proc. 15th Int. Workshop on RE Magnets and their Applications, Dresden*, eds L. Schultz and K.-H. Müller (Werkstoff-Informationsgesellschaft, Frankfurt) pp. 915–923.
- Oesterreicher, K., and H. Oesterreicher, 1984, *Phys. Status Solidi A* **85**, K61.
- Ohashi, K., Y. Tawara, T. Yonayama and N. Kobayashi, 1987, in: *Proc. 9th Int. Workshop on RE Magnets and their Applications, Bad Soden, Germany*, eds C. Herget and P. Poerschke (Deutsche Physikalische Gesellschaft, Bad Honnef) Part 1, p. 355.
- Otsuki, E., T. Otsuka and T. Imai, 1990, in: *Proc. 11th Int. Workshop on RE Magnets and their Applications*, ed. S.G. Sanker (Carnegie Mellon University, Pittsburg, PA) Vol. 1, p. 328.
- Panchanathan, V., 1995, *IEEE Trans. Magn.* **31**, 3605.
- Paviprasad, K., S. Kakoo, K. Makita and M. Umamoto, 1995, *Funtai oyobi Funmatsu-yakin* **42**, 1305.
- Ping, D.H., K. Hono, H. Kanekiyo and S. Hirosawa, 1999, *Acta Mater.* **47**, 4641–4651.
- Pinkerton, F.E., and C.D. Fuerst, 1992, *Appl. Phys. Lett.* **60(20)**, 2558.
- Rodewald, W., and P. Schrey, 1989, *IEEE Trans. Magn.* **MAG-25**, 3770.
- Sagawa, M., and H. Nagata, 1993, *IEEE Trans. Magn.* **29**, 2747.
- Sagawa, M., S. Fujimura, N. Togawa, H. Yamamoto and Y. Matsuura, 1984a, *J. Appl. Phys.* **55**, 2083.
- Sagawa, M., S. Fujimura, H. Yamamoto, Y. Matsuura and K. Hiraga, 1984b, *IEEE Trans. Magn.* **MAG-20**, 1584.
- Sagawa, M., S. Hirosawa, H. Yamamoto, S. Fujimura and Y. Matsuura, 1987, *Jpn.J. Appl. Phys.* **26**, 785.
- Sagawa, M., S. Fujimura, H. Yamamoto and S. Hirosawa, 1988, Japanese Patent No. 63-38555.
- Sagawa, M., P. Tenaud, F. Vial and K. Hiraga, 1990, *IEEE Trans. Magn.* **26**, 1957.
- Sakata, M., K. Ikuma, R. Watanabe, M. Iwasa, H. Miyadera and K. McAloon, 1992, *J. Magn. Soc. Japan* **16**, 135.
- Sakurada, S., A. Tsutai, T. Hirai, Y. Yanagida, M. Sahashi, S. Abe and T. Kaneko, 1996, *J. Appl. Phys.* **79**, 4611.
- Sakurada, S., T. Hirai and A. Tsutai, 1997, *J. Magn. Soc. Japan* **21(4-1)**, 181. In Japanese.
- Schnitzke, K., L. Schultz, J. Wecker and M. Katter, 1990, *Appl. Phys. Lett.* **57**, 2853.
- Schrefl, T., J. Fidler and H. Kronmüller, 1994a, *Phys. Rev. B* **49**, 6100.
- Schrefl, T., R. Fisher, J. Fidler and H. Kronmüller, 1994b, *J. Appl. Phys.* **76**, 7053.
- Schultz, L., J. Wecker and E. Hellatein, 1987, *J. Appl. Phys.* **61**, 3583.
- Schultz, L., K. Schnitzke and J. Wecker, 1988, *J. Appl. Phys.* **64**, 5302.
- Shen, B.G., L.S. Kong, F.W. Wang and L. Cao, 1993, *Appl. Phys. Lett.* **63**, 2288.
- Shimoda, T., K. Akioka, O. Kobayashi and T. Yamagami, 1988, *J. Appl. Phys.* **64**, 5290.
- Shimotomai, M., Y. Fukuda, A. Fujita and Y. Ozaki, 1990, *IEEE Trans. Magn.* **26**, 1939.
- Shimotomai, M., Y. Fukuda, A. Fujita, Y. Ozaki and Y. Kitano, 1994, *Trans. Mater. Res. Soc. Japan* **14B**, 997.
- Skomski, R., and J.M.D. Coey, 1993, *Phys. Rev. B* **48**, 15812.
- Smith, P.A.I., J.F. O'Sullivan and J.M.D. Coey, 1998, in: *Proc. 15th Int. Workshop on RE Magnets and their Applications, Dresden*, eds L. Schultz and K.-H. Müller (Werkstoff-Informationsgesellschaft, Frankfurt) pp. 205–214.
- Steyaert, S., J.M. Le Breton and J. Teillet, 1996, *J. Phys.: Condens. Matter.* **8**, 10721.
- Stoner, E.C., and E.P. Wohlfarth, 1948, *Philos. Trans. R. Soc.* **240**, 599.

- Strnat, K.J., 1976, in: Proc. 2nd Int. Workshop on Rare-earth Cobalt Permanent Magnets and their Applications, Dayton, OH, p. 1.
- Strnat, K.J., 1988, in: Ferromagnetic Materials, Vol. 4, eds E.P. Wohlfarth and K.H.J. Buschow (North-Holland, Amsterdam) pp. 131–209.
- Strnat, K.J., and R.M.W. Strnat, 1991, *J. Magn. Magn. Mater.* **100**, 38–56.
- Sugimoto, S., O. Gutfleisch and I.R. Harris, 1997, *J. Alloys Compounds* **260**, 284.
- Takeshita, T., 1995, *J. Alloys Compounds* **231**, 51.
- Takeshita, T., and R. Nakayama, 1989, in: Proc. 10th Int. Workshop on RE Magnets and their Applications, Kyoto (The Society of Non-traditional Technology) p. 551.
- Takeshita, T., and R. Nakayama, 1992, in: Proc. 12th Int. Workshop on RE Magnets and their Applications, Canberra, ed. Hi-Perm Lab. (REM XII Committee) (Research Center for Advanced Materials and Material Processing) p. 670.
- Takeshita, T., and M. Watanabe, 1989, in: Proc. 10th Int. Workshop on RE Magnets and their Applications, Kyoto (The Society of Non-traditional Technology) Part I, p. 477.
- Tenaud, P., F. Vial and M. Sagawa, 1990, *IEEE Trans. Magn.* **MAG-26**, 1930.
- Teresiak, A., M. Kubis, N. Mattern, M. Wolf and K.-H. Muller, 1998, in: Proc. 10th Int. Symp. on Magnetic Anisotropy and Coercivity in RE-TM Alloys, Dresden, eds L. Schultz and K.-H. Muller (Werkstoff-Informationsgesellschaft, Frankfurt) pp. 115–124.
- Tomida, T., P. Choi, Y. Maehara, M. Uehara, H. Tomizawa and S. Hirosawa, 1996, *J. Alloys Compounds* **242**, 129.
- Tomida, T., N. Sano, K. Hanafusa, H. Tomizawa and S. Hirosawa, 1999, *Acta Metall.* **47**, 875.
- Toussaint, J.C., B. Kevorkian, O. Fuchart and J. Voiron, 1998, in: Proc. 15th Int. Workshop on RE Magnets and their Applications, Dresden, eds L. Schultz and K.-H. Muller (Werkstoff-Informationsgesellschaft) pp. 1001–1020.
- Umeda, T., T. Okane and W. Kurz, 1996, *Acta Mater.* **44**(10), 4209.
- van Lier, J., J.X. Zhang and H. Kronmüller, 1998, in: Proc. 10th Int. Symp. on Magnetic Anisotropy and Coercivity in RE-TM Alloys, Dresden, eds L. Schultz and K.-H. Muller (Werkstoff-Informationsgesellschaft) pp. 3–11.
- van Lier, J., M. Seeger and H. Kronmüller, 1999, *Z. Metallkd.* **90-2**, 92.
- Wada, M., and F. Yamashita, 1990, *IEEE Trans. Magn.* **26**(5), 2601.
- Wagner, C., 1933, *Z. Phys. Chem.* **21**, 25.
- Wendhausen, P.A.P., B. Gebel, N.M. Dempsey, K.-H. Muller and J.M.D. Coey, 1994, in: Proc. 13th Int. Workshop on RE Magnets and their Applications, Birmingham, eds C.A.F. Manwaring, D.G.R. Jones, A.J. Williams and I.R. Harris (REM XIII Committee) pp. 831–840.
- William, C.J., and K.S.V.L. Narasimhan, 1987, *J. Appl. Phys.* **61**, 3766.
- Yamada, M., H. Kato, H. Hiroyoshi, H. Yamamoto and Y. Nakagawa, 1987, *J. Magn. Magn. Mater.* **70**, 328.
- Yamamoto, T., T. Hidaka, T. Yonayama, H. Nishio and A. Fukuno, 1996, in: Proc. 14th Int. Workshop on Rare-earth Magnets and their Applications, São Paulo, eds F.P. Missel, V. Villa-Boas, H.R. Rechenberg and F.J.G. Landgraf (World Scientific, Singapore) pp. 121–137.
- Yoneyama, T., T. Yamamoto and T. Hidata, 1995, *Appl. Phys. Lett.* **67**, 3197.
- Yoshikawa, N., H. Yamada, Y. Iwasaki, K. Nagata and Y. Kasai, 1994, in: Proc. 13th Int. Workshop on RE Magnets and their Applications, Birmingham, eds C.A.F. Manwaring, D.G.R. Jones, A.J. Williams and I.R. Harris (REM XIII Committee) pp. 635–644.
- Yuri, Y., and T. Ohki, 1994, in: Proc. 13th Int. Workshop on RE Magnets and their Applications, Birmingham, eds C.A.F. Manwaring, D.G.R. Jones, A.J. Williams and I.R. Harris (REM XIII Committee) pp. 645–654.



## Chapter 209

### POLYSULFIDES

INGA G. VASILYEVA

*Institute of Inorganic Chemistry, Siberian Branch Russian Academy of Sciences,  
 630090 Novosibirsk, Russia*

#### Contents

Symbols	567	7. Structural properties	588
Introduction	568	7.1. Structural analysis	588
1. A historical account	568	7.2. Isostructural lines	589
2. The occurrence of polysulfides	570	7.3. Structural chemistry	591
3. Preparative methods	572	8. Thermodynamic properties	594
3.1. General remarks	572	8.1. General remarks	594
3.2. The higher (hyperstoichiometric) polysulfides	573	8.2. Heat capacity and entropy	595
3.3. Disulfides and the lower (hypostoichiometric) polysulfides	573	8.3. Enthalpy of formation, atomization energy	597
3.4. Compositional characterization	575	8.4. Vaporization	597
4. Phase equilibrium	576	9. Chemical bonding	599
4.1. $T-x$ diagrams	576	10. Electronic structure	601
4.2. $P-T$ diagrams	578	11. Physical properties	602
4.3. $P_S-T-x$ diagrams	579	11.1. Electrical properties	602
4.4. Correlation between the $T-x$ and $P_S-T-x$ diagrams	582	11.2. Magnetic properties	603
4.5. Isotypical lines	582	11.3. Optical properties	604
5. Crystal growth	583	11.4. Other properties	605
6. Diagnostic properties	585	12. Concluding remarks	605
		References	605

#### Symbols

Å	Ångström ( $10^{-10}$ m)	$m^*$	effective charge of ions
$a, b, c$	lattice constants	$M(H)$	magnetization at magnetic field $H$
at.%	atomic percentage	$n$	refractive index
$C_p(T)$	molar heat capacity measured at temperature $T$ and at constant pressure	$P$	pressure
$E_g$	energy gap	$P_S$	partial sulfur pressure
$\Delta G_f^0(T)$	free energy of formation at temperature $T$	$r$	radius
$H_c$	magnetic field along $c$ -axis	R	symbol for a rare-earth element
$\Delta H_f^0(T)$	enthalpy of formation at temperature $T$	$R_\Omega$	resistance
		S	sulfur

$S^\circ(T)$	standard entropy at temperature $T$	$x$	concentration
$S_1S_2V$	solid(1)–solid(2)–vapor three-phase equilibria	$Z$	number of formula units per cell
$T$	absolute temperature	$\chi$	magnetic susceptibility
$T_a$	anharmonic contribution at temperature $T$	$\mu_B$	Bohr magneton
$T_C$	Curie temperature	$\theta_p$	paramagnetic Curie temperature (Curie–Weiss constant)
$T_N$	Néel temperature	$\rho$	specific resistance
$X$	symbol for an anion, S, Se or Te		

## Introduction

The rare earths form several binary sulfides of various compositions and crystal structures. Most of them have been well studied by now. Only for polysulfides has complete knowledge not yet been obtained. This work is an attempt to present recent results, to show how they have altered the general idea on the fundamental properties of polysulfides and to call attention to those interesting compounds which need additional investigation.

### 1. A historical account

Attempts to find an analogy between  $CeS_2$  and  $CeO_2$  containing tetravalent cations led to the formula  $Ce_2S_3 \cdot S$  with trivalent Ce (Biltz 1911, Klemm et al. 1930). The formula was derived from magnetic measurements, the chemical behavior of  $CeS_2$ , and the volume of its unit cell which is close to that of  $LaS_2$  with trivalent La. According to the formula, disulfides were described as compounds containing sulfur in excess of the rare earth's trivalent stoichiometry requirements and with properties inconsistent with those of classical salts. The question how sulfur in  $CeS_2$  is bound to the normal sulfide was of minor importance. The 1950–1960s were a period of activity in the synthesis of disulfides. They were obtained as powders for all light lanthanides, for some heavy lanthanides, and for Y (Flahaut and Guittard 1956a). Their structures were identified and their thermal stability was estimated. At the same time a sulfur deficiency in the disulfides was recognized. This characteristic seemed to be typical of the heavy elements only (Flahaut and Guittard 1957, Flahaut et al. 1959). Why this hypostoichiometry appears even in excess sulfur was not clear, and interest arose in the study of the structures and properties of these compounds. During the 1970s the composition nomenclature of the polysulfides increased considerably because of the development of preparative chemistry. Webb and Hall (1970) synthesized the stoichiometric disulfides for all lanthanides under high pressure. For the light elements, in addition to disulfides, hyperstoichiometric compounds,  $LaS_{2.33}$  and  $NdS_{2.67}$  (Eliseev et al. 1972) and the reduced polysulfides,  $LaS_{1.94}$ ,  $LaS_{1.75-1.80}$ ,  $PrS_{1.98}$ ,  $PrS_{1.70}$ , and  $SmS_{1.94}$  (Ring and Tecotzky 1964) have been prepared. The occurrence of the latter compounds as intermediates during disulfide synthesis was unexpected. Later the reduced polysulfides were detected as individual phases in the

La, Nd, and Eu systems through systematic studies of phase diagrams (Grizik et al. 1970, Eliseev and Uspenskaya 1972a, Loginova 1974, Loginova et al. 1975, Ananth et al. 1974). Eliseev and Grizik (1977) published the first review on nonstoichiometry of the disulfides. Usually reviews on rare-earth sulfides included only one or two pages with data concerning the polysulfides (Flahaut and Laruelle 1968, Samsonov and Drozdova 1972, Jarembash and Eliseev 1975, Eliseev and Grizik 1977, Flahaut 1979). By the early 1980s a large body of information on compositions and structural types of the polysulfides had been gathered, but information was very conflicting. The disulfides were taken as phases of continuously variable composition in a wide range or as exactly stoichiometric compounds without any homogeneity ranges. The reduced polysulfides were considered to be individual phases or compositions lying within homogeneity ranges. Poor and improper identification of the polysulfides may add to the confusion. Therefore, attempts to correlate compositions and structures of the polysulfides, on the basis of X-ray powder diagrams and common chemical analysis, were not successful at that time. Identification of the polysulfides became more reliable when structural research on single crystals came into use. The structures of the following stoichiometric disulfides were solved:  $\text{YbS}_2$  by Teske (1974);  $\text{LaS}_2$  by Dugué et al. (1978); and  $\text{NdS}_2$  by Borisov et al. (1979). Polytypes of  $\text{LaS}_2$  with different structures were established. It was expected that dimorphic behavior should also show other light elements.

Other areas of investigation began to develop when high-quality crystals with  $\text{mm}^3$  dimensions were obtained by Vasilyeva et al. (1985). Special techniques to characterize the crystals individually have been devised and, thus, precise experimental data on compositions and densities were obtained in addition to those from structural researches. The disulfide stoichiometry began to become apparent in association with their structural features. The structure of the disulfides consists of alternating sheets of composition  $[\text{RS}]_n$  and layers of  $(\text{S}_2)_n$  with the chemical formula,  $(\text{RS})_n^+(\text{S}_2)_n^{2-}$ . According to this formula the disulfides are arranged in analogy to the  $(\text{CeS})_2\text{As}_2$  compound, one of a large group of compounds classified by Flahaut (1976). The role of the geometric factor in the arrangement of the  $[\text{RS}]_n$  sheet, and the polymerization of sulfur in the  $(\text{S}_2)_n^{2-}$  layer, became the subject of many researches at this period. Many attempts were made to find the factors responsible for the stability of the different structural types and to clarify the polymorphism phenomena of the disulfides (Wichelhaus 1977, Eliseev and Grizik 1977, Yanagisawa et al. 1979, Bénazeth et al. 1981, Kuzmicheva et al. 1981). Electronic structure calculations on the basis of the structural data for  $\text{LaS}_2$  were performed by Zhukov et al. (1990). The availability of well-characterized crystals made it possible to study thermodynamic properties and some physical properties. Features of low-temperature magnetic behavior and memory phenomena of  $\text{CeS}_2$  were observed by Klimenko et al. (1991b); thin crystals of  $\text{NdS}_2$  and  $\text{DyS}_{1.84}$  showed transparency over a wide spectral range (Shilkina et al. 1987a). These properties point to potential areas of practical use of the polysulfides.

As to the nonstoichiometric polysulfides, they seemed to escape notice. Lack of information on how to grow crystals with a desired composition was a main obstacle in the development of this area. Powder-preparative chemistry could hardly provide

reliable data for these compounds. Progress in the preparation and identification of new hypostoichiometric polysulfides has appeared through systematic studies of the  $P_S-T-x$  diagrams coupled to precise structural research using single crystals (Podbereskaya et al. 1997, Vasilyeva and Belyaeva 1999, Vasilyeva and Belaya 1999, Vasilyeva et al. 1999). A series of distinctive intermediate phases of fixed and very close compositions in the systems  $RS_{1.50}-RS_{2.00}$  with  $R=La, Pr, Nd, Sm$  and  $Dy$  were observed. All these phases may be described by the generic formula  $R_nS_{2n-1}$ . The compositions of the hypostoichiometric polysulfides and their homogeneity ranges were determined from these diagrams without the necessity to prepare the phases beforehand in the pure state. According to the  $P_S-T-x$  diagrams, the conditions for growing crystals were known and some hypostoichiometric polysulfides were obtained as single crystals. Structural researches on  $SmS_{1.90}$ ,  $DyS_{1.76}$ , and  $DyS_{1.84}$  single crystals have shown that sulfur deficiency in these compounds results in the formation of different types of superstructures (Tamazyan et al. 1994, Podbereskaya et al. 1998, 1999). In all structures the  $[RS]_n$  sheet remains virtually unchanged and the  $(S)_n$  layer is modified by special distributions of statistically occupied and vacant sulfur positions with the formation of  $-(S_n)^{2-}$  chains of different length. These features of the hypostoichiometric polysulfides offered a clearer view of nonstoichiometry in the disulfides with the  $PbFCl$ -type structure. Chemical bonding and the geometric compromise between the  $(RS)^+$  and  $(S_2)^{2-}$  structural fragments has become the subject of investigation in order to predict changes in the physical properties of the disulfides, when sulfur deficiency or additional metal atoms occur.

Possible areas of application are suggested by peculiarities in the physical properties associated with the nonuniform layered structure of the polysulfides. However, knowledge of these properties is far from complete. Presently, the most developed application of  $LaS_2$  is the production of  $La_2S_3$  as a material for atmospheric infrared optical windows. As initial products for high-temperature and high-pressure technological processes the disulfides provide uniformity and strict stoichiometry of the final ceramics or crystals (Volinetz et al. 1977, Prokofiev 1993).

## 2. The occurrence of polysulfides

The compositional classification of polysulfides is based on three groups: the higher (hyperstoichiometric) polysulfides,  $RS_{2+x}$ ; stoichiometric disulfides,  $RS_{2.0}$ ; and lower (hypostoichiometric) polysulfides,  $RS_{2-x}$ . The classification covers all known compounds up to 1985, with compositions varying in the range from  $RS_{2.67}$  to  $RS_{1.70}$ . The prime interest has been in the stoichiometric disulfides; researches with other polysulfides occurred rarely. The histogram in fig. 1 reflects this situation clearly. The compositions are grouped in two lines, of the  $RS_{2.0}$  and  $RS_{1.90}$  compositions (within the accuracy of common chemical analysis), and the lines are typical for both light and heavy lanthanides. The lines of the  $RS_{1.75}$  and  $RS_{1.70}$  compositions are not quite conclusively demonstrated. The  $RS_{1.75}$  line is more typical of the light lanthanides, while the  $RS_{1.70}$  line is dominated by the heavy elements. There is a large scatter in the compositional range between  $RS_{1.85}$

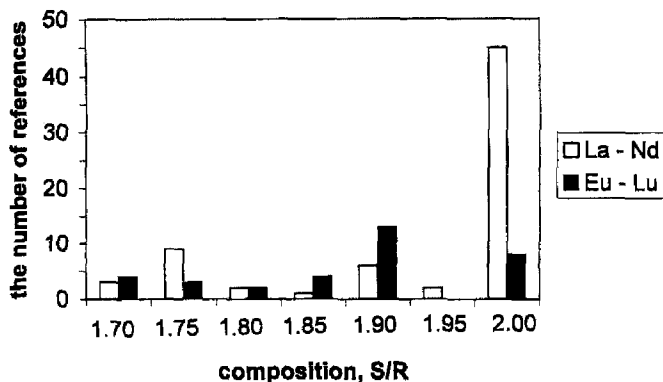


Fig. 1. The number of polysulfides of different compositions reported in the period from 1908 to 1985.

and  $RS_{1.80}$ , and here it is difficult to find arguments in support of a concrete composition. It is seen that the extension of each of the observed isotypical lines does not conform to the known rule of periodicity for other lanthanide compounds. Thus there is reason to believe that some compositions reported in the literature are doubtful. Because of this, it is easily understood why authors studying the  $T-x$  diagrams chose, among all polysulfides, only one or rarely two phases as highly reliable and/or in equilibrium. For instance, the phases  $LaS_{2.0}$  and  $LaS_{1.7}$  were depicted in the phase diagram of the La-S system (Bach 1986); the phases  $YbS_{2-x}$ ,  $YbS_{1.70}$  were involved in the Yb-S system (Eliseev et al. 1981); only  $CeS_2$  was shown for the Ce-S system (Jarembash and Eliseev 1975); and  $Eu_2S_{3.81}$  was found as the only polysulfide in the Eu-S system (Ananth et al. 1974). Therefore, an accurate description of the phase equilibria in these systems requires re-examination of all powder data.

No marked difference is observed between the chemical properties of the polysulfides of any composition. Being powders of micron dimensions they evaporate incongruently at  $\sim 600^\circ\text{C}$  in vacuum. The dissociation temperature has a tendency to decrease along the lanthanide series (Flahaut et al. 1959, Ring and Tecotzky 1964). Polysulfides are considered to melt incongruently, losing sulfur and forming  $R_2S_3$ , except  $Eu_3S_4$  for the Eu polysulfide (Ananth et al. 1974). The polysulfides, except for cerium, are stable in air up to  $500-600^\circ\text{C}$ . The process of oxidation begins together with sulfur loss and leads to the formation of oxysulfides, oxysulfates or oxides with the temperature process (Radzikovskaya and Marchenko 1966, Ananth et al. 1974, Takashi 1973).  $CeS_2$ , a fine powder, is pyromorphic and decomposes in air at  $300^\circ\text{C}$  to form gaseous  $SO_2$  and solid  $Ce(SO_4)_2$ . The polysulfides are stable in water, but dissolve in nonoxidizing acids, evolving free sulfur. The full oxidation of sulfur up to  $SO_4^{2-}$  ions is possible only in strong oxidizing media, for instance,  $HNO_3 + Br_2$  (Radzikovskaya and Marchenko 1966),  $HBr + Br_2$  (Stuve 1981), or  $H_2O_2$  (Picon and Patrie 1956). The polysulfides are practically insoluble in alkalis (Webb and Hall 1970). Other properties of nonstoichiometric and stoichiometric polysulfides will be described in the following sections.

### 3. Preparative methods

#### 3.1. General remarks

Several comprehensive reviews on preparative methods of sulfide compounds are available (Samsonov and Radzikovskaya 1961, Flahaut and Laruelle 1968, Aloman 1968, Jarembash and Eliseev 1975). The following methods are suited for the preparation of the polysulfides: (a) reaction of sulfur with metals; (b) reaction of oxides or salts with  $\text{H}_2\text{S}$  or  $\text{CS}_2$  in an inert gas, Ar or  $\text{N}_2$ ; (c) reaction of sulfides with sulfur. Synthesis between chlorides and a NaCNS melt was performed by Balashevskii and Valtzev (1983), but has not been used thereafter. Metathesis reactions between alkali metal polychalcogenides ( $\text{Na}_2\text{S}_2$  and  $\text{K}_2\text{S}_2$ ) and lanthanoid trihalides ( $\text{PrCl}_3$ ,  $\text{LaCl}_3$ ) were realized at  $\sim 300^\circ\text{C}$ , resulting in appropriate disulfides (Chen and Dorhout 1995). An ammonia-thermal synthesis is known for  $\text{YbS}_2$  (Teske 1974). However, this procedure is rather complex, specific and of little synthetic value for the other lanthanides, except maybe Eu, which also dissolves in water-free ammonia. Advantages and disadvantages will now be discussed for each method separately.

**Method (a).** There are limitations in using this procedure. It is difficult to work with free metals, and the rare-earth metals are not available without gaseous impurities. During synthesis, products may be contaminated by Si, and also by oxygen and nitrogen whose diffusion through quartz becomes appreciable at temperatures above  $900^\circ\text{C}$ . Multiphase products after the first reaction must be crushed in a dry inert gas. The advantage of the procedure is the possibility to vary the sulfur partial pressure in the reaction zone and obtain the polysulfide of the desired stoichiometry. A modified version of this method is the application of high pressures and high temperatures to R-S mixtures. The procedure is not free from the above disadvantages, and the end products may be heterogeneous. Yanagisawa and Kume (1986) have considered the heterogeneity of the polysulfide phases.

**Method (b).** This method employs the oxides or salts as starting materials and has several advantages. Oxides are available in high purity and at rather low cost, and the compounds are convenient for preparative procedures. Disadvantages are the necessity to use high temperatures for reducing oxides (moderate temperatures for salts and hydroxides), to use toxic sulfidizing agents, and to clean them from oxygen. Kinetic problems arise as well, because of the formation of a thick product layer on the unreacted starting solid. All these make the process of rather limited importance.

**Method (c).** Facilities to work with the starting products are combined here with reasonably low temperatures of synthesis. Besides, polysulfides with a minimum content of oxygen may be prepared in this process (Loginova 1974) because oxygen is removed from the starting sulfides during sulfidization. But a kinetic problem is important for this process as with the above procedures, especially if attaining equilibrium for the reaction is visually controlled. Loginova (1974) used an apparatus with automatic recording and balancing of the sample weight; this is more convenient but has a low sensitivity. It was not surprising that the time to reach the equilibrium state of the  $\text{LaS}_{1.5} + \text{S} \rightarrow \text{LaS}_2$  reaction under identical conditions was found to vary, from 25 to 250 hours. Therefore a non-equilibrium state for samples prepared in short times is expected. The kinetics of

the  $RS_{1.5}(\text{solid}) + 0.5S(\text{gas}) \rightarrow RS_2(\text{solid})$  reaction was studied for the La-S and Gd-S systems. The process of  $LaS_2$  formation is controlled by the rate of the chemical reaction, while for  $GdS_2$  formation, sulfur diffusion into the solid sesquisulfide restricts the reaction rate. The different radii of these elements were explained to be the main factor responsible for the different kinetics of these disulfide formation processes (Loginova 1974). Synthesis of  $RS_2$  from the  $R_2S_3(\text{solid}) + S(\text{solid})$  mixtures has also been carried out under high pressures and high temperatures (Yanagisawa and Kume 1973, 1986). The process appears to hold considerable promise for the preparation of stoichiometric polysulfides of the heavy elements, which could not be normally prepared under ordinary sulfur pressure.

### 3.2. *The higher (hyperstoichiometric) polysulfides*

Both methods – high-pressure high-temperature technique and isopiestic experiments under high sulfur pressures ( $P_{\text{partial}}$ ) – have been used to synthesize the higher polysulfides. Isopiestic experiments have been performed for the systems with Gd (Vasilyeva and Kurochkina 1981), Nd (Gorbunova and Vasilyeva 1985), Er (Gorbunova and Vasilyeva 1986), Sm (Vasilyeva and Belyaeva 1999), Dy (Vasilyeva et al. 1999), and Pr (Vasilyeva and Belaya 1999). High-quality silica closed ampoules were used to keep the  $R_2S_3 + S$  mixtures (with ratio  $S/R_2S_3 \geq 3$ ) at  $700^\circ\text{C}$  and under sulfur pressure in 5, 10, or 20 atm. This sulfur pressure appeared to be sufficient to prevent decomposition of  $RS_2$ . The final products were identified compositionally and structurally, and in none of the experiments were hyperstoichiometric phases observed. Neither were they detected in any high-pressure experiments. Only disulfides of Yb, Nd, and Ce may be synthesized with pressures of 30–90 kbar and temperatures of  $1000\text{--}2000^\circ\text{C}$  applied to mixtures even with the ratio  $S/R \geq 3$ . The mixtures were taken as  $Yb + 3S$  or  $YbS_{1.50} + 3S$  (Eliseev et al. 1976, 1978), as  $NdS_{1.50} + 3S$  and  $CeS_{1.50} + 3S$  (Yanagisawa and Kume 1973, 1986). These results seem contrary to the earlier information referring to existence of the higher polysulfides.  $NdS_{2.67}$  and  $YbS_{2+x}$  were synthesized as very small crystals by the chemical transport reaction with iodine, however, without a direct determination of their actual composition (Uspenskaya and Eliseev 1972).  $LaS_{2.33}$  was detected during a phase-diagram study by a weighing method recording the composition increasing (Loginova 1974). These composition values are tentative because, as stated by the authors themselves, the characterizations were not highly accurate. We can agree with these authors' opinion, because the choice of these indirect techniques for compositional identification of the polysulfides was truly unsuccessful. In view of all these results, the disulfides should be taken as the higher polysulfides for the  $RS_{1.50}\text{--}S$  systems.

### 3.3. *Disulfides and the lower (hypostoichiometric) polysulfides*

To our knowledge, the only study where the disulfides of La, Pr, and Nd were prepared from metals and sulfur is by Bucher et al. (1975). Metal, in the form of turnings, and sulfur were heated in double sealed quartz tubes at a temperature of  $1150^\circ\text{C}$  for 2–3 days. The intermediate multiphase product was dissolved in a large amount of liquid sulfur, and was kept at  $500\text{--}600^\circ\text{C}$  for 10–14 days. The high-pressure high-temperature variant

(500–1900°C, 14–70 kbar) was used to prepare disulfides of Nd, Gd, Tb, Dy, Ho, Er, Tm, Yb, and Lu from the R+2S mixtures (Webb and Hall 1970).

The interaction of La and Nd oxides with H<sub>2</sub>S begins at 700°C and results in the corresponding disulfides (Aloman 1968). For CeS<sub>2</sub> this reaction goes to form a mixture of CeS<sub>2</sub>, Ce<sub>2</sub>S<sub>3</sub>, and CeO<sub>2</sub> (Flahaut and Guittard 1956b). The reaction between (RO)<sub>2</sub>CO<sub>3</sub> (R=La, Pr, Nd) and H<sub>2</sub>S takes place at temperature ~650°C, also giving the disulfides (Sallavaud and Rene 1970). The same temperature was suitable for the following reaction: R<sub>2</sub>(SO<sub>4</sub>)<sub>3</sub> + H<sub>2</sub>S(gas) → RS<sub>2</sub>, R=La, Ce, Pr and Sm (Biltz 1908, 1911, Klemm and Rockstroh 1927). Another sulfidizing agent, CS<sub>2</sub> (in an inert gas), was used in the reactions with oxides, and LaS<sub>2</sub> was prepared at 600°C (Takashi 1973); a H<sub>2</sub>S/CS<sub>2</sub>/Ar mixture and a temperature of 850°C were suitable for CeS<sub>2</sub> formation (Vasilyeva et al. 1998a). Le Rolland et al. (1994) prepared LaS<sub>2</sub> using the interaction between solid La<sub>2</sub>O<sub>3</sub> or La(OH)<sub>3</sub> and gaseous CS<sub>2</sub> at 500°C.

The most popular procedure for obtaining disulfides is the reaction between solid R<sub>2</sub>S<sub>3</sub> and gaseous sulfur at 600°C (Biltz 1911, Picon and Patrie 1956, Flahaut and Guittard 1956a,b, 1957, Radzikovskaya and Samsonov 1961, Grizik et al. 1970, Loginova 1974, Golovin et al. 1975, Kriklya 1986). Under these conditions a low-temperature modification of the disulfides may be prepared. To obtain the high-temperature form for R=Ce, Pr, and Nd the high-pressure high-temperature technique was applied to the corresponding mixtures (Yanagisawa and Kume 1973, 1986, Yanagisawa et al. 1979).

It is not quite clear what conditions are suitable for the preparation of the lower (hypostoichiometric) polysulfides. Logically they are formed after the disulfides when the R+2S mixture, under the same high pressure, is heated up to higher temperatures (Webb and Hall 1970, Eliseev et al. 1976, 1978). But why they occur when sulfur is used in excess of the disulfide stoichiometry (Ring and Tecotzky 1964) remains an enigma. In general, different final products may be obtained with the same reaction and identical conditions. Based on identification of the polysulfide compounds by X-ray powder diagrams and chemical wet analysis, Loginova (1974) and Golovin et al. (1975) reported that the stoichiometric disulfides may be obtained for Sm and even for Gd using the RS<sub>1.5</sub>(solid) + S(gas) reaction. However the same experiments by Flahaut et al. (1959) yielded only hypostoichiometric compounds for the heavy elements. This all leads Eliseev and Grizik (1977) to argue that there are many polysulfide phases in the RS<sub>1.5</sub>-S systems: 5 for La and Yb, 4 for Nd, 3 for Ce and Sm, and 2 for other elements. Unfortunately, no serious effort was made by Eliseev and Grizik in their review to estimate what compositions are correct and what ones are in error.

Another problem to be discussed is the nonequilibrium state of the powdered polysulfides prepared by solid-gas interactions. In these cases the rate-controlling process is most often the sulfur diffusion in solids. A thick product layer formed on the unreacted starting solid inhibits the sulfur diffusion, resulting in a nonequilibrium state. To describe this state, one can use some indicators which are shared by many sulfide materials (Vaughan and Craig 1978). First, there is a greater number of phases on the surface of the solids than would follow from Gibbs' rule; the duration of the experiment has a dramatic effect on the number of phases and the compositional identity of the final products.



Second, there is no reproducibility of the resulting compositions in duplicate experiments. Third, the final products of the same gross composition reactions, for instance,  $R + 2S$  or  $RS_{1.50} + 0.5S$ , are not always identical, and depend on the origin of the starting products and the sequence of temperature and pressure variation. With these principles, one can suggest that the powdered polysulfides prepared by different authors (see sect. 3.3) can hardly be related to equilibrium materials. A multiphase surface state of powders has a serious effect on many properties and, thus, merits detailed consideration here. It is apparent that special means must be used to provide data on the gross composition and the spatial variation of the sulfur content over the grain.

### 3.4. Compositional characterization

There are indirect and direct means for determining the composition of the powdered polysulfides. Indirect determinations of the composition are inferred from the change of weight of  $RS_{1.5, \text{ powder}}$  reacting with gaseous sulfur (Loginova et al. 1975); from picnometric density measurements and X-ray powder diagrams (Webb and Hall 1970, Eliseev et al. 1976); and from the shape of the Raman spectra being similar to those expected for the disulfides (Golovin et al. 1975, Le Rolland et al. 1991). Direct methods are based on wet chemical analysis, where metal and sulfur are determined by volumetric and/or gravimetric methods (Biltz 1911, Flahaut and Guittard 1956a, Loginova 1974, Yanagisawa and Kume 1973, Bolgar et al. 1987b, Takashi 1973). Mironov and Kamarzin (1979) discuss the metrological features of the analysis (precision, accuracy, and specificity). They showed that the sulfur content may be determined within a relative error of 2%, at best. In reality this error grows to 3–5% (Loginova 1974, Takashi 1973), and then, within this error,  $RS_{2.00}$  and  $RS_{1.90}$  may be characterized with high probability as phases of like composition. A set of analytical procedures to determine selectively amounts of  $S^{2-}$ ,  $(S_2)^{2-}$ , and  $S^0$ , as a chemisorbed form, was described by Radzikovskaya and Marchenko (1966). Selective analysis should give information on the real polysulfide stoichiometry, eliminating the amount of chemisorbed sulfur from its total. However, this technique has rarely been applied to polysulfide analysis. Sulfur absorption by sulfide powders and even single crystals is a well-known phenomenon (Rau 1978). It was found that for powders of the lanthanide polysulfides the amount of sulfur absorbed, dependent on many factors, might be quite significant. Therefore, this kind of sulfur should be considered as a real source of random errors resulting in incorrect values for polysulfide composition.

There are limited possibilities to establish the compositional inhomogeneity of powdered particles of the polysulfides. A new chemical method, differentiating dissolution, may be strongly recommended for this purpose (Vasilyeva et al. 1998a). This method was really effective in quantitatively characterizing the phase and chemical nonuniformity of  $CeS_2$ – $CeS_{1.5}$  mixtures. Another effective indicator of the compositional nonuniformity of the polysulfide powders is measurement of the sulfur pressure over the polysulfides. All other factors being equal, the more nonuniform powdered polysulfide produces a higher pressure. Indeed, three  $LaS_2$  powdered samples prepared in perfect analogy, except for time (experiment durations 8, 25, and 240 hours), showed the same pressure of 100 Torr

at temperatures 600, 650 and 720°C, respectively. The homogeneity of the last-named sample seems to have been achieved by very prolonged action on the solid by the gaseous sulfur.

*Final comment.* The failure of common analytical methods to recognize the fine compositional differences of the polysulfides is evident. Therefore, new means, both analytical and physico-chemical, are desirable. Systematic studies of the phase diagrams should be the most suitable for this purpose.

#### 4. Phase equilibrium

Systematic studies of the phase diagrams of the polysulfide systems have not been performed. This is easily explained by the high melting points and sulfur pressures of polysulfides, the reactivity of melts toward many container materials, and there being too little diffusion in solids below the Tamman temperature. The selection of experimental techniques which are adequate for these polysulfide properties is troublesome. The possible occurrence of an inexhaustible source of errors in phase-diagram construction becomes actuality if the study of the polysulfides is performed along traditional paths. Therefore, the data available in the literature on the phase diagrams of these systems are considered here together with the techniques used and their potentials.

##### 4.1. $T-x$ diagrams

For most of the R-S systems, experimental data in the range 60–100 at.% sulfur have not been obtained, and some authors have plotted on their diagrams only the compositional lines corresponding to the most credible polysulfides, such as  $\text{LaS}_2$  and  $\text{LaS}_{1.7}$  (Bach 1986);  $\text{YbS}_{2-x}$  and  $\text{YbS}_{1.70}$  (Eliseev et al. 1981);  $\text{CeS}_2$  (Jarembash and Eliseev 1975); and  $\text{Eu}_2\text{S}_{3.81}$  (Ananth et al. 1974). Only for two systems, Eu-S and Nd-S, have experiments been performed in a wide compositional range. However, the DTA investigation in the  $\text{Eu}_3\text{S}_4$ -S region was restricted to an upper temperature of 600°C and in the field the phase boundaries  $\text{Eu}_2\text{S}_{3.81}$  and  $\text{Eu}_3\text{S}_4$  with sulfur in solid, liquid and vapor state were determined (Ananth et al. 1974). The Nd system was accurately studied up to  $\text{NdS}_3$  using the X-ray powder analysis, and the phases  $\text{NdS}_{1.75}$  and  $\text{NdS}_{2.0}$ , both of varying composition, were established (Eliseev and Uspenskaya 1972b). Flahaut et al. (1959), who studied the  $\text{LaS}_2$ - $\text{LaS}_{1.5}$  system showed that  $\text{LaS}_2$  is a phase without homogeneity range. Ring and Tecotzky (1964), on the contrary, observed wide composition ranges for La, Pr, Sm, Gd, Tb, Ho, and Y hypostoichiometric polysulfides according to their X-ray diffraction patterns. All these data on homogeneity ranges of the polysulfides are collected in table 1. It is clear that the correctness of these data depends essentially on the details of the preparation and characterization methods used in these studies for the powdered polysulfide samples.

Little is known on the melting of the polysulfides. The peritectic temperature, 910°C, was determined by DTA for the reaction  $\text{YbS}_{1.70}(\text{solid}) \rightarrow \text{Yb}_3\text{S}_5(\text{solid}) + \text{L}$ , with a sulfur

Table 1  
Phases and homogeneity ranges in the  $RS_{1.5}$ - $RS_{2.0}$  systems

Element	Compositional range (S:R)	Element	Compositional range (S:R) <sup>3</sup>
La	2.0 <sup>1</sup>	Eu	1.92-1.87
	1.97-1.94; 1.88-1.78 <sup>2</sup>		
	1.91-1.76 <sup>3</sup>		
Pr	2.0-1.7 <sup>3</sup>	Gd	1.80-1.70
	1.98; 1.70 <sup>2</sup>		
Nd	2.33; 2.00, 1.80; 1.75-1.67 <sup>4,5</sup>	Tb	1.80-1.74
	1.98-1.80 <sup>3</sup>		
Sm	2.0-1.82 <sup>3</sup>	Ho	1.72-1.67
	1.94; 1.895 <sup>5</sup>		
		Tm	1.78-1.72
		Yb	1.76-1.70

#### References

<sup>1</sup> Flahaut et al. (1959)

<sup>2</sup> Ring and Tecotzky (1964)

<sup>3</sup> Eliseev and Grizik (1977)

<sup>4</sup> Eliseev and Uspenskaya (1972a,b)

<sup>5</sup> Jarembash and Eliseev (1975)

content of 70 at.% (Eliseev et al. 1981). No study of the liquidus region was carried out for this diagram. Quite a low peritectic temperature, 900°C, was established for the reaction  $NdS_2(\text{solid}) \rightarrow NdS_{1.5}(\text{solid}) + L$  (Uspenskaya 1972). With this in mind, Eliseev et al. (1981) suggested that peritectic-type diagrams must be typical of the  $RS_{1.50}$ - $RS_{2.0}$  systems, as that was observed in the  $RX_{1.50}$ - $RX_{2.0}$  systems with  $X = \text{Se}$  and  $\text{Te}$ . However, another type of experiments, where  $NdS_2$  and  $ErS_{1.85}$  crystals were heated in a closed quartz tube at 1100°C under sulfur pressures of  $\leq 20$  atm in excess of equilibrium, showed no evidence at all for polysulfide fusion (Gorbunova and Vasilyeva 1985, Gorbunova et al. 1990). Congruent melting was also established for the powdered polysulfides, when they were very rapidly heated in an open crucible in vacuum (Picon and Patrie 1956, Flahaut and Guittard 1956b). The initial composition was supported to hold constant up to melting, although a negligible sulfur condensation appeared. Recently a new high-temperature thermomicroscopic technique with the original heating and recording systems was described, where, in order to prevent decomposition of the samples, very rapid heating is performed in the camera with a pure helium pressure of about 3 atm (Gibner and Vasilyeva 1998). This apparatus is sensitive to all types of phase transitions, solid-solid, solid-liquid, solid-vapor, and liquid-vapor, and automatically records peaks, where for every transition there is a very specific profile of the peak. The occurrence of the solid-vapor peak is an important indicator of changes in the polysulfide initial composition, and the peak intensity allows the degree of the polysulfide decomposition before melting to be estimated. The experimental procedure of melting point determination for easily decomposing compounds in an open crucible was developed by Vasilyeva et al. (1998b). The melting points of some polysulfides were measured in this way and the results together with data obtained previously are listed in table 2. They are quite close to each

Table 2  
Melting points of the lanthanide polysulfides (°C)

Rapid heating	LaS <sub>2</sub>	CeS <sub>2</sub>	PrS <sub>2</sub>	NdS <sub>2</sub>	NdS <sub>1.90</sub>	SmS <sub>2</sub>	DyS <sub>1.84</sub>	DyS <sub>1.76</sub>	ErS <sub>1.85</sub>	ErS <sub>1.75</sub>
Vacuum	1650	1700	1780	1760		1730				
Pressure 3 atm.				1720	1760		1570	1640	1620	1660

other, although  $T_m$  values were superior for those polysulfides which were heated in vacuum and, hence, could lose sulfur before melting.

On the basis of all these experiments it should be noted that the melting behavior of polysulfides depends on a "pressure piston" in the systems. The liquidus being the projection of the monovariant line of the three-phase equilibria including sulfur vapor must be represented in the  $T-x$  diagrams together with the vapor line. But it is experimentally difficult to directly measure the equilibrium sulfur pressure at melting points. Gorbunova and Vasilyeva (1985) and Gorbunova et al. (1990) used an alternative variant. The pressures were measured at moderate temperatures in silica Bourdon gauges, and subsequently extrapolated with a justified assumption to the temperatures ranging up to melting.

#### 4.2. $P-T$ diagrams

A high-pressure high-temperature technique was used to prepare heavy-element stoichiometric disulfides, which could not be accomplished normally under sulfur pressure. Therefore, most of the experiments were performed with a single composition, 66.6 at.% sulfur, rather than in a wide compositional range. Several isobaric sections were studied in the YbS<sub>2.0</sub>-YbS<sub>1.5</sub> system, and a change in positions of phase fields with pressure was observed (Eliseev et al. 1976, 1978, 1981). Applying a pressure of 14-70 kbar at 400-1900°C to the R+S mixtures, Webb and Hall (1970) synthesized the stoichiometric disulfides for all heavy lanthanides. These compounds, having a  $r_{\text{cat}}/r_{\text{an}}$  ratio smaller than that for the disulfides of the light elements, were structurally identical with the latter obtained normally. From these results it is evident that such behavior of the polysulfides along the La-Lu series obeys the Wentorf general pressure homologous rule (Wentorf 1963). According to this rule, only compounds with ionic-covalent bonds may behave in a similar way, and this can be extended to the lanthanide disulfides.

New orthorhombic polymorphs for the light-element disulfides were obtained by high-pressure high-temperature procedures (Yanagisawa and Kume 1973, 1986, Yanagisawa et al. 1979). For these phases the positions of equilibrium lines of the monoclinic  $\rightarrow$  orthorhombic transformation for the Ce, Pr, and Nd disulfides were determined. No melting curves were presented, no attention was given to the different slopes of the polymorphic lines in the seemingly single-type diagrams, and the absence of reliable crystallographic characteristics for the final products was also a weakness of these studies. Merrill (1982) summarized these data in a survey where the  $P-T$  diagrams for AB<sub>2</sub>-type compounds including the R elements were described, and the solid-state equilibrium phase

Table 3  
Characteristics of tensimetric methods

	Method (a)	Method (b)	Method (c)
Pressure range (atm)	$10^{-3}$ –2	0.5–1.5	5–20
Temperature range (°C)	100–1100	600–1100	up to 700
Sensitivity of microbalance (g)	$10^{-6}$	$2 \cdot 10^{-3}$	–
Kind of reaction	$RS_2 \rightarrow R_2S_3 + S$	$R_2S_3 + S \rightarrow RS_2$	$R_2S_3 + S \rightarrow RS_2$
Time to achieve steady state ( <i>h</i> )	120–240	25	190
Means of composition determination	tensimetric calculations	addition to weight	chemical analysis
Error in composition (at. pct)	0.1	3–5	2–3
Means of homogeneity range determination	breaking points of $S_1S_2V$ – $S_2V$ lines	X-ray powder diagrams	chemical analysis
Limit of determination (at. pct)	$\leq 0.07$	$\leq 3$	$\leq 2$

boundaries were emphasized. Some regularities in the behavior of the phase equilibria for the polysulfide systems along the La–Lu series may be noted. The stability ranges of isostructural disulfides shift to lower temperatures going from La to Lu. The solid–solid lines shift to higher pressure going from La to Sm. Even with these regularities, the information on the  $P$ – $T$  diagrams is scant and inconsistent. Indeed, the phase state in these systems needs further investigation.

#### 4.3. $P_S$ – $T$ – $x$ diagrams

Tensimetric methods are effective in studying phase equilibria of the polysulfide systems because the lanthanides are nonvolatile components at relevant temperatures (Strotzer et al. 1941, Lazarev et al. 1978, Vlach and Chang 1981). Direct sulfur pressure measurements by a silica Bourdon gauge, referred to as method (a) below, and two variants of buffer isopiestic-type measurements with sulfur transfer, methods (b) and (c), were carried out to construct the  $P_S$ – $T$ – $x$  diagrams of the  $RS_{1.50}$ – $S$  systems. Method (a) is based on the registration of transitions from three-phase equilibria,  $S_1S_2V$ , to two-phase equilibria,  $SV$ , and vice versa, when the phase state change occurs as a result of incongruent vaporization of the higher polysulfide in a closed system. The compositions of the intermediate polysulfides are calculated from the initial sample composition, which is known in advance, and the vapor phase in the points where complete decomposition of one of the condensed phases has taken place. The accuracy and sensitivity of the composition determination is achieved due to the precise characteristics of the initial sample (its weight and stoichiometry), and accurate measurements of the other experimental parameters such as pressure, temperature, and the gauge volume. In method (b) the composition is determined by chemical analysis after quenching the sample at the end of a run. In method (c) the composition is monitored continuously by means of a balance. The detailed parameters of these tensimetric methods are given in table 3.

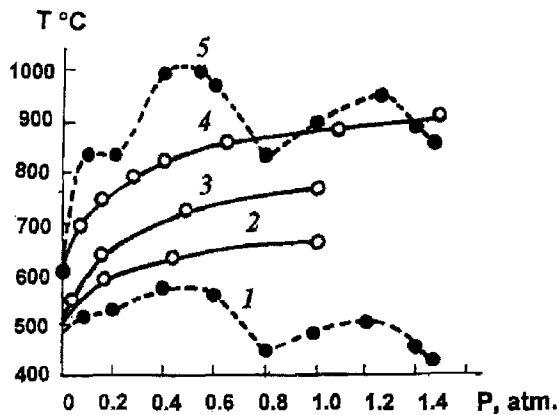


Fig. 2.  $P_S$ - $T$  phase diagrams for the  $\text{SmS}_{1.50}$ - $\text{SmS}_{2.00}$  system: dashed lines, data from method (c); solid lines, data from method (a). Designation of monovariant lines: (1)  $\text{S SmS}_{2.0}$  V; (2)  $\text{SmS}_{1.90}$   $\text{SmS}_{1.89}$  V; (3)  $\text{SmS}_{1.89}$   $\text{SmS}_{1.86}$  V; (4)  $\text{SmS}_{1.86}$   $\text{SmS}_{1.50}$  V; (5)  $\text{SmS}_{2.0}$   $\text{SmS}_{1.50}$  V.

The  $P_S$ - $T$ - $x$  diagrams are studied for several systems. The La, Ce, Sm, and Gd systems were studied by method (c) (Loginova 1974, Loginova et al. 1975). For the Pr, Nd, Sm, Gd, Dy, and Er systems both method (a) and method (b) were used (Gorbunova and Vasilyeva 1985, Vasilyeva 1985, Vasilyeva and Gorbunova 1986, Gibner and Vasilyeva 1990, Vasilyeva and Belaya 1999, Vasilyeva and Belyaeva 1999, Vasilyeva et al. 1999). A considerable difference in topology between diagrams established using methods (c) and (a) is observed. Grossly nonstoichiometric phases with wide compositional ranges, such as  $\text{CeS}_{1.82}$ - $\text{CeS}_{2.53}$  (although the composition of the higher Ce polysulfide is overestimated unjustifiably),  $\text{SmS}_{2.0}$ - $\text{SmS}_{1.82}$ , and  $\text{GdS}_{2.0}$ - $\text{GdS}_{1.82}$  are the main results of method (c). The main results of methods (a) and (b) for these systems are no hyperstoichiometric polysulfides, no strict stoichiometric disulfides for the heavy lanthanides, and the occurrence of a series of individual intermediate phases spaced compositionally very closely. Most of the intermediate polysulfides may be represented compositionally as a homologous series of compounds with the generic formula  $\text{R}_n\text{S}_{2n-1}$ .

The difference between diagrams constructed on evidence obtained by methods (a) and (c) for the Sm system is clearly visible in fig. 2. Both the compositions of the Sm polysulfides and the positions of the lines representing the phase boundaries do not agree with each other. Features of the diagram based on the measurements of method (c) are the abnormal mutual arrangement of the phase fields and the  $P_S$ - $T$  lines lying higher in relation to those of method (a), which leads one to consider this diagram to be "non-equilibrium". It seems plausible that in method (c) a steady state was assumed to be the equilibrium state, considering that the monitoring of the polysulfide weight change was not very sensitive in the experiment. Another example, where the kinetics are of primary importance to the topology of the polysulfide diagram, is shown in fig. 3 by the example of the  $T$ - $x$  diagram of the  $\text{DyS}_{1.50}$ - $\text{DyS}_{1.84}$  system. In this study the criterion for an equilibrium state in the system (invariantness of pressure to time) was intentionally varied from 1 to 2 Torr per day (Vasilyeva et al. 1999). This change was sufficient to fix the invariantness of pressure on the second instead of the ninth day, and to assume a steady

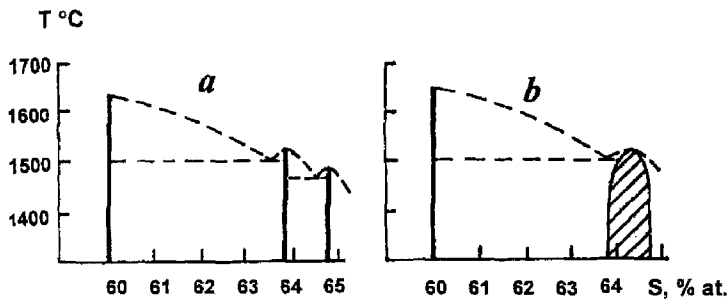


Fig. 3.  $T$ - $x$  phase diagram for the  $\text{DyS}_{1.50}$ - $\text{DyS}_{2.00}$  system: (a) equilibrium and (b) nonequilibrium state.

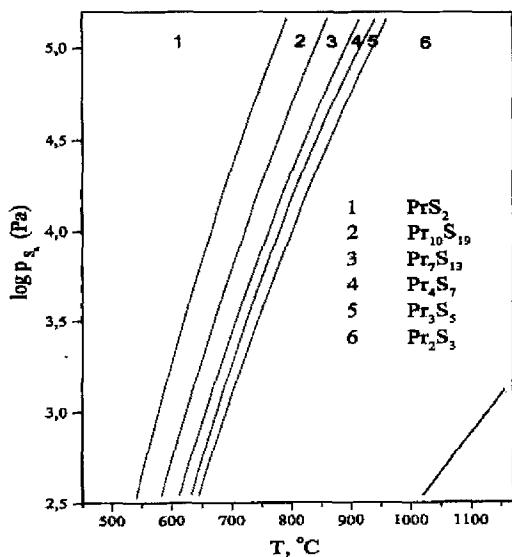


Fig. 4. Solidus portion of the pressure-dependent diagram for the  $\text{PrS}_{1.50}$ - $\text{PrS}_{2.00}$  system. Phase stability fields are marked as 1-6.

state instead of equilibrium one. As a result, the equilibrium phase diagram with two individual polysulfides is modified to that with one nonstoichiometric phase, see fig. 3. Therefore, the method of automatically monitoring the weight change with low sensitivity is not suitable for studying phase equilibria in polysulfides systems.

The solidus portion of the pressure-dependent equilibrium phase diagram of the  $\text{PrS}_{2.0}$ - $\text{PrS}_{1.5}$  system constructed by methods (a) and (b) is shown in fig. 4. A series of new sulfur-deficient polysulfides,  $\text{PrS}_{1.900(2)}$ ,  $\text{PrS}_{1.846(6)}$ ,  $\text{PrS}_{1.766(8)}$ , and  $\text{PrS}_{1.702(7)}$ , in addition to the strict stoichiometric  $\text{PrS}_2$  has been found, separated by miscibility gaps. The intermediate polysulfides are seen to have narrow fields of stability. Therefore, it is difficult to prepare a single-phase intermediate polysulfide, especially when the desired thermodynamic parameters are unknown. On the other hand, the information resulting from these diagrams on the nonstoichiometric polysulfide compositions opens

the possibility to estimate the correctness of polysulfide compositions which were determined chemically, as is customary in the preparative chemistry.

#### 4.4. Correlation between the $T-x$ and $P_S-T-x$ diagrams

The correlation between  $T-x$  phase diagrams and diagrams of log pressure vs. inverse temperature, called Van 't Hoff diagrams, has been illustrated by the example of the Nd and Er systems (Gorbunova and Vasilyeva 1985, Gorbunova et al. 1990). This correlation was used to reach a conclusion concerning the true constitution of the Nd system and to estimate the equilibrium sulfur pressures for the Nd and Er polysulfides at their melting points. The operational details of the procedure are as follows. Possible forms of the Van 't Hoff diagrams were derived for the Nd and Er systems in accordance with the reported  $T-x$  diagrams. Two types of diagrams for Nd, with  $\text{NdS}_2$  either peritectically decomposing at  $900^\circ\text{C}$  (Uspenskaya 1972) or congruently melting at  $1720^\circ\text{C}$  (Gorbunova and Vasilyeva 1985), and one type for Er, with  $\text{ErS}_{1.85}$  congruently melting at  $1620^\circ\text{C}$ , were taken into account. Next the  $P_S-T$  lines for all the polysulfides were experimentally determined at temperatures from  $400$  to  $1100^\circ\text{C}$ , and the slopes of these lines relative to each other and to the line for pure sulfur were analyzed to be compared with the possible forms of the Van 't Hoff diagrams. The fact that none of the vapor lines showed any evidence of inflecting and that they had no tendency to a mutual intersection verified the validity of the  $T-x$  diagrams with congruently melting polysulfides. Knowing that  $\text{NdS}_2$  and  $\text{ErS}_{1.85}$  showed no transitions up to melting, the equilibrium sulfur pressures as extrapolated to the melting points were estimated to be  $\sim 180$  atm for  $\text{NdS}_2$  and  $\sim 128$  atm for  $\text{ErS}_{1.85}$ . The correlation procedure is very useful especially for those systems for which data on the phase equilibrium are scarce and conflicting.

#### 4.5. Isotypical lines

The construction of isotypical lines would be worthwhile to find a compositional principle for the homologous series and to make an estimation of the correctness of available dissimilar data. All new phases suggested from the  $P_S-T-x$  diagrams and crystallization experiments, together with previous values for powdered polysulfides determined chemically, are collected in table 4 with indications of their accuracy. There is some disagreement on these magnitudes. Therefore, a line could be assumed to be actually existing if it included a sufficient number of reliably determined compositions. Among all these compositions, first preference was given to values resulting from tensimetric and crystallization experiments, as they are the most credible. The correctness of values obtained chemically for powdered samples was considered in some detail before their insertion in the line. On this basis one can easily construct two isotypical lines:  $\text{RS}_{2.000}$  for  $\text{R}=\text{La}-\text{Nd}$ , and  $\text{RS}_{1.900}$  for  $\text{La}-\text{Eu}$ . From this point of view the  $\text{RS}_{1.766}$  and  $\text{RS}_{1.700}$  lines are probable, but not as reliable, especially with regard to their estimated extension along the  $\text{La}-\text{Lu}$  series. Little can be said about other lines and phases not belonging to these lines but being members of the homologous series  $\text{R}_n\text{S}_{2n-1}$ . Some compositions, e.g.  $\text{RS}_{1.80}$ , seem to be quite tentative; others, e.g.  $\text{RS}_{1.893}$ ,  $\text{RS}_{1.863}$  and  $\text{RS}_{1.833}$  having



Table 4  
Representation of compositions known for the lanthanide polysulfides

Compositions derived from tensimetric experiment ( $\pm 0.004$ )	Compositions of powdered samples from the chemical method ( $\pm 0.08$ )	Compositions of crystals from the chemical method ( $\pm 0.01$ )
RS <sub>2.000</sub> R = La–Nd	RS <sub>2.00</sub> R = La–Lu	RS <sub>2.00</sub> R = La–Nd
RS <sub>1.900</sub> R = La–Nd, Sm, Eu	RS <sub>1.90</sub> R = La–Ho, Y	RS <sub>1.90</sub> R = Sm
RS <sub>1.893</sub> R = Sm	–	–
RS <sub>1.875</sub> R = Nd	–	–
RS <sub>1.863</sub> R = Sm	–	RS <sub>1.86</sub> R = Dy
RS <sub>1.850</sub> R = Nd, Pr, Er	RS <sub>1.85</sub> R = Nd, Pr, Sm, Dy, Er	RS <sub>1.85</sub> R = Er, Gd
RS <sub>1.833</sub> R = Dy, Gd	RS <sub>1.80</sub> R = La, Gd, Tb	RS <sub>1.84</sub> R = Dy
RS <sub>1.766</sub> R = Pr, Dy	RS <sub>1.75</sub> R = La, Pr, Nd, Tb, Ho, Y	RS <sub>1.76</sub> R = Dy
RS <sub>1.700</sub> R = Pr	RS <sub>1.70</sub> R = La, Pr, Gd, Ho, Er, Yb, Y	RS <sub>1.68–1.70</sub> R = Ho, Lu

their stability field on the  $P_S$ – $T$ – $x$  diagrams, are reliably identified (Vasilyeva and Belaya 1999). The intermediate phase compositions RS<sub>1.900</sub>, RS<sub>1.893</sub>, RS<sub>1.846</sub>, RS<sub>1.766</sub> and RS<sub>1.702</sub>, described by the generic formula  $R_nS_{2n-1}$  seem to be realized by the loss of one sulfur atom. The mechanism of this loss, and the distribution of the vacant sulfur sites in the structures of these intermediate polysulfides of the homologous series, must be solved.

*Final comment.* Complete thermodynamic and kinetic studies have been made to identify new individual polysulfide phases. The static membrane gauge method appears to be the most promising for controlling the equilibrium state in the systems. This method is also the main source in constructing  $P_S$ – $T$ – $x$  equilibrium diagrams, which provide valuable data for crystal-growth processes of the intermediate polysulfides.

## 5. Crystal growth

An important aspect of preparative procedures is the growth of single crystals or films of the polysulfides. It is difficult to grow crystals or films from the melt or from the vapor because of the high melting points and incongruent vaporization of these compounds. No information is available about growing polysulfide films by a specific technique. However, the EuS<sub>1.9</sub> or GdS<sub>1.9</sub> phases were detected by Schienbein et al. (1978) in films prepared by the action of an electron beam on the precursors EuS or GdS. However, the formation of these phases was not associated with direct deposition from the vapor. Interaction of EuS or GdS films with atomic sulfur, accumulated under these films at high deposition rates, led to the occurrence of the polysulfides.

Three types of procedures were used to obtain crystals of polysulfides: from water-free ammonia, by a chemical transport method, and crystallization from fluxes of a different origin. The first procedure was effective in growing small YbS<sub>2</sub> crystals only (Teske 1974). Crystals of LaS<sub>2.0</sub> and NdS<sub>2.0</sub> were prepared by chemical transport with

iodine ( $5 \text{ mg/cm}^3$ ), and mass transport took place from the hot to the cold zone (gradient  $\sim 100^\circ\text{C}$ ) (Uspenskaya and Eliseev 1970, Eliseev et al. 1971, 1972). Well-faceted crystals are usually grown in a diffusion regime: any supersaturation in the gaseous phase results in poor crystallinity. Sulfur and bromine did not transfer polysulfides at all. There are short accounts, without details, on growing  $\text{YbS}_{2-x}$  crystals (Eliseev et al. 1981) and  $\text{GdS}_{2-x}$  crystals (Azizov et al. 1984) by chemical transport.

Flux methods appear to be more effective for growing polysulfide crystals. The following groups of possible solvents were investigated: solvents with a common cation ( $\text{NdI}_3$ ); solvents with a common anion ( $\text{Na}_2\text{S}_2$ ,  $\text{Na}_2\text{S}_{2.8}$ ,  $\text{Na}_2\text{S}_4$ , and sulfur); indifferent solvents (KCNS, Pb, KCl, KI, and KI+KCl or KBr+KI eutectics). Crystallization from a  $\text{NdI}_3$  flux met with failure because of the very high reactivity of the melts towards oxygen and crucible materials. Crystals of  $\text{LaS}_2$ ,  $\text{NdS}_2$ , and  $\text{PrS}_2$  grew from a sulfur melt at  $500\text{--}600^\circ\text{C}$ , but remained small,  $<0.5 \text{ mm}$  (Bucher et al. 1975). The sodium polysulfides are very attractive fluxes because of their properties. They melt at low temperatures, produce the desired gaseous sulfur medium, and form sulfur species  $(\text{S}_n)^{2-}$  in the melt (Ziemann and Buess 1979). The  $(\text{S}_2)^{2-}$  species is identical with the structural fragments,  $(\text{S}_2)^{2-}$ , of the polysulfides, and their concentration in the system would favor the kinetics and mechanism of polysulfide crystallization. Taylor (1980) discussed the stereochemical role of the dimeric species in such a mechanism for other disulfides. A  $\text{Na}_2\text{S}_5$  melt in autoclaves under a pressure of about 10 atm was used in an attempt to grow La disulfide crystals (Scheel 1974). However, hypostoichiometric polysulfides,  $\text{LaS}_{1.9}$  and  $\text{LaS}_{1.7-1.8}$ , rather than the expected disulfide, crystallized in this case. The question why a mixture of the two polysulfides is formed was left unanswered. Contrary to this study, all attempts to grow  $\text{NdS}_2$  and  $\text{DyS}_{1.84}$  crystals from  $\text{Na}_2\text{S}_2\text{--Na}_2\text{S}_5$  fluxes have not been successful. Ternary compounds,  $\text{NaNdS}_2$  or  $\text{NaDyS}_2$ , rather than the polysulfides, grew preferentially under all conditions. The occurrence of the ternary compounds was shown to be the result of a complex chemical interaction between ions generated by the flux and the polysulfide in the melts. It is not surprising, then, that the polysulfides showed a high solubility in these fluxes, 4–10 mass% at  $650^\circ\text{C}$  (Shilkina and Vasilyeva 1984, 1986).

Indifferent solvents are more suitable for the polysulfides.  $\text{LaS}_2$  was grown from the KI+KCl eutectic by Dugué et al. (1978) and Bénazeth et al. (1981);  $\text{TbS}_2$  was prepared from the KI+KBr eutectic by Kuzmicheva et al. (1983),  $\text{NdS}_2$  and  $\text{DyS}_{1.84}$  were obtained from a melt of KI alone (Shilkina et al. 1987a). The solubility of  $\text{NdS}_2$  and  $\text{DyS}_{1.84}$  was studied in many fluxes, and it was found to be at the level of 0.3–0.8 mass% at  $900^\circ\text{C}$ , in KCl, KI and the KI+KCl eutectic. In the Pb and KCNS melts the polysulfides did not dissolve at all (Vasilyeva et al. 1985, Shilkina et al. 1987a). Crystals of all the lanthanide polysulfides, except Eu, Yb, and Tm, were grown from a KI flux at a temperature of  $715^\circ\text{C}$ . Sulfur amounts and temperatures were chosen in such a way that stoichiometric disulfides should be realized without decomposing. The growth mechanism was not specifically studied. Nevertheless, "layer-by-layer" growth was presumed on the basis of the stepped relief of the crystal surface and the fact that spiral growth patterns were revealed through etching figures (Shilkina and Vasilyeva 1984). As a rule, the polysulfides grew from the fluxes as single crystals and as their agglomerates.

The average composition of the crystals was determined by wet chemical analysis for a weight of  $\sim 0.3$  g with accuracy  $\sim 1.5\%$ . It was  $RS_2$  for the La–Nd elements, and  $RS_{1.90}$  for Sm. The analysis shows that the crystals of these elements grown from the eutectic flux correspond precisely in composition to the higher polysulfides observed in these systems by the tensimetric technique. One can concede that in these growth experiments the higher polysulfides are crystallized as a single-phase product. For the heavy elements the parallel weights led to the dispersion of analytical results and the composition was determined as  $RS_{1.85-1.82}$  for  $R = \text{Dy, Er, Gd}$ , and  $RS_{1.70-1.68}$  for  $R = \text{Ho, Lu}$ . This fact together with the large variability in external morphology and in color of the crystals for these systems rather suggests a heterophase crystallization. Other authors also observed heterophase crystallization of the polysulfides. Two kinds,  $\alpha$  and  $\beta$ , of solid modifications of  $\text{LaS}_2$  grew from the  $\text{KCl} + \text{KI}$  eutectic (Bénazeth et al. 1981);  $\text{LaS}_{1.94}$  grew together with  $\text{LaS}_{1.7-1.8}$  from the  $\text{Na}_2\text{S}_5$  melt (Scheel 1974);  $\text{NaNdS}_2$  and  $\text{NdS}_2$  are collectively crystallized from sodium polysulfide fluxes (Shilkina and Vasilyeva 1984). The heterophase mixtures require more extensive identification than just a structural study of one or two single crystals sampled randomly from a wide variety of crystals. In an attempt before structural studying to divide the crystals into different groups on the basis of identity of some their properties, different diagnostic properties of the polysulfides were tested (Vasilyeva et al. 1985, 1999).

*Final comment.* The spontaneous growth from fluxes does not always provide only the desired phase. In the case of heterophase growth a first selection of the crystals on the basis of some diagnostic properties is the best way to avoid an incorrect representation of the phase state in the polysulfide systems.

## 6. Diagnostic properties

Color, external morphology, luster, reflection, hardness, and density may be diagnostic properties of individual polysulfides, if these properties are not affected by the preparation conditions. For small crystals ( $\leq 0.5$  mm) a first selection was performed using color (Uspenskaya 1972, Bucher et al. 1975, Wichelhaus 1977) or external morphology. It turns out that structurally identical crystals may show different habits due to different kinds of twinning (Kuzmicheva et al. 1983). Flux-grown crystals were reasonably large, and some of their properties were measured. For  $\text{PrS}_2$ ,  $\text{NdS}_2$ ,  $\text{SmS}_{1.9}$  and  $\text{DyS}_{1.84}$  crystals, properties such as external morphology, color, density, microhardness and specific spectroscopic parameters were tested to find the best indicator for first selection (Vasilyeva et al. 1999, Vasilyeva and Belyaeva 1999, Podberezskaya et al. 1997, Vasilyeva and Belaya 1999). These crystals were  $(3-5) \times 10^{-3}$  g in weight and  $3 \times 4$  mm in size; special procedures were developed to measure their properties and to accurately determine the composition of any individual crystal of such size. Molecular-emission spectroscopy was used to determine the composition with an accuracy of  $\sim 1\%$  (Bachturova and Chuchalina 1982); a microburette method was used for density measurements with an accuracy of  $\sim 0.5\%$ , and the characteristic Raman spectra were recorded with a spatial resolution of  $\sim 1$  mm<sup>2</sup>.

Usually 20–30 crystals from each of these systems were analyzed to verify the crystal identity. As an illustration, some combined results are presented here.

*Morphology.* Flux-grown crystals of the Pr, Nd, Sm, and Dy polysulfides were in the form of thin plates, rectangular parallelepipeds, truncated pyramids, and some irregular shapes. Going from the light to heavy lanthanides, the thickness of the plates increased from 0.02 to 0.3 mm, however these thick plates were not single-crystalline. For the Pr, Nd, and Sm crystals no single preferred form is observed. The Dy crystals can easily be separated into two groups, as square and extended plates according to their external morphology.

*Composition.* No difference in composition between individual crystals analyzed was established for the Pr, Nd, and Sm polysulfides. The individual Dy crystals show no repeatability in composition, even if taken from one morphological group. These irregularities were suggested to be evidence of a compositional nonuniformity not only between the crystals but locally within individual Dy crystals as well. The nonuniformity is expected to be in the  $\mu\text{m}$  range. Therefore, a first mechanical separation of the Dy crystals by morphology has not the desired effect.

*Color.* The color of the polysulfides was found to be ineffective in distinguishing between them, since the perceived color may involve different extrinsic effects, such as particle size, crystal perfection, or surface states. This is clearly the case since for the  $\text{LaS}_2$  powdered disulfides with identical particle size one may observe colors from deep yellow to red-orange; for  $\text{NdS}_2$  the color can vary from red to black-brown. A slight difference in color between the polysulfides along the La–Gd series may be noted only for thin  $\sim 100\ \mu\text{m}$  crystals. A deep yellow color for  $\text{LaS}_2$  is modified to light brown for  $\text{GdS}_{1.85}$ . Moreover, pleochroism is observed for these thin crystals under the polarizing microscope. All thick crystals, irrespective of R element and, thus, of composition, are of grey color with a mirror-smooth surface which was of the basal (010) plane according to Raman-spectroscopic identification (Kolesov and Vasilyeva 1992). The grey color was caused by structural macrodefects, such as flux inclusions, dislocations, block boundaries, and twins, which were independently detected by different means (Vasilyeva and Belaya 1999, Shilkina et al. 1987a, Kuzmicheva 1994, Podberezskaya et al. 1999).

*Microhardness.* The microhardness was measured on the mirror-smooth surface to be 400, 412, 450 and  $445\ \text{kg/mm}^2$  for the  $\text{PrS}_2$ ,  $\text{NdS}_2$ ,  $\text{SmS}_{1.9}$  and  $\text{DyS}_{1.83}$  crystals, respectively. One can see that these values are independent of the composition within the experimental error of 10%. It appears that the microhardness value is determined mainly by the internal morphology of these crystals rather than their composition and, hence, may not be a diagnostic parameter for these quite imperfect flux-grown crystals.

*Density.* This property was found to be useful for a first selection of the polysulfide crystals. In each of the Nd, Pr and Sm systems 20–30 crystals selected randomly showed identical density, giving a good proof of phase uniformity of all these crystals. For the Dy crystals there was considerable scatter in density values, and only a histogram based on  $\sim 100$  measurements with well-defined maxima allowed the polysulfides with different density and hence with different compositions to be observed. At least two polysulfide phases were identified according to this histogram. The scatter still persists between the

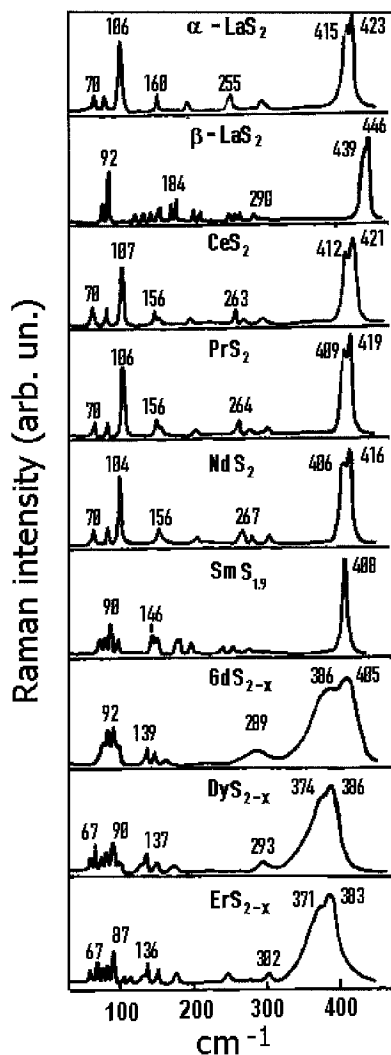


Fig. 5. The Raman spectra of the lanthanide polysulfides.

density of Dy crystals from a single morphological group. This is additional evidence of a local compositional nonuniformity within the individual Dy crystal.

*Spectroscopic properties.* Golovin et al. (1975) and Le Rolland et al. (1991, 1994) have attempted to identify the powdered polysulfide phases using Raman spectroscopy, but characteristic peaks for these compounds were not clearly recognized. Kolesov and Vasilyeva (1992) used a precise Raman procedure with metal isotopes, polarized light, and the crystal oriented intentionally according to its crystallographic axes; their results are presented in fig. 5. A very specific peak for the  $(\text{S}_2)^{2-}$  anion, one structural component of the definite structure, was established. This peak was suggested to be a “fingerprint”

for the  $\alpha$ - and  $\beta$ -forms of the light lanthanide polysulfides, and for  $\text{SmS}_{1.90}$ . The peak loses its specificity for the polysulfides of the heavy elements because of broadening. This broadening may be caused by different effects, such as a heterophase local state in the  $\mu\text{m}$  range, or any atomic disordering in the anion layer. The effects may manifest themselves singly or together, and this makes further identification difficult.

*Final comment.* The density and spectroscopic peculiarities were found to be good indicators for a first phase identification of flux-grown crystals even if the crystals show a microlocal compositional nonuniformity. The local micro-nonuniformity detected for Dy crystals is a very interesting finding and calls for further investigation as to which thermodynamics or kinetics are responsible for the heterophase crystallization in this system. On the other hand, it is desirable to gather accurate data on the density and composition before a structural study of the crystal is undertaken. These data allow some errors in the structural study to be prevented, since twinning is a characteristic property of the polysulfide crystals (Bénazeth et al. 1981, 1982).

## 7. Structural properties

### 7.1. Structural analysis

Classification of the polysulfides according to structural data has already been attempted, but these reviews were representative rather than comprehensive (Samsonov and Radzikovskaya 1961, Flahaut and Laruelle 1968, Jarembash and Eliseev 1975, Eliseev and Grizik 1977, Flahaut 1979, Porcher and Caro 1983). At that time, single-crystal investigations were not extensive and powder data were summarized. In the earlier studies, the cubic lattice was thought to be maintained for the disulfides of all lanthanides according to the powder X-ray diagrams. Later, the anti- $\text{Fe}_2\text{As}$  structure (tetragonal cell,  $P4/nmm$ , with  $a_0 \approx 4 \text{ \AA}$  and  $c_0 \approx 8 \text{ \AA}$ ) or superstructures of this type were proposed for disulfides. The sulfur-deficient compounds were described through pseudo-tetragonal cells,  $2a_0, 2a_0, c_0$ , although they really had lower symmetry (Flahaut 1979). The first single-crystal studies (Dugué et al. 1978, Borisov et al. 1979) showed that the stoichiometric  $\text{LaS}_2$  and  $\text{NdS}_2$  have low symmetry, the orthorhombic  $Pnma$  cell with  $a = 2a_0$ ,  $b = 2c_0$ ,  $c = a_0$ , and the monoclinic  $P2_1/c$  with  $a = 2a_0$ ,  $b = c_0$ ,  $c = a_0$ , respectively. These are superstructures of the anti- $\text{Fe}_2\text{As}$  type with distortions. Later, twinning was found to be typical of the disulfides, and special procedures taking account of the twinning effect were developed (Bénazeth et al. 1981, 1982). An extended treatment on the subject by Magarill et al. (1992) gave the structural data together with the techniques used in the structural studies (powder, photo and single-crystal methods). On the basis of the complete structure information for polysulfides and polychalcogenides, a full revision of these data was made by Podberezskaia et al. (1996). The symmetry and unit cell parameters for the polysulfides were considered and their relationship with those of the  $\text{PbFCl}$  or anti- $\text{Fe}_2\text{As}$  structural prototypes was analyzed. The data recommended as most correct for the polysulfides were taken and supplemented by the latest results for

Table 5  
Structural types and lattice parameters of the polysulfides

Space group	Compound	<i>a</i>	<i>b</i>	<i>c</i>	$\beta$	<i>d</i> <sub>calc</sub>	<i>d</i> <sub>exp</sub>
P2 <sub>1</sub> /c, Z=2 ( $\alpha$ -form)	LaS <sub>2</sub>	8.18	4.03	8.13	90	4.90	4.87
	CeS <sub>2</sub>	8.107	4.075	8.084	89.80	5.07	5.05
	PrS <sub>2</sub>	8.079	4.054	8.058	$\approx$ 90	5.16	5.16
	NdS <sub>2</sub>	8.015	4.012	7.988	90	5.39	5.36
Pnma or Pn2 <sub>1</sub> /a, Z=8 ( $\beta$ -form)	LaS <sub>2</sub>	8.131	16.34	4.142	–	4.90	–
	CeS <sub>2</sub>	8.103	16.221	4.093	–	5.06	–
	PrS <sub>2</sub>	8.025	16.125	4.062	–	5.17	–
P2 <sub>1</sub> /m, Z=2 C2/c, Z=4	NdS <sub>2</sub>	7.977	16.012	4.027	–	5.38	–
	TbS <sub>2</sub>	3.8123	3.8599	7.887	90.10	6.72	–
P4 <sub>2</sub> /n, Z=20 P2 <sub>1</sub> /n, Z=40	YbS <sub>2</sub>	9.32(6)	4.74(4)	9.02(5)	118.3(9)	4.47	–
	SmS <sub>1.90</sub>	8.796	–	15.889(3)	–	5.707	5.71
C112 <sub>1</sub> /m, Z=48	DyS <sub>1.84</sub>	11.009(2)	11.531(2)	11.023(1)	91.152	6.303	6.30
	DyS <sub>1.76</sub>	15.429(3)	15.730(3)	11.539	89.97	–	6.18

the lower polysulfides (Podberezskaya et al. 1998, 1999, Belaya et al. 2000). These are given in table 5. The structures have tetragonal, orthorhombic and monoclinic symmetry. They are all superstructures relating to the PbFCl-type by means of different orientations and cell parameters. The superstructures have a tendency towards formation of closest-packed structures in which a maximum possible symmetry is combined with a minimum cell volume. According to Podberezskaya et al. (1997), the PbFCl-type rather than the anti-Fe<sub>2</sub>As or anti-Cu<sub>2</sub>Sb types commonly occurring in literature, is preferable for the compounds where F, Pb, and Cl positions are occupied respectively by (S<sub>2</sub>)<sup>2-</sup>, R<sup>3+</sup>, and S<sup>2-</sup> ions. Böttcher et al. (2000) systematized the layer compounds RS<sub>2</sub> and their derivatives on the basis of structure of the aristotype structure ZrSSi.

### 7.2. Isostructural lines

The data given in table 5 show that the polysulfides with compositions derived from structural studies tend to classify in the same manner as the compositions derived from tensimetric studies, see sect. 4.5. Structural studies of the polysulfides using single crystals are quite scanty, and only for the RS<sub>2</sub> isotypical line has reliable structural information been obtained for all members of the series (Podberezskaya et al. 1997, Tamazyan et al. 2000a). Two structural types, the  $\beta$ -orthorhombic form, Pnma, and the  $\alpha$ -monoclinic form, P2<sub>1</sub>/a, were established for the strict stoichiometric disulfides of La, Ce, Pr and Nd. The  $\alpha$ - and  $\beta$ -structures belong to a series of polytypes resulting in different arrangements of the layers (Yanagisawa et al. 1979, Bénazeth et al. 1981, Kuzmicheva et al. 1981, Yanagisawa and Kume 1986). The  $\alpha \rightarrow \beta$  transition takes place under pressure, a driving force for sheet displacement, and the pressure applied is a

function of ionic radius of the La–Nd elements (Yanagisawa and Kume 1986). Therefore, the  $\beta$ -phases of  $\text{CeS}_2$ ,  $\text{PrS}_2$  and  $\text{NdS}_2$  could only be synthesized at high pressure, when the radius ratios were improved for the compressibility of the sulfur ions (Merrill 1982). The temperature effect and kinetics of the  $\alpha \rightarrow \beta$  transition have defied explanation. The transition for  $\text{LaS}_2$  was found to be reversible with the upper limit of thermal stability of the  $\alpha$ -form at about  $750^\circ\text{C}$  (Bénazeth et al. 1981) and irreversible according to the study of Le Rolland et al. (1994). In this study two new phases,  $\alpha'$ - $\text{LaS}_2$  and  $\gamma$ - $\text{LaS}_2$ , were observed during the reconstructive phase transformation:  $\alpha'$ - $\text{LaS}_2$  as a metastable phase and  $\gamma$ - $\text{LaS}_2$  as a disordered intermediate between the  $\alpha$  and  $\beta$  phases. This experiment demonstrates that the polysulfide transformation is controlled by both thermodynamics and kinetics. Le Rolland et al. (1994) related the tetragonal  $\gamma$ - $\text{LaS}_2$  phase to a new polymorph with the anti- $\text{Fe}_2\text{As}$  structure and with a spatially averaged disordered structure with local symmetry lower than tetragonal. The answer as to whether this  $\gamma$ -phase is truly a polymorph or not may be obtained only after refinement of its composition and after studying the structure with a single crystal. No transition of  $\alpha$ -form to  $\beta$ -form at all was observed for  $\text{CeS}_2$ ,  $\text{PrS}_2$  and  $\text{NdS}_2$  during quenching experiments in the temperature range between 800 and  $1100^\circ\text{C}$  (Bénazeth et al. 1981, Chen and Dorhout 1995). It is not known whether these temperatures really reflected the thermodynamic stability fields, or a kinetic factor limits reorganization of the (RS) and  $(\text{S}_2)^{2-}$  layers for these elements. Podberezskaya et al. (1997) and Prokofiev (1993) gave a fresh insight in the transition kinetics in the polysulfides in the context of a stereochemical argument. They suggest that not only temperature but also the sulfur vapor composition and especially the  $\text{S}_2$  content must be principal factors controlling the kinetics transitions of such type.

Both  $\text{TbS}_2$  and  $\text{YbS}_2$  are not structural analogs of the series with the light-lanthanide disulfides. The  $\text{YbS}_2$  monoclinic cell is not related to the preceding schemes: all the sulfur atoms are in  $(\text{S}_2)^{2-}$  pairs, and this compound is a disulfide of divalent Yb.  $\text{TbS}_2$  may be a member of a new structural branch, which will be typical for the heavier disulfides, but efforts to prepare the strict stoichiometric disulfides of other heavy rare earths as single crystals have been scarce.

In the case of the  $\text{RS}_{1.90}$  isotypical line ( $R = \text{La–Eu}$ ) the structure has been solved only for  $\text{SmS}_{1.90}$ . This compound actually has the  $\text{Sm}_{10}\text{S}_{19}$  formula and monoclinic structure,  $P4_2/n$  (Podberezskaya et al. 1999, Tamazyan et al. 2000b). However, the formula and symmetry can be given for all members of this line. The statement can be confirmed as follows. First, phases of exactly the same composition, but with selenium anion, were found for the La, Ce, Pr, Nd and Sm elements (Urland et al. 1989, Plambeck-Fischer et al. 1989, Grupe and Urland 1991), and the  $\text{SmS}_{1.90}$  polysulfide is structurally identical with these  $\text{RSe}_{1.9}$  compounds (Podberezskaya et al. 1996). Second, the spectroscopic peaks of the  $(\text{S}_2)^{2-}$  layer, fingerprints for  $\text{PrS}_{1.9}$  and  $\text{NdS}_{1.9}$ , are similar to that for  $\text{SmS}_{1.90}$  (Vasilyeva and Belaya 1999).

The region around the  $\text{RS}_{1.85 \pm 0.02}$  composition includes several close polysulfides (see sect. 4.5). All these compositions are not homologues, and it is not surprising then, that no analogy occurs in the spectroscopic peaks of such compositions (Vasilyeva and Belaya 1999). The structure has been solved only for  $\text{DyS}_{1.834}$  (crystallographic formula  $\text{Dy}_{24}\text{S}_{44}$ ,



$Z=24$ ) by Podberezskaya et al. (1998), and there are no arguments for extending this structure to other members of the region. However, structural data are known for  $\text{DySe}_{1.837}$  (Lee and Foran 1994, 1996),  $\text{YbSe}_{1.83}$  (Kim and Oh 1995) and  $\text{SmTe}_{1.84}$  (Park et al. 1998). These structures were stated to be different large superstructures. Therefore, for the other polysulfide members one would also expect the formation of different superstructures, which will be closely related to each other, but not isostructural.

For the  $\text{RS}_{1.76}$  compositional line (see table 4) the structure has been solved only for  $\text{DyS}_{1.760}$  (crystallographic formula  $\text{Dy}_{24}\text{S}_{42}$ ,  $Z=24$ ). It is noteworthy that the  $\text{DyS}_{1.76}$  structure, which is monoclinic  $C112_1/m$  (Kuzmicheva 1994), is quite specific and is not found among the other polychalcogenides. Indeed, among the 15 kinds of sulfur atoms in the polysulfide layer two vacancies appear together with three sites filled partially by S atoms, with occupancy factors 0.37, 0.64 and 0.90 for S(13), S(14), and S(15), respectively, as shown in fig. 6. Therefore, the best answer as to whether this specific structure will be typical of other polysulfides with the same composition, is to make further structural studies with their single crystals.

Reliable structural data for the  $\text{RS}_{1.70}$  line are missing. The Raman band of the anion layer for the  $\text{PrS}_{1.70}$  polysulfide was found to be broad (Vasilyeva and Belaya 1999). The broadening may result from a disorder of the sulfur and vacant sites since the number of vacancies in the anionic fragment of the  $(\text{S}_2)^{2-}$  layer must increase in  $\text{RS}_{1.70}$  as compared with the  $\text{RS}_{1.83}$  and  $\text{RS}_{1.76}$  polysulfides. The known structure of  $\text{YbS}_{1.70}$  ( $\text{Cu}_2\text{Sb}$  type, space group  $P4b2$ ) has been suggested according to the powder diffraction patterns, and it belongs to a high-pressure modification. Since it is known that polytellurides of  $\text{RTe}_{1.73}$  composition may be prepared at normal conditions (Burns et al. 1979), serious efforts should be made to routinely obtain the polysulfides of this composition as perfect single crystals.

### 7.3. Structural chemistry

For understanding the chemical origin of the sulfide compounds, systematics by basic structural motifs were suggested by Bokii (1964) and Flahaut (1976). But the little-explored rare-earth polysulfides were outside the systematics. When Dugué et al. (1978) showed that the structures of  $\text{RS}_2$  and  $(\text{CeS})_2\text{As}_2$  are formed by structural principles which are similar to basic structures in the Flahaut systematics, the crystallochemistry of the polysulfides began to evolve. Their structure was described by alternating sheets of  $(\text{RS})_n$  composition and layers of  $(\text{S})_n$ . In the sheets the sulfur atoms are isolated, and are  $\text{S}^{2-}$  anions, while in the layers the sulfur atoms form disulfide,  $(\text{S}_2)^{2-}$  anions with a short S–S distance ( $\sim 2.104 \text{ \AA}$ ). An exception to this general arrangement is known for  $\text{YbS}_2$ , as a disulfide of divalent Yb, where all the sulfur atoms are in  $(\text{S}_2)^{2-}$  pairs.

The idea that the symmetry of the polysulfides is controlled by mutual geometrical conjugation of the separate  $\text{R}^{3+}$ ,  $\text{S}^{2-}$  and  $(\text{S}_2)^{2-}$  layers was presented by Podberezskaya et al. (1997). From this point of view, the structure is described by an alternation along the period,  $c_0 \approx 8 \text{ \AA}$  in the parent  $\text{PbFCl}$  structure, layers of  $-(\text{S}_2)^{2-}-\text{R}^{3+}-\text{S}^{2-}-\text{S}^{2-}-\text{R}^{3+}-(\text{S}_2)^{2-}-$ , where each layer has tetragonal symmetry  $4mm$ . The

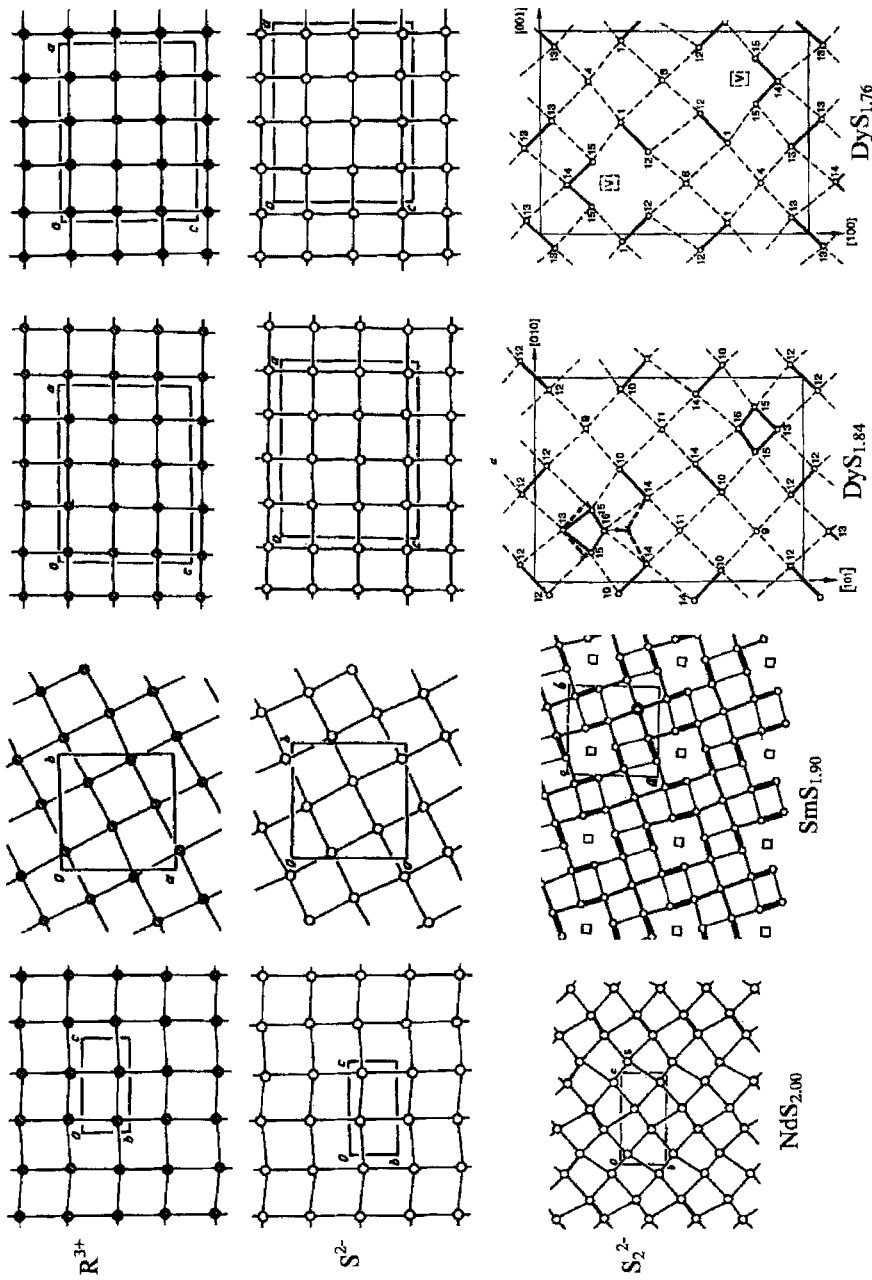
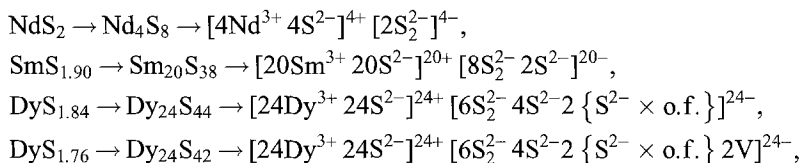


Fig. 6. Arrangement of  $R^{3+}$ ,  $S^{2-}$  and  $(S_2)^{2-}$  layers perpendicular to the  $c$ -direction of the PbFCl-type structure:  $NdS_2$  ( $2P_1/c$ ),  $SmS_{1.90}$  ( $P4_2/n$ ),  $DyS_{1.84}$  ( $P2_1/m$ ), and  $DyS_{1.76}$  ( $P2/m$ ).

periodicity in the  $R^{3+}$  and  $S^{2-}$  layers is achieved by the nonvalent contacts between the  $S^{2-}$  ions. The contacts are specified due to the minimal possible lattice constants in the polysulfides. The side of the large base, over which the  $S^{2-}$  ion is centered in a distorted square antiprism, is given as  $a_0 = 2r_{S^{2-}} \cong 4 \text{ \AA}$ . The other base of the antiprism consists of  $(S_2)^{2-}$  ions, and the side of the square of this layer may be taken to be  $a\sqrt{2} = a_0$ . The arrangement of the  $R^{3+}$ ,  $S^{2-}$  and  $(S_2)^{2-}$  layers for this series of polysulfides,  $NdS_{2.0}$ ,  $SmS_{1.9}$ ,  $DyS_{1.84}$ , and  $DyS_{1.76}$ , of differing symmetry and composition is given in fig. 6. The square nets of  $R^{3+}$  and  $S^{2-}$  are similar, and the (RS) layers, being in proper relation, are shifted relative to each other by  $\frac{1}{2}$  the diagonal square. The interlayer  $S^{2-}-S^{2-}$  bonds vary within 3.342–3.842  $\text{\AA}$ , and the average bond at 3.59  $\text{\AA}$  is slightly shorter than the doubled  $S^{2-}$  ionic radius. Irrespective of the symmetry and unit cell parameters, the structure of the (RS) layer is virtually the same for all compounds. The polysulfide  $(S_2)^{2-}$  layer is very sensitive to the S/R ratio and shows much more variation in the arrangement. According to the structural data, the crystallographic formulas of the polysulfides are



where o.f. is the occupancy factor, and V stands for a vacancy.

For  $DyS_{1.84}$  the partially filled sites, S(13), S(15), and S(16) shown in fig. 6 have o.f. 0.388, 0.474 and 0.155, respectively. The models proposed for the arrangement of the anion layer are confirmed by the good agreement between experimental and calculated densities. The formulas demonstrate that a decrease in S/R ratio results in some  $S^{2-}$  sites being occupied only partially, and even in vacant sites as in the case of  $DyS_{1.76}$ . The vacancies reduce the coordination of the Dy atoms (Tamazyan et al. 1994). Following the formulas, it is clear that in all cases there is electrical equilibrium between the stable  $(RS)^{n+}$  and the varying  $[(S_2)^{2-}-S^{2-}]^{n-}$  fragments. To conserve this charge balance when sulfur content decreases, the dimensions and symmetry of the unit cell of reduced polysulfides are varied relative to the PbFCl type, to form definite superstructures.

Another aspect relating to the structural studies of these phases is the close relationship between the polysulfide structures composed of the three mutually stacked  $R^{3+}$ ,  $S^{2-}$  and  $(S_2)^{2-}$  layers. When the unit cell parameters of the phases of one or several related compositions are commensurate, block structures or microtwins are formed, as pointed out by all authors who studied these compounds (Tamazyan et al. 1994, 2000a,b, Podbereskaya et al. 1996, 1998). Twinning, in turn, may lead to incorrect determination of the crystal symmetry, especially if the photo method was used in the study. Since the majority of structural studies for the reduced polysulfides utilized this method, only investigations where the composition was refined on the basis of more exact recordings of the intensities and adequate corrections for absorption may be taken into account.

Table 6  
Experimental methods for studying the thermodynamic properties of the polysulfides

Method	Temperature range (K)	Compound	Parameters measured
(a) Adiabatic calorimetry	5–315	$\alpha$ -RS <sub>2</sub> (R = La–Nd); $\beta$ -LaS <sub>2</sub> , DyS <sub>1.84</sub>	$C_p^o(T)$ , $S_{298}^o$ , $H_{298}^o - H_0^o$ <sup>1</sup>
(b) Drop calorimetry	298–1800	LaS <sub>2</sub> , PrS <sub>2</sub> , SmS <sub>2</sub> (cub.)	$H_T^o - H_{298}^o$ , $C_p^o(T)$ , $S^o(T)$ , $\Phi^o(T)$ <sup>2</sup>
(c) Solution calorimetry	298	$\alpha$ -NdS <sub>2</sub> , DyS <sub>1.84</sub>	$\Delta_f H_{298}^o$ , $\Delta H_{sol}^o$ <sup>3</sup>
(d) Vapor pressure measurement, static tensimetry	298–1100	$\alpha$ -RS <sub>2</sub> (R = La–Nd), SmS <sub>1.90</sub> , RS <sub>1.85</sub> (R = Gd, Er, Dy)	$\Delta_r H^o(T)$ , $\Delta_f H^o(T)$ , $\Delta_r H_{298}^o$ <sup>4</sup>

#### References

<sup>1</sup> Tagaev et al. (1989a,b)

<sup>2</sup> Kriklya (1986)

<sup>3</sup> Shilkina et al. (1987b, 1990)

<sup>4</sup> Vasilyeva and Belaya (1999), Vasilyeva and Belyaeva (1999), Vasilyeva et al. (1999)

## 8. Thermodynamic properties

### 8.1. General remarks

Dissolution heats of the La and Ce disulfides have been measured in early 1900s (Biltz 1908). However, systematic thermodynamic studies began only in the 1980s, even though separate thermodynamic data of the light-element disulfides, such as  $\Delta_f H_{298}$ ,  $\Delta_{at} H_{298}$ ,  $\Delta_f G_{298}$  and  $S_{298}^o$ , were estimated by different methods. These data have been collected and treated specially for the handbook by Gordienko and Fenochka (1979). Later some thermodynamic parameters of the La, Ce and Pr polysulfides were published by Bolgar and Gordienko (1990). The scarcity of thermodynamic data is easily explained: it is in part due to experimental difficulties and the absence of well-certified samples of polysulfides. The unfavorable kinetics of formation and dissociation of polysulfides limit the possibility of accurate measurements for both the chemical reaction enthalpy by calorimetry and the Gibbs energy by a technique measuring vapor pressure. For the polysulfides it is a problem to find suitable solvents, which are bound to accurately reflect the stoichiometry of the polysulfides. Studies of solid–vapor interaction cannot employ dynamic tensimetric techniques and methods of bomb combustion in sulfur atmosphere. Thus, only measurements of low- and high-temperature heat capacity and static tensimetry were coming into use as soon as high-quality samples of the polysulfides were prepared. A list of methods used for the polysulfides is given in table 6. Two types of samples were examined in these experiments: high-quality crystals and powders of micron dimensions. The crystals were of monoclinic and orthorhombic structure, the powders were cubic, according to the X-ray powder diagrams. Taking into account the “pseudo-mériédrie” effect (Bénazeth et al. 1981) the powders of cubic symmetry must actually be monoclinic. Therefore, thermodynamic data obtained with powders of cubic

Table 7  
Heat capacity and entropy of the lanthanide polysulfides

	LaS <sub>2</sub>	LaS <sub>2</sub>	CeS <sub>2</sub>	PrS <sub>2</sub>	NdS <sub>2</sub>	SmS <sub>2</sub> <sup>1</sup>	DyS <sub>1.84</sub>
<i>Method (a)</i>							
Structural type	orthorh.	monocl.	monocl.	monocl.	monocl.		monocl.
$C_p^\circ(298\text{ K}) \pm 0.3\%$ , J/mol K	70.37	71.58	71.58	73.76	73.40		73.40
$S^\circ(298\text{ K}) \pm 5\%$ , J/mol K	91.41	92.26	104.6	106.4	107.8		104.2
<i>Method (b)</i>							
Structural type		cubic.		cubic.	cubic.	cubic.	
$C_p^\circ(298\text{ K}) \pm 0.3\%$ , J/mol K		71.98		74.31	74.90	75.72	
<i>Method of estimation</i>							
Structural type		cubic	cubic				
$S^\circ(298\text{ K})$							
Mills (1974)		89.8	91.9				
Mustafaev et al. (1977)		89.9	92.0				
Latimer (1954)		78.6	78.6				

<sup>1</sup> The composition must be SmS<sub>1.90</sub>.

symmetry may be correlated with data measured with crystals of monoclinic symmetry. Thermodynamic properties obtained for the polysulfides are accepted as correct when values from different sources agree within experimental error.

## 8.2. Heat capacity and entropy

The low-temperature heat capacity has been measured from samples contained in an adiabatic calorimeter with continuous and impulse heating. For high-temperature measurements, samples in thin-walled tantalum ampoules were placed in a differential calorimeter. The background information obtained is given in table 7. The small difference (~1.0%) between the  $C_p(298\text{ K})$  value of low-temperature measurements and that extrapolated to 298 K from high temperatures was explained by the different quality of crystals and powders used in these experiments (Tagaev et al. 1989a). The close agreement of the two kinds of measurements allows the thermodynamic parameters to be recommended as reliable. Heat capacity equations, enthalpy, entropy increments, and energy function in the low-temperature (Tagaev et al. 1989a,b) and high-temperature range (Kriklya 1986) have been tabulated.

An attempt to represent the  $C_p(T)$  function for the isostructural disulfides as a general-purpose dependence was made by Tagaev et al. (1989a) and Bolgar et al. (1987a,b), and the dependence was thought to hold at high temperatures. At low temperatures the heat capacity of the disulfides shows a complicated behavior because of the Schottky component, magnetic phase transition, and the thin structural features of dimorphs. This behavior requires the low-temperature heat capacity to be experimentally measured for each new polysulfide, even if isostructural. Anomalies contributing to the heat capacity at

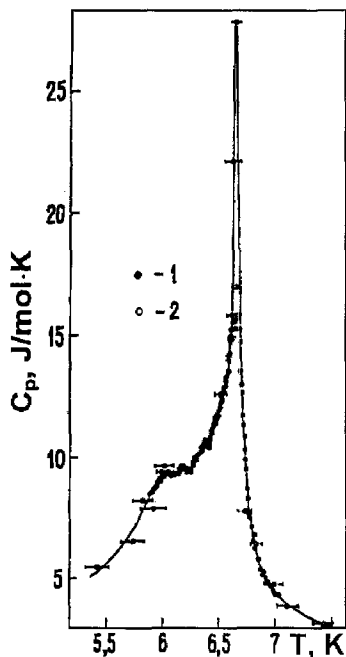


Fig. 7.  $C_p$  of  $\alpha$ -CeS<sub>2</sub> as a function of temperature: dots, continuous heating; stroked dots, pulse heating.

low temperatures were studied in detail by Tagaev et al. (1989a,b). A significant difference in heat capacity between the  $\alpha$ -LaS<sub>2</sub> and  $\beta$ -LaS<sub>2</sub> forms was observed only at very low temperatures where the  $C_p$  behavior is determined mainly by the long-range order of crystal structures. The magnitude as a Debye temperature function was calculated, and the temperature at which an anharmonic contribution appears was found to be  $T_a = 160$  K for  $\alpha$ -LaS<sub>2</sub> and  $T_a = 200$  K for  $\beta$ -LaS<sub>2</sub>. Lattice anisotropy was observed through the Debye parameter varying in the range from 300 K up to 380 K (Beresovskii et al. 1988, 1989, Tagaev et al. 1989a). The heat capacity of  $\alpha$ -CeS<sub>2</sub> measured at low temperature shows a  $\lambda$ -type curve with a main maximum at 6.7 K and an additional maximum at 6.0 K (fig. 7). This result together with the magnetic susceptibility indicates the phase transition of the first-type simulated by ferromagnetic ordering. The transitions are characterized by the entropy  $S_{\max} = 0.94R \ln 2$  and  $S'_{\max} = 0.02R \ln 2$  (Tagaev et al. 1989a). According to these experiments, the La-Nd disulfides were characterized as quasi-dimensional compounds where the number of bonds between the (RS)<sup>+</sup> and (S<sub>2</sub>)<sup>2-</sup> layers is less than those within each of the layers (Beresovskii et al. 1989). For the nonstoichiometric polysulfides the heat capacities are available only for SmS<sub>1.90</sub> and DyS<sub>1.84</sub> (Kriklya 1986, Shilkina et al. 1990).

*Entropy.* Experimental values for the entropy, either measured or estimated, are known mainly for disulfides of the light elements. They are shown in table 7 together with the heat-capacity values. The estimated values of the entropy are determined less appropriately. For nonstoichiometric polysulfides the entropy values are still not known.

Table 8  
The standard heat of formation for the lanthanide polysulfides ( $\Delta_f H_{298}^\circ$ , kJ/mol)

	LaS <sub>2</sub>	CeS <sub>2</sub>	PrS <sub>2</sub>	NdS <sub>2</sub>	SmS <sub>1.90</sub>	SmS <sub>1.89</sub>	SmS <sub>1.86</sub>	DyS <sub>1.84</sub>
Structure	cub.	cub.	monocl.	monocl.	tetrag.	?	?	monocl.
Method (d), $\pm 10\%$			568	557.1	539	540	545	586
Method (c), $\pm 5\%$				580.7				547
<i>Method of estimation</i>								
Structure	cub.	cub.	cub.	cub.				
Finogenov (1973)	603.6	598.6	589.4	580.2				
Gordienko and Fenochka (1979)	622.8	611.5						

### 8.3. Enthalpy of formation, atomization energy

The enthalpy of formation has been determined for NdS<sub>2</sub> and DyS<sub>1.84</sub> by means of solution calorimetry (Shilkina et al. 1987b). The accuracy of the  $\Delta_f H_{298}^\circ$  values obtained calorimetrically depends on the accuracy of the solution enthalpy measured in these experiments. The scatter in these values is believed to occur because HCl was used as a solvent. According to Stuve (1981) HCl, indeed, may hardly be an effective solvent for the polysulfides. Tensimetric equipment allows the sulfur vapor above the polysulfide to be accurately measured over a wide range of temperatures and pressures (Gibner and Vasilyeva 1990, Vasilyeva and Gibner 1987). In these experiments, as opposed to solution calorimetry, the initial vaporization data were precise, but the other values employed in the high-temperature cycles were quite rough. This resulted in uncertainty in the enthalpy of formation calculated from the tensimetric data with the second law. Estimated values of the enthalpy, derived from the reduced cycle with the calorimetric data available in the literature, were presented by Finogenov (1973).

Experimental and estimated values of the enthalpy of formation are given in table 8. It may be deduced that, in the present state of study of the polysulfides, these values agree and, thus, appear to be reliable. The data suggest that the tensimetric static method should be taken presently as the primary method for obtaining accurate thermodynamic data for the polysulfides.

*Atomization energy.* Finogenov (1973) calculated the atomization energy for the light-element disulfides. The calculation is based on a linear correlation between the enthalpy of formation of the sulfides in the RS–RS<sub>1.33</sub>–RS<sub>1.5</sub>–RS<sub>2.0</sub> series. The following values for the disulfides were presented (in kJ/mole): 1412 for La; 1610 for Ce; 1506 for Pr; and 1453 for Nd.

### 8.4. Vaporization

Incongruent evaporation of solid disulfides has been shown by numerous studies: the vaporization began at temperatures of 600–700°C and the vapor was found to consist only of sulfur species (Biltz 1911, Picon and Patrie 1956, Flahaut and Guittard 1956b,

Table 9  
Thermochemical parameters of evaporation for the lanthanide polysulfides<sup>a</sup>

Reaction	$\ln P_{S_2}$ (atm)	$\Delta_r H_T^\circ$ (kJ/mol)	$\Delta_r S_T^\circ$ (J/mol K)	$T$ (K)
$20\text{PrS}_{2.000}(\text{s}) = 20\text{PrS}_{1.900}(\text{s}) + \text{S}_2(\text{g})$	19.31–20328/ $T$	160.9±1.2	161.0±1.2	800–1052
$37\text{PrS}_{1.900}(\text{s}) = 37\text{PrS}_{1.846}(\text{s}) + \text{S}_2(\text{g})$	17.15–19311/ $T$	160.5±2.2	142.5±2.1	952–1110
$25\text{PrS}_{1.846}(\text{s}) = 25\text{PrS}_{1.766}(\text{s}) + \text{S}_2(\text{g})$	17.60–20582/ $T$	171.1±1.4	146.4±1.3	909–1220
$30\text{PrS}_{1.766}(\text{s}) = 30\text{PrS}_{1.702}(\text{s}) + \text{S}_2(\text{g})$	16.37–19669/ $T$	168.8±1.6	141.0±1.4	980–1220
$10\text{PrS}_{1.702}(\text{s}) = 10\text{PrS}_{1.500}(\text{s}) + \text{S}_2(\text{g})$	16.80–20401/ $T$	169.6±5.5	139.7±4.8	909–1220
$20\text{NdS}_{2.000}(\text{s}) = 20\text{NdS}_{1.900}(\text{s}) + \text{S}_2(\text{g})$	17.36–17.895/ $T$	148.3±9.5	143.8±9.9	670–950
$80\text{NdS}_{1.900}(\text{s}) = 80\text{NdS}_{1.875}(\text{s}) + \text{S}_2(\text{g})$	20.36–22586/ $T$	187.8±5.6	169.8±5.8	780–1070
$14\text{NdS}_{1.875}(\text{s}) = 14\text{NdS}_{1.857}(\text{s}) + \text{S}_2(\text{g})$	21.13–20819/ $T$	201.0±7.4	175.6±7.3	780–1000
$5.6\text{NdS}_{1.857}(\text{s}) = 5.6\text{NdS}_{1.500}(\text{s}) + \text{S}_2(\text{g})$	17.15 19311/ $T$	173.1±7.8	146.8±7.0	780–1170
$286\text{SmS}_{1.900}(\text{s}) = 286\text{SmS}_{1.893}(\text{s}) + \text{S}_2(\text{g})$	14.75–15166/ $T$	126±15	123±18	700–840
$6.7\text{SmS}_{1.893}(\text{s}) = 6.7\text{SmS}_{1.863}(\text{s}) + \text{S}_2(\text{g})$	19.05–19598/ $T$	163±3.7	58±4.2	1030–1145
$35\text{SmS}_{1.863}(\text{s}) = 35\text{SmS}_{1.500}(\text{s}) + \text{S}_2(\text{g})$	17.86–19983/ $T$	166±2.0	148±1.8	1030–1145
$5.9\text{GdS}_{1.84}(\text{s}) = 5.9\text{GdS}_{1.50}(\text{s}) + \text{S}_2(\text{g})$	26.0–23144/ $T$	192.3±9.9	179±10	700–1100
$5.7\text{ErS}_{1.85}(\text{s}) = 5.7\text{ErS}_{1.50}(\text{s}) + \text{S}_2(\text{g})$	24.1–23764/ $T$	198±16.0	200.0±18	785–970

<sup>a</sup> References:

PrS<sub>x</sub>: Vasilyeva and Belaya (1999),  
NdS<sub>x</sub>: Gorbunova and Vasilyeva (1986),  
SmS<sub>x</sub>: Vasilyeva and Belyaeva (1999),

GdS<sub>x</sub>: Vasilyeva and Kurochkina (1981),  
ErS<sub>x</sub>: Vasilyeva and Gorbunova (1986).

Takashi 1973). The interest in the sulfur loss process has been to obtain the sesquisulfides in a desired modification. No attempts have been made to understand what intermediate products appear in the process. The first quantitative dependence,  $\log P_S = f(1/T)$ , for the dissociation reaction  $\text{RS}_2(\text{s}) \rightarrow \text{RS}_{1.5}(\text{s}) + \text{S}_2(\text{g})$  (R = La, Ce) was based on calorimetry experiments (Biltz 1911) and it was mentioned that the dissociation reaction proceeds with a very low velocity. The direct interaction,  $\text{RS}_{1.5}(\text{s}) + \text{S}_2(\text{g}) \rightarrow \text{RS}_2(\text{s})$ , (R = La, Ce, Sm and Gd), on the contrary, was studied by means of an isopiestic method (Loginova 1974, Ponomarev and Puchlii 1990). This is the case, as already noted in sect. 4.3, for non-equilibrium conditions and, therefore, the isopiestic method most often provided invalid data. To obtain equilibrium data, both the dissociation reaction and a very sensitive static gauge method were utilized. Substantial progress in the tensimetric experiments was achieved when perfect crystals rather than powders began to be used as starting samples. In this way the dissociation of the following higher polysulfides has been studied: PrS<sub>2</sub> (Vasilyeva and Belaya 1999); NdS<sub>2</sub> (Gorbunova and Vasilyeva 1986); SmS<sub>1.90</sub> (Vasilyeva and Belyaeva 1999); GdS<sub>1.85</sub> (Vasilyeva and Kurochkina 1981); DyS<sub>1.84</sub> (Vasilyeva et al. 1999); and ErS<sub>1.85</sub> (Vasilyeva and Gorbunova 1986). Since the higher polysulfides



dissociate stepwise, the thermodynamic parameters of the vaporization were obtained not only for starting, but also for the intermediate polysulfides. The pressure equations, enthalpy and entropy for these polysulfides (except Dy) are given in table 9. The standard thermochemical data of the dissociation reactions could not be calculated due to a lack of desired thermal functions for the intermediates involved in the high-temperature cycles. As the data of table 9 suggest, the vapor pressure of the  $RS_2$  and  $RS_{1.90}$  compounds increases going from La to Nd. The same dependence has been found for the  $RS_{1.85}$  line with  $R = Nd, Gd$  and  $Er$  (Vasilyeva and Gorbunova 1986).

One paper (Gingerich et al. 1972) describes the mass-spectroscopic determination of the heats of atomization of the  $CeS_2(g)$ ,  $Ce_2S(g)$ ,  $Ce_2S_2(g)$  and  $Ce_2S_3(g)$  molecules. In the study, gas-phase reactions over  $Au-Ce-CeS-BN-C$  mixtures were investigated by the Knudsen technique using a tungsten effusion cell. The enthalpy of the reaction  $CeS_2(g) + Ce(g) = 2CeS(g)$  was determined by the third-law method to be  $168.1 \pm 4.2$  kJ/mole. From this value and the literature data on the dissociation energy of  $CeS(g)$ , the heat of atomization of gaseous  $CeS_2$  was calculated to be  $\Delta_{atom}H_0^\circ = 961.4 \pm 50$  kJ/mole.

*Final remark.* Even with all these data, it is felt that the database of basic thermodynamic properties for the lanthanide polysulfides remains incomplete, especially for the nonstoichiometric compounds.

## 9. Chemical bonding

The subject of chemical bonding and stability of polysulfides arose from the very first study (Biltz 1908), where their dissolution in unoxidizing acids was found to fall out of line for the classical salts due to the appearance of sulfur. It took many years to accumulate the different types of data necessary to understand, to some degree of certainty, the chemical bonding in the polysulfides. Up to now this phenomenon has not been explained properly.

At first, the ionic model seemed to be adequate for describing the structures and properties of the disulfides. Trivalent metals were manifested in the compounds, except in  $YbS_2$  where  $Yb^{2+}$  occurs. The compounds had high symmetry, and melted at high temperatures (Flahaut et al. 1959). To these arguments the following facts, borne out by the ionic model, were added: a high acceptor ability of sulfur building a stable  $s^2p^6$  configuration (Samsonov and Radzikovskaya 1961), and high effective charges observed on the atoms of the  $LaS_2$  compound according to Raman spectroscopy (Golovin et al. 1975). The thermal stability (Ring and Tecotzky 1964), and the compressibility of sulfur ions under pressure (Webb and Hall 1970) in the series of lanthanide polysulfides has also been explained by means of a set of ionic radii. However, structural study of  $LaS_2$  (Dugué et al. 1978) allows this compound to be related to compounds of Flahaut's structural systematics (Flahaut 1976). Due to this, more complicated bonding should be typical of the lanthanide disulfides. Besides, following the crystallochemical formula  $(RS)^+(S_2)^{2-}$  the polysulfides are Mooser-Pearson phases and, therefore, they

are expected to be semiconductors without specific contacts between the metal atoms (Pearson 1977). Indeed, the semiconducting character of the La, Pr, and Nd polysulfides was confirmed experimentally by Bucher et al. (1975). That the covalence contribution increases along the series of  $RS \rightarrow RS_{1.5} \rightarrow RS_2$  sulfides ( $R = \text{La, Pr and Sm}$ ) was shown by means of heat-capacity measurements (Bolgar et al. 1987a,b). Increasing covalence in the chemical bonding of the polysulfides was shown through Madelung energy calculation following the ionic model. The energy value for  $\text{PrS}_2$  was about 10% higher than that for the appropriate Pr oxide. An effect of electrostatic repulsion between the nearest cation neighbors along the  $b$ -axis was observed in  $\text{PrS}_2$ . This interaction seems to be a principal factor determining the structural stability of the disulfides (Yanagisawa and Kume 1986).

This is all true when the stoichiometric disulfides are considered. What happens to chemical bonding upon sulfur loss remains unknown. A possible solution of the problem appeared when the structures of  $\text{SmS}_{1.90}$  (Podberezskaya et al. 1999, Tamazyan et al. 2000b),  $\text{DyS}_{1.84}$  (Podberezskaya et al. 1998), and  $\text{DyS}_{1.76}$  (Tamazyan et al. 1994) were resolved. Formally, the chemical bonding may be characterized by the ionic formulas and by the interatomic distances in the structural series of the  $RS_2 \rightarrow RS_{1.90} \rightarrow RS_{1.84} \rightarrow RS_{1.76}$  compounds. These distances are compared with the known radii (metallic, ionic, covalent) taken from the Table of ionic radii in the ICSD databank (CRISTIN 1986). Considering the structures as alternating square nets,  $-(S_2)-R-S-S-R-(S_2)-$ , two types of distances, within each layer ( $-(S_2)-(S_2)-$ ;  $R-R$ ;  $S-S$ ;) and between the layers ( $R-S$ ;  $S-(S_2)$ ;  $S-S$ ), have been analyzed. In the sheet  $(R-S-S-R)$  or  $(RS)^+$  all the  $R-R$  and  $S-S$  distances are close to the sum of the appropriate metallic radii for  $R$  and ionic radii for  $S^{2-}$ , and the  $R-S^{2-}$  distances are close to the sum of the ionic radii of these elements. This means that the chemical bonding in this sheet is preferably ionic.

A dramatic change occurs in the arrangement of the  $(S_2)^{2-}$  layer of the nonstoichiometric polysulfides (see also sect. 7.3). In the disulfides the  $(S_2)^{2-}$  layer consists only of "normal"  $(S_2)^{2-}$  pairs with identical  $S-S$  distances,  $\sim 2.11-2.16 \text{ \AA}$ . In this case, the  $(S_2)^{2-}$  pair may be considered as a real ligand compensating the charge of two  $(RS)^+$  sheets. Based on the argument that the electronic density of the ligand is not affected by decreasing sulfur content in the nonstoichiometric polysulfides, a transformation of some  $(S_2)^{2-}$  pairs into isolated  $S^{2-}$  ions should be taken into account. Thus, two kinds of sulfur atoms, formally univalent and divalent, are present in the nonstoichiometric polysulfides. However, such a description seems to be too simplified. Indeed, according to structural studies of  $\text{DyS}_{1.84}$  three types of  $S-S$  distances were recognized. The shortest distances,  $< 2 \text{ \AA}$ , are for the  $S(13)-S(15)$  and  $S(16)-S(15)$  pairs if these positions are statistically disordered; normal distances,  $\sim 2.16 \text{ \AA}$ , occur for the covalently bonded  $S(12)-S(12')$  and  $S(10)-S(14)$  pairs; the remaining  $(S_2)^{2-}-(S_2)^{2-}$  distances are between 2 and  $3.6 \text{ \AA}$ , that is, longer than the sum of the covalent radii but shorter than that of the ionic radii. If the  $S(15)$  and  $S(16)$  positions are filled, this would lead to sulfur atomic shifts in the direction indicated by arrows in fig. 6, and to the occurrence of  $-(S_3)^{2-}$  and  $-(S_4)^{2-}$  sulfur chains. In the opinion of Podberezskaya et al. (1999), in an S-deficient layer the chemical bonding is realized

by a cooperative interaction of the covalently and ionic-covalently bonded  $(S_2)^{2-}$  pairs. The average distances between the rearranged  $(S_2)^{2-}$  layer and  $(RS)^+$  sheets decrease, which indicates some increase in the covalent contribution to the chemical bonding between these structural fragments going from stoichiometric to hypostoichiometric polysulfides.

## 10. Electronic structure

The present electronic-structure calculation is based on a linearized muffin-tin orbital method (Zhukov et al. 1990). As the structural model was taken the idealized structure of  $\alpha$ - $LaS_2$  where a small distortion from the square form of the Flahaut pyramid foundations and the non-equivalent positions of the  $(S_2)^{2-}$  pairs were ignored. This simplification was assumed to have no noticeable effect on the energy-band structure calculated. Figure 8

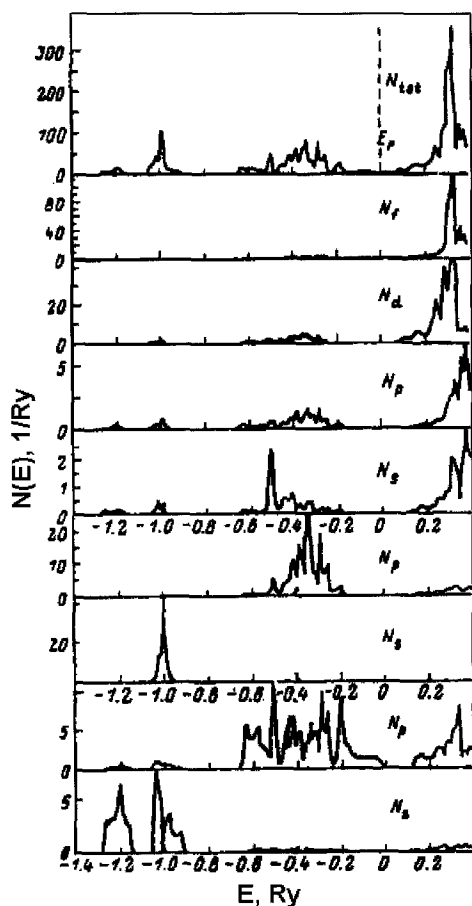


Fig. 8. Total ( $N_{tot}$ ) and partial density states calculated for  $LaS_2$ .

shows the band structure of  $\text{LaS}_2$ . According to the chemical formula,  $(\text{LaS})^+(\text{S}_2)^{2-}$ , the most prominent feature in this electron-band structure is the presence of the  $(\text{S}_2)$  pair, resulting in the splitting of all energy zones. Due to the strong S–S bond in the pair, its bonding ( $\sigma, \pi$ ) and antibonding ( $\sigma^*, \pi^*$ ) orbitals lie lower and higher, respectively, than the atomic orbitals of sulfur from the  $(\text{LaS})^+$  sheets. The lowest band with the sulfur s orbital consists from three peaks of the s state of both sulfur species. In the p band the 2p atomic orbitals of sulfur from the sheet are characterized by noticeable impurities of the La p and d states. The sulfur pair forms five p zones with the upper zone on an antibonding orbital. After the fifth zone a gap occurs since the sixth antibonding zone, being pushed upward, lies above the Fermi level. The conduction zone is formed on 60–80% from the p orbital of sulfur pairs with an impurity of the La 5d states. This hybridization indicates some participation of the La 5d states in the chemical bonding of the disulfide. The total number of electrons in the valence band is 10, and it is fully occupied: of 6 valence electrons from two La atoms, 4 electrons go to sulfur in the sheet and two are transmitted to the  $(\text{S}_2)$  pair. This explains the occurrence of a semiconducting gap at the Fermi level. The width of the gap was calculated to be 0.95 eV, and it was characterized as an indirect band gap between the top of the valence band and the bottom of the conduction band ( $\Gamma$ –R or R–X or M– $\Gamma$ ). These findings are supported by a variety of experimental determinations of the band gap.

## 11. Physical properties

The physical properties of the polysulfide are a very difficult topic, and at present our knowledge of this field is mainly qualitative and fragmentary. Nevertheless, the field is not only interesting but also of importance for polysulfides to be turned to practical use.

### 11.1. Electrical properties

Obtaining reliable data here depends on the quality of the test samples. The resistance data available for the polysulfides were taken from papers by Bucher et al. (1975), Loginova (1974), Shilkina et al. (1987a), Gorbunova et al. (1990) and Le Rolland et al. (1994), and collected in table 10 which clearly illustrates the preceding comment. According to the magnitudes, the polysulfides, even the nonstoichiometric ones, are generally interpreted

Table 10  
Electrical properties of the lanthanide polysulfides at room temperature

Formula	R	Sample	$R_{\Omega}$ ( $\Omega$ )	$\rho$ ( $\Omega$ cm)	References
$\text{RS}_2$	La, Pr, Nd	small crystals	very high		Bucher et al. (1975)
$\text{RS}_2$	La, Ce, Sm, Gd	powders, pressed		$10^6$ – $10^7$	Loginova (1974)
$\text{RS}_2$	Ce, Pr, Nd	crystals, good geometric forms		$10^7$ – $10^8$	Shilkina et al. (1987a)
$\text{RS}_{1.85}$	Gd, Er, Dy	crystals, good geometric forms		$10^9$ – $10^{11}$	Gorbunova et al. (1990)
$\text{LaS}_{2-x}$		powders, pressed	$\sim 10^{10}$		Le Rolland et al. (1994)

taken to be semiconductors (Bucher et al. 1975, Loginova 1974, Vasilyeva 1988). It is further argued that the nonstoichiometry of  $RS_{2-x}$  affects neither the charge of the metal nor the total charge of the  $(S_2)^{2-}$  ligand. No experiments have been performed to explain the conductivity mechanism in the compounds. The polaron conductivity mechanism observed for  $\gamma$ - $LaS_2$  by Le Rolland et al. (1994) could hardly be extended to other polysulfides, as this phase had charged sulfur defects.

### 11.2. Magnetic properties

Numerous magnetic measurements of powders have been carried out to characterize the valence of the lanthanide atom in the polysulfides through their magnetic behavior (Klemm et al. 1930, Domange et al. 1959, Flahaut and Guittard 1956b, Flahaut et al. 1959, Jarembash and Eliseev 1975, Samsonov and Drozdova 1972, Bucher et al. 1975, Yanagisawa and Kume 1986, Le Rolland et al. 1994). Because of the differing quality of the samples, there is a discrepancy between the experimental and expected values. However, this went unrecognized.  $LaS_2$  was found to be diamagnetic, while other polysulfides showed paramagnetic behavior. A slight Van Vleck paramagnetism for  $PrS_2$  and a Néel temperature  $T_N = 2.2$  K for  $NdS_2$  were determined by Bucher et al. (1975). For the  $LaS_2$  polymorphs the magnetic properties have been studied in more detail (Le Rolland et al. 1994). Unlike the ordered  $\alpha$  and  $\beta$  phases, which were diamagnetic at all temperatures,  $\gamma$ - $LaS_2$ , a new tetragonal polymorph with a spatially averaged disordered structure, was slightly paramagnetic at room temperature and showed evidence of antiferromagnetic ordering below 50 K. This behavior was explained as being due to the presence of paramagnetic  $S^-$  defects and rapid S–S-bond switching in the S–S basal planes.

Detailed measurements of the magnetic susceptibility and remanent magnetization between 1.5 K and 100 K in fields of  $10^{-2}$ – $10^2$  Oe have been carried out with the most optimal crystals of  $\alpha$ - $CeS_2$  and  $\alpha$ - $NdS_2$  (Klimenko et al. 1991a,b). The magnetic susceptibility of  $\alpha$ - $CeS_2$  obeys a Curie–Weiss law with an anisotropic effective magnetic moment and Curie–Weiss temperatures:  $P = 2.1\mu_B$ ,  $\theta = +7.8$  K along the  $b$ -axis; and  $P = 1.5\mu_B$ ,  $\theta = -0.8$  K perpendicular to the  $b$ -axis. No anisotropy was observed in the  $ac$  plane. A complicated magnetic behavior was observed for  $\alpha$ - $CeS_2$  (strong dependence of dc susceptibility on the thermomagnetic prehistory, cooling rate and applied field, remanent and memory phenomena) in low fields (0.1–100 Oe) below  $T_N$  (Klimenko et al. 1991a). Magnetization curves at 4.2 K show a sharp metamagnetic transition at  $H_c = 5$  kOe for a field along  $b$  and a linear dependence  $M(H)$  up to 30 kOe for the perpendicular direction. Neutron scattering experiments were performed and calculated magnetic neutron intensities were obtained for long-range antiferromagnetic ordering corresponding to a Shubnikov space group  $P2_1/c$ , with ordered magnetic moments of magnitude  $\mu_{Ce}^{3+} = 1.54\mu_B$  oriented along  $[100]$ . The temperature dependence of the largest magnetic peak 010/200/002 yields  $T_N = 7.2 \pm 0.3$  K, in reasonable agreement with the bulk magnetic measurements. Similar measurements were started on  $\alpha$ - $NdS_2$  and indicate a first-order magnetic phase transition at 1.85 K (Klimenko et al. 1991b). Neutron scattering experiments are now very desirable in order to accurately establish the magnetic ordering and the crystal-field splitting in the layered compound.

Low-temperature ESR spectroscopy in the range 110–190 K was used by Le Rolland et al. (1994) to characterize the metastable and disordered  $\alpha'$ -LaS<sub>2</sub> phase, which was slightly paramagnetic, due to paramagnetic S<sup>-</sup> defects. A single sharp resonance with  $g=2$  was observed at 190 K, corresponding to an itinerant-electron signal. Below 170 K this is joined by a broad signal at slightly lower field, which would correspond to localized paramagnetic centers. The structure of the disordered  $\alpha'$ -LaS<sub>2</sub> phase was shown to consist of local domains arranged in a disordered fashion. This finding may be valuable for understanding the dynamics of sulfur defects in the (S<sub>2</sub>)<sup>2-</sup> basal planes occurring in non-stoichiometric polysulfides.

Bucher et al. (1975) recorded the NMR spectra of PrS<sub>2</sub>. The spectra, which showed a rather complex feature: field-dependent linewidth and frequency, that was not analyzed further.

### 11.3. *Optical properties*

There is not much information available about the optical properties of the polysulfides. As a rule, IR and Raman spectroscopy have been used to study the phonon spectra and to identify the structural type of the compounds (Golovin et al. 1975, Le Rolland et al. 1991, 1994). But with powder samples, the technique was limited to identifying all the variety of structural types for the polysulfides. Working with crystals of good quality, direct structural identification was done for all polysulfide crystals available (Shilkina et al. 1987a, Kolesov and Vasilyeva 1992). It was shown that the structural fragment (S<sub>2</sub>)<sup>2-</sup> has a spectroscopic feature and, being a “fingerprint”, may be used in structural diagnostics of the polysulfides.

Some studies resulted in data on the electronic structure of the polysulfides. The effective charge,  $m^*$ , was determined for RS<sub>2</sub> with R=La, Ce, Sm, and Dy (Golovin et al. 1975).  $E_g$  was found for the polysulfides of all elements, except Eu, Yb, and Tm, from IR absorption spectra and from VIS and near-IR reflection spectra (Kolesov and Vasilyeva 1992). The  $E_g$  value, transparency range, and transmission coefficient were determined for NdS<sub>2</sub> and DyS<sub>1.84</sub> from IR transmission spectra (Gorbunova et al. 1990, Shilkina et al. 1987a). The major results of the above studies may be summarized as follows: both hypo- and stoichiometric polysulfides are semiconductors with practically identical  $E_g \approx 1.4$  eV derived from reflection spectra of the powdered samples, and 2–2.5 eV derived from transmission spectra of the LaS<sub>2</sub> and NdS<sub>2</sub> crystals of 10  $\mu\text{m}$  thickness. The values were interpreted as indirect and direct gaps, respectively, which is in good agreement with energy band calculations. The high transparency in the range from 2 up to 14 microns was observed for the NdS<sub>2</sub> and DyS<sub>1.84</sub> crystals of 10–100  $\mu\text{m}$  thickness. The intensities were 50% and 20%, respectively, relative to 70% calculated theoretically. The transparency decreased for the DyS<sub>1.84</sub> crystals because the structural perfection of these crystals was worse than that for NdS<sub>2.00</sub>. The origin of two selective absorption bands at 2.5 and 5  $\mu\text{m}$  was not studied. The transmission coefficient calculated from the spectra was  $n=2.24$  for both Nd and Dy polysulfides, which was in good agreement with  $n=2.2$  measured by an immersion technique.

#### 11.4. *Other properties*

An attempt to obtain information on crystal-field splitting of the energy levels in the Pr, Nd, Sm, and Er polysulfides was made by Tagaev et al. (1989a) using optical absorption spectroscopy and luminescence. The polysulfide crystals, being of high optical density, have not shown luminescence under a xenon lamp with an exciting power of 1 kW. The "crystal thickness" effect for Sm and Er polysulfides was in these cases essential in obtaining well-resolved spectra. Therefore, reliable crystal-field data were obtained only for  $\alpha$ -PrS<sub>2</sub> and  $\alpha$ -NdS<sub>2</sub>. Some observations, for example on two differently coordinated Er centers in ErS<sub>1.85</sub>, indicate a local structural nonuniformity of the hypostoichiometric polysulfide crystals. This was also detected by structural methods.

An absorption X-ray spectroscopic technique precluding the "thickness effect" was applied to study the R valence state and the  $f^n$ -electron configuration for Ce and Eu polysulfides (Efremova et al. 1976). The L<sub>III</sub> spectra showed no Ce(IV) in CeS<sub>2</sub>, but 23% Eu(II) with the  $f^7$  configuration was observed in the EuS<sub>1.90</sub> compound. The technique was suggested to be a very sensitive quantitative tool for determining impurity levels of ions with higher-valent states (Efremova et al. 1979).

*Final comment.* No applications of the polysulfides are known at present; however, one may expect future applications utilizing their specific magnetic, semiconducting and optical properties for the design of different types of functional materials (Kuznetsov et al. 1997).

## 12. Concluding remarks

This review has summarized the present (beginning in 1908) state of the art of lanthanide polysulfide chemistry. It is intended to provide a factual background and to intimate the most intriguing areas for chemists and physicists who wish to enter this area. The  $P$ - $T$ - $x$  phase diagrams, oriented crystallization, the fabrication of large isometric and high-quality crystals, electronic structure calculations, and peculiarities of physical properties seem to be the most appealing features of the field. While attempts have been made at some generalizations, there is need for additional systematic study. Such studies will undoubtedly further our understanding, not only of the chemistry and the materials science of the lanthanide polysulfides, but also of the chemistry of nonstoichiometric inorganic compounds in general.

## References

- Aloman, A., 1968, Rev. Chim. Român. **19**, 507.  
Ananth, K.P., P.J. Gielisse and T.J. Rockett, 1974, Mater. Res. Bull. **9**, 1167.  
Azizov, T.K., B.G. Tagiev and A. Guseinov, 1984, Elektricheskie i fotoelektricheskie svoistva monokristallov GdS<sub>x</sub>, Preprint 117 (Azerbadzainskaya Akademiya Nauk, Institut Fiziki, Baku) pp. 1-5.  
Bach, H., 1986, unpublished data.  
Bachturova, N.F., and L.S. Chuchalina, 1982, Zh. Anal. Khim. **37**, 1217.

- Balashvskii, G.F., and V.K. Valtzev, 1983, *Zh. Neorg. Khim.* **28**, 1677.
- Belaya, S.V., N.V. Podberezhskaya, N.V. Pervuchina, S.A. Magarill, I.G. Vasilyeva and S.V. Borisov, 2000, *Russ. Chem. Sustainable Dev.* **8**, 103 [Khim. Ustoichivogo Rasv. **8**, 31].
- Bénazeth, S., M. Guittard and J. Flahaut, 1981, *J. Solid State Chem.* **37**, 1981.
- Bénazeth, S., D. Carré and P. Laurelle, 1982, *Acta Crystallogr. B* **38**, 33.
- Beresovskii, G.A., I.G. Vasilyeva, L.G. Gorbunova, I.E. Paukov and A.B. Tagaev, 1988, *Zh. Fiz. Khim. SSSR* **62**, 1677.
- Beresovskii, G.A., V.N. Naumov, I.E. Paukov, A.B. Tagaev, I.G. Vasilyeva and T.Yu. Shilkina, 1989, in: *Aktualnie Voprosi Fiziki i Khimii Soedinenii Redkozemelnych Elementov (Institut Fiziki, Sibirskoe Otdelenie Akademii Nauk, Krasnoyarsk)* pp. 56–57.
- Biltz, W., 1908, *Berichte* **41**, 3341.
- Biltz, W., 1911, *Z. Anorg. Allg. Chem.* **71**, 427.
- Bokii, G.B., 1964, *Kristalokhimiya i Structura Arsenidov, Sulfidov, Arsenosulfidov i ich Analogov (Sibirskoe Otdelenie Akademii Nauk SSSR, Novosibirsk)* 187 pp.
- Bolgar, A.S., and S.P. Gordienko, 1990, in: *Fizika, Khimia Redkozemelnych Poluprovodnikov*, ed. K.E. Mironov (Nauka, Sibirskoe Otdelenie Akademia Nauk, Novosibirsk) p. 45.
- Bolgar, A.S., A.I. Kriklya and L.N. Kartuzova, 1987a, *Poroshk. Metall. Kiev N 2*, 90.
- Bolgar, A.S., A.I. Kriklya and L.N. Kartuzova, 1987b, *Teplofiz. Vys. Temp. B* **25**, 919.
- Borisov, S.V., N.V. Podberezhskaya, N.V. Koshemyak and V.I. Alekseev, 1979, in: *Proc. II Vsesoyuznoi Konf. po Fizike, Khimii Redkozemelnych Poluprovodnikov, Leningrad, 1979 (Akademiya Nauk SSSR, Leningrad)* pp. 69–71.
- Böttcher, P., Th. Doert, H. Arnold and R. Tamazyan, 2000, *Z. Kristallogr.* **215**, 246.
- Bucher, E., K. Andres, F.J. di Salvo, J.P. Maita, A.C. Gossard, A.S. Cooper and G.W. Hull Jr, 1975, *Phys. Rev. B* **11**, 500.
- Burns, J., D. Damien and R.G. Haire, 1979, *Acta Crystallogr. B* **35**, 143.
- Chen, J.H., and P.K. Dorhout, 1995, *J. Solid State Chem.* **117**, 318.
- CRISTIN, 1986, *Table of ionic radii from ICSD (CRISTIN) Data Bank, FIZ Karlsruhe (Inst. für Anorg. Chem. der Universität, Bonn)*.
- Domange, L., J. Flahaut and M. Guittard, 1959, *C.R. Acad. Sci. Paris C* **249**, 697.
- Dugué, G., D. Carré and M. Guittard, 1978, *Acta Crystallogr. B* **34**, 403.
- Efremova, N.N., L.D. Finkelshtein, N.S. Samsonova and S.A. Nemmonov, 1976, *Isv. Akad. Nauk SSSR, Ser. Fiz.* **40**, 420.
- Efremova, N.N., L.D. Finkelshtein, N.I. Lobachevskaya, V.G. Bamburov, N.I. Ignat'eva and M.I. Simonova, 1979, in: *Tugoplavkie Soedineniya Redkozemelnych Metallov (Nauka, Sibirskoe Otdelenie, Novosibirsk)* pp. 177–180.
- Eliseev, A.A., and A.A. Grizik, 1977, in: *Redkozemelnye Poluprovodniki (Nauka, Leningradskoe Otdelenie, Leningrad)* pp. 146–177.
- Eliseev, A.A., and S.I. Uspenskaya, 1972a, in: *Sbornik Trudov, Khimiya i Khimicheskaya Technologia (Institut Tonkoi Khimicheskoi Technologii, Moscow)* p. 333.
- Eliseev, A.A., and S.I. Uspenskaya, 1972b, *Zh. Neorg. Khim.* **17**, 2569.
- Eliseev, A.A., S.I. Uspenskaya and A.A. Fedorov, 1971, *Russ. J. Inorg. Chem* **16**, 768 [*Zh. Neorg. Khim.* **16**, 1485].
- Eliseev, A.A., S.I. Uspenskaya and T. Kalganova, 1972, *Zh. Neorg. Khim.* **17**, 2340.
- Eliseev, A.A., G.M. Kuzmicheva, V.V. Evdokimova and V.I. Novokshanov, 1976, *Zh. Neorg. Khim.* **21**, 2900.
- Eliseev, A.A., G.M. Kuzmicheva and V.I. Jashnov, 1978, *Zh. Neorg. Khim.* **23**, 492.
- Eliseev, A.A., O.A. Sadovskaya and G.M. Kuzmicheva, 1981, *Zh. Vses. Khim. Ova im. D.I. Mendeleeva* **26**, 612.
- Finogenov, A.D., 1973, *Issledovanie termodinamicheskikh svoystv sulfidov of Ce grupi, Avtoreferat dissertation (Institut Stali i Splavov, Moscow)* p. 25.
- Flahaut, J., 1976, *Ann. Chem.* **1**, 27.
- Flahaut, J., 1979, in: *Handbook on the Physics and Chemistry of Rare Earths, Vol. 4*, eds K.A. Gschneidner Jr and L. Eyring (North-Holland, Amsterdam) ch. 31.
- Flahaut, J., and M. Guittard, 1956a, *C.R. Acad. Sci. Paris C* **243**, 1210.
- Flahaut, J., and M. Guittard, 1956b, *C.R. Acad. Sci. Paris C* **243**, 1419.
- Flahaut, J., and M. Guittard, 1957, *C.R. Acad. Sci. Paris C* **245**, 2291.
- Flahaut, J., and P. Laruelle, 1968, in: *Progress in Science and Technology of the Rare Earths 1968*,



- Vol. 3, ed. H. Reiss (Pergamon Press, Oxford) pp. 151–208.
- Flahaut, J., M. Guittard and M. Patrie, 1959, *Bull. Soc. Chem. France*, N 10/12, 1917.
- Gibner, Ya.I., and I.G. Vasilyeva, 1990, *Zavod. Lab.* **56**, 45.
- Gibner, Ya.I., and I.G. Vasilyeva, 1998, *J. Thermal Anal.* **53**, 151.
- Gingerich, L.A., C. Pupp and B.E. Campbell, 1972, *High. Temp. Sci.* **4**, 236.
- Golovin, Yu.M., K.I. Petrov, E.M. Loginova, A.A. Grizik and N.M. Ponomarev, 1975, *Zh. Neorg. Khim.* **20**, 283.
- Gorbunova, L.G., and I.G. Vasilyeva, 1985, *Izv. Sib. Otd. Akad. Nauk SSSR, Ser. Khim. Nauk* N 5, 49.
- Gorbunova, L.G., and I.G. Vasilyeva, 1986, *Izv. Sib. Otd. Akad. Nauk SSSR, Ser. Khim. Nauk* N 5, 77.
- Gorbunova, L.G., Ya.I. Gibner and I.G. Vasilyeva, 1990, in: *Fizika i Khimiya. Redkozemelnich Poluprovodnikov, 1987* (Nauka, Sibirskoe Otdelenie Akademii Nauk SSSR, Novosibirsk) pp. 123–128.
- Gordienko, S.P., and G.Sh. Fenochka, 1979, *Termodinamika Soedinenii Lanthanidov* (Naukova dumka, Kiev) sect. 9.
- Grizik, A.A., E.M. Loginova and N.M. Ponomarev, 1970, in: *Redkozemelnie Metalli i Soedineniya* (Naukova dumka, Kiev) pp. 196–203.
- Grupe, M., and W. Urland, 1991, *J. Less-Common Met.* **170**, 271.
- Jarembash, E.I., and A.A. Eliseev, 1975, *Chalkogenidi Redkozemelnich Elementov* (Nauka, Moscow) pp. 5–14.
- Kim, S.-J., and H.-J. Oh, 1995, *Bull. Kor. Chem. Soc.* **16**, 515.
- Klemm, W., and J. Rockstroh, 1927, *Z. Anorg. Allg. Chem.* **163**, 253.
- Klemm, W., R. Meisel, H. Urlich and H.U. v. Vogel, 1930, *Z. Anorg. Allg. Chem.* **190**, 123.
- Klimenko, A.G., S.M. Ishikaev, A.B. Tageev, I.G. Vasilyeva, M.M. Karpenko, P. Fisher, A. Furrer and U. Staub, 1991a, *Neutronen-Streuung*, Progress Report LNS-154, February 1991 (Laboratorium für Neutronenstrahlung, Eidg. Technische Hochschule, Zürich) pp. 56–57.
- Klimenko, A.G., S.M. Ishikaev, A.B. Tageev, I.G. Vasilyeva, M.M. Karpenko, P. Fisher, A. Furrer and U. Staub, 1991b, *J. Appl. Phys.* **69**, 4630.
- Kolesov, B.A., and I.G. Vasilyeva, 1992, *Mater. Res. Bull.* **27**, 775.
- Kriklya, A.I., 1986, *Termodinamicheskie Svoistva Redkozemelnich Metallov*, Avtoreferat dissertation (Institut Problem Materialovedeniya, Kiev) pp. 1–20.
- Kuzmicheva, G.M., 1994, *Zh. Neorg. Khim.* **39**, 412.
- Kuzmicheva, G.M., A.A. Eliseev and S.U. Chalina, 1981, *Zh. Neorg. Khim.* **26**, 1480.
- Kuzmicheva, G.M., A.A. Eliseev, I.G. Orlova and B.V. Muchin, 1983, *Zh. Neorg. Khim.* **28**, 1337.
- Kuznetsov, F.A., P. Klevtsov, S.V. Borisov, A. Pavluk, Ya. Vasiliev, L. Kozeeva, A. Kamarzin, V. Sokolov and I. Vasilyeva, 1997, *New oxide and sulfide materials*, in: *Proc. Int. Symp. on Laser and Nonlinear Optical Materials*, Singapore, 1997, ed. T. Sasaki (Data Storage Institute, Singapore) pp. 211–217.
- Latimer, V.M., 1954, *Okislitelnie Sostoyania Elementov, ich Potentiali* (Inostrannaya Literatura, Moscow) p. 135.
- Lazarev, V.B., J.H. Greenberg and B.A. Popovkin, 1978, in: *Current Topics in Materials Science*, Vol. 1, ed. E. Kaldis (North-Holland, Amsterdam) pp. 657–695.
- Le Rolland, B., P.F. McMillan and P. Colombet, 1991, *C.R. Acad. Sci. Paris* **312**, 217.
- Le Rolland, B., P. Moline, P. Colombet and P.F. McMillan, 1994, *J. Solid State Chem.* **113**, 312.
- Lee, S., and B.J. Foran, 1994, *J. Am. Chem. Soc.* **116**, 154.
- Lee, S., and B.J. Foran, 1996, *J. Am. Chem. Soc.* **118**, 9139.
- Loginova, E.M., 1974, *Fisiko-khimicheskie issledovaniya redkozemelnich metallov zerievoi gruppi v oblasti  $Me_2S_3$ – $MeS_2$* , Avtoreferat dissertation (Nauchni Proektni Institut Redkometalnoi Promishlennosti, Moscow) pp. 1–25.
- Loginova, E.M., A.A. Grizik, N.M. Ponomarev and A.A. Eliseev, 1975, *Izv. Akad. Nauk SSSR, Neorg. Mater.* **11**, 749.
- Magarill, C.A., N.V. Podberezskaya, N.V. Peruvuchina, E.N. Epatova, T.S. Yudanov and S.V. Borisov, 1992, *Kristallostrukturnie charakteristiki polychalkogenidov redkozemelnich elementov*, Preprint No. 92-05 (Institut Neorganicheskoi Khimii, Sibirskoe Otdelenie Akademii Nauk, Novosibirsk) pp. 5–61.
- Merrill, L., 1982, *J. Phys. Chem. Ref. Data* **11**, 1005.
- Mills, K.G., 1974, *Thermodynamic Data for Inorganic Sulfides, Selenides and Tellurides* (Butterworth, London) pp. 120–129.
- Mironov, K.E., and A.A. Kamarzin, 1979, in: *Tugoplavkie Soedineniya Redkozemelnich Metallov*

- (Nauka, Sibirskoe Otdelenie Akademii Nauk SSSR, Novosibirsk) pp. 161–167.
- Mustafaev, F.M., T.Ch. Azizov, A.S. Abbasov and I.Ya. Alev, 1977, Termodinamicheskie svoystva redkosemelnich elementov, Preprint N 50 (Azərbayca Akademiyası, Institut Fiziki, Bakı) pp. 3–15.
- Park, S.-M., S.-J. Park and S.-J. Kim, 1998, *J. Solid State Chem.* **140**, 300.
- Pearson, W.B., 1977, *The Crystal Chemistry and Physics of Metals and Alloys*, Part I (Mir, Moscow) ch. 5.
- Picon, M., and M. Patrie, 1956, *C.R. Acad. Sci. Paris C* **243**, 1769.
- Plambeck-Fischer, P., W. Abriel and W. Urland, 1989, *J. Solid State Chem.* **78**, 164.
- Podberezhskaya, N.V., S.A. Magarill, N.V. Pervuchina, I.G. Vasilyeva and S.V. Borisov, 1996, *J. Struct. Chem.* **37**, 963 [*Zh. Strukt. Khim. Russ.* **37**, 1140].
- Podberezhskaya, N.V., I.G. Vasilyeva, S.V. Borisov, S.A. Magarill and N.V. Pervuchina, 1997, in: *Proc. III Mezhdunarodnoi Konf. Kristallov: Rost, Svoystva, Realnaya Struktura, Primenenie, Aleksandrov, 1997* (Vserossiiskii Nauchnyi Issledovatel'skii Institut Sintesa, Mineralogicheskaya Serya, Aleksandrov) pp. 453–465.
- Podberezhskaya, N.V., D.U. Naumov, I.G. Vasilyeva, N.V. Pervuchina, S.A. Magarill and S.V. Borisov, 1998, *Zh. Strukt. Khim. Russ.* **39**, 872.
- Podberezhskaya, N.V., N.V. Pervuchina, I.G. Vasilyeva, S.A. Magarill and S.V. Borisov, 1999, *Zh. Strukt. Khim. Russ.* **40**, 520.
- Ponomarev, N.M., and Zh.A. Puchlii, 1990, in: *Fizika, Khimiya Redkosemelnich Poluprovodnikov*, ed. K.E. Mironov (Nauka, Sibirskoe Otdelenie Akademii Nauk, Novosibirsk) pp. 92–101.
- Porcher, P., and P. Caro, 1983, *J. Less-Common Met.* **93**(Part 1), 151.
- Prokofiev, A.V., 1993, *Virashivanie kristalov sulfidov i selenidov redkosemelnich elementov*, Avtoreferat dissertation (St. Petersburg Gosudarstvenni Universitat) pp. 1–15.
- Radzikovskaya, S.V., and V.I. Marchenko, 1966, *Sulfidi Redkosemelnich Metallov* (Akademiya Nauk Ukrainskoi SSR, Institut Problem Materialovedenia, Kiev) sect. 1, p. 111.
- Radzikovskaya, S.V., and G.V. Samsonov, 1961, *Dokl. Akad. Nauk Ukr. SSR* **2**, 74.
- Rau, H., 1978, *J. Phys. Chem. Solids* **38**, 879.
- Ring, S., and M. Tecotzky, 1964, *Inorg. Chem.* **3**, 182.
- Sallavaud, G., and P. Rene, 1970, *C.R. Acad. Sci. Paris C* **271**, 1460.
- Samsonov, G.V., and S.V. Drozdova, 1972, *Sulfidi Redkosemelnich Metallov* (Metallurgia, Moscow) pp. 92–94.
- Samsonov, G.V., and S.V. Radzikovskaya, 1961, *Usp. Khim.* **30**, 60.
- Scheel, H., 1974, *J. Cryst. Growth* **24–25**, 669.
- Schienbein, K., G. Mair and K. Reichelt, 1978, *Thin Solid Films* **52**, L5.
- Shilkina, T.Yu., and I.G. Vasilyeva, 1984, *Izv. Sib. Otd. Akad. Nauk SSSR, Ser. Khim. Nauk N 3*, 35.
- Shilkina, T.Yu., and I.G. Vasilyeva, 1986, *Izv. Sib. Otd. Akad. Nauk SSSR, Ser. Khim. Nauk N 5*, 73.
- Shilkina, T.Yu., L.G. Gorbunova and I.G. Vasilyeva, 1987a, *Izv. Akad. Nauk, Neorg. Mater.* **23**, 1103.
- Shilkina, T.Yu., I.G. Vasilyeva and Yu.G. Stenin, 1987b, *Termodinamicheskie issledovanie polisulfidov Nd i Dy*, in: *Trudi IV Vses. Konf. Fizika i Khimiya Redkosemelnich Poluprovodnikov*, Novosibirsk, 1987 (Akademiya Nauk SSSR, Sibirskoe Otdelenie, Novosibirsk) p. 119.
- Shilkina, T.Yu., G.A. Beresovskii and I.G. Vasilyeva, 1990, *Termodinamicheskie issledovanie polisulfidov disprosiya*, in: *Trudi V Vses. Konf. Fizike i Khimii Redkosemelnich Poluprovodnikov*, 29–31 May, 1990, Saratov (Gosudarstvenni Universitat, Saratov) p. 11.
- Strotzer, E., W. Bieltz and K. Meisel, 1941, *Z. Anorg. Allg. Chem.* **247**, 415.
- Stuve, J.M., 1981, *Inf. Circ. Bur. Mines US*, No. 8853, p. 161.
- Tagaev, A., V.N. Naumov, I.G. Vasilyeva and I.E. Paukov, 1989b, *Zh. Fiz. Khim.* **63**, 2266.
- Tagaev, A.B., V.N. Naumov, G.A. Beresovskii, I.E. Paukov, I.G. Vasilyeva and L.E. Reznik, 1989a, *Termodinamicheskie i spektralnie karakteristiki disulfidov redkosemelnich metallov cerievoi gruppi*, Preprint N 89-11 (Institut Neorganicheskoi Khimi, Novosibirsk) pp. 3–43.
- Takashi, T., 1973, *Bull. Tokyo Inst. Technol.* No. 117, 41.
- Tamazyan, R., H. Arnold, V.N. Molchanov, G.M. Kuzmicheva and I.G. Vasilyeva, 2000a, *Z. Kristallogr.* **215**, 272.
- Tamazyan, R., H. Arnold, V.N. Molchanov, G.M. Kuzmicheva and I.G. Vasilyeva, 2000b, *Z. Kristallogr.* **215**, 346.
- Tamazyan, R.A., V.N. Molchanov, G.M. Kuzmicheva and I.G. Vasilyeva, 1994, *Zh. Neorg. Khim. Russ.* **39**, 417.

- Taylor, P., 1980, *Am. Mineral.* **65**, 1026.
- Teske, C.L., 1974, *Z. Naturforsch.* **29**, 16.
- Urland, W., P. Plambeck-Fischer and M. Grupe, 1989, *Z. Naturforsch. B* **44**, 261.
- Uspenskaya, S.I., 1972, in: *Rost kristallov*, Vol. 9 (Nauka, Moscow) p. 225.
- Uspenskaya, S.I., and A.A. Eliseev, 1970, *Izv. Vyssh. Uchebn. Zaved., Ser. Khim. Khim. Technol.* **13**, 620.
- Uspenskaya, S.I., and A.A. Eliseev, 1972, *Russ. J. Inorg. Chem.* **17**, 1344 [*Zh. Neorg. Khim.* **17**, 2569].
- Vasilyeva, I.G., 1985, *Izv. Akad. Nauk, Neorg. Mater.* **6**, 1043.
- Vasilyeva, I.G., 1988, in: *Proc. VII Vses. Conf. po Khimii, Fizike i Technicheskomu Primeneniyu Khalkogenidov, Uzgorod*, 1988, part II (Akadem. Nauk, SSSR, Uzgorod) p. 140.
- Vasilyeva, I.G., and S.V. Belaya, 1999, *J. Solid State Chem.* **146**, 211.
- Vasilyeva, I.G., and E.I. Belyaeva, 1999, *J. Solid State Chem.* **142**, 261.
- Vasilyeva, I.G., and Ya.I. Gibner, 1987, in: *Proc. IV Vses. Konf. po Fizike i Khimii Redkozemelnich Poluprovodnikov, Novosibirsk*, 1987 (Akad. Nauk SSSR) p. 73.
- Vasilyeva, I.G., and L.G. Gorbunova, 1986, *Izv. Akad. Nauk SSSR, Neorg. Mater.* **22**, 897.
- Vasilyeva, I.G., and L.N. Kurochkina, 1981, *Zh. Neorg. Khim.* **26**, 1872.
- Vasilyeva, I.G., T.Yu. Shilkina and N.V. Podberezskaya, 1985, *Polisulfid Dy: rost kristallov, struktura, svoistva*, in: *Proc. VI Vses. Konf. po Rostu Cristalov, Zachkadsor*, 1985, Vol. II (Akad. Nauk Armyansk. SSR, Erevan) pp. 35–36.
- Vasilyeva, I.G., B.M. Ayupov, A.A. Vlasov, V.V. Malakhov, P. Macaudiere and P. Maestro, 1998a, *J. Alloys Compounds* **268**, 72.
- Vasilyeva, I.G., E.I. Belyaeva and Ya.I. Gibner, 1998b, *J. Thermal Anal.* **52**, 403.
- Vasilyeva, I.G., T.Yu. Shilkina, N.V. Podberezskaya and D.Yu. Naumov, 1999, *Russ. J. Inorg. Chem.* **44**, 153 [*Zh. Neorg. Khim.* **44**, 193].
- Vaughan, D.J., and J.R. Craig, 1978, *Mineral Chemistry of Metal Sulfides* (Cambridge University Press, London) sect. 7.
- Vlach, K.C., and Y.A. Chang, 1981, *Inf. Circ. Bur. Mines US Dep. Inter*, No. 8853, pp. 385–406.
- Volinetz, F.K., G.N. Dronova, N.V. Vekshina and I.A. Mironov, 1977, *Izv. Akad. Nauk, Ser. Neorg. Mater.* **13**, 526.
- Webb, A., and T. Hall, 1970, *Inorg. Chem.* **9**, 1084.
- Wentorf, R.H., 1963, in: *Physics and Chemistry of High Pressure* (Society of Chemical Industry, London) pp. 185–190.
- Wichelhaus, W., 1977, in: *Proc. 17 Hauptversamml. Ges. Dtsch. Chem., München (Frankfurt/M.)* p. 76.
- Yanagisawa, Y., and S. Kume, 1973, *Mater. Res. Bull.* **8**, 1241.
- Yanagisawa, Y., and S. Kume, 1986, *Mater. Res. Bull.* **21**, 379.
- Yanagisawa, Y., F. Kanamuro and S. Kume, 1979, *Acta Crystallogr. B* **35**, 137.
- Zhukov, V.P., N.I. Medvedeva, I.G. Vasilyeva and Ya.I. Gubnanov, 1990, *Fiz. Tverd. Tela Leningrad* **32**, 3676.
- Ziemann, H., and W. Buess, 1979, *Z. Anorg. Allgm. Chem.* **455**, 69.

## Chapter 210

# HALF-SANDWICH TETRAPYRROLE COMPLEXES OF RARE EARTHS AND ACTINIDES

Dennis K.P. NG

*Department of Chemistry, The Chinese University of Hong Kong, Shatin, N.T., Hong Kong, China*

Jianzhuang JIANG

*Department of Chemistry, Shandong University, Jinan 250 100, China*

Kuninobu KASUGA

*Department of Material Science, Faculty of Science and Engineering, Shimane University, Matsue 690-8504, Japan*

Kenichi MACHIDA

*Collaborative Research Center for Advanced Science and Technology, Osaka University, 2-1 Yamadaoka, Suita, Osaka 565-0871, Japan*

---

### Contents

Symbols	611	2.4. Electrochemical properties	639
1. Introduction	612	2.5. Photophysical properties	643
2. Half-sandwich complexes of porphyrins	613	3. Half-sandwich complexes of phthalocyanines	645
2.1. Synthesis and reactivity	613	3.1. Synthesis and reactivity	645
2.2. Structure	623	3.2. Structure	647
2.3. Spectroscopic properties	626	3.3. Spectroscopic and electrochemical properties	648
2.3.1. <sup>1</sup> H NMR spectra	626	4. Outlook	650
2.3.2. Electronic absorption spectra	628	References	651
2.3.3. ESR spectra	636		
2.3.4. Other spectroscopic studies	638		

---

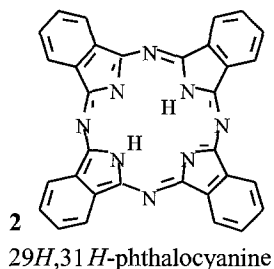
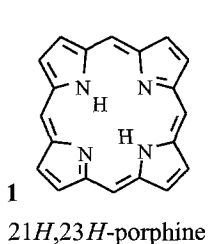
### Symbols

acac	acetylacetonate	HTPP	dianion of 5-(4-hydroxyphenyl)-10,15,20-triphenylporphyrin
CD	circular dichroism	Nc	dianion of naphthalocyanine
DMF	<i>N,N</i> -dimethylformamide	Nc''	dianion of octasubstituted 2,3-naphthalocyanine
DMSO	dimethylsulfoxide	OAc	acetate
HTMPP	dianion of 5-(4-hydroxyphenyl)-10,15,20-tris(4-methoxyphenyl)porphyrin		

OBTPP	dianion of $\beta$ -octabromo- <i>meso</i> -tetraphenylporphyrin	TFPP	dianion of <i>meso</i> -tetrakis(3-fluorophenyl)-porphyrin
OCTPP	dianion of $\beta$ -octachloro- <i>meso</i> -tetraphenylporphyrin	THF	tetrahydrofuran
OEP	dianion of $\beta$ -octaethylporphyrin	tmhd	2,2,6,6-tetramethyl-3,5-heptanedionate
Pc	dianion of phthalocyanine	TMP	dianion of <i>meso</i> -tetramesitylporphyrin
Pc''	dianion of octasubstituted phthalocyanine	TMPP	dianion of <i>meso</i> -tetrakis(4-methoxyphenyl)porphyrin
Por	general porphyrinato dianion	TMPyP	<i>meso</i> -tetrakis(4- <i>N</i> -methylpyridinium)-porphyrinate
R	rare earth	TmTP	dianion of <i>meso</i> -tetra( <i>m</i> -tolyl)porphyrin
SCE	saturated calomel electrode	TNTBP	dianion of <i>meso</i> -tetra(1-naphthyl)-tetrabenzoporphyrin
TBP	dianion of tetrabenzoporphyrin	ToCIPP	dianion of <i>meso</i> -tetrakis(2-chlorophenyl)-porphyrin
TBPP	dianion of <i>meso</i> -tetrakis(4- <i>tert</i> -butylphenyl)porphyrin	ToTP	dianion of <i>meso</i> -tetra( <i>o</i> -tolyl)porphyrin
TBTPP	dianion of $\beta$ -tetrabromo- <i>meso</i> -tetraphenylporphyrin	TpCIPP	dianion of <i>meso</i> -tetrakis(4-chlorophenyl)-porphyrin
TCB	1,2,4-trichlorobenzene	TPP	dianion of <i>meso</i> -tetraphenylporphyrin
TCTPP	dianion of $\beta$ -tetrachloro- <i>meso</i> -tetraphenylporphyrin	TPyP	dianion of <i>meso</i> -tetra(4-pyridyl)porphyrin
TDBPP	dianion of <i>meso</i> -tetrakis(3,5-di- <i>tert</i> -butylphenyl)porphyrin	TSPP	<i>meso</i> -tetrakis(4-sulfonatophenyl)-porphyrinate
TDCPP	dianion of <i>meso</i> -tetrakis(3,5-dichlorophenyl)porphyrin	TTP	dianion of <i>meso</i> -tetra( <i>p</i> -tolyl)porphyrin

## 1. Introduction

Tetrapyrrole derivatives such as porphyrins (e.g. **1**) and phthalocyanines (e.g. **2**) have aroused a widespread interest in various disciplines owing to their diverse and intriguing properties. Having a highly delocalized  $\pi$  system, these macrocyclic compounds exhibit a wide range of novel optical, electrical, magnetic, and spectroscopic properties. These characteristics together with their extraordinary stability render them useful in the fields of materials science, catalysis, biology, and medicine. The development in these areas has been well documented in the handbooks edited by Leznoff and Lever (1989–96), and by Kadish et al. (2000).



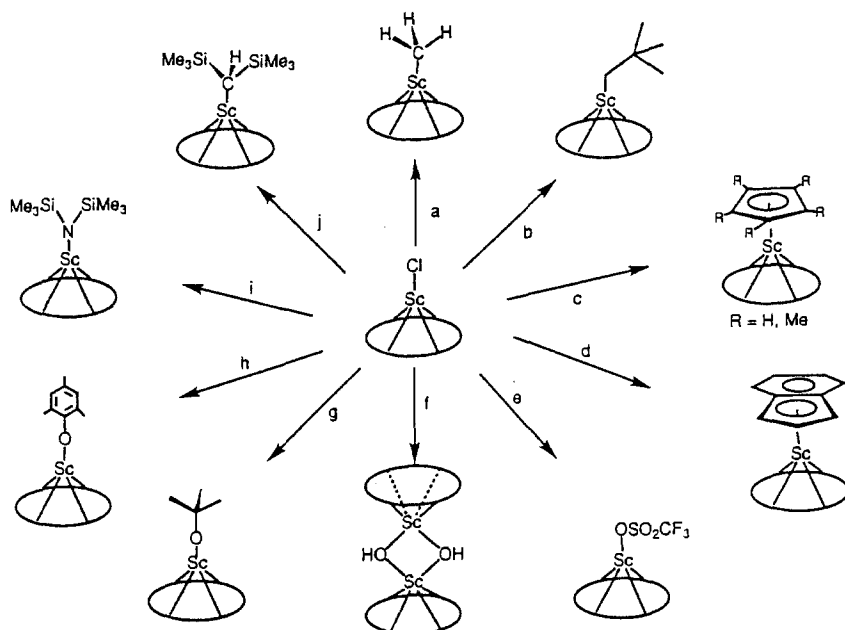
When these macrocycles are complexed with rare-earth and actinide ions through binding with the four nitrogen atoms in the core, the unique nature of the metal ions

is incorporated in the complexes, resulting in characteristic features. The first examples of this class of compounds, namely  $R(\text{Pc})_2$  ( $R = \text{Pr, Nd, Er, Lu}$ ), appeared in 1965 (Kirin et al. 1965); these are now well-known electrochromic materials. To date, a vast number of porphyrinato and phthalocyaninato complexes of virtually the whole series of rare earths and actinides is known. As these metal ions are normally larger than the core size of these macrocyclic ligands, the metal centers are situated out of the ring, forming either half-sandwich complexes with other uni- and/or bidentate ligands, or sandwich-type complexes in which the metal centers are sandwiched between the macrocycles. The former series of compounds can serve as potent and specific NMR shift reagents, and have also been used to probe the structures of proteins and other biological molecules (see below). They are also important precursors for the class of sandwich compounds which have found their promising role in materials science (Jiang et al. 1998a, 1999a, Buchler and Ng 2000). The bis(porphyrinato) rare-earth complexes  $R(\text{Por})_2$ , first reported by Buchler et al. (1983), have also been proposed as structural and spectroscopic models for the "special pair" found in the reaction center protein of photosynthetic bacteria. The purpose of this article is to provide a comprehensive and up-to-date review of the half-sandwich porphyrinato and phthalocyaninato complexes of rare earths and actinides. As the current status in the research of sandwich-type complexes of these tetrapyrrole derivatives has been extensively reviewed recently (Jiang et al. 1997a, 1998a, 1999a,b, Ng and Jiang 1997, Buchler and Ng 2000), they will not be included in this article and will only be mentioned in necessary. Rare-earth complexes of expanded porphyrins such as texaphyrins and sapphyrins have emerged as important derivatives which have found various biomedical applications. Since their chemistry and applications have also been summarized recently (Sessler et al. 1994, Sessler and Weghorn 1997, Jasat and Dolphin 1997), they will not be covered in this article either.

## 2. Half-sandwich complexes of porphyrins

### 2.1. *Synthesis and reactivity*

The first members of this family of compounds were reported by Buchler et al. (1971). By treating  $\text{Sc}(\text{acac})_3$  with  $\text{H}_2(\text{OEP})$  in imidazole at  $170^\circ\text{C}$ , the half-sandwich compound  $\text{Sc}(\text{OEP})(\text{acac})$  was obtained which could be purified by sublimation. At higher reaction temperature ( $235^\circ\text{C}$ ),  $\text{Sc}(\text{OEP})(\text{OAc})$  was produced instead, showing that the acac ligand underwent thermal decomposition. These compounds are very labile toward acids, and imidazole was found to be an ideal solvent. By using anhydrous  $\text{ScCl}_3$  and  $\text{H}_2(\text{TTP})$  as the starting materials, Sewchok et al. (1988) isolated the half-sandwich compound  $\text{Sc}(\text{TTP})\text{Cl}$ , which upon alkaline hydrolysis is converted to the dimer  $[\text{Sc}(\text{TTP})]_2\text{O}$ . Treatment of anhydrous  $\text{ScCl}_3$  with  $\text{H}_2(\text{Por})$  ( $\text{Por} = \text{TPP, OEP}$ ) in pyridine at  $200^\circ\text{C}$  also leads to the formation of the respective  $\mu$ -oxo porphyrin dimers  $[\text{Sc}(\text{Por})]_2\text{O}$  ( $\text{Por} = \text{TPP, OEP}$ ), which are extremely sensitive to dissociation and demetallation in the presence of trace amounts of acid (Gouterman et al. 1975).



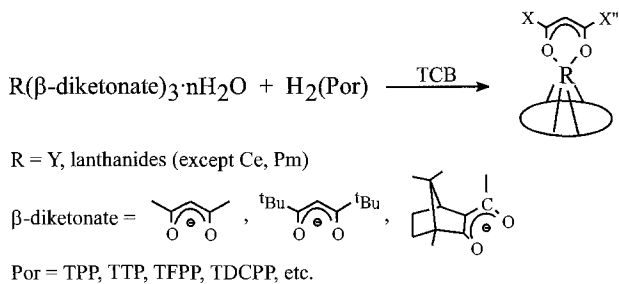
Scheme 1. Derivatives of [Sc(OEP)]. Conditions: (a)  $\text{Me}_2\text{Mg}$  in toluene; (b)  $\text{Np}_2\text{Mg}$  in toluene; (c) NaCp in THF,  $\text{LiCp}^*$  in THF,  $\text{Li}(\text{MeCp})$  in THF; (d) Na(Ind) in THF; (e) TMSOTf in toluene; (f)  $\text{H}_2\text{O}$  in  $\text{CH}_2\text{Cl}_2$ ; (g)  $\text{LiOCMe}_3$  in toluene; (h)  $\text{LiO}(\text{Me}_3\text{C}_6\text{H}_3)$  in toluene; (i)  $\text{NaN}(\text{TMS})_2$  in toluene; (j)  $\text{LiCH}_2\text{SiMe}_3$  in toluene. (From Arnold et al. 1993 with permission.)

An efficient high-yield route to gram quantities of  $\text{Sc}(\text{OEP})\text{Cl}$  was developed later (Arnold and Hoffman 1990, Arnold et al. 1993, Brand and Arnold 1995); it involves the metathesis reaction of  $\text{ScCl}_3(\text{THF})_3$  and  $\text{Li}_2(\text{OEP})(\text{THF})_2$  in toluene:



The procedure does not require high-boiling solvents which are difficult to remove without resorting to chromatography that frequently results in the formation of oxo species. This half-sandwich compound is a versatile precursor to a wide range of alkyl, amide, and alkoxide derivatives of [Sc(OEP)] as shown in scheme 1. The organometallic sandwich compounds  $\text{Sc}(\text{OEP})(\text{ring})$  (ring =  $\eta\text{-C}_5\text{H}_5$ ,  $\eta\text{-C}_5\text{Me}_5$ ,  $\eta\text{-C}_5\text{H}_4\text{Me}$ ,  $\eta\text{-C}_9\text{H}_7$ ) can also be synthesized by treating  $\text{Sc}(\text{OEP})\text{Cl}$  with the corresponding metallic species  $\text{M}(\text{ring})$  ( $\text{M}=\text{Li}, \text{Na}$ ). Hydrolysis of all  $\text{Sc}(\text{OEP})\text{R}$  derivatives results in the formation of the bis( $\mu$ -hydroxide) dimer  $[\text{Sc}(\text{OEP})(\mu\text{-OH})]_2$  (scheme 1).

The reactivity of the yttrium and lutetium analogs  $\text{R}(\text{OEP})\text{L}$  [ $\text{R}=\text{Y}, \text{Lu}$ ;  $\text{L}=\text{CH}(\text{SiMe}_3)_2$ ,  $\text{O-2,6-C}_6\text{H}_3\text{tBu}_2$ ] has also been studied (Schaverien 1991, Schaverien and Orpen 1991). These compounds can be prepared by treating the corresponding  $\text{RL}_3$  with  $\text{H}_2(\text{OEP})$  in toluene. The alkyl derivatives undergo facile protonolysis with  $\text{HO-2,6-C}_6\text{H}_3\text{tBu}_2$ ,  $\text{HC}\equiv\text{C}^t\text{Bu}$ , or  $\text{H}_2\text{O}$  to afford the monomeric alkoxide  $\text{R}(\text{OEP})(\text{O-2,6-C}_6\text{H}_3\text{tBu}_2)$ , or the



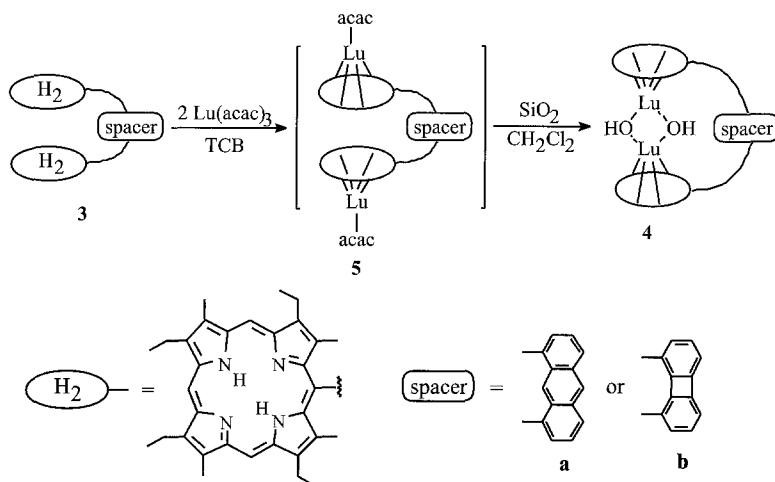
Scheme 2.

dimeric alkynyl or hydroxide species  $[\text{R}(\text{OEP})\text{L}]_2$  ( $\text{L} = \text{C}\equiv\text{C}^t\text{Bu}$ , OH). The alkyl derivatives  $\text{R}(\text{OEP})[\text{CH}(\text{SiMe}_3)_2]$  can also be generated by treating  $\text{R}(\text{OEP})(\text{O}-2,6\text{-C}_6\text{H}_3^t\text{Bu}_2)$  with  $\text{LiCH}(\text{SiMe}_3)_2$ . Reaction of  $\text{Y}(\text{OEP})(\text{O}-2,6\text{-C}_6\text{H}_3^t\text{Bu}_2)$  with two equiv. of  $\text{MeLi}$  in ether yields  $\text{Y}(\text{OEP})(\mu\text{-Me})_2\text{Li}(\text{OEt}_2)$ , which upon treatment with  $\text{AlMe}_3$  in hexane gives  $\text{Y}(\text{OEP})(\mu\text{-Me})_2\text{AlMe}_2$ . Interestingly, this bimetallic complex can selectively activate oxygen molecules to afford the  $\mu$ -methoxy complex  $\text{Y}(\text{OEP})(\mu\text{-OMe})_2\text{AlMe}_2$ .

The "acac" method reported by Buchler et al. (1971) was modified subsequently by Wong et al. (1974) who developed a general procedure for  $\text{R}(\text{Por})(\text{acac})$ . In a typical procedure, hydrated  $\text{R}(\text{acac})_3 \cdot n\text{H}_2\text{O}$  is treated with  $\text{H}_2(\text{Por})$  in refluxing 1,2,4-trichlorobenzene (TCB) for 3–4 h, after which the solvent is removed under reduced pressure and the product is purified by column chromatography. This method is applicable for yttrium (Wong and Horrocks Jr 1975, Buchler et al. 1988) and virtually the entire lanthanide series (except  $\text{R} = \text{Ce}, \text{Pm}$ ) (Horrocks Jr and Wong 1976, Wong 1983). Other  $\beta$ -diketonato ligands such as those derived from 3-acetylcamphor and 2,2,6,6-tetramethyl-3,5-heptanedione (Htmhd) may be equally well used as reactant. A variety of free base porphyrins such as  $\text{H}_2(\text{TPP})$ ,  $\text{H}_2(\text{TTP})$ ,  $\text{H}_2(\text{TFPP})$ , and  $\text{H}_2(\text{TDCPP})$  can be employed to complex with lanthanide ions using this methodology (scheme 2). These compounds are reasonably soluble in organic solvents and are stable to air. Upon treatment with  $\text{HCl}$  gas in organic solvents, the complexes are decomposed spontaneously giving the dications  $\text{H}_4(\text{Por})^{2+}$ .

Treatment of  $\text{RCl}_3$  ( $\text{R} = \text{Y}, \text{Sm-Lu}$ ) with  $\text{H}_2(\text{OEP})$  in imidazole melt at  $210^\circ\text{C}$  gives the corresponding half-sandwich complexes  $\text{R}(\text{OEP})(\text{OH})$  (Gouterman et al. 1976, Srivastava 1978). This method can be extended to the water-soluble porphyrin  $\text{H}_2(\text{TSPP})$  using  $\text{R}(\text{acac})_3$  ( $\text{R} = \text{Gd-Lu}$ ) or other lanthanide salts such as chlorides and nitrates as the metal source (Horrocks Jr and Hove 1978). However, based on the analytical and  $^1\text{H}$  NMR spectroscopic data, it has been found that imidazole remains bound to the latter porphyrin complexes which can thus be formulated as  $\text{R}(\text{TSPP})(\text{OH})(\text{imidazole})_x$  ( $x \leq 2$ ). Actually, in view of the size of the lanthanide ions and by analogy to the crystal structures of related rare-earth phthalocyaninates (see below), all these half-sandwich complexes should be regarded as octacoordinated species in which water molecules are likely present to saturate the coordination sites (Buchler et al. 1986, 1988). These water-soluble macrocycles, having a paramagnetic metal center, can function as NMR shift reagents





Scheme 3.

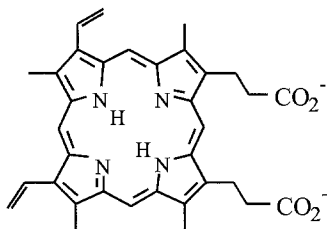
for biological molecules and other water-soluble substrates. For all these compounds, the lighter lanthanide porphyrins are very susceptible to hydrolysis and the stability increases for heavier congeners.

By treating the anthracenyl- and biphenylenyl-bridged cofacial porphyrins **3a** and **3b** with  $\text{Lu}(\text{acac})_3 \cdot 3\text{H}_2\text{O}$  in refluxing 1,2,4-trichlorobenzene, Lachkar et al. (1997) have isolated the corresponding dilutetium complexes **4**·MeOH, which contain two bridging hydroxyl groups and a MeOH molecule being coordinated to one of the lutetium centers. It is believed that the acac complexes **5** are the initial products which undergo hydrolysis during chromatographic purification on a silica gel column (scheme 3).

The first actinide porphyrin  $\text{Th}(\text{TPP})(\text{acac})_2$  has also been synthesized and purified in a similar fashion except that  $\text{Th}(\text{acac})_4$  is employed as the source of metal (Wong and Horrocks Jr 1975). Like the lanthanide analogs, this compound is also stable in air and water, and reacts rapidly with hydrogen chloride to form  $\text{H}_4(\text{TPP})^{2+}$ , but at a somewhat slower rate. Treatment of  $\text{MCl}_4$  ( $\text{M} = \text{Th}, \text{U}$ ) with  $\text{H}_2(\text{Por})$  ( $\text{Por} = \text{TPP}, \text{OEP}$ ) in benzonitrile and pyridine also gives the corresponding actinide porphyrins  $\text{M}(\text{Por})\text{Cl}_2 \cdot 2\text{PhCN}$ , which react with  $\text{Na}(\text{acac})$  in THF to give the respective  $\text{M}(\text{Por})(\text{acac})_2$  (Dormond et al. 1984, 1986). The uranium complex  $\text{U}(\text{OEP})\text{Cl}_2 \cdot 2\text{PhCN}$  can be converted to  $\text{U}(\text{OEP})\text{Cl}_2 \cdot 2\text{THF}$  and  $\text{U}(\text{OEP})\text{Cl}_2$  upon recrystallization in a mixture of  $\text{CH}_2\text{Cl}_2$  and THF or heating at  $200^\circ\text{C}$  under vacuum, respectively. Recrystallization of  $\text{U}(\text{TPP})\text{Cl}_2$  from THF/1,2-dichloroethane/heptane, however, gives the mono-THF adduct  $\text{U}(\text{TPP})\text{Cl}_2(\text{THF})$ , which has been structurally characterized (Girolami et al. 1987).

The reactivity of  $\text{Th}(\text{Por})\text{Cl}_2 \cdot 2\text{PhCN}$  ( $\text{Por} = \text{TPP}, \text{OEP}$ ) has been further explored by Kadish et al. (1988). Reaction of these complexes with aqueous  $\text{Na}_2\text{CO}_3$  in oxygen-

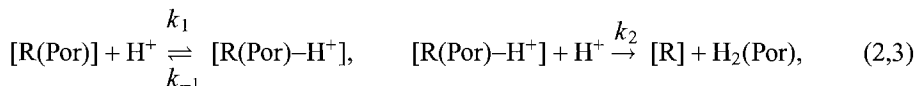
free THF leads to the formation of  $\text{Th}(\text{Por})(\text{OH})_2$ , which trimerize in the solid state. These trimeric porphyrins  $[\text{Th}(\text{Por})(\text{OH})_2]_3$  exist in different forms of aggregation in solutions depending on the concentration of the porphyrins. The compounds are trimeric at polarographic and  $^1\text{H}$  NMR concentrations, but dissociate into monomers as the concentration is decreased from ca.  $10^{-4}$  to  $10^{-7}$  M in PhCN or THF.



6

The ytterbium(III) complex of protoporphyrin IX,  $\text{Yb}(\text{Por-IX})(\text{acac})$  (**6**), has been prepared similarly using the hydrated  $\text{Yb}(\text{acac})_3$  and free base protoporphyrin IX as the starting materials and 4-phenylpyridine as solvent (Horrocks Jr et al. 1975). This compound, containing a naturally occurring porphyrin, is soluble in an aqueous NaOH solution and has been used to re-constitute apomyoglobin using 0.05 M Trishydrochloride (pH 8.0) as the buffer. It is noted that the acac ligand present in  $\text{Yb}(\text{Por-IX})(\text{acac})$  is very likely replaced by  $\text{OH}^-$  (or  $\mu$ -oxo moiety) under alkaline conditions, but it provides no obstacle to reconstitution. The related europium(III), gadolinium(III), and lutetium(III) myoglobins have also been prepared in a similar manner (Srivastava 1980a,b). The formation of these lanthanide porphyrin-globin conjugates provides a new route for the introduction of lanthanide-ion probes into biomolecules.

Wei et al. (1993) have synthesized a related gadolinium(III) hematoporphyrin derivative (HPD) by treating  $\text{Gd}(\text{NO}_3)_3 \cdot 5\text{H}_2\text{O}$  with HPD in 1,2,4-trichlorobenzene at  $215^\circ\text{C}$ . The complex can be used as a tumor localizer to probe a malignant neoplasia and a photosensitizer for photodynamic therapy. In an attempt to examine the *in vitro* stability of lanthanide porphyrins in aqueous solution, which may shed light on their *in vivo* behavior, the kinetics of the acid solvolysis reactions of a series of water-soluble lanthanide porphyrins formulated as  $[\text{R}(\text{TMPyP})(\text{OH})(\text{H}_2\text{O})_3]\text{I}_4$  ( $\text{R} = \text{Pr-Lu}$ , except Pm) have been studied (Haye and Hambricht 1988). These compounds can be prepared by treating  $\text{Na}_2(\text{TPyP})$  with the corresponding  $\text{R}(\text{OAc})_3$  in refluxing DMF followed by *N*-methylation in chloroform with methyl iodide. They can also be synthesized directly from  $[\text{H}_2(\text{TMPyP})]\text{I}_4$  and  $\text{R}(\text{OAc})_3$  in imidazole melts at  $120^\circ\text{C}$ . The kinetic data are in accord with the following mechanism:



with a pseudo-first-order rate constant  $k_{\text{obs}} = k_1[\text{H}^+]^2 / \{(k_{-1}/k_2) + [\text{H}^+]\}$  indicating that two protons are required for solvolysis. Interestingly, a  $0.1 \text{ \AA}$  increase in the ionic

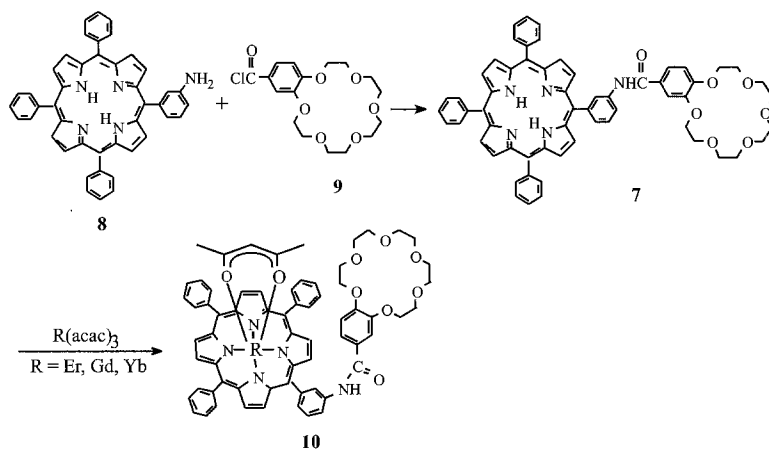
radius of the metal center leads to a remarkable 32 000-fold increase in the rate constant at high  $[H^+]$ . This is consistent with the previous observation that the heavier lanthanide porphyrins are more stable to solvolysis. For this series of compounds, complexes from europium(III) onward are of sufficient stability to protons at the physiological pH 7.4. A related study on the kinetics of demetallation of  $R(TPP)X$  ( $R = Sc, Y, Sm-Lu$ ;  $X = Cl, Br, OAc$ ) in AcOH/EtOH mixtures has also been reported (Lomova et al. 1987–1989).

Hambright et al. (1988) have also studied the kinetics of displacement of the  $Gd^{III}$  ion from the gadolinium(III) complex of TSPP by ethylenediaminetetraacetate (EDTA) giving  $Gd(EDTA)^-$  and  $H_2(TSPP)$  as the main products. This represents the first example of metal removal from a metalloporphyrin by a chelating ligand. A mechanism has been proposed to account for the kinetic data. The water-soluble lanthanide complexes of TMPyP also undergo demetallation in the presence of EDTA (Haye and Hambright 1991). Similar to the acid solvolysis reactions, a linear relationship between  $\log k$  and the ionic radius of the metal center can be established, and complexes with smaller metal center are more stable toward demetallation by EDTA.

The stability of  $Gd(TPP)(acac)$  in the presence of various amines has also been investigated (Radzki and Giannotti 1993). The porphyrin forms 1:1 complexes with morpholine, pyrimidine, imidazole, and 1-methylpyrrolidine, which can be considered as bidentate ligands, and 1:2 complexes with monodentate amines  $N(C_nH_{2n+1})_3$  ( $n = 2, 4, 5, 8$ ) forming octahedral complexes. The relatively large formation constants of these adducts, as determined by spectrophotometric methods, are consistent with the observation that the  $Gd(TPP)(acac)$ -amine adducts are stable in solution and resist photodemetallation. Radzki and Giannotti (1994) have also employed absorption spectroscopy to study the steady-state photolysis of  $Gd(TPP)(acac)$  in toluene containing triethylamine as an electron donor or  $CCl_4$  as an electron acceptor. These reactions produce a gadolinium complex of tetraphenylchlorin or a monooxidized  $\pi$ -radical cation, respectively.

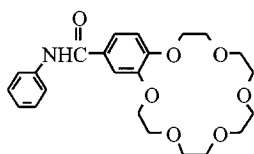
Complexes of 1:1 stoichiometry have also been identified by spectrophotometric titration of  $Gd(TPP)(acac)$  with vitamin E in  $CHCl_3$  or cyclohexane solution (Radzki and Krausz 1995), and of  $Gd(TMPyP)(acac)$  with various nucleobases and nucleosides in mixed MeOH/ $NH_3/H_2O$  solutions (Radzki and Krausz 1996). Although the structures of the complexes remain elusive, the interactions are stronger for metallated porphyrins than for non-metallated analogs, showing that the metal is involved in complex formation.

Apart from the potential biomedical applications, gadolinium(III) porphyrins can also be used as a novel circular dichroism (CD) probe for chirality of amino acids. The achiral porphyrin receptor  $Gd(TDBPP)(acac)$ , prepared from  $Gd(acac)_3$  and  $H_2(TDBPP)$ , forms 1:1 supramolecular complexes with chiral amino acids which exhibit strong, chirality-specific CD bands due to the exciton coupling. By using *N*-acetyl-L-phenylalanine and L-phenylalanine methyl ester instead of unprotected phenylalanine as the guests, only weak CD signals are induced, indicating that the guest phenylalanine may be bound to the gadolinium as a bidentate ligand. As the induced CD bands observed around the Soret band are very strong, the absolute configuration of the amino acids can be sensitively determined from the sign of CD signals (Tamiaki et al. 1997).

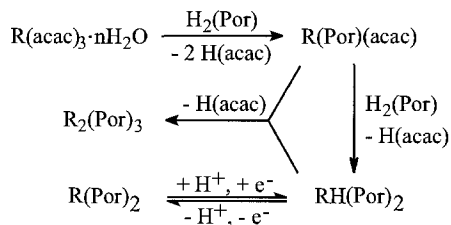


Scheme 4.

In an attempt to develop more efficient receptors for amino acids, Tsukube et al. (1999) have recently modified the lanthanide porphyrins R(TPP)(acac) (R = Er, Gd, Yb) by linking a benzo-18-crown-6 moiety in one of the phenyl rings of TPP. The synthesis involves the treatment of R(acac)<sub>3</sub> (R = Er, Gd, Yb) with the free base porphyrin **7**, which can be prepared by the condensation reaction of the amino-substituted H<sub>2</sub>(TPP) **8** and 4-chlorocarbonylbenzo-18-crown-6 (**9**) (scheme 4). The resulting complexes **10**, having a crown ether unit and a coordinatively unsaturated metal center which are highly complementary to the NH<sub>3</sub><sup>+</sup> and CO<sub>2</sub><sup>-</sup> sites, respectively, of zwitterionic amino acids, are expected to offer synergistic binding of amino acids. The extraction ability of the erbium(III) conjugate **10** (R = Er) for several amino acids and dipeptides is higher than that of Er(TPP)(acac), with and without the presence of the model compound **11**. The gadolinium and ytterbium analogs **10** (R = Gd, Yb), however, extract tryptophan with comparable efficiencies to those with corresponding mixtures of R(TPP)(acac) and **11**, showing that the nature of the lanthanide center is an important factor in designing effective conjugate receptors. Similar to Gd(TDBPP)(acac), the erbium(III) conjugate also exhibits chirality-specific CD signals via complexation with chiral amino acids, enabling it to be useful as a sensitive CD probe for determining the chirality of amino acids.

**11**

As mentioned in the Introduction, the half-sandwich complexes R(Por)(acac) are important intermediates or precursors for the preparation of a whole range of sandwich



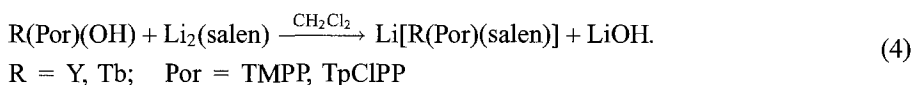
Scheme 5.

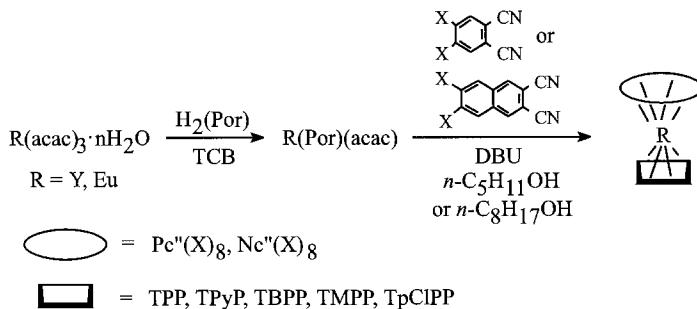
compounds of porphyrins and phthalocyanines (Ng and Jiang 1997, Buchler and Ng 2000). The homoleptic bis- and tris(porphyrinato) rare-earth complexes  $\text{R(Por)}_2$  and  $\text{R}_2(\text{Por})_3$  are usually prepared by treating  $\text{R(acac)}_3 \cdot n\text{H}_2\text{O}$  with the corresponding  $\text{H}_2(\text{Por})$  in 1,2,4-trichlorobenzene. It is believed that  $\text{R(Por)(acac)}$  is formed initially according to the mechanism shown in scheme 5. Treatment of  $\text{R(TPP)(acac)}$  [R = Sm (Spyroulias et al. 1995a), Dy (Bertini et al. 1996), Yb (Bertini et al. 1996), Lu (Spyroulias and Coutsolelos 1996)] or  $\text{M(TPP)Cl}_2$  (M = Th, U) (Kadish et al. 1993) with  $\text{Li}_2(\text{OEP})$  leads to the formation of the respective heteroleptic bis(porphyrinato) complexes  $\text{RH(OEP)(TPP)}$  or  $\text{M(OEP)(TPP)}$ , respectively. Similarly, reaction of  $\text{R(Por)(acac)}$  (R = Y, Ce, Sm, Eu, Gd, Er, Lu; Por = TPP, TPyP, TBPP, TMPP, TpClPP) (Lachkar et al. 1988, Chabach et al. 1992, 1995, Jiang et al. 1996, 1997b, 1998b) or  $\text{M(Por)Cl}_2$  (M = Th, U; Por = OEP, TPP, TTP) (Kadish et al. 1993) with  $\text{Li}_2(\text{Pc})$  gives the corresponding mixed double-decker complexes  $\text{R(Pc)(Por)}$  or  $\text{M(Pc)(Por)}$ . The former reactions may also give the triple-decker complexes  $\text{R}_2(\text{Pc})(\text{Por})_2$  and  $\text{R}_2(\text{Pc})_2(\text{Por})$  depending on the nature of the lanthanide metals and the macrocycles, and the ratio of these reactants.

The above methodology has been extended by Chabach et al. (1996) who prepared a series of novel triple-deckers in which two different metal ions are sandwiched by three macrocycles. Reaction of  $\text{R}^1(\text{Por})(\text{acac})$  ( $\text{R}^1 = \text{Y, Gd, Lu}$ ; Por = OEP, TPP), generated *in situ*, with the double-deckers  $\text{R}^2(\text{Pc})(\text{TPP})$  ( $\text{R}^2 = \text{La, Ce}$ ) results in the formation of the respective mixed triple-deckers  $(\text{Por})\text{R}^1(\text{Pc})\text{R}^2(\text{TPP})$  in good yields.

The half-sandwich complexes  $\text{R(Por)(acac)}$  (R = Y, Eu; Por = TPP, TPyP, TBPP, TMPP, TpClPP) also act as a template to induce tetramerization of dicyanobenzenes  $\text{C}_6\text{H}_2\text{X}_2(\text{CN})_2$  (X = H,  $\text{C}_7\text{H}_{15}$ ,  $\text{OC}_5\text{H}_{11}$ ) or 2,3-dicyanonaphthalenes  $\text{C}_{10}\text{H}_4\text{X}_2(\text{CN})_2$  (X = H,  $\text{SC}_{12}\text{H}_{25}$ ) in the presence of 1,8-diazabicyclo[5.4.0]undec-7-ene (DBU) giving the respective double-decker complexes  $\text{R(Por)[Pc}''(\text{X})_8]$  or  $\text{R(Por)[Nc}''(\text{X})_8]$ , respectively (Jiang et al. 1998c, 1999c,d) (scheme 6).

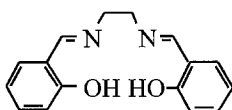
A series of pseudo-sandwich complexes containing a porphyrinato ligand and the Schiff-base ligand derived from bis(salicylideneimino)ethane  $\text{H}_2(\text{salen})$  (**12**) have been prepared by Buchler and Hammerschmitt (1991). Treatment of  $\text{R(Por)(OH)}$  (R = Y, Tb; Por = TMPP, TpClPP) with  $\text{Li}_2(\text{salen})$  in  $\text{CH}_2\text{Cl}_2$  gives the salts  $\text{Li}[\text{R(Por)(salen)}]$  in 62–80% yields:



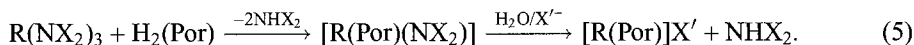


Scheme 6.

The pseudo-sandwich structure of these complexes has been inferred by the  $^1\text{H}$  NMR study of the analogous zirconium complex  $\text{Zr}(\text{OEP})(\text{salen})$  which exhibits a square antiprismatic configuration at 295 K, while the two ligands freely rotate around each other at 373 K.

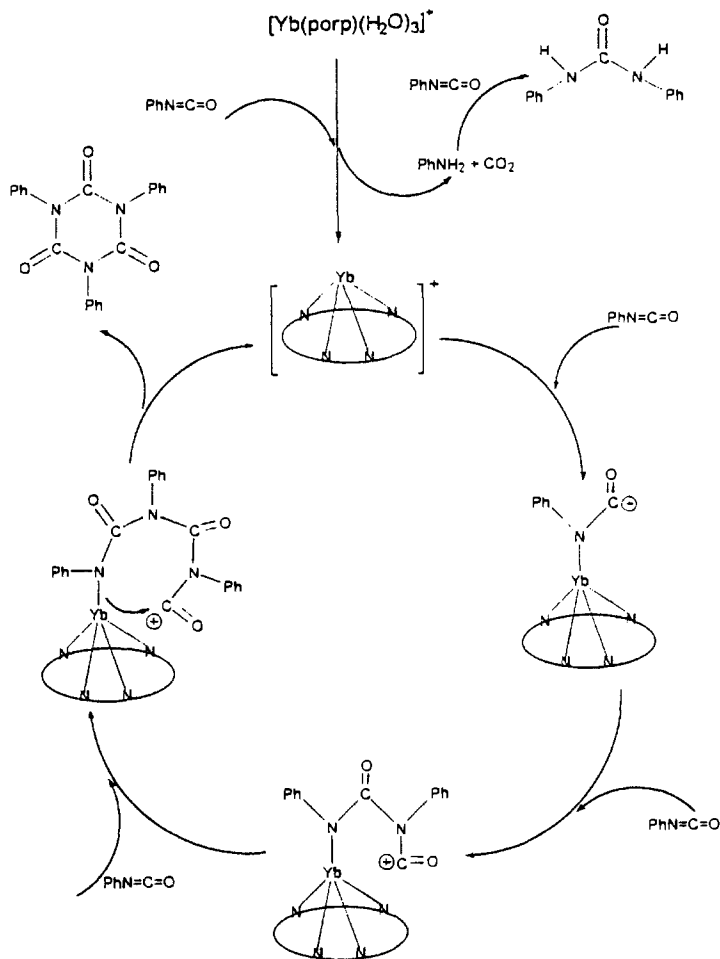
12  $\text{H}_2(\text{salen})$ 

A new synthetic route to half-sandwich lanthanide porphyrinates has recently been developed by Wong et al. (1999); it involves lanthanide amides as the precursors:



Reaction of an excess of  $\text{R}[\text{N}(\text{SiMe}_3)_2]_3 \cdot n[\text{LiCl}(\text{THF})_3]$  ( $\text{R} = \text{Y, Er, Yb}$ ), generated *in situ* from the reaction of anhydrous  $\text{RCl}_3$  with 3 equiv. of  $\text{Li}[\text{N}(\text{SiMe}_3)_2]$  in THF, with free base porphyrins  $\text{H}_2(\text{Por})$  ( $\text{Por} = \text{TMPP, TTP}$ ) in refluxing bis(2-methoxyethyl) ether/THF leads to the formation of the cationic monoporphyrinates  $[\text{R}(\text{TMPP})(\text{H}_2\text{O})_3]\text{Cl}$  ( $\text{R} = \text{Y, Er, Yb}$ ) or  $[\text{Yb}(\text{TTP})(\text{H}_2\text{O})_2(\text{THF})]\text{Cl}$ . These purple complexes are stable in air and have been spectroscopically and structurally characterized. The ytterbium(III) complex  $[\text{Yb}(\text{TMPP})(\text{H}_2\text{O})_3]\text{Cl}$  undergoes metathesis with an excess of  $\text{AgBF}_4$  in THF, leading to the disproportionation of  $\text{Ag}^{\text{I}}$  to silver metal and  $\text{Ag}^{\text{II}}$ , and the isolation of the silver(II) porphyrin  $\text{Ag}(\text{TMPP})$ .

The catalytic activity of these novel cationic lanthanide monoporphyrinates has also been studied (Wong et al. 1999). The ytterbium complex  $[\text{Yb}(\text{TMPP})(\text{H}_2\text{O})_3]\text{Cl}$ , but not the yttrium and erbium analogs, can effectively catalyze the conversion of phenyl isocyanate into its cyclic trimer, 1,3,5-triphenyl-*s*-triazine-2,4,6-trione. The complex appears to be a living catalyst as the resulting mixture can be re-used without losing any of its activity in the first three cycles. A plausible mechanism has been proposed as



Scheme 7. (From Wong et al. 1999 with permission.)

shown in scheme 7. The ytterbium porphyrin first reacts with phenyl isocyanate to give aniline and the coordinatively unsaturated cationic species  $[\text{Yb}(\text{TMPP})]^+$ , which then acts as a Lewis acid to catalyze the cyclic trimerization of phenyl isocyanate. The isolation of 1,3-diphenylurea, formed in the reaction of aniline and phenyl isocyanate, is in accord with the proposed mechanism.

Rare-earth complexes of porphyrins also show catalytic activity in the radical oxidation of unsaturated hydrocarbons by various oxidizing agents such as potassium hydrochlorite and *tert*-butyl hydroperoxide (Kochnev et al. 1991). Styrene, for example, undergoes oxidation to give a mixture of the aldehydes PhCHO and PhCH<sub>2</sub>CHO, and the epoxide PhCHCH<sub>2</sub>O. The oxidation of saturated and aromatic hydrocarbons is also promoted by

rare-earth porphyrins through a similar radical mechanism (Vedernikov et al. 1993). It is believed that the action of the catalyst is to activate the oxidizing agent.

## 2.2. Structure

The half-sandwich structure of R(Por)(acac) was first inferred from the dipolar shift ratios observed in the  $^1\text{H}$  NMR spectra of R(TTP)(acac) (R=Eu, Yb) by assuming an axial symmetry (Horrocks Jr and Wong 1976). The out-of-plane displacement of the metal center was determined to be 1.80 Å for the  $\text{Eu}^{\text{III}}$  complex and 1.60 Å for the  $\text{Yb}^{\text{III}}$  analog, giving Eu–N and Yb–N distances of 2.69 and 2.56 Å, respectively. The calculations were later refined by Babushkina et al. (1986) who employed a new treatment for the paramagnetic NMR shifts which is based on an *ab initio* estimation of the coefficients describing the anisotropy of the magnetic susceptibility, proportional to the pseudo-contact shifts. The new model takes the  $\beta$ -diketonato ligand into consideration which experiences a restricted rotation along the axis through the metal ion and the center of the porphyrin ring, giving a complex with non-axial symmetry. It was found that the metal ion is closer to the macrocyclic plane than had been estimated previously.

The first X-ray crystal structure of half-sandwich porphyrinato complexes appeared in 1986. Dormond et al. (1986) reported the structure of  $\text{Th}(\text{OEP})(\text{acac})_2$  in which the thorium atom is octacoordinated by the four nitrogen atoms of the macrocycle and the four oxygen atoms of the two acac groups forming a nearly perfect antiprism. The thorium atom is closer (by  $\sim 0.1$  Å) to the oxygen atom plane which is consistent with the Th–O bond being shorter (mean value 2.40 Å) than the Th–N bond (mean value 2.50 Å). By comparing the powder X-ray diffraction patterns, the uranium complex  $\text{U}(\text{OEP})(\text{acac})_2$  was found to be isomorphous with the thorium analog.

Figure 1 gives the molecular structure of  $\text{U}(\text{TPP})\text{Cl}_2(\text{THF})$ . The uranium atom is 1.29 Å out of the porphyrin  $\text{N}_4$  plane, forming a 4:3 piano stool structure. The TPP ring is slightly “saucer-shaped” with the four nitrogen atoms forming the bottom of the dish with its convexity toward the uranium atom. This distortion may optimize  $\sigma$  and  $\pi$  bonding

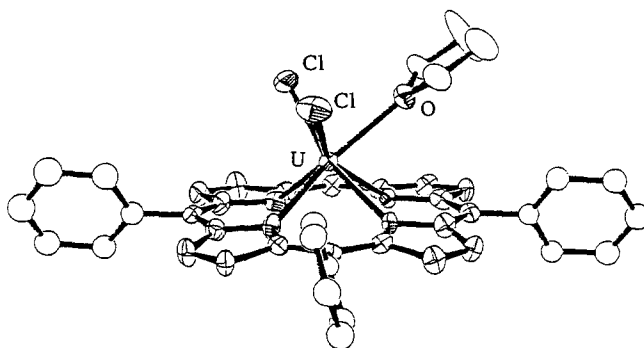


Fig. 1. Molecular structure of  $\text{U}(\text{TPP})\text{Cl}_2(\text{THF})$  (rear phenyl ring omitted for clarity). (From Girolami et al. 1987 with permission.)



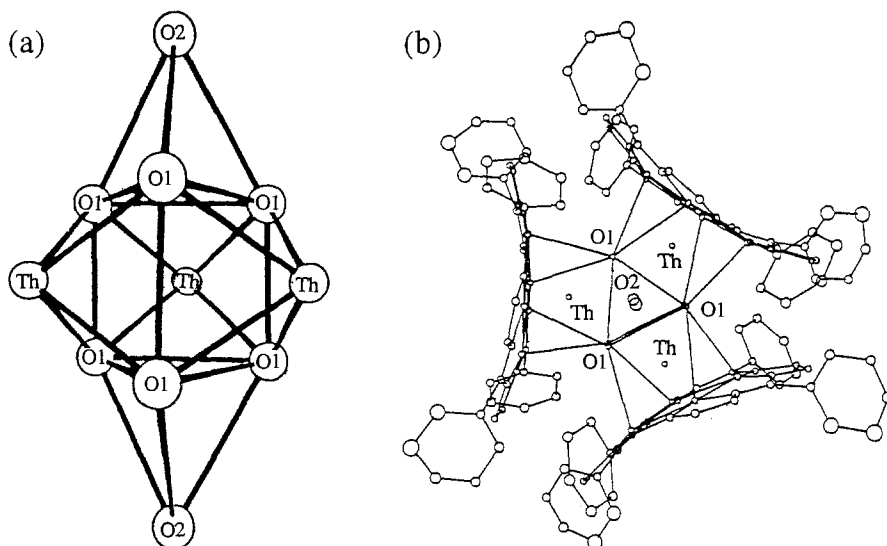


Fig. 2. (a) ORTEP drawing of the  $\text{Th}_3(\text{OH})_6(\text{OH}_2)_2$  core. (b) Projection of the trimeric unit along the  $c$ -axis. (From Kadish et al. 1988 with permission.)

between the nitrogen atoms and the metal center, as it allows the  $sp^2$  hybrids to point toward the metal rather than to the center of the porphyrin ring (Girolami et al. 1987).

The trimeric structure of  $[\text{Th}(\text{TPP})(\text{OH})_2]_3 \cdot 2\text{H}_2\text{O}$  has been confirmed by Kadish et al. (1988). The six hydroxyl ligands in the molecular unit form a trigonal prism of which the triangular faces are capped by two water molecules and the rectangular faces are capped with three thorium atoms (fig. 2a). The three domed TPP units lie parallel to the threefold axis (fig. 2b) and each of the thorium atom assumes a distorted square antiprismatic geometry. The Th–Th separation is  $3.960(3) \text{ \AA}$  and does not suggest any metal–metal interaction.

Scandium(III) porphyrins are the major class of half-sandwich porphyrinato complexes which have been structurally characterized. The crystal structures of seven derivatives:  $\text{Sc}(\text{TTP})\text{Cl} \cdot 2(\text{C}_{10}\text{H}_7\text{Cl})$ ,  $[\text{Sc}(\text{TTP})_2\text{O} \cdot 6\text{THF}]$ ,  $\text{Sc}(\text{OEP})(\eta\text{-C}_5\text{H}_5)$ ,  $\text{Sc}(\text{OEP})\text{Me} \cdot 1.5\text{CH}_2\text{Cl}_2$ ,  $\text{Sc}(\text{OEP})[\text{CH}(\text{SiMe}_3)_2]$ ,  $\text{Sc}(\text{OEP})(\eta\text{-C}_9\text{H}_7)$  and  $[\text{Sc}(\text{OEP})(\mu\text{-OH})_2]$ , are known (Sewchok et al. 1988, Arnold and Hoffman 1990, Arnold et al. 1993). For  $\text{Sc}(\text{TTP})\text{Cl}$ , the scandium atom is  $0.68 \text{ \AA}$  above the  $\text{N}_4$  plane forming a square pyramidal geometry. The two 1-chloronaphthalene molecules are distorted in the lattice and cannot be resolved. The scandium atom in  $\text{Sc}(\text{OEP})\text{Me}$  and  $\text{Sc}(\text{OEP})[\text{CH}(\text{SiMe}_3)_2]$  is also coordinated in a regular square pyramidal fashion and sits atop the  $\text{N}_4$  plane at a distance of  $0.66$  and  $0.71 \text{ \AA}$ , respectively. The structures of  $\text{Sc}(\text{OEP})(\eta\text{-C}_5\text{H}_5)$  and  $\text{Sc}(\text{OEP})(\eta\text{-C}_9\text{H}_7)$  show clearly that the scandium center is sandwiched between the OEP macrocycle and the  $\eta\text{-C}_5\text{H}_5$  or  $\eta\text{-C}_9\text{H}_7$  ring, although the essentially planar indene ligand is tilted with respect to the porphyrin ring in the latter structure. The metal center sits  $0.78\text{--}0.80 \text{ \AA}$  from the mean plane of the nitrogens and  $2.196\text{--}2.233 \text{ \AA}$  from that of the  $\eta\text{-C}_5\text{H}_5$  or  $\eta\text{-C}_9\text{H}_7$

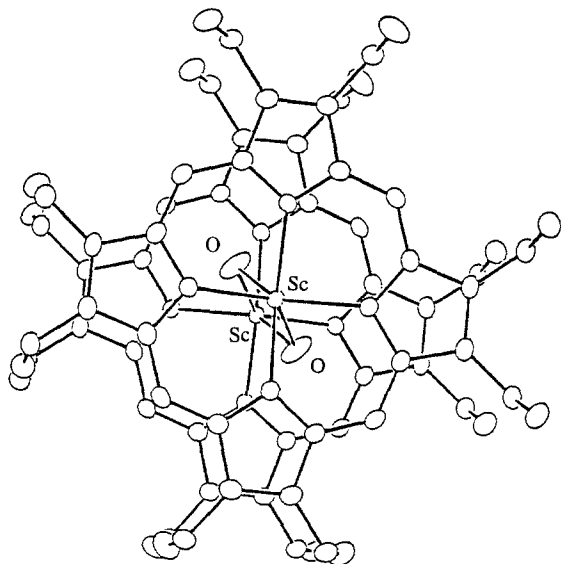


Fig. 3. ORTEP view of  $[\text{Sc}(\text{OEP})(\mu\text{-OH})_2]_2$  looking down the Sc-Sc vector. (From Arnold et al. 1993 with permission.)

ring. The OEP ligand in all these complexes is slightly domed and ruffled, except in  $\text{Sc}(\text{OEP})(\eta\text{-C}_9\text{H}_7)$  where the porphyrin ring is remarkably planar. Both of the complexes  $[\text{Sc}(\text{TTP})_2\text{O}]$  and  $[\text{Sc}(\text{OEP})(\mu\text{-OH})_2]$  adopt a dimeric structure. As shown in fig. 3, the two OEP rings of the latter are eclipsed with a separation of 5.06 Å between the  $\text{N}_4$  planes. The Sc-O-Sc bond angle for both complexes is  $\sim 110^\circ$  with an average Sc-O bond length of  $\sim 2.08$  Å.

The first molecular structure of half-sandwich lanthanide porphyrins was reported by Schaverien and Orpen (1991). The lutetium alkyl complex  $\text{Lu}(\text{OEP})[\text{CH}(\text{SiMe}_3)_2]$  has a structure resembling that of the scandium analog (Arnold et al. 1993), exhibiting a square pyramidal geometry. The five-coordinated lutetium atom lies 0.918 Å above the  $\text{N}_4$  plane, and the porphyrin ring also displays a saucer shape.

The molecular structures of the anthracenyl- and biphenylenyl-bridged bisporphyrins **4a** and **4b** (scheme 3) have also been determined (Lachkar et al. 1997). In both structures, the two lutetium atoms are bridged by two  $\text{OH}^-$  anions, and one of the metal centers is also weakly bonded to a MeOH molecule, giving one hexacoordinated and one heptacoordinated lutetium atoms. The dihedral angle between the two  $\text{C}_{20}\text{N}_4$  mean planes is  $19.7^\circ$  and  $27.1^\circ$  for **4a** and **4b**, respectively. The anthracenyl and biphenylenyl connectors are planar within experimental error, and nearly orthogonal to the porphyrin core mean planes. The porphyrin macrocycles again have a convex shape with some ruffling.

The coordination sphere of the terbium atom in  $[\text{Tb}(\text{OCTPP})(\text{OAc})(\text{DMSO})_2]$  consists of the four nitrogen atoms of the porphyrin and the oxygen atoms of the bidentate acetate and two DMSO solvent molecules forming a square antiprismatic geometry. The porphyrin ring also manifests a marked saddle distortion, and the displacement of the

individual chlorine atoms from the  $N_4$  mean plane is relatively large (1.03–2.18 Å). The dihedral angles between the phenyl rings and the porphyrin mean plane vary from 49.03° to 49.74°, which can minimize unfavorable steric interactions between the phenyl and the flanking chloride substituents (Spyroulias et al. 1997). The structural data are similar to those of the cationic porphyrins  $[R(TMPP)(H_2O)_3]Cl$  ( $R = Y, Er, Yb$ ) in which two of the aqua ligands are disordered with a site occupancy of 0.5. The R–N distances and the separation between the two parallel mean planes formed by four nitrogen atoms and four oxygen atoms follow the order  $Yb^{III} < Er^{III} < Y^{III}$ , reflecting an increase in ionic radii: 98.5 < 100.4 < 101.9 pm. The analogous ytterbium complex  $[Yb(TTP)(H_2O)_2(THF)]Cl$ , however, adopts a monocapped trigonal prismatic structure in which the seven-coordinated ytterbium center lies 1.090 Å above the  $N_4$  mean plane and 1.676 Å below the  $O_3$  mean plane defined by the two aqua ligands and the THF molecule (Wong et al. 1999).

According to an extended X-ray absorption fine structure study, the gadolinium center in  $[Gd(TPP)(acac)] \cdot 8H_2O \cdot 3TCB$  is also octacoordinated to the four nitrogen atoms of TPP, two oxygen atoms of acac, and two oxygen atoms of water, with Gd–N and Gd–O distances of 2.32 Å and 2.43 Å, respectively (Jiang et al. 1998d).

### 2.3. Spectroscopic properties

#### 2.3.1. $^1H$ NMR spectra

Because of the paramagnetic nature of some of the lanthanide and actinide ions, not all of the rare-earth and actinide porphyrins give NMR signals. Broadening and substantial shift of signals are usually observed for those compounds which can be characterized with NMR spectroscopy. Figure 4 shows the  $^1H$  NMR spectra of  $Eu(TTP)(acac)$  and  $Yb(TTP)(tmhd)$  recorded at  $-21^\circ C$  along with the assignment. The spectrum for the metal-free  $H_2(TTP)$  is also displayed for comparison. It can be seen that the ortho and

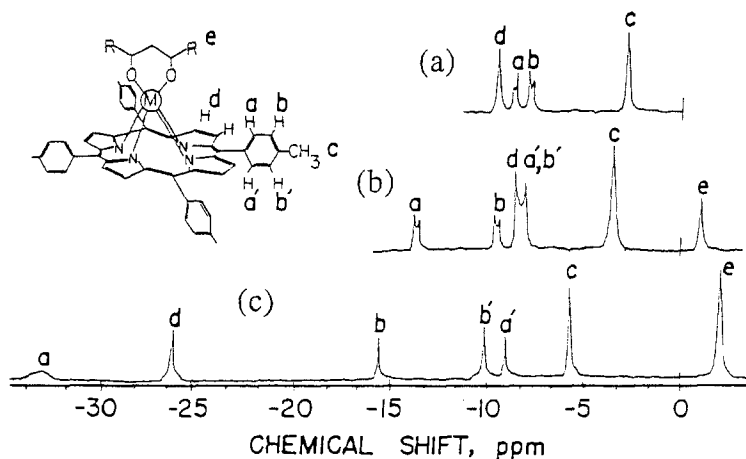


Fig. 4.  $^1H$  NMR spectra of (a)  $H_2(TTP)$ , (b)  $Eu(TTP)(acac)$ , and (c)  $Yb(TTP)(tmhd)$  in  $CDCl_3$  at  $-21^\circ C$ . (From Horrocks Jr and Wong 1976 with permission.)

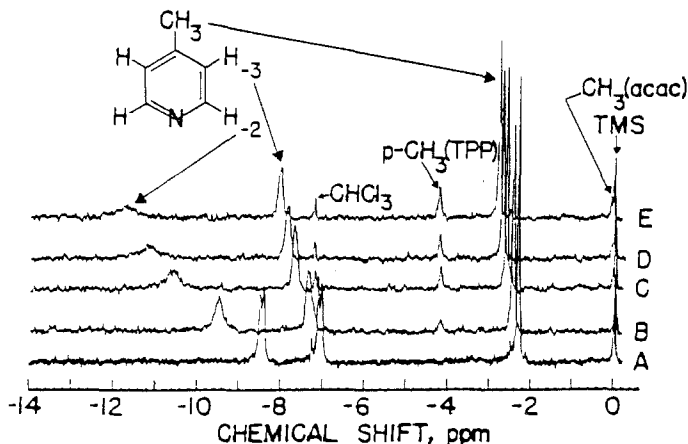


Fig. 5. Effect of increasing concentrations of Yb(TTP)(acac) on the  $^1\text{H}$  NMR spectrum of 4-picoline in  $\text{CDCl}_3$  at  $36^\circ\text{C}$ ;  $R_p = 0.0, 0.021, 0.043, 0.053,$  and  $0.064$  for spectra A–E, respectively. (From Horrocks Jr and Wong 1976 with permission.)

meta aryl protons become non-equivalent upon complexation owing to the out-of-plane displacement of the metal ion and the fact that aryl-group rotation is slow on the NMR timescale at this temperature. Most of the signals are shifted downfield, in particular for the ytterbium(III) complex of which the dipolar shifting ability is ca. 2.2 times that of the prosthetic group in metmyoglobin cyanide, the most effective of the low-spin iron(III) dipolar probes (Horrocks Jr and Wong 1976).

As the complexes  $\text{R}(\text{Por})(\text{acac})$  are not coordinatively saturated, it is not unexpected that the compounds producing sizable shifts may act as shift reagents toward molecules with donor atoms. Figure 5 shows the spectral changes upon addition of successive quantities of Yb(TTP)(acac) to chloroform solutions of 4-picoline. Downfield shifts are observed for all proton signals, and a linear relationship between the observed chemical shifts and the mole ratio of Yb(TTP)(acac) to substrate ( $R_p$ ) is established. It is worth noting that both the substrate and porphyrin resonance shifts are in the same direction, indicating that the picoline ligand also occupies, on the average, the equatorial region where  $(3 \cos^2 \theta - 1) < 0$ , which is consistent only with a significantly out-of-plane displacement of the metal ion. This ytterbium(III) complex also induces downfield shifts for the proton resonances of the aliphatic alcohol 1-pentanol (Horrocks Jr and Wong 1976).

Apart from the ytterbium(III) complex Yb(TTP)(acac), the entire series of lanthanide analogs have also been evaluated as shift reagents toward 4-picoline. Only very small resonance shifts are observed for the early elements (Pr, Nd, Sm, Eu). Sizable upfield (Tb, Dy, Ho) and downfield (Er, Tm, Yb) shifts, however, are observed for the elements at the end of the series. The action of the diamagnetic lutetium(III) porphyrin Lu(TPP)(acac) is unique: it serves as a "ring current" shift reagent. All the proton signals for 4-picoline are shifted upfield in the presence of Lu(TPP)(acac), for which a labile equilibrium between coordinated and uncoordinated ligand is observed. The ring-current shifts, however, are

considerably smaller than the paramagnetic effects induced by the latter half of the lanthanide series (Tb–Yb) (Horrocks Jr and Wong 1976).

The water-soluble lanthanide porphyrins  $R(\text{TSPP})(\text{OH})(\text{imidazole})_x$  ( $R = \text{Ho–Lu}$ ) resemble the TPP and TTP analogs in all these spectral properties except that, apart from the neutral 4-picoline, water-soluble substrates such as the *p*-toluidate anion and the *N*-methylpyridinium cation can also be used (Horrocks Jr and Hove 1978). The gadolinium(III) complex of TSPP is of particular interest. Having a  $\text{Gd}^{\text{III}}$  ion ( $S = \frac{7}{2}$ ) which displays a high relaxivity and a porphyrin moiety which may selectively target to many pathological tissues, this water-soluble complex is potentially useful as a paramagnetic contrast agent for NMR imaging. Both the relaxation times  $T_1$  (spin–lattice) and  $T_2$  (spin–spin) for water are inversely proportional to the concentration of the complex. The effects are comparable to those produced by the free  $\text{Gd}^{\text{III}}$  ion alone in a frequency region close to that used for NMR imaging (Marzola and Cannistraro 1987).

Owing to their diamagnetic nature, porphyrinato complexes of scandium(III) (Buchler et al. 1971, Arnold and Hoffman 1990, Arnold et al. 1993), yttrium(III) (Schaverien 1991, Wong et al. 1999), lutetium(III) (Schaverien and Orpen 1991, Lachkar et al. 1997), and thorium(IV) (Wong and Horrocks Jr 1975, Dormond et al. 1984, 1986, Kadish et al. 1988) usually give normal  $^1\text{H}$  NMR spectra with signals falling in the 0–11 ppm region. The signals for the axial substituents, if any, however may appear at  $\delta < 0$  due to the shielding effect by the porphyrin ring current.

### 2.3.2. Electronic absorption spectra

The formation of  $R(\text{Por})(\beta\text{-diketonate})$  from  $R(\beta\text{-diketonate})_3$  and  $\text{H}_2(\text{Por})$  can be monitored by UV–Vis spectroscopy. As shown in fig. 6, the spectral features are changed remarkably upon complexation. A typical spectrum for the complexes  $R(\text{Por})(\beta\text{-diketonate})$  (fig. 6d) displays an intense B(0,0) (or Soret) band at  $\sim 420$  nm, and Q(2,0), Q(1,0), and Q(0,0) bands at  $\sim 510$ , 550, and 590 nm, respectively (Wong 1983). An additional visible band at  $\sim 400$  nm and an UV band at  $\sim 300$  nm may also be seen, which can be attributed to the B(1,0) band of porphyrins and the  $\pi\text{--}\pi^*$  transition due to the  $\beta\text{-diketonato}$  ligands, respectively (Iwase and Igarashi 1993). Table 1 compiles the electronic absorption data for all compounds in this family. It can be seen that there is only a minor variation in the absorption spectra with changes of the metal center and supporting ligands. Change of porphyrinato ligands, however, may lead to a substantial shift of absorption bands. By replacing TPP with  $\beta\text{-halogenated}$  TPP analogs such as OBTPP and OCTPP, for example, all the absorption bands are remarkably shifted to the red ( $>40$  nm) (Spyroulias and Coutsolelos 1995, Spyroulias et al. 1997).

The solvent effects on the absorption spectrum of  $\text{Gd}(\text{TPP})(\text{acac})$  have been studied by Radzki and Giannotti (1993). As shown in fig. 7, both the Soret and Q(1,0) bands are substantially shifted in different solvents, in particular in solvents with donor atoms. The magnitude is about two times larger than that for metal-free porphyrin  $\text{H}_2(\text{TPP})$  which can be attributed to complex formation between the gadolinium porphyrin and the Lewis base solvents.

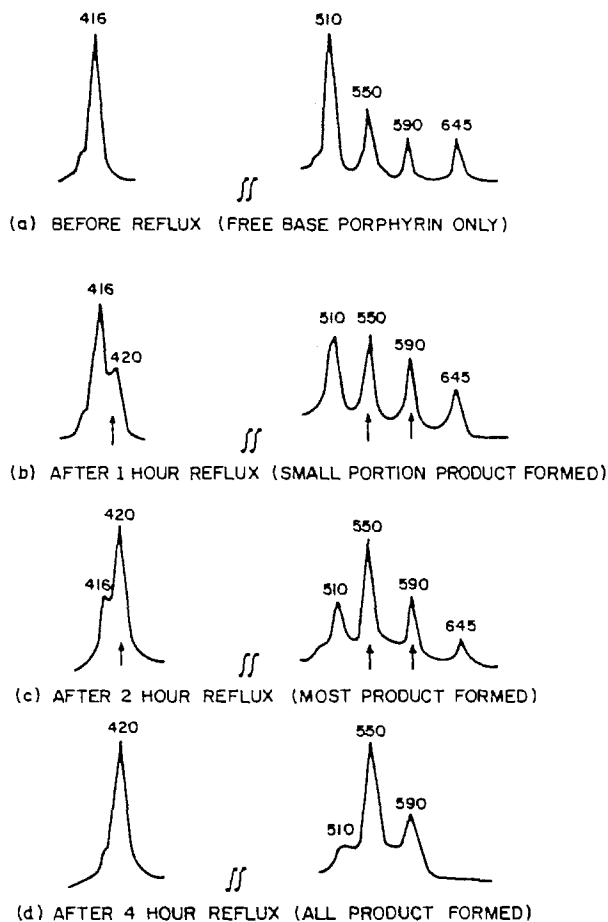


Fig. 6. UV-Vis spectral changes during the reaction of  $R(\beta\text{-diketonate})_3$  with  $H_2(\text{Por})$ . (From Wong 1983 with permission.)

Figure 8 shows the absorption and magnetic circular dichroism (MCD) spectra of  $\text{Yb}(\text{Por-IX})L_n$  with and without interacting with the apomyoglobin. Upon interaction, all the  $B(0,0)$  (397 nm),  $Q(1,0)$  (532 nm), and  $Q(0,0)$  (570 nm) bands intensify and experience a small bathochromic shift to 403, 534, and 572 nm, respectively (fig. 8b). The ellipticities of the Soret and  $Q(1,0)$  bands are very similar as shown in the MCD spectrum (fig. 8a), although the extinction coefficients differ by factors of more than ten. These spectral changes form the basis for the spectrophotometric titration of  $\text{Yb}(\text{Por-IX})L_n$  with apomyoglobin, which reveals a 1:1 stoichiometry of interaction. The sizable and positive extrinsic Cotton effect in the Soret band of  $\text{Yb}(\text{Por-IX})L_n$  induced by the interactions with the globin, as observed in the CD spectra, suggests that the lanthanide porphyrin occupies the heme site of the globin (Horrocks Jr et al. 1975).

As mentioned in sect. 2.1,  $\text{Gd}(\text{TPP})(\text{acac})$  and its derivatives **10** are able to act as novel CD probes for chirality of amino acids (Tamiaki et al. 1997, Tsukube et al. 1999).

Table 1  
UV-Vis data for half-sandwich porphyrinato complexes of rare earths and actinides

Compound	Solvent	$\lambda_{\text{max}}$ (nm) (log $\epsilon$ )				Reference
		B(1,0)	B(0,0)	Q(2,0)	Q(1,0)	
R(TPP)(acac) R = Y, Lu	MeOH	—	418–420	512–515	551–554	587–589 Martarano et al. (1976)
R(TPP)(acac) R = Y, La–Lu (except Ce, Pr, Tm)	acetone	—	418–426	—	544–562	587–608 Wong (1983)
R(TPP)(acac) <sup>a</sup> R = Eu–Lu	— <sup>b</sup>	408–410 (4.60–4.70)	427–433 (5.61–5.68)	515–520 (sh)	556–562 (4.30–4.38)	595–603 (3.70–3.90) Iwase and Igarashi (1993)
Gd(TPP)(acac)	toluene	—	422.5 (5.39)	515.0 (3.50)	555.0 (4.07)	593.1 (3.57) Radzki and Giannotti (1994)
	DMSO	—	430.0 (5.47)	520.2 (3.54)	560.3 (4.04)	599.2 (3.54)
	Et <sub>3</sub> N	—	427.1 (5.29)	518.0 (3.04)	559.1 (4.05)	598.0 (3.38)
	toluene + CCl <sub>4</sub>	—	423.5	516.0	556.2	592.0
	chloroform	—	425 (5.43)	517 (3.48)	553 (4.12)	591 (3.64) Radzki and Krausz (1995)
	cyclohexane	—	426 (5.32)	517 (3.46)	556 (4.04)	593 (3.52)
Sm(TPP)(acac)	DMSO	—	430.6 (4.55)	520 (3.68)	564 (4.13)	599 (3.76) Radzki et al. (1987)
R(Por)(acac)	benzene	—	417–419 (5.58–5.62)	512–513 (3.48–3.51)	552–553 (4.25–4.29)	586–591 (3.30–3.67) Wang et al. (1986)
Por = TPP, ToCIPP						
Dy(Por)(acac)	DMF	—	427–428 (5.64–5.69)	520 (3.46–3.63)	559–560 (4.26–4.29)	596–599 (3.60–3.88) Coutsolelos and Spyroulias (1994)
Por = TPP, ToTP, TmTP, TTP, TMP						
R(TPP)(tmhd)	acetone	—	424–427	—	544–558	589–594 Wong (1983)
R = La, Nd, Sm, Tb, Dy, Ho, Tm						
Sc(TPP)L <sub>x</sub>	CCl <sub>4</sub> -MeOH	395	417	508	547	585 Gouterman et al. (1975)
[Sc(TPP)] <sub>2</sub> O	CCl <sub>4</sub>	~390	406	515	550	591 Gouterman et al. (1975)

continued on next page

Table 1, continued

Compound	Solvent	$\lambda_{\max}$ (nm) (log $\epsilon$ )				Reference	
		B(1.0)	B(0.0)	Q(2.0)	Q(1.0)		
Sc(TTP)Cl	CH <sub>2</sub> Cl <sub>2</sub>	—	422	518	556	596	Sewchok et al. (1988)
[Sc(TTP)] <sub>2</sub> O	toluene	—	414	516	550	592	Sewchok et al. (1988)
R(TTP)(acac) R = Pr, Eu	acetone	—	426	—	556	597	Wong (1983)
[Yb(TTP)(H <sub>2</sub> O) <sub>2</sub> (THF)]Cl	CHCl <sub>3</sub>	—	422 (5.76)	—	551 (4.51)	589 (3.97)	Wong et al. (1999)
[R(TMPP)(H <sub>2</sub> O) <sub>3</sub> ]Cl	CHCl <sub>3</sub>	—	424–425	—	552–555	593	Wong et al. (1999)
R = Y, Er, Yb			(5.29–5.60)	—	(4.14–4.32)	(3.94–4.00)	
Er(TDCPP)(acac)	acetone	—	426	—	556	597	Wong (1983)
Er(TFPP)(acac)	acetone	—	423	—	553	592	Wong (1983)
Yb(TFPP)(tmhd)	acetone	—	422	—	533	590	Wong (1983)
R(HTPP)(acac) R = Ho, Tm–Lu	CHCl <sub>3</sub>	—	423	518	554	594	Liu et al. (1994a)
R(HTMPP)(acac) R = Dy, Er	CHCl <sub>3</sub>	—	425	518	554	594	Liu et al. (1993a)
R(TPyP)(acac)	<sup>b</sup>	—	421	512	550	587	Liu et al. (1993b)
R = Dy, Ho, Yb, Lu			(5.38–5.44)	(3.57–3.62)	(3.98–4.00)	(3.37–3.44)	
Gd(TPyP)(OH)	water (pH = 2)	—	430	520	560	600	Jiang et al. 1994
[Gd(TMPP)(OH)] <sub>4</sub>	water (pH = 7)	—	423	—	562	616	Jiang et al. (1994)
[Sm(TMPP)(acac)] <sub>4</sub>	DMSO	—	430 (4.53)	514 (3.38)	560 (3.44)	590 (3.15)	Radzki et al. (1987)
R(TPyP)(acac)	DMF	—	429–430	520–522	560–561	601–603	Spyroulias et al. (1995b)
R = Sm–Tb			(5.41–5.51)	(3.62–3.72)	(4.49–4.55)	(3.73–3.83)	
[R(TMPP)(acac)] <sub>4</sub>	DMF	—	452–455	517–522	574–577	619–620	Spyroulias et al. (1995b)
R = Sm–Tb			(4.88–4.98)	(3.52–3.57)	(3.87–3.95)	(3.55–3.64)	
	water	—	434–438	520–524	560–564	592–600	
			(5.17–5.31)	(3.61–3.82)	(4.15–4.27)	(3.71–3.81)	

continued on next page



Table 1, continued

Compound	Solvent	$\lambda_{\max}$ (nm) (log $\epsilon$ )				Reference	
		B(1.0)	B(0.0)	Q(2.0)	Q(1.0)		Q(0.0)
R(TSPP)(OH)(imidazole) <sub>x</sub> R = Gd–Lu	water	–	~415 (5.67–5.80)	~510 (3.51–3.62)	~545 (4.23–4.34)	~575 (3.49–3.60)	Horrocks Jr. and Hove (1978)
Na <sub>4</sub> [Sm(TSPP)(acac)]	DMSO	–	432 (4.22)	520 (3.34)	562 (3.87)	602 (3.52)	Radzki et al. (1987)
Gd(TSPP)L <sub>x</sub>	water (pH = 7)	–	419 (5.74)	514 (3.81)	552 (4.36)	587 (3.76)	Hambright et al. (1988)
Yb(TSPP)(OH)(imidazole) <sub>2</sub>	<sup>b</sup>	–	420 (5.79)	510 (3.52)	545 (4.33)	575 (3.59)	Zhuang and Gao (1995)
R(TBP)Cl <sub>x</sub> R = Y, Lu	DMF	399–403	426 (4.96–4.98)	–	580–581	627 (4.49)	Vinogradov and Wilson (1995)
R(TNTBP)(acac)	CHCl <sub>3</sub>	–	459–460 (4.76–4.80)	–	607–609 (2.91–2.94)	652–653 (3.41–3.46)	Liu et al. 1994b
R = Dy–Tm, Lu							
R(OBTPP)(acac)	CH <sub>2</sub> Cl <sub>2</sub>	357–370 (3.84–4.44)	470–475 (4.65–5.00)	546–557 (3.18–3.49)	606–615 (3.42–3.71)	663–675 (3.50–3.82)	Spyroulias and Coutsolelos (1995)
R = Sm–Lu							
Tb(TCTPP)(OAc)	CH <sub>2</sub> Cl <sub>2</sub>	–	432 (5.25)	563 (4.20)	596 (3.76)	–	Spyroulias et al. (1997)
Tb(OCTPP)(OAc)	CH <sub>2</sub> Cl <sub>2</sub>	–	460 (4.77)	553 (3.69)	598 (3.85)	652 (3.89)	
Tb(TBTPP)(OAc)	CH <sub>2</sub> Cl <sub>2</sub>	–	432 (5.20)	569 (4.15)	596 (3.64)	–	
Tb(OBTTPP)(OAc)	CH <sub>2</sub> Cl <sub>2</sub>	–	474 (4.65)	552 (3.48)	612 (3.42)	669 (3.50)	
Bisporphyrin 4a	benzene	336 (4.52)	402 (5.44)	501 (3.23)	538 (4.33)	575 (4.33)	Lachkar et al. (1997)
Bisporphyrin 4b	benzene	337 (4.49)	398 (5.48)	503 (3.15)	539 (4.24)	574 (4.22)	

continued on next page

Table 1, continued

Compound	Solvent	$\lambda_{\max}$ (nm) (log $\epsilon$ )				Reference	
		B(1,0)	B(0,0)	Q(2,0)	Q(1,0) Q(0,0)		
Sc(OEP)L							
L = acac	benzene	335	406	—	538	574	Buchler et al. (1971)
L = OAc	benzene	335	406	—	538	574	
	<i>n</i> -BuOH:3-MeC <sub>3</sub> H <sub>7</sub> (3:7)	385	404	498	534	571	Gouterman et al. (1975)
L = Cl	THF	—	398 (5.4)	—	534 (4.2)	572 (4.5)	Arnold and Hoffman (1990)
	CH <sub>2</sub> Cl <sub>2</sub>	337 (4.2)	406 (5.4)	—	538 (4.1)	576 (4.2)	Arnold et al. (1993)
L = Me	hexanes	332 (4.7)	392 (5.4)	—	534 (4.5)	576 (4.6)	
	hexanes	332 (4.6)	392 (5.4)	—	538 (4.3)	574 (4.5)	
L = CH <sub>2</sub> CMe <sub>3</sub>	CH <sub>2</sub> Cl <sub>2</sub>	—	390 (5.3)	—	530 (4.0)	570 (4.3)	
L = CH(SiMe <sub>3</sub> ) <sub>2</sub>	CH <sub>2</sub> Cl <sub>2</sub>	—	390 (5.4)	—	532 (4.1)	568 (4.4)	
L = $\eta$ -C <sub>3</sub> H <sub>5</sub>	CH <sub>2</sub> Cl <sub>2</sub>	—	390 (5.4)	—	532 (4.1)	568 (4.4)	
L = $\eta$ -C <sub>3</sub> Me <sub>5</sub>	CH <sub>2</sub> Cl <sub>2</sub>	—	402 (5.5)	—	532 (4.3)	568 (4.6)	
L = $\eta$ -C <sub>3</sub> H <sub>7</sub> Me	CH <sub>2</sub> Cl <sub>2</sub>	333 (4.3)	402 (5.4)	—	534 (4.2)	570 (4.4)	
L = $\eta$ -C <sub>9</sub> H <sub>7</sub>	CH <sub>2</sub> Cl <sub>2</sub>	332 (4.3)	402 (5.3)	—	536 (4.2)	572 (4.4)	
L = OSO <sub>2</sub> CF <sub>3</sub>	hexanes	335 (4.3)	391 (5.2)	404 (5.2)	538 (4.1)	576 (4.2)	
L = O <sup>t</sup> Bu	CH <sub>2</sub> Cl <sub>2</sub>	336 (4.1)	399 (5.5)	—	534 (4.0)	570 (4.2)	
L = OC <sub>6</sub> H <sub>2</sub> Me <sub>3</sub>	CH <sub>2</sub> Cl <sub>2</sub>	335 (4.2)	400 (5.4)	—	534 (4.1)	572 (4.3)	
L = N(SiMe <sub>3</sub> ) <sub>2</sub>	CH <sub>2</sub> Cl <sub>2</sub>	—	394	~500	537	573	Gouterman et al. (1975)
[Sc(OEP)] <sub>2</sub> O	CCl <sub>4</sub>	335 (4.6)	404 (5.7)	—	536 (4.4)	574 (4.6)	Arnold et al. (1993)
[Sc(OEP)( $\mu$ -OH)] <sub>2</sub>	CH <sub>2</sub> Cl <sub>2</sub>	334	404	—	538	574	Buchler et al. (1988)
Y(OEP)(acac)	<sup>b</sup>	383–385	402–405	—	534–536	571–573	Gouterman et al. (1976)
R(OEP)(OH) R = Y, Eu, Gd, Ho–Lu	<i>n</i> -BuOH:3-MeC <sub>3</sub> H <sub>7</sub> (3:7)						

continued on next page

Table 1, continued

Compound	Solvent	$\lambda_{\max}$ (nm) (log $\epsilon$ )				Reference	
		B(1.0)	B(0.0)	Q(2.0)	Q(1.0)		
Th(TPP)(acac) <sub>2</sub>	acetone	—	422	—	550	599	Wong (1983)
	MeOH	—	419	510	551	591	Martarano et al. (1976)
	THF	—	418 (5.66)	512 (3.93)	550 (4.36)	590 (3.79)	Tran-Thi et al. (1992)
M(TPP)L <sub>2</sub> , M = Th, U; L = acac, Cl	DMSO	—	424 (5.21)	518 (3.43)	553 (4.21)	588 (3.52)	
	<sup>b</sup>	—	418–428	509–512	550–553	586–594	Dormond et al. (1986)
M(OEP)L <sub>2</sub> , M = Th, U; L = acac, Cl	<sup>b</sup>	—	404–408	—	534–536	572–574	
M(OEP)(acac) <sub>2</sub>	PhCN	—	410–414	—	538	575–577	Kadish et al. (1989)
M = Th, U			(4.91–5.46)	—	(3.78–4.23)	(3.95–4.49)	
[Th(TPP)(OH) <sub>2</sub> ] <sub>3</sub>	THF	332	414–430	—	552–560	587–602	Kadish et al. (1988)
	THF	—	416.5 (6.05)	514.0 (4.28)	552.0 (4.83)	594.0 (4.18)	Tran-Thi et al. (1992)
CH <sub>2</sub> Cl <sub>2</sub>		—	415.8 (6.02)	515.0 (4.18)	552.0 (4.76)	588.0 (4.11)	
	<i>n</i> -C <sub>7</sub> H <sub>14</sub>	—	415.0	510.0	551.0	589.0	
[Th(OEP)(OH) <sub>2</sub> ] <sub>3</sub>	PhCN	328	396–403	—	536–539	573–575	Kadish et al. (1988)

<sup>a</sup> A  $\pi$ - $\pi^*$  transition due to the acac ligand is also observed at 298–300 nm with log  $\epsilon$  = 4.40–4.41.

<sup>b</sup> Not mentioned.

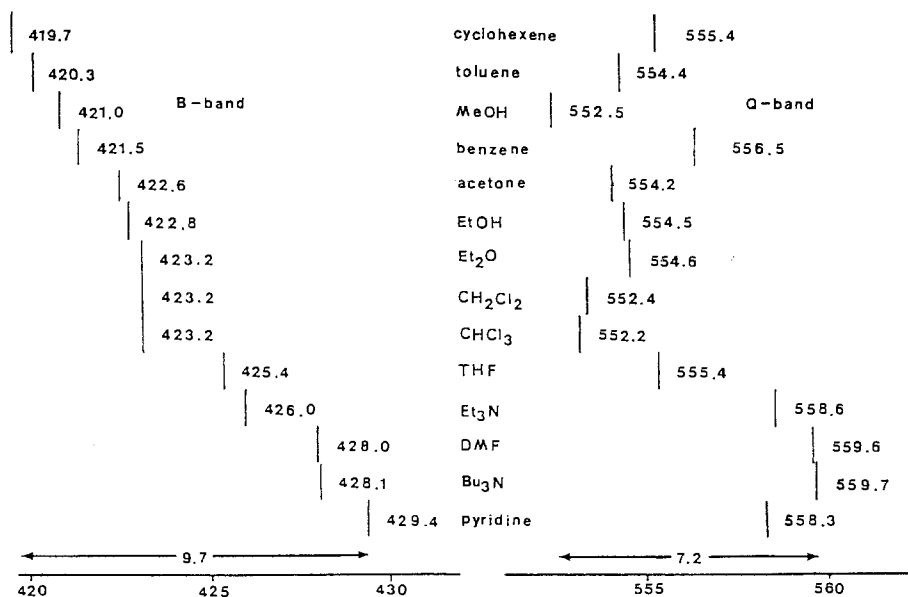


Fig. 7. Absorption positions of the B(0,0) and Q(1,0) bands of Gd(TPP)(acac) in various solvents. (From Radzki and Giannotti 1993 with permission.)

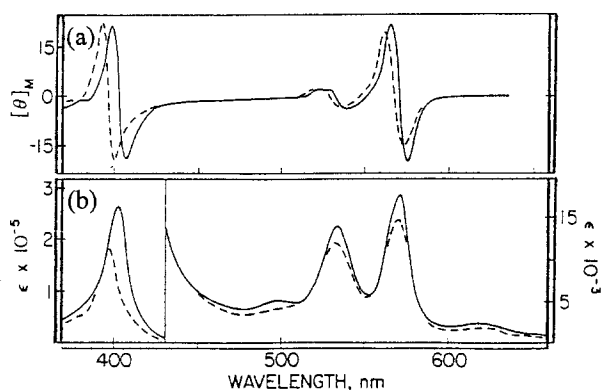


Fig. 8. (a) MCD and (b) UV-Vis spectra of Yb(Por-IX)L<sub>n</sub> (dashed curves) and Yb(Por-IX)globin (solid curves) in 0.05 M Trishydrochloride (pH 8.0). (From Horrocks Jr et al. 1975 with permission.)

Figure 9a shows the visible spectral changes of Gd(TPP)(acac) in CH<sub>2</sub>Cl<sub>2</sub> after being shaken with an aqueous solution of L-phenylalanine. The Soret band is slightly red-shifted and a small new shoulder at ~438 nm appears. Interestingly, the solution also gives CD peaks around the region of Soret and Q bands (fig. 9b). The former exhibits a reverse or normal S-shape depending on the chirality of phenylalanine; racemic D,L-phenylalanine induces no CD signals because Gd(TPP)(acac) has no chirality. This experiment shows clearly that phenylalanine is extracted from the aqueous phase into the CH<sub>2</sub>Cl<sub>2</sub> solution

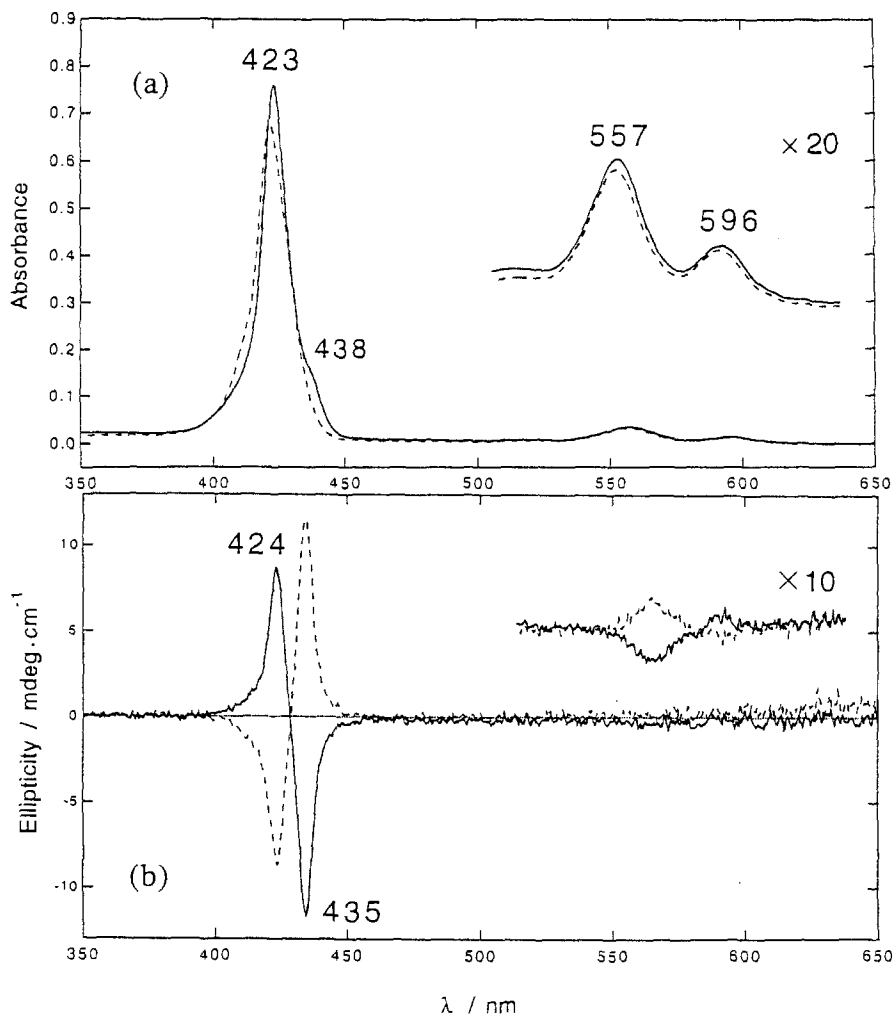


Fig. 9. (a) Visible spectra of Gd(TPP)(acac) in  $\text{CH}_2\text{Cl}_2$  after shaking with an aqueous solution of L-phenylalanine (solid curves) or water (dashed curves). (b) CD spectra of Gd(TPP)(acac) in  $\text{CH}_2\text{Cl}_2$  after shaking with an aqueous solution of L-phenylalanine (dashed) or D-phenylalanine (solid). (From Tamiaki et al. 1997 with permission.)

in which a chiral supramolecular complex is formed between the achiral Gd(TPP)(acac) and the chiral phenylalanine.

### 2.3.3. ESR spectra

ESR spectroscopy is a useful technique to characterize the porphyrinato complexes having unpaired electrons. As reported by Coutsolelos and Spyroulias (1994), all the ESR spectra of Dy(Por)(acac) (Por = TPP, ToTP, TmTP, TTP, TMP), recorded in the solid state or in

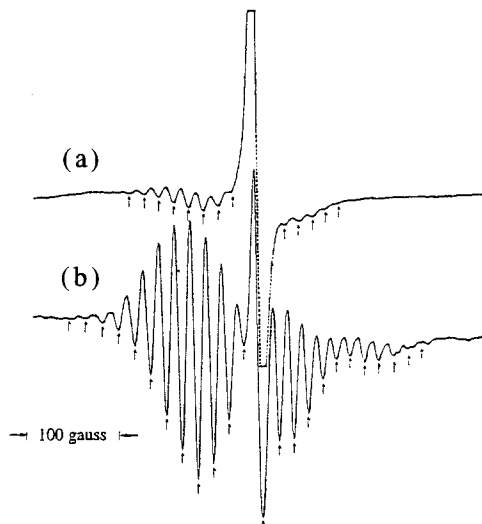


Fig. 10. ESR spectra of (a)  $\text{Eu}(\text{OBTTP})(\text{acac})$  and (b)  $[\text{Eu}(\text{TMPyP})(\text{acac})]^{4+}$  in the solid state at 290 K. (From Spyroulias and Coutsolelos 1995 with permission.)

frozen solutions in toluene, show a signal at  $g = 2.000(7)$  with a peak-to-peak separation between 7.3 and 13.6 G. Hyperfine coupling due to neighboring atoms and probably  $\text{Dy}^{\text{III}}$  ( $I = \frac{5}{2}$  for both isotopes) is only observed for the TMP analog, giving six bands with a hyperfine coupling constant of 87 G. The solid-state ESR spectra of  $\text{R}(\text{TPyP})(\text{acac})$  and  $[\text{R}(\text{TMPyP})(\text{acac})]^{4+}$  ( $\text{R} = \text{Sm}, \text{Eu}, \text{Tb}$ ) are similar, which is exemplified by the spectrum of  $[\text{Eu}(\text{TMPyP})(\text{acac})]^{4+}$  as shown in fig. 10b (Spyroulias et al. 1995b). The observed  $g$ -value ( $\sim 2.00$ ) indicates a free radical, and the hyperfine structure consists of more than 20 lines with a hyperfine coupling constant of 16.9 G, which may be attributed to a superposition of three sets of nine lines [due to four equivalent  $^{14}\text{N}$  ( $I = 1$ )] produced by the anisotropic signal. The octabromo analogs  $\text{R}(\text{OBTTP})(\text{acac})$  ( $\text{R} = \text{Sm} - \text{Lu}$ , except Gd) behave similarly with the exception that a smaller number of lines is observed in the hyperfine structure [see for example the spectrum of  $\text{Eu}(\text{OBTTP})(\text{acac})$  in fig. 10a] (Spyroulias and Coutsolelos 1995).

The ESR spectra of  $\text{Gd}^{\text{III}}$  porphyrins are remarkably different. Due to an  $^8\text{S}_{7/2}$  ground state and a long spin-lattice relaxation time, ESR spectra of  $\text{Gd}^{\text{III}}$  complexes are easily observable at all temperatures, and are usually anisotropic. As shown in fig. 11b, the ESR spectrum of  $\text{Gd}(\text{TPP})(\text{acac})$  exhibits a highly anisotropic  $g$ -factor and consists of six major peaks in the region 0–6 G. This is typical of an S-state ion with a large zero-field splitting. The OBTTP counterpart  $\text{Gd}(\text{OBTTP})(\text{acac})$ , however, gives a single broad signal with a  $g$ -value of 2.3099 (fig. 11a). The difference can be ascribed to the destabilization of the  $a_{2u}$  energy level of OBTTP compared with TPP and hence to the interaction between the porphyrin and the metal orbitals (Spyroulias and Coutsolelos 1995).

By using a time-resolved ESR technique, Ishii et al. (1996) have determined the zero-field splitting and anisotropic  $g$ -values of the half-sandwich complexes  $\text{Y}(\text{Por})(\text{acac})$  ( $\text{Por} = \text{OEP}, \text{TPP}$ ) and their double-decker derivatives in the lowest excited triplet ( $T_1$ )

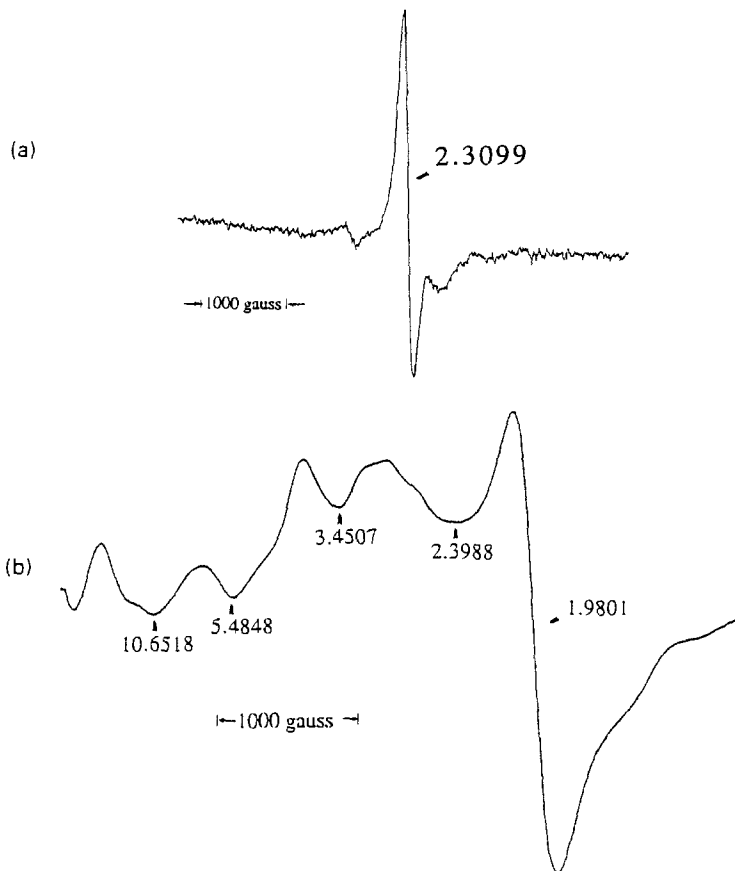


Fig. 11. ESR spectra of (a) Gd(OBTPP)(acac) and (b) Gd(TPP)(acac) in the solid state at 290 K. (From Spyroulias and Coutsolelos 1995 with permission.)

states. The zero-field splitting parameter  $D$  of  $[\text{Y}(\text{OEP})]^+$  is smaller than that of  $\text{Zn}(\text{OEP})$  and its  $g_{zz}$  is smaller than that of  $[\text{Y}(\text{TPP})]^+$ . Based on the temperature dependence of the steady-state ESR spectra, this may be due to a spin-orbit coupling between the Jahn-Teller-split  $T_1$  and  $T_2$  states. The spin density on the  $\text{Y}^{\text{III}}$  ion has been estimated as 0.011 for  $\text{Y}(\text{OEP})(\text{acac})$  in the  $T_1$  state.

#### 2.3.4. Other spectroscopic studies

Many half-sandwich porphyrinato complexes have also been characterized with IR and Raman spectroscopy. The spectra display characteristic bands due to the different vibrational modes of porphyrins and the coordinated supporting ligands (Liu et al. 1985, Wang et al. 1986, Coutsolelos and Spyroulias 1994). For the common acac complexes, the M-O stretch appears in the range  $355\text{--}364\text{ cm}^{-1}$  for  $M = \text{Sm}\text{--}\text{Lu}$  (Liu et al. 1985) and

390–410  $\text{cm}^{-1}$  for  $M=\text{Th, U}$  (Dormond et al. 1986). The acac ligand also displays two marker bands near 1570 and 1520  $\text{cm}^{-1}$  assignable to the  $\nu(\text{C}-\text{O})$  and  $\nu(\text{C}-\text{C})$  stretches (Nakamoto 1997). The  $M-\text{Cl}$  stretching band for  $M(\text{Por})\text{Cl}_2$  ( $M=\text{Th, U}$ ) appears at 255–265  $\text{cm}^{-1}$  (Dormond et al. 1986).

Tatsumi and Tsutsui (1980) studied the X-ray photoelectron spectra of  $\text{R}(\text{TPP})(\text{acac})$  ( $\text{R}=\text{Sm, Gd, Er, Yb}$ ) and  $\text{R}(\text{OEP})(\text{OH})$  ( $\text{R}=\text{Eu, Gd, Yb, Lu}$ ), and the respective metal-free porphyrins. The N 1s spectra collapse to a single peak upon complexation, with a binding energy between the corresponding metal-free porphyrin doublet. The single N 1s peak indicates that the four pyrrolic nitrogen atoms are equivalent, leading to four equalized R–N interactions. There is no significant difference in the binding energies of these lanthanide porphyrins (398.0–398.4 eV) showing that the electronegativities of lanthanides are very similar to each other. It has also been revealed that the full width at half maximum (fwhm) value of the N 1s peak is linearly related to the number of unpaired electrons in the complex. The  $\text{Gd}^{\text{III}}$  complexes, having an  $f^7$  configuration, show the largest fwhm values. The broadening can be rationalized by the multiplet splitting of the N 1s core level arising from an exchange interaction between the ionized core and unpaired valence electrons induced on the nitrogen atoms.

Similar results have also been observed for other porphyrinato complexes including  $\text{Dy}(\text{TPP})(\text{acac})$ ,  $\text{R}(\text{HTMPP})(\text{acac})$  ( $\text{R}=\text{Dy, Er}$ ),  $\text{Yb}(\text{TMPP})(\text{acac})$ ,  $\text{R}(\text{HTPP})(\text{acac})$  ( $\text{R}=\text{Ho, Tm, Yb, Lu}$ ), and  $\text{R}(\text{TPyP})(\text{acac})$  ( $\text{R}=\text{Dy, Ho, Yb, Lu}$ ) for which the C 1s (287.05–288.00), O 1s (532.00–538.15 eV), and R  $nd$  spectra have also been measured (Liu et al. 1993a,b, 1994a). It is worth noting that although the N 1s spectrum of  $\text{H}_2(\text{TPyP})$  shows three bands at 400.1, 398.0, and 398.7 eV assignable to the pyrrole NH, pyridine N, and pyrrole N atom, respectively, there is only a single peak at 398.6–399.0 eV for  $\text{R}(\text{TPyP})(\text{acac})$ , showing that the R–N and pyridine N peaks are accidentally coincident (Liu et al. 1993b).

The Mössbauer spectra of a series of  $\text{Eu}^{\text{III}}$  porphyrins  $\text{Eu}(\text{Por})(\text{acac})$  have been recorded, all of which show a singlet with unresolved quadrupole splitting (Oliver et al. 1991). The isomer shifts at 80 K (relative to  $\text{EuF}_3$ ) are in the 0–1  $\text{mm s}^{-1}$  range characterizing the  $\text{Eu}^{\text{III}}$  oxidation level. The high stability of  $\text{Eu}^{\text{III}}$  is also supported by the magnetic susceptibility data of  $\text{Eu}(\text{TPP})(\text{acac})$  (3.40 BM at 298 K), which lies in the range 3.12–3.63 BM found for trivalent europium oxide and sulfate.

#### 2.4. Electrochemical properties

Although the redox behavior of double- and triple-decker porphyrinato complexes has been well documented, the electrochemical properties of half-sandwich analogs remain little studied. The first systematic study of the electrochemistry of this class of tetrapyrrole derivatives was reported by Kadish et al. (1991). The complex  $\text{Eu}(\text{TPP})(\text{facam})$  was examined, and was found to have higher stability in the oxidized and reduced forms than the corresponding acac and tmhd analogs. The compound can be prepared by treating  $\text{Eu}(\text{TPP})(\text{acac})$  with 3-(trifluoroacetyl)camphor (Hfacam) and sodium hydroxide in an EtOH/water mixture. As shown in fig. 12, the cyclic voltammograms of  $\text{Eu}(\text{TPP})(\text{facam})$



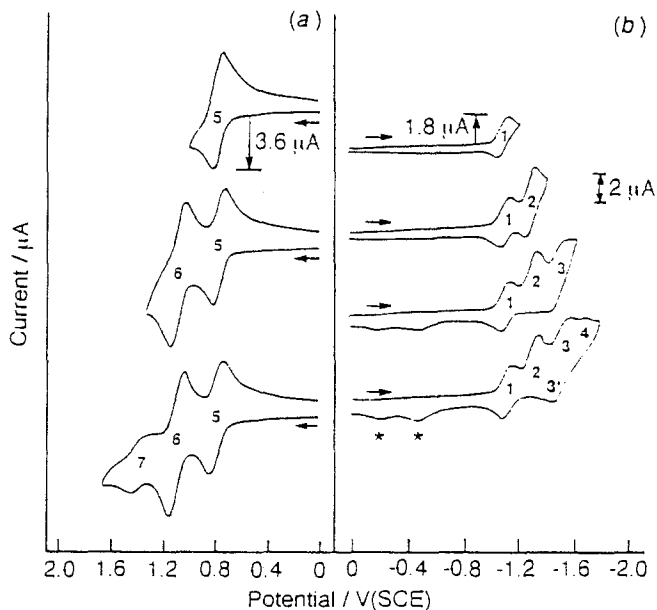
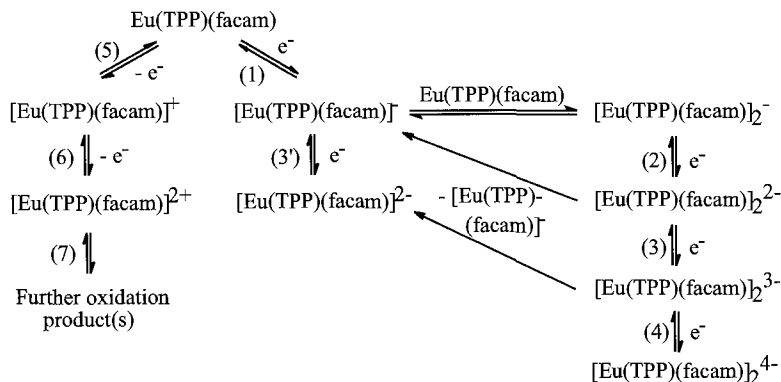


Fig. 12. Room temperature cyclic voltammograms of  $\text{Eu}(\text{TPP})(\text{facam})$  in  $\text{PhCN}$  containing  $0.1 \text{ mol dm}^{-3}$   $[\text{Bu}_4\text{N}][\text{ClO}_4]$  at a scan rate of  $1.0 \text{ V s}^{-1}$ . The starred peaks are due to reoxidation products of the decomposed reduced porphyrin and are assigned to  $\text{Eu}(\text{TPP})$  units lacking the  $\text{facam}$  axial ligand. (From Kadish et al. 1991 with permission.)

in  $\text{PhCN}$  show four reductions (labeled 1–4) and three oxidations (labeled 5–7). While the first two oxidations are characterized by a reversible one-electron transfer, each of the four reductions involves only 0.5 electron per mole of  $\text{Eu}(\text{TPP})(\text{facam})$  as revealed by controlled potential coulometry. The first two reductions are well-defined in  $\text{PhCN}$ , but one or more chemical reactions occur after peaks 2, 3, and 4, leading to a decreased anodic peak current for processes 2 and 4 and the appearance of new oxidation peaks at  $E_p = -0.45$  and  $-0.20 \text{ V}$  for a scan rate of  $1.0 \text{ V s}^{-1}$  (fig. 12). All these observations suggest the presence of both monomers and dimers in solutions and can be accounted for by the mechanism shown in scheme 8, which involves a global addition or abstraction of 2.0 electrons.

The electrochemical behavior of the  $\text{acac}$  analogs  $\text{R}(\text{TPP})(\text{acac})$  ( $\text{R} = \text{Eu-Lu}$ ) is remarkably different (Iwase and Igarashi 1993). As revealed by cyclic voltammetry and rotating-disk experiments as well as thin-layer coulometry, these compounds exhibit two oxidation waves ( $E_{1/2} = 0.60\text{--}0.76, 0.92\text{--}0.94 \text{ V}$ ) and two reduction waves ( $E_{1/2} = -1.32$  to  $-1.37, -1.67$  to  $-1.69 \text{ V}$ ), all of which correspond to a reversible one-electron transfer process. The second reduction may be associated with a dissociation reaction of the  $\text{acac}$  ligand which is supported by thin-layer spectroelectrochemistry. By contrast, the  $\text{Sm}^{\text{III}}$  analog  $\text{Sm}(\text{TPP})(\text{acac})$  undergoes four reversible oxidations ( $E_{1/2} = 0.41, 0.59, 0.80, 1.03 \text{ V}$ ) and one reversible reduction ( $E_{1/2} = -1.51 \text{ V}$ ). The coulometric results suggest that all these

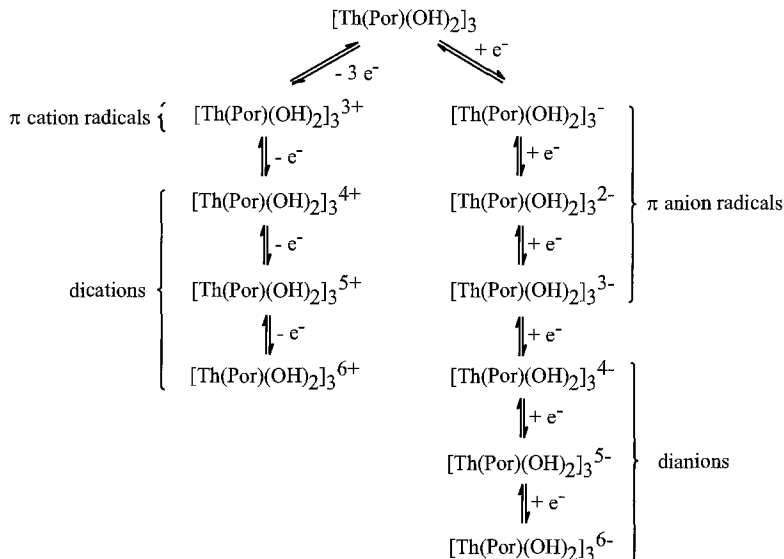


Scheme 8.

processes are attributed to the dimer  $[\text{Sm(TPP)(acac)}]_2$ . By examining the UV-Vis spectral changes during electrolysis, it has been found that all the oxidation and reduction waves for this series of compounds are due to the porphyrin ring.

The electrochemistry of the water-soluble complex  $\text{Yb(TSPP)(OH)(imidazole)}_2$  in basic, neutral, and slightly acidic solutions has also been studied (Zhuang and Gao 1995). The cyclic voltammograms show a cathodic peak at about  $-1.24$  V, which is independent of pH, while the corresponding anodic peak does not appear. This process has been attributed to a two-electron irreversible surface electrochemical reduction with the reactant strongly adsorbed on the surface of the mercury electrode. As new couples due to imidazole and metal-free porphyrin appear in the second scan, it suggests that the complex is unstable and undergoes decomposition after the reduction. By using the chronocoulometric technique which can determine the amount of electroactive reactant adsorbed on the electrode, it has also been found that a monolayer is formed in the saturation coverage of the electrode. Since the data for the ytterbium complex coincide well with those of  $\text{H}_2(\text{TSPP})$ , it can be concluded that the center of adsorption and the redox reactions is the porphyrin ring, and the  $\text{Yb}^{\text{III}}$  ion does not take part in the redox processes.

The actinide complexes  $\text{M(OEP)(acac)}_2$  ( $\text{M} = \text{Th, U}$ ) exhibit a reversible one-electron reduction ( $E_{1/2} = -1.57$  and  $-1.56$  V vs. SCE, respectively) and two oxidations ( $E_{1/2} = 0.76$  V and  $E_{\text{pc}} = 1.15$  V for  $\text{M} = \text{Th}$ ;  $E_{1/2} = 0.58$  V and  $E_{\text{pc}} = 1.26$  V for  $\text{M} = \text{U}$ ). The first oxidation is again a one-electron reversible process while the second oxidation is irreversible and couples with a fast chemical reaction. The  $\text{Th}^{\text{IV}}$  complex gives an additional irreversible oxidation at  $1.23$  V which is due to a product of the chemical reaction. During controlled potential electrolysis, the UV-Vis spectra of both complexes are changed remarkably. The Soret band due to the OEP ring is greatly attenuated during electrochemical reduction, showing that this process is porphyrin-based. The oxidation processes, however, are more complicated. Based on the spectroelectrochemical study, the first oxidation of  $\text{Th(OEP)(acac)}_2$  is also attributed to the OEP ring, but



Scheme 9.

for the uranium(IV) analog the oxidation is metal-centered with the formation of an  $U^V$  intermediate (Kadish et al. 1989).

The electrochemistry of  $[\text{Th(Por)(OH)}_2]_3$  (Por = OEP, TPP) is of particular interest as they contain three redox active metalloporphyrin units (Kadish et al. 1988). The cyclic voltammogram of the OEP complex recorded in THF at  $-72^\circ\text{C}$  shows three reversible one-electron reduction couples at  $-1.49$ ,  $-1.70$ , and  $-1.87$  V vs. SCE. As the temperature rises to room temperature, the third reduction becomes irreversible, and it has been shown that it involves a one-electron transfer followed by a fast chemical reaction (probably dissociation) and an additional one or more electron reduction (an electrochemical ECE-type mechanism). The UV-Vis spectrum of the electroreduced species  $[\text{Th(OEP)(OH)}_2]_3^-$  shows absorption bands at 411, 456, and 799 nm, and its ESR spectrum displays a signal at  $g = 2.003$ , both of which are characteristic of a porphyrin  $\pi$  radical anion. Further one-electron reduction doubles the molar absorptivities of the absorption bands at 456 and 799 nm, indicating that the second reduction is also based on porphyrin. The TPP analog  $[\text{Th(TPP)(OH)}_2]_3$  also exhibits three reversible one-electron reductions at  $-1.13$ ,  $-1.27$ , and  $-1.36$  V at  $-55^\circ\text{C}$ , which are shifted by 360–510 mV relative to the respective processes for  $[\text{Th(OEP)(OH)}_2]_3$  at  $-72^\circ\text{C}$ . Three additional irreversible reductions at  $-1.76$ ,  $-2.00$ , and  $-2.10$  V are also observed for this complex when the potential is scanned to  $-2.20$  V which may be due to the formation of dianions localized on each of the three porphyrin units. Spectroelectrochemical data also indicate that the initial three reductions occur at porphyrin based orbitals.

The oxidation processes of  $[\text{Th(Por)(OH)}_2]_3$  (Por = OEP, TPP) have also been investigated (Kadish et al. 1988). As shown by cyclic voltammetry and rotating-disk

experiments,  $[\text{Th}(\text{OEP})(\text{OH})_2]_3$  undergoes a reversible three-electron oxidation at 0.66 V in THF at  $-72^\circ\text{C}$ , which according to the spectroelectrochemical study can be assigned as removal of an electron from each of the three porphyrin rings. Three additional less well-defined oxidation processes are also revealed at 0.99–1.14 V at  $-72^\circ\text{C}$ . The TPP analog  $[\text{Th}(\text{TPP})(\text{OH})_2]_3$  also exhibits a three-electron porphyrin-based oxidation at 1.08 V, but the process is irreversible at  $-55^\circ\text{C}$  or at room temperature. The overall redox processes of these trimeric complexes are summarized in scheme 9.

### 2.5. Photophysical properties

Photophysical properties of the diamagnetic  $\text{R}(\text{TPP})(\text{acac})$  ( $\text{R} = \text{Y}, \text{Lu}$ ) and  $\text{Th}(\text{TPP})(\text{acac})_2$  have been studied by Martarano et al. (1976). Figure 13 shows the uncorrected fluorescence spectra of  $\text{Y}(\text{TPP})(\text{acac})$  in MeOH upon excitation at 400 and 425 nm. Interestingly, in addition to the normal  $\text{S}_1 \rightarrow \text{S}_0$  fluorescence bands, labeled Q(0,0) and Q(1,0), B(0,0) fluorescence is also seen in the former case, which can be attributed to an unusual emission from the second excited state,  $\text{S}_2 \rightarrow \text{S}_0$ . The lutetium(III) and thorium(IV) analogs show similar luminescence properties. The quantum yield of this Soret fluorescence is essentially the same for all three complexes ( $\Phi_f = 0.001, 0.001,$  and  $0.0004$  for  $\text{M} = \text{Y}, \text{Lu},$  and  $\text{Th}$ ), even though the atomic number increases greatly from yttrium to thorium. This absence of the heavy-atom effect indicates that the radiationless decay of  $\text{S}_2$  proceeds primarily through internal conversion, presumably to  $\text{S}_1$ . By contrast, the quantum yield of the normal fluorescence ( $\text{S}_1 \rightarrow \text{S}_0$ ) exhibits a clear heavy-atom effect ( $\Phi_f = 0.006, 0.001,$  and  $0.0001$  for  $\text{M} = \text{Y}, \text{Lu}, \text{Th}$ ) showing that this emission is mainly internally quenched by intersystem crossing to the lowest triplet state. All these compounds phosphoresce strongly at 764–779 nm ( $\Phi_p = 0.01, 0.02,$  and  $0.03$  for  $\text{M} = \text{Y}, \text{Lu}, \text{Th}$ ) with lifetimes which decrease markedly with increasing atomic number of the metal ion ( $\tau_p = 29, 2.8, 0.3$  ms).

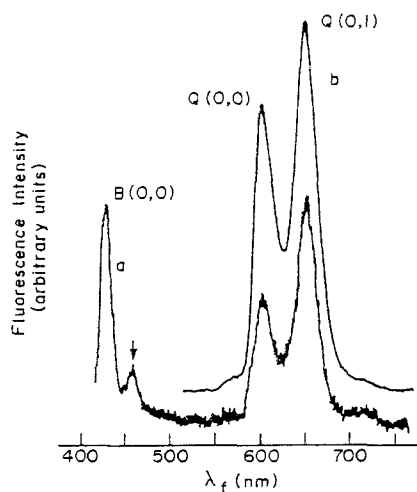


Fig. 13. Uncorrected fluorescence spectra of  $\text{Y}(\text{TPP})(\text{acac})$  in MeOH at room temperature, with excitation at (a) 400 nm and (b) 425 nm. The arrow indicates a solvent Raman peak. (From Martarano et al. 1976 with permission.)

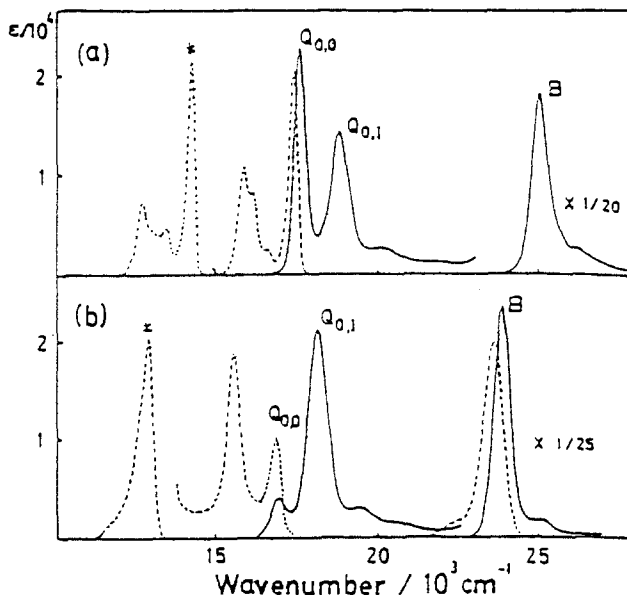


Fig. 14.  $T_1$ ,  $S_1$ , and  $S_2$  emission (dashed curves) and absorption (solid curves) spectra of (a)  $Gd(OEP)(OH)$  and (b)  $Gd(TPP)(OH)$ . The asterisks indicate phosphorescence. (From Kaizu et al. 1986 with permission.)

The paramagnetic erbium(III) porphyrins  $Er(TPP)(L)$  ( $L = OH, tmhd$ ) also fluoresce from the  $S_1$  and the  $S_2$  state, but the OEP analog  $Er(OEP)(OH)$  shows only an emission due to  $S_1 \rightarrow S_0$  (Kaizu et al. 1986). Quenching of  $S_2$  emission in the latter complex, like other diamagnetic metal OEP complexes, is attributed to a fast relaxation to the  $S_1$  state. Similarly, an  $S_2$  emission is observed for  $Gd(TPP)(OH)$  but not for  $Gd(OEP)(OH)$  (fig. 14). The  $Gd^{III}$  porphyrins also show a strong  $T_1 \rightarrow S_0$  phosphorescence even at room temperature (fig. 14) which has never been detected for  $Er^{III}$  analogs. Due to the perturbation by the paramagnetic metal ions, both  $Er^{III}$  and  $Gd^{III}$  porphyrins exhibit an enhanced rate of intersystem crossing. It leads to a strong phosphorescence for the latter complexes [ $\Phi_p = 0.01$  and  $0.001$ ,  $\tau_p = 70$  and  $34 \mu s$  for  $Gd(OEP)(OH)$  and  $Gd(TPP)(OH)$ , respectively in MeOH at room temperature], but for the former, it results in fast relaxation to the low-lying ( $f, f^*$ ) excited states and therefore  $T_1$  emission is totally quenched. There are no sizable differences in quantum yields ( $\Phi_f \approx 2.0 \times 10^{-4}$ ) and lifetimes ( $\tau_p$  of the order 0.1 ns) of the  $S_1$  emission of these  $Er^{III}$  complexes in MeOH. Upon irradiation in an absorption band of coordinated tmhd around 300 nm,  $Er(TPP)(tmhd)$  emits from both porphyrin  $S_2$  and coordinated  $\beta$ -diketone  $T_1$  states. This implies that the rate of interligand energy transfer from the  $\beta$ -diketone  $S_1$  state to the porphyrin  $S_2$  state is not as fast as intersystem crossing within the  $\beta$ -diketone. Also energy transfer between the  $\beta$ -diketone  $T_1$  and porphyrin  $S_2$  is rather inhibited.

Gouterman et al. (1976) have also reported the luminescence properties of a series of rare-earth complexes  $R(OEP)(OH)$  ( $R = Y, Eu, Gd, Ho-Lu$ ). The closed-shell yttrium(III)

and lutetium(III) complexes show moderately strong fluorescence [Q(0,0): 573–576 nm; Q(1,0): 629–630 nm] and phosphorescence [T(0,0): 698–701 nm; T(1,0): 740 nm] due to the OEP ring, with the latter having lifetimes of 55 ms (for R = Y) and 7.8 ms (for R = Lu) at 77 K. All the other open-shell lanthanide complexes exhibit weak porphyrin fluorescence [Q(0,0): 574–580 nm; Q(1,0): 630–635 nm] while the Gd<sup>III</sup> analog (f<sup>7</sup>) also shows a very strong porphyrin phosphorescence at 702 nm with a lifetime of 103 μs at 77 K. The ytterbium(III) complex Yb(OEP)(OH) (f<sup>13</sup>) also gives an f-shell emission,  $^2F_{5/2} \rightarrow ^2F_{7/2}$ , at 975 nm.

The lutetium(III) tetrabenzoporphyrin, probably having a formula of Lu(TBP)CIL<sub>x</sub>, exhibits a S<sub>1</sub> → S<sub>0</sub> fluorescence at 632 nm in DMF. It has been found that the intensity is two-fold higher for deoxygenated samples than aerated samples showing that the S<sub>1</sub> and T<sub>1</sub> excited states have relatively close energies and are in equilibrium. Due to the heavy-atom effect, this compound shows a relatively intense T<sub>1</sub> → S<sub>0</sub> phosphorescence at 803 nm in DMF at room temperature with a quantum yield of 3.5% and a lifetime of 870 μs. By contrast, the yttrium(III) analog is essentially non-emissive; both fluorescence and phosphorescence are almost too weak to be observed (Vinogradov and Wilson 1995).

Photophysical properties of Th(TPP)(acac)<sub>2</sub> have also been examined and compared with those of the trimeric species [Th(TPP)(OH)<sub>2</sub>]<sub>3</sub> (Tran-Thi et al. 1992). The fluorescence of the porphyrin <sup>1</sup>(π,π\*) state is severely quenched in both compounds (Φ<sub>f</sub> = 8–40 × 10<sup>-5</sup>, τ<sub>f</sub> = 0.25 ns in THF) due to the presence of heavy thorium(IV) center(s) giving a long-lived triplet state (τ<sub>p</sub> ≈ 208 μs). The triplet yield of the trimer (0.38), however, is drastically reduced with respect to that of the monomer (1.00) even though the former contains three thorium atoms. This has been attributed to the enhancement of the probability of deactivation of the singlet excited states via an internal conversion pathway.

### 3. Half-sandwich complexes of phthalocyanines

#### 3.1. Synthesis and reactivity

Although rare-earth phthalocyanines have a longer history than the porphyrin analogs, their chemistry has been relatively little studied. The first examples of this series of compounds were reported by Gurevich and Solov'ev (1961) who isolated the phthalocyanines of europium, gadolinium, and ytterbium in the reaction of *o*-cyanobenzamide C<sub>6</sub>H<sub>4</sub>(CN)CONH<sub>2</sub> with the corresponding metal chlorides. The composition of these compounds was not known until 1964 when Plyushchev and Shklover (1964) treated ErCl<sub>3</sub>·5H<sub>2</sub>O with phthalonitrile C<sub>6</sub>H<sub>4</sub>(CN)<sub>2</sub> in the molar ratio 1:4 at 270–280°C. Based on the analytical data, the dark green crystalline product was formulated as Er(Pc)Cl·2H<sub>2</sub>O. Analogous yttrium, lanthanum, and other rare-earth complexes can also be prepared similarly. Since the metal chlorides are hygroscopic and contain a high water of crystallization, metal formates R(HCO<sub>2</sub>)<sub>3</sub>·*n*H<sub>2</sub>O (R = Sm, Er) were used instead to prepare the corresponding phthalocyaninato complexes R(Pc)(HCO<sub>2</sub>) (Shklover and Plyushchev

1964). Kirin et al. (1965, 1967) and Kirin and Moskalev (1971) employed rare-earth acetates as the starting materials to prepare metal phthalocyaninates. It was demonstrated that apart from the monomeric half-sandwich complexes, the reactions also gave bis(phthalocyaninato) sandwich complexes, both of which remained poorly characterized at that time. These half-sandwich compounds are susceptible to de-complexation giving metal-free  $H_2(Pc)$  upon heating in *o*-bromonaphthalene or treatment with concentrated sulfuric acid (Shklover and Plyushchev 1964). When a DMF solution of  $R(Pc)Cl$  is treated with  $NH_4OH$ ,  $R(Pc)(OH)\cdot H_2O$  is formed which is thermally unstable. Upon heating to  $240^\circ C$ , this compound converts to the dimeric species  $[R(Pc)]_2O$  (Ni et al. 1987).

An alternative procedure to half-sandwich rare-earth phthalocyanines was reported by Sugimoto et al. (1982) who treated rare-earth tris(1,3-diphenyl-1,3-propanedionato) complexes  $R(dppd)_3$  ( $R = Y, Sm-Yb$ ) with  $Li_2(Pc)$  in acetone or ethylmethylketone to give the corresponding  $[R(Pc)(dppd)(Hdppd)](sol)_2$  (for  $R = Y$  or  $Sm-Tm$ ,  $sol = Me_2CO$ ; for  $R = Yb$ ,  $sol = EtCOMe$ ). The use of  $MeOH$  as solvent led to the formation of  $[R(Pc)(dppd)](MeOH)_2$  ( $R = Y, Eu-Yb$ ). The presence of solvent and the  $\beta$ -diketonato ligands in the complexes was supported by elemental analyses and spectroscopic measurements. These complexes are stable both in the solid state and in aprotic solvents, but in protic solvents such as  $MeOH$  the complexes decompose gradually to give  $H_2(Pc)$ . Interestingly, by treating  $R(tmhd)_3$  ( $R = Y, Sm-Yb$ ) with  $Li_2(Pc)$  in refluxing THF under an argon atmosphere, a series of novel bridging phthalocyaninato rare-earth dimeric complexes  $[R(tmhd)_2]_2(\mu-Pc)$  were produced which was structurally characterized for  $R = Sm$  (Sugimoto et al. 1983a). In the presence of oxygen, the reactions however gave the half-sandwich complexes  $R(Pc^{\cdot-})(tmhd)_2$  ( $R = Y, Nd, Sm-Lu$ ) in which the  $Pc$  ligand exists as a radical anion (Sugimoto et al. 1983b).

Recently, Nemykin et al. (1998) have also prepared a series of half-sandwich complexes containing a phthalocyanine radical anion. Treatment of rare-earth  $\beta$ -diketonates  $RX_3$  [ $R = Sm, Eu, Gd, Lu$ ;  $X = 1,1,1,2,2,3,3$ -heptafluoro-7,7-dimethyloctane-4,6-dionate (hfdmod), 1,1,1-trifluoro-4-phenylbutane-2,4-dionate (tfpbd) or 3-heptafluorobutyryl-D-camphorate (hfbc)] with metal-free phthalocyanine  $H_2(Pc)$  in DMSO gives the novel  $R(Pc^{\cdot-})X_2$  as red-brown crystals in up to 6% yield. The major products (up to 86%) are the normal blue  $R(Pc)X$  which contain a dianionic  $Pc$  ring. The complexes  $R(Pc)X_2$  are highly soluble in nonpolar solvents such as benzene,  $CHCl_3$ , and hexane, and the solutions remain red for a week. The complexes are even more stable in the solid state.

Treatment of  $Lu(OAc)_3 \cdot nH_2O$  with phthalonitrile in the presence of 1,8-diazabicyclo[5.4.0]undec-7-ene (DBU) in 1-hexanol gives the sandwich compound  $Lu(Pc)_2$  and the half-sandwich complex  $Lu(Pc)(OAc)(H_2O)_2$  (De Cian et al. 1985). Both compounds were structurally characterized and the latter was believed to be an intermediate in the formation of the former complex. A solid-state reaction of  $Lu(OAc)_3$  and phthalonitrile may also lead to the formation of  $Lu(Pc)(OAc)$  and  $Lu(Pc)_2$ , along with the metal-free phthalocyanine  $H_2(Pc)$ . The ratio of these products depends on the reaction temperature and reaction time (Clarisse and Riou 1987). The 1,2-naphthalocyanine analog  $Lu(1,2-Nc)(OAc)$  has recently been prepared in 56% yield by treating  $Lu(OAc)_3$  with  $Li_2(1,2-Nc)$  in 1,2,4-trichlorobenzene (Guyon et al. 1998).

Reaction of anhydrous  $R(\text{OAc})_3$  and diiminoisoindoline in refluxing DMF under an inert atmosphere affords a blue powder formulated as  $R(\text{Pc})(\text{OAc})_2\text{H}$ . The analogous  $R(\text{Pc})(\text{TTA})_2\text{H}$  (HTTA = thenoyltrifluoroacetone) and  $R(\text{Pc})(\text{NPA})$  ( $\text{H}_2\text{NPA}$  = 4-nitrophthalic acid) can also be prepared similarly using  $R(\text{TTA})_3$  and  $R(\text{HNPA})_3$  as the starting materials, respectively (Ni et al. 1987).

The first actinide phthalocyanines  $M(\text{Pc})(\text{acac})_2$  ( $M = \text{Th}, \text{U}$ ) were reported by Guillard et al. (1987). The synthesis involves the reaction of  $M(\text{acac})_4$  ( $M = \text{Th}, \text{U}$ ) with  $\text{Li}_2(\text{Pc})$  in THF (31 and 45% yield, respectively). Treatment of  $\text{MCl}_4$  with  $\text{Li}_2(\text{Pc})$  or  $\text{H}_2(\text{Pc})$ , however, does not lead to the formation of the half-sandwich complexes.

### 3.2. Structure

Structural data for half-sandwich phthalocyaninato complexes are extremely rare. Strictly speaking, only one compound in this family, namely  $\text{Lu}(\text{Pc})(\text{OAc})(\text{H}_2\text{O})_2$  (De Cian et al. 1985), has been structurally characterized so far, although the molecular structure of the bridging phthalocyaninato dimeric complex  $[\text{Sm}(\text{tmhd})_2]_2(\mu\text{-Pc})$  (Sugimoto et al. 1983a) is also known. Figure 15 shows the structure of the former complex in which the lutetium center is bound to four isoindole nitrogens of the phthalocyanine ring, two oxygen atoms of an acetate anion, and two oxygen atoms of two water molecules, forming a slightly distorted square antiprism. The lutetium atom is sandwiched between the  $\text{N}_4$  mean plane and the four-oxygen mean plane with a Lu–plane distance of 1.26 and 1.36 Å, respectively, and the two planes make a small dihedral angle of  $1.9^\circ$ . As shown in fig. 15, the phthalocyanine ring deviates largely from planarity and is convex in shape. By contrast, the phthalocyaninato ligand in  $[\text{Sm}(\text{tmhd})_2]_2(\mu\text{-Pc})$  is essentially planar and bridges two samarium atoms, each of which is coordinated by the four isoindole nitrogens of the phthalocyanine ring and by four oxygen atoms of two  $\beta$ -diketonato ligands (fig. 16).

The molecular structure of  $R(\text{Pc})\text{Cl}$  has also been calculated by the INDO method (Ni et al. 1987). The results show that, for a stable geometric configuration, the rare-earth ion is located at the central axis out of the phthalocyanine ring. As the atomic number of the metal ion decreases, the metal-to-ring distance increases from 1.50 Å (for the Lu complex) to 2.30 Å (for the La complex) and the total energy also increases from

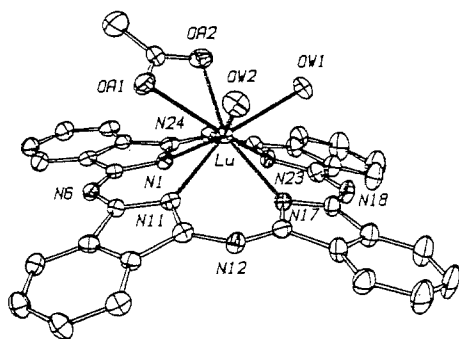


Fig. 15. ORTEP plot of  $\text{Lu}(\text{Pc})(\text{OAc})(\text{H}_2\text{O})_2$ . Ellipsoids are scaled to enclose 50% of the electron density. Hydrogen atoms are omitted. (From De Cian et al. 1985 with permission.)



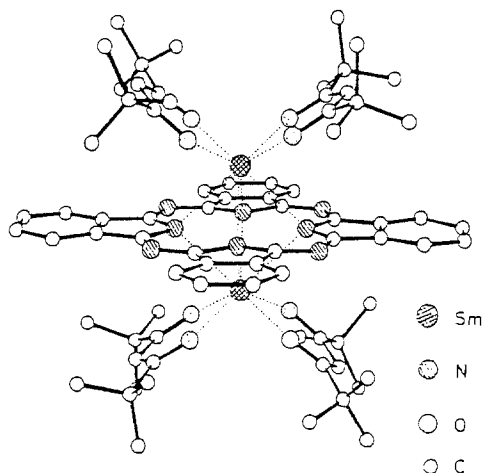


Fig. 16. Molecular structure of  $[\text{Sm}(\text{tmhd})_2]_2(\mu\text{-Pc})$ . (From Sugimoto et al. 1983a with permission.)

–335.4 au (for the Lu complex) to –195.0 au (for the La complex). This is in agreement with the experimental results showing that the  $\text{R}(\text{Pc})\text{Cl}$  complexes for heavy lanthanides can be synthesized readily, but for the light lanthanide analogs, the complexes can only be obtained with difficulty and with lower yield.

### 3.3. Spectroscopic and electrochemical properties

Half-sandwich complexes  $\text{R}(\text{Pc})\text{X}$  give typical UV–Vis spectra of metallophthalocyanines. The spectrum of  $\text{Lu}(\text{Pc})(\text{OAc})(\text{H}_2\text{O})_2$ , for example, shows a B band at 342 nm ( $\log \epsilon = 4.67$ ) and a Q band at 673 nm ( $\log \epsilon = 5.14$ ), together with two vibronic bands at 608 and 645 nm (De Cian et al. 1985). For complexes with a phthalocyanine radical anion such as  $\text{R}(\text{Pc}^{\cdot-})(\text{tmhd})_2$  ( $\text{R} = \text{Y}, \text{Nd}, \text{Sm}–\text{Lu}$ ) (Sugimoto et al. 1983b) and  $\text{R}(\text{Pc}^{\cdot-})\text{X}_2$  ( $\text{R} = \text{Sm}, \text{Eu}, \text{Gd}, \text{Lu}$ ;  $\text{X} = \beta\text{-diketonate}$ ) (Nemykin et al. 1998), the absorption spectra are remarkably different: the Q band is greatly diminished and a new radical band at  $\sim 500$  nm appears. As shown in fig. 17, the spectrum of  $\text{Tb}(\text{Pc}^{\cdot-})(\text{tmhd})_2$  shows absorption bands at  $\sim 330, 500, 620,$  and  $680$  nm. The broad band at 500 nm is characteristic of complexes having a  $\text{Pc}^{\cdot-}$  ligand such as  $\text{Li}(\text{Pc}^{\cdot-})$  and  $\text{R}^{\text{III}}(\text{Pc}^{2-})(\text{Pc}^{\cdot-})$  and is not observed in normal complexes having a  $\text{Pc}^{2-}$  ligand. Upon reduction with  $[\text{Bu}_4\text{N}][\text{BH}_4]$ , the intensity of the Q band increases dramatically and the radical band disappears, giving a normal spectrum of metallophthalocyanines. The absorption spectra of these complexes are practically independent of the nature of the central ion and the type of the axial ligand.

The presence of the phthalocyanine radical anion in  $\text{R}(\text{Pc}^{\cdot-})(\text{tmhd})_2$  ( $\text{R} = \text{Y}, \text{Nd}, \text{Sm}–\text{Lu}$ ) is also supported by the magnetic, ESR and Raman spectroscopic studies (Sugimoto et al. 1983b). The magnetic moment of the diamagnetic  $\text{Y}^{\text{III}}$  and  $\text{Lu}^{\text{III}}$  is 1.65 BM which is close to the free-spin value. Their ESR spectra, both in the solid state and in benzene solution, show a signal centered at the free-spin value at  $g = 2.001$ . The shape and  $g$ -value are characteristic of those of  $\text{H}(\text{Pc}^{\cdot-})$  and  $\text{Li}(\text{Pc}^{\cdot-})$ . Complexes with paramagnetic rare-earth elements are ESR-silent, probably due to the spin–spin relaxation

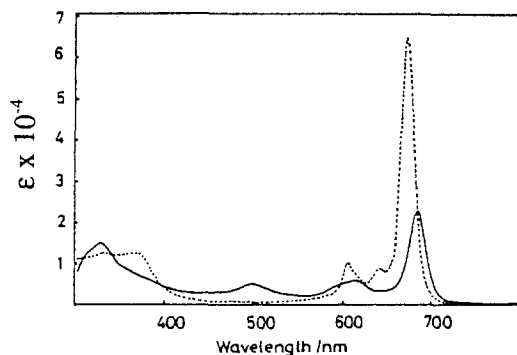


Fig. 17. Absorption spectra of  $\text{Tb}(\text{Pc}^{\ominus})(\text{tmhd})_2$  in benzene (solid curve) and upon addition of an equimolar amount of  $[\text{Bu}_4\text{N}][\text{BH}_4]$  (dashed curve). (From Sugimoto et al. 1983b with permission.)

effect. By comparing the Raman spectra of  $\text{Er}(\text{Pc}^{\ominus})(\text{tmhd})_2$ ,  $\text{Er}(\text{Pc})(\text{dppd})(\text{Hdppd})$  and  $\text{H}(\text{Pc}^{\ominus})$ , it has been found that the marker bands for  $\text{Pc}^{\ominus}$  are strong peaks at about 1600, 1170, and 1100  $\text{cm}^{-1}$ .

NMR data for half-sandwich rare-earth phthalocyanines are extremely rare. Ni et al. (1987) have measured the  $^1\text{H}$  and  $^{13}\text{C}$  NMR spectra of a series of  $\text{R}(\text{Pc})(\text{OAc})_2\text{H}$  ( $\text{R} = \text{Sm}-\text{Lu}$ ) and  $\text{R}(\text{Pc})\text{Cl}$  ( $\text{R} = \text{Er}-\text{Lu}$ ). Due to the intrinsic nature of the metal ions, the signals for the  $\alpha$  and  $\beta$  protons of the phthalocyanine ring span a wide region. Figure 18 shows the variation of  $^1\text{H}$  NMR shift of the  $\alpha$  protons and the OAc methyl protons in  $\text{R}(\text{Pc})(\text{OAc})_2\text{H}$  ( $\text{R} = \text{Sm}-\text{Yb}$ ) relative to those of the diamagnetic lutetium analog. It is noted that the  $\Delta\delta_\alpha/\Delta\delta_\beta$  values remain almost constant for these complexes, showing that the shifts are mainly due to a dipolar contribution.

The  $^1\text{H}$  NMR spectrum of the diamagnetic  $\text{Th}(\text{Pc})(\text{acac})_2$  shows a typical  $\text{AA}'\text{BB}'$  multiplet for the aromatic protons in the normal region ( $\text{H}_\alpha$ ,  $\delta$  9.61;  $\text{H}_\beta$ ,  $\delta$  8.29). Such a

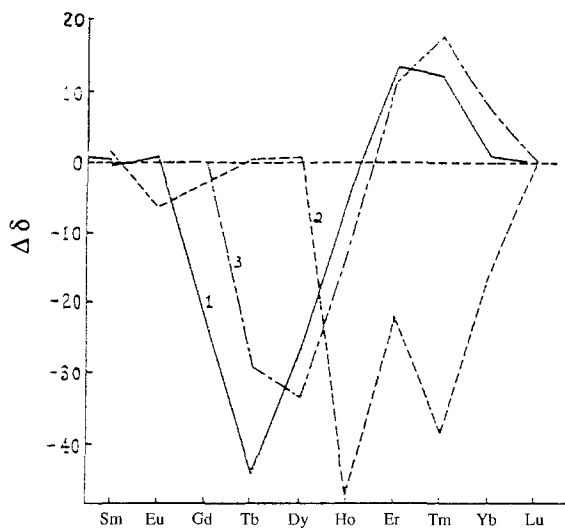


Fig. 18. Variation of  $^1\text{H}$  NMR shift of half-sandwich lanthanide phthalocyanines: (1)  $\alpha$  protons; (2) methyl protons of the OAc group; (3) induced shift calculated by Bleaney's equation. (From Ni et al. 1987 with permission.)

multiplet is also observed for the  $H_\alpha$  ( $\delta$  6.73) and  $H_\beta$  ( $\delta$  5.86) protons in the paramagnetic complex  $U(Pc)(acac)_2$ , but is upfield-shifted by approximately 3 ppm. The methine and methyl protons of  $Th(Pc)(acac)_2$  give bands at  $\delta$  4.45 and 1.50, respectively, while the corresponding proton signals for the uranium analog appear at  $\delta$  13.04 and  $-7.91$ . These data suggest that these two complexes are *cis*-coordinated by two acetylacetonate ligands and have the metal ion out of the macrocyclic ring (Guilard et al. 1987).

The electrochemistry of  $Lu(Pc)(OAc)_2H$  has also been studied (Ni et al. 1987). The complex undergoes a reversible one-electron oxidation at 0.58–0.65 V vs. SCE and a quasi-reversible one-electron reduction at  $-0.98$  to  $-1.09$  V, depending on the solvents. The electron-transfer rate constants for both redox processes in different solvents have also been calculated: they range from 0.9 to 3.6  $cm\ s^{-1}$ . Similarly, the naphthalocyanine analog  $Lu(1,2-Nc)(OAc)$  also exhibits one oxidation (0.36 V vs. ferrocenium/ferrocene) and one reduction process ( $-1.28$  V vs. ferrocenium/ferrocene) as revealed by cyclic voltammetry (Guyon et al. 1998).

The actinide complexes  $M(Pc)(acac)_2$  ( $M=Th, U$ ) undergo two reversible one-electron reductions (for  $M=Th$ ,  $E_{1/2}=-0.85$  and  $-1.29$  V; for  $M=U$ ,  $E_{1/2}=-0.83$  and  $-1.28$  V), and one reversible one-electron oxidation (for  $M=Th$ ,  $E_{1/2}=0.73$  V; for  $M=U$ ,  $E_{1/2}=0.79$  V) in PhCN. The potential difference between the first oxidation and the first reduction of these complexes (1.58–1.62 V) is comparable with the average separation (1.56 V) between the highest occupied and the lowest unoccupied molecular orbitals of other metallophthalocyanines when both the oxidation and the reduction occur at the conjugated  $\pi$ -ring system. According to the coulometric studies and by observing the UV–Vis and ESR spectral changes during electrolysis, it can also be concluded that all of these processes involve a one-electron transfer in the Pc ring. The two reductions are also reversible on the spectroelectrochemical time scale, but the first oxidation is not reversible on a time scale of 5–8 min.

#### 4. Outlook

In the previous sections, the current status of studies of the half-sandwich porphyrinato and phthalocyaninato rare-earth and actinide complexes including their synthesis, spectroscopy, and electrochemistry has been summarized. By incorporating the intriguing electronic and optical properties of the tetrapyrrole derivatives and the unique nature, in particular the paramagnetic properties, of the heavy metal centers, these complexes are potentially useful as biological probes for biomolecules, imaging agents, and photosensitizers in photodynamic therapy, and may also find applications in materials science, although studies in these directions are still in their infancy. We hope the grounding provided in this article will stimulate further research into this novel and important family of complexes.

## References

- Arnold, J., and C.G. Hoffman, 1990, *J. Am. Chem. Soc.* **112**, 8620.
- Arnold, J., C.G. Hoffman, D.Y. Dawson and F.J. Hollander, 1993, *Organometallics* **12**, 3645.
- Babushkina, T.A., L.G. Koreneva and V.F. Zolin, 1986, *Magn. Reson. Chem.* **24**, 1026.
- Bertini, I., A.G. Coutsolelos, A. Dikiy, C. Luchinat, G.A. Spyroulias and A. Troganis, 1996, *Inorg. Chem.* **35**, 6308.
- Brand, H., and J. Arnold, 1995, *Coord. Chem. Rev.* **140**, 137.
- Buchler, J.W., and P. Hammerschmitt, 1991, *Liebigs Ann. Chem.* 1177.
- Buchler, J.W., and D.K.P. Ng, 2000, in: *The Porphyrin Handbook*, Vol. 3, eds K.M. Kadish, K.M. Smith and R. Guilard (Academic Press, San Diego, CA) ch. 20.
- Buchler, J.W., G. Eikermann, L. Puppe, K. Rohbock, H.H. Schneehage and D. Weck, 1971, *Liebigs Ann. Chem.* **745**, 135.
- Buchler, J.W., H.-G. Kapellmann, M. Knoff, K.-L. Lay and S. Pfeifer, 1983, *Z. Naturforsch. B* **38**, 1339.
- Buchler, J.W., A. De Cian, J. Fischer, M. Kihn-Botulinski, H. Paulus and R. Weiss, 1986, *J. Am. Chem. Soc.* **108**, 3652.
- Buchler, J.W., J. Hüttermann and J. Löffler, 1988, *Bull. Chem. Soc. Jpn.* **61**, 71.
- Chabach, D., M. Lachkar, A. De Cian, J. Fischer and R. Weiss, 1992, *New J. Chem.* **16**, 431.
- Chabach, D., M. Tahiri, A. De Cian, J. Fischer, R. Weiss and M. El Malouli Bibout, 1995, *J. Am. Chem. Soc.* **117**, 8548.
- Chabach, D., A. De Cian, J. Fischer, R. Weiss and M. El Malouli Bibout, 1996, *Angew. Chem. Int. Ed. Engl.* **35**, 898.
- Clarisse, C., and M.T. Riou, 1987, *Inorg. Chim. Acta* **130**, 139.
- Coutsolelos, A.G., and G.A. Spyroulias, 1994, *Polyhedron* **13**, 647.
- De Cian, A., M. Moussavi, J. Fischer and R. Weiss, 1985, *Inorg. Chem.* **24**, 3162.
- Dormond, A., B. Belkalem and R. Guilard, 1984, *Polyhedron* **3**, 107.
- Dormond, A., B. Belkalem, P. Charpin, M. Lance, D. Vigner, G. Folcher and R. Guilard, 1986, *Inorg. Chem.* **25**, 4785.
- Girolami, G.S., S.N. Milam and K.S. Suslick, 1987, *Inorg. Chem.* **26**, 343.
- Gouterman, M., L.K. Hanson, G.-E. Khalil, J.W. Buchler, K. Rohbock and D. Dolphin, 1975, *J. Am. Chem. Soc.* **97**, 3142.
- Gouterman, M., C.D. Schumaker, T.S. Srivastava and T. Yonetani, 1976, *Chem. Phys. Lett.* **40**, 456.
- Guilard, R., A. Dormond, M. Belkalem, J.E. Anderson, Y.H. Liu and K.M. Kadish, 1987, *Inorg. Chem.* **26**, 1410.
- Gurevich, M.G., and K.N. Solov'ev, 1961, *Dokl. Akad. Nauk SSSR* **5**, 291.
- Guyon, F., A. Pondaven, J.-M. Kerbaol and M. L'Her, 1998, *Inorg. Chem.* **37**, 569.
- Hambright, P., C. Adams and K. Vernon, 1988, *Inorg. Chem.* **27**, 1660.
- Haye, S., and P. Hambright, 1988, *J. Chem. Soc., Chem. Commun.*, p. 666.
- Haye, S., and P. Hambright, 1991, *J. Coord. Chem.* **22**, 315.
- Horrocks Jr, W.DeW., and E.G. Hove, 1978, *J. Am. Chem. Soc.* **100**, 4386.
- Horrocks Jr, W.DeW., and C.-P. Wong, 1976, *J. Am. Chem. Soc.* **98**, 7157.
- Horrocks Jr, W.DeW., R.F. Venteicher, C.A. Spilburg and B.L. Vallee, 1975, *Biochem. Biophys. Res. Commun.* **64**, 317.
- Ishii, K., Y. Ohba, M. Iwaizumi and S. Yamauchi, 1996, *J. Phys. Chem.* **100**, 3839.
- Iwase, A., and A. Igarashi, 1993, *Electrochim. Acta* **38**, 689.
- Jasat, A., and D. Dolphin, 1997, *Chem. Rev.* **97**, 2267.
- Jiang, J., K. Machida and G. Adachi, 1994, *J. Rare Earths* **12**, 161.
- Jiang, J., T.C.W. Mak and D.K.P. Ng, 1996, *Chem. Ber.* **129**, 933.
- Jiang, J., W. Liu, J. Lin and D.K.P. Ng, 1997a, *Huaxue Tongbao*, p. 14.
- Jiang, J., R.L.C. Lau, T.W.D. Chan, T.C.W. Mak and D.K.P. Ng, 1997b, *Inorg. Chim. Acta* **255**, 59.
- Jiang, J., D.K.P. Ng and J. Xie, 1998a, *Univ. Chem.* **13**, 6.
- Jiang, J., W. Liu, W.-F. Law and D.K.P. Ng, 1998b, *Inorg. Chim. Acta* **268**, 49.
- Jiang, J., M.T.M. Choi, W.-F. Law, J. Chen and D.K.P. Ng, 1998c, *Polyhedron* **17**, 3903.
- Jiang, J., T.-D. Hu, J.-L. Xie, C. Li and J.-Z. Zhang, 1998d, *Chin. J. Chem.* **16**, 425.
- Jiang, J., D.K.P. Ng, D. Du and S. Sun, 1999a, *Univ. Chem.* **14**, 5.

- Jiang, J., D.K.P. Ng, W. Liu, J. Xie and S. Sun, 1999b, *Huaxue Tongbao*, p. 2.
- Jiang, J., J. Xie, M.T.M. Choi, Y. Yan, S. Sun and D.K.P. Ng, 1999c, *J. Porphyrins Phthalocyanines* **3**, 322.
- Jiang, J., D. Du, M.T.M. Choi, J. Xie and D.K.P. Ng, 1999d, *Chem. Lett.*, p. 261.
- Kadish, K.M., Y.H. Liu, J.E. Anderson, P. Charpin, G. Chevrier, M. Lance, M. Nierlich, D. Vigner, A. Dormond, B. Belkalem and R. Guilard, 1988, *J. Am. Chem. Soc.* **110**, 6455.
- Kadish, K.M., Y.H. Liu, J.E. Anderson, A. Dormond, M. Belkalem and R. Guilard, 1989, *Inorg. Chim. Acta* **163**, 201.
- Kadish, K.M., G. Moninot, J.-M. Barbe and R. Guilard, 1991, *J. Chem. Soc., Chem. Commun.*, p. 1124.
- Kadish, K.M., G. Moninot, Y. Hu, D. Dubois, A. Ibnlfassi, J.-M. Barbe and R. Guilard, 1993, *J. Am. Chem. Soc.* **115**, 8153.
- Kadish, K.M., K.M. Smith and R. Guilard, eds, 2000, *The Porphyrin Handbook* (Academic Press, San Diego, CA).
- Kaizu, Y., M. Asano and H. Kobayashi, 1986, *J. Phys. Chem.* **90**, 3906.
- Kirin, I.S., and P.N. Moskalev, 1971, *Russ. J. Inorg. Chem.* **16**, 1687.
- Kirin, I.S., P.N. Moskalev and Y.A. Makashev, 1965, *Russ. J. Inorg. Chem.* **10**, 1065.
- Kirin, I.S., P.N. Moskalev and Y.A. Makashev, 1967, *Russ. J. Inorg. Chem.* **12**, 369.
- Kochnev, D.O., B.N. Solomonov and A.N. Vedernikov, 1991, *Mendeleev Commun.*, p. 117.
- Lachkar, M., A. De Cian, J. Fischer and R. Weiss, 1988, *New J. Chem.* **12**, 729.
- Lachkar, M., A. Tabard, S. Brandès, R. Guilard, A. Atmani, A. De Cian, J. Fischer and R. Weiss, 1997, *Inorg. Chem.* **36**, 4141.
- Leznoff, C.C., and A.B.P. Lever, eds, 1989–96, *Phthalocyanines, Properties and Applications*, 4 volumes (VCH, New York).
- Liu, G., Y. Zhang and W. Xu, 1985, *J. Chin. Rare Earth Soc.* **3**, 81.
- Liu, G., Z. Ma and X. Liu, 1993a, *Synth. React. Inorg. Met. Org. Chem.* **23**, 1145.
- Liu, G., Z. Ma, X. Liu and D. Li, 1993b, *Acta Chim. Sinica* **51**, 791.
- Liu, G., T. Shi and X. Liu, 1994a, *Polyhedron* **13**, 2255.
- Liu, G., T. Shi, X. Cao and X. Liu, 1994b, *Synth. React. Inorg. Met. Org. Chem.* **24**, 1127.
- Lomova, T.N., L.G. Andrianova and B.D. Berezin, 1987, *Zh. Fiz. Khim.* **61**, 2921.
- Lomova, T.N., L.G. Andrianova and B.D. Berezin, 1988, *Koord. Khim.* **14**, 453.
- Lomova, T.N., L.G. Andrianova and B.D. Berezin, 1989, *Zh. Neorg. Khim.* **34**, 2867.
- Martarano, L.A., C.-P. Wong, W.DeW. Horrocks Jr and A.M.P. Goncalves, 1976, *J. Phys. Chem.* **80**, 2389.
- Marzola, P., and S. Cannistraro, 1987, *Physiol. Chem. Phys. Med. NMR* **19**, 279.
- Nakamoto, K., 1997, *Infrared and Raman Spectra of Inorganic and Coordination Compounds*, 5th Ed. (Wiley, New York).
- Nemykin, V.N., V.Y. Chernii and S.V. Volkov, 1998, *J. Chem. Soc., Dalton Trans.*, p. 2995.
- Ng, D.K.P., and J. Jiang, 1997, *Chem. Soc. Rev.* **26**, 433.
- Ni, J., F. Shi, Z. Li and S. Yin, 1987, *Inorg. Chim. Acta* **139**, 165.
- Oliver, F.W., C. Thomas, E. Hoffman, D. Hill, T.P.G. Sutter, P. Hambright, S. Haye, A.N. Thorpe, N. Quoc, A. Harriman, P. Neta and S. Mosseri, 1991, *Inorg. Chim. Acta* **186**, 119.
- Plyushchev, V.E., and L.P. Shklover, 1964, *Russ. J. Inorg. Chem.* **9**, 183.
- Radzki, S., and C. Giannotti, 1993, *Inorg. Chim. Acta* **205**, 213.
- Radzki, S., and C. Giannotti, 1994, *J. Photochem. Photobiol. A Chem.* **80**, 257.
- Radzki, S., and P. Krausz, 1995, *Monatsh. Chem.* **126**, 51.
- Radzki, S., and P. Krausz, 1996, *Monatsh. Chem.* **127**, 51.
- Radzki, S., P. Krausz, S. Gaspard and C. Giannotti, 1987, *Inorg. Chim. Acta* **138**, 139.
- Schaverien, C.J., 1991, *J. Chem. Soc., Chem. Commun.*, p. 458.
- Schaverien, C.J., and A.G. Orpen, 1991, *Inorg. Chem.* **30**, 4968.
- Sessler, J.L., and S.J. Weghorn, 1997, *Expanded, Contracted & Isomeric Porphyrins* (Pergamon Press, Oxford).
- Sessler, J.L., G. Hemmi, T.D. Mody, T. Murai, A. Burrell and S.W. Young, 1994, *Acc. Chem. Res.* **27**, 43.
- Sewchok, M.G., R.C. Haushalter and J.S. Merola, 1988, *Inorg. Chim. Acta* **144**, 47.
- Shklover, L.P., and V.E. Plyushchev, 1964, *Russ. J. Inorg. Chem.* **9**, 186.
- Spyroulias, G.A., and A.G. Coutsolelos, 1995, *Polyhedron* **14**, 2483.

- Spyroulias, G.A., and A.G. Coutsolelos, 1996, *Inorg. Chem.* **35**, 1382.
- Spyroulias, G.A., A.G. Coutsolelos, C.P. Raptopoulou and A. Terzis, 1995a, *Inorg. Chem.* **34**, 2476.
- Spyroulias, G.A., M.P. Sioubara and A.G. Coutsolelos, 1995b, *Polyhedron* **14**, 3563.
- Spyroulias, G.A., A. Despotopoulos, C.P. Raptopoulou, A. Terzis and A.G. Coutsolelos, 1997, *Chem. Commun.* 783.
- Srivastava, T.S., 1978, *Bioinorg. Chem.* **8**, 61.
- Srivastava, T.S., 1980a, *Curr. Sci.* **49**, 429.
- Srivastava, T.S., 1980b, *Curr. Sci.* **49**, 900.
- Sugimoto, H., T. Higashi and M. Mori, 1982, *Chem. Lett.* 801.
- Sugimoto, H., T. Higashi, A. Maeda, M. Mori, H. Masuda and T. Taga, 1983a, *J. Chem. Soc., Chem. Commun.*, p. 1234.
- Sugimoto, H., T. Higashi and M. Mori, 1983b, *Chem. Lett.*, p. 1167.
- Tamiaki, H., N. Matsumoto and H. Tsukube, 1997, *Tetrahedron Lett.* **38**, 4239.
- Tatsumi, K., and M. Tsutsui, 1980, *J. Am. Chem. Soc.* **102**, 882.
- Tran-Thi, T.H., A. Dormond and R. Guillard, 1992, *J. Phys. Chem.* **96**, 3139.
- Tsukube, H., M. Wada, S. Shinoda and H. Tamiaki, 1999, *Chem. Commun.*, p. 1007.
- Vedernikov, A.N., D.O. Kochnev, D.A. Suslov and B.N. Solomonov, 1993, *Dokl. Akad. Nauk* **330**, 200.
- Vinogradov, S.A., and D.F. Wilson, 1995, *J. Chem. Soc., Perkin Trans. 2*, p. 103.
- Wang, W., Y. Yang and J. Zhang, 1986, *Chin. J. Appl. Chem.* **3**, 58.
- Wei, C.-C., W.-S. Hsu, Y. Tominaga, J.-C. Tsai and C.-Y. Chai, 1993, *Nucl. Instr. Meth. Phys. Res. B* **75**, 195.
- Wong, C.-P., 1983, *Inorg. Synth.* **22**, 156.
- Wong, C.-P., and W.DeW. Horrocks Jr, 1975, *Tetrahedron Lett.* 2637.
- Wong, C.-P., R.F. Venteicher and W.DeW. Horrocks Jr, 1974, *J. Am. Chem. Soc.* **96**, 7149.
- Wong, W.-K., L. Zhang, W.-T. Wong, F. Xue and T.C.W. Mak, 1999, *J. Chem. Soc., Dalton Trans.*, p. 615.
- Zhuang, Q.-K., and X.-X. Gao, 1995, *Electrochim. Acta* **40**, 959.

## SUBJECT INDEX

- Abragam relaxation 93, 101  
absorption spectra of complexes 644  
absorption X-ray spectra of polysulfides 605  
acid solvolysis 617  
actinide intermetallics 140  
actinide monochalcogenides 154–170  
actinide mononictides 154–170  
activation volume 558  
adiabatic calorimetry of polysulfides 594  
AlB<sub>2</sub> superstructures 486  
AlB<sub>2</sub> type 464  
Al<sub>75.5</sub>Mn<sub>20.5</sub>Si<sub>4</sub> 281  
α-CeS<sub>2</sub> 596, 603  
α-LaS<sub>2</sub> 589, 590, 596, 601, 603  
α'-LaS<sub>2</sub> 590, 604  
α-NdS<sub>2</sub> 603, 605  
α-PrS<sub>2</sub> 605  
α-YbAuBi 484  
α-YbAuGe 474  
α-YbPdSn 476  
amino acids 629  
amino acids probe 618  
amorphous atomic structure 277  
amorphous materials 172, 268, 272, 277–279  
– a-R–Co 8  
– a-R–Fe 8  
– a-SmCo<sub>2</sub> 49  
– a-SmFe<sub>1.6</sub> 49  
– a-(SmFe<sub>2</sub>)<sub>99.26</sub>B<sub>0.74</sub> 49  
– a-Sm(Fe<sub>0.58</sub>Co<sub>0.42</sub>)<sub>1.54</sub> 49  
– a-(Tb,Dy)<sub>0.42</sub>Fe<sub>0.58</sub> 22  
– a-(Tb,Dy)(Fe,Co)<sub>n</sub> 47  
– a-(Tb,Dy)(Fe,Co) 16  
– a-(Tb<sub>1-x</sub>Dy<sub>x</sub>)<sub>0.42</sub>Fe<sub>0.58</sub> 22  
– a-TbCo<sub>2</sub> 49  
– a-Tb<sub>0.27</sub>Dy<sub>0.73</sub>Co<sub>2</sub> 49  
– a-Tb<sub>0.27</sub>Dy<sub>0.73</sub>Fe<sub>2</sub> 49  
– a-Tb<sub>0.27</sub>Dy<sub>0.73</sub>(Fe<sub>0.45</sub>Co<sub>0.55</sub>)<sub>2</sub> 49  
– a-TbFe<sub>2</sub> 49  
– a-Tb(Fe<sub>0.45</sub>Co<sub>0.55</sub>)<sub>2</sub> 49  
– a-Tb(Fe<sub>0.55</sub>Co<sub>0.45</sub>)<sub>1.5</sub> 48
- AnAl<sub>2</sub> 185  
AnT<sub>2</sub> 191  
AnX compounds 154–170  
AnX<sub>2</sub> compounds 178, 179  
AnX<sub>3</sub> compounds 175  
analysis of polysulfides 575  
anisotropic bonded Sm–Fe–N magnet 556  
anisotropic spin fluctuations 120, 124, 127, 135, 136, 210  
anisotropy  
– after deposition under magnetic polarisation field 48  
– after HDDR processing 533  
– axial 134  
– biaxial 26  
– CEF 120, 127, 217  
– coefficient 13  
– constant 36  
– contributions 35  
– field-annealing induced 32  
– magnetic 167, 211, 277, 340, 342  
– magneto-crystalline 214  
– multilayers 38  
– parallel 21  
– perpendicular 17, 21  
– pseudogap 296, 312  
– random 30  
– uniaxial 32  
anomalous f-element 154  
anomalous rare earth 285  
antiferromagnetic (AF) ordering in YbTX phases 488, 492  
antimonides YbTSb 481  
apomyoglobin 617, 629  
array of particles in W/Fe/W 559  
Arrhenius law 206, 212  
arsenides 480  
asperomagnetic state 172  
asperomagnetism 277  
atomic-exchange-interaction (AEI) 559  
atomization energy 597

- Au–Au contacts 470  
 Au–Au interlayer bonding 481  
 aurophilicity 470  
 autocorrelation function 272  
 BCS (Bardeen–Cooper–Schrieffer)  
   – interaction 250  
   – superconductors 292, 379  
 band structure  
   – near the Fermi level of rare-earth magnets 524  
   – of compounds having 2p electrons 519  
   – of lanthanide–transition-metal (3d–4f) compounds 519, 524  
 bcc-Fe 522  
 Bessel function 118, 181, 232, 253, 303, 322, 379, 395, 397, 405  
 $\beta$ -LaS<sub>2</sub> 578, 589, 590, 596, 603  
 $\beta$ -YbAuBi 484  
 $\beta$ -YbAuGe 474  
 $\beta$ -YbPdSn 476  
 Bi<sub>2</sub>Sr<sub>2</sub>(Ca,Y)Cu<sub>2</sub>O<sub>-8</sub> 266  
 Bi<sub>1-2</sub>Sr<sub>-2</sub>CaCu<sub>2</sub>O<sub>-8</sub> 265  
 Bi<sub>2</sub>Sr<sub>2</sub>(Nd,Ce)Cu<sub>2</sub>O<sub>-8</sub> 266  
 Bi<sub>1-2</sub>Sr<sub>-2</sub>(Nd,Ce)Cu<sub>2</sub>O<sub>-8</sub> 265  
 bilinear ferromagnetic interaction 171  
 biquadratic exchange 189  
 bismuthides YbTbBi 483  
 bonded magnets 555, 556  
 borocarbide superconductors 253  
 Brillouin function 129, 132, 163, 189, 213, 216, 226, 228, 230, 232, 240, 267, 326, 357, 372  
 CEF (crystalline electric field) 120, 127, 140, 142, 145, 150, 152, 165, 185, 202, 209, 210, 213, 217, 227, 237, 254, 282, 287, 303, 376, 380  
   – anisotropy 498  
   – interactions 310  
   – splitting 142, 144, 145, 147, 148, 191, 252, 296, 300, 304, 305, 326, 343, 383, 390, 401, 411, 493, 605  
 CaCuGe type 473  
 CaCu<sub>5</sub> structure 520  
 Caln<sub>3</sub> type 457  
 canonical spin glass 268  
 catalytic cyclic trimerization of phenyl isocyanate 622  
 catalytic oxidation of unsaturated hydrocarbons 622  
 Ce–S system 571, 580  
 CeAg 171, 172  
 CeAg<sub>0.97</sub>In<sub>0.03</sub> 171, 172  
 CeAgSb<sub>2</sub> 234  
 CeAl<sub>2</sub> 179–181, 286, 292  
 CeAl<sub>3</sub> 181, 286, 321, 322  
 CeAs 156, 162, 164, 165  
 Ce<sub>3</sub>Au<sub>3</sub>Sb<sub>4</sub> 286, 350  
 CeB<sub>6</sub> 96, 97, 286, 327  
 CeBa<sub>2</sub>Cu<sub>3</sub>O<sub>6+ $\delta$</sub>  260  
 Ce<sub>3</sub>Bi<sub>4</sub>Pt<sub>3</sub> 293  
 CeCoGe<sub>3</sub> 403  
 CeCoGe<sub>3-x</sub>Si<sub>x</sub> 394, 403  
 CeCu<sub>5</sub> 210, 286, 323, 324  
 CeCu<sub>6</sub> 286, 328, 397  
 Ce(Cu<sub>1-x</sub>Ni<sub>x</sub>)<sub>2</sub>Ge<sub>2</sub> 394, 402  
 CeCu<sub>5-x</sub>Al<sub>x</sub> 323, 324  
 CeCu<sub>5</sub>Au 395, 396  
 CeCu<sub>5.5</sub>Au<sub>0.5</sub> 397, 398  
 CeCu<sub>5.7</sub>Au<sub>0.3</sub> 396  
 CeCu<sub>5.9</sub>Au<sub>0.1</sub> 395, 397  
 CeCu<sub>6-x</sub>Au<sub>x</sub> 394–396, 398  
 CeCu<sub>5-x</sub>Ga<sub>x</sub> 273, 323  
 CeCu<sub>2</sub>Ge<sub>2</sub> 334, 402  
 CeCu<sub>x</sub>Ni<sub>1-x</sub>Sn 273, 292, 306–308  
 CeCu<sub>0.1</sub>Ni<sub>0.9</sub>Sn 294  
 CeCu<sub>0.2</sub>Ni<sub>0.8</sub>Sn 274  
 CeCu<sub>2</sub>Si<sub>2</sub> 286, 331, 332  
 CeCu<sub>2.2</sub>Si<sub>2</sub> 276  
 CeCu<sub>2</sub>(Si<sub>1-x</sub>Ge<sub>x</sub>)<sub>2</sub> 334  
 CeCuSn 218  
 CeCu<sub>2</sub>Sn<sub>2</sub> 286, 342, 347  
 CeCu<sub>2</sub> structure 460  
 CeFe<sub>2</sub> 13  
 CeFe<sub>2</sub>Ge<sub>2</sub> 341  
 Ce<sub>3</sub>Fe<sub>4</sub>P<sub>12</sub> 293  
 CeGa<sub>6</sub> 215  
 CeGe 232  
 Ce<sub>0.85</sub>La<sub>0.15</sub>NiSn 294  
 Ce<sub>0.9</sub>La<sub>0.1</sub>RhSb 294  
 Ce<sub>0.87</sub>La<sub>0.13</sub>Ru<sub>2</sub>Si<sub>2</sub> 339  
 Ce<sub>1-x</sub>La<sub>x</sub>Ru<sub>2</sub>Si<sub>2</sub> 335  
 Ce<sub>0.95</sub>La<sub>0.05</sub>Ru<sub>2</sub>Si<sub>2</sub> 335  
 Ce<sub>7</sub>Ni<sub>3</sub> 286, 394, 403, 404, 406  
 CeNi<sub>2</sub>Ge<sub>2</sub> 402  
 CeNiSn 286, 293–296, 298–300  
 CePb<sub>3</sub> 286, 323  
 CePd<sub>3</sub> 292, 408  
 CePd<sub>2</sub>Al<sub>3</sub> 286, 347  
 Ce<sub>3</sub>Pd<sub>20</sub>Ge<sub>6</sub> 351  
 CePdSb 286, 316, 317



- $\text{Ce}_3\text{Pd}_{20}\text{Si}_6$  351  
 $\text{CePdSn}$  286, 294, 301  
 $\text{CePd}_2\text{Sn}_2$  286, 342, 346  
 Ce polysulfides 580, 602  
 $\text{CePt}_x\text{Ni}_{1-x}\text{Sn}$  305, 308  
 $\text{CePt}_{0.12}\text{Ni}_{0.88}\text{Sn}$  294  
 $\text{CePt}_{0.2}\text{Ni}_{0.8}\text{Sn}$  294  
 $\text{CePt}_2\text{Si}_2$  286, 394, 406  
 $\text{CePtSn}$  232, 286, 294, 295, 301, 302  
 $\text{CePt}_2\text{Sn}_2$  268, 273, 286, 333, 342–345  
 $\text{CeRhAs}$  293  
 $\text{CeRh}_3\text{B}_2$  286, 348, 349  
 $\text{CeRhSb}$  286, 293–295, 312–314  
 $\text{CeRh}_2\text{Si}_2$  222, 224, 286  
 $\text{CeRu}_2$  189, 208, 286, 292, 319, 320  
 $\text{Ce}(\text{Ru}_{1-x}\text{Fe}_x)_2\text{Ge}_2$  340, 341  
 $\text{Ce}(\text{Ru}_{0.85}\text{Rh}_{0.15})_2\text{Si}_2$  339  
 $\text{Ce}(\text{Ru}_{1-x}\text{Rh}_x)_2\text{Si}_2$  335  
 $\text{CeRu}_2\text{Ge}_2$  286, 340, 341  
 $\text{CeRu}_2(\text{Ge}_{1-x}\text{Si}_x)_2$  341  
 $\text{CeRuSi}_2$  286, 329, 330  
 $\text{CeRu}_2\text{Si}_2$  286, 335–337  
 $\text{CeS}_2$  578, 589, 590, 597, 599, 604, 605  
 $\text{CeS}_{2.53}$  580  
 $\text{CeSb}$  156, 166, 286, 292  
 $\text{Ce}_3\text{Sb}_4\text{Pt}_3$  293  
 $\text{CeSi}$  232  
 $\text{CeSn}_3$  292, 408, 409  
 $\text{CeTSn}$  293–304, 308  
 $\text{Ce}_{0.74}\text{Th}_{0.26}$  410  
 $\text{Ce}_{1-x}\text{Th}_x$  292, 409  
 chemical bonding 477, 485, 599, 600  
 chemical kinetics 65  
 chemical properties  
   – polysulfides 571  
   –  $\text{YbTX}$  487  
 chemical stability of  $\text{YbTX}$  487  
 circular dichroism 618  
   – probes 629  
 coercive fields 47  
 coercivity 548  
   – of anisotropic  $\text{Nd}_2\text{Fe}_{14}\text{B}$ -based magnets 536  
   – temperature coefficient of 537  
 coexistence of superconductivity and magnetism  
   251–254, 257, 259, 260, 267, 285, 317, 334,  
   339, 352, 367, 370, 376  
 coherence of spin fluctuations 311  
 cold grown  $(\text{Tb}_{0.3}\text{Dy}_{0.7})_{1-x}\text{Fe}_x$  47  
 collinear spin structure 193  
 colossal magnetoresistance (CMR) 246  
   compensation point 190  
   competing interactions 236, 237  
   compositional classification of polysulfides 570  
   compression molding 556  
   conduction electrons 154, 239, 287  
   – compressibility 139  
   – density 185  
   conical spin structure 118, 132, 137, 277  
   contact field 89, 96, 130, 133, 137, 138, 185,  
   190, 240  
   continuous beam 73  
   Coqblin–Schrieffer model 493  
   correlation functions 124, 135  
   correlation lengths 127, 275, 353, 371, 398,  
   399  
   critical concentration 306, 307, 311, 395, 403  
   critical exponent 120, 133, 137  
   critical phenomena 120, 128, 203, 211, 216, 225,  
   228, 240, 246, 340, 352  
   critical pressure 395, 404, 412  
   criticality class 120, 128  
   crystal growth  
   – disulfides 584  
   – heterophase crystallization 585  
   – indifferent solvents 584  
   – morphology 586  
   – polysulfides 583, 584  
   crystalline disorder 399  
   crystallization temperature 19  
   crystallographic formulas 593  
   cubic compounds 142, 152  
   cuprates 255–267  
   Curie–Weiss behavior 488  
   Curie temperature 12–14  
   –  $\text{a-TbCo}_2$  14  
   –  $\text{a-TbFe}_2$  14  
   – amorphous RT alloys 15  
   – concentration dependence 15  
   cyclic voltammograms 640  
  
 d-electron density 307, 311, 409  
 3d electron density 341  
 3d–3d exchange coupling 48  
 3d–5d hybridisation 10  
 decoupling 100, 101, 103, 263, 271, 273, 283,  
   306, 333, 403  
 demagnetizing field 90, 185  
 density functional methods 483  
 density of states (DOS) 287, 296, 462  
   – rare-earth magnet 525

- density of states (DOS) (*cont'd*)  
 –  $\text{Y}_2\text{Fe}_{17}$  and  $\text{Y}_2\text{Fe}_{17}\text{N}_3$  compounds 518, 520
- diffuse spin motion 161, 317
- dilute spin glass 269, 270, 277
- dipolar field 89, 129, 137
- dipolar interactions 127
- dipolar sums 89, 117, 133, 134, 159, 167, 179, 194, 206, 223, 230, 328, 410
- disordered magnetism 109, 118, 235, 247, 267–284, 305, 311, 326, 336, 344, 373, 375, 381, 384, 385, 399, 405
- dissociation reactions  
 – thermochemical characteristics 598, 599  
 – thermochemical parameters 598
- disulfides 573, 599
- domain magnetization 91, 107
- domain wall motions 20, 33
- double-decker complexes 620
- drop calorimetry of polysulfides 594
- Dy–S system 581  
 – phase diagrams 580
- DyAg 102, 172–174, 272, 277–279
- DyAl<sub>2</sub> 179, 184, 185
- DyBa<sub>2</sub>Cu<sub>3</sub>O<sub>6+ $\delta$</sub>  262
- DyD<sub>2,0</sub> 209
- DyD<sub>2,13</sub> 209
- DyFe<sub>2</sub> 13
- DyFeO<sub>3</sub> 244
- Dy metal 133–135, 138, 139
- DyMn<sub>2</sub> 204, 205
- DyNi<sub>2</sub> 189, 191
- DyNi<sub>5</sub> 213
- Dy polysulfides 602
- DyS<sub>1,76</sub> 578, 589, 592, 593
- DyS<sub>1,83</sub> 586
- DyS<sub>1,84</sub> 578, 589, 592, 593, 597, 598, 600, 604
- DyS<sub>2</sub> 604
- DySb 156, 167
- (Dy<sub>1-x</sub>Y<sub>x</sub>)Mn<sub>2</sub> 205
- dynamic cluster 180
- dynamic depolarization 100
- dynamic relaxation 94, 108
- dynamical scaling 212
- $E_g$  form 604
- EPR (electron paramagnetic resonance) 63  
 – spectra 494
- ESR (electron spin resonance) spectra 636–638, 648  
 – low-temperature 604
- easy axis 143  
 – in Gd 127
- easy magnetisation direction (EMD) 14, 17
- effective charges 604
- effective mass 284, 287
- electric field gradient 498
- electric potential 141
- electrical properties  
 – polysulfides 602, 603  
 – YbTX phases 495–497
- electrochemical potentials between grain-boundary phases and the Nd–Fe–B and Nd–(Fe,Co,Ni)–B main phases 550
- electrochemical properties 639, 648
- electron correlations 284
- electron count 464, 481
- electron localization function ELF 472
- electron paramagnetic resonance, *see* EPR
- electron spin resonance, *see* ESR
- electron–nuclear relaxation 110, 117, 194, 269, 314, 354
- electronegativities 482
- electronic absorption spectra 628
- electronic moment 89, 92
- electronic specific-heat coefficient 501
- electronic structure 462, 601, 602
- emission 644
- enthalpy of formation of polysulfides 597  
 – measurement techniques 597
- entropy of polysulfides 596  
 – CeS<sub>2</sub> 595  
 – LaS<sub>2</sub> 595
- equiatomic aluminides YbTAl 456
- equiatomic gallides YbTGa 463
- Er–S system 580
- Er–S system, pressure-dependent phase diagram 582
- ErAl<sub>2</sub> 179, 184
- ErBa<sub>2</sub>Cu<sub>3</sub>O<sub>6+ $\delta$</sub>  263
- ErFe<sub>2</sub> 13, 189
- ErFe<sub>6</sub>Al<sub>6</sub> 235
- Er metal 120, 133, 136, 138
- ErNi<sub>5</sub> 213, 214
- ErNi<sub>2</sub>B<sub>2</sub>C 254
- Er polysulfides 580, 602
- ErRh<sub>4</sub>B<sub>4</sub> 251
- ErS<sub>1,75</sub> 578
- ErS<sub>1,85</sub> 578, 582, 598, 605
- Eu–S system 571, 576
- EuAs<sub>3</sub> 209

- EuAuGe type 468  
 EuBa<sub>2</sub>Cu<sub>3</sub>O<sub>6+δ</sub> 260  
 EuBa<sub>2</sub>Cu<sub>3</sub>O<sub>-7</sub> 265  
 EuO 120, 239, 240  
 Eu(OBTPP)(acac) 637  
 EuPdAs 292, 410, 411  
 Eu polysulfides 577  
 EuS<sub>1.90</sub> 605  
 [Eu(TMPP)(acac)]<sup>4+</sup> 637  
 Eu(TPP)(facam) 640  
 Eu(TTP)(acac) 626  
 exchange-coupled magnets 517, 540–547  
 – (BH)<sub>max</sub> > 1 MJ/m<sup>3</sup> (120 MGOe) 541  
 – multi-phase permanent magnet flakes and powders 544  
 – multilayer thin films 541  
 exchange-coupling parameter 15  
 exchange energies 15, 26, 29  
 exchange field 15  
 exchange interactions 4, 15  
 exchange-spring-magnets, *see* exchange-coupled magnets  
 exciton condensation 412  
 extended domain wall (EDW) 41  
 extended Hückel calculations 458  
 extended Zintl formulation 467  
 extrusion technique 556
- 4f charge density 5, 11  
 f-electron delocalization 61, 154, 188, 285, 290  
 f-electron magnetism 251  
 FFLO state 320, 376  
 FFT (fast Fourier transform) 111, 114, 256, 339  
 4f magnetism 61, 124  
 5f magnetism 61  
 FTr<sub>2</sub>B<sub>2</sub>C (F = R, Th, U) 253  
 4f–5d exchange interaction mechanism 11  
 4f–3d exchange interactions 14, 518  
 fast fluctuation limit 100, 103, 124, 126, 272, 318, 337  
 fast Fourier transform, *see* FFT  
 Fe–Fe interatomic distances 521, 522  
 Fe<sub>2</sub>B 533, 534  
 Fe<sub>3</sub>B 534, 546  
 Fe<sub>3</sub>B/Nd<sub>2</sub>Fe<sub>14</sub>B nanocomposite magnet 552  
 Fe<sub>3</sub>B–Nd<sub>2</sub>Fe<sub>14</sub>B nanostructures 543  
 FeCo nanostructure layers 49  
 Fe<sub>65</sub>Co<sub>35</sub> phase 541
- Fe K-edge absorption spectra of the series of R<sub>2</sub>Fe<sub>14</sub>B compounds 525  
 Fe K-edge integrated XMCD signals 526  
 – for R<sub>2</sub>Fe<sub>14</sub>B compounds 526  
 Fe oxides 550  
 Fe<sub>2</sub>P-type structure 459  
 FeSi 293  
 FeSiBNbCu (Finemet) 48  
 Fermi liquid 289, 291, 328, 335, 363, 364  
 Fermi-liquid-type behavior in YbTX phases 496  
 ferromagnetic (F) ordering  
 – α-CeS<sub>2</sub> 596  
 – YbTX phases 488  
 ferromagnetic Kondo lattice 493  
 field anisotropy 126  
 field cancellation 277  
 field correlation 125  
 field distribution 93, 95, 97, 104, 144, 162, 256, 269, 273–276, 283, 309, 322, 338, 339, 358  
 field fluctuations 95, 100, 103, 124, 160, 182, 215, 389  
 Finemet 48  
 fluctuation rate 94, 100, 102, 104, 125  
 fluorescence spectra 643  
 Fourier components 153, 155, 161  
 frustration 267, 279–281
- (Ga,Nb)- and (Cu,Nb)- dopants 528  
 γ-YbAuGe 474  
 γ-Fe dendritic phases 547  
 γ-LaS<sub>2</sub> 590, 603  
 gap  
 – charge 297  
 – closure 299, 304–306, 314, 315  
 – formation 247, 293  
 – Haldane 283  
 – spin 297  
 Gaussian 93, 97, 100, 103, 114, 272  
 Gaussian-broadened Gaussian 274, 308  
 GdAl<sub>2</sub> 179, 184  
 GdBa<sub>2</sub>Cu<sub>3</sub>O<sub>6+δ</sub> 261  
 GdBa<sub>2</sub>Cu<sub>3</sub>O<sub>-7</sub> 265  
 GdCo<sub>2</sub> 189  
 GdFe<sub>2</sub> 13, 189  
 Gd/Fe multilayers 40  
 GdGa<sub>6</sub> 216, 217  
 Gd<sub>3</sub>Ga<sub>5</sub>O<sub>12</sub> 280  
 Gd<sub>2</sub>In 232  
 Gd<sub>x</sub>La<sub>1-x</sub>Al<sub>2</sub> 186

- Gd metal 78, 84, 106, 120, 126, 128–131  
 GdMn<sub>2</sub> 202, 203  
 GdNi<sub>2</sub> 189, 191  
 GdNi<sub>5</sub> 120, 210, 212, 228, 380  
 Gd(OBTTPP)(acac) 638  
 Gd(OEP)(OH) 644  
 Gd polysulfides 577, 580, 602  
 GdRh<sub>4</sub>B<sub>4</sub> 252  
 GdS<sub>1.84</sub> 598  
 GdS<sub>1.85</sub> 598  
 Gd(TPP)(OH) 644  
 Gd(TPP)(acac) 635, 638  
 Gd<sub>x</sub>U<sub>1-x</sub>Al<sub>2</sub> 186  
 Gd<sub>0.696</sub>Y<sub>0.304</sub> 231  
 germanides YbTGe 471  
 giant magnetoresistance 245–248  
 giant magnetostriction 1–50  
 grain-boundary phase in Nd–Fe–B magnets 529  
 grain-boundary phases of Nd(Ni,Fe) and/or Nd(Co,Fe) compounds 549  
 Griffiths phase 311, 400
- H<sub>2</sub>CrO<sub>4</sub> 549  
 HDDR (hydrogenation, disproportionation, desorption, recombination) process 516, 530  
 – Nd–Fe–B 557  
 HD (hydrogenation–disproportionation) process 534  
 HF, *see* heavy-fermion  
 HF (hydrofluoric acid) 549  
<sup>1</sup>H NMR spectra 626  
 HP–YbCuAl 457  
 HP–YbNiAl 457  
 H<sub>3</sub>PO<sub>4</sub> 549  
 HT–YbAuSi 467  
 H<sub>2</sub>(TTP) 626  
 half-sandwich, *see* tetrapyrrole complexes  
 Hall coefficient 497  
 Hall measurements 496  
 hard magnets 248–250  
 – *see also* permanent magnets  
 heat capacity 595, 596  
 – CeS<sub>2</sub> 595  
 – DyS<sub>1.84</sub> 595  
 – LaS<sub>2</sub> 595  
 – NdS<sub>2</sub> 595  
 – PrS<sub>2</sub> 595  
 – SmS<sub>2</sub> 595  
 heavy-atom effect 643  
 heavy-fermion antiferromagnet 488  
 heavy-fermion behavior 154, 169, 176, 197, 285, 287, 292, 293, 296, 361, 364, 383, 384, 403, 518  
 heavy-fermion compounds 284, 393, 488  
 heavy-fermion materials 210, 276  
 heavy-fermion systems 319–393, 500  
 heavy-hole gas 304  
 heavy-hole state 313  
 heavy-mass state 501  
 Heisenberg ferromagnet 117, 128, 212, 239  
 helical spin structure 132, 134, 196  
 Helmholtz coils 76, 89  
 heterogeneous magnetic materials 50  
 HfRhSn 475  
 high-energy-product magnets 526, 529  
 – Nd–Fe–B (444 kJ/m<sup>3</sup>) 530  
 high magnetic fields 82, 224  
 high-pressure investigations of YbTX 502  
 high-symmetry site 157, 162, 174, 176, 223, 233, 356, 377  
 high-temperature modification of YbAuSi 468  
 high-T<sub>c</sub> superconductivity 255  
 Hill behavior 154, 175, 191  
 histogram 76  
 HoAl<sub>2</sub> 179, 184  
 HoBa<sub>2</sub>Cu<sub>3</sub>O<sub>6+δ</sub> 260, 262  
 HoBa<sub>2</sub>Cu<sub>3</sub>O<sub>7</sub> 150, 254  
 HoD<sub>2,0</sub> 209  
 HoD<sub>2,12</sub> 209  
 HoF<sub>3</sub> 243  
 HoFe<sub>2</sub> 13  
 Ho<sub>2</sub>Fe<sub>14</sub>B 249  
 HoFeO<sub>3</sub> 244  
 Ho<sub>2</sub>In 233  
 Ho<sub>0.7</sub>Lu<sub>0.3</sub>Rh<sub>4</sub>B<sub>4</sub> 252  
 Ho metal 132, 133, 138, 139  
 HoMo<sub>6</sub>S<sub>8</sub> 251  
 HoNi<sub>2</sub> 189  
 HoNi<sub>2</sub>, 191  
 HoNi<sub>2</sub>B<sub>2</sub>C 253  
 Ho polysulfides 577  
 HoRh<sub>4</sub>B<sub>4</sub> 252  
 homogeneity ranges  
 – hypostoichiometric polysulfides 576, 577  
 – YbAuIn 465  
 homologous series R<sub>n</sub>S<sub>2n-1</sub> 582  
 hopping 115, 121, 148, 361  
 Hund's rule 142  
 hybridization 154, 191, 221, 287, 290, 293, 295, 296, 301, 307, 334, 341, 394, 395

- hydrogen states 65
- hydrogenation disproportionation desorption  
recombination, *see* HDDR
- hydrogenation–disproportionation, *see* HD  
process
- hydrolyzability 465
- hyperfine coupling 146, 147
- hyperfine field 89
- hyperfine interaction 497
- hyperstoichiometric polysulfides 573
- hypostoichiometric polysulfides 574, 600  
– crystal growth 584
- hysteresis 110, 194, 204, 330  
– Tb<sub>0.27</sub>Dy<sub>0.73</sub>Co<sub>2</sub> thin film 30
- i-Gd<sub>3</sub>Mg<sub>42</sub>Zn<sub>50</sub> 282
- IR absorption spectra 604
- IR transmission spectra 604
- i-Tb<sub>8</sub>Mg<sub>42</sub>Zn<sub>50</sub> 282
- i-Dy<sub>8</sub>Mg<sub>42</sub>Zn<sub>50</sub> 283
- implantation depth 88
- impurities 289, 295, 298, 356, 358, 374
- incommensurate magnetic structure 491
- incommensurate spin density wave 254, 336,  
339
- incommensurate spin structure 118, 181, 216,  
227, 255, 301, 323, 335, 379, 387, 404
- indium and thallium compounds YbTlIn and YbTTl  
464
- induced-moment spin glass 149, 310
- inelastic neutron scattering 505
- inhomogeneity 177, 178, 198, 200
- inhomogeneous behavior 234
- inhomogeneous broadening 94, 182, 184
- inhomogeneous freezing 187, 270, 276, 277
- inhomogeneous magnetic order 309
- inhomogeneous magnetic properties 332
- inhomogeneous magnetism 305, 369, 374, 384,  
387
- inhomogeneous transition 323
- initial asymmetry 68, 110, 113
- injection molding magnets 556
- insulators 70, 115, 238, 265
- interaction parameter  $\eta$  560
- intergranular diffusion 551
- interlayer interactions 468
- interlayer Sn–Sn bonding 477
- intermediate valence 291, 292, 318, 348,  
408–412, 494
- interstitial field 63
- interstitial site 70, 115
- interstitial susceptibility 96
- isomer shift 498
- isostructural lines  
– RS<sub>1.70</sub> 591  
– RS<sub>1.76</sub> 591  
– RS<sub>1.85</sub> 590, 591  
– RS<sub>1.90</sub> 590  
– RS<sub>2</sub> 589–591
- isotropic Sm<sub>2</sub>Fe<sub>17</sub>N<sub>3</sub> powders 540
- isotropy 97, 99
- isotypical lines of polysulfides 570, 571, 582,  
583
- itinerant magnet 233
- itinerant magnetism 160, 193, 201, 291, 352
- i-Y<sub>8</sub>Mg<sub>42</sub>Zn<sub>50</sub> 283
- J* multiplets 141
- Jahn–Teller effect 242
- Jander's model 551
- jump process 201
- jump time 122
- KHg<sub>2</sub> structure 460
- KHg<sub>2</sub> superstructures 471
- Kagomé systems 193, 268, 273, 279, 333, 345
- kinetics 617
- Knight shift 82, 89, 93, 95, 128, 146, 148, 149,  
152, 164, 166, 171, 185, 210, 213, 220, 265,  
298, 300, 313, 325, 356, 362, 365, 367, 368,  
373, 378, 379, 405, 408, 409, 412
- Kondo disorder 397, 399, 403
- Kondo effect 306, 487, 518  
– two-channel 397, 400
- Kondo impurities 495
- Kondo insulators 291, 293–319, 408
- Kondo interaction 293, 301, 313, 314, 325, 342,  
383, 388, 390, 394, 496  
– multichannel 394
- Kondo lattice 154, 273, 276, 318, 338, 382
- Kondo metals 224, 293–319
- Kondo minimum 495
- Kondo model 290
- Kondo necklace 290, 291, 311, 330, 341, 342,  
388, 407
- Kondo screening 342
- Kondo semiconductors 291
- Kondo semimetals 291, 293–319
- Kondo temperature 287, 290, 306, 337

- Korrington relaxation 117, 183, 195, 215, 296, 391, 403  
 Kramers ion 144  
 Kubo–Toyabe 98, 103, 114  
 Kubo golden rule (KGR) 275  
  
 $L_{III}$  absorption edge measurements 504  
 $L_{III}$  absorption spectra 493  
 LMTO band structure calculations 480  
 LT-YbAuSi 467  
 $L_3$  XANES spectrum 504  
 $L$ – $S$  coupling of  $R \leftrightarrow Fe$  moments 526  
 (La,Sr)<sub>2</sub>CuO<sub>4</sub> 257  
 (La,Tb)<sub>2/3</sub>Ca<sub>1/3</sub>MnO<sub>3</sub> 246  
 La–Lu system 578, 579  
 La–S system 571  
 LaAg<sub>1-x</sub>In<sub>x</sub> 171  
 LaAl<sub>2</sub> 180  
 La<sub>1-x</sub>Ca<sub>x</sub>MnO<sub>3</sub> 246  
 La<sub>0.15</sub>Ce<sub>0.85</sub>NiSn 298, 304  
 La<sub>x</sub>Ce<sub>1-x</sub>RhSb 312–314  
 La<sub>0.1</sub>Ce<sub>0.9</sub>RhSb 313  
 LaCuO<sub>2.5</sub> 284  
 La<sub>2</sub>CuO<sub>4</sub> 257  
 LaF<sub>3</sub> 243  
 La<sub>1.6-x</sub>Nd<sub>0.4</sub>Sr<sub>x</sub>CuO<sub>4</sub> 258  
 LaNi<sub>5</sub> 210  
 LaNiO<sub>3</sub> 245  
 LaNi<sub>2</sub>Si<sub>2</sub> 222  
 La polysulfides 577, 580, 602  
 LaS 168  
 LaS<sub>2</sub> 578, 589, 597, 601, 604  
 LaS<sub>2.33</sub> 573  
 LaSn<sub>3</sub> 408  
 La<sub>2-x</sub>Sr<sub>x</sub>CuO<sub>4</sub> 244, 256  
 La<sub>1-x</sub>Sr<sub>x</sub>MnO<sub>3</sub> 246  
 La<sub>0.74</sub>Th<sub>0.26</sub> 410  
 lanthanide intermetallics 140  
 lanthanide metals 123  
 lanthanide–transition metal compounds 10  
 Larmor precession 67  
 lattice defect 121  
 lattice parameters of polysulfides 589  
 lattice pressures 197  
 Laves-phase compounds  
   – RCo<sub>2</sub> 12  
   – RFe<sub>2</sub> 11  
 least-squares fitting 112  
 Level Crossing Resonance 62, 82  
 LiGaGe-type structure 457  
  
 LiHoF<sub>4</sub> 243  
 LiTbF<sub>4</sub> 243  
 ligand electrons 154  
 linear muffin-tin orbital (LMTO) method 517  
 linewidth 498  
 local field 88, 116, 129  
 local field cancellation 157, 160, 162, 174, 177, 234, 355, 377  
 local moment 374, 376  
 local shrinkage and expansion in  $c$ -plane of Th<sub>2</sub>Fe<sub>17</sub> crystal structure 523  
 local-spin-density approximation 522  
 local spin-density functional (LSDF) method 517  
 localized magnets 219  
 localized moments 285  
 Lorentz field 90  
 Lorentzian 95, 98, 104, 114, 149, 162, 173, 177, 199, 269  
 low-carrier heavy-fermion systems 155  
 low-carrier systems 292, 350, 383, 385, 386, 408  
 low-energy excitations 338  
 LuFe<sub>2</sub> 189  
 LuNiO<sub>3</sub> 245  
 LuRh<sub>4</sub>B<sub>4</sub> 252  
  
 MORE facility 74, 80  
 magnesium and zinc compounds YbTMg and YbTZn 485  
 magnetic after-effects 558  
 magnetic anisotropy 107, 140, 150, 167, 213, 227  
 magnetic annealing 48  
 magnetic circular dichroism 629  
 magnetic domains 106  
 magnetic excitation 146  
 magnetic frustration 140, 193, 197, 199, 201, 206, 233, 235, 279, 319, 343, 381  
 magnetic hysteresis loops, sandwich Tb–Co/Nd–Co/Tb–Co 43  
 magnetic instability 175, 311, 328, 334, 348, 390, 394, 400, 404, 406, 407  
 magnetic insulation among grains 551  
 magnetic interactions 3  
 magnetic moment  
   – 3d-sublattice 32  
   – lanthanide sublattice 16, 32  
 magnetic phase diagram 201, 208, 218, 219, 225, 245, 256, 258, 266, 308, 311, 358, 402

- magnetic phase transition temperature 47  
 magnetic polaron 246  
 magnetic properties  
   – of polysulfides 603, 604  
   – of  $YbTX$  phases 487–495  
 magnetic short-range order 495  
 magnetic softness 48  
 magnetic subsites 122, 159, 182  
 magnetic superconductors, *see* coexistence of  
   superconductivity and magnetism  
 magnetic susceptibility, high field 30  
 magnetic X-ray scattering 64, 243, 355  
 magnetization  
   – field-annealing effects 30  
   – saturation 13, 14  
   – spontaneous 30  
   – TbFe 39  
   –  $Tb_{0.4}Fe_{0.6}(4.5\text{ nm})/Fe(6.5\text{ nm})$  multilayer 39  
   – TbFe/Fe 38  
   – TbFe/Fe and TbFe/FeCo multilayer 38  
   – TbFe/FeCo 38  
   – TbFe/Fe multilayer 39  
   –  $Tb_{1-x}Fe_x$  films 17  
 magnetization direction 13  
 magnetization process 20  
   – amorphous R–T alloys 16  
   – sandwich films 41–43  
 magneto-volume effects 520, 524  
 magnetocrystalline coupling constant 15  
 magnetoelastic coefficients 9, 10, 26, 32–34,  
   49  
   – concentration dependence 31  
   – determination 9  
   – measurement principle 7  
   – multilayers 38  
   –  $Tb_{0.27}Dy_{0.73}(Co_xFe_{1-x})_2$  31, 32  
 magnetoelastic coupling 50  
 magnetoelastic energy 20  
 magnetoelastic field-annealing effects 31  
 magnetoelastic ratio 36  
 magnetoelastic susceptibility 48  
 magnetoresistance 496  
 magnetostriction 1–50  
   – a- $(SmFe_2)_{99.26}B_{0.74}$  alloy 25  
   – a- $(Tb_{1-y}Dy_y)_{0.42}Fe_{0.58}$  films 23  
   – a- $Tb_{1-x}Co_x$  25  
   – a- $Tb_{1-x}Co_x$  alloys 25  
   – a- $Tb_{1-x}Fe_x$  25  
   – a- $Tb(Fe_{0.45}Co_{0.55})_{2.1}$  33  
   – a- $Tb_{1-x}Fe_x$  thin films 18  
   –  $\alpha$ -mode 6  
   – annealing effect 18, 19  
   – applications 43, 44  
   – coefficients 5, 9, 49  
   – concentration dependence 22  
   – deposition conditions 18, 19  
   – determination 7, 9  
   –  $DyFe_2$  12  
   –  $\epsilon$ -mode 7  
   – expression 6  
   – field-annealing effects 31, 33, 34  
   –  $\gamma$ -mode 7  
   –  $GdAl_2$ ,  $GdNi_2$  and  $GdFe_2$  12  
   –  $HoCo_2$  and  $ErCo_2$  12  
   – Joule 5  
   – magnetisation dependence 20, 21, 23, 24, 33  
   – measurement principle 8  
   – mechanisms 5  
   – microstructure dependence 22, 23  
   – modes 6  
   – multilayers 38, 40  
   – sandwich films 41–43  
   –  $(Sm,Tb)Fe_2$ –B alloys 25  
   – Sm–Co thin films 36  
   – Sm–Fe thin films 24  
   –  $Sm_{0.37}Co_{0.63}$  36  
   –  $SmFe_2$  12  
   –  $(SmFe_2)_{100-x}B_x$  25  
   – sperimagnetic cone dependence 28  
   – substrate temperature effect 18, 19  
   – surface 40  
   –  $(Tb,Dy)$ –Fe thin films 21  
   –  $(Tb_{1-y}Dy_y)_{0.42}Fe_{0.58}$  alloys 23  
   –  $(Tb_{1-y}Dy_y)_{0.42}Fe_{0.58}$  films 22  
   – Tb–Fe thin films 17  
   –  $Tb_{0.32}Co_{0.68}$  34  
   –  $Tb_{0.36}Co_{0.64}$  36  
   –  $TbCo_{2.1}$  34  
   –  $TbCo_2$ ,  $DyCo_2$  12  
   –  $Tb_{0.27}Dy_{0.73}(Co_{0.83}Fe_{0.17})_2$  28  
   –  $Tb_{0.27}Dy_{0.73}(Co_{0.83}Fe_{0.17})_2$  and  $Tb_{0.27}Dy_{0.73}Fe_2$   
     26  
   –  $Tb_{0.27}Dy_{0.73}Fe_2$  28  
   –  $(Tb_{0.3}Dy_{0.7})Fe_2$  24  
   –  $(Tb_{1-x}Dy_x)(Fe_{0.55}Co_{0.45})_{2.1}$  35  
   –  $(Tb_{0.27}Dy_{0.73})(Fe_{1-x}Co_x)_2$  films 29  
   –  $(Tb_{1-x}Dy_x)(Fe_{0.45}Co_{0.55})_{2.1}$  thin films 33  
   –  $TbFe_2$  12  
   –  $Tb_{0.32}(Fe_{0.45}Co_{0.55})_{0.68}$  34  
   –  $Tb_{0.36}(Fe_{0.5}Co_{0.5})_{0.64}$  34

- magnetostriction (*cont'd*)  
 – Tb(Fe<sub>0.45</sub>Co<sub>0.55</sub>)<sub>2.1</sub> 34  
 – Tb(Fe<sub>0.55</sub>Co<sub>0.45</sub>)<sub>2.1</sub> 35  
 – Tb<sub>0.4</sub>Fe<sub>0.6</sub>(4.5 nm)/Fe(6.5 nm) multilayer 39  
 – Tb<sub>1-x</sub>Fe<sub>x</sub> films 18, 19  
 – temperature dependence 35  
 – thickness dependence 40  
 – volume 6  
 magnetostrictive devices 44–46  
 magnetostrictive hysteresis loops  
 – sandwich Tb–Co/Nd–Co/Tb–Co 43  
 – TbFe/FeCo multilayer 40  
 – TbFe/Fe multilayer 39  
 magnetostrictive softness 49  
 magnetostrictive susceptibility 26, 48, 49  
 Markovian dynamics 269, 272, 345  
 Markovian process 94, 100, 122  
 mass enhancement 386  
 maximum entropy 114, 205, 265, 266  
 Maxwellian 97  
 mean-field approximation (MFA) 299  
 mechanical stability 487  
 melting points of polysulfides 577, 578  
 metal–insulator transition 245, 247, 412  
 metallic behavior of YbTX phases 493  
 metallic conductors of YbTX phases 496  
 metamagnetic transitions of YbTX phases 488  
 metamagnetism 149, 204, 224, 350, 404  
 metamagnets in YbTX phases 488  
 MgAgAs-type structure 481  
 MgCu<sub>2</sub>-type phase 457  
 MgZn<sub>2</sub> structure 460  
 missing fraction 70, 238, 244  
 mixed valency of YbTX phases 488  
 mixture of  $\alpha$ -Fe and Nd<sub>2</sub>Fe<sub>14</sub>B phases 543  
 (Mo,Fe)<sub>3</sub>B<sub>2</sub> 528  
 mode-coupling theory 128, 212  
 modified Bloch–Grüneisen expression 496  
 modulated spin structure 208, 210, 217, 226, 232,  
 237, 301, 338, 339, 404  
 molecular dynamics 316  
 moment collapse 168, 233  
 moment instability 201, 204  
 moment localization 207, 305  
 moment stabilization 199  
 momentum tuning 86  
 monoclinic distortion 344, 346  
 monoclinic SrAgGe type 468  
 Moriya limit 117, 184, 191  
 Mössbauer spectroscopy 63, 497, 550, 639  
 motional narrowing 94, 100, 104, 191, 207, 315,  
 349, 356, 389, 397  
 $\mu_0 H_c$  48  
 multi-*k* structures 152, 162, 170, 223, 243, 361  
 multichannel Kondo interaction 290, 394  
 multilayer 47  
 muon beams 71  
 muon bonding 115, 239, 244, 257  
 muon diffusion 70, 114, 121, 135, 179, 194, 206,  
 210, 212, 244  
 muon gate 78  
 muon implantation 69  
 muon-induced effects 71, 148, 151, 191, 239,  
 263, 326, 373  
 muon lifetime 63  
 muon production 67  
 muon properties 66  
 – negative 63  
 muon site 114, 129, 135, 179, 190, 206, 222,  
 223, 225, 234, 239, 241, 261, 324, 326, 328,  
 335, 359, 380, 403, 405  
 muon spin precession 93  
 muon spin relaxation 62  
 – measurements 493  
 – rate  
 – – parallel 124  
 – – perpendicular 124  
 muon spin resonance, *see*  $\mu$ SR  
 muon spin rotation 62  
 muon stopping 70  
 muon trapping 185, 205, 206  
 muonium 70, 114, 238  
 $\mu$ SR (muon spin resonance) 55–414  
 – asymmetry spectrum 78, 112  
 – high pressure 83  
 – high temperature 81  
 – longitudinal field 102  
 –  $\mu$ SR facility 81  
 –  $\mu$ SR spectrometer 76  
 – – beam collimation 85  
 – – beam spot 85  
 – reviews 65  
 – studies of  
 – –  $\alpha$ -Fe<sub>2</sub>O<sub>3</sub> 244  
 – – Cr<sub>2</sub>O<sub>3</sub> 244  
 – transverse field 93  
 – zero field 97  
 $\mu$ SR spectroscopy  
 – background counts 112  
 – background signal 113



- backward-forward ratio 112
- baseline 113
- $\beta$  decay 68
- counting statistics 80
- dead time 73, 101, 108, 276, 282, 357
- decay channel beam 75
- degrader 75
  
- NMR (nuclear magnetic resonance) 64, 65, 604, 649
  - shift reagents 615, 627
- NP-YbCuAl 457
- NP-YbNiAl 457
- n-R-Fe 8
- n-Tb<sub>0.27</sub>Dy<sub>0.73</sub>Fe<sub>2</sub> 49
- nanocrystalline films 24
- Nb<sub>3</sub>Sn 251
- (Nd,Ce)<sub>2</sub>CuO<sub>4</sub> 258, 259
- (Nd,Zr)<sub>2</sub>(Fe,Co,Ga)<sub>4</sub>B 533
- (Nd,Ca)CuO<sub>2.5</sub> 284
- Nd<sub>1-2x</sub>Ca<sub>x</sub>Th<sub>x</sub>Ba<sub>2</sub>Cu<sub>3</sub>O<sub>7- $\delta$</sub>  265
- (Nd<sub>0.125</sub>Sm<sub>0.875</sub>)<sub>0.5</sub>Sr<sub>0.5</sub>MnO<sub>3</sub> 247
- Nd-Co (Nd<sub>3</sub>Co) phase 527
- Nd-Co/Tb-Co/Nd-Co 41
- Nd-Fe-B 556
- Nd-Fe-C systems 556
- Nd-(Fe<sub>1-x-y</sub>Co<sub>x</sub>Ni<sub>y</sub>)-B 549
- Nd-S system 576, 580
  - pressure-dependent phase diagram 582
- NdAl<sub>2</sub> 179, 184
- NdBa<sub>2</sub>Cu<sub>3</sub>O<sub>6+ $\delta$</sub>  264
- Nd<sub>3</sub>Co 551
- Nd<sub>0.25</sub>Co<sub>0.75</sub>/Tb<sub>0.28</sub>Co<sub>0.72</sub>/Nd<sub>0.25</sub>Co<sub>0.75</sub> 49
- NdCu 528
- NdCu<sub>2</sub> 208, 528
- Nd<sub>2</sub>CuO<sub>4</sub> 258
- Nd(Fe,Co,Ni)<sub>2</sub> 549
- NdFe<sub>12</sub>B<sub>6</sub> 543
- Nd<sub>2</sub>Fe<sub>23</sub>B<sub>3</sub> 543
- Nd<sub>4.5</sub>Fe<sub>77</sub>B<sub>18.5</sub> 546
- Nd<sub>4.5</sub>Fe<sub>76.8</sub>B<sub>18.5</sub>Cu<sub>0.2</sub> 546
- Nd<sub>4.5</sub>Fe<sub>75.8</sub>B<sub>18.5</sub>Cu<sub>0.1</sub>Nb<sub>1.0</sub> 546
- Nd<sub>4.5</sub>Fe<sub>75.8</sub>B<sub>18.5</sub>Cu<sub>0.1</sub>Nb<sub>1.0</sub> ribbon 547
- Nd<sub>2</sub>Fe<sub>14</sub>B magnets 249, 516-518, 532, 548, 549
  - coatings
  - - Al-ion plating 550
  - - Ni plating 550
  - corrosion 548
  - - initial stage 551
  - - oxygen, carbon and/or nitrogen effects 549
  - - passivating currents 550
  - effect of alloying additions
    - - Al 549, 550
    - - Co 527, 529, 536, 538, 548, 551
    - - Cr 543, 549
    - - Dy 527, 529, 536, 543, 548-550
    - - Ga 536, 543, 549
    - - Mo 528, 549
    - - Nb 549
    - - Si 538
    - - Tb 543
    - - Ti 549
    - - V 549, 551
    - - V and Mo 528
    - - Zr 536, 549
  - effect of oxide additions 549
  - liquid-phase sintering 527
  - MQ-1 538
  - MQ-2 538
  - MQ-3 539
  - MQP-B powder 537
  - Nd-rich phase 527, 529, 550
  - oxidation 552-555
    - - logarithmic law 553
    - - long-range quantum tunneling 554
    - - parabolic law 551, 552
  - radial anisotropic ring magnets 555
  - rapid solidification 538, 539, 547
- Nd<sub>4.5</sub>Fe<sub>76</sub>B<sub>18.5</sub>Nb<sub>1.0</sub> 546
- Nd<sub>1.1</sub>Fe<sub>2</sub>B<sub>4</sub> phase 528, 529, 549
- Nd<sub>2</sub>Fe<sub>14</sub>BH<sub>x</sub> 532, 535
- NdGa<sub>6</sub> 216
- Nd<sub>5</sub>(Ga,Fe)<sub>3</sub> 528
- Nd<sub>3</sub>(Ga,Fe) 528
- NdH<sub>2</sub> phase 534
- NdH<sub>2 ± x</sub> phase 532, 533
- Nd<sub>0.7</sub>La<sub>0.3</sub>NiO<sub>3</sub> 245
- Nd(OH)<sub>3</sub> 550, 551
- Nd<sub>2</sub>O<sub>3</sub> phase 527
- Nd oxide 550
- NdPdAs 410, 411
- Nd polysulfides 577, 602
- NdRh<sub>2</sub>Si<sub>2</sub> 228
- NdRu<sub>2</sub>Si<sub>2</sub> 225
- NdS<sub>1.857</sub> 598
- NdS<sub>1.875</sub> 598
- NdS<sub>1.900</sub> 598
- NdS<sub>2.000</sub> 578, 582, 586, 589, 590, 592, 593, 597, 598, 603, 604

- NdS<sub>2.67</sub> 573  
 Nd<sub>1-x</sub>Sr<sub>x</sub>MnO<sub>3</sub> 246  
 neutron scattering 64  
   – polysulfides 603  
 Ni<sub>2</sub>In structure 468  
 nickel deficiency 482  
 non-equilibrium state  
   – polysulfides 575, 576  
 non-Fermi liquid 291, 311, 331, 393–407  
 noncollinear spin structure 156, 160, 162  
 nonequilibrium state of polysulfides 574  
 NpAl<sub>2</sub> 188  
 NpCo<sub>2</sub> 191  
 NpFe<sub>2</sub> 191  
 NpNi<sub>2</sub> 191  
 NpO<sub>2</sub> 240, 242  
 nuclear magnetic ordering 147  
 nuclear moments 89, 92, 262  
 Nucleation Expansion Model 559  
 Nucleation Model 559  
  
 “one-third” asymptote 98, 100, 101, 270, 308  
 “one-third” signal 108, 279, 321, 349  
 optical exponent 221  
 orbital angular momentum 124, 141, 154, 183  
 origin of the remanence-enhancement phenomenon 541  
 orthoferrites 243  
 oxidation of Sm<sub>2</sub>Fe<sub>17</sub>N<sub>3</sub> powders 553  
  
 paramagnetic clusters 127, 215  
 paramagnetic contrast agent 628  
 paramagnetic limit 116, 144  
 parity violation 67  
 Pauli paramagnet 201  
 Pauli paramagnetism 488  
 PbMo<sub>6</sub>S<sub>8</sub> 251  
 penetration depth 251, 253, 255, 258, 264–266, 365, 379  
 permanent magnets 248, 515–561  
   – 2-17 structure 520  
   – *see also* Nd<sub>2</sub>Fe<sub>14</sub>B magnets *and* SmCo<sub>5</sub>-type magnets *and* Sm<sub>2</sub>Fe<sub>17</sub>N<sub>x</sub> magnets  
   – casting methods 555  
   – hot-pressing 555  
   – hot-working 555  
   – mechanical alloying 538, 540  
   – melt-spinning 538, 540  
   – mesoscopic 537  
   – micromagnetism 558  
   – nanocomposite 537  
   – – Cr-doped Fe–Fe<sub>2</sub>B–Nd<sub>2</sub>Fe<sub>14</sub>B 557  
   – – Fe<sub>3</sub>B–Nd<sub>2</sub>Fe<sub>14</sub>B mixtures 543  
   – – industrialization of Sm–Fe 547  
   – – Nd–Tb–Fe–Cr–B 545  
   – – Nd<sub>4.5</sub>(Fe<sub>1-x</sub>Cr<sub>x</sub>)<sub>77</sub>B<sub>18.5</sub> 543  
   – – Nd<sub>2</sub>Fe<sub>14</sub>B + α-Fe 543  
   – – Nd<sub>4.5</sub>Fe<sub>73</sub>Ga<sub>1</sub>Co<sub>3</sub>B<sub>18.5</sub> 543  
   – – Sm–Zr–Fe–N + α-Fe 539  
   – plasma-activating process 555  
   – rapid quenching 538, 539  
   – sintered 526  
   – thin film coatings of Zn, In, and Cu 550  
 perovskites 243  
 persistent spin fluctuations 236, 273, 284, 298, 343, 390, 392  
 phase de-locking 161, 174  
 phase diagrams of polysulfides 571, 576–583  
 phase segregations 19  
 phonon-induced relaxation 214  
 phosphides and arsenides YbTP and YbTAs 479  
 photoemission of YbTX phases 505  
 phthalocyanines 645–650  
   – electrochemistry 650  
   – phosphorescence spectra 643  
   – photophysical properties 643  
   – reactivity 645  
   – structure 647  
   – synthesis 645  
 pion decay 67  
 planar anisotropy 255, 265  
 plumbides YbTPb 478  
 point charge model 142  
 point-contact spectroscopy of YbTX phases 503  
 polaron 91  
 polyanions in YbTX phases 462  
 polycrystalline films 24  
 polycrystalline Terfenol-D film 46  
 polysulfides 567–605  
   – analysis 575, 585, 586  
   – applications 605  
   – chemical bonding 599–601  
   – chemical properties 571  
   – color 586  
   – compositional classification 570, 571  
   – crystal growth 583–585  
   – crystals 587, 588, 604  
   – density 586, 587

- electrical properties 602, 603
- electronic structure 601, 602
- historical account 568
- interatomic distances 600
- magnetic properties 603, 604
- melting 576-578
  - - determination of 577
  - - sulfur pressure 582
- microhardness 586
- neutron scattering experiments 603
- non-equilibrium state 575, 576
- optical properties 604
- phase equilibrium 576-583
- powders 586, 587, 604
- preparative methods 572-576
- pressure-dependent phase diagrams 581
  - - techniques for 579
- samples 594, 595
- structural arrangement 591-593
- structural interatomic distances 600, 601
- structural representation 588, 589
- structure types 589
- thermodynamic properties 594-599
  - - measurement techniques 594
- vaporization 597-599
  - - measurement techniques 597, 598
- porphyrins 613-645
  - reactivity 613
  - structure 623
  - synthesis 613
- positron angular distribution 69
- power exponential 101, 255
- power-exponential relaxation 271, 272, 277, 305, 309
- (Pr,Ca)CuO<sub>2.5</sub> 284
- Pr-S system 581
  - pressure-dependent phase diagram 581, 582
- PrAl<sub>2</sub> 96, 179, 184
- PrBa<sub>2</sub>Cu<sub>3</sub>O<sub>6+δ</sub> 260
- PrBa<sub>2</sub>Cu<sub>3</sub>O<sub>7</sub> 264
- Pr<sub>1-x</sub>Ca<sub>x</sub>MnO<sub>3</sub> 247
- PrCo<sub>2</sub>Si<sub>2</sub> 224-226, 336
- PrCu<sub>2</sub> 149, 152, 208
- Pr<sub>2</sub>CuO<sub>4</sub> 258
- Pr<sub>2</sub>Fe<sub>14</sub>B 249
- Pr<sub>2</sub>Fe<sub>14</sub>B magnets 555
- PrIn<sub>3</sub> 148, 176
- PrInAg<sub>2</sub> 289, 382
- Pr metal 146
- PrNi<sub>5</sub> 147, 148, 152, 210
- PrP<sub>x</sub> 149, 310
- PrP 150, 402
- PrPb<sub>3</sub> 148
- Pr polysulfides 577, 602
- PrRu<sub>2</sub>Si<sub>2</sub> 150, 227
- PrS<sub>1.702</sub> 598
- PrS<sub>1.766</sub> 598
- PrS<sub>1.846</sub> 598
- PrS<sub>1.900</sub> 598
- PrS<sub>2-x</sub> 581
- PrS<sub>2</sub> 578, 581, 586, 589, 590, 597, 598, 603, 604
- Pr<sub>1/2</sub>Sr<sub>1/2</sub>MnO<sub>3</sub> 247
- precursor state 156, 157, 163, 166, 167, 172, 193, 204, 303
- preparative methods
  - polysulfides 572-576
  - YbTX phases 455, 456
    - - fluxes for 456
- pressure-induced magnetization of Yb<sup>2+</sup> 502
- protoporphyrin IX 617
- pseudo-quadrupolar interaction 146
- pseudogap 291, 295, 296, 312
- pulsed beam 71
- pyrochlores 279
- quadrupolar ordering 170, 326, 351
- quadrupole splitting 497
- quantum critical point 311, 331, 334, 341, 360, 376, 381, 394, 403, 407
- quantum diffusion 65, 213
- quantum spin liquid state 197, 199
- quasicritical behavior 299
- quasicrystals 273, 277, 281-283
- quasistatic field 106
- (R,Ce)<sub>2</sub>CuO<sub>4</sub> 257
- R-T sandwich films 41
- RAl<sub>2</sub> 179
- RBa<sub>2</sub>Cu<sub>3</sub>O<sub>6+δ</sub> 244
- RCMMV (range-correlated moment magnitude variation) model 275
- (RC)<sub>2</sub>(NiB)<sub>2</sub> 255
- RFe<sub>4</sub>Al<sub>8</sub> 236
- RFe<sub>6</sub>Al<sub>6</sub> 235
- R<sub>2</sub>Fe<sub>14</sub>B 249
- R<sub>2</sub>Fe<sub>14</sub>B spectra 526
- RFe<sub>9.5</sub>Mo<sub>2.5</sub> 234
- RGa<sub>6</sub> 215, 283
- RH<sub>2±x</sub> (R = Nd, Sm) 533
- R<sub>2</sub>In 232

- RKKY (Ruderman–Kittel–Kasuya–Yosida)  
 interaction 146, 183, 239, 285, 287, 306, 325,  
 342, 394, 403, 412
- $\text{RMn}_2$  193
- $\text{RMO}_6\text{X}_8$  ( $\text{X} = \text{S}, \text{Se}$ ) 251
- R monochalcogenides 239
- $\text{RNi}_2\text{B}_2\text{C}$  254
- $\text{RNiO}_3$  245
- $\text{RRh}_4\text{B}_4$  251, 252
- $\text{RS}_{1.70}$  570, 582, 583
- $\text{RS}_{1.75}$  570
- $\text{RS}_{1.766}$  582, 583
- $\text{RS}_{1.80}$  571, 582
- $\text{RS}_{1.85}$  570
- $\text{RS}_{1.90}$  570, 582, 583
- $\text{RS}_{2.0}$  570, 582, 583
- $\text{R}_n\text{S}_{2n-1}$  homologous series 580
- $\text{RT}_2$  compounds 189
- $\text{RX}$  compounds 154–175
- $\text{RX}_2$  compounds 178, 179
- $\text{RX}_3$  compounds 175–178
- radiation damage 71
- radiolysis 239
- Raman spectra of polysulfides 587, 588, 604
- random axial anisotropy 15
- random spin system 93
- random switching 273
- randomness 199, 223, 277, 309
- randomness of moment orientation 325
- rare-earth monochalcogenides 154–170
- rare-earth monpnictides 154–170
- reaction velocity 547
- reduced dimensionality 215, 283, 284
- relativistic effect 471, 480
- relaxation function 94, 297
- relaxation limits 101
- remanence 203, 330
- enhancement 540
- – in  $\text{Nd}_2\text{Fe}_{14}\text{B}$  559
- – in  $\text{SmCo}_5$  559
- – in  $\text{Sm}_2(\text{Fe}_{0.8}\text{Co}_{0.2})_{17}\text{N}_{2.8}$  559
- resistivity of  $\text{YbTX}$  phases 495–497
- phonon contribution 496
- root-exponential relaxation 246, 269, 272
- rotating frame 82
- $\text{RuSr}_2\text{GdCu}_2\text{O}_8$  266, 267
- ruthenates 266, 267
- SCR (self-consistent renormalization) relaxation  
 193, 195, 340
- S state ion 126, 144, 202
- sandwich
- complexes 613
- compounds 620
- films, configuration 42
- $[\text{Sc}(\text{OEP})(\mu\text{-OH})_2]$  625
- Schottky anomaly 143, 342
- second moments 93, 227
- self-trapping 71, 91
- semiconductors 70, 238
- semimetallic heavy-fermion system ( $\text{YbPtBi}$ )  
 496
- short-range correlations 395, 398
- short-range order 119, 151, 195, 197, 199, 201,  
 202, 208, 219–269, 280, 309, 319, 348, 486
- silicides  $\text{YbTSi}$  466
- sine-wave spin structure 136
- sine wave structure 181
- single-ion anisotropy 124, 127, 202, 261, 263
- singlet ground state 145, 147, 149, 150, 227,  
 262
- sinusoidally modulated spin structure 230
- site averaging 121, 162, 190, 210, 213, 249,  
 315
- site exchange 115
- site potential calculations 116, 295
- slow spin dynamics 117, 161
- slow spin fluctuations 307, 315, 330, 332, 356
- $\text{Sm-Co/Co-Zr/Sm-Co}$  multilayer films 559
- $\text{Sm-Co}$  system 516
- $\text{Sm-Fe-X}$  systems 521
- $\text{Sm-S}$  system 580
- pressure-dependent phase diagram 580
- $\text{SmB}_6$  293
- $\text{SmCo}_5$ -type magnet 516, 520, 532
- $\text{SmFe}_2$  13
- $\text{Sm}_2\text{Fe}_{17}$  532
- $\text{Sm}_2(\text{Fe,Ga})_{17}$  carbides 539
- $\text{Sm}_2(\text{Fe,Ga})_{17}\text{C}_2$  540
- $\text{SmFeB/TbFeB}$  multilayers 40
- $\text{Sm}_2\text{Fe}_{17}\text{C}_x$  516, 540
- $\text{Sm}_2\text{Fe}_{16}\text{Ga}$  533
- $\text{Sm}_2\text{Fe}_{17}\text{N}_x(-\text{C}_y)$  compounds 520
- $\text{Sm}_2\text{Fe}_{17}\text{N}_x$  magnets 518
- $\text{Sm}_2\text{Fe}_{17}\text{N}_3$  516, 541
- $\text{SmFeO}_3$  244
- $\text{SmH}_{2 \pm x}$  533
- $\text{SmIn}$  232
- $\text{Sm}_{0.9}\text{La}_{0.1}\text{S}$  292, 412
- $\text{Sm}$  polysulfides 577, 602

- $\text{SmRh}_4\text{B}_4$  252, 253  
 $\text{SmS}$  293  
 $\text{SmS}_{1.86}$  597  
 $\text{SmS}_{1.863}$  598  
 $\text{SmS}_{1.89}$  597  
 $\text{SmS}_{1.893}$  598  
 $\text{SmS}_{1.9}$  586, 589, 592, 593, 597, 598  
 $\text{SmS}_2$  578, 604  
 $\text{Sm}_2\text{Se}_3$  383  
 $\text{Sm}_3\text{Se}_4$  289, 383, 384, 408  
 $\text{Sm}_3\text{Te}_4$  289, 384, 385  
 small-moment magnetism 312  
 $[\text{Sm}(\text{tmhd})_2]_2(\mu\text{-Pc})$  648  
 $^{119}\text{Sn}$  and  $^{170}\text{Yb}$  Mössbauer spectroscopic 497  
 $\text{SnMo}_6\text{S}_8$  251  
 solution calorimetry of polysulfides 594  
 Sommerfeld constant 155, 176, 197, 284, 325, 329, 340, 342, 348, 352, 383, 388, 392, 393  
 specific coherent length ( $L$ ) 558  
 specific heat of  $\text{YbTX}$  phases 500–502  
 spectroscopic properties 626, 648  
 sperimagnetic cone angle 27, 31  
 – a-Tb–Co films 29  
 sperimagnetic structure 14, 15, 27  
 speromagnetism 14  
 spin autocorrelation functions 276  
 spin bunching 134  
 spin canting 175, 177, 204  
 spin clusters 276  
 spin correlations 157, 166, 169, 171, 180, 183, 199, 201, 214, 247, 297, 305, 307, 313, 319, 346, 376, 388, 392  
 spin density wave 230, 379, 388  
 spin disorder 169, 177, 236  
 spin fluctuations 120, 128, 161, 166, 173, 176, 187, 192, 193, 199, 204, 206, 207, 237, 272, 280, 297, 300, 311, 318, 364, 389, 390  
 spin freezing 149, 187, 199, 206, 248, 255, 267, 270, 271, 273, 276, 279, 302, 305, 310, 320, 331, 333, 351, 400  
 spin-freezing temperature 492  
 spin glass 100, 104, 119, 186, 255, 268, 272, 279, 303, 400  
 spin-glass-like clusters 195, 197, 246  
 spin-glass-like domains 387  
 spin-glass-like state 201, 206, 263, 269, 277, 305, 309, 319, 375, 402  
 spin ladders 275, 284  
 spin magnetism 126  
 spin-Peierls transition 284  
 spin relaxation 401  
 spin reorientation 118, 220, 244, 258, 354, 362  
 spin-singlet pairs 345  
 spin-slip structure 132, 134, 303  
 spin turning 118, 129, 132, 230, 341  
 spin wave 106, 317  
 spin–lattice relaxation 140  
 spin–orbit coupling 4, 5, 141  
 spontaneous spin precession 106, 149, 163, 166, 190, 223, 242, 249  
 sporadic paramagnetism 334  
 spring-magnet-type multilayers 37  
 – structure 37  
 $\text{Sr}_{2.5}\text{Ca}_{11.5}\text{Cu}_{24}\text{O}_{41}$  334  
 $\text{SrCr}_3\text{Ga}_4\text{O}_{19}$  273  
 $\text{Sr}(\text{Cu}_{1-x}\text{Zn}_x)_2\text{O}_3$  275  
 $\text{Sr}_4\text{Cu}_6\text{O}_{10}$  284  
 $\text{Sr}_{2-x}\text{Nd}_{1+x}\text{Mn}_2\text{O}_7$  247  
 $\text{Sr}_2\text{RMn}_2\text{O}_7$  248  
 $\text{Sr}_2\text{RuO}_4$  266  
 $\text{Sr}_2\text{YMn}_2\text{O}_7$  248  
 stannides  $\text{YbTsn}$  474  
 static relaxation 94, 108  
 Stevens factor 10, 36, 37, 142  
 Stoner–Wohlfarth coherent rotation equation 559  
 Stoner factor 186  
 stopping range 74  
 stress 20, 26  
 – film thickness dependence 27  
 stretched exponential 101  
 – relaxation 272  
 stripe magnetic order 245, 258, 259  
 strong collision model 100, 149  
 structure  
 – of  $\text{Lu}(\text{Pc})(\text{OAc})(\text{H}_2\text{O})_2$  647  
 – of tetrapyrrole complexes 623, 648  
 subgroup 464  
 substrates for thin films  
 – glass 8  
 – Si [100] 8  
 – Si [110] 8  
 – Ta 8  
 – W 8  
 superconductivity 250–267, 285, 292, 331, 352, 358, 364, 370, 376  
 superexchange 244, 257, 283  
 superparamagnetism 351  
 superstructures of  $\text{YbTX}$  phases 468, 475, 478, 486

- surface anisotropy 4  
 surface beam 74  
 surface coating methods 550  
 surface contribution 50  
 surface magnetostriction 4  
 symmetry-breaking field 367  
 symmetry reduction 484  
 synthesis of YbTX phases 455, 456
- (Tb<sub>0.3</sub>Dy<sub>0.7</sub>)<sub>0.33</sub>Fe<sub>0.67</sub> 24  
 Tb–Co/Nd–Co/Tb–Co 41  
 Tb–Fe thin films 17  
 TbBa<sub>2</sub>Cu<sub>3</sub>O<sub>6+δ</sub> 260  
 Tb<sub>0.28</sub>Co<sub>0.72</sub>/Nd<sub>0.25</sub>Co<sub>0.75</sub>/Tb<sub>0.28</sub>Co<sub>0.72</sub> 49  
 TbCo<sub>2</sub>Ni<sub>1-x</sub>C<sub>2</sub> 235, 237  
 TbCu<sub>7</sub>-type material 539  
 Tb<sub>0.27</sub>Dy<sub>0.73</sub>(Co<sub>0.83</sub>Fe<sub>0.17</sub>)<sub>2</sub> 27  
 Tb<sub>0.27</sub>Dy<sub>0.73</sub>(Co<sub>x</sub>Fe<sub>1-x</sub>)<sub>2</sub> films 30, 33  
 Tb<sub>0.27</sub>Dy<sub>0.73</sub>Fe<sub>2</sub> 27, 49  
 TbDyFe 48  
 (Tb<sub>0.27</sub>Dy<sub>0.73</sub>)(Fe<sub>1-x</sub>Co<sub>x</sub>)<sub>2</sub> 29  
 (Tb<sub>1-x</sub>Dy<sub>x</sub>)(Fe<sub>0.55</sub>Co<sub>0.45</sub>)<sub>2.1</sub> 36  
 TbDyFe + Zr 47  
 Tb<sub>0.27</sub>Dy<sub>0.73</sub>Fe<sub>2</sub> alloys 12  
 TbDyFe/Fe multilayers 48  
 (Tb<sub>0.3</sub>Dy<sub>0.7</sub>)Fe<sub>2</sub> films 24  
 TbDyFe/Finemet multilayers 48  
 TbF<sub>3</sub> 243  
 TbFe<sub>2</sub> 13  
 Tb(Fe<sub>0.45</sub>Co<sub>0.55</sub>)<sub>2.1</sub> 47  
 Tb(Fe<sub>0.55</sub>Co<sub>0.45</sub>)<sub>1.5</sub>/(Fe<sub>0.85</sub>Co<sub>0.15</sub>) multilayers 48  
 TbFe/FeCoBSi multilayers 48  
 TbFe/FeCo multilayer 38  
 TbFe/Fe multilayer 38  
 TbGa<sub>6</sub> 216, 217  
 TbMn<sub>2</sub> 203  
 Tb<sub>2</sub>Mo<sub>2</sub>O<sub>7</sub> 280  
 TbNi<sub>5</sub> 106, 152, 213  
 TbNi<sub>2</sub>B<sub>2</sub>C 255  
 Tb(Pc<sup>-</sup>)(tmhd)<sub>2</sub> 649  
 Tb polysulfides 577  
 TbS<sub>2</sub> 589, 590  
 Tb<sub>2</sub>Ti<sub>2</sub>O<sub>7</sub> 279, 280  
 Terfenol 12  
 Terfenol-D 13  
 tesseral harmonics 141  
 tetracritical point 353  
 tetragonal distortion 159, 193, 391  
 tetragonal PbFCl type 468  
 tetrahedral network 483
- tetrapyrrole complexes 611–650  
 – half-sandwich  
 – – phthalocyanines 645–650  
 – – porphyrins 613–645  
 t-Fe<sub>3</sub>B phase 534  
 ThAs 155  
 ThMn<sub>12</sub>-type structures 516  
 Th<sub>3</sub>(OH)<sub>6</sub>(OH<sub>2</sub>)<sub>2</sub> 624  
 Th<sub>2</sub>Zn<sub>17</sub>-type structures 516  
 Th<sub>2</sub>Zn<sub>17</sub> and Th<sub>2</sub>Ni<sub>17</sub> structures 521  
 thermalization of muons 69, 114  
 thermoelectric power of YbTX phases 503  
 three-dimensional atom-probe microanalysis  
 (3D-APM) 546  
 TiNiSi structure 460  
 TiNiSi type 463  
 tie line of the Fe–Nd<sub>2</sub>Fe<sub>14</sub>B phases 542  
 tilting angle 130  
 time resolution 72, 73, 80  
 time to digital converter 76  
 time window 64  
 TmAl<sub>2</sub> 179, 184  
 TmFe<sub>2</sub> 13, 189  
 TmNi<sub>5</sub> 214  
 TmNi<sub>2</sub>B<sub>2</sub>C 254  
 Tm polysulfides 577  
 TmSe 293  
 TmTe 293  
 transferred hyperfine field 499  
 transuranium compounds 188  
 triple-decker complexes 620  
 twinning  
 – polysulfides 593  
 – YbAuSn 478  
 two-channel Kondo effect 397, 400  
 two-component structure 318, 321, 333, 337,  
 340, 355, 363, 373, 378, 404  
 two-magnon processes 213, 214, 240
- UAl<sub>2</sub> 176, 186, 187, 288  
 UAs 156  
 U<sub>14</sub>Au<sub>51</sub> 288, 370  
 UAuGe 481  
 UBe<sub>13</sub> 288, 364  
 UBe<sub>13-y</sub>B<sub>y</sub> 366  
 UCd<sub>11</sub> 288, 364  
 U<sub>x</sub>Ce<sub>1-x</sub>NiSn 304  
 UCoAl 222  
 UCo<sub>2</sub>Si<sub>2</sub> 229  
 UCu<sub>5</sub> 210, 288, 361, 363

- UCu<sub>5-x</sub>Pd<sub>x</sub> 394, 398  
 UCu<sub>2</sub>Sn 319  
 UGa<sub>3</sub> 175  
 UGe<sub>2</sub> 288, 337, 352  
 UGe<sub>3</sub> 178  
 U(Ge<sub>x</sub>Ga<sub>1-x</sub>)<sub>3</sub> 175  
 U(Ge<sub>1-x</sub>Ga<sub>x</sub>)<sub>3</sub> 178  
 UIn<sub>3</sub> 175, 176, 288, 292  
 UIrGa 221  
 U<sub>0.75</sub>La<sub>0.25</sub>Ru<sub>2</sub>Si<sub>2</sub> 375  
 U<sub>1-x</sub>La<sub>x</sub>Ru<sub>2</sub>Si<sub>2</sub> 374  
 U<sub>x</sub>La<sub>1-x</sub>S 169  
 U<sub>1-x</sub>La<sub>x</sub>S 167  
 U Mn<sub>2</sub> 207  
 UN 156, 160  
 UNiAl 220, 221  
 UNi<sub>2</sub>Al<sub>3</sub> 288, 376, 379, 380  
 UNi<sub>4</sub>B 288, 381, 382  
 UNiGa 219, 220  
 UO<sub>2</sub> 240–242  
 UP 156, 160  
 UPd<sub>3</sub> 209, 400  
 UPd<sub>4</sub> 400, 401  
 U(Pd<sub>x</sub>Pt<sub>1-x</sub>)<sub>3</sub> 352  
 UPd<sub>2</sub>Al<sub>3</sub> 288, 376, 378, 379  
 UPd<sub>2</sub>Ge<sub>2</sub> 229  
 UPt<sub>3</sub> 288, 352–355  
 U(Pt<sub>1-x</sub>Pd<sub>x</sub>)<sub>3</sub> 358–360  
 U<sub>2</sub>Pt<sub>2</sub>In 394, 407  
 UPt<sub>2</sub>Si<sub>2</sub> 229  
 U(Rh<sub>0.35</sub>Ru<sub>0.65</sub>)<sub>2</sub>Si<sub>1</sub> 375  
 URh<sub>2</sub>Ge<sub>2</sub> 288, 375  
 URhIn 221  
 URh<sub>2</sub>Si<sub>2</sub> 229, 370, 373  
 URu<sub>2</sub>Si<sub>2</sub> 288, 370, 372, 373  
 US 156, 167, 168  
 USb 156, 160, 288, 292  
 USn<sub>3</sub> 175, 176, 288, 292  
 U(Sn<sub>1-x</sub>In<sub>x</sub>)<sub>3</sub> 175, 177  
 U(TPP)Cl<sub>2</sub>(THF) 623  
 UTe 156, 167  
 U<sub>1-x</sub>Th<sub>x</sub>Be<sub>13</sub> 364–366  
 U<sub>1-x</sub>Th<sub>x</sub>Be<sub>13-y</sub>B<sub>y</sub> 364, 367  
 U<sub>1-x</sub>Th<sub>x</sub>Pt<sub>3</sub> 352, 357  
 U<sub>0.95</sub>Th<sub>0.05</sub>Pt<sub>3</sub> 357  
 UV–Vis spectra 628–630, 648, 649  
 U<sub>1-x</sub>Y<sub>x</sub>Ru<sub>2</sub>Si<sub>2</sub> 374  
 U<sub>0.95</sub>Y<sub>0.05</sub>Ru<sub>2</sub>Si<sub>2</sub> 375  
 U<sub>2</sub>Zn<sub>17</sub> 288, 368  
 ultra-low temperatures 81  
 ultra-slow muons 87  
 uniaxial pressure 84, 297  
 uniaxial symmetry 125  
 universal correlation 255  
 uranium monochalcogenides 167  
 (V,Fe)<sub>3</sub>B<sub>2</sub> 528  
 VIS and near-IR reflection spectra 604  
 V<sub>2</sub>O<sub>3</sub> 549  
 valence change 494  
 valence charge density distribution 463  
 valence fluctuations 141, 383, 410  
 Van Vleck moment 93  
 Van Vleck susceptibility 145, 391  
 Van Vleck width 98, 229  
 vapor pressure measurement of polysulfides 594  
 weak ferromagnet 493  
 weak interaction 67  
 weak-moment magnetism 118, 168, 229, 242, 285, 298, 315, 320, 328, 334, 355, 358, 362, 365, 370, 371, 386, 403  
 weak temperature-independent paramagnetism (TIP) 488  
 Wigner–Seitz (W–S) cell 523  
 – volume in bcc-Fe 521  
 world-wide market for rare-earth bonded magnets 557  
 X-ray photoelectron spectra 639  
 Y<sub>1-2x</sub>Ca<sub>x</sub>Th<sub>x</sub>Ba<sub>2</sub>Cu<sub>3</sub>O<sub>7</sub> 265  
 YBa<sub>2</sub>Cu<sub>3</sub>O<sub>6+δ</sub> 256, 259, 261  
 YBa<sub>2</sub>Cu<sub>3</sub>O<sub>6+x</sub> 256  
 YBa<sub>2</sub>Cu<sub>3</sub>O<sub>7-δ</sub> 88  
 YCo<sub>2</sub> 206, 207  
 YCoC-type structure 466  
 YCo<sub>2</sub>Si<sub>2</sub> 335  
 YF<sub>3</sub> 243  
 Y<sub>1-x</sub>Fe<sub>x</sub> 14  
 YFe<sub>2</sub> 189  
 Y<sub>2</sub>Fe<sub>17</sub> 522  
 Y<sub>6</sub>Fe<sub>23</sub> 233  
 Y<sub>2</sub>Fe<sub>14</sub>B 525  
 Y<sub>2</sub>Fe<sub>17</sub>N<sub>3</sub> 522  
 YFeO<sub>3</sub> 244  
 YLiSn type 483  
 YMn<sub>2</sub> 110, 193–195  
 YMn<sub>12</sub> 233

- $Y_6Mn_{23}$  233  
 $Y(Mn_{1-x}Al_x)_2$  199  
 $Y(Mn_{1-x}Fe_x)_2$  199, 200  
 $Y_6(Mn_{1-x}Fe_x)_{23}$  233  
 $Y_2Mo_2O_7$  279  
 $YNi_2B_2C$  253  
 $YNiO_3$  245  
 $Y_2O_3$  549  
 YPdSi type 468  
 $Y_{1-x}Pr_xBa_2Cu_3O_{-7}$  264  
 $YRh_4B_4$  252  
 $YRu_2Si_2$  222, 335  
 $Y_{0.97}Sc_{0.03}Mn_2$  199  
 $Y(Sc)Mn_2$  197  
 $Y_{0.97}Sc_{0.03}Mn_2$  197  
 $Y_{0.97}Sc_{0.03}(Mn_{0.9}Al_{0.1})_2$  199  
 $Y(TPP)(acac)$  643  
 $Y(Tb)Mn_2$  196  
 $Y_{0.6}U_{0.4}Pd_3$  401  
 $Y_{0.8}U_{0.2}Pd_3$  401  
 $Y_{0.9}U_{0.1}Pd_3$  401  
 $Y_{1-x}U_xPd_3$  394, 400, 402  
 $Y_{0.5}Yb_{0.5}BiPt$  386  
 Yb-S system 571  
 $YbAgAl$  457  
 $YbAgBi$  484  
 $YbAgGa$  464  
 $YbAgGe$  474  
 $YbAgPb$  479  
 $YbAgSb$  482  
 $YbAgSi$  467  
 $YbAgSn$  476  
 $YbAgZn$  485  
 $Yb_4As_3$  289, 385, 408  
 $YbAuAl$  457  
 $YbAuBi$  484  
 - phase transition 483  
 $YbAuCu_4$  289, 300, 390, 391  
 $YbAuGa$  464  
 $YbAu_{0.67}Ge_{1.33}$  474  
 $YbAuGe$  474  
 $YbAu_{1.24}Ge_{0.76}$  474  
 $YbAuIn$  465  
 $YbAu_{1.27}In_{0.73}$  465  
 $YbAuMg$  485  
 $YbAuSb$  482  
 $YbAu_{0.63}Si_{1.37}$  467  
 $YbAu_{0.88}Si_{1.12}$  467  
 $YbAu_{1.25}Si_{0.75}$  467  
 $YbAuSn$  476  
 $YbB_{12}$  289, 292, 293, 314-316  
 $YbBa_2Cu_3O_{6+\delta}$  260  
 $YbBiPt$  289, 386, 387  
 $YbCdGe$  474  
 $YbCdIn$  465  
 $YbCdPb$  479  
 $YbCdSn$  476  
 $YbCoAl$  457  
 $YbCoC$  467  
 $YbCoGe$  474  
 $Yb_2Cu_9$  289, 392  
 $Yb(Cu_{1-x}Ni_x)_2Si_2$  318  
 $YbCuAl$  493, 494  
 - yttrium doping 494  
 $YbCuBi$  484  
 $YbCuGa$  464  
 $YbCuGe$  474  
 $YbCuPb$  479  
 $YbCuSb$  482  
 $YbCuSi$  467  
 $YbCu_2Si_2$  318  
 $YbCuSn$  476  
 $YbCuZn$  485  
 $YbFeSi$  467  
 $YbGaAl$  457  
 $YbHgPb$  479  
 $YbHgSn$  476  
 $YbIrSn$  476  
 $YbLiAs$  480  
 $YbLiBi$  484  
 $YbLiGe$  474  
 $YbLiSb$  482  
 $Yb_{1-x}Lu_xB_{12}$  315, 316  
 $YbMgGe$  474  
 $YbMgPb$  479  
 $YbMgSi$  467  
 $YbMgSn$  476  
 $YbNi_5$  215  
 $YbNiGa$  464  
 $YbNiGe$  474  
 $YbNiSb$  482  
 $YbNiSn$  289, 318, 337, 338, 476  
 $Yb(Pd,Pb)$  479  
 $YbPdAl$  457  
 $YbPdAs$  480  
 $YbPdBi$  484  
 $YbPdGa$  464  
 $YbPdGe$  474  
 $YbPdIn$  465  
 $YbPdP$  480



- YbPdPb 479  
YbPdSb 289, 388, 389, 482  
YbPdSi 467  
YbPdSn 476  
– structural transformation 478  
YbPdTi 466  
Yb polysulfides 577  
YbPtAl 457  
YbPtAs 480  
YbPtBi 484, 496, 497  
YbPtGa 464  
YbPtGe 474  
YbPtIn 465  
YbPtP 480  
YbPtSb 482  
YbPtSi 467  
YbPtSn 476  
YbRhAl 457  
YbRhGa 464  
YbRhGe 474  
YbRhSn 476  
YbS<sub>2</sub> 589–591  
YbS<sub>2+x</sub> 573  
YbS<sub>2.0</sub>–YbS<sub>1.5</sub> system 578  
Yb(TTP)(tmhd) 626  
YbZnGa 464  
YbZnGe 474  
YbZnIn 465  
YbZnPb 479  
YbZnSn 476  
ytterbium ternary compounds 453–506  
  
zinc doping 259  
Zn(C<sub>2</sub>H<sub>5</sub>)<sub>2</sub> 550  
Zr and Mo additives to R–T thin films 47  
ZrNiAl type 459